



Kyoji Sassa · Paolo Canuti · Yueping Yin *Editors*

Landslide Science for a Safer Geoenvironment

Volume 3
Targeted Landslides



 Springer

Landslide Science for a Safer Geoenvironment

Kyoji Sassa • Paolo Canuti • Yueping Yin
Editors

Landslide Science for a Safer Geoenvironment

Volume 3: Targeted Landslides

 Springer



Editors

Kyoji Sassa
UNITWIN Headquarters Building
Kyoto University Uji-Campus
Uji, Kyoto, Japan

Paolo Canuti
ICL - International Consortium on Landslides
Florence, Italy

Yueping Yin
Center of Geo-Hazards Emergency Technology, MLR
Beijing, China

ISBN 978-3-319-04995-3 ISBN 978-3-319-04996-0 (eBook)
DOI 10.1007/978-3-319-04996-0
Springer Cham Heidelberg New York Dordrecht London

Library of Congress Control Number: 2014938096

© Springer International Publishing Switzerland 2014

This work is subject to copyright. All rights are reserved by the Publisher, whether the whole or part of the material is concerned, specifically the rights of translation, reprinting, reuse of illustrations, recitation, broadcasting, reproduction on microfilms or in any other physical way, and transmission or information storage and retrieval, electronic adaptation, computer software, or by similar or dissimilar methodology now known or hereafter developed. Exempted from this legal reservation are brief excerpts in connection with reviews or scholarly analysis or material supplied specifically for the purpose of being entered and executed on a computer system, for exclusive use by the purchaser of the work. Duplication of this publication or parts thereof is permitted only under the provisions of the Copyright Law of the Publisher's location, in its current version, and permission for use must always be obtained from Springer. Permissions for use may be obtained through RightsLink at the Copyright Clearance Center. Violations are liable to prosecution under the respective Copyright Law.

The use of general descriptive names, registered names, trademarks, service marks, etc. in this publication does not imply, even in the absence of a specific statement, that such names are exempt from the relevant protective laws and regulations and therefore free for general use.

While the advice and information in this book are believed to be true and accurate at the date of publication, neither the authors nor the editors nor the publisher can accept any legal responsibility for any errors or omissions that may be made. The publisher makes no warranty, express or implied, with respect to the material contained herein.

Cover Illustration: The Loess landslide, 100 m long, 70 m wide, with a volume of 180,000 m³, occurred in Dongxiang town, Gansu Province, China, in March 2011. The landslide destroyed major roads and tens of houses, but 760 people were evacuated successfully due to early warning.

Printed on acid-free paper

Springer is part of Springer Science+Business Media (www.springer.com)

Foreword for *International Consortium on Landslides*



United Nations
Educational, Scientific and
Cultural Organization

Organisation
des Nations Unies
pour l'éducation,
la science et la culture

Organización
de las Naciones Unidas
para la Educación,
la Ciencia y la Cultura

Организация
Объединенных Наций по
вопросам образования,
науки и культуры

منظمة الأمم المتحدة
للتربية والعلم والثقافة

联合国教育、
科学及文化组织

More than 200 million people are affected every year by natural hazards, and the impact is deepening—especially in developing countries, where they can set back healthy growth for years. Globally, an estimated one trillion United States dollars have been lost in the last decade alone.

We may not be able to stop disasters, but we can reduce their risks and their consequences. Mitigating the effects of natural hazards requires education, training, and capacity building at all levels. Fundamentally, it calls for new thinking—to move from reaction after disasters to action before.

Landslides are important in this regard, given the tragic loss of life and the economic disruption they cause. More than ever, we need to address landslides in ways that are integrated and coordinated internationally. This is the goal guiding the *International Consortium on Landslides* and its International Programme on Landslides, focusing on research, education, and capacity building in landslide risk reduction, working with international, governmental, and non-governmental actors.

Associated with the *International Consortium on Landslides*, UNESCO has accompanied the International Programme on Landslides from its inception, as an innovative initiative for cooperative research and capacity building in landslide risk mitigation. In the same spirit, UNESCO and Kyoto University established a University Twinning and Networking Cooperation Programme on landslide risk mitigation for society and the environment in March 2003, in order to deepen cooperation in this vital area.

This publication is an essential tool for both organizations and individuals to deepen understanding of landslide phenomena and to reduce their risks. Drawing on latest scientific developments, this volume presents a range of initiatives under way across the world and puts forward recommendations on risk mitigation. At a time when the consequences of climate change are deepening, this work provides a benchmark reference to strengthen the resilience of societies under pressure. I wish to thank all participants in the *International Consortium on Landslides* and all involved in this important work. Let me highlight especially Professor Kyoji Sassa, Chairperson of the

Consortium, for his tireless efforts. In this spirit, I look forward to further strengthening UNESCO's cooperation with the *International Consortium on Landslides*.



A handwritten signature in blue ink that reads "Irina Bokova". The signature is written in a cursive, flowing style.

Ms. Irina Bokova
Director-General of UNESCO

Foreword

Landslide, floods, drought, wildfire, storms, tsunami, earthquakes, and other types of natural hazards are increasingly affecting the world. For the first time in history the world has experienced 3 consecutive years (2010–2012) where annual economic losses have exceeded \$100 billion due to an enormous increase in exposure of industrial assets and private property to extreme disaster events. During the period of 2000–2012, 2.9 billion people were affected by disasters, economic damage is equivalent of USD 1.7 trillion, and 1.2 million people were killed by disasters.¹

The Global Assessment Report (GAR), a regular publication by the United Nations on disaster risk levels, trends, and analysis of the underlying causes, found that most of the small-scale recurrent disasters such as landslides are not effectively accounted for by authorities. The same report also found that while landslides and other recurrent natural hazards are responsible for only a small proportion of global disaster mortality, they account for a very significant proportion of damage to public assets, such as health and educational facilities and infrastructure, as well as to the livelihoods, houses, and assets of low-income groups.

Extensive risk associated with localized, mainly weather-related hazards with short return periods. These highly localized yet frequent hazards include surface water and flash flooding, landslides, fires, and both agricultural and hydrological drought. They are exacerbated by badly managed urban development, environment degradation, and poverty.²

The *Hyogo Framework for Action 2005–2015: Building the Resilience of Nations and Communities to Disasters (HFA)*, adopted at the 2nd World Conference on Disaster Reduction (WCDR, Kobe, Hyogo, Japan, in January 2005), represents the most comprehensive action-oriented policy guidance in universal understanding of disasters induced by vulnerability to natural hazards and reflects a solid commitment to implementation of an effective disaster reduction agenda. In order to ensure effective implementation of HFA at all levels, tangible and coordinated activities must be carried out. Since 2005, we have seen many activities and initiatives developed to implement HFA in various areas. As a concrete activity in the area of landslide risk reduction, the International Programme on Landslides has maintained the momentum created in 2005 through organizing the two World Landslide Forums in 2008 in Tokyo and in 2011 in Rome, being led by the International Consortium on Landslides. It is my great pleasure to see the valuable development for the last 8 years.

There is a growing evidence of the need for a strong science basis to understand the causes and impacts of landslides as well as the most effective measures to reduce landslide risk. This book includes a number of substantive articles on landslide risk reduction. Applying science into practice is one of the key words for the global endeavour. I expect this book as well as the Third World Landslide Forum to make a substantive contribution for that purpose in the area

¹ Disasters refers to drought, earthquake (seismic activity), epidemic, extreme temperature, flood, insect infestation, mass movement (dry and wet), storm, volcano, and wildfire/Data source: EM-DAT: The OFDA/CRED International Disaster Database/Data version: 12 March 2013 - v12.07.

² Global Assessment Report on Disaster Risk Reduction 2013: http://www.preventionweb.net/english/hyogo/gar/2013/en/home/GAR_2013/GAR_2013_2.html

of landslide risk reduction by the promotion of exchange of experience and achievements in science and facilitating discussion on sustainable disaster risk management.

Recognizing that disaster reduction needs interdisciplinary and multi-sectoral action, we build on partnerships and take a global approach to disaster reduction. Therefore, we welcome better cooperation between government authorities and the international community including scientific community that play a critical role in helping people make life-changing decisions about where and how they live before the disaster strikes, in particular high-risk urban areas.

Once the ten-year mark has been passed in 2015, the world will have a new disaster risk reduction framework. Consultations on elements for the post-2015 framework (“HFA2”) are currently ongoing. Multi-stakeholders, including academic and scientific institutions, are encouraged to be engaged in the ongoing consultation towards HFA2, which is expected to be adopted at the Third World Conference on Disaster Risk Reduction in March 2015 in Sendai, Japan.

Scientist, international, and regional institutions have a responsibility to assist with the tools, knowledge, and capacity to understand their risk and take the most effective measures to reduce them. The knowledge on landslides is a key part of the equation and the work and outcome of The Third World Landslide Forum in June 2014 in Beijing will be important contribution to these efforts and ongoing consultation towards 2015. UNISDR is fully behind the community of practice working on landslide risk.



A handwritten signature in black ink, appearing to read 'Margareta Wahlström'.

Ms. Margareta Wahlström
**Special Representative of the UN Secretary-
General for Disaster Risk Reduction, Chief
of UNISDR**

Preface: Landslide Science for a Safer Geoenvironment

The Third World Landslide Forum (**WLF3**) was held at the China National Convention Center, Beijing, China, on 2–6 June 2014. WLF is the triennial conference of the International Consortium on Landslides (**ICL**) and the International Programme on Landslides (**IPL**).

ICL (The International Consortium on Landslides) launched at the Kyoto Symposium in January 2002 is an international non-governmental and non-profit scientific organization promoting landslide research and capacity building for the benefit of society and the environment. Major activities of the ICL are the publication of a bimonthly full-colour journal “Landslides: Journal of the International Consortium on Landslides”, the International Programme on Landslides including IPL Projects in many countries/regions, and the Triennial World Landslide Forum and promotion of ICL regional and thematic networks and the World Centres of Excellence on Landslide Risk Reduction (WCoE). All activities involve cooperation by ICL-supporting organizations and other various stakeholders (national and local governments, civil society, and private sectors) contributing to landslide risk reduction.

The IPL is a programme of the ICL. It is developed in partnership with ICL-supporting organizations. The programme is managed by the IPL Global Promotion Committee including ICL and ICL-supporting organizations: the United Nations Educational, Scientific and Cultural Organization (UNESCO), the World Meteorological Organization (WMO), the Food and Agriculture Organization of the United Nations (FAO), the United Nations International Strategy for Disaster Risk Reduction (UNISDR), the United Nations University (UNU), the International Council for Science (ICSU), the World Federation of Engineering Organizations (WFEO), and the International Union of Geological Sciences (IUGS). The IPL contributes to the United Nations International Strategy for Disaster Reduction.

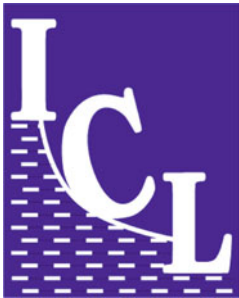
ICL-IPL invites relevant organizations and programmers to promote Landslide Science for a Safer Geoenvironment.

The International Consortium on Landslides (ICL)

- ICL was established by adopting its statutes in January 2002. The headquarters was registered as a legal body under the Japanese law for non-profit-making organizations (NPO) in the Kyoto Prefectural Government, Japan, in August 2002.
- ICL established the UNITWIN (University Twinning and Networking) Cooperation Programme on Landslide Risk Mitigation for Society and the Environment with UNESCO and Kyoto University in March 2003. The UNITWIN Headquarters Building was constructed by ICL and Kyoto University at the Kyoto University Uji Campus in September 2004. The programme was developed to promote landslide and water-related disaster risk management for society and the environment in November 2010.
- ICL founded “*Landslides*”: *Journal of the International Consortium on Landslides* in 2004. It was established as a quarterly journal published by Springer Verlag. It was approved as an ISI journal in 2005 and moved to a bimonthly journal from Vol. 10 in 2013.
- ICL founded the International Programme on Landslides (IPL) in partnership with seven global stakeholders by adopting the 2006 Tokyo Action Plan. It exchanged MoU to

promote IPL with the United Nations Educational, Scientific and Cultural Organization (UNESCO), the World Meteorological Organization (WMO), the Food and Agricultural Organization of the United Nations (FAO), the United Nations International Strategy for Disaster Reduction (UNISDR), the United Nations University (UNU), the International Council for Science (ICSU), and the World Federation of Engineering Organizations (WFEO) in 2006.

- The IPL Global Promotion Committee (IPL-GPC) was established following the 2006 Tokyo Action Plan to manage IPL activities including IPL projects, the World Landslide Forum (WLF) every 3 years, and the World Centres of Excellence for Landslide Risk Reduction (WCoEs) to be identified at WLFs.
- ICL headquarters in Kyoto, Japan, was approved as a scientific research organization (No. 94307) which can receive scientific grants from the Ministry of Education, Culture, Sports, Science and Technology (MEXT), Japan, in March 2007 and registered in the cross-ministerial research and development management system of all ministries of Japan in May 2008.
- ICL was approved as an NGO having operational relations with UNESCO in April 2007. It was reclassified as an NGO with consultative partnership with UNESCO in March 2012.
- ICL-IPL organized the First World Landslide Forum (WLF1) at the United Nations University, Tokyo, in November 2008.
- ICL-IPL organized the Second World Landslide Forum (WLF2) at the Food and Agriculture Organization of the United Nations, Rome, in October 2011.
- ICL-IPL is organizing the Third World Landslide Forum (WLF3) at the China National Convention Center, Beijing, in June 2014.
- ICL-IPL will organize the Fourth World Landslide Forum (WLF4) in Ljubljana, Slovenia, in May 29–June 2, 2017.



The symbol of ICL was designed as below.

I is a symbol of cultural heritage at landslide risk

C symbolizes the moving landslide mass

L is a symbol of retaining wall to stop landslides for its risk reduction.

The greatest discussion on C whether the Consortium should stand still or might be inclined during dynamic motion.

The International Programme on Landslides (IPL)

- The United Nations World Conference on Disaster Reduction was held on 18–22 January 2005 in Kobe, Japan. At this conference, the ICL proposed the organization of a thematic session to develop the IPL within the WCDR, and it was approved by the United Nations Secretariat for the International Strategy for Disaster Risk Reduction. With financial support from the Cabinet Office of Japan, the Ministry of Education, Culture, Sports, Science and Technology of the Government of Japan (MEXT), and the Disaster Prevention Research Institute of Kyoto University, the thematic conference Session 3.8 “New International Initiatives for Research and Risk Mitigation of Floods (IFI) and Landslides (IPL)” was organized together with ICL-supporting organizations and also the flood group.
- The thematic session 3.8 was opened with the addresses by Koichiro Matsuura (Director-General of UNESCO), Michel Jarraud (Secretary-General of WMO), and others. The session was chaired by Hans van Ginkel (Rector of UNU). The ICL proposed a **Letter of**

- Intent** to promote further joint global activities in disaster reduction and risk prevention through “Strengthening research and learning on ‘Earth system risk analysis and sustainable disaster management’ within the framework of the ‘United Nations International Strategy for Disaster Reduction’ (ISDR)”. This Letter of Intent was agreed and signed by heads of seven global stakeholders of UNESCO, WMO, FAO, UNISDR, UNU, ICSU, and WFEO.
- Based on this Letter of Intent, ICL, UNESCO, WMO, FAO, UNISDR, UNEP, UNU, and Kyoto University jointly organized the Round Table Discussion (RTD) “Strengthening research and learning on earth system risk analysis and sustainable disaster management within UN-ISDR as regards landslides—towards a dynamic global network of International Programme on Landslides (IPL)” on 18–20 January 2006 at Elizabeth Rose Hall of the United Nations University, Tokyo, Japan. The RTD was cosponsored by Japanese and international governmental and non-governmental organizations. The 2006 Tokyo Action Plan was adopted as the result of RTD.
 - The 2006 Tokyo Action Plan decided to develop the International Programme on Landslides (IPL) which is managed by IPL Global Promotion Committee. It is formed by ICL member organizations, ICL-supporting organizations which have exchanged the Memorandum of Understanding with ICL to promote ICL, and organizations which provide Subvention to IPL.
 - The ICL exchanged the Memoranda of Understanding with each of seven global stakeholders: UNESCO, WMO, FAO, UNISDR, UNU, ICSU, and WFEO to promote the 2006 Tokyo Action Plan within 2006. Then, IPL was formally launched as a programme of the ICL in partnership with ICL-supporting organizations aiming at organizing work in response to the ICL goals.
 - The logo of IPL in Fig. 1 is a simple design of ICL and ICL-supporting organizations which have exchanged MOU with ICL to promote ICL-IPL.



Fig. 1 Logo of the International Programme on Landslides (IPL)

The World Landslide Forum

The First World Landslide Forum: Implementing the 2006 Tokyo Action Plan on the International Programme on Landslides (IPL)

WLF1 was organized at the United Nations University, Tokyo, in November 2008. It was a global cross-cutting information and cooperation platform for all types of organizations from academia, United Nations, governments, private sectors, and individuals that are contributing to landslide research and education and who are willing to strengthen landslide and other related earth system risk reduction.

- Plenary sessions were (1) Open forum “Progress of IPL Activities”, (2) Plenary symposium “Global Landslide Risk Reduction”: A special Report and four keynote lectures, (3) Public Forum on “Protection of Society and Cultural and Natural Heritage, (4) “Landslides for Children”, (5) High-level panel discussion “Landslides in Global Change—How to mitigate risk? Toward the Second World Landslide Forum in 2011”.
- Parallel sessions were (1) A look from space, (2) Case Studies and National Experiences, (3) Catastrophic slides and avalanches, (4) Climate change and slope instability, (5) Landslides threatening heritage sites, (6) Economic and Social Impact of Landslides, (7) Education, Capacity Building and Public Awareness for Disaster Reduction, (8) Environmental Impact of Landslides, (9) Landslides in General, (10) Landslides and multi-hazards, (11) Mapping: inventories, susceptibility, hazard and risk, (12) Monitoring, prediction and early warning, (13) Policy and Institutional framework for Disaster Reduction, (14) Rainfall, debris flows, and wildfires, (15) Landslide Disaster Mitigation Engineering Measures, (16) Watershed and Forest Management for Risk Reduction, (17) Landslides in Dam Reservoirs.
- One full-colour book—Landslides-Disaster Risk Reduction—including all papers in plenary sessions and introduction of all parallel sessions was published, two monocolour proceedings for full papers were accepted for parallel sessions, and papers accepted for poster papers were printed and also are uploaded in the ICL web in full colour.
- 430 people from 48 countries and several other international organizations participated (175 from Japan, and 255 from abroad).

The Second World Landslide Forum: Putting Science into Practice

WLF2 was organized at the Headquarters of the Food and Agriculture Organization of the United Nations (FAO) on 3–9 October 2011. It was jointly organized by the IPL Global Promotion Committee (ICL, UNESCO, WMO, FAO, UNISDR, UNU, ICSU, WFEO) and two ICL members in Italy: the Italian Institute for Environmental Protection and Research (ISPRA) and the Earth Science Department of the University of Florence with support from the Government of Italy and many Italian landslide-related organizations.

- 864 people from 63 countries and several international organizations participated. Attendance was larger than expected, and twice the attendance at the First World Landslide Forum 2008 in Tokyo.
- 25 Technical sessions were held, and 465 full papers were submitted. All accepted papers were edited in seven full-colour volumes titled as “**Landslide Science and Practice**” as below.
 - Vol. 1 Landslide inventory and susceptibility and hazard zoning
 - Vol. 2 Early warning, instrumentation and monitoring
 - Vol. 3 Spatial analysis and modelling
 - Vol. 4 Global environmental change (420 pages)
 - Vol. 5 Complex environment (520 pages)
 - Vol. 6 Risk assessment, management and mitigation (430 pages)
 - Vol. 7 Social and Economic Impact and Policies (430 pages)

The Third World Landslide Forum: Landslide Risk Mitigation Toward a Safer Environment

WLF3 will be organized on 2–6 June 2014 in Beijing, China.

Three full-colour volumes (Vol. 1–Vol. 3) will be published by Springer, titled as Landslide Science for a Safer Geoenvironment. 303 papers will be published in three full color volumes. One monocolour proceedings which contains 123 full papers and an abstract volume will be published by the Chinese Organizing Committee. Volume 1 includes Plenary lectures, and selected papers from the side events. Volume 2 includes papers accepted in sessions for methods of landslide studies. Volume 3 includes papers accepted for methods of landslide studies. Front matters include two Forewords from Ms. Irena Bokova, Director-General of UNESCO and Ms. Margareta Wahlström, Special Representative of the UN Secretary General for Disaster Risk Reduction, Chief of UNISDR, and Preface by Kyoji Sassa (Executive Director), Paolo Canuti (President) and Yueping Yin (Incoming President) of ICL. Back matters include “Landslide Technology and Engineering in Support of Landslide Science” and “ICL Structure”.

Plenary sessions are:

1. High-Level Panel Discussion toward a Safer Geoenvironment
2. Plenary Lectures “Progress in Landslide Science”
 - Runqiu HUANG: Progress in Large-Scale Landslide Studies in China
 - Farrokh NADIM: Progress in Living with landslide risk in Europe
 - Rex BAUM: Progress in Regional landslide hazard assessment
 - Kyoji SASSA: Progress in Landslide Dynamics
3. Round Table Discussion “Major achievement in WLF3 and development toward WLF4”

Parallel sessions are:

Special Sessions

A1 International Programme on Landslides, A2 Thematic and Regional Networks on Landslides, A3 Policy, Legislation and Guidelines on Landslides, A4 Climate & Landuse Change Impacts on Landslides, A5 Recognition and Mechanics of Landslide, A6 General Landslide Studies

Sessions for Methods of Landslide Studies

B1 Physical Modeling and Material Testing, B2 Application of Numerical Modeling Techniques to Landslides, B3 Remote Sensing Techniques for Landslide Mapping and Monitoring, B4 Hazard Mapping, B5 Monitoring, Prediction and Warning of Landslides, B6 Risk Assessment, B7 Remedial Measures & Prevention Works, B8 Risk Reduction Strategy, B9 Inventory and Database

Sessions for Targeted Landslides

C1 Debris Flows, C2 Rock-Slope Instability and Failure, C3 Earthquake-Induced Landslides, C4 Rain-Induced Landslides, C5 Landslides in Cultural/Natural Heritage Sites, C6 Urban Landslides, C7 Landslides in Cold Regions, C8 Landslide in Coastal and Submarine Environments, C9 Natural Dams and Landslides in Reservoirs

Side Events

D1 Student Session, D2 Landslide Teaching tools, D3 Dialogues on Country Landslide Issues

Other ICL-IPL Activities

Other ICL-IPL activities include (1) IPL Projects, (2) ICL Regional and thematic networks, (3) World Centre of Excellence on Landslide Risk Reduction, (4) ICL Landslide Teaching Tools.

Landslides: Journal of the International Consortium on Landslides

The ICL decided to create a new international journal on landslides “Landslides: Journal of the International Consortium on Landslides” at the First Board of Representatives of ICL held at the UNESCO Headquarters, Paris on 19-21 November 2002. The ICL planned to publish full color journal presenting full color photos and colored maps & figures to attract policy makers, government officers and citizens as well as scientists and engineers in many fields.

The first issue of the journal *Landslides* was published from Springer Verlag in April 2004 as the core project of the International Programme on Landslides (IPL). This journal was the first full-colour scientific journal without a full-colour printing fee. The field of landslides is very wide in the related basic science fields. Common information source which all readers may understand is a full-colour photo of landslides. Landslide researchers from geology, geomorphology, geotechnology, geophysics, and landslide dynamics may obtain various aspects of information from the colour photos. The journal “Landslides” aims to promote landslide research and investigation in the developing countries as well as in developed countries. Published papers of most international journals are shared by researchers in the developed countries. *Landslides* have made the following five categories to promote contribution from developing countries and young researchers.

Within these categories, “Original articles” will deal with the frontiers of landslide science and technology. “Recent landslides” will accept recent landslide reports from developing countries where many landslide disasters will occur and “Technical note” will accept case studies of landslides in the less reported countries. “ICL-IPL activities” will report for international information dissemination and cooperation. As a central tool of the global landslide community, the journal is planned to provide different functions.

1. Original paper (6–12 pages): original research and investigation results.
2. Review paper (6–12 pages): review of current research and development of technology in a thematic area of landslides.
3. Recent landslide (less than 6 pages): reports of recent landslides including location (latitude/longitude), plan, section, geology, volume, movement, mechanism, and associated disasters.
4. Technical note (less than 6 pages): research notes, review notes, case studies, progress of technology, and best practice in monitoring, testing, investigation, and mitigation measures.
5. ICL-IPL activities: progress of IPL projects and ICL committee activities.



Fig. 2 Cover of “Landslides”, Vol.11, No.2, 2014

“Landslides” have published 513 articles in 42 issues in Volume 1–Volume 10 since 2004. Volumes 1–9 were 4 issues per year. The total pages in Vol. 9 were 569 pages containing 47 papers. Vol. 10 from 2013 was 6 issues per year. The total pages in Vol. 10 are 851 pages containing 68 papers. Figure 2 presents the front and back cover of Vol.11, No.2, 2014. The design of the cover is the same from the founding issue in 2004.

“Landslides” was identified as an SCI journal by Thomson Reuters in 2005. The impact factor was 2.216 in the 2011 Journal Citation Report, and it was 2.093 in 2012 Journal Citation Report. This journal is the core activity of ICL-IPL to share information on scientific and technological development and to develop “Landslide Science” toward a Safer Geoenvironment.

IPL Projects

IPL Projects are proposed by one or more ICL members or by IPL-Global Promotion Committee (IPL-GPC) by submitting the [IPL project proposal form](#) by 30 March every year. Proposal form will be evaluated by IPL Evaluation Committee. The proposer or a member of the project is requested to orally explain the project in the IPL-GPC which will be organized together with the Board of Representatives (BOR) of ICL each year. IPL-GPC will decide the approval of proposed project based on the evaluation committee report, oral presentation, and discussion. Each IPL Project leader with ongoing status is requested to submit an annual report of the project by 30 March each year.

The IPL project may authorize the leader and the accepted project by the IPL Global Promotion Committee. The project, leaders, and the annual report are uploaded in IPL WEB <http://www.iplhq.org/>. The progress and the research results are invited to contribute to **Landslides: Journal of the International Consortium on Landslides**. The achievements of IPL Projects are evaluated every 3 years. Three successful IPL projects will be identified at the World Landslide Forum. The leaders will receive US\$3,000 per project together with a certificate.

ICL Regional and Thematic Networks

Establishment of ICL networks was proposed at the 10th Session of Board of Representatives of ICL held at the headquarters of the Food and Agriculture Organization of the United Nations (FAO) in Rome, Italy, on 5 October 2011. The networks were approved at the 10th anniversary meeting of ICL held on 17–20 January 2012 in Kyoto, Japan. The regional and thematic networks are platforms for cooperation within ICL member organizations and non-ICL member organizations in each region and each thematic field.

Current networks are:

ICL Regional Networks

- (1) Adriatic-Balkan Network, (2) Latin America Network, (3) North-East Asia Network, (4) South-East Asian Network for Landslide Risk Management

ICL Thematic Networks

- (1) Landslides Risk Management Network, (2) Capacity Development Network, (3) Landslides in Cold Regions Network, (4) Landslides and Cultural & Natural Heritage Network, (5) Landslide Monitoring and Warning Network

World Centre of Excellence on Landslide Risk Reduction

The Global Promotion Committee (GPC) of the International Programme on Landslides (IPL) will identify World Centres of Excellence on Landslide Risk Reduction at the World Landslide Forum organized every 3 years within eligible organizations, such as universities,

institutes, NGOs, government ministries, and local governments, contributing to “Risk Reduction for Landslides and Related Earth System Disasters”. An independent Panel of Experts, set up by the Global Promotion Committee of International Programme on Landslides (IPL-GPC), endorses the WCoEs.

Objectives of WCoE:

To strengthen the International Programme on Landslides (IPL) and IPL Global Promotion Committee

To create “A Global Network of entities contributing to landslide risk reduction”; and

To improve the global recognition of “Landslide Risk Reduction” and its social-economic relevance, and entities contributing to this field

Twelve World Centres of Excellence (WCoEs) 2008–2011 were identified at the First World Landslide Forum in November 2008 at UNU in Tokyo, Japan. Fifteen WCoEs for 2011–2014 were identified at the Second World Landslide Forum in October 2011 at FAO, Rome, Italy. New WCoEs for 2014–2017 will be identified and announced at WLF3. WCoEs are cores of ICL regional and thematic networks.

ICL Landslide Teaching Tools

ICL Landslide Teaching Tools aim to provide various teaching materials to ICL members and other landslide institutions and entities for their efforts to educate university students, local government officers, people in non-governmental organizations, and local communities. Tools include text including figures and full-colour photos, PDFs of published papers, guidelines and laws, and PPTs for lectures.

Copyright and Responsibility for Each Teaching Tool

ICL called for contributions and compiled the accepted teaching tools. Copyright and responsibility for the content of each tool lie with its contributing organization. Each tool may be updated by the contributing organization.

The Teaching Toolbox contains five parts:

1. Mapping and Site Prediction
2. Monitoring and Early warning
3. Testing and Numerical Simulation
4. Risk Management and Others
5. Country Practices and Case Studies

The Teaching Toolbox contains three types of tools:

1. The first type are TXT-tools consisting of original texts with figures.
2. The second type are PDF-tools consisting of already published reference papers, manuals, guidelines, laws, codes, and others. They are on the accompanying CD as pdf files.
3. The third type are PPT-tools consisting of Powerpoint[®] files made for lectures. They are on the accompanying CD as ppt files.

ICL invites landslide research organizations and their experts to jointly develop effective and practical Landslide Teaching Tools. The copyright and the updating responsibility belong to the contributing organization.

A Call for ICL-IPL Partners

The International Consortium on Landslides (ICL) and partners of the International Programme on Landslides (IPL), including the United Nations Educational, Scientific and Cultural Organization (UNESCO), the World Meteorological Organization (WMO), the Food

and Agricultural Organization of the United Nations (FAO), the United Nations Office for Disaster Risk Reduction (UNISDR), the United Nations University (UNU), the International Council for Science (ICSU), the World Federation of Engineering Organizations (WFEO), and the International Union of Geological Sciences (IUGS), invite related international programmes and initiatives from natural sciences (earth sciences and water sciences), engineering sciences, human and social sciences, and governmental and non-governmental programmes to promote science and technology and their applications for landslide risk mitigation and to support this initiative by joining the International Networking and Partnerships aimed at enhancing capacities, in particular in the developing world, to reduce risk and vulnerabilities and build resilience related with landslides, and contribute to a safer Geoenvironment in support of UNISDR.

The “Third World Conference on Disaster Risk Reduction of the United Nations (3rd WCDRR)” will be organized in Sendai, Japan, on 14–18 March 2015, succeeding the 2nd WCDR (Kobe, 18–22 January 2005). ICL-IPL is examining an activity for 3rd WCDRR to enhance partnerships and agree with relevant organizations and programmes on ICL-IPL SENDAI PARTNERSHIPS 2015–2024 for Landslide Disaster Risk Reduction for a Safer Geoenvironment.

Kyoji Sassa
Executive Director of ICL



Paolo Canuti
President of ICL



Yueping Yin
Incoming President of ICL



ICL-IPL Secretariat

ICL office: The International Consortium on Landslides
138-1 Tanaka Asukai-cho, Sakyo-ku, Kyoto 606-8226, Japan

IPL office: UNESCO-KU-ICL UNITWIN Headquarters
Kyoto University Uji Campus, Uji Kyoto 611-0011, Japan

Email: secretariat@iclhq.org

URL: <http://icl-iplhq.org/> and <http://www.iclhq.org/>

List of Editors

Editors

Kyoji Sassa
International Consortium on Landslides
Kyoto, Japan

Yueping Yin
Center of Geo-Hazards Emergency Technology, MLR
Beijing, China

Paolo Canuti
International Consortium on Landslides
Florence, Italy

Associate Editors

Eileen and Mauri McSaveney
GNS Science,
Lower Hutt, New Zealand

Lynn Highland
U.S. Geological Survey
Denver, Colorado, USA

Vol.1 Part Editors

Part 2
Matjaž Mikoš
University of Ljubljana,
Ljubljana, Slovenia

Part 4
Sálvano Briceño
International Consortium on Landslides
Kyoto, Japan

Part 6
Luciano Picarelli
Seconda Univ. di Napoli
Aversa, Italy

Part 8
Bin He
Nanjing Institute of Geography & Limnology, CAS
Nanjing, China

Part 3
Snjezana Mihalić Arbanas
University of Zagreb
Zagreb, Croatia

Part 5
Vit Vilimek
Charles University
Prague, Czech Republic

Part 7
Peter Bobrowsky
Geological Survey of Canada
Ottawa, Ontario, Canada

Vol.2 Part Editors

Part 1
Binod Tiwari
California State University, Fullerton
Fullerton, California, USA

Part 3
Vern Singhroy
Canada Centre for Remote Sensing
Ottawa, Ontario, Canada

Part 5
Željko Arbanas
University of Rijeka
Rijeka, Croatia

Part 2
Marc-Andre Brideau
BGC Engineering Inc.
Vancouver, British Columbia, Canada

Part 4
Rex Baum
U.S. Geological Survey
Denver, Colorado, USA

Part 6
Huabin Wang
Huazhong University of Science and Technology
Wuhan, Hubei, China

Part 7
Sebastian Fischer
Technische Universität Darmstadt
Darmstadt, Germany

Part 9
Snježana Mihalić Arbanas
University of Zagreb
Zagreb, Croatia

Vol.3 Part Editors

Part 1
Giovanni Crosta
Università degli Studi di Milano Bicocca
Milano, Italy

Ko-Fei Liu
National Taiwan University
Taipei, Taiwan

Part 3
Kazuo Konagai
Yokohama University
Tokyo, Japan

Fawu Wang
Shimane University
Matsue, Shimane, Japan

Part 5
Jan Vlcko
Comenius University, Bratislava
Bratislava, Slovakia

Part 7
Ying Guo
Northeast Forestry University
Harbin, China

Part 9
Alexander Strom
JSC “Hydroproject Institute”
Moscow, Russian Federation

Part 8
Farrokh Nadim
International Centre for Geohazards at NGI
Oslo, Norway

Part 2
Jan Klimeš
Institute of Rock Structure and Mechanics, CAS
Praha, Czech Republic

Part 4
Binod Tiwari
California State University, Fullerton
Fullerton, California, USA

Part 6
José Chacón
University of Granada
Granada, Spain

Part 8
Michael Strasser
ETH Zurich
Zurich, Switzerland

Contents

Part I Debris Flows

Introduction: Debris Flows	3
Giovanni B. Crosta and Ko-Fei Liu	
Formation Condition, Disaster Characteristics and Developing Trend Analysis on Debris Flows in Moxi River Basin, SW China	5
Huayong Ni, Zongliang Li, Yongbo Tie, and Zhi Song	
Dendrogeomorphic Chronologies of Debris Flows for the Crimean Mountains (Ukraine)	13
Karel Šilhán, Tomáš Pánek, Jan Hradecký, and Markus Stoffel	
Experimental Study on the Rheological Behaviour of Fine-Grained Soils with Sand Content and Liquidity Index (Water Content)	19
Hyo-Sub Kang and Yun-Tae Kim	
Hazard Management in a Debris Flow Affected Area: Case Study from Spreitgraben, Switzerland	25
Daniel Tobler, Isabelle Kull, Mylène Jacquemart, and Nils Haehlen	
Control Effect of Vegetation on Debris Flows: A Case Study in Batang County, Southwest China	31
Yanchao Gao, Hua Ge, and Wei Xu	
Efficiency of Slot-Check Dam Group on Debris Flow Control in Shengou Basin, Kunming, China	37
Yuhua Zou, Kaiheng Hu, Xiaoqing Chen, and Wei Zhong	
The Influence of Accumulated Precipitation on Debris Flow Hazard Area	45
Ko-Fei Liu, Shih-Chao Wei, and Ying-Hsin Wu	
Concrete Torrent Check-Dams and Debris-Flow Magnitudes	51
Matjaž Mikoš, Andrej Kryžanowski, Manica Martinčič, and Jošt Sodnik	
A New Concept of Moraine-Supplied Debris Flow Prevention in Alpine Area, Moxi Basin, SW China	57
Yongbo Tie, Chuan Tang, and Zongliang Li	
Analysis on Blocking of Dadu River by Extra Massive Debris Flows at Moxi River	63
Zhi Song, Wanmo Zheng, Renji Ba, and Hao Fu	

Part II Rock-Slope Instability and Failure

Introduction: Rock-Slope Instability and Failure	69
Simon Loew and Jan Klimeš	

Supporting Rockfall Countermeasure Design in Difficult Conditions	71
Federico Agliardi and Giovanni B. Crosta	
Design Approach for Rockfall Protections with Simple Drapery Systems	77
Alberto Grimod and Giorgio Giacchetti	
Effect of Large Impacts Against Rockfall Barriers	83
Giorgio Giacchetti and Alberto Grimod	
Design Approach for Rockfall Barriers Tested According to ETAG 027	91
Alberto Grimod and Giorgio Giacchetti	
Design Approach for Secured Drapery Systems	99
Alberto Grimod and Giorgio Giacchetti	
Study on Damage Deterioration of Rock Slope Under Dynamic Loads	107
W.B. Jian and X.T. Xu	
Pore Pressure Transients in Brittle Translational Rockslides	115
Simon Loew and Thomas Strauhal	
The Rockfall Potential of the Southwestern Part of Kastamonu Castle (Turkey) Based on 2-D and 3-D Analyses	123
Mutluhan Akin, Tamer Topal, and Muge K. Akin	
Approach for Systematic Rockslide Mapping of Unstable Rock Slopes in Norway	129
Reginald L. Hermanns, Thierry Oppikofer, Freddy X. Yugsi Molina, John F. Dehls, and Martina Böhme	
Part III Earthquake-Induced Landslides	
Introduction: Earthquake-Induced Landslides	137
Fawu Wang, Kazuo Konagai, Hideaki Marui, Mohammadreza MahdaviFar, and Gabrielle Scrasecia-Mugnozza	
Landslides Triggered by the Ms 7.0 Earthquake of 20 April 2013 in Lushan, SW China	141
Genlong Wang, Maosheng Zhang, Jing Peng, and Hua Zhu	
Characteristics of Ground Acceleration and Features of Landslides Triggered by the Lushan Earthquake (China)	149
W.P. Wang, Y.P. Yin, B. Li, Z. Feng, N. Zhang, and Y. Gao	
Characteristics of Deep-Seated Landslides Induced by Different Type Earthquakes in Inland Japan	157
Baator Has, Toko Takayama, Kiichiro Ogawa, and Satoshi Onoda	
Investigation of Tandikat Landslide, West Sumatra, Indonesia	161
Fikri Faris and Fawu Wang	
Study on the Distribution of Large-Landslides Triggered by Wenchuan Earthquake	169
Xiaojun Chang, Dewei Wang, Weiya Ge, Lunwu Wei, Wanmo Zheng, and Yeqi Tang	
Large Slope Instabilities in Northern Chile: Inventory, Characterization and Possible Triggers	175
Giovanni B. Crosta, Reginald Hermanns, Paolo Frattini, Elena Valbuzzi, and Andrea Valagussa	

A Preliminary Spatial Distribution Analysis of Landslides Triggered by the 2010 Haiti Earthquake	183
Chong Xu	
Did the 2008 Wenchuan Earthquake Lead to a Net Volume Loss?	191
Chong Xu, Xiwei Xu, Tolga Gorum, Cees J. Westen, and Xuanmei Fan	
Hazard and Risk Related to Earthquake-Triggered Landslide Events	197
Hans-Balder Havenith	
Multi-stage Statistical Landslide Hazard Analysis: Earthquake-Induced Landslides	205
Chyi-Tyi Lee	
Quantitative Probabilistic Hazard Analysis of Earthquake-Induced Rockfalls	213
Andrea Valagussa, Paolo Frattini, and Giovanni B. Crosta	
Triggering Mechanism of Earthquake Induced Landslides	219
Zaheer Abbas Kazmi and Kazuo Konagai	
Landslides of Liquefaction Caused by Single Source of Impact Pamir-Hindu Kush Earthquakes in Central Asia	225
Rustam Niyazov and Bakhtiar Nurtaev	
Dynamics of Large and Rapid Landslides with Long Travel Distances Under Dense Gas Expanding Power	233
Zhong-qi Quentin Yue	
Investigation to the Local Site Effects During Earthquake Induced Ground Deformation Using Microtremor Observation in Yogyakarta, Central Java-Indonesia	241
Zaw Lin Kyaw, Subagyo Pramumijoyo, Salahuddin Husein, Teuku Faisal Fathani, and Junji Kiyono	
Indicators for Earthquake-Induced Soil Slides in the Flatlands of an Alpine Fringe Area	251
Philip Leopold, Jason N. Goetz, Gerhard Heiss, and Erich Draganits	
Using Dendrochronological Analysis for Dating Earthquake-Triggered Landslides (By the Example of SE Altai, Russia)	257
Roman Nepop, Anna Agatova, Vladimir Myglan, Andrey Nazarov, and Valentin Barinov	
Environmental Effects of Shuanghe Giant Landslide in Jiuzhai, Sichuan, China	263
Yunsheng Wang, Xin Zhang, Xinze Li, and Shuo Mao	
Part IV Rain-Induced Landslides	
Introduction: Rain Induced Landslides	271
Binod Tiwari and José Cepeda	
Rainfall-Induced Landslides: Slope Stability Analysis Through Field Monitoring	273
Massimiliano Bordoni, Claudia Meisina, Davide Zizioli, Roberto Valentino, Marco Bittelli, and Silvia Chersich	
Performance of I–D Thresholds and FLAIR Model for Recent Landslide Events in Calabria Region (Southern Italy)	281
Davide Luciano De Luca, Pasquale Versace, and Giovanna Capparelli	

Failure and Post-failure Characteristics of Mine Deposits in Korea	287
Sueng Won Jeong, Sung-Sik Park, and Hiroshi Fukuoka	
Multi-stage Statistical Landslide Hazard Analysis: Rain-Induced Landslides	291
Chyi-Tyi Lee	
Topographic and Pedological Rainfall Thresholds for the Prediction of Shallow Landslides in Central Italy	299
Silvia Peruccacci, Maria Teresa Brunetti, Silvia Luciani, Maria Costanza Calzolari, Devis Bartolini, and Fausto Guzzetti	
Catastrophic Landslide in Nižná Myšľa Village (Eastern Slovakia)	305
L'ubomír Petro, Vlasta Jánová, Andrej Žilka, Peter Ondrejka, Pavel Liščák, and Dominik Balík	
Effect of Rainfall and Building Construction on a Marginal Slope in Triggering Landslide	313
Binod Tiwari and Sneha Upadhyaya	
Utilization of Inferred Landslide Hazard Information as a Web Based Decision Making Tool for Landslide Disaster Risk Reduction and Early Warning	319
Kumari M. Weerasinghe	
Part V Landslides in Cultural/Natural Heritage Sites	
Introduction: Landslides in Cultural/Natural Heritage Sites	333
Jan Vlccko and Claudio Margottini	
Notes on a Landslide That Formed the Only Known True Inland Lake in South Africa	335
S.G. Chiliza and S. Diop	
Rock Slope Potential Failures in the Siq of Petra (Jordan)	341
Giuseppe Delmonaco, Claudio Margottini, Daniele Spizzichino, and Bilal Khrisat	
Instability Processes Affecting the Katskhi Pillar Monastery (Georgia)	349
Claudio Margottini, Luca Maria Puzzilli, Alberico Sonnessa, and Daniele Spizzichino	
Investigating Natural Hazards in the Peruvian Region of Nasca with Space-Borne Radar Sensors	357
Deodato Tapete, Francesca Cigna, Rosa Lasaponara, and Nicola Masini	
Deformations Dynamics in Response to Seasonal Temperature Oscillations: An Example from Pravecicka Brana Rock Arch (Czech Republic)	363
Jan Vlccko, Martin Brček, and Vladimír Greif	
Risk Assessment and Countermeasure of Rock Falls in Sanbang Mountain of Jeju Island, Korea	369
Su-Gon Lee, Stephen R. Hencher, Gi-Hyong Cho, Ji-Won Kim, Sung-Bu Cho, Ho-Dam Lee, Sun-Hyun Park, Paul Lee, Gun-Su Kim, and Young-Suk Lee	
Part VI Urban Landslides	
Introduction: Urban Landslides	377
José Chacón	

Typology of Rainfall-Triggered Landslides in the Urban Area of Antonina, Southern Brazil	379
Jefferson Picanço, Carolina Athayde Pinto, Maria José Mesquita, Mayra Moraes, Luiz Felipe Soares, and Francisco Cardoso	
Rockfall Runout Modelling for Hazard Characterization and Countermeasure Design in Urban Area	385
Paolo Frattini, Giovanni B. Crosta, and Andrea Valagussa	
Re-evaluation of Landslide Caused by Hurricane Mitch 1998, Tegucigalpa Honduras	393
Kiyoharu Hirota and Shizuka Kamiya	
11th May, 2013 Laipuitlang Rockslide, Aizawl, Mizoram, North-East India	401
Laldinpuia, S. Kumar, and T.N. Singh	
Geological Investigation of Slumping Localities in Saiha Town, Southern Mizoram, North-East India	407
Laldinpuia	
Probabilistic Back Analysis of a Cut Slope: A Case Study of Slope Failure Event in Precinct 9, Putrajaya, Malaysia	413
Soon Min Ng, Mohd Ashraf Mohamad Ismail, and Ismail Abustan	
A New Appraisal of the Ancona Landslide	419
Veronica Tofani, Andrea Agostini, Teresa Nolesini, Luca Tanteri, Ascanio Rosi, and Nicola Casagli	
Urban Landslides at the South of Sierra Nevada and Coastal Areas of the Granada Province (Spain)	425
José Chacón, Clemente Irigaray, Tomás Fernández del Castillo, Rachid El Hamdouni, Jorge Jiménez-Perálvarez, Pedro Alameda, José Moya, and José Antonio Palenzuela	
Recent Landslide Activity in La Paz, Bolivia	431
Nicholas J. Roberts, Bernhard Rabus, Reginald L. Hermanns, Marco-Antonio Guzmán, John J. Clague, and Estela Minaya	
Part VII Landslides in Cold Regions	
Introduction: Landslides in Cold Regions	441
Ying Guo, Marina O. Leibman, Marten Geertsema, and Sumio Matsuura	
Vegetation Dynamics of Landslide Affected Slopes (Central Yamal)	443
Ksenia Ermokhina	
Landslides in the Isolated Patches Permafrost Zone, Northeastern British Columbia (NTS Mapsheet 94G East Half)	451
Marten Geertsema and Vanessa N Foord	
Cryogenic Landslides in Paragenetic Complexes of Slope and Channel Processes in the Central Yamal Peninsula	457
Anatoliy Gubarkov and Marina Leibman	
The Impact of the Shrub Roots on the Stability of Soil Cut Slope in Seasonal Frozen Regions	463
Ying Guo, Wei Shan, Hua Jiang, and Zhaoguang Hu	
Formation Mechanism and Deformation Characteristics of Cut Layer Rock Landslide in Island Permafrost Region	471
Hua Jiang, Wei Shan, Zhaoguang Hu, and Ying Guo	

Dynamics of Vegetation on Cryogenic Landslides of Different Age in Central Yamal (West Siberian Arctic)	481
Olga Khitun, Irina Czernyadjeva, and Marina Leibman	
Assessment of Landsliding Hazard in Typical Tundra of Central Yamal, Russia	487
Artem Khomutov and Marina Leibman	
Cryogenic Landslides in the Arctic Plains of Russia: Classification, Mechanisms, and Landforms	493
Marina Leibman, Artem Khomutov, and Alexandr Kizyakov	
Fluctuations in the Pore-Water Pressure of a Reactivated Landslide in a Snowy District	499
Sumio Matsuura, Takashi Okamoto, Hikaru Osawa, Tatsuya Shibasaki, Kazutoki Abe, and Yasuhiko Okada	
Landslide Deformation Monitoring and Analysis of Influence Factors at K178 + 530 of the Bei'an to Heihe Expressway	503
Zhaoguang Hu, Wei Shan, and Hua Jiang	
Rockslides in the Open Pit of Kumtor Goldmine (Kyrgyzstan)	511
Isakbek Torgoev and Almazbek Torgoev	
Mass Movement in the Waste Dump of High-Altitude Kumtor Goldmine (Kyrgyzstan)	517
Isakbek Torgoev and Bektur Omorov	
Study of Plant-Soil-Permafrost System on Landslide-Affected Slopes Using Geochemical Methods on Yamal, Russia	523
Nataliya Ukraintseva, Marina Leibman, Irina Streletskaya, and Tatiana Mikhaylova	
Permafrost Distribution Study Based on Landsat ETM+ Imagery of the Northwest Section of the Lesser Khingan Range, China	529
Chunjiao Wang, Wei Shan, Ying Guo, Zhaoguang Hu, and Hua Jiang	
Transglacial Hazards: Karakoram and NW Himalaya, Inner Asia	535
Kenneth Hewitt	
Part VIII Landslides in Coastal and Submarine Environments	
Introduction: Landslides in Coastal and Submarine Environments	545
Michael Strasser, Yonggang Jia, Yasuhiro Yamada, and Roger Urgeles	
Geotechnical Characteristics and Slope Stability Analysis on the Deeper Slope of the Ligurian Margin, Southern France	549
Fei Ai, Annika Förster, Sylvia Stegmann, and Achim Kopf	
Reconstruction and Tsunami Modeling of a Submarine Landslide on the Ionian Margin of Calabria (Mediterranean Sea)	557
Silvia Ceramicola, Stefano Tinti, Filippo Zaniboni, Daniel Praeg, Peter Planinsek, Gianluca Pagnoni, and Edy Forlin	
Marine Erosion and Slope Movements: SE Coast of the Krk Island	563
Čedomir Benac, Sanja Dugonjić Jovančević, Igor Ružić, Martina Vivoda, and Josip Peranić	
Assessment of Rock Slope Stability for A Coastal Area Near Kusadasi, Aydin, Turkey	569
Yavuz Kaya and Tamer Topal	

Analysis of Quaternary Mass Transport Deposits Based on Seismic Data in Southern Deep-Water Region of Qiongdongnan Basin, South China Sea	575
Dawei Wang, Shiguo Wu, Genshun Yao, Fuliang Lü, and Michael Strasser	
Flank-Collapse on Ta'u Island, Samoan Archipelago: Timing and Hazard Implications	583
Shaun P. Williams, Tim R. Davies, Timothy T. Barrows, Matthew G. Jackson, Stanley R. Hart, and Jim W. Cole	
The 1977 Gioia Tauro Harbour (South Tyrrhenian Sea, Italy) Landslide-Tsunami: Numerical Simulation	589
Filippo Zaniboni, Alberto Armigliato, Katharina Elsen, Gianluca Pagnoni, and Stefano Tinti	
Part IX Natural Dams and Landslides in Reservoirs	
Introduction: Natural Dams and Landslides in Reservoirs	597
Alexander Strom, Hans-Balder Havenith, and Fawu Wang	
Catastrophic Debris Flow in the Hako Creek: Tributary of the Wabi Shebelle River, Ethiopia	599
Anatoliy Zhirkevich	
A Conceptual Event-Tree Model for Coseismic Landslide Dam Hazard Assessment	605
Xuanmei Fan, Runqiu Huang, Cees J. van Westen, Qiang Xu, Hans-Balder Havenith, and Victor Jetten	
Analysis of Waves Generated by Zhaojun Bridge Rockfall in Xingshan County, Three Gorges Reservoir, on December 28, 2012	609
Huang Bolin, Yin Yue-ping, Wang Shichang, and Liu Guangning	
Development Characteristics of the Landslides in Jurassic Red-Strata in the Three Gorges Reservoir, China	615
Haibo Miao, Kunlong Yin, and Bin Lin	
Influence of Geotechnical Properties on Landslide Dam Failure Due to Internal Erosion and Piping	623
Austin Chukwueloka Okeke, Fawu Wang, and Yasuhiro Mitani	
Sarez Lake Problem: Ensuring Long-Term Safety	633
Alexander Strom	
Geophysical Monitoring of Artificial Landslide Dam of Kambarata Hydro Power Plant-2 (Kyrgyzstan)	641
Isakbek A. Torgoev, Hans-Balder Havenith, and Almaz D. Torgoev	
Using Microtremor Array Survey to Evaluate the Possibility of Piping-Induced Landslide Dam Failure	649
Fawu Wang, Hisao Hayashi, Austin Chukwueloka Okeke, Yasuhiro Mitani, Hufeng Yang, Yohei Kuwada, and Shinya Baba	
Impact of Water Level Fluctuation on the Reservoir Landslide Stability	659
Qiang Yang, Zhennan Ye, Weicui Ding, and Youlong Gao	
Stability Analysis of Reservoir Slope Considering the Change of Mechanical Parameters of the Materials	665
Ming Zhang and Ruilin Hu	

Field Identification and Characteristics of the Ancient Shuangjiaping Translational Landslide	673
Zhao Yong, Xu Mo, Guo Jian, Kang Xiaobing, and Song Ci	
Field Monitoring and Stabilization Analysis of Landslide: A Case Study	679
Tingkai Nian, Dongchen Li, Kai Liu, Haiyang Xu, and Yanjun Zhang	
Preliminary Global Catalogue of Displacement Waves from Subaerial Landslides	687
Nicholas J. Roberts, Robin McKillop, Reginald L. Hermanns, John J. Clague, and Thierry Oppikofer	
Internal Structure of Landslide Dams Triggered by Earthquake/Rainfall and Their Instability	693
Gonghui Wang	
Influence of Water Level Drawdown on Landslide Movement in Reservoir	703
Hufeng Yang and Fawu Wang	
Landslide Technology and Engineering in Support of Landslide Science	709
Kyoji Sassa	

Part I

Debris Flows



Introduction: Debris Flows

Giovanni B. Crosta and Ko-Fei Liu

Abstract

Debris flows are a major hazard worldwide causing impressive damages to structures and infrastructures. Their study is approached by different methods by a vast community of researchers spread over the world. This session is focused on debris flows and a total number of ten contributions has been accepted for publication in the conference volume. These contributions by researchers from different parts of the world cover most of the subjects of interest in the study of debris flows, from triggering events to rheological properties determination, damages, design and efficiency of retention structures, role of vegetation, dating, hazard zonation and alarming.

Keywords

Debris flow • Introduction • Review

Introduction

Debris flows are considered as one type of movement within the landslide classification. Nevertheless, the mechanics and physics involved are quite variable and their understanding and modelling is complicated by the extreme changes in behaviour as a function of the type of affected soils and environmental conditions. The possibility to observe single or multiple coalescent sources, the rate of movement, the length of the transportation and their extreme variability, the presence of single and multiple steep surge fronts, the overflowing and deposition of lateral levees, the progressive spatial and temporal grain size selection and grading, the role of organic debris, the loss and entrainment of water

along the path are the major characteristics of these phenomena with respect to most common landslide types.

Therefore, they can be put as intermediate phenomena between rock/debris avalanches and hyper-concentrated floods, characterized by unsteady and non-uniform motion. Thus methodologies adopted for their study are quite different as well as the type of problems that they cause to the affected areas. Usually, debris flows are studied from different points of view, namely: initiation, flowing, deposition, hazard assessment, monitoring, alerting and design of countermeasures. Empirical formulas, small and large-scale experiments, numerical models and field investigation have been developed and all frequently used tools.

Empirical formulas are affected by a large uncertainty and requires high quality and robust datasets and their use is prevalently limited to regional predictions for initial hazard zonation or identification of possible triggering conditions.

Small and large scale experiments are a fundamental mean for understanding processes, collecting well controlled data under specific conditions and are fundamental for the validation of numerical models and for ex ante predictions.

Numerical models have been developed for different types of phenomena and starting from sets of observations and assumptions. They use different types of numerical

G.B. Crosta (✉)

Department of Earth and Environmental Sciences, Università degli Studi di Milano Bicocca, P.za della Scienza 4, 10126 Milano, Italy
e-mail: giovannibattista.crosta@unimib.it

K.-F. Liu

Department of Civil Engineering, Hydrotech Research Institute, National Taiwan University, Taipei 10617, Taiwan
e-mail: kfliu@ntu.edu.tw

solution schemes but progressively become more and more capable to include different observed behaviours (levee, deposition, steep surges, material recirculation, erosion and entrainment).

As editor of this C1 session we have been positively impressed to find that papers in this session covered many different aspects concerning debris flows. Some of the papers provide excellent field examples of investigation and countermeasures. Some of the papers gives interesting experimental and numerical studies of relevant topics. We think that even if this is a small set manuscripts, chosen among a wider initial set, these can still stimulate ideas, discussion and improvements for any serious attendant to the world landslide forum and interested in the research field.

Summary of Presented Contributions

In the following we present a concise summary of the subjects treated in each of the papers presented to the session.

The description of rheological properties is still an interesting subject even if there is a progressive development of models based on mixture theory. Nevertheless, models based on simple rheological models are still the most popular and controllable codes for debris flow modelling and direct applications. Kang and Kim analyse the effect of sand content (0, 5, 10 and 15 %) and liquidity index on the rheology of a fine-grained mixture and observe a shear thinning behaviour.

Debris flow initiation in a study area located at the margin of the Tibetan Plateau (China) is analysed by Ni et al. They discuss the conditions controlling the generation of debris flows in this area characterized by an exceptional production of loose debris, and the relationship between daily rainfall and antecedent rainfall (6 days) required to trigger instabilities with a quasi-periodic style.

The relationship between cumulated rainfall and the extent of endangered areas is studied by Ko-Fei et al. This can be an extremely useful tool for civil protection actions and hazard zonation, as well as for associating a return period to areas of different extent. The cumulated rainfall values are quite consistent (300 to 500 mm/24 h) and typical of extreme typhoon conditions. The Debris-2D code is used for flow simulations and determination of invasion areas.

The problem of torrent stabilization and possible single and multiple (chain) collapse of check dams has been recently described as an important process. Multiple chain collapses can generate very large debris flows by remobilization of deposits of past debris flows. Mikos et al. study the problem at some catchment in Slovenia showing by numerical simulations (Flo-2D) the extent of the endangered zone by deposition. The design of flexible barriers by means of a simplified analytical approach, already developed by the

authors, is presented in the contribution by Segalini et al. and tested against some experimental data.

Vegetation is known to play an important role in debris flow triggering, evolution and dating, and two contributions to this session investigate some of these aspects. In particular, Silhan et al. complete a dendrogeomorphic study for an area in the Crimean Mts (Ukraine), including 8 torrent catchments close to the town of Yalta. A massive effort involving the sampling of 1,122 cores from 566 black pines, allowed to date 2,215 debris flow events since AD 1701. The resulting computed mean decadal frequency amounts to 6.9 events with a maximum during the 1940s.

Relationships between vegetation and debris flow susceptibility are explored by Gao et al. for the Batang County in the Sichuan Province (China). By collecting data about 151 debris flows, on open slopes (33 events) and gullies (118 events). They confirm the negative relationship between vegetation coverage and open slope debris flows, and observe that this is not true for gully debris flows.

Very large debris flows can induce the formation of natural dams along major valley bottoms. Song et al. investigate the case of the Moxi river (same catchment studied by Ni et al. in this session) debris flow which caused the Dadu river blockage. The authors quantify the required size of the blocking debris flow dam on the basis of sediment characteristics and valley bottom geometry.

Hazard management strategies for a small but extremely active torrent in Switzerland, which has been recently affected by an increase in debris flow activity, is presented by Tobler et al. The 2009–2012 events are described presenting the progressive evolution in channel morphology. The authors discuss the entire hazard assessment and risk management chain, from triggering to countermeasure design and alarming.

To reduce hazard and then risk, efficient countermeasures are required and among them slot check dams are frequently adopted. Zou et al. examine the efficiency of a “slot-check dam groups” in the Shengou basin (Dongchuan district, China). Equilibrium deposit profiles and grain size data are discussed, and a semi-empirical relationship for the slot check dam efficiency is presented on the basis of slot check dam geometry and catchment’s characteristics.

Conclusions

10 contributions out of the 21 submitted to this session have been selected on the basis of their presentation and technical significance. These contributions present case studies and models developed worldwide and that can be considered useful to experts and public officers involved in debris flow modelling, monitoring and risk assessment. Furthermore, this subject is considered an extremely important one in the country hosting this WLF3 edition and as such will raise more attention and discussion during the conference.



Formation Condition, Disaster Characteristics and Developing Trend Analysis on Debris Flows in Moxi River Basin, SW China

Huayong Ni, Zongliang Li, Yongbo Tie, and Zhi Song

Abstract

Moxi river basin is located on the east piedmont of Mt. Gongga. Based on field investigation, 49 typical debris flows which could threat local residents and important equipments directly have been identified. In this paper, formation condition, initiation mechanism, typical characteristics and developing trend were analyzed, and countermeasures were put forward. Conclusions were drawn as follows: (1) It is the special geo-environment background made the solid materials very loose and abundant. More than $3 \times 10^7 \text{ m}^3$ loose solid materials are prone to be supplied to debris flow by means of collapse, landslides, erosion and entrainment. (2) Debris flows were principally triggered by the intense intraday rainfall and antecedent effective rainfall accumulating for 6 days before debris flows occurred. Their quantitative equation was established with a power-law relation and can be employed as disaster warning line. (3) Debris flows in Moxi river basin usually occur in group quasi-periodically and present chain effect. (4) Up to 43 gullies are differentiated at stages of their formation and developing. Combined with influence of climate trend, the occurrence probability of debris flows will still be high in this drainage in future. (5) As Moxi river basin is a famous scenic spot, prevention of debris flow should be given priority there and combined with the tourism planning. It is of great importance to protect Moxi platform through avoiding lateral erosion and collapse.

Keywords

Debris flow • Moxi river basin • Formation condition • Characteristic • Developing trend • Prevention

H. Ni (✉)

State Key Laboratory of Geo-Hazard Prevention and Geo-environment Protection, Chengdu University of Technology, Chengdu 610059, China

Chengdu Institute of Geology and Mineral Resources, China
Geological Survey, Chengdu 610081, China
e-mail: nihuayong@126.com

Z. Li • Y. Tie • Z. Song

Chengdu Institute of Geology and Mineral Resources, China
Geological Survey, Chengdu 610081, China
e-mail: 517830823@qq.com; 229883592@qq.com; 35842126@qq.com

Introduction

Debris flow is a very rapid to extremely rapid flow of saturated debris in a deep channel, such as a gully or a ravine (Hung et al. 2001) and is usually initiated by the erosion and entrainment of hillslope and channel material by overland flow (Berti et al. 2005), or some times triggered by outburst of reservoirs built in the channels (Godt and Coe 2007). Many geomorphological papers deal with the role of debris flows as a very active agent of landscape evolution and sediment transfer in mountain areas (Caine 1980). Debris flows commonly induce serious disaster in mountain area, particularly due to their great velocity, long run-out distance

and huge capacity to transport large, heavy objects such as tree and rock.

Moxi river basin is located at transition terrains from the Tibetan Plateau to Sichuan Basin in SW China (Fig. 1). Its special geographical and geological configuration are very favourable for generation of debris flows and 49 debris flow gullies have been identified on basis of field investigation combined with RS interpretation. Moreover, there are two towns, Moxi town and Xinxing town, one national geological park, Gongga mountain national geological park, and about 14,000 residents living in this basin. The usual location of towns, villages, as well as houses of inhabitants in valleys and alluvial fans at foothill of mountain ranges has implied that many of the local residents are in hazard zones (Ni et al. 2010). Over past 50 years, tens of debris flow events happened, and direct economic loss has been estimated up to 60 million dollars. As debris flows in Moxi River basin have typical characteristics of various types, complex formation mechanism, high occurrence frequency and serious threat, this basin has been regarded as a museum of natural debris flows in SW China (Ni et al. 2010). In this paper, formation condition, initiation mechanism and representative characteristics of the debris flow in Moxi river basin are discussed firstly, and then developing trend and potential hazard are analyzed. Finally, some advices on mitigation measures are put forward in order to guide the government to prevent debris flow hazard in future.

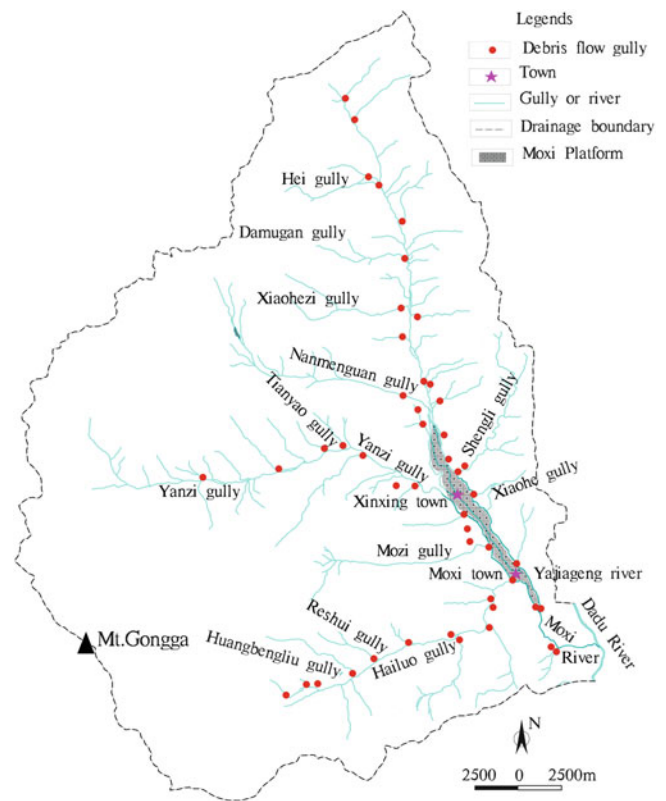


Fig. 1 Location of Moxi river basin and distribution of debris flow which is symbolized by red dot

Geomorphological and Geological Setting

Geomorphology

Moxi river basin can be seen as a typical landform-leaping belt in SW China. Gongga Mountain whose altitude of the highest peak is 7,556 m erects at the west edge of Moxi river basin (Fig. 1), as a result, relative elevation reaches up to 6,580 m there. Along the right bank of Moxi river, there are many branches and most valleys in this river basin are deeply incised with depth from tens to hundreds of meters. Shape of most valleys belong to V type with steep slopes whose gradients predominately between 25° and 60° . Major drainage basins are associated with Yajiageng river and Yanzi valley with drainage areas of 507.5 km^2 and 351.2 km^2 , respectively. In addition, Moxi river basin is famous for abundant contemporary glacier generating on a low altitude about 4,500 m. In southeast of this basin, there is a stripe-like platform named Moxi platform which is the most populated region as the existence of Moxi town and Xinxing town.

Geological Context

In SW China, there are three major faults i.e. Xianshui river fault, Longmen mountain fault and Anning river fault. Moxi river basin is located just near their junction site. Among these faults, Xianshui river fault along which many earthquakes ever broke out extends through Moxi river basin along NW direction. The south-extending part of Xianshui river fault is called Moxi fault. In addition, Caoke Syncline and Maoping Anticline are developed in NW of Moxi river Basin. The peak values of ground acceleration (PGA) is between 0.2 g and 0.4 g. The neotectonic movements are quite active in Moxi river basin and more than 20 earthquakes with magnitude over MS 6.0 have ever broke out. The intense neotectonic movements result in the rocks cracked and fragmented.

The stratum outcropped in this area are characterized by widespread Permian metamorphic rocks in west zones and sporadic Devonian deposits along Moxi fault belt. Magmatic rocks are mainly granites and distributed widely in Moxi river basin. Quaternary deposits such as deluviums, eluviums, colluviums, as well as moraine deposits are distributed widely along valleys and gentle slopes. Deposits

Table 1 Parameters of rainfall (unit in mm) at different altitude in Moxi river basin

Altitude (m)	Annual maximum precipitation	Annual average precipitation	Monthly average precipitation
1,600	1113.6	897.8	81.4
3,000	2,160	1941.5	161.8
Altitude (m)	Monthly maximum precipitation	Daily maximum precipitation	Daily average precipitation
1,600	300.5	75.3	2.8
3,000	438.5	91	5.3

on slopes are deep (>5 m in depth) but loose. Plenty of loose materials, such as sands, gravels and pebbles can be seen in every channel. All the loose solid materials both on slopes and in gully beds can be prone to supply to debris flows.

Climate and Rainfall

Typical continental monsoon climate characterized with vertical varieties is presented in this basin. According to observation, average temperature of elevation of 1,600 m and 3,400 m is 13 °C and 1 °C respectively. Generally speaking, the temperature drops 0.67 °C as altitude ascends per 100 m and daily temperature difference is up to 20 °C.

As for characteristic of rainfall, one intense precipitation belt is at altitude of 3,000 m with annual average precipitation of 1941.5 mm. Based on rainfall observation data during 1989 and 2005 recorded by Gongga Station of Alpine Forest Ecosystem, Chinese Academy of Science, some precipitation parameters at 1,600 m and 3,000 m are shown in Table 1 respectively. It can be seen that the precipitation at 3,000 m is far more than that of 1,600 m. In addition, precipitation in Moxi river basin isn't well-proportioned as far as the seasonal distribution is concerned and most rains fall in wet seasons from May to September.

Formation Condition of Debris Flow

It has been a general knowledge that steep topography, rich loose materials and intense precipitation are 3 pre-requisite elements for occurrence of debris flow. As above-mentioned, the special geographical and geological configuration of this river basin is extremely suitable for generation and formation of debris flow.

Favourable Landform Condition

In order to understand contribution of landform factor to formation of debris flow, two eigenvalues are considered.

Table 2 Drainage morphology index δ of debris flow gullies in Moxi river basin

δ	≤ 0.2	0.2–0.4	0.4–0.6	0.6–0.8	0.8–1	≥ 1
Number	2	18	13	7	3	6

One is the drainage morphology index which can be used to indicate the shapes and developing stages of debris flow drainages (Shen and Gong 1986), and the other is the gully gradient which could indicate potential energy and hydraulic condition.

Calculation results of drainage morphology index and gully gradient are given in Tables 2 and 3 respectively. About 60 % of debris flow drainage morphology index in Moxi river basin are more than 0.4, indicating a favorable condition for flood conflux. And up to 88 % of debris flow gully gradient are over 300 ‰, presenting the steep landform and favorable potential energy.

Abundant Solid Material Supply

As afore-mentioned, the intense neotectonic movements make rocks in this river basin cracked and fragmentized and the cold climate with large difference in temperature causes rocks physically weathered seriously. As a result, loose solid material are distributed widely and abundantly in this basin. On basis of RS interpretation, field survey and former research, distribution and corresponding volumes of the solid material supplied to debris flows have been identified and calculated. The whole loose solid materials are estimated to be more than $4 \times 10^8 \text{ m}^3$ in volume. Based on further analysis of the engineering geological characteristics and stability assessment, as one debris flow event occurred, the loose solid material that can be supplied to debris flow once are estimated as much as $3 \times 10^7 \text{ m}^3$ in volume. These solid materials are deposited both on the slopes and gully beds. The former deposits consist mainly of moraine deposits of both early Gongga glacier age and late Gongga glacier age, Quaternary deluviums, eluviums, colluviums, and landslides. These kinds of solid material are mainly distributed along the middle and upper reaches of Hailuo gully, Yanzi gully, Yajiageng gully, Nanmenguan gully, and so on. The deposits in gully beds mainly include the Early Holocene debris flow and alluvium deposits such as sands, gravels, pebbles.

Based on field investigation, source material of debris flows in Moxi river basin were classified into four types: collapse deposits, landslide deposits, flood or original debris flow deposits on gully beds and moraine deposits. Though types of source material in this basin are various, the collapse and landslides consist of the predominant types in this basin.

In addition, supplying methods of source material in this basin is also different. Generally speaking, in this drainage basin, three supplying means can be found: rill or slope

Table 3 Debris flow gully gradient J in Moxi river basin

J (‰)	≤200	200–400	400–600	600–800	800–1,000	≥1,000
Number	2	18	13	7	4	6

erosion, collapse or landslides, and entrainment. Field investigation indicated that most debris flows are supplied by several ways among which collapse or landslides and erosion are the most important supplying method during the occurrence of debris flow in this basin.

Sufficient Rainfall and Water Supply

In Moxi river basin, water contributed to debris flow occurrence is mainly from rainfall and snow melting. Among these two resources, rainfall plays an important role in debris flow occurrence whereas the role played by snow-melting water is limited (Ni et al. 2010). Every debris flow event occurring in history was always associated with process of intense rainfall.

Numrous studies (e.g., Fiorillo and Wilson 2004; Cannon et al. 2008; Guzzetti et al. 2008; Pelfini and Santilli 2008) analyzed the empirical relation between debris flow occurrence and rainfall condition. In order to further study relation between debris flows occurrence and corresponding triggering condition of rainfall in Moxi river basin, nine debris flow events occurring in recent years between 1989 and 2005 (Ni et al. 2010) were collected and corresponding rainfall records were analyzed. According to the rainfall records from Gongga Station of Alpine Forest Ecosystem, it can be seen that it is daily intense rainfall and antecedent effective rainfall contribute to debris flow occurrence and antecedent effective rainfall usually fell 6 days before debris flows occurred. The relation between intraday rainfall and antecedent effective rainfall was confirmed as follows:

$$R_0 = 104.29R_a^{-0.2772}$$

where R_a represents the effective antecedent rainfall fell 6 days before debris flow occurred (mm), R_0 is the intraday rainfall fell when debris flow occurred (mm). The correlation coefficient is 0.74.

The regressive power-law function can be seen not only as rainfall condition of debris flow occurrence in Moxi river basin but as a basic warning line accordingly. Through supposing certain antecedent effective rainfall, thresholds of intraday rainfall can be calculated and employed to warn debris flow. For example, warning information should be released under the following three cases: (1) antecedent effective rainfall more than 42.7 mm and intraday rainfall more than 25 mm; (2) antecedent effective rainfall more than 35.3 mm and intraday rainfall more than 50 mm; (3) intraday rainfall more than 100 mm.

Table 4 Velocity and discharge of debris flows occurred on August 11, 2005

Debris flows	Flow velocity (m/s)	Peak discharge (m ³ /s)
Nanmen gully	9.2	1,925
Yajiageng river	8.8	1,933
Yanzi gully	13.6	1,627
Moxi river	7.9	2,388

Representative Characteristics of Debris Flows

Quasi-periodic Occurrence

Temporally speaking, debris flow in Moxi river basin primarily occurred in rainy seasons. However, debris flows didn't occur every year. According to interview and literature referring, it can be found that serious debris flow events ever occurred in 1935a, 1954a, 1967–1969a, 1989–1990a and 2003–2005a. Therefore, in the eyes of many researchers, debris flow occurrence in this river basin has quasi-periodic characteristic and re-occurrence period of serious debris flow hazards is about 10–15 years (Cheng 2002).

Group Occurrence

Spatially speaking, in terms of the serious debris flow disaster events occurred in past years, debris flows in this drainage basin usually broke out from many gullies almost at the same time. Taking 2005-8-11 debris flow as example, stroken by rainstorms, more than ten gullies broke out debris flows from 18:00 p.m. on August 11 to 06:00 a.m. on August 12 in this basin. These debris flow gullies mainly include Yanzi valley, Yajiageng river, Nanmenguan gully, Shengli gully, Xiaohe gully, Xiongjia gully, Gaojia gully, as well as some other small ravines. Group occurrence of debris flows usually makes it more difficult to mitigate disaster.

Huge Dynamic Capability

Several events indicated that debris flows in Moxi river basin usually have huge dynamic capability. On July 26, 1989, an extremely huge debris flow broke out from Yanzi gully (Lü 1992). The velocities were calculated between 8.2 and 11.7 m/s and peak flow discharge reached 6775.2 m³/s. Flow velocities and peak discharges of typical debris flows occurred on August 11, 2005 were calculated and displayed in Table 4.

Table 5 Relation between integral of area-altitude curve and its geomorphologic significance

Integral (S)	Erosion rate (E)	curve form	Evolution stage	Developing stage of debris flow
<0.35	>65 %	Concave	Old	Recessionary period
0.35–0.6	40–65 %	Linear	Maturity	Frequent occurrence period
0.6–1	<40 %	Convex	Youth	Formation period

It can be seen from the calculation results that debris flow traveled with very rapid speed and large discharge. In addition, some huge boulders carried by debris flows are widespread at the downstream or at mouth of the gullies. Diameter of the largest boulder was surveyed up to 23 m (Ni et al. 2010).

Disaster Chain Effect

Debris flows in Moxi river basin ever caused catastrophic disasters in history. As far as mode of damage is concerned, debris flows usually induced disaster chain effect. Two types of damage should be mentioned and given much attention. One is the eroding hazard to the slopes of Moxi platform along both Yanzi gully and Yajiageng river caused by debris flows. After the occurrence of 2005-8-11 debris flow, many collapses and landslides were triggered on both sides of the platform and Moxi platform was shortened about 1 m averagely in width. Another is the blocking of Moxi debris flows to Dadu River. It was reported that debris flows occurred on July 26, 1989 and August 11, 2005 ever blocked Dadu River and caused huge loss. Further study indicated that Dadu River is prone to be blocked if debris flow reaches $84.26 \times 10^4 \text{ m}^3$ in volume (Song et al. 2010).

Developing Trend Analysis

Landform Evolution and Developing Stage Analysis

Area-altitude method was adopted to differentiate evolution stage of debris flow drainage in Moxi river basin. According to Stranler theory, the integral of area-altitude curve can be used to indicate erosion condition of land surface and developing stage of landform. Relation between integral of area-altitude curve and its geomorphologic significance are enlished in Table 5.

As far as landform evolution of debris flow gully drainage is concerned, formation of debris flow is also associated with the developing stage (Table 5). The integrals of corresponding area-altitude curve of 49 debris flow gullies in this basin were calculated and the evolution stage of debris flow drainage are all differentiated based on area-altitude analysis. Results indicate that 6 gullies are at the

topographic youth age and 43 gullies at topographic maturity age. In this river basin, there are no debris flow gullies that are at the topographic old age.

The differentiation results of the evolution stage of debris flow drainage based on area-altitude analysis are consistent with field observation well. On the basis of field survey, it was found that the headward erosion and lateral erosion are seriously occurred in many gullies in this basin. Serious erosion proves the youth and maturity age in terms of the topographic evolution stage. In addition, gully length and drainage area are usually considered as two other important parameters which can represent the evolution trend of drainage landform. Statistics indicate that relation between gully length and drainage area of debris flow gullies in this river basin can be fitted as a power law form:

$$L = 1.94A^{0.49}$$

where A is drainage area (km^2) and L presents main gully length (km). $R^2 = 0.8585$.

According to the regression relation between main gully length and drainage area, it can be found that drainage evolution whose area is less than 25 km^2 is highly associated with the change of gully length and that when the area is over 25 km^2 the gully length takes on slow evolution. As 85.7 % of drainage areas of debris flows in this river basin are less than 25 km^2 , it can be concluded that most debris flow gullies will be eroded headward seriously in future and the debris flows will occur still frequently.

Climate Change and Influence on Debris Flows

Based on both the former researches and the observation records from Gongga Station of Alpine Forest Ecosystem, the annual temperature in the east slope of Mt. Gongga has been taking on a warming trend. Glacier fluctuation in Moxi river basin is well associated with this point. Based on fluctuation observation of glacier bottom at Hailuogou spot in this basin, during 1930 and 2008, the glacier tongue had been back off 1,878 m (Liu et al. 2011). In terms of the formation condition of debris flows in this basin, the hydro-thermal combination is related to their occurrence and it is reported that 13 serious debris flow events ever occurred in recent 40 years and 7 of them occurred in the years when the hydro-thermal condition was warm and humid (Xu et al. 2007). Therefore, from trend of climate change involving

rainfall and temperature, it can be predicted that climate will be more favorable for formation and occurrence of debris flows in Moxi river basin.

Conclusions and Prevention Advice

Due to the special geomorphological and geological setting, debris flow gullies are widely distributed in Moxi river basin. Debris flow has been seen as the most serious geological hazard in this basin. On the basis of field investigation, 49 debris flows which threat towns, villages, scenic spots, as well as transportation and water-power project located at mountain foothills have been identified. Up to $4 \times 10^8 \text{ m}^3$ loose solid material are deposited both on the slopes and gully beds and prone to be supplied to debris flows in the way of collapse and landslide, erosion and entrainment. From typical debris flow events occurred in recent years, it is revealed that the occurrence of debris flows in Moxi river basin have quasi-periodic characteristic temporally speaking and group characteristic in terms of occurrence space. In addition, debris flows in this basin usually have huge dynamic capability and the disaster process usually have chain effects including the erosion to Moxi platform and the block to Dadu River.

According to Stranler theory, as for phase of landform evolution, all debris flow gullies in this drainage basin are at youth age and maturity age. Meteorological records indicate both the rainfall and temperature presume a trend of rising. As a result, debris flows will still occur frequently in future and disaster situation will still be urgent. In order to prevent debris flow hazards in this basin, on basis of field investigation, the following prevention advice on was put forward:

Firstly, to further study the triggering condition and to establish the monitoring and warning system. As triggering factors are concerned, most debris flows in this river basin are initiated by rainfall. However, due to the different geological and geomorphological settings in different regions, rainfall thresholds to trigger the flows as well as soil destabilization are different. In addition, some of the debris flows, such as Hailuo gully, Yanzi gully and Nanmenguan gully in this basin, are initiated jointly by rainfall and glacier melting. Therefore, triggering condition of debris flow initiation in this basin should be further studied. Then, as the risk of debris flow disaster is high, a monitoring and warning system should be established. If critical condition is satisfied to trigger debris flow, warning information should be released automatically and corresponding preparedness should be started timely.

Secondly, as the erosion of debris flows has been leading to collapse on both sides of Moxi platform and then threat the infrastructures and residents at edge of the platform, some lateral embankments should be built at the

place where is the most likely to be eroded by debris flows so as to protect the Moxi platform.

Thirdly, prevention of debris flow should be associated with infrastructure, land protection and tourism developemnt. The debris flows occurred on August 11, 2005 had resulted in the roads and bridges destroying and more than 1,000 visitors were blocked in Hailuogou scenic spot. More than 6,000 residents were seriously affected because of destroyed supplying establishments of both water and electricity in this disaster event.

Last but not least, comprehensive prevention system should be planned thoroughly based on the whole basin. In this basin, in terms of prevention of tributary debris flows, in order to avoid blocking of Yajiangeng River, Yanzi gully, Moxi River and even Dadu River, some tributaries including Nanmenguan gully, Shengli gully, Xiaohe gully, Xiaohezi gully, Yanzi gully, Hailuo gully, Mozi gully, Longbaiwei gully, Tianyao gully and Dagan gully should be given enough attention and advertence. Debris flow broke out in above-mentioned tributary gullies ever broke out debris flows in later nineteenth century and beginning of twentieth century and are likely to occur in future. They usually bring about hazards by carrying solid materials to Yanzi gully and Yajiangeng river so as to increase debris flow magnitude, or even by blocking the two main gullies and then produce huge flow discharge after outburst.

Acknowledgements This research is financially supported by the National Science Foundation of China (grant No. 41102226) and the Project of China Special Project of Basic Work of Science and Technology (grant No. 2011FY110100-1). The authors would like to thank Ko-Fei Liu and Prof. Giovanni Crosta for their constructive comments on the paper revision.

References

- Berti M, Genevois R, Simoni A (2005) Experimental evidences and numerical modeling of debris flows initiated by channel runoff. *Landslides* 2:171–182
- Caine N (1980) The rainfall intensity-duration control of shallow landslides and debris flows. *Geogr Ann* 62A:23–27
- Cannon S, Gartner J, Wilson R (2008) Storm rainfall conditions for floods and debris flows from recently burned areas in southwestern Colorado and southern California. *Geomorphology* 96:250–269
- Cheng G (2002) Study on the quasi-period of breaking out debris flow under storm. *J Nat Disasters* 11(4):49–54 (in Chinese)
- Fiorillo F, Wilson R (2004) Rainfall induced debris flows in pyroclastic deposits, Campania (Southern Italy). *Eng Geol* 75:263–289
- Godt J, Coe J (2007) Alpine debris flows triggered by a 28 July 1999 thunderstorm in the central Front Range, Colorado. *Geomorphology* 84:80–97
- Guzzetti F, Peruccacci S, Rossi M, Stark C (2008) The rainfall intensity-duration control of shallow landslides and debris flows: an update. *Landslides* 5:3–17
- Hungr O, Evans S, Bovis M et al (2001) A review of the classification of landslides of the flow type. *Environ Eng Geosci* 7(3):221–238

- Liu Q, Liu S, Zhang Y et al (2011) Surface ablation features and recent variation of the lower ablation area of the Hailuoguo glacier, Mt. Gongga. *J Glaciol Geocryol* 33(2):227–236 (in Chinese)
- Lü R (1992) An extremely heavy debris flow in Gongga mountain. *J Glaciol Geocryol* 14(2):174–177 (in Chinese)
- Ni H, Zheng W, Li Z et al (2010) Recent catastrophic debris flows in Luding county, SW China: geological hazards, rainfall analysis and dynamic characteristics. *Nat Hazards* 55:523–542
- Pelfini M, Santilli M (2008) Frequency of debris flows and their relation with precipitation: a case study in the Central Alps, Italy. *Geomorphology* 101:721–730
- Shen Y, Gong G (1986) *Conspectus of river geomorphology*. Science Press, Beijing (in Chinese)
- Song Z, Ba R, Liu Y (2010) Analysis on blocking of the Dadu River by a giant debris flow of Moxi River: quantitative calculation of scale of a debris flow and flow of different frequencies by rain-flood method. *J Catastrophol* 25(2):73–75 (in Chinese)
- Xu X, Ma D, He D et al (2007) Analysis on hydro-thermal combination of debris flow occurrence in Mt. Gongga region. *J Mt Sci* 25(4): 431–437 (in Chinese)



Dendrogeomorphic Chronologies of Debris Flows for the Crimean Mountains (Ukraine)

Karel Šilhán, Tomáš Pánek, Jan Hradecký, and Markus Stoffel

Abstract

The Crimean Mountains (Ukraine) are renowned for the highest occurrence in debris flows along the northern coast of the Black Sea, but information on their origin, frequency and triggers is widely lacking. This study therefore aims at reconstructing a regional time series of debris flows in eight catchments located on the slopes above Yalta. Dendrogeomorphic analyses were performed on 1,122 increment cores selected from 566 black pines (*Pinus nigra ssp. pallasiana*) with clear signs of damage induced by past debris-flow activity. We date a total of 215 debris flows back to AD 1701 and observe a mean decadal frequency of 6.9 events, with a peak in activity during the 1940s (20 events).

Keywords

Debris flows • Dendrogeomorphology • Crimean mountains

Introduction

Debris flows (DF) represent one of the more common and widespread geohazards and an effective geomorphic process of sediment transfer in mountain environments (Rickenmann 1999). Optimal datasets on DF also contain information on magnitude-frequency relations of DF (Jakob and Friele 2010; Stoffel 2010). Data on the temporal frequency, magnitude and on meteorological conditions controlling DF activity are even more important in the densely populated regions (Pasuto and Soldati 2004) such as the southern slopes of the Crimean Mountains (Ukraine), where DF and other types of mass movements have been reported to occur frequently (Pánek et al. 2009; Šilhán et al. 2012).

K. Šilhán (✉) • T. Pánek • J. Hradecký
Department of Physical Geography and Geoecology, University of Ostrava, Chittussiho 10, Ostrava 710 00, Czech Republic
e-mail: karel.silhan@osu.cz; tomas.panek@osu.cz; jan.hradecky@osu.cz

M. Stoffel
Dendrolab.ch, Institute of Geological Sciences, University of Berne, Baltzerstrasse 1+3, 3012 Berne, Switzerland
e-mail: markus.stoffel@dendrolab.ch

Despite the recent progress in dendrogeomorphic research on DF and related techniques, concern emerged about the suitability and capability of trees of different age to record geomorphic disturbance with equal confidence (Bollschweiler and Stoffel 2010; Šilhán et al. 2012).

This study therefore focuses on the first reconstruction of regional DF histories in the sub-Mediterranean Black Sea region. The main objectives of this work are to (1) reconstruct spatio-temporal patterns of DF activity on the southern slopes of the Crimean Mountains (Ukraine).

Study Area

The Crimean Mountains (Ukraine) are a part of the Caucasus–Crimean fold-and-thrust belt that forms the northern fringe of the Black Sea basin (Fig. 1) (Pánek et al. 2009). The highest ridges of the Crimean Mountains are >1,200 m a.s.l. and asymmetrically shifted to the Black Sea coast, thereby forming very steep southern slopes with local relief >1 km (measured in 1 km² windows). The slopes are formed by mechanically weak claystone-dominated flysch units of the Upper Triassic-Lower Jurassic overlain by very thick (>1 km), strongly karstified Upper Jurassic

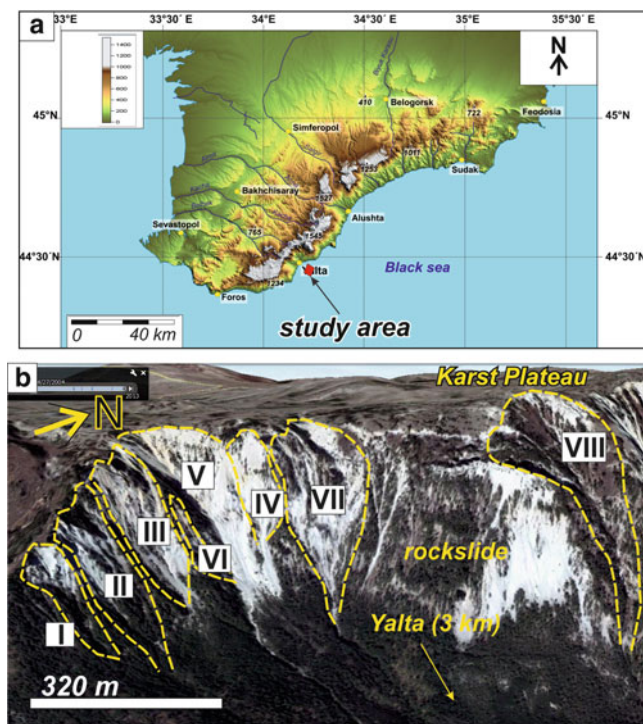


Fig. 1 Study area. (a) Localization of the Crimean Mountains. (b) Localization of study area in the vicinity of the town of Yalta. (c) Oblique Google Earth satellite image showing the morphological context of studied debris flow basins

limestones (Derenyuk et al. 1984). As a result of this contact between physically different lithologies, the very pronounced local relief, active seismicity, relatively high annual precipitation (>1,000 mm), coastal abrasion and intense anthropogenic activity, the southern slopes of the Crimean Mountains must be considered extremely prone to various types of mass movements (Pánek et al. 2009; Šilhán et al. 2012, 2013). DF activity in the area is largely concentrated to the highest areas of the mountains above the densely populated agglomeration of Yalta, which is the major economic center of the southern Crimean coast.

The area under investigation is situated in the steepest and highest portions of the coastal slopes of the Crimean Mountains, approximately 4 km W of Yalta (44°28.7'N/34°04.5'E; Fig. 1). The study area is dominated by eight adjacent torrential catchments draining the eastern slopes of Ai Petri Mt. (1,234 m a.s.l.); the main characteristics of the individual torrents are presented in Table 1. Lithology is characterized by thin-bedded, strongly fractured Upper Jurassic limestones, highly susceptible to weathering and mass movements (Šilhán et al. 2012). The piedmont area of the torrents is gently inclined (<20°), with terraced slopes with several generations of DF cones, talus and/or landslide lobes (Fig. 1). Within this study, dendrogeomorphic work focused on the most active parts of the torrents with recent

(±200 years) DF levees and lobate deposits with signs of DF damage in trees (Fig. 1).

Annual precipitation totals in the uppermost parts of source areas reach 1,050 mm and the temperature is 7.5 °C, whereas the lowermost part of the accumulation zone of debris flow receives 580 mm of total annual precipitation and its mean temperature is 13 °C.

Methods

Geomorphic mapping was realized at a 1:5,000 scale and focused on erosional (gullies, debris flow channels) and depositional (lateral levees, lobes) landforms related to DF activity. Tree-ring analysis focused on black pines (*Pinus nigra* ssp. *Pallasiana*) with signs of growth disturbances related to DF activity (stem burial, tilting and wounding). Each tree was sampled with two increment cores. In addition, we sampled 40 old but undisturbed *P. nigra* individuals to construct reference chronology. All samples were processed following the standard dendrogeomorphic procedure described by Stoffel and Bollschweiler (2008). Increment curves of disturbed trees were then compared with the reference chronology to identify and correct false and/or missing rings. Dating of DF was based on the identification of anomalies in the increment curves and by visual inspection of the increment cores. Within this study, dendrogeomorphic analysis was restricted to (i) abrupt growth suppression, (ii) abrupt growth release, (iii) the presence of callus tissue and (iv) reaction wood.

Dating of DF events was based on a semi-quantitative approach (Bollschweiler et al. 2007; Bollschweiler and Stoffel 2010), where ≥ 2 trees located in the same flow line had to exhibit strong growth disturbances to be considered DF events. We also computed decadal frequencies so as to demonstrate possible temporal trends in DF activity (Stoffel et al. 2008; Bollschweiler and Stoffel 2010). Event years were considered local events if DF activity was restricted to ≤ 3 torrents in a given year and regional events as soon as DF occurred in four or more torrents.

Results

A total of 1,122 increment cores from 566 *P. nigra* trees were sampled in eight active DF torrents. Mean age of trees at sampling height is 102.1 yr (SD 83.2 year). Dendrogeomorphic analyses of the *P. nigra* trees yielded information on 1,271 growth disturbances related to DF activity. Abrupt growth suppression (37.6 %) and compression wood (36.4 %) were observed most frequently in the full sample, followed by abrupt growth release (14.9 %) and the presence of callus tissue (11.1 %).

Table 1 Basic morphometrics parameters of individual catchments

Catchment	I	II	III	IV	V	VI	VII	VIII
Orientation	NE	NE	NE	NE	E	E	E	SE
Area (km ²)	0.02	0.04	0.07	0.04	0.1	0.01	0.1	0.3
Altitude range (m)	160	268	310	170	365	227	355	525

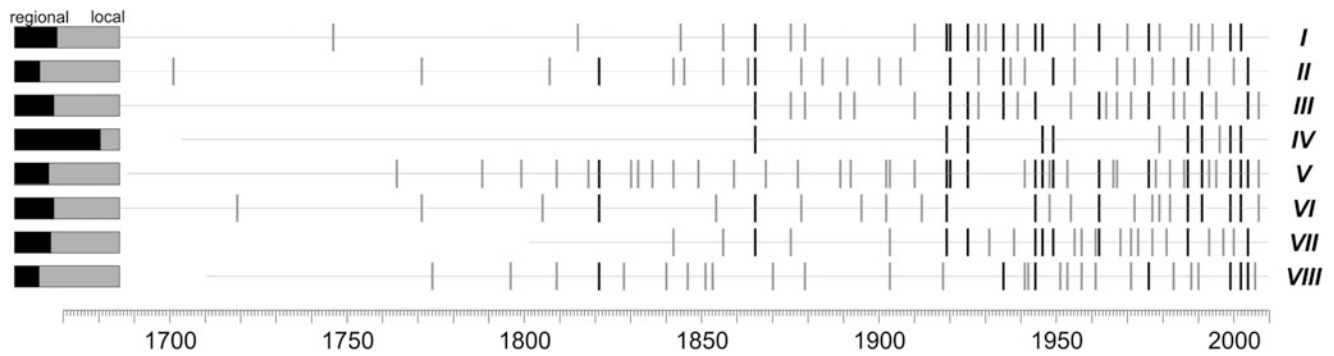


Fig. 2 Annual frequency of debris flow and ratio of regional and local events in individual catchments

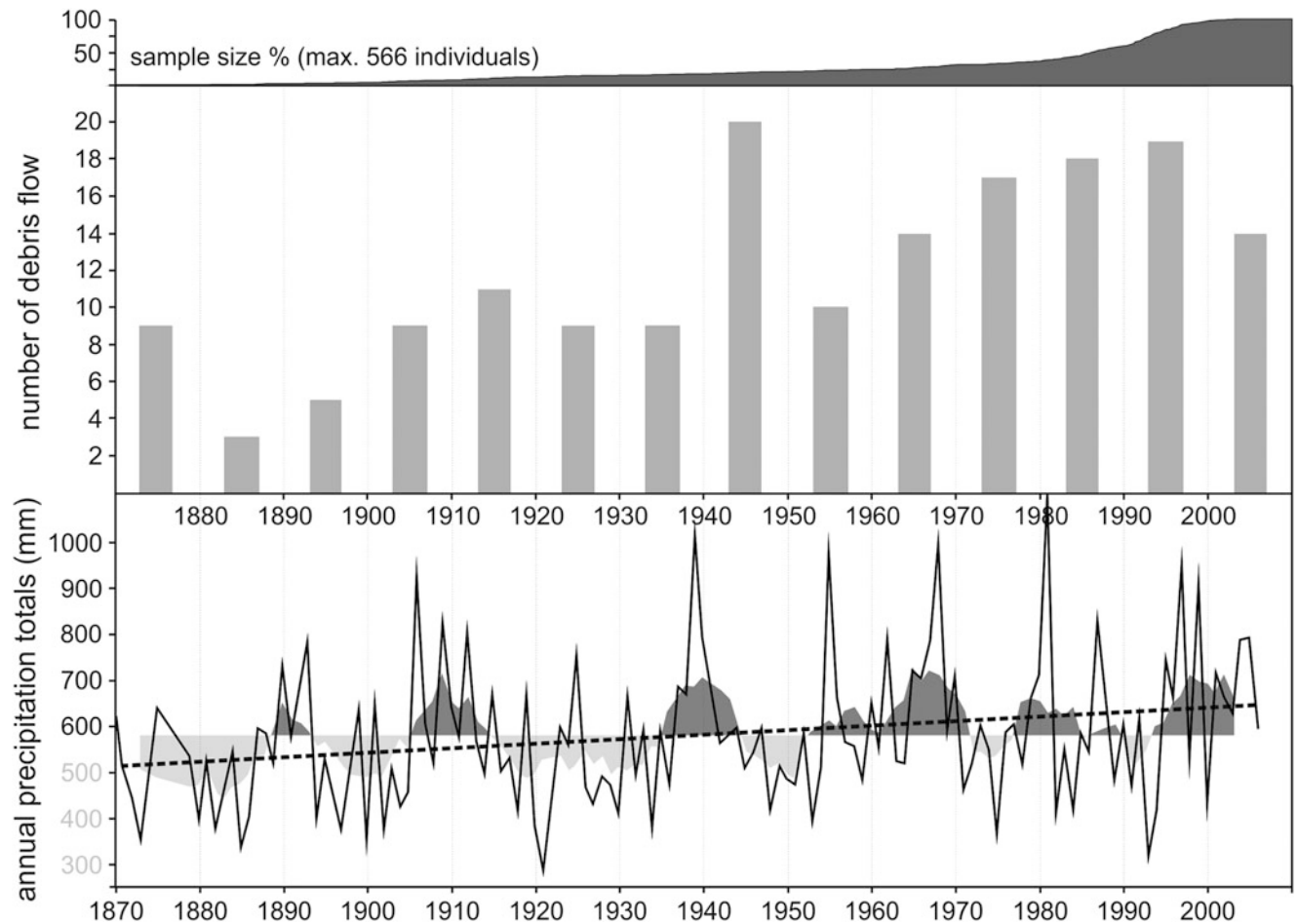


Fig. 3 Decadal frequency of debris flow and annual precipitation totals

A total of 215 DF has been dated in 105 event years in the eight torrents, with the oldest event dated to AD 1701 (Fig. 2). On the temporal scale, DF activity remained at a comparable level between the 1840s and 1930s, with the exception of the 1880s and 1890s for which activity was significantly reduced. DF activity was at its peak in the 1940s for which 20 events have been reconstructed (recurrence interval: 0.5 year). A gradual (and apparent) increase in activity can be observed since the 1950s, and up to 1990s, whereas the last decade (2000s) is again characterized by less marked activity (Fig. 3).

Sixteen event years (out of 105; 15.2 %) are considered here as regional events, as they have been recorded in four or more torrents in the same year. The remaining 89 event years (84.8 %) are considered more localized phenomena, since they have triggered DF in one to three catchments. Regional and local events are presented by 75 and 140 DF, respectively.

Discussion

The nature of growth disturbances in trees will ultimately be driven by the nature of the process itself. In our case, signs of past DF activity were mostly visible in the form of abrupt growth suppression reflecting stem burial and/or root disroutines. In contrast, abrupt growth releases were scarce in our case and thus point to the negligible role of tree fertilizing processes during minor burial events or the elimination of neighbors. Compression wood was mostly present in the younger trees (with flexible stems) and may therefore appear more important as compared to other DF sites. In the same line of thoughts we do not consider the abundance of compression wood in our dataset as a sign of high magnitude DF, even more as the scarcity of callus tissue suggests that the impact forces of individual DF are not very strong.

The reconstructed decadal frequency of DF (6.9 events/decade) is clearly higher than the one obtained by Procter et al. (2011) for the Western Austrian Alps (3.2), where DF events are triggered from sediment-limited limestone environments, or by Šilhán and Pánek (2010) for medium-high mountain of middle Europe. At the same time, the reconstructed decadal DF activity is much smaller than that reconstructed for the permafrost-dominated catchments of the Valais Alps in Switzerland (18.5; Bollschweiler and Stoffel 2010). The causes of debris generation seem to be slightly different in our case as compared to high-mountain environments, where increased frequency of DF is often driven by higher temperatures influencing permafrost degradation and dynamics of rock glaciers (Kääb et al. 2005; Lugon and Stoffel 2010).

The largest number of regional events can be found in catchment IV, a narrow system of limited area, where triggering precipitation events are unlikely to be limited to its territory and likely to activate DF in adjacent catchments as well. On the contrary, catchment VII is somewhat isolated with respect to the other catchments and thus has the largest amount of local events. This evidence suggests highly site-specific effects of downpours in mountainous regions.

Conclusion

Dendrogeomorphic investigation of eight torrents situated on the southern slopes of the Crimean Mountains and next to the coast of the Black Sea enabled dating of 215 debris flows by means of tree-ring analysis of 1,122 increment cores sampled from 566 *P. nigra* trees. We reconstruct a mean decadal DF frequency of 6.9 events. As a result we call for more work in the Black Sea region which has been neglected considerably in the past as far as dendrogeomorphic work is concerned.

Acknowledgments This research was supported by the project of the Czech Science Foundation no. P209/12/0317: “Late Quaternary evolution of the complex gravitational slope deformations on the southern slopes of the Crimean Mountains (Ukraine)”.

References

- Bollschweiler M, Stoffel M (2010) Tree rings and debris flows: recent developments, future directions. *Progr Phys Geogr* 34:625–645
- Bollschweiler M, Stoffel M, Ehmisch M, Monbaron M (2007) Reconstructing spatio-temporal patterns of debris-flow activity using dendrogeomorphological methods. *Geomorphology* 87:337–351
- Derenyuk NE, Vanina MV, Gerasimov MY, Pirovarov SV (1984) Geological map of the Crimea. Geological Ministry of Ukraine, Kiev, scale 1:200,000 (in Russian)
- Jakob M, Friele P (2010) Frequency and magnitude of debris flows on Cheekye River, British Columbia. *Geomorphology* 114:382–395
- Kääb A, Huggel C, Fischer L, Guex S, Paul F, Roer I, Salzmann N, Schlaefli S, Schmutz K, Schneider S, Strozzi T, Weidmann Y (2005) Remote sensing of glacier- and permafrost-related hazards in high mountains: an overview. *Nat Hazards Earth Syst Sci* 5:527–554
- Lugon R, Stoffel M (2010) Rock-glacier dynamics and magnitude-frequency relations of debris flows in a high-elevation watershed: Ritigraben, Swiss Alps. *Global Planet Change* 73:202–210
- Pánek T, Hradecký J, Šilhán K, Smolková V, Altová V (2009) Time constraints for the evolution of a large slope collapse in karstified mountainous terrain of the southwestern Crimean Mountains Ukraine. *Geomorphology* 108:171–181
- Pasuto A, Soldati M (2004) An integrated approach for hazard assessment and mitigation of debris flow in the Italian Dolomites. *Geomorphology* 61:59–70
- Procter E, Bollschweiler M, Stoffel M, Neumann M (2011) A regional reconstruction of debris-flow activity in the Northern Calcareous Alps Austria. *Geomorphology* 132:41–50

- Rickenmann D (1999) Empirical relationships for debris flows. *Nat Hazards* 19:47–77
- Šilhán K, Pánek T (2010) Fossil and recent debris flows in medium-high mountains (Moravskoslezské Beskydy Mts, Czech Republic). *Geomorphology* 124:238–249
- Šilhán K, Pánek T, Hradecký J (2012) Tree-ring analysis in the reconstruction of slope instabilities associated with earthquakes and precipitation (the Crimean Mountains, Ukraine). *Geomorphology* 173–174:174–184
- Šilhán K, Pánek T, Hradecký J (2013) Implications of spatial distribution of rockfall reconstructed by dendrogeomorphological methods. *Nat Hazards Earth Syst Sci* 13:1817–1826
- Stoffel M (2010) Magnitude-frequency relationships of debris flows – a case study based on field surveys and tree-ring records. *Geomorphology* 116:67–76
- Stoffel M, Bollschweiler M (2008) Tree-ring analysis in natural hazards research – an overview. *Nat Hazards Earth Syst Sci* 8:187–202
- Stoffel M, Conus D, Grichting MA, Lièvre I, Maître G (2008) Unraveling the patterns of late Holocene debris-flow activity on a cone in the Swiss Alps: Chronology, environment and implications for the future. *Global Planet Change* 60:222–234



Experimental Study on the Rheological Behaviour of Fine-Grained Soils with Sand Content and Liquidity Index (Water Content)

Hyo-Sub Kang and Yun-Tae Kim

Abstract

Rheological properties such as yield stress and viscosity is the main parameters to determine the fluidity of the debris flow. In this study, to evaluate effects of sand content and liquidity index (water content) on the rheological properties of fine-grained soils, several series of laboratory tests were performed on specimens with various sand contents of 0, 5, 10, and 15 % or with various liquidity indices ranging from 5 to 12.3. The flow behavior was strongly influenced by liquidity index (water content) and sand content. The overall shape of the flow curves of specimens had characteristics of a shear thinning fluid, with a decrease in viscosity as shear rate increased. The yield stress and viscosity gradually decreased as the liquidity index increased. At a given liquidity index, yield stress and viscosity of soil increased with an increase in sand content. Also, the yield stress and viscosity tend to increase with increasing concentration by volume (C_v) of the fluid matrix. The values of the four coefficients α_1 , α_2 , β_1 , and β_2 were obtained by regression analysis for each fine-grained soil.

Keywords

Rheological characteristics • Rheological model • Viscosity • Shear stress

Introduction

Debris flow is a kind of natural mixtures of soil, rock, and water that is fast moving (Malet et al. 2005). Debris flows generally generate as unconsolidated material becomes saturated and unstable, either on a hillslope or in a stream channels. These flows are accelerated downhill by gravity and tend to follow steep mountain channels. They may reach long distances and high velocities, which make them serious geological hazards affecting vast areas of inhabited regions (Takahashi 1991). Individual landslides can be widely scattered in space and time, but a substantial portion of the annual landslide loss is associated with a few major catastrophic events such as the debris flow. Such movement

usually occurs following soil saturation due to fairly intense and short-duration rainfall events. Mud and debris flows originate on steep slopes or landslide areas. The zone of sediment transport typically has a steep channel system, at the end of which a sudden break in slope on the valley floor induces deposition to form a conical debris fan (O'Brien and Julien 1988). The behavior of debris flow is difficult to characterize owing to nonhomogeneous mixture with various components that may range from clay to large boulders including water. Rheological properties such as yield stress and viscosity is the main parameters to determine the fluidity of the debris flow. The run-out distance, depth, velocities, and impact force of debris flow could be related to characteristics of rheological properties of the soils (Imran et al. 2001; Locat et al. 2004). Therefore, flow behavior can be quite complex according to soil type, liquidity index, grain sizes, and sand content.

This paper examines rheological characteristics of fine-grained soils with various sand contents and various

H.-S. Kang • Y.-T. Kim (✉)
Department of Ocean Engineering, Pukyong National University,
Busan 608-737, Republic of Korea
e-mail: monkle0@hanmail.net; yuntkim@pknu.ac.kr

liquidity indices to investigate effects of sand content and liquidity index on the rheological behaviors, particularly viscosity and yield stress. From experimental test results, some general conclusions are drawn about the effects of sand content and liquidity index on rheological properties.

Properties of Material

To evaluate effects of sand content and water content on the rheological properties of fine-grained soils, rheological test was performed on various mixtures. The materials used in the research were weathered granite soil and kaolin clay. Mixtures consist of four different sand contents of 0, 5, 10, and 15 %. The grain-size distributions of S0, S5, S10, and S15 samples are shown in Fig. 1. Soil mixtures used for this study were composed of average particle sizes ranging from 6.54 to 31.52 μm .

A series of rheological investigations were carried out on these mixtures; S0, S5, S10, and S15. These mixtures had their physical and geotechnical properties as listed in Table 1. These mixtures have specific gravity values in the ranges of 2.77 to 2.67, liquid limit (LL) and plastic index (PI) values in the ranges of 49.6 to 33.3 % and 14.1 to 4.6 %, respectively. All these mixtures are classified into ML, fine-grained soil according to USCS.

Rheometer Test

The rheological analysis of soil samples was carried out using a cone-and-plate rheometer (AR2000ex, TA Instruments). Figure 2 shows the rheometer apparatus used in the present study for the testing. The rheometer used in this study is a cone-and-plate rheometer (TA instrument). Figure 2a shows

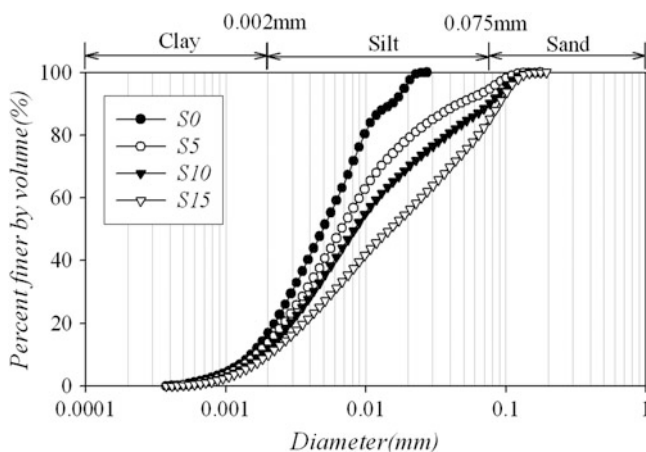


Fig. 1 Particle-size distribution curves of soil samples

Table 1 Properties of soil samples used in the study

Soil sample	S0	S5	S10	S15
Specific gravity (G_s)	2.77	2.73	2.68	2.67
Liquid limit (LL)	49.6	43.7	38.9	33.3
Plastic limit (PL)	35.5	33.7	30.8	28.7
Plasticity index (PI)	14.1	10.0	8.1	4.6
Clay content (%)	17	14	12	10
Silt content (%)	83	81	78	75
Sand content (%)	0	5	10	15
Average particle size (D_{50} , μm)	6.5	16.3	22.8	31.5
USCS	ML			

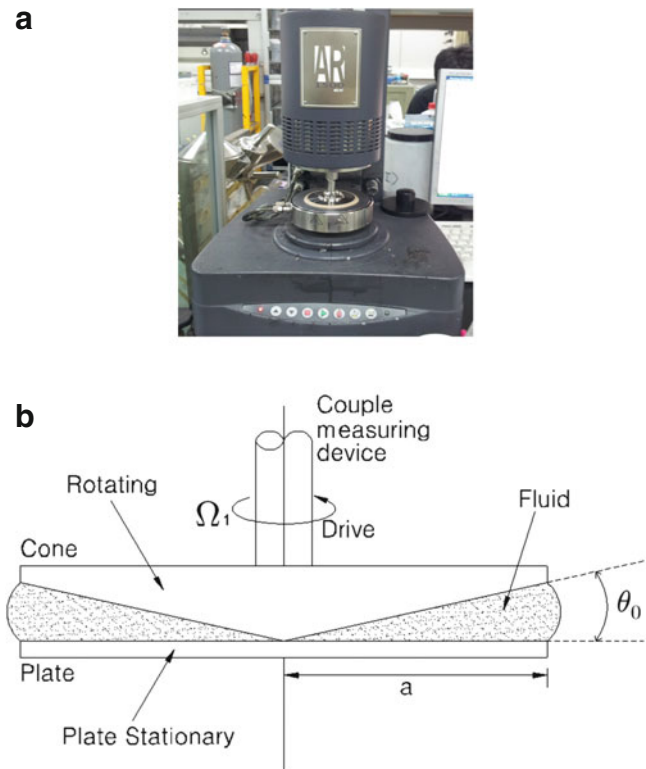


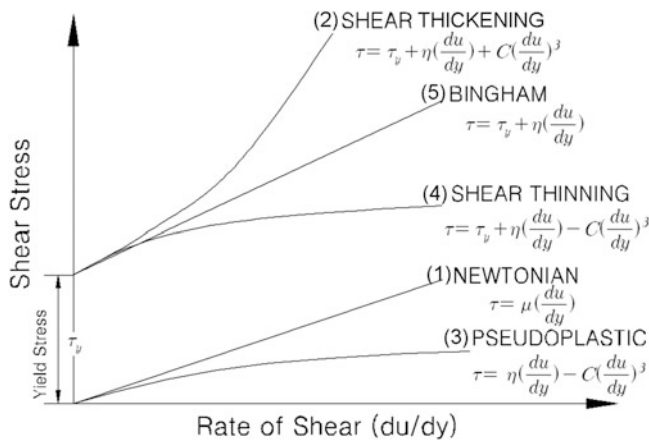
Fig. 2 Cone-plate rheometer (a) Rheometer, (b) The concept of cone-plate rheometer

concept of the cone-and-plate rheometer. The device consists of rotating plate 60 mm in diameter and 2° in cone angle. The rheometer can be operated in the controlled shear rate mode where the shear rate is fixed and the required torque is measured, or in the controlled shear stress mode where the shear stress is applied and the resulting shear rate is measured.

Table 2 shows mixtures tested in this study. A total of 12 samples were prepared in the tests. Three different liquidity indices were applied for each specimen with same sand content. All tests were carried out at a controlled temperature of 20°C .

Table 2 Mixtures with various sand content and liquidity indices

Soil sample	S0			S5				S10			S15		
Sand content (%)	0			5				10			15		
Liquidity index (LI)	5.0	6.2	8.3	4.0	5.0	6.0	8.0	5.0	5.9	7.9	8.0	9.3	12.3


Fig. 3 Major types of fluids (1) Newtonian; (2) Thickening; (3) Pseudoplastic; (4) Thinning; (5) Bingham

Rheological Models

The several types of flow are shown in Fig. 3, where viscosity corresponds to the slope of these curves. Thickening liquids are those for which the viscosity increases with shear rate. Fluidizing or pseudoplastic liquids have an opposite behavior, as the viscosity decreases with increasing shear rate. Thinning fluids are fluidizing bodies characterized by a yield stress and slowly decreasing viscosity at higher shear rates. Other liquid-like materials reach a constant viscosity, but only after reaching their yield stress—these are called Bingham fluids (Locat and Demers 1988).

Results and Discussion

Shear Stress-Shear Rate Behavior

All rheological tests were performed at the same condition except different sand content and liquidity index. Figure 4 shows the shear stress-shear rate and viscosity-shear rate curves obtained for the soil sample with sand content of 5%. But the soil sample has different liquidity indices ranging from 5.0 to 8.0. It can be seen that shear stress and viscosity decreases when the liquidity index increases. It is found that the shear stress rapidly increases towards yield stress, but once it reaches yielding point, it increases more slowly. The overall shape of the flow curves for the fine-grained soils used in this study has characteristics of a shear thinning fluid, with a decrease in viscosity as shear rate increases.

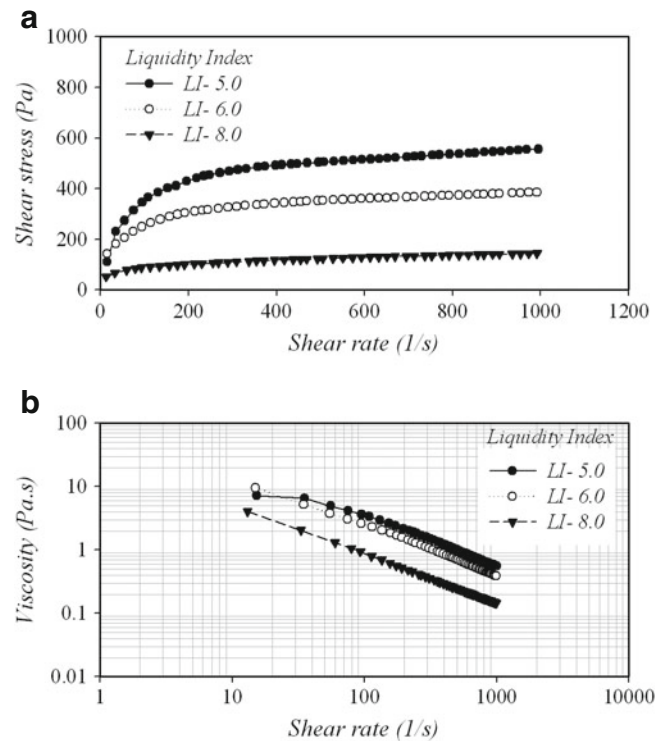

Fig. 4 A series of flow curves obtained for the soil sample with sand content of 5% (a) Shear stress-shear rate curves, (b) Viscosity-shear rate curves

Figure 5 shows the shear stress-shear rate and viscosity-shear rate curves obtained for the soil sample with liquidity index of 8. But the soil sample has different sand contents ranging from 0 to 15%. It can be seen that shear stress and viscosity increases as the sand contents increases, except for soil sample of low sand content (i.e., 0, 5%).

Relation Between Volumetric Concentration and Rheological Properties

The parameter related to unit weight is a solid concentration by volume (C_v) as proposed by O'Brien (2003). The solid volumetric concentration C_v , i.e., the ratio of the amount of solids to the total mixture, is defined as;

$$C_v = \frac{V_{solid}}{V_{solid} + V_{water}} \quad (1)$$

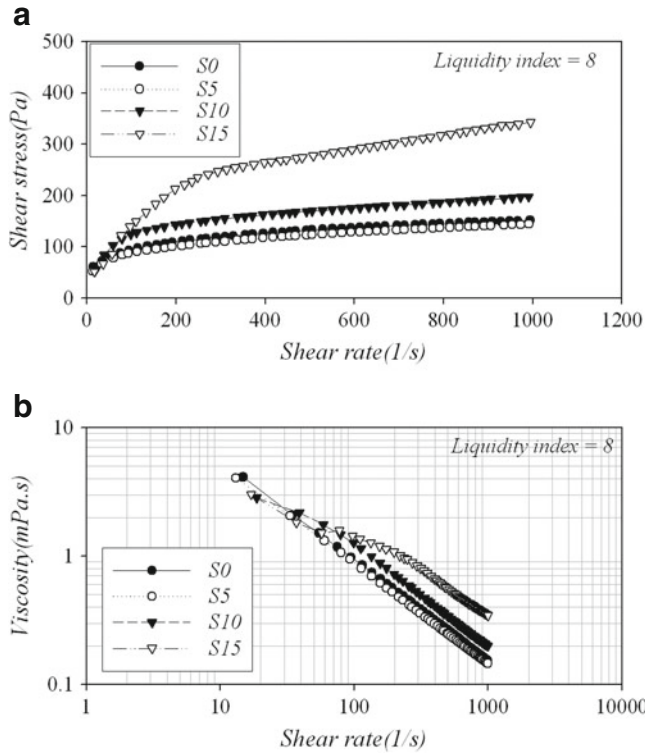


Fig. 5 A series of viscosity-shear rate curves obtained for the soil sample with liquidity index of 8 (a) Shear stress-shear rate curves, (b) Viscosity-shear rate curves

where V_{solid} is volume of solid part, and V_{water} is volume of pore water. For full saturated material, C_v may be written as (Widjaja 2011):

$$C_v = \frac{1}{1 + e} \quad (2)$$

where e is void ratio.

Figure 6 shows the relationship between rheological properties of soil sample and volumetric concentration. It can be seen that shear stress and viscosity increase as the volumetric concentration increases. The higher sand content of samples (S15) in Fig. 5 have lower values of yield stress and viscosity when compared with lower sand content of the samples (S0).

At sediment concentrations above 20 % the flow was treated as a non-Newtonian fluid, where yield strength and viscosity become important parameters (Pierosn and Scott 1985).

They assumed that viscosity(η) and yield stress(τ_y) depended on both empirical coefficients and sediment concentration as follows:

$$\tau_y = \alpha_1 e^{\beta_1 C_v} \quad (3)$$

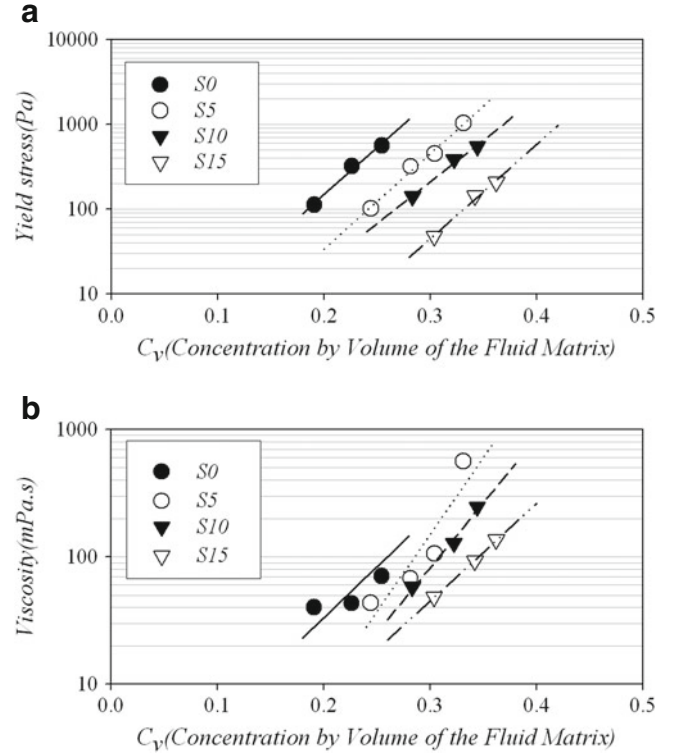


Fig. 6 Empirical relationships relating viscosity and yield stress on varying the solid concentration in volume (a) Relationship between yield stress and C_v , (b) Relationship between viscosity and C_v

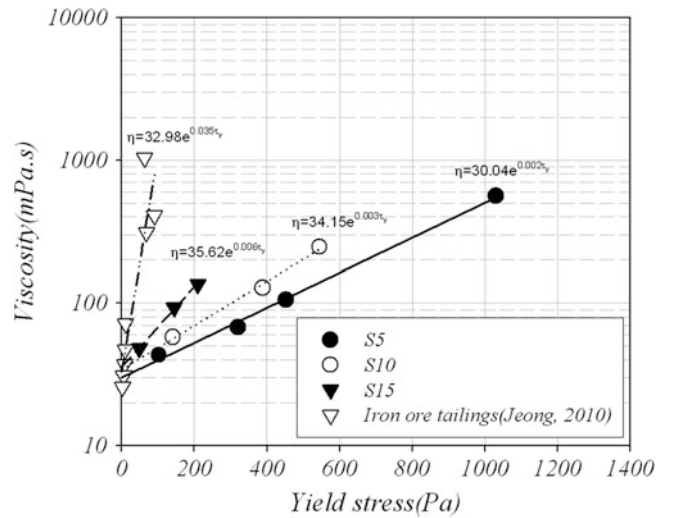


Fig. 7 Relation between viscosity and yield stress with sand content

$$\eta = \alpha_2 e^{\beta_2 C_v} \quad (4)$$

where α_1 , α_2 , β_1 , β_2 and are the empirical coefficients obtained by regression analysis and C_v is the volumetric concentration in the flow. Based on these correlations,

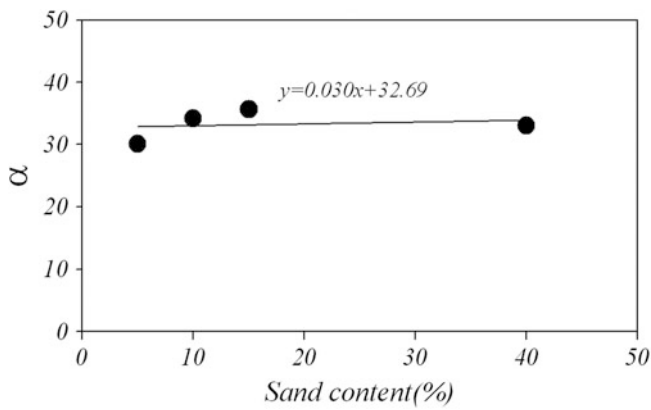


Fig. 8 Relation between α and sand content

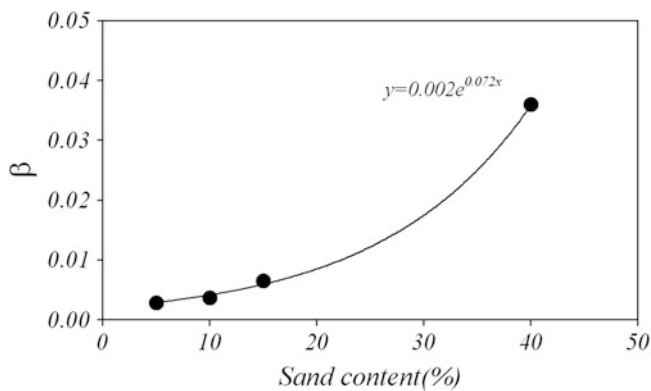


Fig. 9 Relation between β and sand content

Table 3 Coefficients for viscosity and yield stress

Soil sample	$\tau_y = \alpha_1 e^{\beta_1 C_v}$		$\eta = \alpha_2 e^{\beta_2 C_v}$	
	α_1	β_1	α_2	β_2
S0	0.915	25.47	0.848	18.36
S5	0.193	25.87	0.035	27.87
S10	0.236	22.67	0.072	23.46
S15	0.02	25.59	0.226	17.64

viscosity and yield stress for a given soil can be calculated from the volumetric concentration and empirical coefficient.

Relation Between Viscosity and Yield Stress

Figure 7 shows the relationship between viscosity and yield stress of soil sample and volumetric concentration. It can be seen that correlation between viscosity and yield stress. Relationship of viscosity and yield stress can be expressed as follows:

$$\eta = \alpha e^{\beta \tau_y} \tag{5}$$

where α , β and are the empirical coefficients obtained by regression analysis (Figs. 8 and 9; Table 3).

Conclusion

To evaluate the effects of sand content and liquidity index on the rheological properties of soils, several series of laboratory tests were performed on several specimens with sand content of 0, 5, 10, and 15 % or with liquidity index ranging from 5 to 12.3. Some conclusions are as follows:

The flow behavior is strongly influenced by liquidity index and sand content. The overall shape of the flow curves has characteristics of a shear thinning fluid, with a decrease in viscosity as shear rate increases.

The yield stress and viscosity decreased as the liquidity index increased.

The shear stress and viscosity decreases as the volumetric concentration increases. The empirical coefficients (α_1 , α_2 , β_1 and β_2) obtained by regression analysis. The viscosity and yield stress for a given soil can be calculated from the volumetric concentration and empirical coefficient.

Acknowledgments This research was supported by the Public Welfare & Safety Research Program through the National Research Foundation of Korea(NRF) funded by the Ministry of Science, ICT & Future Planning (2012M3A2A1050977).

References

Imran J, Parker G, Locat J, Lee H (2001) 1D numerical model of muddy subaqueous and subaerial debris flows. *J Hydraul Eng* 127 (11):959–968

Locat J, Demers D (1988) Viscosity, yield stress, remoulded strength, and liquidity index relationships for sensitive clays. *Can Geotech J* 25:799–806

Locat J, Lee HJ, Locat P, Imran J (2004) Numerical analysis of the mobility of the Palos Verdes debris avalanche, California, and its implication for the generation of tsunamis. *Mar Geol* 203 (3–4):269–280

Malet J-P, Laigle D, Remaitre A, Maquaire O (2005) Triggering conditions and mobility of debris flows associated to complex earthflows. *Geomorphology* 66:215–235

O’Brien JS (2003) Reasonable assumptions in routing a dam break mudflow. In: Rickenmann D, Chen CL (eds) *Debris-flows hazard mitigation: mechanics, prediction, and assessment*. Millpress, Rotterdam, pp 683–693

O’Brien JS, Julien PY (1988) Laboratory analysis of mudflow properties. *J Hydraul Eng* 114(8):877–887

Pierosn TC, Scott KM (1985) Downstream dilution of a lahar: transition from debris flow to hyperconcentrated streamflow. *Water Resour Res* 21(10):1511–1524

Takahashi T (1991) *Debris flows*. Balkema, Rotterdam, 165 p

Widjaja B (2011) Case study of mudflow using FLO-2D. In: Fragomeni S, Venkatesan S, Lam NTK, Setunge S (eds) *Incorporating sustainable practice in mechanics of structures and materials*. CRC Press, Leiden, pp 533–537



Hazard Management in a Debris Flow Affected Area: Case Study from Spreitgraben, Switzerland

Daniel Tobler, Isabelle Kull, Mylène Jacquemart, and Nils Haehlen

Abstract

Since 2009 every year several extremely erosive debris-flows occurred in the Spreitgraben near Guttannen. It started with small and harmless flows. Within 3 years they became huge, destructive events with enormous hazard potential. During this period a total amount of 650,000 m³ bedload has been transported into the main river. Strong erosion along the debris flow channel caused considerable deposition at the confluence of the channel and the Aare river. Until now, no constructive protection measure to stop the process evolution has been planned due to the intensity of the erosion and deposition.

Important infrastructures are affected more and more; the major gas pipeline between Germany and Italy had to be relocated and two houses to be abandoned. The main road between the two adjacent villages is endangered in different places or has been locally destroyed already. The only reasonable solution to face these natural hazard processes is land use planning, meaning to avoid any sort of human activity in the fast growing zone of deposition.

As a temporary measure an extensive and sophisticated early warning system has been installed. A profound knowledge of the ongoing processes is the base for a reliable hazard and risk management. By means of a debris flow model scenario based predictions for the near future have been simulated. Hazardous areas have been defined. They build the base for the safety and monitoring concept. In a project handbook the role, task, responsibilities and cooperation with all affected infrastructure owners and public authorities is defined.

The case study focuses on the hazard management in a highly endangered area with an enormous vulnerability. The devastating debris flows push the authorities to adapt yearly to new situations.

Keywords

Debris flow • Hazard management • Modelling • Early warning system • Prediction

D. Tobler (✉) • I. Kull
Natural Hazard Department, GEOTEST SA, Birkenstrasse 15, 3052
Zollikofen, Switzerland
e-mail: daniel.tobler@geotest.ch; isabelle.kull@geotest.ch

M. Jacquemart
GEOPRAEVENT AG, Technoparkstrasse 1, 8005 Zürich, Switzerland
e-mail: mylene.jacquemart@geopraevent.ch

N. Haehlen
KAWA, Natural Hazard Department, Schloss 2, 3800 Interlaken,
Switzerland
e-mail: nils.haehlen@vol.be.ch

Introduction

General Introduction

The village of Guttannen is situated at approximately 1,000 m AMSL in the eastern Bernese Oberland on the northern side of the main Alpine divide. It is surrounded by high mountains—natural hazards are a major element in the village's history. In winter the village is regularly cut off

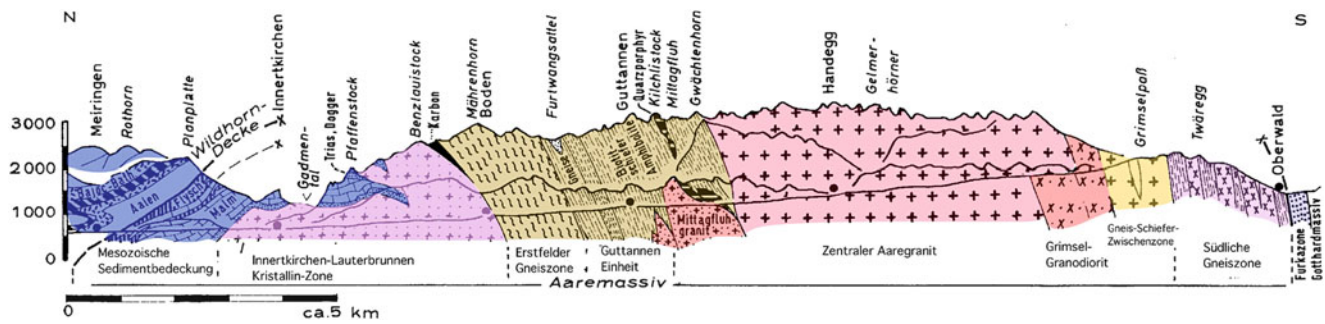


Fig. 1 Geological profile along the Grimsel mountain pass road between the village of Meiringen in the North and Oberwald in the South. The summit of Ritzlihorn is situated in the Guttannen formation

from the outside world by large avalanches. Now the same fate is threatening for the summer months due to the debris flows in the nearby Spreitgraben. Since the major rockfalls on the Ritzlihorn (3,263 m AMSL) in 2009, debris flows have occurred each year, transporting large volumes of bedload into the valley river. Not only the road access to the village of Guttannen is affected, however, but also whole parts of the village itself, as well as the international gas pipeline between Germany and Italy.

Geology and Geomorphology

The sheer rock faces of the Ritzlihorn south-west of Guttannen extend down to the slighter flatter terrain of the Schafegg (2,500 m AMSL). This prominent bedload deposition adjoins a further steep slope that drops down to the cone neck of the Spreitgraben. The dominant feature of the Spreitgraben is the large Holocene cone that extends down to the Aare river and bears witness to a former debris flow deposition area.

Geologically speaking, the rock formations of the Ritzlihorn are made up essentially of highly foliated gneisses (crystalline rock of the Aare Massif, Fig. 1). The rock shows intensive shearing due to clusters of steep parallel joints. The summit area of the striking, pyramid-shaped flank that drops away to the north-east is disintegrating into a pile of rubble due to weathering. The steep foliation of the mountain together with the high proportion of phyllosilicates makes the rock mass especially vulnerable to weathering. This is a major factor in the formation of debris flows.

According to the index map of potential permafrost distribution in Switzerland (BAFU 2005) and Gruber (2012), the summit area of the Ritzlihorn is situated in the area with widespread permafrost (Hasler et al. 2011). The observations on the coarse-block summit flanks and measurements of the base temperature of the snow cover in winters 2010/2011 as well as 2011/2012 confirm the index

and is built of strongly shisted Biotit-Plagioklas-Gneise [modified after Gwinner (1978)]

map. It is highly likely that the debris flows have their origin in the areas of degrading permafrost.

Catchment

The catchment of the Spreitgraben covers an area of 4.7 km² and extends from 950 m AMSL at the confluence with the Aare to the summit of the Ritzlihorn at 3,263 m AMSL. The mean altitude is just under 2,400 m AMSL. The mean gradient in the catchment is 63 % and the mean gradient of the channel in the cone area is 30 %. The catchment basin is principally oriented towards the north to north-east. It can be roughly subdivided into a very steep upper area of rock and boulders with numerous channels, and a lower cone area (Haehlen 2012).

In winter the Spreitlau is one of the biggest avalanche courses in the Canton of Berne. As a result of recurrent road closures, an avalanche gallery was constructed in 1968 at the spot where the cantonal road crosses the graben.

Events 2009–2012

The events of 2009, initiated out of the rockfall depositions at 2,500 m AMSL, transported approximately 100,000 m³ of bedload to the receiving water of the Aare (Fig. 2). The debris flows caused substantial degradation in the Spreitgraben. In 2010 the source of the debris flows shifted to the area of the cone neck at approximately 2,000 m AMSL. The events began in mid-July 2010 and became progressively larger. The two largest events are likely to have been caused by the sudden release of water that had been dammed up in the cone neck below the firm fields. These old-snow fields are located at the transition from the steep mountain flank to the flatter debris fan. Through small-scale debris flow activity from the unconsolidated rock depositions (e.g. Schafegg), bedload was transported underneath the snowpack and then blocked the drainage channels under the snowpack. The release of the



Fig. 2 Bedload deposition in the Aare river 2009 (left) and 2011 (middle) illustrated in an orthophoto (Haehlen 2012). Debris flow modelling using the RAMMS simulation program (forecast for 2011, right, GEOTEST 2012)

dammed-up water produced very large debris flows peaking at between 500 and 600 m³/s. In total, some 250,000 m³ of bedload was carried to the Aare in 2010 (GEOTEST 2010). One-third originated in the rockfall depositions on the Schafegg, and the other two-thirds were erosions from the old Spreitgraben fan.

A feature of the debris flows of September and October 2011 was the fact that, unlike in the previous years, they did not originate in the area of the rockfall depositions on the Schafegg. The detached in another graben system to the west. No mass displacements had previously been observed in this new graben system.

Presumably, a combination of winters with little snow, a warm spring and a hot August–September resulted in the graben that had been snow-covered for decades being uncovered (Haehlen 2012). From below these firn fields there emerged very extensive debris depositions with easily mobilisable material that had previously been covered and frozen hard, but were now exposed to heat and weathering. In the events of 2011 a total of 260,000–300,000 m³ of material was carried to the Aare. The evolution of the degradation in the graben is shown in Fig. 3.

The bedload volumes of the events in the different years were evaluated in detail using aerial photographs and various digital terrain models. For an interpretation of the data, the overall development of the contributing bedload sources plays a major role (Table 1).

Debris Flow Triggers

The analyses of the events of 2009–2011 show that the most important parameters for triggering of debris flows were temperature, antecedent soil moisture and precipitation (GEOTEST 2010, 2012). Alongside the above-mentioned factors, the availability of easily mobilisable bedload from

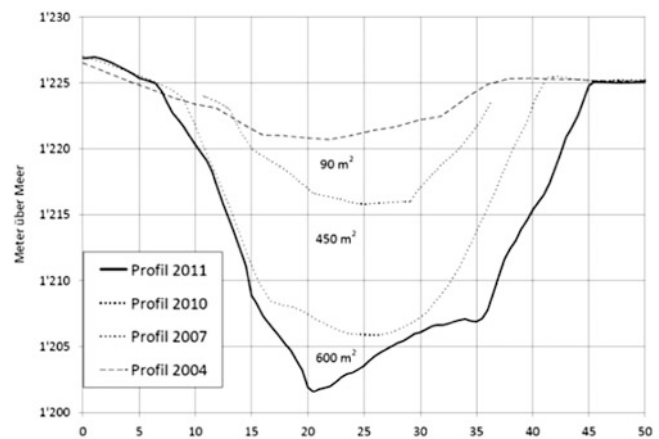


Fig. 3 Evolution of the graben cross-section at 1,200 m AMSL (Haehlen 2012) with indication of channel section area. Topmost line = profil 2004, actual channel = profil 2011

Table 1 Bedload balances 2009–2012 without discharge through Aare river (GEOTEST 2012)

Bedload source	Volume 2009 (m ³)	Volume 2010 (m ³)	Volume 2011 (m ³)
Cone	65,000	120,000	230,000
Firn area	0	30,000	50,000
Schafegg	35,000	100,000	0
Σ _{Deposition}	100,000	230,000	260,000

In 2012 no debris flow event occurred

the rockfall depositions and, potentially, blockages in the area of the firn fields play an important role in the origination of debris flows. The influence of the main meteorological parameters is described below.

Precipitation

The minimum rainfall intensity to trigger a debris flow in 2009–2010 was around 10 mm/h, whereby up until 2010 no

rain gauges with a high-resolution measurement interval were installed in the area. The recordings from the high-resolution precipitation stations of Transitgas AG show that in 2011 total rainfall of at least 40 mm with intensities of 3 mm/h or more were necessary to trigger major debris flows (Haehlen 2012). To date, however, it has not been possible to define a critical volume and/or intensity of rainfall leading to the triggering of a debris flow, as the aforementioned thresholds were also reached several times in 2011 without a debris flow occurring. Additional factors alongside precipitation are likely to play a decisive role in triggering debris flows.

Temperature

The first debris flows between 2009 and 2011 occurred after 24 days of average daytime temperatures above zero on the Jungfrauoch at 3,580 m AMSL (Haehlen 2012). This indicates that a large heat input is needed into the higher parts of the Spreitgraben catchment before a debris flow begins. Alongside this, the temperature curve during the precipitation event is crucial. If the average daytime temperature at 2,900 m AMSL was below 2 °C, no debris flows were recorded even with heavy and short rainfall (GEOTEST 2012).

Antecedent Soil Moisture

In 2009 it initially required at least 100 mm of rainfall over 14 days in order for a subsequent rainfall to trigger debris flows; from the autumn of 2009, 30–50 mm over 14 days was already sufficient. In 2011, there was antecedent soil moisture of at least 40 mm in all three debris flow cases (GEOTEST 2012).

Damage Potential and Protection Measures

The damage potential encompasses the cantonal road (avalanche gallery), the international gas pipeline between Germany and Italy, and a number of houses (see situation in Fig. 4). The gas pipeline was endangered in two locations: where it crosses the Spreitgraben in the vicinity of the avalanche gallery, and further down the valley near the wastewater-treatment facility. During the winter months of 2010/2011, the pipeline was re-laid on the opposite side of the valley near where the Spreitgraben joins the Aare. There it appears to be safe (for the time being). The building immediately opposite the confluence of the Spreitgraben and the Aare was already abandoned and eliminated in 2010.

From the ex-post modelling of the major events of the last 3 years and the forecast modelling for the immediate future carried out using the RAMMS debris flow model, it is clear



Fig. 4 Ritzlihorn's north face with Spreitgraben and Aare river in a Google Earth view

that there is an increasingly large damage potential. Assuming debris flow events of similar magnitude to those in 2011, the damage potential now also extends to certain parts of the settlement (Flesch, Leen) and to the Guttannen wastewater-treatment facility. The cantonal road is endangered in several places, and there might also be additional danger points affecting the gas pipeline.

In many places, constructive measures as part of integrated risk management strategies have successfully mitigated debris-flow threats (Phillips 2006). At the Spreitgraben site, though considered, non-destructive and organizational measures were favoured due to several factors. On one side, the expected erodible volumes and limited space make the construction of retention and deflection dams extremely hard. On the other side, debris-flow, rockfall and avalanche hazards impede extended constructions works, and lastly, the landscape impact of passive measures is significantly lower as well (Tobler et al. 2012).

Integrated Risk Management

Introduction

Owing to the existence of an enormous damage potential a comprehensive, high-tech monitoring and alarm system is in place today. The original simple monitoring system has been refined to create a comprehensive early-warning and alarm service. It is designed to automatically close endangered areas of the cantonal road as well as to inform local

authorities of the current situation via SMS, pager or telephone. The system is running redundantly, allowing for a constant monitoring of the situation in case of secondary events and first-instance trigger line disruption. An online data portal provides users around-the-clock data accessibility of all system components. The whole system may be divided in an alarm-, early warning and research system (Jacquemart et al. 2013).

Alarm System

The components of the alarm system can be assigned to alerting or reacting systems, where the first are designed to detect the debris-flow activity and the latter respond in the form of road closure and information dissemination.

Primary debris-flow detection systems are located at the neck of the debris cone (orange, yellow and green dots in Fig. 5). Trigger lines provide a very reliable yet simple approach to detecting debris flows and mass movements in general. The breaking points of the trigger lines can be precisely defined due to industrially produced pull linkages and the state of the trigger lines can be monitored continuously. Additionally, the simple design of the trigger lines makes them easy and inexpensive to replace after an event. In other setups, the trigger line force is also monitored separately, permitting the detection of false alarms, e.g. due to cable damage.

Two gauge radars with specifically implemented algorithms allow for distance measurements to turbulent surfaces. They provide essential information on flow height in case of debris-flow events. In normal operating mode, the gauge radars trigger flow height warnings, but they are also used as backup alarm triggers in case of secondary events. Two geophones serve as backup alarm systems and data verification, detecting vibrations linked to debris-flow activity.

Alarms issued from any of the alerting devices are transmitted to the data control station via a remote control cable. From there, traffic lights and LED information panels are automatically activated. Four traffic lights ensure the closure of the avalanche gallery as well as the area around Boden (Fig. 5), where the Aare River passes beneath the cantonal road.

Early Warning System

Investigations have shown that the debris-flow hazard potential depends heavily on medium-term meteorological conditions as well as debris availability (Geotest 2010, 2012; Haehlen 2012). A weather station mounted on the debris-flow cone therefore supplies local meteorological

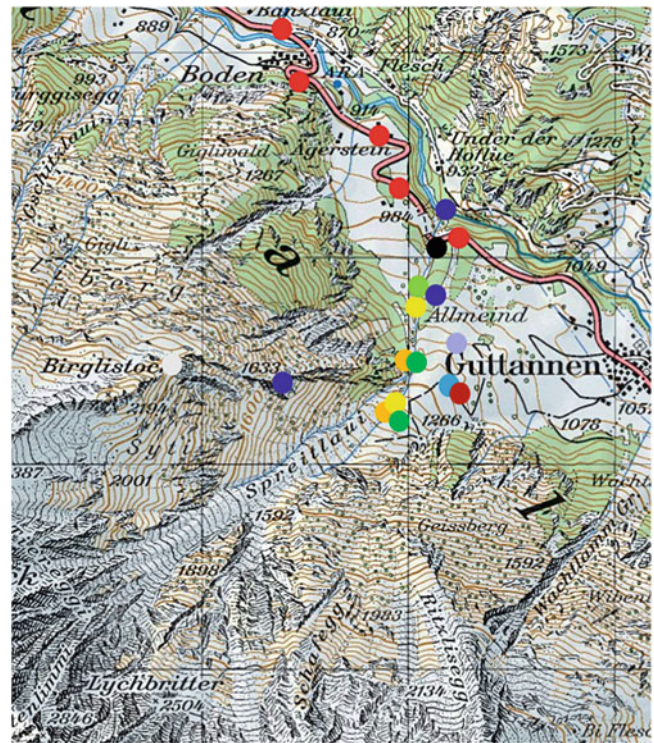


Fig. 5 Monitoring and early warning system consisting of trigger lines (orange), gauge radar (yellow), geophones (green), webcams (dark blue), data station with radio communication (black), rain gauge (bright blue), temperature sensor (brown), laser scanner (bright green), FMCW Doppler radar (purple) and red lights at the road (red)

data to authorities and decision makers at all times. Repeated terrestrial InSAR measurements of the Ritzlihorn northeast face procure information on debris availability and rock fall activity. Webcam images from cameras above the channel, by the avalanche gallery and the Spreitgraben-Aare confluence provide important information on hazard predisposition and serve as useful organizational tools in case of debris-flow events.

Research and Monitoring System

In cooperation with the Swiss Federal Office for the Environment, laser profile scanners that were originally designed for traffic monitoring are being tested at the Spreitgraben site. These scanners provide high resolution data of channel cross section geometry and debris-flow dynamics, supplying essential information for process understanding. The setup of the scanners, mounted at a distance of approximately 1 m from each other, is intended to permit the extraction of flow velocity data based on correlation analysis. Additionally, it is foreseen to excerpt information on grain size distribution and hydrographs from the laser data. The extraction of such parameters from debris flow observations should provide

useful model input data. As another part of the research system, a FMCW Doppler radar system is being tested. The Doppler radar is expected to detect debris flows in the rupture zone, thus roughly doubling the warning time provided to date by the trigger lines. It detects debris flows by measuring flow velocities, similar to the way traffic velocities are monitored. Tests with moving targets have yielded promising results, but the system has not yet been tested in an emergency situation. The detectability of a moving debris flow amongst raindrops blown in the direction of the radar constitutes the largest uncertainty hereby.

Data Transmission

Apart from the direct alarm transmission via remote control cable to the control station, all data is transmitted to the data servers via GPRS network. Aside from the first-order data such as precipitation or webcam images, system status information is also transmitted at regular intervals. This allows for a constant surveillance of logger temperature, battery voltage, logger response time etc. A secure wireless alarm transmission has also been successfully tested and will be implemented in summer 2014. This allows for redundant alarm transmission in case of cable damage. All issued warnings and alarms are automatically distributed as prioritized SMS to authorities and decision makers, via the Swisscom eAlarm net. SMS that are not confirmed by the recipient are automatically forwarded as telephone calls to defined numbers. In case of an event, telephone conferences can be launched by specified users, in order to initiate appropriate measures as soon as possible.

Surveillance Concept

The entire alarm-, early-warning- and monitoring system forms an integral part of the comprehensive safety and surveillance concept. The concept defines the functioning and the individual elements of the surveillance, as well as the tasks and responsibilities of all other parties involved. Responsibilities are assigned to the involved parties and instructions for action are described. In a project handbook all necessary actions and links between stakeholders are diagrammed. In case of an event, every single person knows his role and room of operation. This tried and tested concept has proven to be an extremely efficient and indispensable aid/document in the case of an event.

In case of an event, communication between the major parties involved (commune, road operator, gas pipeline operator, utility operators and endangered private households) is essential. The faster, better and more accurate the communication, the faster clarity about the situation is achieved, enabling the right decisions to be taken within the shortest possible timeframe.

Conclusions

The enormous debris flows in Spreitgraben of the last few years seem to continue over the next years. To handle the huge amount of bedload deposition as well as the hazard and risk management are major tasks for all involved parties—especially the authorities. As a matter of urgency a vast, sophisticated early warning system has been established. A profound knowledge of the ongoing processes is the precondition for reliable hazard and risk management. Scenario-based debris flows have been simulated for the near future in order to estimate the deposit progress of depositions and to define areas at risk. These simulations form the basis for the safety and monitoring concept.

The state-of-the-art infrastructure installed at the Spreitgraben, drawing on a variety of technologies, allows for a very advanced debris-flow monitoring and alerting, and has provided successful detection and surveillance of past events.

References

- Bundesamt für Umwelt (BAFU) (2005) Hinweiskarte der potenziellen Permafrostverbreitung der Schweiz
- GEOTEST AG (2010). Guttannen, Murgang Spreitloui—Analysen und Prognosen. Report No. 09237.8, Zollikofen, 63 p (unpublished)
- GEOTEST AG (2012). Guttannen, Murgang Spreitloui—Analyse und Prognose. Report No. 1409237.3, Zollikofen, 39 p (unpublished)
- Gruber S (2012) Derivation and analysis of a high-resolution estimate of global permafrost zonation. *Cryosphere* 6:221–233
- Gwinner MP (1978) *Geologie der Alpen*, 2nd edn. Schweizerbart, Stuttgart
- Haehlen N (2012) Murgänge Spreitgraben 2011—Ereignisse und Erkenntnisse. Oberingenieurkreis I, Thun, 8 p (unpublished)
- Hasler A, Gruber S, Haeberli W (2011) Temperature variability and offset in steep alpine rock and ice faces. *Cryosphere* 5:977–988
- Jacquemart M, Tobler D, Graf Chr, Meier L (2013) Advanced debris-flow monitoring and alarm system at Spreitgraben. In: *Proceedings IAEG 2013, Torino* (in press)
- Phillips M (2006) Avalanche defense strategies and monitoring of two sites in mountain permafrost terrain, Pontresina, eastern Swiss Alps. *Nat Hazards* 39:353–379
- Tobler D, Kull I, Haehlen N (2012) Hazard management in a debris flow affected area. *GRF, Davos*, pp 692–695



Control Effect of Vegetation on Debris Flows: A Case Study in Batang County, Southwest China

Yanchao Gao, Hua Ge, and Wei Xu

Abstract

Batang County is located in Sichuan Province, southwest China, on the southeast margins of the Qing-Tibet plateau. A wide range of vegetation is distributed from the high altitude mountains to the deep gorges. Batang County is prone to debris flow, of which 151 debris flows were identified by remote sensing techniques (SPOT5) and field surveying in 2009. Based on geomorphology conditions, debris flows can be classified into 33 slope debris flows (SDFs) and 118 gully debris flows (GDFs). The SDFs vegetation coverage was significantly lower than the GDFs vegetation coverage. 72 % of the SDFs have a vegetation coverage below 50 %, and 70 % of the SDFs have a forest coverage below 10 %. However, more than 80 % of the GDFs have a vegetation coverage over 40 %, and only 35 % of GDFs have a forest coverage below 10 %. There is a negative correlation between the SDFs and vegetation coverage. This means that the lower the vegetation coverage, especially forest coverage, the more frequently SDFs occur. This correspondence relationship does not exist in the GDFs. Forest coverage excludes the impacts of shrubland and meadows, thus more accurately reflects the constraining effects of vegetation on debris flow. Vegetation controls debris flow in two ways. (1) Vegetation intercepts rainfall to reduce the volume and velocity of surface runoff, which decreases surface soil erosion. (2) Vegetation roots reinforce the soil, and increase soil shear strength. The primary cause of SDF is surface erosion. The roots of herbs, bushes and trees entwine together to form a dimensional anchorage net which reinforces soil integrity, increases resistance to erosion, and restrains movement by soil particles. The primary cause of GDF is landslides. When a landslide *slide face* is deeper than 3 m, vegetation roots are sparse, have no consolidation capabilities, and vegetation is ineffective at constraining SDF. However, GDF has multiple sources, and happens where the depth of soil is greater than 3 m. In this case, vegetation roots cannot fix the deeper soil body, thus GDF cannot be restrained.

Keywords

Vegetation • Control • Slope debris flow • Gully debris flow • Batang County

Y. Gao (✉)
Chengdu Center, China Geological Survey, Chengdu 610081, Sichuan,
China

Institute of Mountain Hazards and Environment, Chinese Academy of
Sciences, Chengdu 610041, China

University of Chinese Academy of Sciences, Beijing, China
e-mail: gaoyc@imde.ac.cn

H. Ge • W. Xu
Chengdu Center, China Geological Survey, Chengdu 610081, Sichuan,
China
e-mail: 15264427@qq.com; 304934559@qq.com

Introduction

It has been reported that debris flows from a wide range of mountainous environments periodically result in the loss of lives and property damage. A consensus exists that vegetation is one of the most important factors related to debris flows. Many scientists believe that there is a negative correlation between the vegetation coverage and the frequency of debris flows, forest harvesting increases in landslides and

debris flows (Brardinoni et al. 2002; Jakob et al. 2005; Sidle and Ochiai 2006).

But evidence found in recent years indicated that vegetation does not play a simple inhibiting role in debris flow activity. The debris flows occurred frequently before and after human deforestation in Dongchuan, Yunnan, southwest China (Wei and Li 2012). The oldest deposit of debris flow located in Jiangjia valley, southwest China, formed during the Late Pleistocene, while human deforestation did not begin until three centuries ago for copper smelting. Coincidentally, the oldest deposits in Bailongjiang River drainage basin of Gansu, northwest China, formed during the Middle Pleistocene.

In recent years, a number of large-scale debris flows were discovered in dense vegetation areas such as Taiwan, Philippines and Venezuela (Chen et al. 2006; Evans et al. 2007; Pérez 2001). The relationship between vegetation and debris flows needs to be studied comprehensively. The control effects of vegetation on different types of debris flows will provide the basis for their prevention and mitigation. Batang County, located in Sichuan province, southwest China, is highly prone to debris flows and has a wide range of vegetation types.

In this paper, we discussed the relationship between different types of debris flows and vegetation in order to find the control effects of vegetation on debris flow and the driving force mechanism.

Setting

Batang County is located in Sichuan Province, southwest China, on the left bank of the Jinshajiang River. It flows from north to south through the Qing-Tibet plateau. The county area is 8,186 km² and it is covered by mountains and canyons. The highest peak, Dangjiezhenla Mount, has an elevation of 6,060 m, while the lowest valley has an elevation of 2,240 m.

The main fault in the region is the Batang-Moxi Fault which is NS-trending. The Triassic [metamorphic rocks](#) such as slate and phyllite outcrop widely. In the history of the region, there were several earthquakes with magnitudes over 6.0. One earthquake with a magnitude reaching Ms 7.5 on the Richter scale shocked the county in 1870, and an epicentral intensity of 10.

Batang County has a sub-humid continental monsoon climate. Records from 1984 to 2005 indicate that the average annual precipitation was 503.69 mm, and the maximum annual precipitation was up to 828.8 mm in 1998. The maximum daily precipitation reached 42.3 mm, while the maximum rainfall intensity was 25.1 mm/h. The precipitation was not uniformly distributed over the year, with 90 % of the precipitation falling in the wet season from May to

September. The complex geological setting and intense human activities such as deforestation make the area very susceptible to debris flows.

According to Batang [County Annals](#) (2001), the forest coverage of Batang County was 9.3 %, and the vegetation coverage was 68.91 %. A wide range of vegetation is distributed from the high altitude mountains to the deep gorges. The shrubland is distributed among the dry-hot valleys between 2,200 m and 2,800 m. Deciduous, broad-leaved and scrub trees, such as birches, aspen and seabuckthorn are distributed between 2,800 m and 2,900 m. Coniferous and broad-leaved mixed trees, such as pine, fir and poplar are distributed between 2,900 m and 3,300 m. Subalpine coniferous trees are distributed between 3,400 m and 4,200 m. The alpine open trees and thickets are distributed between 4,200 m and 4,500 m. Alpine grasslands are distributed above 4,500 m.

The Relationship Between Vegetation and Different Types of Debris Flow

Material and Methods

The data from Batang debris flows were obtained through surveys, previous data collection and contributions from local residents.

Based on geomorphic and sedimentation conditions, debris flows can be classified as slope debris flow (SDF) and gully debris flow (GDF). Some scientists named them as hillslope debris flows and channelized debris flows (Chen et al. 2009). There are not formal, universally accepted definition of SDF and GDF. The SDF usually does not have a complete drainage area. The surface unconsolidated soil on the top or middle of the slope is eroded by storms and the deposits accumulate in the foothill. They have the landform characteristics of a small gully length (<300 m) and drainage area (<0.01 km²), and steep slope (>30°). When a GDF occurs, erosion, transportation and deposition all occur in the large basin within the mountain range. They have a large gully length (>300 m) and drainage area (>0.1 km²), and mild slope (<30°) (Chen et al. 2009). The source of SDF generally appear as surface erosion while the sources of GDF in large drainage areas usually are diverse, such as landslide, surface erosion and bed erosion. Both the scale and run out of GDF are larger than SDF.

There were 118 GDFs and 33 SDFs accounted in Batang County in 2009. Figures 1 and 2 show the typical characteristics of these two types.

Vegetation coverage data were obtained during the wet season, from May to September, 2009, when vegetation growth flourishes. We got the vegetation coverage through SPOT5 remote sensing data, and interpreted them with in-

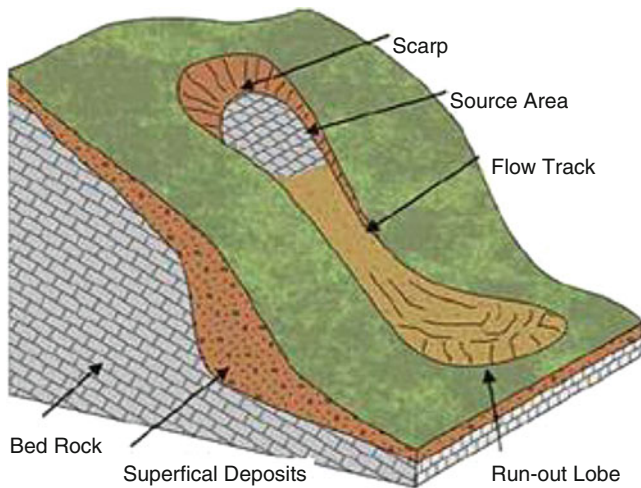


Fig. 1 A typical slope debris flow (Nettleton et al. 2005)

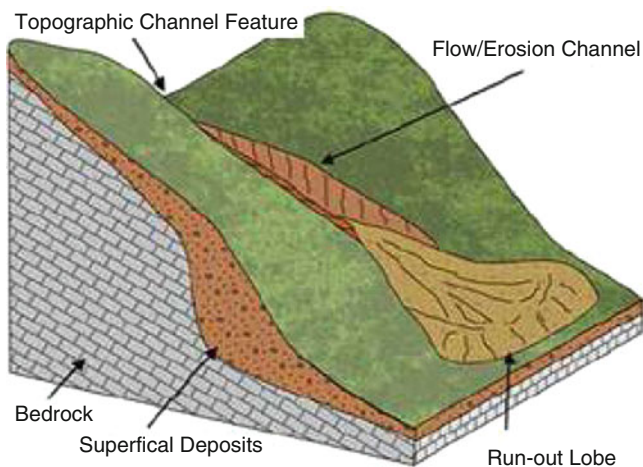


Fig. 2 A typical gully debris flow (Nettleton et al. 2005)

situ survey. Based on the vegetation in the region, the land uses are simplified into four categories: forest, shrubland, grassland, and barren.

Correlation Analysis Between Vegetation and Different Types of Debris Flows

Due to the deeper roots, forest has better capability to conserve soil and water, than shrub and grass. Thus we describe the vegetation using two indicators: forest coverage and vegetation coverage. Vegetation coverage includes forest, shrubland and grassland. The coverage was divided into ten ranges: 0–10 %, 10–20 %, 20–30 %, 30–40 %, 40–50 %, 50–60 %, 60–70 %, 70–80 %, 80–90 %, and 90–100 %. Then we classified SDF and GDF into these vegetation coverage ranges. The debris flows data were normalized for comparison because the number of GDFs was nearly four times of the

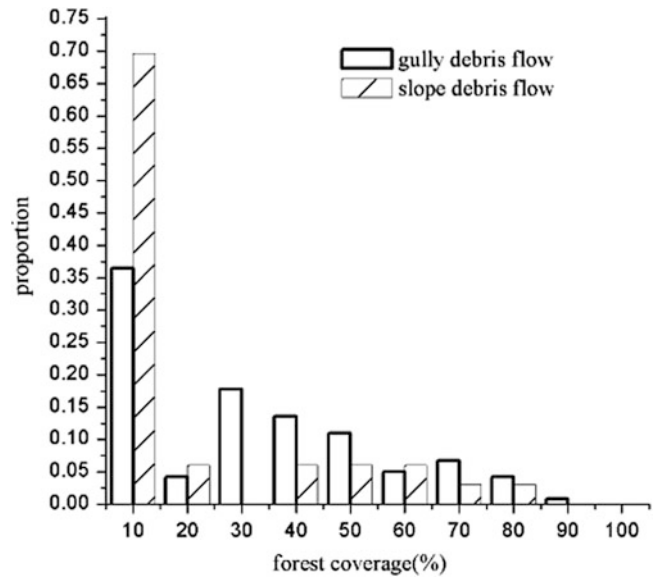


Fig. 3 The vegetation coverage in two types of debris flows

SDFs. Figure 4 shows the correlation between vegetation coverage and the two types of debris flows. The horizontal axis represents ten levels of vegetation coverage, and the vertical axis shows the proportion of the two types in each level. Figure 5 shows the correlation between forest coverage and debris flows using the same criteria.

As seen in Fig. 3, SDF vegetation coverage is significantly lower than the GDF. 72 % of the total SDF has a vegetation coverage of under than 50 %. The vegetation coverage in GDF is discretely distributed, which can be found in each level. 80 % of the total GDF has a vegetation coverage of greater than 40 %. This means that even in dense vegetation regions, debris flows can still easily occur.

The vegetation-debris flow correlation is more significant in Fig. 4. 70 % of the SDF has a forest coverage below 10 %, which means that there is a negative correlation between the SDF and forest coverage. Only 35 % of GDF forest coverage was below 10 percent. The other 65 % is discretely distributed.

The function between vegetation (forest) coverage and debris flows frequency is difficult to obtain because of the absence of debris flow frequency. However, a quantitative evaluation can be drawn through this comparison. In short, the lower the vegetation coverage, especially forest coverage, the more SDFs occur. This correspondence relationship does not exist in GDFs.

Vegetation Distribution in Two Types of Debris Flows

SDF and GDF were indexed. Figure 5 shows the vegetation coverage in each slope hazard and indicates that the vegetation in SDFs are sparse. Most of the slopes are barren and

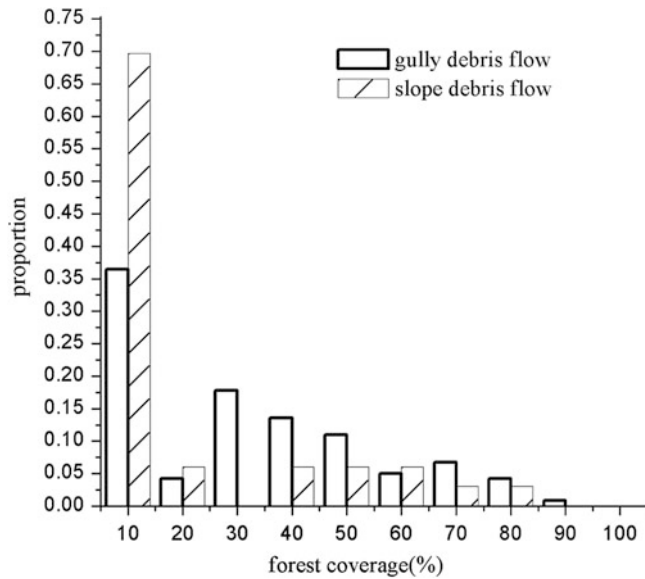


Fig. 4 The forest coverage in two types of debris flows

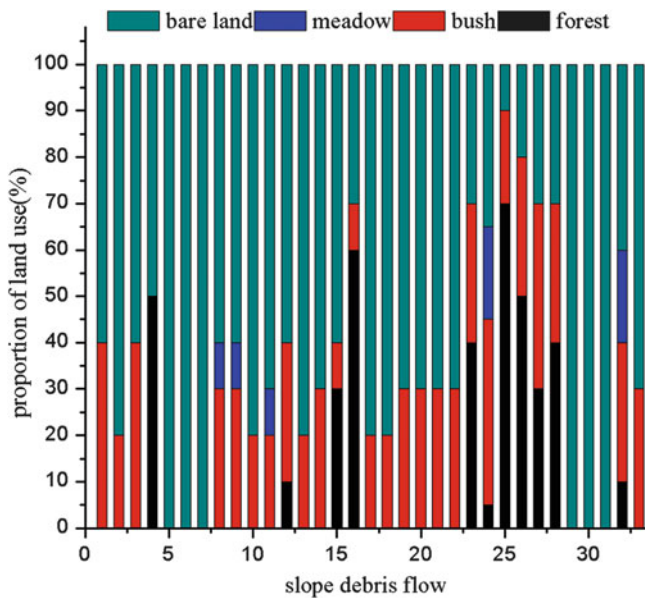


Fig. 5 The proportion of land uses in slope debris flows. The *horizontal axis* represents the debris flow index, and the *vertical axis* represents the proportion of different land uses such as forest, shrubland, grassland and barren land in each slope debris flow

shrub distributed loosely, even when there is little forest and grassland. Six slope debris flows are completely bare. Figure 6 shows the vegetation coverage in each gully hazard using the same criteria. The vegetation in gullies is generally denser than sloped ones.

The proportion of different types of land uses in Figs. 5 and 6 are normalized. Tab.1 shows the vegetation coverage in each type for GDF and SDF. The land uses in the SDF are distributed as follow: 64.39 % barren land, 21.52 % shrubland, 11.97 % forest, and 2.12 % grassland. The distribution

in GDF was: 43.29 % bare land, 28.18 % shrubland, 23.04 % forest, and 5.58 % grassland. The grassland accounted for the smallest proportion in both types. One reason is that the alpine valleys are not conducive to grassland. Another reason is that the grassland has a poor control effect over debris flow. Once a debris flow occurs, the grassland will be destroyed and turned to bare land.

We can draw three conclusions through the analysis above. (1) Vegetation exhibits a good control effect on slope debris flows. There is a negative correlation between the vegetation coverage, especially forest coverage and SDF. 70 % of the SDF occurred when there was less than 10 % forest coverage. (2) There is no significant correlation between vegetation coverage and gully debris flow. The GDF occurs in either lush vegetation drainage or bare drainage. (3) Forest coverage is more effective when controlling debris flows. The reason is that vegetation coverage contains the area of shrubland and grassland, and their control effect on debris flow is very weak. However, forest coverage can eliminate this interference (Table 1).

Discussions

Vegetation Control Effect on Debris Flow

The debris flow encompasses sediment, boulders and flood water. The vegetation control effects on debris flow works in two ways: reducing flow and reducing sediment. The tree leaves, bush leaves and grass overlap together to form protective nets and absorb some rainfall and ease surface soil erosion from rainfall. On the other hand, vegetation can reinforce soil on a slope by its roots. Roots and rhizomes of vegetation interact with soil to produce a composite material. The roots are fibres of relatively high tensile strength and adhesion embedded in a matrix of lower tensile strength, thus the effective cohesion of the whole material increases (Schmidt et al. 2001). Most vegetation roots are concentrated at the top 1 m of soil and are supported by strong tap-roots. The forest reinforcement is better than other vegetation reinforcements due to its strong root system.

The Source of the Two Types of Debris Flows

The vegetation control has different effects on SDF and GDF. This diversity exists because SDF and GDF have different causes as previously mentioned in the definition. Generally there are three kinds of sources: surface erosion, landslides and bed erosion. Most debris flows were composed of more than one source. The source types and proportion in different kinds of debris flows have been counted

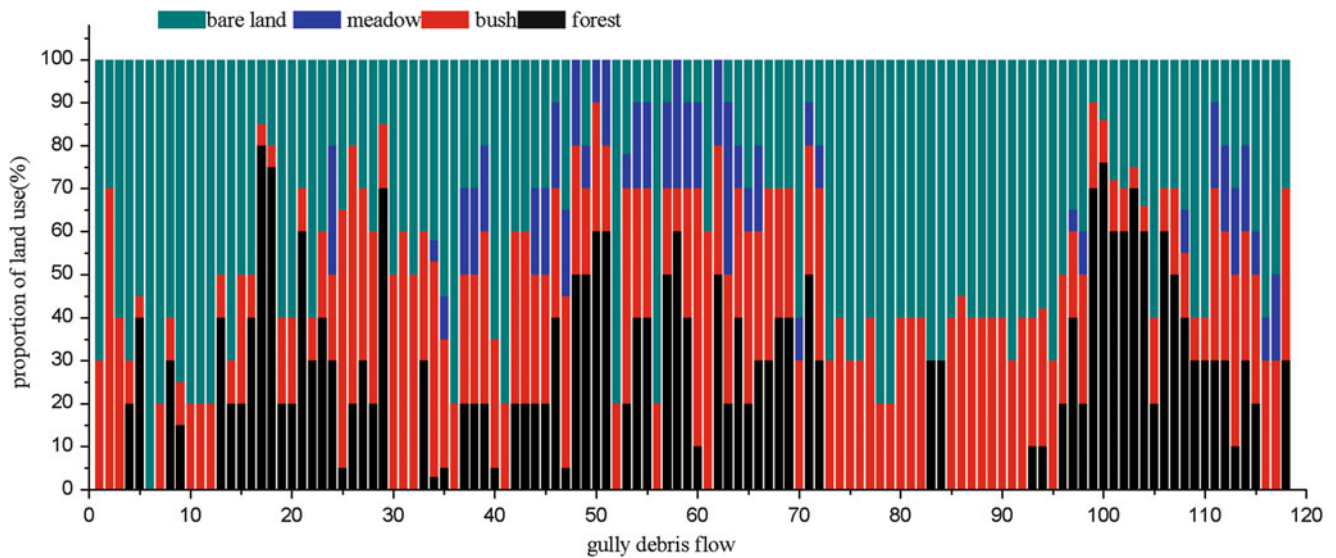


Fig. 6 The proportion of land uses in gully debris flows. The *horizontal axis* represents the debris flow index, and the *vertical axis* represents the proportion of different land uses such as forest, shrubland, grassland and barren land in each gully debris flow

Table 1 The land uses coverage in two types of debris flow (%)

Debris flows	Forest	Shrubland	Grassland	Barren
GDF	23.04	28.18	5.58	43.29
SDF	11.97	21.52	2.12	64.39

as follow. If a SDF has two source (i.e. surface erosion and landslide), then this hazard will be accounted both in the surface erosion sort and the landslide sort. Out of 33 SDFs, there were 27 in which surface erosion existed, thus the probability of surface erosion in SDF was 81.82 %. Figure 7 indicates the probability of three kinds of loose source of debris flows. In SDF, landslide probability was 49.70 %, and bed erosion probability was 21.21 %. In GDF, surface erosion probability was 33.39 %, landslide probability was 83.90 %, and bed erosion probability was 58.47 %. The scales of each source have not been statistically analyzed in this paper, but the distribution characteristics are similar to source frequency when sample sizes were large enough. That is because when the sample size is large, the source frequency can be used to replace source distribution.

Figure 7 indicated that most of sources in SDF were surface erosion. There were a few landslides in deep grooves, while bed erosion only took a small part. Surface erosion was the main component of SDF. The GDF usually has larger drainage, so their sources were more complex than the SDF. Landslides were the main component of GDF.

The Control Effect on Different Kinds of Sources

The main cause of SDF is surface erosion. The roots of herbs, bushes and trees entwine together to form a

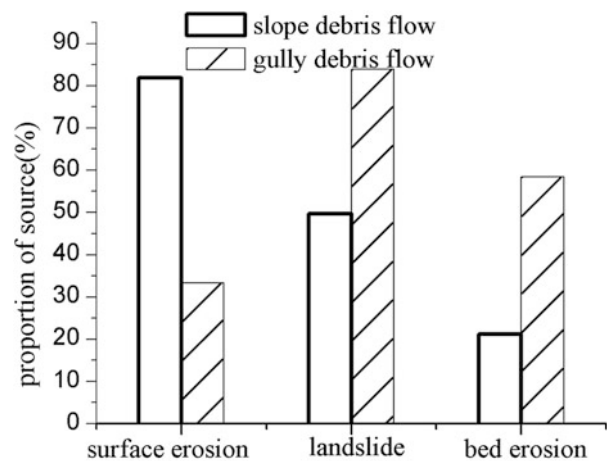


Fig. 7 The proportion of causes in two types of debris flows

dimensional anchorage net which reinforces soil integrity, resistance to erosion, and restrains soil particle movement. The tap-roots of trees even anchor into the bed rock. Loose sediment on the slope was reinforced, and the necessary source for SDF was reduced. So vegetation coverage and SDF have a desirable negative correlation. Slope surface runoff is less likely to occur in dense vegetation regions.

Roots and rhizomes of vegetation interact with soil and produce a composite material, where high tensile roots are entwined in a matrix of lower tensile strength. As a result, cohesion of the whole material is enhanced.

The cause of GDF was diverse, and vegetation was ineffective at controlling it. When loose sediment in a gully was primarily landslide, especially with a landslide

slide face deeper than 3 m, vegetation roots were sparse and had no consolidation capabilities. If the slope is partially unstable and the wind is strong, the slope can slide as a whole due to the pulling force from roots. This will strengthen the debris flows. Vegetation has limited capability in reducing volume of surface runoff. When the rainfall intensity and precipitation exceed a certain threshold, the surface soil becomes saturated, and all the rainfall will turn to surface runoff. This runoff will eventually converge into valleys runoff.

Conclusions

Vegetation is usually considered as one of the most important factors impacting debris flows, and bio-engineering is usually considered as an important means of comprehensive mitigation. Through studying the vegetation coverage and forest coverage in different types of debris flows from Batang County, Sichuan Province, we found that vegetation, especially forest vegetation, has a significant control effect on slope debris flow. However, the control effect of vegetation on gully debris flows is not negligible because of the different causes. Surface erosion is the main cause of slope debris flow, while vegetation roots can reinforce the loose sediment on the slope to restrain surface yield. The causes of gully debris flows are diverse, and landslides are usually the main component. Vegetation roots and forest tap-roots are sparse in sliding surface, and were ineffective at soil reinforcement. This shows that vegetation cannot control the gully debris flow.

Recognizing the different effects that vegetation has on debris flow is significant for the prediction and prevention of debris flows. Slope debris flows rarely occur in dense vegetation regions, so bio-engineering

can be used as a method for slope debris flow mitigation. When thick landslides and heavy rainfall occur in a valley, a large scale debris flow may be induced. So the vegetation coverage should not be used as a criterion for distinguishing whether a debris flow tends to occur nor should it be used as a control method for debris flows.

References

- Brardinoni F, Hassan MA, Slaymaker HO (2002) Complex mass wasting response of drainage basins to forest management in coastal British Columbia. *Geomorphology* 49:109–124
- Chen H, Dadson S, Chi YG (2006) Recent rainfall-induced landslides and debris flow in northern Taiwan. *Geomorphology* 77 (1–2):112–125
- Chen JC, Lin CW, Wang LC (2009) Geomorphic characteristics of hillslope and channelized debris flows: a case study in the shitou area of central Taiwan. *J Mt Sci* 6:266–273
- Evans SG, Guthrie RH, Roberts NJ (2007) The disastrous 17 February 2006 rockslide-debris avalanche on Leyte Island, Philippines: a catastrophic landslide in tropical mountain terrain. *Nat Hazard Earth Syst Sci* 7:89–101
- Jakob M, Bovis M, Oden M (2005) The significance of channel recharge rates for estimating debris-flow magnitude and frequency. *Earth Surf Process Landforms* 30:755–766
- Nettleton IM, Martin S, Hencher S (2005) Debris flow types and mechanisms. Crown Press, Edinburgh, 119p. ISBN 0-7559-4649-9
- Pérez FL (2001) Matrix granulometry of catastrophic debris flows (December 1999) in central coastal Venezuela. *Catena* 45 (3):163–183
- Schmidt KM, Roering JJ, Stock JD (2001) The variability of root cohesion as an influence on shallow landslide susceptibility in the Oregon Coast Range. *Can Geotech J* 35(5):955–1024
- Sidle RC, Ochiai H (2006) Landslides: processes, prediction, and land use, vol 18, Water resources monograph. American Geophysical Union, Washington, DC
- Wei DL, Li YH (2012) The geochemistry analysis of debris flow sediment in the Quaternary at the east fringe of Qinghai-Tibetan Plateau. *Res Soil Water Conserv* 19(6):292–298 (in Chinese)



Efficiency of Slot-Check Dam Group on Debris Flow Control in Shengou Basin, Kunming, China

Yuhua Zou, Kaiheng Hu, Xiaoqing Chen, and Wei Zhong

Abstract

Slot-check dams are widely applied to mitigate debris flow hazards in China. This paper aims at providing an analysis of their performance in the field and establishing a verification to evaluate the efficiency of the slot-check dam group and a single slot-check dam in sediment control. The study area is Shengou basin in Dongchuan district, Kunming in China, where debris flows directly threatens the safety of more than sixty thousand people living in the major city. The analysis is based on a relatively detailed field knowledge consisting of topographical, sediment data and geometry of the group of five slot-check dams at Shengou basin. The results suggest that the conserving sediment volume of each dam has a close relationship with its relative location in the group, gradually decreasing from upstream to downstream. The channel slope has a little influence on the conserving effect. The accumulated sediment volume upstream a check dam strongly depends on its sub-catchment characteristics and increases with the controlled catchment area of the dam and the distance from the dam to the upstream most. A semi-empirical relationship between the conserving efficiency for each subsystem of the group, defined as the percentage of its conserved sediment volume, and the subsystem's catchment parameters is developed.

Keywords

Slot-check dam group • Efficiency • Debris flow • Hazard mitigation

Introduction

Open check dams are commonly used to control sediment transport associated with debris flows (Fiebiger 1997; Heumader 2000; Armanini and Larcher 2001; Catella et al. 2005; Huebl and Fiebiger 2005). Slot-check dam, an open-type check dam, has been shown to be efficient in reducing

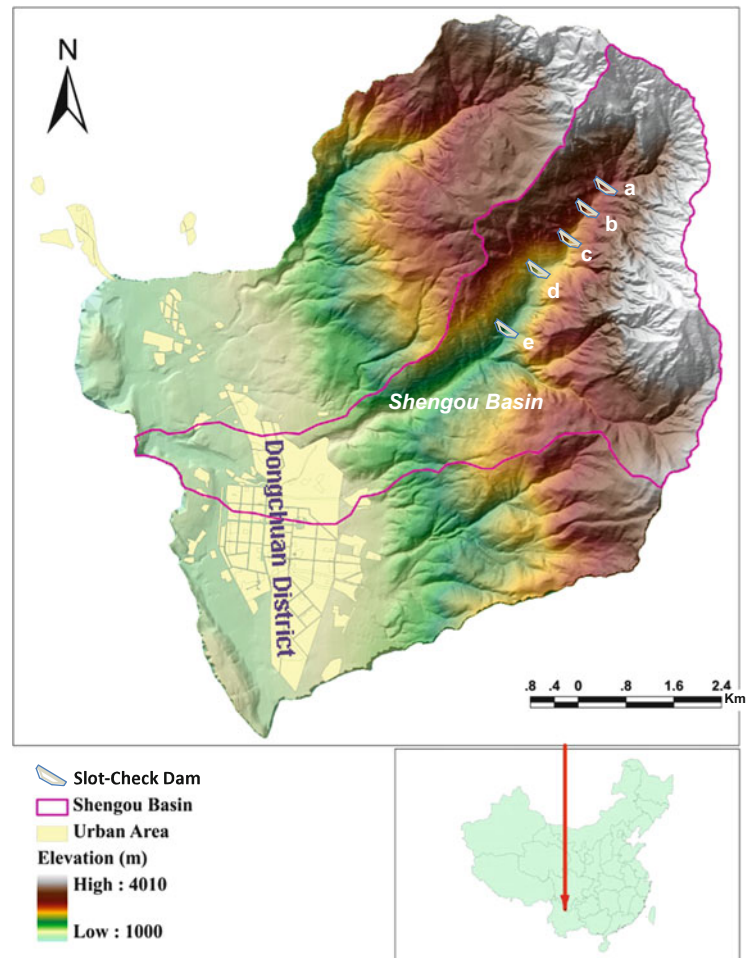
debris flow run-out intensity (Remaître et al. 2008; Jia et al. 2011); it can trap a great amount of sediment with its storage capacity and perfectly protect the downstream area (Li 1997; Mizuyama 2008).

Recent theoretical and experimental study (Jia et al. 2011) clarify partly the capturing process of deposits upstream a slot-check dam during a debris flow event. However, there is no quantitative evaluation on slot-check dam group performance in the field.

This paper is aimed at evaluating the efficiency of a slot-check dam within a slot-check dam group and the efficiency of the group in the field in order to provide a quantitative method for estimating the long term efficiency of slot-check dam group in debris flow hazards mitigation.

Y. Zou • K. Hu (✉) • X. Chen • W. Zhong
Key Laboratory of Mountain Hazards and Earth Surface Processes,
Institute of Mountain Hazards and Environment, CAS, Chengdu
610041, China
e-mail: zyh@imde.ac.cn; khhu@imde.ac.cn; xqchen@imde.ac.cn;
liutenantz@imde.ac.cn

Fig. 1 The slot-check dam group in Shengou basin



Study Area

Physiographic Settings

Shengou basin covers an area of about 32 km² and is located in the northeastern Dongchuan district, extending 103°09'07" ~ 103°15'00"E and 26°04'47" ~ 26°09'03"N (Fig. 1). It is a tributary of the right bank of Xiaojiang River, and a typical debris-flow gully in the mountainous regions of southwestern China. The basic parameters of Shengou basin are listed in Table 1.

Hydrology

Shengou basin pertains to a subtropical monsoon climate zone where precipitation in rainy season accounts for 88 % of total annual precipitation.

The rainfall of the basin during the rainy season in 2012 was recorded by a rain gauge at a distance of about 5.8 km upstream (elevation 2574 m, latitude 26°8'8.6", longitude

Table 1 Main characteristics of Shengou basin (Catchment area A ; Relative altitude H_m ; Main stream length L ; Average slope S ; Average width B)

A (km ²)	H_m (m)	L (km)	S (%)	B (m)	$Q_p = 0.01/\text{m}^3/\text{s}$	
					Flood	Debris flow
31.77	2,520.00	13.55	20.30	51.20	118.95	282.86

103°13'46.2"). The total rainfall in the region during the monitoring period (June to November 2012) was 945.8 mm, with heavy rains occurring three times, twice in July and once in September, and their 24-h rainfall intensities were 62.4 mm, 59.7 mm and 76.2 mm, respectively. The monthly rainfall intensities from June to November 2012 are shown in Fig. 2.

History of Debris Flows

Historically, two large-scale debris flows occurred in Shengou basin, causing seven casualties and the destruction of 375 hm² of farmland. Recent small-scale debris flow

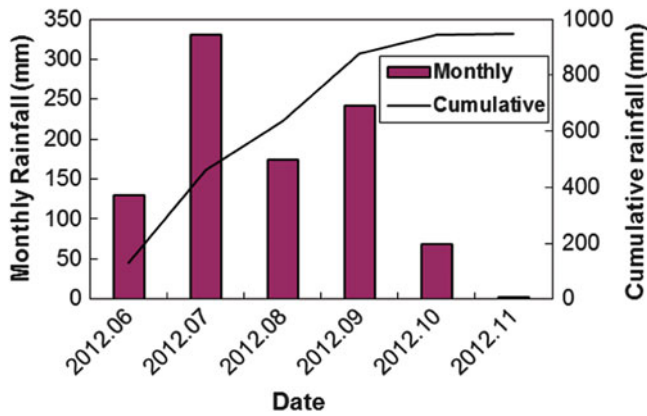


Fig. 2 Rainfall intensity of Shengou basin during the rainy season in 2012

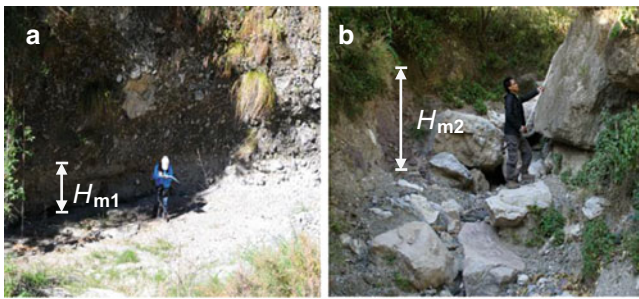


Fig. 3 The mud marks recognized in Shengou gully: (a) in the main channel, (b) in the branch channel, where H_{m1} , H_{m2} show the height of the mud marks

events have been recognized by the mud marks left on the banks in Shengou Gully (Fig. 3).

Debris-flow hazards greatly threaten the safety of more than sixty thousand people living in the downstream urban area since Shengou river flows directly across the major city of Dongchuan.

The Slot-Check Dam Group in Shengou Gully

In order to control sediment transport and mitigate debris flow hazard, a slot-check dam group had been built in the upper region of Shengou basin (Fig. 1). The main characteristics of the slot-check dams are listed in Table 2. The performance of the slot-check dams has been investigated and recorded (Fig. 4).

The mean particle size of debris flow deposits at the upstream and downstream side of each dam are compared in Fig. 5. Mean particle size of deposits at the upstream side of each dam is larger than that at its downstream side. It means larger boulders in debris flow had been blocked and deposited

Table 2 Basic parameters of the slot-check dams (Length of dam L_d ; Height of dam H_d ; Height of drainage hole in dam h ; Width of drainage hole in dam b ; Design discharge Q_{proj} and Relative return time T_r)

Slot-check dam	L_d (m)	H_d (m)	h (cm)	b (cm)	Q_{proj} (m^3/s)	T_r (years)
a	63.9	8.0	50	40	96.55	100
b	79.0	12.0	40	40	96.55	100
c	65.5	10.0	40	40	96.55	100
d	100.0	10.5	50	40	96.55	100
e	62.0	6.0	50	40	96.55	100

at the upstream side of the dams and the finer part drained through the open slots of dams. Maximum decrease in the mean size is about 3.4 mm for the dam *a*, and minimum is about 1.8 mm for the dam *e*. Therefore, the conserving function was utilized most fully for the first dam, and the conserving effect gradually decreased from upstream to downstream dams. Moreover, the mean particle size of deposits at upstream side of each dam is not equal to but larger than that at downstream side of its upper dam, since coarse grains had been generated by lateral erosion at both sides of the gully and gathered at the upstream side of each dam. In general, the mean particle size of deposits was step by step decreased by the slot-check dam group which reflects the effectiveness of the slot-check dam group in debris flow hazard mitigation.

Equilibrium deposits had been blocked and formed upstream each dam. Characteristics of deposits upstream the dams are measured on Nov. 29th (Table 3).

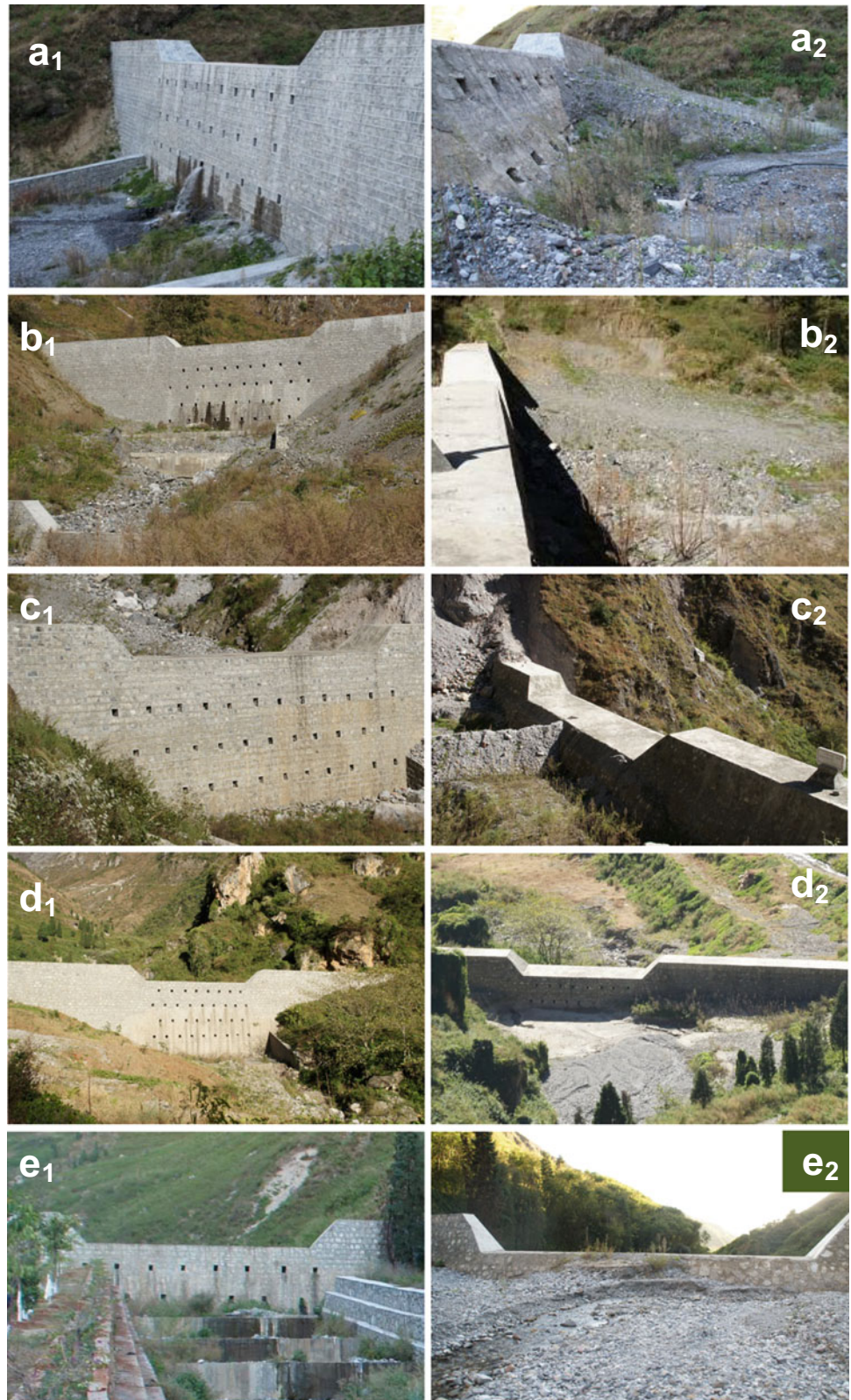
Figure 6 shows the sketch of deposits stored within the slot-check dam group where sediments with different mean particle size were blocked by the slot-check dam at each step. It shows that the channel slope has no big influence on the dam's conserving capability. The dam's function largely depends on its relative location in the group.

From the field investigation, the base of each check dam is not exposed. Hence, bed erosion between each couple of check dams is not serious. Except for the upstream source, the sediments stored within each couple of check dams mainly come from the bank and the lateral slope on both sides of the gully, rather than from the bed.

Analytical Studies

The volume of deposit stored within each slot-check dam storage and the accumulated volume of deposits upstream each dam are related to the control catchment area at that point and the distance from the dam to the most upstream point in the catchment (Fig. 7). The volume within the dam storage initially increases with the increase of its controlled catchment area (Fig. 7a). But after the volume increases to a

Fig. 4 Performance of slot-check dams in Shengou basin on Nov. 29th, 2012 (**a₁–e₁**. View from the downstream, and **a₂–e₂**. View from the upstream of the five check dams, i.e. **a–e** in Fig. 1)



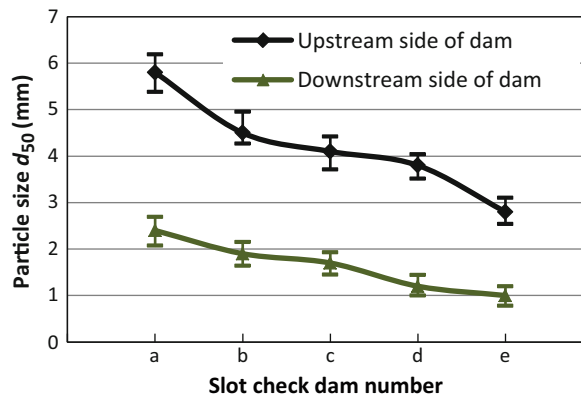


Fig. 5 Mean particle size of debris flow deposits at the upstream and downstream side of each dam

Table 3 Deposits upstream each slot-check dam measured on Nov. 29th, 2012 (Height of deposit upstream the slot-check dam H_s ; Volume of deposit stored within the storage of the slot-check dam V_s)

Slot-check dam	H_s (m)	V_s (10^3m^3)
a	2.90	7.20
b	6.20	26.40
c	7.40	32.80
d	6.10	29.00
e	4.60	14.50

maximum value at a dam located at the midstream, it decreases with the controlled catchment area. However, the accumulated volume upstream the slot check dam always increases with the controlled area, initially it increases sharply, then slightly and gradually approaches to a stable value. About 60 percent of sediment has been blocked upstream the third dam.

The relationship between the deposit volume stored upstream the slot-check dam and the distance from the dam to the first dam in the check dam group is similar. The accumulated deposit volume upstream the slot check dam

approaches to a stable value when the dam sits far away from the first dam in the group.

The efficiency of a slot-check dam within a group consisting of a series of slot-check dams η_i can be represented by the ratio of the volume of sediment stored upstream it the total volume within the dam group V_m :

$$\eta_i = \frac{V_i}{V_m} \quad (1)$$

where V_i is the accumulated volume of deposit stored upstream the dam. The efficiency of slot-check dam in the dam group associated with the characteristics of the catchment mountain is listed in Table 4.

Intuitively, the sediment volume stored upstream each dam is related to the characteristics of the catchment area A_p and the geometry of the opening slots of dam M_p :

$$V_i = f(A_p, M_p) \quad (2)$$

$$\text{where } \begin{cases} A_p = \alpha A_{ci} L_{ci} \\ M_p = (1 - \varepsilon_i) m_i \end{cases} \quad (3)$$

$$\eta_i = \frac{\alpha A_{ci} L_{ci} (1 - \varepsilon_i) m_i}{A_c L_c} \quad (4)$$

where α is a shape coefficient:

$$\alpha = \frac{A_c}{L_c^2} \quad (5)$$

and A_{ci} is the catchment area controlled by the slot-check dam; L_{ci} is the distance from the dam to the most upstream point of the region; ε_i is the open rate of the dam; m_i is the coefficient of transport capacity of the slot-check dam, related to the opening size of the slot of check dam to the representative particle size of debris flow, $0 < m_i < 1$. For a stony debris flow (Mizuyama et al. 1995),

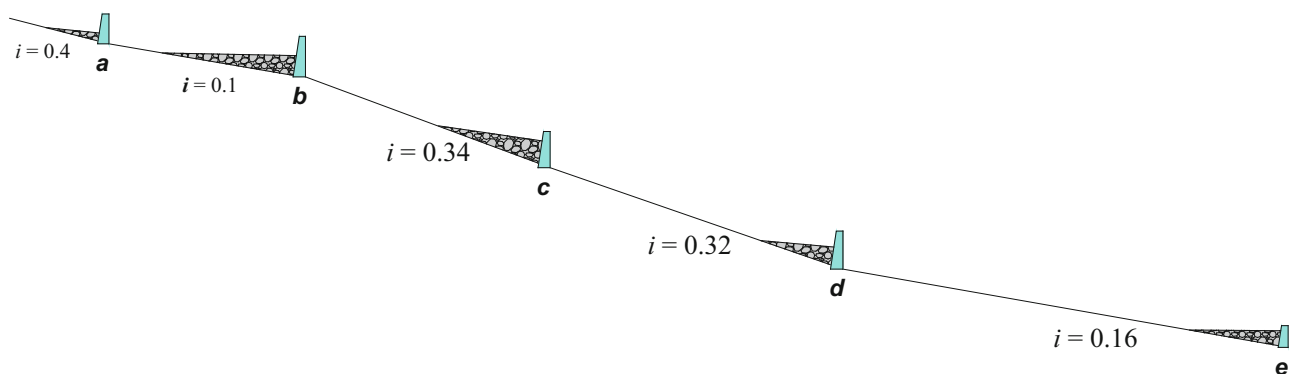


Fig. 6 Sketch of equilibrium deposit upstream each slot-check dam (i = slope gradient of the reach sector)

Fig. 7 Relationship between the volumes of sediment stored upstream the slot-check dam and (a) the drained catchment area, and (b) the position of the check dam along the river

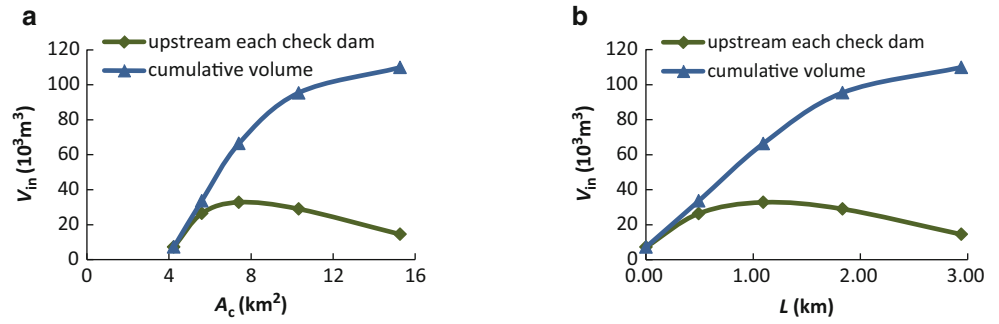


Table 4 The efficiency and associated catchment parameters of each slot-check dam in the dam group (Volume of deposits stored within the storage of each couple of dams v_i ; Efficiency of a slot-check dam in the group η_i ; Efficiency of a slot-check dam in the group calculated by the efficiency model $\bar{\eta}_i$)

Slot-check dam	A_{ci} (km^2)	L_{ci} (km)	v_i (10^3 m^3)	V_i (10^3 m^3)	η_i	$\bar{\eta}_i$
a	4.24	1.97	7.20	7.20	0.07	0.16
b	5.60	2.46	26.40	33.60	0.31	0.42
c	7.41	3.06	32.80	66.40	0.60	0.53
d	10.32	3.80	29.00	95.40	0.87	0.74
e	15.26	4.91	14.50	109.90	1.00	1.00

$$m_i = 1 - 0.11 \left(\frac{B_{\min}}{D_{95}} - 1 \right)^{0.36} C_a^{-0.93} \quad (6)$$

where B_{\min} is the minimum space of slots, C_a is the sediment concentration at the peak discharge occurring at the front part of the debris flow and D_{95} is 95 percent grain size.

Conclusions

The slot-check dam group, an interconnected defense system, plays an important role in sediment transport control. Large boulders in debris flows are blocked and deposited whereas the finer grains flow downstream through the open slots. Equilibrium deposits formed upstream each slot-check dam within the check dam group which prevents the downward development of movable solid material and protects the downstream area.

Field investigation on a slot-check dam group at Shengou shows that the mean grain size of sediments decreases by 3.4 ~ 1.8 mm when conserved by a check dam in the group. Therefore, the utilization of the dams' conserving function gradually decreases from upstream to downstream. The dam's conserving effect largely depends on its relative location in the group, and has no significant relationship with the channel slope. The accumulated volume upstream a check dam always increases with the dam's controlled area and the distance from the dam to the most upstream point, and gradually approaches to a stable value. Then, a semi-empirical relationship between the conserving efficiency for each subsystem of the group and the subsystem's catchment

parameters is proposed. Comparison of the efficiency of the dam group in sediment control with that of a single dam in the group could be employed to evaluate quantitatively the role of each single dam and of the whole group at mitigating debris flow hazards. This will be useful for designing such a slot-check dam group.

Acknowledgments This research was substantially supported by Knowledge Innovation Project of The Chinese Academy of Sciences (Approval No. KZZD-EW-05), the National Natural Science Foundation of China (No. 41072270) and the Natural Science Foundation of Institute of Mountain Hazards and Environment, CAS (No. SDS-QN-1304).

References

- Armanini A, Larcher M (2001) Rational criterion for designing opening of slit check dam. *J Hydraul Eng* 127(2):94–104
- Catella M, Paris E, Solari L (2005) Case study: efficiency of slit-check dams in the mountain region of Versilia basin. *J Hydraul Eng* 131(3):145–152
- Fiebigger G (1997) Structures of debris flow countermeasures. In: Proceedings of 1st international conference on debris-flow hazards mitigation: mechanics, prediction, and assessment. ASCE, New York, NY, pp 596–605
- Heumader J (2000) Technical debris-flow countermeasures in Austria—a review. In: Proceedings of 2nd international conference on debris-flow hazards mitigation: mechanics, prediction, and assessment. ASCE, Taipei, pp 553–564
- Huebl J, Fiebigger G (2005) Debris-flow mitigation measures. In: Jakob M, Hungr O (eds) Debris-flow hazards and related phenomena. Springer, Berlin, pp 445–487
- Jia ST, Cui P, Chen XQ, Huang K, Li Q (2011) Experimental study of regulating barrage and transportation properties of debris flow by

- silt-trap dam. Chin J Rock Mech Eng 30(11):2338–2345 (in Chinese)
- Li DJ (1997) The application of permeable dam in debris flow control. Chin J Geol Hazard Control 8(14):60–66 (in Chinese)
- Mizuyama T (2008) Structural countermeasures for debris flow disasters. Int J Erosion Control Eng 1(2):38–43
- Mizuyama T, Kobashi S, Mizuno H (1995) Control of passing sediment with grid-type dams. J Jpn Erosion Control Eng Soc 47(5):8–13 (in Japanese)
- Remaître A, Van Asch TWJ, Malet JP, Maquaire O (2008) Influence of check dams on debris-flow run-out intensity. Nat Hazard Earth Syst Sci 8:1403–1416



The Influence of Accumulated Precipitation on Debris Flow Hazard Area

Ko-Fei Liu, Shih-Chao Wei, and Ying-Hsin Wu

Abstract

Debris flow warning system in Taiwan uses effective accumulated precipitation as warning criteria. Little research studied the affected area associated with different accumulated precipitation. The Taipei DF024 potential debris flow torrent is used as an example to study the relation between affected area and accumulated precipitation. Three accumulated precipitations in 24 h, 300 mm, 500 mm (official warning criteria) and 700 mm, are chosen for comparison. Average rainfall intensity per hour is calculated from accumulated rainfall through the Monobe Formula. Total flow rate is estimated by the Rational Formula and discharge hydrograph. Maximum debris flow volume is determined by the Equilibrium Concentration Formula. From field investigation, all source of debris are distributed on landslide areas and river bed. DEBRIS-2D is used to simulate debris flows. The results show that hazard area is proportional to precipitation, and the thickness of maximum debris flow accumulation is between 1.62 m and 2.13 m. The relation between accumulated precipitation and hazard area can provide officials additional information on resident evacuation.

Keywords

Accumulated precipitation • DEBRIS-2D • Hazard area

Introduction

The effective accumulated precipitation in 24 h is used as warning threshold for debris flow disaster warning in Taiwan (Lee et al. 2006). According to Soil and Water Conservation Bureau in Taiwan, there are 1,660 potential debris flow torrents in Taiwan and 50 potential debris flow torrents in

Taipei (the capital of Taiwan). In Taiwan, the warning threshold value of debris flow is separated into nine brackets between 200 mm and 600 mm (each bracket is 50 mm), and the value for potential debris flow torrents in Taipei are usually set between 500 mm and 600 mm. When the accumulated rainfall reaches the warning level, all residents in the affected area must be evacuated.

In addition to providing a rainfall warning threshold value for each potential debris flow torrent, the Soil and Water Conservation Bureau also gives local residents an evacuation map with debris flow affected area for evacuative reference. With this evacuation map, the local officers can design an evacuative plan that can help local residents retreat to a shelter before the rainfall warning threshold value is reached.

Presently, delineating debris flow affected area uses an empirical method (Ikeya 1995) which includes only topographical data. As a result, debris flow affected areas is

K.-F. Liu (✉)
Department of Civil Engineering, National Taiwan University, Taipei
10617, Taiwan

Hydrotech Research Institute, National Taiwan University, Taipei
10617, Taiwan
e-mail: kfliu@ntu.edu.tw

S.-C. Wei • Y.-H. Wu
Department of Civil Engineering, National Taiwan University, Taipei
10617, Taiwan
e-mail: d01521001@ntu.edu.tw; wu.ahsin@gmail.com

independent of rainfall. In reality, a higher accumulated rainfall usually induces a larger landslide mass or debris flow. For some high-population area, such as Taipei, the error in delineate affected area can have serious consequence. With different accumulated precipitations, therefore, the variation of debris flow affected areas will be important information for evacuative plan and residential retreat.

In order to consider the effect of accumulated precipitation on debris flow affected area, a two-dimensional debris flow simulation is required to provide more precise result. We use DEBRIS-2D (Liu and Huang 2006) to assess debris flow in the present study. The Taipei DF024 potential debris flow torrent is chosen as an example to demonstrate the effect of accumulated precipitation.

Simulation of Debris Flow

Introduction to DEBRIS-2D Simulation Program

The debris flow simulation program, DEBRIS-2D, was developed in 2006 (Liu and Huang 2006). In DEBRIS-2D, the bulk of debris flow is regarded as a continuum and non-Newtonian fluid. As for non-Newtonian fluid, the adopted constitutive relation is the three-dimensional generalized one proposed by Julien and Lan (1991) as follows

$$\tau_{ij} = \left(\frac{\tau_0}{\varepsilon_{II}} + \mu_d + \mu_c \varepsilon_{II} \right) \varepsilon_{ij}, \text{ for } \tau_{II} \geq \tau_0, \quad (1)$$

$$\varepsilon_{II} = 0, \text{ for } \tau_{II} < \tau_0, \quad (2)$$

where $(i, j) = \{x, y, z\}$;

$$\varepsilon_{II} = \left(\frac{1}{2} \varepsilon_{ij} \varepsilon_{ij} \right)^{1/2} \text{ and } \tau_{II} = \left(\frac{1}{2} \tau_{ij} \tau_{ij} \right)^{1/2} \quad (3)$$

Where $\varepsilon_{ij} = \frac{1}{2} \left(\frac{\partial u_i}{\partial x_j} + \frac{\partial u_j}{\partial x_i} \right)$ denotes strain-rate tensor; τ_0 is the yield stress; μ_d and μ_c are dynamic viscosity and turbulent-dispersive coefficient respectively. Equation (1) denotes the constitutive relation in the region where the shear stress is greater than yield stress; Eq. (2) is for the region with shear stress less than yield stress.

The governing equations are mass and momentum conservation equations with shallow water assumption. The coordinate system is the Cartesian coordinate with the average bed elevation as x-axis. From the analysis of field data, Liu and Huang (2006) found that shear layer thickness is less than 10 % of total flow depth. So the shear layer can be ignored to the leading order. After simplification and rearrangement, the resulting governing equations in conservative form are conservation of mass

$$\frac{\partial H}{\partial t} + \frac{\partial(uH)}{\partial x} + \frac{\partial(vH)}{\partial y} = 0, \quad (4)$$

and conservation of momentum in x and y directions

$$\begin{aligned} \frac{\partial(uH)}{\partial t} + \frac{\partial(u^2H)}{\partial x} + \frac{\partial(uvH)}{\partial y} = & -gH \cos \theta \left(\frac{\partial B}{\partial x} + \frac{\partial H}{\partial x} \right) \\ & + gH \sin \theta - \frac{1}{\rho} \frac{\tau_0 u}{\sqrt{u^2 + v^2}}, \end{aligned} \quad (5)$$

$$\begin{aligned} \frac{\partial(vH)}{\partial t} + \frac{\partial(uvH)}{\partial x} + \frac{\partial(v^2H)}{\partial y} = & -gH \cos \theta \left(\frac{\partial B}{\partial y} + \frac{\partial H}{\partial y} \right) \\ & - \frac{1}{\rho} \frac{\tau_0 v}{\sqrt{u^2 + v^2}}, \end{aligned} \quad (6)$$

where $H(x, y, t)$ is the flow depth; $B(x, y, t)$ is the bed topography; $u(x, y, t)$ and $v(x, y, t)$ are depth-averaged velocities in x - and y - direction respectively; $\tan \theta$ is the average bottom slope; τ_0 and ρ are debris-flow yield stress and density, which are all assumed to be constant here; g is the gravitational acceleration. Since the bottom shear layer is ignored, the yield stress becomes the dominant bottom stress.

With nonlinear treatment, the initiation criterion for any originally stationary debris pile is derived as

$$\begin{aligned} \left(\frac{\partial B}{\partial x} + \frac{\partial H}{\partial x} - \tan \theta \right)^2 + \left(\frac{\partial B}{\partial y} + \frac{\partial H}{\partial y} \right)^2 \\ > \left(\frac{\tau_0}{\rho g \cos \theta H} \right)^2 \end{aligned} \quad (7)$$

The derivatives of B and H represent pressure effect and $\tan \theta$ is the gravitational effect. The right hand side is the resistance from yield stress. According to (7), debris flow can start to move only if pressure and gravitational effects exceed the yield stress effect.

Debris-2D uses finite difference method for the governing equations (4), (5) and (6). In spatial discretization, the first-order upwind method is applied to discretize convective term and central difference method is used for the remaining terms. The explicit third-order Adams-Bashforth method is used for time advancing. During computation the time step Δt is fixed and holds the Courant-Friedrichs-Lewy condition, and the volume of debris flow bulk is conserved.

For start of computation, Debris2D uses (7) to determine where debris flow can be initialized. If (7) is not satisfied, the mass stays stationary with zero velocities and unchanged flow depth. During computation, if the maximum velocity in the whole computational domain is less than numerical error, the computation terminates automatically.

Debris Flow Simulation

The main inputs needed in DEBRIS-2D are topography and initial debris source distribution. The only rheological parameter, yield stress, can be measured from field samples (Liu and Huang 2006; Coussot and Boyer 1995). From field investigation on landslide locations, one can find the dry debris volume and its corresponding locations. Thereafter, the debris flow volume can be determined by equilibrium concentration formula (Takahashi 1981), the equilibrium solid volume concentration can be expressed as

$$C_{d\infty} = \frac{\rho \tan \theta}{(\sigma - \rho)(\tan \phi - \tan \theta)} \leq 0.603, \quad (8)$$

where ρ is water density; σ is the density of dry debris (around 2.65 g/cm^3); ϕ is internal friction angel (about 37°); θ is average creek bottom slope. With the calculated equilibrium concentration, the input volume of debris flow can be estimated by two steps. Firstly, we assume there will be enough water from rainfall to initialize all dry debris in field. Thus the dry material available determines total flow. We refer this as debris-controlled debris flow. The volume of debris-controlled debris flow V_1 can be calculated as

$$V_1 = \frac{V_d}{C_{d\infty}}. \quad (9)$$

Then we must check if there is enough water from the catchment. If the water volume available V_w is less than $V_1(1 - C_{d\infty})$, then only part of the dry debris source can be mobilized. The total amount of debris flow will be controlled by limited water volume. We refer this type as rainfall-controlled debris flow. The volume of rainfall-controlled debris flow V_2 can be calculated as

$$V_2 = \frac{V_w}{1 - C_{d\infty}}. \quad (10)$$

The real volume input for debris flow is the smaller one between V_1 and V_2 (Liu et al. 2009).

Verification and Application of DEBRIS-2D

DEBRIS-2D program was verified by analytical solution and flume test with error under 0.2 % for predicting front location (Liu and Huang 2006). As all input parameters are determined by physical procedures, no calibration or back-calculation is needed for inputs of DEBRIS-2D.

DEBRIS-2D has also been verified with real events. Liu and Huang (2006) simulated the debris flow hazard area in Nantou County, Taiwan from Typhoon Herb. The hazard

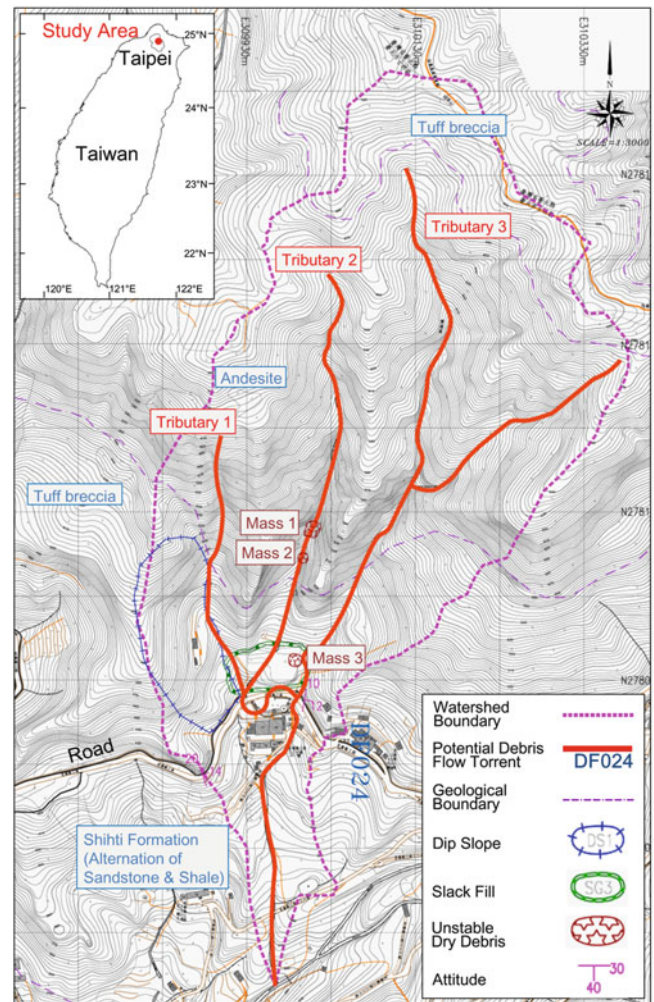


Fig. 1 Geology graph of Taipei DF024 debris flow potential stream (from Geotechnical Engineering Office, Public Works Department of Taipei City 2011)

Table 1 Conversion of debris flow volume

No.	(1) Dry debris volume V_d (m^3)	(2) Debris flow volume V_1 (m^3)
Mass 1	864	1,432.84
Mass 2	345.60	573.13
Mass 3	2,050	3,399.67
Total	3,259.60	5,405.64

zone achieves good agreement compared with field measurements with error less than 5 %. Liu and Wu (2010) assessed the debris flow event in Inje, northeast South Korea in 2006, and the simulated flow depth and distribution agreed with the field investigation very well. Tsai et al. (2011) used this program in 2006 to simulate the debris flow in Daniao tribe, eastern Taiwan. The hazard area predicted agrees very well with the real event occurred in 2009.

Table 2 Estimating for total volume of debris flow

(1) Accumulated rainfall (mm)	(2) Concentration time (min)	(3) Average rainfall intensity (mm/h)	(4) Effective rainfall intensity (mm/h)	(5) Peak flow rate (cm)	(6) Debris flow volume V_2 (m ³)	(7) Erosion area (m ²)
300	22.22	204.48	153.36	2.53	4,249.47	NA
500	16.79	411.27	308.45	5.09	6,456.28	1,050.64
700	13.96	651.63	488.73	8.06	8,504.22	3,098.58

For mitigation of debris flow, DEBRIS-2D also has been applied in vulnerability risk assessment (Liu and Li 2007), hazard loss estimation (Liu et al. 2009), and design of countermeasure (Liu and Wu 2014). DEBRIS-2D also has been compared with FLO-2D (Wu et al. 2013); the results show that DEBRIS-2D gives better assessment in hazard area delineating and flow depth predicting, especially for granular debris flow. Under above-mentioned successful validation and applications in real debris flow events, DEBRIS-2D is proven to be a trustworthy and practical tool for assessment of debris flow hazard.

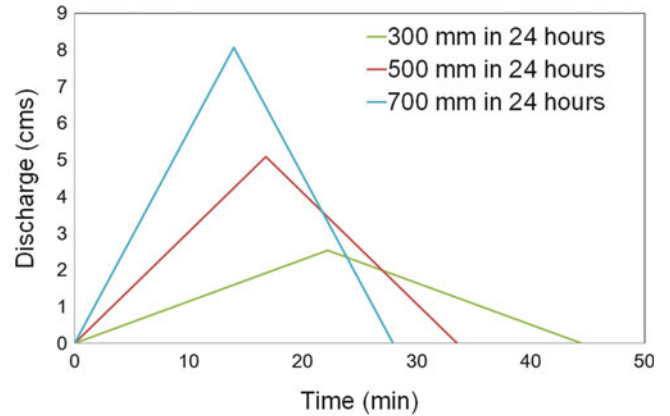
Case Study of Taipei DF024

Description of Taipei DF024

The Taipei DF024 potential debris flow torrent is located in Taipei, Northern Taiwan (Fig. 1). The watershed area and average slope of Taipei DF024 is approximately 31 ha and 36 % ($\approx 21.8^\circ$) respectively. There are three tributaries in the upstream as shown in Fig. 1. The average stream length is about 950 m. The average total annual precipitation is 3163 mm. From Soil and Water Conservation Bureau, the debris flow warning threshold value is set to be 500 mm in 24 h.

The geology formation in the upstream of Taipei DF024 is Andesite with deformed rock. In the midstream, the major geology formation is Tuff breccia with some slack fill. The Shihti formation, alternation of Sandstone and Shale, is distributed in the downstream part with mild slope.

According to field investigation (Geotechnical Engineering Office, Public Works Department of Taipei City 2011), the total solid volume is approximately 3,260 m³ and distributed on the hillside and stream bed of tributary 2 (Fig. 1). From field examination, there is no surface water flow in tributary 1 and 3. From interview of local residents, we learned that there is no surface water in tributary 1 and 3, even in typhoon or torrential rainfall events. Therefore, we don't consider the possibility of debris flow in tributary 1 and 3. With the deposit material brought from tributary 2, the yield stress is measured as 750 Pa and is used in all simulations.

**Fig. 2** Triangular hydrograph for tributary 2

Debris-Controlled Debris Flow

From field investigation, one can find the dry debris volume V_d and its corresponding locations, as shown in column (1) of Table 1. With the water density of 1 g/cm³, the equilibrium concentration $C_{d\infty}$ is calculated as 0.685 by (7), so 0.603 is used. The volume of debris flow V_1 were calculated by (9) and shown in column (2) of Table 1.

Rainfall-Controlled Debris Flow

For accumulated rainfall effect, we choose three different accumulated precipitations in 24 h for comparison: 300, 500 (official warning threshold value) and 700 mm. By using the Monobe formula, one can find the relation between average rainfall intensity per hour I and accumulated rainfall in 24 h R_{24} as

$$I = (R_{24}/24)(24/t_c)^{2/3}, \quad (11)$$

where t_c is concentration time and the value can be estimated through kinematic wave formula (Wooding 1965) as follows

$$t_c = \left(\frac{n_o L_o}{\sqrt{S_o} i_e^{0.67}} \right)^{0.6} + \frac{B}{2i_e L_o} \left(\frac{2i_e n_c L_o L_c}{\sqrt{S_c} B} \right)^{0.6}, \quad (12)$$

where n_o and n_c are roughness coefficients for surface flow and channel flow respectively; L_o and L_c are surface-flow

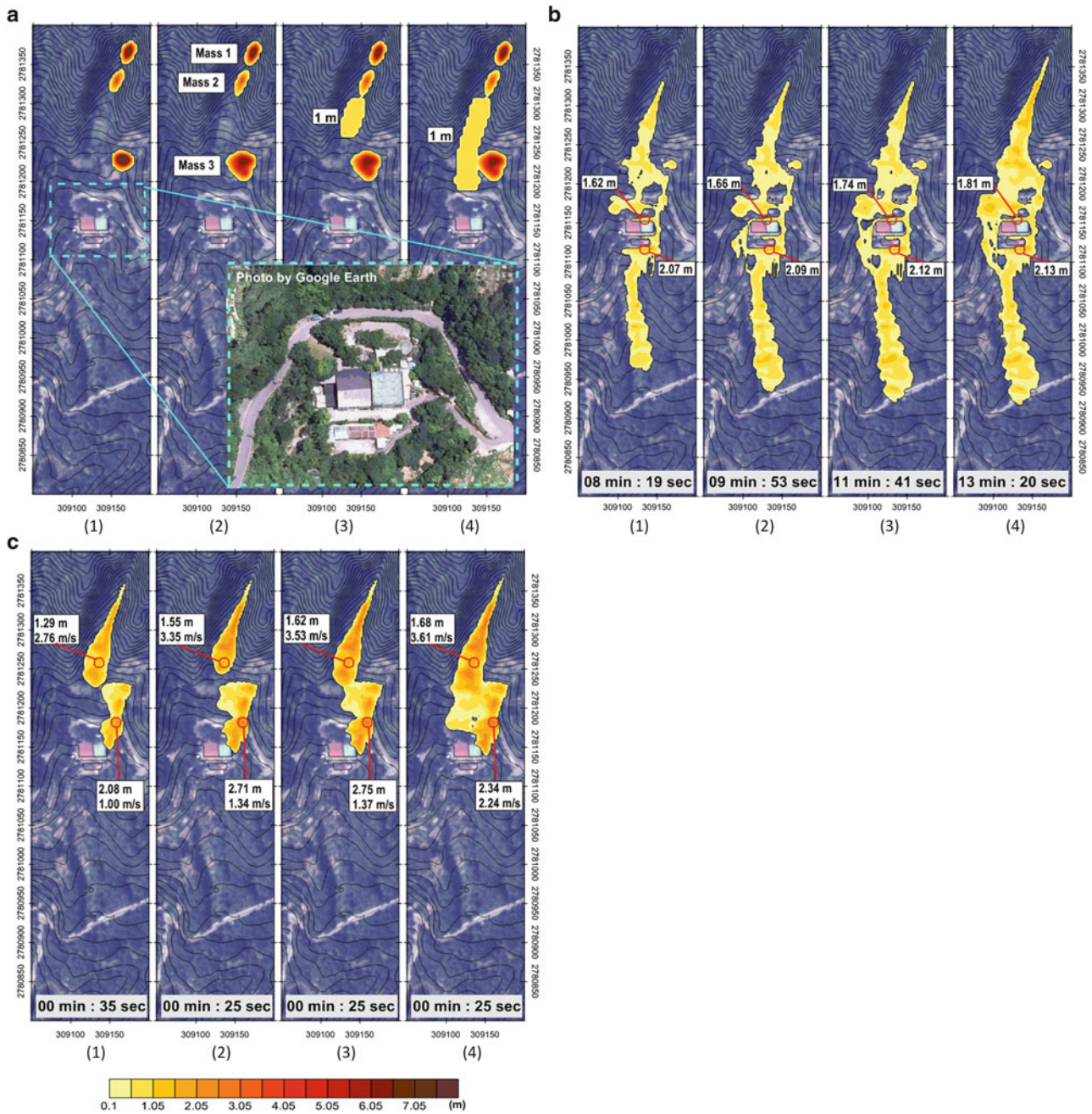


Fig. 3 Distribution of Debris flow depth at different time. The figure from *left to right* are: (1) 300 mm, (2) 423 mm, (3) 500 mm and (4) 700 mm of accumulated rainfall in 24 h. (a) Initial mass distribution, (b) The time while debris flow front hit the house, and (c) Final deposition

length and channel length respectively; S_o and S_c are surface-flow slope and channel slope respectively; B is channel width; i_e is effective rainfall intensity. n_o and n_c has been calibrated as 1 and 0.6 (Lee 2003). From Digital Terrain Model, L_o , L_c , S_o , S_c , B were measured as 65.08 m, 586.67 m, 0.5, 0.39, 2 m, respectively. By recursive calculation, the average and effective rainfall intensity were determined by (11) and (12), as shown in column (3) and (4) of Table 2.

The peak flow rate Q_p is estimated by the Rational formula and the corresponding triangular hydrographs shown in Fig. 2. With the triangular hydrographs, the total water volume V_w can be calculated as $0.5 \cdot Q_p \cdot t_c$. With equilibrium concentration formula, the volumes of debris flows V_2 are calculated as shown in column (6) of Table 2. If $V_2 - V_1$ is negative, it means available debris amount controls the total volume of debris flow. Otherwise, rainfall controls the

total volume of debris flow. From field survey, the maximum erosion depth can be estimated as 1 m. Therefore, we assume the extra debris flow volume ($V_2 - V_1$) will be induced from bed erosion, and the erosion area is calculated in Table 2 and the distribution is shown in Fig. 3a.

Simulation Results

We consider four different 24 h accumulated rainfall for debris flow volume in the simulation: (1) 300 mm: water is not enough to mobilize all dry debris, (2) 403 mm: water is just enough to mobilize all dry debris, (3) 500 mm: stream bed erosion begins, and (4) 700 mm: serious stream bed erosion occurs. The simulation results are shown in Fig. 3.

When the front of debris flows reaches residential area, the maximum velocities are at the upstream part of debris flow, and the velocities are 2.76 m/s, 3.35 m/s, 3.53 m/s, and 3.61 m/s (see Fig. 3b). But the maximum flow depth is located at the county road, and the corresponding depths are 2.08 m, 2.71 m, 2.75 m, and 2.34 m, respectively. The corresponding velocities at the maximum flow depth locations are 1.00 m/s, 1.34 m/s, 1.37 m/s, and 2.24 m/s, respectively.

The residential houses in the field are one story concrete house of 3 m height. Houses are assumed to be intact during the event. For the final deposition in Fig. 3c, the thickness of maximum debris flow accumulation occurs around the house and increase with accumulated rainfall. In front of the houses, it is the county road. The maximum final deposition depths are between 1.62 m and 1.81 m. The maximum accumulated depths behind the houses are between 2.07 m and 2.13 m. The final affected area is larger for larger accumulated rainfall. But the difference is not so significant. The furthest reaches of debris flows compared with the front of debris flow with smallest accumulated rainfall as 0 m have the difference 26 m, 39 m, and 43 m, respectively.

The simulation results indicated that county road will be blocked in all cases, so the evacuative plan must avoid using this county road or the evacuation time should start even earlier before warning. The local residents also need to pay attention to the muddy water after debris flows stop.

Conclusions

We use four different accumulated precipitations to assess the debris flow affect area. The results show that hazard area increases as accumulated precipitation

increases. The thickness of maximum debris flow accumulation is between 1.62 and 2.13 m as shown in Fig. 3c. The county road in front of the house will be covered by debris flows in all cases. The relation between accumulated precipitation and hazard area can provide officials additional information on resident evacuation route and design of countermeasure.

Acknowledgments The authors wish to thank Geotechnical Engineering Office, Public Works Department of Taipei City Government for financially supporting of this research and providing valuable survey data.

References

- Coussot P, Boyer S (1995) Determination of yield stress fluid behavior from inclined plane test. *Rheol Acta* 34(6):534–543
- Geotechnical Engineering Office, Public Works Department of Taipei City Government (2011) 2011 Assessment and field investigation of debris flow potential creek in Taipei city creeks (in Chinese)
- Ikeya Hiroshi (1995) Investigation of disaster on debris flow. Sankai Tong (in Japanese)
- Julien PY, Lan Y (1991) Rheology of hyperconcentrations. *J Hydraul Eng* 117(3):346–353
- Lee KT (2003) Development of the watershed digital topography information system for integrated basin management (IV) (in Chinese)
- Lee MH, Jan CD, Kuo FH (2006) Rainfall threshold criteria for debris flow occurrence and its application in Taiwan. In: 2006 AJT international symposium on sediment-related disaster prevention, Tainan, pp 15-1–15-7
- Liu KF, Huang MC (2006) Numerical simulation of debris flow with application on hazard area mapping. *Comput Geosci* 10(2):221–240
- Liu KF, Li HC (2007) The assessment of debris flow emergency measures. *J City Plan* 34(1):57–73 (in Chinese)
- Liu KF, Li HC, Hsu YC (2009) Debris flow hazard assessment with numerical simulation. *Nat Hazard* 49:137–161
- Liu KF, Wu YH (2010) The assessment of debris flow hazard in Korea using Debris2D. In: INTERPRAEVENT 2010-international symposium in Pacific Rim, Taipei, Taiwan, pp 820–827
- Liu KF, Wu YH (2014) The influence of countermeasure on debris flow hazards with numerical simulation. In: Sassa K (ed) *Landslide science for a safer geo-environment*, vol 1. Springer, Heidelberg. doi:10.1007/978-3-319-04999-1_66
- Takahashi T (1981) Debris flow. *Annu Rev Fluid Mech* 13:57–77
- Tsai MP, Hsu YC, Li HC, Liu KF (2011) Application of simulation technique on debris flow hazard zone delineation: a case study in the Daniao tribe, Eastern Taiwan. *Nat Hazard Earth Syst* 11:3053–3062
- Wooding RA (1965) A hydraulic model for the catchment-stream problem. I. Kinematic-wave theory. *J Hydrol* 3(3):254–267
- Wu YH, Liu KF, Chen YC (2013) Comparison between FLO-2D and Debris-2D on the application of assessment of granular debris flow hazards with case study. *J Mt Sci* 10(2):293–304



Concrete Torrent Check-Dams and Debris-Flow Magnitudes

Matjaž Mikoš, Andrej Kryžanowski, Manica Martinčič, and Jošt Sodnik

Abstract

Large sediment-retention dams, built in a cascade (a chain of check dams), can impose hazard (hyper-concentrated sediment flow, debris flow), if they fail during torrential flash floods or when destroyed by overtopping by a debris flow initiated on slopes or in natural torrential channels. Using estimates of specific annual sediment yields in torrential watersheds on one hand, one can use the area of the watershed and the storage volume of torrential check dams in order to estimate the maximum potential of sediment stored in the retention volume of the check dams—as a first approximation for the magnitude of the debris flows initiated by the dam failure. On the other hand, one can use debris-flow susceptibility maps to estimate likelihood for triggering of potential debris flows in torrential watersheds under investigation (we used debris-flow susceptibility map of Slovenia in the scale 1:250,000). A field study on the status of several tens of check dams in the Upper Sava River in NW Slovenia with regard to the question whether they should be taken as a possible debris-flow source was performed.

Keywords

Check dams • Debris flows • Hazard assessment • Risk mitigation • Torrent control

Introduction

Debris flows are rapid type of mass movements on slopes or in steep torrential channels. They are multiphase (at least two-phase) flow of water (fluid phase) and debris (solid phase) of different sizes (clay to boulders) and forms. In some cases vegetation (tree trunks and branches) constitutes a third (solid) phase (e.g. Takahashi 2007). Debris flows may

be earthquake-triggered (during strong earthquakes) or rainfall-triggered (during heavy rainfalls—monsoon, local thunder storms); they may also be caused by sudden failures of natural or man-made dams (Costa 1985; Costa and Schuster 1987), such as:

- Post-quake breaching of landslide dams,
- Overtopping of earthen dams,
- During glacial lake outburst floods (GLOF), or
- After failures of torrential check-dams filled with sediments.

In Slovenia, a small central European country with intensive torrential processes in mountainous and hilly headwaters (average annual specific sediment production around 500 m³/year/km², in sediment sources or after large mass movement events also much larger; Mikoš et al. 2006), state legislation concerning large dams and spatial consequences of their failure exists. This does not cover concrete torrential check dams as one of the structure types under consideration (there are more than 1,000 torrential check dams in Slovenia according to a national inventory of water structure).

M. Mikoš (✉) • A. Kryžanowski • M. Martinčič
Faculty of Civil and Geodetic Engineering, University of Ljubljana,
Jamova c. 2, 1000 Ljubljana, Slovenia
e-mail: matjaz.mikos@fgg.uni-lj.si; andrej.kryzanowski@fgg.uni-lj.si;
manica.martincic@gmail.com

J. Sodnik
Faculty of Civil and Geodetic Engineering, University of Ljubljana,
Jamova c. 2, 1000 Ljubljana, Slovenia

Water Management Company Kranj, M. Vadnova 5, 4000 Kranj,
Slovenia
e-mail: jost.sodnik@vgp-kranj.si

When developing a new approach to estimate hazard due to failure of large dams, the existing legislation was taken as the starting point. Even though no torrent check dams are listed in the list of existing water infrastructure in Slovenia, and in vast majority they cannot be defined as large dams according to ICOLD criteria (i.e. not high enough), they can impose hazard to environment and infrastructure—when they fail. Especially large sediment-retention dams, built in a cascade (a chain of concrete check dams), can impose hazard (hyper-concentrated sediment flow, debris flow), if they fail during torrential flash floods or when destroyed by overtopping by a debris flow initiated on slopes or in natural torrential channels. The main reason for their failure may be low intensity of their maintenance in the past period prior to extreme events, or wrong assumptions during their design (not taking rare debris flow events into account).

National Research Program “Hydrotechnics, Hydraulics, and Geotechnics” (2004–2008 and 2009–2013)

Assessment of Debris-Flow Magnitudes in Slovenia

Classification of torrential fans considering the Melton’s number (maximum elevation difference in a torrential catchment divided by the square root of the catchment area; Melton 1965) and the fan slope was prepared for the Upper Sava River tributaries in NW Slovenia. Using past events, two limit values are given in literature: the Melton number = 0.3 and torrential fan gradient = 4° (7 %) (for a review on process types on torrential fans see e.g. Rickenmann and Scheidl 2013). These limit values should provide a criterion good enough for classification of torrential fans into three groups (debris-flow prone, transitional, and torrential fans). In the investigated area, 8 out of 18 torrential fans were recognized as fans prone to debris-flow risk (Sodnik and Mikoš 2006) (Figs. 1 and 2).

Other 10 torrential fans in the investigated area were recognized as transitional fans, where debris flows are possible but probability of their occurrence is rather low (Sodnik and Mikoš 2006).

National Research Project “Earth- and Concrete Dams of the Strategic Importance in the Republic of Slovenia” (2011–2012)

Inventory of Large Dams

In Slovenia, 41 large dams are officially registered by the Slovenian National Committee on Large Dams (SLOCOLD 2013; 22 dams for hydropower production, 14 dams for

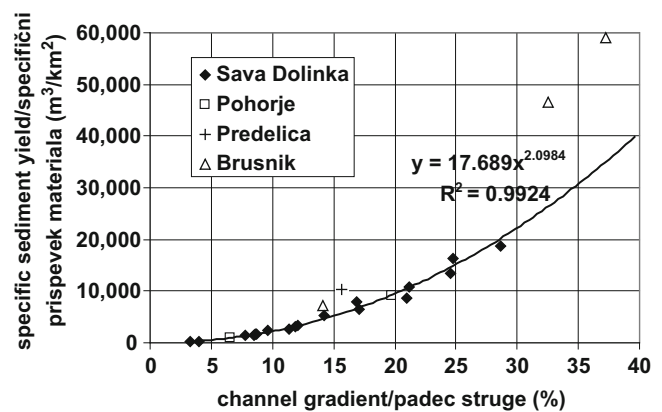


Fig. 1 Specific annual sediment yield (m^3/km^2) as a function of torrential channel gradient (%) for selected torrents in Slovenia (from Sodnik and Mikoš 2006)

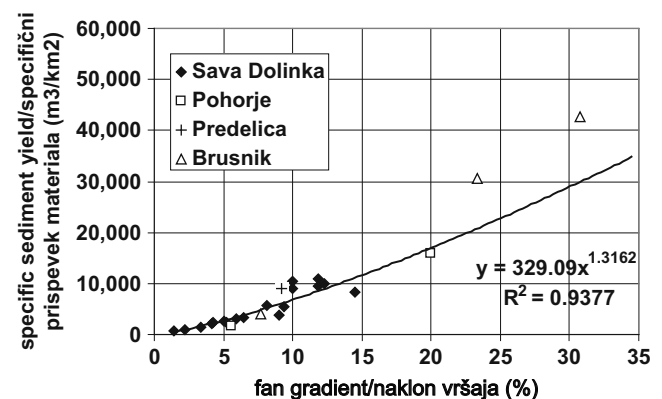


Fig. 2 Specific annual sediment yield (m^3/km^2) as a function of torrential fan gradient (%) for selected torrents in Slovenia (from Sodnik and Mikoš 2006)

water management; 3 historical dams—so-called Klavže barrages from eighteenth Century, 2 dumping tailing barrages) that have fulfilled the ICOLD criteria.

Torrent Check Dams as Debris-Flow Sources

Large dams represent a threat when considering their collapse. In Slovenia large dams are covered with legislation and assessment of spatial consequences of their failure has been completed. Since Slovenia is an alpine country numerous torrential structures were built in last century. All these structures are considered in legislation as less demanding structures with regard to their construction, and no risk assessment is required when planning and building them. In Slovenia, there are over one thousand torrential structures (such as concrete check dams) but no hazard assessment exists for them in case of their failure.

Within the framework of the research project, we proposed a procedure for qualitative evaluation of the hazard

Table 1 Results of the hazard assessment

I. Basic dam parameters	II. Availability of technical documentation	III. Operation parameters	IV. Possible hazards	V. Structure and hydraulic equipment conditions	Overall mark and hazard level	
10–13	10–13	14–17	16–20	14–17	64–79	Low
14–18	14–18	18–23	21–26	18–23	80–105	Low to medium
19–24	19–24	24–31	27–36	24–31	105–140	Medium
25–31	25–31	32–42	37–49	32–42	141–191	Medium to high
32–40	32–40	43–56	50–64	43–56	192–256	High

rate due to failure of large dams. The same procedure was tested for concrete torrent check dams in the Upper Sava valley.

The risk evaluation procedure for (reinforced) concrete torrential structures was developed considering the following parameters (Kryžanowski et al. 2012, 2013; Table 1):

- Basic structure parameters (constructional height, volume of water and sediment deposits, design flood/discharge).
- Availability of technical documentation (design documentation, operation instructions, emergency plans in the case of failure, alarming plans).
- Operation parameters (purpose of the structure, monitoring, alarm systems).
- Possible hazards (collapse, no supervision, design system, no/bad maintenance).
- Conditions of structures and hydraulic equipment (construction, sediment deposits, hydraulic equipment).

Each parameter was ranked according to a 3-level scale of impact (large, medium, and low) on the failure risk, based on a professional judgment (skills, experiences, field expertise).

The rank values of single parameters were scored with increasing steps, and then the ranks were summed up. The final failure hazard evaluation is based on a 5-level hazard scale (low, medium, large and two intermediate levels; Table 1).

For ranking purposes, also known (historical) facts and field conditions should be taken into account (due to long life cycle, importance of proper maintenance) that have been gained during previously conducted field surveys of torrential structures and their documentation.

The rankings followed a scheme applied for large dams, and should be for concrete torrent check dams further tested on a larger set of torrent check dams. The problem lies in the fact that in Slovenia, debris flows are rather rare events, and there does not exist a large database on debris flows that would make such a testing an easy task.

In Table 2, the ranking results of 22 torrent check dams in The Sava Dolinka River valley are shown. The ranking results show that most of surveyed concrete check dams is in medium to high class of failure hazard, seven

of them in class of high failure hazard. The Suhelj torrent case study showed that also smaller torrential structures can represent a considering threat and that such structures should also be considered with comparable methods as large dams.

The results of mathematical modeling of potential debris flows on the fan using a two-dimensional numerical model (Flo2D) confirm that a potential debris flow initiated by a check dam failure in this torrent truly impose hazard to the torrential fan.

Suhelj Torrent in NW Slovenia

A Chain of Check Dams

The Suhelj Torrent was estimated by the field expertise, field evidence and the analysis of watersheds susceptible to debris flows, and as one of the most hazardous torrential watersheds in Slovenia. The main reason is an active sediment source in the upper-most part of the watershed, close to the mountain ridge (Fig. 3). The activity of the torrent was handled in the past by a system of over 10 torrent check dams. During an extreme event in the watershed, failure of a dam may force the failure of the next downstream one with a possible initiation of a debris flow generated from the deposited torrential sediments stored behind the check dams.

The hazard level of the Suhelj torrent check dams is high (Table 2), due to the low budget spent in the last two decades for maintenance and the very poor state of the structures with constructional damages (Fig. 4) in combination with high possible hazards. Some structures are threatening to collapse therefore considering a failure scenario is justified (Fig. 5).

For failure of check dams in a cascade, two scenarios were considered:

1. Partial failure of a check dam during a torrential flood which results in a hyper-concentrated flow in the downstream channel.
2. Complete failure of a check dam. A complete failure results in a channelized debris flow with much greater peak discharge in the downstream channel.

These two different scenarios can be taken as input parameters (inflow hydrograph) for mathematical modeling



Fig. 3 The uppermost part of the Suhelj Torrent watershed is a source of occasional smaller debris flows or hyper-concentrated sediment-laden flows



Fig. 4 Example of a collapsed check dam



Fig. 5 Example of a filled concrete check dam in the Suhelj Torrent with a filtering function

Table 2 Hazard ranking for 22 examined torrential structures

Structure torrent	Overall mark	Hazard level
Bela	186	Medium to high
Dobršnik	182	Medium to high
Graben na pruhu	196	High
Hladnik	198	High
Javornik	178	Medium to high
Klemucov graben	186	Medium to high
Kotarica	194	High
Krotnjek	186	Medium to high
Mlinca	174	Medium to high
Nadiža1	170	Medium to high
Nadiža2	174	Medium to high
Pišnica1	178	Medium to high
Pišnica2	182	Medium to high
Potok	192	High
Presušnik1	170	Medium to high
Presušnik2	170	Medium to high
Presušnik3	170	Medium to high
Suhelj1	198	High
Suhelj2	202	High
Suhelj3	200	High
Tofov graben	172	Medium to high
Završnica	178	Medium to high

of potential debris flows in order to assess debris-flow hazard on a torrential fan. Certainly, also other parameters should be determined, the most problematic being the rheological parameters of such a potentially wet or dry debris flow that are hard to determine in advance. In the case of the Suhelj Torrent, data on rheological properties (viscosity, yield shear stress) were obtained using excavated old torrential deposits on the fan and performing laboratory tests.

Therefore, many times only average values for rheological properties of debris material may be used – a sensitivity analysis using values in the predetermined interval is to be performed as well in order to get the maximum reach-out zone of a potential debris flow not only due to its magnitude but also due to different material rheological properties (Sodnik et al. 2009, 2012a, b). A detailed sensitivity analysis

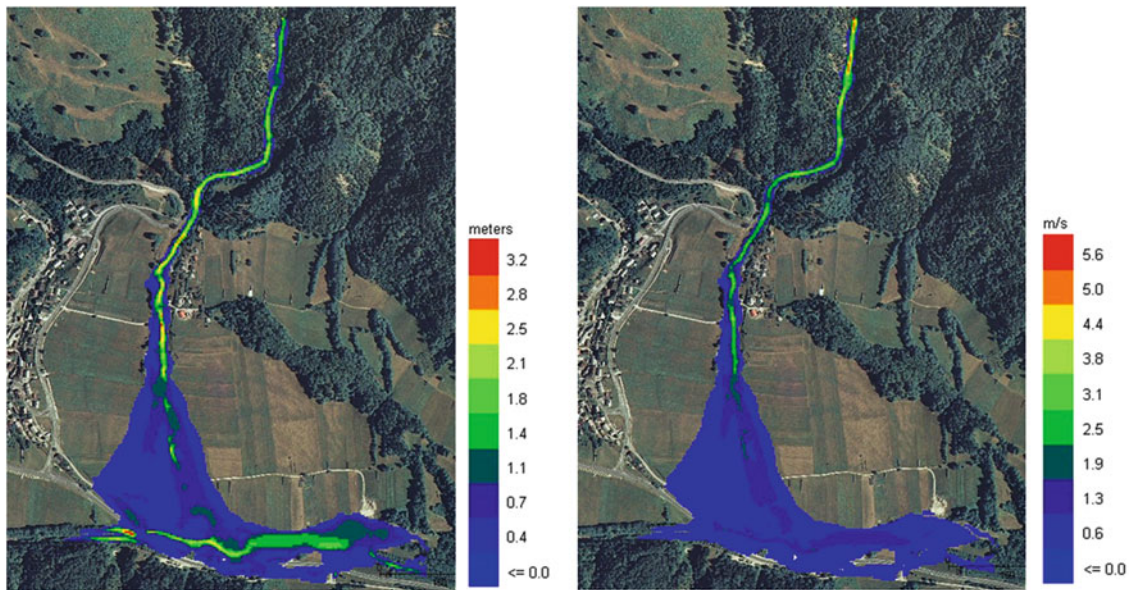


Fig. 6 Maximum debris-flow depths (*left*) and maximum debris-flow velocities (*right*) on the Suhelj torrential fan. The numerical two-dimensional model Flo-2D used numerical grid 5 5 m: debris-flow ($C_v=0.42$) $Q_{\max}=34 \text{ m}^3/\text{s}$, and flash flood $Q_{100}=24 \text{ m}^3/\text{s}$

with Flo2D showed that the main impact on modeling results is due to the magnitude (scenario) of a debris-flow event and the quality of topographic data (DEM) (Sodnik et al. 2009).

The importance of the magnitude for a reliable debris-flow hazard assessment put forward the question whether torrent check dams can influence the magnitude of a potential event. When assessing debris-flow hazard and preparing debris-flow hazard maps, most important modeling results are maximum flow depths and maximum flow velocities.

In the Suhelj torrent case study, publicly available DEM5 was used as input topographic data (grid 5×5 m). Different magnitudes were used as debris flow scenarios and different inflow hydrographs were applied. In Fig. 6 results of the model with a hydrograph with peak discharge $34 \text{ m}^3/\text{s}$ are presented. Peak discharge of water with 100-year return period is $24 \text{ m}^3/\text{s}$. Peak discharge of the hydrograph is the most important parameter when modeling maximum flow depth and maximum flow velocities. Potential failure of a concrete check dam or series of concrete check dams increases peak discharge of a channelized debris flow; therefore, we must estimate sediment budget of torrent check dam. With combination of inflow hydrograph defined from the characteristics of the headwaters and sediment budget of potentially failed check dam we get the “new peak discharge”. Further research must be targeted on systematic surveys of existing concrete check dams and their condition and assessment of failure probability. Combining check dam sediment budgets and watershed magnitude, worst case scenarios for debris flow events must be defined and applied for debris-flow hazard assessment.

Conclusions

Large dams represent a threat when considering their collapse. Large dams are more visible and consequences are more imaging to broad masses. In Slovenia large dams are covered with legislation and assessment of spatial consequences of their failure exists or should exist. Since Slovenia is an alpine country numerous torrential structures were built in the last century. All these structures are considered as easy or less demanding structures and no risk assessment is required when planning and building them. Now we have over one thousand torrential structures as check dams in Slovenia but no hazard assessment in case of their failure.

The newly proposed qualitative evaluation of the hazard rate due to failure of concrete torrent check dams was tested for a chain of concrete torrent check dams in a selected torrent. Case study of the Suhelj torrent shows that also smaller torrential structures can represent an important threat and that such structures should also be considered with comparable methods as large dams. The results of mathematical modeling of potential debris flows on the fan using a two-dimensional numerical model (Flo2D) confirm that a potential debris flow initiated by a failure of check dams in this torrent truly imposes hazard to the torrential fan.

Systematic evaluation of existing torrential structures should be carried out and specific guidelines for designing must be prepared. Our study points out the gap in existing practice and legislation and real situation on the

ground. Numerous structures in poor condition represent a threat to population, settlements and infrastructure that should be evaluated and managed.

Acknowledgments The study was supported by the Research Agency of Slovenia (ARRS) through the research programme P2-0180 “Hydrotechnics, hydraulics and geotechnics” and by the Ministry of Defence of the Republic of Slovenia through the research project “Earth- and concrete dams of the strategic importance in the Republic of Slovenia (2011–2012)”.

References

- Costa JE (1985) Floods from dam failures. US Geological Survey Open-File Report 85–560, Denver, Colorado, USA. p 54. <http://pubs.usgs.gov/of/1985/0560/report.pdf>. Accessed 28 July 2013
- Costa JE, Schuster RL (1987) The formation and failure of natural dams. US Geological Survey Open-File Report 87–392, Denver, Colorado, USA. p 39. <http://pubs.usgs.gov/of/1987/0392/report.pdf>. Accessed 28 July 2013
- Kryžanowski A, Širca A, Humar N, Ravnikar Turk M, Žvanut P, Mikoš M, Četina M, Rajar R, Polič M (2012) Earthfill and concrete water retention dams of strategic importance in the Republic of Slovenia – VODPREG, Final report, University of Ljubljana, Ljubljana. p 161. http://www.sos112.si/slo/tdocs/naloga_97.pdf. Accessed 30 July 2013
- Kryžanowski A, Širca A, Ravnikar Turk M, Humar, N (2013) The VODPREG Project: Creation of dam database, identification of risks and preparation of guidelines for civil protection, warning and rescue actions. In: Proceedings of the 9th ICOLD EU Club Symposium, April 2013, Venice, Italy
- Melton MA (1965) The geomorphic and paleoclimatic significance of alluvial deposits in Southern Arizona. *J Geol* 73:1–38
- Mikoš M, Fazarinc R, Ribičič M (2006) Sediment production and delivery from recent large landslides and earthquake-induced rock falls in the Upper Soča River Valley, Slovenia. *Eng Geol* 86 (2–3):198–210
- Rickenmann D, Scheidl C (2013) Debris-flow runout and deposition on the fan. In: Schneuwly-Bollschweiler M, Stoffel M, Rudolf-Miklau F (eds) Dating torrential processes on fans and cones. Springer, Dordrecht, p 423. ISBN 978-94-007-4335-9
- SLOCOLD (2013) Large dams in Slovenia. URL: http://www.slocold.si/e_pregrade_seznam.htm. Accessed: 30 July 2013
- Sodnik J, Mikoš M (2006) Estimation of magnitudes of debris flows in selected torrential watersheds in Slovenia. *Acta geographica Slovenica* 46(1):93–123, http://giam.zrc-sazu.si/zbornik/ags46-1-4-SodnikMikos_str-93-123.pdf. Accessed 30 July 2013
- Sodnik J, Petje U, Mikoš M (2009) Terrain topography and debris-flow modelling. *Geodetski vestnik* 53(2):305–318, http://www.geodetski-vestnik.com/53/2/gv53-2_305-318.pdf. Accessed 28 July 2013
- Sodnik J, Podobnikar T, Mikoš M (2012a) Using lidar data for debris flow modelling. In: Proceedings of the 12th Congress INTERPRAEVENT, 23–26 April, 2012, Grenoble, France. pp 573–583
- Sodnik J, Vrečko A, Podobnikar T, Mikoš M (2012b) Digital terrain models and mathematical modelling of debris flows. *Geodetski Vestnik* 56(4):826–837, http://www.geodetski-vestnik.com/56/4/gv56-4_826-837.pdf. Accessed 28 July 2013
- Takahashi T (2007) Debris flows: mechanics, prediction and countermeasures. Taylor and Francis, Leiden, 448 p. ISBN 978-0-415-43552-9



A New Concept of Moraine-Supplied Debris Flow Prevention in Alpine Area, Moxi Basin, SW China

Yongbo Tie, Chuan Tang, and Zongliang Li

Abstract

It is found that there are large quantities of debris flows in the alpine area with the moraine as their loose source in southwestern China. Since the longitudinal slope of such debris flow gully is extremely steep, it is hard to carry out the engineering to control the debris flow in the midstream and the upstream of the basin. Besides, when the debris flows run out, they are in high speed, with destructive force and causing hazards rapidly without any warning. On analyzing the formation of this type of debris flow developed in the alpine area in southwestern China, this paper aims to find a new way to reducing the hazards caused by this type of debris flow, and proposes the “Key Section Prevention” concept model. Then, this paper selects Huangbengliu—one of the branches at the left bank of Hailuo Valley in Moxi basin as the study site, and based on the survey, the “Key Section” concept is applied to guide the design of the mitigation plan. With new design conception, this engineering successfully defends two debris flow events in 2010, and avoids the casualty of 30 local persons and the economic losses of 8 million Yuan. It proves to be useful to prevent this type of debris flow hazard in the alpine area by adopting the “Key Section” concept model. The findings can be useful for the prevention of the moraine-supplied debris flow in Moxi Basin; meanwhile, they can offer a new idea for the mitigation of this type of debris flow hazard in southwestern China.

Keywords

Moraine • Debris flow hazards prevention • Alpine area • “Key Section” model • Moxi Basin

Y. Tie (✉)

Department of Hydrogeology and Environgeology, Chengdu Center of China Geological Survey (Chengdu Institute of Geology and Mineral Resource), Chengdu 610081, China

State Key Laboratory of Geohazard Prevention and Geoenvironment Protection, Chengdu University of Technology, Chengdu 610059, China

e-mail: tyongbo@cgs.cn

C. Tang

State Key Laboratory of Geohazard Prevention and Geoenvironment Protection, Chengdu University of Technology, Chengdu 610059, China

e-mail: tangc707@gmail.com

Z. Li

Department of Hydrogeology and Environgeology, Chengdu Center of China Geological Survey (Chengdu Institute of Geology and Mineral Resource), Chengdu 610081, China

e-mail: 517830823@qq.com

Introduction

The debris flow becomes the common concern in all mountainous areas in the world for its sudden outbreak and the serious disasters it may cause (Ardell et al. 2007; Tie 2013). Heavy rainstorms and steep slopes in the mountainous areas in southwestern China provide necessary topographical and hydrodynamic conditions for the formation of the debris flow (Wang and Fan 1987). Moreover, abundant loose source at the high location in the basin is another determining factor for the formation of the debris flow, too (Benn and Lehmkuhl 2000). The moraines generated by the glacials in the alpine area are hundreds-of-meters thick and they provide main loose source for the formation of the debris flow (Clarhal and Kleman 1999; Lehmkuhl 1997; Lehmkuhl and

Owen 2005; Bodo 2006). The moraine-supplied debris flow is a special geological hazard occurred at the alpine area, and its source supply is mainly from the moraine with rich volume, few historical records of events and the steep channel of the gully (Tie and Li 2011). Besides, when the moraine-supplied debris flow runs out, it affects a wide area with its high speed and long runout distance. Thus, it is a typical geomorphological hazard in the mountainous area in southwestern China. To effectively reduce the hazards from this type of debris flow, a systematic engineering from the upstream to the downstream of the gully must be established (Gentile et al. 2008). However, this requires large sum of capital and plenty of time to accomplish in the alpine area with a poor condition. Therefore, the debris flow cannot always be controlled timely and effectively. Furthermore, the slow development of the economy in the mountainous area and the single approach for the fund at the present cause the prevention engineering often being laid aside or it even cannot be carried out (Tie and Li 2011). Therefore, it is necessary to find some way both to minimize the invested capital and to make the effective plans to reduce the hazards from these debris flows in the alpine area (Cui 2009).

Study Area

The typical moraine-supplied debris flow selected in this paper is Huangbengliu in Moxi basin and it is the branch gully at the left bank of Hailuo Valley. Moxi basin is located at the east slope of Mountain Minya Konk, with an area of 904 km², and it belongs to Ganzi Autonomous Prefecture of Tibetan in Sichuan Province (Fig. 1). The No. 3 Camping Zone of Hailuo Valley Scenic Spot is located at the mouth of the gully, and it is destroyed by the debris flows occurred in 1987 and 2005. The basin area of this gully is 2.0 km², the peak height is 4,900 m and the minimum height is 2,970 m above the sea level, with a 1,930-m relative altitude difference. The length of the gully is 3.2 km, and its average longitudinal is 532 ‰. The bedrock is composed of the fine-grained granite with the biotite. The surface of the basin is covered with Quaternary deposits only. According to the era, it is divided into Pleistocene deposits and Holocene deposits. According to its formation type, it is divided into the moraine, the alluvial deposits, the colluvial deposits and the debris flow deposits. The source of the debris flow is mainly from the moraines located between 3,240 m and 3,900 m above the sea level, and its volume is around $135 \times 10^4 \text{ m}^3$.

According to the historical records and the survey data, the return period of Huangbengliu debris flow is 2–5 years, and it is a typical high-frequency debris flow gully. Though its volume is medium to small, the debris flow generated in

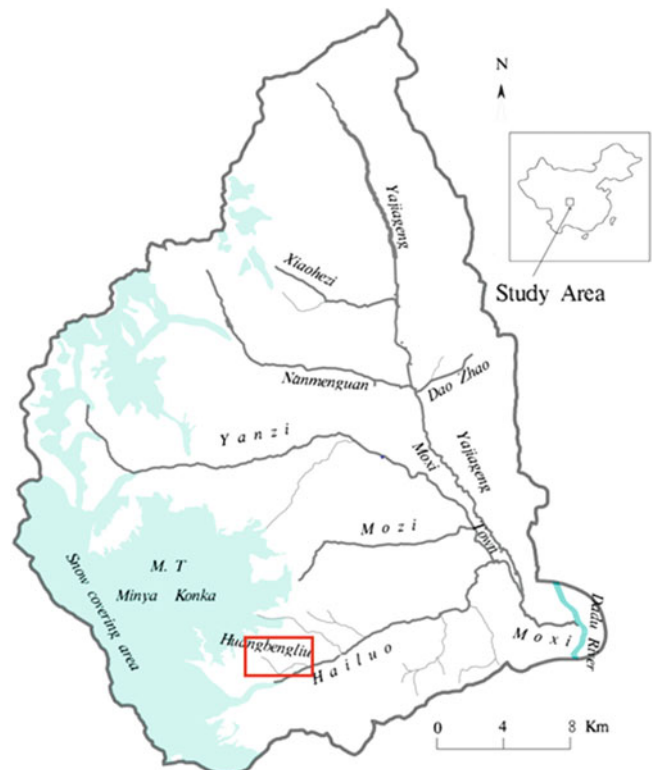


Fig. 1 Characteristics figure of Moxi Basin (Note: the area in red frame is the study area—Huangbengliu)

Huangbengliu endangers No. 3 Camping Zone of Hailuo Valley Scenic Spot, where there are lots of tourism infrastructures as shops, roads, parking lots, cableway stations and sidewalks, etc. Now, Huangbengliu debris flow still threatens 110 residents and 70 million Yuan. Tourists come here every summer, and the maximum number of tourists is around 2,000, so, the potential hazards of the debris flow are rather high.

“Key Section” Conception

The “Key Section” prevention model of the moraine-supplied debris flow means when the engineering is restricted by the landform condition of the basin and when it is difficult to carry the engineering out systematically, selecting the key sections where the hazard is caused directly by the debris flow to carry out the engineering, thus it can reduce risks from the debris flow. To determine the key sections for the prevention in the gully is most crucial. Normally, during the debris flow process, under the action of the inertia, the debris flow runs along the straight line when its path changes to curve, and its kinetic energy is rather powerful. When reaching the bend of the gully, the debris flow rushes directly to the cut bank with its initial inertia, its mud level will exceed the height over the bank at

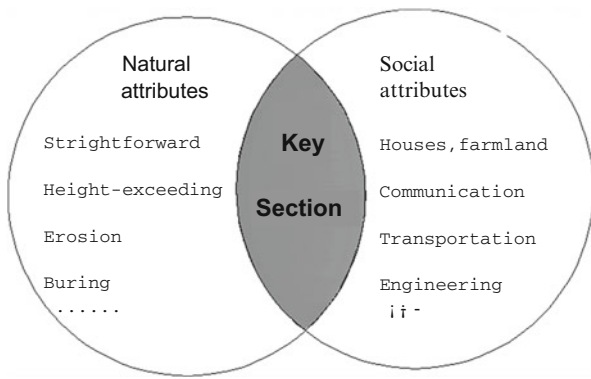


Fig. 2 Conceptual model of the “key section”. The straightforward means that it is affected by the inertia during the movement of the debris flow, its path always keeps straight, and this can cause the debris flow run out of its path at the bend channel zone and cause hazards. At the same time, the strightforwrad always causes the height-exceeding at the bend channel, too

the bend channel and cause the hazards, it is named the “height-exceeding” phenomenon. Therefore, the aim of the engineering in the bend channel section is to avoid the hazards caused by the “height-exceeding”. In some other sections, the debris flow rushes and laterally erodes the channel bed, causing the collapse of the slope, directly endangering the houses and infrastructures along the bank. Thus, the slope and the bed of the gully should be protected to reduce the potential risks from the debris flow in these special sections. Also, after reaching the mouth of the gully, since most of the landforms at the mouth are gentle, the debris flow becomes slow and it begins to deposit, then it buries the house, the farmland, the powerstation and the road and then it causes the hazards. Therefore, the design of the engineering in this section should be taken to accelerate the velocity of the debris flow to make it pass the protection zone quickly.

To prevent the debris flow hazard requires two elements: the debris flow (natural attributes) and the victims (social attributes) (Fig. 2). Then, when determining the “key section” in the debris flow prevention engineering, two important attributes must be considered: the natural attribute, that is, the phenomenon such as the “height-exceeding” at the bend and the bury and the erosion caused by dynamics features of the debris flow at the channel; the social attribute, that is, there must be victims threatened by the debris flow at the key section. The victims include the people, the houses, the farmland, the transport facilities, the communications facilities and other things closely related to human beings’ working and living. Not all the bend sections or the erosion sections of the channel are the key sections. If it is found through the survey that the debris flow rushes out of the channel at the bend section for several times, but there aren’t any victims as the houses, the farmland or the facilities in its

buried area, then this section cannot be considered as the key section when making the plan for the prevention engineering. That is to say, the key section should cover both the natural attribute and the social attribute (Fig. 2).

The Practice of “Key Section” Prevention Model in Huangbengliu Debris Flow

Since the initiation zone of Huangbengliu debris flow is located in a relatively high-latitude area and the average longitudinal slope of the gully is large, it is rather difficult to carry out the engineering at the upstream or the mid-stream, and it restricts the systematic prevention of the debris flow seriously. Based on the mechanism analysis of the formation of the debris flow, the downstream is considered most when designing the plan for Huangbengliu debris flow prevention. The guiding principle is “draining at the deposit zone and controlling at the key section”. Based on this principle, the “Key Section” prevention conception is proposed. In June of 2010, supported by the project from China Geological Survey, Huangbengliu is chosen as the test site for preventing and controlling the debris flow hazards with the new concept. Guided by the “Key Section” Model, two key sections are selected. The first key section (Key Section 1 in Fig. 3) is located at the left bank at the downstream of Huangbengliu gully. The debris flows rushed out of the channel at this key section for many times in the past and destroyed the houses and the forestland because the channel bended here (see the direction pointed by the black arrow in Fig. 3). The second key section (Key Section 2 in Fig. 3) is located at the left bank of the deposit zone of Huangbengliu debris flow. It is the region where the houses, the residents and the tourism infrastructures distribute densely. The debris flow buried and destroyed the constructions here for many times in history, bearing severe potential risks (Fig. 3).

According to the definition of the “key section”, Key Section 1 bears the natural attribute of being strightforward from the debris flow and the social attributes of affecting the houses and the forestland in No. 3 Camping Zone of Hailuo Valley Scenic Spot. Key Section 2 bears the natural attributes of “height-exceeding” and being buried by the debris flow and the social attributes of affecting the houses, the residents and the tourism infrastructures from No. 3 Camping Zone, too. So, two “key sections” in Huangbengliu debris flow are chosen in the prevention engineering.

Design of Key Section 1

Having selected the key sections, the prevention engineering is designed based on the combination of the dynamics

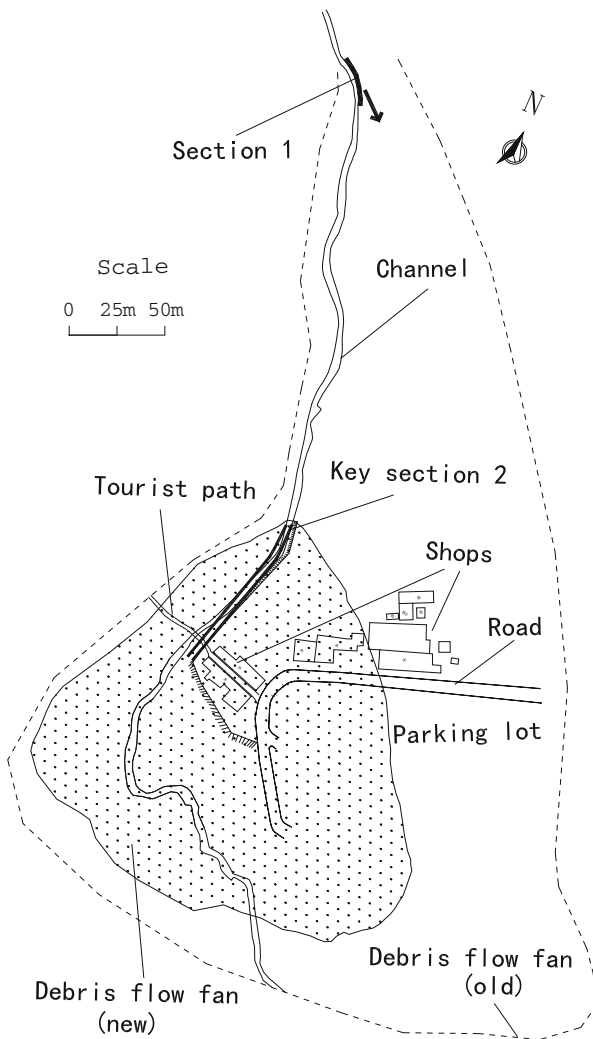


Fig. 3 Sketch map of the accumulation zone and the distribution of the key sections in Huangbengliu debris flow

parameters of Huangbengliu debris flow at different key sections, degree of its sedimentation and erosion and the features of the victims. Key Section 1 is at the flowing zone of the channel, here the debris flow runs fast, impacts strongly and reaches the high level, and moves along the straight line, easily runs out of the channel. Therefore, the designed engineering should be able to both resist the impact and prevent the debris flow from running out of the channel. That is to say, while guaranteeing the height of the engineering, its anti-overturn force should also be considered at the left bank of the channel.

Designing a 60-m-long anti-impact wall to block up the debris flow and keep it flowing along the channel. The stone in deposit zone is sufficient and this can save the cost of engineering, so, the anti-impact wall is designed with the grouted rubble. The body of the wall is 4 m high and 2.6 m wide at the bottom, the top of the wall is 1 m wide, the slope gradient of the side wall facing the channel is 1:0.4, the back

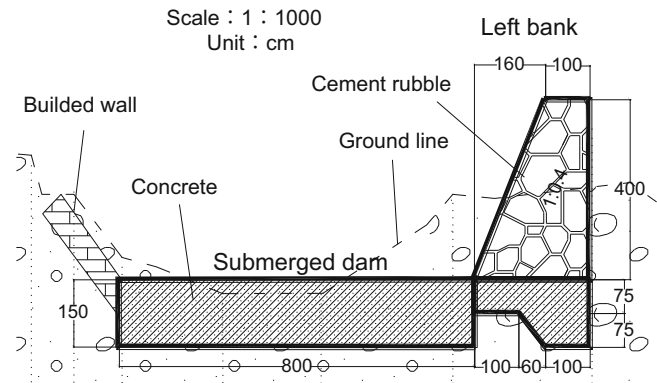


Fig. 4 Design sketch map and completed anti-impact wall at Key Section 1 of Huangbengliu debris flow

of the wall is upright. The anti-impact force of the body of the wall per unit area exceeds the impact force by the debris flow it can bear. Meanwhile, the weight of the anti-impact wall is heavy, its foundation is poured with 1.5-m-thick C25 concrete to bear it (Fig. 4).

In addition, it is found through the survey that since this key section is in the flowing zone and the longitudinal slope of the channel here is relatively steep, the debris flow still features the lateral erosion and the incision to the channel bed. In order to avoid the erosion and the destruction towards the foundation of the anti-impact wall by the debris flow in the future, the submerged dam anti-perpendicular to the anti-impact wall is constructed every 10 m along the channel. It is beneath the bottom of the channel bed, its top is in the same horizontal line to the bed of the channel, thus it can avoid the incision and the undercutting to the foundation of the anti-impact wall by the debris flow (Fig. 4).

Design of Key Section 2

Key Section 2 is in the deposit zone at the mouth of the gully. The longitudinal slope here is relatively gentle, and the debris flow moves slowly and causes the burying to the buildings. Since shops, parking lots and lots of tourism

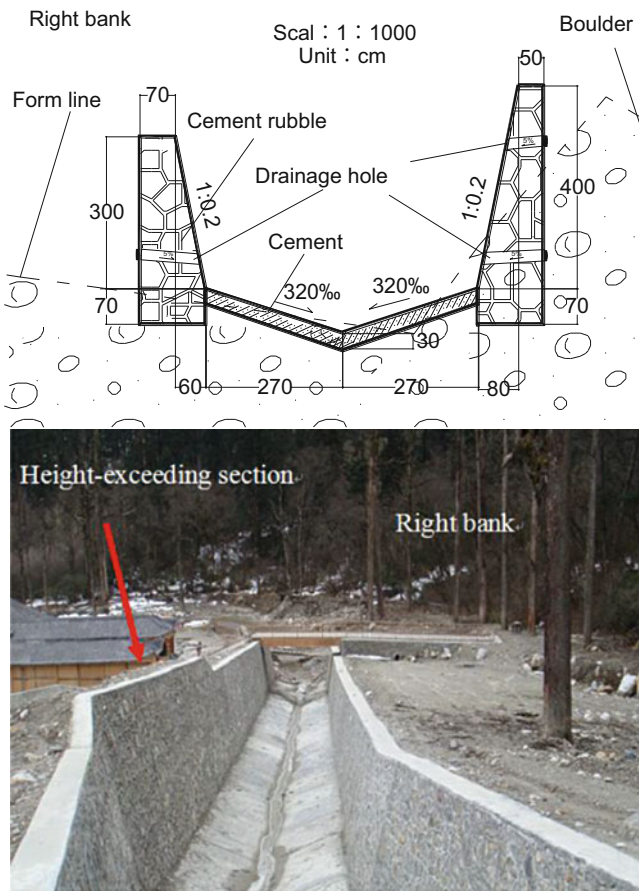


Fig. 5 Design sketch map and completed drainage canal at Key Section 2 of Huangbengliu debris flow

infrastructures distribute densely at the left side of the deposit zone, the potential risk of the debris flow is extremely high. Therefore, when designing the engineering for this section, the primary consideration is to avoid the burying at the left side. That is to say, the engineering intervention is needed to speed up the movement of the debris flow here. Based on the dynamic characteristics and the hazard features of the debris flow, designing a 75 m-long drainage canal at this section, and its length is longer than the length of the channel at the protection zone. Besides, since the bending amplitude of the channel here is large, the drainage canal is designed as “bend improvement”, in order to straighten the path of the debris flow under the constraint of the drainage canal. Meanwhile, the constraint from the drainage canal narrows the flowing cross section, when the volume of debris flow is large, part of the section may be blocked up and the debris flow will run over the bank and cause the hazards. Therefore, the two side walls of the drainage canal are not designed as the symmetric height as they are in the common practice, but as “left bank higher, right bank lower” structure. The side wall at the left bank of the drainage canal is 4 m high, the side wall at the right bank

is 3 m high. Both are made of the grouted rubble; and the slope gradient of the side wall facing the channel is 1:0.2, the back of the wall is upright (Fig. 5).

The unsymmetrical structure can reduce the workload on constructing the wall at the right bank; also, it can sharply broaden the flowing section of the drainage canal. The bottom of the drainage canal is made of the concrete, and it is designed as “V” shape to speed up the movement of the debris flow. The cross slope ratio (I_{cross}) of the body of the drainage canal is 320%, the longitudinal slope ratio ($I_{\text{longitudinal}}$) of the bottom is 140% (Fig. 5).

During the implementation of the prevention engineering for the key sections at Huangbengliu gully, the debris flow occurred twice on July 17th and on July 31st in 2010. However, although only the anti-impact wall has been almost completed and the drainage canal engineering is still under construction, it seems that the key section engineering played a role during these two debris flow processes, because the debris flow didn't run over the channel nor caused any hazards. The engineering protected 30 persons as well as more than 8 million Yuan. The new “Key Section” conception model proves to be effective in controlling the debris flow hazards at Huangbengliu gully.

Conclusions and Discussions

From the point of geomorphology, the process of the transportation, the erosion and the deposit of the debris flow reflect the evolution stage of the earth surface in the mountainous area (Marta et al. 2007; Owen and Benn 2005). So, more and more practice indicate that it is difficult to completely control the debris flow through the engineering; besides, there are limitations by doing so.

In the past decades, China has completed lots of engineerings for the prevention of the debris flows, and gained obvious social and economic benefits (Cui 2009). These prevention and control engineerings are guided by various principles and diversified plans are proposed according to different formation features of the debris flows. After 2008 Wenchuan earthquake, large quantities of loose source generated by the earthquake provide necessary condition for the formation of the debris flow in this region. Affected by the later rainfalls, the debris flow occurs almost every year in certain area of Wenchuan earthquake region, and they are in high frequency, in large scale and always cause serious hazards. The scholars, the government, the media and the public all pay unprecedented attention to the debris flow processes in Wenchuan earthquake region (Huang 2011). Therefore, the study of these debris flows and their preventions becomes the important issue at present (Tang 2010). Five years have been passed, the number of the engineerings in Wenchuan earthquake region is still growing. No doubt, the heavy input of the capital

for the systematic engineerings as reinforcing the loose soil at the upstream, blocking up the flow at the mid-stream and draining away the debris flow at the downstream has effectively reduced the hazards caused by these debris flows and also has good returns.

However, these prevention engineering are not universally applicable, for they are carried out in emergency for mitigating the hazards and in the condition of adequate fund. For the prevention of most of the debris flow hazards, especially those generated by the debris flows occur frequently in the mountainous area in western China, it is impractical to put large sum of money to carry out the prevention and control engineering systematically. Therefore, for the moraine-supplied debris flow gully, whose initiation zone is in the high-latitude area, its loose source is rich, the accessibility of its basin is weak and the altitude difference is large (or the longitudinal slope of its gully is steep), when the systematic prevention and control method cannot be carried out at the upstream, the midstream and the downstream, the conception “control the key section at the downstream” should be more considered and put into practice. Meanwhile, when there is no breakthrough in the technology for the debris flow prevention and control engineering, it is especially important to find new methods by which simple technology is used, little capital is invested and good results are gained to prevent the debris flow hazards. The “Key Section” prevention and control conception can provide a new idea for the mitigation of the debris flows in the mountainous area in southwestern or even other regions in China.

Acknowledgments This research supported by The National Natural Science Foundation of China (Project No. 41101086), Special Research Fund of State Key Laboratory of Geo-hazard Prevention and Geoenvironment Protection, Chengdu University of Technology (SKLGP2012K003) and geological survey project from China Geological Survey (Project No. 12120113010200). The author also thank Mr. Giovanni Crosta, Mr. Ko-Fei Liu and innominate peer reviewers

for their valuable comments and suggestions which improved the quality of the paper.

References

- Ardell M, Cesca M, Huggel C et al (2007) Numerical modeling of debris flow run-out in the Swiss Alps. *Geol Soc Am Abstracts with Programs* 39:438–445
- Benn DI, Lehmkuhl F (2000) Mass balance and equilibrium-line altitudes of glaciers in high-mountain environments. *Quat Int* 65 (66):15–29
- Bodo D (2006) Late Quaternary glacier advances in the upper catchments area of the Indus River (Ladakh and Western Tibet). *Quat Int* 154–155:87–99
- Clarhal A, Kleman J (1999) Distribution and glaciological implications of relict surfaces on the Ultevis plateau, northwestern Sweden. *Ann Glaciol* 28:202–208
- Cui P (2009) Advances in debris flow prevention in China (in Chinese). *Sci Soil Water Conserv* 7(5):7–13
- Gentile F, Bisantino T, Liuzzi GT (2008) Debris-flow risk analysis in south Gargano watersheds (Southern-Italy). *Nat Hazards* 44:1–17
- Huang RQ (2011) After effect of geohazards induce by The Wenchuan Earthquake (in Chinese). *J Eng Geol* 19(2):145–151
- Lehmkuhl F (1997) Late Pleistocene, late-glacial and Holocene glacier advances on the Tibetan Plateau. *Quat Int* 38–39:77–83
- Lehmkuhl F, Owen LA (2005) Late quaternary glaciation of Tibet and the bordering mountains: a review. *Boreas* 34:87–100
- Marta C, Sara L, Giovanni M, Philip D (2007) Recent debris flow occurrences associated with glaciers in the Alps[J]. *Global Planet Change* 56:123–136
- Owen LA, Benn DI (2005) Equilibrium-line altitudes of the Last Glacial Maximum for the Himalaya and Tibet: an assessment and evaluation of results. *Quat Int* 138–139:55–78
- Tang C (2010) Activity tendency prediction of rainfall induced landslides and debris flows in the Wenchuan Earthquake areas. *J Mount Sci* 28(13):341–349
- Tie YB (2013) Prediction of the run-out distance of the debris flow based on the velocity attenuation coefficient. *Nat Hazards* 65:1589–1601
- Tie YB, Li ZL (2011) The preliminary study of moraine supplied-rainstorm debris flow mechanism in Moxi Basin (in Chinese). *Bull Soil Water Conserv* 31(4):195–199
- Wang F, Fan CY (1987) Climatic changes in the Qinghai-Xizang (Tibetan) region of China during the Holocene. *Quatern Res* 28:50–60



Analysis on Blocking of Dadu River by Extra Massive Debris Flows at Moxi River

Zhi Song, Wanmo Zheng, Renji Ba, and Hao Fu

Abstract

The smallest volume of the blocking of Dadu River by the debris flow at Moxi River is 842,600 cubic meters according to the calculations of the total source and the minimum size of the blocking. In the total source of the debris flow at different frequencies, when P equals 2 % (50-year of recurrence), the total source of Moxi River is 830,000 m³, so it is quite possible to have a blocking incident.

Keywords

Blocking • Rain-flood method • Total source

Overview of Environmental Geological Conditions and Blocking Disaster at the Basin of Moxi River

The basin of Moxi River, covering an area of 923 square kilometers is located on the right bank of Dadu River and in the southwest of Luding County, Ganzi Tibetan Autonomous Prefecture, Sichuan Province, with the geographic coordinates of north latitude 29°31'07"–29°55'45" and east longitude 101°49'40"–102°10'19". The provincial highway No. 211 passes through the east of the basin, Moxi-Yulingong Highway passes through in the middle of the

basin, and the transport conditions in the basin area are convenient and fine.

This area is situated in the east of Minya Konka, on the joint between Western Sichuan Plateau and Sichuan Basin, which is geologically high in the east and west sides and low in the central and southeastern parts. The highest peak of Minya Konka is 7,556 m above sea level, and the lowest point is the convergence of Moxi River and Dadu River, with an elevation of 976 m, so the height difference between the highest and lowest points is 6,580 m. Generally, the height difference between the hill and valley in the area is 1,500–3,000 m. The main peak in the west are snow mountains in the direction of nearly SN, and the area above an altitude of 5,000 m is accumulated snow that is not melting all year round, where contemporary glaciers, Quaternary moraine and colluvial deposit are abundant.

Because of the extrusion effects of the Qinghai-Tibet plate and the Yangtze plate and a series of SN tectonic zones produced in Indo-Chinese and Yanshanian periods, the main mountain ranges and rivers in the river alternate with each other, in a direction of north to south. In addition, under the massive action of the glaciers, rivers cut and crush the surface, forming the landform of high and steep mountains and canyon with huge height difference between the hill and valley.

This area is mainly affected by the warm-wet air by the southeast monsoon and from Sichuan Basin, featuring a

Z. Song (✉)

China Geological Survey, Chengdu Center, No. 2 of N-3-Section of First Ring Road, Chengdu 610081, China

Southwest Jiao Tong University, Chengdu 610081, China
e-mail: 35842126@qq.com

W. Zheng • R. Ba

China Geological Survey, Chengdu Center, No. 2 of N-3-Section of First Ring Road, Chengdu 610081, China
e-mail: 1050736347@qq.com; 365041380@qq.com

H. Fu

Sichuan Institute of Forestry Survey and Planning, Chengdu 610081, China
e-mail: 1433949204@qq.com



Fig. 1 Blocking incident of debris flow at Moxi River

subtropical monsoon climate. The work area, Moxi River, is at the tributary of Dadu River. Moxi River has 26 tributaries, and the trunk stream is 43 km in length, with the basin area of 923 km². The head and rear drop is more than 3,000 m, slope 51.3 ‰, average annual discharge 23.62 m³/s and low water discharge 9 m³/s. The hydropower theoretical reserve is 4,600 kW.

In August 2005, swarms of debris flows occurred to the basin of Moxi River. After confluence, an extra massive debris flow was formed at Moxi River. After the debris flow enters Dadu River, a huge sedimentation fan has been created. At 21:00, August 11, Dadu River was blocked for some time, which made the water of Dadu River sedimented up to Caihong Bridge, with the sedimentation length about 3 km, and buried large tracts of farmlands on both banks (Chen and Pi 2006).

According to the introduction by the local villagers, the flood peak duration of the debris flow at Moxi River is 2.5 h, and the duration of blocking of Dadu River is about 10–20 min. When Dadu River burst, the water washed out the highways along the river at 2 km downstream. With the erosion of the Dadu River water, the debris flow deposits moved downstream, forming a stone ridge about 1,500 m long, larger on the top and smaller at the bottom. The drifting logs are seen everywhere on the sedimentation fan (Fig. 1).

Quantitative Calculation of the Smallest Primary Size for the Blocking of Moxi River by Debris Flow

The debris flow blocks the main river from converging, which often leads to great disasters. The inundation disaster will be caused at the upstream of the blocking. Once the blocking bursts, massive flood or debris flow disaster will occur to the downstream.

The scale of one debris flow shall be selected to analyze whether the debris flow at Moxi River may block Dadu River.

Assume that the debris flow ditch is orthogonal to the main river (Fig. 2), the main river width is B_w , the main river water depth H_w , is the bottom slope of the main river,

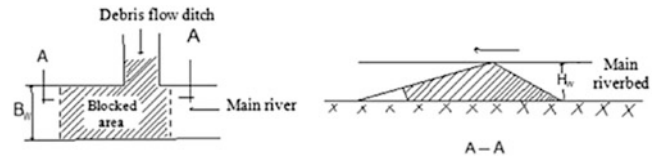


Fig. 2 Diagram of blocking of Main River by debris flow

which is generally small and can be regarded as the horizontal level (Tian et al. 1993). The gradient at the upstream of the blockage is large, which should meet the internal friction angle ϕ of this soil under the condition of saturation. The gradient at the downstream of the blockage can be the initial gradient where the water-rockflow occurs to the riverbed substances, which is 14°, and the soil volume V_{cs} required for blocking the main river is:

$$V_{cs} = (1/2 \tan 14^\circ + 1/\tan \phi) B_w H_w^2 \quad (1)$$

The debris flow at Moxi River is watery debris flow with low unit weight. As soil can be easily separated from water, sand fine and fine particles below are carried away by main river water. The blockage is only coarse particles above sand, the conversion factor for the natural and artificially compacted volumes is 0.7, and the size for blocking the main river at the convergence section is (Tian et al. 1993):

$$\begin{aligned} V_c &= 0.7 V_{cs} / (C_v - p_s C_v) \\ &= (1/2 \tan 14^\circ + 1/2 \tan \phi) 0.7 B_w H_w^2 / (C_v - p_s C_v) \end{aligned} \quad (2)$$

Where, V_c is the required quantity for blocking the main river by the primary debris flow at the convergence section, measured in cubic meter:

P_s is soil particle weight percentage of the sand particles in debris flow and soil particle beneath, which is confirmed by referring to the soil grain size distribution curve of the debris flow.

Based on the measured typical section of Dadu River (ditch of Moxi River), it can be inferred that the section of Dadu River B_w is 220 m, H_w should be the highest water level, 20 m, ϕ_{sw} 25°, C_v 0.45 and $C_v P_s$ 0.225. It is calculated by the above equation that the smallest scale of one debris flow for blocking Dadu River by Moxi River is 842,600 cubic meters.

Discharge of Debris Flows of Different Frequencies and Total Source at Moxi River

It is a calculation method based on the assumption that the debris flow happens with storms at the same frequency and simultaneously and the storm and flood design discharge of

the calculated section is completely converted to the debris flow discharge. The calculation procedure is to first calculate the storm flood discharge of a small basin under the different frequencies of the section by the hydrological method (refer to the hydrological manual for the calculation methods), then select the blockage coefficient before calculating the debris flow discharge as follows.

$$Q_c = (1 + \Phi) Q_p \cdot D_c \quad (3)$$

Where:

Q_c —debris flow flood peak discharge with the frequency of P (m^3/s);

Q_p —storm design discharge with the frequency of P (m^3/s);

Φ —correction factor of debris flow sediments;

D_c —debris flow blocking coefficient

First, calculate the flood discharge Q_p of debris flow ditch within the basin of Moxi River, and take the maximum peak discharge at the moment of the storm, calculated as per the equation (Zhou et al. 1993):

$$Q_p = 0.278(S_p/\tau n - \mu)F \quad (4)$$

In the equation, S_p is the rain force of a certain frequency, mm/h. The calculation formula is as follows:

$$S_p = H_{ip} \cdot t^{n-1} \quad (5)$$

H_{ip} —storm water quantity with the design frequency of the maximum t hours

n—storm parameters;

τ —Conflux duration, h;

L—Length of main ditch, km;

J—gradient of the main ditch, ‰;

F—basin area, km^2 ;

μ —Runoff yield parameter, mm/h;

The gross primary debris flow Q_w can be determined by calculation method and measurement method. The measurement method is of high precision, but the measurement is a rough estimate as appropriate measurement conditions are not available. According to the duration T(s) of the debris flow and the maximum discharge $Q_c(m^3/s)$, the process is generalized as a pentagon according to the characteristics of abrupt rise and falling of debris flow, as shown in the following equation (Huang and Zhao. 2010):

$$Q_w = KTQ_c \quad (6)$$

The K value in the equation varies with the size of the basin area (F):

When $F < 5 km^2$, $K = 0.202$

$F = 5 \sim 10 km^2$, $K = 0.113$

$F = 10 \sim 100 km^2$, $K = 0.0378$

The basin area of Moxi River is $923 km^2$, with the main ditch of 42.5 km long and main ditch longitudinal slope of

Table 1 Characteristic value of debris flow of different frequencies at Moxi River

	P=20 %	P=10 %	P=5 %	P=2 %	P=1 %
Peak discharge (m^3/s)	1,706	2,028	2,342	2,722	3,013
Debris flow discharge (m^3/s)	2,559	3,042	3,513	4,083	4,520
Total source (10^4)	52	62	72	83	92

10.2 %. The blocking coefficient is determined as 1.5 according to Specification of Geological Investigation for Debris Flow Stabilization. The peak discharge of the extra large debris flow last for 2.5 h on August 11, 2005, which can be deemed as the debris flow duration at different frequencies by analogy.

By means of parameter determination and quantitative calculations, the characteristic values of the debris flow of different frequencies at Moxi River are shown in Table 1.

Through the calculations of the total source and smallest size for blocking the river, the smallest total source for blocking Dadu River by Moxi River is 842,600 cubic meters. During the calculation of the total source of the debris flow of different frequencies, when P equals 2 % (50-year of recurrence), the total source of Moxi River is $830,000 m^3$, so it is quite possible to have a blocking incident.

Results and Discussion

1. The rain-flood method is used to indirectly determine the total source of the debris flow at different frequencies to reversely infer that the extra massive debris flow may have a recurrence period of 50 years at Moxi River.
2. There are a lot of complicated causes for an extra large debris flow blocking incident, so this article, while attempting to carry out quantitative analysis with an ideal model, may result in some deviation.
3. Because the debris flow of Moxi River broke out at night, where there are fewer residents. The duration of the debris flow was estimated by locals by counting the bursting noise and violation, which may have errors.
4. This paper intends to have a tentative analysis on the river blocking incident of extra massive debris flow, and provide basis to the recurrence rate with a theory, in order to realize disaster prevention and reduction.

Acknowledgments This research has been supported by The China Geological Survey Project: Monitoring and prewarning on geologic hazards in the key areas along the dadu river valley (Project No. 1212011014017).

References

- Chen XQ, Pi C (2006) 050811 Extra massive debris flow disasters and disaster mitigation strategies. *J Soil Water Conserv* 26(3):122–125
- Huang RQ, Zhao QH (2010) Basic characteristics and preliminary mechanism analysis of large scale rockslide sturzstrom at Wenjiagou triggered by Wenchuan earthquake. *J Eng Geol* 18(2):168–177
- Tian LQ, Wu J, ZC K (1993) Debris flow erosion, handling and accumulation. Chengdu Cartographic Publishing House, Chengdu, p 450
- Zhou BF, Li D, Lv RR (1993) Guide for prevention of debris flows. Science Press, Beijing, 350

Part II

Rock-Slope Instability and Failure



Introduction: Rock-Slope Instability and Failure

Simon Loew and Jan Klimeš

Abstract

This text summarizes topics of the contributions included in the Rock-Slope Instability and Failure chapter.

Keywords

Hazard analysis • Risk mitigation • Displacement monitoring • Process modeling

This session includes contributions on fundamental mechanisms related to the formation of rock-slope instability, as well as new methods developed for hazard analysis and risk mitigation, at many spatial and temporal scales. As discussed in contributions to this session, investigations of larger-volume rock-slope instabilities are based on the study of preconditioning through rock faulting and jointing, erosion, retrogressive slope failure, stress transfer, groundwater flow and chemical weathering. Fundamental research topics related to long-term slope displacement include cyclic loading from seismic, hydraulic and thermal forces causing fatigue and progressive damage as preparatory factors leading to slope failure. Even though the mechanisms causing accelerating rock-slope deformation prior to failure are not fully understood, detailed displacement monitoring over time, when correlated with critical environmental factors, provide a reliable early warning indicator. All these components are

integrated in new best practices developed for identification and classification of regional large-volume rock slope hazards and risks.

The post-failure behavior of smaller-volume rock slope failures is often assessed through dynamic rockfall modeling delivering the spatial distribution and intensity of rock block movements. As discussed in this session, the design of counter measures for such rock slope failures requires an understanding of structure and deformation in the release area as well as friction, mobility and ground interactions of the released rock masses in the transit and deposition areas. The design of effective rock-fall barriers is based on detailed case-history analyses, large-barrier performance tests, and sophisticated mathematical models. The rockfall-fence design and implementation should follow standard codes of practice, which are also illustrated in contributions to this session.

S. Loew (✉)

Department of Earth Sciences, ETH Zürich, 8092 Zürich, Switzerland
e-mail: simon.loew@erdw.ethz.ch

J. Klimeš

Institute of Rock Structure and Mechanics, Czech Academy of Sciences, 12809 Prague, Czech Republic



Supporting Rockfall Countermeasure Design in Difficult Conditions

Federico Agliardi and Giovanni B. Crosta

Abstract

Rockfall protection is a major issue in areas exposed to severe rockfall hazard. The design of structural countermeasures, usually required to ensure such protection, needs careful evaluation of rockfall trajectories, distribution and intensity of impacts, and magnitude and variability of involved dynamic quantities. Protection against rockfalls from high rock walls is especially difficult, due to the widespread occurrence of rockfall sources, the spatial variability of block volumes and rockfall trajectories, and the high involved kinetic energies. In these cases, complex design and construction issues related to massive countermeasures must be addressed. We show the potential of 3D rockfall modelling to support challenging countermeasure design by discussing a case study in the Southern Alps (Italy). Here subvertical limestone cliffs up to 600 m high impend on a narrow strip of flat land, with potentially unstable individual block volumes ranging between 0.5 and 15 m³. Slope benching and a massive embankment were designed to protect a sector of this area. We explicitly integrated countermeasure design geometry into a HRDEM, calibrated modelling parameters by the back analysis of previous rockfalls, and performed predictive simulations considering different block size scenarios. Countermeasure design was verified according to the spatial pattern, heights and overpassing probabilities of expected trajectories. Design optimisation scenarios including additional flexible barriers were also evaluated. Finally we discuss the advantages and requirements of 3D for design support applications.

Keywords

Rockfall • 3D modelling • Countermeasures

Introduction

Rockfalls are widespread and cause significant damages to life and property. Therefore, rockfall protection is an important issue when planning the development of new urban or industrial facilities in exposed areas. Rockfall protection includes risk assessment, identification of mitigation options, and design of structural countermeasures (Agliardi

et al. 2009; Volkwein et al. 2011). This requires a careful quantification of rockfall onset susceptibility and block size distributions in the potential source areas, expected rockfall trajectories, distribution and intensity of impacts, and magnitude and statistical variability of involved kinematic and dynamic quantities (i.e. velocity, kinetic energy, fly height). Different approaches exist to support countermeasure design, using empirical criteria or mathematical modelling techniques. Nevertheless, most approaches presented in the literature or adopted in rockfall engineering were conceived during the last decades in a 2D analysis environment, suitable for the application of simple analytical solutions or early mathematical modelling tools. Methods accounting

F. Agliardi (✉) • G.B. Crosta
Department of Earth and Environmental Sciences, University of
Milano-Bicocca, Piazza della Scienza 4, Milano 20126, Italy
e-mail: federico.agliardi@unimib.it

for rockfall runout on real slopes in 2D or 3D mostly focus on the design of rigid or flexible barriers (Frattini et al. 2012), whereas embankment design methods usually decouple rockfall trajectory modelling from embankment verification (Lambert and Bourrier 2013; Lambert et al. 2013).

Rockfall protection in areas impended by very high, subvertical rock walls is particularly challenging. In these settings, the widespread occurrence of rockfall sources (individual unstable volumes or large rock mass sectors prone to block or mass falls), high variability of release mechanisms, block volumes and rockfall trajectories, and high and scattered values of kinetic energy and fly height are expected. This often results in significant runout model uncertainty and poorly constrained design inputs. In these cases, massive structural countermeasures (i.e. large embankments, slope engineering, rock sheds, composite structures) are usually adopted to achieve acceptable levels of risk reduction (Agliardi et al. 2009). Nevertheless, they require additional design and construction issues to be addressed, including the 3D geometrical and dynamic effects of both the slope and structures.

We discuss the case study of Valmadrera, near Lecco (Southern Alps, Italy) to show the potential of state-of-the-art 3D rockfall runout modelling to support design and verification of large structural rockfall countermeasures.

Case Study

The study area is located near Lecco, on the eastern branch of the Como lake (Fig. 1a). It is a narrow strip of flat land (30–150 m wide) impended by 450–600 m high cliffs, forming the eastern side of Mt. Moregallo (Fig. 1b) and made of thickly bedded limestone and dolostones of the Dolomia Principale formation. The sedimentary succession was involved in ENE-WSW trending km-scale folding, resulting in significant spatial variability of bedding attitude and intensity. In the study area, a slope-scale S-verging syncline fold (Fig. 1b) results in gently S-dipping bedding in the southern sector and steeply N-dipping bedding in the northern part. Structural features have a strong topographic expression, with a 3D slope morphology characterised by subvertical cliffs directly impeding on the shoreline, almost lacking talus materials, and by structurally-controlled chutes and slope breaks (Fig. 1).

Geomechanical features of rock masses also show significant spatial variability depending on large-scale folding. In the northern fold limb, three main discontinuity sets (including bedding) bound tabular blocks in the volume range 0.5–5 m³. In the fold hinge zone, discontinuities are closer and more scattered, resulting in rock mass strength degradation and higher susceptibility to individual block falls up to 15 m³ and mass falls up to some thousands metre cube.

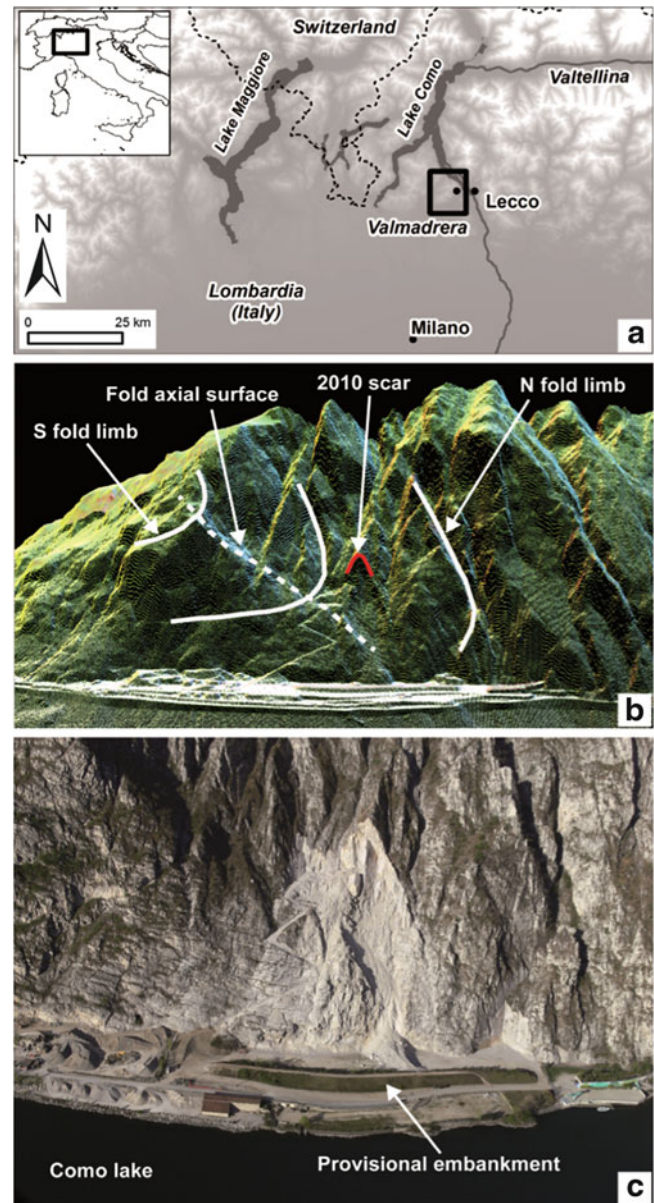


Fig. 1 General settings of the study area. (a) location map; (b) LIDAR point cloud providing a detailed 3D morphological description of both the slope and the area affected by rockfalls. Main structural features are also outlined; (c) oblique aerial view from the East. Source and deposit of the 2010 rockfall, as well as the existing embankment are showed

Rockfall onset susceptibility is lower in the southern fold limb, where blocks in the volume range 0.5–2 m³ are prone to instability near sharp slope breaks.

The studied slope sector (Fig. 1c) suffered several rockfall events during the last decades (1981, 1983, 2006, 2009, 2010), of which a large one affected a former industrial plant (dismantled after the 1981 event), a quarry and an abandoned area. Large blocks identified by bathymetric surveys near the shoreline also suggest long term rockfall activity in the area. Most evidence of rockfall activity concentrates

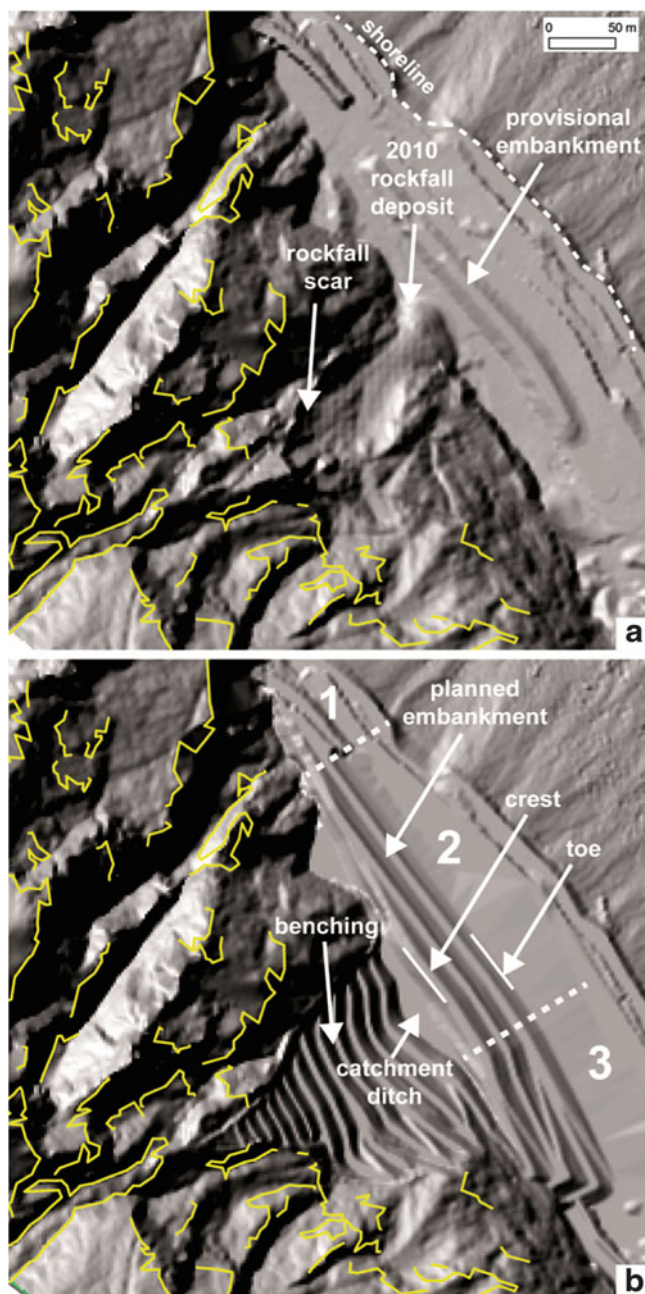


Fig. 2 Explicit geometrical modelling of planned protection structures. (a) original HRDEM (cell: 2 m) from airborne LiDAR (courtesy Regione Lombardia), with release area and accumulation of the 2010 rockfall outlined. *Yellow lines* are distributed rockfall sources. (b) modified HRDEM accounting for the design layout, including slope benching and a 30 m high embankment. Embankment sectors and reference distances for design verification are also showed

around the fold hinge zone, which was protected by a 260 m long and 7 m high embankment (Figs. 1c and 2a). Nevertheless, plans for new area development increased the level of required risk mitigation through rockfall protection. Thus, a massive protection structure was designed (Fig. 2b), consisting of a combination of rock slope benching (with

15 m high and 6 m wide excavated benches) and a 30 m high benched embankment bounding a 10 m deep hybrid catchment ditch.

3D Rockfall Modelling

Modelling Approach: Hy-STONE

Design and construction of such a massive protection structure is challenging and affected by significant uncertainties, related to complex 3D slope morphology, severe expected dynamic conditions, and construction issues. Thus, design scenarios require careful verification and optimisation based on information provided by state-of-the-art runout modelling.

We supported this tasks by performing high-resolution 3D mathematical rockfall modelling through the Hy_Stone simulator (Agliardi and Crosta 2003; Crosta et al. 2004; Frattini et al. 2008; Agliardi et al. 2009). The code is able to simulate the trajectories of non-interacting blocks (i.e. fragmental rockfalls) falling over a three-dimensional topography represented as a vector Triangulate Regular Network (Agliardi and Crosta 2003). This is derived from a raster DEM at any resolution (up to sub-metric cell size), allowing full exploitation of increasingly available high-resolution, remotely-sensed topographic data (e.g. from airborne LiDAR, Terrestrial Laser Scanning, Digital Photogrammetry). The simulator core engine is based on a hybrid algorithm (i.e. mixed kinematic-dynamic) capable to simulate free fall, impact and rolling processes (and related transitional states), with different damping relationships available to account for energy loss by rolling and impact, including an elasto-viscoplastic model for block impacts on soft ground or fill (di Prisco and Vecchiotti 2006).

Most model input parameters are spatially distributed. They are provided to the code as raster matrices consistent with DEM extent and resolution. Main inputs include: source cell locations; block number, shape and mass; energy damping coefficient values; initial conditions.

The stochastic nature of rockfall processes and the spatial variability of related parameters are accounted for by the accuracy of 3D topography and by random sampling of most parameters from different probability density distributions (e.g. normal, negative exponential). Countermeasures and structures can be included in the simulation implicitly (specifying their geometry and energy absorption capacity; e.g. flexible barriers) or explicitly (including their geometry in the DEM; e.g. embankments, large structures).

The code produces outputs in raster and vector formats, including: rockfall frequency (i.e. number of trajectories passing through each cell), bounce height, rotational and translational velocity and kinetic energy, as well as

information about motion type, impact locations and values of impact and rebound angles at each computed point along fall paths.

Model Set-Up

A high-resolution DEM (HRDEM) with cell size of 2 m, derived by airborne LiDAR and bathymetric surveys (courtesy of Regione Lombardia) and integrated by Terrestrial Laser Scanner data postdating the 2010 rockfall event (Fig. 2a), was adopted as 3D base topography for initial parameter calibration and subsequent design-oriented analysis.

The original HRDEM was modified in order to explicitly include the geometry of planned structural countermeasures for modelling. A detailed Triangulated Irregular Network was generated in ArcGISTM starting from original design plans in vector format, and then converted to raster and merged into the original HRDEM (Fig. 2b).

A surface lithology map (including artificial slope material inferred from countermeasure design plans) and a vegetation map were combined to obtain different unique-condition classes of natural and engineered slope units (Table 1). Initial values of energy restitution (en, et) and rolling friction ($\tan\phi_r$) coefficients have been assigned to different classes, based on experience and literature values calibrated in similar contexts and with consistent topographic datasets (Agliardi et al. 2009).

Rockfalls sources (i.e. release locations) are spread over the entire rock slope. In order to achieve a safe reduction of the number of source cells for modelling purposes, we considered linear rockfall sources (Fig. 2), either mapped in the field (i.e. associated to observed or potential instability) or corresponding to cliff-top envelopes (i.e. areas with slope gradient exceeding 55°). Based on available data and field rock mass assessment, we simulated individual block volumes following a negative exponential distribution between 0.5 m³ (modal) and 14 m³ (maximum).

Preserved field evidence of rockfall paths, impact and rolling scours, and fallen block locations are almost lacking in this rockfall setting, which is characterised by the absence of a well-developed talus slope and by a narrow exposed area. Therefore, model parameter calibration chiefly relied on the back analysis of the 2010 rockfall, well documented and evident in the field (Fig. 2a). Damages to structures (i.e. small buildings, retaining structures, pavements) provided additional calibration constraints.

Calibrated restitution and friction parameters (Table 1) allowed simulating 20,500 rockfall trajectories (10/source cell) in the design scenarios described by the modified HRDEM (Fig. 2b). Random sampling of block sizes (negative exponential probability density distribution) and

Table 1 Calibrated mean values of impact restitution (en, et) and rolling friction coefficients ($\tan\phi_r$)

Slope units	en	et	$\tan\phi_r$
Outcropping bedrock	0.65	0.85	0.30
Grass-covered bedrock	0.60	0.75	0.35
Bush-covered bedrock	0.65	0.80	0.35
Forested bedrock	0.60	0.70	0.40
Excavated bedrock (benches)	0.55	0.80	0.40
Reinforced fill (embankment)	0.30	0.65	0.55
Granular impact layer (ditch)	0.25	0.65	0.55
Granular material (bench steps)	0.30	0.65	0.55

of restitution and friction coefficients (normal probability density distribution) was allowed, in order to account for uncertainty and spatial variability. 3D modelling results (Figs. 3 and 4) provided information for design verification and optimization.

Modelling Support to Embankment Design

Embankments are massive earthworks, usually 3–25 m high, up to 100 m long, and mostly associated to an hybrid catchment ditch paved with an impact layer in loose granular material (Lambert and Bourrier 2013). Design of such structures involves addressing issues related to their influence on block trajectories, structural stability under loading, as well as accessibility and cost efficiency (Lambert and Bourrier 2013). Embankments are appropriate to ensure both protection and durability when high kinetic energy and frequency of rockfall events are expected. In fact, although flexible barriers with energy absorption capacity exceeding 5,000 kJ are now available, they are usually unable to stand more than one impact without repair or replacement. However, embankment are expensive structures, and need careful design to ensure favourable cost-benefit balance.

Critical information for massive rockfall protection structure design include: (a) maximum height of rockfall trajectories at a proposed embankment location (constraint on embankment size); (b) design impact energy (constraint on embankment construction); (c) overpassing probability on long-term, i.e. considering a high number of rockfall events (constraint on cost-efficiency including residual risk). Common application of 2D rockfall simulators to define these parameters led specialists to focus on statistical estimators of block trajectory height and energy, e.g. 99th or 95th percentiles of calculated distributions. Nevertheless, these estimators are largely affected by uncertainties due to the number of simulated trajectories, limitations in the physics of rockfall simulators (e.g. rebound modelling), and lack of calibration constraints (Lambert et al. 2013). Moreover, modelling literature for natural slopes (Agliardi and Crosta 2003; Frattini et al. 2012) suggests that 3D topography and

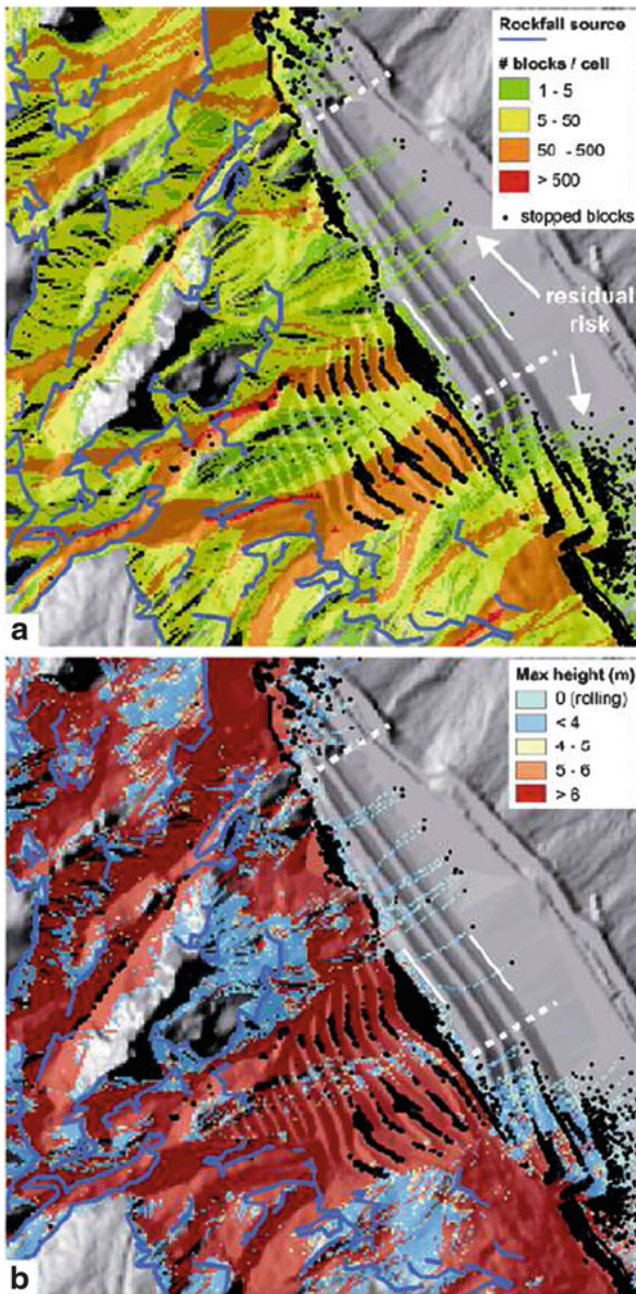


Fig. 3 Design verification (embankment performance and residual risk), based on evaluation of simulated rockfall paths (a), maximum height (b), and spatial distribution and frequency of arrested blocks (a, b)

slope roughness may affect rockfall dynamics (trajectory, height, energy distributions) more than model parameters. When dealing with massive countermeasures (engineered slopes, embankments), structures themselves are strongly three-dimensional.

We addressed all the listed design issues by simulating a large number of 3D block trajectories from spatially-distributed sources, and including a high-resolution description of the actual geometry of the structure (Figs. 3 and 4).

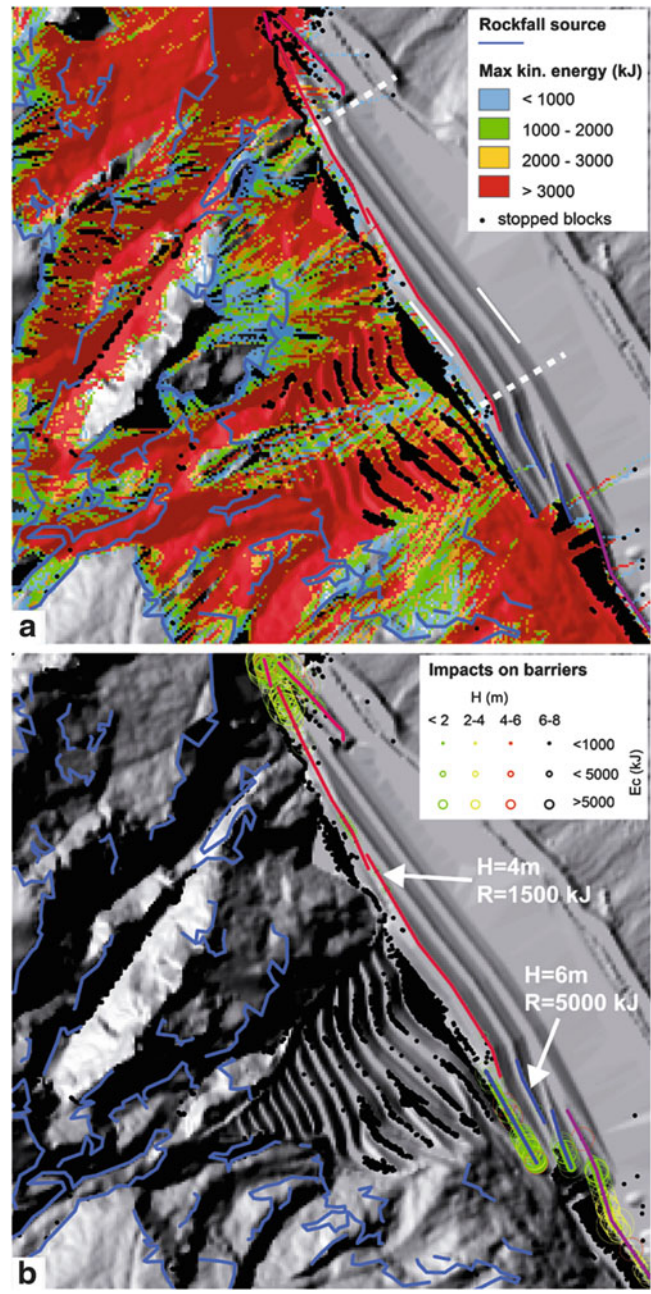


Fig. 4 Design optimisation (flexible barriers), based on evaluation of simulated maximum kinetic energy (a), frequency and spatial distribution of impact locations and energies (b), and location of arrested blocks (a, b)

Stochastic modelling allowed accounting directly for the variability of: (a) rockfall magnitude, i.e. block sizes corresponding to events with different occurrence probabilities; (b) 3D rockfall paths (i.e. lateral dispersion); (c) rockfall intensity (i.e. height, energy). The verification of design performance chiefly considered the spatial frequency of blocks reaching the ditch and the embankment, the height of trajectories above the slope or the embankment, and the location of arrested blocks (Fig. 3).

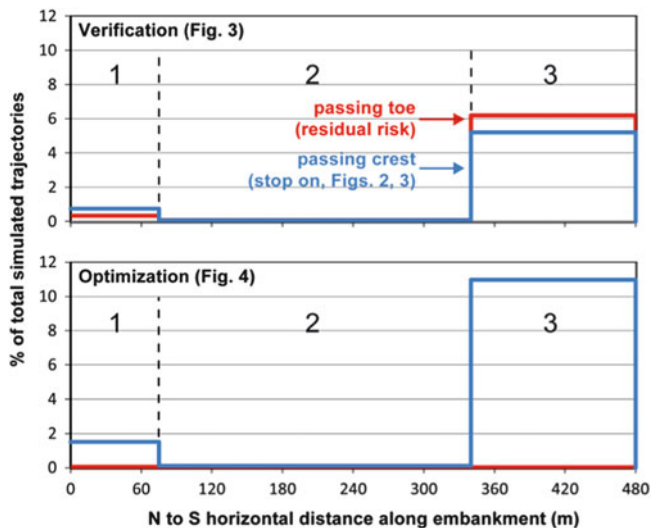


Fig. 5 Spatial distribution of rockfall trajectories passing embankment crest but stopping on the structure (RC residual capacity) and passing the toes (RR residual risk) in each embankment sector (see Fig. 2)

We divided the structure into three sectors with homogeneous cross-section and orientation to the slope (1–3 in Fig. 2). For each sector, counts of blocks arrested at different locations with respect to the embankment allowed quantifying: (a) the embankment’s technical efficiency, EE (probability that blocks stop on up slope benches or in the ditch); (b) the embankment’s residual capability of acting as a benched “collector” slope, RC (i.e. probability that blocks overpass the crest but stop on the embankment; Figs. 2b and 3); (c) the residual risk, RR (i.e. probability that blocks pass the embankment toe and run out in the protected areas; Figs. 2b and 3).

Model results for the design scenario suggested an EE index of 87.32 %, a RC of 6.04 %, and a RR of 6.64. Most rockfall trajectories passing embankment’s crest were clustered in the right sector (3 in Fig. 2b) where the ditch volume is minimum. Only few outlier trajectories overpassed the main body (2 in Fig. 2b) after low-angle bounces on slope benches (Fig. 5).

The relatively high residual risk outlined by the design verification analysis (Fig. 5) pointed to the need of design improvements. These could have been achieved by either increasing the embankment size and ditch capacity (most expensive option) or by completing the structure with a set of flexible barriers up to 5,000 kJ in capacity (less expensive option). We performed 3D modelling to test the latter design optimization scenarios (Fig. 4), and found that a suitable array of flexible barriers would reduce residual risk (RR) to <0.1 % (Fig. 5), thus providing a cost-efficient design improvement option. Hy_Stone capability of providing full information about impacts against flexible barriers (i.e. along-barrier location, height, and energy of individual

impacts; Fig. 4b) provided valuable information to refine their design.

Conclusions

Rockfall protection of areas impended by high subvertical rockwalls remains challenging, due to uncertain design block size, extreme scattering of expected rockfall paths and dynamics, and difficult model calibration. In the past, analysis approaches to design massive protection structures were focused on rigid 2D design schemes, usually supported by poor modelling constraints. We suggest that high-resolution, stochastic 3D runout modeling, explicitly accounting for the real geometry of protection structures and suitably calibrated by event data, is able to provide the required spatial distributed information and modelling constraints for a reliable countermeasure design, without the need of coupling separate models for rockfall runout and structure verification.

Acknowledgments We thank the municipality of Valmadrera for logistic support and Mr. Pensa and Dr E. De Maron for providing TLS and design data. Research was supported by a contract with the Municipality of Valmadrera and partly by PRIN 2010–11 program (2010E89BPY_007).

References

- Agliardi F, Crosta GB (2003) High resolution three-dimensional numerical modelling of rockfalls. *Int J Rock Mech Mining Sci* 40:455–471
- Agliardi F, Crosta GB, Frattini P (2009) Integrating rockfall risk assessment and countermeasure design by 3-D modeling techniques. *Nat Hazard Earth Syst Sci* 9:1059–1073
- Crosta GB, Agliardi F, Frattini P, Imposimato S (2004) A three dimensional hybrid numerical model for rockfall simulation. *Geophys Res Abstracts* 6:04502
- di Prisco C, Vecchiotti M (2006) A rheological model for the description of boulder impacts on granular strata. *Geotechnique* 56:469–482
- Frattini P, Crosta GB, Carrara A, Agliardi F (2008) Assessment of rockfall susceptibility by integrating statistical and physically based approaches. *Geomorphology* 94:419–437
- Frattini P, Crosta GB, Agliardi F (2012) Rockfall characterisation and modeling. In: Clague JJ, Stead D (eds) *Landslides: types, mechanisms and modeling*. Cambridge University Press, Cambridge, pp 267–281
- Lambert S, Bourrier F (2013) Design of rockfall protection - embankments: a review. *Eng Geol* 154:77–88
- Lambert S, Bourrier F, Toe D (2013) Improving three-dimensional rockfall trajectory simulation codes for assessing the efficiency of protective embankments. *Int J Rock Mech MiningSci* 60:26–36
- Volkwein A, Schellenberg K, Labiouse V, Agliardi F, Berger F, Bourrier F, Dorren LKA, Gerber W, Jaboyedoff M (2011) Rockfall characterization and structural protection—a review. *Nat Hazards Earth Syst Sci* 11:2617–2651



Design Approach for Rockfall Protections with Simple Drapery Systems

Alberto Grimod and Giorgio Giacchetti

Abstract

Simple drapery systems are composed of a steel mesh held by a top longitudinal cable fixed with an anchoring system. They are simple, fast and cost effective rockfall protection remediation. Moreover, they can be used on any kind of slope. Their main use is on rocky slope with a steep gradient (higher than 45°). The goal of these interventions is to control the falls of the rocks, which are driven toward to the toe of the slope with slow velocity and low energy. The falling blocks, generally with a diameter up to 1.0 m, are then collected and pile up into a trench (or into a “pocket of mesh”). Because of the highly variable nature of rockfall behaviour these structures cannot be standardized, but they have to be analyzed and designed for each case. Maccaferri has developed a new calculation procedure (MacRO 2) as a practical tool to define the mesh and the related supporting structure composed by up-slope cable and anchors. This paper analyses the theoretical aspects at the base of the analysis for a simple drapery installation, the main steps used for the calculations, and presents a case study in Québec (CAN).

Keywords

Simple drapery • Rockfall protection • Steel mesh • Design

Simple Drapery System

A simple drapery system consists of a rockfall mesh installed along a slope. The drapery is hung as a curtain (Fig. 1), suspended by longitudinal ropes and anchors at the crest. Anchors are positioned in the crest (and if need at the toe too) of the slope and their distance depends on the design and the prevailing instability conditions at the site. They are commonly located in a line and are fitted with suitable terminations (often eye nuts or plates or similar) to accept the crest rope. Once the crest anchors and the upper

longitudinal cable are installed, the mesh can be fixed to them and left free all along the slope (Grimod and Giacchetti 2013).

If the mesh is fixed at the bottom, the falling debris can pile up into a pocket (Fig. 1-left and Fig. 2). Otherwise, if the mesh is left opened at the bottom, a ditch or a fence has to be built in order to collect the falling material (Fig. 1-right). In this second case the maintenance cost is reduced due to the low stresses acting on the mesh.

In comparison to other types of rockfall interventions (i.e. secured drapery systems, rockfall barriers, etc.), the simple drapery is cheaper, and its maintenance is easier, but on the other hand it cannot be considered the remedy for shallow instabilities, because it can only mitigate the effect of the falling trajectories. This system is usually installed on high rocky slopes, where pin drapery systems are not cost effective, or where rockfall fences or rockfall embankments cannot be installed due to the uneven or high gradient of the slope.

A. Grimod (✉)
Gierrevu s.r.l., Passage du Verger n.5, 11100 Aosta, Italy
e-mail: albertogrimod@yahoo.it

G. Giacchetti
Officine Maccaferri SpA, Via Kennedy n.10, 40069 Zola Predosa (Bo), Italy
e-mail: giorgio.giacchetti@maccaferri.com

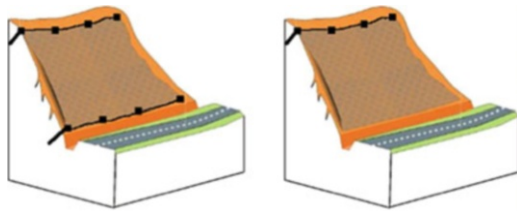


Fig. 1 Example of two types of simple drapery systems: on the left the mesh is fixed at the bottom; on the right the mesh is left opened



Fig. 2 Example of debris accumulated at the bottom of a fixed drapery system

Design of a Simple Drapery System

Calculation Approach

The design of simple drapery depends of different variables related to the geometry of the slope, the type of the mesh and the hypothetical debris accumulated at the base of the system. The most accurate research available on this topic was developed by the Washington State Department of Transportation (Muhunthan et al. 2005).

Using these studies and the results obtained from several laboratories and field tests, Maccaferri has developed a new calculation approach (MacRO 2) that can be used to define the type of mesh, the diameter of the up-slope longitudinal cable and the steel and geometric characteristic (diameter and length) of the up-slope anchors. MacRO 2 allows designers to have a quick and easy solution to the problem. The equations and the procedures at the base of this new formulation are quite simple and rough, but they give reliable and fast results considering the low accuracy level of the input data (i.e. case study presented in the paper).

Nevertheless, even if the design method allows for a quick and simple calculation approach, onsite observations are always recommended in order to achieve a good design, with the ultimate goal of protecting property and human lives.

Table 1 Suggested values of the friction angle at the interface mesh-ground (δ)

Friction angle mesh-ground	Main characteristics of the slope
$\delta > 60^\circ$	Very rough surface: the slope is uneven and undulating and has many prominent protrusions.
$35 < \delta < 60^\circ$	Undulating surface: the slope is undulating and with a few small protrusions.
$25 < \delta < 35^\circ$	Planar surface: the slope is smooth and with a few undulations.
$\delta < 25^\circ$	Smooth surface: the slope is really smooth and in certain point the mesh does not touch the ground surface.

Mesh Design

The simple drapery system must be designed considering all the possible weights able to transmit stresses on the mesh per linear meter, such as the proper weight of the chosen mesh, the weight of the debris accumulated at the toe of the system and the possible external weight (i.e. snow and/or ice).

The three loads mentioned above using the formulations described on the researches performed by the U.S. Department of Transportation FHA (note: formulas 1, 2 and 4 are multiplied by 1 m in order to obtain load per linear meter).

The total load due to the proper weight of the mesh (W_M) can be described with the following:

$$W_M = \frac{\gamma_M \cdot H_S}{\sin \beta} \cdot (\sin \beta - \cos \beta \cdot \tan \delta) \cdot g \quad (1)$$

Where: γ_M is steel mesh unit weight, H_S is the total height of the slope, β is the inclination of the slope (Fig. 3), δ is the friction angle between the mesh and the slope (see Table 1), and g is the acceleration of gravity.

The interface developed between the mesh and the slope may contribute to stability of the mesh system. From table it is possible to underline the friction angle recommended for different type of slope (Sasiharana et al. 2006; Muhunthan et al. 2005).

At this point the stress transmitted from the debris to the mesh (W_D) can be identifying:

$$W_D = \frac{1}{2} \gamma_D \cdot H_D^2 \cdot \left(\frac{1}{\tan B_D} - \frac{1}{\tan \beta} \right) \cdot (\sin \beta - \cos \beta \cdot \tan \phi_D) \cdot g \quad (2)$$

Where: γ_D is the debris unit weight, H_D is the debris accumulation height, ϕ_D is the debris friction angle, B_D is the debris external inclination value (Muhunthan et al. 2005) (Fig. 3):

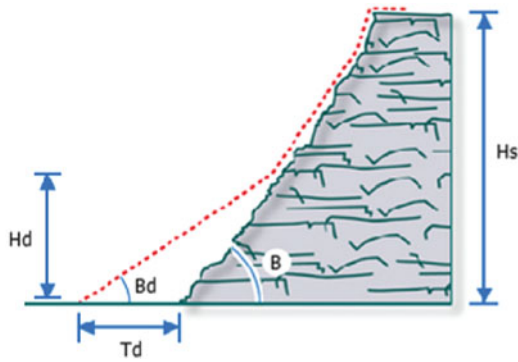


Fig. 3 Geometrical input data to calculate the stress on the mesh due to the debris accumulation

$$B_D = \arctan\left(\frac{H_D}{T_D + \frac{H_D}{\tan\beta}}\right) \quad (3)$$

Where: T_D is the debris accumulation width (Fig. 3).

The last load acting on the mesh is due to the external loads (i.e. snow thickness) acting above the mesh (W_S). Note: for slope with a gradient (β) higher than 60° the snow load (if any) can be neglected since the snow cannot be accumulated if the inclination is too steep.

$$W_S = \frac{\gamma_S \cdot t_S \cdot H_S}{\sin\beta} \cdot (\sin\beta - \cos\beta \cdot \tan\phi_S) \cdot g \quad (4)$$

Where: γ_S is the external load unit weight (i.e. snow unit weight), t_S is the thickness of the external load (i.e. snow thickness), which is considered constant along the entire length of the mesh, and ϕ_S is the friction angle between soil and the external load (i.e. for the snow it depends on the roughness of the soil. According to the Swiss guideline for snow and avalanches (2007), this value can be considered equal to $\tan\phi_S = 0.55-0.50$, for smooth surfaces, and $\tan\phi_S = 0.60$, for rough surfaces).

Safety Coefficient on the Mesh Design

To design the drapery system at the limit equilibrium state, three safety coefficients have to be introduced in the calculation in order to increase the acting forces and decrease the resisting one.

The safety coefficient applied to reduce the resisting forces is introduced in order to decrease the nominal tensile strength of the mesh ($\gamma_{MTS} \geq 1.0$). From the in-situ evidences and the in-situ (Bertolo et al. 2009) and laboratory (i.e. according to UNI 11437: 2012; EN 1538: 2008; ASTM A975: 1997) tests, this factor should not be lower than 2.0).

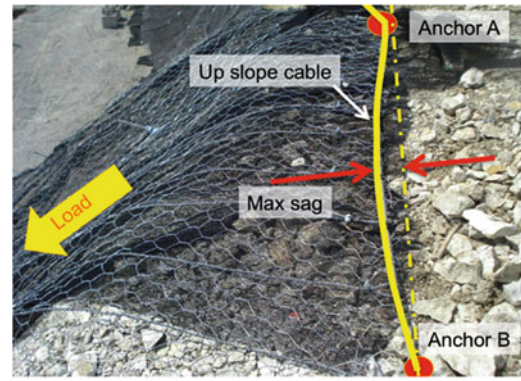


Fig. 4 Example of the deformation of the up-slope longitudinal cable between two anchors

The safety coefficients introduced to increase the acting forces of the system are: γ_{VL} , which is applied on the variable loads, such as the snow thickness and the debris accumulation (≥ 1.0 ; suggested value according to the Euro Code = 1.5), and γ_{PL} , which is applied on the permanent loads, such as the proper weight of the drapery (≥ 1.0 ; suggested value according to the Euro Code = 1.3).

The acting and resisting forces at the limit equilibrium state can be calculated introducing the partial safety coefficients listed above:

The total stress on the revetment (S_w) will be:

$$S_w = (W_D + W_S)\gamma_{VL} + W_M\gamma_{PL} \quad (5)$$

The Serviceability tensile strength of the mesh (R_m) is calculated as:

$$R_m = T_m/\gamma_{MTS} \quad (6)$$

Where: T_m is ultimate longitudinal tensile strength of the mesh, which is defined by laboratory tests.

The design is satisfied if:

$$R_m - S_w \geq 0 \quad (7a)$$

Thus, the safety factor of the mesh is equal to:

$$FS_{\text{mesh}} = R_m/S_w \geq 1 \quad (7b)$$

Cable Design

The mesh is secured on the longitudinal up-slope cable, which is fixed to the crest anchors (Fig. 4). In order to calculate the stress distribution and the deformation of the rope, designers must know the maximum load acting on the drapery (defined in formula (5)) and the spacing between the up-slope anchors. To calculate the total tensile strength

acting on the rope, and consequently verify the longitudinal upper cable, the principle of the catenary is adopted.

The cable is verified if the following equation is satisfied:

$$T_{WLC} F_{CBL} \geq 0 \quad (8)$$

Where: T_{WLC} is the cable working load limit, which is defined as

$$T_{WLC} = T_{CBL} / \gamma_{CBL} \quad (9)$$

Where: T_{CBL} is the ultimate tensile strength of the designed rope (it depends on the steel grade, the type of core and the diameter of the rope; this value is define on the different standards available worldwide, i.e. ASTM 1023/A or EN 12385, etc.), γ_{CBL} is the safety coefficient (≥ 1.0) used to decrease T_{CBL} , and F_{CBL} is the maximum tensile strength acting on the cable (calculated with the catenary theory).

Thus, the safety factor of the cable is:

$$FS_{cable} = T_{WLC} / F_{CBL} \geq 1 \quad (8a)$$

Moreover, using this theory is possible to define the maximum length of the rope and its maximum sag between two anchors.

Anchor Design

The design of the anchors may be divided in two different steps: first of all it is necessary to design the anchor diameter, considering the shear load transmitted from the system, composed by the mesh + cable; then the minimum anchor length has to be defined taking into account the geotechnical soil characteristics.

Evaluation of the Anchor Diameter

With the catenary theory is possible to define the maximum force acting on the intermediate and lateral anchor. These two forces have to be related to the working shear resistance of the designed anchors:

$$S_{bar(j)} N_{(j)} \geq 0 \quad (10a)$$

Where: $S_{bar(j)}$ is the working shear resistance of the anchor j:

$$S_{bar(j)} = \frac{Y_{bar(j)} / \gamma_{ST}}{\sqrt{3}} \quad (11)$$

Where: $Y_{bar(j)}$ is the yield strength of the steel bar j:

$$Y_{bar(j)} = ESS_{(j)} \sigma_{adm(j)} \quad (12)$$

Where: $ESS_{(j)}$ is the effective area of the steel bar j:

$$ESS_{(j)} = \frac{\pi \cdot (\phi_{E(j)} - 2c_{(j)})^2 - \phi_{I(j)}^2}{4} \quad (13)$$

Where: $\sigma_{adm(j)}$ is the yield stress of the steel of the bar j; $\phi_{E(j)}$ is the external diameter of the steel bar j; $c_{(j)}$ is the possible thickness of corrosion on the external crown of the steel bar j; $\phi_{I(j)}$ is the internal diameter of the steel bar j; γ_{ST} is the safety coefficient for the steel strength of the bar (> 1.0); $N_{(j)}$ is the force that the cable and the mesh develop on the anchor j (calculated with the catenary solution); and j is the position of the anchor, which can be intermediate or lateral.

Thus, the safety factor of the different cable may be calculated as follows:

$$FS_{anchor(j)} = S_{bar(j)} / N_{(j)} \geq 1 \quad (10b)$$

Evaluation of the Anchors Length

The evaluation of anchor length takes into account the aspects listed below.

The anchor plays an important role because it must support all the system. Its length must be deep enough to reach the stable section.

The steel bar and the grout are exposed to weathering influences (ice, rain, salinity, temperature variations, etc.).

The minimum theoretical length of the anchor (j) is described by the equation:

$$Lt(j) = L_{s(j)} + L_p \quad (14)$$

Assuming: L_s as the minimum foundation length (calculated with Bustamante and Doix 1985), and L_p as the length of plasticization. This second length is the portion of the stable rock mass that loses its strength (plastification) due to the bend deformation of the anchor bar stressed by a load. The values of L_p depend on the type of rock. Suggested values are: 0.10–0.15 m, for hard rock (i.e. granite); 0.15–0.25 m, for weak rock (i.e. marl); 0.25–0.45, for very weak rock (i.e. siltstone), and 0.25–0.45, for heavy jointed rocks.

$$L_{s(j)} = \frac{P}{(\pi \cdot \phi_{DRILL} \cdot \tau_{LIM} / \gamma_{GT})} \quad (15)$$

Where: ϕ_{DRILL} is the diameter of the drill-hole; τ_{LIM} is the bond stress between grout and rock; γ_{GT} is the safety coefficient applied on the adhesion grout—rock; and P is the maximum pull-out force, which is calculated with the catenary theory.

The length of the anchor defined by the previous formulas has to be considered as a preliminary value. The final

suitable length of the anchor has to be evaluated during drilling in order to verify the exact nature of the soil. Moreover, pull-out tests on the anchors must be done to compare the calculation with the real in-situ condition (Grimod and Giacchetti 2013).

Suitable Meshes for Simple Drapery Systems

It is nowadays evident the wide range of meshes available on the market: single twisted or double twisted wire meshes, steel geocomposites with cables and wires (generally called Steelgrid), cable meshes, cable panels and ring nets. In order to be able to choose the best drapery, designer must consider different aspects related to the fabric and the performance of the meshes. Table 2 resumes the main characteristics to be evaluated during the design and gives some advices for the right choice (Figs. 5 and 6).

The New Concept of Mesh Reinforced with Woven Cables (Steelgrid)

According to the studies developed by Muhunthan et al. (2005), the inclusion of vertical ropes in addition to a top horizontal rope reduces the stress concentration on the mesh, as well as along the top horizontal rope, but only if the longitudinal cables are woven into the mesh and not applied on the mesh at the job site. In this way, the mesh (Steelgrid) is able to transfer the total load acting on the system (S_w) directly to the anchors, and consequently to reduce the tension on the net.

The following figure highlights (on the left) that the higher stress is on the mesh (bigger black arrow), which deforms transversally (necking) and stretches longitudinally (elongation). Using the Steelgrid geocomposite mesh (Fig. 7—right) the forces acting at the bottom of the system are directly transferred to the interwoven cables which reduce the load on the mesh increasing the reaction on the top anchors.

Figure 7 shows that Steelgrid allows high loads to be supported by the drapery system with less deformation on the mesh and lower loads on the crest line ropes. In this way the maintenance of the system can be dramatically reduced.

Case Study

Simple Drapery Systems are commonly used to protect workers, building and infrastructure from rock fall hazards. This case study describes a typical application of a simple drapery system used to protect a hydro-electric power station, Manic 2, Québec (CAN). The solution was designed to control rockfalls with a system that would be easy to install, economic and low maintenance, and of course reliable. The

Table 2 Rockfall meshes features and advices to use them as a simple drapery

Feature to be considered	Advices for simple drapery
Unravelling phenomena	Single twist mesh (i.e. chain link) is not recommended due to its high possibility to unravel if a wire is cut or broken (Fig. 5).
Resistance to the dynamic impacts	Cable panel and ring nets are recommended due to their high dynamic resistance (up to 50 kJ for ring nets).
Tensile resistance	It depends on the input data parameters, but generally it should not be lower than 50 kN/m.
Weight	The weight of the mesh is extremely important because it allows to the drapery to reduce the movement of the blocks along the slope (Fig. 6).
Capacity to transfer load to the top anchors	Mesh with woven cables (Steelgrid) is able to transmit the load directly to the top anchors, and consequently reduce the stress on the mesh (see next paragraph).
Easy installation	No overlap should be required. Workers should work in safety when they “climb” on the mesh: some chain link mesh can be really slippery.

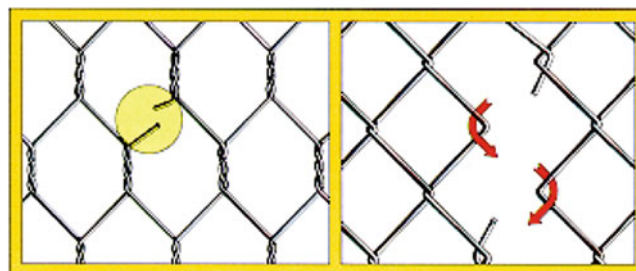


Fig. 5 Comparison between the behaviour of a double twist mesh (left) and a single twist mesh (right) if a wire is cut or broken. The single twist (chain link) suffer of unravelling, while the double twist mesh does not propagate the rupture



Fig. 6 Example of a heavy drapery (HEA cable panel, weight > 2.0 kg/m²): the mesh is able to keep in place the blocks along the slope (red arrows)

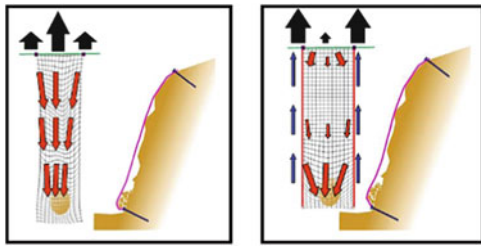


Fig. 7 Distribution of the forces on a simple drapery system: with standard meshes (*left*); with Steelgrid mesh (*right*)



Fig. 8 Detail of the simple drapery system installation. *Left*: limited space between the slope and the hydro-power generation station; *Right*: detail of the snow accumulation on the mesh

design was determined considering two main aspects: the visual impact needed to be kept at a minimum and the selected system had to have low maintenance requirements.

The average height of the slope was around 40 m and the falling block size was supposed to be up to 60 cm in diameter. A simple drapery system was the most cost-effective solution: pin draperies systems were considered too expensive due to the high amount of anchors to be install, and rockfall barriers or rockfall embankment were not suitable due to limited room at the toe of the slope (Fig. 8).

According to the design developed with MacRo 2 approach, more than 4,500 m² of Steel Grid HR30 were installed to protect the power generation plant. This mesh is a double twist wire mesh with 8 mm cables woven longitudinally every 30 cm in order to develop tensile strengths up to 180 kN/m. The rock anchors (yield stress 517 MPa) were drilled 2.5 m in depth and spaced of 3.0 m. The upper longitudinal cable, used to hold the mesh, was 16 mm in diameter (type 1,700 MPa, IWSC).

The last important aspect considered during the design was the life time of the mesh: an alloy Zinc(95 %) + Aluminium (5 %) coating was chosen to guarantee at least the 35

years of lifespan required by Hydro Quebec (the owner of the station).

Conclusion

Simple drapery systems are effective rockfall protection solutions for rock slopes. These types of interventions are cost effective, easy to install, and are characterized by a low level of maintenance. It is recommended in areas where other mitigation systems (i.e. pinned drapery or rockfall barriers) cannot be applied because of their cost and/or the morphology of the site is not suitable.

Based on the researches done by Muhunthan et al. (2005) and the in-situ and laboratory tests, Maccaferri has developed a calculation approach (MacRo 2) that can be used to design all the components of the drapery system: the mesh, the crest cable and the top anchors.

A new concept of mesh can be used as a simple drapery system in order to reduce the stress acting on the mesh, and consequently the maintenance costs; even if the amount of debris volume potentially accumulated at the base of the slope is larger. This mesh (Steelgrid) is composed of steel cables interwoven longitudinally in a double twist wire mesh.

References

- ASTM A975 (1997) (reapproved, 2003) Standard specification for double-twisted hexagonal mesh gabions and revet mattresses (metallic-coated steel wire or metallic-coated steel wire with polyvinyl chloride (PVC) coating). ASTM International, West Conshohocken, PA
- Bertolo P, Oggeri C, Peila D (2009) Full scale testing of draped nets for rock fall protection. *Canad Geotechn J* 46:306–317
- Bustamante M, Doix B (1985) Une méthode pour le calcul des tirants et des micropieux injectés. *Bull. Liaison Labo. Ponts et Chaussées*, Paris, 149
- EN 15381 (2008). Geotextiles and geotextile-related products - characteristics required for use in pavements and asphalt overlays
- Grimod A, Giacchetti G, (2013) New design software for rockfall simple drapery systems. 23rd World Mining Congress. 11–15 August 2013. Montreal QC, Canada
- Muhunthan B, Shu S, Sasiharan N, Hattamleh OA, Badger TC, Lowell SM, Duffy JD, (2005) Analysis and design of wire/mesh cable net slope protection - final research report. Washington State Transportation Commission - Department of Transportation, U.S. Department of Transportation - Federal Highway Administration
- Sasiharan N, Muhunthan B, Badger TC, Shu S, Carradine DM (2006) Numerical analysis of the performance of wire mesh and cable net rockfall protection systems. *Eng Geol* 88:121–132, Elsevier
- UNI 11437 (2012). Rockfall protection measures: tests on meshes for slope coverage. UNI Ente Nazionale Italiano di Unificazione



Effect of Large Impacts Against Rockfall Barriers

Giorgio Giacchetti and Alberto Grimod

Abstract

High energy absorption deformable barriers represent one of the most common measure against rock falls. In order to define the performances of these fences, manufacturers may test their structure in accordance with the European Technical Guideline ETAG 027. The guideline describes all the procedure to perform full-scale crash tests. Moreover, it defines the parameters that must be recorder during the test in order to characterize the fence in term of energy capacity, maximum elongation, residual height and efforts transmitted during the impact to the different anchoring systems (lateral bracing cable, up-slope bracing cable and post foundations). According to ETAG 027, the foundations are not part of the “tested kit”, so designers must verify these elements taking into account the soil properties of the site and the different national design codes available. Difficulties can rise for the post foundations. These elements must be built where strong machineries cannot operate and where the material is very difficult to be transported. In these scenarios, the post foundations can be more expensive than the fence, thus the solutions with rockfall barriers might be reject because the global solution is not cost-effective. The paper describes, in the detail, a case study where very light post foundations where adopted on a 5,000 kJ rockfall barrier. Although the fence was impacted by several blocks able to develop energies higher than the nominal capacity of the fence, the barrier and its foundation system perform properly and they were able to dissipate all the required energy.

Keywords

Rockfall barrier • Rockfall protection • Foundation • Case study • Intervention strategy

Introduction

Even if rockfall barriers are one of the most cost effective remedial solutions as protection against rockfall events, quite often their design remains quite uncertain. The energy capacity and the height of the structure seem to be the only

parameters to be considered during rockfall barrier designs. In the reality, several practical problems must be taken into account, such as the fact that rockfall barriers are generally built in remote or inaccessible areas, where their construction and maintenance can be really difficult and expensive. For instance, several times the foundations of the posts require both strong reinforced concrete plinth and deep anchoring systems.

Other two main aspects must be evaluated: the barrier maintenance and the foundation size. These aspects are strictly related between each other. Designers should be able to answer to the following issues: how is it possible to reduce the barrier maintenance and, in the meantime, increase the lifespan? Can the post foundations, which

G. Giacchetti (✉)
Officine Maccaferri SpA, Via Kennedy n.10, 40069 Zola Predosa, BO,
Italy
e-mail: giorgio.giacchetti@maccaferri.com

A. Grimod
Maccaferri Canada Ltd, 400 Collier MacMillan Drive, Unit B,
Cambridge, ON, Canada N1R 7H7

require a large construction effort, be minimized? The solution requires the knowledge of the behaviour of rockfall barriers, and a more comprehensive design approach.

Rockfall Barrier Behaviour and Design Approach

The behaviour of rockfall barriers can be defined mainly by full-scale tests (crash-tests), which can be used also for the calibration of numerical models. At the present the most important procedure to carry out the crash tests is described by the European Guideline ETAG 027—2008 (“Guideline for European Technical Approval of Falling Rock Protection Kits”). Manufacturers follow ETAG 027 to certify and define the performances of their rockfall barriers.

It has to be clear that ETAG 027 test must be considered as an index test, and the rated energy capacity of the barrier must be considered as nominal (Brunet et al. 2013). For this reason designers should apply reduction coefficients to the nominal energy level of the barrier. Moreover, designer should take into account where and how the barriers have to be installed. For example, when two or more independent barriers have to work as one, the contiguous lateral modules should be overlapped because the lateral functional modules could represent a weak point.

Designers should also consider the uncertainties affecting the rockfall analysis such as the parameters related to the geomechanical, topographic and geologic surveys (Peila et al. 2006). The new Italian standard for “Rockfall protective measures” (UNI 11211:4—2012) represents a very interesting and innovative design approach that takes into account the reliability of the mentioned surveys. Moreover, the standard allows considering both the maximum (MEL) and serviceability energy level (SEL), as defined by the ETAG 027. The choice between a design developed with MEL or SEL (1/3 of the MEL) approach depends on several aspects, such as the possibility to maintain the barrier, the initial economical budget, the allowable risk, the lifespan of the structure, etc.

Field Experience

Barrier foundations should be designed considering the forces directly measured or calculated by crash tests (Turner et al. 2009). In both serviceability and ultimate limit state design approaches, foundations must be designed considering the forces at the maximum energy level, the geotechnical parameters of the soil and the appropriate national provisions. For many designers this means to transfer directly their knowledge from the structural engineering to the deformable rockfall barriers. In these terms the post



Fig. 1 Installation of large steel-reinforced-concrete plinth for a post foundation. The barrier’s energy level is 2,000 kJ. Location: Niagara Falls (ON, Canada)

foundations are generally built with large steel-reinforced concrete plinths, as they avoid settlements and resist to large forces (Fig. 1).

Field experience shows that when the barrier withstands a MEL impact, the damages are very severe and basically rebuild a new barrier is cheaper and safer than repair the impacted one. Even if after a large impact the damages seem to be light or negligible, the probability of micro ruptures on cables, posts, meshes and connection components is very high. Thus, the barrier foundations could suffer of any type of cracks especially on the pins connecting the footplates. With regards to the footplate system, very rarely the “fuse” device, aimed at saving the foundation, is effective.

Opposite is the fence behaviour during a SEL impact. In this case, the damages are usually small and the required maintenance is negligible. The anchoring systems usually do not have any damages and rarely anchors need to be replaced. Strong concrete plinth designed for MEL impacts, appears really redundant and not cost effective. Moreover, the stiffness of the concrete plinth might cause issues on the fence, because the bottom of the post is not able to deform as much as the upper portion. Thus, a “deformable” foundation helps to dissipate energy and make the barrier safer. This concept forces structural engineers to change drastically their mentality during rockfall barriers designs. In these terms the concrete plinth have to be thought as aimed at getting a regular support surface and make easier the installation of the footplate. Its construction should be fast and easy in any environmental condition. The plinth contribution to the bearing capacity of the footplate may be negligible. With this approach, the contribution of the foundation concrete block can be neglected during the design of the post foundations.

The steel bars must directly connect the footplate to the ground. In the case where a concrete plinth is foreseen, the bars have to pass throughout the plinth in order to allow the support of the footplate and in the meantime, to make the foundation more flexible (Grimod and Giacchetti 2013). Using



Fig. 2 Light foundation: the steel footplate is directly lying on soil and tree roots without any plinth. The barrier has energy level of 3,000 kJ. Location: Kirchstrasse, See (Austria)



Fig. 3 Installation of the post on the footplate directly lying on soil. The barrier has energy level 3,000 kJ. Location: Kirchstrasse, See (Austria)

flexible anchors the risk of ruptures on the footplate and of the collapse of the barrier is reduced. In this way, the rockfall fence can maintain an appreciable residual height, and consequently increase the level of safety after the first impact. It has to be underlined that, if the residual height is dramatically reduced, the barrier cannot catch any secondary impact.

The Austrian agency for forest and avalanches (WLV) suggests that the footplate should lie directly on the ground, without any concrete plinth but only fixed by means of anchor bars (Figs. 2 and 3).

Case Study

An interesting case was observed at the km 425 of the Highway A3 (Salerno-Reggio Calabria), which is the most strategic and important road in southern Italy (Fig. 4).

In May 2010 a large rock volume (approx. 8 m³) reached the HWY. Fortunately the consequences for the human life were not remarked (Fig. 5). The detachment area was located approx. 250 m in elevation above the road. In this area, a vertical cliff crowns the 35° inclined slope. The total fallen volume was 1,200 m³: 85–90 % of the debris arrested within the first 50 m from the cliff toe, and almost 10–15 % of the debris continued running for the next 60 m. Ten blocks stopped by the highway, and only reached the road.

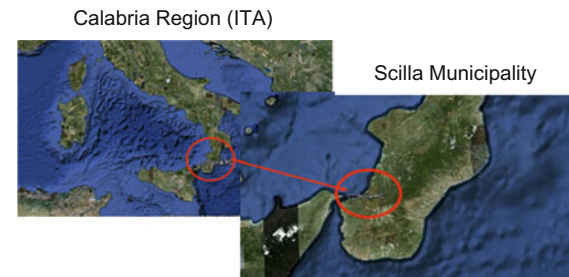


Fig. 4 Location of the case history: Paci Viaduct, km 425 of the highway A3 Salerno-Reggio Calabria, Municipality of Scilla, Calabria Region (Italy)



Fig. 5 Large block fell on the Highway A3 at km 425 (2010—Italy)

The administration asked for a very fast and cheap remedial solution, because the road could not be closed for a long period of time and moreover an alternative route was already under construction and it was planned to be opened in the next couple of years. The geomechanical survey pointed out that on the detachment area there was furthermore 1,000 m³ unstable rock mass, and that the situation was very risky for the safety work yard as well as for the traffic along the highway. The interventions have been organized with the following order: (a) temporary barrier by the highway with two levels of containers filled of sands; (b) drape the unstable cliff by using HEA cable panels aimed to protect the work yard, and, if a further fall would happen, to wrap the falling rocks around and reduce their falling energy and velocity; (c) primary rockfall barrier line to catch the large multiple impacts; (d) subsidiary rockfall barrier line, to be placed just below the main one, in order to stop the rocks that the first barrier could not intercept.

The best position of the primary rockfall barrier has been figured out with a rockfall simulation (Azzoni et al. 1995). The rockfall trajectories analysis was calibrated considering the distribution of the end-points in the case of blocks with 70 m³ in volume (Fig. 6).

The energy capacity, the height and the position of the barrier was defined using the UNI 11211:4 design standard, the MEL design criteria, and previous experiences on large impacts (Giacchetti and Invernizzi 2010). For the specific project two parallel lines of 5,000 kJ deformable rockfall

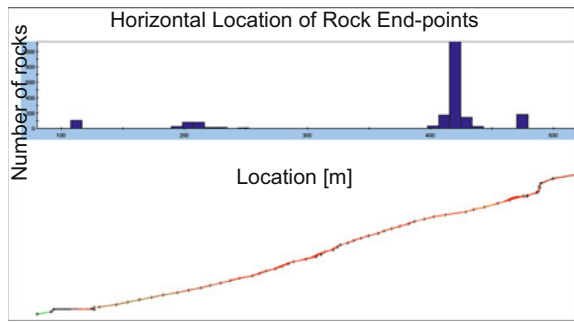


Fig. 6 Location of the end points along the slope. The statistical distribution is similar to the evidence on site: different restitution coefficient has been used to calibrate the model (software RocFall 4—RocScience)



Fig. 7 Effects of the large impact on the primary barrier, at km 425 of the highway A3 (2011—Italy). The post is 6 m long

barriers, 6 m in height and 70 m long, were built. In order to reduce the installation time, and consequently increase the safety condition for the workers, the posts footplates were directly founded on the soil by means of vertical steel rebars, without any concrete plinth.

Seven months later (January 2011), another portion of the cliff collapse at the same location. A fast swarm of large blocks hit the primary barrier, which resisted and preserved a residual height of 35%. Only one block was able to reach the second barrier downslope. Fortunately, no boulders were able to overpass the second fence and reach the HWY A3. The total volume arrested by the upslope fence was estimated in 50+ m³: the largest block had a volume of approx. 7 m³ (Fig. 7). Considering the impact footprint on the barrier, the actual falling velocity (estimated between 9 and 15 m/s) was 2–3 times greater than the calculated one (4.5 m/s), and the total energy was exceeded the nominal capacity of the fence, which was severely damaged. Finally, the trajectories of the block was analysed: it has been hypothesized that the largest blocks mainly rolled on the slope, and impacted the lower longitudinal cables; while the other boulders (1–2 m³ in volume) jumped along the slope and impacted anywhere on the barrier. One of them

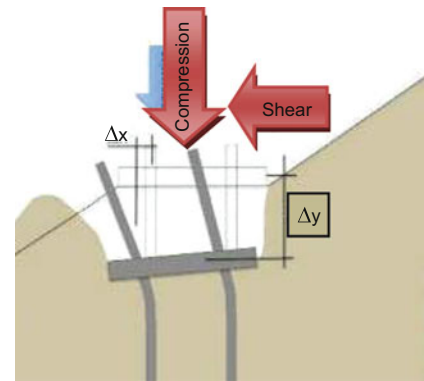


Fig. 8 The vertical (Δy) and horizontal (Δx) settlements of the footplate represents a benefit in terms of energy dissipation by the stiffest zone of the barrier



Fig. 9 Settlement of a footplate after the impact. The displacement was approx. 0.2 m vertically, and 0.1 m horizontally to downslope, km 425 highway A3 (2011)

was also able to reach the second fence. The height of the bounce of this block was estimated in 3.5–4.0 m.

The great performance of the barrier was related to the high residual height that allowed being effective for multiple impacts. Moreover, a relevant aspect was the weakness of the footplates that allowed dissipating the high energy (Fig. 8). Several foot plates sunk in the soil and stripped the vertical anchor bars for approx. 0.2–0.3 m. The bending of several rod heads showed the action of a lateral stress, in accordance with the theoretical calculations and the crash test measurements (Fig. 9).

Other Experiences of Large Impacts

Several impacts on rockfall barriers were recorded by Maccaferri during the last few years. This paragraph shows some of the most interesting real cases, where rockfall fences were able to withstand unusual impacts.



Fig. 10 3,000 kJ barrier impacted by an energy higher than the nominal one. Location: Arnad (Aosta, Italy—2008)

Arnad, Aosta (Italy): Impact with Energies Exceeding the Nominal Barrier Capacity (November 2008)

In Arnad (Italy) a 3,000 kJ barrier was stressed by multiple block impacts. The total energy developed by the rock-boulders was higher than the nominal one of the fence. Two spans were involved in the impact, one post was tilt down-slope and one was bended by a rock that impacted directly against it. The barrier withstood approx. 30 m³ of blocks, the biggest of which had a volume of approx. 12 m³ and energy approx. 4,000 kJ (1,000 kJ higher than the nominal barrier capacity). This boulder impacted directly against the post of the fence (Fig. 10). The minimum residual height of the barrier was still around 50 % of the nominal one (the barrier could still be classified in category A according to ETAG 027) (Giacchetti and Invernizzi 2010).

Even if the foundation of the posts were pretty light (four steel bars, 2.0 m long, drilled through a base concrete block 20–30 cm high), they were not damaged by the impacts. The concrete block of the impacted post was cracked in several points, but the main foundations (the steel bars) were able to absorb all the impacts.

Colle Santa Lucia, Belluno (Italy): Impact of a Large Block Against the Post of a 2,000 kJ Barrier (April 2013)

A 2,000 kJ barrier was impacted by three blocks. One of them, of approx. 4 m³ (approx. 11,000 kg) crashed directly against one of the intermediate post.

The impact velocity was estimated (by a simulation based on a back analysis) equal to 22 m/s. The other two blocks impacted against the barrier: the smallest one (~0.6 m³) impacted against the interception structure, while the largest one impacted on the upper part of the fence, by the upper longitudinal cable. The three boulders developed a total cumulative energy of 5,000+ kJ.



Fig. 11 Effect of the impact against the post of a 2,000 kJ barrier. Location: Colle Santa Lucia (Belluno, Italy—2013)

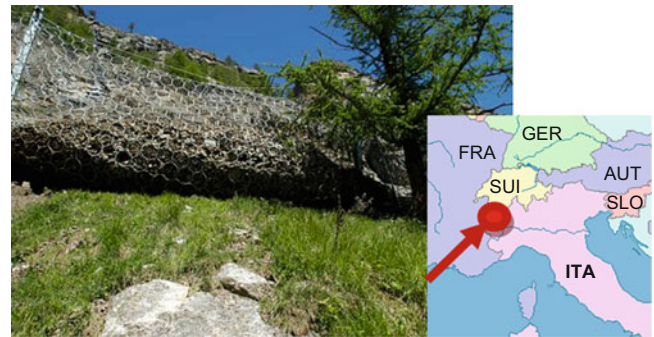


Fig. 12 2,000 kJ rockfall barrier impacted by a large debris flow. Location: Valsavarenche (Aosta, Italy—2008)

Even if one post was directly impacted, the structure was able to maintain a considerable residual height: 30–35 % of the nominal one. The deformation of the mesh, after the three impacts, was approx. 6 m.

The foundations of the post were composed of four steel bars. The base plates of the barrier were installed directly in contact with the ground, without any concrete base-plinths. After the impact, the footplate of the impacted post and the rod bars were lifted from the ground for approx. 0.3–0.4 m. The steel bars bent due to the action of lateral shear stresses (Fig. 11). It could be observed that, probably the designer under-designed the length of the rod bars. In any case, these foundations allowed dissipating the energy on the stiffest portion of the barrier.

Valsavarenche, Aosta (Italy): Impact of a Large Debris Flow Against a 2,000 kJ Rockfall Barrier (May 2008)

A large debris flow, composed by mud, rock blocks and trees impacted against a rockfall barrier after extreme raining events (Fig. 12). The barrier was designed to withstand a rockfall event with a capacity of 2,000 kJ. The height of the fence was 4 m, and the total length was 80 m.

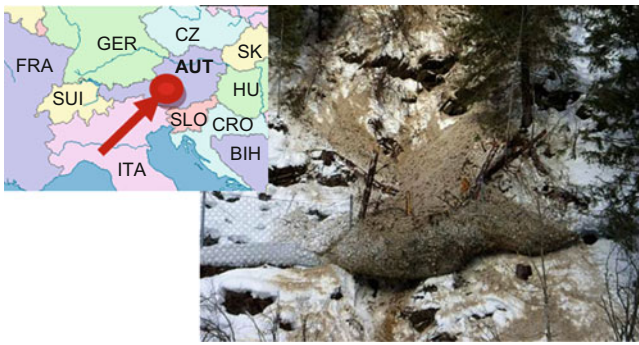


Fig. 13 Effect of a snow avalanches impacted against a rockfall barrier. Location: Patrich, Neder (Austria—2012)

The phenomena involved four spans (40 m) of the barrier, and the total volume of debris was estimated in approx. 200 m³. The barrier performed very well, and it was able to stop all the material and therefore, protect the road downslope. Eight energy dissipater devices worked at their maximum capacity. The barrier maintained a residual height higher than 60 %. The maximum downslope deformation was approx. 4.0 m (Ferrero and Segalini 2009).

The foundations of the posts of the barrier, composed by a micropile 4.0 m long, four short steel bars 1.0 m long, and a shallow concrete plinth (50 × 50 × 40 cm), were not damaged by the debris flow. The impact against the barrier was slow, thus the efforts transmitted to the foundations were not impulsive as generally occur for rockfall impacts.

Patrich, Neder (Austria): Impact of an Avalanche Against 3,000 kJ Barrier (April 2012)

Even if rockfall barriers are not designed to stop avalanches, this case presents a 3,000 kJ that was able to stop a snowslide during its motion (Fig. 13).

The rockfall barrier was installed in order to protect a little village, but during the winter an avalanche occurred and impacted against the barrier (Size 2 according to the Canadian Classification, McClung and Schaerer 1993: mass approx. 100–150 tonnes, run 100–150 m, pressure approx. 5–10 kPa). The high velocity, energy and pressures involved in the snow-motion damaged a few component of barrier. The avalanche impacted against 1.5 spans (approx. 15 m) of the fence. The lateral post (impacted as well) bent and tilted downslope and almost all the energy dissipater devices of the involved spans worked at their maximum capacity.

To conclude, the 3,000 kJ rockfall barrier stopped an avalanche composed by rock debris and big trees. In the impacted span the minimum residual height was evaluated

higher than 50 % of the nominal one, and the downslope deformation approx. 3.5–4.0 m.

The posts were founded with two steel rebars, 5 m long. A small concrete plinth 40 × 40 × h = 10–15 cm were built to give a flat base to the footplate of the barrier. After the impact no damages and no-pull-out were remarked on the bars. Only, a few cracks were noticed on the concrete blocks, due to the high normal stress acting on the posts.

Conclusion

ETAG 027 guideline allows the comparison between different rockfall barriers in term of main performances, such as energy capacity, maximum elongation and residual height. The design of these structures must consider suitable safety coefficients. In these terms a good procedure is suggested by the Italian standard UNI 11211:4. Designers should consider the reality of the natural hazards (i.e. single or multiple impacts), the real behaviour of the tested barrier (tested according to ETAG 027), the installation issues, and the concept of service and ultimate energy level (as per ETAG 027). The field experiences show that this is a useful approach, because it allows designing effective structures, which take into consideration the defence requirements, the construction difficulties, and the maintenance problems.

The design of the post foundations should be included into the same logical approach. At the present, several times is remarked that the post-anchoring systems represent a technological and economic problem for the rockfall fences. “Flexible” post-foundations, easy to build in any slope condition and fit for dissipating energy, represents a good solution for one of the more critical barrier component. Obviously, the “light foundation” implicates a radical change into the designers mentality since they should admit settlements. In these terms, instead of “post foundation system” it would be better to talk about “post base system”.

References

- Azzoni A, La Barbera G, Zaninetti A (1995) Analysis and prediction of rockfalls using a mathematical model. *Int J Rock Mech Min Sci* 32:709–724
- Brunet G, Giacchetti G, Grimod A (2013) Rockfall barrier behavior under multiple impact events. 64th highway geology symposium, New Hampshire, USA, 9–12 September 2013
- EOTA (2008) ETAG 027: guideline for European technical approval of falling rock protection kits, Brussels. <http://www.eota.be>
- Ferrero AM, Segalini A (2009) Rapporto di valutazione dell'efficienza delle barriere di protezione da collate di detrito-Colata di Pont (Pont di Valsavarenche, Ao). GeoDigital Solution Engineering Innovation. Internal Report University of Parma
- Giacchetti G, Invernizzi M (2010) Barriere paramassi impattate con energia eccedente quella nominale: il caso di Amad (AO), in *Lavori Pubblici*, No. 42 – Gennaio/Febrero 2010 (in Italian)

- Grimod A, Giacchetti G (2013) New design approach for rockfall barriers. EuRock 2013, Wroclaw, Poland, 23–26 September 2013
- McClung DM, Schaerer PA (1993) The avalanche handbook. The Mountaineers, Seattle, WA
- Peila D, Oggeri C, Baratono P (2006) Barriere paramassi a rete. Interventi e dimensionamento. GEAM ,Quaderni di studio e di documentazione, n. 26 (in Italian)
- Turner RPE, Turner JP, Duffy JD (2009) Post foundations for flexible rockfall fences. Proceedings 60th highway geology symposium, Buffalo, NY, September 29–October 2
- UNI (2012) UNI 112111-4: 2012 rockfall protective measures – Part 4: definitive and executive design. Ente Nazionale Italiano di Unificazione, Milano Italia (in Italian). <http://www.uni.com>



Design Approach for Rockfall Barriers Tested According to ETAG 027

Alberto Grimod and Giorgio Giacchetti

Abstract

The simplest and easiest way to design a deformable rockfall barrier is to compare the energy level calculated with the rockfall trajectory analyses and the results obtained by the full-scale crash tests performed according to the European Guideline ETAG 027. This calculation approach presents a lot of incertitude due to the difficulties to define the input data, the installation issues and the different performance of a barrier with a configuration that differ from the tested one. Designers should take into account all these aspects and introduce in their design safety coefficients able to increase the energies acting on the structure and reduce the resistances of the fence. Moreover, the performances in term of maximum elongation and residual height should be considered for an accurate design. Maccaferri, which has 130+ years of experiences in the rockfall protection field, uses the European guideline ETAG 027:2008 and the Italian standard UNI 11211:2012 as references for rockfall fence designs. The paper describes the calculation steps and the aspect to be considered in order to carry out a correct design at the service or ultimate limit state.

Keywords

Rockfall barrier • Rockfall protection • Crash test • Design • ETAG 027

Deformable Rockfall Barriers

Deformable barriers are classified as rockfall passive protection systems, because they are generally installed at a certain distance from the detachment area. Thus, their goal is to intercept rock masses that can fall from a certain area located up-slope. According to the European Guideline ETAG 027 (Guideline for European technical approval of falling rock protection kits), issue by EOTA (European Organisation for Technical Approval) in 2008, a deformable rockfall barrier is

defined as a kit of different elements. The “kit” must be able to stop a block that impact against it. The rockfall barrier is therefore considered as an ensemble of components such as: an interception structure (usually a steel mesh), a support structure (steel post) and several connection elements (i.e. cables, energy dissipater devices, etc.). The structure is then anchored to the soil by foundations able to transmit to the ground the forces developed by the impact (Fig. 1). Considering that rockfall fences are never installed in the same type of soil (rock, loose material, etc.) the anchoring systems are not considered as a part of the “kit” (ETAG 027).

To understand and compare the behaviour of these complex structures the EOTA issued the European Guideline ETAG 027, which is the new reference standard for determining the quality and performance of the rockfall barriers. This guideline allow to manufacturers to perform the full-scale crash test on their barriers, in fact ETAG 027 define all the procedures to carry out the full-scale test. Several other

A. Grimod (✉)
Gierrevu s.r.l., Passage du Verger n.5, 11100 Aosta, Italy
e-mail: albertogrimod@yahoo.it

G. Giacchetti
Officine Maccaferri SpA, Via Kennedy n.10, 40069 Zola Predosa, BO, Italy
e-mail: giorgio.giacchetti@maccaferri.com

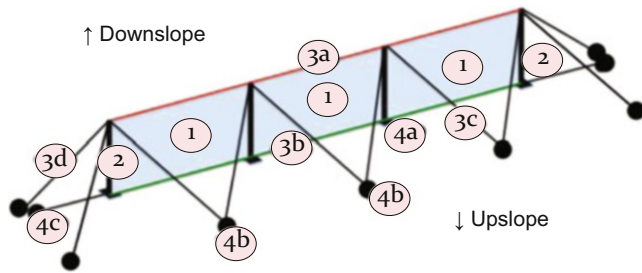


Fig. 1 Functional modules (interception structure): (1); post: (2); upper longitudinal cable: (3a); lower longitudinal cable: (3b); upslope bracing cable: (3c); lateral bracing cable: (3d); post foundation: (4a); upslope bracing cable foundation: (4b); lateral bracing cable foundation: (4c)

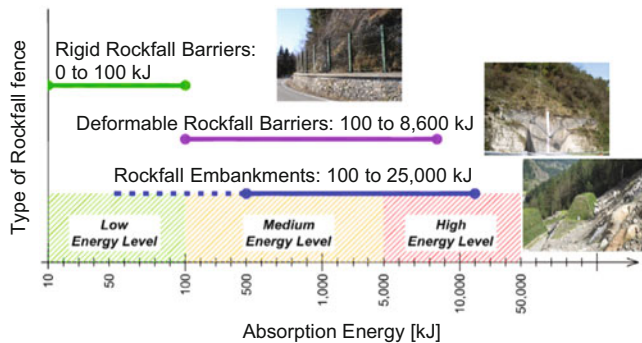


Fig. 2 Correlation between the energy level and the type of rockfall fence suggested: rigid barriers (energy absorption 0–100 kJ: low energy level); deformable barriers (100–8,600 kJ: medium-high energy level); rockfall embankments (up to 25,000 kJ: low to very high energy level) (Grimod et al. 2013a)

guidelines (i.e. Swiss Code WSL 2001) or recommendations (AASHTO 2003) are available worldwide, but the European one is strictest, and it establishes also the factory controls that producers must follow on the materials composing the kit.

At the time of writing, 8,600 kJ (27 tons travelling at 90 km/h) is the maximum capacity for a deformable rockfall fence tested in accordance with ETAG 027 (Fig. 2).

Design Approach for Rockfall Barriers

Rockfall Trajectories Analysis

The first step to design a rockfall barrier is to define the trajectories of the potential unstable blocks along the slope. This study can be performed with commercial software, which allows the user to define in any point of the slope the energy, the velocity, the height of the bounces, and the end point of the falling masses (Fig. 3).

The input data of the rockfall simulations are based upon the results of geomechanical, geological and topographic

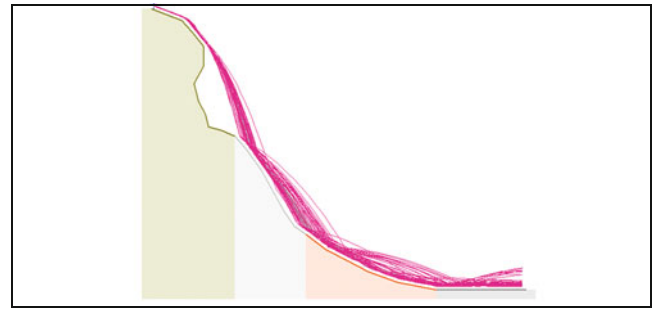


Fig. 3 Example of a rockfall simulation (RocFall 5.0)

surveys. The goal of the geomechanical survey is to characterize the unstable area in order to identify the number and the dimension of the potential blocks that can fall. Then, the geological survey must be completed in order to identify the different soils present along the slope, and consequently define the restitution coefficients and/or the friction parameter block-soil in every area of the slope. In this way the model of the motion of the boulder can be describe. Finally, the topography survey is aimed to identify the geometry of the detachment area and the slope below. In this way the location of the rockfall barriers can be defined. Obviously the precision of the topographic survey is advisable, but it should be recalled that many software perform the best results when the points of the topographic section are 5–10 m spaces.

In order to have reliable results, the rockfall simulations should always consider no less than 1,000 trajectories (Giani 1997; UNI 2012; Giacchetti and Zotti 2012).

Moreover, to validate the trajectory analysis a back analysis is always recommended. This practically means that the statistical distribution of the end-point (figured out with the calculation models) should match the real distribution of the blocks found along the slope. This validation can be done changing the dynamic coefficients of the trajectory (usually defined by coefficients of restitution for the bouncing, and by friction angle for the rolling motion). It should be noticed that the dynamic coefficients, which describe the viscous behaviour of the impact, basically depends on several factors like the ground type, the slope roughness, and the shape, the size and the velocity of the boulder. The dynamic coefficients reported in the technical literature, (Spang 1987; Azzoni et al. 1995; Giani 1992, 1997; Hoek 1986), which often are not related to any of the previous factors, must be intended as indicative.

Serviceability and Ultimate Limit State

ETAG 027 introduces an innovative concept for the absorption energy of the fence. The guideline specifies that, if manufacturers want to test and certified their barriers, they need to perform two different types of tests on their systems:

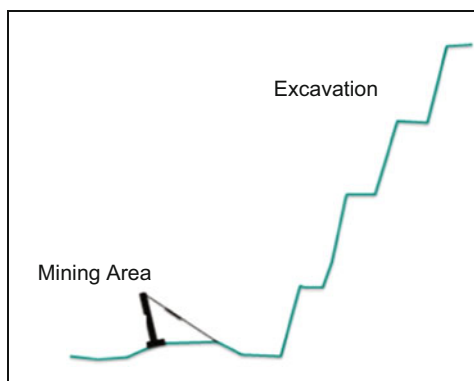


Fig. 4 Example of a rockfall barrier designed at the maximum energy level (MEL): easy maintenance and high risk admitted (i.e. mining industry)

at the Maximum Energy Level (MEL) and at the Serviceability Energy Level (SEL), which is 1/3 of the MEL. For instance, a 3,000 kJ barrier must be tested at 3,000 kJ (MEL) and at 1,000 kJ (SEL) as well. This approach allows designers to develop their design at the service and ultimate limit state.

The SEL criterion is normally used in order to reduce the maintenance costs of the barrier, when the site is vulnerable to multiple impacts and a very low risk is admitted. This approach is obviously the most expensive, because it is necessary to use a barrier with a capacity three times higher than the minimum required, but on the other hands it can increase significantly the safety condition of the area. A typical application of a SEL-design is at the entrance of the tunnel portals (Grimod and Giacchetti, 2013a).

The MEL criterion is normally adopted when there is a low frequency of rock falls or only one boulder is expected to fall, if the maintenance can be easily done and/or if the risk level admitted is high. Using this approach, the initial cost of the structure is certainly lower than the one designed at the SEL, but the maintenance cost can be higher and the safety level is surely lower. Typical uses of rockfall barriers designed at the maximum energy level could be for temporary works, or installations at the base of a re-profiled slope, as often happens in mining applications (Grimod and Giacchetti, 2013a) (Fig. 4).

Installation Aspects

Designers should consider that the full-scale crash tests on the barriers are performed in ideal condition, which are often very different from the in-situ one. Here below are listed the main differences that can be easily observed:

- In the test facility the barrier is assembled as a perfect plane, and the boulder hits in the center of the central



Fig. 5 Example of a difference in post elevations which may modifies the barrier behavior because it induces anomalous stress conditions: low stress in one direction of the panel (*continuous line*) and high stress in the other one (*dash line*). Location: Autostrada A22—km 62 + 640 and km 63 + 150, Bolzano (Ita)

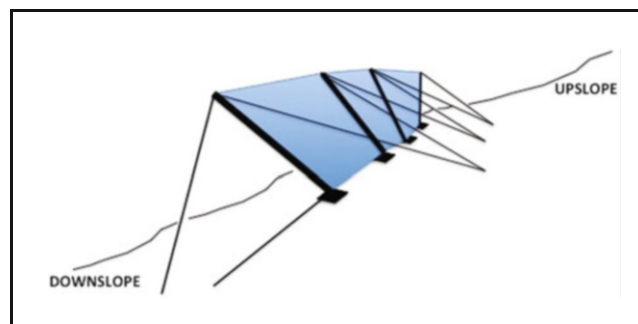


Fig. 6 Example of a barrier configuration with the post not parallel

module. But the impacts in the field can happen at any point on the barrier (on top, on the bottom, the corners, on the post, etc).

- Many times the impact on the barriers is due to multiple rocks, whereas the test is done with a single rock. Multiple impacts constitute one of the most severe conditions for a barrier, especially when they involve two or more functional barrier modules or spans.

Then, concerning barrier installation on a slope, the main difficulties are the following:

- The barriers are tested with three functional modules (30 m in length), whereas on the slopes they are often assembled with longer or shorter lengths.
- Most frequently, after the installation on the slope, the barrier is not perfectly planar, as it may be installed on a very irregular slope—so that the functional modules show different elevation on the foundation of the posts (Fig. 5), planar distortions (Fig. 6), and planimetric deviations (Fig. 7).

Since the crash test cannot describe the barrier behaviour for all the real impact conditions, the test must be considered as an index test. Thus, the rated energy capacity of the barrier must be considered as nominal (Brunet et al. 2013).

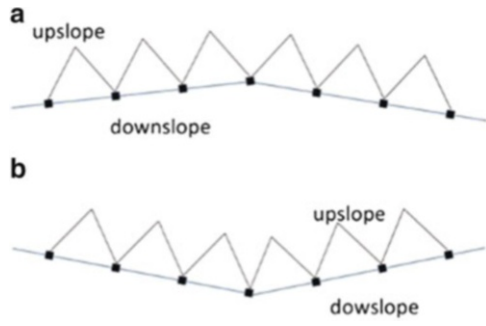


Fig. 7 Example of two possible planimetric distortion of installed rockfall barrier: large deformation in case (a), and possible tilt of the post in base (b)

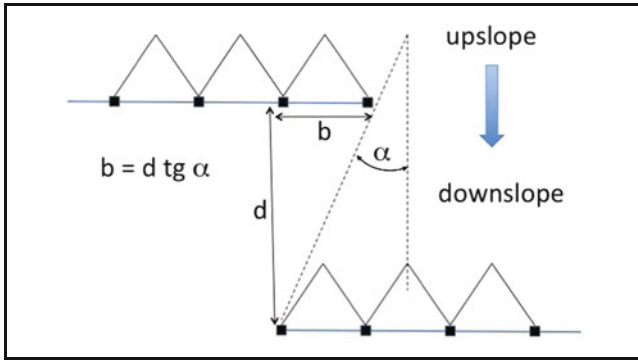


Fig. 8 Procedure for the calculation of the overlap and the distance between two barriers

For this reason the designer should apply some safety coefficients in order to reduce the nominal energy level of the barrier, and increase the energies acting on the structure.

Another important aspect, to be considered during the design is the location of the barriers. For instance, when two or more independent barriers have to work as one, the contiguous lateral modules should be overlapped because the lateral functional modules could represent weak points. A simple and safe rule for the overlapping is the following (Giacchetti and Zotti 2012): (a) the spacing between the two alignments must be enough to allow the deformation of the upslope barrier without interference with the downslope barrier (distance d in Fig. 8); (b) the overlapping must be minimum half module-width. When the barriers are far from each other, the minimum overlap can be estimated with the following formula (distance b in Fig. 8):

$$b = d \cdot \operatorname{tg} \alpha \quad (1)$$

Where b is the overlap, d is the distance between the barriers, and α is the deviation angle of the trajectory from the maximum gradient ($\alpha = 10^\circ$ when the shape of the boulders is spherical and the slope morphology is regular, and $\alpha = 45^\circ$ when the shape is tabular and the slope is uneven).

Minimum Energy of the Barrier

The following formulas describe the steps to design a rock fall barrier according to UNI 11211:4—2012 and Peila et al. 2006. The equation at the base of this design method is the following:

$$E_{sd} < E_{\text{barrier}} / \gamma_E \quad (2)$$

Where: E_{sd} is the design energy level developed by the block against the barrier (see formula (3)); E_{barrier} is the energy absorbed by the barrier (as defined with the crash test carried out according to ETAG 027 at the MEL or SEL); γ_E is the safety coefficient related to the energy level adopted during the design ($\gamma_E > 1.0$ for MEL approach; $\gamma_E = 1.0$ for SEL approach) and to the length of the barrier ($\gamma_E > 1.0$ if the barrier is shorter than 30 m; $\gamma_E = 1.0$ if the barrier is at least 30 m long).

The design energy of the boulder (E_{sd}) is defined with the classical formula of the kinetic energy increased by a safety coefficient ($\gamma_R \geq 1.0$), which considers the human risk. In the formula the spin effect of the falling rock can be neglected because generally it corresponds to approx. 5–15 % of the total energy.

$$E_{sd} = \left(\frac{1}{2} M_d v_d^2 \right) \gamma_R \quad (3)$$

Where: M_d and v_d are respectively the mass and the velocity of the design block

As per Eq. (3), designers must define the design mass and velocity, which are defined as following:

$$M_d = (\operatorname{Vol}_B \gamma) \gamma_{\text{VOL}} \gamma_\gamma \quad (4)$$

$$v_d = v_t \gamma_{\text{Tr}} \gamma_{\text{Dp}} \quad (5)$$

Where: Vol_B is the volume of the design block and γ is the unit weight of the rock; γ_{VOL} is the safety coefficient related to the precision of the design block survey ($\gamma_{\text{VOL}} \geq 1.0$); γ_γ is the safety coefficient related to the evaluation of the unit weight of the rock ($\gamma_\gamma \geq 1.0$); v_t is the velocity calculated with the rockfall simulation and considering the 95° percentile of the velocities; γ_{Tr} is the safety coefficient related to the reliability of the rock fall simulation ($\gamma_{\text{Tr}} \geq 1.0$); and γ_{Dp} is the safety coefficient related to the quality of the topographic survey ($\gamma_{\text{Dp}} \geq 1.0$).

Minimum Height of the Barrier

The minimum height of the barrier has to be defined considering the design height (h_d) plus a free zone ($f_{\text{min}} \geq 50$ cm) which cannot be impacted.

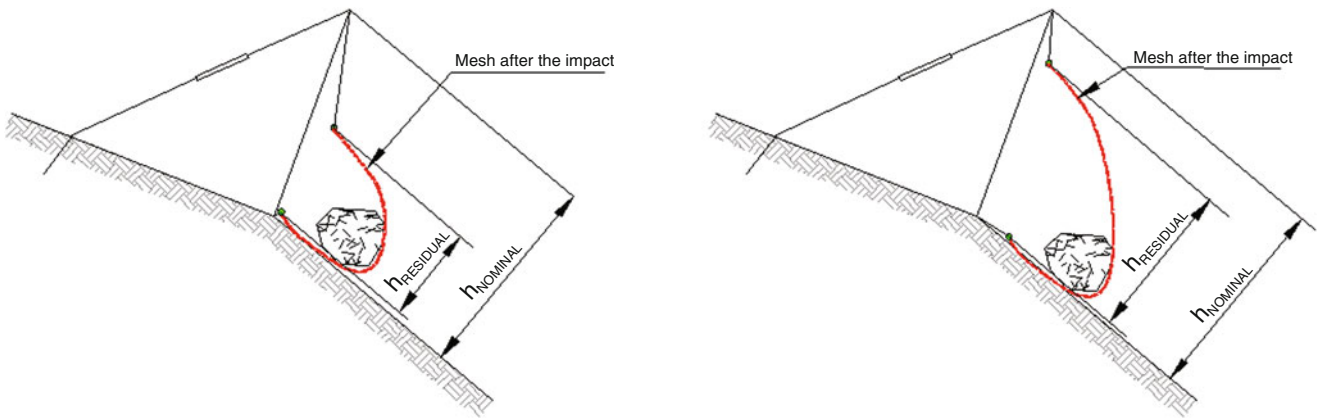


Fig. 9 Advantage having a high residual height of the barrier. *Left:* barrier with a residual height > 50 %; *Right:* barrier with a residual height = 75 %. Both are classified in Category A (according to ETAG

027/2008), but the second barrier has a higher safety margin if impacted by a second block (Grimod and Giacchetti, 2013b)

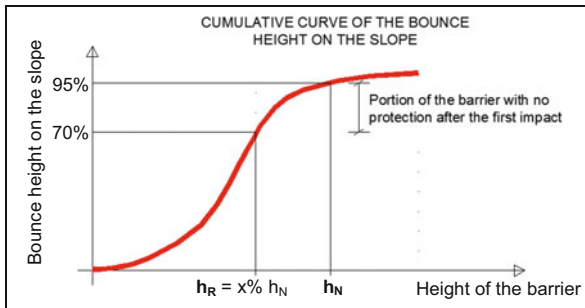


Fig. 10 Example of the reduction of the safety level of the barrier after the first impact

$$H_{tot} = H_d + f_{min} \tag{6}$$

Where: H_{tot} is the nominal height of the tested barrier according to ETAG 027; H_d is the design height of the trajectories define with the following equation:

$$H_d \geq H_t \gamma_{Tr} \gamma_{Dp} + R_{block} \gamma_R \tag{7}$$

Where: H_t is the height of the trajectories defined with the numerical simulations and considering the 95° percentile of the heights; R_{block} is the average radius of the design block; and γ_R is the safety coefficient applied on the radius of the block ($\gamma_R \geq 1.0$).

Minimum Distance Between the Barrier and the Protected Area

The minimum distance between the barrier and the structure to be protected is determined as follow:

$$D_A \geq D_b \gamma_d \tag{8}$$

Where: D_A is the minimum distance between the barrier and the protected zone; D_b is the maximum dynamic deformation of the barrier, measured in accordance with ETAG 027 after the full-scale crash test at the MEL; and γ_d is the safety coefficient related to the energy level adopted during the design ($\gamma_d > 1.0$ for MEL approach; $\gamma_d = 1.0$ for SEL approach), to the length of the barrier ($\gamma_d > 1.0$ if the barrier is shorter than 30 m) and to barrier-span impacted by the boulder ($\gamma_d > 1.0$ if the lateral span of the barrier may be impacted).

Residual Height of the Barrier

Another fundamental aspect, which is not mentioned in the calculation, is the residual height of the fence after the MEL impact. In order to evaluate the risk of the protected area after a rockfall impact on the barrier, designers should know the exact residual height of the barrier.

ETAG 027 defines the residual height (h_R) as the minimum distance between the lower and the upper longitudinal cable, measured orthogonally to the reference slope after the test and without removing the block from the interception structure. Moreover, it classifies the barriers in three categories based on the residual height: when $h_R > 50\%$ of the nominal height (h_N), the fence is classified in Category A; if $30\% h_N < h_R < 50\% h_N$ the barrier is in Category B; and if $h_R < 30\% h_N$ the barrier is in Category C.

To guarantee a high safety level of the protected area it is mandatory to use a rockfall barrier with the highest residual height. In this way, if the barrier is impacted by a block, the high of the interception structure does not change. Thus, the probability that other falling blocks jump above the impacted barrier can be reduced (Fig. 9).

The analysis of multiple impacts can be done comparing the probabilistic distribution of the height of the trajectories with the residual height of the barrier chosen in the design.

Table 1 Performance of the Maccaferri rockfall barriers

Barrier type	Energy level (kJ)	Nominal height (m)	Residual height (%)	Max elongation (m)
RMC 050/A	536	3.0	74.4	3.70
RMC 100/A	1,073	3.5	68.8	4.45
RB 1500	1,637	4.0	61.7	5.80
RMC 200/A	2,083	4.0	72.3	5.25
RMC 300/A	3,136	5.0	73.8	6.05
RMC 500/A	5,254	6.0	69.8	6.50
RMC 850/A	8,644	7.0	57.6	8.10

Values measured during the MEL crash-tests carried out according to ETAG 027

Table 2 Residual height (HR) and maximum elongation (El.) of the most common energies used for rockfall barriers

Energy (kJ)	Manuf. 1		Manuf. 2		Manuf. 3	
	HR (%)	El. (m)	HR (%)	El. (m)	HR (%)	El. (m)
500	68	4.90	50	5.20	75	3.70
1,000	60	8.54	69	4.87	69	4.45
2,000	60	8.96	56	7.19	72	5.25
3,000	64	9.23	59	7.22	74	6.05
5,000	61	8.15	65	8.62	70	6.50

Comparison between three different manufacturers (Manuf.)

The following graph explains how this analysis may be carried out. The specific example (Fig. 10) shows that, after the first impact, the reliability of the simulation drop from 95 % to 70 % of the bounce height on the slope, this means that the allowable probability increase from 5 % to 30 %.

Main Barrier Features in the Design

In order to reduce the technological limits of the fence, designers must evaluate the results of full-scale tests in terms of residual height and maximum elongation. Table 1 summarizes the features of the Maccaferri rockfall barrier portfolio.

To increase the safety level after the first impact, a high residual height is strictly recommended and, a low deformation of the barrier is also suggested when the distance between the fence and the protected zone is limited. Considering these two barrier characteristics, Maccaferri has developed its rockfall barriers in order to have the high performances: high residual height and minimum downslope elongation (Table 1). Table 2 presents the comparisons between the most common energies used for rockfall barrier. In this way, the reader may easily figure out the variety of the performances of some of the barriers available in the market.

Other important parameters have to be considered during the barrier design are the effort that the structure transmit to the foundations. These values are measured during the crash-tests in order to define the type and length of the foundations of the barrier, which depend on the type of soil.

Conclusion

The European Organization for Technical Approval issued in 2008 a Guideline (ETAG 027) which defines a standardized procedure that manufactures may follow to test their rockfall fences at the full scale. Thanks to these full-scale tests it is possible to understand the performances of the deformable rockfall barriers. This guideline is essentially the only test and construction framework utilized by manufacturers all around the world, but unfortunately it describes the performance of the barrier only in ideal conditions and it does not take into consideration all the technological limits of these structures which must be considered during the design phase.

A new approach had been defined by the Italian Standard (UNI 11211:4—2012) in order to design the barrier at ultimate and serviceability limit state. To increase the safety level of the protected area, the forces acting on the barrier are increased and the barrier resistances are reduced.

Extreme attention must be focused on the performance of the barrier in term of residual height and deformation, in order to increase the safety level of the protected area once the barrier is hit.

References

- AASHTO (2003) Recommended procedures for the testing of rock-fall. Standing committee on highways prepared by Jerry D. Higgins
- Azzoni A, La Barbera G, Zaninetti A (1995) Analysis and prediction of rockfalls using a mathematical model. *Int J Rock Mech Min Sci* 32:709–724
- Brunet G, Giacchetti G, Grimod A (2013) Rockfall barrier behavior under multiple impact events. 64th highway geology symposium, New Hampshire, USA, 9–12 September 2013
- EOTA (2008) ETAG 027: guideline for European technical approval of falling rock protection kits, Brussels. <http://www.eota.be>
- Giacchetti G, Zotti IM (2012) Design approach for rockfall barriers. Proceedings of the XI national congress of geotechnic, San José, Costa Rica, 9–10 August 2012
- Giani GP (1992) Rock slope stability analysis. Balkema, Rotterdam
- Giani GP (1997) Rockfall. Hevelius Edizioni, Benevento
- Grimod A, Giacchetti G (2013a) High energy rockfall barriers: a design procedure for different applications. 23rd world mining congress, Montreal, QC, Canada, 11–15 August 2013
- Grimod A, Giacchetti G (2013b) New design approach for rockfall barriers. EuRock 2013, Wroclaw, Poland, 23–26 September 2013
- Hoek E (1986) Rockfall: a computer program for predicting rockfall trajectories. Unpublished internal notes, Golder Associates, Vancouver
- Peila D, Oggeri C, Baratono P (2006) Barriere paramassi a rete. Interventi e dimensionamento. GEAM, Quaderni di studio e di documentazione n26
- Spang RM (1987) Protection against rockfalls – stepchild in the design of rock slopes. 6th international congress on rock mechanics, Montreal, Canada. pp 551–557
- UNI (2012) UNI 112111-4: 2012 rockfall protective measures – Part 4: definitive and executive design. Ente Nazionale Italiano di Unificazione, Milano Italia (in Italian). <http://www.uni.com>
- WSL (2001) Guideline for the approval of rockfall protection kits. Swiss Agency for the Environment, Forests and Landscape (SAEFL), Berne, Switzerland



Design Approach for Secured Drapery Systems

Alberto Grimod and Giorgio Giacchetti

Abstract

Secured drapery systems are composed of a steel rockfall mesh and a pattern of nails disposed with different configurations along the slope. The goal of this solution is to stabilize the superficial portion of the rock slope (by the nails) and keep in place the unstable rock material (by the mesh). The design procedure can be very complicated due to the difficulties to obtain accurate input data in order to define the geomechanical models. This paper describes a simplified design approach, which combines the in-situ evidence and the experience of designers with the results of full scale tests on mesh. The proposed calculation allows one to define the best type of mesh and the nail characteristics both at Ultimate and Serviceability Limit State.

Keywords

Rockfall protection • Steel mesh • Pin drapery • Design • Nails • Anchors

Secured Drapery Systems

Secured drapery systems (or pin drapery) are composed of anchors and a steel mesh (rockfall net). They are really common rockfall mitigation measures, because they can stabilize the superficial portion of the rock slope, maintain the rocks in place and consequently reduce the maintenance cost compared to the simple drapery system. The goal of this system is to improve the superficial rock face stability and maintain the debris/rock on place in the slope: for this reason it can be classified as an active protection measure.

This kind of intervention is typically recommended where the number of unstable blocks is too large and/or if their dimension is too small to be consolidating by single nails (Zotti and Giacchetti 2012).

A. Grimod (✉)
Gierrevu s.r.l., Passage du Verger n.5, 11100 Aosta, Italy
e-mail: albertogrimod@yahoo.it

G. Giacchetti
Officine Maccaferri SpA, Via Kennedy n.10, 40069 Zola Predosa, BO,
Italy
e-mail: giorgio.giacchetti@maccaferri.com

The stability of the superficial rock face is attained using anchors (Fig. 1). These elements are steel bars (called nails) which generate their resistance only if the rock movements or deformations occur: the nail resistance is passively generated. From a geotechnical point of view these elements must be considered as passive, because no pre-stress is applied to them.

Characterization of the Mesh

The design of the mesh requires the identification of the main performances of the mesh, such as the tensile strength and the deformation under a punch load.

The first parameter (tensile resistance) is defined with laboratory tests able to figure out the maximum traction load applicable on the mesh (normally identify in kN/m). These tests are performed following different standards available around the world (i.e. [ASTM A975](#) or [EN 15381:2008](#)).

To analyze the behavior of the mesh under a punch load, and obtain load-displacement curves in 2012 the Italian Organisation for Standardization issued the [UNI 11437](#)

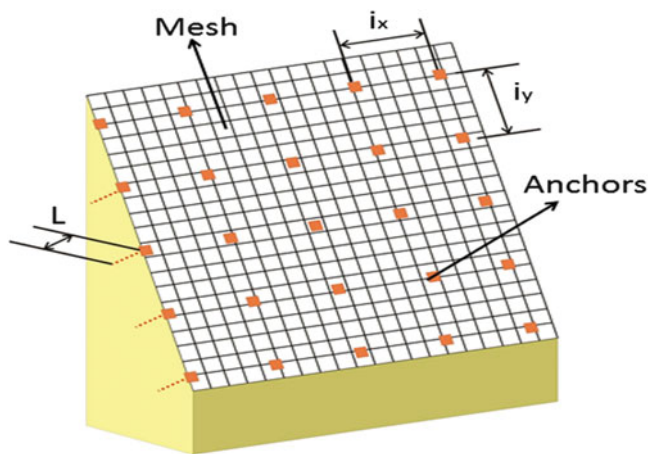


Fig. 1 Pin drapery system: the intervention is composed by a rockfall mesh and a pattern of anchors (L = length of the anchors; i_x and i_y = distance between the anchors, horizontally and vertically)

(Rockfall protection measures—Tests on meshes for slope coverage), which defines, for the first time around the world, a standardized methodology to carry out laboratory punch tests on a sample 3.0×3.0 m.

The most relevant research to analyze the performance of the mesh stressed by a punch test was performed in Pont Boset (Aosta, Italy) by the Polytechnic of Turin (Bertolo et al. 2009). The goal of the research was to study the real behavior of different type of mesh installed on a rock slope. The meshes were anchored to the rock with a pattern of four nails, disposed on the corner of a square having dimension 3.0×3.0 m. The falling block was simulated by a piston connected to a punch device (diameter = 1.5 m); the piston was installed in order to develop a 45° pressure against the mesh. The maximum elongation of the piston was approx. 1.2 m.

This study showed that the effect of constrains, scale and inclination of the load affect the performance of the mesh in terms of capability to contain the deformations. From the graphs below (Fig. 2) it is possible to define the difference between the results obtained in laboratory (with a sample 1×1 m and 3×3 m) and during the in-situ tests (Bertolo et al. 2009).

The graphs show that there is a direct proportion between the sample size and the displacement, as well as between the sample size and the punch resistance (scale effect). The magnitude of this scale effect depends upon the deformability of the fabric. In the case of the single twist mesh, where there is a large freedom of movement and stretch for the wire onto the fabric, the scale effect is emphasized, whereas on the double twist one, in which the wire cannot move, this effect is lower.

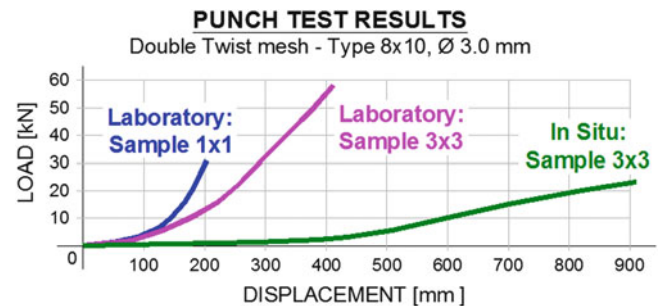


Fig. 2 Difference between the load-displacement curves obtained on different punch tests on a double twist mesh, type 8×10 , wire diameter 3.0 mm and steel strength between 350 and 550 MPa. Blue curve: laboratory test on a small simple (1×1 m) (Agostini et al. 1988)

Design of the Components of the Secured Drapery

Design of pin drapery systems could be complex due to the numerous variables and input data needed to define an accurate model: topographic survey, rock mass properties, joint characteristics, mesh type, type of anchors and other boundary conditions. Often the solution to the problem requires complex numerical analyses which are not practical for every project, especially if the size of the intervention is limited and/or the solution has to be found in a really short time and with limited economic resources.

This new simplified design approach is developed in order to obtain a design tool that can give reliable results in a really short time and with a low amount of input data. A more precise estimation of the problem would require an accurate geomechanical survey and an analysis according to the Goodman & Shi theory (Goodman and Shi 1985).

This simplified design method is based on several hypotheses on the behavior of the mesh and on the rock-slope characteristics. Here below are summarized the assumptions at the base of the approach (Grimod and Giacchetti 2013):

1. According to the in-situ evidence and the punch tests (both in laboratory and in-situ) previously described, the mesh is modeled as a deformable and flexible structure which is not able to transmit any load to the rock. The mesh is activated only if a load starts to push against it. Pre-stresses on the mesh do not develop any forces in the rock mass.
2. The full-scale tests and the in-situ evidence show that meshes are stressed mainly in the longitudinal way (longitudinal tensile strength). In the 80–90 % of the pin drapery installations a transversal resistance up to 15–20 kN/m is enough to guarantee the performance of the system.

3. Considering that superficial instabilities stabilized with pin drapery systems have a thickness no higher than 1.0 m, the approach considers an undefined slope characterized by a constant unstable thickness and a constant slope inclination;
4. In the calculation a limit equilibrium condition of the unstable blocks is considered. In this way the worst configuration is taken into account.

Input Data

The data used as input may be grouped into four main categories:

1. Geotechnical, geomechanical and slope parameters: to define the proper geomechanical model of the slope;
2. Nail configuration and characteristics: to define the maximum volume to be stabilized;
3. Mesh;
4. Seismic action acting on the system.

A constant inclination of the slope (β) and a continuous constant unstable superficial thickness (s) has to be identified, as well as the unit weight of the rock (γ).

Moreover, the intrinsic characteristics of the most critical joint set have to be described in term of roughness (JRC), joint compressive strength (JCS) and inclination (α). These last three parameters can be characterized by a geomechanical survey or with a visual analysis of the instability and then using the literature. JCS is measured by the Schmidt hammer. In a simplified way JCS can be considered as $1/3$ of the UCS (Unconfined Compressive Strength). JRC is measured by the Barton "comb". Its values are between 0 (smooth) and 20 (very rough joint). If the joint is weathered or clay covered, it is better to take low values of JRC . Higher are the values of JCS and JRC , and higher is the resistance of the anchor under shear stress.

Once the rock and the instability are defined, the structural component of the system must be imposed. The yield resistance of the steel (σ_{ST}), the nail diameter (ϕ) and inclination (θ_0) must be identified, as well as the anchor distance (i_x and i_y) in order to figure out the dimension of the maximum block to be stabilized. The nail inclination is generally between 10° and 30° from the horizontal. Note that the nail resistance decreases significantly if the inclination of the bar deviates to much from the perpendicular of the sliding surface.

Another important parameter is the bond stress (τ_{LIM}) between the grout and the rock. This tangential tension can be determined on site, with in-situ pull-out tests on existing anchors, or using the literature.

Additionally, the mesh has to be chosen. The net is characterized, as previously described by a tensile strength

and its capacity to contain the deformation under a punch load.

The last parameter that could be taken into consideration during the calculation is the seismic coefficient (c).

Calculation Approach

The Limit State Design (LSD) approach is used in this simplified calculation. This method provides margin of safety by introducing safety coefficients: partial factors, which decreases the resisting forces to produce the design strength (R_d), and load factors, which increases the acting forces to produce the design load (E_d) (as per EN 1997 1, 2005).

The equation at the base of the LSD calculation method is described with the following formula:

$$R_d \geq E_d \quad (1)$$

Thus, all the safety factors on the different components of the system must be at least equal to 1.0:

$$R_d/E_d \geq 1.0 \quad (2)$$

Feature of the Instability

Using the geomechanical parameters of the slope, it is possible to calculate the dilatancy of the sliding surface with the Barton-Bandis resistance criteria.

First of all the effective joint compressive strength (JCS) and the effective roughness (JRC) have to be evaluated as following:

$$JCS = JCS_0 \left(\frac{L_G}{L_0} \right)^{(-0.03 \cdot JRC_0)} \quad (3)$$

$$JRC = JRC_0 \left(\frac{L_G}{L_0} \right)^{(-0.02 \cdot JRC_0)} \quad (4)$$

Where: JCS_0 and JRC_0 are respectively the compressive strength and the roughness of the most critical joint set, L_0 is the length of the joint, and L_G is the length of the sliding joint, assumed equal to i_y , which is the vertical distance between the nails.

The formulas above take into account the worst scenario, because they consider the maximum potential dimension of the block, which is defined by the distance between the nails: this is the maximum dimension of the block that can fall. Of course, in the reality, smallest blocks usually fall. These one will be maintained in place by the mesh, which must be properly designed.

Then the normal stress acting on the average slip surface (σ_{PLAN}) has to be calculated:

$$\sigma_{PLAN} = \frac{W}{i_x \cdot i_y} \cos \alpha \quad (5)$$

Where: i_x is the horizontal distance between the nails and W is the total unstable weight controlled by one anchor. This value is defined by the volume of rock between the nails (Vol) multiplied by the rock unit weight, as per the following formula.

$$W = Vol \cdot \gamma = (i_x \cdot i_y \cdot s) \cdot \gamma \quad (6)$$

At this point the initial dilatancy of the most critical joint set can be determined with the Barton-Bandis criteria (Barton and Bandis 1982; Bandis 1990):

$$\delta \cong \frac{JRC}{3} \log_{10} \left(\frac{JCS}{\sigma_{PLAN}} \right) \quad (7)$$

Calculation of the Nails

The design of the anchoring system has to be divided into two parts. The first one takes into consideration the capability of the nail to stabilize the superficial portion of the rock-slope, thus the minimum bar diameter has to be designed; while the second has to define the minimum theoretical length of the steel bar.

To define the minimum bar diameter to be used to contrast the shear force developed by the unstable block a few parameters have to be defined, such as the effective cross section of the steel bar (Φ_{EFF}), the nail inclination from the horizontal (ε) and the design yield stress of the steel of the anchor (σ_{ADM}). These three elements can be calculated with the following equations:

$$\Phi_{EFF} = \frac{\pi(\phi_E - 2t_C)^2}{4} - \frac{\pi \cdot \phi_I^2}{4} \quad (8)$$

$$\varepsilon = 90 - \beta - \theta_0 \quad (9)$$

$$\sigma_{ADM} = \frac{\sigma_{ST}}{\gamma_{ST}} \quad (10)$$

Where: ϕ_E and ϕ_I are respectively the external and the internal diameter of the nail (if the steel bar is hollowed), and the t_C is possible corrosion crown to be considered in the calculation. β is the inclination of the slope and θ_0 is the inclination of the bar from the perpendicular to the slope. γ_{ST}

is the partial safety coefficient to be applied to the yield stress of the steel of the bar.

The stabilizing contribution of the nail is (R) (Pellet et al. 1995; Ferrero et al. 1997; Goodman 1989):

$$R = \phi_{EFF} \cdot \sigma_{ADM} \sqrt{\frac{1 + \tan^{-2}(\varepsilon + \delta)}{1 + \tan^{-2}(\varepsilon + \delta) \frac{16}{4}}} \quad (11)$$

At this point the limit equilibrium (Eq. 1) can be rewritten considering the contribution of the nail (Hoek and Bray 1981):

$$W(\sin \beta - c \cdot \sin \beta \cdot \tan \phi) + R \geq W(\sin \beta + c \cdot \cos \beta) \quad (12)$$

Where: Φ is the residual friction angle of the joint. This parameter is really difficult to define by in situ surveys, especially on weathered surficial rock masses and moreover it is not reported in literature like JCS. In order to simplify the calculation procedure the value of the residual friction angle of the joint is imposed equal to 45° , thus the tangent of Φ can be neglected ($\tan \Phi = \tan 45^\circ = 1$). This is a strong but realistic hypothesis at the base of this simplified calculation approach.

Introducing the partial and the load factors, and neglecting the $\tan \Phi$, the stability condition will be:

$$W \sin \beta (1 - c) / \gamma_{RW} + R \geq W(\sin \beta + c \cdot \cos \beta) \cdot \gamma_{DW} \quad (13)$$

Where γ_{RW} and γ_{DW} are respectively the total partial factor and the total load factor which describe the ineptitudes of the input data (as per the LSD method):

$$\gamma_{RW} = \gamma_T \cdot \gamma_W \cdot \gamma_B \geq 1.0 \quad (14)$$

$$\gamma_{DW} = \gamma_{MO} \cdot \gamma_{OL} \geq 1.0 \quad (15)$$

Where: γ_T , γ_W and γ_B are the partial coefficients that take into account the incertitude to define respectively the thickness of the instability ($\gamma_T = 1.20-1.30$), the unit weight of the rock ($\gamma_W = 1.00-1.05$) and rock behaviour, such as weathering or solid rock ($\gamma_B = 1.00-1.05$). While, γ_{MO} and γ_{OL} are the load coefficients that take into account respectively the incertitude on the morphology of the slope ($\gamma_{MO} = 1.10-1.30$) and the possible external load, such snow or ice ($\gamma_{OL} = 1.00-1.20$).

The safety factor of the nail can be defined as:

$$FS_{NAIL} = \frac{FS_{SLP}}{FD_{SLP}} \geq 1.0 \quad (16)$$

Where: FS_{SLP} is the total of the stabilizing force acting on the system, and FD_{SLP} is the total of the driving force acting on the sliding plane:

$$FS_{SLP} = W \sin \beta (1 - c) / \gamma_{RW} + R \quad (17)$$

$$FD_{SLP} = W (\sin \beta + c \cdot \cos \beta) \cdot \gamma_{DW} \quad (18)$$

The second part of the nail design has to evaluate the minimum theoretical length, which is defined as:

$$L_{TOT} = L_S + L_I + L_P \quad (19)$$

Where: L_S is the minimum length of the bar in the stable portion of the rock. This length is defined with the Bustamante-Doix formulation (Bustamante and Doix 1985). In the formula Φ_{DRILL} = drilling diameter; P = maximum pull-out force acting on the anchor (see formula 22). This force is the maximum force between the pull-out force transmitted to the nail by the mesh (P_{mesh}) and the one due to the slope instability (P_{rock}); τ_{LIM} is the bond stress between grout and rock; and γ_{GT} is the safety coefficient applied on the adhesion grout—rock:

$$L_S = \frac{P}{\left(\pi \cdot \phi_{DRILL} \cdot \tau_{LIM} / \gamma_{GT} \right)} \quad (20)$$

L_I is the minimum length of the bar in the unstable portion of the rock:

$$L_I = \frac{s}{(\cos \varepsilon)} \gamma_{DW} \quad (21)$$

L_P is the length of plasticization of the unstable rock mass, generally assumed between 10 and 50 cm, depending on the characteristic of the rock: suggested values are: 0.10–0.15 m, for hard rock (i.e. granite); 0.15–0.25 m, for weak rock (i.e. marl); 0.25–0.45, for very weak rock (i.e. siltstone), and 0.25–0.50, for heavy jointed rocks.

$$P = \max\{P_{mesh}; P_{rock}\} \quad (22)$$

$$P_{mesh} = (M_{B-DRV} - M_{B-STB}) \cos(\alpha + \theta_0) \cdot i_x \quad (23)$$

$$P_{rock} = |FS_{SLP} - R - FD_{SLP}| \cos(\beta + \theta_0) \quad (24)$$

Where: M_{B-DRV} = sum of the driving forces acting on the sliding plane (see Eq. 31); and M_{B-STB} = sum of the stabilizing forces acting on the sliding plane (see Eq. 32).

Mesh Design at the Ultimate Limit State and Serviceability Limit State

The mesh (facing) has to be able to contain the potential unstable blocks that could fall between the nails. These failures are supposed to slide along the most critical joint set (inclined with α) and push against the facing with a certain force (F) which can be divided tangentially (T) and normally (M) to the mesh.

Moreover, the mesh has to be designed in order to contain its deformation (bulging) and consequently reduce the possibility to have the stripping of the anchors. The most suitable mesh suggested for a pin drapery system should have and high tensile strength (to contrast the force T) but above all a higher membrane stiffness in order to have a facing that can contain the deformations due to the force M .

The first parameter to be identified is the maximum rock volume that can slide between the anchors and then push against the facing is:

$$V = V_A + V_B + V_C \quad (25)$$

$$V_A = \frac{1}{2} i_y^2 \cdot \tan(\beta - \alpha) \quad (26)$$

if $\{\beta > \alpha \text{ or } \alpha > \beta - \tan^{-1}(s/i_y)\}$, and $\{\alpha = \beta - \tan^{-1}(s/i_y)\}$

$$V_B = s \cdot [i_y - s / \tan(\beta - \alpha)] \quad (27)$$

if $\{\alpha < \beta - \tan^{-1}(s/i_y)\}$

$$V_C = \frac{1}{2} s^2 / \tan(\beta - \alpha) \quad (28)$$

if $\{\alpha < \beta - \tan^{-1}(s/i_y)\}$

Then, the maximum weight that can slide between the anchors can be calculated (M_B), and consequently the maximum punching force acting on the facing (M):

$$M_B = V \cdot \gamma \quad (29)$$

$$M = (M_{B-DRV} - M_{B-STB}) \cdot \sin(\beta - \alpha) i_x \quad (30)$$

$$M_{B-DRV} = M_B (\sin \alpha + c \cdot \cos \alpha) \gamma_{DW} \quad (31)$$

$$M_{B-STB} = M_B \cdot \sin \alpha (1 - c) / \gamma_{RW} \quad (32)$$

At this point it is possible to define the deformation angle of the mesh (from the slope surface):

$$\rho_P \approx \tan^{-1}(2 \cdot Z_{bulg} / i) \quad (33)$$

Where Z_{bulg} is the displacement of the chosen mesh related to the punch load M . This value is defined on the load-displacement curves determined by the punch-tests. While, i is the average spacing between the anchors

$$(i_x \cdot i_y)^{0.5} \quad (33a)$$

At the ultimate limit state, the mesh is verified if the following condition is satisfied:

$$T_{ADM} - T \geq 0 \quad (34)$$

Where: T_{ADM} is the design tensile strength of the mesh, which is calculated dividing the ultimate tensile strength of the mesh (T_m) by a partial factor (γ_M); and T is the maximum tensile strength developed by the unstable blocks against the mesh.

$$T_{ADM} = T_m / \gamma_M \quad (35)$$

$$T = M \cdot \sin \beta; \quad \text{if} \left(\frac{M}{i_x \cdot \sin(\beta - \alpha - \rho_p)} \right) \geq M \cdot \sin \beta \quad (36)$$

$$T = \frac{M}{i_x \cdot \sin(\beta - \alpha - \rho_p)}; \quad \text{if} \left(\frac{M}{i_x \cdot \sin(\beta - \alpha - \rho_p)} \right) < M \cdot \sin \beta \quad (37)$$

The safety factor of the mesh at the Ultimate Limit State can be defined as following:

$$FS_{MESH-ULS} = \frac{T_{ADM}}{T} \geq 1.0 \quad (38)$$

The calculation of the mesh can be also done at the Serviceability Limit State. Designers must impose a maximum allowable bulging of the mesh (Bulg), which has to be compared to the bulging of the mesh stressed by the load transmitted by the unstable blocks (M). Using the load-displacement curves it is possible to define the following safety factor of the mesh at the Serviceability Limit State:

$$FS_{MESH-SLS} = \frac{\text{Bulg} / \gamma_{M-BULG}}{Z_{bulg}} \geq 1.0 \quad (39)$$

Where γ_{M-BULG} is the partial factor applied to the maximum allowable bulging of the mesh. The authors suggest that this value should not be lower than 1.50 ($\gamma_{M-BULG} = 1.5$, if the facing is properly installed on a regular

surface slope; $\gamma_{M-BULG} = 3.0$, if the mesh is installed improperly on a slope with uneven morphology) (Grimod and Giacchetti 2013).

Conclusion

Secured drapery systems are used to protect rock slopes affected to superficial rockfall phenomena. The system is composed of nails (steel bars), which contribute to stabilize the slope, and by a mesh, which contains the debris or the rock blocks that might move between the nails. To reduce the deformation of the system, steel wire ropes can be applied on the mesh. The system is considered passive, because both mesh and anchors start to develop their resistance only if one or more blocks start to move.

The design procedure can be very complex due to the difficulties in finding the correct input data to insert in the geomechanical model. A simplified approach to designing secured drapery systems is introduced. The calculation method is based on in-situ experiences and on laboratory and full-scale tests carried out on the meshes. The proposed calculation procedure gives the designer the tools to define the proper anchoring system (distance and length of the nails) and the best mesh to be adopted. The results can be obtained with a low amount of simple input data and in a very short time. Moreover, from the design and installation experience gained by the authors, it is possible to conclude that the calculation approach described in the paper give reliable results too.

References

- Agostini R, Mazzalai P, Papetti A (1988) Hexagonal wire mesh for rock-fall and slope stabilization. Publication edited by Officine Maccaferri SpA, Bologna, Italy
- ASTM A975 (1997) (reapproved 2003) Standard specification for double-twisted hexagonal mesh gabions and revet mattresses (metallic-coated steel wire or metallic-coated steel wire with polyvinyl chloride (PVC) coating). ASTM International. www.astm.org
- Bandis SC (1990) Scale effect in the strength and deformability of rocks and roc joints. In: Da Cunha P (ed) Scale effects in rock mechanics, Proceedings of the international workshop scale effects in rock masses. Balkema, Rotterdam, pp 59–76
- Barton NR, Bandis SC (1982) Effects of block size on the shear behaviour of jointed rock. 23rd U.S. symposium on rock mechanics, Berkeley, pp 739–760
- Bertolo P, Oggeri C, Peila D (2009) Full scale testing of draped nets for rock fall protection. Can Geotech J 46:306–317
- Bustamante M, Doix B (1985) Une méthode pour le calcul des tirants et des micropieux injectés. Bulletin Laboratoire Central des Ponts et des Chaussées, n. 140, Nov–Dec, ref. 3047
- EN 1997 1 (2005) Eurocode 7: Geotechnical design – Part 1: General rules European Standard. CEN European Committee for Standardization. <http://standards.cen.eu/dyn/www/f?p=CENWEB:5>

- EN 15381 (2008) Geotextiles and geotextile-related products – characteristics required for use in pavements and asphalt overlays European Standard. CEN European Committee for Standardization. <http://standards.cen.eu/dyn/www/?p=CENWEB:5>
- Ferrero AM, Giani GP, Migliazza M (1997) Interazione tra elementi di rinforzo di discontinuità in roccia - atti “Il modello geotecnico del sottosuolo nella progettazione delle opere di sostegno e degli scavi – IV Conv. Naz. Ricercatori universitari – Hevelius, pp 259–275
- Goodman RE (1989) Rock mechanics, 2nd edn. Wiley, New York, pp 169–171
- Goodman RE, Shi G (1985) Block theory and its application to rock engineering. Prentice-Hall, London
- Grimod A, Giacchetti G (2013) A new design approach to design pin drapery systems. GeoMontreal 2013, Montreal, Canada, 29 September–3 October 2013
- Hoek E, Bray JW (1981) Rock slope engineering. IMM, London
- Pellet F, Egger P (1995) Analytical model for the behaviour of bolted rock joints and practical applications. In: Widmann R (ed) Proceedings of international symposium anchors theory and practice. Balkema, Rotterdam
- UNI 11437 (2012) Rockfall protection measures: tests on meshes for slope coverage. UNI Ente Nazionale Italiano di Unificazione
- Zotti IM, Giacchetti G (2012) Superficial consolidation for rock slopes. XI Congreso Nacional de Geotecnia, Congeo, Costa Rica. San José, 9–10 August 2012



Study on Damage Deterioration of Rock Slope Under Dynamic Loads

W.B. Jian and X.T. Xu

Abstract

One concern to abrupt failure of rock slope is caused by cumulative damage under dynamic load, and the damage deterioration of rock mass strength is one of the important factors. At the University of Fu Zhou, both laboratory tests and numerical simulation were carried out to study the survival conditions of slope due to the deterioration of geotechnical parameters under dynamic loads. Sandstone fatigue curve and damage evolution rule deduced based on damage mechanics theory could be obtained from fitting the laboratory test data. Relevance between safety factor and fatigue life of rock slope in Sha County was simulated by the finite element method. By means of numerical calculations, the relationship between survival ratio, safety factor and damage factor under dynamic load could be achieved by combining with Weibull distribution function expression of survival ratio and cumulative damage factor. Results show that safety factor of the slope will decrease with its consumption life increasing, and the early changes in safety factor have more sensitivity, it also possessing a middle transition section characteristic before the slope developed to sudden failure; the longer residual life is and the higher safety factor becomes, the greater slope survival ratio will be. Taking the characteristics and median cumulative damage factor as a norm of slope security evaluation respectively, the former indicates that the slope owns a life of more than 35.89 years and its safety factor is greater than 1 but smaller than 3.281; the later means that a higher safety factor is called for meeting the slope survival requirements. Finally, the paper points out that during slope engineering design not just slope safety factor should be considered but also combining safety factor with durability based on the slope sudden failure features and service life requirement.

Keywords

Damage deterioration • Survival ratio • Cumulative damage factor • Safety factor

Introduction

With the rapid development of China's economy, a lot of infrastructures (such as highways, railways and hydropower plants, etc) get vigorous development, and constantly extending to the mountains, causing slope engineering problems become increasingly prominent. For rock mass as foundation or slope, fatigue damage (rock mass strength degradation) caused by the environment vibration due to the continuing vehicle and wave loads and others can make it generate large breaking deformation at lower stress levels,

W.B. Jian (✉) • X.T. Xu
Institute of Geotechnical and Geological Engineering,
Fuzhou University, Fuzhou 350108, China

Department of Resources and Urban-Rural Development,
Fuzhou University, Fuzhou 350108, China
e-mail: jwb@fzu.edu.cn; xxtmdd@163.com

leading to “structural” fail. The influence of dynamic loading is being taken into account gradually in durability design and stability evaluation of slope in mountain highway constructions. Relative to static problems of slope, slope dynamic issues become more complex, but are not properly studied (Huang et al. 2008; He et al. 2009).

Currently, there have been a number of ground-breaking research in areas, such as: the basic deformation characteristics (Ge et al. 2003; Jafari et al. 2004; Bagde and Petros 2005), acoustic emission characteristics (Jiang et al. 2004; Fan et al. 2009), preliminary law of mesoscopic damage crack extending to fracture (Ge 2008; Erarslan et al. 2012), damage characteristics based on real-time ultrasonic velocity method (Fan 2008) and non-linear dynamic damage mechanics theory (Qiu 2005; Li 2008) in the fatigue damage process of rocks under dynamic load. In the respect of analyzing slope engineering reliability, Wang et al. (2006) established 3D random damage fields of the rock mass in different excavation stages and adopted mean value and standard deviation of the damage tensor to express the dynamic variation rule of time and space in different stages. Slope reliability can also use the Fuzzy stochastic theory to evaluate, Wang et al. (2011) applied the fuzzy stochastic theory to evaluate slope reliability, and introduced the subordinate function of stability factor to perform fuzzy reliability estimate of the actual working condition of the slope in order to consider fuzzy stochastic features of random variables. However, few research studies on reliability have been focused on “survival ratio” or “damage probability” when rock damage accumulates to approach failure. Therefore, in order to study the survival conditions of slope under dynamic loads, this paper carried out the following work: (1) From the damage mechanics basic theory, use reasonable dissipation potential function to analyze the development law of rock fatigue damage, establish fatigue damage model considering initial cumulative damage factor, then, determine the model parameters by fitting the experimental data. (2) Introduce Weibull distribution of cumulative damage factor to establish the relationship between survival ratio and cumulative damage factor. (3) Combining practical projects, the safety factor and service life (i.e., the size of the cumulative damage factor) are combined by numerical simulation method and finally achieve the purpose of using the relationship between survival ratio, service life and safety factor to show the health situation of rock slope in its whole life cycle, which can provide an idea for reliability analysis of slope engineering research. The above research is of important theoretical and practical significances to the evaluation on the durability of existing slope engineering as well as prediction of its service life under long term dynamic loads.

Establishment of Damage Model

The fatigue damage of rock is caused by irreversible micro-damage accumulation under cyclic load. Due to accumulated plastic deformation is small in each cycle of high-cycle fatigue (phenomenon that rock material can withstand multiple repeated loads under low stress level), it is called micro-plastic strain (represented with $\dot{\kappa}$, Ge et al. 2003). In order to establish fatigue damage equation expressed by cycle number, fatigue damage should be regarded as associated with micro-plastic strain (Xie 1990). The damage dissipation potential function ϕ considering the micro plastic strain can be written in the following form:

$$\phi(Y, P, \dot{\kappa}, T, \varepsilon^P, D) = \frac{Y^2}{2S_0} \frac{\dot{\kappa}}{(1-D)^{\alpha_0}} \quad (1)$$

By orthogonal rule, the damage rate can be written as:

$$\dot{D} = -\frac{Y}{S_0} \frac{\dot{\kappa}}{(1-D)^{\alpha_0}} \quad (2)$$

Damage dissipation rate is given by:

$$Y = -\rho \frac{\partial \phi}{\partial D} = \frac{\sigma^2}{2E} \quad (3)$$

Micro-plastic strain can be described as:

$$\dot{\kappa} = \left[\frac{|\sigma - \bar{\sigma}|}{K(1-D)} \right]^\beta \frac{\langle \dot{\sigma} \rangle}{1-D} \quad (4)$$

Equation (2) is transformed to the following equation through the Eqs. (3) and (4):

$$\dot{D} = \frac{\sigma^2 |\sigma - \bar{\sigma}|}{B(1-D)^\alpha} \langle \dot{\sigma} \rangle \quad (5)$$

where: $B = 2ES_0K$, $\alpha = \alpha_0 + \beta + 3$, $\bar{\sigma} = (\sigma_{\max} + \sigma_{\min})/2$, $\bar{\sigma}$ is the mean stress, S_0 , α_0 , K , β are material parameters, the symbol $\langle \rangle$ is defined as $\langle \chi \rangle = (|\chi| + \chi)/2$.

Integrate formula (5) over a stress cycle, there is

$$\int_D^{D+\frac{\delta D}{N}} dD = \int_0^{\sigma_{\max}} \frac{\sigma^2 |\sigma - \bar{\sigma}|^\beta}{B(1-D)} d\sigma$$

$$\text{i.e. } \frac{\delta D}{N} = \frac{[(\bar{\sigma} + \sigma_a) \sigma_a]^{\frac{\beta+3}{2}}}{(3+\beta)B(1-D)^\alpha}$$

Put D and N on both sides of the equation, then integrate respectively:

$$\int_0^D \frac{dD}{(1-D)^\alpha} = \int_0^N \frac{[(\bar{\sigma} + \sigma_\alpha)\sigma_\alpha]^{\frac{\beta+3}{2}}}{(3+\beta)B} dN$$

$$\frac{1-(1-D)^{1+\alpha}}{1+\alpha} = \frac{[(\bar{\sigma} + \sigma_\alpha)\sigma_\alpha]^{\frac{\beta+3}{2}}}{(3+\beta)B} N + A \quad (6)$$

Where: $\sigma_\alpha = \Delta\sigma$, $\Delta\sigma$ is the difference between maximal principal stress and minor principal stress.

For periodic cyclic load, the initial conditions can be written as:

$$\begin{cases} N = 0; D = 0; A = 0 \\ N = N_f; D = 1 \end{cases} \quad (7)$$

Substitute Eq. (7) into Eq. (6), then:

$$D = 1 - \left(1 - \frac{N}{N_f}\right)^{\frac{1}{\alpha+1}} \quad (8)$$

To consider the initial cumulative damage factor, the Eq. (8) can be expressed by:

$$D = 1 - (1 - D_0) \left(1 - \frac{N}{N_f}\right)^{\frac{1}{\alpha+1}} \quad (9)$$

Weibull Distribution Model of Slope Service Life

The distribution function of Weibull distribution can be defined as (Chen 2002):

$$F(N) = 1 - \exp\left[-\left(\frac{N-N_0}{N_a-N_0}\right)^b\right] \quad (10)$$

Where: N_0 , N_a , b is three parameters of the expression of Weibull distribution; N_0 is the lower limit, also known as minimum life parameters; N_a is the characteristic life parameters; b is describing shape parameters. When $N = N_0$, the $F(N_0) = 0$, that is the damage probability of life less than N_0 is zero; When $N = N_a$, $F(N_a) = 1 - 1/e = 0.632$, that is the damage probability of service life less than N_a is 0.632, and the probability of 0.5 corresponds to the medium life. The Weibull probability distribution can be used to analyze the differential element destruction of rock as its features of easy integration, mean value and value range greater than zero, etc., can meet the statistic characteristics of rock compression failure (Xu and Wei 2002). What count is that the service life and cumulative damage factor D is relevant for a slope, and to display the residual life of slope

under a given survival ratio, the Weibull distribution model of cumulative damage factor can be established to describe the differential element destruction of rock, the expression is:

$$F(D) = 1 - \exp\left[-\left(\frac{D-D_0}{D_a-D_0}\right)^b\right] \quad (11)$$

Take two Natural logarithm of the Eq. (11), then

$$\ln\ln(1-F(D))^{-1} = b\ln(D-D_0) - \ln(D_a-D_0)$$

Make $y = \ln\ln(1 - F(D))^{-1}$, $x = \ln(D - D_0)$, $c = \ln(D_a - D_0)^b$.

Equation (11) can be transformed into linear equations $y = bx - c$, and b , c can be solved by least square method.

Test Conditions and Results

The tested rock is sandstone from Sha Country region located in the central north of Fujian province, China. The sandstone was moderately weathered. The rock specimen was sauch and its structure was blocky. INSTRON1342 electro hydraulic servo loading system was used to do the fatigue test, the upper limit level (the ratio of maximum stress to static strength) of load in constant amplitude fatigue test was varied from 0.8 to 0.9, and the lower limit stress level (the ratio of lower stress to static strength) remained unchanged at 0.1. In cyclic test, it was performed with a given sinusoidal loading waveform whose frequency was 5 Hz. Then the results that uniaxial compressive strength of the sandstone specimen is 20.02 MPa and the ultimate tensile strength (σ_{uts}) is 0.6 MPa. Figure 1 shows the $S-N$ relationship of sandstone fatigue strength under cyclic load, and the relationship between specimen damage quantity and cycle ratio in Fig. 2 reflects the quantitative damage condition under different fatigue cycles. Moreover, the fitting result of the measured data in Fig. 2 shows the initial damage factor is 0.082.

Numerical Analysis of Slope Damage and Deterioration

The rock mass of subgrade slope is always disturbed by dynamic loads. When the stress in the rock suddenly rises because of the ambient disturbance, stress spreads to around, leading the micro-crack in the internal of rock to burgeon, expand and injuries begin slowly to accumulate, once it reaches the threshold, slope reaches its service life and undergoes complete damage. Jian et al. (2009) and Peng (2009) studied the relationship between rock strength

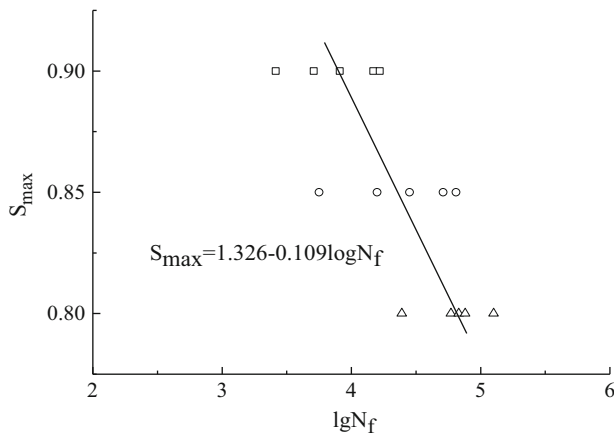


Fig. 1 Fatigue curve of sandstone under cyclic loading

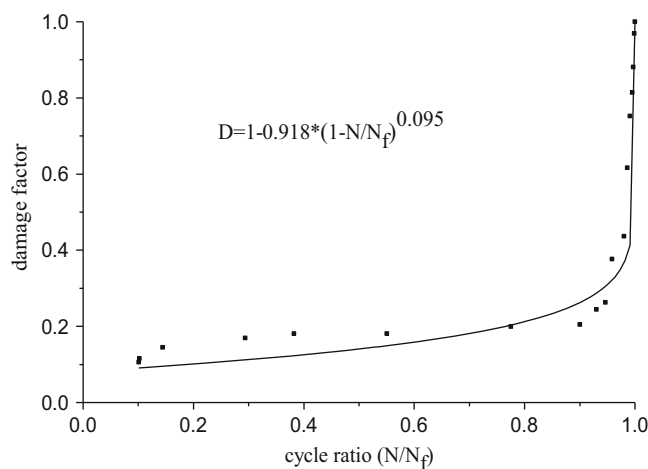


Fig. 2 Curve between sample damage factor and cycle ratio

parameters (material nonlinearity), safety factor and service life through the finite element shear strength reduction method, observing that the method could well reflect slope damage accumulation with simultaneous degradation of geotechnical parameters (damage accumulation corresponds to service life of slope, while the deterioration of geotechnical parameters matches with the attenuation of safety factor).

To display the survival state of slope in this process, consider the influence of geometrical nonlinearity and material nonlinearity on the stability coefficient of slope on the basis of Peng’s idea and the attenuation of rock-soil body strength index is not proportional with safety factor but related to damage factor, then introduce survival ratio to reflect the dynamic variation of slope service life in the process of degradation.

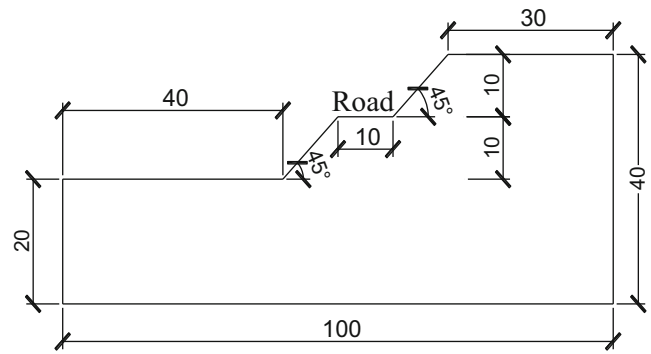


Fig. 3 Typical profile map of slope/m

Model Calculation and Parameters

Take the slope of Sha Country which is located in the San Ming as research object. The slope consists of homogenous medium-weathered sandstone and its typical profile is shown in Fig. 3. There are two such slopes whose angle is 45° and height is 10 m, as shown in Fig. 3. The rock material parameters value of Table 1 is based on the laboratory test results. Choosing the periodic harmonic traffic load of Peng’s (2009) thesis as the form of cyclic load, the expression is: $F = 192 \sin[4\pi(t - 0.125)] + 192, kN$. The rock fatigue damage curve ($S-N$) can be obtained by the fitting results of Fig. 1, the form is: $S_{max} = 1.326 - 0.109 \lg N_f$.

Stability Analysis Method Considering Damage

The steps of stability analysis considering damage methods can be seen from Fig. 4. In particular: (1) Imposing peak of fatigue load (384 kN) on slope, then using the finite element strength reduction method to calculate the safety factor under first fatigue loading, when the computation is converged, the safety factor is 7.705 (the whole rigidity of slope improves after considering the geometrical nonlinearity and then safety factor increases); (2) Slope service life can be obtained by finite element analysis method and the specific steps are as follows: choose the peak fatigue load which is converted into stress actually needed to impose on the slope, and input units sine wave to conduct “structural” cyclic stress analysis, then set up $S-N$ curves of sandstone and select the product of initial values and $(1 - D)$ to consider the degradation value of ultimate compressive strength σ_{uts} , rock mass finally come into state of dilatancy creep due to the weathering and micro-cracks extend under periodic loading, so choosing σ_{uts} as

Table 1 Physical and mechanical parameters of sandstone

Constitutive model	Unit weight γ (kN/m^3)	Elastic modulus E (GP_a)	Poisson's ratio ν	Cohesive strength c (kP_a)	Internal friction angle ψ ($^\circ$)	Dilatancy angle φ ($^\circ$)
M-C	25.8	20	0.25	380	33	0

Fig. 4 Flow chart of stability analysis method of consideration damage

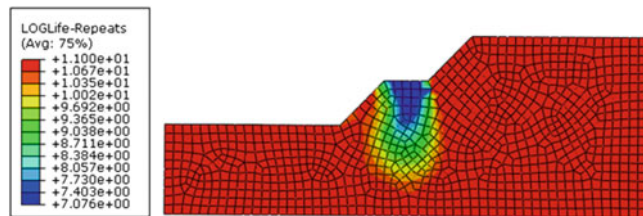
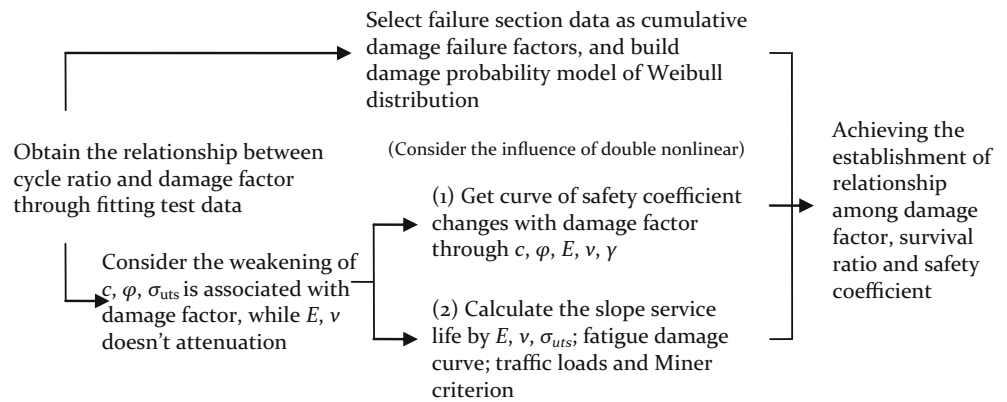


Fig. 5 Service life logarithmic diagram of slope

assessment indicators is feasible. United Kingdom bridge specification BS5400 (BS 1999) recommends that the service life of bridge under traffic loads can be conducted by using Miner cumulative damage rule, and it is worth noting that the bridge and road slope need to coordinate work together, so the Miner rule is also adopted here. The service life logarithmic diagram of slope obtained from numerical calculation is shown in Fig. 5. As it can be seen from Fig. 5, life of fatigue hot spot is being $10^{7.076}$ (11,913,000 times). According to the literature statistics (Peng 2009) the daily times of standard fatigue car is 584, that is to say, after 55.89 years the slope may occur fatigue instability failure.

Relationship Between Safety Factor and Cumulative Damage Factor

Based on reduction ideas of strength reduction *FEM*, geotechnical parameters reduction of any intermediate state has corresponding safety coefficient (the attenuation amplitude of c and $\tan\psi$ can be expressed as the product of damage factor from Stability analysis method considering damage and their initial values). The consumption life can be defined by the life of safety factor of 7.705 minus life of any

intermediate condition (part of the calculation results are shown in Table 2). This also means the “structural” reliability analysis of slope engineering can be reflected in the designed durable years. Once according to the requirements of service life 30 and 50 years, the corresponding safety coefficient is 4.769 and 7.528, while service life is required 100 years, the further engineering reinforcement measure is needed.

Relationship Between Cumulative Damage Factor and Survival Ratio

This section uses the Weibull distribution principle to analyze the probability of test data. Through the trial, choose the median rank algorithm as the sample distribution function: $F_n(t_i) = i - 0.3/n + 0.4$ (n is the total number of chosen test data sorted from small to large). Although the assumption to obey Weibull distribution of rock differential element destruction could completely fail only when the stress reaches infinity, the fact is that rocks had all been destroyed after a certain displacement occurs. Therefore, the fitting data should be chose based on the previous period of the completely destroyed (Xu and Wei 2002). So, selected the sharp ascent stage from Fig. 2 as failure data, the value of selection damage factor and its fitting results can be seen in Table 3 and Fig. 6 respectively. The ultimate expression of the Weibull distribution function is

$$F(D) = 1 - \exp \left[- \left(\frac{D - 0.082}{0.589} \right)^{1.4736} \right]$$

From the above equation we can get that the characteristic of cumulative damage factor of 0.672, this means survival

Table 2 Calculation results of numerical simulation

Safety factor/ <i>K</i>	Cohesive strength <i>c</i> (kPa)	Internal friction angle ψ (°)	Service life N_f	Consumption life N_i	Cumulative damage factor <i>D</i>
7.705	380	33	11,913,000 (55.89 years)	1	0
7.528	373.21	32.41	10,660,000 (50 years)	1,253,000	0.105
4.769	250.21	21.73	6,395,000 (30 years)	5,518,000	0.463
1	49.32	4.28	844	11,912,156	1

Table 3 Data test sheet of damage factor

<i>i</i>	1	2	3	4	5	6
<i>D</i>	0.199	0.244	0.263	0.377	0.436	0.617
<i>i</i>	7	8	9	10	11	–
<i>D</i>	0.752	0.814	0.881	0.934	0.989	–

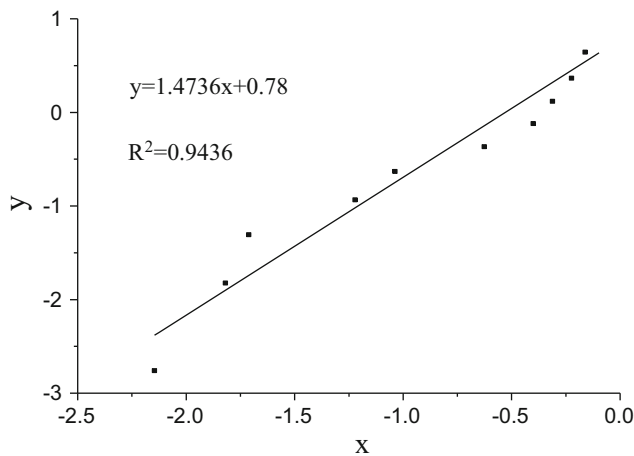


Fig. 6 Results of data fitting

ratio is 0.368 when fatigue damage factor is less than the characteristics of cumulative damage factor under dynamic load. Besides, median cumulative damage factor of 0.538 corresponds to survival rate of 0.5. Due to the results from sections “relationship between safety factor and cumulative damage factor” and “relationship between cumulative damage factor and survival ratio”, the dynamic changes between safety factor, service life (damage factor) and survival ratio can be reflected, and the final calculated results are shown in Figs. 7, 8, and 9.

Figure 7 shows that the safety factor representing slope stability in its whole cycle life decreases with the reduction of slope fatigue life, the early changes in safety factor has more sensitive and the middle part of the curve is a transition section; then the descend range of safety factor starts to increase after about 45 years later. In the rest 5 years of slope service life, it is characterized by developing rapid and sudden failure.

Figures 8 and 9 show the relationship respectively between both survival ratio and residual life and safety factor of slope.

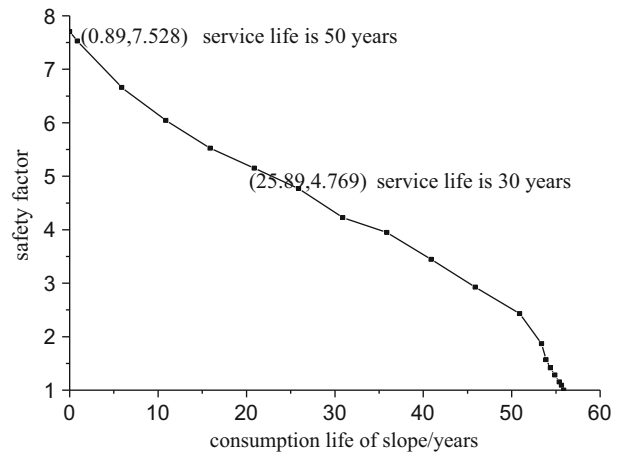


Fig. 7 Trend graph between consumption life and safety factor of slope

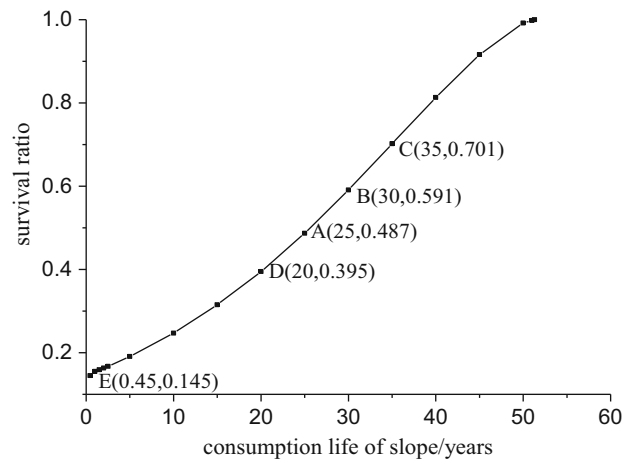


Fig. 8 Trend graph between residual life and survival ratio of slope

The longer residual life and higher safety factor are, the greater slope survival probability is. When the characteristic of the cumulative damage factor is taken as criterion, the slope can live more than 35.89 years without overall reinforcement measure and have less than 3.281 safety coefficient. While when the median cumulative damage factor is considered as norm, the remaining life of is about 25 years of life and the safety factor should have been more than 3.673 (point A in Fig. 9) to meet the requirement. The survival

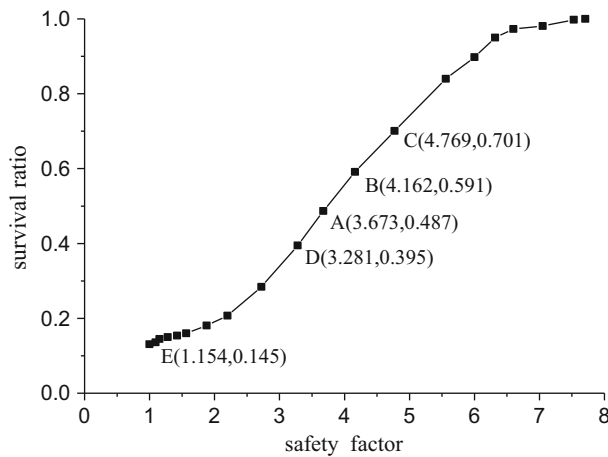


Fig. 9 Trend graph between safety factor and survival ratio of slope

ratio (0.145) and safety factor (1.154) of E point in Fig. 9 is in the later slope of service life.

Conclusions

1. In the whole cycle life of slope, the safety factor and survival ratio of slope would decrease with the reduction of fatigue life. Taking the characteristics cumulative damage factor as a norm of slope security evaluation, the slope has a life more than 35.89 years and its safety factor is greater than 1 but smaller than 3.281, while considering the median cumulative damage factor, a higher safety factor is called for meeting the slope survival requirements. This requires us to think seriously about the concept that slope has a stable state if its safety factor is larger than 1, and what reinforcement measures we should do to fit the different norms of cumulative damage factor and slopes service life.
2. Deterioration value of geotechnical parameters is assumed to be linearly proportional to damage factor, in fact, the degradation is far more complex, therefore, further test is needed to reveal the degradation path. Although strength reduction method reflects attenuation of geotechnical parameters, using service life in elastic stage to correspond with safety coefficient of elastic-plastic stress state is conservative. In order to solve the problem, we can use the limit equilibrium method to calculate the safety factor.
3. Slope engineering design should consider the durability design of resonance resistance and fatigue resistance except meeting the requirements of bearing capacity, stability and deformation control. Of course, the proposed idea considering service life as one way of the durability and borrowing the concept of fatigue to study the reliability of slope long-term stability are also worth further discussion.

Acknowledgments The authors would like to acknowledge the financial support from National Nature Science Foundation of China (41072232) and research grants (2010J01254) provided by the Natural Science Foundation of Fujian Province, China.

References

- Bagde MN, Petros V (2005) Fatigue properties of intact sandstone samples subjected to dynamic uniaxial cyclical loading. *Int J Rock Mech Min Sci* 42(2):237–250
- BS, B. B. S. (1999) 5400 1980, Steel, concrete and composite bridges part 10: code of practice for fatigue
- Chen CY (2002) Fatigue and fracture. Huazhong University of Science and Technology Press, Wuhan, 198p. ISBN 7-5609-2596-0
- Erarslan N, Liang ZZ, Williams DJ (2012) Experimental and numerical studies on determination of indirect tensile strength of rocks. *Rock Mech Rock Eng* 45(5):739–751
- Fan XF (2008) Research on rock fatigue damage developing and rocky slope response under cycle loading. Ph. D. Thesis, Fuzhou University, China
- Fan XF, Wu ZX, Jian WB (2009) Analysis of acoustic property of sandstone fatigue damage under cyclic loading. *Rock Soil Mech* 30(S1):58–62
- Ge XR (2008) Deformation control law of rock fatigue failure, real-time X-ray CT scan of geotechnical testing, and new method of stability analysis of slopes and dam foundations. *Chin J Geotech Eng* 30(1):1–20
- Ge XR, Jiang Y, Lu YD, Ren JX (2003) Testing study on fatigue deformation law of rock under cyclic loading. *Chin J Rock Mech Eng* 22(10):1581–1585
- He Z, Xu WY, Shi C, Li MW, Zhao Y (2009) 3D dynamic response back analysis of failure mechanisms of a high dip bedding rock slope in earthquake. *Rock Soil Mech* 30(11):3512–3518
- Huang RQ, Pei XJ, Li TB (2008) Basic characteristics and formation mechanism of the largest scale landslide at DaGuangBao occurred during the WenChuan earthquake. *J Eng Geol* 16(6):730–741
- Jafari MK, Pellet F, Boulon M (2004) Experimental study of mechanical behavior of rock joints under cyclic loading. *Rock Mech Rock Eng* 37(1):3–23
- Jian WB, Li R, Peng J, Fan XF (2009) Study of the fatigue degradation of rock slope under cyclic loading. In: Tang CA (ed) *RaSiM 7: controlling seismic hazard and sustainable development of deep mines*. Rinton, New York, pp 1519–1524
- Jiang Y, Ge XR, Ren JX (2004) Deformation rules and acoustic emission characteristics of rocks in process of fatigue failure. *Chin J Rock Mech Eng* 23(11):1810–1814
- Li SC (2008) Deformation and damage law and its nonlinear characteristics of rock under cyclic load. Ph. D. Thesis, Chongqing University, China
- Peng J (2009) Study on fatigue stability of rock slope under traffic loading. MS Thesis, Fuzhou University, China
- Qiu ZB (2005) Theory of non-linear dynamic damage mechanics and numerical modeling. Ph. D. Thesis, Zhejiang University, China
- Wang JC, Chang LS, Chen YJ (2006) Study on probability damage evolutionary rule of jointed rock mass slope. *Chin J Rock Mech Eng* 25(7):1396–1401
- Wang Y, Song XL, Zhang X, Wang C, Yu HM (2011) Fuzzy random reliability analysis of slope engineering. *China J Yangtze River Sci Res Inst* 28(9):30–34
- Xie HP (1990) Damage mechanics of rock and concrete. China University of Mining and Technology Press, Xuzhou, 308p. ISBN 7-81021-298-2
- Xu WY, Wei LD (2002) Study on statistical damage constitutive model of rock. *Chin J Rock Mech Eng* 21(6):787–791



Pore Pressure Transients in Brittle Translational Rockslides

Simon Loew and Thomas Strauhal

Abstract

In a recent paper (Loew and Strauhal, Pore pressure distributions in brittle translational rockslides. In: Italian Journal of Engineering Geology and Environment, Book Series (6): International Conference on Vajont 1963-2013 – thoughts and analyses after 50 years since the catastrophic landslide, pp 181–191, 2013) we showed how variable extents, depths and hydraulic properties of slope parallel sliding zones and fractured rockslide masses can explain most of the observed steady-state hydrogeologic features of translational rockslides, such as seepage faces or pore pressure distributions. In this paper we extend this analysis to transient conditions, controlled both by annual recharge variations from snow-melt and summer rainstorms and hydropower reservoir level fluctuations. We apply a geometrically simple 2D numerical model to investigate and explain characteristic transient pressure variations, as observed in highly instrumented rockslides at the Mica Reservoir in British Columbia. We characterize pore pressure transients and seepage forces above and below major sliding zones at different elevations above the reservoir level. Sliding plane geometry or toe constraints caused by thick alluvial deposits at the valley bottom explain why reservoir level fluctuations significantly impact slope movements and stability, even though the induced pressure variations are relatively small and only impact smaller parts of the rockslide rupture planes.

Keywords

Rockslide • Transient pore pressure • Groundwater • Fractured rock • Transient model

S. Loew (✉)

Engineering Geology, ETH Zurich, Sonneggstrasse 5, 8092 Zurich, Switzerland
e-mail: simon.loew@erdw.ethz.ch

T. Strauhal

alpS – Centre for Climate Change Adaptation, Grabenweg 68, 6020 Innsbruck, Austria

Institute of Geology, University of Innsbruck, Innrain 52, 6020 Innsbruck, Austria

e-mail: strauhal@alps-gmbh.com

Introduction

Translational and roto-translational rockslides are characterized by deformations along one or several sliding zones oriented subparallel to the slope. The compartments between these sliding zones show diverse kinematic behaviour ranging from extensional faulting to compressive thrusting and buckling, and thus strong hydraulic heterogeneity. The sliding zones are composed of sandy-gravelly breccia and/or clayey-silty gouge. While fine-grained fault gouges typically act as a hydraulic barrier for pressure compartments, the rest of the sliding zone material (i.e. fault breccia and fractured rock) is characterized by a high hydraulic conductivity and consequently acts as a conduit for preferential groundwater

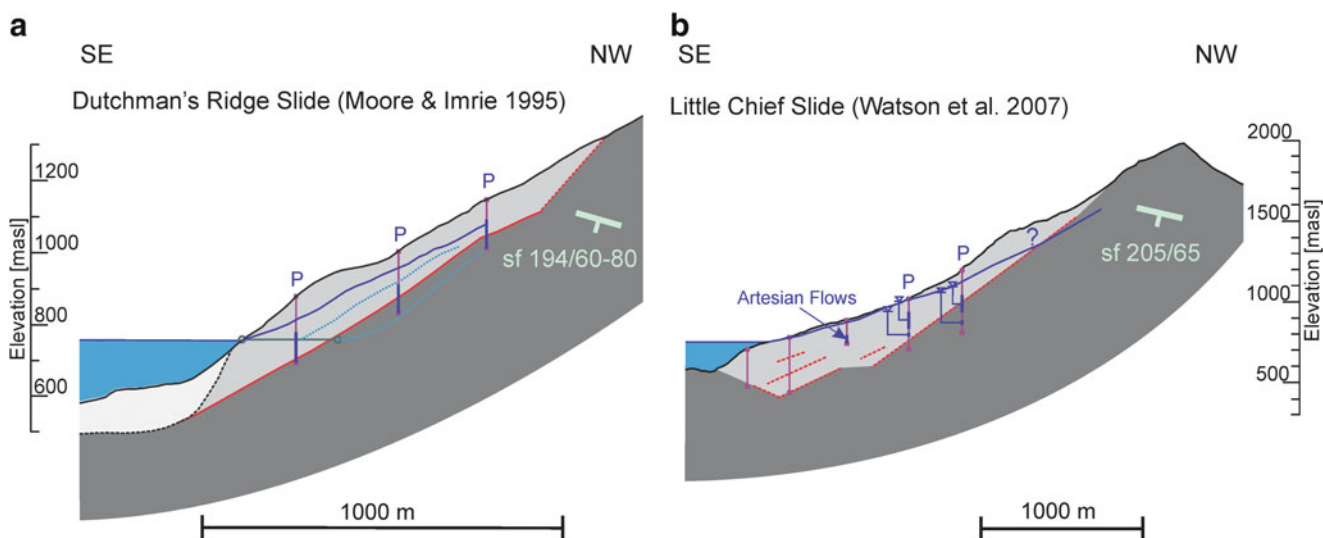


Fig. 1 Sections of the Dutchman's Ridge Slide (a) and Little Chief Slide (b) at the Mica Reservoir in British Columbia (in part from Moore and Imrie 1995 and Watson et al. 2007). Shown are orientation of main foliation (sf), sliding zones (red lines), piezometer boreholes (P) and

piezometric lines (dark blue: phreatic groundwater table in rockslide mass, light blue: pore pressure level above and below basal sliding plane before and after drainage at Dutchman's Ridge Slide)

flow with higher hydraulic conductivities than the rest of the fractured rockslide mass.

This article is based on observations and steady-state groundwater pressure simulations made for six case studies in brittle translational rockslides, presented in Loew and Strauhal (2013). Here we will focus on transient pore pressure fields in translational rockslides. We will first review the hydraulic field observations made at Dutchman's Ridge and Little Chief slides in British Columbia and then extend the model described in Loew and Strauhal (2013) to transient boundary conditions caused by precipitation, snowmelt and reservoir level fluctuations. The response of this model in terms of transient pore pressures is investigated, and finally we briefly discuss the potential consequences in terms of stability and displacement rates of translational rockslides.

Hydraulic Observations at the Dutchman's Ridge and Little Chief Slides

The first detailed hydraulic investigations of brittle rockslides adjacent to hydropower reservoirs were carried out at the Columbia River (British Columbia) in the late sixties. These investigations included the Downie Slide, the Dutchman's Ridge Slide (Moore 1992) and the Little Chief Slide (Watson et al. 2007). All of these rockslides are located in metamorphic rocks (granodiorites, gneisses and schists) and overrode Quaternary glacial till in the landslide toe area. Downie Slide differs from the other two sites by its type (sagging morphology) and shallow dip angles of slope and sliding planes (18°). Only the steeper Dutchman's Ridge and

Little Chief rockslides, which were creeping with annual rates of about 6–14 mm prior to drainage, are discussed in this paper.

The main foliation and bedding at Dutchman's Ridge Slide is dipping with $60\text{--}80^\circ$ obliquely into the slope, which has a mean dip angle of 35° . Basal sliding of about 115 million m^3 of rock takes place along a 1.5–40 m thick cataclastic fault zone at a depth of 100–250 m which dips with about 29° towards the reservoir (Fig. 1). At Dutchman's Ridge Slide an 870 m long drainage gallery with 17,000 m of draining holes was constructed between 1986 and 1988 below and within the sliding mass.

At Dutchman's Ridge Slide the distribution of groundwater pressures was measured with 267 sensors installed in 1–2 m long monitoring intervals isolated by Westbay multi-packers. Within the rockslide mass these systems recorded phreatic groundwater levels about 50–100 m below ground surface in the upper and middle slope area prior to drainage (Fig. 1). Tectonic and gravitational shear zones at Dutchman's Ridge Slide act as efficient boundaries of pressure compartments, with the basal shear zone being the most important pressure barrier. Before drainage construction pressure heads below the basal shear zone ranged between 0 and 126 m, with an average of 36 m (Fig. 1).

Groundwater pressure sensors showed differences in the intensity of reaction to reservoir level fluctuations or natural recharge (snowmelt/rainfall) events, depending on the piezometric level and distance to the shore line (Moore and Imrie 1995; Fig. 2). Pressure levels in the slope were only influenced by reservoir level fluctuation below or within 20 m of the current reservoir elevation (Fig. 2, P23).

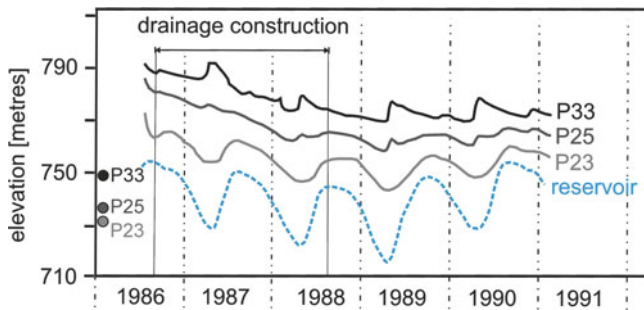


Fig. 2 Transient piezometric pressure levels and reservoir levels in the Dutchman's Ridge Slide (after Moore and Imrie 1995)

Piezometric pressure levels 40 m above the concurrent reservoir level show characteristic natural pressure fluctuations controlled by snowmelt in spring and groundwater depletion during the remaining time of the year (Fig. 2, P33). A further piezometer is showing pressure responses in the intermediate range with groundwater recharge signals superimposed on reservoir level fluctuations (Fig. 2, P25). This even holds when monitoring intervals are below reservoir levels (Fig. 2, circles). At the shoreline, tracked reservoir level fluctuations induce groundwater pressure variations without any significant time lag.

Little Chief Slide occurs in a quasi-planar slope north of Dutchman's Ridge and covers nearly the entire slope dipping about 30° towards the reservoir. The volume of the slide is estimated to be about 900 million m^3 (Watson et al. 2007). At the ridge crest near elevation 2,000 masl foliation is locally parallel to the head scarp dipping about 65° towards SW. The sliding planes are less clearly defined than at Dutchman's Ridge. A steeply dipping fault occurs near the head scarp but not in favourable downslope orientation. Inclinometer data indicate two rupture planes in the lower slide sector (at a depth of about 200–300 m and 100 m bgs), possibly with a rotational geometry (Fig. 1, 36° in upper slope area, $16\text{--}22^\circ$ in slope toe area).

At Little Chief Slide initial hydraulic measurements during reservoir filling were made in leaky inclinometers. In 2004/2005 three multiple piezometers with 66 monitoring intervals were installed in the lower, middle and upper parts of the slope, showing locally perched groundwater and unsaturated zones. A 100 m deep monitoring interval in the mid-slope sector (about 900 masl), covered by glacial till, showed stable artesian pressure conditions (Fig. 1). Inclinometers and piezometers along the shoreline showed similar response as shown in Fig. 2 for Dutchman's Ridge Slide. A soft clayey zone in the basal shear zone also created a high pressure differential (75 m over a packer spacing of only 1.5 m, Watson et al. 2007).

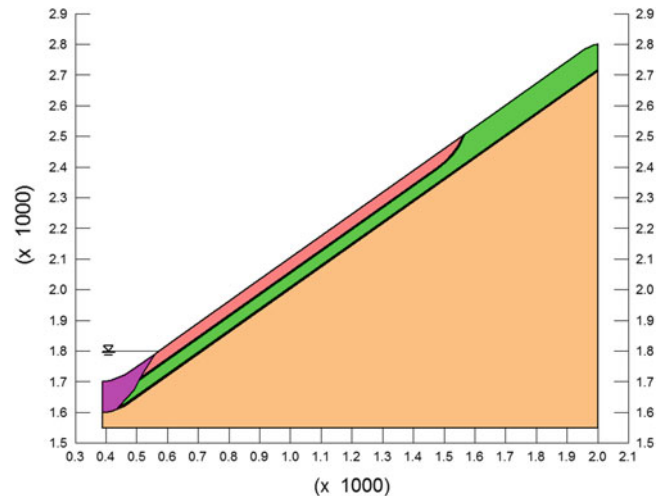


Fig. 3 Geometric setup and zonation of the generic translational rockslide model. Scale is shown in metres

Generic Translational Rockslide Model

Model Structure and Geometry

The numerical model presented in the following investigates rockslides, in which the large-scale water flow can be approximated by a simplified two dimensional flow system. This simplification is usually most suitable for quasi-planar slopes where gravitational deformation occurs parallel to the slope (e.g. Little Chief Slide). However there are many translational rockslides showing a more complex topography, like ridges or fluvial incisions at the lateral boundaries (Dutchman's Ridge Slide), which might act as receiving streams inducing a local three dimensional flow field component. This kind of groundwater flow is neglected in the two dimensional approach presented below.

A generic translational rockslide model was set up in the finite element code Geo-Slope SEEP/W 2012 (Geo-Slope International Ltd 2013) for numerical analyses of saturated/unsaturated pore pressure variations in rockslides with similar material properties and geometries as the case studies described above (Loew and Strauhal 2013). The model represents translational rockslides with single or multiple planar sliding surfaces oriented parallel to a linear slope with a dip angle of 35° (Fig. 3). A basal sliding zone with a typical thickness of 5 m was defined 100 m below ground surface and is heading up to the crest. A secondary sliding zone with a thickness of 5 m is located at a depth of 50 m and runs from the toe up to mid-slope region. Homogeneous materials with variable properties are distributed within the model domains, which are called *stable rock mass*, *sliding*

zone and *rockslide mass*. Depending on the allocation of these materials to the different model zones, large and small rockslides can be analysed. Like in the examples shown in Fig. 1, a region of *alluvial deposits* is located at the toe. The finite element model was discretized with about 120,000 nodes, consisting of a mesh of quads and triangles. The node density was adjusted to the region size.

For steady-state modelling a fixed reservoir level at the toe of the slope (total head at an altitude of 1,800 masl), potential groundwater infiltration of 300 mm/a along the slope area from the crest (altitude of 2,800 masl) to the toe (altitude of 1,800 m) and potential seepage face along the whole slope were defined as boundary conditions. Transient models were calculated with (1) annual variations in groundwater recharge by snowmelt in spring (total recharge of 260 mm during 60 days) and three summer/fall rainstorm periods (recharge of 12, 12 and 16 mm during 7, 7 and 10 days, respectively, e.g. Hansmann 2012), (2) annual filling and draining of the reservoir with lake levels between 1,770 and 1,800 masl and (3) a combination of both transient groundwater infiltration rates along the slope and transient reservoir levels. For modelling of (1) and (2) the other boundary condition was kept constant as in the steady-state model. All transient simulations are based on coefficients of volumetric compressibility of $4.5\text{e}-8 \text{ kPa}^{-1}$ for the stable rock mass and $8.9\text{e}-5 \text{ kPa}^{-1}$ for the rockslide mass.

The bottom and right boundaries of the model were defined as no flow boundaries. The bottom model boundary should have a minor impact on the numerical results, as the hydraulic conductivity of the stable rock mass usually decreases with increasing depth (e.g. Masset and Loew 2010).

Saturated and Unsaturated Hydraulic Conductivity

Saturated hydraulic conductivities of all model materials were estimated based on published parameters for comparable sites and rock types. Saturated hydraulic conductivities of the base case model are as follows: $1\text{E}-4 \text{ m/s}$ for the *rockslide mass* (Pisani et al. 2010; Thoeny 2008), $1\text{E}-7 \text{ m/s}$ for the *stable rock mass* (Woodbury et al. 1987), $1\text{E}-9 \text{ m/s}$ for the *sliding zone* (Fischer et al. 1998) and $1\text{E}-5 \text{ m/s}$ for the *alluvial deposits* (Bergmeister 2012). Besides these base case parameters also an alternative parameter scenario (called parameter variation) with lower hydraulic conductivities of the *stable rock mass* ($4.5\text{E}-7 \text{ m/s}$) and the *rockslide mass* ($8.9\text{E}-7 \text{ m/s}$) has been investigated under transient conditions.

Since many translational rockslides (including Dutchman's Ridge Slide) show large unsaturated zones (Loew and Strauhal 2013), it is necessary to define hydraulic conductivity functions and water-saturation functions (characteristic

curves) for each model material. These functions describe the relationship between hydraulic conductivity and water saturation. Further, they define the correlation between saturation and capillary pressure and pressure head (Mualem 1976; Van Genuchten 1980). The characteristic curves applied in this study are similar to the ones used and explained in Loew and Strauhal (2013).

Hydraulic Behaviour of the Generic Translational Rockslide Model

Spatial Pore Pressure Distributions

Figure 4 illustrates the differences in pore pressure distribution between the base case parameter set and the parameter variation for a translational rockslide with a clayey *sliding zone* at 50 m depth extending to an elevation of 2/3 slope height. For the base case model parameters no significant seepage zone occurs above the reservoir level due to the highly conductive *rockslide mass*. Most of the discharge occurs below the reservoir level.

The position of the main phreatic groundwater surface, which is defined as zero pore pressure boundary at an assumed air pressure of zero is clearly higher and steeper for the parameter variation model with lower hydraulic conductivities. For the parameter variation model, a saturated perched aquifer with significant thickness develops above the sliding zone due to the lower hydraulic conductivities. The reduction in rockslide hydraulic conductivity also leads to a seepage face extending about 50 m above the reservoir level (Fig. 4).

Pore Pressure Transients

In both models pore water pressure transients for (1) transient slope water infiltration rates (snowmelt and precipitation), (2) transient reservoir levels and (3) transient slope infiltration superimposed on transient reservoir levels were investigated. These simulations required much computing time, as the results shown represent just the last 14 months at the end of a 5 year simulation period (required to reach stationary conditions). Figures 5 and 6 show the results of the modelled pore pressure transients as sampled at several observation points along the sliding zone at the slope toe of the rockslide both for the base case and the parameter variation.

Saturated pore water pressures (positive pressures) respond to reservoir level fluctuations without systematic time lags, both for base case and parameter variation (Figs. 5c and 6c). The time shift of the reaction to reservoir level fluctuations increases slightly below the *sliding zone* and with increasing distance to the reservoir. Reaction amplitudes

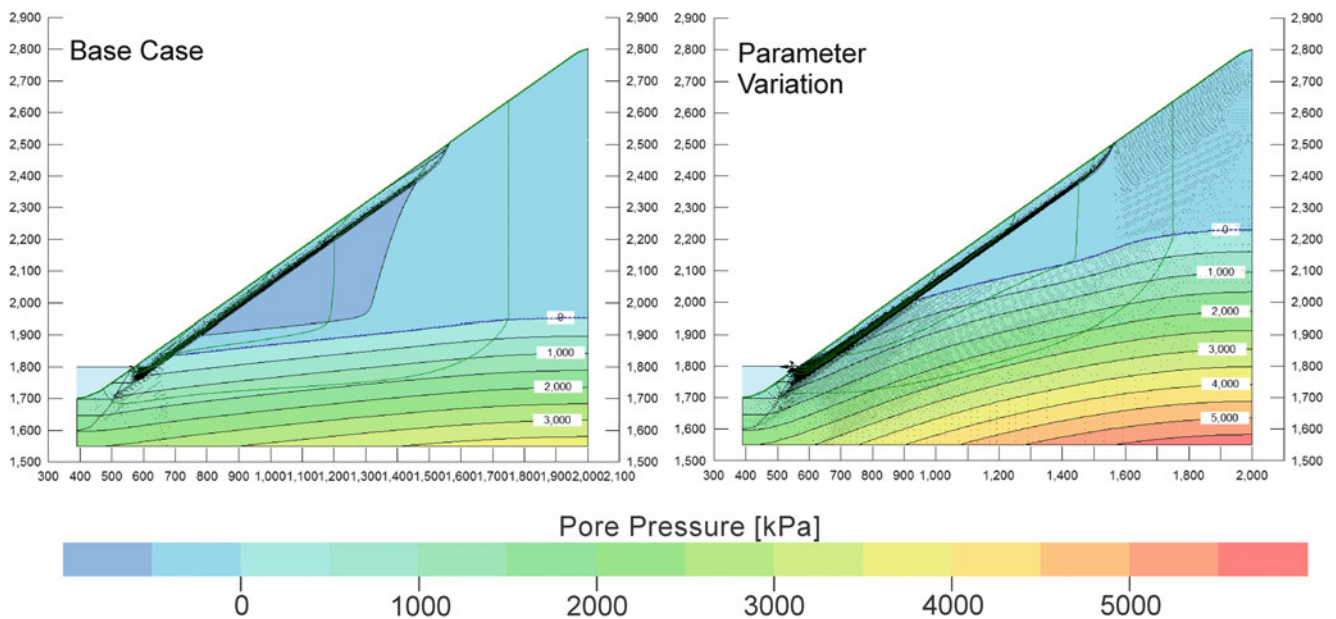


Fig. 4 Modelled pore pressure distributions [kPa] and flow lines for the base case parameter set (*left*) and the parameter variation (*right*)

systematically decrease with elevation and distance to the groundwater table (30 m water level change corresponds to approx. 300 kPa). Above the groundwater table negative pore pressures of up to 600 kPa develop for the base case parameters. For the decreased hydraulic conductivities of the parameter variation pore pressure cycles disappear about 50 m above the maximum reservoir level.

In contrast, the pore pressure response to groundwater recharge from snowmelt (Fig. 5b) is significantly delayed for all monitoring points below the *sliding zone* and not significantly delayed for monitoring points above the *sliding zone*. Pressures below the reservoir elevation (1,800 masl) remain stable. Pressure delay for the base case parameter set is substantially larger than for the parameter variation, systematically increases with elevation, and reaches peak values about 2.5 months after the end of the snowmelt period. Damped reaction to snowmelt is also measurable below the lake level.

In contrast to snowmelt, short-term summer rainstorms do not have a visible impact on the saturated (positive) pore water pressures at the toe of the slope for the base case parameter set. However, for the reduced hydraulic conductivities of the parameter variation, pore water pressures systematically increase with a short time lag of a few days after every rainstorm. This time lag is increasing while getting closer to the reservoir with a maximum of about 15–20 days after the end of the infiltration events.

In the base case scenario the superposition of both transient reservoir and slope water infiltration (Fig. 5d) leads to the strongest pressure differentials across the *sliding zone* in late summer (up to 400 kPa). For the parameter variation (and

fully saturated conditions) the pressure differentials have similar magnitudes but do not show significant seasonal changes. The faster reaction to snowmelt of the parameter variation is amplified by the synchronous increase of the reservoir level, leading to very strong pressure increases by up to about 300 kPa in early spring (Fig. 6d).

Discussion and Conclusions

Model Assumptions

The presented generic rockslide model is a substantial geometrical and hydraulic simplification of natural conditions. For example, metamorphic rocks are characterized by a heterogeneous spatial distribution of conductive fractures leading to preferential groundwater flow and hydraulic anisotropy (e.g. Masset and Loew 2010). The models investigated in this study only consider homogeneous and isotropic equivalent continuum conductivity functions. The results presented in this paper only include the simplest geometry with a single planar sliding zone dipping 35° extending to about 2/3 of the slope height.

For a detailed hydraulic analysis of pressure and flow in brittle rockslide problems it is essential to implement characteristic curves. In this study, these functions have only been estimated roughly. While it is assumed, that this uncertainty does not have a major influence on the resulting saturated groundwater flow distributions, the magnitudes of negative pore water pressures in the unsaturated zones remain

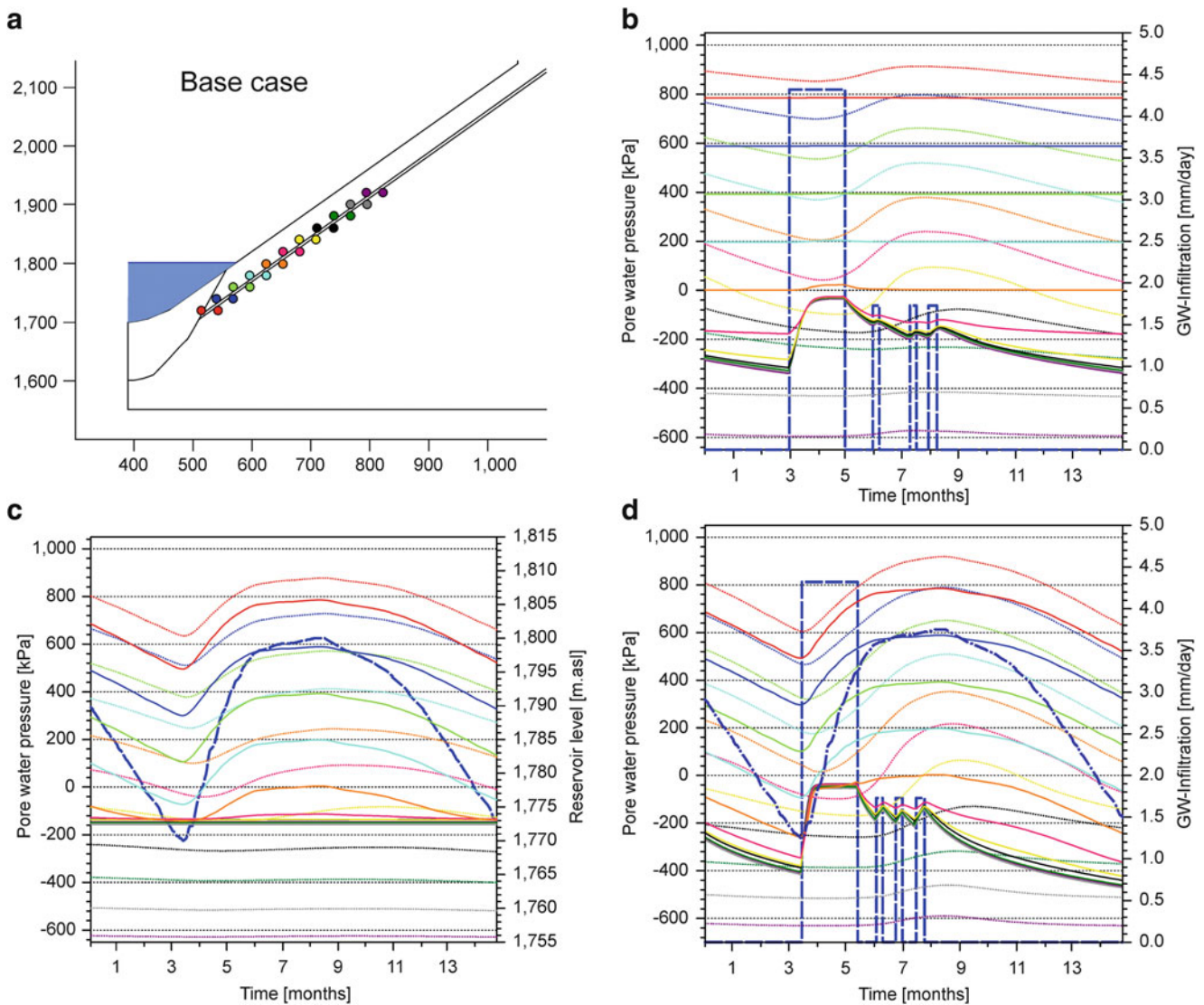


Fig. 5 Transient model results for base case scenario. (a) Locations of observation points, (b) variations in pore water pressure resulting from transient groundwater infiltration rates, (c) variations in pore water pressure resulting from transient reservoir level and (d) variations in pore water pressure resulting from both transient groundwater

infiltration rates and reservoir level. Pore pressure transients above the sliding zone are illustrated as *solid lines*, those below the sliding zone as *dotted lines*. Transient boundary conditions are illustrated as *thick blue lines*

uncertain. Especially creeping rock masses with large total displacements are often characterized by intense fracturing and large fracture apertures. The capillary pressure threshold lies at an upper aperture limit of about 4 mm (Wang and Narasimhan 1993). Consequently, no negative pore pressures might be expected within substantial parts of the *rockslide mass* but in the *stable rock mass* and the *sliding zone*.

Comparison of Model Results and Observations

Even though we only present results from an extremely simple model, the numerical simulations presented in this

study reproduce and explain several key hydrogeological field observations at the case study locations.

It can be shown that, similar to the Dutchman's Ridge Slide, most of the naturally infiltrating bedrock recharge is drained by the highly conductive *rockslide mass*. Consequently, most of the water flow occurs above the *sliding zone* and low pressure or even negative pressure conditions develop below the basal shear zone. Low saturation further decreases hydraulic conductivity and groundwater recharge. A reduction in *stable rock mass* hydraulic conductivity leads to a significant increase in saturation and the elevation of the water table. A decrease of the hydraulic conductivity of the *rockslide mass* leads to increased saturation levels and

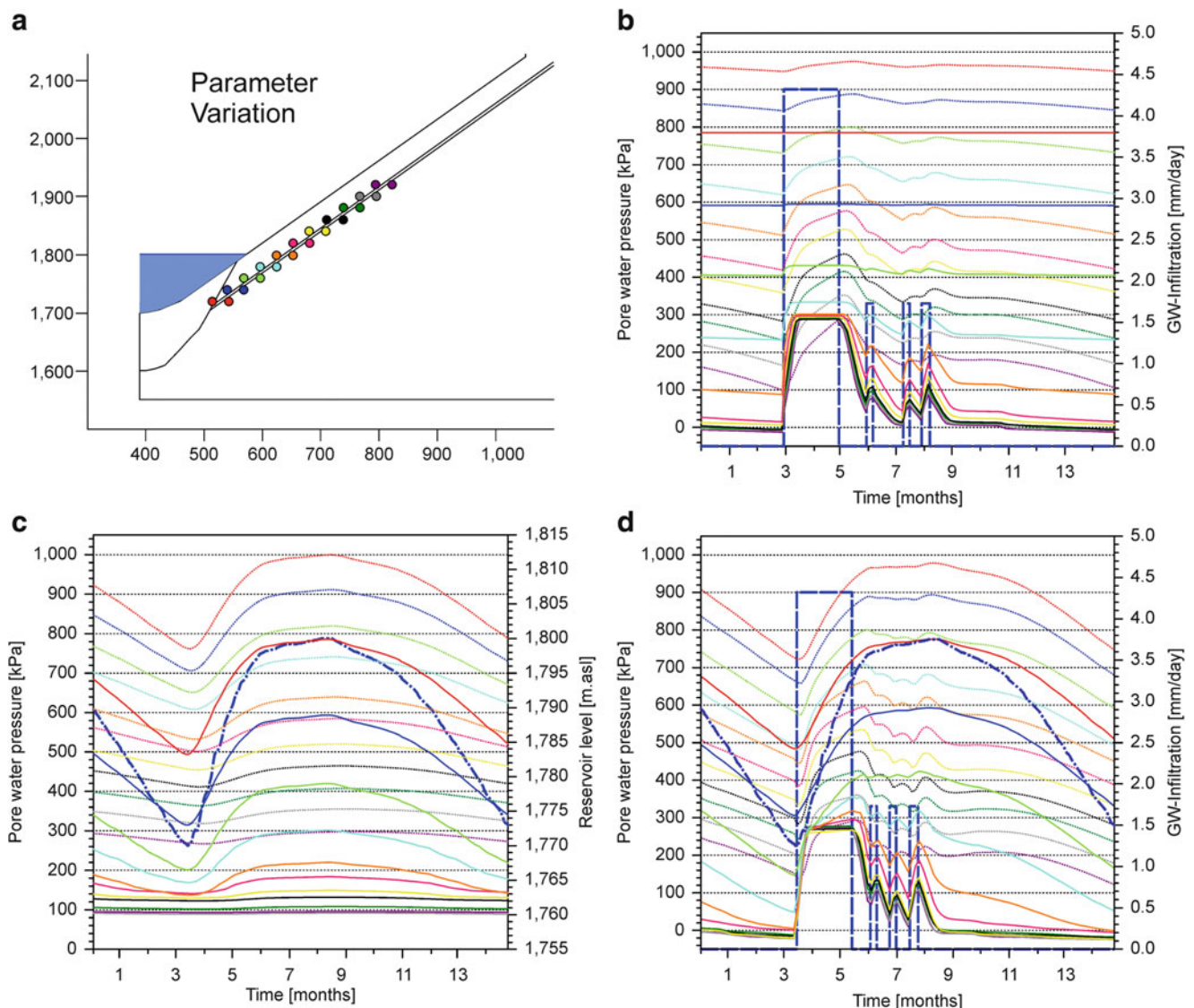


Fig. 6 Transient model results of the parameter variation scenario. (a) Locations of observation points, (b) variations in pore water pressure resulting from transient groundwater infiltration rates, (c) variations in pore water pressure resulting from transient reservoir level and (d) variations in pore water pressure resulting from both transient

groundwater infiltration rates and reservoir level. Pore pressure transients above the sliding zone are illustrated as *solid lines*, those below the sliding zone as *dotted lines*. Transient boundary conditions are illustrated as *thick blue lines*

seepage faces, and the formation of a perched aquifer above deep unsaturated zones (as observed for example at the Little Chief Slide). The model reproduces well the significant pressure differentials observed across clayey sliding zones at the Dutchman's Ridge and Little Chief Slides. In case of multiple sliding zones with clayey shear zone materials, more complex flow and pressure distributions develop, as observed at the Little Chief Slide and illustrated in Loew and Strauhal (2013).

As observed at the Dutchman's Ridge and Little Chief Slides, the time lag between reservoir level fluctuations and groundwater pressure changes within the *rockslide mass* and

stable rock mass is short, and the amplitudes reduce with distance to the reservoir. Both, in the case studies and the numerical models, no reactions to lake level variations are measured 30–50 m above the current lake level (Fig. 2). As pressure diffusion is controlled by hydraulic diffusivity, i.e. the ratio between hydraulic conductivity and storage, changes in time lags could also be explained by variations in saturated storage (or volumetric compressibility and porosity). Infiltrating water by snowmelt is usually influencing the groundwater regime of a rockslide much stronger than summer or fall rainstorms. Deep groundwater pressure reactions to snowmelt in spring are typically delayed by

weeks to months. Due to the superposition and temporal correlation between reservoir level and snowmelt recharge, the steepest gradients in pore pressure (especially above the *sliding zone*) develop in spring, leading to typical annual saw-tooth pressure histories as observed at the Dutchman's Ridge Slide (Fig. 2). A direct response in pore pressure to slope water infiltration from rainstorm events can mainly be observed in simulations with significant perched aquifers (reduced hydraulic conductivity of *rockslide mass*). The pressure differentials observed across clayey sliding zones in the slope toe area always show hydraulic head gradients directed towards the slope face (pressure heads at monitoring points of equal elevation below sliding zone are bigger than above) inducing significant seepage or uplift forces. The pressure gradients change during the year, with highest modelled gradients in later summer or fall.

Even though pore pressure changes induced by lake level variations only occur up to 20–40 m above the lake elevation, and thus impact less than 50 % of total basal sliding zone length, the impact of reservoir filling on slope stability is significant. This is clearly seen in the displacement records at Dutchman's Ridge Slide, where reservoir filling most probably re-activated a dormant rockslide having seen a long history of downslope creep (Moore 1992). This could be because typical reservoir level induced pore pressure variations can have larger amplitudes than natural recharge induced pore pressure changes (Figs. 5 and 6). In addition, both case study landslides have an abutment in the slope toe area, either caused by alluvial overburden (Dutchman's Ridge Slide) and/or a passive wedge from roto-translational slide geometry (Little Chief Slide), which is substantially weakened by the local increase of pore pressures.

On the other hand, low or even negative pore water pressures, as suggested by the groundwater models below the upper part of the basal sliding zone, can have a positive impact on the stability of a slope (Vanapalli 1994). For example Fredlund (1995) illustrated the influence of suction on the classical stability limit-equilibrium relationship in a porous medium slope:

$$\tau = c' + (\sigma_n - u_a) \cdot \tan(\phi') + (u_a - u_w) \cdot \tan(\phi_b)$$

where τ is the shear strength, ϕ' is the effective angle of internal friction, ϕ_b is the angle of the shear strength-suction relationship, c' is the effective cohesion, σ_n is the total normal stress on shear surface, u_a is the pore-air pressure (often equal to atmospheric conditions) and u_w is the pore water pressure. During snowmelt, these suction pressures can decay over large portions of the sliding planes and thus impact the rockslide creep displacements and stability in a complex manner, requiring detailed monitoring and modelling investigations.

Acknowledgements The authors would like to thank the Tiroler Wasserkraft AG, ILF Consulting Engineers Ltd., GEO.ZT GmbH, and FFG (COMET) for supporting this work and Andrew Watson for field visits in BC.

References

- Bergmeister K (2012) Brenner base tunnel under construction. *Tunnel* 1:18–30
- Fischer U, Kulli B, Flühler H (1998) Constitutive relationships and pore structure of undisturbed fracture zone samples with cohesionless fault gouge layers. *Water Resour Res* 34(7):1695–1701
- Fredlund DG (1995) The stability of slopes with negative pore-water pressures. In: Ian Boyd Donald symposium on modern developments in geomechanics, Monash University, Melbourne, Australia, 7 June 1995, pp 99–116
- Geo-Slope International Ltd (2013) Seepage modeling with SEEP/W—an engineering methodology. June 2013 edition, Canada, 197 p
- Hansmann J (2012) Analysis of transient surface deformations above the Gotthard Base Tunnel (Switzerland). Dissertation, ETH Zürich, No. 20177, Zürich, 180 p
- Loew S, Strauhal T (2013) Pore pressure distributions in brittle translational rockslides. *Italian Journal of Engineering Geology and Environment, Book Series (6): International Conference on Vajont 1963-2013 – thoughts and analyses after 50 years since the catastrophic landslide*, pp 181–191
- Masset O, Loew S (2010) Hydraulic conductivity distribution of crystalline rocks, derived from inflows to tunnels and galleries in the Central Alps, Switzerland. *Hydrogeol J* 18(4):863–891
- Moore DP (1992) Panelist contribution: stabilization of Downie Slide and Dutchman's Ridge. In: International conference on soil mechanics and foundation engineering. ICSMFE conference XII, Balkema, Rio de Janeiro, pp 3063–3065
- Moore DP, Imrie AS (1995) Stabilization of Dutchman's Ridge. In: Bell R (ed) International symposium on landslides. ISL VI. Balkema, Christchurch, pp 1783–1788
- Mualem Y (1976) A new model for predicting the hydraulic conductivity of unsaturated porous media. *Water Resour Res* 12(3):513–522
- Pisani G, Castelli M, Scavia C (2010) Hydrogeological model and hydraulic behaviour of a large landslide in the Italian Western Alps. *Nat Hazards Earth Syst Sci* 10:2391–2406
- Thoeny R (2008) Dynamic fluid electrical conductivity logging for identification and characterization of preferential groundwater flow in the Aknes rockslide (Norway). MSc Thesis, ETH Zurich, Zürich, 105 p
- Van Genuchten MT (1980) A closed-form equation for predicting the hydraulic conductivity of unsaturated soils. *Soil Sci Soc Am J* 44: 892–898
- Vanapalli SK (1994) Simple test procedures and their interpretation in evaluating the shear strength of an unsaturated soil. Ph.D. Thesis, University of Saskatchewan, Saskatoon, SK, Canada, 433 p
- Wang JSY, Narasimhan TN (1993) Unsaturated flow in fractured porous media. In: Bear J, Tsang CF, de Marsily G (eds) Flow and contaminant transport in fractured rock. Academic, San Diego, CA, 560 p
- Watson AD, Moore DP, Stewart TW, Psutka JF (2007) Investigations and monitoring of rock slopes at Checkerboard Creek and Little Chief Slide. In: Eberhardt E, Stead D, Morrison T (eds) Rock mechanics: meeting society's challenges and demands. Taylor & Francis, Vancouver, pp 1015–1022
- Woodbury AD, Smith L, Dunbar WS (1987) Simultaneous inversion of hydrogeologic and thermal data: 1. Theory and application using hydraulic head data. *Water Resour Res* 23(8):1586–1606



The Rockfall Potential of the Southwestern Part of Kastamonu Castle (Turkey) Based on 2-D and 3-D Analyses

Mutluhan Akin, Tamer Topal, and Muge K. Akin

Abstract

Urbanization around steep rock slopes with jointed rock masses is mostly under the threat of rockfalls. Numerous catastrophic rockfall hazards have been reported throughout the world due to the downslope movement of detached rocks. It is quite critical to determine the rockfall potential of a location considering rockfall trajectories, run-out distances, bounce heights and the kinetic energies of falling rocks. Therefore, the determination of rockfall paths requires the use of rockfall simulations. In practice, 2-D and 3-D models are most commonly employed during rockfall event modeling. The rockfall trajectories are simulated on a slope profile with X and Y axis in 2-D models, whereas 3-D models encompass a real space with X, Y and Z axis to calculate the rockfall paths. In this study, the rockfall potential of the southwestern part of the Kastamonu Castle, which is situated on a steep sandstone hill, was evaluated on the basis of 2-D and 3-D rockfall analyses using RocFall v.4.0 and ROTOMAP software, respectively. The close vicinity of the Kastamonu Castle, especially the southwestern region, is surrounded by residential houses and these settlements were adversely affected by disastrous rockfalls in the past. Based on 2-D and 3-D simulations, two different preliminary rockfall hazard maps were prepared and rockfall high-risk areas were defined. Both the 2-D and 3-D analyses pointed out that the southwestern part of the castle is under the great danger of rockfalls of which the weight of falling blocks may reach up to 10 tons. Finally, it is concluded that the maximum fall-out distances in 3-D analyses are more remote than those of 2-D analyses in the study area.

Keywords

Rockfall • 2-D analysis • 3-D analysis • Kastamonu • Fall-out distance

M. Akin (✉)

Department of Mining Engineering, Yuzuncu Yil University, Van 65080, Turkey
e-mail: mutluhanakin@gmail.com

T. Topal

Department of Geological Engineering, Middle East Technical University, Ankara 06800, Turkey
e-mail: topal@metu.edu.tr

M.K. Akin

Department of Civil Engineering, Yuzuncu Yil University, Van 65080, Turkey
e-mail: mugeakink@gmail.com

Introduction

Rockfalls may cause catastrophic events in urban areas and along transportation routes resulting in a certain amount of property loss as well as casualties. Since rockfalls are disastrous, they have been investigated in mountainous terrains throughout the world (Dorren 2003; Marquinez et al. 2003; Piacentini and Soldati 2008; Tanarro and Muñoz 2012; Youssef and Maerz 2012). The determination of rockfall paths and the maximum run-out distances is of great importance for the locations under the threat of rockfall. In addition, the bouncing heights and kinetic energies of the falling rocks should also be well-established for proper design of



Fig. 1 Location map of the study area and a general view of the W-SW slope of the Kastamonu Castle

preventive measures. In rockfall hazard evaluations, 2-D and 3-D rockfall analyses are commonly employed to model or simulate the rockfall event. The basic dissimilarity between 2-D and 3-D simulations is the X, Y and Z coordinates of the modeled rockfall terrain. The rockfall paths are analyzed on a slope profile with X and Y axis in 2-D models. In contrast, 3-D models require a real space with X, Y and Z axis to calculate the rockfall trajectories (Dorren et al. 2011).

In the literature, numerous studies on both 2-D and 3-D rockfall analyses have been published (Descœudres and Zimmermann 1987; Guzzetti et al. 2002; Ayala-Carcedo et al. 2003; Jaboyedoff et al. 2005; Corominas et al. 2005; Lan et al. 2007; Topal et al. 2007, 2012; Frattini et al. 2008). However, there is no scientific consensus on the accuracy of 2-D or 3-D rockfall models considering run-out distances, rockfall trajectories, bounce heights and energies (Lambert and Nicot 2011).

Kastamonu is one of major provinces in the western Black Sea Region of Turkey with many touristic destinations involving the Kastamonu Castle (Fig. 1). The residential houses particularly around the southwestern foothill of the castle were subjected to rockfalls in the past (Fig. 2).

The rockfall potential of the southwestern part of the Kastamonu Castle, situated on a steep sandstone hill with a



Fig. 2 A large fallen block stopped by a street lamp and garden wall in the southwestern foothill of the castle

height of 112 m, was evaluated on the basis of 2-D and 3-D rockfall analyses. Eventually, two different preliminary rockfall hazard maps were prepared for the southwestern region of the castle and rockfall high-risk areas were defined considering the run-out distances based on 2-D and 3-D analyses. The prepared maps in this study are preliminary as there are still ongoing analyses for the entire castle perimeter.

2-D Rockfall Analyses

RocFall v.4.0 software of Rocscience (2002) was used for the 2-D rockfall analysis which were carried out along six profiles on the S-SW foothills of the Kastamonu Castle. It should be stated that the analyzed slopes are not vegetated as can be recognized from the photo in Fig. 1. RocFall v.4.0 (Rocscience 2002) is a software performing statistical analyses of rockfalls based on lumped-mass method considering the mass of a boulder to be a single point moving through the air along a trajectory with X and Y coordinates.

The most important coefficients of the 2-D rockfall analysis are the normal (R_n) and tangential (R_t) coefficients of restitution. For the assessment of these coefficients, the positions of the fallen sandstone blocks were placed on the available topographic map at a scale of 1:1,000. The weight of each block was predicted using the volume and the unit weight of the block. Consequently, an average block mass of about 10 tons was assumed on the basis of site evidences.

Table 1 Parameters used in 2-D rockfall analyses

Parameters	Value
Normal coefficient of restitution	0.35 ± 0.05
Tangential coefficient of restitution	0.62 ± 0.05
Friction angle (°)	30 ± 2
Slope roughness (°)	2
Initial velocity (m/s)	1 ± 0.5
Number of throws	1,000
Minimum velocity cut-off (m/s)	0.1
Sampling interval	50

Back analysis was then performed to estimate the coefficients of restitution for the sandstone in the study area. Based on the analysis, the normal and tangential coefficients of restitution of the rocks were determined as 0.35 and 0.62, correspondingly. The friction angle and slope roughness were considered as 30° and 2, respectively. For the initial velocity, a value of 1 m/s was considered (Table 1).

As a particular note, during the rockfall analyses, it was assumed that the falling of blocks initiates just below the castle wall since this elevation is the highest point that rockfall may occur. The fall-out distances of falling blocks on six different profiles ranges between 36 and 88 m. Furthermore, the bounce height of blocks attains as high as 7.3 m on a profile whereas the maximum kinetic energy is around 250 kJ.

The rockfall danger zone map produced in accordance with 2-D rockfall analysis for the southwestern region of the Kastamonu Castle is shown in Fig. 3. It can be easily noticed from Fig. 3 that the maximum run-out distances of falling blocks exceeds the settlement boundary indicating a certain rockfall danger for the residential houses in the close vicinity.

3-D Rockfall Analyses

3-D rockfall analyses were carried out using the ROTOMAP software by Scioldo (1991). Before the analyses, a 3-D model of the hill where the castle is settled was generated in the same computer code. Contrary to 2-D rockfall analyses, rockfall initiation was modeled along a detachment line surrounding the castle wall. A total of 1,000 rockfalls were simulated using minimum (0.5 m/s) and maximum (1.5 m/s) initial velocities. Parameters employed in the ROTOMAP rockfall simulations are presented in Table 2.

The limit value of the angle that defines the transition from aerial motion to sliding–rolling motion plays an important role in the analysis. This angle is created between the tangent to the path of a rebounding block and the tangent of the slope profile at the impact point. The transition between bouncing and rolling is established when this angle is lower than a chosen threshold value (Scioldo 1991).

Table 2 Parameters used in 3-D rockfall analyses

Parameters	Value
Fly limit angle (°)	9
Colliding limit angle (°)	9
Bouncing limit angle (°)	9
Number of starting points	1,000
Number of initial velocities	1
Minimum initial velocity (m/s)	0.5
Maximum initial velocity (m/s)	1.5
Number of initial directions	1
Maximum angular deviation (°)	50
Boulder mass (t)	10
Normal coefficient of restitution	0.35
Tangential coefficient of restitution	0.62
Friction coefficient of rolling boulders	0.5

The same normal (R_n) and tangential (R_t) coefficients of restitution used in 2-D analyses (0.35 and 0.62) were employed in 3-D analyses. Moreover, the friction coefficient of the rolling boulders (0.5) was selected based on literature data (Descoedres and Zimmermann 1987).

The rockfall trajectories and run-out distances obtained from 3-D rockfall analyses performed using the ROTOMAP software is illustrated in Fig. 4.

It should be indicated that in the rockfall trajectory map, bouncing is represented by red color, whereas green lines indicate rolling rocks. Thus, rolling is the main movement type for the investigated terrain as can be seen in Fig. 4. Blocks bounce mostly on the southwestern hills of the castle and a maximum of 5.5 m bouncing was determined in the ROTOMAP software, although maximum bouncing was found to be 7.3 m in 2-D analyses.

3-D rockfall analyses point out a rockfall danger zone as the maximum run-out distances are beyond the settlement boundary on the southwestern region. The rockfall danger for the southwestern side of the castle determined in 2-D rockfall analyses is verified by 3-D analyses.

The highest kinetic energy values were found in the southwestern side of the castle. Similar to 2-D analyses, the kinetic energy of falling blocks reaches a maximum value of 250 kJ on the southwestern side of the castle according to 3-D analyses. In other words, both 2-D and 3-D analyses reveal the same kinetic energy values for the southwestern section.

Comparison of 2-D and 3-D Rockfall Analyses

In the literature, there are few studies concerning the accuracy of rockfall models (Dorren et al. 2011). According to Labiouse (2004), similar run-out distances can be obtained if the model parameters are well-calibrated. However, bounce heights and kinetic energies may vary along rockfall

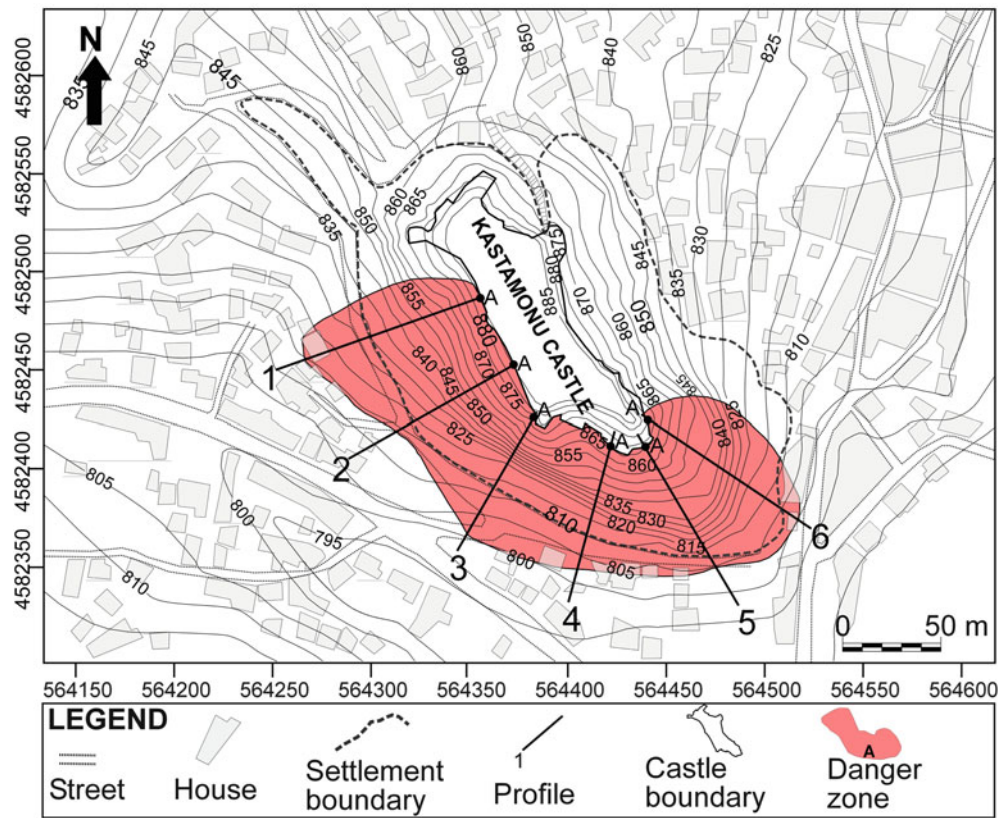


Fig. 3 Rockfall danger zone map of the southwestern part of the Kastamonu Castle based on 2-D analyses

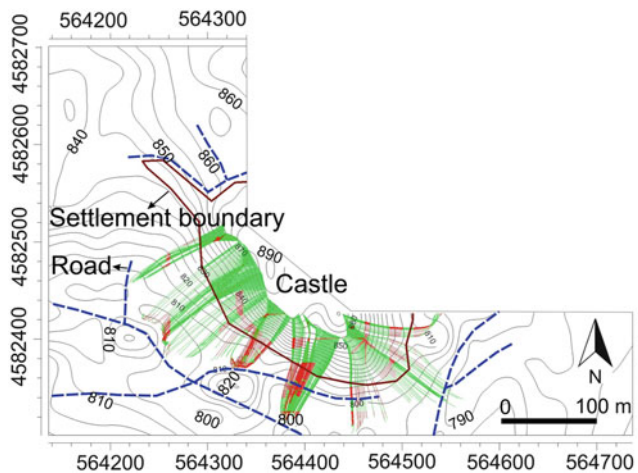


Fig. 4 Rockfall danger zone map of the Kastamonu Castle based on 3-D analyses

trajectories in 2-D and 3-D rockfall simulations. In addition, the selection of rockfall profiles is of great importance in complex terrain as the profile roughness significantly affects the rockfall model (Labieuse 2004).

In this study, the maximum run-out distances for the southwestern hill of the castle obtained from 3-D analyses are further than those of 2-D analyses (Figs. 3 and 4). Once

the maximum run-out distance in 2-D model is 88 m, the rockfall trajectories can reach more than 100 m in 3-D analyses. There is also slight difference in bounce heights of the models. A maximum of 7.3 m bouncing was calculated in 2-D analyses, whilst the maximum bounce height is 5.5 m in 3-D model. Despite the inaccuracy of run-out distances and bounce heights, the same maximum kinetic energy value (250 kJ) was determined in both models.

The run-out distance variation in both models may be attributed to the accuracy of the terrain models used in the analyses. It is quite complicated to determine one model is more accurate. However, it is clear that the southwestern side of the Kastamonu Castle is under great danger of rockfalls and remedial measures should be implemented. Both 2-D and 3-D models reveal that falling boulders exceed the settlement boundary.

Conclusions

In this study, rockfall hazard in the southwestern region of the Kastamonu Castle was investigated through 2-D and 3-D rockfall models and the obtained results were compared. Both simulations indicate a critical rockfall danger zone for the southwestern side of the castle. Although the maximum run-out distances in two models are far beyond the settlement boundary, quite different

results were obtained considering the rockfall path distances and bounce heights. The maximum run-out distances obtained from 3-D analyses are further than those of 2-D analyses and the bounce heights of 2-D analyses are higher than 3-D simulations. The same kinetic energy values were calculated from both models.

As rockfall danger is obvious for the Kastamonu Castle, remedial measures should be taken. Boulders that have a tendency to fall down should be removed and fences with sufficient height and kinetic energy absorbance capacity should be set up around the castle.

Acknowledgments This study is financially supported by METU-BAP Project. The authors gratefully acknowledge Kastamonu Municipality for their support during the field study and providing technical documents related to the Kastamonu Castle.

References

- Ayala-Carcedo FJ, Cubillo-Nielsen S, Alvarez A, Domínguez MJ, Laín L, Laín R, Ortiz G (2003) Large scale rockfall reach susceptibility maps in La Cabrera Sierra (Madrid) performed with GIS and dynamic analysis at 1:5,000. *Nat Hazards* 30:325–340
- Corominas J, Copons R, Moya J, Vilaplana JM, Altimir J, Amig'o J (2005) Quantitative assessment of the residual risk in a rockfall protected area. *Landslides* 2(4):343–357
- Descoedres F, Zimmermann TH (1987) Three-dimensional dynamics calculation of rockfall. In: *Proceedings of the 6th international congress on rock mechanics*, Montreal, vol 1, pp 337–342
- Dorren L (2003) A review of rockfall mechanics and modelling approaches. *Progr Phys Geogr* 27:69–87
- Dorren L, Domaas U, Kronholm K, Labiouse V (2011) Methods for predicting rockfall trajectories and run-out zones. In: Lambert S, Nicot F (eds) *Rockfall engineering*. Wiley, London, 435 p
- Frattoni P, Crosta G, Carrara A, Agliardi F (2008) Assessment of rockfall susceptibility by integrating statistical and physically based approaches. *Geomorphology* 94:419–437
- Guzzetti F, Crosta GB, Detti R, Agliardi F (2002) STONE: a computer program for the three-dimensional simulation of rock-falls. *Comput Geosci* 28:1079–1093
- Jaboyedoff M, Dudt JP, Labiouse V (2005) An attempt to refine rockfall hazard zoning based on the kinetic energy, frequency, and fragmentation degree. *Nat Hazards Earth Syst Sci* 5:621–632
- Labiouse V (2004) Fragmental rockfall paths: comparison of simulations on alpine sites and experimental investigation of boulder impact. In: *9th International symposium on landslides*, Rio de Janeiro, Balkema, pp 457–466
- Lambert S, Nicot F (2011) *Rockfall engineering*. ISTE, Wiley, New York, 435 pp
- Lan H, Derek Martin C, Lim CH (2007) Rockfall analyst: a GIS extension for three-dimensional and spatially distributed rockfall hazard modelling. *Comput Geosci* 33(2):262–279
- Marquinez J, Menéndez R, Farias P, Jiménez M (2003) Predictive GIS-based model on rockfall activity in mountain cliffs. *Nat Hazards* 30:341–360
- Piacentini D, Soldati M (2008) Application of empiric models for the analysis of rockfall runout at a regional scale in mountain areas: examples from the Dolomites and the northern Apennines (Italy). *Geogr Fis Dinam Quat* 31:215–223
- Rocscience (2002) RocFall software-for risk analysis of falling rocks on steep slopes. Rocscience user's guide, 59 p
- Scioldo G (1991) ISOMAP and ROTOMAP, 3D surface modelling and rockfall analysis. Geo and Soft, Torino, Italy
- Tanarro LM, Muñoz J (2012) Rockfalls in the Duraton canyon, central Spain: inventory and statistical analysis. *Geomorphology* 169:17–29
- Topal T, Akin M, Ozden AU (2007) Assessment of rockfall hazard around Afyon Castle. *Environ Geol* 53(1):191–200
- Topal T, Akin MK, Akin M (2012) Rockfall hazard analysis for an historical Castle in Kastamonu (Turkey). *Nat Hazards* 62:255–274
- Youssef AM, Maerz NH (2012) Development, justification, and verification of a rock fall hazard rating system. *Bull Eng Geol Environ* 71:171–186



Approach for Systematic Rockslide Mapping of Unstable Rock Slopes in Norway

Reginald L. Hermanns, Thierry Oppikofer, Freddy X. Yugsi Molina, John F. Dehls, and Martina Böhme

Abstract

Systematic mapping of unstable rock slopes has been carried out in Norway since 2005. More than 300 unstable or potential unstable rock slopes have been detected and characterized so far. This utilises a standardized hazard and risk classification system that was established in 2012. The determination of the hazard and risk level follows a new standard approach for the systematic mapping of the analyzed sites that is iterative, starting with simple assessments. However the higher the hazard/risk level of a site is, the larger the amount of geological information collected, and the more detailed the run-out models and consequence analyses that will be carried out. This approach allows mapping resources to be focused on sites with higher risk level, delivering products with different levels of detail. Rock slope failures that would not result in any loss of life, as there is no life line or building in the run-out area, are mapped without a probability assessment. These analyses thus have no scale for the hazard class. Rock slope failures that can result in loss of life are analyzed using qualitative hazard analyses, thus the mapping products are hazard maps with qualitative probability classes. The work on this mapping approach is still ongoing; methods for assessment of the occurrence and consequences of secondary processes (e.g., triggering of displacement waves in water bodies, river damming and outburst floods) need still to be defined. An iterative approach will also be developed to analyze those processes.

Keywords

Rock slope instability • Detection • Mapping • Displacement measurements • Run-out analysis • Consequence analysis • Hazard classification • Risk classification

Introduction

Although rock slope failures are relatively rare events on a global scale, with its 100,000 km long coastline, Norway has historically experienced 2–6 large rockslides per century

that have produced several tens of meters high displacement waves and resulted in the death of dozens of people (e.g., Hermanns et al. 2006; Devoli et al. 2011). In response to this high rockslide exposure, the Geological Survey of Norway (NGU) began in 2005 to map unstable rock slopes (e.g., Böhme et al. 2011; Bunkholt et al. 2011; Henderson and Saintot 2011; Oppikofer et al. 2013). Since 2009, this activity has been financed through the Norwegian Water Resources and Energy Directorate (NVE).

Standardization of the mapping approach is crucial in order to guarantee that the products of the hazard and risk classification are comparable and reproducible. The establishment of the hazard and risk classification for unstable

R.L. Hermanns (✉) • T. Oppikofer • F.X. Yugsi Molina • J.F. Dehls • M. Böhme
Geological Survey of Norway, P.O. Box 6315 Sluppen, 7491 Trondheim, Norway
e-mail: reginald.hermanns@ngu.no; thierry.oppikofer@ngu.no; freddy.molina.yugsi@ngu.no; john.dehls@ngu.no; martina.bohme@ngu.no

rock slopes in 2012 (Hermanns et al. 2012, 2013a) has set the frame work to define the level of detail required for the mapping of unstable rock slopes according to their level of hazard. This paper describes that approach, which is also summarized in a flowchart diagram in Fig. 1.

Mapping Approach

Goals

Goals of these ongoing mapping activities are to find all rock slopes that could fail catastrophically and to determine areas that would be affected by their failure in order to communicate possible consequences to Norwegian society. Catastrophic failures are here defined as rock slope failures that involve substantial fragmentation of the rock mass during run-out and that impact an area larger than that of a rockfall, hence also include rock slope failures that might cause a displacement wave or damming of valleys (Hermanns and Longva 2012).

Since the beginning of 2013, mapping activities have focused on collecting information to be used for the implementation of the hazard and risk classification system (Hermanns et al. 2012) recently developed by a team of Norwegian and international experts. This classification became the standard procedure for defining the risk level that will be used to decide on further actions (that will be specified in an upcoming NVE document) on the investigated sites. The consequence analysis within this classification system focuses on loss of life only.

The results of the evaluation using this classification system have allowed developing a systematic mapping approach, as presented in Fig. 1. This approach is set up so that mapping activities for sites that cannot cause catastrophic rock slope failures, or that do not show signs of past deformation or do not have consequences in case of failure, are discarded from further investigations after the reconnaissance phase. This allows detailed, costly investigations to be focused on the medium- and high-risk sites.

This mapping approach guarantees a similar level of geological information for all sites with the same risk level over the entire country. However, detail of geological information is not even for sites with different risk levels. Additional geological data will have to be collected in future at sites where the risk level changes due to external factors (e.g., increase in potential consequences due to new buildings).

Due to the difference in the amount and detail of geological data, outcomes will be different too: maps of the run-out area of the majority of low-risk sites will represent hazard maps without a hazard class (qualitative probability of

failure), while they will represent hazard maps with qualitative hazard classes for all medium- and high-risk sites and some of the low-risk sites.

Investigation Stages

Detection of Unstable Rock Slopes

Detection of (potential) unstable rock slopes is carried out using expert-based analysis of optical remote sensing imagery to search for morphological features of unstable slopes such as opening of cracks, displacement of blocks, high fracture density of bedrock, and satellite-based radar interferometry (InSAR) (Fig. 1).

Reconnaissance

On steep slopes and high mountain plateaus in Norway the bedrock is often bare or covered only by thin Quaternary deposits. Old inherited tectonic structures are thus readily visible and may appear as cracks, especially on slopes where they are subject to preferential erosion. However, superficial processes such as solifluction can be detected by InSAR techniques and mistaken for signs of rock slope deformation. Therefore, all detected sites undergo an initial reconnaissance.

Reconnaissance is carried out from any spot with easy access to the site and good visibility or from a helicopter. In this step, rock slopes with no real signs of deformation of large rock volumes are divided in three categories: (A) unstable rock slopes that are too small to cause a catastrophic failure in the above-defined sense. These sites are however prone to rockfalls, and other available mapping products such as the national rockfall susceptibility map or rockfall hazard maps define the susceptibility/hazard levels of those areas (see <http://www.skrednett.no>). (B) Rock slopes that have no structural or lithological conditions that could lead to a catastrophic rock slope failure in the future. (C) Rock slopes that have the structural or lithological conditions for failure in the future, but no sign of past or present displacements or deformation (potential unstable rock slopes). Category C sites have to be followed up by a revision after several years to decades, as they might become active unstable rock slopes. The fast development of remote sensing data with increasing resolution and acquisition cycles will make this possible.

Preliminary Consequence Analyses

At the end of the reconnaissance phase a preliminary consequence analysis will be carried out for all unstable rock slopes. Sites with evidently no consequences (no buildings or life lines in the potential run-out area) are evident low-risk sites and no further investigations will be made. Nonetheless, the volume will be assessed and an automated run-out

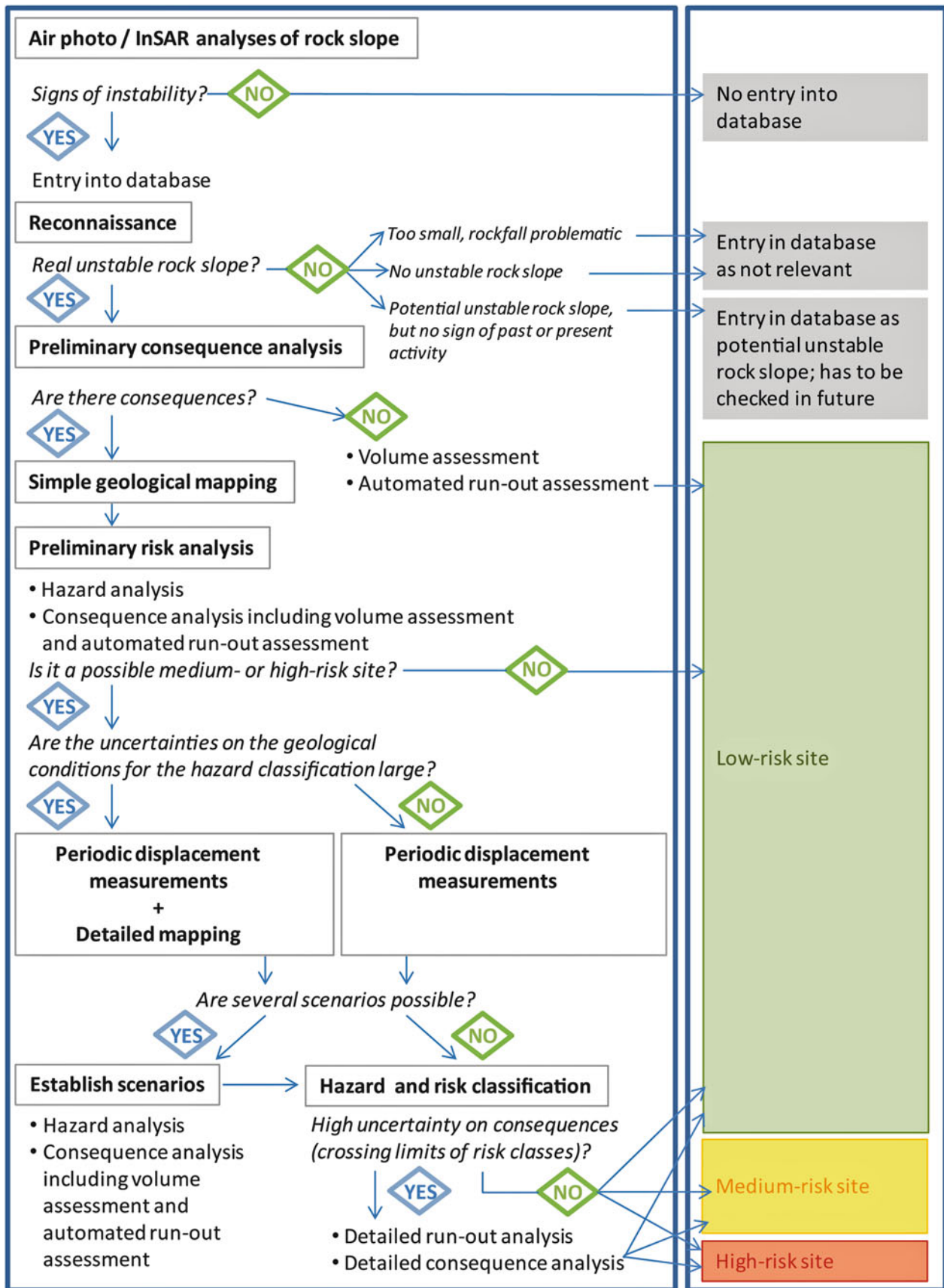


Fig. 1 The flowchart shows the mapping approach for unstable rock slopes in Norway. Potential unstable rock slopes that do not display signs of past displacements and sites without possible consequences are discarded from more intensive geological studies at an early stage

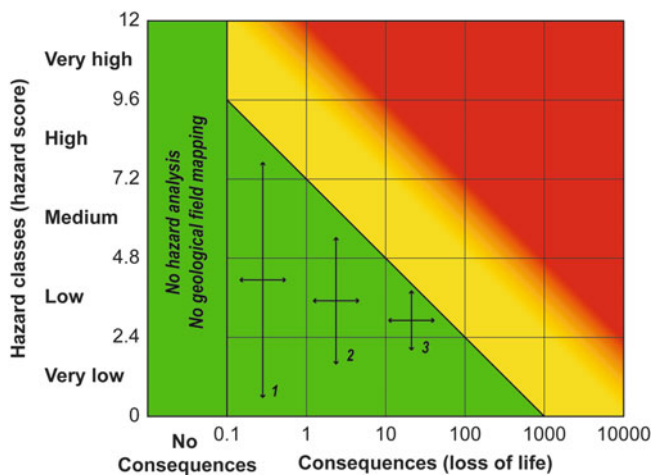


Fig. 2 Risk matrix, showing the risk classes (*green* is low, *yellow* is moderate and *red* is high). The diagram also shows under which conditions no geological field mapping will be carried out (no consequences) and 3 examples with increasing consequences (1–3) that require decreasing uncertainty levels and hence increasing certainty of geological observations

analysis will be calculated to indicate areas that could potentially be hit by a catastrophic failure (hazard map without a qualitative probability assessment) (Figs. 1 and 2). Unstable rock slopes with evident consequences (buildings, life lines or water bodies in the run-out area) will be further investigated according to the flowchart in Fig. 1.

Simple Geological Mapping

During simple geological mapping geological information on all criteria that are necessary for the hazard classification are collected, including morphological and structural development (e.g., back scarp, potential sliding structures, lateral release surfaces, morphological expression of rupture surface, kinematic analysis) and signs of activity (displacement rates, acceleration, increase of rockfall activity, past events) (see also: Hermanns et al. 2012, 2013a). Uncertainty on these observations might be high (especially for the displacement rates, since no monitoring data are being collected at that stage of investigation). A first hazard analysis will be performed as indicated in Hermanns et al. (2012, 2013a). For all sites an automated run-out analysis is calculated and consequences are assessed. Sites with no consequences are categorized as low-risk sites. For all other sites a preliminary risk analysis is carried out following Hermanns et al. (2012, 2013a). Low-risk sites with low consequences might have large uncertainty on the geological observations (example 1 in Fig. 2). For all possible medium- or high-risk sites, i.e., the yellow and red zones in the chart presented in Fig. 2, the amount of geological observations has to be increased to reduce the uncertainty margins (examples 2 and 3 in Fig. 2). Two situations are possible

based on this simple geological mapping: (A) the geological conditions are well understood, or (B) the geological criteria could not entirely be assessed by the simple geological mapping. For the former, periodic displacement measurements need to be carried out, while for the latter further geological mapping is necessary, in addition to periodic displacement measurements.

Periodic Displacement Measurements and Detailed Geological Mapping

At all sites that are assessed as potential medium- or high-risk sites, local conditions have to be understood better in order to reduce uncertainties in the hazard analysis. In general the easiest way to reduce uncertainties is to use monitoring equipment in order to assess the current displacement rates. A wide variety of monitoring techniques is currently used by NGU, including extensometers, differential Satellite Global Navigation Systems (dGNSS), satellite- and ground-based InSAR with and without reflectors, terrestrial laser scanning and photogrammetry.

In addition, sites with complex geology require additional geological field mapping. These are sites where simple kinematic models (planar sliding, wedge sliding, flexural or block toppling) cannot explain the observed deformation and more complex kinematic models have to be developed. These could be sites with a combination of two failure mechanisms, such as bi-planar sliding, slide toppling, or a combination of sagging and rock slide. Sites with a strong change in the structural conditions over the slope (e.g., folding) also fall into this group.

Establish Scenario and Hazard and Risk Classification

Scenarios are developed following structural and morphological mapping, in combination with results of displacement measurements. A single failure scenario is likely if the structures over the entire unstable slope do not vary and the entire unstable slope deforms uniformly. In contrast, if the displacement rates vary over the instability and the whole unstable rock slope is divided in compartments with different behaviour, different failure scenarios have also to be taken into account. Two general cases of scenarios exist: (A) individual compartments of a larger unstable rock slope lie beside each other and each one could fail independently of the other, or (B) individual compartments are subareas within a larger unstable rock slope and could fail without causing the failure of the total unstable rock slope; the failure of the total unstable rock slopes however includes also its subareas.

For each scenario the hazard and automated run-out analyses followed by consequence analyses have to be performed, leading to the risk classification. If the

uncertainties on the consequences are high, detailed run-out analyses become necessary.

Mapping Products

The information product will be published through the existent database of unstable rock slopes in Norway (Bunkholt et al. 2013) and includes the location and extent of the unstable area, mapping status and recommendations for follow-up activities. This information will become of public access through <http://www.skrednett.no> in 2014. The result of the hazard and risk classification will be added once all necessary data have been collected and the classification performed. In addition, run-out areas for each site will be published once the analysis is carried out. These run-out areas present different quality levels. They represent hazard maps with no qualitative probability analysis for those sites where today consequences are zero (no building or life lines are in the run-out area) and qualitative hazard maps for those areas where loss of life might occur. More specific geological information will continue to be in the category of restricted access. Information for each site will be downloadable in 2014 as factsheets.

Discussion

Due to the geomorphologic conditions of Norway, with one of the world's longest coastlines characterized by high mountains deeply incised by fjords, large rock slope failures occurred repeatedly in the past, often accompanied by secondary effects such as displacement waves and damming of valleys (Blikra et al. 2006; Hermanns et al. 2013b). Therefore, in contrast to other mountain belts in the world, these long-distance effects resulted in a larger death toll than from just the direct impact of the rock slope failure itself. As such events will also occur in the future, and in order to attenuate their deadly consequences, systematic mapping of rock slopes has started in the first decade of the twenty-first century, and today more than 300 (potential) unstable rock slopes are known. This high number of sites necessitated a quantitative hazard and risk classification system to assist in deciding on follow-up activities. This system was elaborated in a large effort combining national and international experts from various disciplines in earth sciences and presented in Hermanns et al. (2012, 2013a).

Subsequently, in order to establish the hazard and risk classification system, it became necessary to adapt the national mapping approach to this system. The goal of this mapping approach is to be cost-effective and to focus mapping resources on sites that are most critical. This goal is met by using an iterative approach: the amount of

collected geological data, quality of run-out modelling, and detail of consequence analyses increase respectively, improving with the increasing risk level for each site and scenario. Hence for high-risk sites, various cycles of hazard analysis, run-out-analysis, consequence analysis and risk analysis are carried out. This leads in parallel to a reduction of the uncertainties in the hazard and risk classification. However, using this approach, the level of detail of the mapping products is not even. Sites where run-out models are calculated from a volume estimate alone do not include an assessment of the hazard level. Also the run-out areas of low-risk sites represent hazard zones with relatively high uncertainties in the likelihood of an event. Uncertainties in the likelihood of an event are smaller for medium- and high-risk sites. This will lead in general to the situation that mapping products for unstable slopes that can cause a larger number of casualties will rely on a sound knowledge of their geological characteristics.

The work on this mapping approach is not finalized and it is an ongoing project. So far it has been decided that secondary effects such as rockslide-triggered displacement waves and rockslide damming will be included. Detail of analysis for these secondary effects should also increase with risk level and follow an iterative approach; however, practises are still under development.

References

- Blikra LH, Longva O, Braathan A, Anda E, Dehls JF, Stalsberg K (2006) Rock slope failures in Norwegian fjord areas; examples, spatial distribution and temporal pattern. In: Evans SG, Scarascia Mugnozza G, Strom A, Hermanns RL (eds) Landslides from massive rock slope failures, NATO science series IV (49), Earth and environmental sciences. Springer, Dordrecht, pp 475–496
- Böhme M, Henderson I, Saintot A, Hermanns RL, Henriksen H (2011) Rock-slope instability investigations in Sogn & Fjordane County, Norway: a detailed structural and geomorphological analysis. In: Jaboyedoff M (ed) Slope tectonics. Geological Society, London. Special Publication, 351, pp 97–112. ISBN:978-1-86239-324-0
- Bunkholt H, Osmundsen PT, Redfield T, Oppikofer T, Eiken T, L'Heureux J-S, Hermanns R, Lauknes TR (2011) ROS Fjellskred i Troms: status og analyser etter feltarbeid 2010. Norwegian Geological Survey Report No. 2011-031, 135 p
- Bunkholt H, Nordahl B, Hermanns RL, Oppikofer T, Fischer L, Blikra LH, Anda E, Dahle H, Sætre S (2013) Database of unstable rock slopes of Norway. In: Margottini C, Canuti P, Sassa K (eds) Landslide science and practice, Volume 3: Spatial analysis and modelling. Springer, Berlin, pp 423–428
- Devoli G, Eikenæs O, Taurisano A, Hermanns RL, Fischer L, Oppikofer T, Bunkholt H (2011) Plan for skredfarekartlegging – Delrapport steinsprang, steinskred og fjellskred. NVE rapport 15/2011. Norgesvassdrags- og energidirektorat, Oslo, 110 p
- Henderson IHC, Saintot A (2011) Regional spatial variations in rockslide distribution from structural geology ranking: an example from Storfjorden, western Norway. In: Jaboyedoff M (ed) Slope tectonics. Geological Society, London. Special Publication, 351, pp 79–96. ISBN:978-1-86239-324-0

- Hermanns RL, Longva O (2012) Rapid rock-slope failures. In: Clague JJ, Stead D (eds) *Landslides: types, mechanisms and modeling*. Cambridge University Press, Cambridge, UK, pp 59–70
- Hermanns RL, Blikra LH, Naumann M, Nilsen B, Panthi KK, Stromeyer D, Longva O (2006) Examples of multiple rock-slope collapses from Kölfels (Ötz valley, Austria) and western Norway. *Eng Geol* 83(1–3):94–108
- Hermanns RL, Oppikofer T, Anda E, Blikra LH, Böhme M, Bunkholt H, Crosta GB, Dahle H, Devoli G, Fischer L, Jaboyedoff M, Loew S, Sætre S, Yugsi Molina F (2012) Recommended hazard and risk classification system for large unstable rock slopes in Norway. NGU-rapport 2012.029, 53 p
- Hermanns RL, Oppikofer T, Anda E, Blikra LH, Böhme M, Bunkholt H, Crosta GB, Dahle H, Devoli G, Fischer L, Jaboyedoff M, Loew S, Sætre S, Yugsi Molina F (2013a) Hazard and risk classification system for large unstable rock slopes in Norway. In: Genevois R, Prestininzi A (eds) *International conference on Vajont – 1963-2013*. Italian Journal of Engineering Geology and Environment, Book series 6, Rome, Italy, pp 245–254
- Hermanns RL, Dahle H, Bjerke PL, Crosta GB, Anda E, Blikra LH, Saintot A, Longva O, Eiken T (2013b) Rock slide dams in Møre og Romsdal county, Norway: examples for the hazard and potential of rock slide dams. In: Margottini C, Canuti P, Sassa K (eds) *Landslide science and practice, Volume 6: Risk assessment, management and mitigation*. Springer, Berlin
- Oppikofer T, Saintot A, Otterå S, Hermanns RL, Anda E, Dahle H, Eiken T (2013) Investigations on unstable slopes in Møre og Romsdal - status and plans after field surveys in 2012. NGU rapport 2013.014 (ISSN 0800-3416), 169 p

Part III

Earthquake-Induced Landslides



Introduction: Earthquake-Induced Landslides

Fawu Wang, Kazuo Konagai, Hideaki Marui, Mohammadreza MahdaviFar, and Gabrielle Scrascia-Mugnozza

Abstract

Earthquake-induced landslide may be the most complicated type among other forms of landslides. In this session, 18 papers were accepted for oral presentation. The contents of the papers covered case study and investigation report, landslide inventory and database, hazard analysis and risk evaluations, triggering mechanism and travelling mechanism, and methodologies.

Keywords

Landslide • Earthquake • Inventory • Mechanisms • Methodology

Earthquake-induced landslide may be the most complicated type among other forms of landslides; this is because of the unpredictable nature of earthquakes. Different types of landslides triggered by earthquake, such as sliding, falling and flowing may occur. Also, because the earthquake may occur in different geological, topographic and climatic conditions, the scale of landslides may change from small scale like rockfall to large scale like giant landslides covering several square kilometers. For disaster reduction, hazard assessment and risk management on earthquake-triggered-landslides becomes important and has proved to be the most

effective way of safeguarding human lives and property from landslides.

In this session, 18 papers were accepted for presentations. The papers covered the most active seismic zones of the world, including Japan, Indonesia and Chile located in the circum-Pacific earthquake belt, Southwestern and North-western China, Taiwan, Altai Russia, Central Asia, and the alpine area. The papers can be classified into five groups, which are: case study and investigation report, landslide inventory and database, hazard analysis and risk evaluation, triggering mechanism and travelling mechanism, and methodologies.

The following is a brief introduction of the paper contents.

F. Wang (✉)

Department of Geosciences, Shimane University, Matsue, Japan
e-mail: wangfw@riko.shimane-u.ac.jp

K. Konagai

Graduate School of Urban Innovation, Yokohama National University, Yokohama, Japan

H. Marui

Research Institute for Natural Hazards and Disaster Recovery, Niigata University, Niigata, Japan

M. MahdaviFar

Geotechnical Engineering Research Center, International Institute of Earthquake Engineering and Seismology, Tehran, Iran

G. Scrascia-Mugnozza

Department of Earth Sciences, University of Rome "La Sapienza", Rome, Italy

Case Study and Investigation Report

Two papers introduced the investigation results on Ms 7.0 earthquake of 20 April 2013 in Lushan, SW China (Wang et al. 2014a, b). A total number of 217 people were reported dead or missing, and 13,000 people were injured due to the earthquake. 539 landslides were triggered by the earthquake, and among them, small and medium-scale landslides with volume ranging from several cubic meters to a few tens of thousand cubic meters were in the majority. These earthquake-triggered landslides were distributed primarily

along the causative faults of Shuangshi-Dachuan Fault and most of them occurred within the buffer zone of $-20\sim 20$ km distance to the causative fault (Wang et al. 2014a). FLAC software was used to analyze the progressive damage difference of numerical models of Donghekou rock landslide affected by the Lushan and Wenchuan earthquakes, respectively. Acceleration of ground motion observation in Lengzhuguan slope suffering from seismic waves of Lushan earthquake indicated that there was symmetrical relationship between predominant frequency and acceleration amplification curves (Wang et al. 2014b). Has et al. (2014) analyzed the characteristics of deep-seated landslides induced by different types of earthquake in inland Japan. They analyzed the distribution and scale of deep-seated landslides induced by Chuetsu earthquake in 2004, Iwate-Miyagi earthquake in 2008, North Nagano Province earthquake in 2011, Fukushima Hamadori earthquake in 2011, and found that in the case of reverse fault earthquakes, the landslides were mostly distributed on the hanging wall of the source fault and the scale of landslides are likely to be larger than that on the foot wall. While in the case of normal fault, the landslides mostly occurred on the hanging wall. These characteristics are coinciding with the PGA distribution of different types of earthquakes, considered to be related with hanging wall effect of reverse fault and normal fault earthquakes. Faris and Wang (2014) reported the investigation results of Tandikat Landslide, West Sumatra, Indonesia triggered by a magnitude 7.6 earthquake, which took hundreds of lives and triggered numerous landslides. The landslides occurred on loose pumice layered mountain during rainfall. The combination of intensive rainfall and strong earthquake was considered to have decreased the slope stability. Pore water pressure caused by the seismic loading was estimated using the strain energy approach. The result shows that shallow landslides due to earthquake are more likely to occur in the area than deep-seated landslides. It shows that slope failure may have occurred prior to the maximum peak of earthquake acceleration implying great influence of pore water pressure generation to slope failure. Through the field surveys and data access, Chang et al. (2014) analyzed the distribution of large landslides triggered by the 2008.5.12 Wenchuan earthquake in China.

Landslide Inventory and Database

Landslide inventory and database may be an effective tool to understand the whole image of landslides triggered by one earthquake event or in a specific region. Crosta et al. (2014) presented a landslide inventory in the area between Pisagua (19.4° Chile) and Tacna (17.5° Peru) to the NE of the Arica bend. Volume estimates and slope stability modelling have been used to characterize the phenomena and the possible

triggering mechanisms. Xu (2014) built an inventory for landslides triggered by the 2010 Haiti earthquake using Geographic Information Systems (GIS) technology and visual interpretation of high-resolutions remote sensing images. Statistical analysis of these landslides spatial distribution using double indices such as landslide number density (LND) and landslide area percentage (LAP) determined how landslide occurrence correlates with controlling parameters. Based on the inventory of landslides triggered by the 2008 Wenchuan earthquake in China, Xu et al. (2014) compare the mass wasting volume due to seismic landsliding to the gain volume caused by rock uplift. The results show that about 5.9 km^3 materials, generated by nearly 200,000 landslides triggered by the Wenchuan earthquake, are distributed in the landslide intensive area. Although the landslide volume is larger than the published volume of tectonic rock uplift ($2.6 \pm 1.2 \text{ km}^3$), it is rather smaller than that from the previous study.

Hazard Analysis and Risk Evaluation

When we live with risk, the hazard analysis is important. Havenith (2014) analyzed how important earthquake-induced landslide hazards are compared to other geohazards at world-wide scale. They tried to answer questions such as: how likely is a seismic versus climatic origin for giant landslides; how is the general geohazards level affected by these low-frequency earthquake-triggered mega-events. Through multi-stage statistical landslide hazard analysis, Lee (2014) used data obtained from the Chi-Chi earthquake-induced landslides as input data set to perform the susceptibility analysis and probability of failure surface analysis. A regular probabilistic seismic hazard analysis was conducted to map different return-period Arias intensities. Finally, a seismic landslide hazard map was produced. While Valagussa et al. (2014) conducted a quantitative probabilistic hazard analysis of earthquake-induced rockfalls. They illustrated a methodology for quantitative probabilistic hazard analysis related to earthquake-induced rockfall events. In their work, they developed a map by using multivariate statistical techniques with morphological and seismic variables.

Triggering Mechanism and Travelling Mechanism

The triggering mechanism and travelling mechanism of landslides triggered by earthquake is fundamental for landslide disaster reduction. Through comprehensive study of the 2004 Mid-Niigata Prefecture earthquake and the 2005 Kashmir earthquake, Kazmi and Konagai (2014) calculated

the seismic stresses for the epicentral areas of the aforementioned earthquakes in the interior of a laterally homogeneous layered half-space using forward modeling. Distribution of landslides for both earthquakes is compared to the square root of the second principal invariant of deviatoric stress tensor and a remarkable correlation is observed. Comparison of the existing landslides and seismic stresses deduced continual build-ups of a similar stress pattern in the past. Niyazov and Nurtaev (2014) analyzed impacts of Pamir-Hindu Kush earthquakes in the foothill areas of Central Asian region for landslides of liquefaction, and classified the liquefactions into three groups: extrusion, thixotropic liquefaction and mudslides of gravitational liquefaction. Yue (2014) mechanistically investigated the dynamics of large and rapid landslides with long travel distance. In addition to many existing theories for friction reduction, the paper puts forward a new cause and mechanism of dense natural gas expansion and its governing equations and numerical results.

Methodologies

Some methodologies were applied directly and indirectly to earthquake-triggered-landslides. Kyaw et al. (2014) made an investigation on local site effects during earthquake-induced ground deformation using microtremor observation in Yogyakarta, Central Java-Indonesia. Leopold et al. (2014) tried to find some indicators for earthquake-induced soil slides in the flatlands of an alpine fringe area. Using dendrochronological analysis of wood penetrating injuries of trees, Nepop et al. (2014) conducted paleoseismological investigations on the high mountain, especially on the seismically active southeastern part of the Russian Altai, and found previously unknown complex of earthquake-induced landslides. Finally, Wang et al. (2014c) analyzed the environmental effects of Shuanghe giant landslide in China. They asserted that the environmental benefits include a wide valley in the ever-reservoir area, providing the people with a convenient site for construction of a new township. As the lacustrine silt sediments lie beneath the new county town, bearing capacity problem and sand liquefaction risk could exist. A road construction cutting in the narrow valley at the toe of the landslide may dam the river again, which could threaten the new town.

We look forward to engaging participants in active discussion on topics bordering on landslides triggered by earthquake in the World Landslide Forum 3 in Beijing.

References

- Chang XJ, Wang DW, Ge WY, Wei LW, Zheng WM, Tang YQ (2014) Study on the distribution of large-landslides triggered by Wenchuan Earthquake. In: Sassa K (ed) *Landslide Science for a Safer Geo-environment*, vol 3, Targeted landslides. Springer, Cham
- Crosta GB, Hermanns R, Frattini P, Valbuzzi E, Valagussa A (2014) Large slope instabilities in Northern Chile: inventory, characterization and possible triggers. In: Sassa K (ed) *Landslide Science for a Safer Geo-environment*, vol 3, Targeted landslides. Springer, Cham
- Faris F, Wang FW (2014) Investigation of Tandikat Landslide, West Sumatra, Indonesia. In: Sassa K (ed) *Landslide Science for a Safer Geo-environment*, vol 3, Targeted landslides. Springer, Cham
- Has B, Takayama T, Ogawa K, Onoda S (2014) Characteristics of deep-seated landslides induced by different type earthquakes in inland Japan. In: Sassa K (ed) *Landslide Science for a Safer Geo-environment*, vol 3, Targeted landslides. Springer, Cham
- Havenith HB (2014) Hazard and risk related to earthquake-triggered landslide events. In: Sassa K (ed) *Landslide Science for a Safer Geo-environment*, vol 3, Targeted landslides. Springer, Cham
- Kazmi ZA, Konagai K (2014) Triggering mechanism of earthquake induced landslides. In: Sassa K (ed) *Landslide Science for a Safer Geo-environment*, vol 3, Targeted landslides. Springer, Cham
- Kyaw ZL, Pramumijoyo S, Husein S, Fathani TF, Kiyono J (2014) Investigation to the local site effects during earthquake induced ground deformation using microtremor observation in Yogyakarta, Central Java-Indonesia. In: Sassa K (ed) *Landslide Science for a Safer Geo-environment*, vol 3, Targeted landslides. Springer, Cham
- Lee CT (2014) Multi-stage statistical landslide hazard analysis – earthquake-induced landslides. In: Sassa K (ed) *Landslide Science for a Safer Geo-environment*, vol 3, Targeted landslides. Springer, Cham
- Leopold P, Goetz JN, Heiss G, Draganits E (2014) Indicators for earthquake-induced soil slides in the flatlands of an alpine fringe area. In: Sassa K (ed) *Landslide Science for a Safer Geo-environment*, vol 3, Targeted landslides. Springer, Cham
- Nepop R, Agatova A, Myglan V, Nazarov A, Barinov V (2014) Using dendrochronological analysis for dating earthquake-triggered landslides (by the example of SE Altai, Russia). In: Sassa K (ed) *Landslide Science for a Safer Geo-environment*, vol 3, Targeted landslides. Springer, Cham
- Niyazov R, Nurtaev B (2014) Landslides of liquefaction caused by single source of impact Pamir-Hindu Kush earthquakes in Central Asia. In: Sassa K (ed) *Landslide Science for a Safer Geo-environment*, vol 3, Targeted landslides. Springer, Cham
- Valagussa A, Frattini P, Crosta GB (2014) Quantitative probabilistic hazard analysis of earthquake-induced rockfalls. In: Sassa K (ed) *Landslide science for a safer geo-environment*, vol 3, Targeted landslides. Springer, Cham
- Wang GL, Zhang MS, Peng J, Zhu H (2014a) Landslides triggered by the Ms 7.0 earthquake of 20 April 2013 in Lushan, SW China. In: Sassa K (ed) *Landslide Science for a Safer Geo-environment*, vol 3, Targeted landslides. Springer, Cham
- Wang WP, Yin YP, Li B, Feng Z, Zhang N, Gao Y (2014b) Characteristics of ground acceleration and features of landslides triggered by the Lushan earthquake (China). In: Sassa K (ed) *Landslide Science for a Safer Geo-environment*, vol 3, Targeted landslides. Springer, Cham

- Wang YS, Zhang X, Li XZ, Mao S (2014c) Environmental effects of Shuanghe giant landslide in Jiuzhai, Sichuan, China. In: Sassa K (ed) *Landslide Science for a Safer Geo-environment*, vol 3, Targeted landslides. Springer, Cham
- Xu C (2014) A preliminary spatial distribution analysis of landslides triggered by the 2010 Haiti earthquake. In: Sassa K (ed) *Landslide Science for a Safer Geo-environment*, vol 3, Targeted landslides. Springer, Cham
- Xu C, Xu XW, Gorum T, van Westen CJ, Fan XM (2014) Did the 2008 Wenchuan earthquake lead to a net volume loss? In: Sassa K (ed) *Landslide Science for a Safer Geo-environment*, vol 3, Targeted landslides. Springer, Cham
- Yue ZQ (2014) Dynamics of large and rapid landslides with long travel distances under dense gas expanding power. In: Sassa K (ed) *Landslide Science for a Safer Geo-environment*, vol 3, Targeted landslides. Springer, Cham



Landslides Triggered by the Ms 7.0 Earthquake of 20 April 2013 in Lushan, SW China

Genlong Wang, Maosheng Zhang, Jing Peng, and Hua Zhu

Abstract

An earthquake measuring 7.0 on the Richter scale occurred in Lushan County in Southwest China's Sichuan Province, at 8:02 A.M, on 20 April 2013. A total number of 217 people were reported dead or missing, and 13,000 people were injured due to the earthquake. Shortly after the earthquake, a group from China Geological Survey carried out field investigations in the earthquake-hit region of Lushan County, Baoxing County and Tianquan County. The results showed that 539 landslides were triggered by the earthquake in the study area. Among them, small and medium-scale landslides with volume ranging from several cubic meters to a few tens of thousand cubic meters were in the majority. These earthquake-triggered landslides were distributed primarily along the causative faults of Shuangshi-Dachuan Fault and most of them occurred within the buffer zone of –20 to 20 km distance to the causative fault.

Keywords

Lushan earthquake • Earthquake landslide • Causative fault • Rockfall • Debris-rock flow

Introduction

On 20 April 2013, at exactly 8:02 (Beijing Time), a catastrophic earthquake (N30.3° and E103.0°) with Ms 7.0 in surface wave magnitude, occurred beneath the steep eastern margin of the Tibetan Plateau in Sichuan, China (Fig. 1). The earthquake was located at the south of the Longmenshan, about 100 km away from Chengdu, and 100 km from the epicenter of Wenchuan Ms 8.0 earthquake, and thus both of these two big earthquakes occurred in the Longmenshan fault system (Liu et al. 2013). It is the largest earthquake that occurred in the same region after the Wenchuan earthquake

(Xie et al. 2013). After the main shock, more than 4,687 aftershocks have been recorded as of 16:00 of 25 April. The number of events with $M > 3.0$ is up to 110 (0 events with mag. 6.0–6.9, 4 events with mag. 5.0–5.9, 21 events with mag. 4.0–4.9, and 85 events with mag. 3.0–3.9). The affected population was 1.99 million from over 19 cities, involving 115 counties. The number of those injured and killed is reported to be 13,000 and 217 as at 12:00, 26 April (Yang et al. 2013).

The strong ground motion triggered by the earthquake caused more than one thousand landslides over a broad area, while aftershocks added further to the landslides (Lan et al. 2013). In the Lushan, Baoxing and Tianquan Counties, which were the hard-hit areas of the earthquake, the number of landslides reached 539 according to field investigations. When it comes to landslide, Vernes (1978) describes it as a wide variety of processes that result in the downward and outward movement of slope-forming materials, including rock, soil, artificial fill, or a combination of these. Therefore, in the work, rockslide, rockfall and debris flow belong to landslide.

G. Wang (✉) • M. Zhang • H. Zhu
Key Laboratory for Geo-Hazards in Loess Area, MLR, Xi'an Regional Center, China Geological Survey, Xi'an 710054, People's Republic of China
e-mail: wang2006@mail.iggcas.ac.cn

J. Peng
Sichuan Geological Circumstance Inspect Center, Chengdu 610081, People's Republic of China



Fig. 1 Location of the Lushan Earthquake

Analyzing the causes and distributions of landslides triggered by an earthquake is important in understanding secondary disasters for future earthquake occurrence. In recent years, large number of studies had focused on landslides triggered by earthquakes (Keefer 2002; Khazai and Sitar 2003; Chigira and Yagi 2006; Wang et al. 2007; Huang and Li 2009; Yin et al. 2009; Qi et al. 2010, 2011; Dai et al. 2011). Nevertheless, very little research has addressed these landslides triggered by the Lushan earthquake. In this paper, we analyzed the available data from the Lushan earthquake to provide insight into the reasons of earthquake-triggered landslides, and to characterize its distributions in the region of Lushan, Baoxing and Tiquan Counties. By understanding the numbers, types and distributions of landslides, it is important to outline the potential dangerous areas of landslides before reconstruction and re-settlement, so as to avoid further disaster occurrence.

Characteristics of the Study Area

The study area is located in a transition region where topography varies abruptly from the steep and rugged Qinghai-Tibet Plateau to the mild Sichuan basin. In other words, the earthquake-affected area is in the mountainous region, and is located at the west hilly edge of Sichuan Basin. It is characterized by rugged topography, steep high mountains, deep valleys and complicated geological structures. The northwest part of the area is higher than the southeast part. Maximum vertical interval reaches some 4,700 m within a horizontal distance of less than 50 km.

The famous Longmenshan fault zone (Wu et al. 2008) crossed the study area with the strike direction NE–SW; it consists of back range fault (F_{1-1} , Longdong Fault and F_{1-2} ,

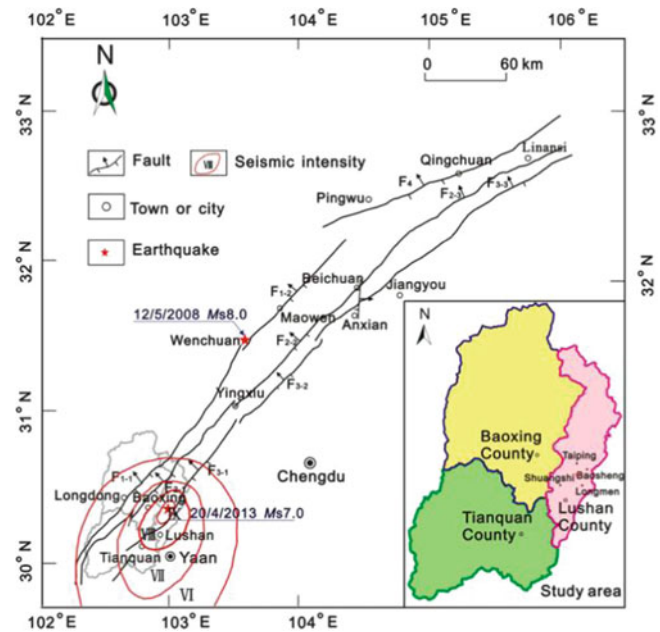


Fig. 2 The distribution of Faults in the Longmenshan fault zone. The Longmenshan fault zone includes back range faults (F_{1-1} and F_{1-2}), central faults (F_{2-1} , F_{2-2} and F_{2-3}) and front range faults (F_{3-1} , F_{3-2} and F_{3-3})

Maowen Fault), Central fault (F_{2-1} , Wulong Fault; F_{2-2} , Beichuan-Yingxiu Fault and F_{2-3} , Beichuan-Linansi Fault), and outet-hill fault (F_{3-1} , Shuangshi Fault; F_{3-2} , Guanxian-Anxian Fault and F_{3-3} , Jianguyou Fault). The epicenter of the Lushan earthquake is located in the footwall of the Shuangshi fault (F_{3-1}), 1.5 km east of it (Fig. 2). Field work indicated that there was no significant rupture on the ground; therefore, researchers have speculated that the causative fault was a buried fault. The focal depth was around 13 km according to the research CNEC (<http://www.cenc.ac.cn/>), so the 4.20 Lushan earthquake was a shallow-focus earthquake. The shallow centroid depth probably contributed to these new added landslides.

In the study area, except for the Cambrian (\in), the rest of the strata from the Pre-Sinian (Z) to the Quaternary (Q) are widely outcropped, mainly with mudstone, sandy mudstone, conglomerate, limestone and dolomitic limestone. Field investigations indicate that majority of the landslides occurred in the Cretaceous siltstone and mudstone, which generally have low shear strength and are heavily fractured. Furthermore, rockfalls were generated in the Triassic limestone, which is generally hard, with fragmented rock mass.

Annual average rainfall in Lushan County, Baoxing County and Tianquan County are 1,313.1 mm, 1,101.5 mm and 1,663 mm, respectively. In Lushan County, the maximum recorded daily and hourly rainfall intensity in 1978 was 188 mm and 86 mm, respectively. Rainy season starts in May and ends in October. On the average, 91 % of the annual precipitation falls during this period. Therefore,

Table 1 Comparison of landslides in various counties before and after the earthquake

Region	Lushan County		
Types	Rock slide	Rock fall	Debris flow
Before the earthquake	87	15	5
After the earthquake	86	186	0
Region	Baoxing County		
Types	Rock slide	Rock fall	Debris flow
Before the earthquake	11	52	35
After the earthquake	52	108	0
Region	Tianquan County		
Types	Rock slide	Rock fall	Debris flow
Before the earthquake	60	10	5
After the earthquake	46	60	1

during the rainy season, high rainfall following the Lushan earthquake will probably increase the landslide occurrences and consequent threat to lives and property.

Major Characteristics of the Landslides

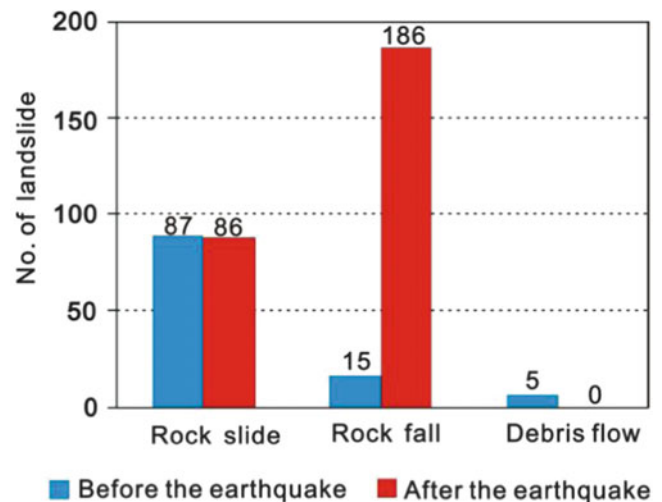
The Number of Landslides

The study area is tectonically active, and earthquakes frequently occur. The region was also affected by the 12th May 2008 Ms = 8.0 Wenchuan earthquake, and evidence suggested that 139 landslides occurred in three years after the earthquake. For the 20th April 2013 Ms = 7.0 Lushan earthquake, the strong ground motion, combined with steep and rugged topography, and soft and erodible lithologic substrate, caused 539 landslides in the study area (6,787 km²). According to the reports of CENC (China Earthquake Networks Center), the seismic intensity of the epicenter reached 9°.

The number of landslides in the study area has been examined as shown in Table 1. For example, before the earthquake, there were about 107 landslides in nine towns in Lushan County. However, except for the debris flow, the amount of rockslides and rockfalls increased after the earthquake. From statistical data, about 272 new landslides, including 86 rockslides and 186 rockfalls have been triggered by the earthquake (Fig. 3). Moreover, the number of landslides in Baoxing County and Tianquan County also increased to 160 and 107, respectively, after the earthquake. The statistical analysis above indicates that the number of new rockfalls triggered by the earthquake reached 354 in the three Counties, accounting for about two-third of the total landslides.

The Type of Landslides

The landslides triggered by the Lushan earthquake can be classified into three categories: (a) Rockslide; (b) rockfall;

**Fig. 3** Comparison of mountain disaster in Lushan County before and after the earthquake

and (c) debris flow. Although the major characteristics of landslides were similar to those observed by authors in 2008 Wenchuan earthquake in the mountainous regions of southwest China, the scale of landslides in the study area is much smaller because of lesser earthquake magnitude (Ms = 7.0).

Rockslide

Field investigations indicated that most of the rockslides triggered by the earthquake were small and medium-scaled. These small and medium-scaled ones, which generally ranged in volume from several cubic meters to a few tens of thousand cubic meters, were surface landslides and shallow landslides, mainly developed in weathered and steep rock slopes (including natural slopes and cut slopes). Figure 4 shows that two small-scale landslides occurred in the period of 20 April 2013, in the epicentral region of Lushan County. Although these small-to-medium landslides were small in size, they endangered roads and cars. As shown in Fig. 5, along the regional road S210 in Baoxing County, more than two small-scale rockslides were identified by means of aerial photographs.

In contrast, large-scale rockslide triggered by the earthquake is very rare; for instance, there is only one large-scale rockslide (> 10⁶ m³) in each of the three Counties. As shown in Fig. 6, the Sanlongshan rockslide (located in Taiping Town) is the only large-scale one in all the landslides in Lushan County. More importantly, the Sanlongshan landslide poses a continuing hazard from remobilization and flow during intense, prolonged rainfall.

Rockfall

According to Vernes (1978), a rockfall is a fragment of rock (a block) detached by sliding, toppling, or falling, that falls

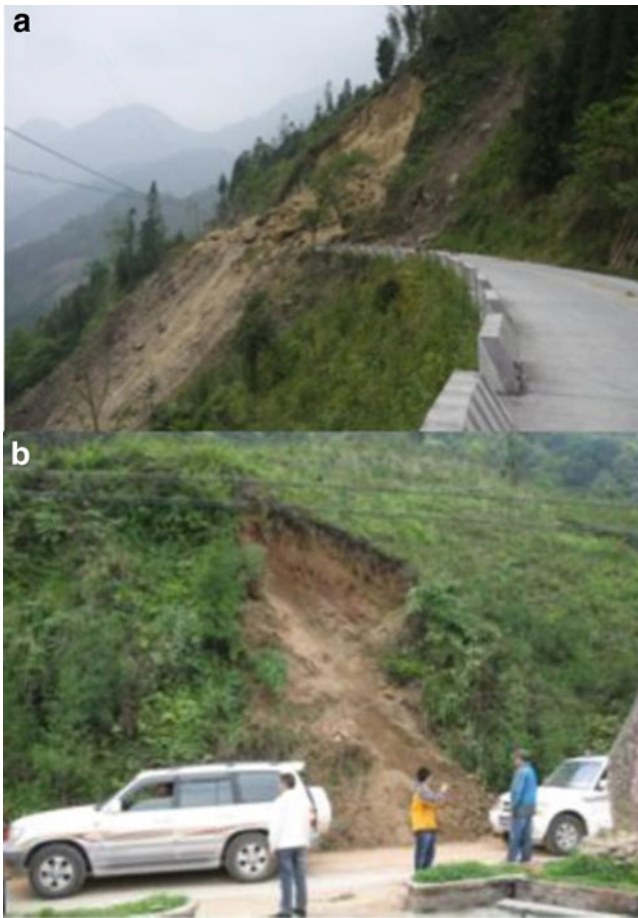


Fig. 4 Shallow or surface landslides triggered by Lushan earthquake. (a) Located at Dachuan Town, the landslide blocked the road. (b) A landslide on the road from Shuangshi to Taiping Town in the epicentral region of Lushan County



Fig. 5 Less than 300 m, more than two landslides have been found along the regional road S210 in Baoxing County

along a vertical or subvertical cliff, and proceeds downslope by bouncing and flying along parabolic trajectories or by rolling on talus of debris slopes. Earthquake-induced rockfalls are different from the one induced by rainfall or

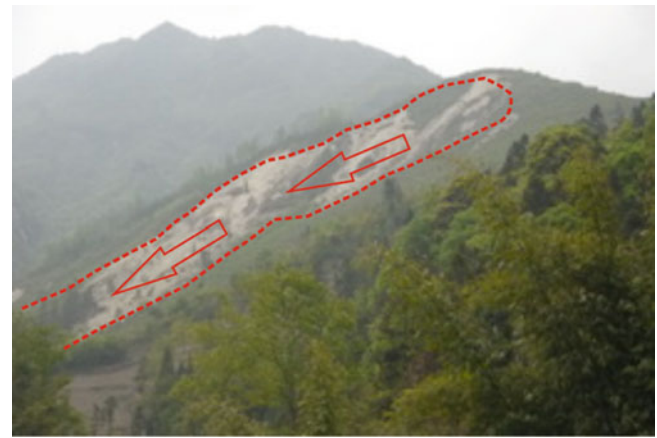


Fig. 6 The Sanlongshan large scale landslide, located at the Taiping Town of Lushan County

weathering because they maybe the result of strong inertia force from movement of the causative faults in the epicentral region.

Among many landslides found in the study area (epicentral region), rockfalls were in the majority. Statistics indicated that these rockfalls triggered by the earthquake ranged in volume from a few dm^3 to $10,000 \text{ m}^3$. In spite of its small size, the rockfalls caused considerable damage and disruption of roadways and also damaged properties below the slopes. Figure 7 shows several examples of rockfall, which blocked the regional road of Lushan County. Along the road from Linguan Town to Shuangshi Town, we estimated to be 2–3 rockfalls per 100 m with volume range from several cubic meters to hundreds of cubic meters.

Figure 8a shows a boulder-sized hole on a protective net at a local sports center at the time of the earthquake. The rockfall involving a volume of about $2.7 \times 10^3 \text{ m}^3$ was located at $\text{N}30.304^\circ$ and $\text{E}103.042^\circ$ in Baosheng Town of Lushan County. As shown in Fig. 8b, a boulder fell into a building in Baoxing County. The rockfall, located at $\text{N}30.378^\circ$ and $\text{E}103.814^\circ$, is composed of granite, dolomite and limestone. The volume of the rockfall was estimated to be about $6 \times 10^3 \text{ m}^3$. Figure 8c, d (photographed in Fentou Village, Baosheng Town, Lushan County), also provided some scenes of building damages caused by boulders at that time.

Debris Flow

Because of a relatively small earthquake magnitude (seismic acceleration $< 0.5 \text{ g}$), only one debris-rock flow was found at the Damiao Village of Laochang Town in Tiquan County. The Damiao debris-rock flow was located at $\text{N}31.150^\circ$ and $\text{E}102.767^\circ$ in a tributary of the Laochang River. The debris-rock flow is composed of sandstone, siltstone and conglomerate (J_3). Field investigations showed that a rock avalanche (Fig. 9a), located at Dabengshan, at an elevation of 1,490 m, was



Fig. 7 Individual boulder falls and rockfall deposits blocking regional road in Lushan County

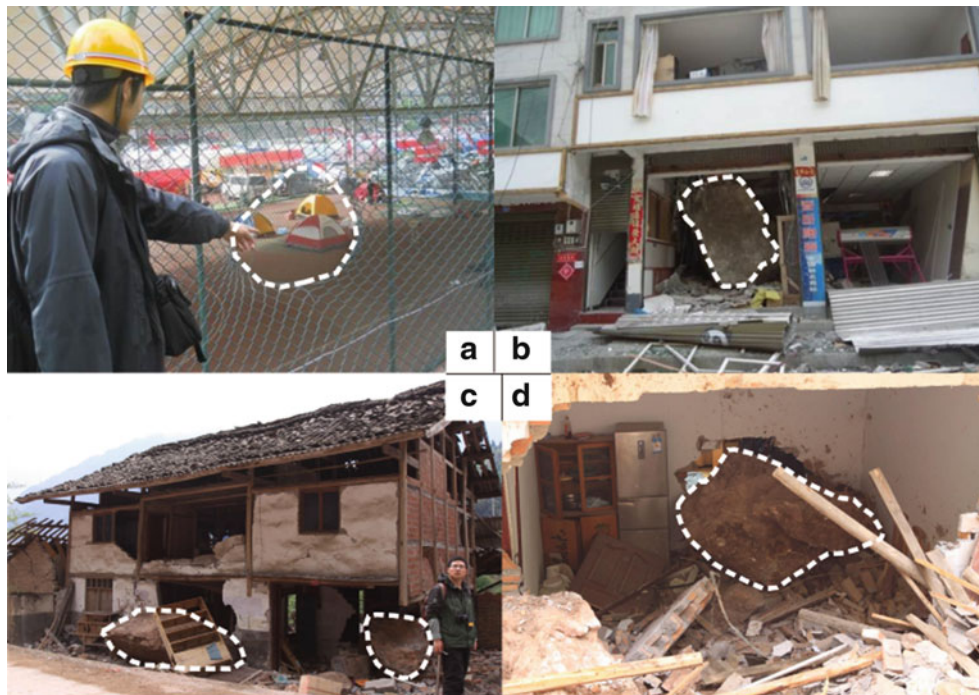


Fig. 8 Damage caused by rockfalls in Lushan earthquake zone. (a) A block broke through a protecting net; (b)–(d) several boulders rushed into buildings

triggered at the time of the earthquake. Then masses of rock fragments moved down the slope, and were divided into two debris-rock flows (Fig. 9b, c) when obstructed by the

hill. The two debris-rock flows finally converged at the lower reaches of the valley, at an elevation of 1,021 m and formed a small-scale dammed with a barrier lake

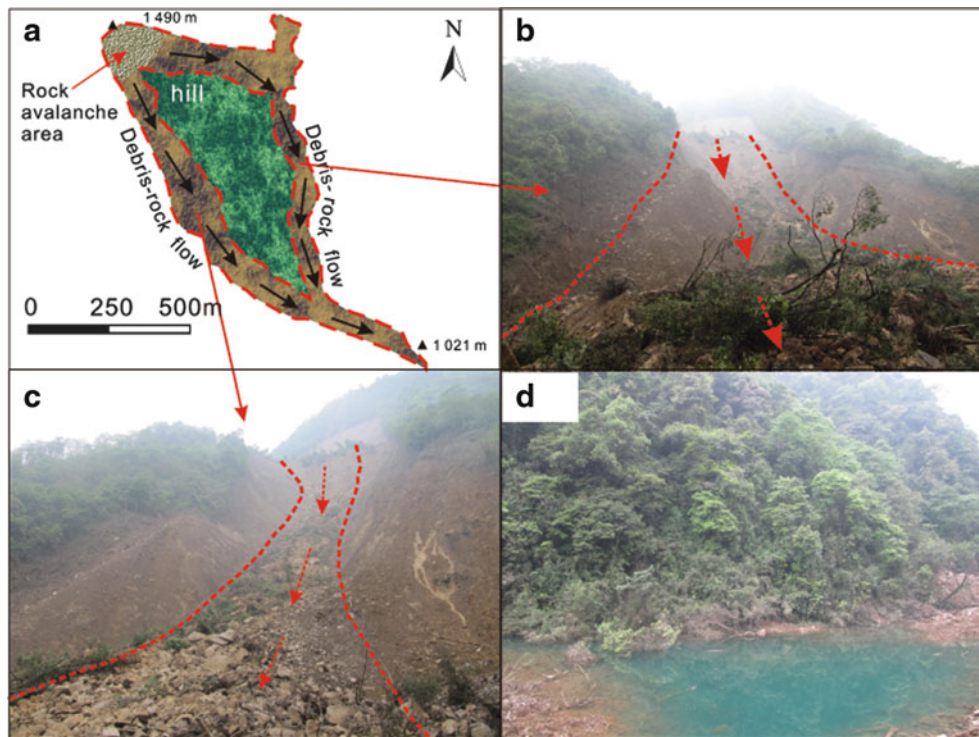


Fig. 9 A debris-rock flow triggered by the earthquake in Tianquan County. (a) The planar shape of the debris-rock flow; (b) the east debris-scoured groove; (c) the west debris-scoured groove; and (d) the small scale debris dammed-lake

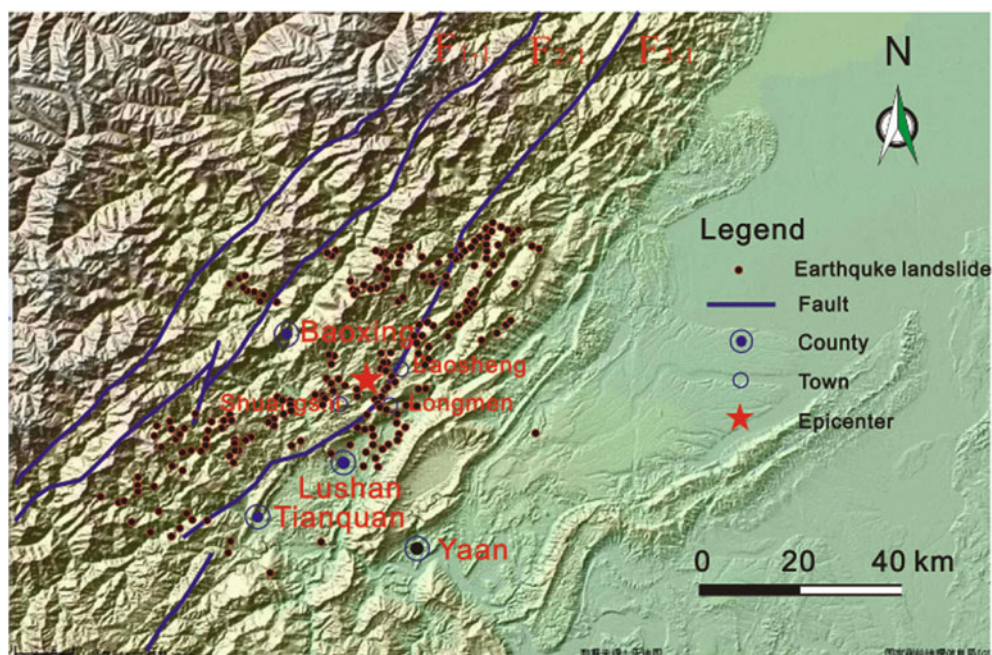


Fig. 10 Distribution of earthquake-triggered landslides on the remote sensing image

(Fig. 9d), which recorded 1 fatality. The rock avalanche had an estimated volume of about $218 \times 10^4 \text{ m}^3$. Measurements showed that the vertical drop of debris from the head scarp to the distal deposits is 369 m, and

the maximum horizontal runout distance of debris is 1,220 m. It is noted that the heavy rainfall following the Lushan earthquake will probably increase the debris flow occurrences on areas inhabited by people.

Table 2 Statistics of landslides in different towns of Lushan County

Town	Distance to the epicentre (km)	Area (km ²)	Rockslide	Rock fall
Baosheng	3.8	120	6	43
Taiping	4.2	86	39	54
Longmen	5.6	54	4	14
Shuangshi	9.4	80	2	13
Qingren	12.2	67	7	5
Luyang	17.8	5	2	7
Siyan	20.8	24	5	13
Dachuan	24.8	690	17	33
Feixianguan	32	16	4	4

Distributions of Landslide

Although the occurrence of landslide in an earthquake area is a function of various natural and human factors, such as topography, lithology and cut slope, distance from the earthquake source or distance from the causative fault should not be ignored. Qi et al. (2010) stated that the distribution of earthquake-triggered landslides generally decreases with increasing distance to the causative fault, and an obvious increase in landslide incidence occurred locally in the adjacent active faults zone. Dai et al. (2011) also proved that most of the landslides occurred along the major causative fault, and were concentrated on the hanging wall of the fault.

Figure 10 shows that the landslides were distributed primarily along the causative faults of Shuangshi Fault (F₃₋₁). Moreover, it can be seen from Fig. 10 that the number of landslides decreased with increase in distance to the causative fault F₃₋₁, and most of the landslides occurred within the buffer zone of 20 km distance to the causative fault.

In order to clarify the relationship between the landslide and the distance from earthquake source, the authors counted the number of landslides triggered by the earthquake for nine towns (Baosheng, Taiping, Longmen, Shuangshi, Qingren, Luyang, Siyan, Dachuan and Feixianguan) in Lushan County. The results (Table 2) showed that the towns closer to the epicenter such as Baosheng, Taiping, Longmen and Shuangshi, have more landslides, accounting for about 64.3 % of the total landslides in Lushan County. Furthermore, we noticed that distance to the earthquake source for the four towns mentioned above were less than 20 km. The regularity observed in this study is consistent with conclusions of reference, i.e. Keefer (2002), Khazai and Sitar (2003), Xu et al. (2013).

Conclusions

Based on the landslide database collated from Lushan, Baoxing and Tianquan, by means of field investigations, the causes and major characteristics of landslides triggered by the 4.20 Lushan earthquake are presented as follows:

1. The strong ground motion, combined with the steep and rugged topography and the soft and erodible lithologic substrate, caused 539 new landslides in the study area. Among them, the number of rockfall accounts for about two-third of the total landslides.
2. Because of lesser earthquake magnitude (Ms = 7.0), some small and medium-scale landslides ranging from several cubic meters to a few tens of thousand cubic meters are in the majority.
3. The landslides triggered by the earthquake are distributed primarily along the causative faults of Shuangshi Fault (F₃₋₁), which is a Longmenshan front range fault.
4. The number of earthquake landslides is decreasing with increase in distance to the causative fault F₃₋₁, and most of the landslides occurred within the buffer zone of 20 km distance to the causative fault.

Acknowledgments This work was funded by the China Geological Survey and the Key Laboratory of Geo-hazards in the Loess Area. The authors would like to thank Yibi Zhao, Tianyu Liu, Jiangbing Guan, Haokun Qin, Ning Zhang, Wei Yao, Zhixu Wang, Jie Gao, Jianping Zhou, Jianzhong Ma, Bo Zhang and Jidong Guo for their field work in Lushan County, Baoxing County and Tianquan County shortly after the earthquake.

References

- Chigira M, Yagi H (2006) Geological and geomorphological characteristics of landslides triggered by the 2004 Mid Niigata prefecture earthquake in Japan. *Eng Geol* 82:202–221
- Dai FC, Xu C, Yao X, Xu L, Tu XB, Gong QM (2011) Spatial distribution of landslides triggered by the 2008 Ms 8.0 Wenchuan earthquake, China. *J Asian Earth Sci* 40:883–895
- Huang R, Li W (2009) Analysis of the geo-hazards triggered by the 12 May 2008 Wenchuan Earthquake, China. *Bull Eng Geol Environ* 68:363–371
- Keefer DK (2002) Investigating landslides caused by earthquakes—a historical review. *Surv Geophys* 23:473–510
- Khazai B, Sitar N (2003) Evaluation of factors controlling earthquake-induced landslides caused by Chi-Chi earthquake and comparison with the Northridge and Loma Prieta events. *Eng Geol* 71:79–95
- Lan HX, Zhou CH, Gao X, Cheng WM, Wang ZH, Yang ZH, Li LP, Wu YM (2013) Secondary geological hazard assessment and hazard

- mitigation countermeasures in Lushan, Ya'an Earthquake, Sichuan Province. *Progr Geogr* 32(4):499–504 (in Chinese)
- Liu CL, Zheng Y, Ge C, Xiong X, Hsu HT (2013) Rupture process of the Ms 7.0 Lushan earthquake, 2013. *Sci Chin Earth Sci*. doi: [10.1007/s11430-013-4639-9](https://doi.org/10.1007/s11430-013-4639-9)
- Qi SW, Xu Q, Lan HX, Zhang B, Liu JY (2010) Spatial distribution analysis of landslides triggered by 2008.5.12 Wenchuan earthquake, China. *Eng Geol* 116:95–108
- Qi SW, Xu Q, Zhang B, Zhou YD, Lan HX, Li LH (2011) Source characteristics of long runout rock avalanches triggered by the 2008 Wenchuan earthquake, China. *J Asian Earth Sci* 40:896–906
- Vernes DJ (1978) Slope movements: types and processes. In Schuster RL, Krizek RJ (eds) *Landslide analysis and control*, Special Report 176. Transportation Research Board, Washington, DC, pp 11–33
- Wang HB, Sassa K, Xu WY (2007) Analysis of a spatial distribution of landslides triggered by the 2004 Chuetsu earthquakes of Niigata Prefecture, Japan. *Nat Hazards* 41:43–60
- Wu FQ, Fu BH, Li X, Liu JY (2008) Initial analysis of the mechanism of the Wenchuan earthquake (southwest China), 12 May 2008. *Bull Eng Geol Environ* 67:453–455
- Xie ZJ, Jin BK, Zheng Y, Ge C, Xiong X, Xiong C, Hsu HT (2013) Source parameters inversion of the 2013 Lushan earthquake by combining teleseismic waveforms and local seismograms. *Sci China Earth Sci* 7:1–6
- Xu C, Xu XW, Yao X, Dai FC (2013) Three (nearly) complete inventories of landslides triggered by the May 12, 2008 Wenchuan Mw 7.9 earthquake of China and their spatial distribution statistical analysis. *Landslides* doi:[10.1007/s10346-013-0404-6](https://doi.org/10.1007/s10346-013-0404-6)
- Yang J, Chen JH, Liu HL, Zhang K, Ren W, Zheng JC (2013) The Chinese national emergency medical rescue team response to the Sichuan Lushan earthquake. *Nat Hazards* 69:2263–2268.
- Yin Y, Wang F, Sun P (2009) Landslide hazards triggered by the 2008 Wenchuan earthquake, Sichuan, China. *Landslides* 6:139–151



Characteristics of Ground Acceleration and Features of Landslides Triggered by the Lushan Earthquake (China)

W.P. Wang, Y.P. Yin, B. Li, Z. Feng, N. Zhang, and Y. Gao

Abstract

The 2013 Lushan earthquake ($M_s = 7.0$; epicentre located at 30.3°N , 103.0°E), with a focal depth of 13.0 km was triggered by the reactivation of the Longmenshan fault in Lushan County, Sichuan Province, China on 20 April 2013. Although Lushan M_s 7.0 earthquake occurred on the same Longmenshan thrust belt as Wenchuan M_s 8.0 earthquake, they have very different characteristics of ground acceleration and features of landslides. Based on acceleration waveform data provided by national strong motion network center, a preliminary study was made on the main shock acceleration characteristics, especially vertical and horizontal acceleration ratio V_a/H_a with epicentral distance, which indicated that V_a/H_a ratio ranged only from 0.4 to 0.7, significantly less than the near-field earthquakes with the same magnitude. Meanwhile, it also showed that the vertical seismic force was less than the horizontal seismic force. FLAC 6.0 FDM software was used to analyse the progressive damage difference of numerical models of Donghekou rock landslide affected by the Lushan and Wenchuan earthquakes, respectively. Finally, acceleration data of ground motion observation in Lengzhuguan slope suffering from seismic waves of Lushan earthquake indicated that there was symmetrical relationship between predominant frequency and acceleration amplification curves.

Keywords

Lushan M_s 7.0 • Ground acceleration • Features of landslides • V_a/H_a • Site effects • Numerical modelling

W.P. Wang (✉) • Y.P. Yin • N. Zhang
China Institute of Geological Environment Monitoring, No. 20 Dahuisi Street, Haidian District, Beijing 100081, China
e-mail: wangwenpei1985@163.com

B. Li • Z. Feng
Institute of Geomechanics, Chinese Academy of Geological Sciences, 11#, Min Zu Da Xue Nan Lu, Haidian District, Beijing 100081, China

Y. Gao
China Institute of Geological Environment Monitoring, No. 20 Dahuisi Street, Haidian District, Beijing 100081, China

Institute of Geomechanics, Chinese Academy of Geological Sciences, 11#, Min Zu Da Xue Nan Lu, Haidian District, Beijing 100081, China

Introduction

On 20 April 2013, the Lushan earthquake ($M_s = 7.0$; epicentre located at 30.3°N , 103.0°E) occurred in the southwest of Longmenshan tectonic zone in Sichuan Province, China, about 85 km distance from Wenchuan earthquake ($M_s = 8.0$; epicentre located at 31.0°N , 103.4°E), as in Fig. 1. No obvious continuous ruptures were found on the surface, which showed the causative fault can be thought as buried fault near Longmenshan Frontier Fault (Xu et al. 2012).

Due to dense vegetation cover, potential geological disasters were difficult to be found. It can be inferred that many unstable slopes cracked without having collapsed, or loosed without having slipped, as well as unstable rocks hanged without having fallen off. According to geohazard

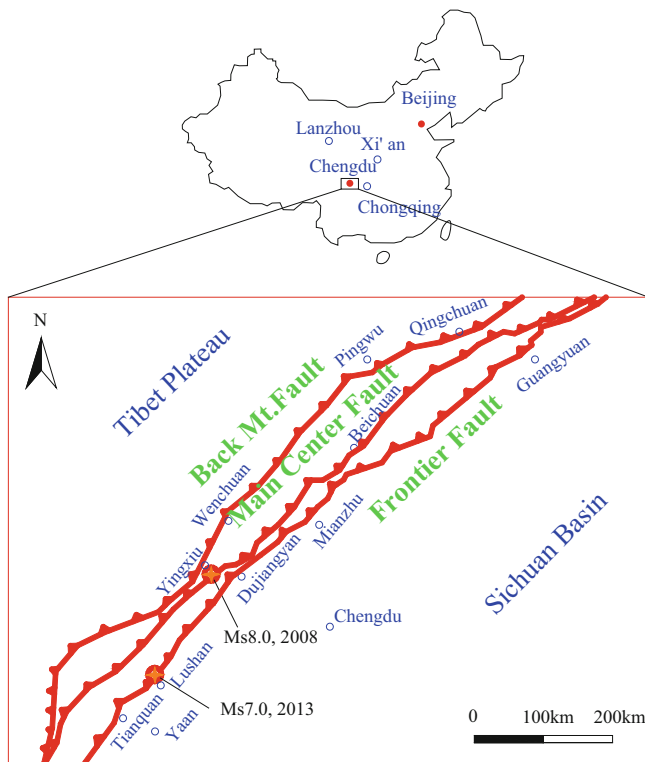


Fig. 1 Location map of the 2008 Wenchuan earthquake and 2013 Lushan earthquake. The red lines are the Back Mt. Fault, the Main center fault and Frontier fault (Yin et al. 2009)

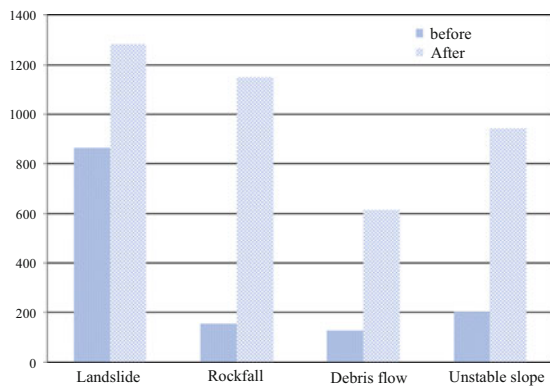


Fig. 2 Comparative histograms of geohazards in the counties affected by the Lushan earthquake before and after the earthquake

investigation before the Lushan earthquake, there were about 1,350 potential geohazard sites in the 36 affected counties (cities) of Sichuan Province. The potential geohazard sites include 866 landslides, 154 rockfalls, 128 debris flows, and 202 unstable slopes. After the earthquake, over 400 landslide experts from the Ministry of Land and Resources of China conducted systematical investigation in the disaster areas using aerial and remote sensing images. The investigations indicate that there were about 3,993 potential geohazard sites in Sichuan Province. The potential



Fig. 3 Vertical air photo of earthquake-triggered geohazards in Baoxing (According to <http://www.scgis.net/>)

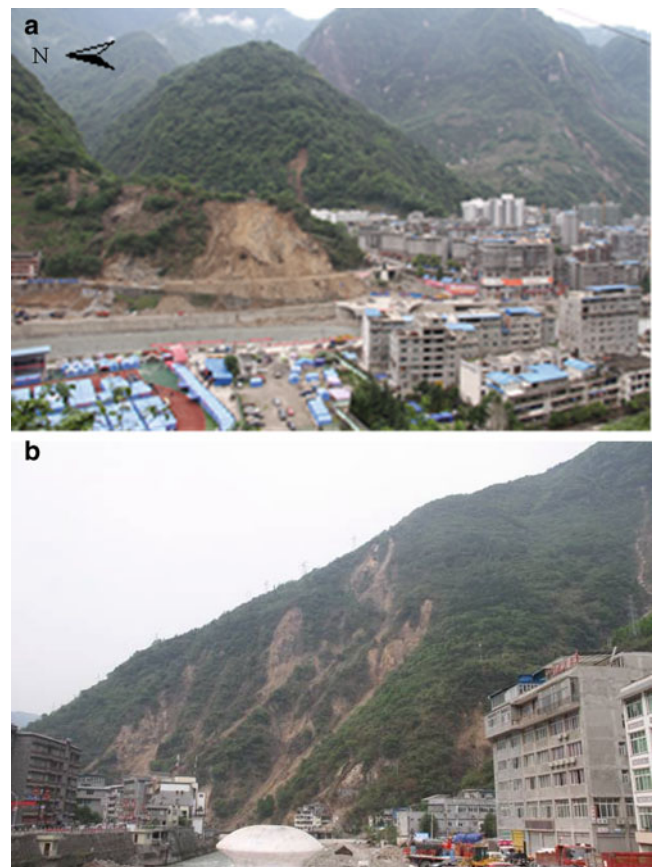


Fig. 4 Earthquake-triggered shallow landslides in Baoxing

geohazard sites include 1,285 landslides (shallow), 1,150 rockfalls, 945 debris flows, and 613 unstable slopes.

Above all, the potential geohazard sites increased by 196 %, among which rockfall incidence increased by 647 %. The rockfall incidence is substantially more when compared to other geohazards. The potential unstable slopes, debris flows, and landslides increased by 203 %, 638 %, and 48 %, respectively (Fig. 2).



Fig. 5 Lenmugou Debris in Baoxing



Fig. 6 Houses destroyed by rock falls in Baoxing

Differed from the Wenchuan earthquake-affected area, landslides, rockfalls, and debris flows were not that big in Lushan earthquake-affected area.

Baoxing town is one of the areas that recorded the highest geohazards from this earthquake (Figs. 3, 4 and 5). It is located in a valley terrace of the Baoxing River. Among the geohazards triggered by the Lushan earthquake, the Lengmugou debris, which is located at the east side of Baoxing town, is aggravated by this earthquake. After the earthquake, the amount of solid source in Lengmugou increased from 2,800,000 m³ to 3,800,000 m³. Fortunately, the emergency project has been fully completed now.

Meantime, a lot of rocks that fell from the slopes caused numerous casualties (Fig. 6).

Characteristics of Ground Acceleration

From 276 acceleration record data including EW, NS and UD directions of China strong ground motion centre, which was collected from seismic stations in Sichuan, Yunnan,

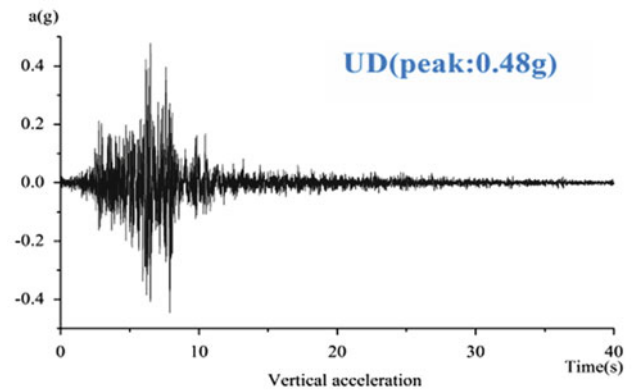
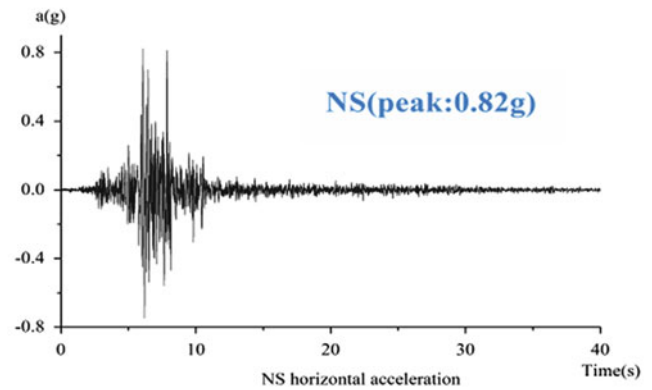
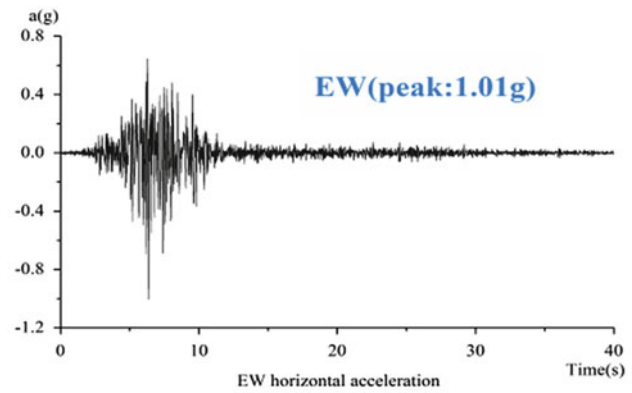


Fig. 7 Acceleration record data of the Lushan Ms 7.0 earthquake at Baoxingdiban Seismic Station, Sichuan

Gansu, Shanxi provinces, the maximum acceleration record data is found in Baoxing-diban seismic station, of which peak acceleration is 101 gal in EW direction, 82 gal in NS direction and 48 gal in UD direction. The main ground motion lasted up to 40 s (Fig. 7).

The ratio of vertical acceleration (Va) and horizontal acceleration (Ha) from the Lushan earthquake is compared with Collier and Elnashi's previous curve (Collier and Elnashai 2001) and Yin's Wenchuan earthquake curve in Fig. 8. It appears that the ratio ranges from 0.4 to 0.7, much less than Wenchuan Ms 8.0's ratio, even less than Ms 6.5's ratio. The ratio drops to about 0.55 at the distance of 30 km

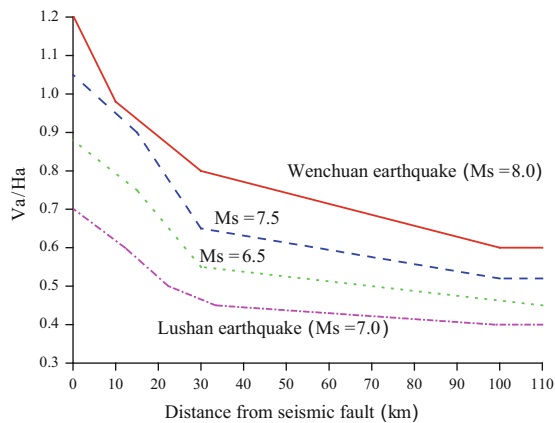


Fig. 8 Comparison of ratio between vertical and horizontal acceleration from the Lushan Ms 7.0 Earthquake with the Coller's curve (modified from Yin 2010)

from the earthquake fault. The vertical acceleration is not large enough to trigger landslides.

As Lushan earthquake is hidden in deep rapture, the seismic source direct influence is reducing, when site effect and propagation path is more important, which is quite different from typical near-fault strong seismic motion, like Wenchuan earthquake.

Features of Landslides

As known, the Wenchuan earthquake has huge seismic forces produced by fault movement, especially the vertical seismic force (Yin et al. 2009), as well as internal dynamic deformation that caused deep-seated landslides. These landslides could move fast and far under big seismic forces.

However, in Lushan earthquake-affected area, huge seismic forces produced by fault movement are not the obvious cause to trigger landslides. Site effects could play a role to trigger landslides that cannot be neglected.

Small shallow slides and rock falls can be seen everywhere in Lushan earthquake-affected area, most of which belong to progressive failure because of shaking, when earthquake-induced damages can further increase the amplification of seismic forces along the slop surface, which could cause more small shallow landslides.

The Case Study

In order to compare the seismic trigger differences of landslides in Lushan earthquake and Wenchuan earthquake, a stress–strain 2D numerical modelling was carried out using FLAC 6.0 (Itasca 2005) FDM software in dynamic

configuration to analyse the 2008 Donghekou rock landslides. It can be seen in Fig. 9.

The Donghekou rock landslides numerical model and material properties chosen can be referred to Sun as well as material damping and boundary conditions. The seismic waves for Lushan earthquake were EW and UD acceleration records on 20 April 2013 in Baoxing-diban seismic station of 40 s while the ones for Wenchuan earthquake were EW and UD acceleration records on 12 May 2008 in Qingping seismic station of first strong seismic sequence for 40 s (Yin et al. 2012).

During the dynamic modelling, where a plasticity state is reached within the model, both strength and stiffness parameters were modified, according to an elastic-perfectly plastic behaviour (Eberhardt et al. 2004; Francesca et al. 2011), by instantaneously zeroing cohesion and reducing the dynamic shear modulus (G) down to the value of the landslide mass.

The results obtained from numerical analysis can be summarised as follows (Fig. 10):

1. Dynamic damage processes of Donghekou rock landslides are nearly same when suffering from Lushan earthquake and Wenchuan earthquake. Damages appear initially along the shallow surface of the slope and then progressively develop internally.
2. Damage process of Donghekou rock landslides suffering from Lushan earthquake stays stable after 20 s, and does not cut through the whole slip surface while the one suffering Wenchuan earthquake cut through the whole slip surface.
3. Wenchuan earthquake firstly forms continuous surface along the back part of the slip surface, then the front part and finally the whole slip surface.
4. Lushan earthquake is easier to cause shallow landslides while Wenchuan earthquake is easier to from deep-seated and entire landslides.

Site Effects

Lengzhuguan slope is located in the southwest of Lushan (Fig. 11), at the distance of nearly 90 km from the Lushan epicentre (Luo et al. 2013). The bedrock is granite.

With the consideration of aftershock activity is more frequent along the Longmenshan fault zone after the Wenchuan Ms 8.0 earthquake, ground motion observation has been implemented in Lengzhuguan slope from top to bottom so as to study the ground vibration characteristics. Fortunately, it also captured the signals produced by Lushan Ms 7.0 earthquake.

The original seismic wave forms can be referred to Luo et al. (2013). The acceleration amplification (the measured

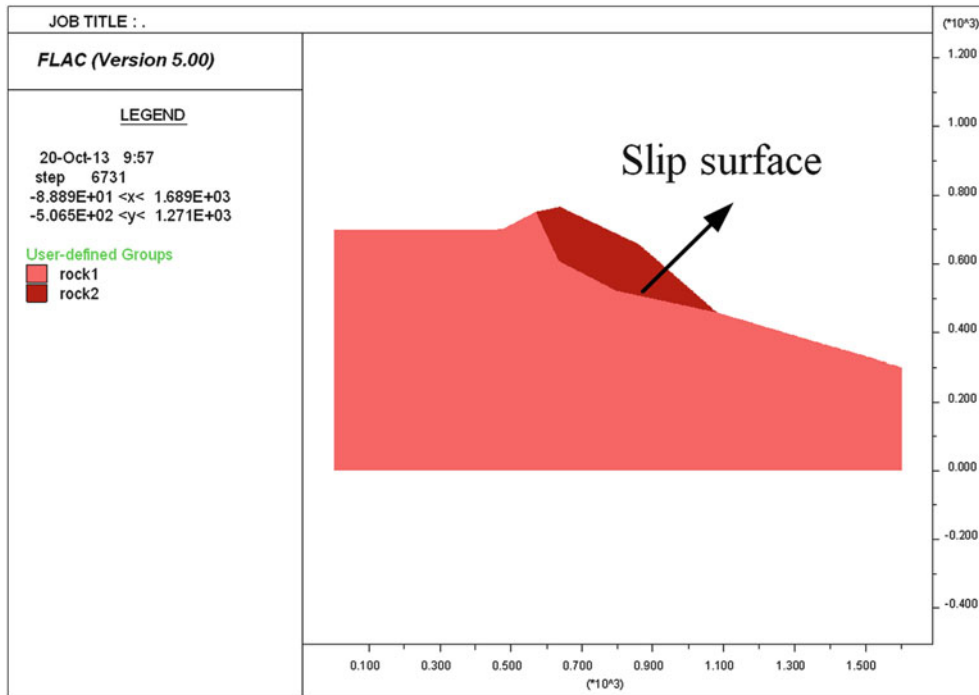


Fig. 9 Section of the diagrammatic sketch and simulation model of the Donghekou rock landslide (Sun et al. 2008)

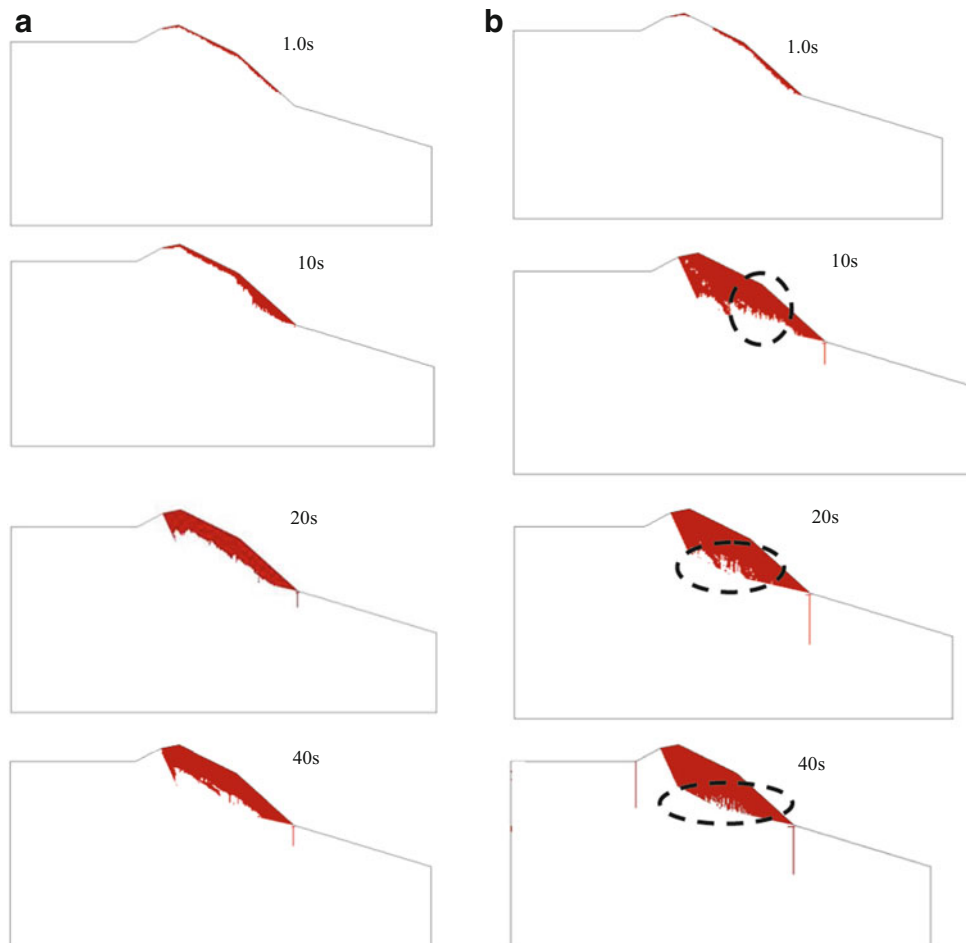


Fig. 10 Rupture model derived from the dynamic numerical modelling by FLAC 6.0. (a) Suffering from Lushan earthquake; (b) suffering from Wenchuan earthquake

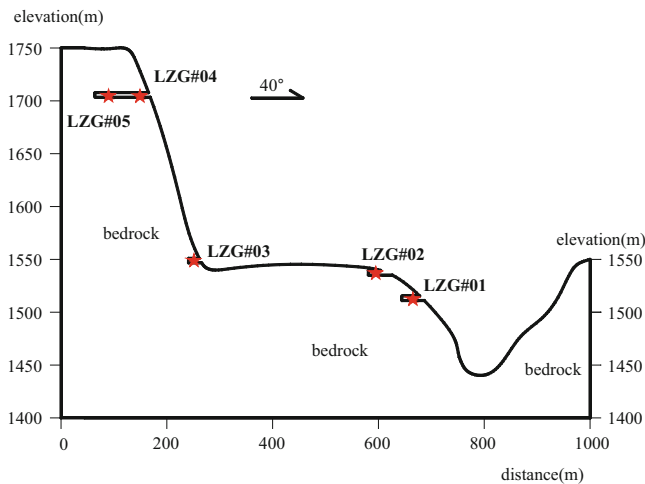


Fig. 11 Section map showing the slope of Lengzhuguan and the monitoring location of ground motion records with four different elevations at Lengzhuguan (Luo et al. 2013)

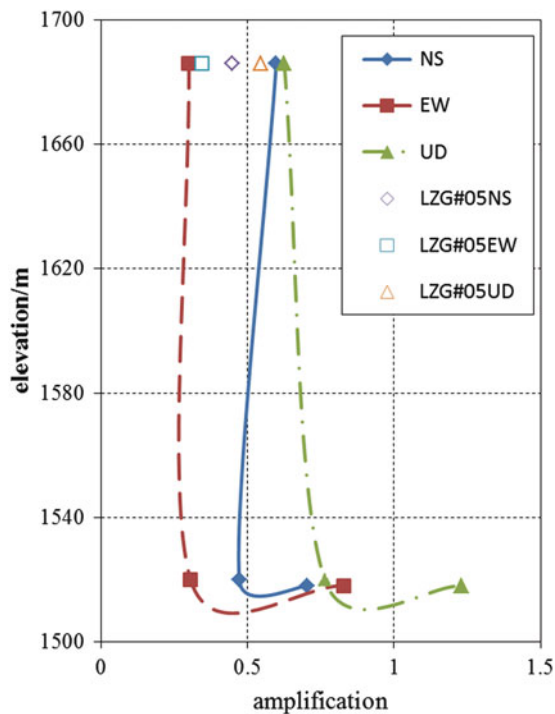


Fig. 12 The acceleration amplification (EW, NS and UD) distribution curves with different elevations; The acceleration amplification can be calculated through the measured peak acceleration of each point against the peak acceleration of LZG#01, except LZG#01 itself. LZG#05 data is shown in form of *single points* as it has the same elevation as LZG#04

peak acceleration of each point divided by peak acceleration of LZG#01) can be shown as follows:

Besides acceleration amplification, predominant frequency is also an important dynamic feature of slope. Without a reference station on nearby stable ground, site-to-

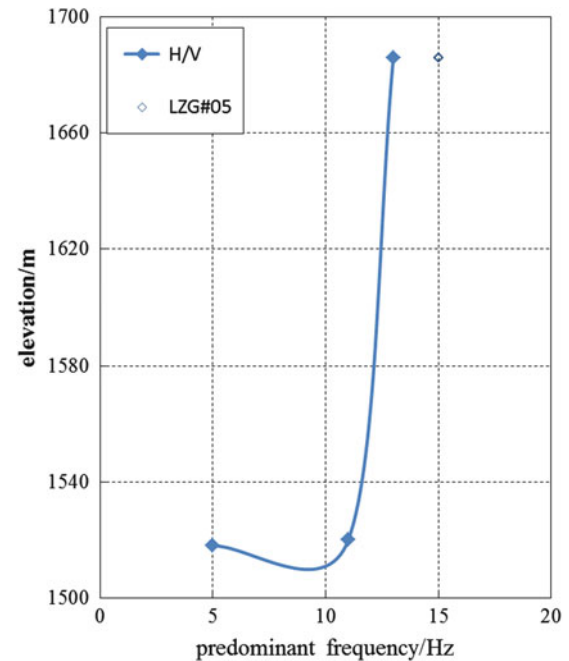


Fig. 13 The predominant frequency distribution curve with different elevations; predominant frequency of EW/UD spectral ratio is almost same as the one of NS/UD; LZG#05 data is shown in form of *single points* as it has the same elevation as LZG#04

reference spectral ratio (SRSR) method is not suitable to quantify site effects. Hence horizontal-to-vertical spectral ratio (HVSr) method with non-reference is much appreciated here.

The results obtained from numerical analysis can be (Figs. 12 and 13) can be summarised as follows:

1. The acceleration amplification of LZG#02, 03, 04 and 05 is smaller than LZG#01, except the vertical acceleration amplification of LZG#01. It shows that the elevation is not the cause of amplification here. Topographic effects play an important role in amplification, especially steep slope and then gentle slope from high to low.
2. Through comparing Figs. 12 with 13, it appears that the predominant frequency curve is symmetrical to amplification, which means in the high steep part of Lengzhuguan slope, the amplification is small and the predominant frequency is big while in the low gentle part, the amplification is big and the predominant frequency is small.
3. The result differences between LZG#04 and LZG#05 are not so big, which represents the inside and outside of the same region.

Conclusions

The 2013 Lushan earthquake-induced geohazards are mainly rock falls and shallow landslides, which are not severer than 2008 Wenchuan earthquake along the same

Longmenshan tectonic zone because of the low earthquake magnitude and hidden in deep rupture. However, the Lushan earthquake has also caused heavy casualties and serious economic losses as well as different characteristics of ground motion and features of landslides.

Based on acceleration record data of China strong ground motion centre, the ratio of vertical acceleration (V_a) and horizontal acceleration (H_a) from the Lushan earthquake is quite small, which means that the seismic source direct influence is reducing, when site effect and propagation path is more important.

Based on elastic-perfectly plastic behaviour, stress-strain numerical models of Lushan earthquake and Wenchuan earthquake are built using FLAC 6.0 software, which has shows that Lushan earthquake is easier to cause shallow landslides while Wenchuan earthquake is easier to from deep-seated and large-scale landslides.

According to ground motion observation in Lengzhuguan slope suffering from seismic waves of Lushan earthquake, the predominant frequency curve is symmetrical to acceleration amplification and topographic effects have played an important role in site effects.

Acknowledgments The research leading to this article was funded by the National Key Technology R&D Program of the Ministry of Science and Technology during the 12th Five-year Plan Period in China (2012BAK10B01). The authors wish to thank China Strong Ground Motion Centre for acceleration record data, Sun Ping for information on the 2008 Donghekou rock landslide event triggered by the Wenchuan

earthquake and Luo Yonghong for information on ground motion observation data of 2012 Lengzhuguan slope. We are also indebted to China Geological Survey Bureau for valuable chance after Lushan earthquake.

References

- Collier CJ, Elnashai AS (2001) A procedure for combining vertical and horizontal seismic action effects. *J Earthq Eng* 5(4):521–539
- Eberhardt E, Stead D, Coggan JS (2004) Numerical analysis of initiation and progressive failure in natural rock slope: the 1991 Randa rockslide. *Int J Rock Mech Min Sci* 41:69–87
- Francesca B, Luca L et al (2011) Earthquake triggering of landslides in highly jointed rock masses: reconstruction of the 1783 Scilla rock avalanche (Italy). *Geomorphology* 129:294–308
- Itasca Consulting Group Inc (2005) FLAC (fast Lagrange analysis of continua) slope user's guide (Version 5.0). Minneapolis, Minnesota
- Luo YH, Wang YS, He Y et al (2013) Monitor result analysis of Lengzhuguan slope ground shock response of Lushan earthquake of Sichuan, China. *J Chengdu Univ Technol* 40(3):232–241
- Sun P, Yin YP, Wu SR et al (2008) Does vertical seismic force play an important role for the failure mechanism of rock avalanches? A case study of rock avalanches triggered by the Wenchuan Ms8.0 Earthquake of May 12, Sichuan, China. *Environ Earth Sci* 66 (5):1285–1293
- Xu XW, Chen GH, Yu GH (2012) Seismic structure of the Lushan earthquake and its relationship with the Wenchuan earthquake. *Chin J Earth Sci Front* 20:1–10
- Yin YP (2010) Catastrophic landslides associated with the M8.0 Wenchuan Ms8.0 Earthquake. *Bull Eng Geol Environ* 70(1):15–32
- Yin YP, Wang FW, Sun P (2009) Landslide hazards triggered by the 2008 Wenchuan Ms8.0 Earthquake, Sichuan, China. *Landslides* 6 (2):139–152
- Yin YP, Wang M, Sun P (2012) Dynamic response characteristics of Daguangbao landslide triggered by Wenchuan earthquake. *Chin J Rock Mech Eng* 31(10):1969–1982



Characteristics of Deep-Seated Landslides Induced by Different Type Earthquakes in Inland Japan

Baator Has, Toko Takayama, Kiichiro Ogawa, and Satoshi Onoda

Abstract

Recent years, a series of strong earthquakes struck inland Japan and triggered a large number of deep-seated landslides, caused serious damage to the focal area of those earthquakes. In this paper, to clarify the characteristics of the landslides induced by recent different type earthquakes, we analyzed distribution and scale of deep-seated landslides induced by Chuetsu earthquake in 2004, Iwate-Miyagi earthquake in 2008, North Nagano Province earthquake in 2011 and Fukushima Hamadori earthquake in 2011.

The results of analysis shown that in the case of reverse fault earthquakes, the landslides were mostly distributed on the hanging wall of the source fault and the scale of landslides was likely to larger than that on the foot wall. On the other hand, in the case of normal fault, the landslides mostly occurred on the hanging wall. However, the number of landslides induced by normal fault was significantly fewer than that induced by reverse fault earthquakes.

These characteristics are coinciding with the PGA distribution of different type earthquakes, considered to be related with hanging wall effect of reverse fault and normal fault earthquakes.

Keywords

Earthquake • Landslide • Japan

Introduction and Study Area

Recent years a series of strong inland earthquakes struck Japan, caused a large number of landslides. These earthquake-induced landslides caused sever damage to the focal areas. To clarify the characteristics of inland earthquake-induced landslides, we analyzed distribution, size of deep-seated landslides induced by recent 4 strong earthquakes that occurred recent year inland Japan (Table 1). The Chuetsu earthquake and the Iwate-Miyagi earthquake occurred in mountainous areas, caused a large number of

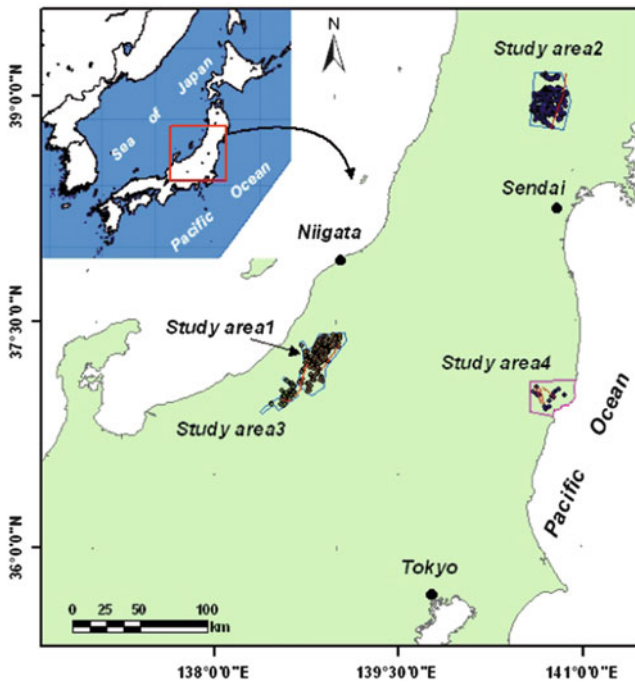
deep-seated landslides (Chigira and Yagi 2005; Yagi et al. 2008), some of them dammed rivers. The Northern Nagano Province earthquake (hereafter, Northern Nagano earthquake) was a larger earthquake that triggered by the huge Tohoku earthquake of 2011, Japan. This earthquake occurred in heavy snow region in winter to spring season, caused some characteristic landslides (Has et al. 2012). The Fukushima Hamadori earthquake (2011, hereafter Fukushima earthquake) occurred just after 1 month of the huge 3.11 earthquake. The Fukushima earthquake occurred on normal fault, a rare case in Japan, while other earthquakes occurred on reverse fault. All of these earthquakes occurred inland central to north eastern Japan with shallow focal depth.

The study areas are focused on the focal area of the earthquakes (Study area 1: Chuetsu earthquake; Study area 2: Iwate-Miyagi earthquake; Study area 3: Northern Nagano

B. Has (✉) • T. Takayama • K. Ogawa • S. Onoda
Asia Air Survey Co., Ltd, 1-2-2 Manpukuji, Asao-ku, Kawasaki
215-0004, Japan
e-mail: has.baator@ajiko.co.jp; tk.takayama@ajiko.co.jp;
ki.ogawa@ajiko.co.jp; sa.onoda@ajiko.co.jp

Table 1 Parameters of earthquakes involved in this study

Earthquake	Date (local)	Epicenter		M (JMA)	Depth (km)	Source ault			Max intensity (JMA)	PGA (gal)
		Lat.	Long.			Strike	Dip	Type		
Chuetsu	Oct. 23, 2004	37°17.5'	138°52.0'	6.8	13	N36E	53NW	Reverse	7	1,750.2
Iwate-Miyagi	Jun. 14, 2008	39°01.7'	140°52.8'	7.2	8	N21E–N11E	41NW	Reverse	6+	4,022.1
Northern Nagano	Mar. 12, 2011	36°59.1'	138°35.8'	6.7	8	N30–70E	NE	Reverse	6+	803.5
Fukushima	Apr. 12, 2011	36°54.7'	140°40.3'	7.0	6	N50W	NW	Normal	6-	745.8

**Fig. 1** Location of study areas

earthquake; Study area 4: Fukushima earthquake). In the case of the Chuetsu earthquake, the landslides data is from Hasi et al. (2011), and in the case of the Northern Nagano earthquake, the landslides data is based on Has et al. (2012). For the Iwate-Miyagi earthquake and Fukushima earthquake, landslides were interpreted using aerial photos and Google Earth images.

The study area is shown in Fig. 1.

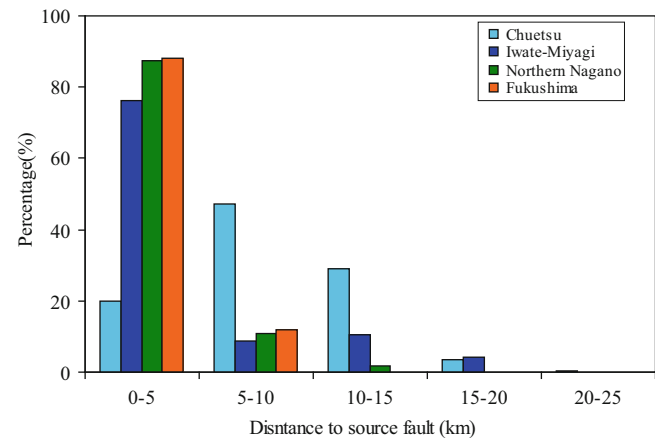
Characteristics of Landslides Distribution

Landslides Distribution with Source Fault

In the cases of reverse fault earthquakes, a large number of deep-seated landslides were triggered. Compared to these reverse fault earthquakes, only dozens of landslides

Table 2 Landslides distribution with source fault

Earthquake	Landslides				
	Total number	Hanging wall (number/%)		Foot wall (number/%)	
Chuetsu	362	350	96.7	12	3.3
Iwate-Miyagi	810	741	91.5	69	8.5
Northern Nagano	111	101	91.0	10	9.0
Fukushima	17	13	80.0	4	20.0

**Fig. 2** Landslides distribution with distance from source fault

induced by the normal fault earthquake of Fukushima (see Table 2). In all cases, the number of landslides occurred on the hanging wall is significantly larger than that on the foot wall. This tendency is same in reverse fault and normal fault.

In this study, the source fault of the Chuetsu earthquake is based on Hikima and Koketsu (2005), while for the Iwate-Miyagi earthquake is based on Hikima et al. (2008). For the Northern Nagano earthquake and the Fukushima earthquake, since there is no source fault model has been recorded, the active faults that considered to initiated the earthquakes are selected as the source fault (AIST 2009).

Figure 2 shows the landslides number frequency with distance from source fault. In all cases in this study, the deep-seated landslides occurred within 25 km from source fault. Compared to reverse fault induced landslides, the

landslides induced by normal fault occurred within short distance from the source fault within 10 km from the source fault.

Landslides Distribution with PGA

The relationship between the deep-seated landslides induced by the earthquakes and peak ground acceleration (PGA) of those earthquakes was analyzed. In the case of the Chuetsu earthquake, the whole landslides occurred in the area where intensity is larger than 500 gal (Hasi et al. 2011). Same as the case of the Chuetsu earthquake, the landslides induced by the Iwate-Miyagi earthquake occurred within an area of the PGA is larger than 500 gal. In the case of the Northern Nagano earthquake, most of the landslides (97.3 %) located in the area where the PGA is larger than 500 gal. However, in the case of the Fukushima earthquake, the landslides occurred in the area where the PGA is larger than 200 gal, mostly in the area of the PGA is 200–500 gal.

Landslides Distribution with Seismic Intensity

Same as the PGA, landslides distribution and seismic intensity (JMA, Japan Meteorological Agency scale) was analyzed. In the case of the Chuetsu earthquake, whole of the landslides occurred in an area where the intensity is larger than 5 *upper* in JMA scale. In the case of the Iwate-Miyagi inland earthquake, all of the landslides in the study area located in the area of intensity larger than 5 *upper*. In the case of the Northern Nagano earthquake, all of the landslides occurred in the area of intensity larger than 6 *lower*. However, in the case of the normal fault earthquake of Fukushima, most of the landslides (88.2 %) occurred in the area where the intensity larger than 5 *upper*.

Characteristics of Landslides Size

Landslides Size with Source Fault

Figure 3 shows the landslide size with distance to source fault. In all cases, both reverse fault and normal fault earthquakes, the size of landslides (area of landslides) shows a tendency that the larger one distributed on the hanging wall of the source fault. However, in the cases of reverse fault earthquakes, the size of landslides is significantly larger than that induced by normal fault earthquake.

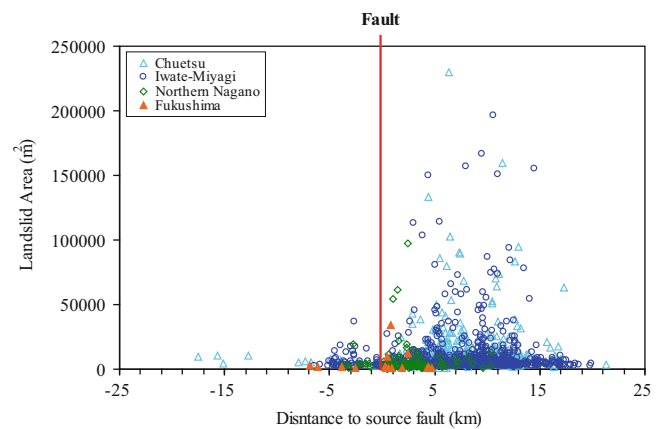


Fig. 3 Landslides size with distance from source fault

Discussion and Conclusions

The distribution and size of the landslides which induced by recent three reverse fault earthquakes and one normal fault earthquake were analyzed in this study. The similar characteristic of landslides distribution was that in both case of reverse fault and normal fault earthquake, the landslides mostly occurred on hanging wall. This may due to the hanging wall effect, about 50 % increase of PGA on the hanging wall compared to foot wall (e.g. Abrahamson and Somerville 1996; Chang et al. 2004). However, reverse fault earthquakes tend to induce a larger number of landslides and bigger landslides compared to normal fault earthquake. These characteristics are coinciding with the different PGA distribution of reverse fault and normal fault. In the case of same magnitude earthquake, the PGA of reverse fault is larger than that of normal fault.

About strike-slip fault earthquakes in inland Japan, like Kobe earthquake (M7.3, 1995) and Western Tottori earthquake (M7.3, 2000), compared to reverse fault and normal fault earthquakes, very few or no deep-seated landslides occurred. This characteristic indicated that different type earthquakes may induce different distribution and size of landslides. For future work, we will conduct detailed analysis of landslides distribution with geology, geomorphology, as well as the PGA, period of seismic wave.

The results of the study are concluded as following:

1. Both of reverse fault and normal fault earthquake induced landslides mostly occur on hanging wall of the source fault.
2. Reverse fault earthquakes tend to trigger a large number and larger size landslides against normal fault earthquake.

3. Most of the landslides occurred within area of the PGA is larger than 500 gal and the seismic intensity is larger than 5 upper in JMA scale.

References

- Abrahamson NA, Somerville PG (1996) Effects of the hanging-wall and footwall on ground motions recorded during the Northridge earthquake. *Bull Seismol Soc Am* 86(1B):S93–S99
- AIST (National Institute of Advanced Industrial Science and Technology) (2009) Active fault database of Japan, June 23, 2009 version. Research Information Database DB095, National Institute of Advanced Industrial Science and Technology http://riodb02.ibase.aist.go.jp/activefault/index_e.html. Last Accessed 10 Jun 2013
- Chang TY, Cotton F, Tsai YB, Angelier J (2004) Quantification of hanging-wall effects on ground motion: some insights from the 1999 Chi-Chi earthquake. *Bull Seismol Soc Am* 94(6):2186–2197
- Chigira M, Yagi H (2005) Geological and geomorphological characteristics of landslides triggered by the 2004 Mid Niigata prefecture earthquake in Japan. *Eng Geol* 82:202–221
- Has B, Noro T, Maruyama K, Nakamura A, Ogawa K, Onoda S (2012) Characteristics of earthquake-induced landslides in heavy snowfall region—Landslides induced by the northern Nagano Prefecture earthquake, March 12, 2011 Japan. *Landslides* 9(4):539–546
- Hasi B, Ishii Y, Maruyama K, Terada H, Suzuki S, Nakamura A (2011) Distribution and scale of landslides induced by recent reverse-fault earthquakes in Japan. *J Jpn Landslide Soc* 48(1):23–38 (in Japanese with English abstract)
- Hikima K, Koketsu K (2005) Rupture processes of the 2004 Chuetsu (mid-Niigata prefecture) earthquake, Japan: A series of events in a complex fault system. *Geophys Res Lett* 32. doi:10.1029/2005GL023588
- Hikima K, Miyazaki S, Koketsu K (2008) Rupture process of the 2008 Iwate-Miyagi Nairiku earthquake (M_j7.2), Japan, inferred from strong motion and geodetic data. *Eos Trans AGU* 89(53), Fall Meet. Suppl., Abstract S51D1789
- Yagi H, Sato T, Yamashina S, Yamazaki T (2008) Aerial photo interpretation map for 2008 Iwate-Miyagi inland earthquake. http://www.landslide-soc.org/education/report/iwate_miyagi_EQ_080728.jpg. Last Accessed 18 May 2010



Investigation of Tandikat Landslide, West Sumatra, Indonesia

Fikri Faris and Fawu Wang

Abstract

A disastrous earthquake struck Padang, West Sumatra Province on September 30, 2009, at 5:16 p.m. with magnitude of 7.6, triggered landslides in Tandikat, Padang Pariaman Regency which took hundreds of lives. These landslides occurred on loose pumice layered mountain during rainfall. The combination of intensive rainfall and strong earthquake probably decreased the slope stability. This study proposes to learn more about initial failure mechanism of earthquake-induced landslide of Tandikat area using strain energy approach.

Integrated study through field investigation, laboratory work and numerical modeling were conducted. Strain energy concept was used to assess pore water pressure increase during cyclic loading. In order to attain dynamic properties required, stress-controlled cyclic triaxial (CTX) test were used. Model of pore water pressure ratio related to cumulative dissipated strain energy (E) was developed. The estimation of E during the actual earthquake motion was performed by finite element code ABAQUS. The predicted excess pore water pressure was used to assess slope stability during earthquake motion using infinite slope assumption.

In terms of initial effective confining pressure, lower effective confining pressure of pumice sand need small E to reach the value of 0.8 of pore pressure ratio than that of higher effective confining stress. The result shows that shallow landslide due to earthquake more likely to occur than deep seated type landslide in the area. From slope stability analysis result, slope failure occurred prematurely prior to maximum peak of earthquake acceleration implying great influence of pore water pressure generation to slope failure.

Keywords

Earthquake • Rainfall • Strain energy

Introduction

Rainfall and earthquake are two separate events which occurred independently. The probability of these events to take place at the same time might be small in the most areas. However, in the perspective of landslide mitigation, the

impact of the inadvertent combination of rainfall and earthquake could be disastrous. Moreover, in some high seismic area which has frequent intense rainfall, the incident of earthquake happened during rainfall has higher possibility to occur than that of common places.

The Tandikat landslides portrayed the one of a kind earthquake-induced landslide occurred during intense rainfall on volcanic deposit strata. These landslides occurred on loose pumice layered mountains during rainfall after M7.6 Padang Earthquake with magnitude of 7.6 struck West Sumatra Province on September 30th, 2009, at 5:16 p.m.

F. Faris (✉) • F. Wang
Shimane University, Research Center of Natural Disaster Reduction,
Matsue 690-8504, Japan
e-mail: fikri.faris.ugm@gmail.com

local time (EERI 2009). The high mobility of the landslide mass deposit spread widely on the valley implies the high water content of the landslide mass.

Particularly in Tandikat area, the study of post-failure mechanism using un-drained ring shear apparatus have been conducted to confirm the grain crushing mechanism of long run-out pumice material (Wang et al. 2010). The study also verified the previous study of Wang and Sassa (2000) about grain crushing susceptibility of long travelled landslide in pyroclastic depositional area using un-drained ring shear apparatus. However, the initial failure mechanism of Tandikat landslide involving infiltrated rainfall and earthquake motion is needed to be examined in order to recognize the risk of earthquake-induced landslide during rainfall in volcanic region. This study emphasized the initial failure mechanism of earthquake-induced landslide in saturated soil by using cyclic triaxial apparatus and strain energy concept to assess the potential of pore pressure increase during earthquake motion.

Seismicity and Climate of West Sumatra

The seismicity of West Sumatra is majorly controlled by Sumatra Fault System which formed as consequence of oblique motion and thrust-faulting of Indo-Australia plate and Euro-Asian plate. This tectonic activity results to frequent earthquakes of high intensity around the west coast of Sumatra. This also results to uplifting of trench basement which runs the length of the Barisan Mountains containing volcanic mountain parallel to the west coast (Aydan 2009).

The contribution of rainfall on earthquake-induced landslides has raised great concern in the volcanic area surrounding west coast of Sumatra Island which has equatorial type of weather. This type of weather usually brings rainfall of high intensity which continues even during dry season period (Sipayung et al. 2007). Based on the latest meteorological research on west coast of Sumatra Island, high intensity rainfall is frequently recorded on late afternoon or evening and is highly controlled by topographical condition of the area which is mostly consist of high mountains (Wu et al. 2009). The fact of high seismicity superimposed by the climate condition brings great concern of landslide occurrence due to earthquake during rainfall.

Geological Condition

The Tandikat landslides occurred on mountainous area around two volcanoes of Mt. Tandikat and Mt. Singgalang. Landslides were distributed widely on steep slopes inclined around 30–50°. The slopes are mainly covered by loose volcanic deposits from the nearby mountains. This



Fig. 1 Widespread development of Tandikat landslides (<http://www.boston.com/bigpicture>)

topographical condition is considered as important contributory factor for landslides in Tandikat (Fig. 1).

According to geological map of Padang (Kastowo and Gerhard 1973) in Fig. 2, landslide distribution was concentrated on the Quaternary volcanic bedrocks which is indicated as Qvf (Quaternary volcanic rocks along flank of volcanoes). The surface deposits consist of silt, sand, and gravel and may include remnants of pumice-tuff. Particularly in the area, impermeable clay stratum is overlain by porous pumice sand layer. According to the landslides scarp and outcrops observation, the pumice sand deposit was clear and distinguishable from the clay stratum (Fig. 3). From the measurement, the thickness of pumice sand layers is about 2–3 m. The difference in permeability may cause the saturation of lower part of the pumice layer when rainfall percolates.

Strain Energy

The concept of strain energy is commonly used to assess pore pressure increase in liquefaction analysis. This concept is based on the idea that under dynamic loading, part of the dynamic energy is dissipated into soil grain connection, generating irrecoverable deformation between soil grains. This dissipated strain energy per unit volume can be determined as the area of the hysteric strain–stress loop which can be attained through experiment (Fig. 4).

The practice of this concept in pore pressure generation analysis was firstly introduced by Nemat-Nasser and Shokoh (1979). Thereafter, numerous energy-based pore pressure models have been developed based on the results of cyclic test. Jafarian et al. (2012) conducted cyclic hollow cylinder torsional tests on the reconstituted specimens of Toyoura sand under initial effective confining pressure to simulate the effect of ground sloping.

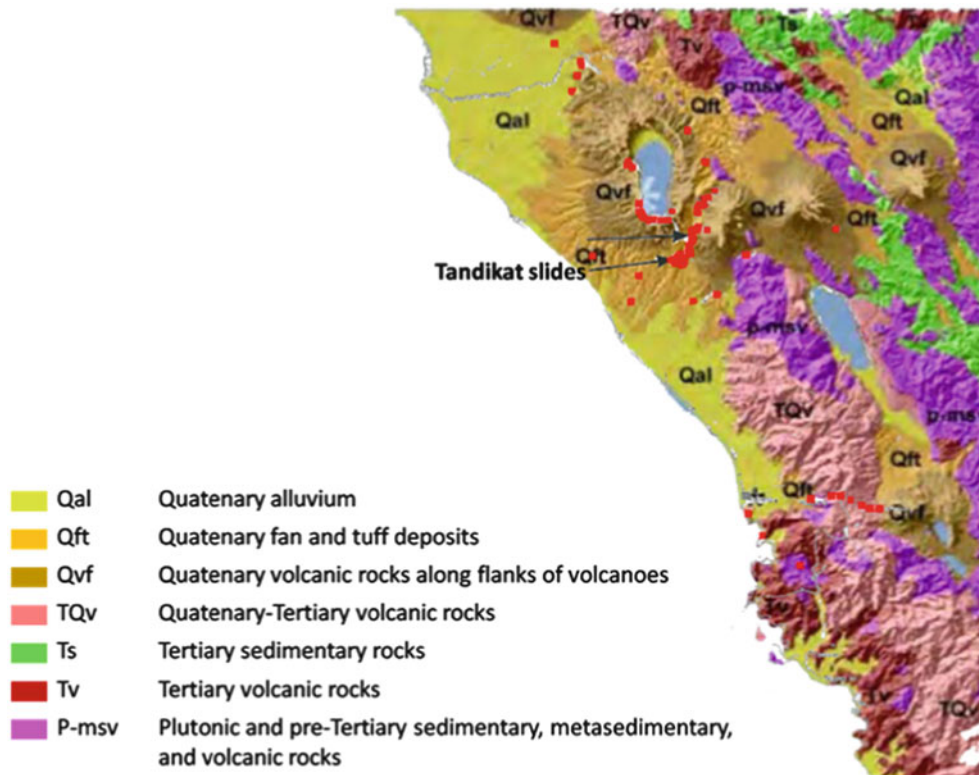


Fig. 2 Simplified geology of the studied area (modified from Kastowo and Gerhard 1973)

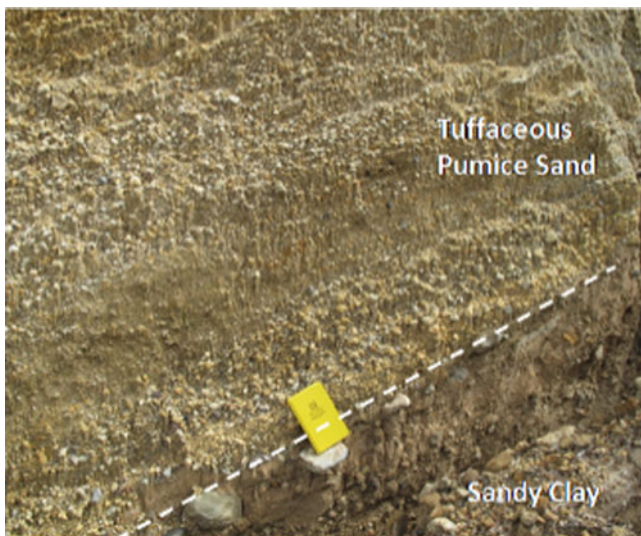


Fig. 3 Outcrop shows distinctive layer of sandy clay overlain by pumice sand

Further research on the dynamic behavior of Tandikat pumice sand to examine the energy-based pore pressure increase has never been conducted. This paper attempted to apply strain energy concept for assessing slope stability during earthquake, especially in pumice deposition area of Tandikat by examining cumulative strain energy, E from

cyclic triaxial results and its correlation with pore pressure increase. The effect of ground sloping was also examined by applying initial shear stress during cyclic triaxial test.

The cumulative enclosed area of the shear stress-strain loop is referred to as dissipated strain energy, which causes residual displacement and pore water pressure build up inside the specimen. Total dissipated strain energy, E , can be calculated using (1). The parameters used in the equation correspond with Fig. 4.

$$E = \frac{1}{2} \sum_{i=1}^{n-1} (\sigma_{d,i+1} + \sigma_{d,i}) \cdot (\varepsilon_{a,i+1} - \varepsilon_{a,i}) \quad (1)$$

where σ_d is the deviatoric axial stress and ε_a is the axial strain.

In order to perform reasonable evaluation of the effect of initial confining pressure on cumulative strain energy, Green et al. (2000) proposed the term of normalized strain energy (E_N) as un-dimensional parameter:

$$E_N = \frac{E}{\sigma'_{v0}} \quad (2)$$

where σ'_{v0} is initial effective confining pressure.

Some value of cumulative strain energy was used as a reference in order to assess the effect of initial effective

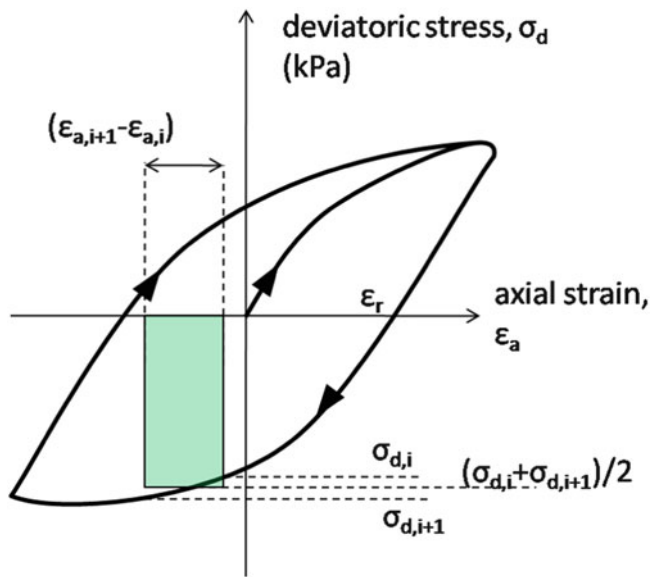


Fig. 4 Typical stress–strain from cyclic triaxial test and parameters in regard to (1)

confining pressure. From cyclic triaxial test result observation, at the initial stage of cyclic loading, only small amount of strain energy is necessary to increase pore pressure ratio rapidly up to 0.8. From this point, additional strain energy does not generate significant pore pressure ratio until the state of liquefaction attained. Therefore, cumulative strain energy required to increase pore pressure ratio up to 0.8 was determined as reference ($E_{ru=0.8}$). Analogously, the normalized cumulative strain energy required to attain 0.8 of pore pressure ratio ($E_{Nru=0.8}$) can be calculated using (2) as well.

Subsequently, from the triaxial test result, the cumulative strain energy and pore pressure ratio were correlated. The model of pore pressure generation developed by Davis and Berrill (2001) was then fitted to the plot of cumulative strain energy vs. pore pressure ratio using the following equation:

$$r_u = 1 - \exp\left(-\alpha \frac{E}{\sigma'_{v0}}\right) \quad (3)$$

where r_u is pore pressure ratio, E is cumulative strain energy, σ'_{v0} is initial effective confining pressure and α is calibration parameter. Later, this model will be utilized using cumulative strain energy generated from finite element analysis in order to evaluate the stability during earthquake.

Laboratory Tests

Disturbed soil sample was taken from pumice sand layer during field investigation to obtain physical and mechanical properties of the soil. Physical properties, such as specific

Table 1 Pumice sand properties obtained from in situ measurement and laboratory tests

Pumice sand properties	Values
Specific gravity	2.66
Bulk density	1.50 g/cm ³
Dry density	0.89 g/cm ³
Relative density	≈50 %
Void ratio, e	2.00
Uniformity coefficient (C_u)	8.19
Coefficient of curvature (C_c)	1.03
Saturated hydraulic conductivity, k_s	8.4×10^{-5} m/s
Internal friction angle, ϕ'	39°

gravity and grain-size distribution, were obtained through specific gravity examination and grain-size distribution test. The results of specific gravity and void ratio are shown in Table 1. High void ratio indicates the loose structure of pumice layer and can be associated with the large and interconnected pores as observed from field investigation.

Mechanical properties of the soil were obtained using static triaxial compression test through consolidated-undrained procedure. The sample was remoulded to form 5 cm in diameter and 10 cm in height cylindrical specimen of the original in situ density. To achieve the required density, determined weight of the dry samples were inserted into a mould with specified volume by using dry pluviation method. In case there was excess soil mass, the mould was impacted slightly to provide extra space for the remaining soil mass. The specimens were then injected with CO₂ gas to ease saturation process before it was saturated with de-aired water. The full saturation of specimens were confirmed if Skempton's B-value was higher than 0.95. After full saturation condition was reached, the specimens were loaded axially inside the triaxial cell with different confining pressure: 20 kPa and 50 kPa with displacement velocity of 0.7 mm/min. The result of the undrained strength parameters is summarized in Table 1.

In order to study the behavior of soil under cyclic loading, stress controlled cyclic triaxial tests were performed with similar procedure of specimen reconstitution as in static triaxial compression test. The tests were performed to study the effect of cyclic loading in the lower part of landslide mass attaching directly to slip surface in its full saturated condition. The tests were conducted in different by effective confining pressure, σ'_{v0} and initial shear stress to examine the effect of overburden pressure and ground sloping condition under cyclic loading. However, to focus on field condition, initial relative density was maintained as the actual relative density measured in situ. The procedure of test is performed in such a way to simulate the stress path in the field. At first, the specimens were consolidated with specified confining pressure after full saturated condition

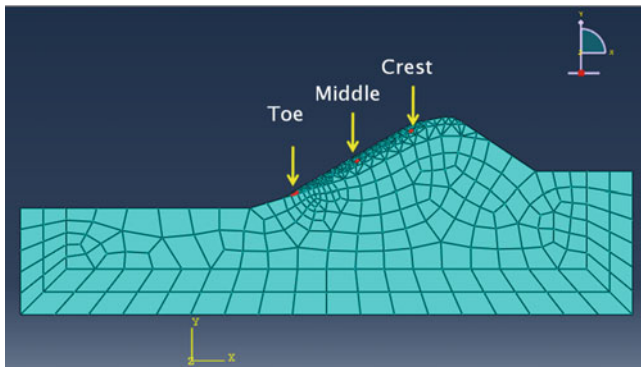


Fig. 5 Model of ABAQUS 2D FEM and slope stability analysis point

has been attained. As the preliminary approximation of irregular motion of earthquake loading, the amplitude of cyclic sinusoidal deviatoric axial stress was taken as 65 % of maximum magnitude of shear stress induced by actual earthquake as proposed by Seed et al. (1975). The cyclic sinusoidal axial stresses were then applied to the specimens at a rate of 1 cycle/s until the ultimate failure state was achieved.

Numerical Analysis and Slope Stability Evaluation

In order to estimate the cumulative strain energy during the actual earthquake motion, finite element procedure was implemented using two dimensional finite element code software ABAQUS. The estimated strain energy was then taken to predict pore water pressure build up based on developed r_u model to evaluate slope stability during earthquake motion. The slope stability analysis was conducted by considering cumulative strain energy obtained from ABAQUS 2D FEM and r_u model developed from laboratory test result. The analysis focused on three different elevation of sliding surface; toe, middle and crest of the slope (Fig. 5). The slope stability analysis simply used the infinite slope assumption to assess factor of safety.

Result and Discussion

The time history of pore pressure of cyclic triaxial test under 45 kPa initial effective confining pressure confirmed the cyclic mobility behavior (Fig. 6). The pore pressure ratio was rapidly increased at the first cycles but did not necessarily reach liquefaction state until some large numbers of cycles. However, the specimen has already undergone large strain before the state of liquefaction was attained.

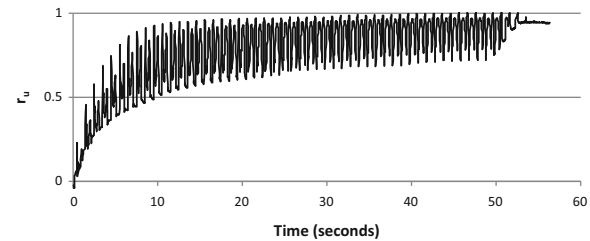


Fig. 6 Time history of pore pressure ratio at $\sigma'_0 = 45$ kPa

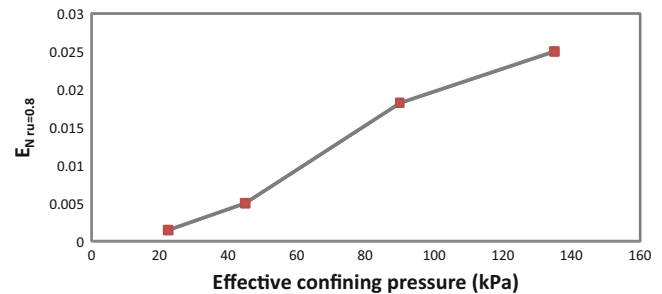


Fig. 7 Plot of total Normalized Strain Energy causing $0.8r_u$ ($E_{N_{ru=0.8}}$) vs. initial effective confining pressure

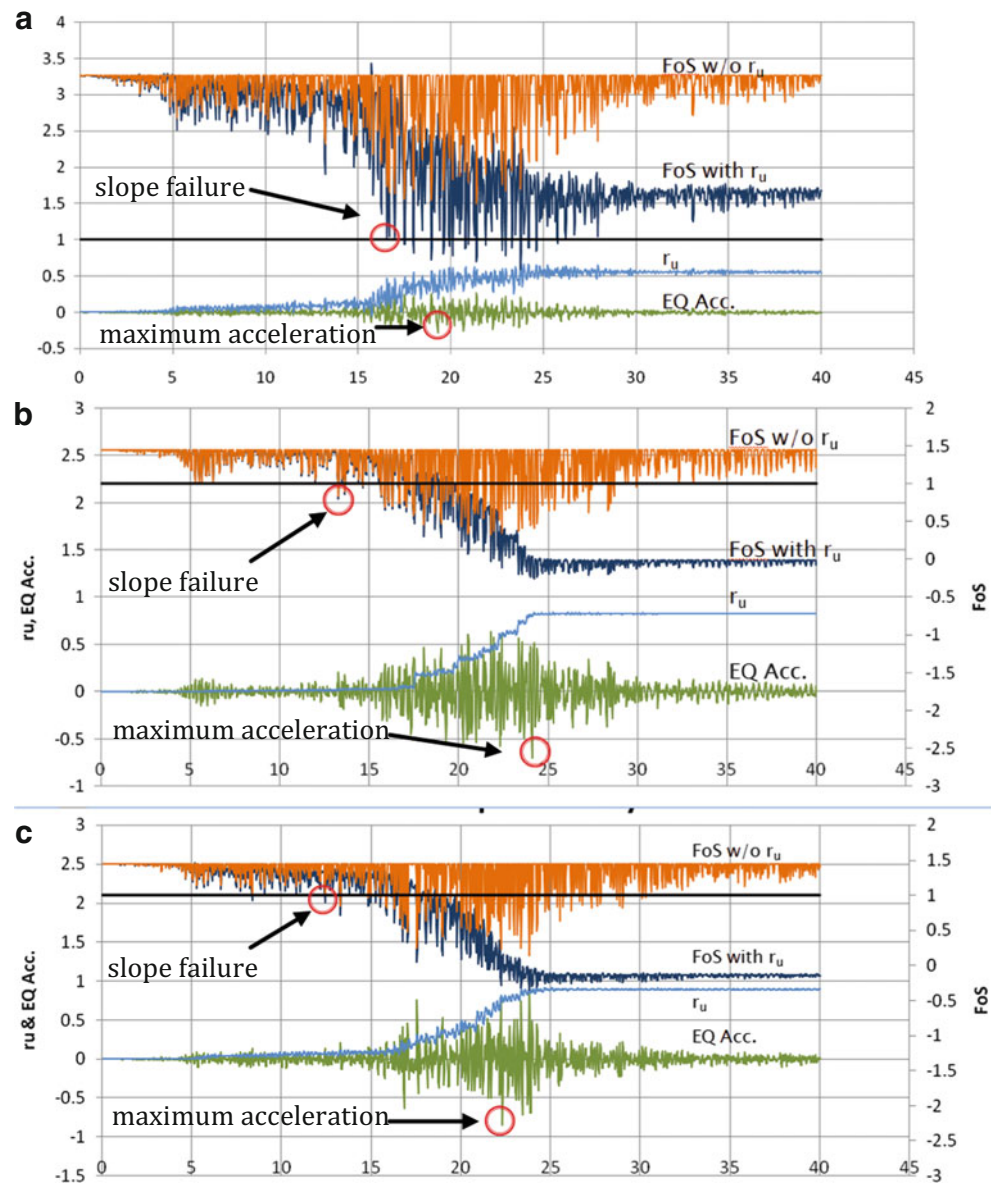
Both static triaxial test and cyclic triaxial tests showed contractive behavior of pumice deposit indicated by excess pore water pressure rise at small strains. Cyclic triaxial test confirmed rapid excess pore water pressure build up during cyclic loading which strongly correlated with cumulative strain energy generation. In terms of initial effective confining pressure, lower effective confining pressure of pumice sand need small cumulative strain energy to reach 80 % of excess pore water pressure than that of higher effective confining stress (Fig. 7). This suggest that shallow landslide due to earthquake tends to occur than deep seated type landslide in the area.

Slope stability analysis result shows premature slope failure due to pore water pressure generation prior to maximum peak of earthquake acceleration. The tendency of pore water generation induced failure is obviously shown at the toe (Fig. 8a). On the other hand, Fig. 8b, c suggests that middle part and crest slope failure happened due to the combination of acceleration amplification and pore water pressure build up. Overall analysis results show that pore water pressure generation during earthquake has great contribution to slope failure.

Conclusion

From the cyclic triaxial test of pumice sand, one may suggests that the developing cumulative strain energy from the earthquake strongly correlated with pore pressure build up. Small portion of strain energy at the initial

Fig. 8 Time history (in s) of factor of safety without considering r_u (FOS w/o r_u), factor of safety by considering r_u (FOS with r_u), r_u and actual earthquake acceleration (EQ Acc.). (a) Toe point, (b) middle point, (c) crest point



stage of earthquake motion could increase pore pressure nearly to critical state. This fact cautiously suggests the risk of earthquake-induced landslide by earthquake smaller than M7.6 Padang Earthquake, providing the soil is on the state of full saturated. Full saturated condition of liquefiable soil could be possibly attained during or after rainfall due to infiltration. Typical rainfall in the mountain range of West Coast of Sumatra sufficiently supports this condition.

From the examination of the effect of initial effective confining pressure on the reference normalized strain energy ($E_{N_{ru}=0.8}$), lower effective confining stress pumice sand needs small strain energy to reach pore pressure ratio of 0.8 than that of higher effective confining stress suggesting the higher tendency of shallow landslide

occurrence instead of deep seated type landslide. This result was confirmed by the fact of many shallow type of landslides occurred in the area.

Overall analysis results show that pore water pressure generation during earthquake has great contribution to premature slope failure prior to maximum peak of earthquake acceleration. The high of pore pressure inside the landslide prior to the failure may cause the high mobility of landslide mass. It advises the severe impact of landslide that may happen in the earthquake prone area during heavy rainfall.

Acknowledgments We appreciate the help of Prof. Dwikorita Kamawati and Dr. T. Faisal Fathani of Gadjah Mada University for providing additional data (SPT and geological logging) used in this

study. The authors are also grateful to Mr. Rahindro Pandhu Mahesworo, S.T, M.T, the Head of Engineering Seismology Data, BMKG Indonesia for providing data of earthquake accelerogram used in this study.

References

- Aydan Ö (2009) A reconnaissance report on the Pariaman-Padang earthquake of September 30, 2009. Japan Society of Civil Engineers, Japan, 36p
- Davis RO, Berrill JB (2001) Pore pressure and dissipated energy in earthquakes-Field verification. *J Geotech Geoenviron* 127 (3):269–74
- EERI (2009) Learning from earthquakes: the M_w 7.6 Western Sumatra earthquake of September 30, 2009. http://www.eeri.org/site/images/eeri_newsletter/2009_pdf/Padang-eq-report-NL-insert.pdf. Last Accessed 8 Apr 2013
- Green RA, Mitchell JK, Polito CP (2000) An energy-based excess pore pressure generation model for cohesionless soils. In: Proceedings of the John Booker memorial symposium, Sydney, New South Wales, Australia, 16–17 November 2000. A.A. Balkema Publishers, Rotterdam, Netherlands
- Jafarian Y, Towhata Y, Baziar MH, Noorzad A, Bahmanpour A (2012) Strain energy based evaluation of liquefaction and residual pore water pressure in sands using cyclic torsional shear experiments. *Soil Dyn Earthq Eng* 35:13–28
- Kastowo D, Gerhard WL (1973) Geologic map of the Padang Quadrangle, Sumatra: Geological Survey of Indonesia, Ministry of Mines Geologic Quadrangle Map, Sumatra, Padang 4/VIII
- Nemat-Nasser S, Shokoh A (1979) A unified approach to densification and liquefaction of cohesionless sand in cyclic shearing. *Can Geotech J* 16(4):659–78
- Seed HB, Idriss IM, Makdisi F, Banerjee N (1975) Representation of irregular stress – time histories by equivalent uniform stress series in liquefaction analysis. Report No. EERC 75-29. Earthquake Engineering Research Center, University of California, Berkeley
- Sipayung SB, Lely QA, Bambang DD, Sutikno (2007) The analysis of rainfall pattern in Indonesia based on global circulation model (GCM) output. *Jurnal Sains Nusantara* 4(2) (in Indonesian)
- Wang FW, Muhammad Wafid A N, Zhang F (2010) Tandikek and Malalak flowslides triggered by 2009.9.30 M_w 7.6 Sumatra earthquake during rainfall in Indonesia, Geoscience Report, Shimane University 29: 1–10
- Wang FW, Sassa K (2000) Relationship between grain crushing and excess pore pressure generation by sandy soils in ring shear tests. *J Nat Disaster Sci* 22(2):87–96
- Wu P, Hara M, Hamada JI, Yamanaka MD, Kimura F (2009) Why a large amount of rain falls over the sea in the vicinity of western Sumatra Island during nighttime. *J Appl Meteorol Climatol* 48:1345–1361



Study on the Distribution of Large-Landslides Triggered by Wenchuan Earthquake

Xiaojun Chang, Dewei Wang, Weiya Ge, Lunwu Wei, Wanmo Zheng, and Yeqi Tang

Abstract

5.12 Wenchuan earthquake in 2008 caused tens of thousands of landslides, avalanches, rockfalls and other secondary geological disasters, and the people in disaster areas suffered a tragic loss of life and property. In particular, the destruction of large area, a wide range of large landslide hazards to human life and property were caused by the catastrophe, and the potential risk still exists. Through the field surveys, data access, etc., the authors analyzed the distribution of large landslides triggered by the Wenchuan earthquake.

Keywords

Large-landslide • Wenchuan Earthquake • Distribution

Introduction

Happened on the Mt. Longmen Fault Zone to the rim of Qinghai-Tibet Plateau on 14:28 of May 12th, 2008, the Wenchuan Earthquake (Ms 8.0) caused a surficial fault zone long 240 km and wide 40 km approximately. The intense earthquake triggered tens of thousands of landslide, collapse, rockfall and other secondary geological disasters, and caused serious loss to the life and property of the people in the disaster area. Especially the super-scale landslide damaging large area and endangering large coverage (its volume is more than $1,000 \times 10^4 \text{ m}^3$) caused huge disaster to the life and property of the local people; even its risk is still latent. Moreover, the super-scale landslide, whichever it is its occurrence or distribution, reflected intuitively the ground failure in the earthquake region to a great extent.

Apparently, it is very important to provide evidences for ascertaining the correlation among earthquake magnitude, seismic intensity and landslide scale, and provide the valuable references for studying the seismic law, seismic prevention and control, and seismic hazard relief to make certain the distribution law of the super-scale landslide triggered by Wenchuan Earthquake (“Wenchuan Larger Seismic Landslide” for short). In accordance with the statistical analysis and investigation research, there are apparent distribution characteristics for Wenchuan Larger Seismic Landslide. By summing up the major distribution characteristics of Wenchuan Larger Seismic Landslide, the paper provides the fundamental information for guiding disaster prevention and reduction, and the further researches.

Overview of Wenchuan Larger Seismic Landslide

Wenchuan Earthquake triggered 33 large-scale landslides in the territory of Sichuan Province. Most of them were the rocky landslides, and few were the soil or detritus landslides. These large-scale landslides happened in a wide range and almost covered the whole principal earthquake area of Wenchuan Earthquake, especially along the banks of the rivers in the severely affected areas and

X. Chang (✉) • W. Ge
Nanjing Center, China Geologic Survey, Nanjing 210016, China
e-mail: shaanxipeople@163.com; 391743801@qq.com

D. Wang
Chengdu Center, China Geologic Survey, Chengdu 610081, China
e-mail: 155343514@qq.com

L. Wei • W. Zheng • Y. Tang
Chengdu Center, China Geologic Survey, Chengdu 610081, China
e-mail: 1196903550@qq.com; 1050736347@qq.com; tyeqi@qq.com

Table 1 The basic characteristics of large landslide induced by Wenchuan Earthquake

No.	Landslide name	Geographic position	Nature of landslide	Crest (m)	Intensity zone	Slope angle (°)	Aspect (°)
01	Qinglingou landslide	Baolun Town, Lizhou	Soil	1,000	VII	48	160
02	Zhengjiashan landslide	Nanba Town, Pingwu	Lithology	1,400	X	35	130
03	Zhaojiafen landslide	Nanba Town, Pingwu	Lithology	1,200	X	34	275
04	Wenjiaba landslide	Nanba Town, Pingwu	Lithology	1,340	X	43	320
05	Weigoucun landslide	Guixi Town, Pingwu	Detritus	1,300	XI	42	115
06	Youtongping landslide	Badi Town, Pingwu	Lithology	1,700	IX	23	275
07	Chenjiaba landslide	Chenjiaba Town, Qingchuan	Lithology	1,300	XI	30	157
08	Taihongcun landslide	Chenjiaba Town, Qingchuan	Soil	1,400	XI	52	120
09	Xinxiancheng landslides	Qushan Town, Beichuan	Lithology	1,130	XI	27	236
10	Tangjiashan landslide	Qushan Town, Beichuan	Lithology	1,200	XI	51	330
11	Kuzhuba landslides	Qushan Town, Beichuan	Lithology	1,280	XI	31	122
12	Wangjiayan landslides	Qushan Town, Beichuan	Lithology	1,600	XI	28	83
13	Wenjiagou landslide	Qingping Town, Mianzhu	Lithology	2,320	X	40	207
14	Xiejiadian landslide	Longmenshan Town, Pengzhou	Lithology	2,170	XI	58	154
15	Dameizilin landslide	Hongbai Town, Shifang	Detritus	1,470	X	31	28
16	Ganhekou landslide	Hongbai Town, Shifang	Lithology	1,427	X	37	312
17	Shuimogou landslides	Hongbai Town, Shifang	Lithology	1,650	X	28	110
18	Yuejiashan landslide	Hongbai Town, Shifang	Lithology	1,600	X	25	106
19	Donghekou landslide	Hongguang Town, Qingchuan	Lithology	1,400	IX	46	90
20	Dongjialiang landslide	Qima Town, Qingchuan	Lithology	1,400	IX	43	107
21	Shibangou landslide	Hongguang Town, Qingchuan	Lithology	1,240	IX	27	25
22	Woqian landslide	Magong Town, Qingchuan	Lithology	1,430	X	41	137
23	Lianhuaxingou landslide	Yingxiu Town, Wenchuan	Lithology	1,800	XI	37	100
24	Niujuangou landslide	Yingxiu Town, Wenchuan	Lithology	1,570	XI	35	119
25	Tiziyan landslide	Sanjiang Town, Wenchuan	Lithology	1,700	IX	26	320
26	Heitupo landslide	Shuimo Town, Wenchuan	Detritus	1,183	X	25	60
27	Daguangbao landslide	Gaochuan Town, Anxian County	Lithology	3,047	X	55	60
28	Laoyingyan landslide	Gaochuan Town, Anxian County	Lithology	1,240	X	46	78
29	Yinshan landslide	Yong'an Town, Anxian	Detritus	1,020	X	32	267
30	Tuqiao Yinshan landslides	Yong'an Town, Anxian	Lithology	1,080	X	28	174
31	Chuanzhumiao landslide	Yong'an Town, Anxian	Lithology	1,140	X	39	115
32	Miaoping landslide	Qiaoting Town, Nanjiang	Lithology	1,500	VII	24	300
33	Zhangguizhai landslide	Huilong Town, Maoxian	Soil	2,293	VII	35	307

Note. The data above comes from the field investigation (except for that of Beichuan) and the reference based on Investigating Report for Secondary Geological Disasters of Wenchuan Earthquake (42 counties)

secondarily severe affected areas in 11 counties, namely Wenchuan, Beichuan, Pingwu, Anxian, Qingchuan, etc. Among which, 8 were in Beichuan, and it was the county in which the earthquake triggered off the large-scale landslide maximally; 5 in Anxian, 4 in Qingchuan, Shifang and Wenchuan, 3 in Pingwu, and 1 respectively in Lizhou District of Guangyuan City, Mianzhu City, Pengzou City, Maoxian, Nanjiang and so on (Table 1 and Fig. 1).

As for the large-scale landslide triggered by Wenchuan Earthquake, the size was different from each other. The largest one was the Daguangbao landslide (Huang et al. 2008) in the northwest of Quanshui Village, Gaochuan Town, Anxian County, which had the volume exceeding 700,000,000 cubic meters. Following, it was the Wenjiagou landslide, which was located in Qingping Town, Mianzhu City, which had the volume of 130,000,000 cubic meters

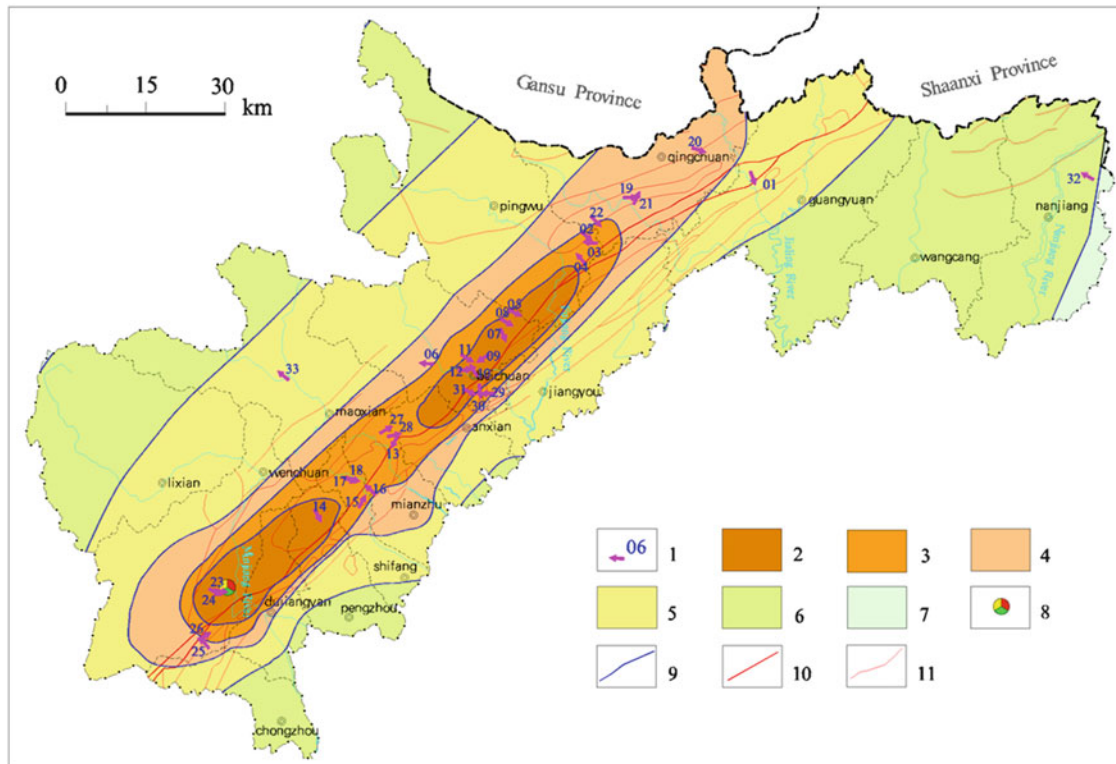


Fig. 1 Distribution of large landslide and seismic intensity (intensity partition data according to China Earthquake Administration, 2008, 9). Legend note: 1. landslide and number (*direction of the arrow* represents

the direction of landslide); 2–7. respectively XI, X, IX, VII, VII, VI degree of intensity zones; 8. Epicenter (Yingxiu); 9. Isoseismal line; 10. Seismogenic fault; 11. secondary faults

(Yin 2009); the rest were the landslides with the volume less than 40,000,000 cubic meters (among which, over 80 % had the volume between 10,000,000 and 20,000,000 cubic meters). The large-scale landslides happened in Wenchuan Earthquake go beyond the scope (MLR 2006) of landslide definition and show “unconventional”; in essence they are the combined disaster caused by collapse, landslide, slungshot, debris flow and other geological disasters, featuring in high-speed and long-distance sliding in most circumstances. By researching the typical landslide cases, Yin (2008) considered that the high-speed and long-distance landslide triggered by Wenchuan Earthquake generated the effects of throwing, colliding, scraping and air cushion (Yin 2009). When the earthquake happened, these landslides caused thousands of people died (or to be buried) and had huge threat to the life and property of the people. Moreover, large-scale landslide accumulation body blocking off creek or river, forming Tangjia Shan, Shibangou, Donghekou, Laoyingyan, etc. more than 30 large dammed lakes, its potentially dangerous consequences are difficult to be predicted (Yin 2008; Cui et al. 2009).

Distribution Characteristics of Super-Scale Landslide in Wenchuan Earthquake

The distribution of super-scale landslide was dually controlled by fracture and landform

1. Distribution characteristics of landform

All the 33 super-scale landslides triggered off by Wenchuan Earthquake were all distributed in the medium and low geomorphologic region of the Longmen mountains; the landform of the local area where the landslide happened was high and steep, and the crest elevation of the landslides was averagely over 1,000 m, and almost 90 % were distributed on the elevation of 1,000 ~ 1,800 m; the highest Daguangbao landslide was over 3,000 m (Fig. 2). The mountains where the landslide happened were comparatively and generally steep, and were distributed on the inclined slope of 20° ~ 60° unevenly. Among which the mountain with the slope of 25° ~ 29° grew the landslide maximally and accounted for 1/4 of the total number; 27 landslides were happened at the landslide of 25° ~ 45° and it was 80 % of the total numbers of landslides (Fig. 3).

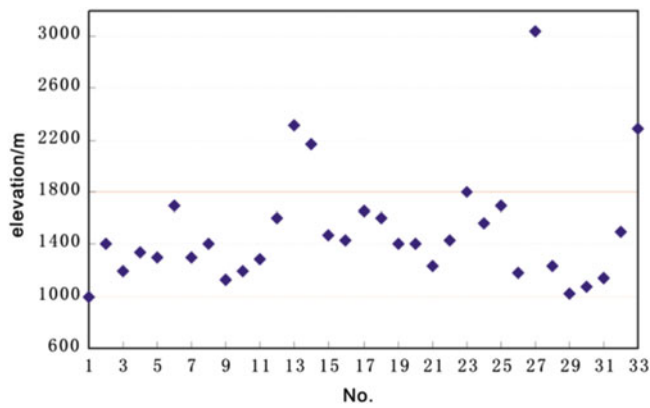


Fig. 2 Landslide top elevation charts

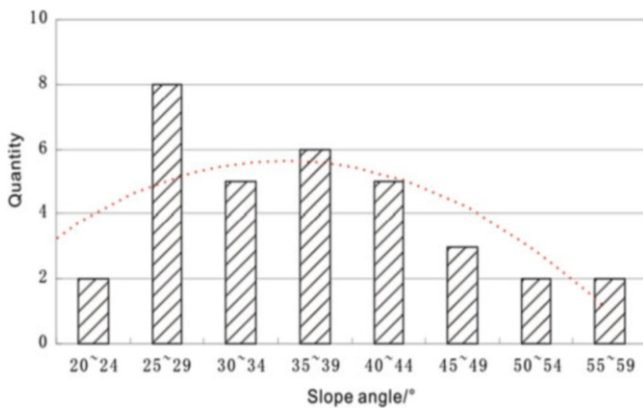


Fig. 3 Landslide slope angle charts

According to the investigation, it was found that the super-scale landslides triggered by Wenchuan Earthquake were distributed at the highly steep slope of branch ditch's origin or the concave banks of rivers. Such landform magnified the earthquake apparently (Zhang et al. 1994; Gao 1979); and the local landform has the apparent round-backed armchair pattern and the broadly open free face, but has no obstruction along the slope direction; all these topographic features provide the advantageous topographic conditions for the high-speed, long-distance and fluidized movement of the landslides.

2. Relation to fracture structure

The distribution of the super-scale landslides triggered by Wenchuan Earthquake were almost distributed in the principal fault zone of the Mt. Longmen, and over 90 % super-scale landslides were mainly distributed in the areas where the earth surfaces were seriously damaged by Wenchuan Earthquake, but there were only two landslides, namely Zhanggui landslide (in Maoxian County) and Miaoping landslide (in Nanjiang County) were distributed on the secondary minor fault. Due to the geographic position where they are far away from the principal fault zone, they are not

damaged too much, but several earthquake fissures with different depth run through their slope.

The asymmetric fracture in the Mt. Longmen causes very apparent hanging side/heading side effect (Huang and Li 2008) to the difference in surface damage, where 27 landslides were distributed at the hanging side (accounting for 80 % or above) and 6 at the heading side. Along the extension direction of the fault zone, the quantity and density of the super-scale landslide increased in the north-eastwards direction of Yingxiu town in the focal area, where three dense landslide belts (zones) were formed, i.e.: Shifang—Mianzhu, Anxian County—Beichuan, and Pingwu—Qingchuan, averagely 13.6 landslides per 100 km. Among which there were the mostly dense landslides in the area of Anxian County-Beichuan, where it was 24.7 landslides per 100 km. As the area approaches to the end of the seismogenic fault, the number of the landslide reduces gradually (Fig. 1). Such statistical results prove the seismic Doppler effect (Chen 2008) proposed by the academician Chen Yuntai.

There is close correlation between the distribution of super-scale landslide and relevant seismic parameters

1. Relation among landslide distribution, seismogenic fault and focal position

In accordance with the results of research on the earthquake source mechanism of Wenchuan Earthquake, the seismogenic fault of Wenchuan Earthquake was a central fault (Yingxiu—Beichuan fault), with the direction of 220°, the inclination 120° and the dip angle 39°; where the seismic wave was spread in the north-eastwards direction along the fault zone (Pan 2008; Li et al. 2008, 2009). 33 super-scale landslides were averagely distributed in the area 90 km away from the seismogenic fault, where over 90 % super-scale landslides were distributed within the area of 10 km at both sides of the seismogenic fault (Figs. 1 and 4).

In view of the characteristic of Wenchuan Earthquake, namely Wenchuan Earthquake happened at multiple points, two meizoseismal areas, i.e.: Yingxiu and Beichuan, were selected as the macroscopic epicenter. Based on Fig. 4, it can be seen that most of landslides were distributed within the area 100 km away from the epicenter. In accordance with the line epicenter measurement proposed by Li et al. (2009), most of the super-scale landslides triggered off by Wenchuan Earthquake were within the area 15 km away from the epicenter; where the number of the landslide reduces sharply as the distance away from the epicenter increases.

2. Super-scale landslide and intensity distribution

The maximum intensity of Wenchuan Earthquake is XI. Based on Figs. 1 and 5, it can be seen that the super-scale landslides of Wenchuan Earthquake were averagely distributed in the area with the intensity of VII or above; the number of the super-scale landslide increased as the

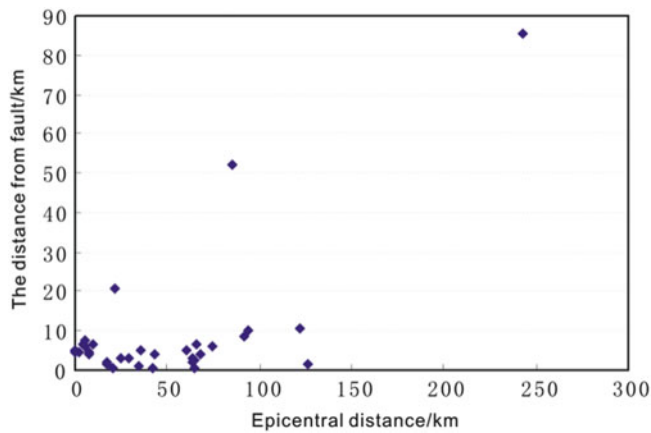


Fig. 4 Landslide and seismic fault/epicenter distance

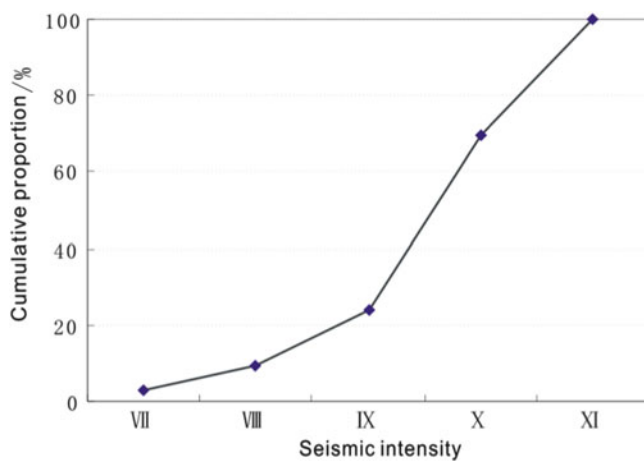


Fig. 5 Large landslide cumulative distribution curve of different seismic intensity

distance to the area of high intensity reduced. Among which 25 super-scale landslides were grown in the area of the intensity X and XI, accounting for 3/4 of the total super-scale landslides, and both of them were the areas where the super-scale landslides grew maximally (Fig. 5). The landslides merely 3 in the area of intensity VII and VIII, less than 10 % of the total; moreover the degree of damage to the landslide was not as obvious as that of the area of high intensity; especially 2 landslides in the area of intensity VII did not move wholly, but certain slope got fissure or sedimentation.

The direction of the super-scale landslide is in conformity with the tectonic stress direction

By investigation and analysis on the main sliding direction of landslide, it can be found that the dominated sliding direction of the super-scale landslides triggered off by Wenchuan Earthquake was NW-SE; which was almost perpendicular to the trend of the seismogenic fault; some landslides slid almost along the fracture direction (Fig. 6).

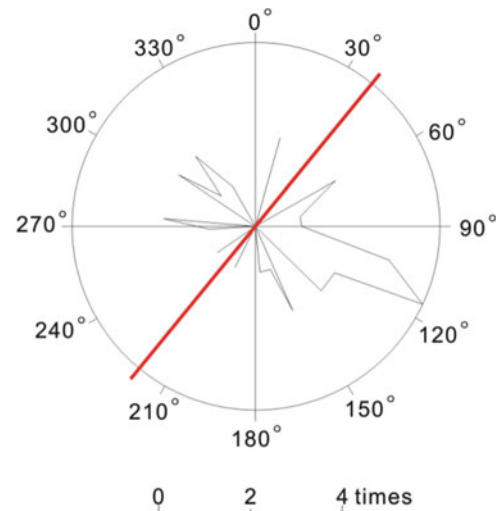


Fig. 6 Rose of the main sliding direction of landslide (red line stand for the main fault strike)

Based on Fig. 1, it can be seen that the sliding direction of the landslides at the hanging side was SE, but the one at the heading side was relatively NW. The landslides happened not only in the spread direction of the seismic wave (Zhang et al. 1994), but also in the “head seismic slope”; where the one at the hanging side is more apparent.

Du et al. (2009) made sliding data inversion for post-earthquake fracture in the research area, where the tectonic stress tensor shows the characteristics of the modern tectonic stress field in the Mount. Longmen area (the latest tectonism period): maximum principal compressive stress direction $76^{\circ} \sim 121^{\circ}$ and close to the EW (Du et al. 2009). By comparing with Fig. 6, it can be seen there is good consistency between the sliding direction of the super-scale landslides and the stress direction of the fault zone (triggered off and caused by Wenchuan Earthquake).

According to the advantageous direction of landslides, it can be taken as a way of researching regional tectonic stress field (Zou et al. 1994). Likewise, if the characteristics of the tectonic stress field of a region are known, the advantageous direction of the seismic landslide or other disaster caused by intense earthquake can be estimated, which is beneficial for the research how to forecast, prevent and relieve the seismic hazard, but also can be used as the reference how to prevent and relieve the geological disasters caused by the earthquake.

Conclusions

1. The super-scale landslide is the response of the inclined slope of sensitive mountains in the earthquake region to $M_s 8.0$ Wenchuan Earthquake; which reflects the degree of seismic damage objectively and directly. Over 90 % landslides happened in the 240 km

principal surface fault zone of Wenchuan Earthquake, and were densely distributed within 10 km at both sides of the seismogenic fault.

2. The super-scale landslide is dually restrained by the fault zone of Wenchuan Earthquake and the local landform. The seismic fault zone dominated the landslide areas and its tectonic stress field decided the advantageous direction of landslides; the medium-mountain landform and the steep landform control the distribution position of super-scale landslides.
3. The predominant direction of the super-scale landslide of Wenchuan Earthquake is NW-SE, which is almost perpendicular to the trend of the seismogenic fault and is in conformity with the stress direction of the fault zone. Such predominant direction is beneficial for us for making analog and reference for the regional seismic landslide research, and disaster prevention and relief.

Acknowledgments This work was supported by land and resources investigated project of China Geological Survey (No. 1212010740309). Hua Ge, Hongfu Zhou, Qiguo Chen, Yongbo Tie, Ping Sun, et al. participated in field survey. Professor Wenyu Fan, Researcher Minghui Li and Engineer Renji Ba provided significant assistance. At this point, to express our heartfelt gratitude for their help.

References

- Chen YT (2008) Reasons, rupture process and mechanism of disaster of Wenchuan earthquake. Tenth annual meeting of China Association of Science and Technology invited report. <http://it.sohu.com/20080918/n259628307.shtml> [2008.9.18]
- Cui P, Han YS, Chen XQ et al (2009) Distribution and risk analysis of dammed lakes induced by Wenchuan earthquake. *J Sichuan Univ (Engineering Science Edition)* 41(3):35–42
- Du Y, Xie FR, Zhang XL et al (2009) The mechanics of fault slip of Ms8.0 Wenchuan earthquake. *Chin J Geophys* 52(2):464–473
- Gao ZH (1979) Analysis on distribution of intensity anomalies in the Beijing region caused by the Tangshan Earthquake. *Seismol Geol* 1(2):74–82
- Huang RQ, Li WL (2008) Research on development and distribution rules of geo-hazards induced by Wenchuan Earthquake on 12th May, 2008. *Chin J Rock Mech Eng* 27(12):2585–2592
- Huang RQ, Pei XJ, Li TB (2008) Basic characteristics and formation mechanism of the largest scale landslide at daguangbao occurred during the Wenchuan earthquake. *J Eng Geol* 16(6):730–741
- Li ZQ, Yuan YF, Li XL et al (2008) Some insights into the macro-epicenter and meizoseismal region of Wenchuan earthquake. *Seismol Geol* 30(3):768–777
- Li Y, Huang RQ, Zhou RJ et al (2009) Geological background of Longmenshan seismic belt and surface ruptures in Wenchuan earthquake. *J Eng Geol* 17(1):3–18
- Ministry of Land and Resources of the People's Public of China (MLR) (2006) Specification of geological investigation for landslide stabilization (DZ/T 0218-2006):1–4
- Pan GT (2008) Regional geological and tectonic background of Wenchuan earthquake. *Decis Mak Advis Newslett* 2008(3):1–8
- Yin YP (2008) Researches on the geo-hazards triggered by Wenchuan earthquake, Sichuan. *J Eng Geol* 16(4):433–444
- Yin YP (2009) Rapid and long run-out features of landslides triggered by the Wenchuan earthquake. *J Eng Geol* 17(2):153–166
- Zhang ZY, Wang ST, Wang LS (1994) Principles of engineering geological analysis. Geological Publishing House, Beijing, 181p, ISBN: 9787116013322
- Zou JC, Shao SM, Jiang RF (1994) Distribution and tectonic implications on the Gulang seismic landslide. *Earthq Res China* 10(2):168–174



Large Slope Instabilities in Northern Chile: Inventory, Characterization and Possible Triggers

Giovanni B. Crosta, Reginald Hermanns, Paolo Frattini, Elena Valbuzzi, and Andrea Valagussa

Abstract

The Western slope of the Andes of Northern Chile is characterized by intense seismicity. The W Escarpment and Precordillera are formed by coarse-grained clastic and volcanoclastic formations. The area has been characterized by a long-term hyper-aridity (Atacama Desert) and its evolution has been characterized by canyon incision into Tertiary paleosurfaces and large slope instabilities. These occurred in the “interfluvial” sectors of the western escarpment and Precordillera, and along the canyon flanks. Landslides affecting the preserved paleosurfaces, dissected by the parallel drainage network, involve volumes of various cubic kilometres and control the drainage network. These mega landslides locally evolved in large rock avalanches. Landslides along the canyon flanks affect volumes generally up to 1 km³ and have been reincised. We present a landslide inventory in the area between Pisagua (19.4° Chile) and Tacna (17.5° Peru) to the NE of the Arica bend. Volume estimates and slope stability modelling have been completed to characterize the phenomena and the possible trigger mechanisms.

Keywords

Northern Chile • Large landslides • Canyon • Erosion • Inventory • Trigger

Introduction

Very large landslides are generally limited in number and their areal density is usually low. Some examples have been described in the literature under different geological and environmental conditions (Abele 1974; Philip and Ritz 1999; Strom and Korup 2006; Penna et al. 2011; Huang and Fan 2013) and some are unique events associated to volcanic edifices. These phenomena can be controlled by extremely strong perturbations or trigger factors

characterized by a very low frequency of occurrence. Therefore, it can be considered a peculiar condition to find exceptionally large landslides with a relatively high density in a well-delimited area. Under these conditions, the presence of very large landslides can strongly control the slope and drainage evolution. In addition, it significantly contributes to erosion resulting in a series of geomorphological evidences both downstream and upstream to the landslide site. Therefore, it becomes important to evaluate the recurrence time, the trigger and predisposing factors to which the occurrence of these phenomena can be associated.

The western slope of the Andes of northern Chile—southern Peru, forming the modern Andean forearc, is characterized by intense seismicity, associated to the subduction of oceanic Nazca plate below the S-American continent at rates between 63 and 84 mm a⁻¹. This area is subdivided, from west to east, in four main morpho-tectonic units: Coastal Cordillera, Central Depression, W-Precordillera and W Cordillera. The Atacama Desert in Northern Chile is characterized

G.B. Crosta (✉) • P. Frattini (✉) • E. Valbuzzi (✉) • A. Valagussa (✉)
Dipartimento di Scienze Geologiche e Geotecnologie, Università degli Studi di Milano Bicocca, Milan, Italy
e-mail: giovannibattista.crosta@unimib.it; paolo.frattini@unimib.it; elena.valbuzzi@unimib.it; a.valagussa2@campus.unimib.it

R. Hermanns
Norges Geologiske Undersøkelse (NGU), Trondheim, Norway
e-mail: Reginald.Hermanns@NGU.NO

by the presence of a hierarchized drainage network cutting through the Precordillera, the Central Depression and the Coastal Cordillera. The large and deep canyons in the lower half of the valleys suggest an important base level lowering. At the same time, the exceptional long term hyper-aridity (probably since Middle Miocene) of the Atacama Desert, and attributed to different causes (e.g. cold upwelling Humboldt Current, Andean rain-shadow effect), is the cause of the preservation of many landforms typical of this landscape. The canyon incision in this part of the Andes has been a recent subject of various studies (Schlunegger et al. 2006; Thouret et al. 2007; Hoke et al. 2007; García et al. 2011) and some suggest the presence of lakes in the Central Depression between Late Miocene and Early Pliocene (Kirk-Lawlor et al. 2013), and so of a possibly wetter climate with respect to present day hyperaridity. This then relates to different mechanisms responsible for the late valley incision.

Few studies on selected mega-landslides show that they occur along the Precordillera slope and sectors with minor valleys affecting mainly interfluvial slopes at the macro scale. These major landslides seem to be controlled by the presence of important NNW trending open fractures and graben like features with a relevant longitudinal continuity (up to 8–9 km). These coincide, in the northernmost part, with the western side of the Oxaya block, characterized by an eastward back-tilting (Minimini and Latagualla landslides, Pinto et al. 2008; Lluta collapse, Strasser and Schlunegger 2005). A completely different type of landslides is observed along the main fluvial valleys cutting deeply through the Precordillera and the Central Depression to reach the Pacific Ocean through the Coastal Cordillera. These valleys are 10–25 km apart from each other.

In the paper, we first describe the study area and some specific issues that are important for the interpretation of the landslide distribution; then, we present a landslide inventory of the area, and finally we investigate the possible seismic trigger.

Study Area

The study area is located in the Northern Chile forearc. It extends between Iquique (19.4°) and Arica (10.0°), and from West to East including the Coastal Cordillera (up to average elevation of 1,500 m a.s.l.), the Central Depression (500–2,300 m a.s.l.) and the Precordillera (up to 3,700 m a.s.l.). These last two are often defined as the Atacama Padiplain and characterised by an interfluvial denudation rate extremely low in the last 6 Ma (Kober et al. 2007). The area of interest for this study is characterized by extremely low precipitations (Arica: 0.5 mm a⁻¹; Iquique: 0.6 mm a⁻¹; Quezada et al. 2010) close to the coast to about 300 mm a⁻¹ in the upper part of the Western Cordillera.

Seismicity in the area is extremely high: this sector of Northern Chile is well known as the Iquique Gap, lacking a major earthquake since 1868/1877 (Kausel and Campos 1992).

The W Escarpment and Precordillera are formed by a coarse-grained clastic formation (conglomerates and sandstones of the Azapa Formation) and volcanoclastic (Oxaya Ignimbrite, rhyolitic-dacitic tuffs, Oligocene and Miocene in age, 26 to 17 Ma), and fluvial deposits (Huaylas and El Diablo Formations.), up to the present day surface (upper El Diablo Formation., 13.7 to 8.3 Ma), in a homoclinal setting (Sucuna homocline, dipping 2–3° to the W). This homocline is affected by NW and NS trending folds (Hauyillillas, Oxaya Anticline from N to S, in the northern sector) about 1 km in amplitude, bounded to the W by the Ausipar Fault, and flexures (Humayani, Moquella and Aroma-Soga to the S) along the Precordillera western limit.

The river network is exorheic in our study area but becomes endorheic to the south, with a trellis to subdendritic pattern moving from north to south (García et al. 2011). A clear zonation of the drainage network can be observed moving downstream from the Western Cordillera towards the Pacific Ocean.

The Precordillera area is characterized by a densely incised (up to 200–250 m deep), poorly organized, parallel drainage network of which wide remnants can be found both in the Chilean and Peruvian territory. This part of the drainage network develops within the Oxaya Formation, and some of the lavas, allowing a dating for the incision ranging between 15 ± 0.6 Ma and 11.2 ± 0.6 Ma, and allowing to relate this with at least part of the El Diablo Formation deposition. The network converges downstream within few deep valleys and subsequently in a single deep canyon cutting through the Coastal Cordillera. These canyons must be younger than 11 Ma and the presence of some ignimbrite layers, dated to 2.7–2.9 Ma, constrains the canyon incision in the Central Depression before Late Pliocene. Nevertheless, not everywhere, such evidences can be found and a different time for the onset of canyon incision is possible moving from North to South. The longitudinal river profiles are characterized by streams with knickpoint bounded segments (Hoke et al. 2007) commonly attributed to localized tectonic disturbance or to the regional uplift. The initiation of the knickzones has been ascribed to folding and faulting, or to a general surface uplift in the Precordillera and tilting of the Western Escarpment. The gently W-dipping Central Depression has been filled by a sequence of Oligo-Miocene sediments and ignimbrites in a sub-horizontal setting with gentle NW trending Neogenic folds and flexures, exposed along the canyon walls. Knickpoint position change moving N to S (Hoke et al. 2007; García et al. 2011; Kirk-Lawlor et al. 2013) with respect to the coastline further supporting a possible time difference for the onset of incision. Incision in

the Central Depression ranges between 300 and almost 1,050 m, with larger values in the western sectors, and the incision rate ranges between 25 and 120 m Ma⁻¹ (García and Herail 2005; García et al. 2011; Farias et al. 2005). For the Precordillera part of the drainage network, two rates can be defined for the parallel poorly organized part (50–60 m Ma⁻¹) and for the more recent canyons for which different rate values can be estimated for different time intervals, with up to fourfold increases (50–270 m Ma⁻¹, García and Herail 2005; García et al. 2011).

Landslides Chronology

Actually, no dating is available for the landslides along the canyon flanks. Nevertheless, some age constrains can be proposed relative to the pediment surface, ignimbritic deposits and strath terraces along the canyons, canyon incision rates and the migration of the knickpoints within the valleys. Pediplain surface age (ca 7–8 Ma) and ignimbritic deposits some tens of meters above the valley bottom (ca 2.5 Ma) give two initial constrains. Incision rates range between 25 m and 137 m Ma⁻¹. In general, it has been suggested that valley incision tends to start later and proceed slower moving southward in the area (Hoke et al. 2007). This is supported by the main knickpoints position with respect to the valley outlet, assuming a linear retrogression of the knickpoints, constant climatic conditions and a minor role of geological and lithological constrains.

For the exorheic valleys, from the Azapa to the Tiliviche valley (northern area, Fig. 1), the distance ranges between 120 and 75 km (so 10 to ca 17 km Ma⁻¹), whereas for the endorheic valleys, from Tarapaca to Ramada (southern area, Fig. 1), it ranges between 75 and 25 km (3.6 to 10.7 km Ma⁻¹). Therefore, assuming a progressive linear increase in time along the valley profile, we could determine the approximate maximum age for each of the landslides along the valley flanks.

At the same time, we should consider some more options: the uniform incision through the entire valley length, at rates slightly changing from West to the East; the fact that some landslide toe lies well above the valley bottom and could have occurred at earlier stages of valley incision. Due to the width (parallel to the river course) of some of the landslides, the total time needed to completely clear the landslide toe and the failure to occur can be quite long with the given erosion/incision rates. For the same reason, failures could have progressively propagated upstream with valley erosion. In this last condition, the groundwater level within the slopes could have been higher than along a well-developed valley flank, so favouring the failure process.

Inventory

The landslide inventory covers an area about 220 km long and 80 km wide, between Iquique and Arica. We mapped landslides, main tectonic structures and other morphological features. Mapping has been performed by use of satellite images and direct field surveys.

A total of 379 landslides have been mapped in the area, prevalently including large phenomena. The landslide area ranges from 2×10^{-3} km² to 464 km² (Lluta landslide). The total area, inclusive of the landslide scarp and of the deposit amounts to about 1.77×10^3 km².

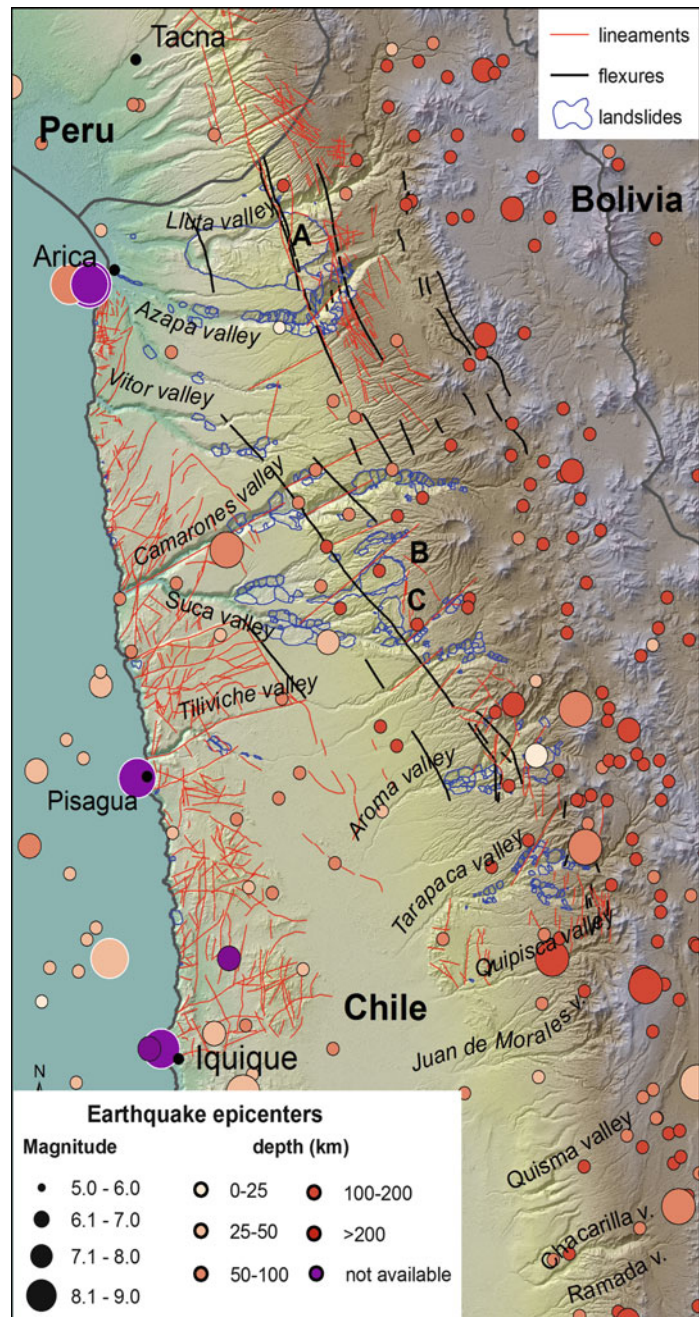
The mega landslides already described in the literature (Strasser and Schlunegger 2005; Pinto et al. 2008) can be classified as large block slides that can evolve in large rock avalanches (e.g. Minimini). Their initiation seems to be strongly associated to the presence of secondary faults and large fractures transversal to the slope. These landslides show evidence suggesting a re-incision by the main canyon network. This seems particularly true for the Lluta collapse where the main “landslide” mass is masked or deleted by the successive erosion. These landslides have been associated mainly to the uplift in the Precordillera (Pinto et al. 2008). Other landslides have been mapped along the Coastal Escarpment and some of the major tectonic escarpments with an E-W trend.

We examined area-frequency distributions of landslides by developing logarithmically binned, non-cumulative size frequency distributions that report frequency density ($f = dN/dA$) as a function of landslide planar area A ($dN =$ number of landslides with an area between A and $A + dA$). The size frequency distribution presents a strong undersampling for smaller landslides, due to the extremely old age of the inventory. For landslides larger than 2×10^6 m², the distribution exhibits a power-law behaviour with scaling exponent, β , equal to -2.24 (Fig. 3).

For comparison, we analyzed the power-law behavior of other earthquake-induced landslide inventories, obtaining similar results, although the geological and seismic conditions may have been very different (Buller, New Zealand, $\beta = -2.42$; Iningahua, New Zealand, $\beta = -2.53$; Northridge, USA, $\beta = -2.39$; Chi-Chi, Taiwan, $\beta = -2.30$; Wenchuan Earthquake, China, $\beta = -2.19$). Landslides along the canyon flanks affect volumes generally lower than 1 km³ and can be mainly classified as large compound slides, complex phenomena and in some cases lateral spreading, supposedly by multiple retrogressive failure events with a relatively long spreading so that deposits often cross or develop along the valley bottom and have been re-incised exposing undeformed bedrock material.

Volume estimates and slope stability modelling have been completed to characterize the phenomena and the

Fig. 1 Study area and landslide inventory (A: Lluta landslide; B: Minimini landslide; C: Latagualla landslide). Earthquake epicenters: post-1900, from USGS ANSS Comprehensive Catalogues (circles with black outline); pre-1900, from Centro Sismológico Nacional, Universidad de Chile (circles with white outline). Flexures from 1:1.000.000 geological map of Chile. Lineaments from photointerpretation



possible trigger mechanisms. Evidences of sharp shear zones at the base of the landslides have been collected and material tested. Large boulder fields and alluvial deposits infill the lower part of the canyons suggesting a long history of dam breaching events.

Seismic Trigger

The northern Chile area is subject to a high seismicity associated to earthquakes of different type: interplate (superficial and intermediate depth), subduction zone earthquakes.

Shallow thrust earthquakes have been historically the most important with magnitude above 8 and return periods around 80–130 years. Megathrust earthquakes have a longer return period. Therefore, it is interesting to analyse the possible landslide triggering by seismic activity and by different seismogenic structures. In the Central Depression and Precordillera areas some superficial earthquakes are associated to east verging fault planes and to the flexures present in the area.

By analysing the frequency size relationships for earthquake-induced landslides from literature, it is possible to observe that the higher the earthquake Magnitude, the

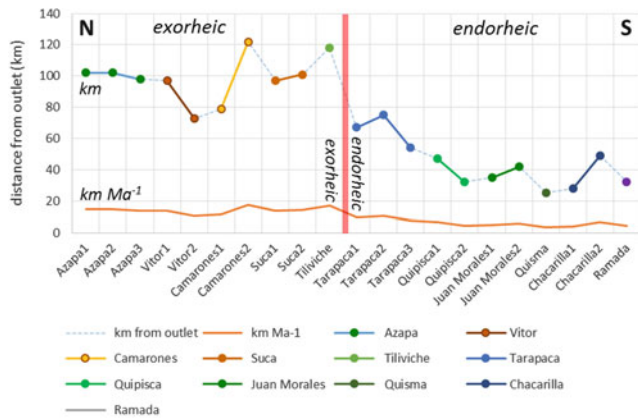


Fig. 2 Distance of river knickpoints from the coastline. See Fig. 1 for river location following the approach by Hoke et al. (2007)

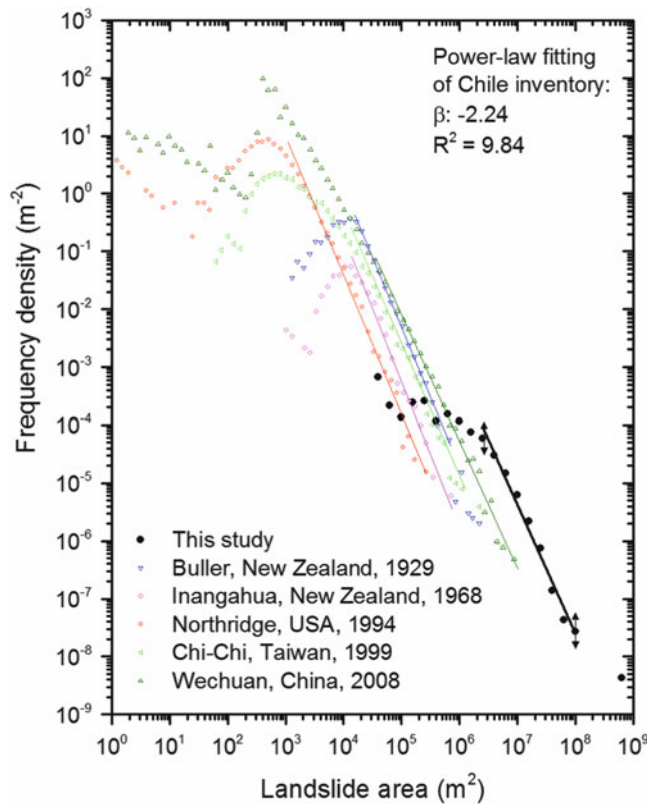


Fig. 3 Frequency density vs. area for the Chile inventory (black dots) and other earthquake-induced landslide inventories from the literature (Buller and Iningahua, Parker 2013; Northridge, Harp and Jibson 1995; Chi-Chi, Liao and Lee 2000; Wenchuan, Parker 2013). Lines represent the fitting curves of the power-law range of each inventory

higher the frequency density curve. To quantify this observation, we used the power-law relationships derived for each inventory to calculate the frequency density associated to selected areas, and we plotted these frequencies as a function of the magnitude of the respective earthquakes (Fig. 4). For

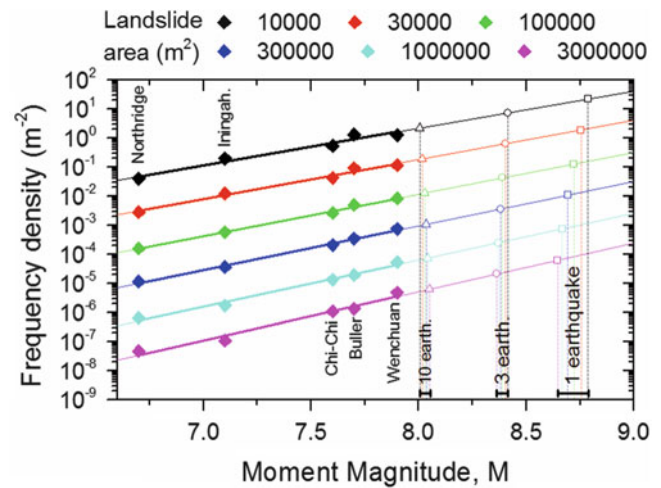


Fig. 4 Relationship between the earthquake Magnitude and the frequency density, f , for earthquake-induced landslides. The extrapolated linear relationships between magnitude and $\log(f)$ was used to calculate the expected Magnitude of earthquake (or multiple earthquakes) required for Chile landslides trigger

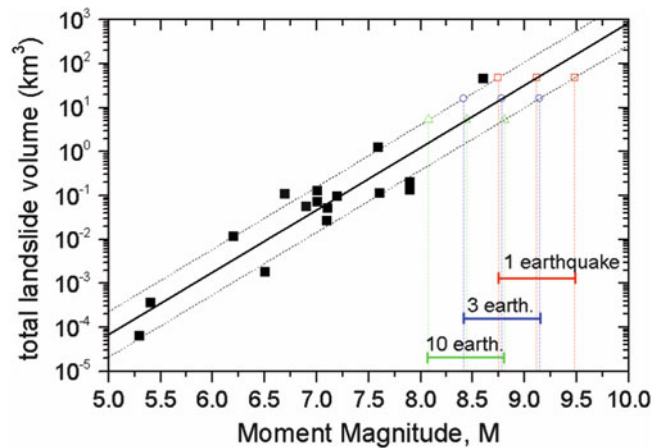


Fig. 5 Relationship between the earthquake Magnitude and the total landslide volume of earthquake-induced landslides. The fitting line (Malamud et al. 2004) was used to calculate the Magnitude of earthquake (or multiple earthquakes) required for Chile landslides

each area value, a clear linear trend exists between earthquake magnitude and logarithm of landslide frequency density. By using these fitting curves and the frequency density of Chile inventory for the selected areas, we derived the Magnitude required to generate such landslide distribution.

The three largest landslides (Lluta, Minimini and Latagualla) have been excluded from this analysis.

For this, we considered three possible scenarios: (1) all landslides triggered during 1 single earthquake; (2) landslides triggered during three equal-magnitude earthquakes; (3) landslides triggered during ten equal-magnitude earthquakes. As a results, we obtained an estimated earthquake magnitude of 8.71 ± 0.05 ,

8.39 ± 0.02 , 8.03 ± 0.02 for scenario 1, 2 and 3, respectively. In order to validate these values, we applied to our inventory a relationship between earthquake Magnitude and total landslide volumes, as reported in Keefer (1994) and Malamud et al. (2004) (Fig. 5).

By introducing the total volumes of landslides calculated from areas by using the relationship proposed by Larsen et al. (2010) for rock slides, we obtained an estimated earthquake magnitude of 9.11 ± 0.36 , 8.77 ± 0.36 , 8.40 ± 0.36 for scenario 1, 2 and 3, respectively. These values are slightly higher than the values estimated above, but this can be due to difficulties to estimate correctly the volumes. In fact, in order to obtain the same magnitudes, the total volume should be about 20 km^3 .

Conclusions

We studied slope instabilities in the Central depression of the western Andean Escarpment, one of the most seismic areas in the world. These landslides are of different types: translational and rotational slides along the main canyons, rockfalls and avalanches. Their size is generally extremely large and this could be attributed to a possible trigger by past strong earthquakes as suggested by the global distribution of mega landslides (Strom and Korup 2006).

Jibson and Keefer (1989) suggests that large to mega landslides are frequently triggered by longer duration shaking, generally related to earthquakes of larger magnitude. The type of observed failures resembles very much some coastal bluff instabilities, affecting sub-horizontal layered deposits characterized by the presence of basal weak layers (Hutchinson 1969; Jibson and Keefer 1989; Le Cossec et al. 2011).

Evolution of these landslides is controlled by:

- Deep valley incision, canyon walls undercutting and lateral migration of the river controlled by valley flank instabilities.
- Presence of weak lithologies and weak basal layers.
- River incision debuttruss the slope toe and especially brings to daylighting the weak basal layers observed at some landslide sites.
- Possible deep groundwater flow above the deep impermeable formations and clay layers.
- Movement along sub-horizontal basal shear zones which can be locally extruded at the slope toe.
- River damming because of the strong lateral components of displacement and successive reincision by the river with dam failure.
- Possible sequence of reactivations by reincision of the deposit.
- The occurrence of high magnitude (8–9) earthquakes as suggested by the analysis of landslide frequency area distributions in comparison with available datasets.

References

- Abele G (1974) Bergstürze in den Alpen. Wissenschaftl. Alpenvereinshefte Nr. 25: 230 p
- Farias M, Charrier R, Comte D, Martinod J, Hérail G (2005) Late Cenozoic deformation and uplift of the western flank of the Altiplano: evidence from the depositional, tectonic, and geomorphologic evolution and shallow seismic activity (northern Chile at 19 degrees 30'S). *Tectonics* 24. <http://dx.doi.org/10.1029/2004TC001667>
- García M, Hérail G (2005) Fault-related folding, drainage network evolution and valley incision during the Neogene in the Andean Precordillera of Northern Chile. *Geomorphology* 65:279–300
- García M, Riquelme R, Farias M, Hérail G, Charrier R (2011) Late Miocene-Holocene canyon incision in the western Altiplano, northern Chile: tectonic or climatic forcing? *J Geol Soc* 168 (4):1047–1060
- Harp EL, Jibson RL (1995) Inventory of landslides triggered by the 1994 Northridge, California Earthquake. <http://pubs.usgs.gov/of/1995/ofr-95-213>, U.S. Geological Survey Open File Report 95-213
- Hoke GD, Isacks BL, Jordan TE, Blanco N, Tomlinson AJ, Ramezani J (2007) Geomorphic evidence for post-10 Ma uplift of the western flank of the central Andes 18°30'–22°S. *Tectonics* 26:TC5021
- Huang R, Fan X (2013) The landslide story. *Nat Geosci* 6:325–326
- Hutchinson JN (1969) A reconsideration of the coastal landslides at Folkestone Warren, Kent. *Geotechnique* 19:6–38
- Jibson RW, Keefer DK (1989) Statistical analysis of factors affecting landslide distribution in the new Madrid seismic zone, Tennessee and Kentucky. *Eng Geol* 27:509–542
- Kausel E, Campos J (1992) The Ms = 8 tensional earthquake of December 1950 of northern Chile and its relation to the seismic potential of the region. *Phys Earth Planet Int* 72:220–235
- Keefer DK (1994) The importance of earthquake-induced landslides to long-term slope erosion and slope-failure hazards in seismically active regions. *Geomorphology* 10:265–284
- Kirk-Lawlor NE, Jordan TE, Rech JA, Lehmann SB (2013) Late Miocene to Early Pliocene paleohydrology and landscape evolution of Northern Chile, 19° to 20° S, Palaeogeography, Palaeoclimatology, Palaeoecology 387: 76–90. <http://dx.doi.org/10.1016/j.palaeo.2013.07.011>
- Kober F, Ivy-Ochs S, Schlunegger F, Baur H, Kubik PW, Wieler R (2007) Denudation rates and a topography-driven rainfall threshold in northern Chile: multiple cosmogenic nuclide data and sediment yield budgets. *Geomorphology* 83:97–120
- Larsen JJ, Montgomery DR, Korup O (2010) Landslide erosion caused by hillslope material. *Nat Geosci* 3:247–251
- Le Cossec J, Duperré A, Vendeville B, Taibi S (2011) Numerical and physical modelling of coastal cliff retreat processes between La Hève and Antifer capes, Normandy (NW France). *Tectonophysics* 510:104–123
- Liao HW, Lee CT (2000) Landslides triggered by the Chi-Chi earthquake. Asian conference on remote sensing
- Malamud BD, Turcotte DL, Guzzetti F, Reichenbach P (2004) Landslides, earthquakes, and erosion. *Earth Planet Sci Lett* 229:45–59
- Parker RN (2013) Hillslope memory and spatial and temporal distributions of earthquake-induced landslides. Durham theses, Durham University
- Penna LM, Hermanns RL, Niedermann S (2011) Multiple slope failures associated with neotectonic activity in the Southern Central Andes (37°–37°30'S), Patagonia, Argentina. *Geol Soc Am Bull* 123 (9–10):1880–1895
- Philip H, Ritz J-F (1999) Gigantic paleolandslide associated with active faulting along the Bogd fault (Gobi–Altay, Mongolia). *Geology* 27:211–214

- Pinto L, Hérail G, Sepúlveda SA, Krop P (2008) A Neogene giant landslide in Tarapacá, northern Chile: a signal of instability of the westernmost Altiplano and palaeoseismicity effects. *Geomorphology* 102:532–541
- Quezada J, Cerda JL, Jensen A (2010) Efectos de la tectonica y el clima en la configuracion morfologica del relieve costero del norte de Chile. *Andean Geol* 37:78–109
- Schlunegger F, Zeilinger G, Kounov A, Kober F, Husser B (2006) Scale of relief growth in the forearc of the Andes of Northern Chile (Arica latitude, 18 degrees S). *Terra Nova* 18:217–223
- Strasser M, Schlunegger F (2005) Erosional processes, topographic length-scales and geomorphic evolution in arid climatic environments: the ‘Lluta collapse’ northern Chile. *Int J Earth Sci (Geol Rundsch)* 94:433–446
- Strom AL, Korup O (2006) Extremely large rockslides and rock avalanches in the Tien Shan mountains, Kyrgyzstan. *Landslides* 3:125–136
- Thouret J-C, Worner G, Gunnell Y, Singer B, Zhang X, Souriot T (2007) Geochronologic and stratigraphic constraints on canyon incision and Miocene uplift of the central Andes in Peru. *Earth Planet Sci Lett* 263:151–166



A Preliminary Spatial Distribution Analysis of Landslides Triggered by the 2010 Haiti Earthquake

Chong Xu

Abstract

Over thirty thousands of landslides were triggered by the January 12, 2010 Haiti earthquake (Mw 7.0). Inventory of landslides triggered by the earthquake was constructed based on Geographic Information Systems (GIS) technology and visual interpretation of high-resolutions remote sensing images. It shows that at least 30,828 landslides occurred related to the earthquake over an area of about 3,200 km². These landslides cover a total area of 15,736 km². Correlations of landslides occurrence with controlling parameters were analyzed. Statistical analysis of these landslides spatial distribution using double indices, including, landslide number density (LND), defines as the number of landslides per one square kilometre, landslide area percentage (LAP), defines as the percentage of the area affected by landslides, to determine how landslides occurrence correlates with controlling parameters. This paper can give reference to landslide controlling parameters selecting for earthquake-triggered landslide hazard mapping. It can also give reference to scientists and policy makers for determining landslide susceptible ranks associated variable of landslide controlling parameters when earthquake in similar magnitude, rupture mechanism, topographic and geologic conditions in future.

Keywords

The 2010 Haiti earthquake • Landslides • Inventory • Landslide number density • Landslide area percentage

Introduction

Preparation of inventories of landslides triggered by recent earthquakes and subsequent landslides spatial distribution analyses are important research directions. Inventories of co-seismic landslides can provide basic dataset for future studies (e.g. Harp et al. 2011; Guzzetti et al. 2012), such as, landslide assessment (e.g. Xu et al. 2012a, b, c; Xu and Xu 2013), geomorphologic evolution (e.g. Keefer 1999; Parker et al. 2011) in earthquake struck areas, etc. And landslide

spatial distribution analysis can help us understanding where is the most easily response to landslides occurrence under probable earthquakes may occur in future. Keefer (1984) and Rodríguez et al. (1999) have analyzed landslides triggered by some historical worldwide earthquakes occurred before 1997. More recently, studies about landslide inventory compiling and landslide spatial distribution related to recent large earthquakes have been published, for example, several research teams produced inventory of landslides triggered by the May 12, 2008 Mw 7.9 Wenchuan earthquake (e.g. Xu 2012; Xu et al. 2009, 2010; Dai et al. 2011; Gorum et al. 2011; Parker et al. 2011; Qi et al. 2010), the most detailed and complete result (e.g. Xu et al. 2013a, b, c) showed that 197,481 individual landslides related to the Wenchuan earthquake were mapped as polygons. After the April 14, 2010 Mw 6.9 Yushu earthquake, result of emergency co-seismic

C. Xu (✉)

Key Laboratory of Active Tectonics and Volcano, Institute of Geology, China Earthquake Administration, Qijiahuozi, Deshengmenwai, P.O. Box 9803, Beijing 100029, China
e-mail: xc1111111@126.com; xuchong@ies.ac.cn

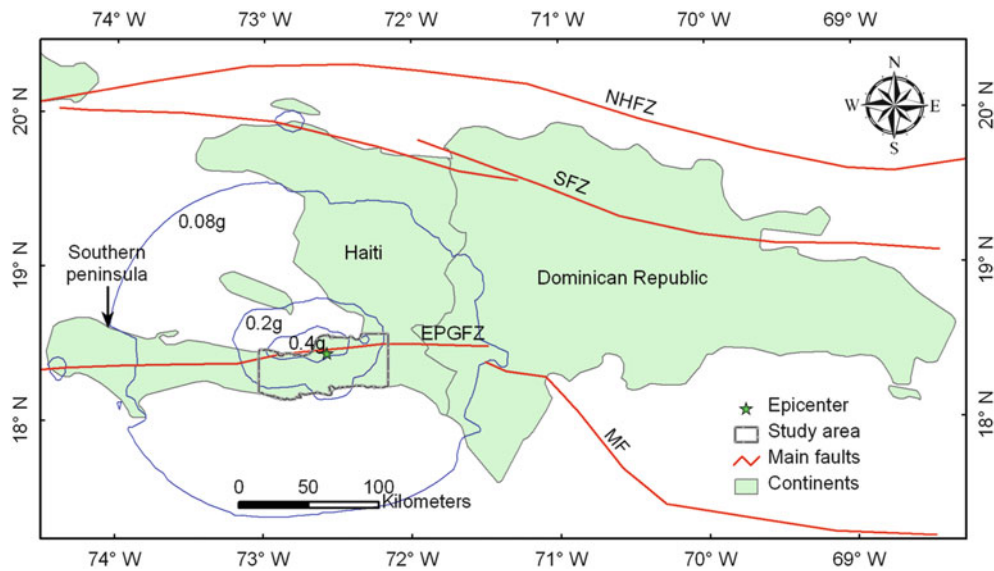


Fig. 1 Tectonic setting of the 2010 Haiti earthquake. Thin green lines show main PGA contour lines. Study area is similar to the approximate landslides limit line

landslide field surveys along main roads showed 282 landslides were triggered by the earthquake (Yin et al. 2010). Subsequently, a more completed landslides inventory contained 2,036 landslides (as polygons) was prepared by visual interpretation of aerial photographs and satellite images in high resolutions (Xu et al. 2012d, 2013d), and landslide hazard analysis (Xu and Xu 2012; Xu et al. 2012e) were carried out. Landslide inventory about other earthquakes were also prepared, such as the May 11, 2011 Mw 5.1 Lorca, SE Spain earthquake (Alfaro et al. 2012), the June 14, 2008 Iwate–Miyagi Nairiku, Japan Mw 6.9 earthquake (Yagi et al. 2009), the July 16, 2007 Niigata Chuetsu–Oki, Japan Mw 6.6 earthquake (Collins et al. 2012), the October 8, 2005 Mw 7.6 Kashmir earthquake (Sato et al. 2007), the October 23, 2004 Mw 6.6 Mid-Niigata, Japan earthquake (Chigira and Yagi 2006), the January 21, 2003 Mw 7.6 Tecomán, Mexico earthquake (Keefer et al. 2006), the September 21, 1999 Mw 7.6 Chi-Chi, Taiwan, China earthquake (Wang et al. 2002), etc. These publications provided very important case studies for co-seismic landslides research in future.

On January 12, 2010, a catastrophic earthquake with Mw 7.0 struck the Port-au-Prince region of Haiti. The epicenter was located at latitude $18^{\circ}27'25''\text{N}$, longitude $72^{\circ}31'59''\text{W}$ with a focal depth of 13 km, approximately 15 km southwest of Port-au-Prince according to USGS (<http://www.usgs.gov>). The earthquake killed more than 230,000 people and caused an estimated \$8 billion in damages, about 100 % of the country's gross domestic product (Calais et al. 2010). In addition, tens of thousands of landslides were triggered by the earthquake from interpretation of aerial photographs and

satellite images in high-resolutions. The main purpose of this paper is to preliminarily analyze spatial distribution of the landslides with slope angle, slope aspect, slope position, distance from drainages, distance from associated fault, and peak ground acceleration (PGA).

Tectonic Setting

From north to south, there are three main fault systems including the North Hispaniola fault zone (NHFZ), the Septentrional fault zone (SFZ), and the Enriquillo-Plantain Garden fault zone (EPGFZ). The three fault zones accommodate the Caribbean-North America relative plate motion in the north-eastern Caribbean (Fig. 1). The Haiti earthquake occurred near the Enriquillo-Plantain Garden Fault (EPGF), which is main structural feature that cuts through the centre of the southern peninsula of Haiti (Mann et al. 1984; Calais et al. 2010). Topographically, the fault is shown as a strong, linear, N85°E-trending element (Prentice et al. 2010). Mechanism of the Haiti earthquake included both thrust and left-lateral strike-slip movements (Jibson and Harp 2011). The earthquake was initially thought to have ruptured the EPGF. As we know, many shallow epicentre earthquakes with Mw 7.0 or greater can produce surface rupture of tens of kilometres, however, it showed that the Haiti earthquake did not produce surface rupture from satellite imagery and field investigations (Prentice et al. 2010). Conclusions in some publications (Calais et al. 2010; Hashimoto et al. 2011) showed that the earthquake ruptured an unrecognized and unmapped north-dipping fault (named

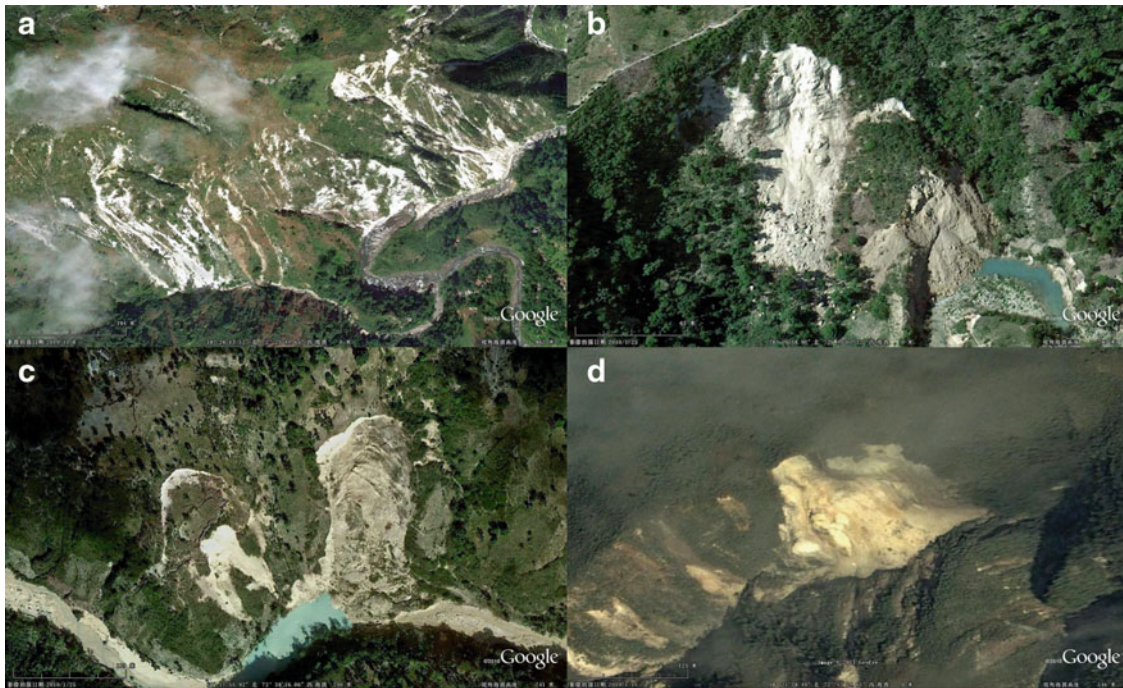


Fig. 2 Several typical landslides triggered by the earthquake. (a) Densely shallow-disrupted landslides, (b) a rock falls, (c) two deep-seated landslides, and (d) a rock avalanche



Fig. 3 Photos taken from helicopter (Jibson and Harp 2011). (a) Several landslides dams resulted in beaded dammed lake; (b) a typical landslide dammed a drainage

Léogâne fault). The two largest M 6.0 and M 5.9 aftershocks respectively occurred seven minutes after the main shock and on January 20, 2010.

Landslides Triggered by the Earthquake

Landslides triggered by the 2010 Haiti earthquake are of various types, including: (1) shallow-disrupted landslides, (2) rock falls, (3) rock avalanche, and (4) deep-seated landslides. Figure 2 shows images of various landslides

triggered by the earthquake from Google Earth last accessed in May 2011. Shallow-disrupted landslide was the most common landslide triggered by the Haiti earthquake in the study area. Some of landslides triggered by the Haiti earthquake are different to classified because of characteristics of two or more landslide types were indicated. Some of the landslides blocked stream drainages (Figs. 2b, c and 3), blocked roads, and threatened infrastructure in many part of Haiti (Jibson and Harp 2011).

The author used images on Google Earth (last accessed September 2011) to prepare a sufficiently detailed inventory

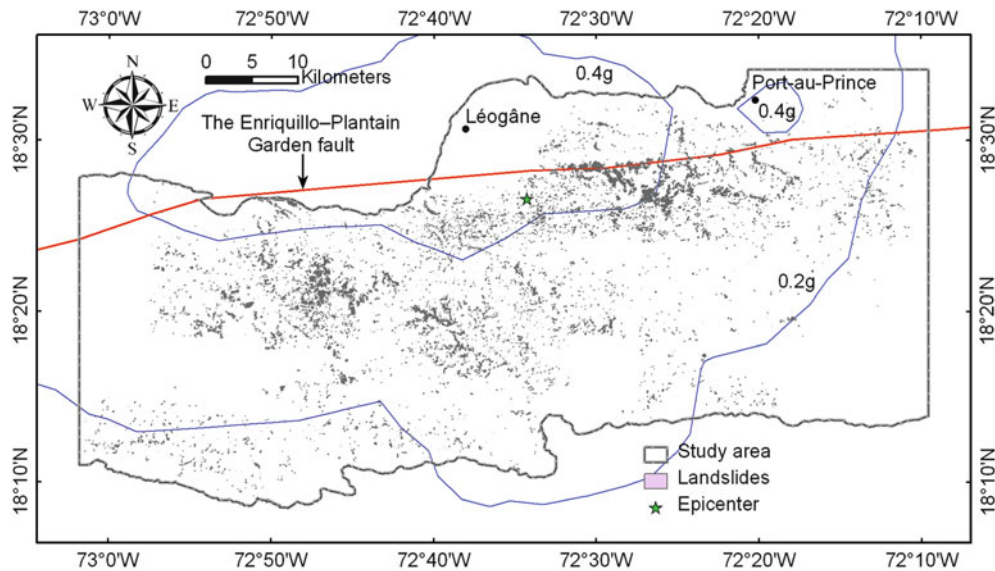


Fig. 4 Spatial distribution of landslides triggered by the earthquake

of landslides triggered by the earthquake. A total of 30,828 landslides were determined from available satellite images in high resolutions over an area of 3,192.85 km² (Fig. 4). These landslides cover about 15.736 km². The LAP (landslide area percentage), which was expressed as a percentage of the area affected by landslides, was $LAP = (15.736 \text{ km}^2 / 3,192.85 \text{ km}^2) \times 100\% = 0.493\%$, and the LND (landslide number density), which was calculated as the number of landslides per square kilometer, was $LND = 30,828 \text{ landslides} / 3,192.85 \text{ km}^2 = 9.655 \text{ landslides/km}^2$.

Relations of Landslides and Controlling Factors

The occurrence of earthquake-triggered landslides can be related to several parameters as following: slope angle, slope aspect, slope position, and PGA. For the Haiti earthquake, the correlation analysis of the landslide distribution was performed for the 30,828 co-seismic landslides, using LND and LAP. The analysis was carried out using digital elevation model of ASTER DEM in 30 m × 30 m resolution. For the purpose of LAP analysis for small landslide area less than about 1,000 m (slightly more than area of one grid in 30 m × 30 m resolution), the ASTER DEM in 30 m × 30 m resolution was resampled into a new DEM in 5 m × 5 m resolution.

Slope Angle

Slope angle is an important controlling factor for co-seismic landslides occurrence. Slope angle map of the study area was

produced from the DEM in ArcGIS Software. Extend of slope angle in the study area was 0°–75.83°. The slope angle map was reclassified into 11 classes in intervals of 5°, including (1): 0–5°, (2): 5–10°, (3): 10–15°, (4): 15–20°, (5): 20–25°, (6): 25–30°, (7): 30–35°, (8): 35–40°, (9): 40–45°, (10): 45–50°, (11): 50–75.83°. Statistical result (Fig. 5) shows the LAP and LND values increasing with slope angle rising except the 11 class (slope angle more than 50°). That is because area of the 11th class is too small to carry out an objective statistical. For showing both LAP and LND on a map, the unit of all LAP values in the following text is set to “‰”.

Slope Aspect

Slope aspect is defined as the direction of maximum slope of the terrain surface. Aspect may affect on co-seismic landslide occurrences through accompanying with directions of seismic wave propagating, crustal block movement, and the earthquake associated fault slipping. Slope aspect in the study area was divided into nine classes from ArcGIS in a conventional classification, such as, flat, north, northeast, east, southeast, south, southwest, west, and northwest. Figure 6 shows the relation of landslide and slope aspect. It shows the east and northeast directions, which are generally consistent with the strike direction of the earthquake associated fault (EPGF) or direction of the Caribbean Plate movement. In other words, the more susceptible slope aspect of the landslides is decided by the direction of crustal block movement during the earthquake.

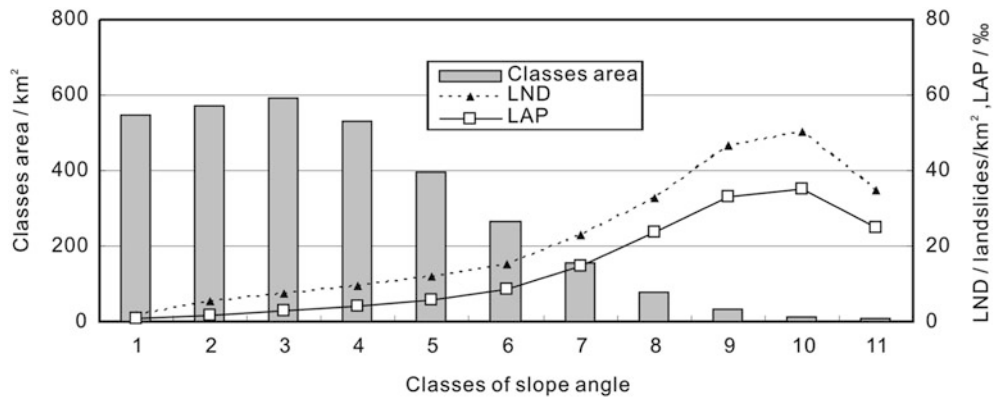


Fig. 5 Relation of landslide and slope angle. (1): 0–5°; (2): 5–10°; (3): 10–15°; (4): 15–20°; (5): 20–25°; (6): 25–30°; (7): 30–35°; (8): 35–40°; (9): 40–45°; (10): 45–50°; (11): 50–75.83°

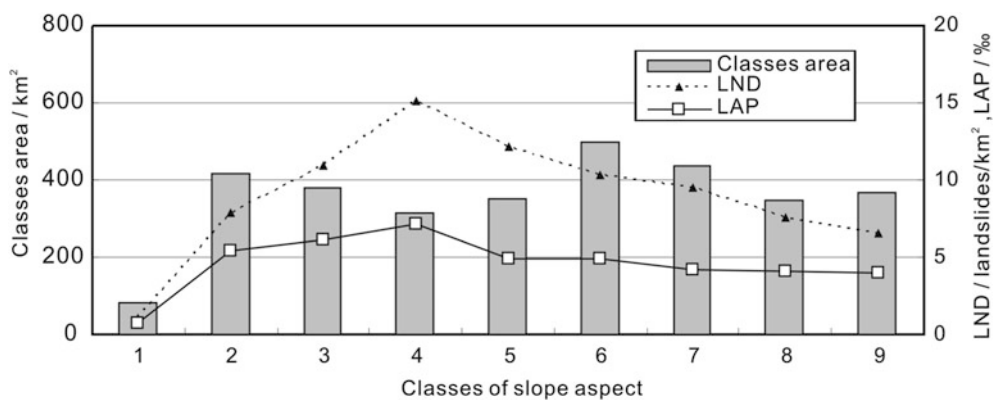


Fig. 6 Relation of landslide and slope aspect. (1): Flat; (2): N; (3): NE; (4): E; (5): SE; (6): S; (7): SW; (8): W; (9): NW

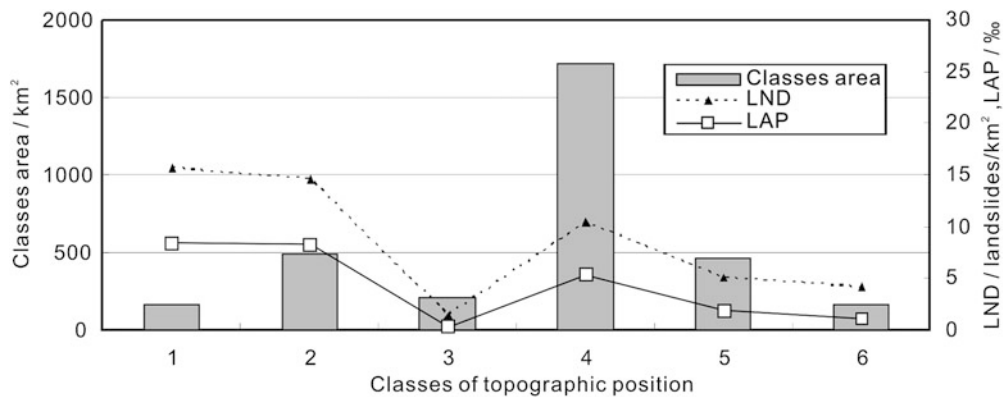


Fig. 7 Relation of landslide and topographic position. (1) Valleys, (2) Lower slopes, (3) Gentle slopes, (4) Steep slopes, (5) Upper slopes, and (6) Ridges

Slope Position

Referencing to Weiss (2001) and Jenness et al. (2013), slope positions were classified into six categories, including, (1) Valleys, (2) Lower slopes, (3) Gentle slopes, (4) Steep slopes, (5) Upper slopes, and (6) Ridges based on DEM. Both LAP and LND values (Fig. 7) show the lower the slope position.

There have no obvious correlations between slope position and landslide occurrences. Gentle slopes showed the lowest landslides abundance. The classes of valleys and lower slopes showed high LAP and LND values, which showed that earthquake-triggered landslides more easily occurred at valleys and lower slopes. This perhaps because loose deposits and weathered layers often appear in areas of the valley.

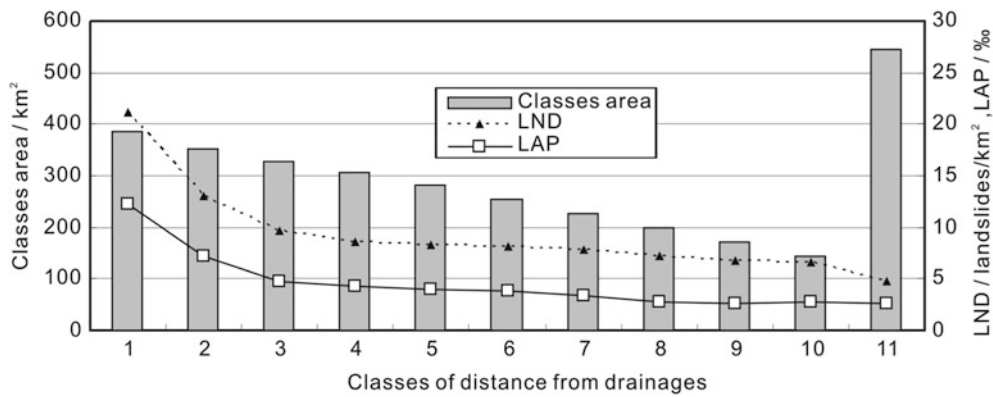


Fig. 8 Relation of landslide and distance from drainages. (1): <100 m; (2): 100–200 m; (3): 200–300 m; (4): 300–400 m; (5): 400–500 m; (6): 500–600 m; (7): 600–700 m; (8): 700–800 m; (9): 800–900 m; (10): 900–1,000 m; (11): >1,000 m

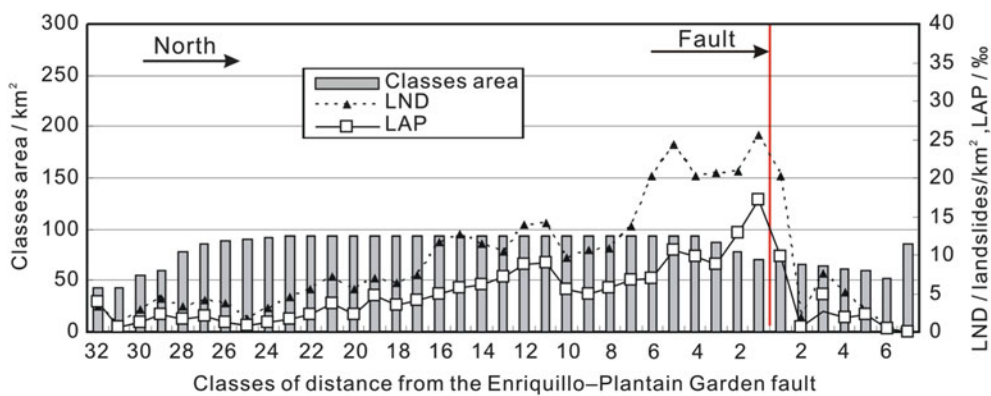


Fig. 9 Relation of landslide and distance from the Enriquillo–Plantain Garden fault. 1 km intervals, seven classes on the North Plate and 32 classes on the South Plate

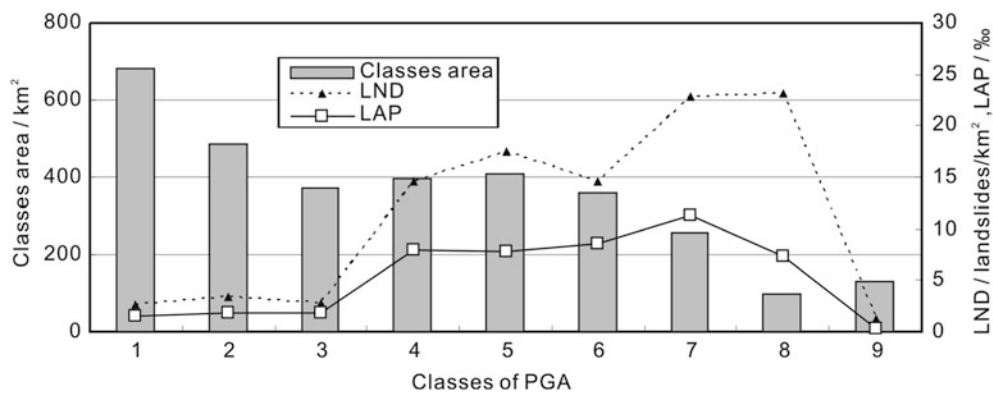


Fig. 10 Relation of landslide and PGA. (1): ≤0.16 g; (2): 0.2 g; (3): 0.24 g; (4): 0.28 g; (5): 0.32 g; (6): 0.36 g; (7): 0.4 g; (8): 0.44 g; (9) ≥0.48 g

Distance from Drainages

The erosion or under-cutting action of the rivers will make natural slopes unstable. Drainages in the study area were mapped from satellite images in high resolution from. There were 11 classes of distance from drainages, including, (1): <100 m; (2): 100–200 m; (3): 200–300 m; (4): 300–400 m;

(5): 400–500 m; (6): 500–600 m; (7): 600–700 m; (8): 700–800 m; (9): 800–900 m; (10): 900–1,000 m; (11): >1,000 m. Relation of the Haiti earthquake-triggered landslides and distance from drainages was shown in Fig. 8. It is observed the closer to drainages, the higher LND and LAP values are.

Distance from Seismogenic Fault

Although some publications (Calais et al. 2010; Hashimoto et al. 2011) showed that the Haiti earthquake ruptured the blind Léogâne fault, in this study, the earthquake associated fault (EPGF) was used to analyze correlation of the landslides with distance from the seismogenic fault. The reasons are: (1) the accurate geographic position of the Léogâne fault is unknown; (2) distance from the Léogâne fault and the EPGF is relatively near; (3) the Léogâne fault is just a sub-branch of the EPGF, and the activity of the fault is controlled by the EPGF. Buffer distance of the EPGF was set to 1 km. The result correlation between LND, LAP values and distance from the EPGF showed the EPGF fault strongly controlled co-seismic landslides occurrence (Fig. 9). Most landslides occurred on the south plate of the fault. The closer to the fault the more landslides occurred except few exceptions, such as classes of about 5 and 12 km south to the fault.

Peak Ground Acceleration

Generally, there was a good correlation between PGA values and occurrences of earthquake-triggered landslides. The PGA map of the 2010 Haiti earthquake was downloaded for the U.S. Geological Survey. It indicated that range of PGA values of the study area is from 0.12 g to 0.7 g. The PGA map was reclassified into nine PGA value classes, including: (1): ≤ 0.16 g; (2): 0.2 g; (3): 0.24 g; (4): 0.28 g; (5): 0.32 g; (6): 0.36 g; (7): 0.4 g; (8): 0.44 g; (9) ≥ 0.48 g. Figure 10 showed the correlations of LAP and LND values with PGA values. LAP and LND values between 0.28 g and 0.44 g are obvious higher than that of PGA values equal to and less than 0.24 g. It demonstrated that PGA strongly affects the landslide occurrences. It is showed abnormal lower LAP and LND values correlate to PGA values equal to and more than 0.44 g. The probable reason is that regional relief of these high PGA value areas (Léogâne seaside town) is rather gentle.

Conclusion

A total of 30,828 landslides triggered by the Haiti earthquake were delineated from visual interpreting of satellite images in high resolutions on Google Earth. These landslides distributed over an area of about 3,200 km² and covered a total area of 15.736 km². These landslides are of various types, including, (1) shallow-disrupted landslides, (2) rock falls, (3) rock avalanche, and (4) deep-seated landslides. Some of the landslides blocked stream drainages. Double indices of LND and LAP were used to correlate earthquake-triggered landslide with several controlling parameters. The results show that the LAP and LND values generally increasing with slope

angle rising. The east and northeast directions were the prefer orientations for landsliding (the direction of the south plate movement during the earthquake). Landslides triggered by the earthquake were more easily occurred on ridges and in valleys. It was found that most of the landslides were occurred on the south plate. The closer to drainages and the EPGF, the higher LND and LAP values are. It showed positive correlation between PGA values and landslide abundance except a few exceptions in Léogâne seaside town. In conclusions, the Haiti earthquake triggered landslides mapping can provide essential and important data for seismic landslide assessment for the Haiti earthquake struck area (Xu et al. 2012f). Statistical result obtained from correlations of landslides abundance and landslide controlling parameters can give reference to scientists interested in earthquake-triggered landslides understanding spatial distribution landslide triggered by a blind-fault generated earthquake in subduction zone.

Acknowledgments This research is supported by the National Natural Science Foundation of China (grant no. 41202235).

References

- Alfaro P, Delgado J, García-Tortosa F, Lenti L, López J, López-Casado C, Martino S (2012) Widespread landslides induced by the Mw 5.1 earthquake of 11 May 2011 in Lorca, SE Spain. *Eng Geol* 137–138:40–52
- Calais E, Freed A, Mattioli G, Amelung F, Jónsson S, Jansma P, Hong SH, Dixon T, Prépetit C, Momplaisir R (2010) Transpressional rupture of an unmapped fault during the 2010 Haiti earthquake. *Nat Geosci* 3(11):794–799
- Chigira M, Yagi H (2006) Geological and geomorphological characteristics of landslides triggered by the 2004 Mid Niigata prefecture earthquake in Japan. *Eng Geol* 82(4):202–221
- Collins BD, Kayen R, Tanaka Y (2012) Spatial distribution of landslides triggered from the 2007 Niigata Chuetsu-Oki Japan Earthquake. *Eng Geol* 127:14–26
- Dai FC, Xu C, Yao X, Xu L, Tu XB, Gong QM (2011) Spatial distribution of landslides triggered by the 2008 Ms 8.0 Wenchuan earthquake, China. *J Asian Earth Sci* 40(4):883–895
- Gorum T, Fan XM, van Westen CJ, Huang RQ, Xu Q, Tang C, Wang GH (2011) Distribution pattern of earthquake-induced landslides triggered by the 12 May 2008 Wenchuan earthquake. *Geomorphology* 133(3–4):152–167
- Guzzetti F, Mondini AC, Cardinali M, Fiorucci F, Santangelo M, Chang KT (2012) Landslide inventory maps: new tools for an old problem. *Earth Sci Rev* 112(1–2):42–66
- Harp EL, Keefer DK, Sato HP, Yagi H (2011) Landslide inventories: the essential part of seismic landslide hazard analyses. *Eng Geol* 122(1–2):9–21
- Hashimoto M, Fukushima Y, Fukahata Y (2011) Fan-delta uplift and mountain subsidence during the Haiti 2010 earthquake. *Nat Geosci* 4(4):255–259
- Jenness J, Brost B, Beier P (2013) Land facet corridor designer: topographic position index tools. <http://www.jennessent.com>
- Jibson RW, Harp EL (2011) Field reconnaissance report of landslides triggered by the January 12, 2010, Haiti earthquake. <http://pubs.usgs.gov/of/2011/1023/>

- Keefe DK (1984) Landslides caused by earthquakes. *Geol Soc Am Bull* 95(4):406–421
- Keefe DK (1999) Earthquake-induced landslides and their effects on alluvial fans. *J Sediment Res* 69(1):84–104
- Keefe DK, Wartman J, Ochoa CN, Rodriguez-Marek A, Wiczorek GF (2006) Landslides caused by the M 7.6 Tecoman, Mexico earthquake of January 21, 2003. *Eng Geol* 86(2–3):183–197
- Mann P, Burke K, Matumoto T (1984) Neotectonics of Hispaniola: plate motion, sedimentation, and seismicity at a restraining bend. *Earth Planet Sci Lett* 70(2):311–324
- Parker RN, Densmore AL, Rosser NJ, de Michele M, Li Y, Huang RQ, Whadcoat S, Petley DN (2011) Mass wasting triggered by 2008 Wenchuan earthquake is greater than orogenic growth. *Nat Geosci* 4(7):449–452
- Prentice C, Mann P, Crone A, Gold R, Hudnut K, Briggs R, Koehler R, Jean P (2010) Seismic hazard of the Enriquillo-Plantain Garden fault in Haiti inferred from palaeoseismology. *Nat Geosci* 3(11):789–793
- Qi SW, Xu Q, Lan HX, Zhang B, Liu JY (2010) Spatial distribution analysis of landslides triggered by 2008.5.12 Wenchuan Earthquake, China. *Eng Geol* 116(1–2):95–108
- Rodríguez CE, Bommer JJ, Chandler RJ (1999) Earthquake-induced landslides: 1980–1997. *Soil Dyn Earthq Eng* 18(5):325–346
- Sato HP, Hasegawa H, Fujiwara S, Tobita M, Koarai M, Une H, Iwahashi J (2007) Interpretation of landslide distribution triggered by the 2005 Northern Pakistan earthquake using SPOT 5 imagery. *Landslides* 4(2):113–122
- Wang WN, Nakamura H, Tsuchiya S, Chen CC (2002) Distributions of landslides triggered by the Chi-chi Earthquake in Central Taiwan on September 21, 1999. *Landslides* 38(4):18–26
- Weiss AD (2001) Topographic position and landforms analysis. http://www.jennessent.com/downloads/tpi-poster-tnc_18x22.pdf
- Xu C (2012) Detailed inventory of the 2008 Wenchuan earthquake triggered landslides and its comparison with global other earthquake events. *Sci Technol Rev* 30(25):18–26 (In Chinese)
- Xu C, Xu XW (2012) The 2010 Yushu earthquake triggered landslides spatial prediction models based on several kernel function types. *Chin J Geophys* 55(9):2994–3005 (In Chinese)
- Xu C, Xu XW (2013) Controlling parameter analyses and hazard mapping for earthquake triggered-landslides: an example from a square region in Beichuan County, Sichuan Province, China. *Arab J Geosci* 6(10):3827–3839
- Xu C, Dai FC, Chen J, Tu XB, Xu L, Li WC, Tian W, Cao YB, Yao X (2009) Identification and analysis of secondary geological hazards triggered by a magnitude 8.0 Wenchuan Earthquake. *J Remote Sens* 13(4):754–762 (In Chinese)
- Xu C, Dai FC, Xu XW (2010) Wenchuan earthquake induced landslides: an overview. *Geol Rev* 56(6):860–874 (In Chinese)
- Xu C, Dai FC, Xu XW, Lee YH (2012a) GIS-based support vector machine modeling of earthquake-triggered landslide susceptibility in the Jianjiang River watershed, China. *Geomorphology* 145–146:70–80
- Xu C, Xu XW, Dai FC, Saraf AK (2012b) Comparison of different models for susceptibility mapping of earthquake triggered landslides related with the 2008 Wenchuan earthquake in China. *Comput Geosci* 46:317–329
- Xu C, Xu XW, Dai FC, Xiao JZ, Tan XB, Yuan RM (2012c) Landslide hazard mapping using GIS and weight of evidence model in Qingshui river watershed of 2008 Wenchuan earthquake struck region. *J Earth Sci* 23(1):97–120
- Xu C, Xu XW, Yu GH (2012d) Study on the characteristics, mechanism, and spatial distribution of Yushu earthquake triggered landslides. *Seismol Geol* 34(1):47–62 (In Chinese)
- Xu C, Xu XW, Lee YH, Tan XB, Yu GH, Dai FC (2012e) The 2010 Yushu earthquake triggered landslide hazard mapping using GIS and weight of evidence modeling. *Environ Earth Sci* 66(6):1603–1616
- Xu C, Xu XW, Yu GH (2012f) Earthquake triggered landslide hazard mapping and validation related with the 2010 Port-au-Prince, Haiti earthquake. *Disaster Adv* 5(4):1297–1304
- Xu C, Xu XW, Yao Q, Wang YY (2013a) GIS-based bivariate statistical modeling for earthquake-triggered landslides susceptibility mapping related to the 2008 Wenchuan earthquake, China. *Q J Eng Geol Hydrogeol* 46(2):221–236
- Xu C, Xu XW, Wu XY, Dai FC, Yao X, Yao Q (2013b) Detailed catalog of landslides triggered by the 2008 Wenchuan earthquake and statistical analyses of their spatial distribution. *J Eng Geol* 21(1):25–44 (In Chinese)
- Xu C, Xu X W, Yao X, Dai F C (2013c) Three (nearly) complete inventories of landslides triggered by the May 12, 2008 Wenchuan Mw 7.9 earthquake of China and their spatial distribution statistical analysis. *Landslides*. doi:10.1007/s10346-013-0404-6
- Xu C, Xu XW, Yu GH (2013d) Landslides triggered by slipping-fault-generated earthquake on a plateau: an example of the 14 April 2010, Ms 7.1, Yushu, China earthquake. *Landslides* 10(4):421–431
- Yagi H, Higaki D, Yamamoto M, Yamasaki T (2009) Distribution and characteristics of landslides induced by the Iwate–Miyagi Nairiku Earthquake in 2008 in Tohoku District, Northeast Japan. *Landslides* 6(4):335–344
- Yin YP, Zhang YS, Ma YS, Hu DG, Zhang ZC (2010) Research on major characteristics of geohazards induced by the Yushu Ms 7.1 earthquake. *J Eng Geol* 18(3):289–296 (In Chinese)



Did the 2008 Wenchuan Earthquake Lead to a Net Volume Loss?

Chong Xu, Xiwei Xu, Tolga Gorum, Cees J. van Westen, and Xuanmei Fan

Abstract

The topographic evolution of mountain landscapes is a coupling process of tectonic rock uplift, landslide erosion, and valley incision etc. A widely accepted notion is that an earthquake will build up the mountainous topography, whereas some researchers suggest that the 2008 Wenchuan earthquake tumbled down the mountain because the wasting mass volume due to landsliding is two to six times larger than the gain volume caused by rock uplift. The purpose of this paper is to compare the wasting mass volume due to seismic landsliding with the gain volume caused by rock uplift related to the 2008 Wenchuan event based on a new detailed landslide inventory prepared by visual interpretation of aerial photos and satellite images of high resolutions. The results show that about 5.9 km^3 materials, generated by nearly 200,000 landslides triggered by the Wenchuan earthquake, are distributed in the landslide intensity area. Although the landslides volume is larger than the published volume of tectonic rock uplift ($2.6 \pm 1.2 \text{ km}^3$), it is rather smaller than that from the previous study. We think it is not enough only to account for the co-seismic landslide volume and uplifted volume in the study of landscape evolution of the Longmenshan mountain area where the Wenchuan event took place. Orogenic evolution is affected by a variety of factors, such as co-seismic and interseismic crustal uplift, and isostatic compensation of mass removed from the surface of the earth which leads to orogenic growth, whereas co-seismic landslides and river erosion can destroy mountainous topography.

Keywords

Landslide • 2008 Wenchuan earthquake • Tectonic rock uplift • River erosion

Introduction

A detailed and accurate landslide inventory is an essential part of assessment of co-seismic landslides hazard. Harp et al. (2011) considered an ideal inventory would cover the entire area affected by an earthquake and include all of the landslides that are possible to detect down to size of 1–5 m in length, and the landslides must also be located accurately and mapped as polygons depicting their true shapes. Such inventories can then be used to perform seismic landslide hazard analysis (e.g. Xu et al. 2012a, b), regional landslide volume calculation (Xu and Xu 2013a, b), and other

C. Xu (✉) • X. Xu
Key Laboratory of Active Tectonics and Volcano, Institute of Geology,
China Earthquake Administration, Qijiahuozi, Deshengmenwai,
P.O. Box 9803, Beijing 100029, China
e-mail: xc1111111@126.com; xuchong@ies.ac.cn; xiweixu@vip.
sina.com

T. Gorum • C.J. van Westen • X. Fan
Faculty for Geo-Information Science and Earth Observation,
University of Twente, Enschede, The Netherlands
e-mail: gorum@itc.nl; westen@itc.nl; fanxuanmei@gmail.com

quantitative analyses (Dai et al. 2011; Gorum et al. 2011; Xu et al. 2013a).

The topographic evolution of mountain landscapes is a coupling process of tectonic rock uplift, landslide erosion, and valley incision, etc. A widely accepted notion is that an earthquake will build up the mountainous topography, whereas Parker et al. (2011) found the Wenchuan earthquake tumbled down the mountain because the wasting mass volume due to landsliding is two to six times larger than the gain volume caused by rock uplift. However, we question their landslide volume estimation to be overestimate of the co-seismic landslide volume due to two limitations in their landslide inventory: (1) the incompleteness of the inventory; and (2) the generalization of landslide mapping (delineating several landslides as one landslide). They have contrary effect on the landslide volume calculation. Which aspect plays a more important role? Only a detailed and complete landslide inventory could answer this question. Further, it will affect judging of the correlation between the wasting mass volume due to seismic landsliding and the gain volume caused by rock uplift related to the 2008 Wenchuan earthquake.

In this work, a detailed and objective inventory of landslides triggered by the 2008 Wenchuan earthquake was prepared by using visual interpretation of aerial photos and satellite images in high resolutions. Then, the wasting mass volume due to seismic landsliding was calculated by landslide “area-volume” formulas. In our opinions, the landscape evolution of the earthquake area is affected by various factors, such as co-seismic and interseismic crustal uplift, isostatic compensation of mass removed from the surface of the earth, co-seismic landslides, and river erosion. The conclusion that the 2008 Wenchuan earthquake led to a net volume loss (Parker et al. 2011) seems too hastily.

Two Important Limitations of the Landslide Inventory Constructed by Parker et al. (2011)

The fact that various factors may affect the quality of landslide inventories (Guzzetti et al. 2012) commonly result in many landslide inventories of poor quality. In our opinion, there are two important limitations in the landslide inventory for the 2008 Wenchuan earthquake constructed by Parker et al. (2011). One relates to the incompleteness of the inventory which might lead to an underestimation of the regional landslide volume, and the other is associated with the grouping of individual small landslides into larger units. The second limitation is more important than the first one, leading to an overestimation of the total landslide volume. These limitations were already acknowledged by Parker et al. (2011) in their supplementary data, but cannot be quantified due to the lack of a complete landslide inventory.

Incomplete Landslides Inventory

Parker et al. (2011) did not use of image visual interpretation for constructing landslide inventory, instead employed a semi-automated detection algorithm and EO-1 and SPOT 5 imagery for the mapping of individual landslides. Their inventory contained 73,367 landslide features across an area of 13,800 km², which is substantially smaller than the entire earthquake affected area. They did not make a comparison between their inventory and the available one of Dai et al. (2011) which contained 56,847 landslides mapped across an area of 41,750 km². When compared with our landslide inventory map, the inventory map of Parker et al. (2011) lacks information on tens of thousands of landslides that occurred in areas in the N, NW, W, and SW direction of the epicenter, as well as in the NE section of the main co-seismic surface rupture.

Overestimation of Individual Landslide Areas

Parker et al. (2011) obtained landslide polygons based on a semi-automated detection algorithm and EO-1 and SPOT 5 imagery, using only post-earthquake images. Although such automatic detection methods can provide a first indication in a short time, the resulting inventory maps tend to be extremely general and include numerous errors when compared with detailed landslide inventory maps prepared by image experts through visual interpretation (Harp et al. 2011). In addition, Parker et al. (2011) did not exclude pre-existing landslides since only the post-earthquake images were used. Considering these factors, there is very possible that bare-rocky areas were mapped as landslides. This can significantly change the results they present in Fig. 2 in their main manuscript, which compares “Net volume changes” of co-seismic uplift and landslides within a swath profile with a width of 1-km in the along-strike distance from the epicenter. The automated image classification method used by Parker et al. (2011) also resulted in the grouping of many single landslide events into larger ones, leading to an exaggeration of the landslide area. This can be observed from the example resented in Fig. 1, from Beichuan County, where they combined the Beichuan Middle-school rock-avalanche with several other rock falls in the neighbouring slope into a single landslide (Fig. 1a). This overestimation of individual landslide areas can change the volumetric calculations considerably. When using the exact area of each landslide (Fig. 1b) and using the conversion to volume indicated in their supplementary data, the area of the individual landslides varies between 1,531 m² (L4) and 123,329 m² (L1) and the volumes range between 2,793 m³ and 1,235,048 m³, using the area-volume conversion formula of $V_{ls} = 0.106 \times A_{ls}^{1.388}$ (Parker et al. 2011). The total

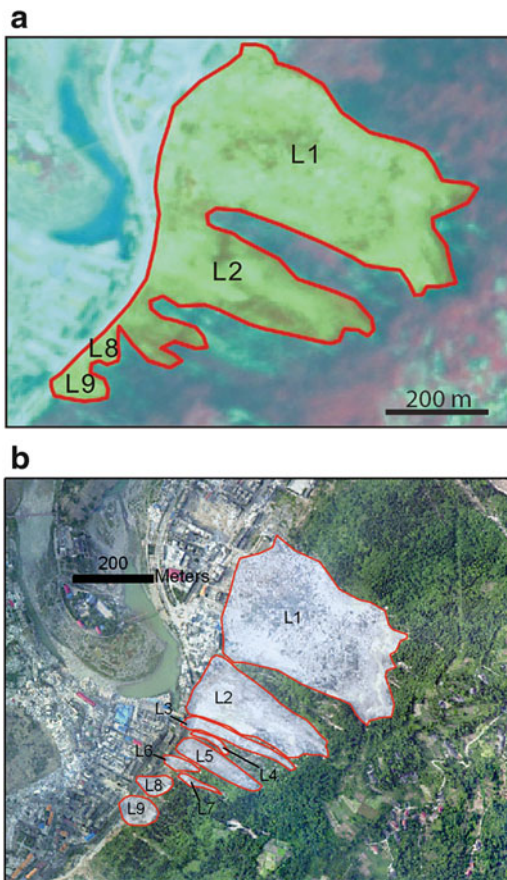


Fig. 1 Comparison of landslide interpretation: (a) an image classification by Parker et al. (2011); (b) for a test area in Beichuan County. Nine individual landslides can be observed clearly in (b), whereas only some of them can be distinguished in (a)

area of the nine landslides (L1–L9) is 192,935 m², and the total volume is 1,612,466 m³. When following Parker et al.'s image classification result (Fig. 1a) the area of the combined landslide is 192,935 m² and the corresponding volume is $0.106 \times 192,935^{1.388} = 2,379,382$ (m³), which is an over-estimation of $2,379,382/1,612,466 \times 100 \% = 147.6 \%$ with respect to the reality.

Data and Methods

Our initial landslide distribution data, as cited by Parker et al. (2011), showed more than 56,000 landslides (Dai et al. 2011; Gorum et al. 2011) triggered by the 2008 Wenchuan earthquake. These landslides were delineated by visual interpretation of high-resolution aerial photos and satellite images over a broad area, using mainly post-earthquake images. Although the inventory contains a large number of landslides, some of the earthquake affected areas still lacked high-resolution post-earthquake remote sensing images, resulted in an incomplete landslide inventory map.

Images Used for Landslides Visual Interpretation

We manually mapped landslides in polygons based on the visual interpretation of pre- and post- earthquake remote sensing images. These images of post-earthquake include aerial photos of 1 m, 2 m, 2.4 m and 5 m resolutions, SPOT 5 of 2.5 m resolution, CBERS02B of 19.5 m resolution, IKONOS of 1 m resolution, ASTER of 15 m resolution, IRS-P5 of 2.5 m resolution, QuickBird of 0.6 m and 2.4 m resolutions, and ALOS of 2.5 m resolution. The images of pre-earthquake consist of SPOT 5 of 2.5 m resolution covering part of the landslides distribution area and ETM + of 15 m resolution throughout the whole landslide area. In addition, a few hundreds of landslides occurred in areas lacking clear images were delineated from visual interpretation of images on Google Earth platform.

Inventory of Landslides Triggered by the Earthquake

An inventory of landslides triggered by the 2008 Wenchuan earthquake was prepared using visual interpretation on a GIS platform, resulting in a total of 197,481 landslides delineated as individual solid polygons (Fig. 2; Xu 2012; Xu and Xu 2012; Xu et al. 2013b), with a total area of about 1,160 km², occurring over an area of about 110,000 km². This landslide distribution map is more detailed than previous ones (e.g. Dai et al. 2011; Gorum et al. 2011; Chigira et al. 2010; Yin et al. 2010; Qi et al. 2010; Huang and Li 2009).

The distribution of the co-seismic landslides triggered by the Wenchuan earthquake (Fig. 2) shows several features as follows: (1) Most of the landslides are concentrated around the Yingxiu-Beichuan co-seismic surface rupture, indicative of a control on the spatial distribution patterns of the landslides. (2) Most of the landslides occurred northeast of the epicentre, consistent with the earthquake rupture mechanism. (3) Most of the landslides occurred on the hanging wall of the seismogenic fault, especially the southwest segment of the fault dominated by thrusting. (4) In the areas of hanging wall of the seismogenic fault but far away from the fault, some co-seismic landslides were also present and mainly distributed along rivers. (5) The area between the two main surface-ruptures also registered high density landslides, but less than the hanging wall area. (6) The landslides in areas northeast to the Beichuan County were distributed in clusters around the surface rupture.

Results

Based on our landslide inventory, we recalculated the landslide volume in the same manner as Parker et al. (2011)

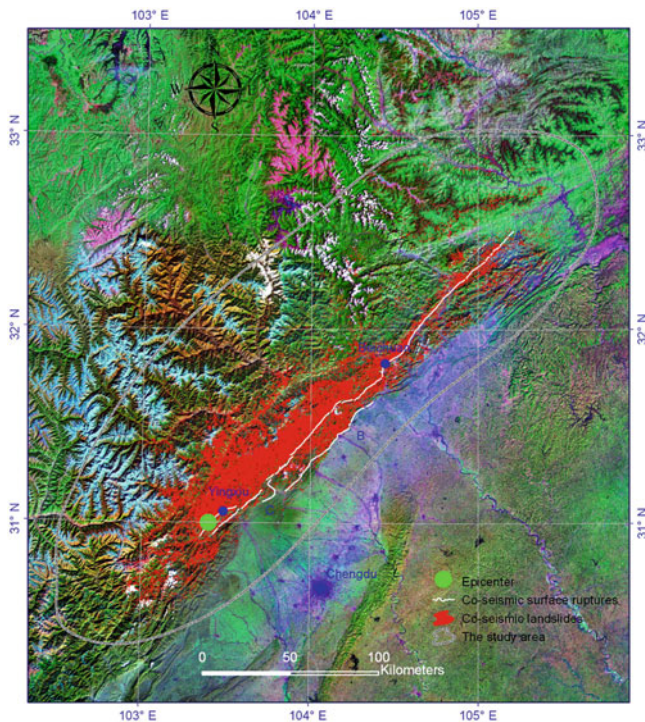


Fig. 2 Distribution of co-seismic surface ruptures (white lines) and earthquake triggered landslides (red polygons). (a) The Yingxiu-Beichuan co-seismic surface rupture; (b) The Guanxian-Jiangyou co-seismic surface rupture; (c) The Xiaoyudong co-seismic surface rupture. The co-seismic surface rupture is revised from Xu et al. (2009)

(Table 1), resulting in volume estimations that are between 49 and 86 % of their results. The volume of the Wenchuan earthquake triggered landslides is about 5.9 km^3 based on the “volume-area” power-law from Parker et al. (2011). Furthermore, a large part of the landslide materials is not likely to be eroded away within a short period of time, as many landslides occurred as rockfalls or large rockslides (Hovius et al. 2011; Fan et al. 2012), e.g. the Daguangbao landslide. Fan et al. (2012) concluded that over 80 % of the co-seismic landslide materials are still suspended on the hillslopes inside the mountain system about 3 years after the earthquake, and the time needed to transport them outside the mountain system largely depends on the stream power, long-term rock uplift as well as the regional climate change. Therefore, the maximum volume loss due to landslides is only 20 % of 5.9 km^3 , which is about 1.2 km^3 , evidently less than the uplifted volume of $2.6 \pm 1.2 \text{ km}^3$ (Parker et al. 2011; de Michele et al. 2010). The uplifted volume of $2.6 \pm 1.2 \text{ km}^3$ from InSAR (de Michele et al. 2010) was the most credible result currently due to the rare GPS vertical data (Shen et al. 2009; Wang et al. 2011) for the Wenchuan earthquake struck area.

The two limitations mentioned above have an opposite effect on the estimation of the total landslide volume calculation. We calculated the total landslide volume in a

Table 1 Comparison of landslide volumes based on our results, as compared with those of Parker et al. (2011)

RS	MidV (%)	MaxV (%)	MinV (%)
L1	4.49/5.73 (78)	4.73/6.14 (77)	4.26/5.35 (80)
L2	6.92/9.36 (74)	7.69/10.75 (72)	6.22/8.15 (76)
L3	10.63/14.9 (71)	11.82/17.1 (69)	9.56/13 (74)
G	8.09/15.2 (53)	8.93/17.2 (52)	7.33/13.4 (55)
FM	5.91/9.08 (65)	15.27/31.28 (49)	2.35/2.73 (86)

“RS” represents several published relationships between individual landslide area and volume. “MidV (%)”, “MaxV (%)”, and “MinV (%)” mean the middle, maximum, and minimum volume values (reference to Parker et al. 2011) of total landslides triggered by the earthquake in “ km^3 ” from this study and from Parker et al. (2011), data in the double brackets mean the percentage ratio of them. “L1”, “L2”, “L3” (Parker et al. 2011) respectively mean all landslides, all bedrock landslides, mixed Himalayan landslides from Larsen et al. (2010). “G” (Parker et al. 2011) represents all landslides from Guzzetti et al. (2009). “FM” means using the landslide “area-volume” relationship from field measurements by Parker et al. (2011)

landslide density area of about $13,800 \text{ km}^2$ based on our own inventory in the same manner as Parker et al. (2011). The results are shown in Table 1. The resulting total landslide volume is much larger than our results, even though their inventory lacked data for some landslide density areas. For some of the area-volume relations, our results are less than 50 % of their results. In our opinion, using the same empirical relationships between area and volume the total landslide volume was between ~ 4 and 8 km^3 , which is much less than the range of ~ 5 – 15 km^3 reported by Parker et al. (2011).

In order to conveniently observe spatial distribution patterns of materials generated by the co-seismic landslides, we divided the study area into 44,041 square cells of size 1 km^2 . Because the area of some giant landslides is larger than 1 km^2 , it is inappropriate to consider such giant landslides as a point to calculate landslide material thickness in an 1 km^2 cell. In this study, we select 20 m as sampling intervals to extract landslide material thickness in co-seismic landslide areas. The nearly 200 thousands co-seismic landslides cover about $1,150.622 \text{ km}^2$ and 2,875,676 points were extracted in 20 m interval. Based on the area-volume conversion formula of $V_{\text{ls}} = 0.106 \times A_{\text{ls}}^{1.388}$ (Parker et al. 2011), landslide material volume can be obtained and each average thickness of the 2,875,676 points were assigned. Then, landslide erosion material average thickness of every 1 km^2 cell were calculated based on the following formula:

$$\text{Thick}_{\text{Average}} = \sum_{i=1}^{2500} \text{Thick}_i \times 400/10^6 \quad (1)$$

where $\text{Thick}_{\text{Average}}$ represents the landslide material thickness of certain 1 km^2 square cell, and every 1 km^2 square area contains 2,500 points in 20 m intervals; i ($1 \leq i \leq 2,500$) means the i point of the 2,500 points in the 1 km^2

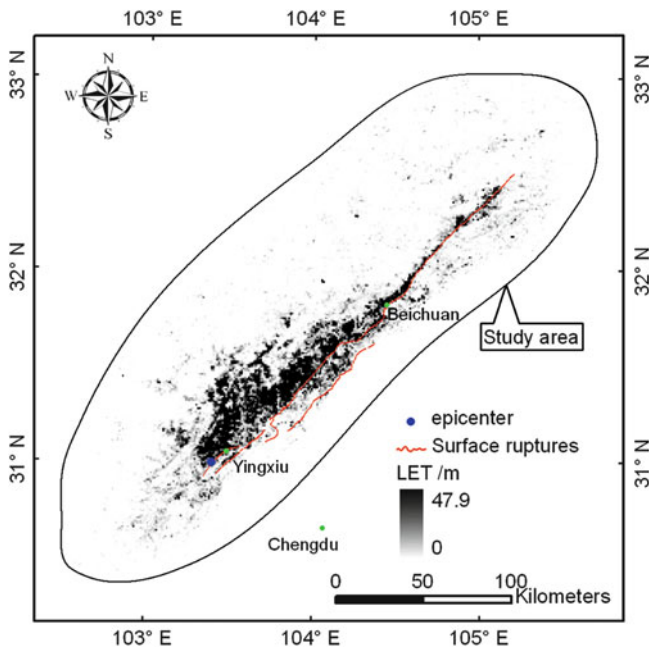


Fig. 3 Distribution map of landslide erosion thickness based on 1 km² cells. *LET* landslide erosion thickness

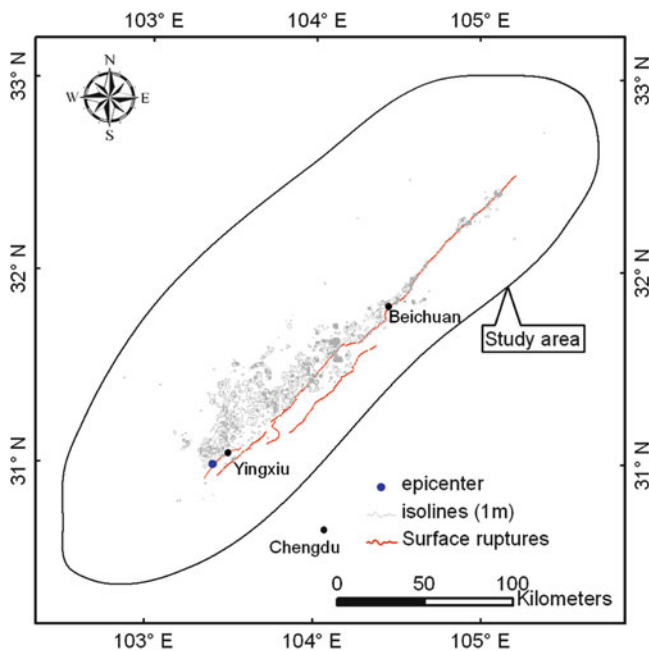


Fig. 4 Isolines of landslide erosion thickness related to the Wenchuan earthquake

cell; and $Thick_i$ is landslide erosion thickness of the i point (area of 20 m × 20 m) with unit meter. Then, a distribution map of landslide erosion thickness based on 1 km² cells (Fig. 3) were constructed. Subsequently, landslide erosion thickness isolines (Fig. 4) were constructed by the Fig. 3 based on 1 m intervals. It can be observed landslide erosion

thickness (*LET*) values of the most study area are less than 1 m. Most *LET* values larger than 1 m are located in the hanging wall of the southwest segment (between Beichuan County and the Yingxiu County) of the Yingxiu-Beichuan co-seismic surface rupture. This indicates high density of the co-seismic landslides occurrence on the hanging wall of the southwest segment of the fault dominated by thrusting.

Conclusions

After the 2008 Wenchuan earthquake, a detailed inventory map of the earthquake-triggered landslides was prepared. This inventory map contains 197,481 individual landslides mapped as individual polygons, with a total area of about 1,160 km². These landslides are distributed over an area of more than 110,000 km². About 5.9 km³ materials were generated by the landslides. Our results show that Parker et al. (2011) overestimated the volume of landslides triggered by the 2008 Wenchuan earthquake, and therefore their conclusion that such major earthquakes led to a net material deficit seems not supported by the data. It is not enough only to account for co-seismic landslide volume and uplifted volume in the study of landscape evolution of the Longmenshan mountain area where the 2008 Wenchuan event took place. Orogenic evolution is affected by a variety of factors, such as co-seismic and interseismic crustal uplift, and isostatic compensation of mass removed from the surface of the earth (Molnar 2012) which can lead to orogenic growth, whereas co-seismic landslides and river erosion can destroy mountainous topography.

Acknowledgments This research was supported by the National Natural Science Foundation of China (grant No. 41202235).

References

- Chigira M, Wu XY, Inokuchi T, Wang GH (2010) Landslides induced by the 2008 Wenchuan earthquake, Sichuan, China. *Geomorphology* 118(3–4):225–238
- Dai FC, Xu C, Yao X, Xu L, Tu XB, Gong QM (2011) Spatial distribution of landslides triggered by the 2008 Ms 8.0 Wenchuan earthquake, China. *J Asian Earth Sci* 40(4):883–895
- de Michele M, Raucoules D, de Sigoyer J, Pubellier M, Chamot-Rooke N (2010) Three-dimensional surface displacement of the 2008 May 12 Sichuan earthquake (China) derived from Synthetic Aperture Radar: evidence for rupture on a blind thrust. *Geophys J Int* 183(3):1097–1103
- Fan XM, van Westen CJ, Korup O, Gorum T, Xu Q, Dai FC, Huang RQ, Wang GH (2012) Transient water and sediment storage of the decaying landslide dams induced by the 2008 Wenchuan earthquake, China. *Geomorphology* 171–172:58–68
- Gorum T, Fan XM, van Westen CJ, Huang RQ, Xu Q, Tang C, Wang GH (2011) Distribution pattern of earthquake-induced landslides triggered by the 12 May 2008 Wenchuan earthquake. *Geomorphology* 133(3–4):152–167

- Guzzetti F, Ardizzone F, Cardinali M, Rossi M, Valigi D (2009) Landslide volumes and landslide mobilization rates in Umbria, central Italy. *Earth Planet Sci Lett* 279(3–4):222–229
- Guzzetti F, Mondini AC, Cardinali M, Fiorucci F, Santangelo M, Chang KT (2012) Landslide inventory maps: new tools for an old problem. *Earth Sci Rev* 112(1–2):42–66
- Harp EL, Keefer DK, Sato HP, Yagi H (2011) Landslide inventories: the essential part of seismic landslide hazard analyses. *Eng Geol* 122(1–2):9–21
- Hovius N, Meunier P, Lin CW, Chen H, Chen YG, Dadson S, Hornung MJ, Lines M (2011) Prolonged seismically induced erosion and the mass balance of a large earthquake. *Earth Planet Sci Lett* 304(3–4):347–355
- Huang RQ, Li WL (2009) Analysis of the geo-hazards triggered by the 12 May 2008 Wenchuan Earthquake, China. *Bull Eng Geol Environ* 68(3):363–371
- Larsen IJ, Montgomery DR, Korup O (2010) Landslide erosion controlled by hillslope material. *Nat Geosci* 3(4):247–251
- Molnar P (2012) Isostasy can't be ignored. *Nat Geosci* 5(2):83
- Parker RN, Densmore AL, Rosser NJ, de Michele M, Li Y, Huang RQ, Whadcoat S, Petley DN (2011) Mass wasting triggered by 2008 Wenchuan earthquake is greater than orogenic growth. *Nat Geosci* 4(7):449–452
- Qi SW, Xu Q, Lan HX, Zhang B, Liu JY (2010) Spatial distribution analysis of landslides triggered by 2008.5.12 Wenchuan Earthquake, China. *Eng Geol* 116(1–2):95–108
- Shen ZK, Sun JB, Zhang PZ, Wan YG, Wang M, Burgmann R, Zeng YH, Gan WJ, Liao H, Wang QL (2009) Slip maxima at fault junctions and rupturing of barriers during the 2008 Wenchuan earthquake. *Nat Geosci* 2(10):718–724
- Wang Q, Qiao XJ, Lan QG, Freymueller J, Yang SM, Xu CJ, Yang YL, You XZ, Tan K, Chen G (2011) Rupture of deep faults in the 2008 Wenchuan earthquake and uplift of the Longmen Shan. *Nat Geosci* 4(9):634–640
- Xu C (2012) Detailed inventory of the 2008 Wenchuan earthquake triggered landslides and its comparison with global other earthquake events. *Sci Technol Rev* 30(25):18–26 (In Chinese)
- Xu C, Xu XW (2012) Comment on “Spatial distribution analysis of landslides triggered by 2008.5.12 Wenchuan Earthquake, China” by Shengwen Qi, Qiang Xu, Hengxing Lan, Bing Zhang, Jianyou Liu [Engineering Geology 116 (2010) 95–108]. *Eng Geol* 133–134:40–42
- Xu C, Xu XW (2013a) Quantitative study on volume, gravitational potential energy reduction and caused regional centroid position change: an example of the 2010 yushu earthquake triggered landslides. *Sci Technol Rev* 31(2):22–29 (In Chinese)
- Xu C, Xu XW (2013b) Response rate of seismic slope mass movements related to the 2008 Wenchuan Earthquake and its spatial distribution analysis. *Chin J Rock Mech Eng* 32(S2):3888–3908 (In Chinese)
- Xu XW, Wen XZ, Yu GH, Chen GH, Klinger Y, Hubbard J, Shaw J (2009) Coseismic reverse- and oblique-slip surface faulting generated by the 2008 Mw 7.9 Wenchuan earthquake, China. *Geology* 37(6):515–518
- Xu C, Dai FC, Xu XW, Lee YH (2012a) GIS-based support vector machine modeling of earthquake-triggered landslide susceptibility in the Jianjiang River watershed, China. *Geomorphology* 145–146:70–80
- Xu C, Xu XW, Dai FC, Saraf AK (2012b) Comparison of different models for susceptibility mapping of earthquake triggered landslides related with the 2008 Wenchuan earthquake in China. *Comput Geosci* 46:317–329
- Xu C, Xu XW, Yu GH (2013a) Landslides triggered by slipping-fault-generated earthquake on a plateau: an example of the 14 April 2010, Ms 7.1, Yushu, China earthquake. *Landslides* 10(4):421–431
- Xu C, Xu XW, Yao X, Dai FC (2013b) Three (nearly) complete inventories of landslides triggered by the May 12, 2008 Wenchuan Mw 7.9 earthquake of China and their spatial distribution statistical analysis. *Landslides*. doi:10.1007/s10346-013-0404-6
- Yin JH, Chen J, Xu XW, Wang XL, Zheng YG (2010) The characteristics of the landslides triggered by the Wenchuan Ms 8.0 Earthquake from Anxian to Beichuan. *J Asian Earth Sci* 37(5–6):452–459



Hazard and Risk Related to Earthquake-Triggered Landslide Events

Hans-Balder Havenith

Abstract

First, we analyse how important earthquake-induced landslide hazards are compared to other geohazards at world-wide scale. Then, we try to estimate where these hazards may have the strongest impacts—at regional and local scale. In this regard, we also consider the short- and long-term effects of geological, tectonic, climatic and morphological conditions. Hazard and risk related to these processes was also analysed based on series of case histories: e.g., the 1920 Haiyuan earthquake-landslide disaster in China, the 1970 Nevado-Huascaran rock avalanche, as well as the 1999 events in Taiwan, 2001 in El Salvador, 2005 in Pakistan, and 2008 in China. Detailed report was provided for events in Central Asia: the 1911 earthquakes in Kemin, Sarez in 1911, Khait in 1949, Gissar in 1989 and Suusamyр in 1992. Particular focus is on mega-events such as the Usoy rockslide in Tajikistan as well as giant prehistoric rockslides in other parts of Central Asia and in the world (including Europe). We will try to answer several questions such as: how likely is a seismic versus climatic origin for giant landslides; how is the general geohazards level affected by these low-frequency earthquake-triggered mega-events. One conclusion is that in semi-arid mountain regions marked by a strong seismic activity, such as those in Central Asia, seismogenic landslides and related long-term effects may represent the most important geohazards. Further, the susceptibility to seismic slope instability is highest along active fault zones and on convex slopes made of soft or fractured materials.

Keywords

Earthquakes • Large landslides • Central Asia • Impacts • Long-term effects

Introduction

During the last 10 years, after a series of disastrous earthquake events in the mountain regions of Taiwan (1999), El Salvador (2001), Pakistan (2005) and China (2008), more attention has been given to landslides triggered by earthquakes.

Previously, landslides have been considered as minor effects of earthquakes compared to the impact of the ground

shaking itself. Schuster and Highland (2001) partly attributed the perception of the relatively small impact of earthquake-triggered mass movements to the fact that many related losses are often referred to as direct consequences of the earthquake.

This study of Schuster and Highland (2001) had been well completed before the $M = 7.6$ earthquake hit the Kashmir mountains on October 8, 2005. For this event, Petley et al. (2006) estimated that about 30 % of the total number of killed people (officially 87,350), i.e. 26,500, had been victims of co-seismic landslides. Less than 3 years later, on May 12, 2008, the Wenchuan earthquake hit the Sichuan and neighbouring provinces of China and caused 'more than 15,000 geohazards (recently, even much higher

H.-B. Havenith (✉)
Department of Geology, University of Liege, B18, 4000 Liege,
Belgium
e-mail: hb.havenith@ulg.ac.be

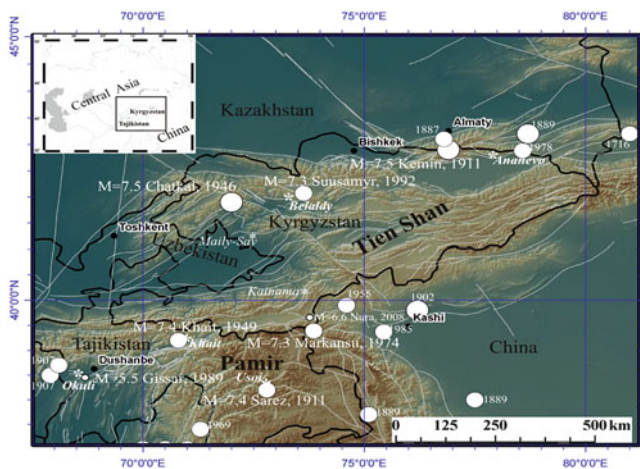


Fig. 1 Map of Tien Shan and Pamir Mountains in Central Asia with location of major faults and earthquakes (*white filled circles* show all recorded $M \geq 7$ earthquakes with the year of occurrence; the magnitude is indicated for analysed events) and related major mass movements (*stars*)

numbers have been published, up to 100,000) in the form of landslides, rockfalls, and debris flows, which resulted in about 20,000 deaths' (Yin et al. 2009).

In this paper, we will evaluate the potential impact of landslide hazards induced by earthquakes on the basis of a review of related geological observations. We focus on the relatively poorly known Central Asian mountain regions, the Tien Shan and Pamir, on the basis of landslide case histories related to the following earthquakes (see location in Fig. 1): $M = 8.2$ Kemin, 1911, $M = 7.6$ Sarez, 1911, $M = 7.4$ Khait, 1949, $M = 5.5$ Gissar, 1989 and $M = 7.4$ Suusamy, 1992.

The documented earthquake case histories of Central Asia will be compared with some of the worldwide most disastrous events, and particularly with the $M = 7.8$ Haiyuan (or Gansu, 1920) and the $M = 7.8$ Peru (1970) earthquakes. These two events caused the greatest number of deaths in history through multiple triggered landslides and a single mass movement, respectively.

Further, our analysis will focus on those types of mass movements, that caused these disasters: rapid flows (mainly) in loess deposits and massive rock avalanches. Actually, those types also induce the highest geological risk in Central Asian regions, such as shown in the following. For a complete review of landslide types triggered by earthquakes, the reader is referred, e.g., to Keefer (1984).

Special attention is paid to long-term effects of earthquakes in mountain regions. Examples is shown for clearly delayed triggering of slope failures after earthquakes and post-seismic increase of landslide activity, such as observed after the Chi-Chi earthquake of 1999 in Taiwan (Dadson et al. 2004). In this regard, we will also analyse previously called 'secondary or tertiary effects' of

earthquakes, such as natural dams and related flooding impacts. In the Tien Shan, the most recent massive natural dam was formed after the Suusamy, 1992—it partly failed in 1993, thus causing a long-runout debris flow and widespread flooding downstream. The 2008 Wenchuan earthquake clearly marked the importance of such effects—which could have killed another few thousands of people if efficient mitigation measures had not been taken by Chinese authorities. For these cases, it will be shown that the term 'consequential hazard' proposed by Korup (2003) should be preferred over 'secondary or tertiary effects' implying a lesser degree of importance.

Factors Contributing to the Seismic Triggering of Landslides

Geology

From our field observations and an extensive literature review (summarized in Havenith and Bourdeau 2010), we conclude that there are no particular geological conditions favouring the seismic triggering of landslides (compared to the aseismic triggering). However, if cross-bedding failure occurred, a seismic triggering is more likely compared to aseismic triggering.

Morphology

Earthquake-induced landslides may be triggered from any surface morphology—even within flat areas, such as lateral spreads, or from steep cliffs, such as rock falls.

Still, several particularities can be outlined. Harp and Crone (2006) noted for effects induced by the 2005 Pakistan earthquake that '... several ridges near the top also are covered with fractures that are concentrated at the ridge crests and the summit'. They conclude that 'these fractures probably are associated with increased levels of shaking due to topographic amplification of the ground shaking'. From our own experience of earthquake-induced landslides in the Tien Shan (see below), it can be concluded that mainly the surface curvature has an influence on seismic slope stability at global scale; particularly, hillcrests and convex surface morphologies are prone to seismic slope failure. The influence of slope angle on seismic slope stability is not clear; in some cases, especially in rocks, steeper slopes are more prone to instability; in others, especially in soft sediments, gentle slopes produce most of the mass movements, indicating that the combined effect of slope and geology has to be taken into consideration. Similarly the influence of the slope aspect on slope stability is connected to environmental and tectonic conditions.

Major Seismic Landslide Events: Focus on Central Asia

Nadim et al. (2006) assessed landslide and avalanche occurrence probabilities worldwide on the basis of morphological, geological, meteorological and seismological data. They clearly showed that all landslide hotspots are located in seismically active mountain ranges. For Central Asia, they estimate that global landslide hazard can be rated as medium to very high. They further noted that some areas in Tajikistan are marked by highest mortality risk due to landslides.

The following case histories document the landslide risk triggered by earthquakes in the Tien Shan and the Pamir Mountains. A comparison will be made with the 1920 Haiyuan (China) and 1970 Peru events to outline the most important factors contributing to landslide hazard and risk in Central Asia.

Central Asian Case Histories

The Kemin $M_s = 8.2$ earthquake of 1911 is one of the strongest events ever recorded in the Tien Shan; it was first analysed by Bogdanovich et al. (1914). The earthquake caused extensive landsliding along the activated fault segments over a length of 200 km. The largest mass movements were two rockslides, one within the Kemin valley and the other north of the lake Issyk-Kul. The first rock avalanche (about $15 \times 10^6 \text{ m}^3$) made of limestone material occurred along the activated Chon Kemin fault at about 60 km W of the epicentre, and is known to have buried a village of yourts with 38 inhabitants. The second ‘Anavevo’ rockslide is one of the most prominent features produced by the Kemin earthquake. Failure took place at the southern end of a mountain ridge, just above the discontinuous Chon Aksu thrust fault also activated by the 1911 Kemin earthquake. Outcrops at the foot of the southwest-oriented slope show particularly disintegrated and weathered granitic rocks within a 100–200 m thick fault zone.

During the same year, 1911, the Sarez earthquake, $M_s = 7.6$, struck the central Pamir Mountains, Tajikistan. Such an earthquake is likely to have triggered hundreds or thousands of mass movements, but only one is well documented: the giant Usoi rockslide, which fell from a 4,500 m high mountain down to an elevation of 2,700 m in the valley (Schuster and Alford 2004). This rockslide has formed a dam with a volume of about $2 \times 10^9 \text{ m}^3$ on Murgab River. According to Schuster and Alford (2004), the location of the slide is related to ‘a high degree of rock fracturing from previous tectonic activity... a major thrust fault with an unfavourable orientation... and... a series of intensively sheared zones forming geometric setting for a typical wedge failure.’ Behind this 600 m high natural dam

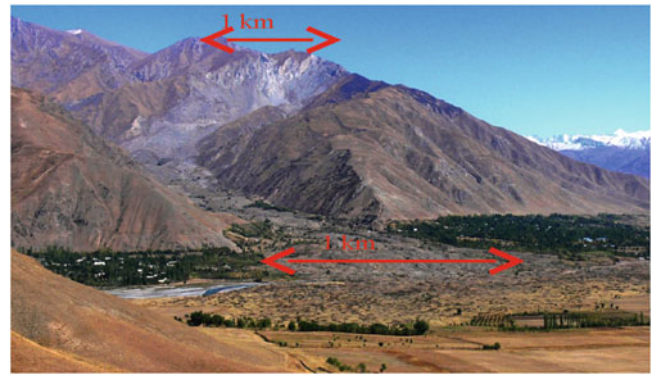


Fig. 2 Khait rock avalanche; view towards the East from Yasman valley (unpublished photograph of 2005 provided by A. Ischuk)

(the highest dam in the world), Lake Sarez and the smaller Lake Shadau had been impounded, the first one with a maximum depth of 550 m. Various scenarios consider the risk related to the failure of the rockslide dam due to internal erosion or overtopping as well as to a flood wave induced by the impact of mass movement into Lake Sarez. Those scenarios are discussed by Schuster and Alford (2004), among others—the worst-case scenario flood wave could affect more than 5 million people living in the Amu Darya river basin.

In 1949, the $M = 7.4$ Khait earthquake in Northern Tajikistan produced one of the most destructive earthquake-triggered landslide events in human history (until that time, according to Leonov 1960). The most catastrophic triggered mass movement is a rock avalanche that had buried the villages of Khait and Kusurak with thousands of inhabitants (Fig. 2); the exact number of fatalities will never be known since ‘during the formidable rule of Joseph Stalin, information about accidents and natural catastrophes was suppressed unless special permission was granted’ (Yablokov 2001). The volume was initially estimated to more than $200 \times 10^6 \text{ m}^3$ (Leonov 1960). However, more recent investigations by Evans et al. (2007) indicated that the total volume would be much lower, of about $40 \times 10^6 \text{ m}^3$. Also Evans et al. (2007) observed that a significant part of the mass movement was made of loess, which probably contributed to the mobility of the initial rockslide. They also indicate that in the Yasman valley opposite to the Khait rock avalanche, massive loess earth-flows are believed to have buried about 20 villages. In total, the Khait rock avalanche and loess earth-flows are likely to have killed more than 10,000 people during the 1949 event. In addition to the catastrophic impacts, Russian geologists described also the general conditions of the earthquake-triggered slope failures. For instance, Leonov (1960) wrote (translated from the Russian original): ‘...involved are also amplification effects that can explain landsliding far from the epicentre...’ This observation had already been pointed out above.

In 1989, a $M_s = 5.5$ earthquake struck the village of Gissar in Tajikistan and triggered a series of earth-flows in loess. At least 200 people were killed and hundreds of houses were buried. According to Ishihara et al. (1990), those slides were all related to extensive liquefaction, which had developed for a horizontal acceleration of about 0.15 g. They associated the liquefaction to the ‘collapsible nature’ of the highly porous loess material (a silt-sized deposit with an average content of clay of 15 % and a low plasticity). The sliding surface of most landslides was located at a depth of about 15 m within the saturated part of the 30 m thick loess deposits. Ishihara et al. (1990) also noted that the scarps of many landslides were located along a water channel installed on the shoulder of the hills. They assumed that ‘water in the channel had been infiltrating in the loess over years leading to final failure during earthquake due to liquefaction of water-bearing loess layer’. This is supported by their observation of muddy water oozing from the earth-flow.

The most recent large seismic event hitting Central Asian mountain regions was the $M_s = 7.3$ Suusamyр earthquake on August 19, 1992, triggering various types of ground failures in the Northern-Central Tien Shan.

Most of the 50 people killed in the remote areas were victims of mass movements. Korjenkov et al. (2004) described a series of ground failures: sagging of mountain slopes, rockfalls, landslides, soil avalanches and flows, mud/debris flows, and also a great variety of gravitation cracks. Extensive ground failures could be observed along the crest and southern slope of the Chet-Korumdy ridge—here, most landslides had developed from previously existing ground instabilities.

It should be noted that only one large rockslide was triggered, the Belaldy rock avalanche (Korjenkov et al. 2004). It has covered a shepherd’s family and a flock of sheep. The situation before and after the earthquake of the rockslide site is shown in Fig. 3. This mass movement had formed a dam on Jalpaksu River with a thickness of about 100 m, a width of 700 m, and volume of more than $40 \times 10^6 \text{ m}^3$. Behind the dam two small lakes were impounded (with an area of 200–300 m^2 in September 1992). In less than a year, the water level had increased enough to induce partial failure of the dam (Korjenkov et al. 2004). This failure resulted in a 20 km long mud- and debris-flow, which caused a lot of damage for infrastructure of Toktogul region. The aerial photograph of 1996 of the Belaldy site (Fig. 3) shows the upper part of the debris flow just below the dam.

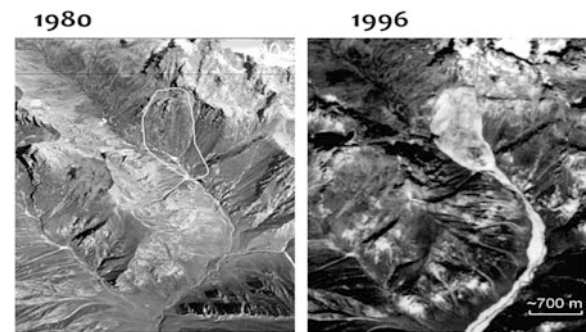


Fig. 3 The Belaldy rock avalanche. Aerial photographs before (left) and after (right) the Suusamyр earthquake

The Most Disastrous Regional and Singular Earthquake-Triggered Landslide Events

As shown previously, earth-flows in loess deposits and rock-debris avalanches proved to be the most catastrophic mass movements in Central Asian mountain regions. Therefore, the 1920 Haiyuan and 1970 Peru earthquakes were selected for comparison since they are known to have triggered, respectively, the most disastrous loess earth-flows and the most catastrophic single rock-debris avalanche.

On December 16, 1920, a $M = 8.5$ earthquake occurred near Ganyan Chi, Haiyuan County of the Ningxia Hui Autonomous Region in China (Zhang 1995). Several hundreds of thousands of houses collapsed and officially 234,117 people died. Zhang (1995) noticed that particularly high intensities were recorded over areas covered by thick loess deposits: ‘...areas with intensity of 8 ... here the damage caused by the slides was more serious than the primary ones caused by the quake. Zhang and Wang (2007) report that about 100,000 people were killed by landslides in loess deposits. Dangjiacha landslide was one of the most catastrophic mass movements triggered by the 1920 earthquake. The landslide formed a dam with a volume of about $15 \times 10^6 \text{ m}^3$. Behind the dam, the largest lake induced by the earthquake had been impounded. Zhang and Wang (2007) observed that loess earth-flows triggered by the Haiyuan earthquake had developed on relatively gentle slopes compared to those triggered by rainfall in the same region. These observations highlight the particular susceptibility of loess areas to ground failure, such as it was clearly shown by Derbyshire et al. (2000) analysing geological hazards affecting the loess plateau of China. The failure mechanisms of loess earth-flows and their connection with liquefaction phenomena will be analysed more in detail in the next section.

On May 31, 1970, the $M = 7.7$ Peru earthquake triggered one of the most catastrophic landslides that have ever occurred: the Nevado Huascarán rock-debris avalanche. This event is not only known for the large number of casualties it has caused, about 18,000, but also for its geologically fascinating aspects (Plafker et al. 1971). The huge mass of rock and ice with a volume of more than $50 \times 10^6 \text{ m}^3$ originated from the west face of the 6,654 m high north peak of Nevado Huascarán at some 130 km east of the earthquake epicentre. The particularity of this debris avalanche is its long travel distance of about 16 km. Before reaching the villages of Yungay and Ranrahirca, the mass slid for more than 2 km over a glacier, filled the valley floor at the foot of the slope and then was channelled through a gorge. Just before the end of the gorge, the avalanche split into two lobes one moving on towards the village of Ranrahirca, one overtopping the 230 m high southern ridge of the gorge and continuing its way to Yungay village. Peak velocities of this rock avalanche were actually estimated at more than 100 km/h (even to about 300 km/h by Plafker et al. (1971)).

Short Conclusions Based on the Case Histories

The Nevado Huascarán and the Khait mass movements show that volume, runout and speed are three important factors contributing to the impact potential of mass movements. The high speed of the Khait rock avalanche is also documented by the following notes from Solonenko (1977): ‘...Its rate was about 100 km/h... A powerful air-wave went before the collapse. It broke constructions, uprooted trees and threw them down for hundreds of metres.’ Further, the Khait rock avalanche is one of the largest (recent) runout mass movements in the Tien Shan. A debris flow developing from a dam breach may, however, have an even longer runout—about 20 km in the case of the partial Belaldy rockslide dam failure. Similarly, loess earth-flows are known to have caused rapid and long runout mass movements. For instance, in the Dzhahal-Abad region, Fergana Valley, Kyrgyz Republic, loess earth-flows had travelled over 7 km in 1994 killing several tens of people. Considering also the previous notes on geological disasters in loess deposits, we believe that earthquake and landslide hazards are particularly high in those regions of Central Asia, which are covered by several tens of meters of loess: the foothill regions of the Fergana Basin rim (Kyrgyz Republic and Tajikistan) and around the town of Dushanbe (Tajikistan) as well as mountain valleys covered by loess up to an altitude of 2,000–2,500 m.

However, a disaster such as the 1920 Haiyuan earthquake is not expected to hit any of those regions for two reasons: first, a $M > 7.5$ earthquake is very unlikely to occur in these

areas; second, the loess cover is significantly thinner than on the loess plateau of China where the thickness can reach 300 m (Derbyshire et al. 2000).

Considering the enormous impact potential of massive rockslides, such as Belaldy or Khait, it is important to assess their occurrence probability. This probability is closely related to the recurrence time of the triggering earthquake (actually, only very few massive non-seismic rock avalanches are known from the Tien Shan)—but also other, climatic, aspects have to be considered as shown below. For the entire Tien Shan and Northern Pamir region, the analysis of Abdрахmatov et al. (2003) showed that a return period of less than 20 years can be estimated for a $M \geq 7$ earthquake—able to trigger massive rockslides. Considering that the last $M \geq 7$ earthquake occurred in 1992, a rough computation of conditional probability indicates that there is a 90 % chance to exceed a 7-magnitude event within the next 10 years. The probability to have such an earthquake—and related mass movements—seems to be highest (with a chance of 90 % to exceed a $M = 7$ earthquake within the next 10 years) along the Tien Shan—Pamir boundary region, where the last $M \geq 7$ earthquake was the Markansu event in 1974 close to the Tajik-Kyrgyz-Chinese border.

Conclusions

A series of case histories of earthquake-induced landslides in Central Asia and a comparison with two worldwide known events have been presented. The volume and mobility (runout and speed) of the mass movements play an important role for related hazard and risk. In this regard, it is not surprising that the most disastrous mass movement known in Central Asia is a long runout rock avalanche with volume of about $40 \times 10^6 \text{ m}^3$, the Khait rock avalanche, which is supposed to have reached a speed of more than 100 km/h.

While these giant rockslides are almost exclusively triggered by large magnitude seismic events ($M \geq 7$) in Central Asian mountain regions, loess earth-flows may also be triggered by smaller earthquakes—or even by climatic factors alone. Here, we presented some examples of fatal loess landslides triggered directly by an $M = 5.5$ earthquake in Tajikistan and we know a series of landslides, which developed even during or after local $4 < M < 5$ earthquakes. The comparison with the Haiyuan earthquake event of 1920 showed that such loess landslides could be very disastrous.

For loess earth-flows, the high impact potential is, however, not only related to the volume and mobility of a single landslide—which are generally lower than that of massive rock avalanches. Here, the high spatial and temporal occurrence probabilities clearly contribute to related risk. The 1920 Haiyuan earthquake triggered thousands of loess earth-flows. $M > 7$ earthquakes able

to trigger at least hundreds of landslides occur almost every 20 years in the Central Asian mountain regions—many of which are covered by several meters of loess, especially in the foothill areas.

The importance of mid- and long-term effects can be outlined both for rockslides and loess landslides. Several case histories showed that one important—if not the most important—long-term consequence of massive rockslides can be the formation of a dam and the impoundment of a natural reservoir. Actually, the largest still existing rockslide dam on earth had formed in 1911 in the Pamir Mountains. The worst-case scenario flood wave triggered by dam failure could affect more than 5 million people living in the Amu Darya river basin.

For many loess landslides, it can be shown that seismic ground motions must not necessarily be the final trigger, but could also be a preparatory factor of slope failure. Relatively weak seismic shaking (e.g. <0.1 g) is able to produce ground fractures, but often without inducing a mass movement. However, these ground fractures can facilitate water infiltration and related increase of groundwater pressures, which could lead to slope instability.

In this regard, it should be emphasized that similar earthquakes may not necessarily trigger the same amount of landslides, due to different climatic conditions and groundwater level at the time of the earthquake: the $M = 6.6$ Nura earthquake in 2008 triggered relatively few landslides due to the occurrence at the end of the dry summer season. Thus, predicting the total hazard of earthquake-triggered landslide events, both seismic and climatic effects have to be taken into consideration. Some local seismic effects have been highlighted, notably amplification of shaking by convex surface morphology and surficial soft materials. Recent works by Chinese colleagues had clearly proofed the morphological effects on the seismic triggering of landslides for the last 2008 Wenchuan earthquake, China.

Finally, the case histories showed that related landslides were not only instantaneous effects of earthquakes—some had already developed before the seismic shock and some continued or started moving well after the shaking. To better assess the short- to long-term effects earthquakes on slopes, landslides need to be monitored by geophysical, seismological and geo-technical systems, coupled to multi-temporal satellite imagery and numerical modeling of multi-event

scenarios. In the frame of new projects on landslide problems in Central Asia, focus will be on the installation of such monitoring—modeling systems.

References

- Abdrakhmatov K, Havenith HB, Delvaux D, Jongmans D, Trefois P (2003) Probabilistic PGA and arias intensity maps of Kyrgyzstan (Central Asia). *J Seismol* 7:203–220
- Bogdanovich MMC, Kark J, Korolkov B, Muchketov D (1914) Earthquake of the 4 January 1911 in the northern districts of the Tien Shan. Commission of Geology Committee, Saint Petersburg, 270 p (in Russian)
- Dadson SJ, Hovius N, Chen H, Dade B, Lin JC, Hsu ML, Lin CW, Horng MJ, Chen TC, Milliman J, Stark CP (2004) Earthquake-triggered increase in sediment delivery from an active mountain belt. *Geology* 32:733–736
- Derbyshire E, Meng X, Dijkstra TA (2000) Landslide in the thick loess terrain of North-West China. John Wiley, Chichester
- Evans SG, Roberts NJ, Ischuk A, Morozova G (2007) Landslides triggered by the 1949 Khait Earthquake, Tien Shan, Tajikistan. *Geophys Res Abstr* 9:10388
- Harp EL, Crone AJ (2006) Landslides triggered by the October 8, 2005, Pakistan earthquake and associated landslide-dammed reservoirs: USGS Open-file Report, 2006-1052
- Havenith HB, Bourdeau C (2010) Earthquake-induced hazards in mountain regions: a review of case histories from Central Asia – an inaugural lecture to the society. *Geol Bel* 13(3):135–150
- Ishihara K, Okusa S, Oyagi N, Ischuk A (1990) Liquefaction-induced flow slide in the collapsible deposit in the Soviet Tajik. *Soil Found* 30:73–89
- Keefer DK (1984) Landslides caused by earthquakes. *Geol Soc Am Bull* 95:406–421
- Korjenkov AM, Mamyrov E, Omuraliev M, Kovalenko VA, Usmanov SF (2004) Rock avalanches and landslides formed in result of strong Suusamy (1992, $M = 7.4$) earthquake in the Northern Tien Shan. Test structures for mapping of paleoseismic deformations by satellite images. In: Buchroithner MF (ed) High mountain remote sensing cartography VII (HMRSC VII), Institute for Cartography of the Dresden University of Technology. Kartographische Bausteine, Band 23, Dresden, 19 p
- Korup O (2003) Geomorphic hazard assessment of landslide dams in South Westland, New Zealand: fundamental problems and approaches. *Geomorphology* 66:167–188
- Leonov NN (1960) The Khait, 1949 earthquake and geological conditions of its origin. In: Proceedings of academy of sciences of the USSR. Geophysical series, 3. pp 409–424 (in Russian)
- Nadim F, Kjekstad O, Peduzzi P, Herold C, Jaedicke C (2006) Global landslide and avalanche hotspots. *Landslides* 3:159–173
- Petley D, Dunning S, Rosser N, Kausar AB (2006) Incipient landslides in the Jhelum Valley, Pakistan following the 8th October 2005 earthquake. Disaster mitigation of debris flows, slope failures and landslides. Universal Academy Press Inc., Tokyo, pp 47–55
- Plafker G, Erickson GE, Concha JF (1971) Geological aspects of the May 31, 1970, Peru earthquake. *Bull Seismol Soc Am* 61: 543–578
- Schuster RL, Alford D (2004) Usoi landslide dam and Lake Sarez, Pamir Mountains, Tajikistan. *Environ Eng Geosci* X(2):151–168

- Schuster RL, Highland LM (2001) Socioeconomic and environmental impacts of landslides in the western hemisphere. USGS Open-File Report, 2001-0276
- Solonenko VP (1977) Landslides and collapses in seismic zones and their prediction. *Bull Int Assoc Eng Geol* 15:4–8
- Yablokov A (2001) The tragedy of Khait: a natural disaster in Tajikistan. *Mt Res Dev* 21(1):91–93
- Yin Y, Wang F, Sun P (2009) Landslide hazards triggered by the 2008 Wenchuan earthquake, Sichuan, China. *Landslides*. doi:[10.1007/s10346-009-0148-5](https://doi.org/10.1007/s10346-009-0148-5)
- Zhang Z (1995) Geological disasters in loess areas during the 1920 Haiyuan earthquake, China. *GeoJ* 36(2–3):269–274
- Zhang D, Wang G (2007) Study of the 1920 Haiyuan earthquake-induced landslides in loess (China). *Eng Geol* 94:76–88



Multi-stage Statistical Landslide Hazard Analysis: Earthquake-Induced Landslides

Chyi-Tyi Lee

Abstract

Landslides are secondary or induced features, whose recurrence is controlled by the repetition of triggering events, such as earthquakes or heavy rainfall. This makes seismic landslide hazard analysis more complicated than ordinary seismic hazard analysis and requires multi-stage analysis. First, susceptibility analysis is utilized to divide a region into successive classes. Then, it is necessary to construct the relationship between the probability of landslide failure and earthquake intensity for each susceptibility class, or find the probability of failure surface using the susceptibility value and earthquake intensity as independent variables. Then, hazard analysis for the exceedance probability of earthquake intensity is performed. Finally, an analysis of the spatial probability of landslide failure under a certain return-period earthquake is drawn. This study uses data obtained from the Chi-Chi earthquake-induced landslides as input data set to perform the susceptibility analysis and probability of failure surface analysis. A regular probabilistic seismic hazard analysis is also conducted to map different return-period Arias intensities. Finally, a seismic landslide hazard map is provided.

Keywords

Landslide • Event landslide inventory • Landslide susceptibility • Seismic landslide hazard • Earthquake-induced landslides • Arias intensity

Introduction

Unlike seismic ground motions, landslides are secondary or induced features that can be triggered by an earthquake or a storm. Their recurrence is controlled by the repetition of the triggering events and so, analysis is not as simple as with earthquake occurrence. Therefore, different approaches must be considered, as well as multi-stage analysis.

Seismic landslide hazard analysis, as introduced by Jibson et al. (2000), is actually multi-stage analysis, including Newmark analysis, and probability of failure analysis. Its product is a map showing probability of seismic triggering of landslides given the Northridge-earthquake shaking

conditions in part of the Oat Mountain quadrangle. A further study has been made applying the Newmark and probability of failure analysis method in Taiwan where the 475-year earthquake intensity was used to construct a seismic landslide hazard map of the Kuohsing quadrangle (Liao 2004; Liao and Lee 2009).

Lee et al. (2008a) proposed a statistical approach to determine the earthquake-induced landslide susceptibility and probability of landslide failure. This approach is similar to Jibson et al.'s (2000) with only the susceptibility stage being different; the former uses a statistical method and the latter uses a deterministic method. Lee (2013b) made an attempt to construct a 475-year seismic landslide hazard map. This paper used the Chi-Chi earthquake-induced landslide data as the training data set to develop a susceptibility model and a probability of failure curve, and further used a 475-year return-period Arias intensity map to construct a 475-year seismic landslide hazard map for the whole of Taiwan.

C.-T. Lee (✉)
Graduate Institute of Applied Geology, National Central University,
No. 300, Zhongda Rd., Zhongli City 32001, Taiwan
e-mail: ct@ncu.edu.tw

However, this approach has a weak point in that the hazard map may include the probability contributed from causative factors and produces a non-zero probability at zero earthquake intensity. To remedy this problem, a new landslide probability of failure relationship must be further developed.

The present study seeks to improve upon Lee's method (2013b) by developing a probability of failure surface instead of a probability of failure curve. The new relationship should avoid mixing the contribution from causative factors. Using this new probability of failure surface and a 475-year return-period Arias intensity map, a new 475-year seismic landslide hazard map for the whole of Taiwan is constructed. The seismic landslide hazard map might reveal the landslide spatial probability at each pixel given a certain earthquake return-period.

Methodology

Susceptibility Model

Our statistical seismic landslide susceptibility analysis method basically follows Lee et al. (2008a). Effective selection of the landslide causative factors and triggering factors should evaluate: (1) the difference between landslide and non-landslide groups; (2) probability of failure curve of a factor; (3) success rate curve of a factor (Lee 2013a). Effective factors are then tested for normality and independence, and the final selection of factors is made.

The construction of a statistical landslide susceptibility model may be performed using a multivariate statistical method (Carrara 1983; Ayalew and Yamagishi 2005; Eeckhaut et al. 2006; Greco et al. 2007). Discriminate analysis was selected in Lee et al. (2008a) to build their susceptibility model with causative factors, triggering factor and an event-based landslide inventory. However, in routine analysis of landslide susceptibility for many different drainage basins in Taiwan in recent years (e.g., Lee and Fei 2011), it has been found that logistic regression is better for three reasons: (1) the shape and concentration of data points in the probability of failure curve are always better when the logistic regression method is used; (2) logistic variables can be used in the logistic regression for categorical data, like the lithology and slope aspects; and (3) although normality is also required in logistic regression, it is not as serious as in discriminate analysis (Lee 2013b). Therefore, the logistic regression method is adopted in the present study.

Probability of Failure Surface

The construction of a probability of failure curve for the susceptibility values is simple: simply plot the mean probability of failure value at each susceptibility bin and fit a

curve. A probability of failure surface is intended to show relationship between the probability of failure and Arias intensity at each susceptibility bin, and to obtain the fit to the surface using the Arias intensity and susceptibility as two independent variables. Note that the susceptibility values used here indicate the event-independent susceptibility without a triggering factor.

A landslide spatial probability map may be produced by transferring the event-independent susceptibility values and Arias intensities to the probability of failure by using a probability of failure surface. When Arias intensities from the training event are used, one can produce a hazard map that reflects the earthquake event. The use of the Arias intensities for a specific earthquake scenario, produces a hazard map that reflects the scenario earthquake.

Temporal Probability of Landslides

Since seismic landslides are induced by earthquakes, their recurrence is controlled by the repetition of the earthquake event. Therefore, we must know the likelihood of earthquake recurrence or the annual exceedance probability of earthquake ground motions. This may be obtained through regular probabilistic seismic hazard analysis (PSHA) (Wong et al. 2004) with a set of fault source models in addition to the regional source models (Cheng et al. 2007) and a proper set of Arias intensity attenuation equations (Lee et al. 2012).

An Arias intensity map for a certain level of exceedance probability or return period for earthquakes is the objective of the PSHA, and this comprises the input data for the seismic landslide hazard mapping. This is commonly a 475-year return period or 10 % exceedance in 50 years. However, there may be other choices of return period or exceedance probability, like a 950-year return period or a 10 % exceedance in 100 years. If the Arias intensities of a 475-year earthquake are used, the hazard map reflects the 475-year earthquake, and may be called a 475-year seismic landslide hazard map.

Both for establishing a susceptibility model and in hazard mapping, the Arias intensity should be topographically corrected. The present study uses the empirical formula proposed by Lee et al. (2008a) for topographic correction of the Arias intensity.

Data

Basic Data

The basic data used in the present study include: 10 m high resolution SPOT images, a 5-m grid digital elevation model (DEM), 1/5,000 photo-based contour maps, 1:50,000 geologic maps, and earthquake strong-motion records. Digital

geological maps (1:50,000) were obtained from the Central Geological Survey, Taiwan. All the vector layers were converted into raster cells of 20 m × 20 m in size and this resolution was used for all subsequent processing and analysis for each landslide factor and the hazard model.

Chi-Chi Landslide Inventory

False-color SPOT images were used for landslide recognition. Landslides were recognized and digitized in GIS and attributes assigned to establish a landslide map table. Each landslide table was then checked in the field and modification was made. An event-triggered landslide was identified by comparing the pre-event and post-event landslide inventories, to produce an event-based landslide inventory. The Chi-Chi earthquake event-based landslide inventory is shown in Fig. 1. For a detailed description of the new Chi-Chi landslide inventory, please refer to Lee (2013a).

Results

Event-Based Susceptibility Model

The Chi-Chi earthquake induced shallow landslides (Fig. 1) and Arias intensities were actually used in the susceptibility analysis. Due to the fact that an event landslide inventory and a triggering factor of the event are used in the development of the susceptibility model, this is called an event-based susceptibility model (Lee et al. 2008a, b).

Causative factors used in the susceptibility model include the following: slope gradient, slope aspect, terrain roughness, slope roughness, total curvature, total slope height, and lithology. For a detailed description of the causative factors and the triggering factor, please refer to Lee (2013a).

Logistic regression is used in the susceptibility analysis and the results of this analysis include a logistical function and the coefficients,

$$\ln \left[\frac{p}{1-p} \right] = 0.089L_1 + 0.259L_2 - 0.538L_3 + 0.550L_4 - 0.067L_5 - 1.179L_6 - 0.435A_1 - 0.172A_2 + 0.209A_3 + 0.288A_4 + 0.345A_5 - 0.339A_7 - 0.715A_8 + 1.068F_1 + 0.184F_2 + 0.137F_3 + 0.827F_4 + 0.234F_5 + 1.220F_6 - 2.331. \quad (1)$$

where L_1 – L_7 are lithological units; F_1 – F_5 are causative factors; F_6 is a triggering factor; and p is the occurrence probability. During the establishment of the logistic equations, the input p is 1 for a landslide grid and 0 for a

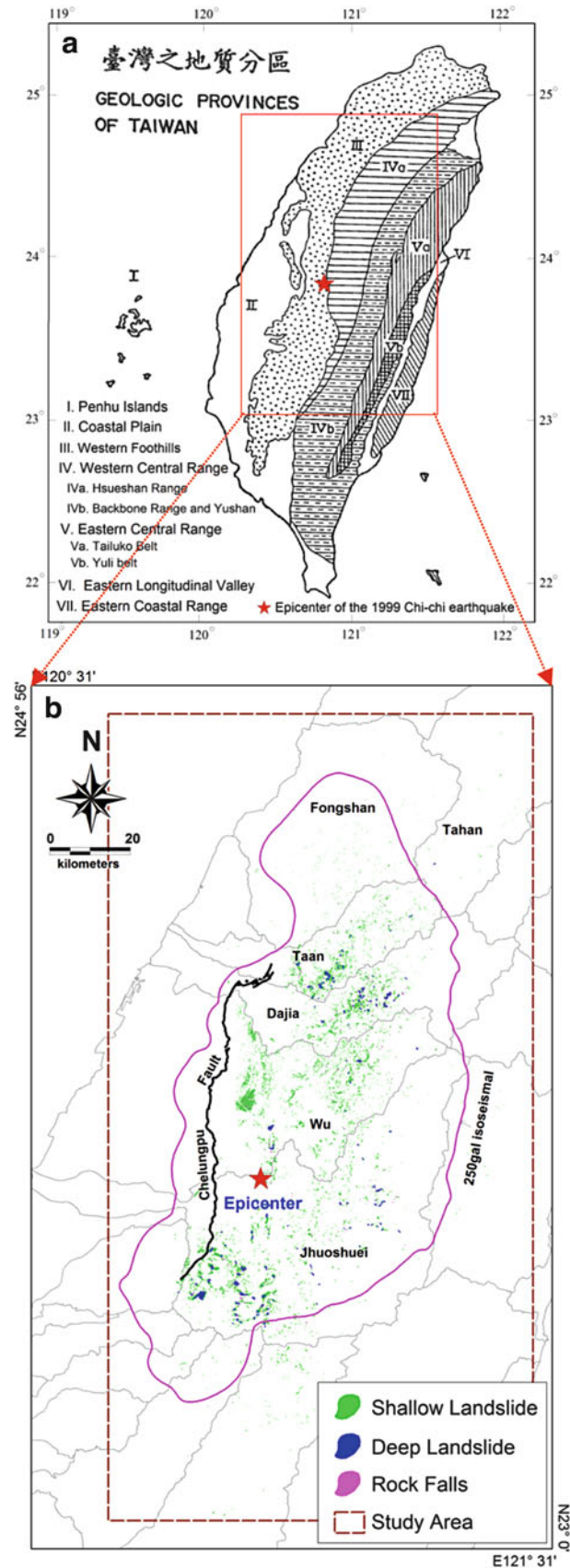


Fig. 1 Landslides triggered by the 1999 Chi-Chi earthquake: (a) index map showing the geology of Taiwan; (b) landslide distribution (the red star indicates the epicenter of the Chi-Chi earthquake)

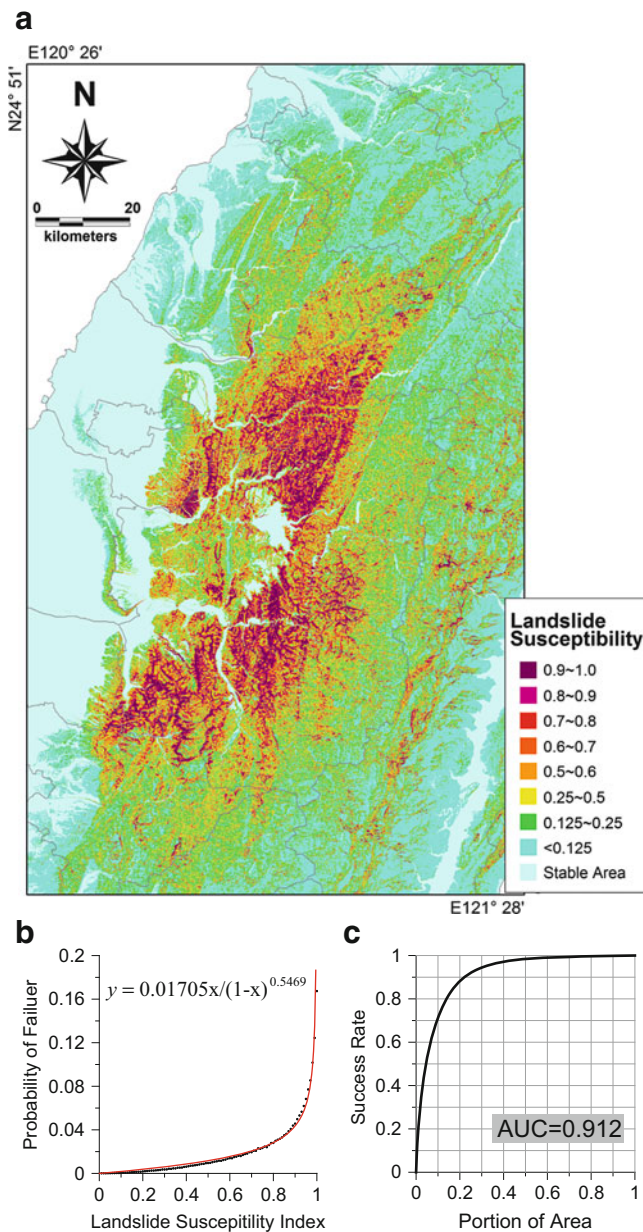


Fig. 2 Susceptibility model for Chi-Chi earthquake-induced landslides: (a) event-dependent landslide susceptibility map; (b) probability of failure curve; and (c) success rate curve

non-landslide grid. After the regression, when the set of factors is given a score at a grid point, the occurrence probability p at that point is derived. It will be in the range of 0–1. This occurrence probability is taken as a susceptibility index λ in this study. Larger values of an index indicate a higher susceptibility to landslides.

The event-based susceptibility model (Fig. 2) explains the event-induced landslide distribution. The probability of failure curve shows a good fit to the $x/(1-x)$ function (Fig. 2b). The area under the curve (AUC) of the success rate curve can be as high as 0.912 (Fig. 2c). The model is further

validated utilizing the Rueili earthquake event landslide inventory (Huang 1999) and Arias intensities; the AUC of the prediction rate curve is 0.769 for the model.

Event Independent Susceptibility Model

The event-based susceptibility model is dependent on the event itself. However, if we extract the triggering factor from the model, then the model becomes event independent, provided that the triggering factor is an independent factor having only small correlation coefficient with any causative factors. This option must be carefully examined before a causative factor is selected.

In this case, the event-based susceptibility model is reduced to an event-independent model by removing the component of the triggering factor from the original model. Here, we call this reduced model an event-independent susceptibility model for the region. Different event-independent susceptibility models for the same region have been compared and good similarity has been found among them (Lee et al. 2004). On this basis, we can use an event-independent susceptibility model to represent the susceptibility of the region with confidence.

Probability of Failure Surface

Starting with testing the relationship between probability of failure and Arias intensity at each event-independent susceptibility bin, it was found that the relation is good; the probability of failure increases with an increase in the Arias intensity and also with an increase in the susceptibility (Fig. 3a). After this finding, it was necessary to find a global fitting surface using the Arias intensity and event-independent susceptibility as two independent variables. The result is shown in Fig. 3b and Eq. (2) as follows:

$$y = 50.316\lambda \left(1 - e^{-12.620\lambda^{1.021}}\right) \left(1 - e^{-0.026\alpha^{2.232}}\right) \quad (2)$$

where x is the corrected Arias intensity; y is the probability of failure, and λ is the event-independent susceptibility.

Arias Intensity from PSHA

The temporal probability of a seismic landslide hazard model may be accounted for by a triggering factor—namely the hazard level of the Arias intensity in the present study. This may be obtained through conducting a regular PSHA (Wong et al. 2004) with a proper set of earthquake source models and Arias intensity attenuation equations.

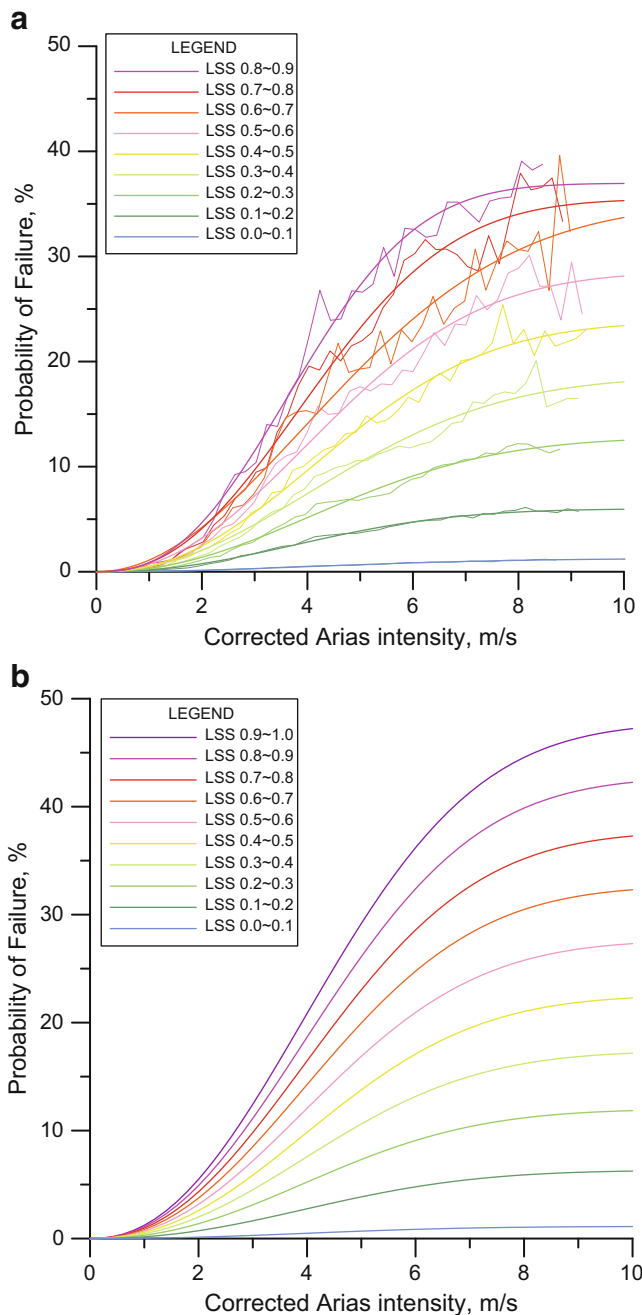


Fig. 3 Probability of failure surface: (a) probability of failure curve at each event-independent susceptibility bin with data and local fit; (b) fit of probability of failure surface, equation shown in the text

I and my students have made efforts to build a modern Taiwan seismic hazard model since the year 2002 (Cheng 2002). This model includes traditional regional sources and model fault sources. In the model, the fault parameters and slip rate for each of the 48 active fault sources are evaluated

(Lee 1999; Cheng 2002). Subduction zone interface and intraslab sources are also considered.

The seismic hazard model of Taiwan (Cheng 2002; Cheng et al. 2007) and a new Arias intensity attenuation relationship (Lee et al. 2012) are used in performing the PSHA, to obtain the different levels of exceedance probabilities as well as return periods for Arias intensity for each grid cell in the study region. The attenuation equations used include the relationships for crustal earthquakes, subduction zone interface earthquakes and intraslab earthquakes (Lee et al. 2012; Hsieh 2008).

Both in establishing a susceptibility model and in hazard mapping, the Arias intensity should be topographically corrected. The empirical formula proposed by Lee et al. (2008a) is used for topographic correction of the Arias intensity in the present study.

Seismic Landslide Hazard Map

The event-independent susceptibility model and the probability failure surface together with an Arias intensity map may be used to construct a seismic hazard map. It is capable of landslide prediction during a scenario earthquake event, provided that the earthquake intensity is known for each study grid cell. However, for hazard mapping, a certain temporal probability or return period for earthquake intensity should be adopted. This is commonly a 475-year return period or 10 % exceedance in 50 years. Other choices of return period or exceedance probability, like a 950-year return period or a 10 % exceedance in 100 years, may also be used.

The 475-year topographically corrected Arias intensity map and the event independent susceptibility model are then applied to the probability of failure model to construct a 475-year seismic landslide hazard map for the whole of Taiwan (Fig. 4).

Conclusion and Recommendation

A multivariate statistical approach with logistic regression has been used to analyse the Chi-Chi earthquake-induced shallow landslides and their controlling factors, and to build an event-dependent susceptibility model. The event-independent model (without a triggering factor), the topographically corrected Arias intensity map, and the actual landslides from the Chi-Chi event, are used to construct a relationship, using the event-independent susceptibility and corrected Arias intensity as independent variables, and is fitted with a probability of failure surface. Then, a 475-year corrected Arias intensity map with the event-independent susceptibility model are input

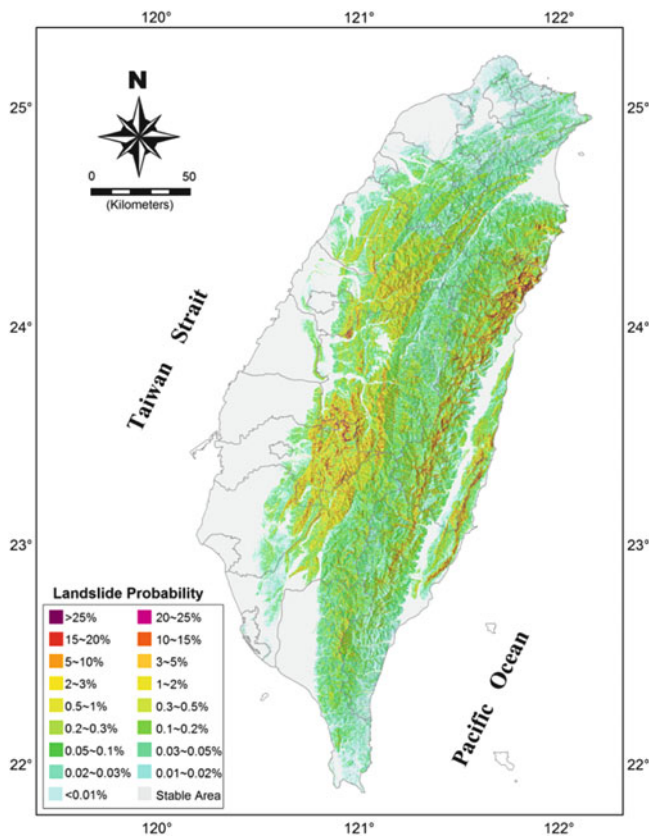


Fig. 4 475-Year seismic landslide hazard map for the whole of Taiwan

into the probability of failure relationship to complete a 475-year seismic landslide hazard map for the whole of Taiwan. The results of the analysis are good, provided that careful validation of the Rueil earthquake-induced landslides is made. We conclude that this statistical approach is feasible for seismic landslide hazard analysis, and that the hazard model can be used to predict landslides after a major earthquake and can be used to produce a seismic landslide hazard map of a wider region.

The statistical approach to seismic landslide hazard has advantages over deterministic methods in that it does not require failure depth, material strength, or groundwater data, and may have a better prediction rate. On the other hand, a deterministic model can be used anywhere once the parameters required by the model are available. The statistical approach, in contrast, may be applicable only in the vicinity of the study region where the model was trained, and may be limited to within or near the earthquake intensity range for which they were trained.

The present proposed hazard model is good for the prediction of landslide spatial probability during an earthquake event, the mapping of the seismic landslide hazard probability for a certain return-period earthquake, decision making for regional planning, site selection, hazard

mitigation, and the estimation of sediment products for a drainage basin after an extreme event. However there is still a lack of output in regards to the landslide magnitude which is very important in risk assessment. This problem needs further study.

References

- Ayalew L, Yamagishi H (2005) The application of GIS-based logistic regression for landslide susceptibility mapping in the Kakuda-Yahiko Mountains, central Japan. *Geomorphology* 65:15–31
- Carrara A (1983) Multivariate models for landslide hazard evaluation. *Math Geol* 15(3):403–427
- Cheng CT (2002) Uncertainty analysis and deaggregation of seismic hazard in Taiwan. Doctoral Thesis, National Central University, Jhongli, Taiwan (in Chinese with English abstract)
- Cheng CT, Chiou SJ, Lee CT, Tsai YB (2007) Study on probabilistic seismic hazard maps of Taiwan after Chi-Chi earthquake. *J GeoEng* 2(1):19–28
- Eeckhaut M, Vanwalleghem T, Poesen J, Govers G, Verstraeten G, Vandekerckhove L (2006) Prediction of landslide susceptibility using rare events logistic regression, a case-study in the Flemish Ardennes. *Geomorphol* 76:392–410
- Greco R, Sorriso-Valvo M, Catalano E (2007) Logistic regression analysis in the evaluation of mass movements susceptibility: the Aspromonte case study, Calabria, Italy. *Eng Geol* 89:47–66
- Hsieh PS (2008) Attenuation relationship of Arias intensity for Taiwan. Master Thesis, National Central University, Jhongli, Taiwan (in Chinese with English abstract)
- Huang TF (1999) Landslides triggered by Jueili earthquake. Master Thesis, National Central University, Jhongli, Taiwan (in Chinese with English abstract)
- Jibson RW, Harp EL, Michael JA (2000) A method for producing digital probabilistic seismic landslide hazard maps. *Eng Geol* 58:271–289
- Lee CT (1999) Neotectonics and active faults in Taiwan. *Proceedings of 1999 workshop on disaster prevention/management & green technology*, Foster City, CA, USA, pp 61–74
- Lee CT (2013a) Re-evaluation of factors controlling landslides triggered by the 1999 Chi-Chi earthquake. In: Ugai K, Yagi H, Wakai A (eds) *Earthquake-induced landslides*. Springer, Berlin, pp 213–224
- Lee CT (2013b) Developing a seismic landslide hazard map for Taiwan. *EGU General Assembly Conference Abstracts* 15
- Lee CT, Fei LY (2011) Landslide hazard analysis and mapping in a wide area. *Sino-Geotech* 129:53–62 (in Chinese with English abstract)
- Lee CT, Huang CC, Lee JF, Pan KL, Lin ML, Liao CW, Lin PS, Lin YS, Chang CW (2004) Landslide susceptibility analyses based on three different triggering events and result comparison. *Proceeding of international symposium on landslide and debris flow hazard assessment*, Taipei, pp 6-1–6-18
- Lee CT, Huang CC, Lee JF, Pan KL, Lin ML, Dong JJ (2008a) Statistical approach to earthquake-induced landslide susceptibility. *Eng Geol* 100:43–58
- Lee CT, Huang CC, Lee JF, Pan KL, Lin ML, Dong JJ (2008b) Statistical approach to storm event-induced landslide susceptibility. *Nat Hazard Earth Syst Sci* 8:941–960
- Lee CT, Lin PS, Hsieh BS, Sung CH (2012) Regional Arias intensity attenuation relationship for Taiwan with considering Vs30. *Bull Seismol Soc Am* 102(1):129–142
- Liao CW (2004) Probabilistic hazard analysis of earthquake-induced landslides – an example from Kouhsing, Taiwan. Doctoral Thesis,

- National Central University, Jhongli, Taiwan (in Chinese with English abstract)
- Liao CW, Lee CT (2009) Probabilistic hazard analysis of earthquake-induced landslides – an example from Kuohsing, Taiwan. Proceeding of the next generation of research on earthquake-induced landslides – an international conference in commemoration of 10th anniversary of the Chi-Chi earthquake, Jhongli, Taiwan, pp 91–92
- Wong I, Thomas P, Abrahamson N (2004) The PEER-lifelines validation of software used in probabilistic seismic hazard analysis. In: Yegian MK, Kavazanjian E (eds) Geotechnical engineering for transportation projects. ASCE GSP 126, pp 807–815



Quantitative Probabilistic Hazard Analysis of Earthquake-Induced Rockfalls

Andrea Valagussa, Paolo Frattini, and Giovanni B. Crosta

Abstract

On May 6, 1976, in the Friuli Venezia Giulia Region (Eastern Italian Alps) a 6.5 Mw earthquake triggered a high number of rockfalls, causing casualties and relevant damages. For ensuring safety to people and infrastructure, as well as for territorial and land use planning, hazard analysis is fundamental. This contribution illustrates a methodology for quantitative probabilistic hazard analysis related to earthquake-induced rockfall events. This methodology is based on Rockfall Hazard Vector (RHV, Crosta and Agliardi, *Nat Hazards Earth Syst Sci* 3:407–422, 2003), which has been modified to incorporate temporal probability. RHV is defined as the magnitude of a three dimensional vector in the Frequency-Energy-Height space. The parameters involved are calculated for each grid cell by using Hy-STONE, a software developed to perform 3D numerical modeling of rockfall propagation over complex terrain. In particular, rockfall annual frequency for each grid cell is assessed by combining the annual onset frequency with the transit frequency simulated by Hy-Stone. For earthquakes-induced rockfalls, the annual onset frequency is defined based on a magnitude-frequency function, which has been spatially downscaled according to a rockfall susceptibility map. This map was developed by using multivariate statistical techniques (e.g. Discriminant Analysis) with morphological and seismic variables (e.g. slope, curvature, PGA, distance from the epicentre ecc.).

Keywords

Rockfall • Earthquake • Hazard analysis

Introduction

Rockfalls are one of the most severe and recurrent dangerous events that occurs where geological and weather conditions are particularly severe for slope stability. The high hazard of rockfalls is mainly due to its dynamic behaviour, with velocities of the blocks between 30 and 100 km per hour, and the difficulty to predict the source areas and the trajectories of the blocks. The trigger of these events is

generally determined by a shear or tension failure along pre-existing planes of discontinuity that separate potentially unstable blocks from the slope.

For the forecast of the rockfall occurrence, two probabilities must be defined: the onset probability and the reach probability. The onset probability depends on several factors such as geological, geomorphological, hydrological conditions that control the stability of the cliffs. The reach probability depends on the path of rockfalls movement related to several factor such as topographical surface, rockfall volume, shape and size of blocks. For the assessment of the reach probability, the rockfall dynamics is performed by using empirical methods (e.g. the “shadow cone” method, Evans and Hungr 1993) or by simulating free-fall, impact, bouncing and rolling motions in a 2D or

A. Valagussa (✉) • P. Frattini • G.B. Crosta
Department of Earth and Environmental Sciences, University of
Milano-Bicocca, p.zza della Scienza 4, Milano 20126, Italy
e-mail: a.valagussa2@campus.unimib.it; paolo.frattini@unimib.it;
giovannibattista.crosta@unimib.it

3D space, through the use of kinematic (e.g. Stevens 1998), hybrid (Pfeiffer and Bowen 1989; Jones et al. 2000; Crosta et al. 2004) or dynamic mathematical models (Descouedres and Zimmermann 1987; Azzoni et al. 1995).

For seismically active areas, the onset probability is controlled by the earthquake occurrence rate. The relationship between landslide and earthquake has been extensively studied in the literature since Keefer (1984). However, only a few studies focused explicitly on rockfalls. In particular, Marzorati et al. (2002) defined a method for the determination of the spatial variability of events and their triggering factors in relation to the earthquake happened in Umbria and Marche regions in the 1977. They define a regression equation in which the density of landslide is related to the slope gradient and to the Peak Ground Acceleration (PGA) values.

In this work, the starting point for the definition of a rockfall hazard map in seismic areas, is the “Rockfall Hazard Vector” approach (RHV) proposed by Agliardi and Crosta (2003). This method has been modified to include probability in order to develop a new simple and readily applicable methodology for earthquake-induced rockfall hazard assessment and zonation in seismic areas.

Methodology

Rockfall hazard at a given location on a slope is described as a function of rockfall annual frequency of transit for each position along the slope of a terrain surface, F_{annual} (year^{-1}), block kinetic energy, E_k (kJ), and trajectory height, H (m). Rockfall hazard is expressed through an index that represents the magnitude of the modified “Rockfall Hazard Vector” (RHV_{mod}):

$$|RHV_{\text{mod}}| = \sqrt{F_{\text{annual}}^2 + E_k^2 + H^2} \quad (1)$$

where F , E_k and H are indices obtained by reclassifying from 1 to 3 f_{annual} , e_k , and h , respectively (Table 1).

The reclassification threshold of e_k and h classes are defined based on the dimension and energy of typical countermeasures (Crosta and Agliardi 2003). The thresholds of f_{annual} have been defined taking into account the individual risk acceptability criteria; in fact assuming that the impact of a block on a person is always lethal, the frequency of transit corresponds to the individual risk, defined, as the probability that an unprotected person, always in the same position, is killed (Bottelberghs 2000). The f_{annual} class thresholds correspond to the limits of tolerability for non-volunteer risk proposed by Geotechnical Engineering Office (1998).

Table 1 Intervals classification of the variables involved

Value	c	e_k (kJ)	h (m)	f_{annual}
1	0–10	0–1,000	0–4	$0–10^{-5}$
2	10–50	1,000–5,000	4–10	$10^{-5}–10^{-4}$
3	>50	>5,000	>10	$>10^{-4}$

The annual frequency of transit for each cell, f_{annual} is obtained by combining the annual onset frequency, f_{onset} (i.e. the expected number of events per year) with the results of the rockfall propagation model:

$$f_{\text{annual}} = f_{\text{onset}} \frac{c}{N} \quad (2)$$

Where c is the number of transits for each cell and N is the total number of blocks simulated in the area.

Based on a statistical and probabilistic analysis, a new procedure for the calculation of f_{onset} of rockfalls triggered by earthquakes is proposed. The first step is the calculation of the potential rockfall unstable area for different return periods by using a discriminant analysis. The second step is the calculation of the expected annual number of events for each return period starting from the calculated unstable area and from rockfall Magnitude Frequency (MF) relationship. The third step is the integration of different scenarios and calculation of the annual onset frequency, f_{onset} .

Case Study

The methodology has been applied to Venzone (Friuli-Venezia Giulia Region, Italy), which was interested by 1976 Friuli earthquake, with high damages and casualties. The area is part of an active geodynamic context. In the last 700 years, in the whole Friuli Venezia Giulia Region, 36 earthquakes occurred with magnitude larger than 5 (Rovida et al. 2011). The areas most affected by the earthquakes are well defined along the valley of the Tagliamento River, where Venzone is located (Fig. 1). According to the seismic hazard map of Italy (Working Group MPS 2004), in this area the peak ground acceleration with a 10 % exceeding probability in 50 years (i.e. return period of 475 years) ranges from 196 to 270 cm/s^2 . These values are the highest in northern Italy.

The Friuli 1976 Earthquake rockfall inventory covers about 630 km^2 . Govi (1976) compiled it through systematic photointerpretation of two series of photographs taken soon after the earthquake at latitudes ranging from 1,800 to 4,000 m. The inventory map, 1:50,000 in scales, includes 1,006 rockfall events mapped as points and, only for larger rockfalls, polygons.

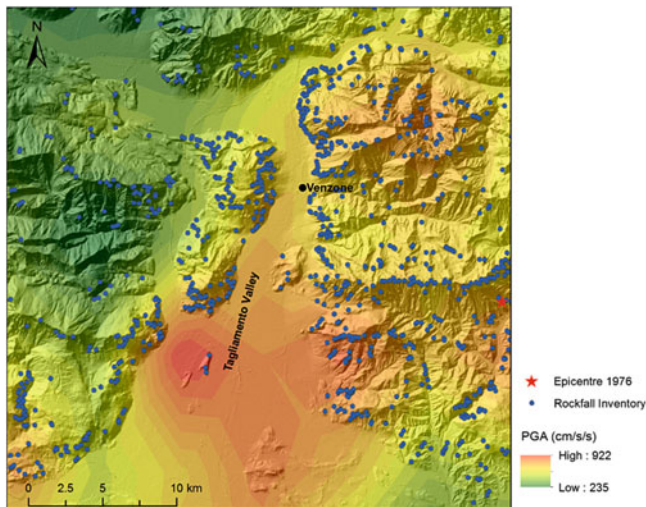


Fig. 1 Study area. Rockfalls (blue circles), the earthquake epicentre (red star, Aoudia et al. 2000) and the PGA values of main 1976 shock (Wald et al. 2006) are shown

Discriminant Analysis for the Assessment of Potential Unstable Areas

The first step for the assessment of f_{onset} of rockfalls triggered by earthquakes is the calculation of the potential rockfall unstable area for different return periods. To do this, a discriminant function analysis has been performed. This analysis allows classifying grid cells along the cliff as stable or unstable (0 and 1) as a function of morphometric variables and a seismic parameter that can be associated to different return periods. The discriminant function analysis is based on a dataset of points that are a-priori identified as stable or unstable. The unstable points correspond to rockfall source areas of events reported in the inventory used for the analysis. The stable group has been created as a set of random points in the cliff area with a distance larger than 50 m from unstable points. This allows to avoid overlapping of the two datasets. The distance of 50 m has been selected considering the spatial uncertainty in the mapping of actual rockfall events.

By a stepwise procedure, the discriminant analysis selects variables that are most relevant for the classification of stable and unstable points. The importance of each predictor is evaluated by the value of the standardized discriminant coefficient (Table 2), whose sign depends on the tendency of the variable to classify objects in either the positive or the negative group. The positive group is represented by cells with rockfall; hence, a positive coefficient indicates a tendency to favour rockfall susceptibility.

Table 2 Variables selected and relative standardized discriminant function coefficients (SDFC)

Variables	SDFC
PGA (cm/s^2)	0.753
Slope	0.896
Aspect	n.s.
Epicenter distance (m)	0.435
$\cos \alpha$	-0.355
Vertical distance (m)	n.s.
Total curvature 10 m	n.s.
Total curvature 30 m	n.s.
Total curvature 90 m	0.078
Profile curvature 10 m	-0.096
Profile curvature 30 m	n.s.
Profile curvature 90 m	n.s.

n.s. = unselected by stepwise procedure. The centroids of the “no rockfall” and “rockfall” groups are -0.141 and 0.835 respectively, the percentage of the correct classification is 69.9 %

Independent Variables

Among the morphological variables, the slope angle, the slope aspect, the vertical distance from ridge, and the curvatures have been considered. Slope aspect is the maximum slope direction and it is related to some factors that may control rockfall occurrence (e.g. wind direction, rainfall, direction of seismic waves) (Dai et al. 2011). The vertical distance of each point from the ridge was used to express the effect of topographic amplification of seismic waves along ridges (Meunier et al. 2008). It is defined through a focal statistic that describes the maximum difference of elevation within a circular window with a radius of 800 m. Total and profile slope curvatures are introduced to account for topographic amplification along ridges and scarps. The effects of curvatures at different scales has been considered through the calculation of these variables with different resolution, by resampling DEMs at 1, 10, 30 and 90 m. Three seismic parameters have been used: the Peak Ground Acceleration (PGA, cm/s^2), the epicentre distance (m) and the difference between the direction of the seismic wave, in plant, and the local slope aspect has been used.

PGA values were obtained from the ShakeMap produced by the U.S. Geological Survey Earthquake Hazards Program (Wald et al. 2006). In the studied area, the value of the PGA ranges between 0.24 and 0.94 g. The epicentre distance was calculated as Euclidean distance in meters of each grid cell from the epicentre of Aoudia et al. (2000). The difference between the direction of the seismic wave, in plant, and the local slope aspect has been calculated as the cosine of the angle ($\cos \alpha$).

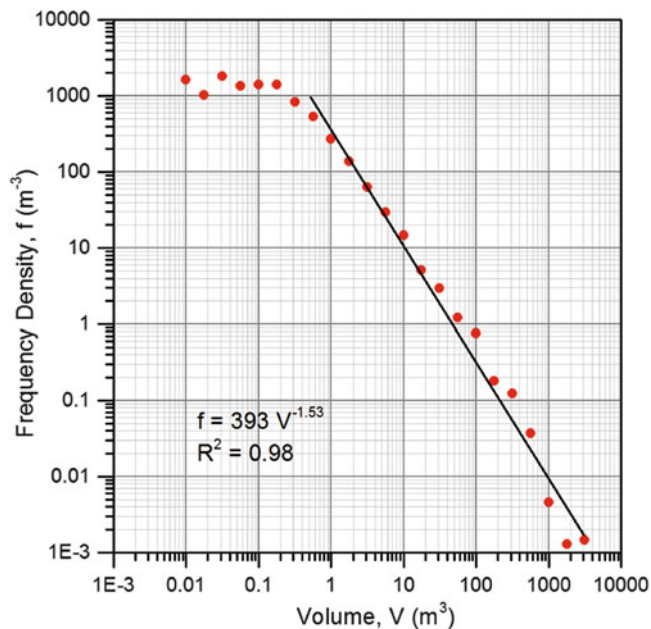


Fig. 2 Magnitude-Frequency relationships (MF) from field survey

Calculation of Annual Onset Frequency

From the results of the discriminant function analysis, the raw discriminant function and the unstable-group membership probability, which is considered as a proxy of the rockfall onset probability, were obtained. The discriminant function is:

$$D = -4.73 + 0.067 \cdot S + 0.0041 \cdot \text{PGA} + 0.00011 \cdot C90m \quad (3)$$

Where S is the slope angle (degree), PGA the peak ground acceleration (cm/s^2) and $C90m$ the total curvature with a resolution of 90 m.

By using, in the discriminant function, PGA values (Working Group MPS 2004) associated to different return periods ($T_r = 30, 50, 72, 100, 140, 200, 475, 1,000, 2,500$ years), it was possible to obtain nine maps of unstable-group membership probability along the cliff.

These maps have been finally reclassified in two classes (stable and unstable) by considering unstable all grid cells with a group-membership probability ≥ 0.5 .

The calculation of the expected annual number of events for each return period, starting from the unstable area maps, can be performed.

Given that the total unstable area is the sum of many different events with different volumes, and assuming that the relative frequency of these events with different volumes follows a known MF relationship (Hungry et al. 1999; Dussauge et al. 2003; Frattini et al. 2012b). Then the number

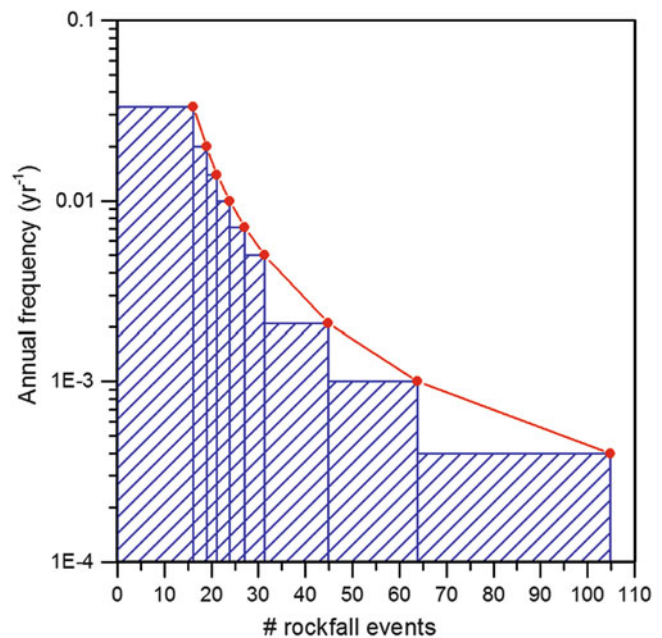


Fig. 3 For each scenarios, expressed in term of annual frequency (year^{-1}), the number of rockfall events is reported. The integral of the area under the curve (red rectangle) represent the total annual number of rockfall events per year

of events was calculated by equating the total area with the integral of the MF curve, expressed in terms of area. For this analysis, the MF relationship of the field-survey volume dataset 2010 has been used (Fig. 2), converting the rockfall volumes, V , in areas, A , considering a cubic shape for rockfalls, $A = V^{2/3}$.

Taking into account all scenarios (Fig. 3), the total annual number of rockfall events amounts to 0.76 per year. This value corresponds to the annual onset frequency, f_{onset} .

Rockfall Propagation Modelling

The rockfall runout simulation was performed by using the 3D model Hy-STONE (Agliardi and Crosta 2003; Crosta et al. 2004). The model is also able to simulate the effect of passive countermeasures, dynamics of “flying rocks” and the effect of vegetation (Frattini et al. 2012a).

Model results are provided in both raster and vector formats, including rockfall frequency, fly height, rotational and translational velocity and kinetic energy, as well as information about motion type, impact locations, impact and rebound angle at each computed point along fall paths.

The simulation performed in this study is based on the following parameters: spherical blocks with a density of $2,600 \text{ kg/m}^3$, mean radius of 0.71 m (max. 2.56 m); sources area steeper than 55° , stochastic exponential distribution for the radius of the blocks, normal for the coefficients of

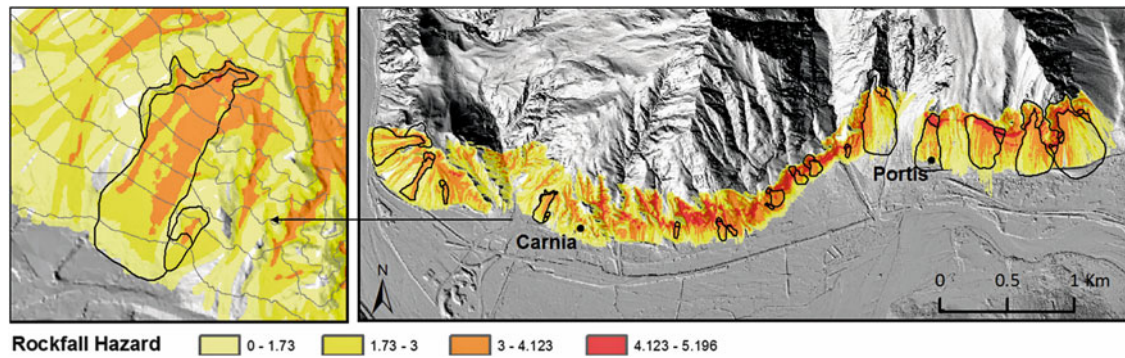


Fig. 4 In the figure are represented the RHV_{mod} and the rockfalls triggered by the 1976 Friuli earthquake come from photo interpretation

restitution and friction angle. A total number, N , of 3,233,830 blocks were simulated, 10 for each grid cell source. The calibration was based on the maximum runout distance identified during the field survey, and the extension of debris talus. The presence of countermeasures of given height and energy absorption was also considered.

Using the modified “Rockfall Hazard Vector” (RHV_{mod}) (Eq. 1) a hazard map was created, on the base of the 3D model. To better show the results, a neighbour statistic has been performed with a radius of 5 m. With this procedure, a new class of risk has been generated with values between 0 and 1.73. This class is considered as an area of residual risk that can be affected only by rare and isolated extreme events.

Comparing the main rockfall events of the 1976 Friuli earthquake identified on the basis of the aerial photo with the hazard map (Fig. 4) a good relation was found. The historical events mostly correspond to the area with a high level of risk, demonstrating the validity of the 3D model, at the basis of the RHV methodology. Differences in the runout of rockfalls are related to the presence of countermeasures aimed at the safety of the urban area.

Discussion

The presented methodology is proposed for the zonation of areas where rockfalls can be triggered by earthquakes. The result is a hazard map where the area is divided into classes with different levels of hazard, from low to high. The method gives also a probability of detachment from the cliff as function of different selected variables. This information is meaningful for any risk calculation, emergency planning, analysis of costs and benefits of different mitigation strategies, and risk management.

Furthermore, the RHV_{mod} , unlike other methods (e.g. RHRS, Pierson et al. 1990; RHV, Agliardi et al. 2003), expressed hazard in absolute terms, as a function of expected annual frequency. Hence, the RHV_{mod} values calculated for different geographical locations can be fully compared. This

is a big advantage when performing different hazard assessments, because the comparability of hazards allows to prioritize the interventions and the building of mitigation structures.

For the definition of an equation (Eq. 3) that related seismic and topographic variables to the rockfall occurrence, the methodology requires a complete description of the rockfall events in term of the position of the source areas for the statistical analysis, and the detached blocks size for the MF relationship. This information has been obtained through field surveys made after the earthquake and in the 2010, respectively.

Moreover, the methodology needs a detailed recording of the seismic parameter of the earthquake such as the PGA values, to allow a correct use of the information in the statistical analysis.

The effect of different lithology was not included because in the study area there is not a great variation on this variable. This may not be valid for other sites with different types of rocks.

Acknowledgments Civil Protection of Friuli Venezia Giulia Autonomous Region for having made available the LiDAR data and the orthophotos of the area.

Autonomous Region of Friuli Venezia Giulia for providing the historical data related to the 1976 Friuli Earthquake.

References

- Agliardi F, Crosta G (2003) High resolution three-dimensional numerical modelling of rockfalls. *Int J Rock Mech Min Sci* 40(4):455–471
- Aoudia A, Saraò A, Bukchin B, Suhadolc P (2000) The 1976 Friuli (NE Italy) thrust faulting earthquake: a reappraisal 23 years later. *Geophys Res Lett* 27:573–576
- Azzoni A, La Barbera G, Zaninetti A (1995) Analysis and prediction of rock falls using a mathematical model. *Int J Rock Mech Mining Sci Geomech Abstr* 32:709–724
- Bottelberghs PH (2000) Risk analysis and safety policy developments in the Netherlands. *J Hazard Mater* 71(1–3):59–84
- Crosta GB, Agliardi F (2003) A new methodology for physically-based rockfall hazard assessment. *Nat Hazards Earth Syst Sci* 3:407–422

- Crosta GB, Agliardi F, Frattini P, Imposimato S (2004) A three-dimensional hybrid numerical model for rockfall simulation. *Geophys Res Abstr* 6:04502
- Dai FC, Xu C, Yao X, Xu L, Tu XB, Gong QM (2011) Spatial distribution of landslides triggered by the 2008 Ms 8.0 Wenchuan earthquake, China. *J Asian Earth Sci* 40(4):883–895
- Descoedres F, Zimmermann T (1987) Three-dimensional dynamic calculation of rockfalls. In: Herget G, Vongpaisal S (eds) *Proceedings of the sixth international congress on rock mechanics*, Montreal. Balkema, Rotterdam, pp 37–42
- Dussauge C, Grasso JR, Helmstetter A (2003) Statistical analysis of rockfall volume distributions: implications for rockfall dynamics. *J Geophys Res* 108(B6):2286
- Evans SG, Hungr O (1993) The assessment of rockfall hazard at the base of talus slopes. *Can Geotechn J* 30(4):620–636
- Frattini P, Crosta GB, Agliardi F (2012a) Rockfall characterization and modeling. In: Clague JJ, Stead D (eds) *Landslides types, mechanisms and modeling*. Cambridge University Press, Cambridge., pp 267–281. ISBN 978-1-107-00206-7
- Frattini P, Crosta GB, Lari S, Agliardi F (2012b) Probabilistic rockfall hazard analysis (PRHA) In: Eberhardt E, Froese C, Turner K and Leroueil S (eds) *Landslides and engineered slopes: protecting Society through improved understanding*. Taylor & Francis Group, London, pp 1145–1151
- Govi M (1976) Map showing the landslides triggered by earthquake (from aerial photographs of May–June 1976)
- Hungr O, Evans SG, Hazzard J (1999) Magnitude and frequency of rock falls and rock slides along the main transportation corridors of southwestern British Columbia. *Can Geotech J* 36:224–238
- Jones CL, Higgins JD, Andrew RD, (2000) *Colorado Rockfall Simulation Program Version 4.0*. Colorado Department of Transportation, Colorado Geological Survey, 127
- Keefer D (1984) Landslides caused by earthquakes. *Geol Soc Am Bull* 95(4):406–421
- Marzorati S, Luzi L, De Amicis M (2002) Rock falls induced by earthquakes: a statistical approach. *Soil Dyn Earthq Eng* 22(7):565–577
- Meunier P, Hovius N, Haines JA (2008) Topographic site effects and the location of earthquake induced landslides. *Earth Planet Sci Lett* 275:221–232
- Pfeiffer TJ, Bowen T (1989) Computer simulation of rockfalls. *Bull Assoc Eng Geol* 26:135–146
- Pierson LA, Davis SA, Van Vickle R (1990) *Rockfall hazard rating system implementation manual*. Federal Highway Administration (FHWA) Report FHWA-OR—EG-90-01. FHWA, U.S. Department of Transportation
- Rovida A, Camassi R, Gasperini P, Stucchi M (eds) (2011) *CPTI11, the 2011 version of the parametric catalogue of Italian earthquakes*. Milano, Bologna. <http://emidius.mi.ingv.it/CPTI>. doi:10.6092/INGV.IT-CPTI11
- Stevens W (1998) *RocFall: a tool for probabilistic analysis, design of remedial measures and prediction of rockfalls*. M.A.Sc. Thesis, Department of Civil Engineering, University of Toronto, ON, Canada
- Wald DJ, Worden C, Quitoriano V, Pankow KL (2006) *ShakeMap® Manual, version 1.0* Technical manual, users guide, and software guide. Techniques and methods 12–A1, USGS. Available at <http://pubs.usgs.gov/tm/2005/12A01/pdf/508TM12-A1.pdf>
- Working group MPS (2004) *Redazione della mappa di pericolosità sismica prevista dall'Ordinanza PCM 3274 del 20 marzo 2003. Rapporto Conclusivo per il Dipartimento della Protezione Civile, INGV, Milano-Roma, aprile 2004, 65 pp. + 5 appendici (in Italian)*



Triggering Mechanism of Earthquake Induced Landslides

Zaheer Abbas Kazmi and Kazuo Konagai

Abstract

Earthquakes are catastrophic events instigating a variety of devastations by the strong ground shaking and/or internal deformations of the earth's crust. Landslides have been reported as the most devastating secondary effect (non-shaking) of deadly historical earthquakes in terms of the loss of lives, properties and disruption of communication facilities. The Mid-Niigata Prefecture Earthquake of 2004 and the Kashmir Earthquake of 2005 are two of the most catastrophic earthquakes of last decade and have triggered numerous landslides and slope failures. Seismic stresses have been calculated for the epicentral areas of both of the aforementioned earthquakes in the interior of a laterally homogeneous layered half-space through the forward modelling. Distribution of landslides for both of the subject earthquakes are compared to the square root of the second principal invariant of deviatoric stress tensor and a remarkable correlation is observed. Comparison of the existing landslides and seismic stresses deduces continual build-ups of a similar stress pattern in the past.

Keywords

Earthquakes • Landslides • Seismic stresses

Introduction

Most of the moderate to large historical earthquakes triggered numerous landslides and slope failures which caused significant damages to seismically active areas. In addition to their direct impacts, landslides and slope failures cause long lasting geotechnical problems in the form of destabilized mountainous slopes due to rock weathering such as debris flows, temporal mass movements, etc. Some of the most catastrophic earthquakes in terms of landslide

disasters in the last two decades include the 1999 Chi-Chi Earthquake of Taiwan (10,000 landslides; WN Wang et al. 2003), the 1995 Hyogoken-nanbu Earthquake of Japan, the 1994 Northridge Earthquake in the USA (11,000 landslides; Harp and Jibson 1996), the 1989 Loma Prieta Earthquake in the USA (1,280 landslides; Keefer 2000), the 2004 Mid-Niigata Prefecture Earthquake in Japan (1,353; Sato et al. 2005) and 2005 Kashmir Earthquake of Pakistan (2,424 landslides; Sato et al. 2007). Quantitative and geospatial study of global losses caused by the most deadly earthquakes in last 40 years (Marano et al. 2010) has shown that deaths from landslides have been the largest among those from other causes than shakes. Kobayashi (1981) has also found that more than half of all deaths in large earthquakes ($M > 6.9$) in Japan between 1964 and 1980 were caused by landslides. We, therefore, need to rationally understand the triggering mechanism and thorough cause investigation for such landslide disasters.

Z.A. Kazmi (✉)

COMSATS Institute of Information Technology, Quaid Avenue, Wah Cantonment 47040, Pakistan
e-mail: zaheer989@gmail.com

K. Konagai

Yokohama National University, 79-1 Tokiwadai, Hodogaya-ku, Yokohama, Japan
e-mail: konagai@ynu.ac.jp

The Mid-Niigata Prefecture Earthquake and 2005 Kashmir Earthquake are the two most catastrophic earthquakes of last decade, in terms of landslide disasters, and have been considered as study areas for the this article. The Mid-Niigata Prefecture Earthquake jolted low-raised mountainous terrain of Higashiyama mountains (Fig. 1) having an actively folded geological structure (Yoong and Okada 2005). In common with other historical earthquakes in active folding regions, the Mid-Niigata Prefecture Earthquake reportedly triggered and/or reactivated thousands of landslides, including 362 landslides with widths of more than 50 m and 12 large-scale landslides with individual volumes of more than one million cubic meters. The economic loss due to these landslides was initially estimated to be about 8 billion US dollars, making this one of the costliest landslide events in history (Kieffer et al. 2006).

The 2005 Kashmir Earthquake also struck rugged mountainous terrain of the northern areas of Pakistan and Pakistan administrated state of Jammu and Kashmir (Fig. 2). The source of the earthquake is about 75 km long NW-SE trending Balakot-Bagh reverse fault (Fig. 2). Due to active seismicity, great relief, heavy monsoon rains, and accelerated erosion due to deforestation and construction, landsliding is one of the most prevalent hazards in the epicentral area. The earthquake triggered thousands of landslides throughout the region in an area of more than 7,500 km², causing more than 1,000 direct fatalities, destroying roads, and disrupting communication links. Blind reverse separation of the causative fault has crushed and disintegrated dolomite slope surfaces along its total stretch. These crushed slopes have been exposed to the extreme weather conditions (heavy monsoonal rains after very dry hot season) and a remarkable increase in slope failures and landslides was also reported due to rock weathering and rain infiltration in the years following the earthquake. Most (>90 %) of the earthquake-induced landslides were rock and debris falls ranging from a few m³ to >10³ m³ in size; but also included debris slides and debris flows (Owen et al. 2008). Sato et al. (2007) interpreted 2,424 landslides in 55 km × 51 km epicentral area (Fig. 2) using 2.5-m-resolution System Pour l'Observation de la Terre 5 (SPOT 5) stereo image.

In this paper, the authors have extended their previous work of obtaining Lagrangian ground displacements and their implications for source inversion analysis (Kazmi et al. 2013) to reveal seismic stress distribution through forward modeling near the surface of a layered half-space. The authors have also tried to develop a cause and effect relation between the landslide disasters and change in the state of stress induced by seismic stresses.

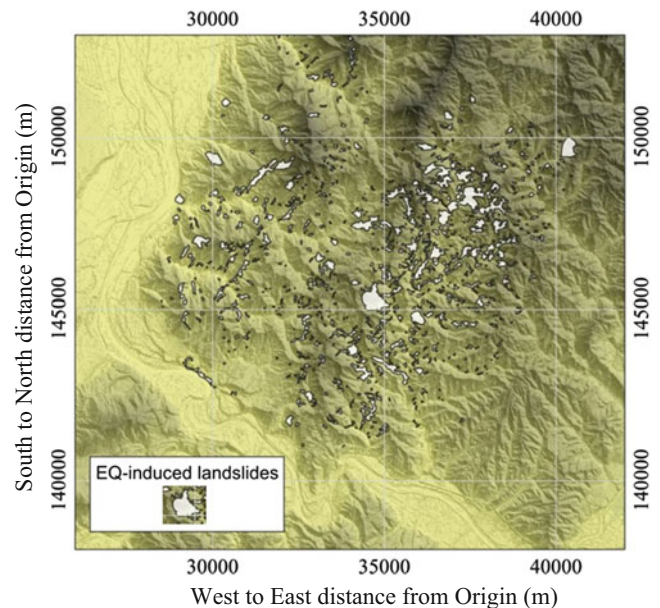


Fig. 1 Epicentral area of the October 23rd 2004 Mid-Niigata-Prefecture Earthquake: The terrain shown above is a digital representation of cartographic information (Digital Elevation Model) in a raster form with pixels arranged in *square*. Topographical mapping is on the JGD2000/Japan Plane Rectangular Coordinate System VIII with its southwest corner located as the origin at 138°30'00" E, 36°00'00" N. White polygons show the distribution of earthquake induced landslides mapped by Oyagi et al. (2008)

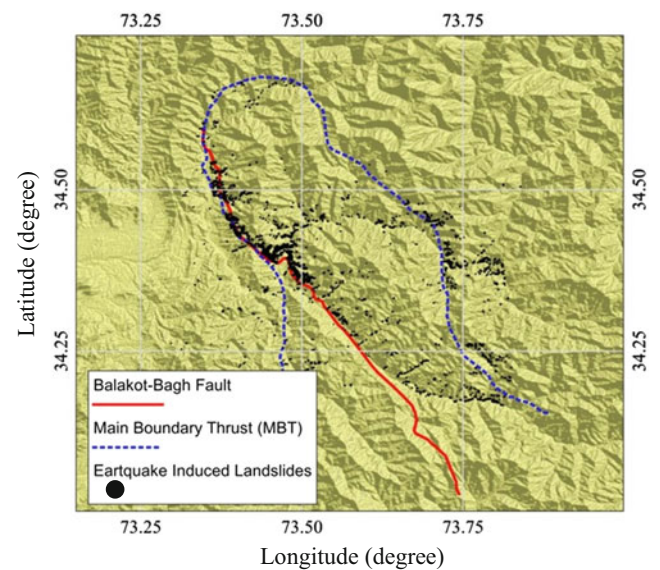


Fig. 2 Tectonic map of 2005 Kashmir Earthquake with the causative Balakot-Bagh Fault overlaid the terrain map. *Black dots* show the distribution of landslides triggered by Kashmir Earthquake (extracted from the satellite data by Sato et al. 2007)

Source Mechanisms

Based on the theory of elastic dislocation (Aki and Richards 1980), linear geodetic inversion analysis has been performed to reveal displacement discontinuity across fault rupture plane from co-seismic surface displacements. The detailed mathematical formulation is available in author's previous work (Kazmi et al. 2013).

Mid-Niigata Prefecture Earthquake

Figure 3 shows the results of spatial distribution of fault slips on a multi-segment fault model embedded in a laterally homogenous layered half space. The maximum simulated value of slip for the main shock is 1.75 m. The detailed geometry of the fault model and discussion on slip pattern is available in authors' previous paper (Kazmi et al. 2013).

2005 Kashmir Earthquake

Figure 4 shows spatial distribution of slip on a 90 km × 30 km fault rupture plane for 2005 Kashmir Earthquake, having strike and dip angles of 320° and 29°, respectively. The largest simulated value of slip has reached 7.6 m. Slips are mainly concentrated in the shallower depth of the rupture plane (Fig. 4) and the slip vectors close to the ground surface are closely matching the crustal deformation pattern.

Sub-Surface Seismic Stress Changes

The analytical solutions for surface and internal deformations generated by shear and tensile faults in a homogenous half-space were derived by Okada (1985, 1992) and are widely used as the forward model for inversion. However, a homogeneous half-space model may oversimplify the real earth, and a model of horizontally layered half-space is considered to be a workaround. To solve for elastic deformation in the layered half-space, there was a progressive development in the numerical techniques and most of them are based on wave number integration method (e.g. Sato 1971; Sato and Matsuura 1973; Singh 1971 etc.). However, the wave number spectra or kernel functions for the layered half space can only be integrated numerically or approximated. The problems of limited number of layers due to exponential growth of the calculation for kernel functions and numerical instability were dealt rationally more recently by Wang (1999), who considered the problem from its physical point of view. Following Wang et al. (2003), seismic stresses/strains are

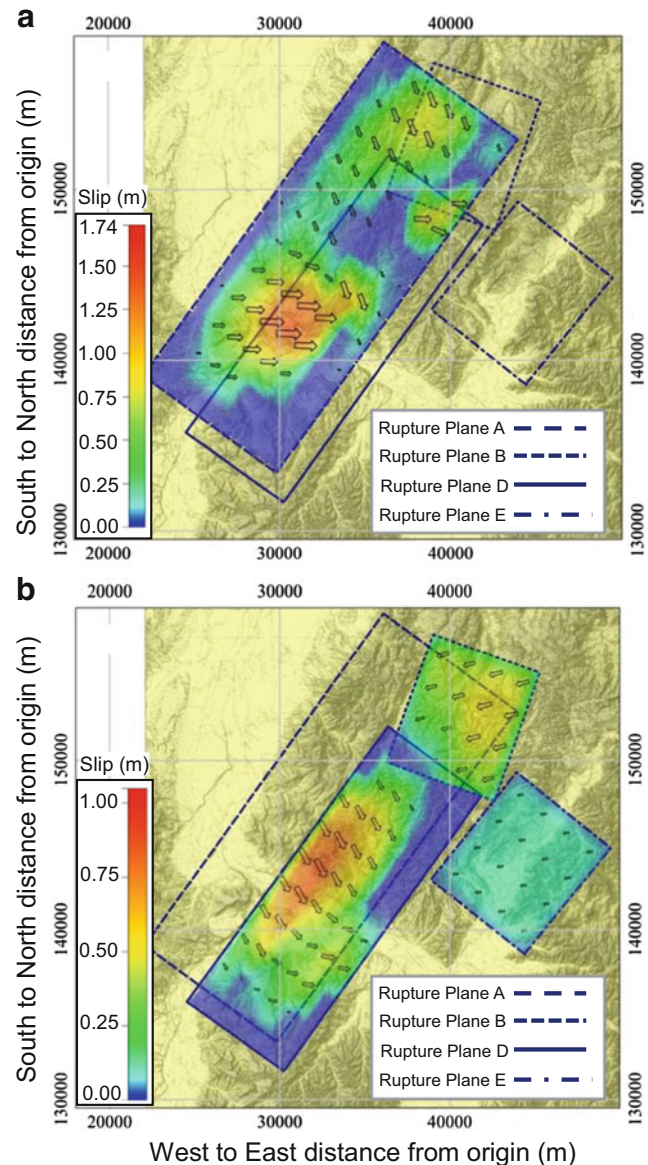


Fig. 3 Surface projections of fault slip distribution obtained by the inverse modeling for (a) main shock (b) three largest aftershocks of Mid-Niigata Prefecture Earthquake (Kazmi et al. 2013). The detailed geometry of the multi-segment fault model is available in authors' previous paper. Topographical mapping is on the JGD2000/Japan Plane Rectangular Coordinate System VIII with its southwest corner located as the origin at 138°30'00"E, 36°00'00"N

calculated in the interior of soil by considering a similar layered half space as was used in inverse modeling.

The partial differential equation governing static deformation in an elastic medium in combination with Hooke's law is given by:

$$(\lambda + 2\mu)\nabla(\nabla \cdot \mathbf{u}) - \mu\nabla \times (\nabla \times \mathbf{u}) = \mathbf{f} \quad (1)$$

where λ and μ are the two Lamé constants, \mathbf{u} is the displacement vector, and \mathbf{f} is the body force.

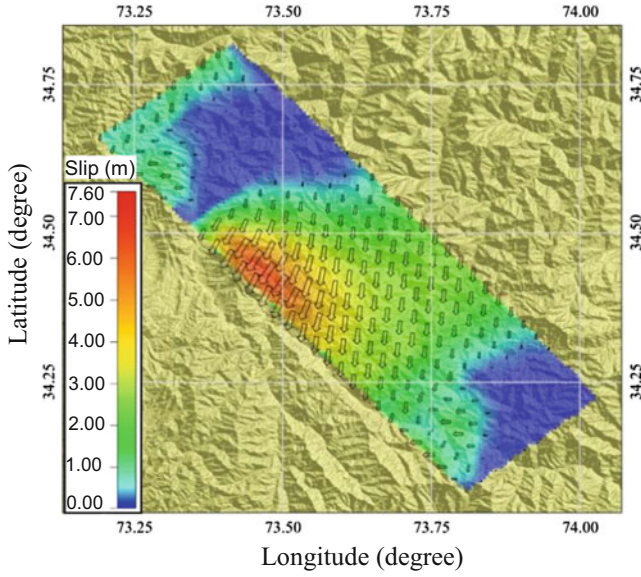


Fig. 4 Surface projections of fault slip distribution obtained by the linear geodetic data inversion. The *color* shows the scale for slip while the *vectors* are to show the direction of slip. *White star* shows the location of hypocenter

By applying Hankel transforms (Aki and Richards 1980), the partial differential equation of static deformation is transferred to a set of ordinary differential equations which are decoupled from each other, and represent P-SV and SH modes. The resulting set of ordinary equations for P-SV mode is given by:

$$\frac{d}{dz}y_m = Ay_m \quad (2)$$

where y_m and A are the generalized displacement vector and coefficient matrix for P-SV mode, respectively, given by:

$$y_m = (U_m E_m V_m F_m)^T \quad (3)$$

$$A = \begin{bmatrix} 0 & \frac{1}{\lambda + 2\mu} & \lambda k / (\lambda + 2\mu) & 0 \\ 0 & 0 & 0 & k \\ -k & 0 & 0 & \frac{1}{\mu} \\ 0 & -\frac{\lambda k}{\lambda + 2\mu} & 4k^2\mu(\lambda + \mu) / (\lambda + 2\mu) & 0 \end{bmatrix} \quad (4)$$

Similarly for the SH mode, the resulting equation is;

$$\frac{d}{dz}x_m = Bx_m \quad (5)$$

with the generalized displacement vector, x_m , and the coefficient matrix, B , given as;

$$x_m = (W_m G_m)^T \quad (6)$$

$$B = \begin{bmatrix} 0 & 1/\mu \\ k^2\mu & 0 \end{bmatrix} \quad (7)$$

The surface of the layer ($z = 0$) is traction-free and the laterally homogeneous layers making up a semi-infinite half space are in welded contact along their boundary planes. The fault planes are modeled by superimposing double couples, single forces, inflations, etc.

Thomson-Haskell propagator algorithm is applied to get the solution of complete boundary value problem. Chain rule property of the Thomson-Haskell Propagator Matrix Method helps to conveniently relate the solutions across different depths. The detailed mathematical formulation of the numerical technique is given by Wang et al. (2003). After obtaining the solution for y_m and x_m , all the components of stresses are obtained by inverse Hankell transformation (Wang et al. 2003). Knowing the stress components, the second principal invariant of deviatoric stress tensor is obtained as;

$$J_2 = \left[(\sigma_x - \sigma_y)^2 + (\sigma_y - \sigma_z)^2 + (\sigma_z - \sigma_x)^2 \right] + \tau_{xy}^2 \quad (8)$$

The second principal invariant of deviatoric stress tensor, J_2 , can be considered as an index for rocks and soils deformability in the absence of reliable rock failure criterion and spatial coverage of soil/rock properties. Although the slip surfaces for different landslides will have large variability, seismic stresses are calculated at a representative depth of 5 m below the ground surface to discuss the landslide triggering mechanism and its relation with the seismic stresses.

Figure 5a shows spatial distribution of the square root of the second principal invariant of deviatoric stress, $\sqrt{J_2}$, for the epicentral area of Mid-Niigata Prefecture Earthquake at 5 m below the ground surface. Parallel belts of large $\sqrt{J_2}$ values are observed at an about 4 km regular interval. All the landslides triggered by this earthquake are found concentrated along the stripes of large $\sqrt{J_2}$ values (white polygons in Fig. 5a). This highlights the importance of the seismic stresses in triggering and/or reactivation of landslides. It is also noted that all the existing landslides that had been identified as of 2000 (National Research Institute for Earth Science and Disaster Prevention 2000) are even more precisely clustered along the higher values of $\sqrt{J_2}$ (white polygons in Fig. 5b). It can be deduced from the concordant behavior of higher $\sqrt{J_2}$ values and landslides existing before that earthquake that a similar pattern of stress distribution might have repeated in the past.

Figure 6 shows the spatial distribution of $\sqrt{J_2}$ values for the whole epicentral area of 2005 Kashmir Earthquake. Higher values of $\sqrt{J_2}$ are aligned along the causative Balakot-Bagh fault and extend in a wider brush towards the hanging wall. It is also worth mentioning that almost

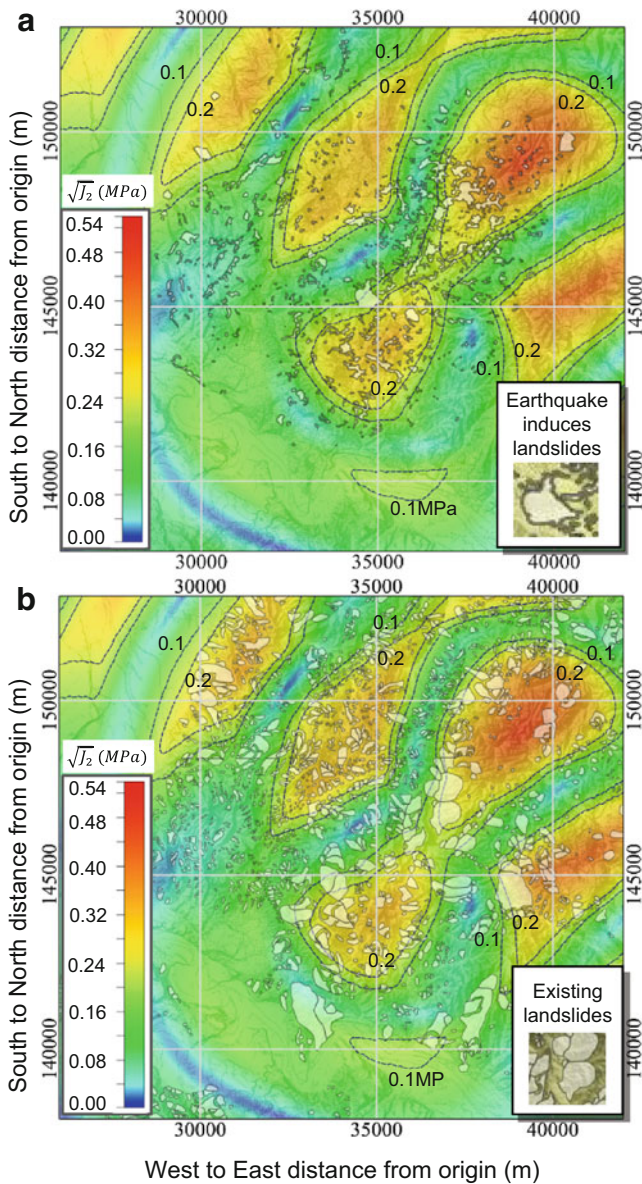


Fig. 5 Distribution of second principal invariant of the stress deviator tensor $\sqrt{J_2}$ over the entire target zone at the depth of 5 m from ground surface, with locations of (a) earthquake induced landslides (Oyagi et al. 2008) and (b) existing landslides (National Research Institute for Earth Science and Disaster Prevention 2000). Topographical mapping is on the JGD2000/Japan Plane Rectangular Coordinate System VIII with its southwest corner located as the origin at $138^{\circ}30'00''E$, $36^{\circ}00'00''N$

all landslides triggered by the Kashmir earthquake (extracted by Sato et al. 2007 from the satellite data) are concordant with the higher values of $\sqrt{J_2}$ (black dots in Fig. 6).

The above mentioned discussion, about two of the most devastating earthquakes in last decade, elaborates the importance of the seismic stresses and their relation to the soils and

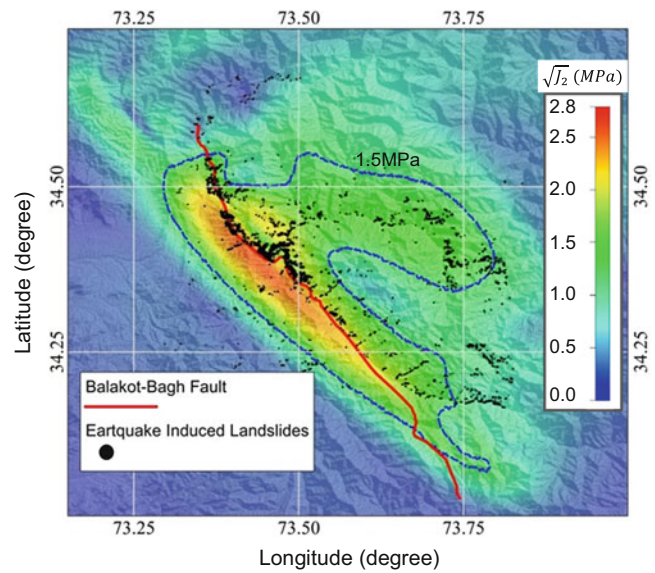


Fig. 6 Distribution of the square root of the second invariant of deviatoric stress tensor $\sqrt{J_2}$ at 5 m depth below the ground surface along with the distribution of landslides triggered by the 2005 Kashmir Earthquake. All the landslides are found remarkably consistent with the large $\sqrt{J_2}$ values

rocks deformability. In a separate work, the authors have also observed that the damages to underground facilities are also located at the higher values of $\sqrt{J_2}$. For a given scenario earthquake, seismic stress distribution can be used to delineate potentially hazardous areas and to carry out protection works for the important and unavoidable locations. It also highlights the importance of monitoring crustal deformations, which will allow us to calculate spatial stress distributions that have been appearing over and over during a long period of geological time.

Assuming that the similar events will be occurring continually, the information will be crucial for taking necessary measures to protect our lives and properties.

Conclusions

Large earthquakes can trigger numerous landslides, which are very often the most devastating secondary effect of an earthquake in terms of all kinds of losses. Estimation of co-seismic stress changes from geodetic data was taken for investigating the causes and triggering mechanisms of landslide disasters.

Based on the theory of elastic dislocation, a source inversion analysis has been performed to obtain spatial distribution of slips on fault ruptures planes for two of the most devastating earthquakes of the last decade, namely Mid-Niigata Prefecture Earthquake (2004) and the Kashmir Earthquake (2005). Through a forward modeling, the seismic stresses were evaluated in the interior of a latterly homogeneous layered half-space. In

the absence of reliable yield criterion and spatial coverage of soil/rock properties, square root of second principal invariant of deviatoric stress tensor $\sqrt{J_2}$, is taken as an index of rock/soil deformability. It was observed that the spatial distribution of landslides triggered by both of the aforementioned earthquakes were found consistent with those of the large values of $\sqrt{J_2}$.

For the Mid-Niigata Prefecture Earthquake, a set of digital data was also available for the locations, sizes and shapes of landslides which existed before the earthquake (mapped in 2000). Spatial pattern of existing landslide clusters were also found concordant with those of large values of $\sqrt{J_2}$, suggesting that the active folding epicentral area of the Mid-Niigata Prefecture Earthquake might have been experiencing similar stress pattern in the past.

Assuming that the similar events with those in the past will be occurring continually in many earthquake-prone zones, the information of co-seismic stress distribution will be important for taking rational measures to protect our lives and properties. Though the method is yet imperfect often with unavailability of important geological and geotechnical data, it is considered to hold great promise to be used in both disaster mitigations and land conservations.

References

- Aki K, Richards PG (1980) Quantitative seismology. W. H. Freeman, San Francisco, CA, 932 pp
- Harp EL, Jibson RW (1996) Landslides triggered by the 1994 Northridge, California earthquake. *Bull Seismol Soc Am* 86:319–332
- Kazmi ZA, Konagai K, Sekiguchi H, Fujita T (2013) Extracting earthquake induced Lagrangian ground displacement and their implication for source inversion analysis. *Soil Dyn Earthq Eng* 48:198–208
- Keefer DV (2000) Statistical analysis of an earthquake-induced landslide distribution—the 1989 Loma Prieta, California event. *Eng Geol* 58:231–249
- Kieffer DS, Jibson R, Rathje EM, Kelson K (2006) Landslides triggered by the 2004 Niigata Ken Chuetsu, Japan, Earthquake. *Earthquake Spectra* 22:S47–S73
- Kobayashi Y (1981) Causes of fatalities in recent earthquakes in Japan. *J Disaster Sci* 3:15–22
- Landslide distribution maps (shape files), National Research Institute for Earth Science and Disaster Prevention, October 2000, <http://lsweb1.ess.bosai.go.jp/gis-data/index.html>
- Marano KD, Wald DJ, Allen TI (2010) Global earthquake casualties due to secondary effects: a quantitative analysis for improving rapid loss analyses. *Nat Hazards* 52:319–328
- Okada Y (1985) Surface deformation due to shear and tensile faults in a half-space. *Bull Seismol Soc Am* 75:1135–1154
- Okada Y (1992) Internal deformation due to shear and tensile faults in a half-space. *Bull Seismol Soc Am* 82:1018–1040
- Owen LA, Kamp U, Khattak GA, Harp EL, Keefer DK, Bauer MA (2008) Landslides triggered by the October 8, 2005, Kashmir earthquake. *Geomorphology* 94:1–9
- Oyagi N, Uchiyama S, Inokuchi T (2008) Map of landslides caused by the 2004 Niigata-ken Chuetsu (Mid-Niigata) Earthquake (MJMA = 6.8). Technical note no. 317, National Research Institute for Earth Science and Disaster Prevention
- Sato R (1971) Crustal deformation due to a dislocation in a multi-layered medium. *J Phys Earth* 19:31–46
- Sato R, Matsuura R (1973) Static deformation due to the fault spreading over several layers in a multi-layered medium. Part I: displacement. *J Phys Earth* 21:227–249
- Sato HP, Sekiguchi T, Kojiro R, Suzuki Y, Iida M (2005) Overlaying landslides distribution on the earthquake source, geological and topographical data: the mid Niigata prefecture earthquake in 2004, Japan. *Landslides* 2:143–152
- Sato HP, Hasegawa H, Fujiwara S, Tobita M, Koarai M, Une H, Iwahashi J (2007) Interpretation of landslide distribution triggered by the 2005 Northern Pakistan earthquake using SPOT 5 imagery. *Landslides* 4:113–122
- Singh SJ (1971) Deformation of a multilayered half-space by stress dislocations and concentrated forces. *Bull Seismol Soc Am* 61:1625–1637
- Wang R (1999) A simple orthonormalization method for the stable and efficient computation of Green's functions. *Bull Seismol Soc Am* 89:733–741
- Wang R, Martin FL, Roth F (2003) Computation of deformation induced by earthquakes in a multi-layered elastic crust. *Comput Geosci* 29:195–207
- Wang WN, Wu HL, Nakamura H, Wu SC, Ouyang S, Yu MF (2003) Mass movements caused by recent tectonic activity: the 1999 Chi-Chi earthquake in central Taiwan. *Island Arc* 12(4):325–334
- Yoong KH, Okada A (2005) Surface deformations associated with the October 2004 Mid-Niigata earthquake: description and discussion. *Earth Planets Space* 57:1093–1102



Landslides of Liquefaction Caused by Single Source of Impact Pamir-Hindu Kush Earthquakes in Central Asia

Rustam Niyazov and Bakhtiar Nurtaev

Abstract

Sudden landslides formed simultaneously in different areas, triggered by single source seismic impacts of Pamir-Hindu Kush earthquakes create great danger in the foothill areas of the Central Asian region. The role of distant deep-foci Pamir-Hindu Kush earthquakes as a “trigger” for the formation and mechanism in dispersive water-encroached soils under the influence of prolonged, low-frequency vibrations is examined. There are three groups of landslides liquefaction—extrusion, thixotropic liquefaction and mudslides of gravitational liquefaction. Results of geodetic measurements of large landslides in Angren coal mine for 22–26 years and the role of the Pamir-Hindu Kush earthquakes in their formation are analyzed. Figures obtained of the overriding criterion of velocity 74.4 cm/day and time 79 days in transition of the mass movement into progressive creep of clay material.

Keywords

Large-scale landslides • Earthquakes • Liquefaction • Trigger • Case study

Introduction

For the Central Asia region the largest excitatory center of seismic activity are deep-focus (100–300 km) Pamir-Hindu Kush earthquakes. The spatial placement of focuses is caused by the movement of the Indian plate to Eurasia in the area (60–70 km²), high level of seismicity and repeatability of events and compact localization of focuses, centered in Afghanistan between the coordinates of 36–37° and 69°40′–71°20′. Every year, there occurred 200 earthquakes, 40 % in the spring, covering Central Asia, Northern India, Afghanistan and North-East Pakistan. Deep-focus earthquakes of Afghanistan in the proximate epicentral area are manifested slightly and intensity increasing at the

distance (Leonov 1965). The role of the deep fault zones as a screen preventing the passage of seismic waves for deep-foci earthquakes is insignificant. The main role in increase of deep earthquakes ground motions is the state of lithology, soil conditions, level of underground water and water content of the rock mass.

Among the four known intercontinental zones where earthquakes occur in intermediate focal depth (Burma, Romania, Spain and the Pamir-Hindu Kush), the latter is the most active and best covered by instrumental measurements and fairly well understood (Molnar et al. 1976).

In the foothill areas of Central Asia at a distance of 340–600 km from the hypocenter, vibrations felt as 2–3 intensity units, duration of oscillations from 90 to 200 s, with maximum amplitude of 0.04–0.3 cm/s, maximum frequency 0.5–1.5 Hz, playing the role of “trigger” and cause the process of liquefaction in watered rocks on the slopes. For 50 years, it was found that in wet years during the earthquakes were formed 125 major landslides and after the earthquakes 81 (Niyazov and Nurtaev 2013).

R. Niyazov
Institute Hydroingeo, Engineering Geology, Olimlar 64, Tashkent
100041, Uzbekistan

B. Nurtaev (✉)
Institute of Geology and Geophysics, Olimlar 49, Tashkent 100041,
Uzbekistan
e-mail: nurtaev@ingeo.uz

Simultaneous Formation of Landslides

In connection with a single source of seismic impact of deep foci earthquakes in the wettest years in March, April recorded several cases of landslides of liquefaction formed at one time. For example in March 10, 1969, as a result of earthquake of M-5.1, H-201 km 6 cases were reported during and 7 after the earthquake.

In 1994, after the earthquake of March 5, M-5.1 landslides occurred at 12 sites in Kyrgyzstan and Uzbekistan.

After strong local earthquake many landslides may occur, however, the number of these cases is insignificant in Uzbekistan, more events registered when as a result of one earthquake occurs several landslides in large area. So, earthquake of March 31, 2012 M-4, 9 H = 229 km, caused simultaneous formation of landslides at 27 sites, of these large liquefaction landslides in 8 sites. In large quantities the landslides are formed simultaneously on 2–3 sites. In addition there are landslides sites Maylusuu, Altynbel, Baypaza, Naugarzan, where the displacement of rocks through fixed years repeated and accelerated. Apparently, except for the impact of area regional factor, precipitation and seismic activity, the formation of landslide depends on condition if local areas of the slope reached the critical state of stability. Devastating earthquakes, when in the area of the epicenter simultaneously formed several hundred landslides, occur once in 100–150 years. In distinction from devastating earthquakes dozen deep-focus earthquakes occurs each year and landslides formed in the wet spring in different locations over long distances of 200–300 km from each other.

Mechanism of Liquefaction Landslides Development

So far number of published works dealing with the mechanism of landslides in fine-grained soil during and after the earthquake is limited. The role of the simultaneous movement of the masses of rocks throughout the area of the landslide, when some landslides after the earthquake have a long movement, others will be stabilized in a short time usually was not considered. Therefore, spatial monitoring of joint influence of factors which determine triggering mechanism of landslide and mechanism of development is a complex and important task for the early warning. Various authors qualified dynamic unstable soils as liquefaction, quicksand, thixotropic and dilatant, etc. Carried out by V.I. Osipov (1988) analysis has allowed him to identify thixotropic, gravitational and quicksand liquefaction. Having these forms of liquefaction it is recommended to identify three

groups of landslides liquefaction: extruding landslides in quicksand liquefaction in small interlayer in the depth of the solid mass; thixotropic liquefaction landslides on the surface of the broad shallow slopes, where there is no static load and mudslides of gravitational liquefaction.

Extruding Landslides in Quicksand Liquefaction

The beginning of their formation associated with the devastating earthquakes, but with long-lasting low-frequency seismic vibrations with intensity 3–4 intensity units. Whole area of the landslide subjected to simultaneous movement at different speed and direction. There is no consistent movement of rocks from the bottom up or top down. This is a deep, long-scale landslides of tens and hundreds of millions m³, slipping on the flat sliding surface, where at the same time formed the graben-like separation wall, lateral shear cracks and flow of ground. Quicksand liquefaction occurs in small interlayer of water-bearing sandy-clay rocks in the depth of the solid mass. The displacement occurs on plastic clay with pinching-out of quicksand mass in the lower zone. Characterized by rare occurrence with concurrent formation of flow of ground while the height of 0.3–0.8 m in the flood plains and river beds and high steep walls of separation in the upper part of the slope graben-like shape, where the lateral shear cracks can be located on the back of the watershed surfaces. There are two forms of flow of ground: one in the form of track laying cover with height of 0.3–0.8 m in sandy-clay soils, the second form—gradual rise of the lower zone for 5–7 m, where the upper stratum is composed of hard rock—limestone, sandstone due to long-term and large horizontal displacements. The duration and amplitude of large horizontal displacements associated with the extent of the landslide and small 4–8° slope of sliding surface. Furthermore, the horizontal displacement is also related to the width of graben zone in separation wall.

Fragmented nature of the landslide surface is another important indicator of seismic impact on the formation of landslides. In some cases the entire surface of the slope is divided into many small (2 × 4 m) blocks, in the other in the separation zone formed elongated transverse cracks, forming blocks of graben-like lows. In the middle, central area it is formed series of transverse and longitudinal cracks. Landslides of extrusion in recent years have been recorded in the 13 sites, 6 of them—in man-made areas.

For the analysis were selected two landslides—Central and Old substation, formed in the zone of Angren graben—synclinal, which are characterized by one type of landslide—extrusion and with similar geological structure (Fig. 1).



Fig. 1 Plan of landslide central A and old substation B

Landslide mass movement with thickness more than 100 m took place by one very flat-dipping 2–4° sliding surfaces in the Paleogene sediments. The process of slope stability loss is characterized by man-made factors, in open pit mine with steep walls and the interval of its service. The trigger which caused the beginning of their formation is long low-frequency vibrations from distant (530–570 km) deep-focus (180–230 km) Hindu Kush earthquakes.

Results of Geodetic Observations

Landslide Central was formed in April 1985 in the Western working board of Angren coal mine. The first crack in the loess rocks with length of 300 m was formed at a distance of 250–280 m from the upper edge of the working board under Baksuk mud-water reservoir. In March, 1987 upper edge of working board come around to the crack on 50–150 m, and its length was increased to 1,300 m, the total volume of the landslide was 58 million m³. The height of the movable part of the board was 145 m, and the was angle 17°. The sliding surface was confined to clays of Suzak formation of Paleogene, lying at the angle 3–4°. Since then, mudslide Central for 25 years (1987–2013) continues to move, the total amount of displacement—more than 260 m (Rp 17). All these years, coal mining was carried



Fig. 2 Cracks on landslide old substation, 1993

out when the volume of the rock mass was taken out from the prism of active pressure was 1.5–2 times more than the volume of material excavated from the knife-edged support in the lower ledges. This technology of open pit development made it possible to constrain landslide displacement velocity at 20–24 mm/day. As a result its length reduced from 750 m in 1990 to 320 m. Maximal thickness from 105 m was reduced to 30 m from the former volume and remained about 20 %, or 10.8 million m³.

However, in May 1993, on the top ledge of the working board from the North up to the Central landslide in the area “Old Substation” (Fig. 2) formed a series of cracks with a length of 100–500 m.

It was formed a threat of cracks connecting process at the site “Old substation” with separation wall of landslide Central. The main cause of deformation was long standing of open-pit benches, as a result of underflow by streams of Sayaksay and Baksuksay, which led to the deformation of underground channels in a washed gravel (inflow of Sayaksay-550 m³/h, Baksuksay-up to 250 m³/h).

From 2000 to 2001 there are started joining process of two landslides. They had a close direction of the displacement vectors (135–150°), but the rate of horizontal displacement in the area “Old substation” is 8–10 times less than in the area of Central landslide.

First activation of the landslide Central from the seismic action occurred in April 6, 2004, after Hindu Kush earthquake of M-6,6, H-187 km. In Angren at a distance 530 km, it was felt as 2–3 intensity units and duration of oscillations over 2.0 min. Landslide movement velocity has risen from 31.4 mm/day (03/08/04) to 117.3 (19.04.04), May (23.05.04) up to 261, in July to 287 mm/day, i.e. increased within 95 days in 10 times. In the following years (2005–2010) the rate of landslide horizontal displacement decreased up to 5–24 mm/day and vertical 1.6–2.4 mm/day.

At the site of the Old substation in 2003–2004 was carried out unloading of the upper ledge, as a result the deformation of loess decreased up to 0.07–0.14 mm/day. The value of horizontal displacement over a 3 year period (2005–2008)

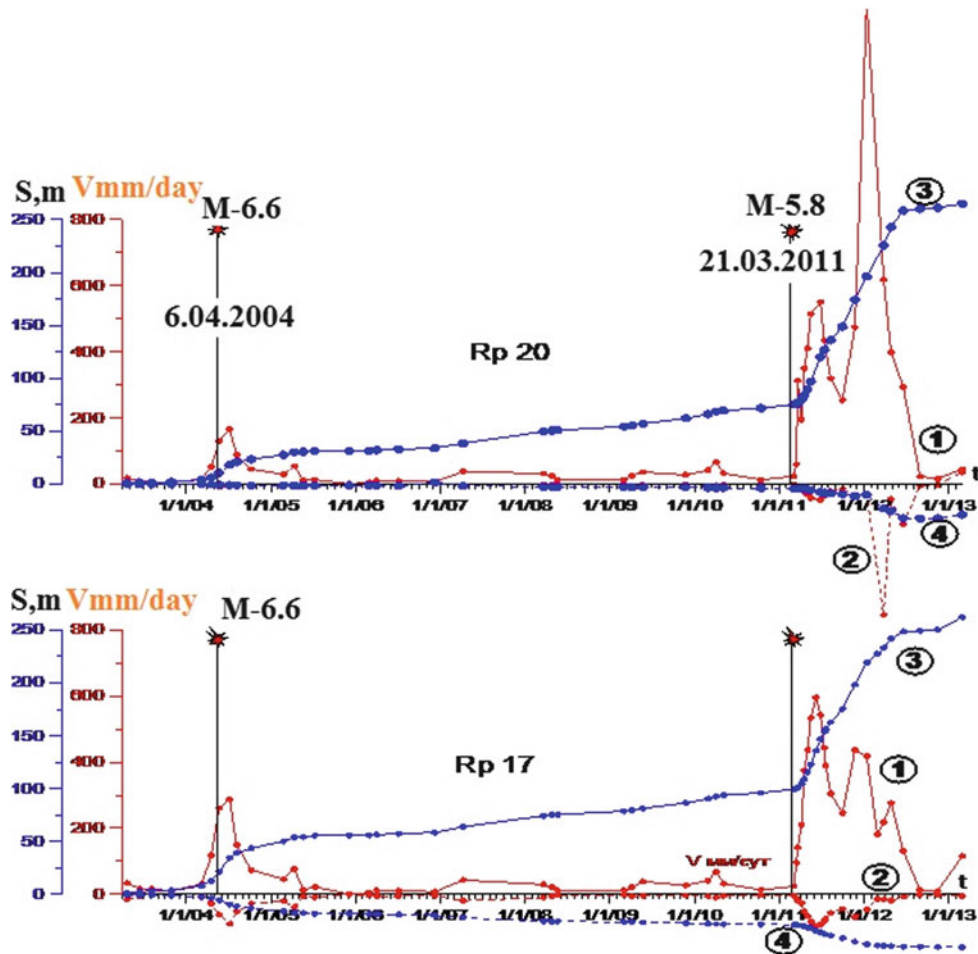


Fig. 3 Graph of behaviour of velocity of horizontal (1) and vertical (2) motions displacements (3,4) for the bench marks Rp17 and Rp20. Landslide central—period from March 11, 2003 up to 2013

was 60–66 mm. Activation of this landslide was observed in October (13.4–18.7 mm/day) and February (23.6 mm/day), with average values 0.6–3.8 mm/day. Perhaps this was due to the Hindu Kush earthquakes occurred 17.09.10, M-6,3, H-220 km. Because maximum displacement (Rp 6) took place from 13.10.10 up to 05.03.11 for 1.8 m with horizontal rate 13 mm/day and vertical 2.9 m, with rate 7 mm/day, i.e. increased during 5 months in 10 times (Fig. 3).

At the same time, in the lower part of the left side of the knife-edged support occurred two block landslides in limestone up to 15–20 m, volumes of 0.8–1.0 million m³. Right flank above the landslide covered by series of longitudinal cracks with length of 40–60 m with amplitude 0.5–2.0 m. Vertical fractures united with transverse deformations. As a result a large single landslide circus formed with width of 1,400 m, length of 900 m, average thickness—100 m. The volume of the landslide is 120–130 million m³.

The separation wall of landslide confined to actual elevation 1,100 m, and the outbreak of the sliding surface 905 m, altitude difference is 200 m at length of 1,000 m. Geological

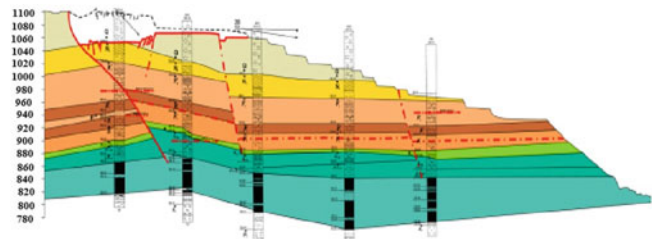


Fig. 4 Geological cross section and sliding surface of landslide old substation

structure of the landslide consists of Quaternary loess with the inclusion of boulder-pebble deposits with thickness in the upper part 65–70 m and 15–20 m in the central part of the pit board. The thickness of the Neogen siltstones and sandstones is 30–35 m. In the lower ledges of the pit Quaternary and Neogene sediments are worked-out and absent. It consists mainly of interbedded strata of Paleogene sandstone, shale, fractured limestone and clays with total thickness up to 40 m deposited on the Cretaceous and Jurassic shale and carbonaceous sediments (Fig. 4).

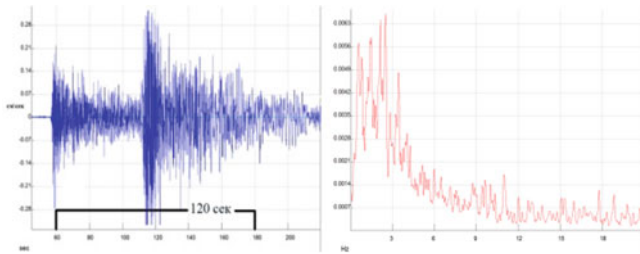


Fig. 5 Velocigrams and spectra of earthquake 21.03.2011

The displacement of rocks confined to 3–4 m zone of contact of limestone with interbedded fine-grained sands and greenish clays of the Paleogene at the actual elevation 905–910 m, 85–90 m above the pit bottom (820–830 m). Lower-lying Cretaceous and Jurassic clay and coal sediments are not deformed.

March 21, 2011 earthquake occurred in the Hindu Kush with $M=5.8$, $H=196$ km. In Angren it was felt in the range of 2–3 units, duration of the vibration was 120 s and amplitude of 0.3 cm/s (Fig. 5).

March 21 morning before the earthquake Geodetic Survey was carried out regular round of geodetic measurements. March 22 carried out repeated GPS measurements. The increase in velocity was negligible, in the lower zone in the area of ground flow—52 mm (Rp 24) and 30 mm (Rp 25). Even less has been in the upper zone—20 mm (Rp 6) and 3–4 mm (Rp 1). However, the whole area of the landslide subjected to the movement. Most sensitive to the earthquake motion turn out to be ground water, in 5–7 h was observed sharp increase of groundwater in 4–5 times, on the pit ledges formed small lakes, length 25 m, width 15 m, depth 1–1.5 m. At the bottom there was a mass water outcrop on the left side. A significant increase was observed of displacement velocity in April 7 from 86 up to 101 mm/day (Rp 6), from 197 to 309 mm/day (Rp 38). Increasing of the speed of the displacement took place within 56–79 days for various bench marks every day at 76, 96, 104, 137 mm/day. In the central zone the rate of displacement within 79 days (22.03–8.06.11) accelerated from 189 to 747 mm/day. In the upper area—from 68 to 385 mm/day. Then the displacement speed began to decrease in 5–7 times in 23.11.11, 15–16 times in 26.03.12. At the present time, it has decreased 40–50 times and in 30.08.12 up to 04.04.13 is 3.4–9.2 mm/day (Fig. 6).

22 cycles of geodetic observations conducted after the earthquake in 26.03.2013 up to 22.03.2011 for 2 years showed that the maximum of horizontal displacement occurred in the central part of the landslide 98.1 m and 3.4 m at the vertical (Rp37). The maximum vertical downwarping of the upper zone was 42.7 m (Rp 6) and the horizontal of 58.6 m. Maximal vertical uplifting occurred in the lower part of ground flow—7.5 m, and it is horizontally

moved on 79 m. Analysis of the relationship between the vertical deformation and horizontal displacements of the upper and lower zone showed that in the upper zone of separation wall in the first 3 months from 22.03.2011 up to 28.06.2011 vertical deformation (32 m) slightly exceeded horizontal (31 m), and then it began to exceed it in the lower zone of the flow of ground. In July 14, it was raised to 9.6 m (Rp 25), and by 23 November, it decreased by 3 m and was 6.3 m. In August 30, 2012, it reached to 7.2 m. To the end of 2011 and beginning of 2012, shape of landslide dramatically changed, throughout its outline aggregating various cracks and block steps as a result formed unified graben-shaped downwarping. In the area of the separation wall it had as width of 140–160 m, height of 43–45 m, a slope angle of 90°. All early stage blocks turn out to be in the area with a gentle base-leveled plain (Fig. 7).

The right side of the graben has expanded up to 250 m and has combined with the Central landslide. The minimal width of graben 70–80 m formed in the left side of the landslide. In these area concentrated all small lakes. Water inflow of groundwater along the northern boundary of the landslide decreased from 1,080 m³/h in March to 314 m³/h in September 2011.

April 4, 2013 in the Hindu Kush occurred earthquake with $M=5.4$, $H=240$ km, in Tashkent at the distance 554 km from the epicenter, it was felt 2–3 intensity units, duration of vibrations was 150 s. Repeated geodetic measurements were performed 3 h after the earthquake, landslide displacement acceleration compared to the previous cycle of 26.03.13 was not registered.

Mechanism of Thixotropic Liquefaction Landslides

In contrast to the quicksand, thixotropic liquefaction occurs in the absence of external static loads, there is no change in pore pressure, and the restoration of their strength is reversible. At influence of long (90–200 s), low frequency (0.5–4 Hz) and a low-amplitude (0.02–0.06 cm/s) seismic effects in fine-grained, slightly compact and wet clayish and heavy powdery loam with low permeability instantly liquefy without any load. A distinctive feature is the ability to transfer large impact energy to the rock mass at small amplitude of the displacement within oscillation period.

It may be assumed that in the basis of the mechanism of thixotropic liquefaction landslides in long-term seismic impact played resonance phenomena, when maximum weakening of soil take place in coincidental occurrence of frequencies of induced oscillations with own frequencies of the solid phase particles. Thixotropic liquefaction landslides occur less frequently, mostly in the period of intensive snow melting and significant rainfall. It coincides with the seismic

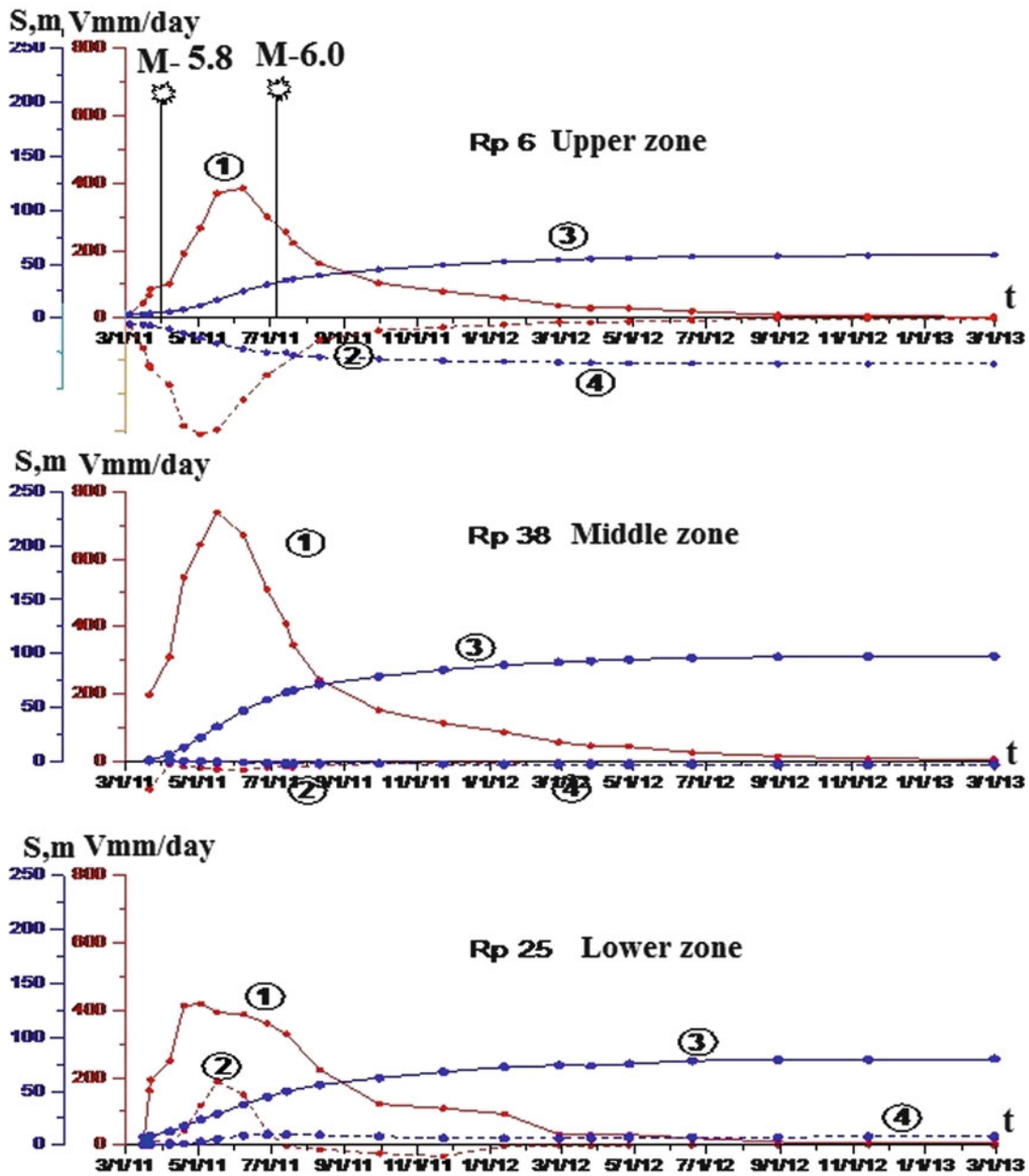


Fig. 6 Graph of behavior of velocity of horizontal (1) and vertical (2) motion and values of displacements (3,4) in upper (bench mark Rp6), middle (Rp38) and lower (Rp25) zones of landslide Old substation for

the period from March 21, 2011 up to March 26, 2013. Hindu Kush earthquakes occurred with M = 5.8 and M = 6.0



Fig. 7 Graben-shaped separation wall of landslide Old substation

impact of Hindu Kush earthquakes with M—4.8–4.9 and more at the depth of 180–240 km, duration of vibrations from 90 to 180 s, frequency of 1–4.5 Hz and amplitude of 0.06–0.27 cm/s.

These landslides are formed at the wide watershed surfaces or steep slopes, where there is groundwater aquifer, which lies on a small (4–7 m) depth with a weak or non-draining system (Fig. 8).



Fig. 8 Landslide thixotropic liquefaction Chaknak, 2009

Thixotropic liquefaction unlike the mud flow is not formed at depth, but on the surface of the ground, without static load. Loess and sandy loam soils on the surface of slope uniformly fragmented and liquefied with emission of underground water to the surface forming small lakes. These landslides are areal, but not deep (3–12 m) and are characterized by small horizontal movement.

Mechanism of Mudflows at Gravitational Liquefaction

In contrast to the thixotropic, gravitational liquefaction occurs on the slopes in the contact zone of loess and sandy-clay soils with clay and appearance of pore pressure. In addition to liquefaction, seismic impact influence on the structure of underground stream, the place and its flow rate. By the change of groundwater flow it is fixed time interval of zone being in the liquefied state. Because of the nature of their formation, they are divided into the mud flows generated during and after the earthquake.

Mud flows of Gravitational Liquefaction Formed During the Earthquake

Connection in time of the long low-frequency earthquake motion and development of landslide registered in 22 sites in wet years. Due to the proximity of recharge and discharge of groundwater they are formed during combination of sharp snowmelt (8–14 cm) and large amount of precipitation (300–450 mm) in March, April, and increasing the flow rate of groundwater in May, June (Niyazov 2009). By the place of formation most major landslides formed in the zones of tectonic dislocations, where the springs discharge are increasing in the springs from 2 to 5 times. The greatest amount of mud flows of gravitational liquefaction formed in wet years during impact of Pamir-Hindu Kush earthquakes with $M=4.5-7.3$ at a depth of 130–252 km (Fig. 9).



Fig. 9 Mudflow Baybaksai, 2005

Mud Flows of Gravitational Liquefaction Formed After the Earthquake

Analysis of landslides by time of formation after the earthquake started in recent years. However, in spite of limited data, the process can occur often in certain years, when the rock massif on the slope reaches a critical state. Basically, it is associated with a temporary underground overlap or changing of groundwater flow direction, subsidence of the slope surface, development of suffosion holes, etc. This is quite a complex natural process associated with various slope processes. They typically occurs 3–5 or 10–15 day after earthquake.

Landslides, which started formation during earthquake and main displacement occurred after 2–3 days, we refer to the group, which was formed during the earthquake. And mud flows, initially experienced some strain, and after 7–15 days or month transferred to the stream by time of formation we refer to occurred after the earthquake.

Even more difficult case of landslide cracks transition to the landslide process, i.e. there are some cracks formed during the earthquake in the spring or autumn, and it moved to the landslide process after 4–6 months, sometimes after few years, when there are no earthquake. These landslides are common, we refer it to the caused by precipitation. Only for mud flows of gravitational liquefaction is characteristic displacement of soils after the earthquake.

Conclusion

Deep-Pamir-Hindu Kush earthquakes at great distances from the source are characterized by prolonged low-frequency vibrations, causing in watered loess and sandy clay soils simultaneous formation of several major of liquefaction in the large area.

Depending on the nature of changes of slopes watering, groundwater flow patterns and morphological features separated three groups of liquefaction landslides. Landslides squeezing in quicksand in a small interlayer, landslides of thixotropic liquefaction on the surface of flat wide slopes, where there is no static load and mudslides of gravitational liquefaction.

The role of the Pamir-Hindu Kush earthquakes as a trigger in the revitalization of movement of landslides squeezing in Angren coal mine is analyzed. Progressive increasing creep rate indexes in clay soils (from 189 up to 744 mm/day) within 79 days are obtained.

References

- Leonov NN (1965) Dzhurm earthquake and geological conditions of its occurrence. In "Earthquakes in the USSR"
- Molnar P, Rautian TG, Khalturin VI (1976) Spectral composition of Pamir-Hindu Kush earthquakes: evidence for a high-Q zone in the upper mantle. Collection of Soviet-American works on earthquake prediction. Dushanbe-Moscow, pp 140–159
- Niyazov RA (2009) Landslides in Uzbekistan. *Gidroingeo*, Tashkent, 208
- Niyazov RA, Nurtaev BS (2013) Modern seismogenic landslides caused by the Pamir-Hindu-Kush earthquakes and their consequences in Central Asia. In: Margottini C et al (eds) *Landslide science and practice*, vol 5. Springer, Heidelberg, pp 343–348
- Osipov VI (1988) Dynamic liquefaction of saturated soils: nature and its determining factors. *Eng Geol* 2:3–32



Dynamics of Large and Rapid Landslides with Long Travel Distances Under Dense Gas Expanding Power

Zhong-qi Quentin Yue

Abstract

This paper mechanistically investigates the dynamics of large and rapid landslides with long travel distance. In addition to many existing theories for friction reduction, the paper puts forward a new cause and mechanism of dense natural gas expanding and its governing equations and numerical results. The dense gas can have a huge amount of time-dependent expansion energy and pressure to deform, suddenly rupture and push the above rock and soil mass. Under gravity, the expanding dense gas and the broken rock and soil debris can rapidly flow, fly, and/or slide over and down the slope. The continued gas expanding and its almost zero shear strength beneath and within the debris solids carry them to powerfully move and travel to much longer distance. This process is rapidly completed and the debris solids deposit suddenly because the expanding dense gas can quickly and completely flow out of the solids and escape into sky.

Keywords

Landslide • Natural gas • Energy • Dynamics • Mechanism • Cause • Frank slide

Introduction

One of the most impressive natural phenomena that can be observed by people on the surface of the Earth is the sudden breaking of large mountain rock mass and subsequent rapid movement of the broken rock fragments over very long horizontal distance upon gentle slope, creek or stream course. The broken rock and/or soil masses for each individual mountain avalanche case are generally greater than 1 million m³ and sometimes can be 1 billion m³.

The broken rock and soil debris can rapidly fly and flow down the hillside slopes. Their speeds can be more than 10 m/s and sometimes more than 100 m/s. They can fly and impact on slope grounds with opposite dip angles. After each impact, they still can flow and move rapidly to some distance. Sometimes, they can make four impacts

before they finally stop on flat ground or slope ground with opposite dip angles. Their horizontal travel distances are normally more than two times greater than their vertical drops. Their travel angles are much less than the angle of repose which is the normal slope angle between 26° and 34° for granular materials such as sands and gravels to be stable and settle when their sliding down slopes.

They usually suddenly happen on mountain slopes that have been stable for many years and do not give any pre-notices or pre-signals to local people. Furthermore, the rapid movements and flows of the broken rock and soil fragments and particles have large momentums and kinetic energies that can give huge impacts and displacement loadings on buildings, structures and/or people on their paths. Therefore, their occurrences are commonly dramatic and can result in devastating disasters to human beings.

One of the most well-known cases is the Frank Slide that occurred in the early morning of April 29, 1903 at the then coal mining town of Frank in the Crownsnest Pass region of southwestern Alberta, Canada (Fig. 1). It was a rockslide–avalanche of 30 × 10⁶ m³ Palaeozoic limestone of about

Z.Q. Yue (✉)
Department of Civil Engineering, The University of Hong Kong,
Pokfulam Road, Hong Kong, China
e-mail: yueqzq@hku.hk

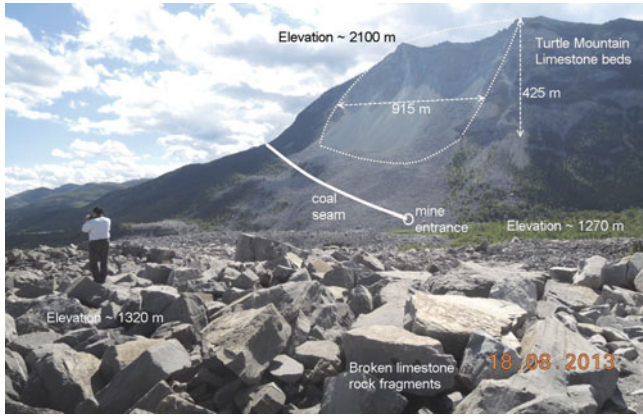


Fig. 1 Site photograph showing the 1903 Frank Slide and its large broken limestone fragments on flat ground

550 m long, 780 m wide and 70 m thick from the east face of Turtle Mountain. The event completed within 100 s. The broken limestone fragments rapidly moved down with an average speed 31 m/s. The debris deposited over a 3.0 km² flat area in front of the slope. The horizontal runout distance was about 3.6 times the vertical drop height. The rock debris destroyed the southern part of the Frank town and buried about 76 people (McConnell and Brock 1904; Kerr 1990; Cruden and Martin 2007).

Issues in Large and Rapid Landslides with Long Travel Distances

In many cases, the large and rapid landslides with long travel distances involve suddenly broken rock and soil fragments and particles. Such broken rock and soil materials are basically granular geo-materials. For granular geo-materials, the process of their sliding down on a slope by gravity would be completed and stopped when the angle of repose is reached. The angle of repose is the minimum angle of a slope for granular debris to move and slide on that slope by gravity force only. This angle of repose is equal to 26° for silts to 36° for gravels. For broken rock fill, its angle of repose can be 40°. Its normal value is about 30°. It is equal to the internal frictional angle of granular materials at loose state. However, the travel angles for such large and rapid landslides with long travel distances are usually much less than their angles of repose. For example, the travel angles for the 1903 Frank slide and the 2001 Las Colinas slide (Evans and Bent 2004) can be 16° and 13°, respectively. This issue can be illustrated in the following kinetic analysis of rock debris sliding down a slope.

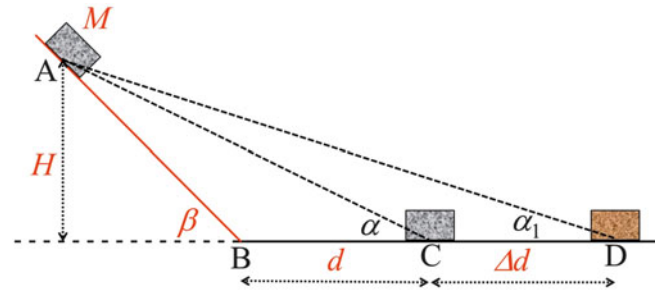


Fig. 2 Mobility and travel distance of debris sliding down slope

Classical Frictional Mechanics and Analysis

Figure 2 shows a typical example of a rock debris sliding down upon a slope (A to B) and continuously moving on a flat ground in front of the slope (B to C). The debris has a mass M at the point A with the height H . The slope surface is a plane with an average slope angle a plane with an average slope β and an average frictional angle ϕ . The ground in front of the slope toe B is a horizontal plane with an average frictional angle ϕ . The total potential energy of the debris is MgH , where g is the acceleration of gravity. Using the Newton's law of motion, the following equations can be obtained under the conditions that $\beta \geq \phi$ and $a(t)$ is the acceleration of the rock mass.

$$\begin{cases} Mg \sin \beta - Mg \cos \beta \tan \phi = Ma(t) & \text{for A to B} \\ -Mg \tan \phi = Ma(t) & \text{for B to C} \end{cases} \quad (1)$$

The maximum velocity V_{AB} of the debris sliding down at the slope toe B can be expressed by

$$V_{AB} = \sqrt{2Hg \left(1 - \frac{\tan \phi}{\tan \beta} \right)} \quad (2)$$

If assuming the energy loss of the impact at the toe point is zero, the debris would have a complete change of its velocity direction to horizontal along the flat ground from B to C. The runout distance d from B to C on the flat ground where the debris stops is

$$d = \left(1 - \frac{\tan \phi}{\tan \beta} \right) \frac{H}{\tan \phi} \quad (3)$$

The travel angle α from A to C can have the following relation.

$$\tan \alpha = \frac{\tan \beta \tan \phi}{\tan \beta + \tan \phi - \tan \phi} \quad (4)$$

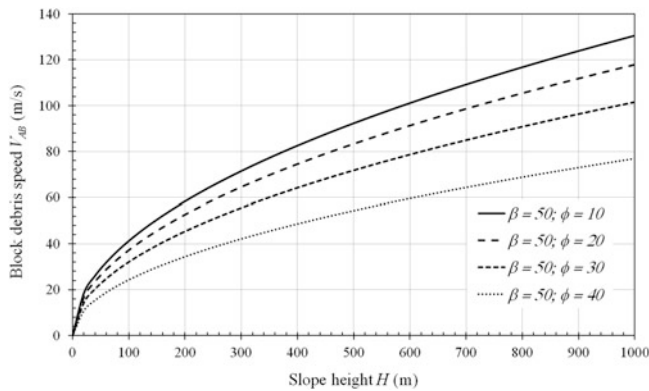


Fig. 3 Variation of the maximum velocity at slope toe with slope height at different slope frictional angles

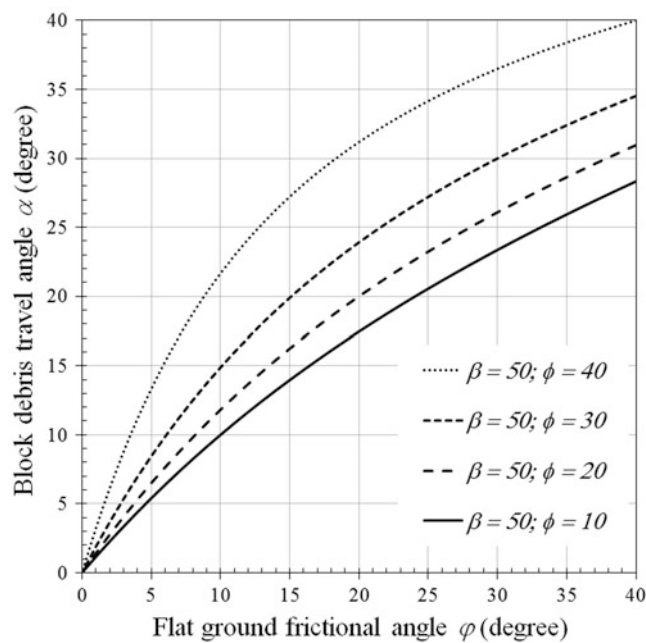


Fig. 4 Variation of the travel angle with flat ground frictional angle at different slope frictional angles

The travel angle depends on the slope angle β , the two frictional angles (ϕ and φ) and is independent to the slope height H and the debris mass M . If $\phi = \varphi$, a special result can be given, i.e., $\alpha = \phi = \varphi$.

Figure 3 shows some typical numerical results for the variations of the maximum velocity V_{AB} at the slope toe. A velocity greater than 10 m/s can be obtained if the slope is more than 10 m high. Reduction in the slope frictional angle ϕ can substantially increase the maximum velocity. Figure 4 shows the variation of the travel angle α with the flat and slope ground frictional angles φ and ϕ . The travel angle α can be significantly reduced to less than the minimum angle of repose 26° if the flat ground frictional angles φ is small.

The reduction in the slope frictional angle ϕ from 40° to 10° can make less than 15° reduction in the travel angle α .

Existing Theories for Frictional Resistance Reductions

From the above mechanical results, it is evident that if the frictional angles or coefficients of the slope and/or flat grounds can be very small, the landslide debris can slide very long distance and have a very small travel angle comparing to the angle of repose for granular materials. In addition, the debris speed can be rapid if the slope is high enough. Accordingly, the existing approach to resolve the issue is to significantly reduce the ground frictional resistance so that the debris can rapidly slide, move and flow one the slope for long distance.

Therefore, many researchers have proposed and developed a variety of theories to reduce the ground frictional angles ϕ and φ since the 1903 Frank slide. As a result, they can well explain the phenomenon that many large landslides (>1 million m^3) reach runout distances exceeding those expected from conventional friction physics. These theories can be classified into the following two groups (Schneider et al. 2011).

The first group is the so-called debris volume effect without lubricants. It includes (1) the apparent friction coefficients map for landslides progressively decrease with increasing volumes; (2) the dispersive pressure in a granular mass that destabilizes and starts moving (the static friction coefficient reduces to a significantly lower dynamic friction); (3) the mechanical fluidization that the avalanche movement itself may result in a volume increase (dilatation) and a further reduction of the internal shear resistance within the shear layer; (4) the decrease of the shear resistance due to grain dilatation externally induced by oscillating ground during an earthquake; (5) the effect acoustic fluidization that the energy needed to cause grain fluctuations may result from an acoustic source; and (6) dynamic fragmentation theory that infers that dispersive pressure can also be generated by the rapid breakage of rock particles within force chains.

The second group is the lubrication & fluidization with lubricants such as water or air. It includes (1) air lubrication where rapid landslides may slide on a thin layer of compressed air after topographic jumps; (2) lubrication by water due to its incompressibility, its higher density and viscosity; (3) lubrication by frictional heating because of layers of molten rock found in several rock-avalanche deposits and refrozen snow observed at the base of snow avalanches; (4) steam generation along thin sliding planes; and (5) air cushion effect and aerodynamics.

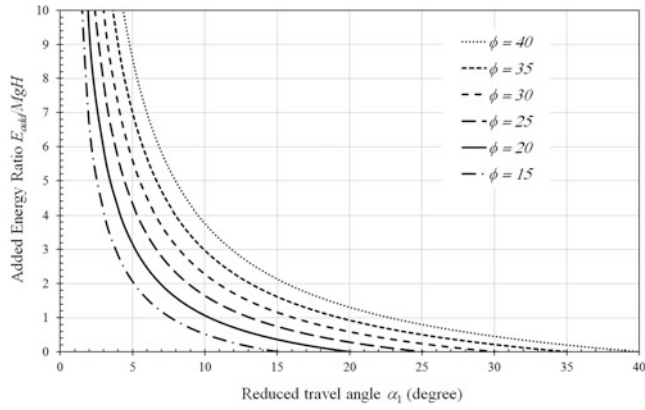


Fig. 5 Additional energy ratio needed for debris to slide and reach the reduced travel angle

However, these theories have encountered various challenges and difficulties. Sometimes, it is difficult to quantify the effects of these effects in reducing the frictional angle or coefficients between the ground and the moving debris. Sometimes, the huge and rapid landslide occurred in dry or little water conditions. The air cushion effect may be possible when the thick sliding debris fly down and cover the air in a narrow valley. However, the air pressure compressed by the flying down debris could be too small to carry and bear the weight and impacting of the moving debris.

Additional Energy Required for Longer Travel Distance

If the slope and flat ground surfaces have the normal frictional angles to be equal to the angle of repose ($\sim 30^\circ$), the rock debris would be able to slide to the position C in Fig. 2. Additional energy is needed for the rock debris to slide to the longer travel distance at the point D with the smaller travel angle α_1 in Fig. 2. The minimum additional energy E_{add} can be assumed to be equal to the frictional work for the debris sliding from the position C and the position D. Because $\Delta d = H(1/\tan \alpha_1 - 1/\tan \alpha)$ and $\alpha = \phi = \varphi$, it can be expressed as follows.

$$E_{add} = \left(\frac{\tan \phi}{\tan \alpha_1} - 1 \right) MgH \quad (5)$$

Figure 5 shows the numerical results for the ratio of the additional energy over the total potential energy of the sliding rock mass E_{add}/MgH with the reduced travel angle α_1 at different frictional angle ϕ . It is evident that the higher ground frictional angle and lower reduced travel angle need more additional energy to overcome the frictional work. For example, if the frictional angle is 25° , the additional energy would be equal to $0.525 MgH$ and $1.020 MgH$ for the travel

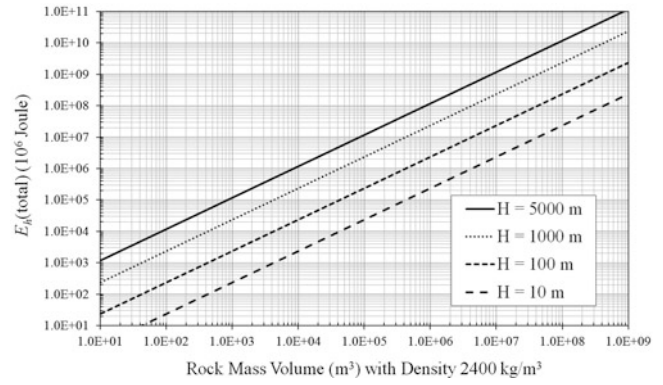


Fig. 6 Total potential energy versus rock mass volume at height H

angle to be reduced from 25° to 17° and 13° , respectively. Figure 6 shows the total potential energy for rock mass of volume from 10 m^3 to 10^9 m^3 with heights from 10 m to 5,000 m.

Dense Natural Gas Expansion Energy

According to Wang and Wang (1989), the energies and works participated in a landslide from the static beginning to the static end can be expressed in the following energy balance equation.

$$E_h + U_d + E_e = W_f + W_i + W_a + W_g + W_m \quad (6)$$

where $E_h (=MgH)$ rock mass potential energy; U_d the rock mass deformation energy; E_e external loading energy such as seismic shocking; W_f frictional resistance work; W_i impact work between moving rock mass and ground; W_a air or water resistance work; W_g work for fracturing and breaking rocks; and W_m impacting work between moving rock fragments. E_h , U_d and E_e are active energies for breaking and moving the rock mass on slope. W_f , W_i , W_a , W_g and W_m are passive energies/works for blocking and stopping the rock mass forward moving, flying, flowing and/or sliding. In particular, $W_f = DMg \cos \beta \tan \phi$, where D the sliding distance.

The author has proposed the volumetric expansion energy E_{gas} of a mount of dense natural gas mass migrated from the deep ground to the slope rock/soil mass to actively cause the slope rock mass to deform, rupture, move, slide and/or fly (Yue 2008, 2009, 2010, 2011, 2012, 2013a, 2013b). Therefore, the general energy balance equation (6) can be re-expressed as follow, where the deformation energy U_d is due to the E_{gas} and includes in it.

$$E_h + E_{gas} = W_f + W_i + W_a + W_g + W_m \quad (7)$$

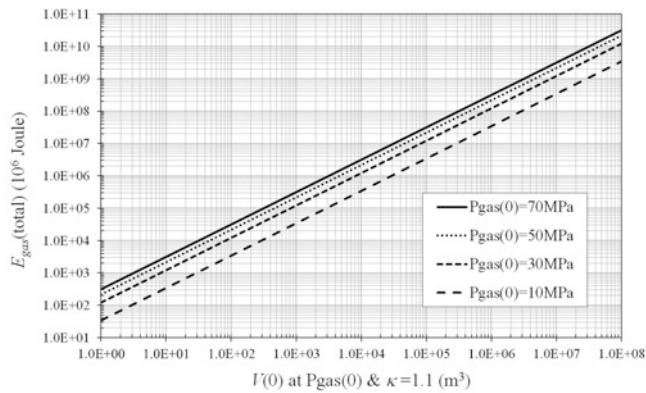


Fig. 7 Total volumetric expansion energy versus the initial gas volume due to reduction of the initial gas pressure to the atmospheric pressure 0.1 MPa

Since a large and rapid landslide can be completed within few seconds to few minutes, its process can be considered as an adiabatic process. Therefore, the volumetric expansion energy $E_{gas}(t)$ released at the time t can be expressed as follows according to the ideal gas laws.

$$E_{gas}(t) = \frac{p_{gas}(0)V_{gas}(0)}{\kappa - 1} \left[1 - \left(\frac{p_{gas}(t)}{p_{gas}(0)} \right)^{1-1/\kappa} \right] \quad (8)$$

where $\kappa > 1$ is the gas specific heat ratio and depends on temperature. At the standard atmospheric pressure $p_a(\approx 0.1 \text{ MPa})$, and a room temperature $25 \text{ }^\circ\text{C}$, $\kappa = 1.66, 1.41$ and 1.31 for helium, hydrogen and methane gases, respectively.

Figure 7 shows the total volumetric expansion energy for dense gas with volume of 1 m^3 to 10^8 m^3 at different initial gas pressure values: $p_{gas}(0) = 10, 30, 50$ and 70 MPa . Comparing with the results in Figs. 6 and 7, it is evident that the dense gas can offer the additional energy sufficient enough to cause the much longer travel distance for the rock debris.

During an adiabatic process of gas expanding due to its surrounding pressure reduction, the gas pressure $p_{gas}(t)$ and its volume $V_{gas}(t)$ at the time t can have the following relationship with its pressure $p_{gas}(0)$ and volume $V_{gas}(0)$ at the original or initial time ($t = 0$):

$$p_{gas}(t)(V_{gas}(t))^\kappa = p_{gas}(0)(V_{gas}(0))^\kappa \quad (9)$$

Figure 8 gives the large gas volumetric expansions due to the reduction of initial high gas pressure. The gas specific heat ratio κ has a significant effect on the degree of the volumetric expansion.

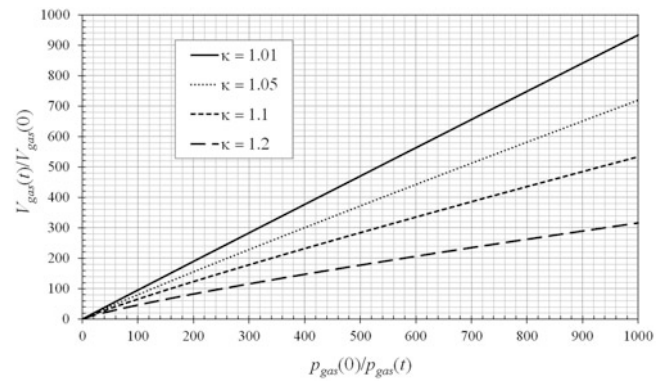


Fig. 8 Volumetric expansion of dense gas with pressure reduction

Mechanism and Mechanics for Dense Gas Expanding Cause

The dense natural gas with high pressure escapes from the deep ground and flows through weak zones and porous channels into the rock and soil masses forming slopes. The slope geomaterials have the strength and can resist the initial loading of the dense gas. The natural gas from deep ground is continuously migrating into and storing in the voids, pores, holes, gaps, openings, apertures and cavities of the geomaterials forming the slope. With time, more and more gas mass would migrate into and store in the geomaterials. Due to high rigidness and relatively well sealing, the slope geomaterials can have little volumetric deformation and some distortional deformation. The gas would increase its pressure and penetrate into various voids and defects. Eventually, the peak equilibrium of forces and deformation can be reach. The expanding power of the gas in the slope geomaterials instantly and rapidly breaks, erupts and/or explodes the slope soil and rock masses. Due to its density is many times greater than the air density ($\sim 1.3 \text{ kg/m}^3$), the dense gas mixed together with the broken debris and continued to offer its remaining expanding powers to the moving and sliding debris. As a result, the debris of large volume can reach the runout distances exceeding those expected from the conventional friction physics and the angles of repose due to gravity only.

Based on fracture mechanics, the minimum pressure $p_{gas}^{tensile}$ of gas in the interior of rock mass to cause all the rock defects to have sudden tensile ruptures can be expressed by the following equation.

$$p_{gas}^{tensile} = 3\sigma_{surrounding} + 2\sigma_{tensilestrength} \quad (10)$$

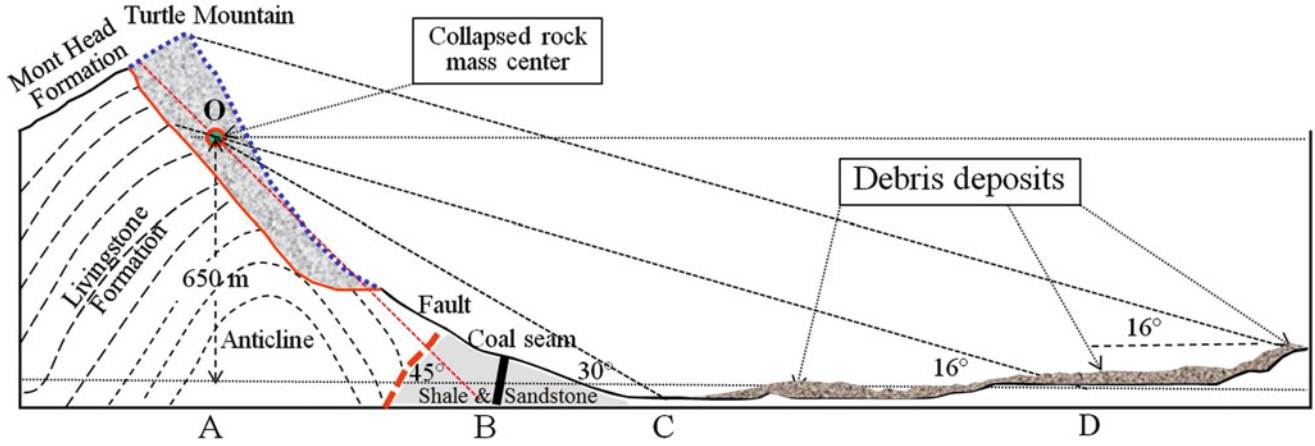


Fig. 9 Cross-section A-B of 1903 Frank Slide (modified after McConnell and Brock 1904)

where $\sigma_{surrounding}$ is the maximum overburden stress, $\sigma_{tensilestrength}$ is the tensile strength of intact rock.

Furthermore, using the Newton's law of motion, the following equations can be obtained under the condition that the dense natural gas is present at the base of rock mass.

$$\begin{cases} Mg \sin \beta + p_{gas}(t)S_1(t) \\ - (Mg \cos \beta - p_{gas}(t)S_2(t)) \tan \phi = Ma(t) & \text{for A to B} \\ p_{gas}(t)S_1(t) \\ - (Mg - p_{gas}(t)S_2(t)) \tan \varphi = Ma(t) & \text{for B to D} \end{cases} \quad (11)$$

where $S_1(t)$ and $S_2(t)$ are respectively the neat areas of the rock mass surfaces with their normal directions parallel and perpendicular to the rock mass moving directions and applied by the gas pressure $p_{gas}(t)$. The above equations are valid if the following conditions are true.

$$\begin{cases} Mg \cos \beta - p_{gas}(t)S_2(t) > 0 & \text{for A to B} \\ Mg - p_{gas}(t)S_2(t) > 0 & \text{for B to D} \end{cases} \quad (12)$$

Due to the gas pressure, the apparent frictional angles ϕ_a and φ_a are changing with time and can be expressed as follows.

$$\begin{cases} \tan \phi_a = \left(1 - p_{gas}(t)S_2(t)/Mg \cos \beta\right) \tan \phi & \text{for A to B} \\ \tan \varphi_a = \left(1 - p_{gas}(t)S_2(t)/Mg\right) \tan \varphi & \text{for B to D} \end{cases} \quad (13)$$

If $Mg \cos \beta - p_{gas}(t)S_2(t) < 0$, the rock debris is flying over the dense and expanding gas from A to B. So, the motion equation (10) for A to B can be re-expressed as

follows using the vertical and horizontal coordinates (x, z) .

$$\begin{cases} Mg - p_{gas}(t)S_z(t) = Ma_z(t) & \text{along } z \text{ axis} \\ p_{gas}(t)S_x(t) = Ma_x(t) & \text{along } x \text{ axis} \end{cases} \quad (14)$$

where $S_x(t)$ and $S_z(t)$ are the near areas of the rock mass surfaces with their normal directions parallel to the axes x and z , respectively.

Secondly, when the rock debris are moving in the B to D zone and if $Mg - p_{gas}(t)S_2(t) < 0$, the rock debris is also flying upon the dense and expanding and leaking gas from B to D. So, the motion equation (13) is also applicable to the motion in B to D.

The gas pressure $p_{gas}(t)$ is controlled by (9). The gas expanding volume $V_{gas}(t)$ is a function of the weight, volume, voids, particle sizes, gas leaking capability, and flying/moving path of the debris. The gas neat areas $S_1(t)$, $S_2(t)$, $S_x(t)$ and $S_z(t)$ are also functions of the gas expanding volume and the properties of the broken rock mass debris.

Case Study and Discussions

Figure 9 shows the geological cross-section of the 1903 Frank Slide according to McConnell and Brock (1993). The collapsed upper limestone mountain rock mass has a total volume of $30 \times 10^6 \text{ m}^3$. Its center may be 650 m above the flat ground in front. Its rupture surface is about 45° . Its central travel angle is about 16° to 18° . The travel angle from the failed peak to the debris far end is 16° . It is clear that the rock debris from the 1903 Frank Slide travelled much farther than the expectation from the conventional frictional mechanics. Almost all the debris are located outside the line (point C in Fig. 9) with the travel angle 30° in Fig. 9.

Since it happened, many opinions have been proposed on the cause of the 1903 Frank Slide. They included an earthquake, a volcano, an explosion of coal gas accumulated in big cave, and combined causes (Kerr 1990). The combined causes are the form and structure of the Turtle Mountain, the removing coal from large chambers in the mine at the base of the mountain and the whether condition of hot a few days before the Slide and very cold (about $-17.8\text{ }^{\circ}\text{C}$) in the night before the Slide (McConnell and Brock 1904). The limestone beddings forming the collapsed Turtle Mountain are in the form of anticline fold, have major deep faults and coal beds.

If assuming the ground surfaces had a frictional angle 30° , the additional energy can be estimated to further displace the collapsed rock debris from the normal travel angle 30° (Point C) to the unusual travel angle 17° to 16° (Point D). Using (5), it is calculated to be $0.9\text{ }MgH$ to $1.0\text{ }MgH$. Since $MgH = 5.0 \times 10^{14}\text{ J}$, the required additional energy is equivalent to 119 kt of TNT, which is huge and unrealistic.

Alternatively, we can use (13) to estimate how much the gas pressure is needed to reduce the ground surface frictional angle from 30° to the apparent frictional angle 16° .

$$\begin{cases} p_{gas}(t) = \frac{Mg \cos \beta}{S_2(t)} \left(1 - \frac{\tan \phi_a}{\tan \phi} \right) & \text{for A to B} \\ p_{gas}(t) = \frac{Mg}{S_2(t)} \left(1 - \frac{\tan \phi_a}{\tan \phi} \right) & \text{for B to D} \end{cases} \quad (15)$$

Using the data discussed above, the following results can be estimated.

$$\begin{cases} p_{gas}(t) \approx 2600 \times 9.8 \times 70 \times \left(1 - \frac{\tan 16^{\circ}}{\tan 30^{\circ}} \right) & \text{for A to B} \\ p_{gas}(t) \approx 2600 \times 9.8 \times 14 \times \left(1 - \frac{\tan 16^{\circ}}{\tan 30^{\circ}} \right) & \text{for B to D} \end{cases} \quad (16)$$

Accordingly, the dense and expanding gas to pad the rock sliding from O to the slope toe has a minimum pressure of 1.0 MPa. The dense and expanding gas to pad the rock debris sliding from the toe to the point D has a minimum pressure of 0.28 MPa. The atmospheric pressure 0.1 MPa is added to the calculated results from (16).

Furthermore, using (10), assuming $\sigma_{surrounding} = 3\text{ MPa}$ and $\sigma_{tensilestrength} = 4\text{ MPa}$, the minimum gas pressure $p_{gas}^{tensile} = 17\text{ MPa}$ for the initial complete ruptures and ejection of the rock mass forming the slope. This minimum pressure 17 MPa is much larger than the results from (15) and (16). These results are considered reasonable.

Using the apparent frictional angle 16° and the equations (1–3), the total time for the rock debris from the center O to the point D is about 53 s to 60 s, is less than the 100 s reported in the literature. The calculated average speed is from 40 m/s to 48 m/s, which is higher than the reported speed 31 m/s.

The reason for the difference is due to that the actual rock mass forming the slope and its broken debris are spread over large areas whilst the modelled rock mass and its debris are combined together at their central points. The interactions and spatial spreading of the broken rock debris need time, which makes the calculated results reasonable. The gas beneath and within the rock and soil debris quickly flow, leak and migrate into upper sky, which left the sudden deposition of the debris solids over the ground.

More detailed analysis on gas cause of Frank Slide will be presented in future publication.

Conclusions

The author has put forward the cause and mechanisms of dense natural gas expanding power for the dynamics of large and rapid landslides with long travel distances. The gas in deep grounds can flow and migrate into and accumulate in the slope geo-materials via special channels such as deep fault. It becomes denser and denser. Eventually, its expansion power deforms and suddenly ruptures the geo-materials. Under gravity, the expanding dense gas and the broken geo-materials rapidly move downward. The author has given relevant governing equations and some numerical results for this gas cause of landslides. The Frank Slide was used as an example to illustrate the cause and mechanism.

Acknowledgments The author thanks the financial support from China Natural Science Foundation (Grant No. 41372336), the National Basic Research Program of China (973 Program, Grant No. 2011CB710600) and many friends and colleagues for their invaluable advices, assistances, discussions, information, data and supports during his independent investigations of the nature of geohazards, earthquakes, volcanoes and the Earth system.

References

- Cruden DM, Martin CD (2007) Before the frank slide. *Can Geotechn J* 49(4):460–476
- Evans SG, Bent AL (2004) The Las Colinas landslide, Santa Tecla: a high destructive flowslide triggered by the January 13, 2001, El Salvador earthquake. *Natural hazards in El Salvador*. The Geological Society of America, Washington, DC, pp 25–38. ISBN-13: 978-0813723754
- Kerr WJ (1990) Frank slide. Barker Publishing, Canada, 48p. ISBN 978-0-9694761-0-8
- McConnell RG, Brock RW (1904) Report on the great landslide at Frank, Alberta, Canada. Canadian Department of Interior, Annual Report, 1903, Part 8

- Schneider D, Huggel D, Haeberli W, Kaitna R (2011) Unraveling driving factors for large rock-ice avalanche mobility. *Earth Surf Proc Landforms* 36:1948–1966
- Wang SJ, Wang SY (1989) Analysis of energy on large-scale high-speed landslide and their catastrophe prediction. In: *Proceedings of selected papers from 1988 Annual national symposium on landslide*. Sichuan Scientific and Technology Publishing House, Chengdu, pp 117–124 (in Chinese)
- Yue ZQ (2008) What caused the catastrophic landslides during the May 12 Wenchuan Earthquake in Sichuan, China. In: *Abstract and oral presentation at the 12th International Conference of International Association for Computer Methods and Advances in Geomechanics (IACMAG)*, Goa, India, 1–6 Oct 2008, p 135
- Yue ZQ (2009) The source of energy power directly causing the May 12 Wenchuan Earthquake: huge extremely pressurized natural gases trapped in deep Longmen Shan faults. *News J China Soc Rock Mech Eng* 86(2):45–50
- Yue ZQ (2010) Features and mechanism of coseismic surface ruptures by Wenchuan earthquake. *Rock stress and earthquake*. Taylor & Francis Group, London, pp 761–768. ISBN 978-0-415-60165-8
- Yue ZQ (2011) On the common energy and gas source for causing earthquakes and natural gas. *Bull Earth Sci Philos (No.1) and Total No. 50*:21–64 (in Chinese)
- Yue ZQ (2012) New cause of gas expanding power for large, rapid and long runout landslides and rock avalanches. Abstracts volume of the first international symposium on new techniques for geohazards research and management, in commemoration of the Zhouqu 2010 Debris Flow Disaster, Gansu Province, Lanzhou, China, 10–15 Sept 2012, p 3
- Yue ZQ (2013a) Natural gas eruption mechanism for earthquake landslides: illustrated with comparison between Donghekou and Papandayan Rockslide-debris flows. *Earthquake-induced landslides*, Chap 51. Springer, Berlin, pp 485–494. ISBN: 978-3-642-32237-2
- Yue ZQ (2013b) Gas-kinetic model for mechanics of large and rapid landslides with long travel distances In: *Proceedings of the international symposium in commemoration of the 5th anniversary of the 2008 Wenchuan Earthquake: long term geo-hazard and risk consequences of areas struck by high magnitude earthquakes*. Chengdu University of Technology, Chengdu, China, 12–13 May 2013, p 32



Investigation to the Local Site Effects During Earthquake Induced Ground Deformation Using Microtremor Observation in Yogyakarta, Central Java-Indonesia

Zaw Lin Kyaw, Subagyo Pramumijoyo, Salahuddin Husein, Teuku Faisal Fathani, and Junji Kiyono

Abstract

Local site effects have an enormous influence on the character of ground motion and play an important role in seismic damage to human being made structures. Several powerful earthquakes have struck Yogyakarta, Indonesia during recent years, one of the destructive which was an Mw 6.3 event that occurred on May 27th, 2006 and caused more than 5,700 fatalities and over 37,000 injuries. Following this event, the single observations of microtremors were densely performed at 274 sites in Yogyakarta City. To provide a good coverage of the study area, the single microtremor observations are designed with a grid spacing of 500 m to the main path of the north–south and east–west of the research area to known in detail the configuration soft rocks and contact hard rock. The predominant periods due to horizontal vertical ratio (HVSRs) are in the range of 0.15–4.00 s. The amplification factor (A_g) and the soil natural frequency (F_g) are generally ranging between 0.70–5.56 and 0.4–3.3 Hz according to results derived from HVSR analysis. It is obviously observed that the thickness of local sediments has great influence on amplification characteristics. In general, the local geology effect is more dominant than the topography effect. The level of soil damage due to the local site effects at the ground deformation location was indicated by the vulnerability index (K_g) and the effective shear strain (γ). Actually, vulnerability index (K_g) varied from 0.6 to 51.3 and the effective shear strain (γ) had values ranging from 300×10^{-6} to $25,000 \times 10^{-6}$ which for $\gamma > 10,000 \times 10^{-6}$ catastrophic landslide or very large deformation will be occurred. This study illustrates how the vulnerability index and the effective shear strain could be used to make preliminary assessment of the research area deformed during the earthquake.

Z.L. Kyaw (✉)

Geology Department, Yangon University, Yangon, Myanmar

Geological Engineering Department, Faculty of Engineering, Gadjah Mada University, Yogyakarta, Indonesia

e-mail: zkyaw.geol@gmail.com

S. Pramumijoyo • S. Husein

Geological Engineering Department, Faculty of Engineering, Gadjah Mada University, Yogyakarta, Indonesia

e-mail: bagyo@ugm.ac.id; shddin@gmail.com

T.F. Fathani

Civil and Environmental Engineering Department, Faculty of Engineering, Gadjah Mada University, Yogyakarta, Indonesia

e-mail: tfathani@gmail.com

J. Kiyono

Department of Urban Management, Graduate School of Engineering, Kyoto University, Katsura Campus, Nishikyo, Kyoto, Japan

e-mail: kiyono.junji.5x@kyoto-u.ac.jp

Keywords

Local site effects • Amplification factor • Natural frequency • Soil vulnerability index • Weak zones • HVSr • Yogyakarta earthquake

Introduction

The Yogyakarta City, the capital of Yogyakarta Special Province, is situated at the southern part of the volcanic arc island of Java. The Yogyakarta City is located in the so-called Yogyakarta Depression area, where is only about 30 km from the Merapi volcano which reaches the elevation of 2,911 m above sea level; it is the most active volcano in Indonesia, and about 40 km from the coast of the Indian Ocean. The eastern part of Yogyakarta City is situated at the centre of the province, in the middle part of Yogyakarta basin. The Basin response depends on the site geometry, impedance contrast, soil properties and constitutive model, and on the complexity and strength of the input solicitation. An earthquake with the magnitude M_w 6.3 occurred near the city of Yogyakarta, on May 27th, 2006 at 5:54 am local time. The earthquake directly affected the provinces of Yogyakarta and Central Java Island. This earthquake caused nearly 5,700 fatalities and above 37,000 injured. More than 135,000 houses were damaged, and 600,000 people were homeless.

It is now well known that local site characteristics may produce large ground motion amplifications during earthquakes. This issue can be investigated by means of the analysis of actual seismic records and the study of synthetic seismogram as well. By last century's middle years, effects of local soil and geological condition were studied mainly in terms of peak accelerations or peak velocities. The effects of topography on surface ground motion have been observed and studied from field experiments. The present paper is attempted to assess the local site effects of weak zones in the city of Yogyakarta, Central Java, Indonesia. The local site effects characterized by high levels of seismicity and weak zones are vulnerable to failure during earthquakes. This can be identified from the Peaks Ground Acceleration (PGA) ranges from 0.2 to 0.25 g and the level 5 of earthquake hazard according to SNI-1726–2010 (Standard National Indonesia).

Background Geology

The geology of Yogyakarta area is controlled by active plate tectonic phenomena such as the active volcano and active subduction of Indian-Australia oceanic plate below the Eurasia continental plate. To the west, a dome of andesitic

breccia and lava flows with the intensive fault formation occurred. Meanwhile at the eastern part of the Yogyakarta City, steep mountains of carbonaceous-volcanic rocks as well as limestone with karst landscape are exposed. The major structure is the north-eastern trending normal fault, well-known Opak fault and defines the eastern limit of a trough extending from Yogyakarta to the coast. The Quaternary succession is dominated by volcanic activities, largely attributable to Merapi volcano. Other important deposits such as littoral clay deposits in the vicinity of Wates, minor valley and terrace alluvium in the main river valleys, deflation materials on limestone and sand dunes adjacent to the coast have also been encountered. The Yogyakarta unit forms the surface outcrop throughout the lowland area of Yogyakarta Basin from Merapi Middle Slope to the coast. The unit consists of an interbedded sequence of sand, gravels, silts and clay. The amount of clay increases southwards. However, the layers of coarse materials have been encountered throughout the basin. Thickness of this unit is variable and up to 45 m in some places. This unit lies unconformable upon the Sleman unit. The Yogyakarta City sits in a broad valley between two groups of roughly north running mountains where Kulon Progo Mountains are to the west and southern mountains to the east. The towering Merapi volcano caps the northeast end of the valley as shown in Fig. 1.

Historical Seismicity

Earthquakes occur almost continuously around the world. Fortunately, most are so small that they cannot be felt. Only a very small percentage of earthquakes are large enough to cause noticeable damage and small percentage of those are large enough to be considered major earthquakes. Throughout recorded history, some of these major earthquakes can be regarded as being particularly significant, either because of their size and the damage they produced or because of what scientists and engineers were able to learn from them.

The Java trench region shows low seismicity compared with the Sumatra subduction zone region but the destructive earthquakes occurred in the past and among them some generated tsunami. The historical earthquake record in this area can be generally divided as the pre-historical period up to about 1840 with the epicentre locations and magnitudes based largely upon felt reports, and an instrumental period

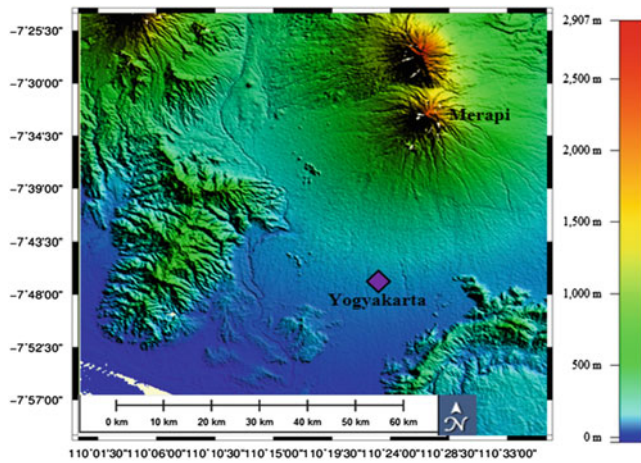


Fig. 1 Topography or altitude map in Yogyakarta area

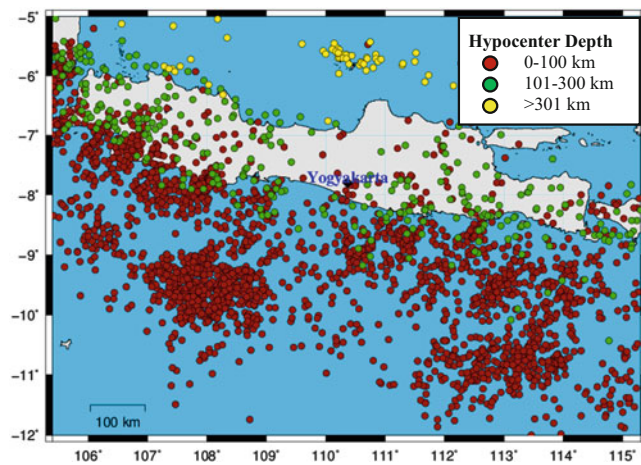


Fig. 2 Historical Seismicity in Java Island ($M_w > 4.0$ and 1840–2013)

which is inferred from the USGS (2013) (NEIC) and ANSS earthquake catalogues. According to the historical and instrumental records, most of the earthquakes which effected on the Yogyakarta special province mostly occurred within the radius of 200 km.

Although the southern part of central Java has relatively low seismicity compared to the east Java and the west Java, it does not mean that Yogyakarta have never or rarely experience devastating earthquakes. Despite from the latest May 27th 2006 event, historical records indicate that Yogyakarta has been struck several times by the earthquake and significant damages were reported as shown in Fig. 2. The Yogyakarta area therefore can be regarded as a seismic prone area and the similar destructive earthquakes can be expected in future. The prevention and mitigation of seismic risk in this area is one of the major needs.

Microtremor Survey

The earth surface is always in motion at different frequencies; even in the absence of active seismic sources. The damages caused by the recent earthquake are concluded as a direct result of local geological conditions affecting the ground motion. These constant vibrations are called microseisms or preferably microtremors. The amplitude of these microtremors is generally too small (10^{-4} – 10^{-2} mm) to be felt by human senses. Microtremors are considered as noise sources in seismological studies. Microtremor is a very convenient tool to estimate the effect of surface geology on seismic motion without other geological information. Moreover the single microtremor observation methods have been developed as a simple and cost effective method to determine the characteristics of the ground properties (Nakamura 1989; Tokimatsu et al. 1994).

In today practice, to provide a good coverage of the study area, the measurement sites are designed with a grid spacing of 500 m to the main path of the north–south and east–west of the research area to known in detail the configuration soft rocks and contact hard rock.

The results of microtremors observations were measured only for five minutes by using the sampling rate of 100 Hz with 3-components. Although they are results from five minutes measurements, it is still enough to get first fundamental period of H/V ratio for most of cases. The first fundamental frequency of H/V ratio mostly reflects the S-wave velocity of sediments and it is therefore used for validation of S-wave velocity structures determined by geotechnical approach.

Moreover, the single microtremors observations of 274 sites in the eastern part of Yogyakarta City show in the Fig. 3. The measurements were carried out during the daytime using a microtremor instrument which is model of Mitutoyo-GPL-6A3P and serial No. 0418707. A single seismic station was used for the microtremor measurements. It was composed of a short-period, three-component seismometer with natural period of 1 s, a 24-bit A/D converter with GPS time, sampling each channel at 100, and a laptop computer to control the system and store the data. At each sites microtremors were recorded with a sampling rate of 100 Hz for five minutes. During the measurements particular attention was given to keep the recordings free from very local noise sources, like e.g. passing pedestrians, vehicles or operating machineries. Meteorological disturbances, e.g. rainfall or gusty wind, did not occur during the observation period. The site's topography and local peculiarities were also considered, e.g. artificial soil replenishments, floor coverings, paved or tarmac roads, and neighbouring elevated structures.

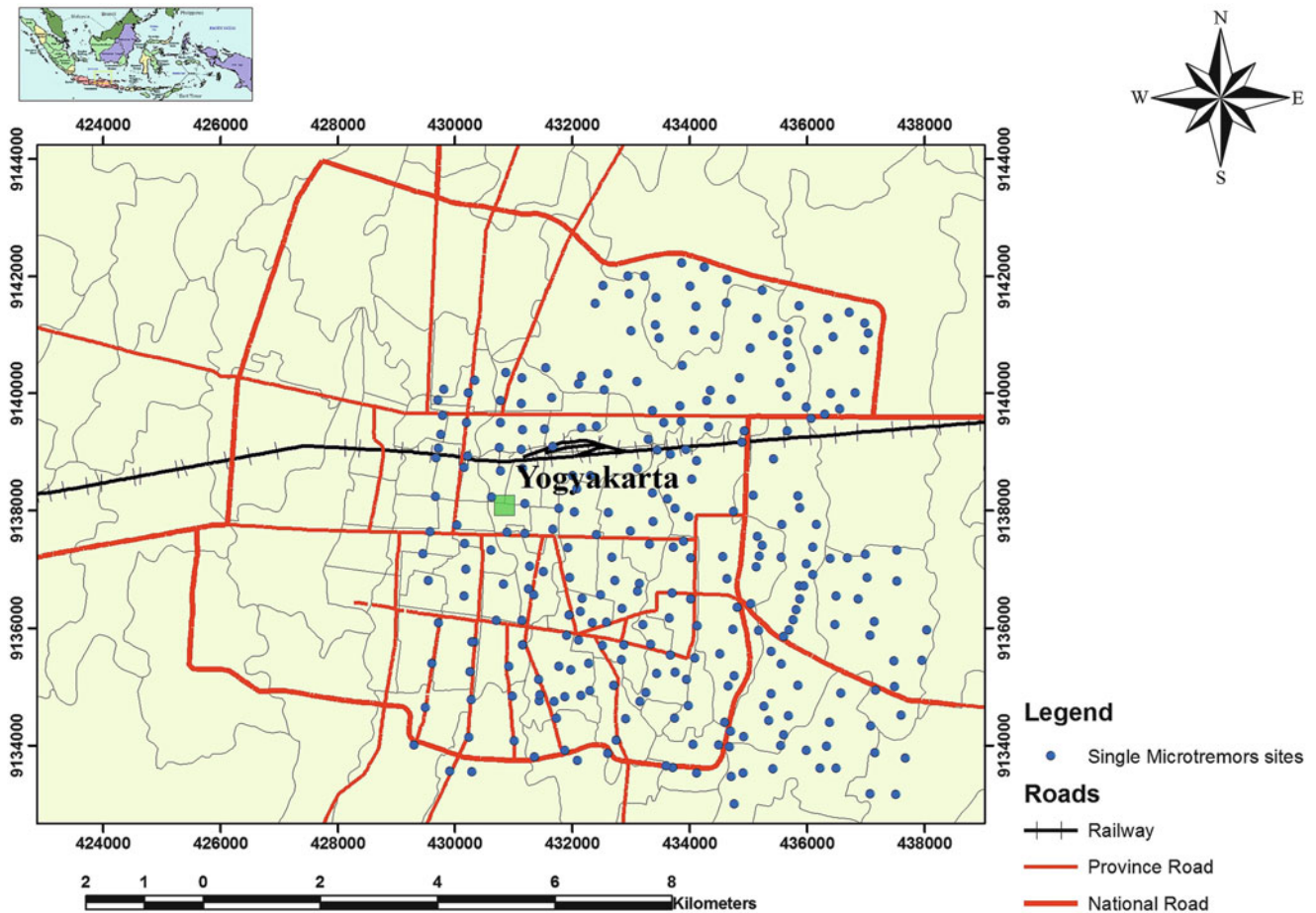


Fig. 3 Station of densely microtremor observations

Application of HVSR

A microtremor is a very small ground motion that can be recorded at the ground surface. It can be produced by a variety of excitations (e.g., wind, traffic, breaking sea waves). A full microtremor record can be described by one vertical and two horizontal components. The analysis was conducted using the recorded microtremor. First, the horizontal and consists in estimating the ratio between the Fourier amplitude spectra of the horizontal (H) to vertical (V) components of ambient noise vibrations recorded at one single station. The peak period of the HVSR is known to correspond to the resonant period of the site.

The procedure generally used to calculate the HVSR consists in the application of (1) to the average amplitude spectra of the three components of motion. This HVSR method postulates the shape of the Fourier spectrum

(Nakamura 2000). Equation (1) shows the method used to calculate HVSR using the observed records:

$$HVSR = \frac{\sqrt{F_{NSi}(\omega)^2 + F_{EWi}(\omega)^2}}{F_{UDi}(\omega)^2} \quad (1)$$

where $F_{NSi}(\omega)$, $F_{EWi}(\omega)$ and $F_{UDi}(\omega)$ denote the Fourier amplitude of the NS, EW and UD components of each interval, respectively, and ω is the frequency.

Predominant Period of H/V Spectrum

Among various kinds of geological explorations by using microtremor records, the horizontal to vertical spectrum ratio (H/V spectrum) is considered most effective (Nakamura 1989). The H/V spectrum only requires observation at single point, which is much easier than the array

observation for the F-K spectrum and the SPAC methods. In this study the potential effectiveness of the H/V spectrum for the investigation of shallow and deep soil structure on the volcanic sediments of lowland sites is discussed with reference to microtremor observations at 274 sites in the eastern part of Yogyakarta City.

Based on the nature of the H/V spectrum mentioned above, the soil structure of the eastern part of Yogyakarta City was estimated. For deep soil, predominant period is estimated from a peak in long period range of the H/V spectrum. On the other hand, the shapes of H/V spectrum are various in the short period range, showing the variety of shallow soil conditions. It is shown that the existence of the clearly contrasted soil layer is almost detected by the peak period of the H/V spectrum considering the microtremor as a Rayleigh wave.

The spectral ratio of horizontal and vertical motion obtained by microtremor observations is called the H/V spectrum. The predominant period of an H/V spectrum is thought to be equivalent to the predominant period of the ground directly beneath the site. H/V spectra at each site in the target area were calculated. The H/V spectrum was classified into three types according to the shape of the spectra (Kiyono et al. 2011).

- Type A: the two distinct peaks (Fig. 4a)
- Type B: a single clear peak (Fig. 4b)
- Type C: without clear peaks

The distinct peaks express the characteristic of the layers for which the shear wave velocity is quite different. According to this interpretation, the lower and higher periods in Type A represent the effects from deep and shallow soil layers, respectively. In Type B, the difference between the two layers is not marked, and the effect of one layer is absorbed into that of the other layer. Type C is an observation site that has hard soil.

Thus, it was established the data for both long and short predominant periods, T_d and T_s . In the eastern part of Yogyakarta City, T_d is between 0.15 and 4.00 s in Fig. 5 and T_s is between 0.1 and 1.00 s in Fig. 6. Although the predominant period does not always indicate the characteristics of an individual layer because typically the actual shaking mode of the ground is complex, it was assumed that the long and short periods reflected information from each layer. If each value of the predominant period obtained is considered to be a realization of a stochastic random field, it can be used the Kriging technique, which is one of the interpolation techniques that considers the covariance of the random field. On the basis of these results, it would appear that it is possible to use the H/V spectral ratio to determine the fundamental periods and establish the seismic microzonation in terms of a predominant period's map of the studied region.

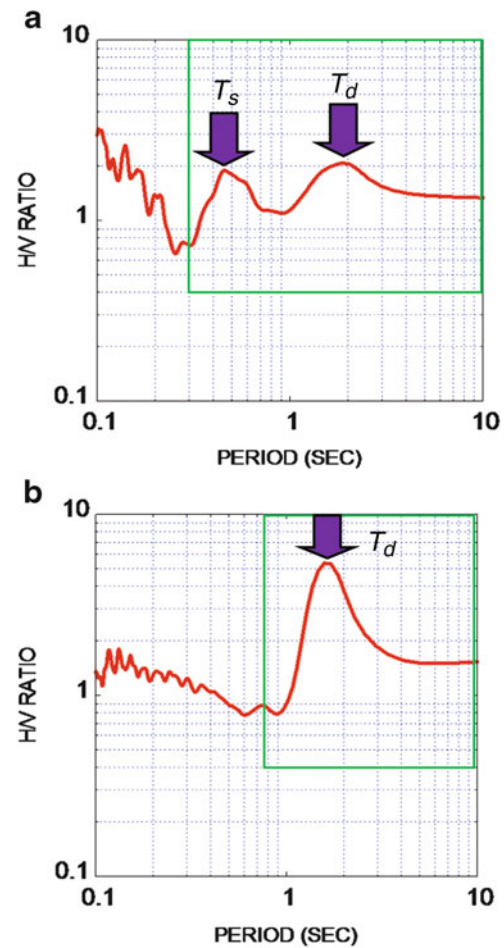


Fig. 4 Typical examples of (a) the two distinct peaks (Location site (157) $7^{\circ}51'56.3''S$, $110^{\circ}24'26.9''E$), and (b) a single clear peak (Location site (167) $7^{\circ}49'1.4''S$, $110^{\circ}24'29.3''E$)

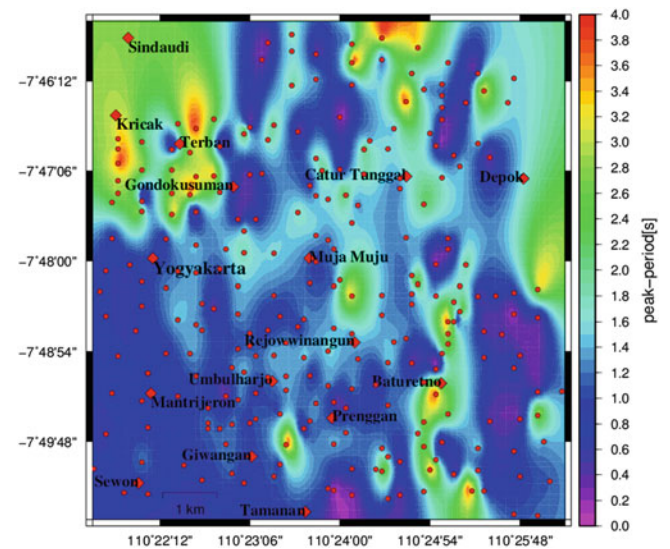


Fig. 5 Spatial distribution of the long predominant period, T_d or seismic microzonation

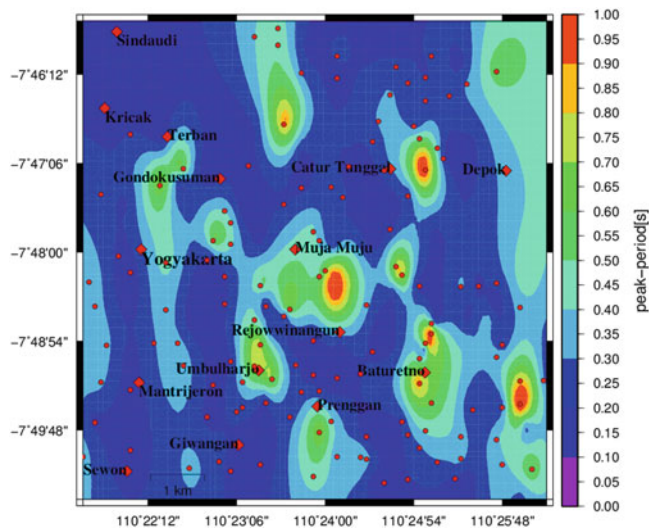


Fig. 6 Spatial distribution of the short predominant period, T_s , or seismic microzonation

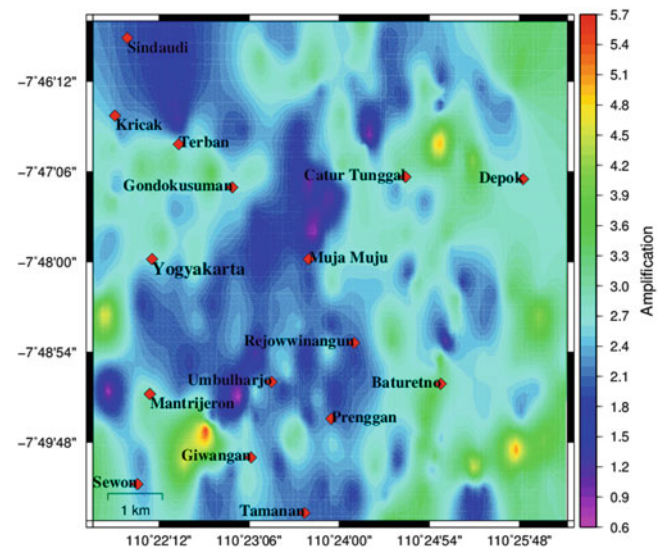


Fig. 7 Spatial distribution of the transfer functions or the amplification factor

Distribution of Amplification Factor and Fundamental Frequency

Earthquake damage is strongly affected by site amplification from bedrock to the ground surface, as well as the size of the earthquake itself. The site amplification of the ground is controlled by factors of the sedimentary layers such as soil density, shear wave velocity, damping characteristics, shape of irregular boundaries and so on. In considering the earthquake disaster prevention measures, knowledge of the amplification characteristics and underlying structures of the ground are very important. The peak magnitude of H/V ratio is generally correlated to site amplification. However, it is only a rude estimation and the site amplification characteristics determined by response analysis is more acceptable and rational. The ratio of amplification of the Fourier spectrum at two layers is called frequency response function, spectral ratio or amplification factor. Amplification ratio is the amplitude of the objective layer to those of the reference layer and is a function with respect to frequency. The objective layer is chosen to be ground surface and reference layer is base and thus, frequency at the peak of the spectral ratio corresponds to predominant period of the ground. The inverse of the frequency, i.e., natural predominant period is also obtained.

In Fig. 7, the amplification factor is generally ranging between 0.70 and 5.56. The high amplification mainly related to thicker sediment area where fundamental frequency is low and vice versa, the lower amplification is in shallow sediment area where high fundamental frequency is

dominant. The highest amplification zones are bounded in Terban, Gondokusuman, Yogyakarta, Mantrijeron, Baturetno, Catur Tunggal and Depok areas where are thick sediment area and it should be taken attention to construct the new huge building plan or project via engineering point of view. The lowest amplification zones are represented dark blue color which is included in Sindaudi, Kricak, north of Terban, south of Yogyakarta, Muja Muja, Rejowwinangun and Umbulharjo, Prenggan, Sewon, Tamanan area (shallow sediment area).

Estimation of the local response of a site is a key component of any analysis of local seismic hazard. Seismic hazard enables us to characterize potential seismic aggressions that need to be taken into account when designing new structures or upgrading existing ones. The experimental methods involving microtremor recordings are useful for determining site effects in regions of moderate seismic activity as Yogyakarta City where ground motion records are few and urban or highly density population where the noise level is high. Therefore, each observation point provides a spectral ratio and enables an estimation of the fundamental frequency and the maximum value of the amplification at the site studied.

As shown in Fig. 8, the fundamental frequency is generally varying between 0.40 and 3.30 Hz and there are three zones of frequency which is low, medium and high frequency zones. Kricak, Terban, Gondokusuman, Catur Tunggal, Depok, Muja Muju, Rejowwinangun, Umbulharjo, Baturetno, Prenggan, Giwangan and Tamanan area are detected the low frequency zones (<1.00 Hz). So it is clear

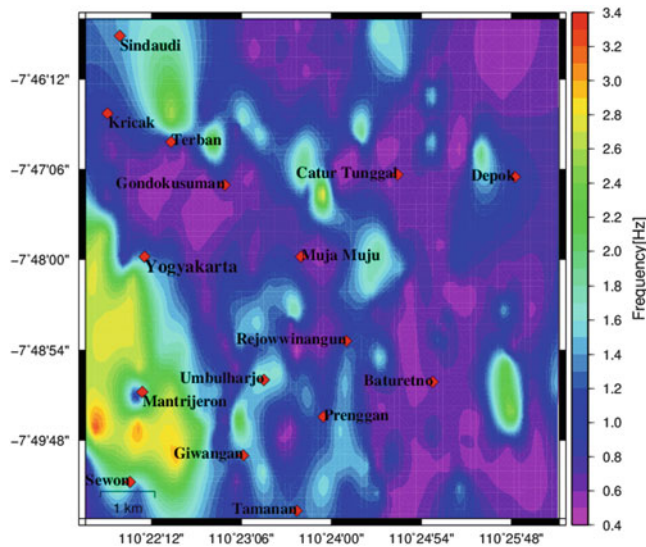


Fig. 8 Spatial distribution of the fundamental frequency

that the low frequency zone is correlated to the thicker sediment and higher amplification zone where it can be expected the ground motion in the future. Sindaudi, south of Yogyakarta and Mantrijeron and Sewon area are observed the medium frequency zones (1.6–2.6 Hz). Moreover, it is notice that small area between Mantrijeron and Giwangan area is including the high frequency zones (>2.8 Hz). And then it means that high frequency zones are related to the shallow sediment and low amplification zone.

Seismic Vulnerability Index and Effective Shear Strain of Ground and Structure

It is provided that the H/V spectral ratio of both microtremor and strong motion is useful for estimation of at least fundamental frequency and its amplification factor. Based on the information of the H/V spectral ratio, vulnerability index K values for ground and various structures are defined. Earthquake damage of members occurs at the time of exceeding the limit of the strain caused by deformation, and it causes the collapse if the stability of the structure lacked. Then the vulnerability index focused on the strain was defined (Nakamura 1997). K value in $10^{-6}/\text{cm/s}^2$ is defined to estimate the strain in the unit of 10^{-6} at particular parts of the structures, by multiplying the maximum acceleration at the engineering basement and the K value. These K values are defined for ground and various structures, as K_g value for ground. K_g value is defined as follows;

$$K_g = A_g^2 / F_g \quad (2)$$

Here F_g and A_g are predominant frequency and amplification factor on surface ground estimated by the H/V spectral ratio, respectively. If maximum acceleration is 100 cm/s^2 at the basement and K_g value is 20, the average strain at the surface ground layer is estimated $2,000 \times 10^{-6}$, and the strain may cause some damage to this ground. Many research groups in worldwide confirmed the relationship between K values and the actual earthquake damages.

In this study the vulnerability indices are defined as an index concerning the presumed value of shear strain for surface ground which is derived from the product of the index and maximum acceleration of the expected earthquake motion. It is expected that these vulnerability indices can rationally estimate the risk of the ground and structures for assumption earthquakes. Furthermore, the validity of these vulnerability indices is expected to be generalized as compared with actual earthquake damage.

$$\gamma = (A_g^2 / F_g) \times (\alpha / \pi^2 v_b) \quad (3)$$

where, γ = Shear strain (in powers of 10^{-6})

A_g = Amplification factor of the surface ground ($=V_b/V_s$)

F_g = Natural frequency of the surface ground (Hz) ($=V_s/4 h$)

α = Maximum acceleration of the basement (g)

v_b = S-wave velocity of the basement (m/s)

Effective strain can be presumed as a value which multiplied by K_g value and the maximum acceleration in case of an earthquake. K_g value is an index peculiar to the measured ground, and it is possible to express the vulnerability of the ground. As shown in equation (2), K_g value can be easily derived from natural frequency F_g and amplification factor A_g which were presumed in each measurement point.

The target of this study is to propose a simple and exact vulnerability index based on the result of microtremor measurements for ground and structures. As a result of this study, it was confirmed that the seismic response characteristics of ground and structures could be exactly obtained from the result of measurements. And also, a widely applicable vulnerability index was proposed from the viewpoint of the strain corresponding to typical deformation of ground and structures. The validity of the proposed vulnerability index was verified by comparing its results with the damage and/or influence of actual earthquakes.

For ground, shear strain γ of surface ground is noticed. Ishihara (1978) compiled the relationship of γ to ground disasters. It indicates that from $\gamma = 1,000 \times 10^{-6}$ ground begins to show non-linear character and in $\gamma > 10,000 \times 10^{-6}$ large deformation and collapse occur.

The value of v_b is expected to be nearly constant in a broad area and K_g is a proper value for measured point. Thus K_g can be considered as an index to indicate easiness of deformation of measured points which is expected useful to detect weak points of the ground.

Distribution of Soil Vulnerability Index and Effective Shear Strain

At each point of single microtremor observation sites, the natural frequency (F_g), amplification factor (A_g), vulnerability index (K_g) and effective shear strain (γ) were determined. Nakamura (1996) introduced a Vulnerability Index Parameter (K_g), which combined A_g and F_g to determine soil damage level due to the local site effects (Nakamura 1996). Thus, K_g can be considered as an index to indicate easiness of deformation of measured points which is expected useful to detect weak points of the ground. To estimate soil vulnerability index (K_g), the value of shear strain (γ) need to be considered. According to Ishihara (1978) ground soil becomes plastic state at about $\gamma = 1,000 \times 10^{-6}$; and for $\gamma > 10,000 \times 10^{-6}$ catastrophic landslide or very large deformation will be occurred (Ishihara 1978). Fig. 9 shows the distribution of vulnerability index (K_g) having values ranging from 0.6 to 51.3. Nakamura (2008) stated that K_g greater than 20 represented that ground deform much. Large values of K_g ($K_g > 20$) were found; these zones were considered as weak zones which may fail during the earthquake.

In Fig. 9, the southeast of the study area is high seismic vulnerability index zone ($K_g > 20$) especially southeast of Baturetno and Prenggan area and the rest area is low zone ($K_g < 20$). Therefore it is expected that the exact area and extend of damage will be able to be predicted by using the investigation data before next the earthquake.

In Fig. 10, the high shear strain zone ($\gamma > 10,000 \times 10^{-6}$) is found in southeast of the research area actually southeast of Baturetno and Prenggan area and the low zone ($\gamma < 10,000 \times 10^{-6}$) is presumed in the rest of the study area. That is why it is obviously observed that these areas were determined as weak zone which may damage during the earthquake. To better understand that an increase of K_g value resulted in a greater possibility earthquake, the effective shear strain calculation was used. For $\alpha = 0.25$ g and $v_b = 500$ m/s it can be determined that effective shear strain varied from 300×10^{-6} to $25,000 \times 10^{-6}$ during an earthquake. Large values of γ were found the eastern part of the studied area especially southeast of the research area; these zones were

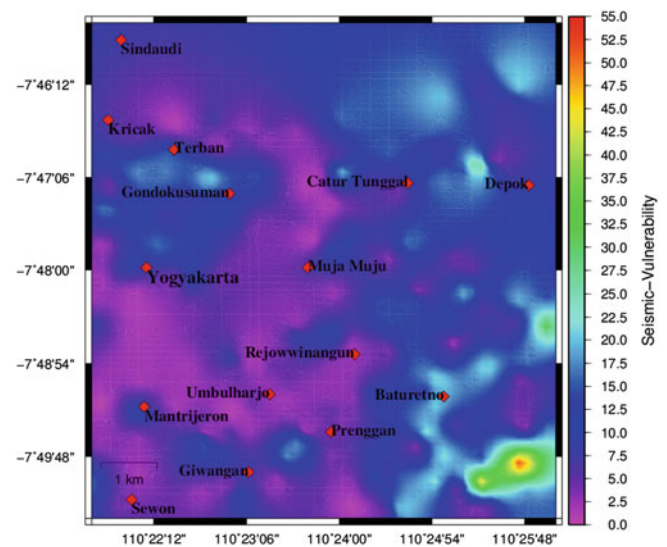


Fig. 9 Spatial distribution of seismic vulnerability index

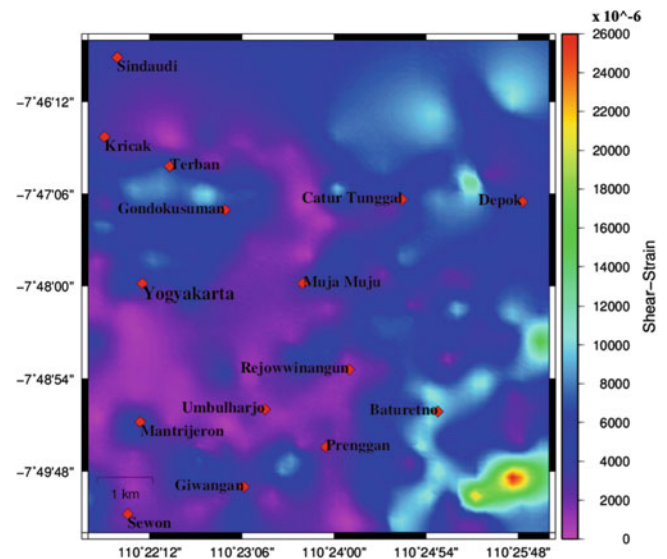


Fig. 10 Spatial distribution of the effective shear strain

considered as weak zones which may fail during the earthquake.

In the comparison, an important remark can be recognized the similar findings of the site investigation results and numerical analysis results. So, it is possible to understand that the distribution of seismic vulnerability index (K_g) and effective shear strain (γ) are corresponding as weak zones which may contribute to increase the aseismic capacity of the research area.

Vulnerability indices (K-values) of ground and structures due to earthquake motions have been proposed. K-values can be calculated from microtremors measured easily everywhere and it is not impossible to estimate the vulnerabilities of all structures and ground concerned. In the near future, the data of K-values will be accumulated and the plan to do vibration rupture experiment to estimate damage degrees precisely from K-values and to examine validity of K-values as vulnerability indices will be done.

Conclusions

The microtremor observations and data analyses were performed useful and practical data for earthquake disaster mitigation in Yogyakarta City. In this research, the 274 of densely single-point microtremor observations which covered almost the whole city area were conducted to estimate the shallow and deep soil structures from the short and long predominant periods in Yogyakarta City. It was obviously confirmed that H/V spectrum for microtremor is horizontal to vertical amplitude ratio of Rayleigh wave including higher modes. By analyzing the shallow and deep soil structure, it will be investigated to grasp the strong ground motion and to mitigate the future damage.

The distribution of frequency is relatively uniform, ranging from 0.40 to 3.30 Hz, where the topographic pattern is associated with the frequency value. The amplification factor is varying from 0.70 to 5.56. The high amplification factor ($A_g > 2.7$) are observed in several main urban area. The topographic effect is not the only one factor controlling of the amplification factor and it can be clearly showed that the geological factors are more dominant to the amplification variation. Finally the distribution of high value of seismic vulnerability index and effective shear strain are corresponding as weak zones or ground deformation or landslide which may contribute to increase the aseismic capacity of Yogyakarta City during the future earthquake.

Acknowledgements This study has been supported financially by ASEAN University Network/the Southeast Asia Engineering Education Development Network, Japan International Cooperation Agency AUN/SEED-Net, JICA, Japan. I would like to thank the students of Geological Engineering Department, Gadjah Mada University who helped me during the microtremor observations in Yogyakarta City-Indonesia, 2012.

References

- ANSS (Advanced National Seismic System) Composite Earthquake Catalog 1970/01-2007/07. <http://www.ncedc.org/anss>
- Ishihara K (1978) Introduction to dynamic soil mechanism, January
- Kiyono J, Ono Y, Sato A, Noguchi T, Rusnardi R (2011) Estimation of subsurface structure based on Microtremor observations at Padang, Indonesia. Division III, Civil Engineering, Environmental Engineering and Geological Engineering. ASEAN Eng J 1(3):69–84, AUN/SEED-Net JICA
- Nakamura Y (1989) A method for dynamic characteristics estimation of surface layers using microtremor on the surface. RTRI Report 4:18–27
- Nakamura Y (1996) Real time information systems for seismic hazards mitigation UrEDAS, HERAS, PIC. Quart Rep RTRI 37 (3):112–127
- Nakamura Y (1997) Seismic vulnerability indices for ground and structures using microtremor. World Congress on Railway Research in Florence, Italy, November
- Nakamura Y (2000) Clear identification of fundamental idea of Nakamura's technique and its applications. In: Proceedings of the 12th World Congress on Earthquake Engineering, Auckland, New Zealand
- Nakamura Y (2008) On the H/V spectrum. In: The 14th World conference on engineering, October 12–17, 2008, Beijing, China
- NEIC (National Earthquake Information Center) USGS Earthquake Catalog 1973/01-2007/07. <http://neic.usgs.gov/neis/epic/>
- Tokimatsu K, Nakajo Y, Tamura S (1994) Horizontal to vertical amplitude ratio of short period microtremors and its relation to site characteristics. J Struct Construct Eng Architect Inst Jpn 475:11–18 (in Japanese)
- USGS (2013) United States geological survey, historical earthquakes in the world since 1900. <http://earthquake.usgs.gov/regional/world/historical.php>



Indicators for Earthquake-Induced Soil Slides in the Flatlands of an Alpine Fringe Area

Philip Leopold, Jason N. Goetz, Gerhard Heiss, and Erich Draganits

Abstract

In Austria's most eastern province Burgenland, an ongoing study of the regional distribution of mass movements has been performed. In this alpine fringe area more than 280 previously unrecognized active mass movements were mapped, most of them are identified as creep or soil slides. We assume that the majority of these landslides were triggered by intense rainfall, but we also found strong indications that at least two large scale movements might be earthquake-induced. These two movements, each covering an area of more than 1 km², are situated in the north of the province. In other parts of the province the dimension of mapped landslides averages only 0.03 km². Compared to the other areas, the hill slopes in the north have the lowest steepness and the lowest annual precipitation. Underground geologic conditions, however, are overall comparable. Earthquakes are only documented in the north of the province and they could have acted as additional trigger for these comparatively large scale landslides with their noticeable different pattern in dimension and volume.

Keywords

Slide • Earthquake • Natural triggers • Burgenland • Basin • Austria

Introduction and Investigated Area

Since 2005, an ongoing study of the regional distribution of mass movements has been performed in the province of Burgenland in Austria (Fig. 1). The province covers three basin landscapes situated in the eastern alpine fringe area: the Eisenstadt basin in the north, the Oberpullendorf basin in the middle and the eastern part of the Styrian basin in the south. In total, more than 280 previously unrecognized

active landslides in loose and weak consolidated sediments have been classified in the province. They have directly and indirectly caused significant damages on buildings and infrastructure.

The geology of the basins is characterised by Neogene and Quaternary sediments, mainly comprising clay, silt, sand and gravel, commonly interbedded. This setup makes the basin areas particular vulnerable to form landslides. The dominant types of movements are slides and creep with secondary slides as discussed within the second WLSF (Leopold et al. 2013). In this paper we want to focus on comparatively large scale landslides in a study region in the Eisenstadt Basin. After discussing general controls, frequency, dimensions and triggers of landslides in all three basin landscapes we want to focus on earthquakes as additional triggering mechanism in the Eisenstadt basin.

P. Leopold (✉) • J.N. Goetz • G. Heiss
Health and Environment Department, AIT–Austrian Institute of
Technology GmbH, Konrad-Lorenz-Straße 24, Tulln 3430, Austria
e-mail: philip.leopold@ait.ac.at; jason.goetz.fl@ait.ac.at; gerhard.heiss@ait.ac.at

E. Draganits
Department of Geodynamics and Sedimentology, University of
Vienna, Vienna 1090, Austria
e-mail: erich.draganits@univie.ac.at

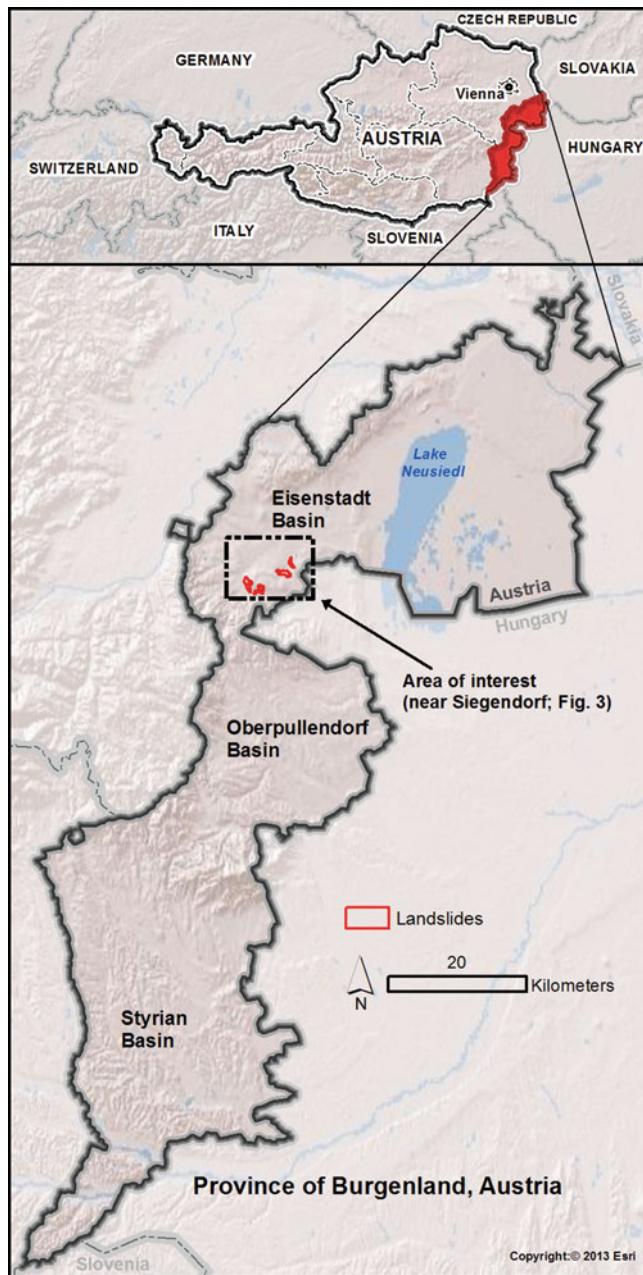


Fig. 1 The province of Burgenland in Austria with its three basin landscapes and the area of interest

Controls, Frequency and Dimensions of Landslides in Burgenland

Natural Controls

Hutchinson (1968) highlighted that mass movements are naturally controlled by geology, climate and topography.

As already stated in the introduction, the geological conditions are comparable in the three basin landscapes of the province (Leopold 2012). Basin sediments are of the same Neogene age and sedimentary composition.

Table 1 Mean annual ground-surface temperature (MAGST) and average annual precipitation (AAP) for the three basin landscapes in the province of Burgenland

Climate	Eisenstadt Basin	Oberpullend. Basin	Styrian Basin
MAGST(°C) 1961–1990	10.2	9.3	8.7
MAGST(°C) 1992–2004	10.7	9.8	9.9
AAP(mm) 1961–1990	606.5	645.5	731.7
AAP(mm) 1992–2004	630.2	685.3	699.1

These sediments are covered with only thin Quaternary deposits. As field investigations could show, these quaternary sediments are not responsible for forming landslides. It is the Neogen interbedded strata, especially the frequent alteration from very fine to coarse sediment layers that makes the area so vulnerable to form landslides (Leopold 2012).

The climate conditions are also rather comparable. To outline the characteristics of the regions we used data for temperature and precipitation provided by ZAMG (<http://www.zamg.ac.at>). We analysed data from seven long term climate observation stations to calculate typical average data for the three basin landscapes, shown in Table 1. Two periods 1961–1990 and 1992–2004 were reviewed to additionally highlight recent climate changes. Mean annual ground-surface temperature (MAGST) shows some variation with the abnormality of a warmer north due to local climate preconditions resulting from the alpine fringe position (Auer et al. 1996). In recent years, the temperature in the south (Styrian basin) increased significantly and the gap to the warmer north is shrinking. The values for the average annual precipitation (AAP) range between 606 mm in the north and 732 mm in the south for the 1961–1990 period, but differences are also decreasing in recent years. However, the southern region still has a slightly higher annual precipitation (Leopold 2012).

Slope is the most important topography parameter in the context of landslides (Soeters and Van Westen 1996). All investigated basin landscapes are characterised by gently dipping hill slopes, typical for landscapes where Neogen loose and weak consolidated sediments form the base material of the basin. To go more into detail we used a DTM with 10 m resolution and performed GIS-based slope angle class analysis. However, in the context of this paper, this analysis is summarized by presenting the average slope angles (Table 2). We used ESRI's "3D-Analyst" to compute an average slope angle for each basin landscape by taking only terrain with Neogen and Quaternary sediments into account. Flat valley plains with recent deposits were excluded. The average slope angle in the south (Styrian basin) is nearly double compared to the northern Eisenstadt basin.

Table 2 Average slope angles for the three basin landscapes. Only terrain with Neogen and Quaternary sediments are taken into account

Topography	Eisenstadt Basin	Oberpullend. Basin	Styrian Basin
Average slope angle	3.5°	4.5°	6.4°

In summary, natural controls are overall comparable in the three basin landscapes. While geological conditions show only little variation, the Styrian basin has higher annual precipitation and significantly steeper terrain.

Anthropogenic Controls

Aside from described natural controls a large volume of published studies highlight the importance of anthropogenic controls on landslides (e.g. Highland and Bobrowsky 2008). The province of Burgenland has a very homogeneous settlement structure. Apart from the capital Eisenstadt (approx. 13,300 inhabitants) all other cities do not exceed a population of 8,000 inhabitants. Settlements are mostly scattered in rural areas. Analogous cultural development and comparable natural conditions (climate, soil and topography) lead to a very homogeneous land use in all of the three basin landscapes. Land cover analysis derived from satellite images show continuous distribution of fields, forests and settlement areas. Contrary to some natural controls, anthropogenic controls do not show significant variances within the entire investigated area.

Frequency and Dimensions

As stated in the introduction, landslides are a very frequent phenomenon in the three basin landscapes of the province. Our investigations have shown an average of 1.2 landslides per every 10 km², with the highest frequency in the south and the lowest frequency in the north of the province (Leopold 2012). Statistical comparisons also have illustrated that the average dimension of the movements in the Oberpullendorf basin and the eastern Styrian basin is only about 0.03 km². In these two basins landslides occur frequently, but only affect small areas.

Comparatively Large Scale Landslides in the Eisenstadt Basin

The Eisenstadt basin, however, shows a very different pattern of landslide dimensions. The basin stands out with a general low frequency of landslides, but with the occurrence of some comparatively large scale landslides. Their location



Fig. 2 Current deformation (red arrow) of the railroad tracks of the “Raaberbahn” caused by the activity of the complex landslide L1. Strong deformation of the drainage trench is also visible

and expansion is shown in Fig. 3. The movement L1 covers an area of 1.08 km² and L2 an area of 1.17 km², the average slope angle of 9° is the same for both landslides. They represent the largest known landslides with continuous active movements within the province. Each of them covers an area more than 30 times larger than the average landslide area in other parts of the province. L1 and L2 are surrounded by other comparatively large scale landslides (Fig. 3), but outside the pictured area in the Eisenstadt basin landslides are about the dimensions of the other basins.

Aside from most mapped movements in the region, where only very little is known about the movement history, at least some references could be traced for the complex movement L1. The railway company “Raaberbahn” has reported stability problems for decades where its railway tracks cross this movement area. According to unpublished reports of “Raaberbahn”, instability started some years after the construction of the tracks in the year 1876. Several measurements and reconstructions have been performed since then, but still until today, long-term stability of the tracks could not be achieved. Figure 2 shows the current situation and the on-going deformation of the railroad tracks.

The measurements performed by “Raaberbahn” included inclinometric surveys. This data together with our detailed geomorphological field mapping enabled us to draw geotechnical cross sections to understand movement mechanisms and to estimate the movement volume. Based on the classification of Hutchinson (1968) we believe that

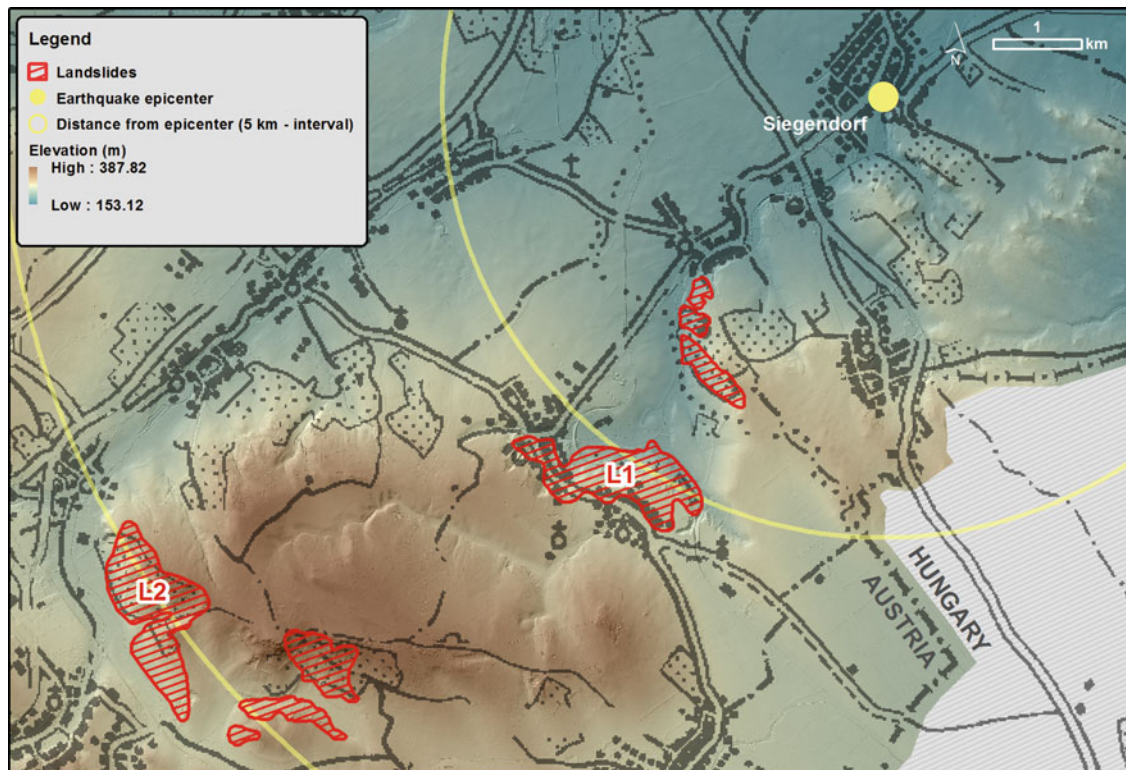


Fig. 3 Large scale landslides in the Eisenstadt basin and the 1888 earthquake epicentre including 5 km contour lines

the movement L1 is in the stage of progressive creep and is therefore also characterised by several secondary rotational slides. We estimate the volume of the movement L1 affected by progressive creep is more than 1 million m³ (Leopold 2012; Leopold et al. 2013).

Triggering Mechanisms of Landslides in Burgenland

Wieczorek (1996) and Highland and Bobrowsky (2008) defined five natural landslide triggers:

- Intense rainfall
- Rapid snowmelt
- Water-level change
- Volcanic eruption
- Earthquake shaking

Intense rainfall is the most important trigger of mass movements in all of the three basin landscapes. As described in the “Natural controls” sub-section, the AAP value is high enough to consider rainfall as an important trigger. Additionally Auer et al. (1996) point out, that the province is characterised by dry winters and wet summers, the predominant AAP percentage falls between May and August. Intense rainfall also occurs frequently over this period. During our

fieldwork, we could repeatedly map new appearances of slides after intense summer rainfalls.

Due to dry winters, a snow depth of more than 10 cm develops very rarely in the basin landscapes (Auer et al. 1996). This is why we excluded the possibility of rapid snowmelt as a trigger for these mass movements. Also water-level changes are not important, because mapped landslides are usually situated far away and at considerably higher elevation compared to the position of the discharge system. Volcanic triggers can also be excluded due to no reported volcanic activity in the greater surroundings.

Apart from intense rainfall, earthquake shaking could be considered as possible trigger mechanism for mass movements in the province. Thereby it is important to take the spatial distribution of recorded and reconstructed (historic) strong earthquakes into account. ZAMG (2013) published a catalogue of earthquakes in Austria with a Richter magnitude greater than 4 dating back to the year 1201. It shows that for the greater area of eastern Styrian basin and Oberpullendorf basin there are no records of strong earthquakes. But there are records of earthquakes with a magnitude of 4.6, two anno 1766 and one anno 1888 in the Eisenstadt basin. Therefore, earthquake shaking has to be considered as a possible trigger for mass movements in the Eisenstadt basin.

Discussion: Indicators for Earthquake-Induced Soil Slides

The reconstructed epicenter of the above mentioned 1888 earthquake event in the Eisenstadt basin is in the village of Siegendorf. The village is situated only 5 km and 10 km, respectively, away from the comparatively large scale landslides L1 and L2 described above. This spatial relationship is shown in Fig. 3. Given the earthquake magnitude and the distance from the mass movements to the epicenter, the work of Keefer (1984, 2002) supports the possibility that these mass movements are indeed within the range of earthquake triggered soil slides. According to the author, earthquakes with a magnitude of 4.6 can induce soil slides up to a distance from 8 to 10 km. In addition, large scale fault systems have been documented near the mass movements and the epicenter (Spahic et al. 2010) indicating at least former strong tectonic activity.

To emphasize our thesis of earthquake induced large scale landslide in the Eisenstadt basin, we would like to combine different indicators outlined in the sections above. Although the natural controls are overall comparable in the three basin landscapes, one would expect more frequent and larger scale landslides in the Styrian basin; this area is characterised by higher annual precipitation and also the terrain is significantly steeper. Usually these are important natural drivers to develop mass movements (Highland and Bobrowsky 2008). In fact, landslides appear to occur more frequently in the Styrian basin, but in relatively smaller dimensions. By far, the largest scale landslides (L1 and L2) are situated in the Eisenstadt basin where both precipitation and slope have the lowest mean values. As differences in anthropogenic controls can be excluded, we suggest different trigger mechanism as possible explanation for this phenomenon. Landslides in the Styrian Basin are only triggered by intense rainfall because other natural triggers obviously can be excluded, and there are no records of earthquakes in this area. Landslides in the Eisenstadt basin can additionally be triggered by reported earthquakes, as represented by the relation between L1, L2 and the reconstructed 1888 Siegendorf event.

Also the above mentioned records of the “Raaberbahn” are supporting our thesis, whereby instability of the railway tracks started some years after the construction in the year 1876. The 1888 earthquake event could have at least reactivated an older complex landslide in the position of L1 and developed large scale secondary slides affecting the tracks.

Conclusion

The most important limitation of the current study lies in the fact that the relationship between comparatively large scale landslides in the Eisenstadt basin and an earthquake strong enough to trigger these landslides cannot be clearly proven

at the present stage of the investigations. However, strong indicators for earthquake-induced soil slides in an alpine fringe area are presented in this study. The potentially affected landslides show a different pattern in dimension and volume compared to other landslides in the area without any possible relation to earthquakes.

Considerably more work needs to be done to further build our knowledge of these large active landslides to establish a verified relationship between landslides and earthquakes in this alpine fringe area. Until now, earthquakes have rarely been considered as a mass movement trigger in this area (Lenhardt 2007) and we want to stimulate this discussion.

Acknowledgments This study was co-funded by the provincial government of Burgenland.

References

- Auer I, Böhm R, Fürst E, Koch E, Lipa W, Mohni H, Potzmann R, Rudel E, Svabik O (1996) *Klimatographie und Klimaatlas von Burgenland*. Zentralanstalt für Meteorologie und Geodynamik, Wien, 293p
- Highland LM, Bobrowsky P (2008) *The landslide handbook—a guide to understanding landslides*. U.S. Geological Survey Circular 1325. Reston, Virginia. (ISBN 1-234-47126-4), 129p
- Hutchinson JN (1968) Mass movement. In: Fairbridge RW (ed) *Encyclopedia of geomorphology*. Reinhold, New York, pp 688–695
- Keefer DK (1984) Landslides caused by earthquakes. *Geol Soc Am Bull* 95:406–421
- Keefer DK (2002) Investigating landslides caused by earthquakes—a historical review. *Surv Geophys* 23:473–510
- Lenhardt W (2007) Earthquake-triggered landslides in Austria-Dobratsch revisited. *Jb Geol B-A* 147:193–199
- Leopold P (2012) *Kriechbewegungen in den neogenen Beckensedimenten des Burgenlandes: Verbreitung, Vergleich natürlicher Einflussfaktoren, Bewegungsmechanismen und Auslöser. (Creep in Neogene basin sediments in Burgenland: Distribution, comparison of natural parameters, movement mechanisms and triggers)*. PhD Thesis Universität Wien, 196p
- Leopold P, Draganits E, Heiss G, Kovács E (2013) A geotechnical explanation for the transition from creep to slides in the alpine foreland. In: Margottini C, Canuti P, Sassa K (eds) *Landslide science and practice, Vol 4. Global Environmental Change*. Springer (ISBN 978-3-642-31337-0). Pp 74–79
- Soeters R, van Westen C J (1996) *Slope Instability Recognition, Analysis, and Zonation. Landslides - Investigation and Mitigation*. Transportation Research Board Special Report, 247. Turner A K, Schuster R L (eds). National Academy Press, Washington D.C.. (ISBN 0-309-06208-X). pp.129-177
- Spahic D, Exner U, Behm M, Grasemann B, Haring A, Pretsch H (2010) Listric versus planar normal fault geometry: an example from the Eisenstadt-Sopron Basin (E Austria). *Int J Earth Sci*. doi:10.1007/s00531-010-0583-5, 11p
- Wieczorek G (1996) Landslide triggering mechanisms. In: Turner A K, Schuster R L (eds) *Landslides - investigation and mitigation*. Transportation Research Board Special Report, 247. National Academy Press, Washington DC. (ISBN 0-309-06208-X). pp.76–90
- ZAMG Zentralanstalt für Meteorologie und Geodynamik (2013) *Catalogue of strong earthquakes in Austria*. <http://www.zamg.ac.at/lexikon/index.php?ts=1319792341> Accessed 12.09.2013



Using Dendrochronological Analysis for Dating Earthquake-Triggered Landslides (By the Example of SE Altai, Russia)

Roman Nepop, Anna Agatova, Vladimir Myglan, Andrey Nazarov, and Valentin Barinov

Abstract

Paleoseismogeological investigations of the high mountain, seismically active southeastern part of the Russian Altai reveal a previously unknown complex of earthquake induced landslides. Using dendrochronological analysis of the wood penetrating injuries of trees (both dead and living ones) caused by seismically induced rockfalls allowed establishing the date of previously unknown strong medieval earthquake. This date was also confirmed by radiocarbon dating of seismically cut fossil soil overlapped by undistorted one. The specified recurrence interval of strong ($M > 7$) earthquakes for the SE Altai (about 400 years during the last 3,000 years) argues the high regional seismicity.

Keywords

Dendrochronology • Paleoseismology • Earthquake triggered landslides • Russian Altai • Late Holocene

Introduction

Paleoearthquake age estimation is one of the key paleoseismological problems. It is a crucial point of specifying the recurrence interval of strong earthquakes and seismic hazard evaluation. The period of instrumental seismological observations is insignificant in comparison with the recurrence interval of strong earthquakes. Thus to estimate this interval the historical data are being involved as well as age evaluations of recognized paleoearthquake induced surface disturbances (both ruptures and gravitational deformations).

With this purpose the radiocarbon method is one of the most exploitable absolute dating techniques. It allows determining the age of soils, tree fragments and other organic materials which were deformed and/or buried during the earthquake. The application of the radiocarbon method is limited by ~50 ka but some problems occurred while using this technique for dating recent (2–3 ka) seismic events due to high relative methodological error and presence of several “plateaus” at the calibration curve.

In case of spreading the forest vegetation in seismically active areas dendrochronological analysis can be used as an additional and/or alternative approach. It has a great potential due to utmost precision of dating. Rings of trees—witnesses of seismic events contain both the evidence for the earthquake and its age. They give the opportunity to date different events which cause the tree injuries and deaths as well as to define the time of forest recolonization on the bared surfaces.

This study presents the first experience of dating strong prehistoric earthquakes within southeastern part of the Russian Altai (SE Altai) on the basis of the dendrochronological analysis and brings new insight into this dating technique.

R. Nepop (✉) • A. Agatova
Institute of geology and mineralogy, Koptjug av. 3, Novosibirsk
630090, Russia
e-mail: agatr@mail.ru; agatr@mail.ru

V. Myglan • A. Nazarov • V. Barinov
Siberian Federal University, Svobodny av. 79, Krasnojarsk 660041,
Russia
e-mail: dend_ro@mail.ru; nelisgar@mail.ru; nelisgar@mail.ru

Study Site and Perspectives of Applying Dendrochronology for Timing Seismically Induced Landforms in the SE Altai

The Altai Mountains are the northern part of the Central Asia collision belt (Fig. 1). They stretch northwest more than 1,500 km across the borders of Mongolia, China, Kazakhstan and Russia, and form a wedge shape narrowest in the southeast and widest in the northwest. The elevation increases in the opposite direction from 400 m a.s.l. to 4,000 m a.s.l. The high-mountain southeastern part of the Russian Altai includes the Chuya and the Kurai intermountain depressions surrounded by ridges with altitudes about 3,500–4,200 m a.s.l.

The SE Altai is the northern extension of the Mongolian Altai, known for its high seismicity (Zhalkovskii and Muchnaya 1975), and is the most seismically active part of the Russian Altai. Almost the whole territory of the SE Altai is characterized by seismic intensity of eight point according to MSK scale. This is evidenced by the numerous large Holocene earthquake induced landslides and recently was supported by the 2003 Chuya earthquake ($M_S = 7.3$) (Agatova and Nepop 2011).

The dendrochronological analysis is a very promising tool and has a great potential for dating the seismically induced landforms here due to several reasons: (1) seismically induced slope processes intrude into the forest stand zone in an immediate vicinity with the modern upper timber limit (which is favorable for carrying out the dendrochronological analysis); (2) arid climate promotes good preservation of wood (up to two thousand years on stone surfaces); (3) a number of long absolute tree-ring chronologies, including the 2,367-years “Mongun” one (Myglan et al. 2012) has been developed for the SE Altai and adjusted Tuva region; (4) the strong Chuya earthquake ($M_S = 7.3$) that strike the SE Altai in 2003 gives the opportunity to analyze the distribution patterns of tree injuries caused by rock falls of specifically seismic origin.

Sampling Strategy and Dating Procedure

Initial Premises

Paleoseismological investigations revealed the repeated reactivation of the same focal zones within the SE Altai. Thus besides the estimating the germination ages of trees growing on the bare surfaces of seismically triggered landslides we have also tested the new approach of timing earthquakes which occurred already after forest regeneration. We suppose that for trees located near the scarps and talus fans (both dead and living ones) wood penetrating

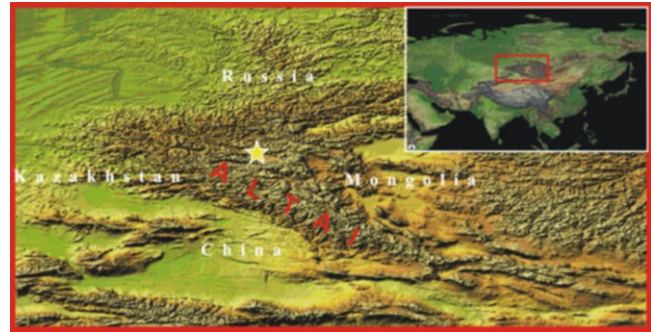


Fig. 1 Studied area. Star shows the location of the southeastern part of the Russian Altai

injures could be caused by earthquake induced rockfalls. It gives the opportunity to date such events within time limit exceeding the recurrence interval of strong earthquakes in the region. Obviously besides earthquake triggered rockfalls there are climatically driven ones. Thus as well as the number of wood penetrating injures, the simultaneity of such anomalies sustained by several trees grown on different earthquake induced landslides was taken as a criterion of their seismic origin. The accuracy of such an approach was supported by data obtained from analyzing injuries occurred on trees due to rock falls triggered by the 2003 Chuya earthquake.

Sampling

Detailed geomorphological investigations and process analyses were carried out using interpretation of aerial photographs, topographic maps (scale of 1:25,000), and field investigations including mapping of landforms and deposits of different genesis. Paleoseismogeological investigation was applied for basing the seismic origin of studied landslides. Samples were collected from trees (both living and dead ones) located on the surfaces of the talus fans and landslides near the scarps or most active talus channels. Cores and wedge shaped samples were taken from living trees and discs—from dead ones. In order to provide reliable dating additional discs were collected from the uninjured parts of tree trunks.

Dating Procedure

Dendrochronological analysis included tree ring width measurements with an accuracy of 0.01 mm using digital LINTAB positioning table coupled to a Zeiss stereomicroscope and TSAP system V3.5 software (Rinn 1996). Growth curves were cross-dated using the standard correlation parameters of TSAP system V3.5 and the

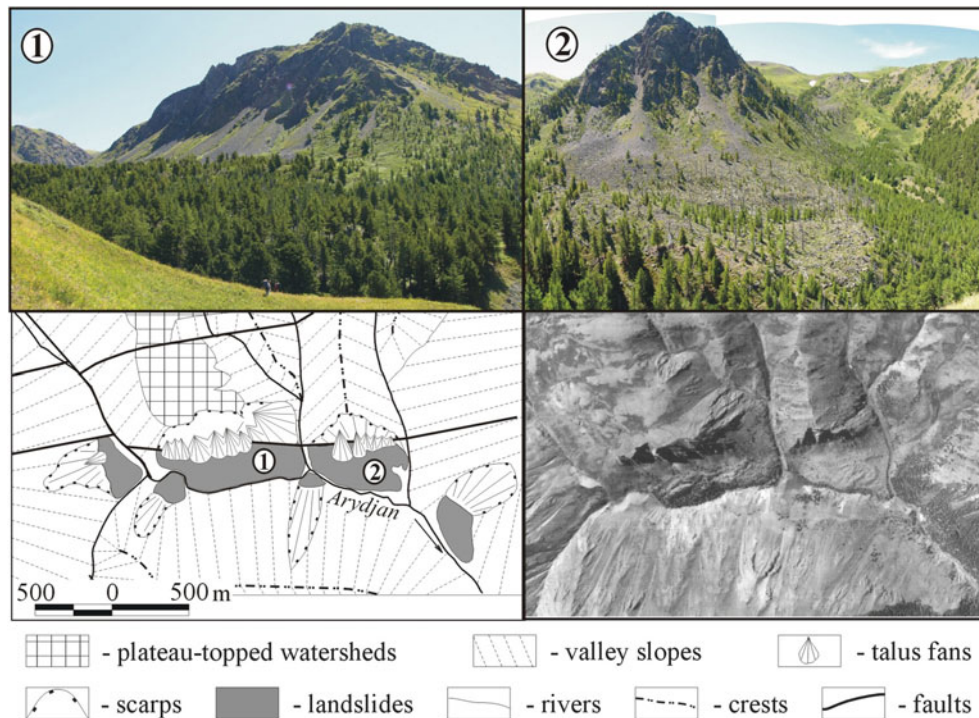


Fig. 2 The largest earthquake triggered landslides in the Arydjan valley (location is shown by star 1, Fig. 3)

dendrochronological software package DPL (Holmes 1983) with visual control of the radial growth curves. The standard procedure of building the tree ring chronologies (Shiyatov et al. 2000) on *Pinus Sibirica* Du Tour and *Larix Sibirica* Ledeb was applied for calendar dating. Anomalies (wood penetrating injuries) in the individual tree ring series were studied for identification and dating of earthquake triggered rock falls. The germination ages of trees growing on the bare surfaces of such landslides were also calculated. An age correction has been applied for the assessment of the colonization time gap and the time of surface stabilization.

Results

Estimating the Ages of Strong Prehistoric Earthquakes

Our paleoseismogeological investigations revealed a previously unknown complex of earthquake induced landslides in the Arydjan valley located at the northern part of the Chagan-Uzun massif (Fig. 2).

To provide the dendrochronological dating the local 1153-years (AD 856 till 2009) tree ring chronology on *Pinus sibirica* Du Tour was built. The year of birth of the eldest examined trees which colonized the surface of the talus fans covering landslide bodies is AD 1069 and 856 for landslides 1 and 2 respectively. From 120 traumatic injuries of tree rings, three and more coincide into the

years 1316, 1422, 1532 and 2003 (Fig. 3). At the same time numerous wood penetrating injuries dated by AD 1532 for trees grown at both landslides are displayed at various heights of tree trunks. This fact implies a high magnitude of a medieval seismic event or/and its nearby epicenter. Same patterns of wood penetrating injuries caused by rockfalls, triggered by the 2003 Chuya earthquake with its epicenter located on the southern border of the Chagan-Uzun massif, allow us to assert that a strong earthquake struck SE Altai in 1532.

In order to estimate the time of creation of earthquake triggered landslides in addition to the germination ages of trees growing on their surfaces, the colonization time gap (about 100 years) and the formation time of talus fans covered landslide bodies, as well as surface stabilization period, should be taken into consideration. Due to these reasons the applied age correction can reach two centuries or more. Thus, it could be asserted that by AD 600–700 the studied seismically triggered landslides in the Arydjan valley already existed (available data do not allow to distinguish the time of landslides formation).

Verifying Dendrochronological Data by Radiocarbon Dating

The previously unknown medieval earthquake is also confirmed by radiocarbon ages of seismically cut fossil soil overlapped by undistorted fossil soil on the southern border

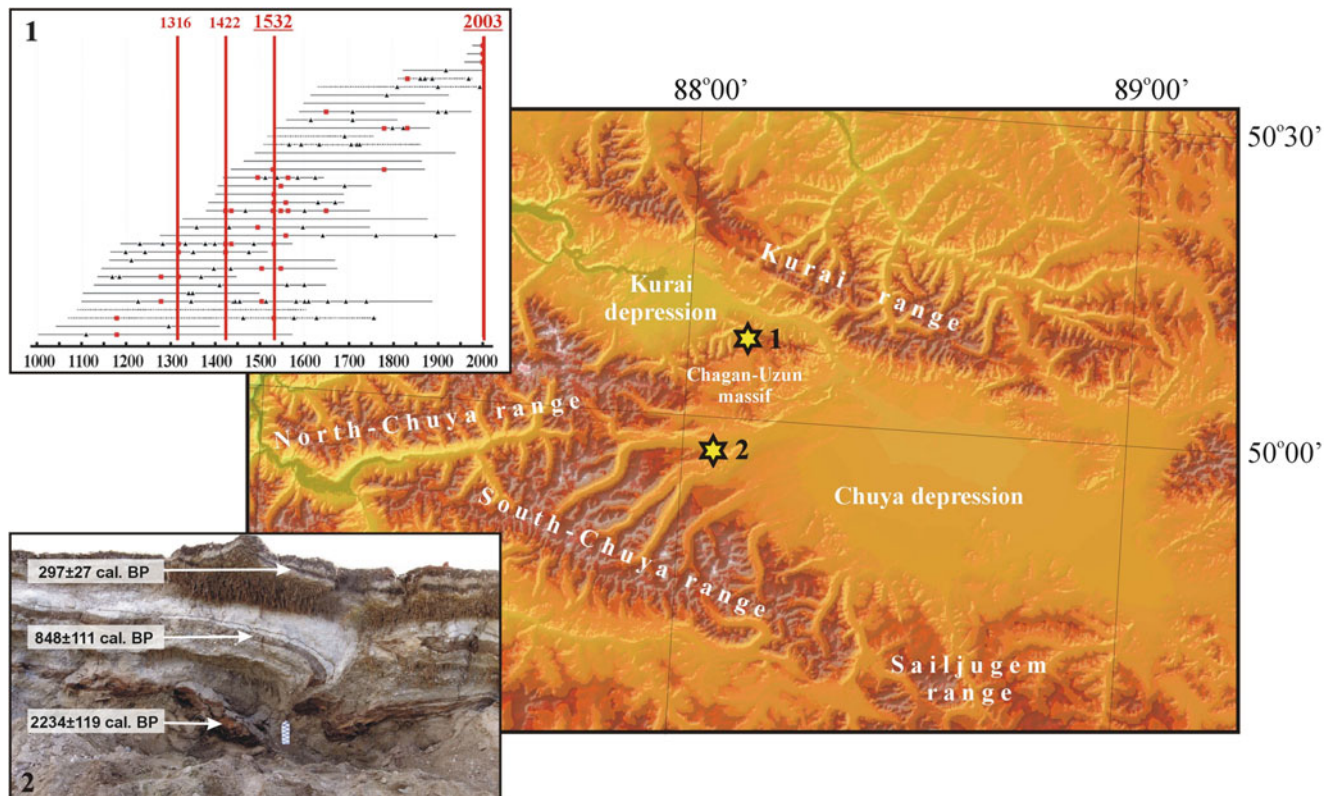


Fig. 3 Southeastern part of the Russian Altai, sampling sites and results of (1) dendrochronological and (2) radiocarbon dating which allowed to establish the date of previously unknown strong medieval earthquake

of the Chagan-Uzun massif. A section of lacustrine and colluvial sediments with the fossil soil layers covering ancient moraines were exhumed in one of the numerous ruptures within the giant landslide triggered by the 2003 Chuya earthquake in Taldura valley. The ages of two seismically deformed fossil soil layers are $2,234 \pm 119$ cal. years BP (IGAN 4090) and 848 ± 111 cal. years BP (IGAN 4105) and the age of undistorted fossil soil covering them is 297 ± 27 cal. years BP (SOAN 8659). Thus the dendrochronologically obtained date of the 1532 seismic event lies within the time range determined by radiocarbon ages of fossil soils.

Specifying the Recurrence Interval of Strong Earthquakes

The obtained data allow us to specify the recurrence interval of strong ($M > 7$) earthquakes for the SE Altai, which can be estimated now as about 400 years during the last 3 ka. Previously this value for the whole Holocene had been estimated as 1,000–3,000 years (Zhalkovskii and Muchnaya 1975) and was later reduced to 500–900 years as a result of extensive paleoseismological research and radiocarbon dating (Rogozhin et al. 2007). New data support the high

seismicity of SE Altai and allow defining the Chagan-Uzun massif as one of the major regional seismogenerating structures.

Conclusion

Dendrochronology has a great potential in paleoseismological investigations due to utmost precision of dating. Rings of trees—witnesses of seismic events contain both the evidence for the earthquake and its age. Analysis of traumas for trees grown on the surfaces of different landslides allows us to mark out tree-ring anomalies caused by specifically seismically triggered rock falls. Thus the date of strong medieval earthquake has been set up using dendrochronological analysis to a year. This date was verified by radiocarbon dating of seismically cut fossil soil overlapped by undistorted one. The ages of the oldest trees settled the bared landslides surfaces give the information about the minimal ages of these landforms. Specified recurrence interval of strong earthquakes ($M > 7$) argues for the high seismicity of the SE Altai.

Besides the obvious applied importance for local paleoseismological investigations the suggested approach can be used for timing landslides and strong paleoearthquakes for regions where instrumental seismic records or historical accounts are not available.

Acknowledgements We would like to thank L.A. Orlova (IGM SB RAS, Novosibirsk) and E.P. Zazovskaya (IG RAN, Moscow) for the radiocarbon dating. The study was partly funded by Russian Foundation for Basic Researches (grant 13-05-00555).

References

- Agatova AR, Nepop RK (2011) Assessing the rate of seismogravitational denudation of the relief of Southeastern Altai: the Chagan_Uzun R. Basin. *J Volcanol Seismol* 5(6):53–62
- Holmes RL (1983) Computer-assisted quality control in tree-ring dating and measurement. *Tree-ring Bull* 44:69–75
- Myglan VS, Ojdupaa O Ch, Vaganov EA (2012) Making the 2367-year tree-ring chronology for Altai-Sayan region (mountain massif Mongun-Taiga) [Postroenie 2367-letnej drevesno-kol'cevoj hronologii dlja Altae-Sajanskogo regiona (gornyj massiv Mongun-Taiga)]. *Archeology, ethnography and anthropology of Eurasia [Arheologija, etnografija b antropologija Evrazii]* 3: 76–83 (in Russian).
- Rinn F (1996) TSAP V3.5. Computer program for tree-ring analysis and presentation. Frank Rinn Distribution, Heidelberg
- Rogozhin EA, Ovsyuchenko AN, Marakhanov AV, Ushanova EA (2007) Tectonic setting and geological manifestations of the 2003 Altai earthquake. *Geotectonics* 41(2):87–104
- Shiyatov S G, Vaganov EA, Kirdjanov AV, Kruglov VB, Mazepa VS, Naurzbaev MM, Khantemirov RM (2000) Methods of dendrochronology. Part I. [Metody dendrohronologii. Chast'I]. Krasnojarsk University Press, Krasnojarsk (in Russian)
- Zhalkovskii ND, Muchnaya VI (1975) Energy distribution of earthquakes and seismic activity in the Altai-Sayan area [Raspredelenie zemletrjasenij po energii i seismicheskaja aktivnost' Altae-Sajanskoj oblasti]. In: Gaiskii VN (Ed) *Seismicity of the Altai-Sayan area [Seismichnost' Altae-Sajanskoj oblasti]*. Nauka Novosibirsk, pp. 5–15 (in Russian)



Environmental Effects of Shuanghe Giant Landslide in Jiuzhai, Sichuan, China

Yunsheng Wang, Xin Zhang, Xinze Li, and Shuo Mao

Abstract

The Jiuzhai county is located in the northwest of Sichuan Province, China with high seismic intensity. There were a series of huge landslide damming events in the geological history resulting in beautiful lake or a wide valley in the reservoir. Shuanghe landslide is one of such landslides. Understanding of the mechanism of this landslide is the key to the future similar slope stability in the region of the similar slope. Based on a geological survey at a large scale, borehole drilling and core sample dating, it reveals that the landslide is located in the right bank of Baishui River, its source region is characterized by the high slope with counter-tilt structure, and the regional maximum geo-stress is perpendicular to the flow direction of Baishui River. Since the middle of Pleistocene, the river has incised intensively, causing the intensive unloading and stress field adjustment. As obvious toppling deformation of the high slope, a huge rock landslide was triggered by a strong earthquake that occurred about 30,000 years ago. The landslide overlapped the second Terrace, the accumulation is composed of huge block with a volume estimated at 250 million m³. The barrier dam existed for a long time until it broke, leaving a wide valley in the front of the barrier dam. Though the main part of Shuanghe landslide is stable, the front part can suffer from the river lateral erosion in the toe of the landslide accumulation. The environmental benefit includes a wide valley in the ever-reservoir area, providing the people with a satisfied site for construction of a new township. As the lacustrine silt sediments lie beneath the new county town, the bearing capacity and sand liquefaction could exist. A road construction cutting in the narrow valley at the toe of the landslide may dam the river again which could threaten the new county town.

Keywords

Shuanghe landslide • Seismic landslide • Giant landslide • Environmental effects

Introduction

Seismic landslides are the main natural hazard in north-west of Sichuan. They change the geological environment of river valley (Casagli and Ermini 1999; Clague and

Evans 1994): the landslide dam serves to block river flow, store water behind the dam, and form a landslide lake. The lifespan of a landslide dam ranges from less than a day to several thousands of years (Costa and Schuster 1991; Dai et al. 2005). When the dam broke, the landslide lake disappeared and formed a wide valley basin, providing a natural site for settlement and cultivation. However, some Pleistocene landslides were not recorded in the human history. Therefore, in this paper, the seismic landslide identifiers are presented. They occurred in groups with large scale in the high intensity

Y. Wang (✉) • X. Zhang • X. Li • S. Mao
State Key Laboratory of Geohazard Prevention and Geoenvironment Protection, Chengdu University of Technology, Chengdu 610059, China
e-mail: wangys60@163.com

(Keefer 1984) and high geo-stress concentration area, linear distribution along the active faults (Papadopoulos and Plessa 2000). The accumulation area generally separated from the source region, and the latter is on the high slope where it is several hundred meters above the river bottom. There is a disturbance zone between the landslide accumulation and underlying beds. Instead of the slide zone of the slides induced by the storm, the composition is as same as that in the source area. The accumulation structure is characteristic of huge block with gravels and soil generally with particle-supported. It happened with high speed and generally dammed the river in transitory or long-lived. If it is long-lived, there is a wide valley in its upper stream and over-burden.

There are many seismic landslides in the Jiuzhai area, Shuanghe landslide is one among them. It formed a river basin on the Baishui River. Jiuzhaigou town is just located in the basin. The Jiuzhaigou town basin is 700–1,000 m wide and 8,000 m long, providing a nice site for the new county town. Based on the field survey, borehole core logging and time dating, it reveals there was strong seismic event in the late Pleistocene, which triggered Shuanghe giant landslide. The giant landslide dammed the Baishui River resulting in a large reservoir. Abundant sediments from the surrounding area filled the valley, and a wide valley section appeared after the dam break.

The Geological Setting

Jiuzhai region is in the north part of the Minshan lift, the famous scenery of Jiuzhaigou is in the area. The new Jiuzhaigou county town is 40 km downstream from the Jiuzhaigou spots. The topography is of the typical canyon area, with the elevation ranging from 1,300 to over 4,500 m above sea level and changing abruptly. The land area with slope gradients greater than 35° accounts for 55 % of the total land. The two regional faults are NW strike Qinling fault and Tazang (Maqin-Lueyang) fault (Hou et al. 2005). The stratigraphy in the block is the Zhuwo Formation of Triassic System, composed of the grey, light grey medium-thickly bedded marble intercalate with a little slate and metamorphic sandstone. It is an area with a high seismic intensity area coming from the adjacent strong earthquake zones including: Wudu, Songpan-Pingwu and Longmenshan. The distance between those the earthquake zones mentioned above is 25 km, 20 km and 170 km respectively. Ms 8.0 earthquake in 1879 had a strong influence, causing lots of avalanches in the Jiuzhai area. The seismic influence intensity is well above VIII (Fig. 1).

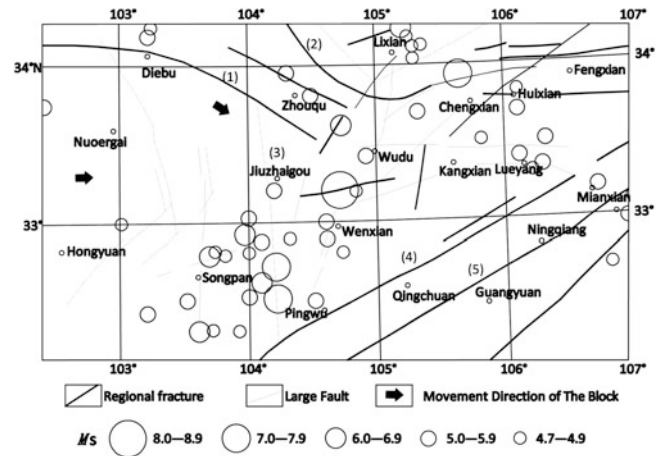


Fig. 1 The regional tectonic skeleton (modified from Hou et al. 2005). (1) Tazang fracture; (2) Qinling fracture; (3) Huya fracture; (4) Qingchuan-Pingwu fracture; (5) the central fracture (Yingxiu-Beichuan fracture)

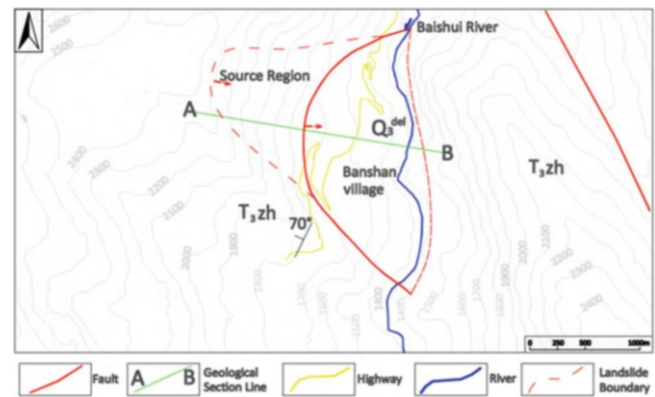


Fig. 2 The geological map of Shuanghe landslide

The Slope Structural Feature of the Landslide Region

The source area of Shuanghe landslide located in the upper part of the slope is 1,000 m above the bottom of Baishui River valley (Fig. 2). The slope is composed of the medium-thinly bedded metamorphic limestone, sandstone and slate, dipping the west, with dipping angle of $65\text{--}70^\circ$ (Fig. 3). As it is a counter-tilt slope with thinly-medium bedded structures, the toppling deformation is in the superficial part of the slope. The deformed strata dipping angles reduce to 10° and deform tensile cracks in the depth of slope about 60 m according to the trench excavation (Fig. 4). As the deformation developed, the crack run-through gradually came true, which provided a nice condition for the large scale failure to take place.

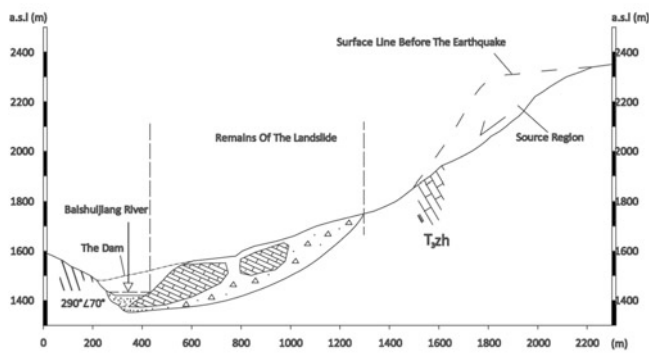


Fig. 3 The geological section of Shuanghe landslide

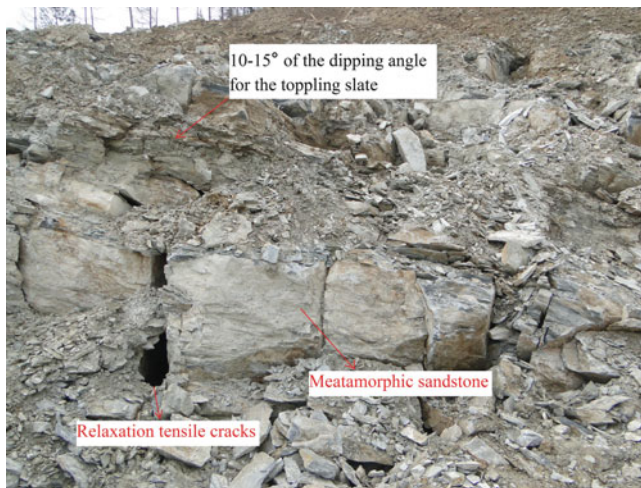


Fig. 4 The toppling of the rockmass in the source region

The bed rock in the lower part of the slope and the bottom of the river is composed of grey thin-medium bedded quartz slate. The strata occurrence is $315^\circ \angle 65-70^\circ$. There are two structural planes: (1) $EW/N \angle 65-75^\circ$, the length is 2–4 m, the distance between the adjacent structural planes larger than 1 m, that of the minority is 20–35 cm; (2) $N40-60^\circ E/SE (NW) \angle 70-80^\circ$, the length is 2–3 m, the distance between the adjacent structural planes is larger than 1 m, that of the minority 20–40 cm.

The Feature of the Landslide Accumulation

The Shuanghe landslide is located on the right bank, the upper reach of Baishui River. It is 3,000 m downstream from the New Jiuzhai county town.

The landslide accumulated in form of a hat-shape (Fig. 5), with a gentle slope in the upper part (slope gradient is $10-35^\circ$) and steep slope in the front part ($50-70^\circ$) (Fig. 2 and Fig. 5). The accumulation is 1,040 m long, 2,400 m wide. The elevation of the front toe is 1,351 m while the

elevation of the back margin is 1,750 m. The total volume of the landslide is about 250 million m^3 . The landslide occupies the river path, forming a bending deep valley in the river section. The narrowest width of the valley is only 46 m. Obvious drop water exists.

According to the borehole in the SZK21, 23, 24 and the adit on dam abutment, the Shuanghe landslide is the one with huge blocks (Fig. 3). The block is composed of the marble with a thickness of 100–160 m, a length of 500–800 m, and a width of 700–1,000 m. The dipping angle of the marble blocks is $40-50^\circ$, which is lower than that of the bed rock. The marble block is with cataclastic texture. The back margin is composed of the soil with block and detritus while the front toe overlaps on the fluvial gravel layer. There is no slip plane found in the accumulation instead a 5–50 m thick disturbed zone between the marble block and the fluvial gravel layer exists (Fig. 6). The layer is 2,500 m long along the river and 200 m wide. The disturbed zone is composed of mixture of fluvial sands, gravel, the block and detritus of marble and slate, without layered clay in the zone. The upper part of the accumulation is composed of the slate clastics and weathering soil. The lithology of the slip bed is quite different from that of the landslide accumulation.

The alluvial gravel thickness ranges from 30 to 50 m, it can be divided into three layers according to the composition, structure and origin from the bottom up:

- (1) Alluvial, fluvial gravels with boulder, pebble and sands, distributing in the lower part, with a thickness about 10–20 m, high density;
- (2) Colluvial, pluvial detritus with solitary stone, sands, distributing in the middle part, with a thickness ranging from 6 to 13 m;
- (3) Alluvial gravel with boulder, sands, distributing in the middle-upper part, with a thickness ranging from 5 to 50 m.

According to borehole No SZK21, 23, 24, there is an old river deep trough on the right bank. The elevation of the deep trough bedrock top beneath the overburden is 1,327.56–1,317.73 m a.s.l., which is much lower than the modern river bottom (1,339.31–1,339.80 m a.s.l.), the landslide is lay on the first layer of the overburden. The time dating of the sand in the layer (1) (electron spin resonance) is 3.64×10^4 years BP.

The Environmental Effects of Shuanghe Landslide

Shuanghe landslide formed in the late Pleistocene, effectively blocked the Baishui River. The dam is about 130 m high, forming a reservoir with a length of 8 km. As huge



Fig. 5 The whole topography of Shuanghe landslide

blocks exist in the landslide accumulation, the outburst did not happen immediately. The thick fine sand accumulation was formed at the bottom of the reservoir. As the filling of the accumulation, the reservoir has become a valley basin. The environment effects can be summed as follows:

- (1) The landslide changed the local topography. Prior the landsliding event, there was a large erosion platform in the source region, as the seismic landslide happened. The platform became narrower, giving rise to two-level platforms on the slope, in which the lower one is landslide platform. Due to the blocking, the original “V” type valley became “U” type one. There are six huge pluvial fans present on the two bank of the wide valley, which provide nice sites for the town and village construction.
- (2) The slope of the River profile was also changed. The general river gradient is 16 ‰, while the slope of the valley plain section (reservoir) is only 6–8.6 ‰. However, the river gradient on dam section is 25 ‰, conforming that the local base level has been uplifted as the formation of the barrier dam.
- (3) An overburden was formed, which may present a series of many potential engineering problems such as: sand liquefaction, uneven settlement and leakage. The ground water level is shallow. Silt and fine sand lens are well developed in the valley plain according to the civil exploration, revealing the hidden danger in the event of strong earthquake events in future.

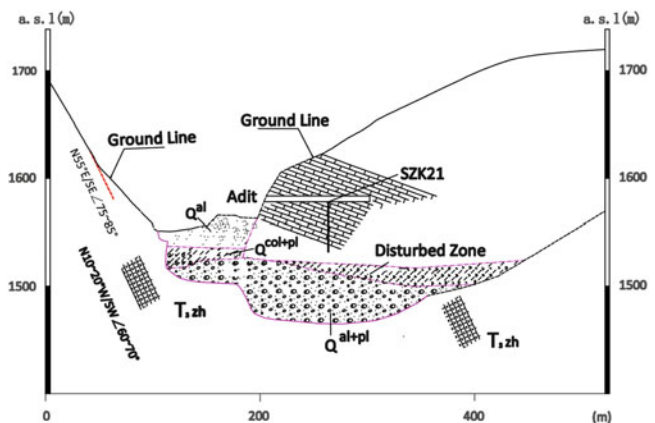


Fig. 6 The geological section of the front of Shuanghe landslide (modified from Jiang Guoyong)

Conclusion

Based on the field investigation and engineering exploration, several conclusions on the Shuanghe landslide are drawn as follows:

- (1) There are lots of historical seismic landslides in the Jiuzhai area where a high seismic intensity exists. The Shuanghe landslide is a typical one among the Jiuzhai seismic landslide group with the source region is located on the high slope.

- (2) The genetic mechanism of the landslide is that the toppling deformation in the superficial part of the high slope of counter-tilt slope with thinly-medium bedded structures, and then the strong earthquake waves under the topography amplification threw the deformed rockmass from the source region to the lower position of the slope.
- (3) The seismic landslide that happened in the late Pleistocene was so huge that dammed the Baishui River, forming a large reservoir.
- (4) There is not any clear slippery plane between the landslide accumulation and the underlying beds, but a disturbed layer does exist according to information suggested by the borehole core samples and excavation data during the construction of the hydropower station.
- (5) The landslide changed the local topography such as the changes on the right bank topography and the river slope gradient.
- (6) There are some potential engineering problems such as sand liquefaction, uneven settlement and leakage.

Acknowledgments This study is financially supported by the National Foundation for Natural Science of China (41072231) and the foundation of China Geological Survey (12120113009700). The authors would like to thank Mr. Jiang Guoyong for providing the borehole

and adit data and Prof. Li Yusheng for his helpful suggestions. We also particularly thank Prof. Wang Fawu and his students, Prof. Xu Yongxin for comments and suggestions to the manuscript.

References

- Casagli N, Ermini L (1999) Geomorphic analysis of landslide dams in the northern Apennine. *Trans Jpn Geomor Un* 20:219–249
- Clague JJ, Evans SG (1994) Formation and failure of natural dams in the Canadian Cordillera. *Geol Surv Can Bull* 464:1–35
- Costa JE, Schuster RL (1991) Documented historical landslide dams from around the world. U.S. Geological Survey Open-File Report 91-239, pp 1–486
- Dai FC, Lee CF, Deng JH, Tham LG (2005) The 1786 earthquake-triggered landslide dam and subsequent dam-break flood on the Dadu River, South-western China. *Geomorphology* 65:205–221
- Hou KM, Lei ZS, Wan FL (2005) Research on the 1879 Southern Wudu M8.0 Earthquake and its coseismic ruptures. *Earthquake Res China* 21(3):295–308 (in Chinese)
- Keefer DV (1984) Landslides caused by earthquakes. *Geol Soc Am Bull* 95(4):406–421
- Papadopoulos GA, Plessa A (2000) Magnitude-distance relations for earthquake-induced landslide in Greece. *Eng Geol* 58:377–386, Special Issue

Part IV

Rain-Induced Landslides



Introduction: Rain Induced Landslides

Binod Tiwari and José Cepeda

Abstract

With current global warming and climate change issues, numbers of rainfall induced landslides have been increasing. This session includes 9 papers that include landslide hazard analysis and monitoring programs, landslides case studies, and effects of landslides on natural slopes as well as mines. The session will discuss on how the numbers and risks of rainfall induced landslides can be reduced.

Keywords

Rainfall induced landslides • Landslide hazard mapping • Warning system • Slope stability • Risk analysis

Rainfall is considered as one among the major causes of landslides. With global warming and climate change, precipitation pattern has been changing in recent years. As a result, numbers of landslide disaster are increasing annually. On the other hand, researches pertinent to rainfall induced landslides and their mitigation have significantly been advanced in the recent years. The session C4: Rainfall Induced Landslides of the World Landslide Forum 3 (WLF3) focuses on the recent advancements pertinent to the research and design practices in the area of rainfall induced landslides.

Session C4 of the WLF3 invited papers from a wide range of topics covering the rainfall induced landslides, including, development and application of methods for susceptibility and hazard assessment, empirical and physically-based thresholds, early-warning systems, assessment and management in regions prone to precipitation-induced landslides, and the geographical extent of the approaches ranging from local (slope scale) to regional scales of the research. Among

more than 20 papers received in this session for possible publication and presentation, eight papers were accepted for publication in section C4, Volume 3 of the proceedings of the WLF3. These eight papers were reviewed and edited by the members of the International Editorial Board of the conference.

This section includes one paper, each, pertinent to the research finding in the area of stability of natural slopes, numerical modelling, and stability of mine deposits. Likewise, two papers, each, included in this section cover the research pertinent to prediction of landslides and catastrophic landslide disasters. Eight papers included in this section are co-authored by 28 researchers from all over the world including Italy, Korea, USA, Taiwan, Slovakia, Japan and Sri Lanka. Among the included papers, three, one, one, one, one, and one are the case studies from Italy, Korea, Taiwan, Slovakia, Nepal, and Sri Lanka, respectively. These papers discuss a wide spectrum of topics related to rainfall induced landslides.

B. Tiwari (✉)
Civil and Environmental Engineering Department, California State
University, Fullerton, 800 N State College Blvd., Fullerton, CA, USA

J. Cepeda
Norwegian Geotechnical Institute, Sognsveien 72, 0855 Oslo, Norway



Rainfall-Induced Landslides: Slope Stability Analysis Through Field Monitoring

Massimiliano Bordoni, Claudia Meisina, Davide Zizioli, Roberto Valentino, Marco Bittelli, and Silvia Chersich

Abstract

Rainfall-induced shallow landslides are hazardous phenomena that could cause several damages to infrastructures and people. To understand the hydrological and mechanical triggering conditions of shallow landslides in an area of Oltrepo Pavese (Northern Apennines, Italy) a field monitoring was conducted. In this work the results of 16 months monitoring are shown, focusing on the hydrological behaviour of the studied materials as function of rainfall and its effect on slope stability.

Keywords

Slope monitoring • Shallow landslides • Stability analysis

Introduction

Rainfall-induced shallow landslides can be defined as slope movements affecting superficial deposits of small thickness (generally lower than 2 m) triggered by very intense rainfall events. The failure surface is generally located along the interface between shallow soils and bedrock or between soil levels with different soil physical properties. Although shallow landslides generally involve small volumes of soil, due to their close proximity to urbanized areas, they cause significant damage to structures and infrastructure and, sometimes, human losses.

In the past, several methods were proposed to monitor slopes susceptible to shallow failures on unsaturated soils. More recent monitoring techniques allowed to focus not only on soil conditions during shallow landslides triggering, but also on unsaturated soils behaviour linked to meteorological and climatic conditions which could play primary roles to promote or inhibit the development of shallow failures. In particular, some authors focused on infiltration, on soil water redistribution determined by evapotranspiration and on redistribution towards underlying permeable bedrocks (Matsushi et al. 2006). Some other authors focused their research on time changes in soil hydrological features (Damiano and Olivares 2010; Smethurst et al. 2012) and on the increase of pore water pressures with possible development of perched water tables in soils that could promote shallow landsliding (Simoni et al. 2004).

This paper describes the results of a field experiment in the North-Eastern Oltrepo Pavese (Northern Apennines, Italy; Fig. 1), where several shallow landslide events occurred in the past. The objectives of the research are: i) to monitor the unsaturated zone response to seasonal and extreme rainfall events to determine how precipitation affects soil hydrological response; ii) to carry out a slope stability analysis by evaluating the factor of safety and its variation with time.

M. Bordoni (✉) • C. Meisina • D. Zizioli • S. Chersich
Department of Earth and Environmental Sciences, University of Pavia,
Pavia 27100, Italy

e-mail: massimiliano.bordoni01@universitadipavia.it; claudia.meisina@unipv.it; davide.zizioli@unipv.it; silviachersich@gmail.com

R. Valentino
Department of Civil, Environmental, Territorial Engineering and
Architecture, University of Parma, Parma 43124, Italy
e-mail: roberto.valentino@univr.it

M. Bittelli
Department of Agricultural Science, University of Bologna, Bologna
40100, Italy
e-mail: marco.bittelli@unibo.it

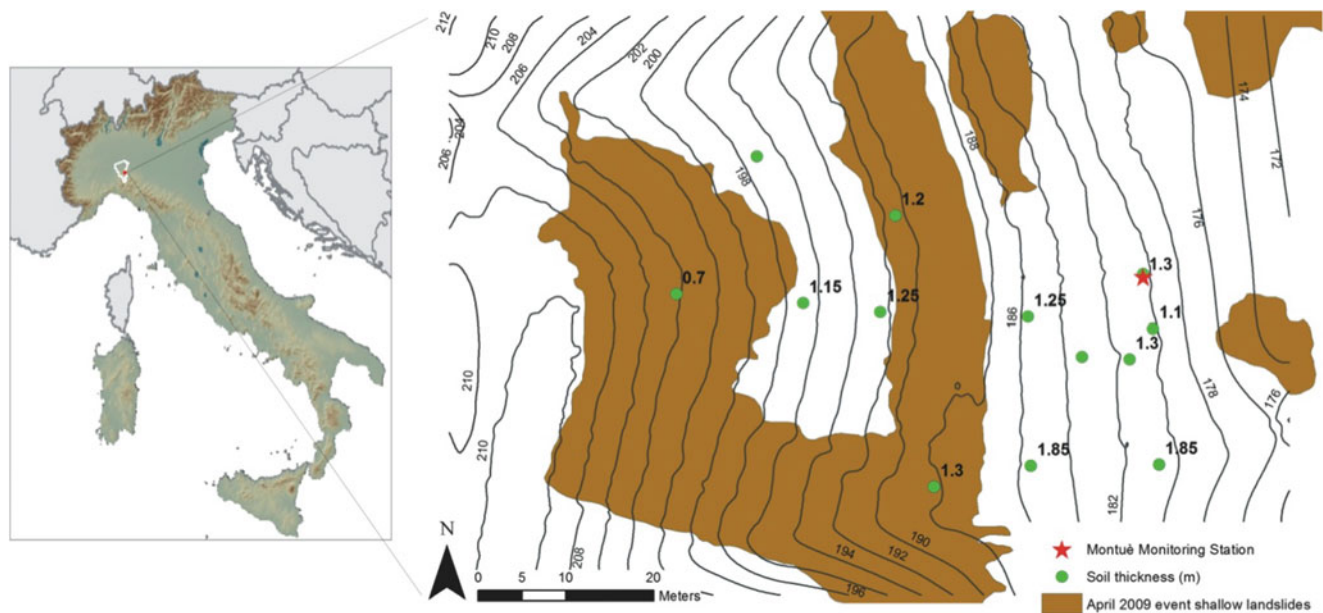


Fig. 1 Studied slope location with measured soil thickness and landslides distribution

Geological Settings and Landslide Distribution of the Test Slope

The study area is located on the northern termination of Pavese Apennines, near Montuè village, in the Canneto Pavese municipality. The test site slope is representative of other sites in Apennines subjected to shallow landslides (Fig. 1): it is characterized by medium-high topographic gradient (26°) and an E-W orientation. The monitoring station is located at 180.5 m a.s.l.

The bedrock is made of gravel, sand and poorly cemented conglomerates, with a low percentage of marls. Superficial soils derived by bedrock weathering and are prevalently clayey-sandy silts and clayey-silty sands with different amount of pebbles and carbonate concretions.

Soil thickness in different points of the test site area was determined through trench and manual pits around the position of the monitoring station (Zizioli et al. 2013). Soil thickness ranges between a few centimeters to 1.85 m, increasing from the top to the bottom of the slopes, also due to the presence of accumulation areas of previous shallow landslides.

In the test site area some shallow landslides (Fig. 1) were triggered on the 27th and 28th April 2009, due to an extreme rainfall event characterized by 160 mm of rain in 62 h (20 % of the annual average amount) with a maximum intensity of 22 mm h^{-1} (Zizioli et al. 2013).

These phenomena tended to be concentrated at the top of the test site slope and in correspondence of slope angle change, from gentle slope to steep slope (Fig. 1). Most of

failure surfaces are located along the contact between shallow soil and weathered bedrock at the depth ranging between 0.5 m and 1.0 m.

Monitoring Equipment

The integrated monitoring station (Fig. 2a) consists of a pluviometer (Model 52203, Young Comp.), a thermo-hygrometer (Model HMP155A, Campbell Sci. Inc.), a barometer (Model CS100, Campbell Sci. Inc.), an anemometer (Model WINDSONIC, Campbell Sci. Inc.) and a net radiometer (Model NR-LITE 2, Campbell Sci. Inc.). Six Time Domain Reflectometer (TDR) probes (Model CS610, Campbell Sci. Inc.) were installed at a depth of 0.2, 0.4, 0.6, 1, 1.2, 1.4 m, respectively, to measure water content in different soil horizons and in the weathered bedrock (Fig. 2).

A combination of field devices were used to measure matric potential. Three tensiometers (Model Jet-Fill 2725, Soilmoisture Equipment Corp.) and three Heat Dissipation (HD) sensors (Model HD229, Campbell Sci. Inc.) were installed at a depth of 0.2, 0.6, 1.2 m corresponding to different soil horizons (Fig. 2). In particular, HD sensors allow to measure only matric potential higher than 10 kPa (Bittelli et al. 2012). So, tensiometers are installed along with the HD sensors to measure matric potential range lower than 10 kPa.

The field data were collected by a CR1000X datalogger (Campbell Sci. Inc.) powered by a photovoltaic panel. In this work, field data acquired during the time span between 27/03/2012 and 23/07/2013 are analyzed.

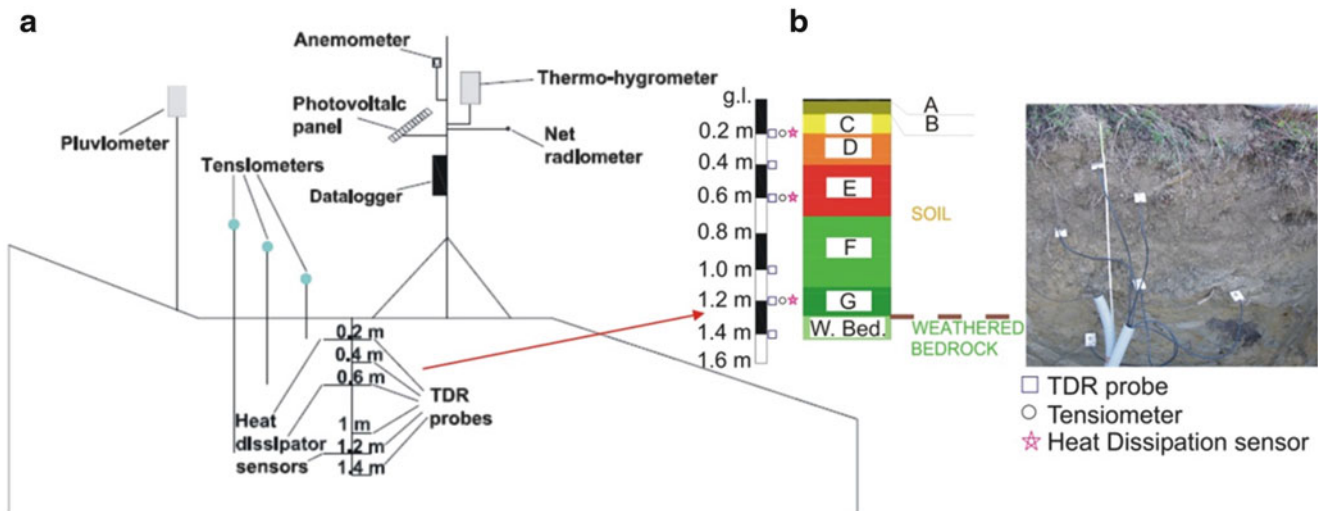


Fig. 2 Field monitoring station used in the test site slope: (a) scheme of soil horizons and weathered bedrock under the monitoring station with corresponding TDR probes, HD sensors and tensiometers (b)

Soil Properties of the Test Site Slope

A pedological description of the soil profile in the test site was performed in a test pit next to the monitoring station. According to the IUSS Working Group WRB (2007) the soil is a Calcic Gleysol. Seven main soil horizons were identified and labeled as indicated in Fig. 2. Weathered bedrock (indicated as W. Bed.) was identified at 1.3 m depth. Selected properties of the investigated soil horizons are shown in Tables 1 and 2.

The soil has low organic carbon content (O.C.) that decreases with depth, and a steady basic pH (Table 1).

Analysis with calcimeter show that carbonate content (Carb. C.) is much higher in the G horizon with values up to 35.29% (Table 1): for this reason it can be considered as a calcic horizon. X-Ray diffraction analysis on *tout-venant* obtained from different levels shows the prevalence of clay minerals (Clay M.) and carbonate minerals (Car. M.) in the shallow soil and the presence of feldspar (Feld. M.) and other minerals (Ot. M.) in the weathered bedrock (Table 1). Based on grain-size distribution, soil has a high silt content, which tends to grow along depth; instead, weathered bedrock has a high sand content (Table 2). According to USCS classification, soil horizons are prevalently lean clay (CL). Liquid limit (w_L) ranges from 38.46 to 41.85, while plasticity index (P_I) ranges from 14.25 to 17.18. Soil and weathered bedrock unit weight (γ) is about 16.70–18.60 kN m⁻³ (Table 2). Unit weight distribution along the vertical profile shows a prominent increase between 0.6–0.7 m from ground level.

Triaxial tests were performed to obtain shear strength parameters (Table 2). D, E and F horizons have friction

angle ϕ' between 31° and 33° without cohesion (c'). G is characterized by a friction angle of 26° and effective cohesion of 29 kPa.

Hydrological properties of C, E and G horizons were determined through laboratory reconstruction of Soil Water Characteristic Curves (SWCC), combining a WSM technique (Hyprop, UMS GmbH, Munich, Germany) with a VPM device (WP4T, Decagon Devices, Pullman, WA). The obtained data were fitted through Marquardt algorithm (1963) to obtain λ , n , θ_s and θ_r parameters of Van Genuchten (1980) equation, required to invert data of HD sensors through Flint et al. (2002) equation. The analyzed horizons had the same value of λ (0.01 k Pa⁻¹) and of θ_r (0.01 m³ m⁻³). C and E also had the same value of θ_s (0.42 m³ m⁻³) and n (1.40). However, G had lower θ_s (0.40 m³ m⁻³) and n (1.34) than shallower horizons.

Hydrological Parameters Dynamics in Relation with Rainfalls

Monitoring station data were used to determine the dynamics of water content and matric potential. Average hourly values of water content and matric potential were considered. Due to break of the tensiometer at 0.2 m depth since November 2012, matric potential in the range between 0 and 10 kPa at this depth was not measured till the end of the analyzed period.

Rainfall data showed a period with poor rainfall events since May 2012 till the last week of October 2012, in particular during summer 2012 (Fig. 3). A wetter period between the second half of October 2012 and May 2013 can be noticed. Main intense rainfall events were recorded

Table 1 Pedological and mineralogical features of the studied slope soil and weathered bedrock

Level	Ped. clas.	Rep. depth (m)	O. C. (%)	pH (H ₂ O)	Carb. C. (%)	Clay M. (%)	Carb. M. (%)	Feld. M. (%)	Ot. M. (%)
C	Ap2	0.2	2.29	8.30	14.12	43	21	21	17
D	2Apgk	0.4	2.34	8.30	15.68	45	19	21	15
E	2Bgk	0.6	1.76	8.60	14.11	43	22	17	18
F	2BCgk	1.0	1.51	8.60	16.08	44	21	16	19
G	3Cbgk	1.2	1.07	8.50	35.29	40	22	22	16
W.B.	W. Bed.	1.4	0.52	8.80	13.70	21	2.0	54	23

Table 2 Geotechnical and physical features of the studied slope soil and weathered bedrock

Level	Rep. depth (m)	Gravel (%)	Sand (%)	Silt (%)	Clay (%)	W _L (%)	P _I (%)	γ (kN m ⁻³)	φ' (°)	c' (kPa)
C	0.2	12.33	12.50	53.92	21.25	39.79	17.18	17.00	–	–
D	0.4	1.50	11.40	59.42	27.68	38.46	14.25	16.70	31	0
E	0.6	8.47	13.23	51.10	27.20	40.32	15.65	16.70	31	0
F	1.0	2.40	12.20	56.40	29.00	39.15	15.94	18.60	33	0
G	1.2	0.50	7.50	65.63	26.37	41.85	16.54	18.25	26	29
W.B.	1.4	0.20	75.00	24.80	0.00	–	–	18.06		

on 1st May 2012 (24.70 mm in 5 h 20 min), 31st August 2012 (17.00 mm in 1 h 30 min), 24–25th March 2013 (29.80 mm in 24 h 20 min) and 4–5th April 2013 (29.50 mm in 26 h). Figure 3b, c show the trends of water content and matric potential for the analyzed period. For different soil horizons, water content ranged between 0.15 and 0.45 m³ m⁻³, while matric potential ranged between 1.50 and 1,129.30 kPa for C and E horizons, while for the G horizon above the weathered bedrock matric potential ranged between 0.40 and 1,898.00 kPa. Water content in the weathered bedrock ranged between 0.17 and 0.35 m³ m⁻³ (Fig. 3a).

Water content and matric potential trends showed different hydrological behaviors in the soil horizons. The horizons up to 0.6 m from ground level depth had quick response towards rainfall in terms of increase in water content and decrease of matric potential during relatively drying periods. These horizons had likewise fast response passing from wetting to drying periods, that reflected in decrease of water content and increase in matric potential (Fig. 3a, b), due to evapotranspiration effects. In the same conditions, for deeper soil horizons, between 0.6 and 1.3 depth, and for weathered bedrock, hydrological parameters were not affected by single rainfall events or evapotranspiration. In fact, only longer rainy or dry periods provoked important changes in water content and matric potential at deeper levels (Fig. 3a, b).

During a prolonged rainy period from March to May 2013, similar values of water content (between 0.35 and 0.42) and matric potential (between 0.40 and 15 kPa) were measured for all different analyzed levels, but in G at 1.2 m near completely saturation conditions were kept for longer period than the above soil horizons (Fig. 3a, b). Weathered

bedrock at 1.4 m reached a water content lower than the shallow soil horizon (Fig. 3a). It is reliable that shallow soil and weathered bedrock are characterized by a very different hydraulic conductivity and then there is a sudden change in permeability at the interface between these two levels. Rain-water accumulates in the G horizon without infiltrating quickly in the weathered bedrock, so the G horizon is firstly saturated during prolonged rainy period with a significant decrease in matric potential.

Factor of Safety Trend with Time

A slope stability analysis has been carried out by evaluating the time trend of the safety factor. To this purpose a model that takes into account soil unsaturated conditions and their variation in time has been applied. The model proposed by Lu and Godt (2008) allows the computation of the safety factor of an infinite slope according to a limit equilibrium analysis. The equation to calculate the safety factor is given by:

$$F_s = \frac{\tan \varphi'}{\tan \beta} + \frac{2c'}{\gamma z \sin 2\beta} - \frac{\sigma^s}{\gamma z} (\tan \beta + \cot \beta) \tan \varphi' \quad (1)$$

where φ' is friction angle, c' is cohesion, β is slope angle, γ is unit weight of the soil, σ^s is the computed suction stress, z is the depth below the ground level. Suction stress groups the inter-particle physico-chemical forces and inter-particle capillary forces which counterbalance the shear stress in unsaturated soils (Lu and Likos 2006). When the soil approaches saturation, the suction stress is reduced, and this phenomenon is the triggering mechanism for landslides. Lu et al.

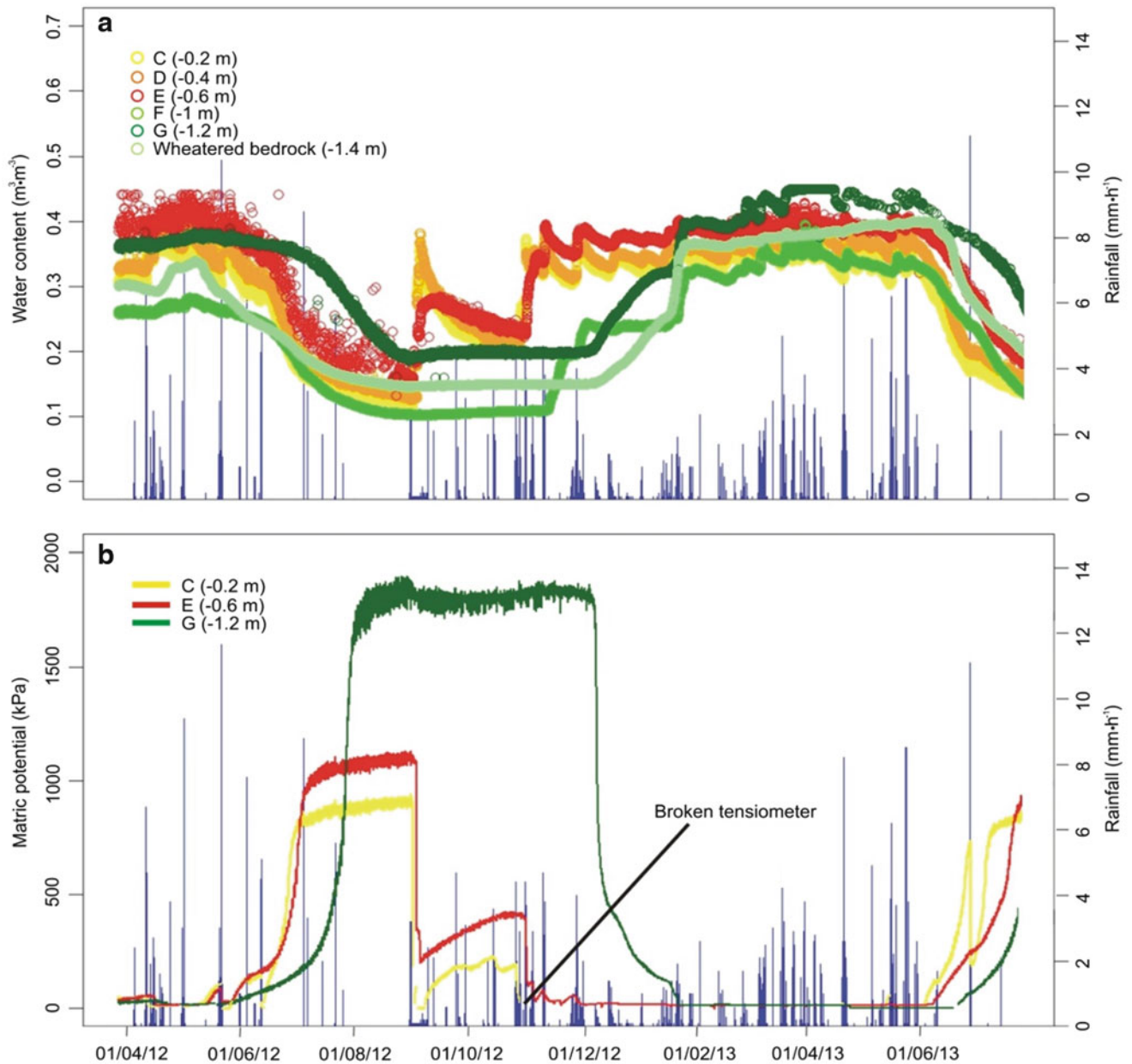


Fig. 3 Time-wise trend of field data at different depths with rainfalls: (a) water content; (b) matric potential

(2010) proposed to evaluate suction stress by using Van Genuchten's (1980) SWCC model:

$$\sigma^s = -\frac{Se}{\alpha} \left(Se^{n(1-n)^{-1}} - 1 \right)^{n-1} \quad (2)$$

where Se is the residual degree of saturation, computed as:

$$Se = \frac{\theta - \theta_r}{\theta_s - \theta_r} \quad (3)$$

By assuming input parameters as reported in Table 2 and the values of van Genuchten parameters found through

laboratory tests, the time-varying trend of F_s computed through Eq. (1) (Fig. 4) showed that the slope stability ($F_s > 1$) was maintained all over the considered time span both at 0.6 and 1.2 m from ground level: this stable condition was reached especially during the less rainy period due to the corresponding high values of suction stress.

For the E horizon, F_s quickly decreased in consequence of prolonged rainy conditions but also for intense and concentrated rainfalls (as on 24–25th March 2013, 29–30th March 2013 and 4–5th April 2013; Fig. 4), approaching conditions of potential instability (safety factor next to 1). Instead, this condition was generally kept steady only for

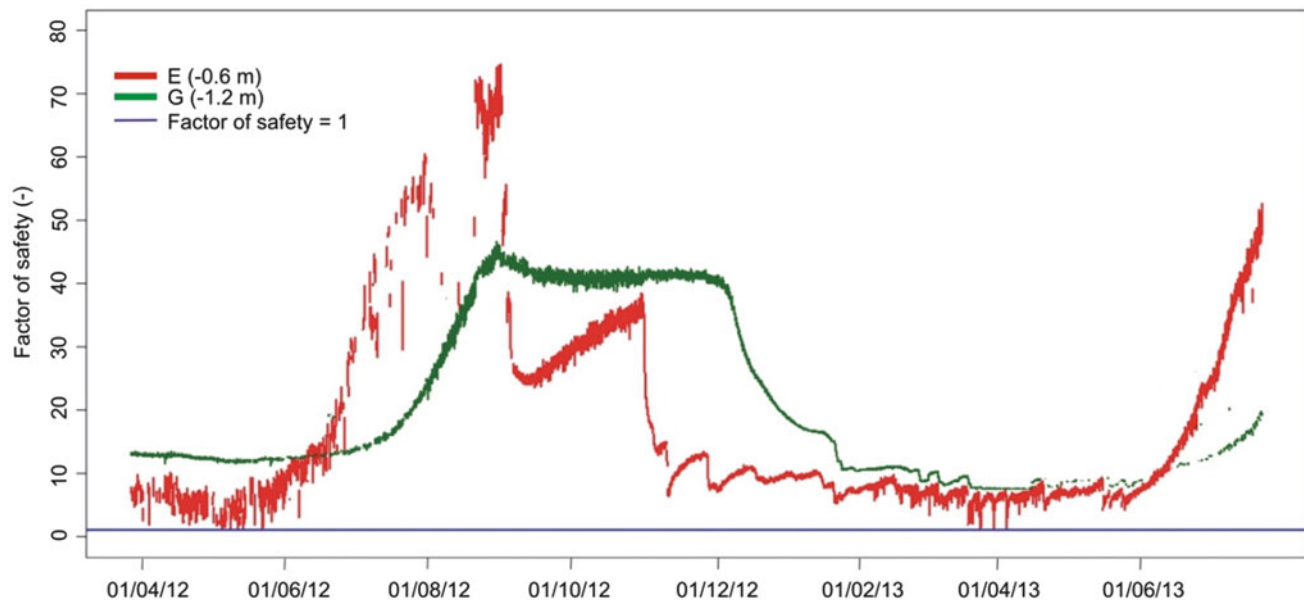


Fig. 4 Time-varying trend of the safety factor computed through Eq. (1) for E and G soil horizons

few hours, demonstrating that a more intense rainfall is necessary to get landslide triggering in most shallow soil horizons. In comparison to the G horizon, F_s had a trend similar to the matric potential of the same soil horizon (Fig. 4). For this horizon seasonal trends could be identified, and in particular a drastic decrease in winter 2013 and a further low decrease during the end of March 2013 (Fig. 4) can be observed. In this time span the amount of cumulative precipitation was of 357.30 mm in 126 days. F_s trend in the G seems not to be affected by single rainfall events, suggesting that the shallow landslide triggering in this soil level could be influenced by cumulative precipitation more than single rainfall events. Instead, the high values of effective cohesion (29 kPa) produced a positive effect on the slope stability: in fact, the estimated values of F_s for this horizon are always higher than 9.50.

Conclusions

Preliminary results concerning the first 16 months of monitoring highlight different hydrological behavior of the soil. The decrease in matric potential and the corresponding increase in water content are higher both after intense and concentrated rainfalls and after prolonged rainy periods for soil horizons to 0.6 m depth, while the deeper soil horizons and the weathered bedrock are affected only by prolonged rainy period. The soil profile G at 1.2 m depth seems acting as less permeable in which infiltrated rainwater accumulates provoking a saturation into the shallower levels.

The analysis of the safety factor trend with time showed that conditions of potential instability are favorable in the E horizon at 0.6 m depth after intense and concentrated rainfalls. This is in good agreement with the event occurred in April 2009, when shallow landslides included soils to a depth of about 0.5–1.0 m in slopes near the sample site. G horizon shows the safety factor much greater than 1 even for long rainy periods due to its high cohesion.

References

- Bittelli M, Valentino R, Salvatorelli F, Rossi Pisa P (2012) Monitoring soil-water and displacement conditions leading to landslide occurrence in partially saturated clays. *Geomorphology* 173–174:161–173
- Damiano E, Olivares L (2010) The role of infiltration processes in steep slope stability of pyroclastic granular soils: laboratory and numerical investigation. *Nat Hazards* 52:329–350
- Flint AL, Campbell GS, Ellett KM, Calissendorf C (2002) Calibration and temperature correction of heat dissipation matric potential sensors. *Soil Sci Soc Am J* 66:1439–1445
- IUSS Working Group WRB (2007) World reference for soil resources 2006, first update 2007. *World Soil Resources Reports* 103, FAO, Rome
- Lu N, Godt J (2008) Infinite slope stability under steady unsaturated seepage conditions. *Water Resour Res* 44:W11404. doi:10.1029/2008WR006976
- Lu N, Likos WJ (2006) Suction stress characteristic curve for unsaturated soil. *J Geotech Geoenviron Eng* 132(2):131–142
- Lu N, Godt J, Wu DT (2010) A closed-form equation for effective stress in unsaturated soil. *Water Resour Res* 46:W05515
- Marquardt DW (1963) An algorithm for least-squares estimation of non-linear parameters. *J Soc Indus Appl Math* 11:431–441
- Matsushi Y, Hattajji T, Matsukura Y (2006) Mechanisms of shallow landslides on soil-mantled hillslopes with permeable and

- impermeable bedrocks in the Boso Peninsula, Japan. *Geomorphology* 76:92–108
- Simoni A, Berti M, Generali M, Elmi C, Ghirotti M (2004) Preliminary result from pore pressure monitoring on an unstable clay slope. *Eng Geol* 73:117–128
- Smethurst JA, Clarke D, Powrie W (2012) Factors controlling the seasonal variation in soil water content and pore water pressures within a lightly vegetated clay slope. *Geotechnique* 62(5):429–446
- Van Genuchten MT (1980) A closed-form equation for predicting the hydraulic conductivity of unsaturated soils. *Soil Sci Soc Am J* 44:892–898
- Zizioli D, Meisina C, Valentino R, Montrasio L (2013) Comparison between different approaches to modeling shallow landslide susceptibility: a case history in Oltrepo Pavese, Northern Italy. *Nat Hazards Earth Syst Sci* 13:559–573



Performance of I–D Thresholds and FLAIR Model for Recent Landslide Events in Calabria Region (Southern Italy)

Davide Luciano De Luca, Pasquale Versace, and Giovanna Capparelli

Abstract

During the period 2008–2010 heavy and persistent rainfall events induced thousands of shallow landslides and hundreds of deep-seated landslides in Calabria Region (Southern Italy), with more than 2,000 crisis points and damages related to about 94 % of the municipalities. These events are comparable, or even worse, with those occurred in the 50's and in the early 70's. In this context, the performance of mathematical models, which are used for the Early Warning System of Calabria Region, is evaluated. In details, Intensity–Duration (I–D) thresholds for several temporal aggregations (hourly and multi daily) of rainfall heights and the hydrological model named FLAIR (Forecasting of Landslides Induced by Rainfall, Sirangelo and Versace 1996) are considered. Moreover, the use of a regional approach for these models was also tested, which is particularly useful when it is necessary to predict the triggering of landslide movements in vast areas where there are concerns not only about the reactivation of pre-existing movements, but also activation of new movements whose exact location is unforeseeable and for which there is no available past information. The obtained results highlight a good model performance, in particular for FLAIR, which can be considered as a general case of I–D rainfall thresholds (Capparelli et al. 2009) and it is characterized by a more flexibility, as it takes into account the real pattern of rainfall heights along the time, and not average values of temporal intensity.

Keywords

Landslides • Rainfall thresholds • Hydrological model • Early warning

Introduction

Modelling of rainfall-induced landslides, for early warning systems, is mostly carried out by using two groups of models (Cascini and Versace 1988): empirical (also named hydrological) and physically-based. The former (Campbell 1975; Caine 1980; Wilson and Wiczorek 1995) usually requires a reduced computational time, with respect to the latter (Baum

et al. 2010; Iverson 2000; Montgomery and Dietrich 1994; Simoni et al. 2007), as only historical data of landslides occurrences and rainfall heights for calibration and validation are used.

In this context, the most common type of empirical models adopted in technical literature is represented by Intensity–Duration (I–D) thresholds (Caine 1980; Guzzetti et al. 2007). As demonstrated in Capparelli et al. (2009), and herein briefly reported, a general framework for I–D schemes and Antecedent Precipitation approaches (D'Orsi et al. 1997; Gabet et al. 2004) is constituted by FLAIR model (Forecasting of Landslides Induced by Rainfalls, Sirangelo and Versace 1996), which takes into account the real pattern

D.L. De Luca (✉) • P. Versace • G. Capparelli
CAMllab Laboratory, University of Calabria, Ponte Pietro Bucci 41/b,
Rende (CS) 87036, Italy
e-mail: davide.deluca@unical.it; pasquale.versace@unical.it;
giovanna.capparelli@unical.it

of rainfall heights along the time, and not average values of temporal intensity.

In this paper a regional approach for FLaiR model, by using ROC methodology (Receiver Operating Characteristics, Fawcett 2006), is described. It was developed at Laboratory of Cartography and Hydrogeological Modelling (CAMIlab) of University of Calabria, and it constitutes a development and improvement of previous works (Versace et al. 2012; Capparelli and Versace 2013), with applications in other areas. The aim is to predict landslide trigger in vast areas, where there are concerns not only about the reactivation of the pre-existing movements, but also activation of new movements whose exact location is unforeseeable and for which there is no available past information.

Applications are related to the provinces of Catanzaro (CZ), Crotona (KR) and Vibo Valentia (VV), located in Calabria region (Southern Italy). These areas were affected by a lot of landslide events, induced by persistent and widespread rainfall phenomena, during the period 2008–2010.

The obtained results were compared with the output of rainfall threshold schemes, adopted in the Early Warning System of Calabria Region. The comparison highlights a significant improvement in the reconstruction of landslides occurrences by using the regional approach of FLaiR model.

Theoretical Background

I–D Thresholds

Intensity–duration (I–D) thresholds are the most adopted models for predicting landslide occurrences induced by rainfall. Since the work of Caine (1980), different I–D schemes were proposed, and Guzzetti et al. (2007) summarized the relationships proposed by 52 authors worldwide. The general form is:

$$I = aD^b \quad D \leq T \quad (1)$$

where I is the average rainfall intensity with a duration D , T is the maximum duration for which (1) is calibrated, and a and b are coefficients. Curves are usually represented in logarithmic scales. Different results may be obtained working with the same set of empirical data (Guzzetti et al. 2008). To overcome this limitation, Guzzetti et al. (2007) developed a methodology, based on a probabilistic approach, to define a threshold model (1).

Moreover, Cepeda et al. (2010) proposed an extension of (1), i.e.:

$$I = [\gamma_1 A_n^{\gamma_2}] D^b \quad (2)$$

where γ_1 and γ_2 are coefficients, A_n is the n -day antecedent precipitation, and the other symbols are defined as previously.

FLaiR Model

FLaiR model (Forecasting of Landslides Induced by Rainfalls) evaluates landslide trigger on the basis of a mobility function $Y(t)$, defined as a convolution between rainfall intensity $I(t)$ and a filter function $\psi(\cdot)$:

$$Y(t) = \int_0^t \psi(t - \tau) I(\tau) d\tau \quad (3)$$

where the filter $\psi(\cdot)$ can assume several mathematical forms (Capparelli and Versace 2011), among which we can consider:

gamma

$$\psi(t) = \frac{t^{\alpha-1} e^{-t/\beta}}{\beta^\alpha \Gamma(\alpha)} \quad t \geq 0, \alpha > 0, \beta > 0 \quad (4)$$

power

$$\psi(t) = mt^{-q} \quad 0 < t < T, m > 0, 0 < q < 1 \quad (5)$$

By using FLaiR model, a landslide event occurs when $Y(\cdot)$ exceeds a critical value Y_{cr} , which is evaluated during the model calibration. In the following subsections, calibration methodology and the proof concerning FLaiR as a general framework for I–D schemes are briefly reported.

FLaiR Calibration at Local Scale

For a given filter $\psi(\cdot)$, characterized by a parameter vector $\underline{\theta}$, it is possible to evaluate all the parameter values for which $Y(t, \underline{\theta})$ assume its k highest values in correspondence with the k known historical movements occurred at a single slope (“ranking” method, Iiritano et al. 1998). The ensemble of all these value sets for $\underline{\theta}$ identifies the admissible parametric region (Fig. 1), and for each set it is possible to define a lower limit function value f_L and an upper limit function

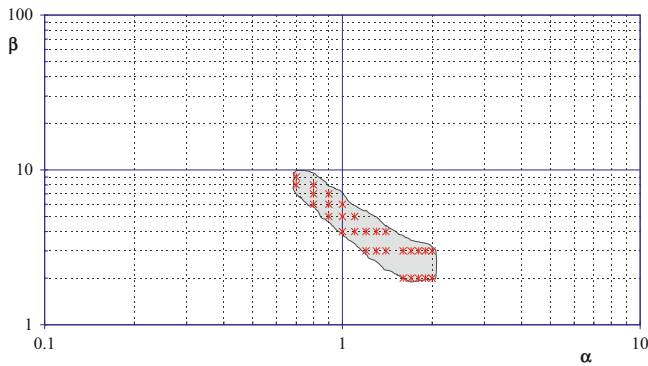


Fig. 1 Example of admissible parametric region for a gamma function (4)

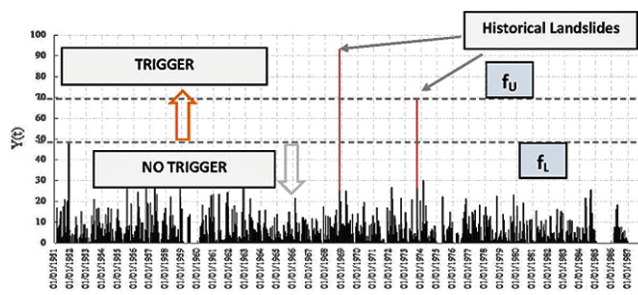


Fig. 2 Example of evaluation for $Y(t)$ and associated f_U and f_L

value f_U for $Y(t, \theta)$. These represent, respectively, the highest value which did not produce any movement and the lowest value for which movements occurred (Fig. 2). The optimal θ set is chosen such as the difference:

$$r = f_U - f_L \tag{6}$$

assumes its maximum value. This estimation allows for the largest possible gap between the mobility function $Y(\cdot)$ values related to a no movement situation and those related to a movement situation. The critical value Y_{cr} is usually set equal to f_U . It is possible to demonstrate that calibration with ranking method is equivalent to use ROC analysis (NGI report 2012), briefly illustrated in the following section related to the regional version of FLaiR model.

FLaiR as a General Framework for I–D Schemes

As already mentioned in the introduction part, FLaiR model constitutes a general framework for all the I–D schemes. In fact, if we consider into the integral of (3):

- a constant rainfall intensity function with (1);
- a power function (5) as a filter, and set $q = 1 - b$ and $m = b/T^b$,

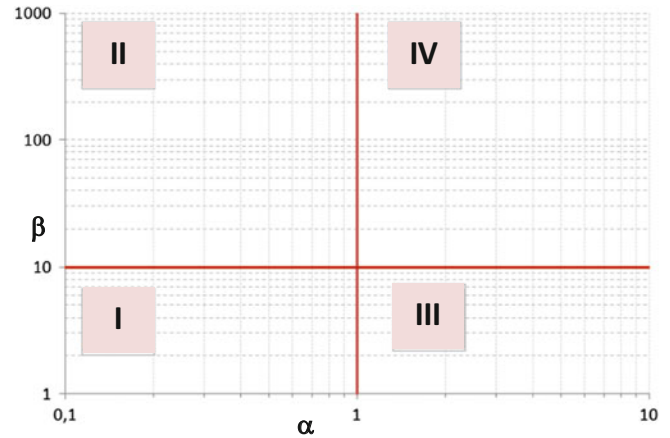


Fig. 3 Gamma function: subdivision of 2D Cartesian system $0\alpha\beta$ into four quadrants

it is easy to demonstrate (Capparelli et al. 2009) that the maximum value of mobility function is:

$$Y_{max} = \frac{a}{T^b} = Y_{cr} \tag{7}$$

and it does not depend on rainfall duration D but only on the parameters in (1) (see also Fig. 3 in Capparelli and Versace 2011). Thus, for each I–D scheme with (1), an unique Y_{cr} of FLaiR is associated, by adopting a power filter with (5).

Regional FLaiR Model

For a given study area, a unique mathematical form has to be selected as filter, and, consequently, the admissible parametric region, the optimal θ set and the correspondent Y_{cr} can be defined for each slope affected by historical landslides.

The next step concerns the organization into homogeneous groups. In this study, a gamma function (4) is considered as a filter, and four different quadrants can be identified on 2D Cartesian system $0\alpha\beta$ (Fig. 3). Each quadrant is associated to a distinct behaviour of gamma function. The boundaries of quadrants were fixed also on the basis of experimental data: $\alpha = 1$ distinguishes the monotonically decreasing functions from the non-monotonic ones, while $\beta = 10$ days separates filters with different process memory. In details, curve I characterizes landslides induced by intense rainfall events with a short duration, while curve IV is representative of movements triggered by prolonged periods of rainfall events.

Estimation of regional values for θ and Y_{cr} , for each characteristic curve of a filter, consists of the following steps:

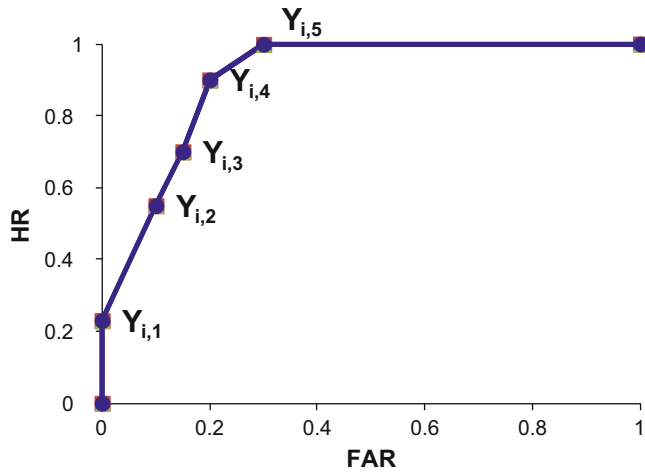


Fig. 4 Example of ROC space

1. Let n be the number of optimal, $\underline{\theta}$ sets inside a quadrant; each set is considered into the filter for FLaIR application (1), by using the time series of all the n correspondent rain gauges. Similarly to the K-mean method of Cluster Analysis (MacQueen 1967), the set comprising the mean values of each scalar parameter is also adopted, thus the total number of used sets is $n + 1$.
2. Let m be the number of historical landslide occurrences (clearly $m \geq n$ as a single rain gauge could be representative of several slopes, and, for a single slope, a number of landslides greater than one could be occurred along a single rainfall time series); the values of mobility function Y_{ij} ($i = 1, \dots, n + 1$ and $j = 1, \dots, m$) are calculated.
3. For each i -th parameter set ($i = 1, \dots, n + 1$) a ROC curve is plotted (Fawcett 2006), for which the Hit Ratio (HR) and False Alarm Ratio (FAR), defined as follows, are considered on vertical and horizontal axis, respectively, of the ROC space:

$$HR = \frac{CA}{CA + MA} \quad (8)$$

$$FAR = \frac{FA}{FA + TN} \quad (9)$$

where CA , MA , FA and TN are, respectively, the number of Correct Alarms, Missed Alarms, False Alarms and True Negatives. The range of both metrics is $[0; 1]$. Each point of a ROC curve is evaluated by considering a value Y_{ij} , determined in the previous step 2, as Y_{cr} (Fig. 4).

4. The i -th parameter set will be representative of the group if its AUC (Area Under ROC Curve) assumes the

maximum value among all the $n + 1$ computed AUC. The perfect condition is $AUC = 1$ (Fawcett 2006).

5. If the i -th parameter set presents the maximum AUC (step 4), then the regional value of Y_{cr} to be adopted will be the minimum value assumed by Y_{ij} .

Study Area Description

The provinces of Catanzaro (CZ), Crotona (KR) and Vibo Valentia (VV), located in Calabria region (Southern Italy), were selected as study area (Fig. 5).

The Early Warning System of Calabria region (Versace et al. 2012) adopted I–D schemes (1), with T set equal to 100 days and rainfall thresholds evaluated by using I–D–F curves (Intensity–Duration–Frequency) characterized by a Return Period R_p equal to 10 years. Moreover, a dimensionless index ξ_{ID} is used, defined as ratio between the rainfall intensity (observed in real time or forecasted) and threshold value, for different durations D . In details, three values, $\xi_1, \xi_{2,ID} = 0.4$, $\xi_{3,ID} = 0.6$, $\xi_{3,ID} = 0.8$ are assumed for comparison with ξ_{ID} evaluated in real time, which are associated to three different steps into an emergency plan of civil protection (e.g. advice, watch and warning, respectively).

In a similar way, the dimensionless index $\xi(t) = Y(t)/Y_{cr}$ is considered for FLaIR model (Capparelli and Tiranti 2010) with the following values: $\xi_1 = 0.4$, $\xi_2 = 0.6$, $\xi_3 = 0.85$.

The landslide database is composed by 268 records (138 for Catanzaro, 47 for Crotona and 83 for Vibo Valentia). Only rainfall-induced landslides and with an exact knowledge of occurrence date were considered, and for each one an associated rain gauge was selected, far at most 10 km from the correspondent slope.

The period until 2007 was chosen for calibration, while the period 2008–2010 was considered for validation. This latter temporal interval was characterized by a lot of landslides (shallow and deep-seated) occurred on the whole Calabria region; several damages affected the transportation system (highway, railway), buildings and two people died on A3 highway on 25 January 2009. Table 1 reports the number of historical landslides considered for both calibration and validation period, and for each province. Concerning validation, a comparison between regional FLaIR and I–D thresholds was carried out (see section “Results and discussion”); with this aim, only slopes with associated rain gauges characterized by at least 30 years of data were considered, in order to obtain a robust estimation of percentiles with $R_p = 10$ years.

Rainfall data includes time series of 64 rain gauges, provided by Multi Risks Center of Calabria region located in Catanzaro.

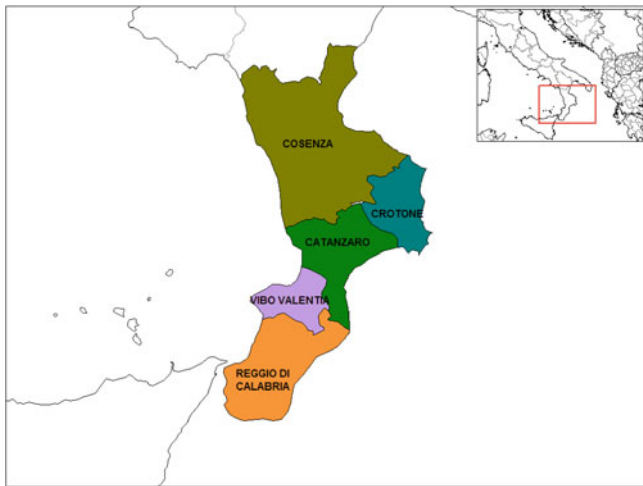


Fig. 5 Study area: provinces of Catanzaro, Crotona and Vibo Valentia

Table 1 Number of investigated landslides for each province in calibration and validation periods

Province	No. of investigated landslides	
	Calibration	Validation
Catanzaro	25	113
Crotone	15	32
Vibo Valentia	8	75

Table 2 Calibration results of regional FLaiR, by using gamma function as filter

Province	Curve	α (-)	β (days)	Y_{cr} (mm/day)
Catanzaro	I	0.3	1	119.5
	III	1.25	6	19.5
	IV	1.2	15	15.5
Crotone	I	0.8	5	41.7
	III	1.1	2	58.5
	IV	1.1	10	16
Vibo Valentia	I	0.1	1	141.7
	III	2.4	2.6	15.4
	IV	1	12	11.9

Results

Gamma function (4) was chosen as filter. For each province, the group correspondent to curve II (Fig. 3) presented no optimal set related to the calibration period, and thus only curves I, III and IV were defined (Table 2), by adopting the procedure previously described. As an example, characteristics curves for Catanzaro province are reported in Fig. 6.

For validation purpose, the comparison between I-D schemes and regional FLaiR was carried out by considering the metric HR (8) related to the percentages $\xi_{3,ID}$ and ξ_3 of

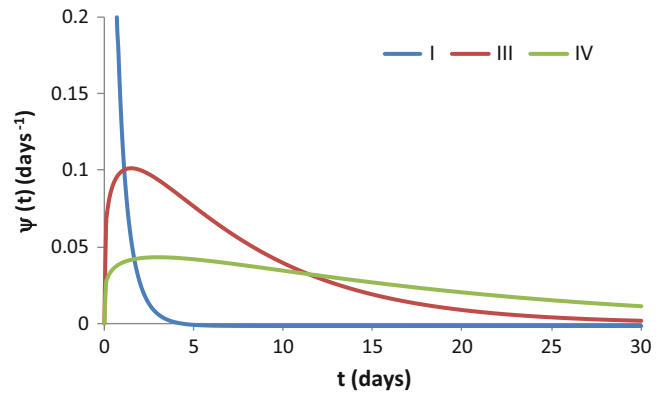


Fig. 6 Characteristics curve for Catanzaro province

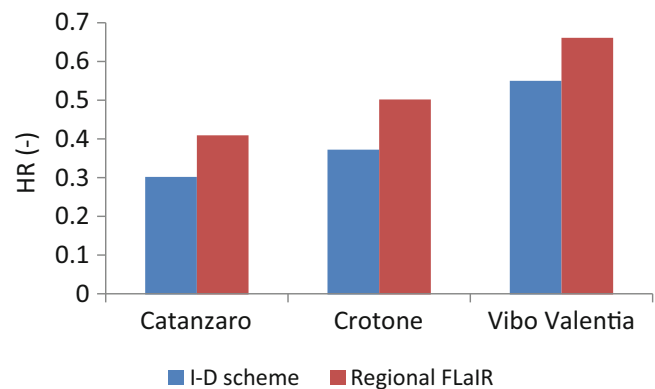


Fig. 7 Validation results: comparison of I-D scheme and regional FLaiR in terms of Hit Ratio (HR)

the critical thresholds. This choice is justified in order to test model performance in terms of activation of civil protection measures. In details, for regional FLaiR, a Correct Alarm was computed if at least one of the characteristic curves (I, III or IV) provided, during the convolution (3), an exceedance of thresholds corresponding to the historical occurrence. The obtained results indicated an improvement of occurrence forecasting with adoption of regional FLaiR. As also illustrated in Fig. 7, percentages of Correct Alarms increased from 30 % to 41 % for Catanzaro, from 37 % to 50 % for Crotone, and from 55 % to 67 % for Vibo Valentia.

Conclusions

The regional version of FLaiR provided acceptable results, as a significant improvement was obtained in modelling landslide occurrence with respect to the I-D relationships used in the Early Warning System of Calabria region. This aspect clearly allows to insert regional FLaiR into a forecasting system for vaste areas.

However, it should be highlighted that simplified hypotheses were adopted, related to uniqueness and

stationarity for Y_{cr} , due to the paucity of the available data (in terms of number on landslides) for calibration.

Better results could be obtained by modelling Y_{cr} as a variable along the time (with higher values during a dry season and smaller values during a wet period), thus adopting a scheme similar to D'Orsi et al. 1997 and Gabet et al. 2004, and by developing the regional approach for other mathematical expressions of the filter.

References

- Baum RL, Godt JW, Savage WZ (2010) Estimating the timing and location of shallow rainfall-induced landslides using a model for transient, unsaturated infiltration. *J Geophys Res* 115:1–26
- Caine N (1980) The rainfall intensity-duration control of shallow landslides and debris flows. *Geogr Ann* 62A(1–2):23–27
- Campbell RH (1975) Soil slips, debris flows and rainstorms in the Santa Monica Mountains and vicinity, Southern California. U.S. Geological Survey Professional Paper 851
- Capparelli G, Tiranti D (2010) Application of the MoniFLaIR as an early warning system for rainfall-induced landslides in Piedmont region (Italy). *Landslides* 7(4):401–410
- Capparelli G, Versace P (2011) FLAIR and SUSHI: two mathematical models for Early Warning Systems for rainfall induced landslides. *Landslides* 8:67–79
- Capparelli G, Versace P (2013) On verification of Forecasting Capability of the FLAIR regional model in Landslide Early Warning. In: Margottini C, Canuti P, Sassa K (eds) *Landslide science and practice*, vol 6. Springer, Heidelberg, pp 773–778
- Capparelli G, Biondi D, De Luca DL, Versace P (2009) Hydrological and complete models for landslides triggered by rainfalls. Proceedings of IWL—the first Italian workshop on landslides, rainfall-induced landslides: mechanisms, monitoring techniques and nowcasting models for early warning systems, Naples, 8–10 June 2009, vol 1, pp 162–173, Doppiavoce Edizioni, Napoli, ISBN: 978-88-89972-12-0
- Cascini L, Versace P (1988) Relationship between rainfall and landslide in a gneissic cover. In: Proceedings of the fifth international symposium on landslides, Lausanne, pp 565–570
- Cepeda J, Hoeg K, Nadim F (2010) Landslide-triggering rainfall thresholds: a conceptual framework. *Q J Eng Geol Hydrogeol* 43(1):69–84
- D'Orsi RN, D'Avila C, Ortigao JAR, Moraes L, Santos MD (1997) Rio-The Rio de Janeiro landslide watch. In: Proceedings of 2nd PSL Pan-Am symposium on landslides, Rio de Janeiro, vol 1, pp 21–30
- Fawcett T (2006) An introduction to ROC analysis. *Pattern Recogn Lett* 27(8):861–874
- Gabet EJ, Burbank DW, Putkonen JK, Pratt-Sitaula BA, Ojha T (2004) Rainfall thresholds for landsliding in the Himalayas of Nepal. *Geomorphology* 63:131–143
- Guzzetti F, Peruccacci S, Rossi M, Stark CP (2007) Rainfall thresholds for the initiation of landslides in central and southern Europe. *Meteorog Atmos Phys* 98:239–267
- Guzzetti F, Peruccacci S, Rossi M, Stark CP (2008) The rainfall intensity-duration control of shallow landslides and debris flows: an update. *Landslides* 5:3–17
- Iiritano G, Versace P, Sirangelo B (1998) Real-time estimation of hazard for landslides triggered by rainfall. *Environ Geol* 35(2–3):175–183. doi:10.1007/s002540050303
- Iverson RM (2000) Landslide triggering by rain infiltration. *Water Resour Res* 36:1897–1910
- MacQueen JB (1967) Some methods for classification and analysis of multivariate observations. In: Proceedings of 5th Berkeley symposium on mathematical statistics and probability, vol 1, University of California Press, Berkeley, pp 281–297
- Montgomery DR, Dietrich WE (1994) A physically based model topographic control on shallow landsliding. *Water Resour Res* 30:1153–1171
- NGI report (2012) Statistical and empirical models for prediction of precipitation-induced landslides. Safeland Project—Deliverable D1.5
- Simoni S, Zanoti F, Bertoldi G, Rigon R (2007) Modelling the probability of occurrence of Avallo landslides and channelized debris flow using GEOTop_FS. *Hydrological processes*. Wiley InterScience
- Sirangelo B, Versace P (1996) A real time forecasting model for landslides triggered by rainfall. *Meccanica* 31(1):73–85
- Versace P, Arcuri S, Biondi D, Capparelli G, Cruscomagno F, De Luca DL, Leone S, Maletta D, Niccoli R (2012). Sistemi di allertamento e difesa del suolo in Calabria (Early warning systems and soil conservation in Calabria, in Italian). In: Proceedings of XXXIII Italian national conference on hydraulics and hydraulic engineering, Brescia, Italy, 10–15 September 2012
- Wilson RC, Wiczorek GF (1995) Rainfall thresholds for the initiation of debris flow at La Honda, California. *Environ Eng Geosci* 1(1):11–27



Failure and Post-failure Characteristics of Mine Deposits in Korea

Sueng Won Jeong, Sung-Sik Park, and Hiroshi Fukuoka

Abstract

A series of ring shear tests were performed on waste rock materials collected from mine deposits in the mountainous region of Korea. The collected samples were classified as gravelly sand soils. After the samples were fully saturated, they were subjected to a normal stresses of 50–100 kPa for 300 s. The test program includes: a measurement of (1) shear stress for a given shearing speed, (2) shear stress as a function of normal stress and (3) strength behavior as a function of shear speed, which varied from 0.01–100 mm/s. A comparison was also made between clayey, sandy and waste rock materials. For the given materials, strain softening behavior was observed regardless of the drainage condition and shearing speed. From the grain size distribution results, we found that the larger grain sizes in the matrix, corresponded to greater fragmentation during shearing. At a relatively high shear speed condition, such as rapid mass movements, the grain crushing effect is more significant.

Keywords

Ring shear test • Mine deposits • Shear stress • Post-failure • Grain crushing

Introduction

To examine failure and post-failure characteristics of the mass movement of a sloped surface material, we need both drained and undrained shear strength characteristics of the soil. These characteristics can be determined using the ring shear apparatus, which allows soil saturation, consolidation,

drainage and shearing at controlled speed. At a relatively low shearing speed, the shearing characteristics in the pre-failure stage can be reproduced, and at a relatively high shearing speed, the failure and post-failure characteristics can be examined. In addition, a strength parameter, such as the residual shear strength, related to the post-failure stage can be used to simulate debris flow.

A series of ring shear tests on waste rock materials collected from mine deposits in the mountainous region of Korea were performed. All tests were performed under full saturation. Thus, normal stress, drainage and shearing speed are the main controlling factors of slope stability. Based on the test results, we will discuss the shear strength characteristics of the mine deposits based on the ring shear test and the effect of grain crushing on ring shear tests. Lastly, the correlation between grain crushing and sediment entrainments will be emphasized.

S.W. Jeong (✉)

Korea Institute of Geoscience and Mineral Resources, 124, Gwahangno, Yuseong-gu, Daejeon 305-350, Republic of Korea
e-mail: swjeong@kigam.re.kr

S.-S. Park

Department of Civil Engineering, Kyungpook National University, Daegu, Republic of Korea
e-mail: sungpark@knu.ac.kr

H. Fukuoka

Research Centre on Landslides, Disaster Prevention Research Institute, Kyoto University, Gokasho, Uji, Kyoto 611-0011, Japan
e-mail: fukuoka@scl.kyoto-u.ac.jp

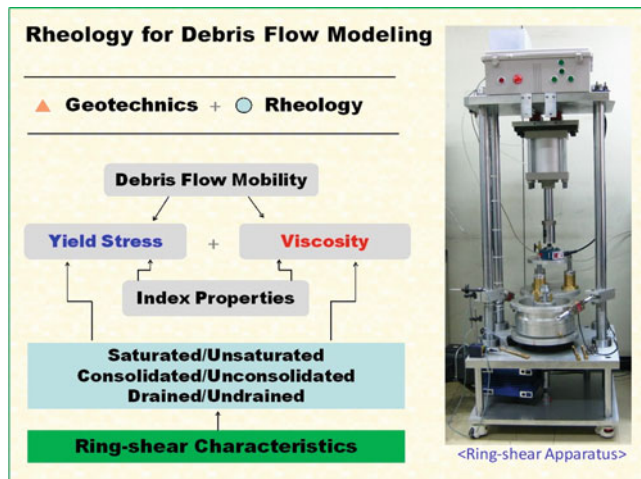


Fig. 1 Ring shear apparatus and rheology for debris flow modelling

Ring Shear Tests

Ring Shear Apparatus

Ring shear tests are often used to measure shear strength of soil and estimate slope stability at the failure and post-failure stage. They are also used for examining the shear behavior of landslide movement along the sliding zone (Sassa 2000; Sassa et al. 2003, 2004; Wang et al. 2002). The ring shear apparatus (Fig. 1) was developed at the Korea Institute of Geoscience and Mineral Resources (KIGAM) in 2011 with the help of the Disaster Prevention Research Institute (DPRI), Kyoto University (Jeong et al. 2011) and was based on the DPRI ver 7 (Fukuoka et al. 2007).

A description of the sample preparation and the test program can be found in Wang et al. (2002) and Sassa et al. (2004). Before testing, the samples were placed in the shear box. The samples were first consolidated by applying a normal stress, and then the samples were sheared by keeping the upper ring fixed while rotating the lower ring. In this study, we performed ring shear tests under drained and undrained conditions at various shearing speeds ranging from 0.01 to 100 mm/s. Figure 1 shows the shearing characteristics of soil obtained with the ring shear test for a given shearing speed.

Determination of Yield Stress and Viscosity

The geotechnical and rheological properties of the soil (i.e., yield stress and viscosity) are required to analyze the mobilization of debris flow. The values can be determined using the ring shear apparatus. Figure 1 shows the determination of

yield stress and viscosity using the ring shear apparatus. Given the saturation, consolidation and drainage condition, the torques (i.e., shear stress) can be measured. For each shear speed, the peak and residual shear stresses were measured. In general, shear stress increases with increasing shearing speed. Therefore, we can obtain a linear regression while plotting shear stress versus shearing speed. In this plot, the y-intercept and slope after yielding represent the yield strength and viscosity, respectively.

Results and Discussion

Ring Shear Characteristics

Figure 2 shows the test results on the waste rock materials taken from the mine deposits in Korea. The materials were classified as gravelly sandy soils. The shear stress obtained with time was examined for different drainage conditions and shear speeds (i.e., drained and undrained conditions at $V = 0.01$ and 100 mm/s). The shearing time for the materials was 300–1,000 s. The preliminary tests were performed at $V = 0.01$ mm/s. The materials exhibit a strain-softening behavior, regardless of the drainage and shearing speed condition. From this finding, it can be concluded that a higher shearing speed corresponded to a higher shear stress (Figs. 1 and 2). At a relatively low shearing speed (i.e., $V = 0.1$ –1 mm/s), the undrained shear stress is greater than the drained shear stress.

Shear Stress as a Function of Shearing Speed

According to previous studies, shear stress is a function of Atterberg limits, particle size distribution, particle shape and shearing speed (Fukuoka and Sassa 1991; Wang et al. 2010; Li et al. 2013). Among these influencing factors, the dependency of shearing speed on shear stress was emphasized in this study. The waste rock materials were subjected to different shearing speeds (i.e., $V = 0.1, 1, 10$ and 100 s) under drained and undrained conditions. Figure 3 shows the relationship between shear stress and shearing speed, both axes plotted in the logarithmic scale. For a given shearing speed, the undrained shear stress is generally greater than the drained shear stress. The difference in shear stress is significant at a low shearing speed (i.e., $V = 0.1$ –1 s). However, with increasing shearing speed, the difference between undrained and drained shear stress is smaller (this may be due to the grain crushing effect). The large difference is approximately 15 kPa at $V = 0.1$ mm/s. After $V = 1$ mm/s, the variation is much more significant.

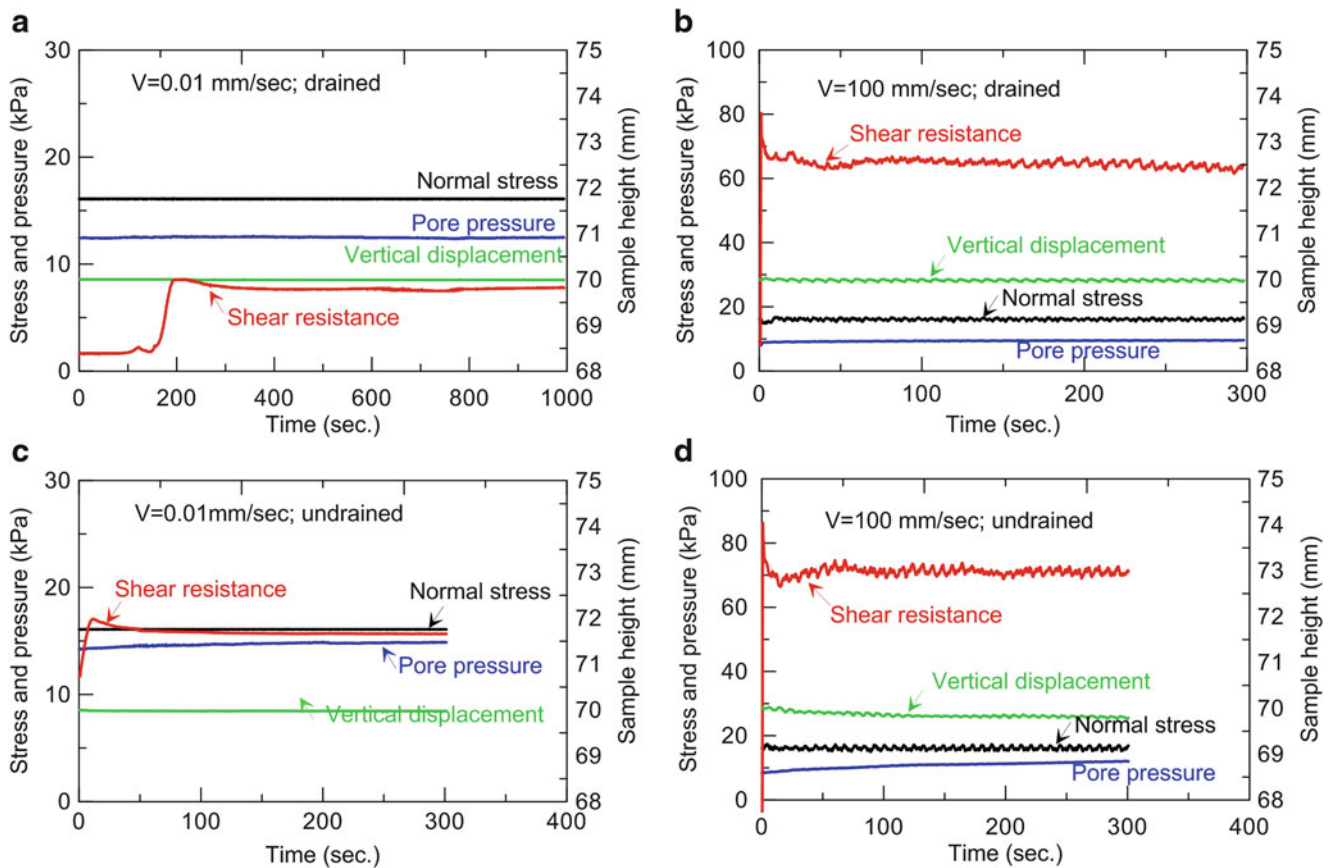


Fig. 2 Shearing characteristics of mine deposits obtained with the ring shear test: (a and b) drained condition and (c and d) undrained condition for a given shear speed ($V = 0.01\text{--}100$ mm/s)

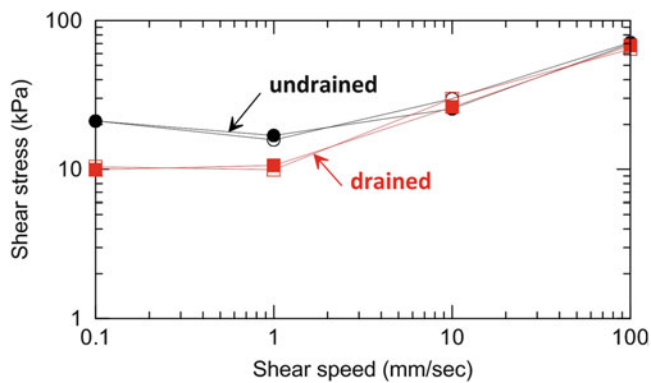


Fig. 3 Shear stress as a function of shearing speed. Shear stresses were determined in peak and residual shear stress levels

Grain Crushing and Post-failure Characteristics

Debris flow mobilization is dependent on several factors. One of the most important factors is the variation in pore water pressure. Grain crushing of granular soils plays an important role in the generation of excess pore pressure (Fukuoka et al. 2006; Okada et al. 2004; Wang and Sassa 2000, 2002; Wafid et al. 2004). The effect of grain crushing

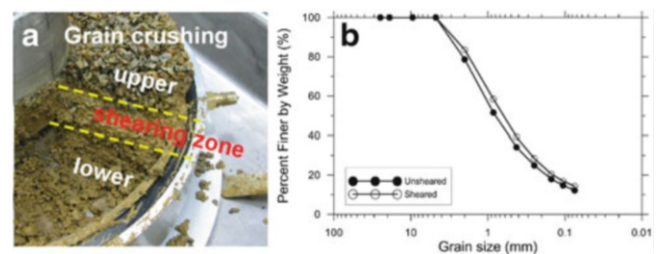


Fig. 4 Grain crushing characteristics (a) observation for shear zone, (b) grain size distribution analysis of samples from the sheared and unsheared zone

depends on stress level, grain resistance and time (Feda 2002). Grain crushing susceptibility can be obtained using a drained ring shear test; however the generation of excess pore water pressure can be measured in an undrained ring shear test. In general, grain crushing is significant under a drained condition, but we performed tests under an undrained condition to validate the link between grain crushing and pore water pressure generation. In addition, grain size distribution analyses of the samples within the sheared and unsheared zone were performed. As shown in Fig. 4, the grain crushing effect in the shear zone is significant.

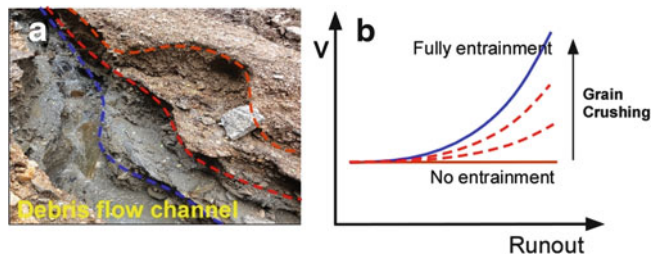


Fig. 5 Grain crushing with sediment entrainment in debris flow channel. V = sediment volume

Grain crushing may also be related to the sediment entrainment. It may result in increasing sediment volume, and consequently, causing highly mobile debris flow characteristics in the channelized flow. Figure 5 shows the debris flow channel observed in a debris flow occurrence in Korea and the relationship between sediment volume and debris flow runout. Due to the grain crushing effect, the mobility of mass movement will increase with increasing sediment volume.

Conclusions

Shear stresses at the failure and post-failure stages depend on the drainage and shearing speed condition. Highly mobile debris flow can be related to the generation of excess pore water pressure due to grain crushing in the debris flow channel. We used the ring shear apparatus to simulate the debris flow mobilization triggered by extreme heavy rainfall. Based on the ring shear tests on mine deposits, the following conclusions were drawn.

1. The materials, tested, exhibit strain softening behavior, regardless of the drainage and shearing speed conditions. In general, the higher the shearing speed, the higher the shear stress.
2. The shear stress is a function of shearing speed. The undrained shear stress is greater than the drained shear stress. The difference in shear stress is significant at low shearing speed. It may be related to the effect of grain crushing.
3. The grain crushing effect is important for estimating the sediment volume of debris flow and its impact on communities. Grain crushing may contribute to the variation in pore water pressure, but this was not considered in this study. More research in this area is needed in the future.

Acknowledgments This research was supported by the Public Welfare and Safety Research Program through the National Research Foundation of Korea (NRF) funded by the Ministry of Science, ICT & Future Planning (Grant No. 2012M3A2A1050983). The authors also would like to thank the KIGAM research project (11-7622, 13-3212) for their support.

References

- Feda J (2002) Notes on the effect of grain crushing on the granular soil behaviour. *Eng Geol* 63:93–98
- Fukuoka H, Sassa K (1991) High-speed high-stress ring shear test on granular soils and clayey soils. USDA Forest Service General Technical Report PSW-GTR-130, pp 33–41
- Fukuoka H, Sassa K, Wang G, Sasaki R (2006) Observation of shear zone development in ring-shear apparatus with a transparent shear box. *Landslides* 3:239–251
- Fukuoka H, Sassa K, Wang G (2007) Influence of shear speed and normal stress on the shear behavior and shear zone structure of granular materials in naturally drained ring shear tests. *Landslides* 4:63–74
- Jeong SW, Fukuoka H, Song YS (2011) Ring-shear apparatus for estimating the mobility of debris flow and its application. *J Korean Soc Civil Eng* 33(1):181–194 (in Korean)
- Li YR, Wen BP, Aydin A, Ju NP (2013) Ring shear tests on slip zone soils of three giant landslides in the Three Gorges Project area. *Eng Geol* 154:106–115
- Okada Y, Sassa K, Fukuoka H (2004) Excess pore pressure and grain crushing of sands by means of undrained and naturally drained ring-shear tests. *Eng Geol* 75:325–343
- Sassa K (2000) Mechanism of flows in granular soils. In: *Proceedings of the international conference of geotechnical and geological engineering, GEOENG2000*, vol 1, Melbourne, Australia
- Sassa K, Wang G, Fukuoka H (2003) Performing undrained shear tests on saturated sands in a new intelligent type of ring shear apparatus. *Geotech Test J* 26(3):1–9
- Sassa K, Fukuoka H, Wang G, Ishikawa N (2004) Undrained dynamic-loading ring-shear apparatus and its application to landslide dynamics. *Landslides* 1:7–19
- Wafid MA, Sassa K, Fukuoka H, Wang GH (2004) Evolution of shear-zone structure in undrained ring-shear tests. *Landslide* 1 (2):101–112
- Wang FW, Sassa K (2000) Relationship between grain crushing and excess pore pressure generation by sandy soils in ring shear tests. *J Nat Dis Sci* 22(2):87–96
- Wang G, Sassa K (2002) Post-failure mobility of saturated sands in undrained load-controlled ring shear tests. *Can Geotech J* 39:821–837
- Wang FW, Sassa K, Wang G (2002) Mechanism of a long-runout landslide triggered by the August 1998 heavy rainfall in Fukushima Prefecture, Japan. *Eng Geol* 63:169–185
- Wang G, Suemine A, Schulz WH (2010) Shear-rate-dependent strength control on the dynamics of rainfall-triggered landslides, Tokushima Prefecture, Japan. *Earth Surf Process Landf* 35(4):407–416



Multi-stage Statistical Landslide Hazard Analysis: Rain-Induced Landslides

Chyi-Tyi Lee

Abstract

Recurrence of rain-induced landslides is controlled by the repetition of rain events. Therefore, rainfall induced landslide hazard analysis is more complicated than a conventional rainfall frequency analysis, and requires multi-stage procedures. It requires a susceptibility analysis to divide a region into successive classes at the first stage. Then, the relationship between the probability of landslide failure and rainfall intensity and/or total rainfall of an event for each susceptibility classes may be constructed, and further fit a probability of failure surface using the susceptibility value, rainfall intensity and/or total rainfall as independent variables. Then, frequency analysis for rainfall parameters at different return periods is performed. Finally, an analysis of the spatial probability of landslide failure under a certain return-period rainfall is drawn. This study selects data for Typhoon Haitang induced landslides in the Kaopin river basin as the training data set to perform a susceptibility analysis and a probability of failure surface analysis. A rainfall frequency analysis is also conducted to map different return-period rainfall intensity and 3-day rainfalls. Finally, a rainfall landslide hazard map is provided.

Keywords

Landslide • Event landslide inventory • Landslide susceptibility • Rainfall-induced landslides • Rainfall landslide hazard

Introduction

Rainfall induced landslide hazard analysis has two major approaches, statistical and deterministic. Statistical approach commonly uses a multi-temporal landslide inventory to build a statistical model (e.g., Carrara 1983; Guzzetti et al. 1999). However, most of the available hazard maps are still of qualitative nature and concentrate basically on determining the susceptibility (van Westen et al. 2006), and temporal probability is also lacking. Guzzetti et al. (2005) attempt to solve the temporal probability problem and introduced a probabilistic model which predicts where landslides will occur, how

frequently they will occur, and how large they will be. But, there still are problems on incompleteness of the inventory, insufficient length of historical records, and a possible mixing of extreme events and/or earthquake disturbance.

Physical based method uses a hydrological model and an infinite slope model to form a landslide prediction model (Montgomery and Dietrich 1994; Iverson 2000; Brenning 2005; Claessens et al. 2007). It is perfect in theory, but has a difficulty in acquiring site specific data, like, failure depth, material strength, and groundwater data.

A new statistical approach called event-based landslide susceptibility analysis (EB-LSA) was introduced recently in Lee et al. (2008b). This new approach is different from the traditional susceptibility analyses in the emphasis of using an event landslide inventory and triggering factors. It is also different from the probabilistic method in the usage of event landslide inventory and triggering factors.

C.-T. Lee (✉)
Graduate Institute of Applied Geology, National Central University,
No. 300, Zhongda Road, Zhongli City 32001, Taiwan
e-mail: ct@ncu.edu.tw

EB-LSA is basically different from the physical based method, but they are similar in the multi-stage nature, including a susceptibility stage for spatial probability of landslides and a rainfall frequency analysis stage for temporal probability of landslides, and both intend to construct a landslide spatial probability or safety factor map for a certain return-period rainfalls. This means both method adopt that recurrence of rain-induced landslide is controlled by the repetition of triggering events.

To construct a 100-year rainfall landslide hazard map was routinely done in the landslide project of Central Geological Survey (CGS), Taiwan, in recent years for each river basin in Taiwan (Lee and Fei 2011). A nationwide storm landslide hazard map will be completed in the end of year 2013 (Lee et al. 2012). However, the approach in the previous studies has a weak point in that the hazard map may include the probability contributed from causative factors and produces non-zero probability at zero rainfall intensity. Therefore, a new landslide probability of failure relationship must be further developed.

The present study upgrades the study of Lee et al. (2012) by developing a probability of failure surface instead of a probability of failure curve. The new relationship should avoid mixing the contribution from causative factors. Using this new probability of failure surface and a 100-year return-period rainfall map, a new 100-year storm landslide hazard map for a major river basin in southern Taiwan is constructed. The rainfall landslide hazard map may reveal landslide spatial probability at each pixel given a certain rainfall return-period.

Methodology

Susceptibility Model

Our rainfall induced landslide susceptibility analysis method basically follows Lee et al. (2008b) which used an event landslide inventory and the triggering factors to build a susceptibility model. This model is called an event-based susceptibility model by Lee et al. (2008a, b), and is accordingly event-dependent. The effective selection of the landslide causative factors and triggering factors, as well as an analytical method, are very important for the construction of a high prediction rate model. Please refer to Lee and Fei (2011) for details of these.

Probability of Failure Surface

The construction of a probability of failure curve in the previous studies is simple: simply plot the mean probability of failure value at each susceptibility bin and fit a curve.

A probability of failure surface is intended to show a relationship between the probability of failure and rainfall parameters at each susceptibility bin, and to obtain the fit to the surface using the rainfall parameters and susceptibility as independent variables. Note that the susceptibility values used here indicate the event-independent susceptibility without a triggering factor.

A landslide spatial probability map may be produced by transferring the event-independent susceptibility values and rainfall factors to the probability of landslide failure at each grid cell by using a probability of failure surface. When rainfall factors from the training event are used, one can produce a hazard map that reflects the rainfall event. The use of the rainfall parameters for a specific rainfall scenario, produce a hazard map that reflects the scenario rainfall event.

Temporal Probability of Landslides

Since rainfall induced landslides are induced features from the heavy rainfall, their recurrence is controlled by the repetition of the rainfall event. Therefore, we must know the likelihood of a rainfall recurrence or the rainfall values at a certain return-period. This may be obtained through a regular hydrological frequency analysis (e.g., Chow 1953; Fowler and Kilsby 2003) with a set of rainfall data from different rain gage stations.

Preparation of a certain return-period rainfall intensity map and 3-day rainfall map for the study region is the objective of the frequency analysis, and is the input data for the rainfall landslide hazard mapping. This is commonly a 100-year return period rainfall. However, it may include other choices of return period, like a 50-year return period. If rainfalls of a 100-year return-period are used, the hazard map reflects the 100-year rainfall, and may be called a 100-year rainfall landslide hazard map.

Data

Basic Data

The basic data used in the present study include: 2.5m high resolution SPOT5 images, a 5-m grid digital elevation model (DEM), 1/5,000 photo-based contour maps, 1:50,000 geologic maps, and hourly rainfall records. Digital geological maps (1:50,000) were obtained from the Central Geological Survey, Taiwan. All the vector layers were converted into raster cells of 10 m × 10 m in size and this resolution was used for all subsequent processing and analysis for each landslide factor and the hazard model.

Event Landslide Inventory

The Typhoon Haitang hit Taiwan on July 16 to 20, 2005. It brought a total rainfall of up to 2,000 mm in the Kaoping river basin, and triggered 15,864 landslides with a total area of 42.8 km², which occupied 1.28 % area of the river basin, or 1.75 % of the slope terrain in the river basin.

False-color SPOT5 images were used for landslide recognition. Landslides were recognized and digitized in GIS and attributes were assigned to establish a landslide map table. Each landslide table was then checked in the field and in the laboratory against 1/5,000 photo-based contour maps, and modifications were made. An event-triggered landslide was identified by comparing the pre-event and post-event landslide inventories, to produce an event-based landslide inventory. The Typhoon Haitang event-based landslide inventory is shown in Fig. 1. The event landslide inventory for the 2009 Typhoon Morakot was prepared in a similar way and will be used for validation of the Haitang event susceptibility model.

Results

Event-Based Susceptibility Model

The Typhoon Haitang induced shallow landslides (Fig. 1) and rainfall data are actually used in the susceptibility analysis. Due to the fact that an event landslide inventory and a triggering factor of the event are used in the development of the susceptibility model, this is called an event-based susceptibility model (Lee et al. 2008a, b).

Causative factors used in the susceptibility model include the following: slope gradient, slope aspect, slope roughness, tangential curvature, relative slope height, and lithology. For a detailed description of the causative factors and the triggering factor, please refer to Lee and Fei (2011).

Logistic regression is used in the susceptibility analysis and the results of this analysis include a logistical function and the coefficients,

$$\ln \left[\frac{p}{1-p} \right] = 0.726L_1 + 0.175L_2 + 1.072L_3 + 3.673L_4 + 2.520L_5 + 2.575L_6 + 2.856L_7 + 2.205L_8 + 3.044L_9 + 3.053L_{10} + 2.940L_{11} + 2.812A_1 + 3.595A_2 + 4.146A_3 + 4.333A_4 + 4.240A_5 + 3.987A_6 + 3.297A_7 + 2.790A_8 + 1.182F_1 + 0.061F_2 + 0.299F_3 - 0.761F_4 + 0.446F_5 - 7.317. \quad (1)$$

where L_1 – L_{11} are lithological units; A_1 – A_8 are slope aspects; F_1 – F_4 are causative factors; F_5 is a triggering factor; and p is

the occurrence probability. During the establishment of the logistic equations, the input p is 1 for a landslide grid and 0 for a non-landslide grid. After the regression, when the set of factors is given a score at a grid point, the occurrence probability p at that point is derived. It will be in the range of 0 to 1. This occurrence probability is taken as a susceptibility index λ in this study. Larger values of an index indicate a higher susceptibility to landslides.

The event-based susceptibility model (Fig. 2) goes a good way to explaining the event-induced landslide distribution. The probability of failure curve shows a good fit to the hyperbolic sine function (Fig. 2b). The area under the curve (AUC) of the success rate curve is 0.776. The model is further validated utilizing the Typhoon Morakot rainfalls and its event landslide inventories; the AUC of the prediction rate curve is 0.728 for the model.

Event Independent Susceptibility Model

The event-based susceptibility model is dependent on the event itself. However, if we extract the triggering factor from the model, then the model becomes event independent, provided that the triggering factor is an independent factor having only small correlation coefficient with any causative factors. This option must be carefully examined before a causative factor is selected.

In this case, the event-based susceptibility model is reduced to an event-independent model by removing the component of the triggering factors from the original model. Here, we call this reduced model an event-independent susceptibility model for the region. Different event-independent susceptibility models for the same region have been compared and good agreement has been found among them (Lee et al. 2004). On this basis, we can use an event-independent susceptibility model to represent the susceptibility of the region with confidence.

Probability of Failure Surface

We tested the relationship between probability of failure and rainfall intensity, as well as total rainfall at each event-independent susceptibility bin. It was found that the relation is good; the probability of failure increases with an increase in the rainfall and also with an increase in the susceptibility. After this finding, it was necessary to find a global fitting surface using a rainfall parameter and event-independent susceptibility as two independent variables. The result is shown in Fig. 3 and (2) and (3) as follows:

$$y = 16.808\lambda \left(1 - e^{-5.924\lambda^{0.942}} \right) \left(1 - e^{-0.0132\tau_1^{2.907}} \right) \quad (2)$$

Fig. 1 Geology of the Kaoping river basin (a) index map showing the geology of Taiwan, (b) landslide distribution of the Kaoping river basin

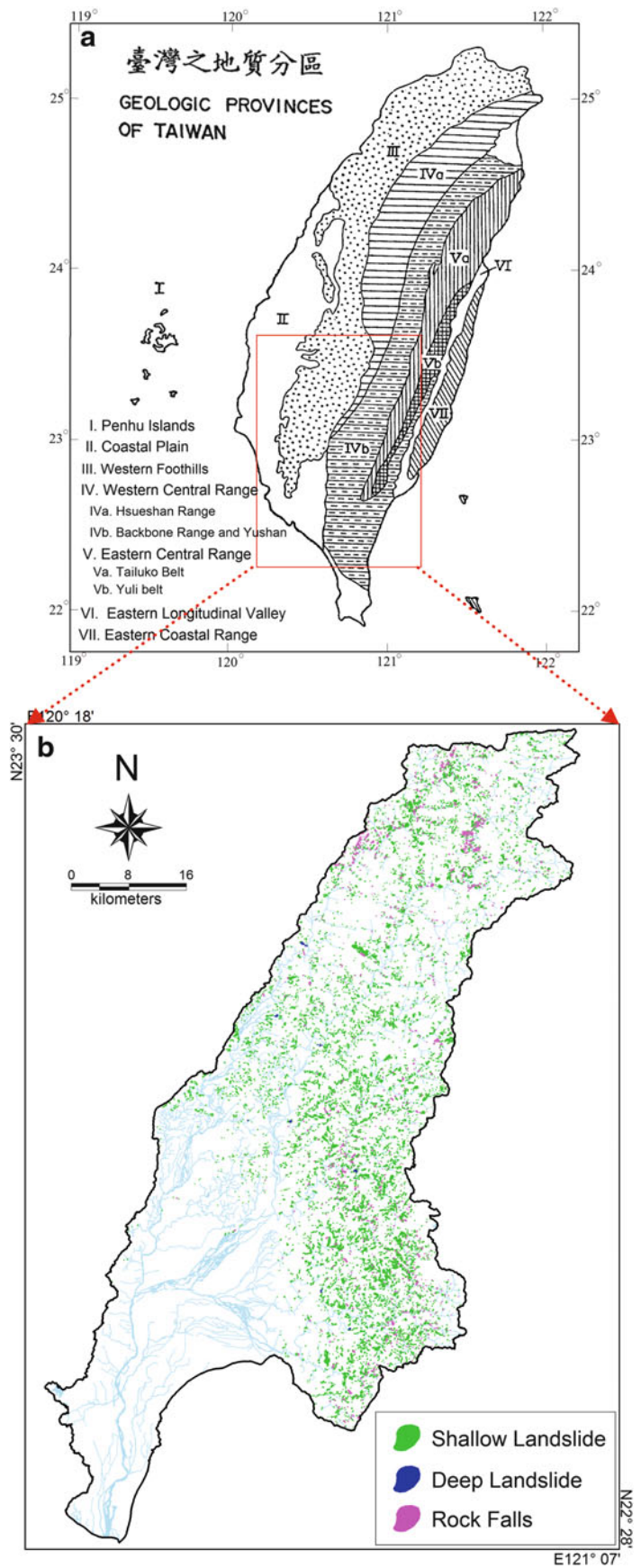
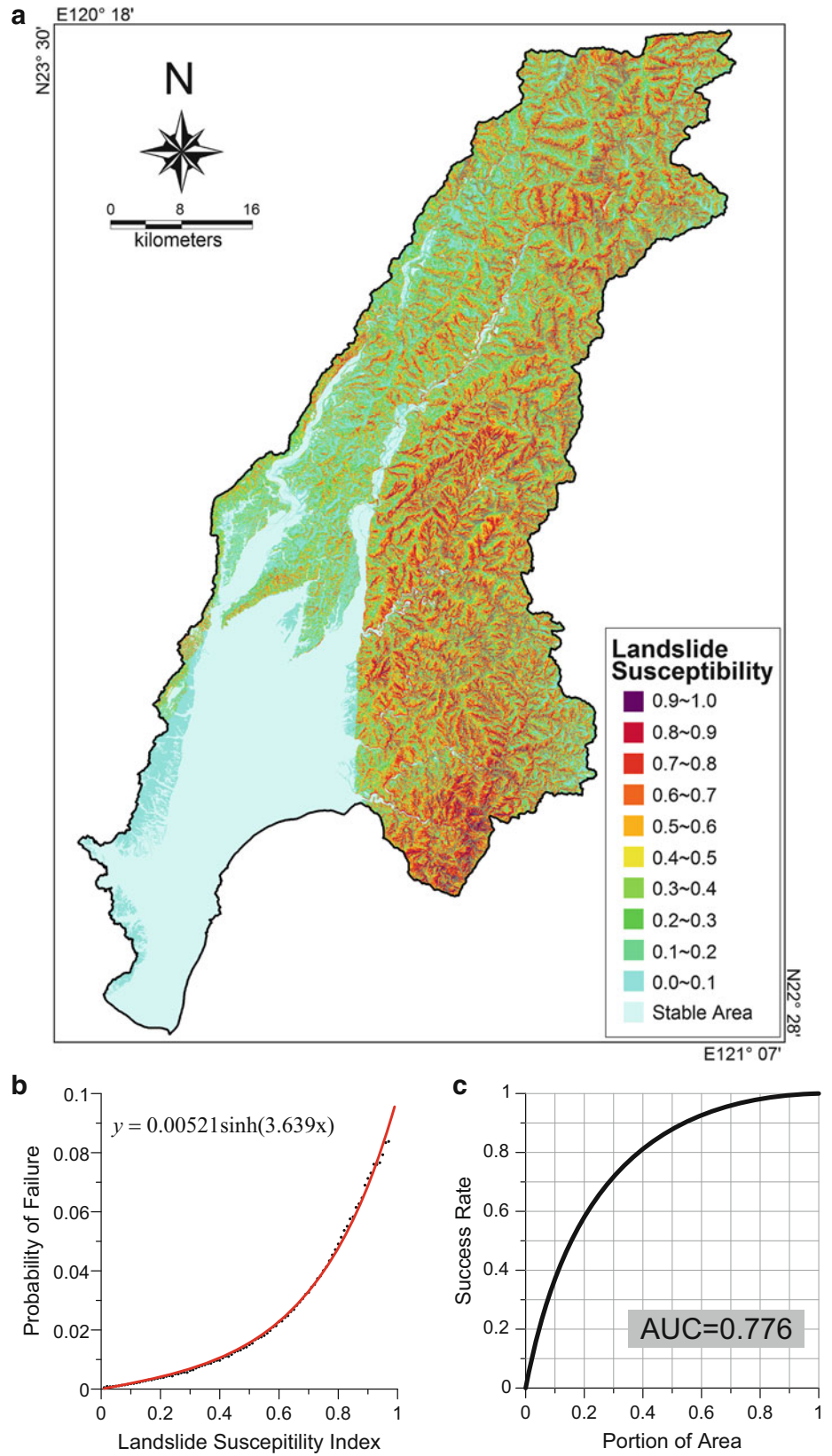


Fig. 2 Susceptibility model for the Haitang event landslides (a) event-dependent landslide susceptibility map; (b) probability of failure curve; and (c) success rate curve



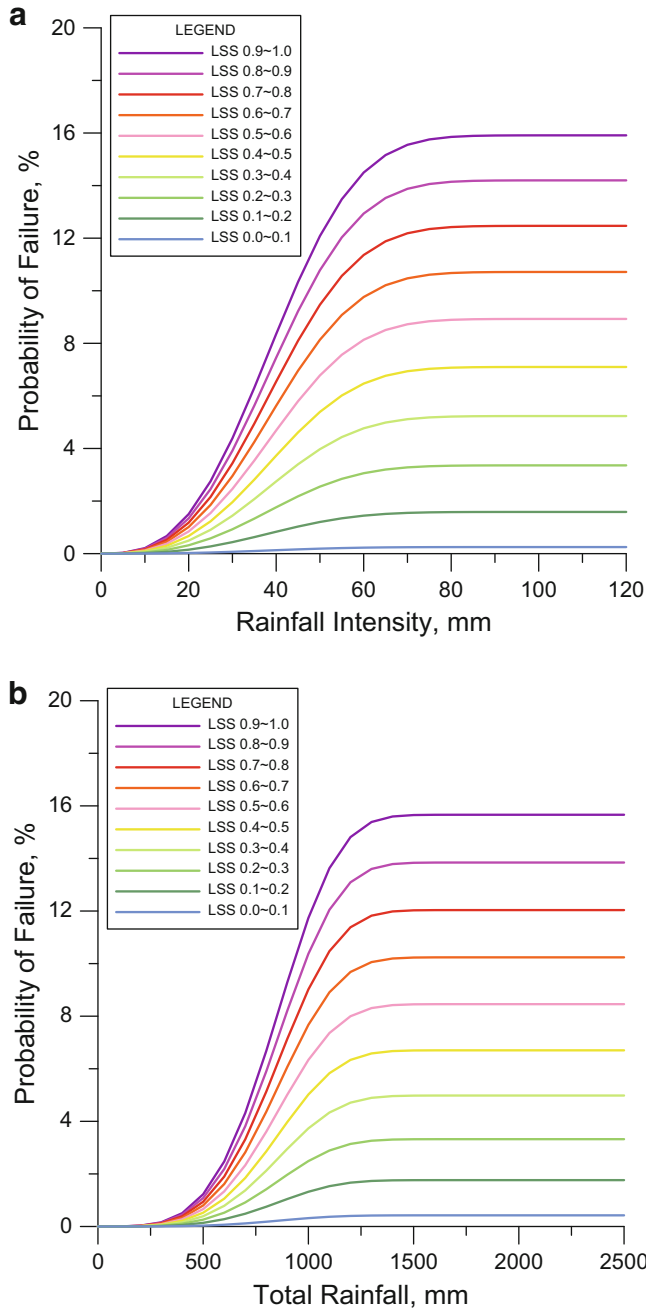


Fig. 3 Probability of failure surface (a) rainfall intensity; (b) total rainfall. Equation shown in the text

$$y = 17.990\lambda \left(1 - e^{-2.542\lambda^{0.461}}\right) \left(1 - e^{-0.000114x_2^{4.085}}\right) \quad (3)$$

where x_1 is the rainfall intensity in centimeter, x_2 is the total rainfall in decimeter; y is the probability of failure, and λ is the event-independent susceptibility. Equation (2) is for rainfall intensity and (3) is for total rainfall.

A global probability of failure surface for two rainfall variables may be built by combining (2) and (3). If the two rainfall variables are totally independent, then the square of global probability of failure is the sum of the square of (2) and the square of (3). If the two rainfall variables are totally dependent, then the square of global probability of failure is the product of (2) and (3). In actual cases, the two rainfall variables are, commonly, in between dependent and independent, but have a correlation coefficient between 0 and 1. In the present study, we propose,

$$y = \left((1 - r)(y_1^2 + y_2^2) + r(y_1 y_2)\right)^{0.5} \quad (4)$$

where y_1 is y of (2), y_2 is y of (3), and r is the correlation coefficients between rainfall intensity and total rainfall.

Rainfall Frequency Analysis

The temporal probability of a rainfall landslide hazard model may be accounted for by the recurrence of the rainfall events. Rainfall values at different return-period may be obtained through a conventional rainfall frequency analysis.

A hydrological team in the CGS landslide project was responsible for rainfall frequency analysis and providing different return-period rainfall values at each study area and also a set of maps for the whole of Taiwan. The present study selects 1-h rainfalls and 3-day rainfalls of 100-year return-period for final mapping of the rainfall landslide hazard. 3-day rainfalls are evaluated as proper to represent the total rainfall of a Typhoon storm event in Taiwan.

Rainfall Landslide Hazard Map

The previously built susceptibility model, which is event-dependent, is good for interpretation of the event landslide distribution. With the addition of the probability failure surface, this model is capable of predicting landslides during a scenario event, provided that the rainfall values are known for each study grid cell. However, for hazard mapping, a certain temporal probability or return period for rainfall values should be adopted. This is commonly a 100-year return period. Other choices of return period, like a 10-year, 20-year, 50-year return-period may also be used.

The 1-h rainfall map and 3-day rainfall map of 100-year return-period, and the event independent susceptibility model are then applied to the probability of failure model to construct a 100-year rainfall landslide hazard map for the Kaoping river basin (Fig. 4).

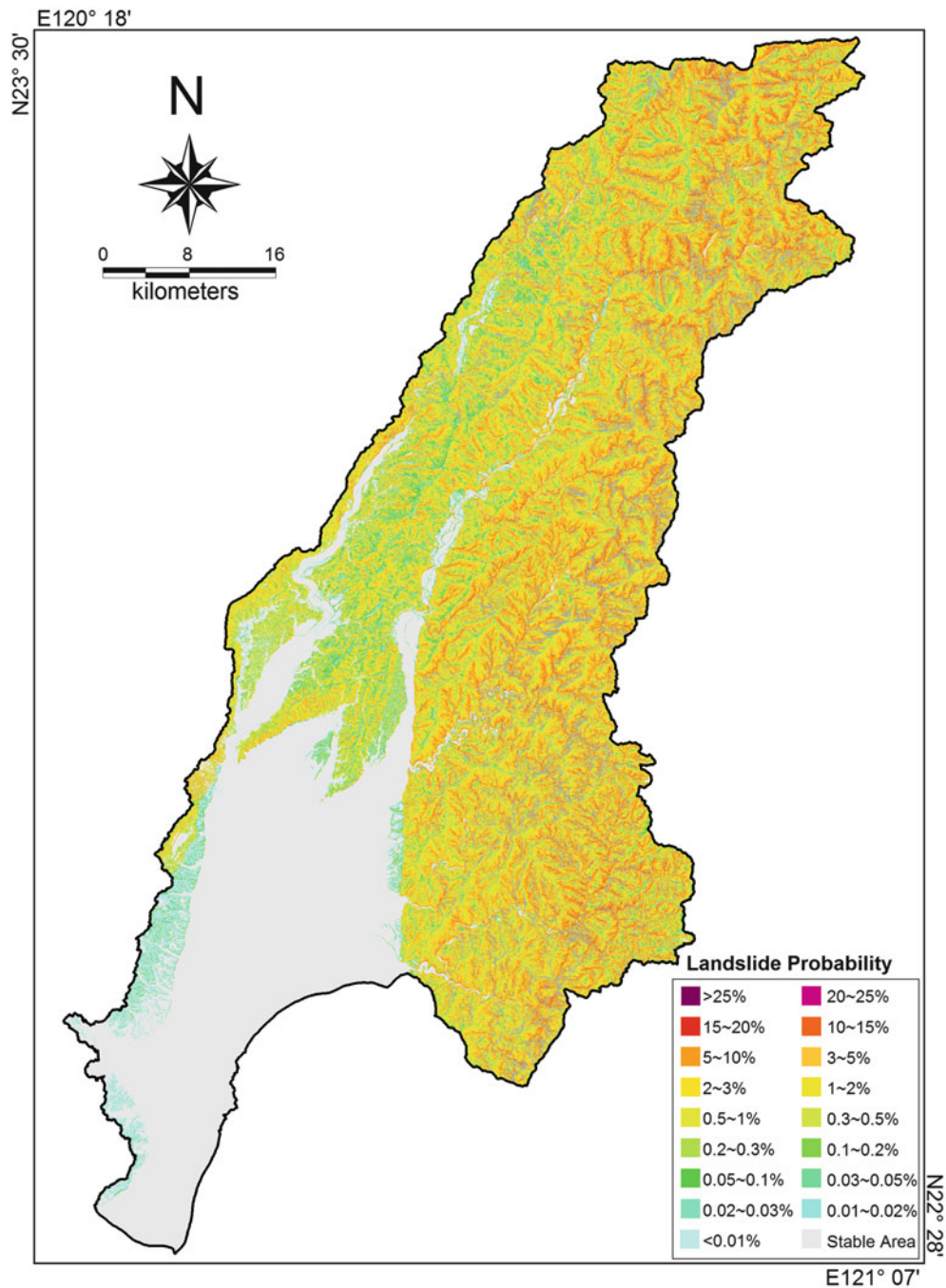


Fig. 4 100-year rainfall landslide hazard map for the Kaoping Basin

Conclusion and Recommendation

A multivariate statistical approach with logistic regression has been used to analyse the Typhoon Haitang induced shallow landslides and their controlling factors, and to build an event-dependent susceptibility model. The event-independent model (without a triggering factor), rainfall intensity map, total rainfall map, and the actual landslides

from the Haitang event, are used to construct a relationship, using the event-independent susceptibility and rainfall parameters as independent variables, and it is fitted with a probability of failure surface. Then, the 100-year rainfall maps together with the event-independent susceptibility model are input into the probability of failure relationship to complete a 100-year rainfall landslide hazard map for the Kaoping river basin. The results of the analysis are good,

provided that careful validation of the Typhoon Morakot induced landslides is made. We conclude that this statistical approach is feasible for rainfall landslide hazard analysis, and that the hazard model can be used to predict landslides after a rainfall event and can be used to produce a rainfall landslide hazard map of a wider region.

The statistical approach to rainfall landslide hazard has advantages over deterministic methods in that it does not require failure depth, material strength, or groundwater data, and may have a better prediction rate. On the other hand, a deterministic model can be used anywhere once the parameters required by the model are available. The statistical approach, in contrast, may be applicable only in the vicinity of the study region where the model was trained, and may be limited to within or near to the rainfall intensity range for which they were trained.

The present proposed hazard model is good for the prediction of landslide spatial probability during a rainfall event, the mapping of the rainfall landslide hazard probability for a certain return-period rainfall, decision making for regional planning, site selection, hazard mitigation, and the estimation of sediment products for a river basin after an extreme event. However there is still a lack of output in regards to the landslide magnitude which is very important in risk assessment. This problem needs further study.

References

- Brenning A (2005) Spatial prediction models for landslide hazards: review, comparison and evaluation. *Nat Hazard Earth Syst Sci* 5(6):853–862
- Carrara A (1983) Multivariate models for landslide hazard evaluation. *Math Geol* 15(3):403–427
- Chow VT (1953) Frequency analysis of hydrologic data with special application to rainfall intensities. University of Illinois Engineering Experiment Station, Bulletin Series, 414, 81p
- Claessens L, School J, Veldkamp A (2007) Modelling the location of shallow landslides and their effects on landscape dynamics in large watersheds: an application for Northern New Zealand. *Geomorphology* 87:16–27
- Fowler HJ, Kilsby CG (2003) A regional frequency analysis of United Kingdom extreme rainfall from 1961 to 2000. *Int J Climatol* 23(11):1313–1334
- Guzzetti F, Carrara A, Cardinali M, Reichenbach P (1999) Landslide hazard evaluation: a review of current techniques and their application in a multi-scale study, Central Italy. *Geomorphology* 31:181–216
- Guzzetti F, Reichenbach P, Cardinali M, Galli M, Ardizzone F (2005) Probabilistic landslide hazard assessment at the basin scale. *Geomorphology* 72:272–299
- Iverson RM (2000) Landslide triggering by rain infiltration. *Water Resour Res* 36:1897–1910
- Lee CT, Fei LY (2011) Landslide hazard analysis and mapping in a wide area. *Sino-Geotechnics* 129:53–62 (in Chinese with English abstract)
- Lee CT, Huang CC, Lee JF, Pan KL, Lin ML, Liao CW, Lin PS, Lin YS, Chang CW (2004) Landslide susceptibility analyses based on three different triggering events and result comparison. In: *Proceeding of international symposium on landslide and debris flow hazard assessment, Taipei*, pp 6-1~6-18
- Lee CT, Huang CC, Lee JF, Pan KL, Lin ML, Dong JJ (2008a) Statistical approach to earthquake-induced landslide susceptibility. *Eng Geol* 100:43–58
- Lee CT, Huang CC, Lee JF, Pan KL, Lin ML, Dong JJ (2008b) Statistical approach to storm event-induced landslide susceptibility. *Nat Hazard Earth Syst Sci* 8:941–960
- Lee CT, Chang CW, Lin SH (2012) Landslide hazard analysis and mapping in a wide region. *EGU General Assembly Conference Abstracts* 14
- Montgomery DR, Dietrich WE (1994) A physical-based model for the topographic control on shallow landsliding. *Water Resour Res* 30(4):1153–1171
- Van Westen CJ, van Asch TWJ, Soeters R (2006) Landslide hazard and risk zonation - why is it still so difficult? *Bull Eng Geol Environ* 65:167–184



Topographic and Pedological Rainfall Thresholds for the Prediction of Shallow Landslides in Central Italy

Silvia Peruccacci, Maria Teresa Brunetti, Silvia Luciani,
Maria Costanza Calzolari, Devis Bartolini, and Fausto Guzzetti

Abstract

In Italy, rainfall induced shallow landslides are frequent phenomena that cause casualties every year. At the national and regional scales, empirical rainfall thresholds can predict the occurrence of single or multiple rainfall-induced shallow landslides. In this work, we updated a historical catalogue listing 553 rainfall events that triggered 723 landslides in the Abruzzo, Marche and Umbria regions, central Italy, between February 2002 and March 2011. For each event, the rainfall duration (D) and the cumulated event rainfall (E) responsible for the failure are known, together with the exact or approximate location of the landslide. To analyse the influence of topography and soil characteristics on the occurrence of rainfall induced shallow landslides, we subdivided the study area in three topographic divisions, and eight soil domains. We analysed the (D , E) rainfall conditions that resulted in the documented shallow landslides in each topographic division and regional soil domain, and we defined ED rainfall thresholds at 5 % exceedance probability level for the two subdivisions. We expect that the new topographic and pedological thresholds will contribute to forecast shallow landslides in central Italy, and in areas characterized by similar morphological and soil settings.

Keywords

Shallow landslides • Central Italy • Rainfall thresholds

S. Peruccacci (✉) • F. Guzzetti

Istituto di Ricerca per la Protezione Idrogeologica, Consiglio Nazionale delle Ricerche, via Madonna Alta 126, Perugia 06128, Italy
e-mail: silvia.peruccacci@irpi.cnr.it; fausto.guzzetti@irpi.cnr.it

M.T. Brunetti • S. Luciani

Istituto di Ricerca per la Protezione Idrogeologica, Consiglio Nazionale delle Ricerche, via Madonna Alta 126, Perugia 06128, Italy

Dipartimento di Scienze della Terra, Università degli Studi di Perugia, Perugia 06123, Italy

e-mail: mariateresa.brunetti@irpi.cnr.it; silvia.luciani@irpi.cnr.it

M.C. Calzolari

Istituto di Biometeorologia, Consiglio Nazionale delle Ricerche, Sesto Fiorentino 50019, Italy

e-mail: c.calzolari@ibimet.cnr.it

D. Bartolini

Istituto di Ricerca per la Protezione Idrogeologica, Consiglio Nazionale delle Ricerche, Sesto Fiorentino 50019, Italy

e-mail: bartolini.devis@gmail.com

Introduction

In Italy, shallow landslides triggered by intense and/or prolonged rainfall cause casualties every year, and represent a serious hazard to the population. At the national and regional scales, the prediction of rainfall induced shallow failures can be achieved by defining empirical rainfall thresholds. In the literature, empirical thresholds are established through the analysis of past rainfall events that have resulted in landslides (for an extensive review see e.g. Guzzetti et al. 2007).

In this work, we updated a historical catalogue of 553 rainfall events that have resulted in 723 landslides in the Abruzzo, Marche and Umbria regions, central Italy, between 2002 and 2011. We exploited this catalogue to determine new cumulative event rainfall—rainfall duration (ED)

thresholds for the possible occurrence of slope failures in central Italy.

To define objective and reproducible thresholds, we adopted the frequentist statistical method proposed by Brunetti et al. (2010) and refined by Peruccacci et al. (2012) to determine regional, lithological and seasonal thresholds in the same study area. It is known that the local topographic (morphological), lithological, soil, and climatic settings influence the occurrence and the spatial distribution of shallow landslides in an area. In this work, we investigated the role of topography and soil types in the cumulative amount (E) and the duration (D) of the rainfall that resulted in shallow landslides in our study area. First, we subdivided the study area in 3 physiographic provinces, and we defined ED rainfall thresholds for the topographic terrain classification. Next, using a small-scale pedological map, we obtain information on the main regional soil domains where landslides were reported, and we calculated ED thresholds for three soil regions. We conclude after discussing the results obtained.

Materials and Methods

Catalogue of Rainfall Events with Landslides

In a previous work (Peruccacci et al. 2012), we compiled a catalogue of 442 rainfall events that triggered 573 documented shallow landslides in the Abruzzo, Marche, and Umbria regions, central Italy, between February 2002 and August 2010. In the Umbria region, the landslide information was obtained searching national, regional, and local newspapers, and reports of landslide events compiled by fire brigades. In the Marche and the Abruzzo regions, newspapers were the only source of information.

A large amount of information on rainfall-induced landslides is required to define reliable rainfall thresholds. In order to collect additional information, we began a collaboration with: (1) the Marche Regional Department for Civil Protection, and (2) provincial fire brigades of the Marche region. As a result, we found information on 111 rainfall events that resulted in 150 documented slope failures in the Marche region. Merging the data, we obtained a new catalogue listing 553 rainfall events in central Italy that have caused 723 landslides in the period between February 2002 and March 2011 (Fig. 1).

Depending on the quality of the available information, we mapped the observed landslides as single points, attributing to each failure a level of mapping accuracy P , in three classes: high, $P_1 < 1 \text{ km}^2$; medium, $1 \leq P_{10} < 10 \text{ km}^2$; and low, $10 \leq P_{100} < 100 \text{ km}^2$ (Peruccacci et al. 2012).

For each rainfall event, the duration D (in hours) and the total event rainfall E (in mm) were determined using hourly

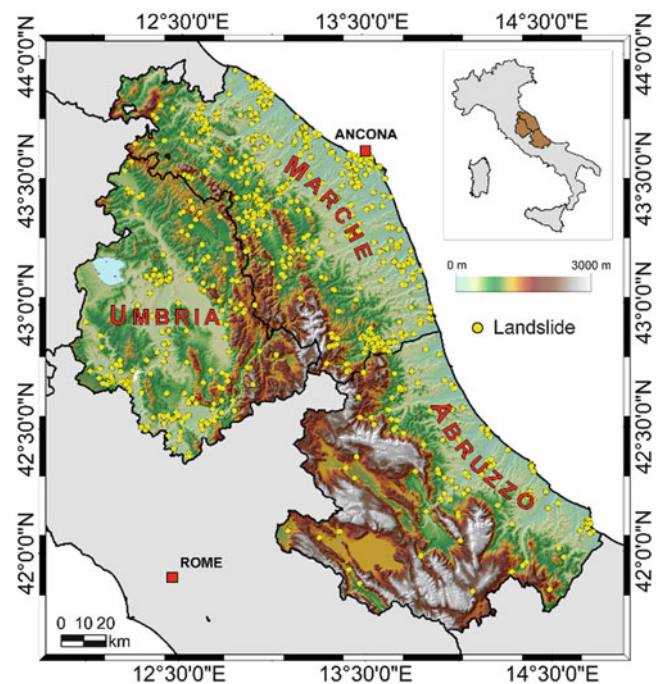


Fig. 1 Map of the study area, including Abruzzo, Marche and Umbria regions (central Italy). Yellow dots show location of 723 rainfall induced landslides

rainfall measurements from a network of 150 rain gauges. Generally, the rain gauge used to reconstruct the rainfall responsible for the failure (i.e. D and E) was selected considering the geographic distance to the landslide, and its elevation with respect to the elevation of the landslide.

In the updated catalogue, the rainfall events that resulted in landslides in central Italy are in the range of duration $1 < D < 1,212 \text{ h}$, and in the range of cumulated rainfall $7.0 < E < 457.2 \text{ mm}$.

Definition of Rainfall Thresholds

Guzzetti et al. (2007, 2008) highlighted the need to define objective and reproducible empirical rainfall thresholds for the possible initiation of landslides.

In this work, we used a frequentist statistical method (Brunetti et al. 2010; Peruccacci et al. 2012) to calculate new ED thresholds in central Italy. The method assumes the threshold curve is a power law:

$$E = (\alpha \pm \Delta\alpha) \times D^{(\gamma \pm \Delta\gamma)} \quad (1)$$

where, E is the cumulated (total) event rainfall (in mm), D is the duration of the rainfall event (in h), " α " is a scaling parameter (the intercept), " γ " is the slope of the power law threshold curve, and " $\Delta\alpha$ " and " $\Delta\gamma$ " are the uncertainties associated to α and γ , respectively.

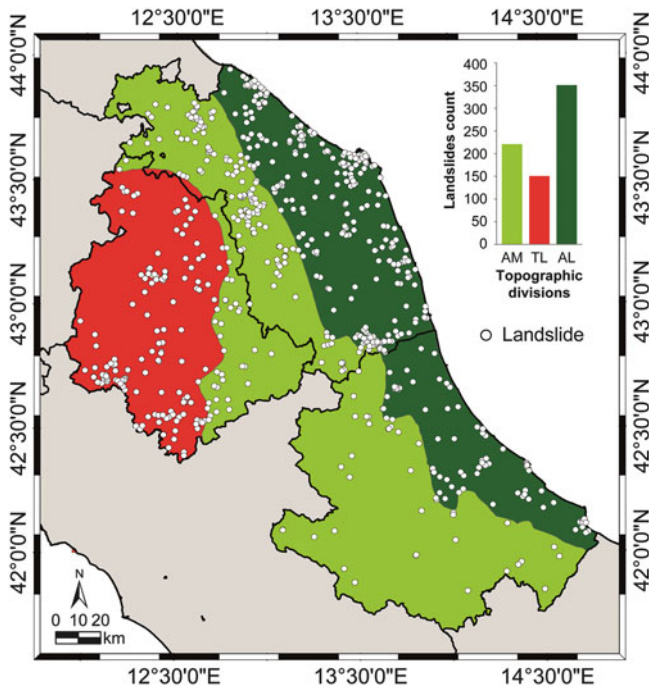


Fig. 2 Simplified topographic division of the study area. AM Apennines Mountain System, TL Tyrrhenian Lowland, AL Adriatic Lowland. White dots show location of rainfall-induced landslides. Histogram shows number of landslides in each physiographic province

The method allows calculating thresholds corresponding to different exceedance probabilities. As an example, assuming the set of the empirical (D , E) data points is sufficiently complete and representative of the conditions that led to slope failures in a study area, the 5 % threshold is the curve that should leave 5 % of the rainfall events with landslides below the threshold.

Results

It is widely believed that landslide occurrence is affected by the local topographic (morphological), lithological, soil, and climatic settings. For this work, we exploited the new catalogue of rainfall events with landslides in central Italy to investigate the role of topography and soil types on rainfall thresholds for the possible initiation of landslides.

Topographical Thresholds

To analyse the influence of topography on the rainfall conditions responsible for the slope failures, we used the topographic divisions of Italy proposed by Guzzetti and Reichenbach (1994). They divided the entire Italian territory into eight major physiographic provinces reflecting physical, geological, and structural changes of the Italian landscape.

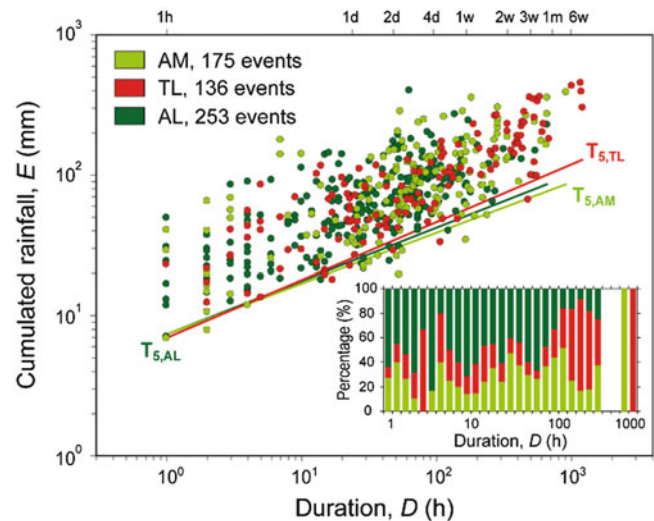


Fig. 3 Rainfall duration D (x -axis) and cumulated event rainfall E (y -axis) conditions that have produced landslides in Apennines Mountain System (AM, light green dots), Tyrrhenian Lowland (TL, red dots), and Adriatic Lowland (AL, dark green dots), in the study area. Coloured lines are 5 % power law thresholds ($T_{5,AM}$, $T_{5,TL}$, $T_{5,AL}$). Data shown in logarithmic coordinates. Bar chart shows proportion of rainfall events for different rainfall durations

According to this topographic division, in the study area we identified three physiographic provinces, namely: (1) Apennines Mountain System, AM; (2) Tyrrhenian Lowland, TL, and (3) Adriatic Lowland, AL (Fig. 2).

Using the procedure adopted by Peruccacci et al. (2012), we attributed each landslide to a specific physiographic province. In particular, each landslide, mapped as a single point, was represented by a circle, with the area of the circle dependent on the mapping accuracy (P_1 , $A = 0.5 \text{ km}^2$; P_{10} , $A = 5 \text{ km}^2$; P_{100} , $A = 50 \text{ km}^2$). The landslide circles were then intersected with the topographic division, and a physiographic province was attributed to each landslide if it covered 75 % or more of the circle. The histogram in Fig. 2 shows the number of failures in each physiographic province.

Figure 3 shows, in logarithmic coordinates, the distribution of the rainfall conditions (D , E) that caused landslides in AM, Apennines Mountain System (175 light green dots), TL, Tyrrhenian Lowland (136 red dots), and AL, Adriatic Lowland (253 dark green dots). Coloured lines are the 5 % ED power law thresholds, $T_{5,AM}$, $T_{5,TL}$, $T_{5,AL}$ (Table 1). Figure 3 also shows the proportion of rainfall events for different rainfall durations. Figure 4 shows $T_{5,AM}$, $T_{5,TL}$, and $T_{5,AL}$ in linear coordinates in the range $1 \text{ h} \leq D \leq 120 \text{ h}$, with the shaded area portraying the uncertainty associated with the thresholds. The uncertainty depends on the number and distribution of the data points. Inspection of Figs. 3 and 4 reveals that $T_{5,AM}$, $T_{5,TL}$, and $T_{5,AL}$ are substantially equivalent and statistically indistinguishable in our study area.

Table 1 Rainfall *ED* thresholds for the possible initiation of landslides in central Italy

#	Label	Area	Events	Threshold	Range	Uncertainty
1	T _{5,AM}	Apennines Mountain System	175	$E = 7.4 \times D^{0.36}$	1 < D < 918	$\Delta\alpha = 1.1, \Delta\gamma = 0.03$
2	T _{5,TL}	Tyrrhenian Lowland	136	$E = 7.0 \times D^{0.41}$	1 < D < 1,212	$\Delta\alpha = 0.8, \Delta\gamma = 0.02$
3	T _{5,AL}	Adriatic Lowland	253	$E = 7.8 \times D^{0.37}$	1 < D < 663	$\Delta\alpha = 0.7, \Delta\gamma = 0.02$
4	T _{5,S1}	Cambisol—Leptosol region with Luvisols of the central Apennine	128	$E = 7.2 \times D^{0.36}$	1 < D < 1,176	$\Delta\alpha = 1.2, \Delta\gamma = 0.04$
5	T _{5,S2}	Cambisol—Regosol region, with Luvisols of eastern Italy	94	$E = 7.1 \times D^{0.42}$	1 < D < 315	$\Delta\alpha = 1.2, \Delta\gamma = 0.04$
6	T _{5,S3}	Cambisol—Regosol region with Vertisols of central and southern Italy	198	$E = 7.9 \times D^{0.37}$	1 < D < 662	$\Delta\alpha = 0.8, \Delta\gamma = 0.03$
7	T _{5,PO}	Post-Orogenic sediments	211	$E = 7.4 \times D^{0.37}$	1 < D < 1,188	$\Delta\alpha = 0.6, \Delta\gamma = 0.02$
8	T _{5,FD}	Flysch deposits	82	$E = 10.3 \times D^{0.37}$	1 < D < 1,212	$\Delta\alpha = 1.5, \Delta\gamma = 0.03$
9	T _{5,CC}	Carbonate complex	88	$E = 9.0 \times D^{0.3}$	1 < D < 663	$\Delta\alpha = 1.5, \Delta\gamma = 0.04$

Label: label of the thresholds. Area: area for which the threshold was defined. Equation: *D*, rainfall duration, in hour; *E*, cumulated event rainfall, in mm. Range: range of validity for the threshold. Uncertainty: uncertainty associated with the intercept α and the slope γ of the threshold curve. Source: # 1–6, this work; # 7–9, Peruccacci et al. (2012)

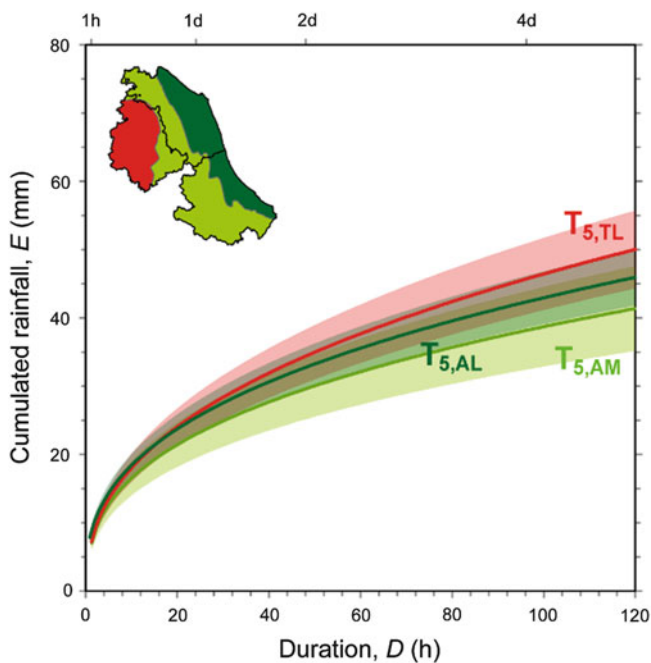


Fig. 4 Cumulated event rainfall—rainfall duration (*ED*) thresholds for AM, Apennines Mountain System; TL, Tyrrhenian Lowland; AL, Adriatic Lowland. Solid coloured lines are 5 % power law thresholds (T_{5,AM}, T_{5,TL}, T_{5,AL}) in linear coordinates. Shaded areas show uncertainty associated with the threshold curves

Pedological Thresholds

To investigate the relationship between soil type and rainfall thresholds, we obtained the pedological information from a synoptic map published by Costantini et al. (2004). They divided the Italian territory into 34 soil regions reflecting morphology, soil water, temperature regime, and more diffused soil types (according to FAO 1990). We partitioned

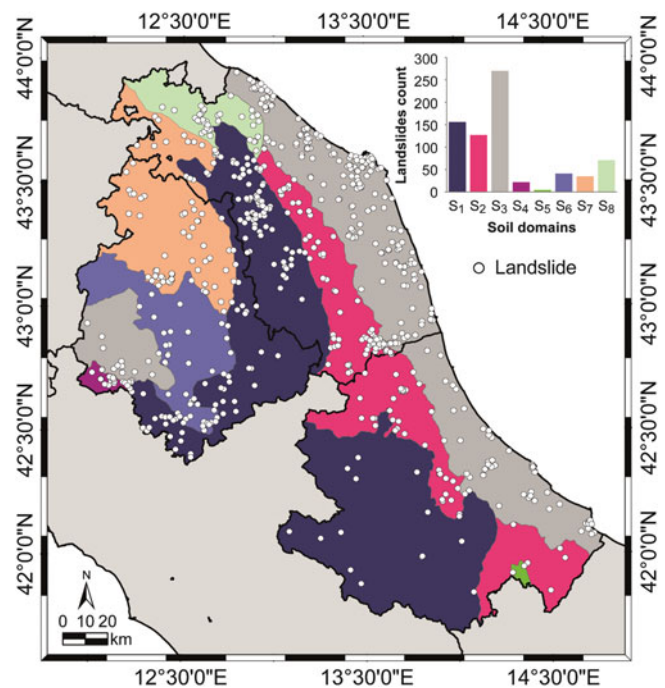


Fig. 5 Simplified pedological division of the study area (from S₁, to S₈). White dots show location of rainfall-induced landslides. Histogram shows number of landslides in each soil region

the study area in eight soil regions from S₁, to S₈ (Table 2, Fig. 5) and we attributed each landslide to a specific soil region. The histogram in Fig. 5 portrays the number of failures in each soil region.

We used this information to determine *ED* thresholds for three soil regions (S₁, S₂, and S₃). For the remaining soil regions, the number of events was insufficient to determine reliable thresholds.

Table 2 Soil regions identified in the study area using the synoptic map published by Costantini et al. (2004)

Code	Soil region
S ₁	16.4: Cambisol—Leptosol region with Luvisols of the central Apennine
S ₂	61.1: Cambisol—Regosol region, with Luvisols of eastern Italy
S ₃	61.3: Cambisol—Regosol region with Vertisols of central and southern Italy
S ₄	56.1: Cambisol—Andosol region with Regosols of central Italy
S ₅	59.7: Cambisol—Leptosol region with Luvisols of the southern Apennine
S ₆	64.4: Cambisol—Fluvisol region with Luvisols and Vertisols of Arno and Tevere rivers and coastal plains in central Italy
S ₇	78.1: Regosol—Cambisol region with Calcisols of the northern Apennine
S ₈	78.2: Regosol—Cambisol region with Calcisols of the middle Apennine

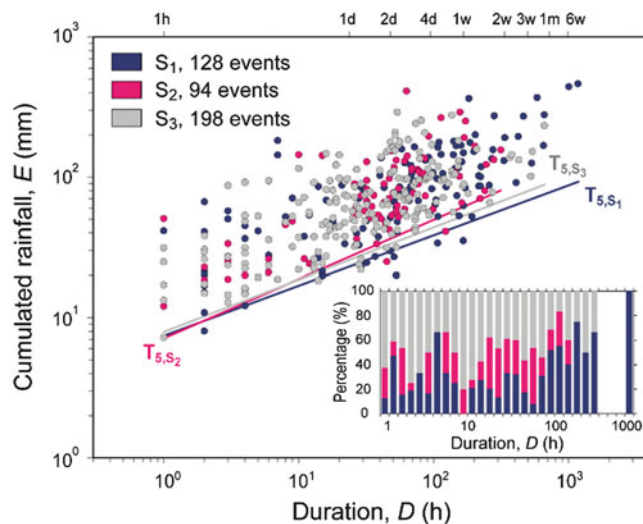


Fig. 6 Rainfall duration D (x -axis) and cumulated event rainfall E (y -axis) conditions that have triggered landslides in S_1 (dark blue dots), S_2 (magenta dots), and S_3 (grey dots), in the study area. Coloured lines are 5 % power law thresholds ($T_{5,S1}$, $T_{5,S2}$, $T_{5,S3}$). Data shown in logarithmic coordinates. Bar chart shows proportion of rainfall events for different rainfall durations

Figure 6 shows, in log-log scale, the ensemble of the rainfall conditions that have resulted in landslides in S_1 (128 dark blue dots), in S_2 (94 magenta dots), and in S_3 (198 grey dots) together with the 5 % ED power law thresholds $T_{5,S1}$, $T_{5,S2}$, and $T_{5,S3}$ (Table 1). Figure 6 also shows the proportion of rainfall events for different rainfall durations. Figure 7 portrays $T_{5,S1}$, $T_{5,S2}$, and $T_{5,S3}$ in linear coordinates in the range $1 \text{ h} \leq D \leq 120 \text{ h}$, with the shaded area showing the uncertainty associated with the thresholds.

Inspection of Figs. 6 and 7 reveals that $T_{5,S1}$, $T_{5,S2}$, and $T_{5,S3}$ are similar. Further inspection of Figs. 6 and 7 indicates

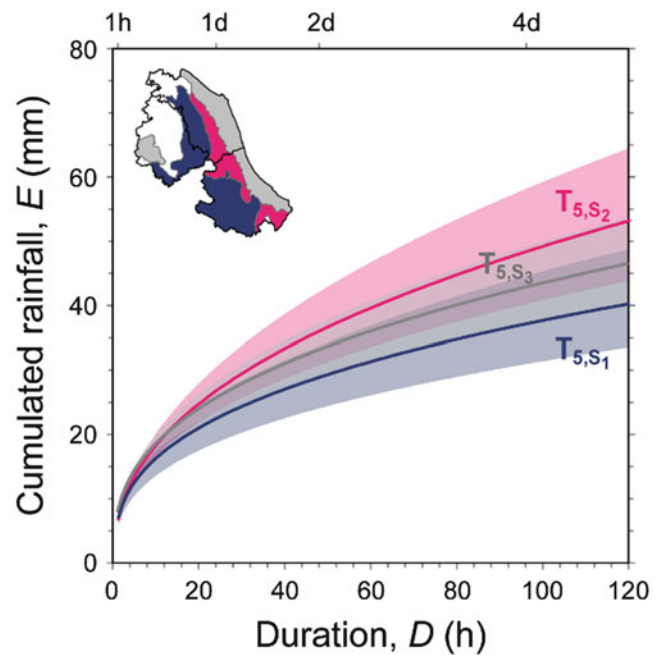


Fig. 7 Cumulated event rainfall—rainfall duration (ED) thresholds for S_1 , S_2 , and S_3 . Solid coloured lines are 5 % power law thresholds ($T_{5,S1}$, $T_{5,S2}$, $T_{5,S3}$) in linear coordinates. Shaded areas show uncertainty associated with the threshold curves

that $T_{5,S2}$ is slightly steeper and higher than $T_{5,S1}$ (i.e., their uncertainties do not overlap completely). This could mean that, increasing rainfall duration, a smaller amount of rainfall is necessary to trigger landslides in S_1 , rather than in S_2 . The trend for each soil region has to be confirmed by collecting a larger number of events.

Discussion and Conclusion

We updated an existing catalogue of rainfall events that resulted in landslides in central Italy. The final catalogue listed information on 553 rainfall events that produced 723 slope failures in the period between February 2002 and March 2011.

Peruccacci et al. (2012) investigated the relationship between lithology and rainfall thresholds in central Italy. They defined ED thresholds and their associated uncertainty for the 3 main lithological domains: post-orogenic sediments PO, flysch deposits FD, and carbonate rocks CC, $T_{5,PO}$, $T_{5,FD}$ and $T_{5,CC}$, respectively (Table 1). In the study area, they found that: (1) threshold for flysch terrain was definitively higher than those for post-orogenic and carbonate sediments, and (2) thresholds for post-orogenic sediments and for carbonate rocks were statistically indistinguishable.

To investigate the influence of other environmental factors on the rainfall conditions responsible for shallow failures in the same study area, we segmented the

catalogue of rainfall event with landslides on topography and soil regions to determined objective cumulated event rainfall—rainfall duration (*ED*) thresholds in central Italy. The analysis of the segmented catalogue reveals that the differences between topographic and pedological thresholds exist but are not large, and the thresholds are substantially equivalent.

Although the size of the data set is significant (553 rainfall events with landslides), we acknowledge that it may be insufficient to identify (subtle) differences in the rainfall conditions required to initiate slope failures due to the different topographic and pedological settings.

Acknowledgments This research was conducted with funding provided by the Italian National Department of Civil Protection (DPC). DB was supported by DPC. DPC provided access to the national rainfall database used in the study. Additional rainfall information was made available by the Marche Regional Department for Civil Protection. We thank provincial fire brigades of the Marche region for providing access to their database on rainfall-induced landslides.

References

- Brunetti MT, Peruccacci S, Rossi M, Luciani S, Valigi D, Guzzetti F (2010) Rainfall thresholds for the possible occurrence of landslides in Italy. *Nat Hazards Earth Syst Sci* 10:447–458
- Costantini EAC, Urbano F, L'Abate G (2004) Soil regions of Italy. http://www.soilmaps.it/download/csi-BrochureSR_a4.pdf. Last accessed 7 Aug 2013
- Guzzetti F, Reichenbach R (1994) Towards a definition of topographic divisions for Italy. *Geomorphology* 11:57–74
- Guzzetti F, Peruccacci S, Rossi M, Stark CP (2007) Rainfall thresholds for the initiation of landslides in central and southern Europe. *Meteorol Atmos Phys* 98:239–267
- Guzzetti F, Peruccacci S, Rossi M, Stark CP (2008) The rainfall intensity-duration control of shallow landslides and debris flows: an update. *Landslides* 5(1):3–17
- Peruccacci S, Brunetti MT, Luciani S, Vennari C, Guzzetti F (2012) Lithological and seasonal control on rainfall thresholds for the possible initiation of landslides in central Italy. *Geomorphology* 139–140:79–90. doi:10.1016/j.geomorph.2011.10.005



Catastrophic Landslide in Nižná Myšľa Village (Eastern Slovakia)

L'ubomír Petro, Vlasta Jánová, Andrej Žilka, Peter Ondrejka, Pavel Liščák, and Dominik Balík

Abstract

Landslides belong to the most significant geodynamic phenomena in the Slovak Republic. According to the recent data more than 21,190 slope failures (mostly landslides) have been registered in the Slovak part of the Western Carpathians. They cover an area of 2,576 km² which represent 5.25 % of the total area of Slovakia. The landslides are concentrated especially in the Flysch and Neovolcanic regions. In May and June 2010 extraordinary rainfalls induced a lot of slope failures in some regions of Slovakia. More than 550 newly evolved landslides were registered especially in the Eastern Slovakia. The most disastrous landslide occurred in the Nižná Myšľa Village in the 4th June 2010. Amidst the village the local infrastructure (roads, gas and water pipelines, wells) and 40 houses were damaged. Twenty nine of them had to be demolished and several others became uninhabitable. Fortunately nobody was injured or died. After the Handlová landslide (1960–1961) it was the 2nd biggest one in Slovakia as concerns damages. The geological conditions of the area are prone for landsliding. The slopes at the western part of village are built by the Neogene high plastic clays with tuff and sand intercalations. The clays are sensitive to swelling and shrinking. The extreme rainfalls (250 mm/month) can be considered as the main triggering factor of sliding. After the landslide event the emergency state had been declared and the engineering geological survey started in June 2010. During the first stage of remedial works the middle part of village was stabilized. Currently, the whole landslide area is permanently monitored geodetically and by set of piezometric and inclinometric boreholes. The second stage of stabilization is in preparation. All the geological works at the landslide are coordinated by the Ministry of the Environment of the Slovak Republic and financed by the Slovak Government.

Keywords

Catastrophic landslide • Heavy rainfalls • Nižná Myšľa Village (Slovakia)

L'. Petro (✉)

State Geological Institute of Dionýz Štúr, Jesenského 8, 040 22 Košice, Slovak Republic

e-mail: lubomir.petro@geology.sk

V. Jánová

Ministry of the Environment of Slovak Republic, Nám. L'. Štúra 1, 812 35 Bratislava, Slovak Republic

e-mail: vlasta.janova@enviro.gov.sk

A. Žilka • P. Ondrejka • P. Liščák • D. Balík

State Geological Institute of Dionýz Štúr, Mlynská dolina 1, 817 04 Bratislava, Slovak Republic

e-mail: andrej.zilka@geology.sk; peter.ondrejka@geology.sk; pavel.liscak@geology.sk; dominik.balik@geology.sk

Introduction

Slope movements belong to the most significant geodynamic phenomena in the Slovak Republic (Western Carpathians). According to the recent data (Kopecký et al. 2008) more than 21,190 slope failures (mostly landslides) have been registered in the Slovak part of the Western Carpathians. They cover an area of 2,576 km² which represent 5.25 % of the total area of Slovakia. The landslides are concentrated especially in the Flysch regions of external parts (Externides),

intra-mountain basins and tectonic depressions (Internides) of the Western Carpathians as well as in the regions built by the Neogene volcanic and sedimentary rocks.

A systematic inventory of landslides in Slovakia started after the Handlová landslide disaster in 1960–1961 (Záruba and Mencl 1982); it comprised three stages and was completed in 1991. Registry of landslides records and database creation were the main aim of the inventory. In 2006 the *Atlas of slope stability maps* of the whole territory of Slovakia at the scale 1:50,000 was prepared by a wide working team of experts from several institutions (Šimeková et al. 2006). The maps summarize results of nearly 50-year regional research in the field of slope failures.

This contribution deals with the second most catastrophic landslide in the history of Slovakia (Czechoslovakia). This study includes the results of engineering geological investigation, remedial measures and monitoring.

Geomorphology and Climatic Conditions

The Nižná Myšľa landslide is located in the southernmost part of the Košice Depression which lies in the eastern part of the Slovak Republic. The depression is located between the Slovak Ore Mts. (SGR) and Slanské vrchy Mts. (Fig. 1). The study area belongs to the Košice – Lučenec Depression and creates a part of the Western Carpathians province (Mazúr and Lukniš in Miklos et al. 2002).

The recent morphology of the Košice Depression reflects the lithology of the region and the geodynamic processes of the last geological periods (Late Neogene and Quaternary). In its southernmost part it is possible to recognize the flat relief of the river plains and terraces, alluvial fans as well as a couple of N-S oriented hilly ridges (Viničná and Varhaňovce) separated by the Hornád, Torysa and Olšava rivers. The relief energy of both ridges is low (differences between valley bottoms and ridges do not exceed 200–250 m) with the altitude up to the 500 m a.s.l. The average slope angle ranges from 5° to 12°. The erosion and slope movements are the most frequent geodynamic phenomena of this area. Numerous gullies and landslides can be found on slopes.

The relief of the adjacent mountains has a character of highlands with altitudes up to 1,000–1,200 m. The slopes on the right side of the Hornád Valley (Slovak Ore Mts.) are built of Palaeozoic rocks and usually have the inclination ranging from 6° to 21°. Erosion and slope movements are not very often. On the other hand the slopes at the left side of the Košice Depression are built by Neogene and Quaternary volcanic and sedimentary rocks (Fig. 2) and are very susceptible to erosion and sliding. A lot of gullies as well as slope failures (landslides, creep, lateral spreads etc.) can be found in these slopes.

The studied region has a typical warm continental climate with 50 or more summer days annually in average (with daily

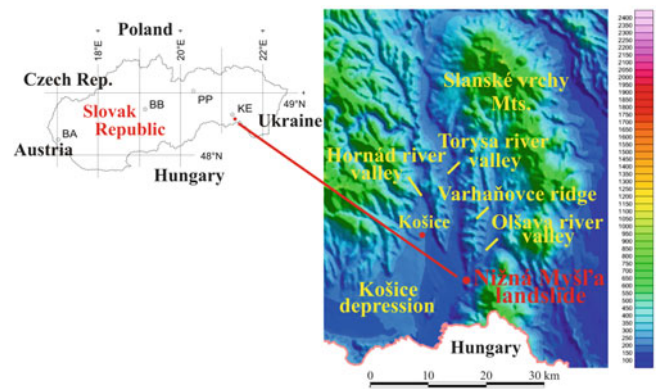


Fig. 1 Digital terrain model of the Eastern part of the Slovak Republic (Western Carpathians) with position of the Nižná Myšľa landslide and adjacent geomorphological units

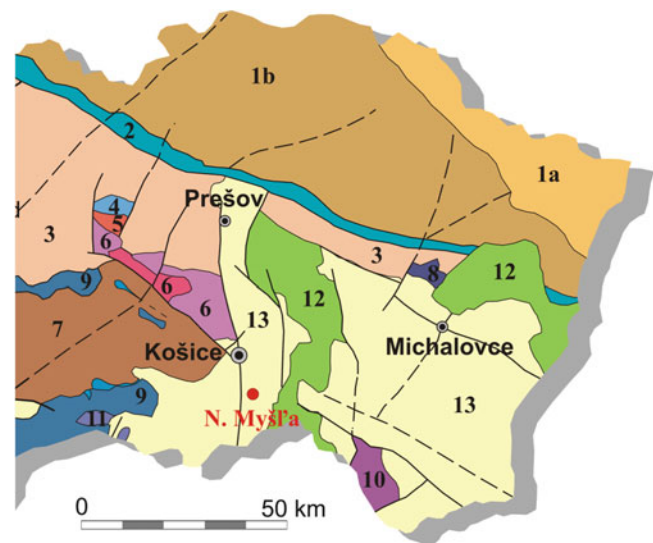


Fig. 2 Tectonic map of the Eastern part of the Western Carpathians with location of Nižná Myšľa landslide. (1) Carpathian Flysch Belt (a—Dukla unit, b—Magura unit), (2) Pieniny Klippen Belt, (3) Inner Carpathians Palaeogene, (4) Hronicum, (5) Tatricum, (6) Veporicum, (7) Gemicum, (8) Fatricum, (9) Silicikum, (10) Zemplinicum, (11) Turnaicum, (12) Neogene volcanics, (13) Neogene backarc basins and Quaternary rocks (adapted from Lexa et al. 2000)

maximum air temperature $\geq 25^\circ\text{C}$). Average yearly air temperature is $\geq 8^\circ\text{C}$, mean temperatures in January are between -3° and -4°C ., in July between 19° and 20°C (Šťastný et al. in Miklos et al. 2002), mean annual precipitation does not exceed 600 mm (Faško and Šťastný in Miklos et al. 2002).

Geological Settings

The Košice Depression is located at the eastern part of Slovakia (Western Carpathians). From the geotectonic point of view it represents the western part of the Neogene

Eastern Slovakian (Transcarpathian) Basin which has all features of typical pull-apart basin (Vass in Rakús, 1998). The depression is filled by the Neogene sedimentary rocks ranging in age from the Karpatian to Pannonian as well as by the volcanic rocks of Sarmatian to Early Pannonian (Fig. 2). The molasse sediments (marine, deltaic and lacustrine-fluvial) belong to the following formations—*Kladzany*, *Klčovo*, *Stretava*, *Kochanovce* and *Sečovce* (Karoli in Kaličiak et al. 1996). The prevailing lithologies include clay and claystone with sand and gravel intercalations, silt and siltstone, gravel, sand, as well as rhyolite and pumice tuff and tuffite. Volcanic rocks (andesites, rhyolites, volcanoclastics) create the eastern border of the Košice Depression and belong to several stratovolcanoes (Kaličiak et al. 1996). In the vicinity of Nižná Myšľa occurs the andesite stratovolcano Bradlo.

Pre-Tertiary (Palaeozoic and Mesozoic) rocks of different lithology (gneiss, migmatite, phyllite, diabase, keratophyre, rhyolite, dacite, tuff, tuffite, granodiorite, magnesite, amphibolite, breccia, conglomerate, sandstone, shale, quartzite, limestone, dolomite) of the *Veporicum* and *Hronicum* units occur at the western part of the Košice Depression (Grecula et al. 2009).

The southernmost part of the N-S oriented Varhaňovce ridge, where the Nižná Myšľa catastrophic landslide is located (Fig. 1) is built of gray silty and calcareous clays and siltstones with intercalations of redeposited rhyolite tuffs and tuffites (Karoli in Kaličiak et al. 1996). These rocks are covered by deluvial clays with angular fragments of weathered tuffs and siltstones (up to 10–15 %) and locally also by fills up to 2 m thickness. The ridge separates alluvial plains of Hornád and Olšava rivers. Both plains are formed by a several meters thick layer of the Quaternary gravels with clay cover.

The fault system of N-S orientation has played a very important role by forming of the Košice Depression. One fault is running through the Hornád river valley and is connected with seismic activity of the Košice area. At the eastern part of the Košice town the earthquake with macroseismic observed intensity of 7° EMS-98 (European Macroseismic Scale) was recorded in 1676 (Procházková et al. 1978).

Landslide History and Feature

First problems with slope stability in the Nižná Myšľa appeared near local cemetery in 1984 (Ondrejka 1984). A systematic study of the area was performed during the 3rd stage of slope failures inventory in Slovakia by the Geological Institute of Dionýz Štúr between 1985 and 1991 (Spišák in Modlitba et al. 1991) as well as during geological mapping of the Košice Depression and Slanské vrchy Mts.

(Spišák and Petro in Kaličiak et al. 1991). The main features of Nižná Myšľa dormant landslide were described in the *Registration form of landslides and other dangerous slope failures* and became a part of landslide database stored in Geofond (Central geological archive in Bratislava). The study area was evaluated from the viewpoint of slope stability in the frame of project entitled *Set of engineering geological maps of the environment of the Košice Depression and Slanské vrchy Mts.* (Petro et al. 1993). The main types of slope failures in the Košice Depression and Slanské vrchy Mts. (including the Nižná Myšľa landslide) were described by Petro and Spišák (1994). Area of Nižná Myšľa was also studied in the scope of the *Atlas of slope stability maps* (Šimeková et al. 2006).

The Nižná Myšľa slope failure was described as dormant landslide with several earth blocks inclined downslope below the main scarp just in the central part of the village (Spišák in Modlitba et al. 1991). The size of blocks did not exceed 40–80 m. Dimensions of this complex landslide were 410 m (length) and 1,810 m (width). Relief of landslide was undulate, in upper part lifted (blocks). The slope oriented to the NW/WNW (southern and central part of the landslide) and to the W (northern part of the landslide), has average gradient between 6° and 7°. The height of striking and uneven main scarp was about 5–7 m. The concave toe at some parts achieved the height of about 5–6 m. According to the landslide morphology the depth of basal slip surface was estimated between 12 and 15 m. The velocity of mass movement was assumed to several cm per year. Damages of buildings and engineering nets had not been recognised in the 90s of the previous century.

Excessive precipitation occurred in Slovak territory during May and June 2010. In some regions the mean monthly precipitation exceeded three or four times the normal values. Besides serious floods a lot of slope failures (mainly landslides) have also been generated primarily in the Flysch regions of Eastern Slovakia. More than 550 failures were registered up to the end of October 2010 (Liščák et al. 2010). The Nižná Myšľa landslide started early morning on 4th June 2010 just after heavy rainfalls. Normal mean monthly precipitations in May and July (period 2005–2009) at the nearest ombrometric station (Vyšný Čaj) were 63 and 83 mm, respectively. However, in the same months in 2010, precipitation values were recorded as 229.7 and 113.7 mm, respectively. The majority of rainfalls were concentrated in the 2nd week of May and 1st week of June (Pecho et al. 2010).

Three active landslides originated within the former dormant one (Fig. 3). The biggest landslide appeared in the southern part of the village and damaged 40 houses, local roads, water and gas pipelines, sewage and electrical lines. About hundred people were evacuated, but fortunately none of them was injured. Up to now 29 houses had to be

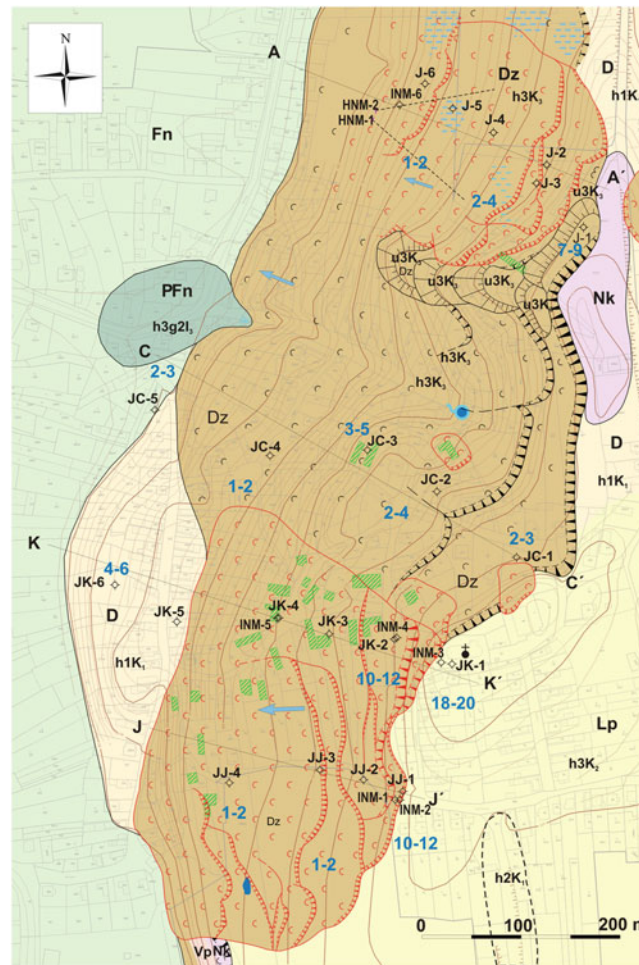


Fig. 3 Engineering geological zoning map of the Nižná Myšľa with delineation of active (*red contours*) and dormant (*black contours*) landslides, position of cross sections, piezometric (J-1–J-6, JC-1–JC-6, JK-1–JK-6, JJ-1–JJ-4), inclinometric (INM-1–INM-6) and subhorizontal dewatering (HNM-1–HNM-6) boreholes, depth of groundwater tables, wet areas and springs, direction of groundwater flow, damaged structures (*green contours*) and main genetic-

lithological units (zones)—Fn—Hornád river flood plain sediments, D—deluvial clayey soils (local with clastic rocks), Dz—sliding sediments (Quaternary and Neogene clays with tuff/tuffite intercalations and fragments), PFn—alluvial fan sediments on the flood plain, Lp—loess-like sediments (clays), Nk—Neogene clayey-gravelly sediments, Vp—Neogene tuffs and tuffites (adapted after Tometz et al. 2010)

demolished because of the strong damage. Some people and their properties were evacuated with the help of army. Major part of Nižná Myšľa was declared as emergency area. In cooperation with the Ministry of Environment of the Slovak Republic (MoE SR), preparation of the investigation and remedial works were started. Based on the sustained damages the landslide is considered as the second worst catastrophic slope failure in Slovakia, after the Handlová catastrophic landslide in 1960–1961 (Záruba and Mencl 1982).

Engineering Geological Investigation

The first stage of the landslide area investigation started immediately after the catastrophe and continued till October 2010. The geological, geophysical and geodetic works were

focused in recognition of engineering geological conditions, determination of soil parameters and slope stability calculations. A set of 23 piezometric, 6 inclinometric and a couple of subhorizontal dewatering boreholes were installed along several profiles across the landslides (Fig. 3). The boreholes were equipped for monitoring purposes. Laboratory tests of soils revealed that sliding slopes are mainly built of high plasticity clays (CH), of less stiff consistency, and sandy clays (CS) of stiff consistency and medium plasticity clays (CI) of stiff consistency. Strongly weathered tuffs and tuffites represent about 10 % and sandy soils (S-F, SC) at 6 % of the moving mass.

The boreholes confirmed the depth of slip surfaces in active landslide at 20 m (Fig. 4) depth.

Investigation also revealed the main causes of sliding. Among natural ones dominate favourable geological setting

of slope (high plasticity clays with montmorillonite interacted by tuff/tuffite conformable with slope), morphological position (slope inclination between 4° and 15° , steep upper and bottom parts of slope, 29° – 40°), hydrogeological conditions (seepage of groundwater from detritic volcanoclastic beds to lower parts of slope, locally confined groundwater level) and climate (heavy rainfalls). During the neotectonic evolution (Pliocene–Quaternary period) the Varhaňovce ridge has been uplifted. By this way the permeable tuff/tuffite layers were elevated to the higher slope position and uncovered by erosion. The uplift of the ridge seems to be recent (Janočko in Karoli et al. 1998). For tectonic and seismic activity of the area (intensity $\leq 7^\circ$ EMS-98) the N-S oriented faults belonging to the Hornád fault system are responsible. One of them is running along the western ridge foot. Among the anthropogenic causes, uncontrolled overloading of slopes by structures, unsuitable engineering practice (unstabilized cuts), poor surface drainage of rainwater and insufficient legislation (Building Law No. 50/1976) are the main. The heavy rainfalls at the beginning of June 2010 represent the main triggering factor of the landslide.

Remedial Measures

After the results and recommendations of implemented investigation the 1st phase of remediation design was prepared. The design comprised a supplementary engineering geological investigation. All the works have been performed by the private company as a winner of public procurement (according to valid Slovak legislation) and financed from the Environmental Fund (State Budget). The Division of geology and natural resources of the MoE SR as a guarantee of the works ensured an independent company for inspection of all activities. A set of 63 boreholes up to the depth of 5–25 m located in 5 new profiles were performed mainly in the most damaged part of the village (Fig. 3) in 2011. Some of these boreholes (43) were equipped for groundwater level measurement; another (17) were coupled by inclinometric casings. In hardly accessible places the dynamic penetration tests (15) were conducted. A complex evaluation of engineering geological, geotechnical and hydrogeological conditions as well as stability of sliding area confirmed its complicated geotectonical setting, the rock mass heterogeneity and mechanism of slope failures.

Based on data obtained from the first and supplementary investigations the set of remedial measures was implemented in the southern part of the village (area to the S of the municipal office) in 2012. The project of remedial measures comprised:

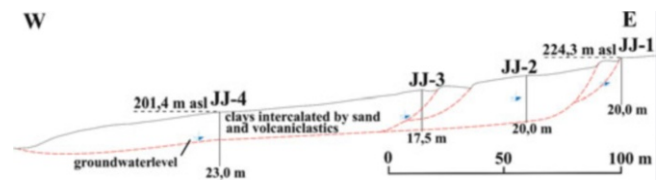


Fig. 4 Simplified cross section J–J' located in the central part of southern active landslide in the Nižná Myšľa Village. The pattern, course and depth of slip surfaces, complicated relief and antithetic earth blocks (adapted after Tometz et al. 2010) are evident from the figure

- Anchored pile walls beneath the St. Matthew Church (Fig. 5) and at the Small and Big German streets (piles of 600 mm in diameter up to 10–13 m depth, anchors of 25 m length with inclination 25° – 35°);
- Deep dewatering of the area (25 subhorizontal boreholes of 55–100 m length drilled from 7 sites, gravel dewatering wall consisting of boreholes of 9.5–10.0 m depth along the Hlboká street);
- Near-surface dewatering of the area (main drain rib along the Repiská street, set of drain ribs of 1–5 m depth under the church);
- Several anchored pile walls (41 piles of 600 mm in diameter up to 10–11 m depth enforced by the 13 tension micropiles up to 15 m depth with inclination of 30°) connected by micropile wall (a few 8 + 8 micropiles up to 10 m depth) for rehabilitation of the municipal office and culture house;
- Finishing works comprise field engineering (filling the depressions and open cracks, elimination of elevations, greening), construction of gabions and reinforcement of pavements (Fig. 6).

Monitoring Results

Systematic monitoring of the Nižná Myšľa landslide started immediately after finishing the first and supplementary investigation, it means since the end of 2010 and the beginning of 2012. Selected piezometric, inclinometric as well as subhorizontal dewatering holes were incorporated into the local monitoring network. The first set of measurements showed a drop in the groundwater table levels and decreased yield of dewatering boreholes. Any significant mass movements or static failures inside the habitable and other type of houses have not been registered in the central part of the village stabilized by remedial measures so far. The inclinometer measurements (21 monitoring bore holes) revealed sliding activity in all non-stabilized parts of the village. Displacements ranging from 0.3 to 4.5 cm at depths between 10 and 16 m have been detected so far (Fig. 7).



Fig. 5 View from the *bottom* to the St. Mathew church in the central part of Nižná Myšľa Village and to local road damaged by the landslide (*left*) as well as to bolted pile wall under construction (Photo: L'. Petro, 4th June 2010/24th November 2011)



Fig. 6 Panoramic view of the central part of the Nižná Myšľa Village destroyed by the catastrophic landslide on 4th June 2010 and the same area after remedial measures (Photo: L'. Petro)

According to these results, in the areas around local school and below the cemetery as well as in the southern part of the village, the supplementary remedial measures will be inevitable.

Conclusion

Regarding the material damages and endangering people, the Nižná Myšľa landslide is designated as the catastrophic one. Fortunately the casualties have not been registered. People from the damaged houses were partially compensated from the State Budget, insurance companies as well as from the foundation, People in Peril Association Slovakia. Thanks to the great effort of the Division of geology and natural resources (MoE SR) as the guarantee of all geological works, the local municipality and geologists from private companies and the State Geological Institute of D. Štúr, the most dangerous parts of the active landslide have been stabilized. This fact is also confirmed by the results obtained from the

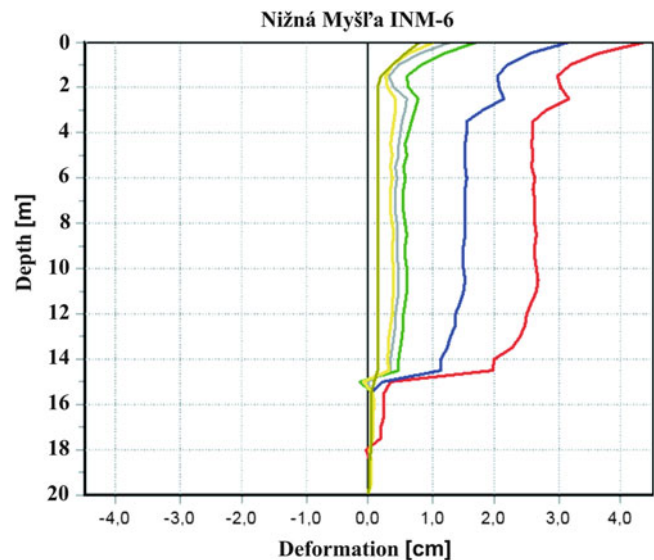


Fig. 7 Results of inclinometer measurements in the INM-6 borehole located in the central part of the Nižná Myšľa Village (above local basic school) since October 2010

local monitoring network. Current inclinometer measurements have shown the ongoing sliding activity in non-stabilized parts of the village. For this reason the supplementary remedial measures will be inevitable.

References

- Grecula P, Kobulský J, Gazdačko L', Németh Z, Hraško L', Novotný L, Maglay J (2009) Geologická mapa Spišského Rudohoria 1:50000. Publ. MŽP SR, Bratislava
- Kaličiak M, Baňacký V, Jacko S, Janočko J, Karoli S, Molnár J, Petro L', Spišák Z, Vozár J, Žec B (1991) Geological map of the Slanské vrchy Mts. and Košice depression—northern part 1:50000. Publ. GÚDŠ, Bratislava
- Kaličiak M, Baňacký V, Janočko J, Karoli S, Petro L', Spišák Z, Vozár J, Žec B, Ivanička J, Vass D (1996) Geological map of the Slanské vrchy Mts. and Košice depression—southern part 1:50000. Publ. GS SR, Bratislava
- Karoli S, Jacko S, Janočko J, Németh Z, Návesňák D, Grecula M (1998) Geologická a tektonická mapa 1:25000. In: Hricko J et al. (eds) "Košice - abiotická zložka životného prostredia". Final Report, GS SR, Košice, 58p
- Kopecký M, Martinčeková T, Šimeková J, Ondrášik M (2008) Atlas zosuvov—výsledky riešenia geologickej úlohy. In: Proc. "Geológia a životné prostredie", Bratislava (18.–19. 9. 2008). Publ. D. Štúra, Bratislava, 105–110
- Lexa J, Bezák V, Elečko M, Mello J, Polák M, Potfaj M, Vozár J, Schnabel G W, Pálenský P, Császár G, Rylko W, Mackiv B (2000) Geological map of Western Carpathians and adjacent areas. MoE SR and Geological Survey of Slovak Republic, Bratislava. ISBN 80-88974-01-1
- Liščák P, Pauditš P, Petro L', Iglárová L', Ondrejka P, Dananaj I, Brček M, Baráth I, Vlačiky M, Németh Z, Záhorová L', Antalík M, Repčiak M, Drotár D (2010) Registration and evaluation of newly evolved slope failures in 2010 in Prešov and Košice regions. Miner Slov 42(2):393–406

- Miklos L et al (2002) Landscape Atlas of the Slovak Republic. The MoE of the Slovak Republic, Bratislava and Slovak Environmental Agency, Banská Bystrica, 344p. ISBN 80-88833-27-2
- Modlitba I, Jánová V, Kováčik M, Krippel M, Liščák P, Petro L', Spišák Z, Vančíková I, Iglárová L', Lobík M, Šarík M, Ondrášik M (1991) Výsledky registrácie svahových deformácií na území Slovenska v roku 1991. Publ. ŠGÚDŠ Bratislava, 57–62
- Ondrejka J (1984) Nižná Myšľa—cintorín—zosuv, inžinierskogeologický prieskum. Technical Report, ÚGV FBERG TU, Košice, 12p
- Pecho J, Faško P, Lapin M, Kajaba P, Mikulová K, Šťastný P (2010) Extrémne atmosférické zrážky na jar a na začiatku leta 2010 na Slovensku. Meteorol. časopis, 13, 69–80
- Petro L', Spišák Z, Polaščinová E (1993) Súbor inžinierskogeologických máp 1:50000. In "Súbor regionálnych máp geofaktorov životného prostredia 1:50000 regiónu Košická kotlina a Slanské vrchy". Publ. MŽP SR, Bratislava
- Petro L, Spisak Z (1994) Slope deformations in the area of Košická kotlina Basin and Slanské vrchy mountains (Eastern Slovakia). In: Balkema AA (ed) Proceedings of the 7th international congress IAEG, Lisboa, Rotterdam, pp 1585–1590
- Procházková D, Brouček I, Guterch B, Lewandowska-Marciniak H (1978) Map and list of the maximum observed macroseismic intensities in Czechoslovakia and Poland. Publications of the Institute of Geophysics of the Polish Academy of Science, vol B-3(122), pp 3–75
- Šimeková J, Martinčeková T, Abrahám P, Baliak F, Caudt L, Gejdoš T, Grenčíková A, Grman D, Hrašna M., Jadroň D, Kopecký M, Kotrčová E, Liščák P, Malgot J, Masný M, Mokrá M, Petro L', Polaščinová E, Rusnák M, Sluka V, Solčiansky R, Wanieková D, Záthurecký A, Žabková E (2006) Atlas máp stability svahov Slovenskej republiky 1:50 000. Publ. MŽP SR Bratislava
- Tometz L, Blišťan P, Harabinová S, Leššo J, Nyárhidy J, Turovský F (2010) Nižná Myšľa – havarijný zosuv, inžinierskogeologický prieskum. Final technical report. Publ. MPŽPaRR SR, Bratislava, pp 1–59
- Vass D (1998) Neogene geodynamic development of the Carpathian arc and associated basins. Geological survey of Slovak Republic, pp 155–188
- Záruba Q, Mencl J (1982) Landslides and their control (Developments in geotechnical engineering, Vol. 31.). Academia, Publ. House of the Czech. Academy of Sciences, Prague, pp 83–94



Effect of Rainfall and Building Construction on a Marginal Slope in Triggering Landslide

Binod Tiwari and Sneha Upadhyaya

Abstract

With an increase in urban population, lands that have been considered marginal for housing development are being utilized for construction of buildings in order to accommodate the increased population. This trend is significantly increasing in the capital city of Kathmandu, Nepal. Utilization of marginally stable lands such as river bank, steep slope, and foot of mountain frequently trigger landslides. This study presents a case study pertinent to the recent collapse of a building that was constructed within a steep slope located close to a river bank. The field visit, geotechnical investigation and pertinent slope stability as well as deformation analysis shows that rise in water table due to continuous rainfall triggered the landslide. Moreover, construction of house within the marginally stable slope contributed in triggering the landslide.

Keywords

Landslides • Rainfall • Limit equilibrium analysis • Strength reduction factor • Geotechnical investigation • Fully softened shear strength

Background

Landslides cause a significant annual loss of lives and properties throughout the world. Although there are several triggering factors associated with landslides, these factors can be broadly divided into two—natural and anthropogenic. Rainfall, earthquake, snow melt, etc. are some of the natural triggering factors. Likewise, unplanned construction practice, encroachment of marginal land for cultivation, unmanaged infrastructure development and building construction, deforestation, excessive use of blasting in road construction, poor drainage/water management, etc. are some of the anthropogenic factors. While it is not possible to control natural factors, understanding potential consequences of those factors and paying attention to likely occurrence of

the extreme events can help in avoiding disasters associated with the landslides triggered by natural factors. However, paying proper attention and implementing proper land use regulation and practice can significantly help in reducing the impacts of landslides triggered by anthropogenic factors.

To accommodate the increasing population in urban area, marginally stable lands are being utilized for agriculture, highway construction and construction of buildings. Moreover, due to a drastic increase in the price of land in urban areas of developing countries, residential areas have been expanded to the banks of river and marginally stable slopes. Such developments are frequently triggering landslides and causing loss of lives and properties. Examples of such unplanned urban development have been evidenced in Kathmandu, the capital of Nepal for more decades. The population of Nepal in 2011 was reported as 26.5 million, which resulted in an annual growth of 1.35 % from 2001 (CBS 2011). The population of greater Kathmandu Valley that includes three major cities and associated villages, in 2011, was 2.5 million, which was close to 10 % of the national population. This shows an annual growth of 3.6 %, which is

B. Tiwari (✉) • S. Upadhyaya
Department of Civil and Environmental Engineering, California State University Fullerton, 800N State College Blvd., Fullerton, CA 92831, USA
e-mail: btiwari@fullerton.edu; upadhyayasneha@csu.fullerton.edu



Fig. 1 Location Map of the study area

approximately three times the national growth rate. The population density of Kathmandu Valley is approximately 2,800 persons per square kilometre. The second largest city, Pokhara, has one tenth of the population of the greater Kathmandu. According to a survey, average annual increase in the land price in the past 10 years is approximately 30 %. This increase in population and land price resulted in an increasing utilization of marginally stable lands for building construction. The aerial photo interpretation in the past three decades clearly shows that construction along the river banks has increased significantly. This can be attributed to both population growth and the rise in land price.

As the marginal lands have been increasingly encroached, potential of natural disasters such as landslides is also increasing in Kathmandu. Number of landslide disasters and losses due to those landslides are increasing annually. This paper describes a case study of a landslide that occurred in September, 2012. The landslide caused a direct loss of a building and temporarily dammed a river. However, the debris mass and change in topography after the occurrence of landslide is currently threatening hundreds of buildings, several hectares of land, several kilometres of roads, and several bridges. This study mainly focuses on the post-landslide geotechnical investigation report and pertinent slope stability analysis results.

Details of the Landslide

The landslide is located in ward no. 5 of Tinthana Village Development Committee (VDC), which is close to the border of Kirtipur Municipality. Presented in Fig. 1 is the

location map of the landslide. As can be observed in Fig. 1, the location is close to Prithwi/ Tribhuwan Highway of Nepal, which is the only road to connect Kathmandu with western part of the country. There is an increasing demand of land to build houses within 10 km radius outside the Kathmandu Ring Road. This location lies within approximately 1 km of the ring road.

The landslide occurred around 1:00 am on September 18, 2012. A house that was located at the center of the landslide area was displaced by approximately 20 m. As the foundation of the house was much shallower than the depth of sliding plane, the house was displaced as a block; that caused relatively less structural damage to the house. According to the interview taken with the residents of the building, the residents did not notice until 3:00 am that the house was displaced. The house was constructed less than 2 years prior to the landslide event. Shown in Fig. 2 is the aerial photograph of the landslide obtained from the Google Earth, taken in March 2, 2013. As can be observed in Fig. 2, the landslide completely blocked the river that is located below the landslide. This river is a major tributary of the Bagmati River, one of the major rivers in Nepal. Length of the landslide (including the toe of the slid mass) is approximately 130 m. Average width of the landslide is approximately 80 m. The data collected during the field visit shows that the length of actual slide was approximately 40 m and the slid mass travelled a distance of 90 m in a gentler slope. As can be observed in Fig. 2, the landslide completely blocked approximately 50 m length of the stream. Fortunately, the river changed the course afterwards and landslide damming did not cause a serious damage. The landslide area is located approximately 60 m away from a major bridge (Fig. 2); therefore, damming and



Fig. 2 Google Earth photograph of the landslide



Fig. 4 Main scarp of the landslide



Fig. 3 Overall view of the landslide area



Fig. 5 A view of the side scarp of the landslide

breakage of the stream could wash away the bridge. The bridge is constructed on a road that connects the local area with two major roads—Salyanthan Road that goes to Kirtipur Town and Tribhuvan/Prithivi Highway, which is a major highway that connects Kathmandu with the western side of the country. As can be observed in Fig. 2, several landslide topographies can be identified along the bank of the river. However, several buildings have been constructed in the area ignoring this fact.

Presented in Fig. 3 is the overall view of the landslide area observed from the main scarp. Position of the building prior to and after the landslide event is shown in the figure. Also presented in the figure is the river that was blocked by the landslide as well as the location of the bridge. Please note that a house that can be observed on the left side of Fig. 3 is a boundary of the landslide; therefore the house was not affected. This house can be observed in Fig. 2 as well.

Main scarp of the landslide is presented in Fig. 4. There are several existing buildings located above the main scarp (as can be seen in Fig. 4). These buildings were not affected with the current landslide. However, as the topography has been drastically changed, all of these buildings are threatened by the extension of the existing landslide. Fig. 5 presents a side scarp of the landslide. As can be observed in Fig. 5, there are several expensive houses that have potential to be affected by the extension of the current landslide.

Field Investigation

Field investigation was conducted two weeks after the landslide event. As can be observed in Fig. 6, the house that was displaced by the landslide mass was structurally damaged below the first floor although the second floor was intact. Columns and walls were broken. Likewise, the well that was



Fig. 6 Damage to the house that was swept away by the landslide

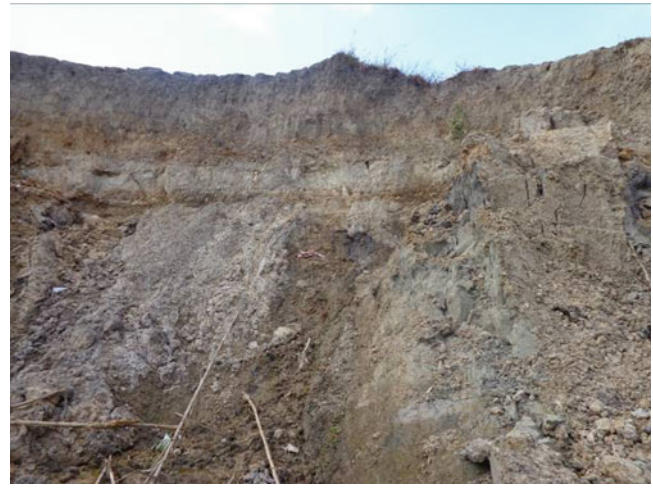


Fig. 8 Exposed spring waters coming out of landslide area



Fig. 7 Natural blocking of the river with landslide debris resulted in reduction of the river width



Fig. 9 Exposed slickensides observed throughout the landslide area

constructed at a side of the building was uplifted by more than 50 cm. The slid mass was distributed throughout the area up to the river. The river was completely blocked. Shown in Fig. 7 is the photograph of the river that was partially blocked. The width of the river reduced to one third of the original width after the landslide (Fig. 7). During the field visit, several natural springs were observed throughout the slope. An example of these locations is presented in Fig. 8. These springs and the water table observed in a well located near the landslide area was helpful to estimate the position of water table during the landslide, which was utilized during the slope stability analysis. The field investigation revealed several slickensides, mainly near the main scarp. Presented in Fig. 9 is an example of those slickensides. The slid mass was composed of a mixture of silty and clayey soils. The slickensides exposed on the

brown clayey material. Soil samples were collected from the main scarp of the landslide area as well as the landslide debris in order to investigate the geotechnical properties of soil.

A high precision total station and GPS devices were used to prepare cross-section of the landslide area. The cross-section obtained during the field investigation was utilized to conduct various deformation and slope stability analyses. Cross-section of the landslide area is presented in Fig. 10.

Soil Test and Stability Analysis Results

The soil test results revealed that the soil has the liquid limit and plasticity index of 45 and 14, respectively. Proportion of clay and silt were 25 % and 74 %, respectively. Based on the USCS classification system, the soil was classified as silt

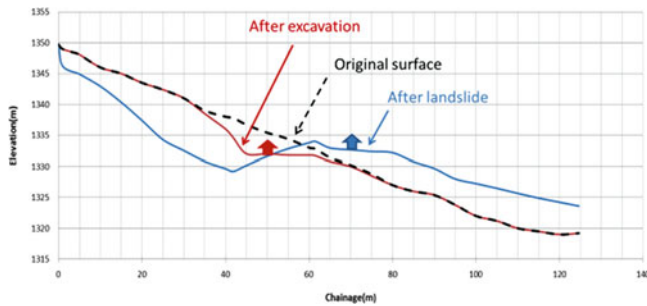


Fig. 10 Cross-section of the landslide area after the landslide event. Estimated profiles of the ground prior to building construction and after the construction of the building are also shown in the figure

(ML) material. Activity of the soil was 0.56 and the fully softened friction angle of soil was 20° . Estimated fully softened shear strength based on the values of the liquid limit, plasticity index, and activity, using the empirical correlation proposed by Tiwari and Ajmera (2011) and Mualem (1974), was 20.5° . This confirms the measured fully softened friction angle.

Presented in Fig. 10 is the cross-section of the landslide obtained from the field investigation; the estimated position of the building and the original ground profile prior to the construction of the building are also presented in Fig. 10. The lowest water table was expected to be in April and was assumed to be 4 m below the highest water table observed during the field investigation.

At first, deformation analysis was performed for the original ground prior to the construction of building using the strength reduction method. Fully softened friction angle of 20° was used for the analysis. The deformation analysis was performed using the commercially available software Phase2, version 8. (RocScience 2011). The potential depth of sliding surface was obtained from the deformation analysis. Then, factors of safety of the slope were calculated with the limit equilibrium method using the calculated sliding surface depth for numerous situations such as—(a) prior to building construction at low water table, (b) prior to building construction at high water table, (c) after the construction of building and low water table condition, and (d) after the construction of building and high water table situation. Spencer's method was used utilizing the commercially available software Slide Version 6 (RocScience 2010) for the limit equilibrium analysis. Based on the deformation analysis result, depth of sliding surface was estimated to be 18.5 m. The calculated factors of safety for the scenarios a, b, c, and d mentioned above were 1.373, 1.081, 1.372, and 0.993, respectively. This shows that although the slope was marginally stable during high water table stage prior to the construction of the building, the construction of the building have contributed in the reduction of the overall stability. The

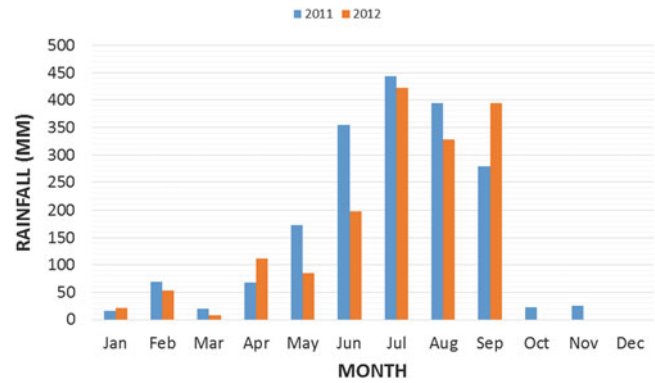


Fig. 11 Amount of monthly precipitation in 2011 and 2012, recorded at Thankot station, near the landslide area. (Source: DMG 2012)

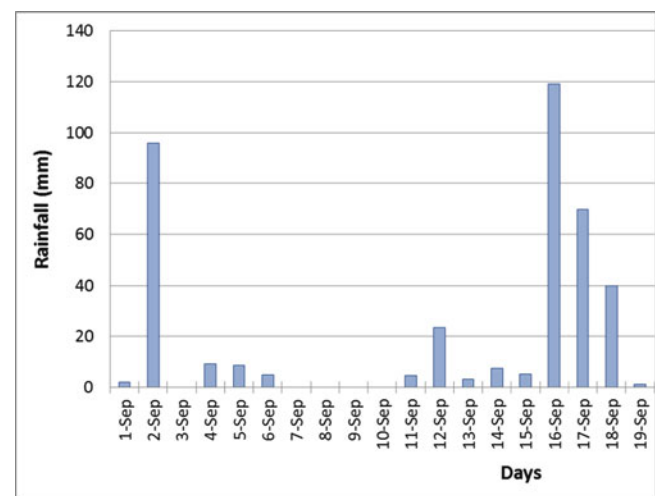


Fig. 12 Amount of precipitation 18 days prior to the landslide event (September 18, 2013) in Thankot station, near the landslide area. (Source: DMG 2012)

building did not contribute much in lowering the factor of safety compared to the the effect of rise in water table. However, it helped in reducing the safety factor further.

Amount of precipitation 3 months prior to the landslide event (i.e. 3 month antecedent rainfall) was calculated and compared with the rainfall in 2011. The rainfall pattern in 2012 was similar to that in 2011. Presented in Fig. 11 is a comparison between monthly rainfall in 2011 and 2012. Precipitation in September 2012 is much higher than that in 2011. Sudden collapse of the slope can be attributed to a rise in water table due to such increase in rainfall. However, high rainfall with daily precipitations ranging from 40 to 120 mm was observed for 3 days prior to the landslide event. A total 3-day precipitation exceeded 230 mm prior to the landslide event. This rainfall could have triggered the landslide. Presented in Fig. 12 is the rainfall pattern in September, 2013, prior to the landslide event.

Summary and Conclusion

Due to a significant growth in population and the land price in Kathmandu valley, slopes that are considered to be marginally stable are being utilized for building construction. As a result, the potential of landslide hazards are increasing every year. On September 18, 2013 a moderate size landslide occurred in the Tinthana VDC of Kathmandu district. The landslide displaced a house, blocked a river and threatened hundreds of houses, roads, and a bridge. The field investigation and slope stability analysis of the landslide showed that excessive rainfall reduced the safety factor of the slope below 1 and triggered the landslide. While the construction of building did not reduce the safety factor significantly, it added to the reduction in safety factor, which was already reduced to the value close to 1 due the rise in ground water table after the rainfall.

Acknowledgments The authors would like to thank the Associated Student Inc. (ASI), California State University, Fullerton, for providing financial support to purchase materials.

References

- Central Bureau of Statistics Nepal (2011) National population and housing census 2011, pp 1–270
- Department of Hydrology and Meteorology Nepal (2012) Annual rainfall inventory of Nepal
- Mualem Y (1974) A conceptual model of hysteresis. *Water Resour Res* 10(3):514–520
- RocScience Inc. (2010) Slide Version 6.0—2D limit equilibrium slope stability analysis. <http://www.rocscience.com>. Toronto, ON
- RocScience Inc. (2011) Phase2 Version 8.0—finite element analysis for excavations and slopes. <http://www.rocscience.com>. Toronto, ON
- Tiwari B, Ajmera B (2011) A new correlation relating the shear strength of reconstituted soil to the proportions of clay minerals and plasticity characteristics. *Appl Clay Sci* 53:48–57



Utilization of Inferred Landslide Hazard Information as a Web Based Decision Making Tool for Landslide Disaster Risk Reduction and Early Warning

Kumari M. Weerasinghe

Abstract

The highlands of Sri Lanka are affected by rain induced landslides and associated land degradation. Over the past 3 decades, the Government of Sri Lanka with the technical cooperation of international institutions such as UNDP, ADPC, NGI and JICA has implemented several programmes for landslide disaster risk reduction in the country. As a result, landslide hazard zonation maps are prepared for all landslide prone districts. The landslide susceptibility information derived from landslide hazard maps serves as the base for risk assessment, issuance of early warning, landslide education, mitigation and issuance of landslide clearance certificates. Many national and private sector organizations utilize the landslide hazard maps for selecting suitable sites for future developments. The major problem faced by the users of hazard maps in printed format is the mismatching which often takes place in relating the zonal boundaries identified in the map with actual ground conditions. Even though this problem can be eliminated by utilizing the maps in digital format, many users in rural areas lack the access to the required GIS software. In the usage of digital format also, misinterpretation of hazard potential occur in borderline cases. The author has attempted to integrate the landslide hazard information with the parcel based land information for developing a web based tool which identifies landslide potential at land parcel level. As the land parcels are demarcated on the ground, this tool can be effectively utilized for planning of development activities and implementing landslide disaster risk reduction activities. A part of the Uva Paranagama Administrative Division of the Badulla district was selected as the study area used for developing this web based tool which can easily be replicated to other areas with the availability of land information. As the internet can be conveniently accessed, a majority of map users will be benefitted by the developed landslide information tool.

Keywords

Landslide information • Disaster Management • Web based decision making tool

Introduction

Landslides are a major natural disaster, which affects life, properties, and economy in the central highlands of Sri Lanka during the monsoons with heavy rainfall (Fig. 1). According to the available records, over 450 human lives have been lost due to devastating landslide events occurred during the past 7 decades (NBRO 2012). The extent of damage caused to the livelihoods, property, infrastructure,

K.M. Weerasinghe (✉)
Landslide Research and Risk Management Division, National Building
Research Organisation, 99/1 Jawatta Road, Colombo 005, Sri Lanka
e-mail: kmweera@yahoo.com

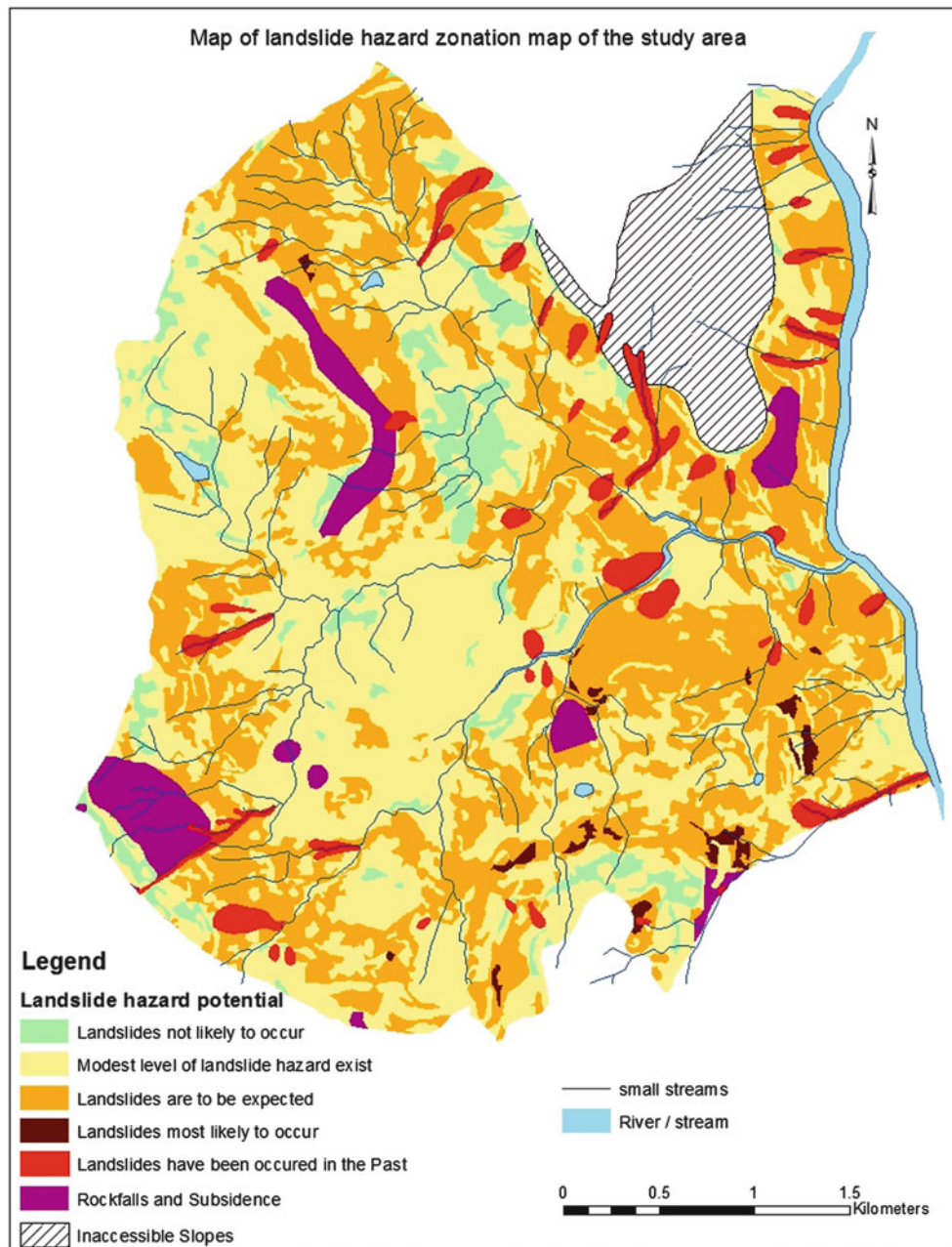


Fig. 1 Landslide hazard zonation map of the study area

national development, flora and fauna and the impact on regional and national economy caused by landslides often goes beyond estimation. The topographical and geological characteristics and the inappropriate land utilization are the major contributory factors of Sri Lankan landslides while rainfall serving as the common triggering factor.

Studying of landslides in the country and landslide hazard zonation mapping are two major programmes implemented by the National Building research Organisation (NBRO) of Sri Lanka for landslide disaster risk reduction in the country (NBRO 1986). The landslide hazard zonation maps which

depict the areas prone to landslide hazards (Fig. 1), and the severity of hazard within each zone, serves as a guide for identification of areas suitable for human settlements and/ other development activities. At present, landslide hazard zonation maps have been accepted as an essential tool in decision making for sustainable development in the central highlands.

The landslide susceptibility information derived by the landslide hazard zonation maps are further analysed along with the information on regional rainfall, for the issuance of landslide early warning. As the reliability of issuing early

warning is highly dependent on the accurate rainfall information measured within the vulnerable areas, with the assistance of UNDP, JICA, NGI and ADPC, NBRO has stepped into the process of installing her own set of automated rain gauges in the areas identified as landslide prone.

As a result of many development activities and adverse land uses have taken place, uncontrolled, within the areas with high landslide potential, the severity of landslide hazard has increased during the past 2 decades (NBRO 1995–2012).

To control the unplanned development and construction activities in the central highlands, and to increase the safety of life and property from future slope instabilities, the Government issued a circular, in February, 2011, making it compulsory for the local authorities and other project approving agencies in hilly areas to obtain NBRO's clearance on landslide vulnerability prior to giving approvals for development and construction activities. During the early years within which this new circular was in effect, all new construction that took place in the central highlands, irrespective of the terrain characteristics and the variations in the severity of landslide potential, were required to obtain landslide clearance from NBRO. At present, landslide hazard zonation maps are being used by the local authorities to identify (i) the areas where landslide potential is very low and can be excluded from requirement to obtain NBRO's landslide clearance and (ii) the areas where landslide potential is medium to high and therefore, obtaining NBRO's landslide clearance is required before approving any development.

Research Problem

The major problem faced by the users of hazard maps is the mismatching which often takes place in relating the zonal boundaries identified in the hazard map with actual ground conditions. Even though this problem is frequently encountered when using the maps in printed format and can be solved by utilizing the maps in digital format, majority of the map users lacks the access and the required skills to utilize the required GIS software.

In the usage of digital format also, misinterpretation of hazard potential occur in borderline cases; For example in Fig. 2, the land parcel "A" belongs to the single landslide hazard zone; interpreted by colour—yellow, where as the land parcel B belongs to two landslide hazard zones interpreted by colours; yellow and orange and the land parcel C belongs to four landslide hazard zones interpreted by colours; green, yellow, orange and red.

Wherever a plot of land belongs to more than one hazard zone (Fig. 2), the overall landslide potential of the site may not always be interpreted, accurately, by the non technical map users and perhaps such interpretations could be bias to individual's needs. Further, Even though the existing



Fig. 2 A part of a landslide hazard zonation map showing a land parcel that belong to one hazard zone (A), a land parcel that belong to two hazard zones (B), a land parcel that belong to several hazard zones (C)

landslide potential of a particular land parcel is very low, the planned development may require excessive ground modifications which may increase the severity of the landslide potential of that land parcel. This aspect needs to be studied by evaluating the existing landslide potential against the terrain characteristics of the area and cannot be identified by studying only the landslide hazard zonation map.

Therefore, a user friendly mechanism to learn the technically inferred landslide potential of a land parcel and to decide on the requirement of obtaining landslide clearance prior to develop that land parcel has become a timely necessity.

Research Objective

The objective of this research is to integrate the landslide hazard information derived from the landslide hazard zonation maps with the parcel based land information, the terrain characteristics and the existing development status for designing a web based tool which allows the user to (a) conveniently identify a land parcel, (b) appraises the landslide potential of the identified site, (c) learn the level of suitability of the land for further development, and (d) if applicable, guides the user on the requirement of obtaining landslide clearance.

Study Area

A part of the Uva Paranagama Administrative Division of the Badulla District was selected as the study area for developing this web based tool (Fig. 3). The selection of this study

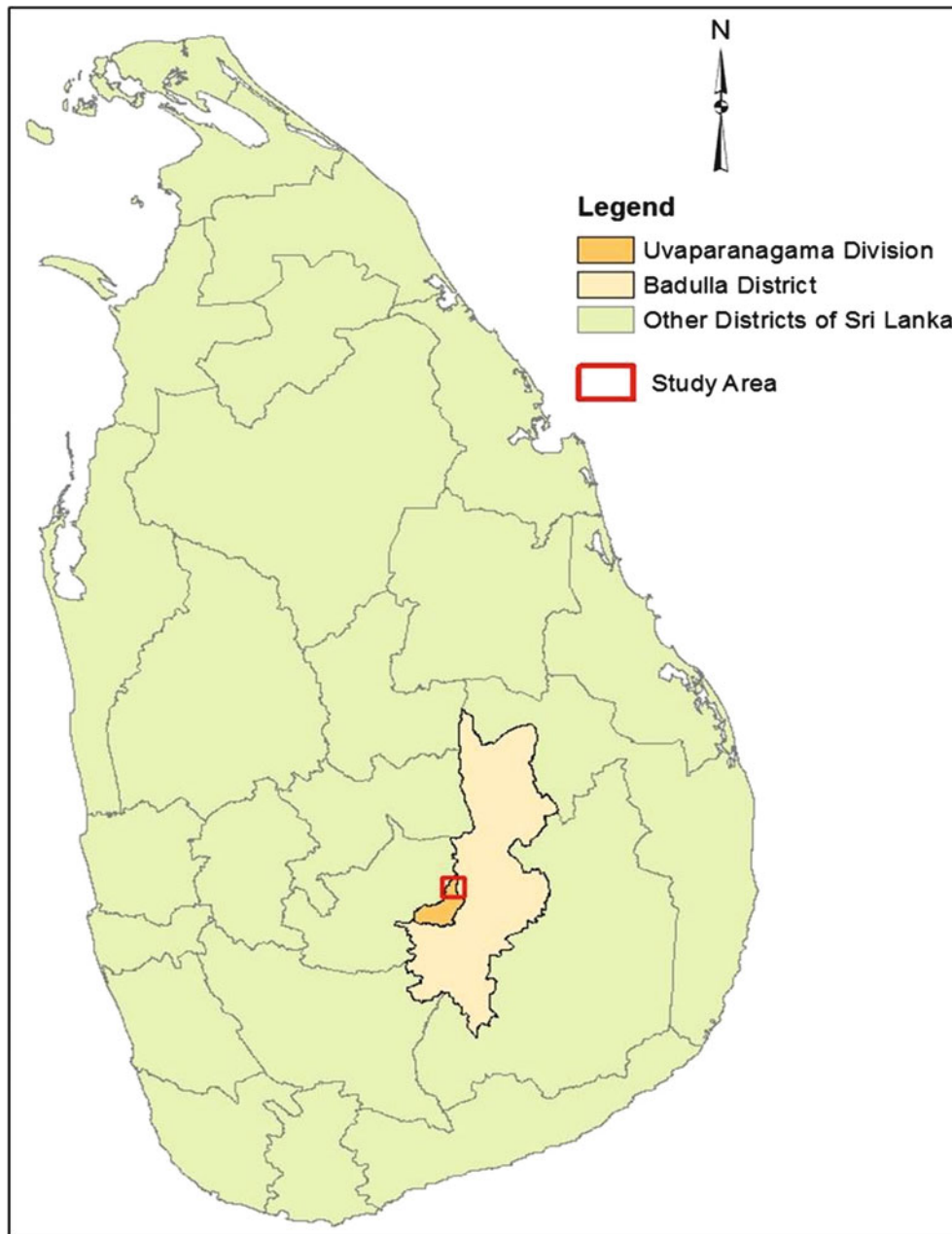


Fig. 3 Location of study area with respect to the country

area was solely based on the facts that the area is potential to landslides (Fig. 1) and the availability of parcel based land information required for decision making. The selected area is spread within 10 Grama Niladhari Divisions which are the village level administrative divisions in the country (Fig. 4). The same tool can easily be replicated to other landslide prone areas and districts also with the availability of parcel level land information.

Development of Database

Geographically referenced information on land parcels within the Uva Paranagama Administrative Division had been prepared to a reasonable accuracy by the Land Use Policy Planning Department (LUPPD) of Sri Lanka and has been made available to NBRO in the form of a digital map

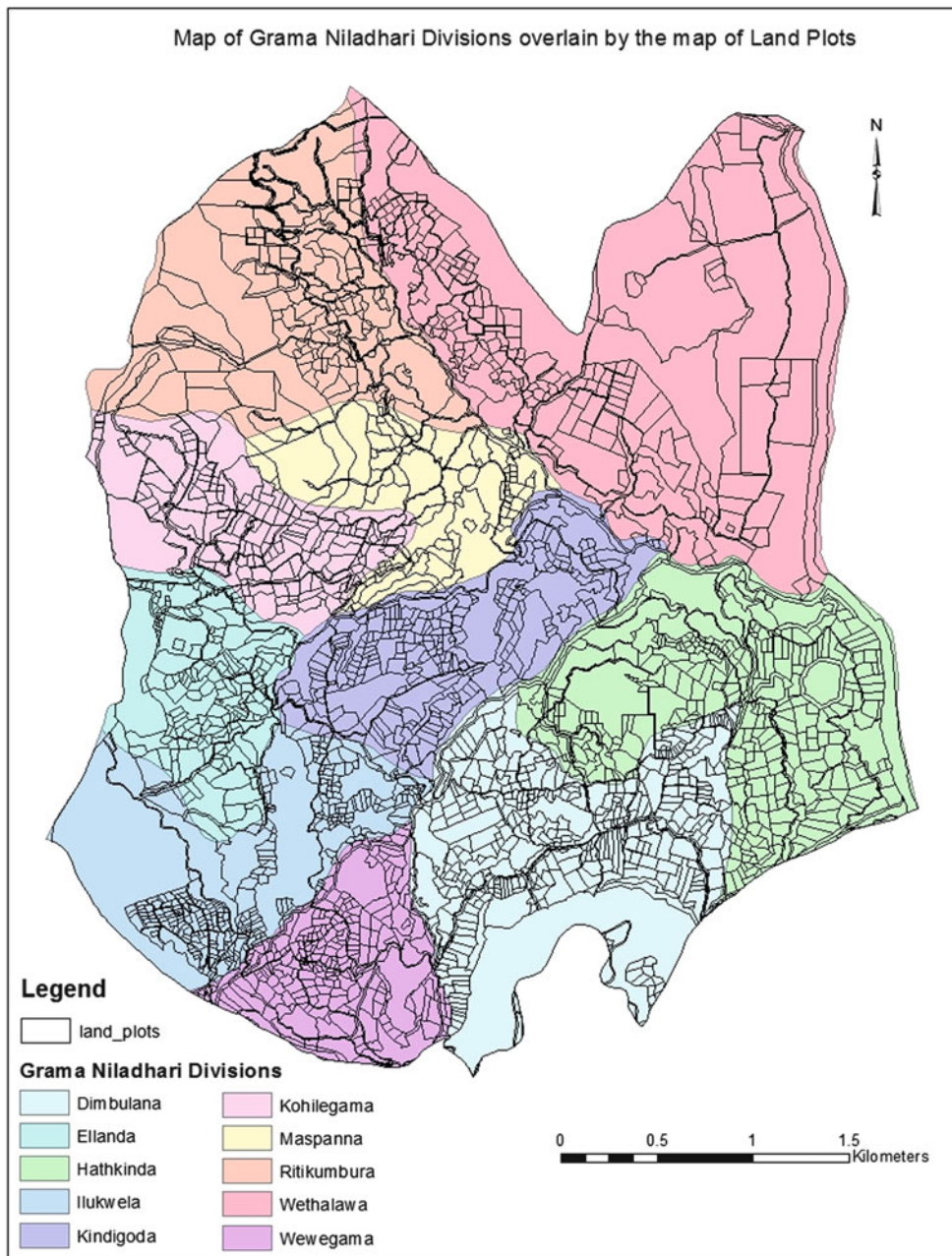


Fig. 4 Distribution of land parcels within 10 Grama Niladhari divisions

layer for utilisation in landslide disaster risk reduction activities in the Badulla District.

The LUPPD database includes a unique plot identification number (Plot_ID), the present land utilization and the extent of each land parcels. The the land extent is expressed in “Perches”, as it is the commonly used unit in Sri lanka to express the extent of land or the land area (Table 1).

This map of land parcels were overlaid on a map of Grama Niladhari Divisions (GND) to determine the relationship between the land parcels and the Grama Niladhari Divisions (Fig. 4) as indicated in Table 2. The standard

Table 1 Part of parcel level information extracted from the LUPPD database

Plot_ID	Land utilization	Area in Perches
9095	Mixed crops	20.82
11185	Mixed crops	294.61
11479	Chena cultivation	74.75
11579	Mixed crops	38.44

names, identification numbers and the codes assigned for the GND by the Department of Census and Statistics of Sri Lanka have been utilized for the developed database also, to

Table 2 Part of the database that indicate the relationship between the land parcel information and the Grama Niladhari divisions

Plot_ID	GND	GND_ID	GND_code
9095	Dimbulana	812745	38A
11185	Ritikumbura	812710	37F
11479	Wethalawa	812715	37A
11579	Maspanna	812720	37

maintain the data sharing capability within government organisations.

The landslide hazard potential of each land parcel was then evaluated by overlaying the map of land parcels on the landslide hazard zonation map of the study area (Fig. 5). The resulting information includes the relationship between the Plot Numbers and the landslide hazard zones (Table 3).

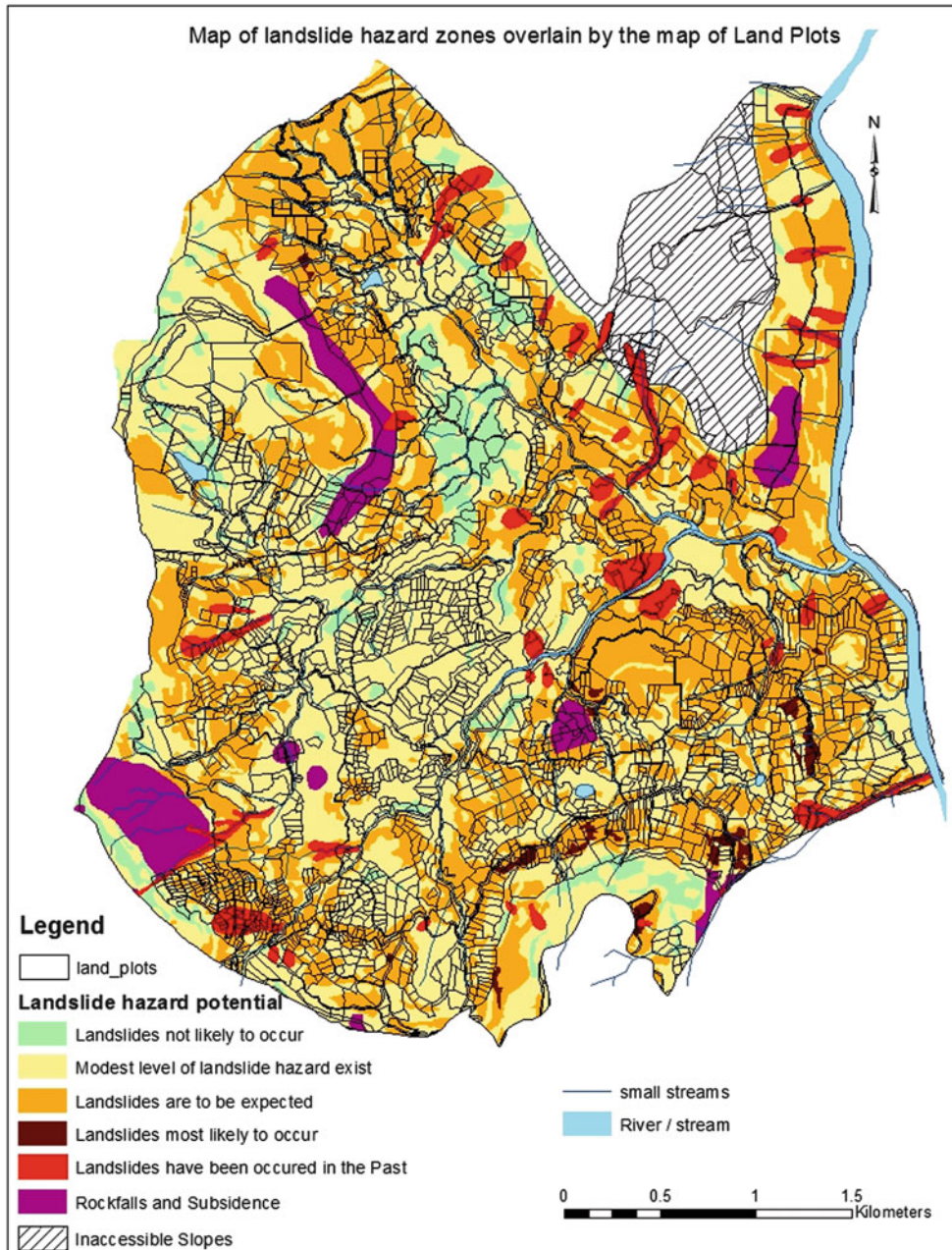
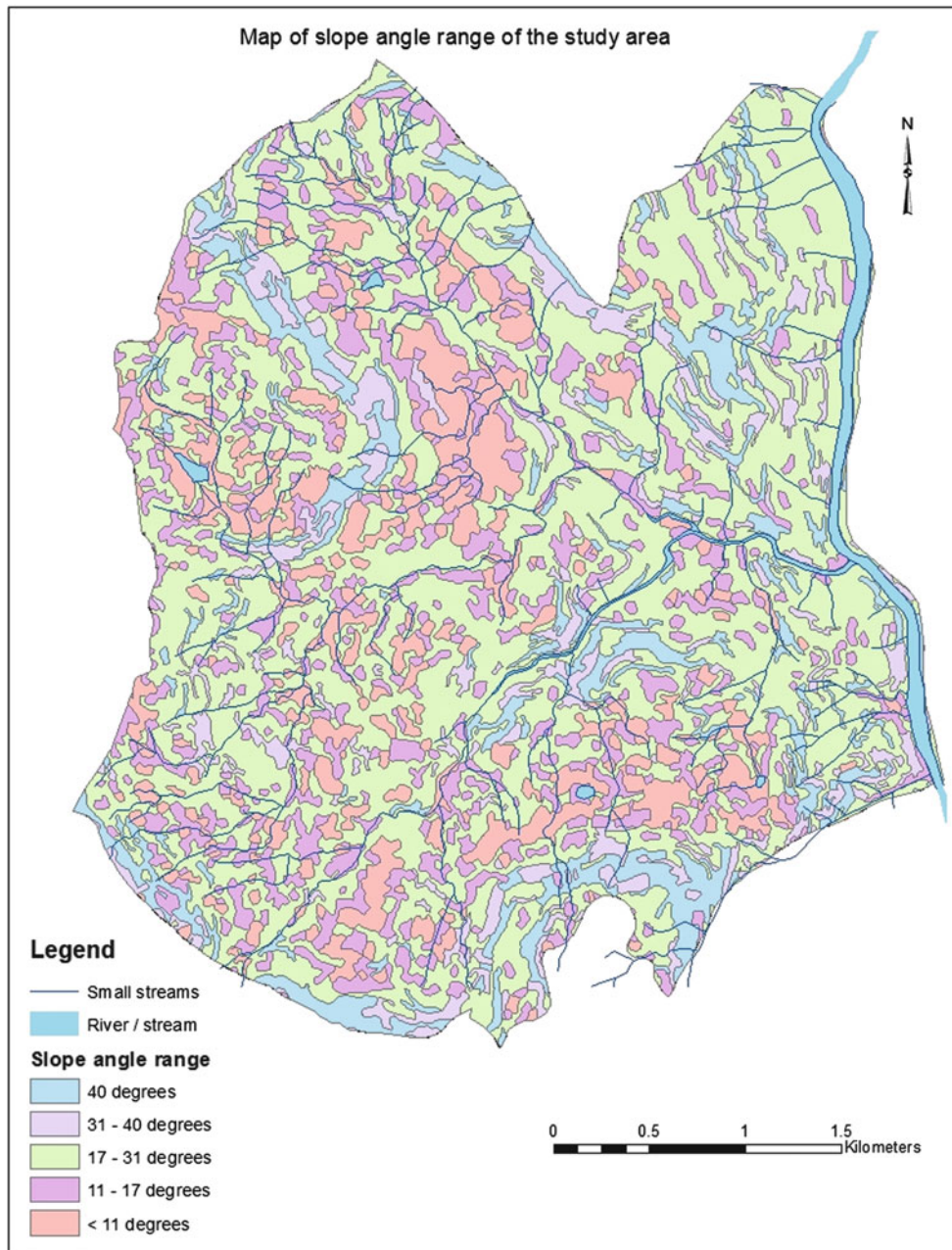


Fig. 5 Distribution of landslide hazard potential within the land parcels

Table 3 Part of the database that indicate the relationship between the land parcel information and the landslide hazard potential

Plot_ID	Landslide hazard potential	
	Lowest severity	Highest severity
9095	Landslides are to be expected	Rock falls have been occurred in the past
11185	Modest level of landslide hazard exist	Landslides are most likely to occur
11479	Modest level of landslide hazard exist	Modest level of landslide hazard exist
11579	Landslides are not likely to occur	Landslides are not likely to occur

**Fig. 6** Distribution of slope angle ranges within the study area

In this situation, there may be more than one hazard zone which lie on a single land plot as previously shown in Fig. 2. In such situations, it is possible either to assign the landslide hazard zone with highest severity as the landslide potential

of that land parcel or to assign the landslide hazard zone which covers the largest portion of the land parcel as the landslide potential of that land parcel. For the database associated with the designed decision making tool both the

landslide hazard potentials with lowest severity and the highest severity were recorded as shown in Table 3 and reviewed when appraising the landslide potential of the land parcel.

One intended utilization of the developed decision making tool is for deciding on the suitability of the land

Table 4 Part of the database that indicate the relationship between the land parcel and the slope angle range

Plot_ID	Slope angle range
9095	Steep
11185	Gently sloping to steep
11479	Moderately steep
11579	Gently sloping

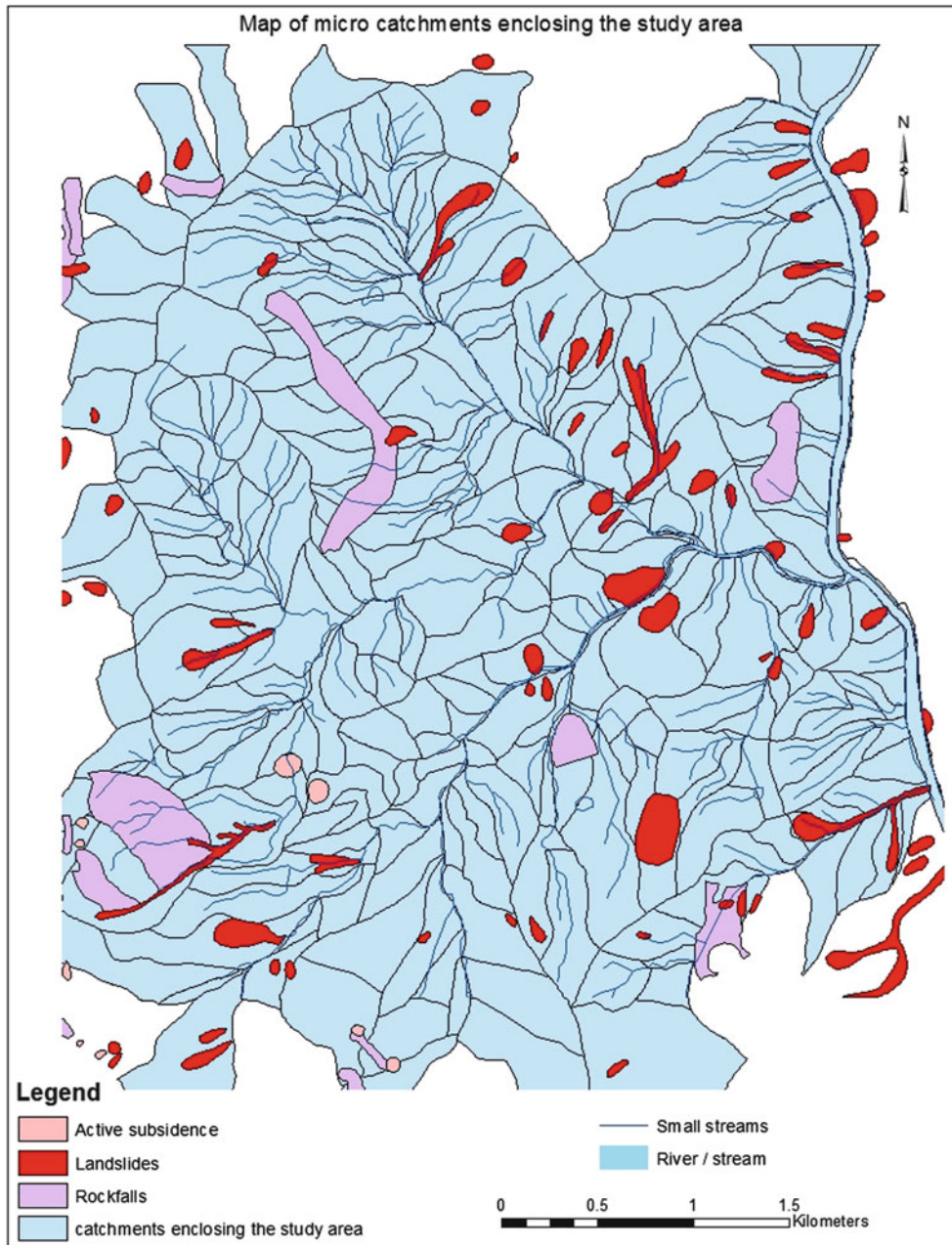


Fig. 7 A map showing the micro catchments where landslides and other instabilities have been occurred in the past

Fig. 8 Interface of the web based tool which allows the user to select a particular land parcel through a series of selection menus

parcel for development and/or deciding on the necessity of obtaining landslide clearance from NBRO prior to planning any construction within the land parcel. The developer may or may not always select the part of land parcel with the lowest landslide hazard potential for his or her planned development.

Therefore, rather than assigning a single landslide hazard potential for a particular land parcel, it was felt as appropriate to review both the landslide hazard potential with lowest severity and the landslide hazard potential with highest severity to decide on (i) whether the land parcel is potential to any form of landslides based on its existing characteristics (ii) whether the land parcel is suitable for development, (iii) will the severity of existing landslide potential be increased due to possible ground modifications introduced by a planned development, or (iv) whether obtaining landslide clearance is required prior to planning any construction or development within that land parcel.

The fact that a landslide, rock fall and a subsidence had been occurred (Table 3) within the land parcel is also taken into account by the developed tool in providing information on the landslide hazard potential of a land parcel to the prospective users.

Even though land parcel is located in an area with low landslide hazard potential, if that parcel is located in a slope, non-engineered slope modifications leading to slope instability may take place during the development or construction stage. Therefore, additional to the information extracted from the landslide hazard zonation maps, for decision making, the steepness of the existing ground is also reviewed

by studying the map of slope angle range (Fig. 6 and Table 4) where the land parcel is located.

Similarly, the existing landslide potential of a particular land parcel may be low but a landslide, rock fall or another form of slope instability has been occurred within the same catchment enclosing the land parcel (Fig. 7). In such situations, if the land parcel is located along the probable flow path of a landslide or any other form of instability, the particular land parcel is also at the risk. Therefore, the fact that any type of slope instability has taken place within a catchment enclosing the particular land parcel is also reviewed by the designed decision making tool.

Development of Interface

The interface of the tool is developed using PHP and Javascript scripting languages on Mysql database. It is accessed by the users through a web portal which allows the users to identify the land parcel through a series of user friendly selection options (Fig. 8). The inputs such as administrative Province, District, Division and the Grama Niladhari Division within which the particular land parcel is located are the basic location specific information known to even non technical users. Once the Grama Niladhari Division is input, the parcel numbers within that Grama Niladhari division is listed through another selection menu through which the user selects the specific parcel.

Once the land parcel is identified, a preliminary evaluation of landslide potential for the selected land parcel will be

Preliminary Evaluation of Landslide Potential of Sites Selected for Housing and Other Development

Select the Province, District and the Administrative Division where your site is located :

Select the Province Select the District Select the Division

Select the Grama Niladhari Division and the Plot Number applicable to your site:

Select the Grama Niladhari Division Select the Plot Number

Appraisal of landslide potential of the selected site:

This site is located in an undulating land
A modest level of landslide hazard exist in this site.
This site is located in a catchment where landslide have been occurred in the past.

Conclusion and Recommendation:

Obtaining landslide clearance is required prior to planning any construction or development in this site.

[Click to apply, online, for construction clearance](#)

[Click to download construction guidelines](#)

Thank you for using this web portal ! - [Click](#) - to let us know any of your comments.

Fig. 9 The results of the evaluation of landslide potential of the selected site is displayed on the screen

performed by reviewing the information on the inferred landslide hazard potential of the land, slope angle range, landslide history, catchment characteristics, existing land use, and the building density of the land parcel for arriving at conclusions and recommendations. The resulting information along with conclusions and recommendations are displayed on the screen as shown in Fig. 9.

For the land parcels where the existing land use is Forest or Forest plantations, the tool will inform the user of the necessity of obtaining clearance from the Forest conservation Department, prior to processing the application for landslide clearance. According to the guidelines for construction in landslide prone areas, the recommended minimum extent of a land parcel in hilly and mountainous areas is 15 Perches. However, due to the scarcity of suitable land in the central highlands, this land extent may perhaps be relaxed to 10 Perches. This requirement is also reviewed by this tool through the evaluation of building density of the selected site.

The interface allows the users to apply for landslide clearance, on line, and also to download guidelines for construction in landslide prone areas (Fig. 9).

Conclusion

The developed tool is a simple straight forward information system which can be utilized by even a non technical user for learning the landslide potential of a specific land parcel. The tool reviews the range of landslide hazard potential zones within which a land parcel is located, the terrain characteristics, present land utilization, present

development status and reasonably interpret the overall landslide hazard potential of the selected land parcel.

As the land parcels are demarcated on the ground, the landslide potential evaluated by this tool can be effectively related to the actual ground conditions. The hazard potential indications are provided along with the conclusions and the recommendations and cannot be misinterpreted based on the individual's needs. The developed tool directly informs the user of the requirement of obtaining landslide clearance, if necessary.

The output of this developed tool can be effectively utilized in evaluating the landslide potential of a site for implementing landslide disaster risk reduction activities. The users of this web portal are not limited to the land owners or developers. Project approving agencies, disaster management institutions, banks and financial facilitators, insurance companies can equally utilize this web portal for decision making pertaining to their specialized services. When utilized along with local level rainfall information, the output of this tool can be utilized for landslide early warning also. As the internet can be conveniently accessed even from the remote areas of the country, a majority of map users will be benefitted by the developed landslide information tool.

Acknowledgments The author of this article expresses her sincere gratitude to the pioneers of the landslide related studies at NBRO, the Government of Sri Lanka, UNDP, JICA, NGI and ADPC the Land Use Policy Planning Department, the Survey Department and the Department of Census and statistics for their contributions.

References

National Building Research Organisation (1995–2012) Investigations on slopes affected by landslide. National Building Research Organisation, Colombo

National Building Research Organisation (1986) Landslide hazards in Sri Lanka. National Building Research Organisation, Colombo
National Building Research Organisation (2012) Inventory of landslide. National Building Research Organisation, Colombo

Part V

Landslides in Cultural/Natural Heritage Sites



Introduction: Landslides in Cultural/Natural Heritage Sites

Jan Vlcko and Claudio Margottini

Abstract

Multi-disciplinary approach in landslide risk assessment related to preservation of historic and natural heritage sites is the challenge for the future. Presented papers document this fact.

Keywords

Historic and natural heritage sites • Multidisciplinary approach

Protection and conservation of cultural and natural heritage sites is one of the most challenging problems facing modern civilization. It involves variety of factors ranging from cultural and humanistic to technical and economical factors intertwining in inextricable patterns. The complexity of factors influencing the protection of cultural and natural heritage sites covers broad variety of disciplines involved in this topic. Especially when natural phenomena, among them especially landslides and related slope phenomena pose the risk to cultural and natural assets, the experts from natural (earth scientists with various specialisation e.g. engineering geologists, geomorphologists, geophysists, etc.) and technical (geotechnical engineers) disciplines are dealing with this serious problem. Also, from several conferences organized throughout the world (eds. Marinis and Koukis 1988, Sassa 2001, 2002, Viggiani 1997, Carslaw and Jaeger (1959) and others) was confirmed that the problem of vulnerability of cultural and natural heritage sites to landslides is an emerging issue still to be properly investigated, which requires multidisciplinary approach and highly qualified expertise in order to preserve the integrity and authenticity

of unique natural environment, geosites, pre-historic sites, earth/rock monuments, archaeological sites, and historic urban landscapes. Within this broad view, adopted solutions, but also investigation and monitoring, are all aimed at minimizing the impact of final conservation works, even during study phases and execution works. On the other hand, reliable and accurate data are required to elaborate correct geological and geotechnical model in relationship with slope failure and instability to achieve, together with historical and archaeological data, the most appropriate mitigation actions.

As far as the future concerns, especially in the countries where the state budget is too low to finance the preliminary studies to elaborate hazard and risk mitigation strategies as well as principles of risk preparedness including risk management to historical built environment and natural sites the landslides will result in one of the major disasters causing loss of world's cultural and natural history which have to be preserved for future generations. This is one of the most important issues why this session was included in the programme of WLF 3.

C-5 session covers contributions that propose new multidisciplinary approaches and describe good practices and case studies in landslide risk assessment and mitigation, showing how strategies and conservation/restoration projects have to be totally "site dependent" in terms of investigations and proposed solutions.

J. Vlcko (✉)

Faculty of Natural Sciences, Dept. of Engineering Geology, Comenius University in Bratislava, Mlynska dolina G, 84215 Bratislava, Slovakia
e-mail: vlcko@fns.uniba.sk

C. Margottini

Dept. Geological Survey of Italy, ISPRA, Via Branconi, 60, 00144 Rome, Italy

References

- Carslaw HS, Jaeger JC (1959) *Conduction of heat in solids*, 2nd edn. Oxford University Press, Oxford, 517 p
- Marinos PG, Koukis GC (eds) (1988) The engineering geology of ancient works. In: *Monuments and historical sites - preservation and protection Symposium*, Athens, 19–23 Sept 1988
- Sassa K (ed) (2001) *Landslide risk mitigation and protection of cultural and natural heritage*. In: *Proceedings of UNESCO/IGCP Symposium*, Tokyo
- Sassa K (ed) (2002) *Landslide risk mitigation and protection of cultural and natural heritage*. In: *Proceedings of international symposium*, Kyoto
- Viggiani C (ed) (1997) *Geotechnical engineering for the preservation of monuments and historic sites*. Balkema, Rotterdam



Notes on a Landslide That Formed the Only Known True Inland Lake in South Africa

S.G. Chiliza and S. Diop

Abstract

Lake Fundudzi is a particular landslide site of great interest situated in the heart of the Soutpansberg Mountains in the Limpopo province of South Africa. The landslide that formed the Lake occurred in the northward dipping quartzitic sandstone of the Fundudzi Formation of the Soutpansberg Group. The Lake is surrounded by lush forests, waterfalls and mountains, and is believed to be sacred to the Vhatavhatsindi clan, the People of the Pool who act as the custodian of the lake. Field observations suggested that the failure mechanism was planar, and the landslide may have occurred by pre-existing conditions, such as the joint pattern. Kinematic analyses using Rocscience Inc. Dips revealed three major joint sets (JS 1, JS 2 and JS 3) in the rock mass which are oriented northeast–southwest, west north west–east south east, and north–south respectively. The main failure plane best correlated with JS 2, which dips towards the lake. The analyses also revealed that the mechanism of failure was planar which is in agreement with field observations. In the year 2008 the South African Heritage Resource Agency (SAHRA) reported that the sacred Lake Fundudzi situated in the mountainous area of Tshiavha village, north of South Africa, was listed on a provisional list of sites to be declared a national heritage site.

Keywords

Heritage site • Lake Fundudzi • Culture • Quartzitic sandstone • Landslide

Introduction

In an attempt to assess landslide hazard, risk, and indicate the spatial distribution of previous events the Council for Geoscience (CGS) identified the Limpopo Province for landslide inventory and susceptibility assessment mapping. It was during this CGS landslide inventory and susceptibility mapping programme that a unique landslide which resulted in the damming of the eastward flowing Mutale River to form the only known true inland lake in South Africa was identified (Van der Waal 1997). Lake Fundudzi is situated in the Soutpansberg Mountains and was formed by an ancient

landslide (~10,000 years ago) event that blocked the course of the eastward-flowing Mutale River (Van der Waal 1997). But the local people see it in a far more mysterious way. They'll point out that three rivers flow into the lake, yet it never overflows and there is no obvious outlet. It is a sacred site where the Vhavenda worship their ancestors (Stayt 1968). This paper presents some notes on the cultural aspects, beliefs associated with this Landslide Lake and kinematic analysis results.

Location

Lake Fundudzi is located in the Mutale River valley of the eastern Soutpansberg Mountains in the Limpopo Province (22°50'22.08"S and 30°18'36"E) near the Kruger National Park. The Limpopo Province is the northern-most province

S.G. Chiliza (✉) • S. Diop
Council for Geoscience, Engineering Geoscience Unit, Pretoria, South Africa
e-mail: gchiliza@geoscience.org.za

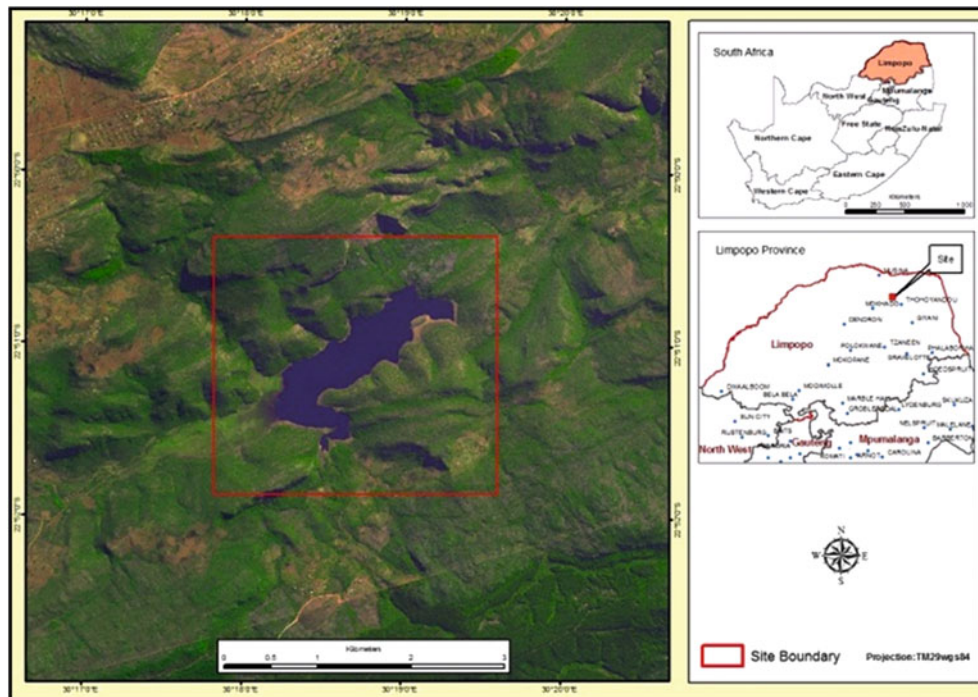


Fig. 1 Locality map of Lake Fundudzi and the landslide

in South Africa and borders Mozambique, Zimbabwe and Botswana. The Lake lies approximately 57 km north east of Makhado and 21 km north-east of Thohoyandou as shown in Fig. 1.

Geological and Structural Settings

The landslide occurred in the northward dipping quartzitic sandstone of the Fundudzi Formation of the Soutpansberg Group. The Soutpansberg Group is partially buried beneath younger Karoo Supergroup sedimentary and volcanic rock of varying thicknesses (Barker et al. 2006). The group consists essentially of reddish arenaceous and minor argillaceous deposits, and reaches a thickness of around 12,000 m. Basic lava, tuff and pyroclasts occur as layers and lenses of variable thickness throughout the succession (Visser 1984).

The rock beds strike in an east–west direction and dip 30° to the north. The rocks of the Soutpansberg are severely faulted by faults of various ages (Van Eeden et al. 1955). Barker (1979), mapped two NW–SE and SW–NE intersecting faults which form the failure lines of each flanking buttress or release surfaces. Several minor rock slides and falls are still active and noticeable on the failure side of each buttress, and were also noted by Janisch (1931). Tension cracks were also observed at the crest of the landslide (Fig. 2).

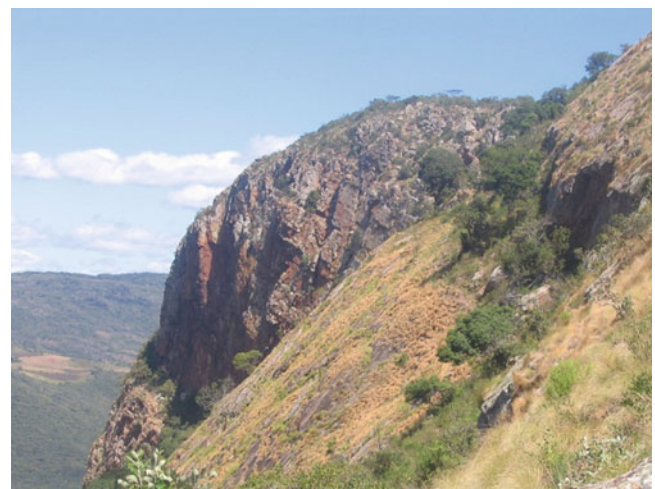


Fig. 2 Smooth planar failure surface with a near vertical tension crack

The Landslide that Formed the Lake

The failure of the mountain at Lake Fundudzi involved occurred on a jointed rock mass which is characterised by three prominent joint sets; two joints and one bedding types of joints. The observed failure mode characterises that of a plane failure in rock slides.

The crest of the landslide scarp is approximately 450 m in length, 220 m above the Lake, and has a slope failure plane surface area of approximately 20 ha (Fig. 3). The calculated



Fig. 3 Lake Fundudzi formed by a landslide

volume of rock that slid down the failure surface is estimated at 10 to 15 million m^3 , while rock blocks travelled a distance of up to 700 m across the valley floor. The failure plane dips approximately 60° to the south into the valley, while bedding planes dip at average of 20° to the north.

Causes of failure are not defined, however with regard to the Lake Fundudzi landslide, pre-existing conditions such as the joints, fractures and faults made the rock mass vulnerable to instability.

The Soutpansberg Mountains also experience high rainfall and as rainfall-induced slides are common in the province; this was also a probable trigger to failure. Available historical records of seismic data indicate a low level of seismic activity for the region, but may also have acted as an additional trigger at the time.

The Lake and Its Surroundings

At full supply lake is a 3 km long and 1 km wide inland freshwater body (Fig. 4). It covers an area of about 144 ha, and a maximum depth of 27 m, at an elevation of 865 m AMSL.

The Mutale River enters the lake at the middle of its bed. It lies in a valley which runs roughly SW–NE. The water level fluctuates considerably between dry and wet seasons. According to Costa and Schuster (1988), Lake Fundudzi is classified as a type 2 landslide dam in terms of material deposits on the valley floor. Type 2 landslide dams are larger and deposited material can cross the valley floor, in some cases to the opposite valley sides.

There is an abundant fish life in the Lake that attracts interest from local communities on a daily basis for self-sustenance through fishing.



Fig. 4 An oblique aerial view of the Lake Fundudzi landslide situated in the Soutpansberg mountains

The Lake hosts a crocodile's community which are relatively calm towards people and live stocks. This was observed during a daylong (8 h) walk around the Lake on the 21st of April 2008. During the visit 4 crocodiles were seen in separate incidents. The crocodiles would crawl into the Lake each time when we were approaching towards them. Walking around the Lake was not pleasant because of the difficult terrain more so on the mountain side where the landslide occurred.

Some Cultural Beliefs About the Lake

The lake is surrounded by lush forests, waterfalls and mountains, and is believed to be sacred to the Tshiavha clan "the People of the Pool who act as the custodian of the lake". The clan is under the leadership of Chief Netshiavha.

It is shrouded in by myths and legends, including the mythical python, the sacred white crocodile and a guardian white lion. There is a wonderful viewpoint that overlooks it and the Sacred Forest. Literature reports that, the great powers of Lake Fundudzi have been kept a closely guarded secret by the Venda people, who have preserved it for generations. The lake is often associated with myth and legends of the Venda people and is believed to be protected by a python god, who has to be pacified annually with gifts of traditionally brewed beer (Khorombi 2000).

In Venda culture, the python is the god of fertility and maidens still perform the famous Domba-python dance in the sacred lake to honour this god (Fig. 5). The young women form a line in which they hold on to the elbows of the maiden in front of them, and using their joint arms, make snake-like movements next to the lake to honour the god (Khorombi 2000).



Fig. 5 Maidens performing the Domba python dance

Fundudzi is also a burial site for the local clans that practice Thevhula. They exhume their dead after 10 or 15 years and burn the bones, releasing the ash into the Lake (Stayt 1968).

Other myths around the lake include a story of mysterious “zombies” which live near at the lake and play the traditional Venda music known as Tshikona.

The lake is surrounded by the Thathe Vondo forest, deemed to be so mystical and filled with spirits that few Venda people venture into it for fear of alleged hauntings and a lightning bird called “Ndadzi”.

It’s believed that on the rare occasion that a visit to the lake is granted, visitors must turn their backs on the lake and view the water from between their legs. This ritual is called “Fundudzi” after which the lake is named (Stayt 1968).

Special permission must be granted by the Netshiavha royal family, to visit the lake. He is a very warm, kind and very welcoming community leader (Fig. 6).

Kinematics of the Landslide

A kinematic analysis based on the Markland’s (1972) test in conjunction with the *Rocscience* software *Dips*, has been conducted on this ancient landslide in order to determine the type of failure mechanism that may have occurred.

The basic technique used in mapping surface or underground exposures is the scanline survey (Brady and Brown 2006). However, due to the hazardous nature of the terrain coupled with the limited rock mass outcrops, it was impossible to carry out a full scale scanline survey. As a result, cell or window mapping was used to collect discontinuity data. Wherever possible, the conditions of the discontinuities such as spacing, roughness, water conditions, and filling were recorded. Mathis (1987) suggested that sparsely scattered joint sets are not readily detected with scanline mapping, but are generally detected by cell mapping; hence local variations



Fig. 6 CGS Scientists at Chief Netshiava’s (wearing a *black hat* and a *tie*) place during the visit

in properties are easily detected resulting in better knowledge of variability. Over 200 discontinuity datasets, where rock mass outcrop exposures permitted, were recorded.

It was observed during field investigation, that the possible mode of failure of the landslide was planar. A kinematic analysis was thus undertaken in order to confirm this. The data obtained from the discontinuity survey was analysed using the *Rocscience Inc. Dips*. The data was plotted as poles and subsequently contoured into pole concentrations to be recognized from essentially random data as prescribed by Hoek and Bray (1981). The pole concentrations were then grouped to determine the major joint sets. This program enables the relationships between discontinuities and the slope face to be established. The determination of these relationships is essential for further kinematic analysis of the major joint sets. Subsequently, the mechanism of failure was determined by analysing the relationship between the major joint sets and the slope face by the Markland’s (1972) test as suggested by Hoek and Bray (1981). The dip and dip direction of the plane of the failed slope was found to be 80°/040°. Based on joint surface conditions which were predominantly slightly rough to rough, a value of 35° was chosen for the frictional angle for quartzitic sandstone as prescribed by Hoek and Bray (1981).

About 200 poles were plotted equal angle, lower hemisphere projection and the poles were contoured. Three sets of joints were subsequently determined: JS 1 (bedding), and JS 2 and 3 (discontinuities) (Fig. 7).

The maximum concentration of poles for JS 1 is approximated at 15°/283°. In the case of joint sets 2 and 3, the maximum pole concentrations are approximated at 85°/237° and 73°/175°, respectively.

In order to analyse for plane failure, the pole friction cone of plunge 90° and 35° dip was estimated to represent the friction of the rock mass. The daylight envelope is visible

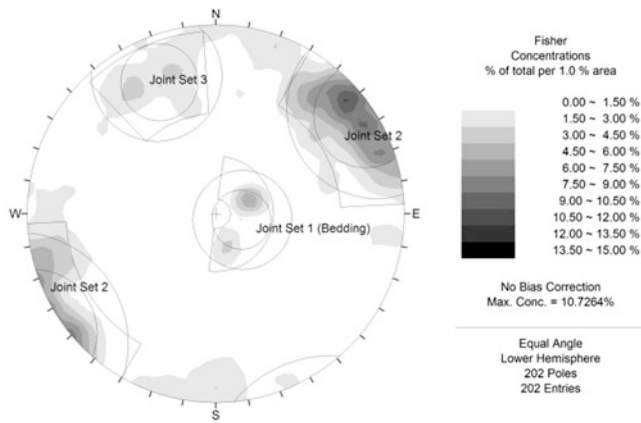


Fig. 7 Stereoplot showing the contoured plot of the poles and the three joint sets

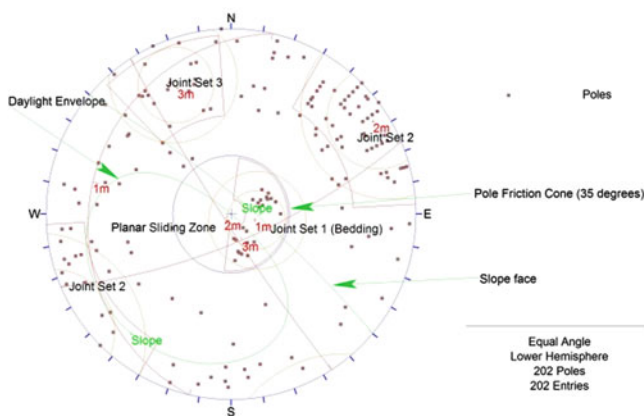


Fig. 8 Stereonet plot showing analysis of plane failure using daylight envelope and friction cone

and marked with a green circle (Fig. 8). According to the Markland's test, any pole that falls outside the cone represents a plane that could slide if kinematically possible. Hence there was no chance for JS 1 to slide because it falls within the friction cone area on the stereonet. Based on the analysis, there is an indication that (JS 2) poles represent planes which would slide and were susceptible to plane failure.

A crescent shaped zone formed by the daylight envelope and the pole friction circle encloses the region of planar sliding. Estimating probability of failure based on poles of JS 3 that fell within this zone was not relevant because the slope had already failed.

The Lake as National Heritage Site

It was reported back in 2008 by South African Heritage Resource Agency (SAHRA) that the sacred Lake Fundudzi situated in the mountainous area of Tshiavha village, north of South Africa, was listed on a provisional list of the sites to be declared as national heritage sites. There have been

delays to this process due to on-going sensitive consultative processes between the custodians of the Lake and SAHRA.

Conclusion

Lake Fundudzi is referred to by many researchers as the only natural freshwater inland lake in South Africa. Studies indicate that the Lake could be 10,000 years old.

It occurred in the northward dipping quartzitic sandstone of the Fundudzi Formation of the Soutpansberg Group. The failed slope rock mass is characterized by two NW–SE and SW–NE intersecting faults which coincide with the release surfaces and an undifferentiated lineament in the scarp area.

The Lake is shrouded by myths and legends, including the myths and pythons. The main spiritual significance of the Lake to the Tshiavha clan is as a graveyard or symbolic tombstone. They exhume their dead after 10 or 15 years and burn the bones, releasing the ash into the lake. Also in Venda Culture, the python is the god of fertility and maidens still perform the famous Domba-python dance in the sacred Lake to honour this god.

An ancient rockslide at Lake Fundudzi was analysed using *Rocscience Inc. Dips* software based on the Markland's test. Three major joint sets were discovered which included bedding. The maximum concentration or joint sets for bedding poles was approximately at $15^{\circ}/283^{\circ}$ and approximated at $85^{\circ}/237^{\circ}$ and $73^{\circ}/175^{\circ}$ for joint sets 2 and 3. The results revealed that joint set 2 (JS 2) poles represent planes that were susceptible to plane failure. From the analysis, plane failure mode was determined based on the orientation of the slope, the orientation of rock discontinuities, and the internal angle of friction of the rock mass. This was found to be consistent with field observations. Future work would involve back-analyses studies in order to investigate the geotechnical conditions that may have led to failure.

For over 5 years now the South Africa Heritage Resources Agency (SAHRA) has earmarked it as a national heritage site and the custodians of the Lake support the proposal.

Acknowledgements Thanks are due to the now retired Mr. C. Forbes of the Council for Geoscience (CGS) for constant motivation, guidance and valuable inputs during the Limpopo landslide project; Dr B.C.W van der Waal formerly of the University of Venda, for helpful discussions on Lake Fundudzi; Chief Netshiavha of the Tshiavha clan for permission to visit Lake Fundudzi; the Council for Geoscience (CGS) for funding and supporting this project.

References

- Barker OB (1979) A contribution to the geology of the Soutpansberg Group, Waterberg Group, Northern Transvaal. M.Sc. thesis (Unpublished), University of the Witwatersrand, Johannesburg, South Africa

- Barker OB, Brandl G, Callaghan CC, Eriksson PG, van der Neut M (2006) The Soutpansberg and waterberg groups and the blouberg formation. In: Johnson MR, Anhaeusser CR, Thomas RJ (eds) The geology of South Africa. Geological Society of South Africa, Council for Geoscience, Johannesburg, Pretoria, pp 301–319
- Brady BHG, Brown ET (2006) Rock mechanics for underground mining, 3rd edn. Springer, Dordrecht
- Costa JE, Schuster RL (1988) The formation and failure of natural dams. *Geol Soc Am Bull* 100:1054–1068
- Hoek E, Bray JW (1981) Rock slope engineering. Institution of Mining and Metallurgy, London, 359pp
- Janisch EP (1931) Notes on the central part of the Soutpansberg and on the origin of Lake Fundudzi. *Trans Geol Surv South Afr* 54:152–162
- Khorombi M (2000) Towards a sustainable land-use plan for the Lake Fundudzi catchment area. M. Inst. Agr. thesis (Unpublished), University of Pretoria, South Africa
- Markland JT (1972) A useful technique for estimating the stability of rock slope when the rigid wedge slide type of failure is expected. Imperial College rock mechanics research reprint no. 19
- Mathis JI (1987) Discontinuity mapping – A comparison between line and area mapping. In: Proceedings of the 6th international congress on Int Soc Rock Mech, vol 2. Balkema, pp 1111–1114
- Stayt HA (1968) The Bavenda (Facsimile of 1931 edition). Frank Cass, London
- Van der Waal BCW (1997) Fundudzi, a unique, sacred and unknown South African lake. *South Afr J Aquat Sci* 23(1):42–55
- Van Eeden OR, Visser HN, Van Zyl JS, Coertze FJ, Wessels JT (1955) The geology of the eastern Soutpansberg and the Lowveld to the north. Explanation Sheet 42 (Soutpansberg). *Geol Surv South Afr*: 117
- Visser DJL (1984) Geological map of the Republic of South Africa and the kingdoms of Lesotho and Swaziland: 1:1000 00 scale. Geological Series, Department of Mineral and Energy Affairs



Rock Slope Potential Failures in the Siq of Petra (Jordan)

Giuseppe Delmonaco, Claudio Margottini, Daniele Spizzichino, and Bilal Khrisat

Abstract

The Siq is a 1.2 km naturally formed gorge that represents the main entrance to Petra (Jordan). Discontinuities of various type (bedding, joints, faults), mainly related to stratigraphic setting, tectonic activity and geomorphological evolution of the slope can be recognized. Structural condition determines a rock-fall potential activity that may involve unstable volumes, from 0.1 m³ up to over some hundreds m³. The latter can be catastrophic according to evolution of the movement (extremely rapid) and involved rock mass volumes. Slope instability, acceleration of crack deformation and consequent increasing of rock-fall hazard conditions could threaten the safety of people walking through the Siq. UNESCO, ISPRA and Jordan local authorities have implemented a project focused on landslide hazard assessment and risk mitigation strategies as a first step for the long-term conservation of the Siq. The paper reports preliminary data on landslide inventory, geomechanical properties of materials and assessment of landslide kinematics that affect the Siq of Petra.

Keywords

Rock fall • Landslide kinematics • Cultural heritage

Introduction

The Siq is a naturally formed deep gorge in the sandstone mountains that connects the urban area of Wadi Musa with the monumental area of Petra (SW Jordan) and represents, since Nabataean times, the main narrow entrance for some thousands tourists that access Petra every day.

Recent active and landslide processes involving the Siq and other parts of the archaeological area have arisen the

attention on the geological conservation of the site as well as on the safety of visitors.

An international project, managed by UNESCO (Siq Stability—Sustainable Monitoring Techniques for Assessing Instability of Slopes in the Siq of Petra, Jordan), has been funded by the Italian Ministry of Foreign Affairs, for the analysis of slope stability conditions of the Siq and implementation of an integrated remote and field monitoring systems aimed at the detection and control of deformation processes.

In the framework of the Siq Stability project activity, the paper reports a preliminary landslide inventory map of potentially unstable blocks and a geotechnical and geostructural analysis with detection of the main potential slope failure types for a further landslide hazard assessment of the Siq area.

G. Delmonaco (✉) • C. Margottini • D. Spizzichino
ISPRA, Italian National Institute for Environmental Protection and
Research, Via V. Brancati 48, Rome 00144, Italy
e-mail: giuseppe.delmonaco@isprambiente.it; claudio.margottini@isprambiente.it; daniele.spizzichino@isprambiente.it

B. Khrisat
Department of Conservation Sciences, Queen Rania Institute of
Tourism and Heritage, Hashemite University, Zarqa, Jordan
e-mail: bilal@hu.edu.jo

Geological and Geomorphological Setting

Petra is located on the eastern side of the Dead Sea Wadi Araba tectonic depression, a ca. 15 km-wide topographic low formed by shearing along the transform separating the Arabian and Sinai plates (Sneh 1996; Ginat et al. 1998). The local stratigraphic succession (Quennel 1951; Bender 1974) starts with a ca. 50 m thick Salib Arkose arenitic formation, overlain by a >500 m thick massive and poorly stratified Cambrian-Ordovician quartz arenites of the Umm Ishrin and Disi formations where the hand-carved rock monuments of Petra are entirely cut. The lithological and petrographic characteristics of the two formations are controlling weathering related conservation problems, affecting, as well, shear strength parameters of the rocks.

The Siq has a length of ca. 1.2 km with a general E-W orientation and a meandering course. It is the natural prolongation of Wadi Musa river before the Nabataeans diverted it through the Wadi Mudhlim tunnel. The difference in height between the beginning at the entrance dam and the current exit at the Treasury is 63 m, at least in the bottom part of the slopes. Actually, the difference in altitude between the path floor and the top of the slopes at the confluence with the Outer Siq is much higher (>200 m). This is due to the morphological setting of the area that presents a stepped-slope shape lower part, where visual survey is possible, and a middle and top sectors where slope faces are only partially observable from the Siq path.

The Siq is surrounded by very steep slopes entirely formed by the Umm Ishrin Sandstone Formation that can be subdivided into three main units, according to texture, mineralogical composition and engineering classification (Fig. 1). The Upper Sandstone, called “honeycomb sandstone”, is composed of white and mauve-red, coarse to medium grained, hard and massive sandstone, forming very steep slopes. It is characterized by typical cavernous weathering caused by solution of cement and consequent granular disintegration that form the typical honeycomb structures. The Middle Sandstone (“tear sandstone”) consists of multi-coloured, medium to fine-grained, well-bedded and friable sandstone. Weathering is diffuse, especially by solution of the ferruginous and manganiferous layers and cements that cause change or the rock face from red-brown to yellow and grey. Cross-bedding structures and presence of interbedded silty and clayey sands are quite common. The Lower Sandstone (“smooth sandstone”) is made of white, medium to coarse-grained, hard massive sandstone.

The Siq geomorphology is the result of long and short-term factors such as tectonic up-lift, erosion due to runoff, differential erosion and weathering of sandstone materials. The slopes, as a general rule, presents a rupestral aspect, mainly massive. Nevertheless, discontinuities of various

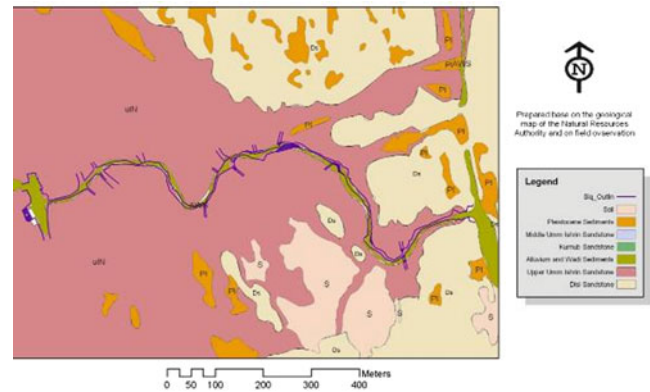


Fig. 1 Geological map of Petra area

types, are present, mainly related to stratigraphical setting (bedding, generally horizontal), tectonic activity (faults, master joints, mainly sub-vertical), geomorphological activity (from vertical to medium-inclined joints). Sub-vertical and medium-angle dipping joints intersecting horizontal bedding are quite frequent in some parts of the Siq stratification and observed during field investigation. This situation may cause potential sliding of blocks, whose dimensions are depending on local, orientation, density and persistence of joints.

Rock slope failures occurring in the Siq of Petra have been recognised (Delmonaco et al. 2012) considering the main failure type (fall, topple, slide) and potential magnitude. All the above geomorphological processes have been collected and elaborated through a geo-database and a preliminary landslide inventory map produced (Fig. 2).

Geotechnical and Structural Analysis

Field investigations have been conducted to reconstruct the structural and geomechanical characteristics of the Siq slope-forming rocks with geotechnical field techniques and laboratory tests on representative core rock samples and blocks of the Umm Ishrin Sandstone Formation. The Siq has been divided into 15 different sectors, following morphological and structural criteria, in order to provide a zoning on potential landslide types and kinematical processes affecting each single sector.

The assessment of the strength parameters (friction angle/cohesion and UCS) and geomechanical indexes (i.e. RMR, GSI, Q system) as per ISRM suggested methods (ISRM 1978, 1981, 1985) have been reconstructed through the execution of scanlines in each sector and: (1) execution of Schmidt-hammer tests on discontinuities and intact rock and point load test with portable equipment for assessment of UCS; (2) tilt tests on core rock blocks for reconstruction of the base friction angle.

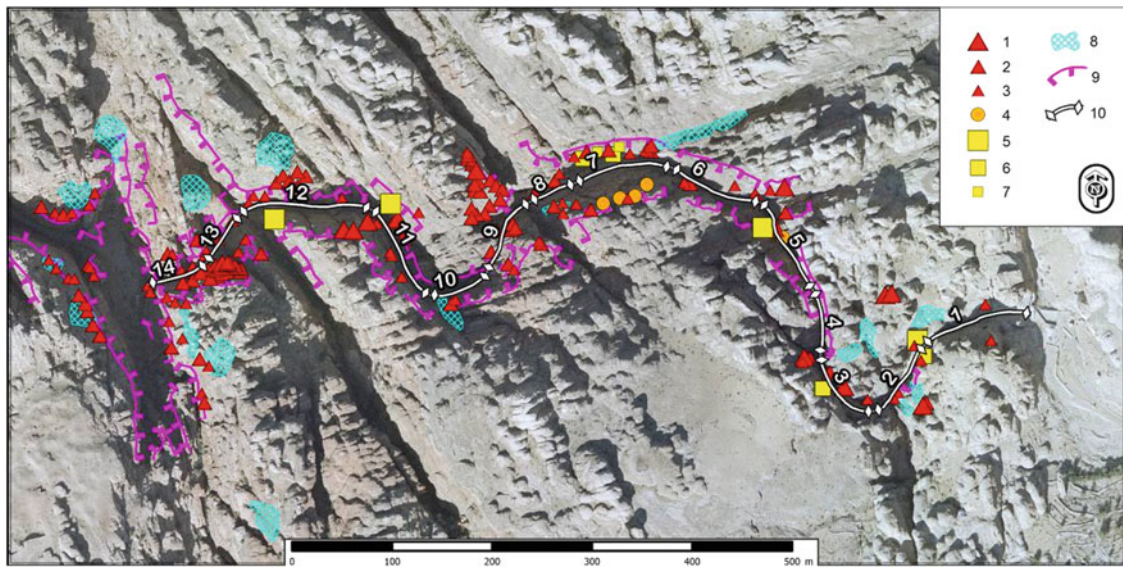


Fig. 2 Landslide inventory map of Petra area. (1) rockfall large; (2) rockfall medium; (3) rockfall small; (4) toppling large; (5) toppling large; (6) slide medium; (7) slide small; (8) unstable debris; (9) scarp; (10) Siq Sector (numbered)

Table 1 Geotechnical parameters estimated from in situ techniques

Natural unit weight (KN/m ³)	JRC	UCS (MPa) (Schmidt Hammer)	φ° (Tilt test)	UCS (MPa) (Point Load test)
19.16–21.68	4–6	–	35–43	115 (hard sandstone)
–	4–6	25–35	35–43	30 (soft sandstone)
GSI	c (MPa)		φ°	E _m (GPa)
72	0.4		43°	12

Table 2 Synthesis of geotechnical parameters from laboratory test

γ _{dry} (KN/m ³)	V _p (Km/s)	V _s (Km/s)	σ _n (MPa) Triaxial tests	σ _t (MPa) Brazilian tests
20.8	2.15	1.18	22.85	2.84
ρ _{dry} (Mg/m ³)	E _{sec} (GPa)	E _{tan} (GPa)	K (σ _n /σ _t)	ν _{dyn}
2.12	6.45	9.46	8.04	0.28

Laboratory tests on core and natural blocks have provided values of UCS, tensile strength and dynamic parameters.

In situ and laboratory analysis are reported in the following Tables 1 and 2.

A rock mass classification (Hoek 2007; Hoek and Brown 1988; Hoek et al. 1992) for the right and left flanks of each sector has reported in Fig. 3.

A geostructural characterization of discontinuities has been done in the Siq sectors in order to provide the reconstruction of the structural setting of the area.

Generally in the Petra area straight, individual joints, with mostly vertical planes, can be followed in the field for long distances (up to 500 m), mainly related to tectonics. The trends of the main high-angle joint systems in the area, mainly vertical are controlled by, firstly, the post-Ordovician pre-Lower Cretaceous stresses which affected the Palaeozoic rocks only, secondly, by the stresses which created the Dead Sea transform fault system (Miocene-recent) and, thirdly, by tectonics within the Ash Shawbak fold belt

(Miocene) (Barjous 1987). Middle-angle joints are related to lateral unloading due to water erosion coupled with tectonic uplift as well as and to the typical petrographic and physical properties of the rocks (e.g. chemical and mineralogical composition, grain size, shape, thickness, homogeneity, porosity, permeability, type of cement).

The intensity of jointing is variable depending on distance from faults and strength of materials (i.e. higher within the siltstone sequences, lower within sandstone layers).

All data collected for blocks/slope areas in the Siq, have been analysed and represented with the geo-structural software DIPS[®] and reported in the Fig. 4.

The rose diagram shows that the major trend of joint systems ranges around a ENE-WSW directions (060–080° and 240–260°) with high slope angles (70–90°) exhibiting a trend parallel to local slope faces. These systems are in accordance with the dominant joint systems surveyed in the area that strike between 60–70° and 160–179° and are characteristic of the Umm Ishrin Sandstone and Disi

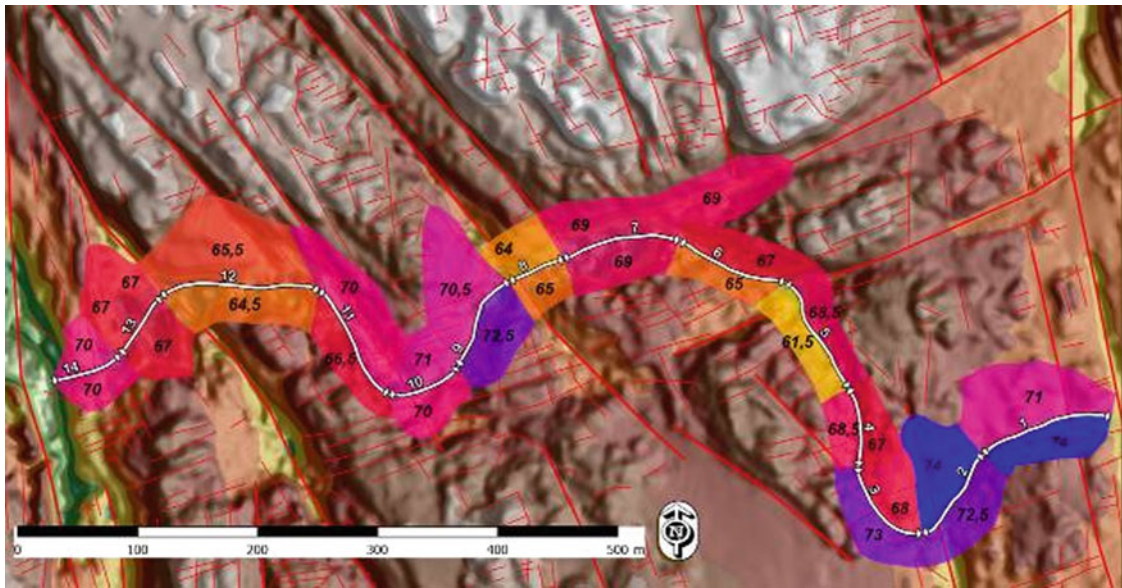


Fig. 3 GSI distribution value for the whole Siq

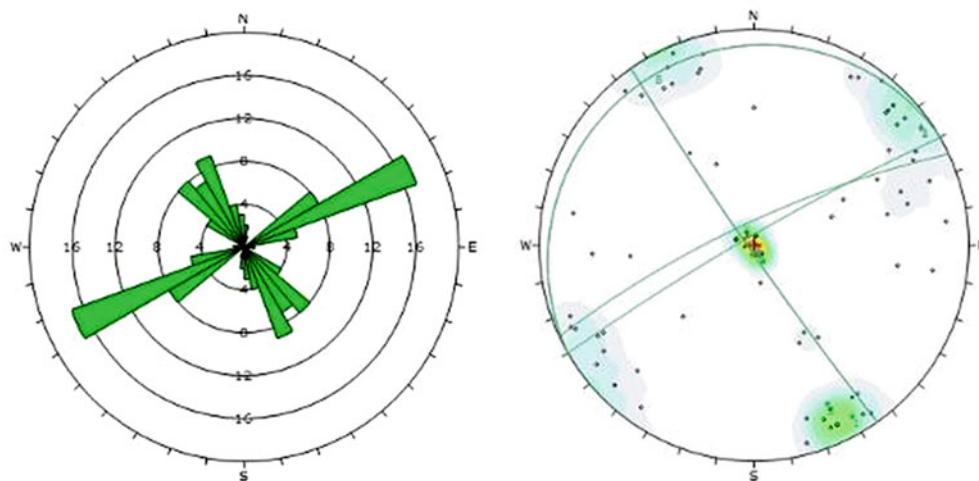


Fig. 4 Rose diagram (*left*) and plot (*right*) of joints surveyed in potential unstable sectors in the Siq

Sandstone Formations (Jaser and Bargous 1992). Also inclined joints, that represent the potential failure plane of sliding-mode blocks, are usually parallel to the main joint directions.

The Fig. 5 reports the main structural setting of the Siq area performed both through satellite image photo interpretation coupled with a field survey.

Kinematic Analysis

The presence of brittle sandstone in the Siq area and in Petra, as a general rule, promotes a block composition of rocks due to high frequency of discontinuities of various origin (i.e. faults, joints). All geomorphological processes and slope

instability, acting along the Siq of Petra, are the results of different structural combination of the main joints families.

Rock slope potential landslides occurring in the Siq of Petra can be classified as toppling (base, direct and oblique), planar and wedge failure modes depending on the type and degree of structural control.

Slope processes differ along the Siq path both in terms of activity, namely their state (temporal evolution), distribution (spatial evolution), style (combination and repetition of different failure mechanism) and as magnitude (landslide intensity and potential volumes).

Toppling is widespread along the whole Siq area due to large presence of sub-vertical and opened discontinuities parallel to the slope faces, locally intersecting sub-horizontal bedding planes of weaker sandstone layers. Figure 6 is

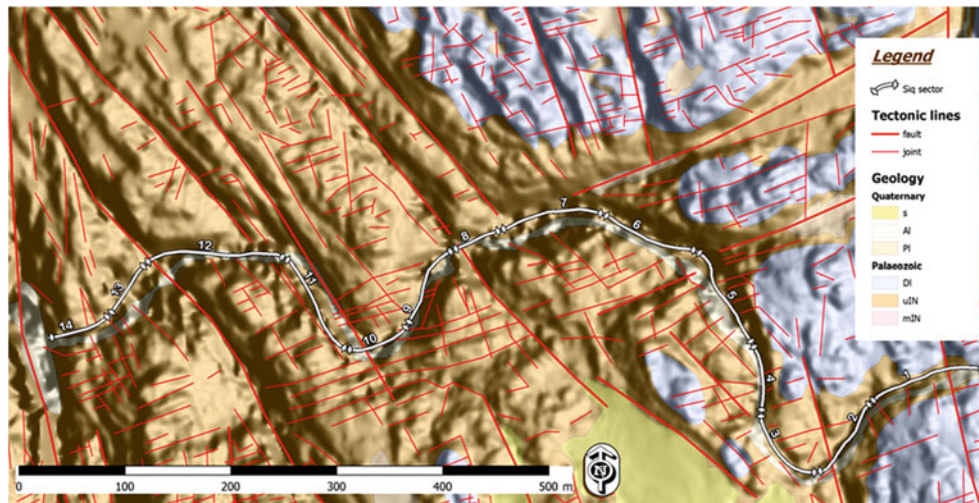


Fig. 5 Sketch of main discontinuities (fault, master joints) of the Siq area performed by aerial photo interpretation and field survey



Fig. 6 Potential toppling failure mode of a large block

representative of a toppling failure mode involving a large volume block, located in sector 5 of the Siq that is deemed as one of the most dangerous.

Planar failures in the Siq can occur along middle-angle dipping joints intersecting sub-vertical discontinuities (Fig. 7). For larger potentially unstable blocks in the Siq,

planar sliding is generally coupled with toppling failure mode.

Wedge failures are not so frequent in the Siq slopes, although they can develop on slope faces where main joints, oriented generally E-W, encounter secondary joints with orientation NNW-SSE.

Potential unstable volumes of wedges are as a general rule $< 10 \text{ m}^3$, though larger volumes can be involved (Fig. 7).

A kinematic analysis has been conducted for the right and left slopes of sectors 1–14 (sector 15 is related to the Treasury area, out of the Siq) using a specific software (DIPS[®]).

The main rock failure types analysed are: block and flexural toppling (Goodman and Bray 1976; Matheson 1983; Hudson and Harrison 1997), plane and wedge failures (Hoek and Bray 1981).

Slope face angles of right and left sectors have been calculated by analysing 10 m sections of the Siq, elaborated by Zamani Group - University of Cape Town, with a laser scanning technique. A general friction angle of 42° , derived by field analysis and laboratory test, has been considered as representative of sandstone materials in the Siq. In some sectors, characterised by different modes of slope angles, distinct elaborations have been produced.

A total of 120 simulations have been calculated for the visible part of the Siq slopes where geostuctural scanlines have been carried out (Fig. 8) and a synoptic table of potential failure types elaborated for further landslide hazard assessment of the Siq sectors.

Conclusion

Geomorphological, geo-structural and geotechnical evidences of the Siq of Petra slope-forming rocks suggest that actual and/or potential instability processes in the Siq

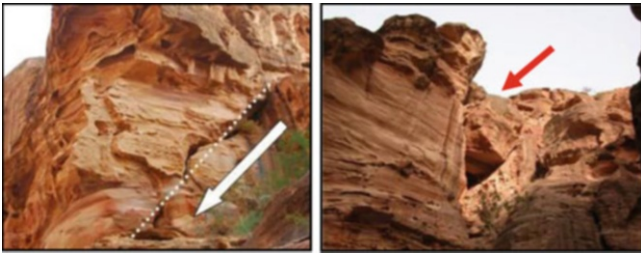


Fig. 7 Planar sliding (*left*) and wedge sliding blocks (*right*)

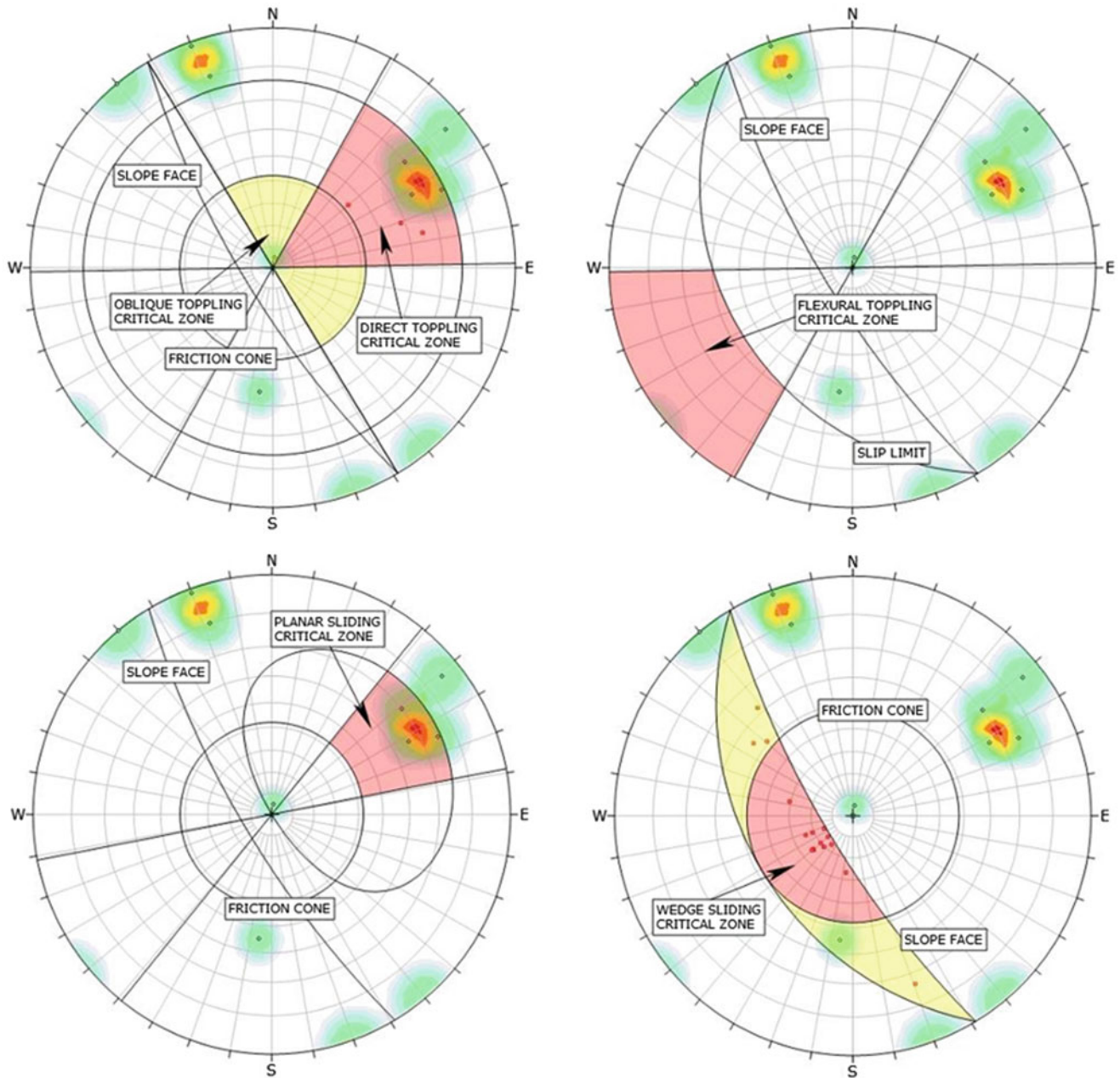


Fig. 8 Example of kinematic analysis for sector 5, *right slope*. From *upper left* to *lower right*: direct toppling, flexural toppling, planar sliding, wedge sliding

are the result of a combination of different predisposing factors in the area mainly depending on presence, frequency and orientation of discontinuities vs. slope orientation.

Potential instability processes and mechanisms observed in the Siq slopes can be referred to three main failure modes (or their combination): planar failure; wedge failure and toppling/flexural failures. Direct toppling and planar sliding are the most common and can develop large blocks.

The volume of blocks are generally $>15 \text{ m}^3$ (medium to large blocks) with evidence of blocks exceeding 500 m^3 . Nevertheless, the presence of many isolated blocks, mostly with a volume $<1 \text{ m}^3$, are widely diffused in the upper part of the Siq and not visible from the ground. Those blocks, along with loose debris outcropping in lateral channels, removable by flowing water produced by heavy rainfall, have to be taken into account for the assessment of hazard and induced risk. In addition, seismicity is another important landslide triggering factor that may cause the falling of rock blocks characterised by stability conditions near to failure.

The implementation of monitoring systems by satellite (SqueeSAR™, TeleRilevamento Europa) and site techniques (crack gauges) has provided preliminary results on slope deformation of major faults/joints systems, affected by negligible displacement in the last 10 years ($<1\text{--}2 \text{ mm}$). Site direct monitoring of cracks in the Siq set up since April 2011, displays very little displacement ($<0.2 \text{ mm}$) mostly connected with seasonal effects of temperature and rainfall on cracks movement.

In this regard, the recent installation of integrated direct monitoring systems (total station, terrestrial photogrammetry and wireless sensor network) on potential unstable blocks and slope sectors can provide an effective tool in order to control the evolution of slope processes and detect the most active parts of the Siq where to address further analysis and suggest landslide hazard mitigation measures.

Acknowledgments This research is part of the UNESCO project “Siq_Stability - Sustainable Monitoring Techniques for Assessing Instability of Slopes in the Siq of Petra, Jordan”, funded by the Italian Development Cooperation and implemented by the UNESCO Amman Office in partnership with ISPRA (Italian Institute for Environmental Protection and Research-Geological Survey of Italy), Zamani Research

Group (University of Cape Town), Petra National Trust (PNT) and in cooperation with the Department of Antiquities of Jordan and the Petra Archaeological Park.

References

- Barjous M (1987) Structural study of the area between Petra and Al Showbak. Unpublished M.Sc. thesis, University of Jordan, Amman
- Bender F (1974) Geology of Jordan. Gebruder Borntraeger, Berlin, 196p
- Delmonaco G, Margottini C, Spizzichino D (2012) Rock-fall hazard assessment in the Siq of Petra, Jordan. The Second World Landslide Forum, 3-9 October 2012, FAO. In: Sassa K, Canuti P, Margottini C (eds) Landslide science and practice, vol 6, Inventory and hazard assessment. Springer, Heidelberg, pp 441–449
- Ginat H, Enzel Y, Avni Y (1998) Translocated Plio-Pleistocene drainage systems along the Arava fault of the Dead Sea transform. *Tectonophysics* 284:151–160
- Goodman RE, Bray JW (1976) Toppling of rock slopes. In: Proceedings of specialty conference on rock engineering for foundations and slopes, ASCE, Boulder, CO, vol 2, pp 201–234
- Hoek E (2007) Practical rock engineering (2007 edition). <http://www.rocksience.com>. Last accessed 15 June 2013
- Hoek E, Bray JW (1981) Rock slope engineering, revised 3rd edn. Institution of Mining and Metallurgy, London
- Hoek E, Brown ET (1988) The Hoek-Brown failure criterion – a 1988 update. In: Curran JH (ed) Proceedings of 15th Canadian rock mechanics symposium. Civil Engineering Dept., University of Toronto, Toronto, pp 31–38
- Hoek E, Wood D, Shah S (1992) A modified Hoek-Brown criterion for jointed rock masses. In: Hudson JA (ed) Proceedings of rock characterization symposium, International Society for Rock Mechanics: Eurock '92. British Geotechnical Association, London, pp 209–214
- Hudson JA, Harrison JP (1997) Engineering rock mechanics: an introduction to the principles. Elsevier, Oxford
- ISRM (1978) Suggested methods for the quantitative description of discontinuities in rock masses. *Int J Rock Mech Min Sci Geomech Abstr* 15:319–368
- ISRM (1981) Rock characterisation testing and monitoring, ISRM suggested methods, Salzburg, 211p
- ISRM (1985) Suggested methods for determining point load strength. *Int J Rock Mech Min Sci Geomech Abstr* 22:51–62
- Jaser D, Bargous MO (1992) Geotechnical studies and geo-logical mapping of ancient Petra city. Town Mapping Project, Bulletin 1, The Hashemite Kingdom of Jordan, Ministry of Energy and Mineral Resources, Natural Resources Authority, 62p
- Mart Y (1991) The Dead Sea Rift: from continental rift to incipient ocean. *Tectonophysics* 197:155–179
- Matheson GD (1983) Rock stability assessment in preliminary site investigations – graphical methods. Transport and Road Research Laboratory Report, LR 1039
- Quennel AM (1951) The geology and mineral resources of (former) Trans-Jordan. *Colon Geol Miner Resour Lond* 2:85–115
- Sneh A (1996) The Dead Sea Rift: lateral displacement and down-faulting phases. *Tectonophysics* 263:277–292



Instability Processes Affecting the Katskhi Pillar Monastery (Georgia)

Claudio Margottini, Luca Maria Puzzilli, Alberico Sonnessa, and Daniele Spizzichino

Abstract

The present work reports the main results of a preliminary hazard assessment affecting Katskhi pillar Monastery stability conditions in western Georgia (Imereti regions). The research activities have been carried out with the support of National Agency for Cultural Heritage of Georgia in Tbilisi, following field survey activities conducted during May and December 2012. The field mission was aimed at the identification of the following main issues: (1) collection of preliminary geological, geomorphological and geomechanical data in order to define the main strength and deformation parameters; (2) geodetic surveying with TLS techniques for the 3D model reconstruction of the site and collection of geometric data for future slope stability analysis; (3) seismic survey with passive technique to achieve information about resonant frequency of the site; (4) preliminary analyses of potential rock slope stability of the pillar; (5) preliminary monitoring project and assessment of stability condition with the implementation of a project proposal for a full analysis on long-term risk assessment for the Katskhi pillar Monastery.

Keywords

Landslide • Katskhi • Cultural Heritage

Historical and Geological Setting of Katskhi Pillar Monastery

The Katskhi pillar is a natural limestone monolith located close to Katskhi village in the western Georgian region of Imereti, near the town of *Chiatura* (Gudjabidze & Gamkrelidze 2003). It is approximately 40 m high, and overlooks the small river valley of Katskhura (Wakhoucht 1842), a right affluent of the Q'virila River (Fig. 1). The rock, with visible church ruins on its top surface (around

150 m²), has been venerated by locals as the Pillar of Life, symbolizing the True Cross, and has become surrounded by legends (Gaprindashvili 1975). It remained unclimbed by researchers and unsurveyed until 1944 and has been more systematically studied from 1999 onward. These studies revealed the early medieval hermitage, dating from the ninth or tenth century. A Georgian inscription dated to the thirteenth century suggests that the hermitage was still extant at that time (Rapp 2003). Religious activity associated with the pillar started to revive in the 1990s and the monastery building had been restored within the framework of a state-funded program by 2009. The Katskhi pillar complex, in its current state consists of a church, a crypt (burial vault), three hermit cells, a wine cellar, and a curtain wall on the uneven top surface of the column. At the base of the pillar there are the newly built church of Simeon Stylites and ruins of an old wall and belfry. The church of St. Maximus the Confessor is located at the south-easternmost corner of the top surface of the Katskhi pillar. A small simple hall church design with

C. Margottini (✉) • L.M. Puzzilli • D. Spizzichino
ISPRA, Italian National Institute for Environmental Protection and Research, Via Vitaliano Brancati 48, Rome 00144, Italy
e-mail: claudio.margottini@isprambiente.it; lucamaria.puzzilli@isprambiente.it; daniele.spizzichino@isprambiente.it

A. Sonnessa
Surveylab, Università La Sapienza, Dica, Rome 00100, Italy
e-mail: sonnessa@uniromauno.it



Fig. 1 Panoramic view of Katskhi Pillar Monastery

the dimensions of 4.5×3.5 m, it is a modern restoration of the ruined medieval church built of stone.

Beneath and south of the church is an elongated rectangular crypt with the dimensions of 2.0×1.0 m, which had served as a burial vault. Digs at the ruined wine cellar revealed eight large vessels known in Georgia as *k'vevri*. Also of note is a rectangular cellar grotto with the entrance and two skylights—on the vertical surface of the rock, some 10-m below the top. At the very base of the pillar there is a cross in relief, exhibiting parallels with similar early medieval depictions found elsewhere in Georgia.

In historical records, the Katskhi pillar is first mentioned by the eighteenth-century Georgian scholar Prince Vakhushiti, who reports in his *Geographic Description of the Kingdom of Georgia*: “There is a rock within the ravine standing like a pillar, considerably high. There is a small church on the top of the rock, but nobody is able to ascend it; nor know they how to do that.” No other written accounts of monastic life or ascents survived. A number of local legends surround the pillar. One of them says that the top of the rock was connected by a long iron chain to the dome of the Katskhi church, located at a distance of around 1.5 km from the pillar.

In July 1944 a group led by the mountaineer Alexander Japaridze and the writer Levan Gotua made the first documented ascent of the Katskhi pillar (Figs. 2 and 3). Vakhtang Tsintsadze, an architecture specialist with the group, reported in his 1946 paper that the ruins found on top of the rock were remains of two churches, dating from

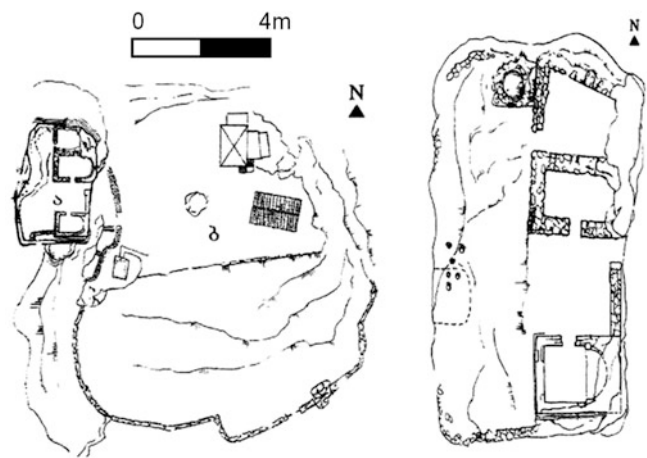


Fig. 2 Archaeological survey carried out by Japaridze during, 1944

the fifth and sixth centuries and associated with a stylite practice (Bardzimasvili 2010), a form of Christian asceticism (Fig. 4).

Since 1999, the Katskhi pillar has become the subject of more systematic research.

Based on further studies and archaeological digs conducted in 2006 (Gagoshidze 2010), an art historian with the Georgian National Museum, re-dated the structures to the ninth to tenth century. He concluded that this complex was composed of a monastery church and cells for hermits. Discovery of the remnants of a wine cellar also undermined

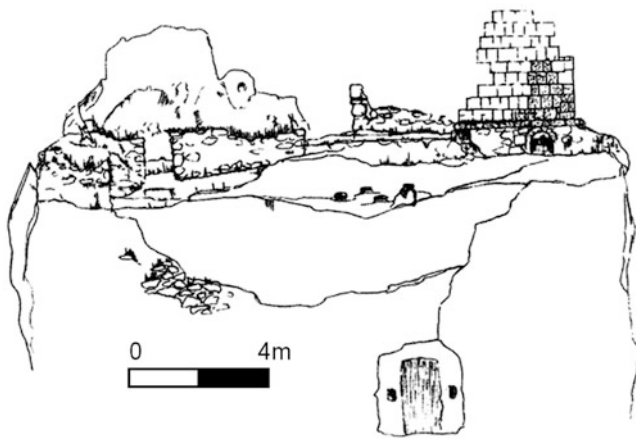


Fig. 3 Detailed map from Japaridze carried out during his first survey, 1944



Fig. 4 Ruins of the monastery before restoration works

the idea of extreme asceticism flourishing on the pillar. In 2007, a small limestone plate with the *asomtavruli* Georgian inscriptions was found, dated to the thirteenth century and revealing the name of a certain “George”, responsible for the construction of three hermit cells. The inscription also makes mention of the Pillar of Life, echoing the popular tradition of veneration of the rock as a symbol of the True Cross. Religious activity started to revive in 1995, with the arrival of the monk Maxim, a native of Chiatura. Between 2005 and 2009, the monastery building on the top of the pillar was restored with the support of the National Agency for Cultural Heritage Preservation of Georgia (NACHPG 2009). The rock is now accessible only through an iron ladder running from its base to the top (Fig. 5).

Site Scale Geotechnical Characterisation

Geo-mechanical characteristics of the pillar, have been reconstructed through field techniques and in situ laboratory tests, performed on rock blocks. A rock mass classifications

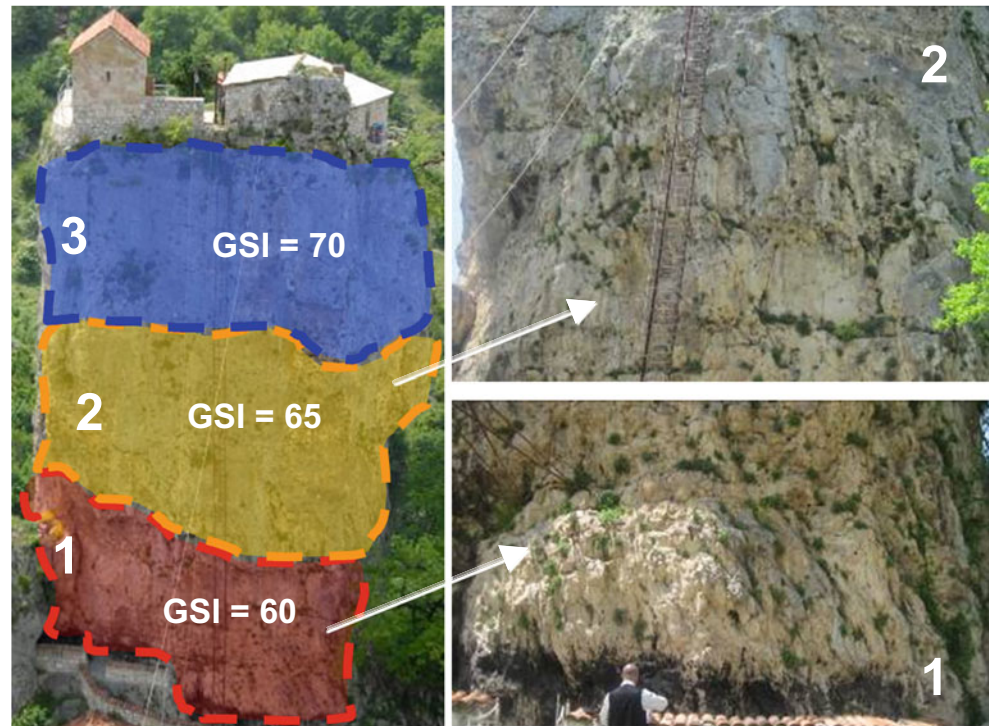
and failure criteria have been implemented (Hoek 2007). More in detail, the following activities have been carried out during 2012 field survey: the pillar has been divided into three different portions from the bottom to the top due to their rock strength characteristics (Fig. 5); field survey implementation through scan lines techniques in order to define the main geomechanical parameters and indexes (e.g. RMR, GSI, Q system); collection of strength and deformation parameters starting from scientific and technical literature as well as from local technical report; Schmidt-Hammer tests on joint surfaces and intact rock blocks for in-situ analysis of UCS; sampling of blocks in the field for the laboratory tests; Point Load tests to provide UCS data from sampled blocks and compare them with in-situ data (ISRM 1978, 1981) (Table 1).

The preliminary site engineering geological investigations for reconstruction of the strength of slope forming materials and geo-structural characteristics of the joints (Barton 1973), have provided the following results. Uniaxial Compressive strength is ranging between 50 and 70 MPa, with an average density of 22.6 KN/m³.

Passive Seismic Analysis

A passive seismic analysis was also carried out during the field survey. Site effects associated with local geological conditions, constitute an important part of any seismic hazard assessment: furthermore passive seismic techniques uses only environmental noise which exists everywhere in nature. The H/V spectral ratio technique of ambient noise recordings relies on the basic idea that the response of underground structures to such kind of vibrations may provide useful indications about their mechanical behaviour under dynamic condition. Interest aroused due to the possibility of using such a small amplitude ground motion for the cost effective seismic characterization of subsoil and the parameterization of building dynamical response. In particular, Horizontal-to-Vertical Noise Spectral Ratios (HVNSR) deduced by single station measurement could be considered, in many cases, as an important tool for a very preliminary seismic characterization providing two basic pieces of information: identification of seismic resonance phenomena induced by the presence of sharp seismic impedance contrasts in the subsoil and the preliminary estimation of the resonance frequencies F_0 of the site. Ambient noise measurements were conducted by using TROMINO Micromed[®], a three-directional digital tromograph with a sampling frequency of 128 Hz and an acquisition time of 16 min, following the procedure described in SESAME European project (SESAME 2004). Five measurements were conducted around the pillar and two measurements on top of the pillar, the latter in order to retrieve meaningful information about possible double-resonance effects of the

Fig. 5 Geological Strength Index zoning



structure. The analysis of the raw spectra of each component for every measurement was firstly conducted, to individuate the possible “anthropogenic” origin of F_0 , usually characterized by sharp peak on all components. For the application of H/V technique we chose a window length of 60 s, being necessary to investigate the wide range of engineering interest between 1 and 20 Hz, using a Khonno-Ohmachi smoothing with $b = 40$ and combining horizontal components NS and EW with a squared average before compute HV spectral ratio. We obtain an average HV curve with its corresponding peak frequency and peak amplitude (F_0 and A_0 respectively) and associated standard deviation values for each measurement. Further analysis were conducted comparing measurements made at the base with the ones collected at the top of Katskhi pillar, using the “structure spectrum” plug-in of Geopsy suite, an advanced signal processing tool aiming at estimating the Transfer function of a system by computing the spectral ratio between the input and the output signals. The “input signal” was represented by ambient vibrations recording at bottom of the pillar, whereas the registration on top was considered as “output signal”: a third signal, represented by the difference of each pair of signals, it’s finally added for the deconvolution (Fig. 6).

Table 1 Synthesis of preliminary geotechnical parameters

Lithology	Natural unit weight (KN/m ³)	JRC	UCS from Schmidt–Hammer test (MPa)	ϕ° Tilt test	UCS from Point Load test (MPa)
Limestone	22.6	6–8	50–70	46°	153

Geodetic Survey

The geodetic surveying was aimed at the three-dimensional (3D) reconstruction of the pillar, and the collection of data for future slope stability analysis of the site. All 3D data were collected in a Local Reference Frame by means of a terrestrial high-resolution laser scanner (TLS). Laser scanning is an automatic contact-free surveying technique (scanning laser range-finder) able to collect 3D surface coordinates at a very high spatial and geometric level of accuracy. All these characteristics make TLS an extremely useful tool in the field of conservation and protection of Cultural Heritage. Surveying activities at Katskhi site were performed using a topographical Riegl Z210i laser scanner both for measuring the 3D coordinates of the models and

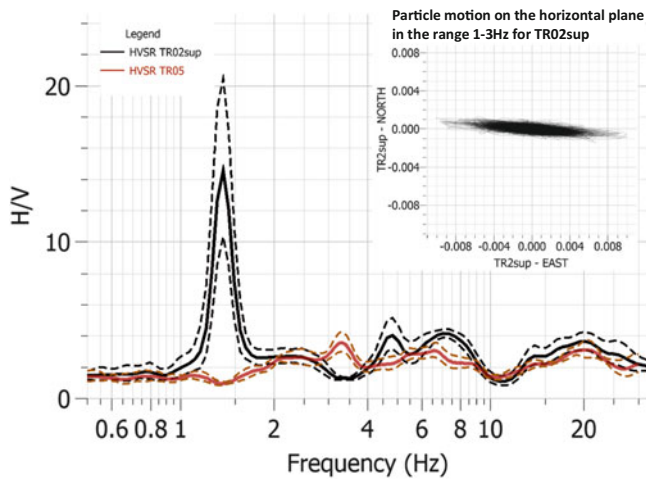


Fig. 6 HV curve with its corresponding peak frequency

acquiring the RGB information linked to the point clouds. This allows obtaining very accurate 3D surface models for archiving uses or further quantitative analyses (Fig. 7).

Types of Rock Slope Failures and Kinematics Analysis

Due to its morphological and geo-structural trend, the Katskhi pillar has been divided into different portions in order to provide zoning on potential landslide types and kinematical processes affecting each single portion (Cruden 1991). Rock slope failures occurring in the Katskhi can be classified into one of the following categories listed below depending on the type and degree of structural control and mechanical properties of rock masses (Cruden & Varnes 1996).

Small Medium Rock Fall and Wedge Failure

The whole pillar is affected (mainly in the lower/middle portion) by diffused small size rockfall and wedge failures, size $< 1 \text{ m}^3$ (Figs. 8 and 9).

These phenomena, although are not directly correlated to the overall stability of the pillar, can be very dangerous for pilgrims and visitors.

Small/Medium Rock Fall and Slide Failure

In the middle portion of the column small block sliding phenomena have been identified and mapped, block size from 1 to 2 m^3 (Fig. 9).

Also in that situation there is no a real hazard for the stability of the entire column but there is a high risk for

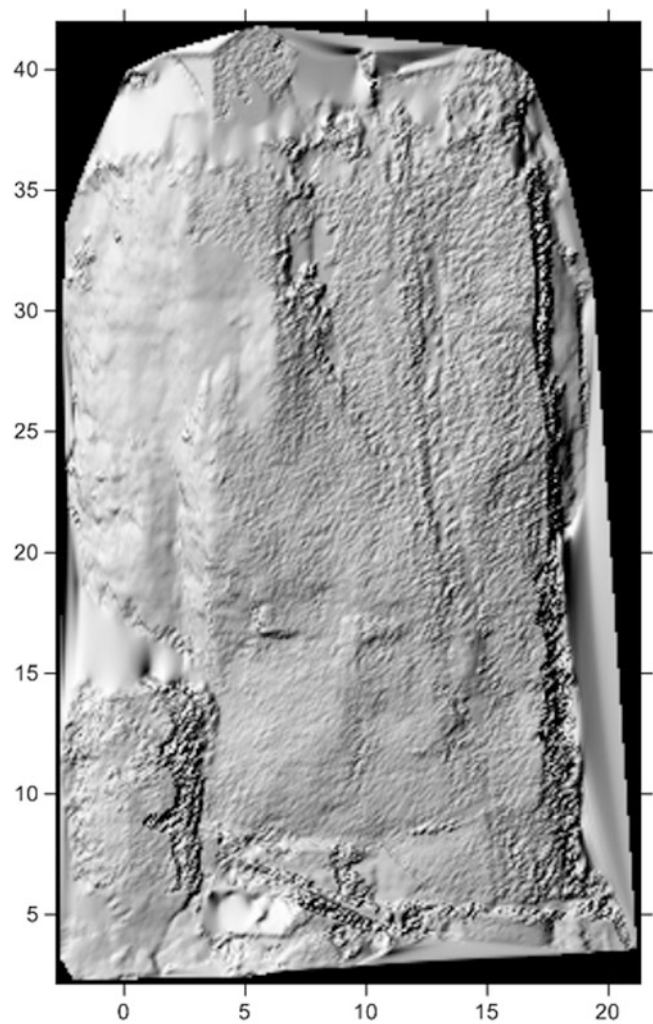


Fig. 7 TLS 3D implemented model



Fig. 8 Small size rockfall in the lower portion of the pillar

tourists, pilgrim and the community of monks and hermits of the site.

Medium Rock Fall, Toppling and Slide Failure

In the upper part of the pillar big portion of unstable rock masses (toppling/sliding) have been detected and mapped



Fig. 9 Rock slide failure detected along the slope face



Fig. 10 Unstable rock masses in the upper portion of the pillar

(Fig. 10). Due to the dimensions of the unstable rock masses also the edge and the boundary of the monastery could be involved.

This situation is the most dangerous involving both the safety of persons and the same Monastery edge.

Structural Analysis

All data collected during field survey have been analysed and represented with the geo-structural software DIPS[®] and reported in the Fig. 11.

The rose diagram shows that the major trend of joint systems ranges around a E-W directions (080–110° and 260–290°) with high slope angles (80–90°). In fact, these trends correspond to the four main slope faces of the rock column. The evolution and final shape of the column are strictly governed by major structural weakness joints.

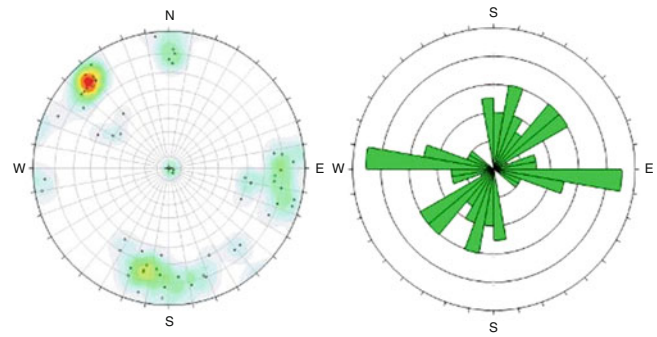


Fig. 11 Rose diagram (right) and plot (left)

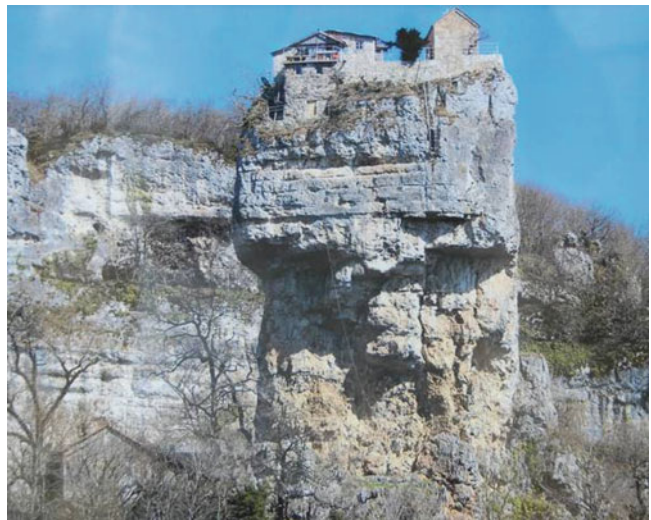


Fig. 12 Western slope of the Katskhi pillar and its overhanging facade

General Stability Condition of the Pillar

Regarding the general conditions of the Katskhi pillar it is currently in stable conditions. The column seems to have no evidence of generalized collapse or instability processes at macro-scale. What we have noticed are a series of medium to small local phenomena of collapse rockfall/sliding of the rock mass due to structural setting and their combination, which increased the risk for pilgrims and visitors. The repetition of such events has created the local morphology. This problem is very pronounced in the western portion of the column that is particularly overhanging (Fig. 12), giving to the column an dangerous eccentricity with a reduction of the useful resistant section. This geometric causative factor could create widespread instability to the entire structure especially in dynamic conditions (presence of an earthquake that is not uncommon in the area).

Conclusion

The present work allowed through a multidisciplinary approach the identification of the following main instability processes affecting the Katskhi pillar Monastery:

- Small rockfall in the lower part of the column;
- Small/medium size rock fall and slide in the middle portion of the column;
- Unstable masses (toppling/sliding) in the upper portion of the pillar;

Due to the above mentioned instability process there is no a real hazard for the stability of the entire column but there is an high risk for tourists, pilgrim and for the community of monks and hermits that live in the site. Although it seems that there are not actually high risk of rapid collapse for the entire Katskhi pillar further analysis should be carried out in order to control and reduce the instability process.

An integrated with low impact monitoring system should be implemented in order to prevent future instability of the column especially under dynamic condition (Margottini & Spizzichino 2009). More in detail the following measures could be sufficient: scaling of small blocks along the façade of the pillar, nails and bolts for the medium size phenomena (reducing the dismantling of the column section and avoiding excessive eccentricity of the pillar loads); installation of wi-fi sensors (clinometers, crack-meters and accelerometers) in order monitoring future stability processes.

Acknowledgments Authors are very grateful to all the National Agency for Cultural Heritage Preservation of Georgia staff members for their support and continuous help.

References

- Bardzimashvili T (2010) Georgian monk builds stairway to heaven, August 27. <http://www.Eurasianet.org>. Accessed 12 May 2012

- Barton NR (1973) Review of a new shear-strength criterion for rock joints. *Eng Geol* 7:287–332
- Cruden DM (1991) A simple definition of a landslide. *Bull Int Assoc Eng Geol* 43:27–29
- Cruden DM, Varnes DJ (1996) Landslide types and processes. In: Turner AK, Schuster RL (eds) *Landslides investigation and mitigation* (Special report 247). Transportation Research Board, Washington, DC, pp 36–75
- Gagoshidze G (2010) კატსხის სვეტი ("Katskhi Pillar"). *Academia*, No. 1:55–68. ISSN 1512-0899
- Gaprindashvili G (1975) *Ancient monuments of Georgia: Vardzia*. Aurora Art, Leningrad, pp 7–25. ISBN 978-1-135-68320-7
- Gudjabidze GE, Gamkrelidze IP (2003) *Geological map of Georgia, 1:500,000*. Georgian State Department of Geology and National Oil Company "Saqnavtobi"
- Hoek E (2007) *Practical rock engineering* (2007 edition). <http://www.roscience.com>
- ISRM – Commission on Classification of Rocks and Rock Masses (1981) Basic geotechnical description of rock masses. *Int J Rock Mech Min Sci Geomech Abstr* 18:85–110
- ISRM – Commission on Standardization of Laboratory and Field Tests (1978) Suggested methods for the quantitative description of discontinuities in rock masses. *Int J Rock Mech Min Sci Geomech Abstr* 15(6):319–368
- Margottini C, Spizzichino D (2009) The management of cultural and environmental heritage sites: a pivot for conservation and enhancement. In: *Proceedings of the first international symposium on Danxia Landform*. The 2nd collection, Danxiashan, Guadong, China, 26–28 May 2009
- National Agency for Cultural Heritage Preservation of Georgia (2009) *Rehabilitation of the monuments of Georgia*. p 142. <http://www.Heritagesites.ge>. Accessed 12 May 2012
- Rapp SH (2003) *Studies in medieval Georgian historiography: early texts and Eurasian contexts, passim*. Peeters, Leuven, retrieved on 26 Apr 2009. ISBN 90-429-1318-5
- SESAME Project – Site EffectS assessment using AMbient Excitations (2004) European Commission Research General Directorate Project No. EVG1-CT-2000-00026. Deliverable 23.12 Guidelines for the implementation of the H/V spectral ratio technique on ambient vibrations: measurements, processing and interpretation
- Wakhoucht (Brosset, Marie-Félicité, transl., 1842) *Description géographique de la Géorgie*. A la typographie de l'Académie Impériale des Sciences, St. Petersburg, pp 365–369



Investigating Natural Hazards in the Peruvian Region of Nasca with Space-Borne Radar Sensors

Deodato Tapete, Francesca Cigna, Rosa Lasaponara, and Nicola Masini

Abstract

ENVISAT ASAR IS2 C-band imagery from the European Space Agency (ESA) archive was processed over the Peruvian region of Nasca, to investigate landscape modifications and dynamics of natural hazards and surface processes. Changes of radar backscattering (σ^0) were computed for the period 2003–2007, and the temporal evolution of the Rio Grande drainage basin was assessed. ASAR amplitude information rather than coherence and phase, was exploited to monitor environmental changes that may cause detrimental effects on natural and cultural heritage. The comparison of multi-platform satellite imagery allowed the detection of aqueduct systems (the so-called ‘*puquios*’) designed by ancient Paracas and Nasca Civilizations (fourth century BC to sixth century AD) for water collection and supply.

Keywords

Land surface processes • Synthetic Aperture Radar • Change detection • Cultural heritage • Nasca

D. Tapete (✉)

Department of Geography, Durham University, South Road, Durham DH1 3LE, UK

Institute of Hazard, Risk and Resilience (IHRR), Durham University, South Road, Durham DH1 3LE, UK

e-mail: deodato.tapete@durham.ac.uk

F. Cigna

British Geological Survey (BGS), Natural Environment Research Council (NERC), Nicker Hill, Keyworth, Nottingham NG12 5GG, UK

e-mail: fcigna@bgs.ac.uk

R. Lasaponara

Institute of Methodologies for Environmental Analysis (IMAA), National Research Council (CNR), Contrada S. Loja, Tito Scalo, Potenza 85050, Italy

e-mail: rosa.lasaponara@imaa.cnr.it

N. Masini

Institute for Archaeological and Monumental Heritage (IBAM), National Research Council (CNR), Contrada S. Loja, Tito Scalo, Potenza 85050, Italy

e-mail: n.masini@ibam.cnr.it

Synthetic Aperture Radar on Nasca Heritage

The Peruvian region of Nasca is widely renowned for the millennial archaeological features—the UNESCO WHL Lines and Geoglyphs of Nasca and Pampas de Jumana, the World’s largest adobe Ceremonial Centre of Cahuachi and the ancient aqueduct systems of *puquios*—which testify a long history of human occupation since 2,000 BC along the tributaries of Rio Grande, i.e. Rio Ingenio, Rio Nazca and Rio Taruga.

Cultural heritage and landscape of Nasca are chronically exposed to natural hazards, mainly flash floods and run-off of sandy materials from unstable slopes. Archaeological evidences testify that the decline of Cahuachi, in the fourth phase of its history (AD 350–400), was due to a series of mudslides and severe earthquake (Masini et al. 2012, and references therein).

To investigate the impact of natural hazards of the heritage and landscape of the region, we implement change detection analysis based on exploitation of satellite Synthetic Aperture Radar (SAR) archives. This research also

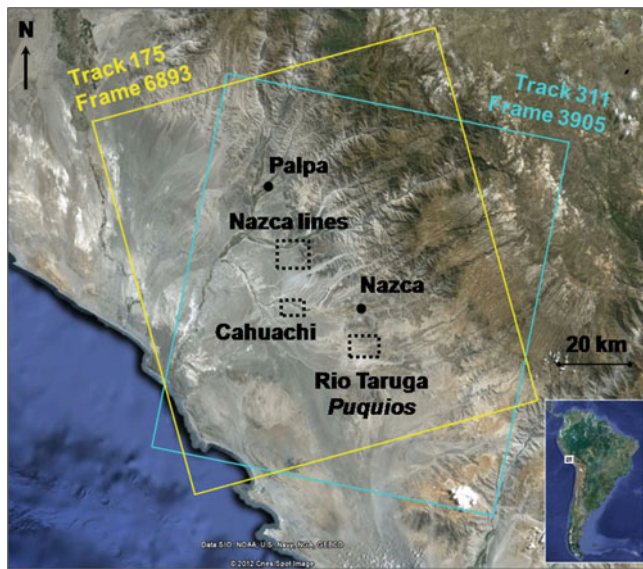


Fig. 1 Areas of interest and ENVISAT ASAR IS2 footprints in ascending and descending mode over the Nasca region, Peru (Google earth © 2012 Cnes/Spot Image) (modified from Cigna et al. 2013)

complements the activities of the Italian mission of heritage Conservation and Archaeogeophysics (ITACA), which involves researchers from the National Research Council (CNR) of Italy. Differently from previous studies that used interferometric coherence (Lefort et al. 2004; Ruescas et al. 2009) and its spatial variation on the micro- and meso-relief scale (Baade and Schullius 2010), our paper presents the results obtained by making the best out of amplitude information contained within SAR imagery.

Input Data and Methodology

The input data that we used for our study cover the whole natural and cultural landscape of the Nasca region in Southern Peru (Fig. 1) and include:

- 8 ENVISAT ASAR IS2 scenes acquired in descending mode between 04/02/2003 and 15/11/2005;
- 5 ENVISAT ASAR IS2 scenes acquired in ascending mode between 24/07/2005 and 11/11/2007.

SAR-based results were also integrated and cross-validated with multispectral Advanced Spaceborne Thermal Emission and Reflection Radiometer (ASTER) data acquired on 30/05/2003, 01/06/2004 and 10/06/2007 in the visible–near-infrared (VNIR), shortwave infrared (SWIR) and thermal infrared (TIR), with spatial resolutions of 15, 30 and 90 m respectively, and derived Normalized Difference Vegetation Index (NDVI) and Water Index (NDWI) maps.

We analysed and reconstructed the temporal evolution of radar signatures of the targets on the ground in the monitoring period 2003–2007. We followed the method of raw data

focusing into Single Look Complex (SLC), absolute radiometric calibration and co-registration described in Cigna et al. (2013) and, finally, we retrieved the time series of radar backscattering coefficient (σ^0).

According to the coded radar terminology (cf. ESA, Radar Glossary 2013), this parameter corresponds with the normalized estimate of the radar return signal (σ) from a distributed target, and it is defined as per unit area on the ground.

For each image pixel i , the temporally averaged backscattering coefficient was obtained using the formula:

$$\bar{\sigma}_i^0 = \frac{1}{n} \sum_{t=t_1}^{t=t_n} \sigma_i^0(t) \quad (1)$$

where

- t_1 and t_n are the acquisition times of the first and last ASAR scenes of the stack, respectively;
- n is the total number of scenes of the stack;
- $\sigma_i^0(t)$ is the pixel backscattering coefficient at time t .

We also derived and geocoded the following products based on the two stacks of co-registered Multi Look Intensity (MLIs) images:

- *Time series of spatially averaged radar signatures for selected Areas Of Interest (AOIs)*—i.e. graphs showing temporal variation of the average σ^0 of the N pixels within each AOI;
- *Image ratios ($R\sigma^0$) of different pairs of spatially filtered MLIs*—which enhance σ^0 changes occurred over the scene during the time interval between two MLIs;
- *RGB (Red-Green-Blue) or RC (Red-Cyan) colour composites of 3 or 2 MLIs respectively*—where pixels with constant σ^0 are shown with grey levels, while those that changed are highlighted with colours of tint corresponding with the scenes recording higher σ^0 .

Results and Discussion

Our study aimed to: (1) explore potentials for monitoring and rapid mapping of land surface processes; (2) create amplitude-based change detection maps to image landscape changes in areas of human occupation; (3) use SAR imagery to improve knowledge of ancient systems of water management.

Monitoring Landforms and Natural Hazards

Assessment of changes in the surface backscattering properties is an effective strategy to map fast land processes and scenes which are rapidly evolving. Mass movement

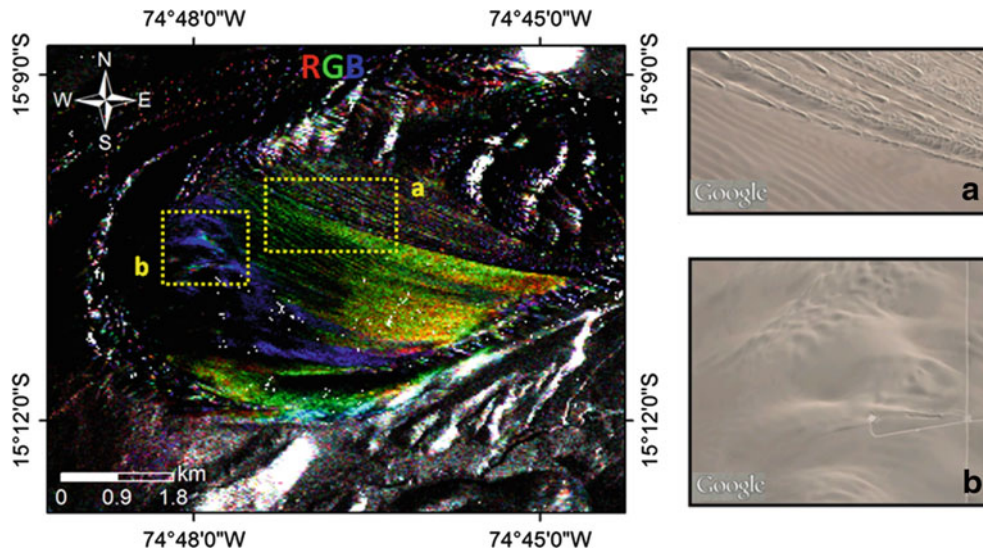


Fig. 2 RGB colour composite of a sand dune south of Cerro Blanco obtained by comparison of ASAR descending scenes acquired on 04/02/2003, 15/04/2003 and 24/06/2003 (red, green and blue channels,

respectively). Google earth (© 2013 DigitalGlobe) views in (a) and (b) correspond with the areas within the yellow dashed boxes (modified from Cigna et al. 2013)

phenomena such as earth/debris flows and sand dune displacements significantly alter the terrain morphology and, consequently, its response to the microwave radiation. Whatever is the event that affected the monitored area, the latter still continues backscattering the incident radiation and σ^0 changes can be estimated over time. Whereas, for instance, the destruction and disappearance of radar targets with stable dielectric properties due to severe natural events and/or human-induced intentional or occasional damages, prevent any Persistent Scatterer Interferometry (PSI) analysis to be performed successfully [see the specific comments reported in Tapete et al. (2012, 2013a) with regard to the impacts on SAR-based archaeological applications].

In arid regions, wind-driven dynamics of sand dune displacements and mass movements triggered by sudden rainfall events are hazards of high relevance. Impacts on cultural features are quite frequent, especially when scatterers and structures are spread over wide regions, which are difficult to monitor periodically.

We tested our approach to investigate surface evolution of a sand dune area located about 30 km south of Cerro Blanco (a mountain considered sacred by the inhabitants of Cahuachi). Figure 2 shows the RGB colour composite of MLIs acquired on 04/02/2003, 15/04/2003 and 24/06/2003. The green-yellow coloured portion is related to an increased reflectivity in February and April 2003. This result clearly suggests the occurrence of movements of sand material, mostly occurred between April and June, which significantly modified the local surface morphology/orientation, and the related radar backscattering.

Comparison with Google earth clarifies the nature of the processes affecting the sand dune surface (Fig. 2a, b).

Amplitude-Based Environmental Assessment

Multi-temporal change detection, complemented with ASTER-based NDVI and NDWI estimates, allows regional-scale zoning of areas affected by σ^0 changes due to seasonal/yearly fluctuations of water availability. This assessment is highly helpful especially over fluvial areas and riverbeds, where long-standing human activity has significantly modified the land use.

A couple of ENVISAR ASAR scenes acquired during the same month of two consecutive years (November 2004 and 2005) were compared to detect yearly changes, and change detection maps were produced (Fig. 3). Orange-red coloured areas over agricultural fields indicate a slightly decreased backscattering from 2004 to 2005, while three localized areas in blue show an increase of σ^0 up to 4–5 times the initial values (Fig. 3). The examination of the ASTER images acquired in June 2003 and 2004 indeed highlights a general decrease in the reflectance in the NIR band and the vegetation cover over the eastern part of this area (Fig. 4), even where increased backscattering is found.

Detection of Ancient Water Systems

Discrimination of σ^0 properties over the monitored scene can lead to the recognition of morphological features attributable to archaeological remains and traces of past human occupation. Besides geometry and surface roughness, soil moisture content and material composition have also an effect on the surface brightness in the radar images.

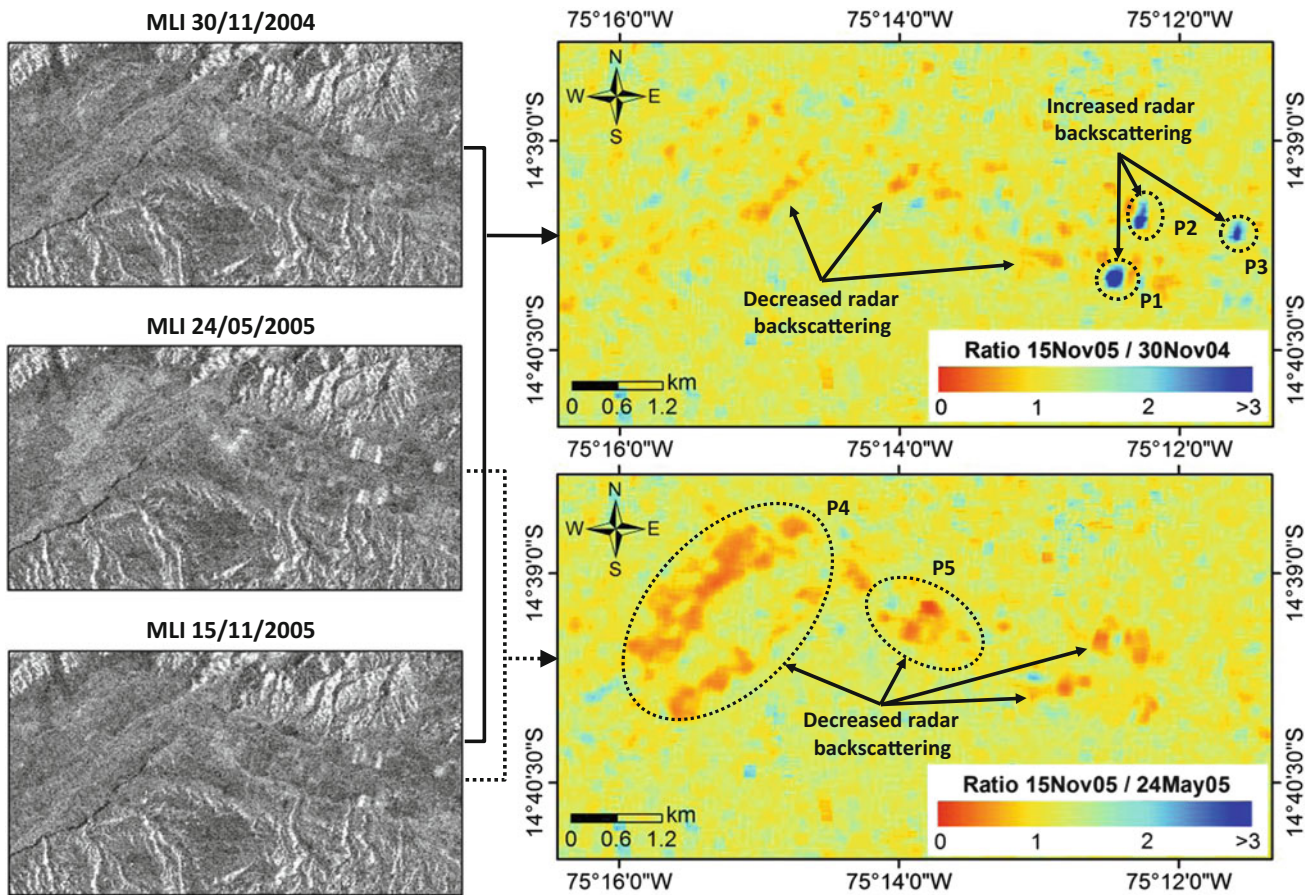


Fig. 3 Amplitude change detection maps obtained over the Rio Ingenio floodplain by ratioing the backscattering coefficient ($R\sigma^0$) estimated in November 2004 and November 2005 (yearly basis), and

May 2005 and November 2005 (intra-year assessment) respectively (modified from Cigna et al. 2013)

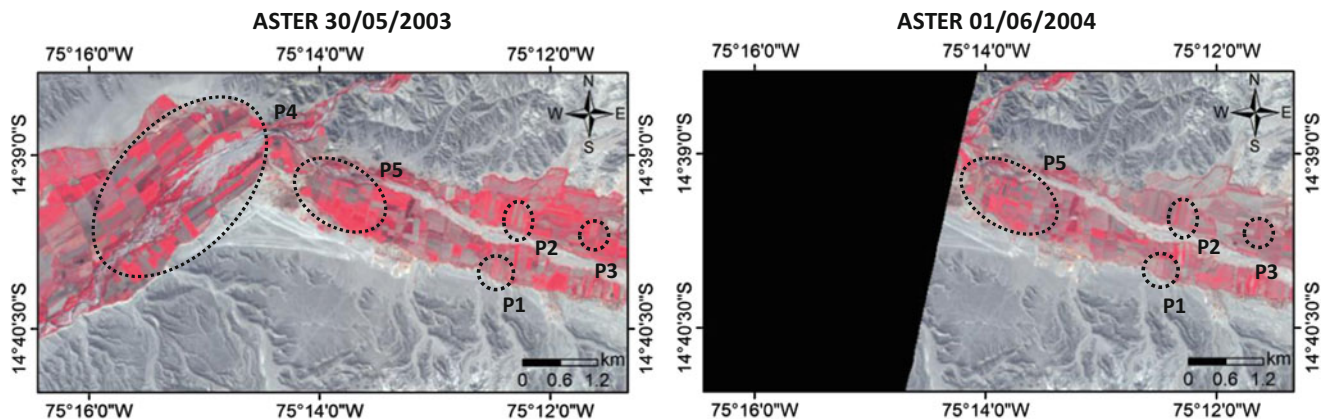


Fig. 4 ASTER 2003 and 2004 RGB composite of bands 3N-2-1 covering the same portion of the Rio Ingenio floodplain shown in Fig. 3 were used to correlate backscattering coefficient changes with

vegetation variations over a similar temporal period. The areas P1-P5 correspond with those affected by $R\sigma^0$ changes (compare with Fig. 3; modified from Cigna et al. 2013)

This aspect was used in this study to distinguish still functioning *puquios*—an ingenious system of water collection and storage through subterranean galleries built by the Nasca Civilization—and those currently abandoned. RC

colour composites of two MLIs acquired on 30/11/2004 and 15/11/2005 and ASTER-derived 2003–2004–2007 NDVI and NDWI suggest changes of soil moisture and vegetation over a large dry hydrographic reticulum lying

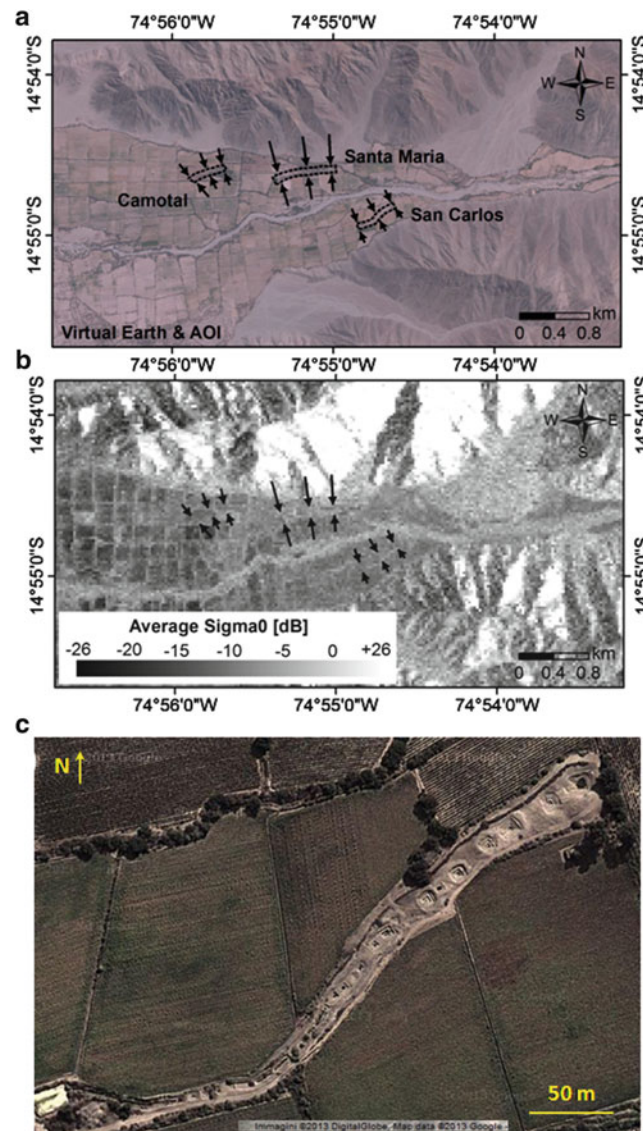


Fig. 5 (a) Virtual Earth image (Google earth © 2012 Cnes/Spot Image) and (b) 2003–2005 average MLI in descending mode of Rio Taruga. (c) Google Maps view of *puquio* San Carlos (© 2013 DigitalGlobe Map data) (modified from Tapete et al. 2013b)

within the desert between the Rio Nazca and the Pampa de Chauchilla (see also Lasaponara & Masini, 2012). Among other features, a linear cyan one was found in correspondence with the track of a young *puquio* (for further detail the reader can refer to Tapete et al. 2013b).

Average MLI over the Taruga Valley allows the identification of the still functioning *puquios* Santa María and San Carlos, as well as of the disused *puquio* Camotal. The latter is distinguished based on different σ^0 likely due to its condition of abandonment (Fig. 5).

The capability of SAR imagery to support the recognition of ancient hydraulic systems (as also proven by other studies

in wet regions, such as Moore et al. 2007) opens perspectives in water resource management from space. Impacts on arid cultural landscapes facing drought can be enormous for local communities. Furthermore, the assessment of the current condition of archaeological features like the *puquios* can inform on the potential impacts of climate change and desertification.

With this regard, high resolution SAR imagery, such as those from recently launched space-borne radar sensors, is expected to provide the most suitable scale of investigation. Nevertheless, an obvious shortcoming is represented by the cost of this type of imagery, with consequent constraints on the actual exploitation for monitoring activities.

From the point of view of scientific investigation over the Nasca region, Baade and Schmullius (2010), for instance, have recently discussed advantages and limits of TerraSAR-X products for multi-scale studies over the Rio Grande drainage basin.

Tapete et al. (in press) have shown the benefits deriving from the unprecedented level of spatial resolution offered by SpotLight and High Resolution SpotLight beam modes of TerraSAR-X and TanDEM-X satellites for local-scale applications over the archaeological landscape of Nasca. Surface features are already appreciable within the SAR images visualised based on their amplitude values.

Concluding Remarks

This study with ENVISAT ASAR data forms the basis for further investigations with other archive (i.e. C-band ERS-1/2) and recently to newly acquired imagery (i.e. TerraSAR-X). This amplitude-based approach complements successfully those exploiting interferometric coherence and phase, and can support a wide range of remote sensing activities including, but not limited to: (1) monitoring of land surface processes which can trigger natural hazards potentially damaging cultural and natural heritage; (2) environmental assessment from regional to local scale; and (3) understanding of past (and future) water resource management strategies. Further research will be also conducted by the authors with high resolution X-band imagery in the framework of the TSX-Archive-2012 LAN1881 project.

Acknowledgments ENVISAT ASAR imagery, auxiliary data and DORIS precise orbits were provided by the European Space Agency (ESA) through the Cat-1 Project Id. 11073. Data processing was carried out using the GAMMA SAR and Interferometry Software, developed by the GAMMA Remote Sensing and Consulting AG (Switzerland) and licensed to the British Geological Survey – Natural Environment Research Council (United Kingdom). ASTER multispectral data and GDEM V2 are products of the Ministry of Economy, Trade, and Industry (Japan) and US National Aeronautics and Space Administration, and were made available through the Land Processes Distributed Active Archive Center (LP DAAC)—Global Data Explorer.

References

- Baade J, Schmullius CC (2010) Interferometric microrelief sensing with TerraSAR-X – first results. *IEEE Trans Geosci Rem Sens* 48(2):965–970
- Cigna F, Tapete D, Lasaponara R, Masini M (2013) Amplitude change detection with ENVISAT ASAR to image the cultural landscape of the Nasca region, Peru. *Archaeol Prospect* 20(2):117–131. doi:10.1002/arp.1451
- ESA (2013) Radar and SAR Glossary. <https://earth.esa.int/handbooks/asar/CNTR5-2.htm>. Last accessed 26 Nov 2013
- Lasaponara R, Masini N (2012) Following the ancient Nasca puquios from space. In: Lasaponara R, Masini N (eds) *Satellite remote sensing. A new tool for archaeology*. Springer, Berlin, pp 269–289. ISBN 978-90-481-8801-7
- Lefort A, Grippa M, Walker N, Stewart LJ, Woodhouse I (2004) Change detection across the Nasca pampa using spaceborne SAR interferometry. *Int J Rem Sens* 25(10):1799–1803
- Masini N, Lasaponara R, Rizzo E, Orefici G (2012) Integrated remote sensing approach in Cahuachi (Peru): studies and results of the ITACA Mission (2007–2010). In: Lasaponara R, Masini N (eds) *Satellite remote sensing. A new tool for archaeology*. Springer, Berlin, pp 307–344. ISBN 978-90-481-8801-7
- Moore E, Freeman T, Hensley S (2007) Spaceborne and airborne radar at Angkor: introducing new technology to the ancient site. In: Wiseman J, El-Baz F (eds) *Remote sensing in archaeology. Interdisciplinary contributions*. Springer, Berlin, pp 185–216. ISBN 978-0-387-44453-6
- Ruescas AB, Delgado JM, Costantini F, Sarti F (2009) Change detection by interferometric coherence in Nasca Lines, Peru (1997–2004). In: *Fringe 2009*, 30 November to 4 December, ESRIN, Frascati, European Space Agency SP-677
- Tapete D, Fanti R, Cecchi R, Petrangeli P, Casagli N (2012) Satellite radar interferometry for monitoring and early-stage warning of structural instability in archaeological sites. *J Geophys Eng* 9(4): S10–S25. doi:10.1088/1742-2132/9/4/S10
- Tapete D, Casagli N, Fanti R (2013a) Radar interferometry for early stage warning of monuments at risk. In: Margottini C et al (eds) *Early warning, instrumentation and monitoring*, vol 2. Springer, Berlin, pp 619–625
- Tapete D, Cigna F, Masini N, Lasaponara R (2013b) Prospection and monitoring of the archaeological heritage of Nasca, Peru, with ENVISAT ASAR. *Archaeol Prospect* 20(2):133–147. doi:10.1002/arp.1449
- Tapete D, Cigna F, Lasaponara R, Masini N (in press) Multi-scale detection of changing cultural landscapes in Nasca (Peru) through ENVISAT ASAR and TerraSAR-X. In: IAEG congress proceedings, Springer, 6 pp



Deformations Dynamics in Response to Seasonal Temperature Oscillations: An Example from Pravcicka Brana Rock Arch (Czech Republic)

Jan Vlcko, Martin Brček, and Vladimír Greif

Abstract

The paper discusses the results of the research devoted to the preservation of natural heritage site carried out at **Pravcicka Brana Rock Arch located in Bohemian Switzerland National Park, Czech Republic.**, the largest natural sandstone bridge in Europe. The aim of the study was laid on the relationship between spatial temperature distribution and rate of displacement, as the response to temperature oscillations and to find out kinematic behaviour (deformations dynamics) of the rock arch using computer modeling to simulate if there exists any potential hazard to sandstone body rock arch to collapse.

Keywords

Rock arch stability • Temperature oscillations • Heat transfer • Temperature penetration depth • Thermo-mechanical model • Pravcicka Brana

Introduction

The investigation of thermally driven coupled processes as consequence of response to changes in heat transfer as a result of temperature oscillations generated processes near the surface are becoming actual in rock slope analysis as related to their stability. Several slope failures, where any significant trigger was estimated and rock failure mechanism remain unclear are recently assigned as hazards triggered by meteorological factors (Vargas et al. 2013; Vlcko et al. 2009; Gunzburger et al. 2005; Grøneng et al. 2011; and others). The heat flow penetrating into the rock mass produces temperature field, which changes with heating and cooling phases as well as with the depth. Temperature oscillations produce thermal strains in rock which result in

its deterioration and are conclusive for mechanical weathering and thus form an initial phase for successive potential hazards (thermally generated creep along discontinuities, rock cliffs bending and tilting, rock falls).

In the recent years several studies based on measuring rock surface temperature or temperature at shallow depths within the rock mass were conducted in order to quantitatively estimate the rate of temperature fluctuations on thermal rock fatigue or thermal shock, respectively (Kerr et al. 1984; McGreevy and Whalley 1982; Hall and Hall 1991; Warke and Smith 1994; Warke et al. 1996; Inigo and Vicente-Travera 2002). Experiments carried out by several researchers pointed out that rate of temperature changes play the most important role. If these exceed $\geq 2^\circ\text{C}/\text{min}$ (Richter and Simmons 1974) regardless of thermometer scale (sub zero or above zero recordings) thermal shock may occur (Hall and André 2001; McKey and Friedmann 1985). Apart of these studies covering the field of temperature generated rock deterioration, several studies which pointed out the existence of thermally driven non reversible or plastic deformations of rocks or rock masses that might be accounted as triggers or controlling factors were carried out (Vargas et al. 2013). Larger rock volume displacements reaching the rate of displacement in mm/year rate were

J. Vlcko (✉) • V. Greif

Department of Engineering Geology, Faculty of Natural Sciences, Comenius University, Bratislava 842 15, Mlynska dolina G, Slovakia
e-mail: vlcko@fns.uniba.sk; greif@fns.uniba.sk

M. Brček

Department of Geotechnics, Faculty of Civil Engineering, Slovak University of Technology, Radlinského 11, 813 68 Bratislava, Slovakia
e-mail: brcek@svf.stuba.sk

described by Vlcko et al. (2005), Vlcko et al. (2009) from UNESCO site Spis Castle, further Bakun-Mazor et al. (2011) and Pasten (2013), or m/s rate along pre-existing fractures (Matsuoka and Sakai 1999; Gunzburger et al. 2004, 2005; Clément 2008; Clément et al. 2008; Gunzburger and Merrien-Soukatchoff 2011; Vargas et al. 2013) or along pre-existing shear plane (Watson et al. 2004).

The main objective of the paper is to present the relationship between spatial temperature distribution, rate of displacement and the existence of thermally driven deformations of sandstone body of Pravcicka brana Rock Arch as the response to temperature oscillations.

Site Under Study

Bohemian Switzerland a small sandstone area in the Central Europe having a characteristic landscape with plateaus, deep canyons, rock cities and labyrinths developed on massive, sub-horizontally stratified sandstones of Cretaceous age, and the rich biodiversity related nature landscape were the main reasons to establish (January 1st, 2000) the Bohemian Switzerland National Park in the NW of Czech Republik. Geomorphological conditions, tectonic and lithological setting and exogeneous geological processes are the reason for higher occurrence of natural geohazards (weathering and erosion e.g. Varilova and Zvelebil 2005). The rock falls are the wide spread hazard characterising the area of National Park. According to 1790–2000 rock fall statistics in the Labe River Canyon, regional recurrence interval for rock falls with volumes of the order of 10^2 m^3 is approximately 3 years and the one for the falls of 10^3 m^3 is about 10 years (Varilova and Zvelebil 2005).

Pravcicka Brana Rock Arch, the best known attraction of the Bohemian Switzerland, is situated on the Czech-Germany border (415 m a.s.l.) north from the city Decin and is the largest natural sandstone bridge in Europe, considered to be the most beautiful natural form in Bohemian Switzerland. The dimensions of the arch are remarkable: the span of the arch at the bottom is 26.5 m, the height is 16 m, width 7.5 m, minimum thickness 2.5 m. The arch is built by marine, shallow water deposited sandstones of Upper Cretaceous (Turonian) age. Relatively massive quartzose sandstones with fracturing in distant spacings along with the formation of basal planes show typical rectangular jointing. The rocks show with quasi cyclical variable grain size (from fine—grained sandstones at the base of the cycle merge into medium-grained and then coarse—are composed of fine-grained quartz sandstone transiting upwards into coarse-grained sandstones to conglomerates). The buttresses are composed of fine-grained quartz sandstone transiting upwards into coarse-grained strata. The tie beam

is built by medium-grained sandstone with occasional conglomerate beds.

Heat Transfer Study: Analytical Approach and In Situ Temperature Observation

Two approaches we adopted: direct in situ measurements and analytical computation. Computed results refer to ideal bodies and provide important standards concerning the heat transfer in rocks. In situ data recordings represent temperature transfer inside the rock mass, if compared with computed ones, it can be determined if the data are error laden (inappropriate recording intervals, unknown structural heterogeneity in the interior of the rock mass, influence of moisture, etc.) or correspond to the real natural conditions. In order to acquire real temperature data at and inside the sandstone rock mass a monitoring net was installed. The net comprised eight high accuracy thermocouples (Pt1000TGL/40) suited for measurements in the range of -30 to $+100$ °C inserted at different depths within the interior of the rock mass. Four thermocouples were embedded at two positions (both eastern and western sides) in longitudinal direction (Fig. 1): one at the rock surface and the three others at selected depths 0.10, 0.40, and 0.90 m. Unfortunately sensors at depth of 0.90 m were shortly after the installation damaged and recorded data were incorrect. Temperatures are acquired hourly and stored in datalogger.

According to Carslaw and Jaeger (1959), the temperature profile along x axis in semi-infinite solid can be found analytically for a given time, T as follows:

$$T(x, t) = T_0 + Ae^{-x/\delta} \sin(\omega t - x/\delta) \quad (1)$$

where A is the harmonic temperature amplitude determined by the spectral analysis of time series from in situ temperature recordings taken from different depths within the rock mass in the certain time period as shown in Table 1, ω is angular frequency of time variations $\omega = 2\pi/\tau$ (s^{-1}), around the mean temperature T_0 for a given period τ (s^{-1}). The penetration depth of temperature changes $\delta = \sqrt{2a/\omega}$ depends on the thermal diffusivity coefficient a ($\text{m}^2 \cdot \text{s}^{-1}$) calculated from the expression (Carslaw and Jaeger 1959):

$$a = (\delta^2 \pi) / \tau \quad (2)$$

where

$$\delta = (Z_j - Z_i) / \ln(A_j/A_i) \quad (3)$$

Z_j and Z_i are the depths (m); represent the rock surface and depth of 0.40 m) and A_j and A_i (°C) corresponding

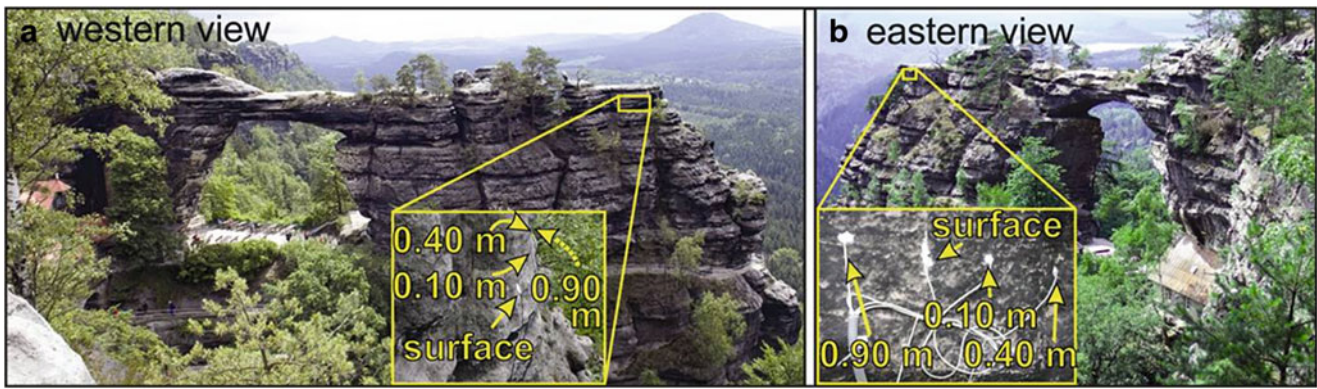


Fig. 1 Location of thermocouples embedded in the Pravcicka Brana Rock Arch

Table 1 Diurnal and annual temperature amplitudes determined directly from in situ recordings taken at three different depths in the rock mass (eastern side of the rock arch)

Temperature amplitude (°C)								
Depth (m)	First year recordings (June 09–May 10)		Second year recordings (June 10–May 11)		Third year recordings (June 11–May 12)		Total period recordings (3 years) (June 09–May 12)	
	Diurnal	Annual	Diurnal	Annual	Diurnal	Annual	Diurnal	Annual
	0.0	4.94	14.98	5.40	14.98	5.26	14.89	5.17
0.10	3.01	15.37	3.29	15.36	3.23	15.31	3.21	15.36
0.40	1.37	12.23	1.39	12.25	1.32	12.31	1.37	12.25

temperature amplitudes. The temperature decay with the time is expressed by the equation

$$t_z = z/(\omega\delta). \tag{4}$$

In order to estimate rock mass response to short-term (diurnal) and long-term-annual (Fig. 2) temperature oscillations, temperature data records at given depths were analyzed and T_{max} and T_{min} as well as the harmonic temperature amplitudes A (°C) and thermal diffusivity a ($m^2 \cdot s^{-1}$) for diurnal (daily) and annual cycles were *calculated*.

From curves in Figs. 3 and 4 is clearly visible that for both diurnal and annual cycles the largest extremes between T_{max} and T_{min} are in summer period, while in winter period the situation is opposite. As far as the temperature attenuation (decay), time lag and the penetration of diurnal temperature wave concerns, expressed in m or in %, the calculated temperature amplitude 0.01 (°C) represents 99.9 % of temperature attenuation corresponding to the depth of 1.5 m (Fig. 4), while for annual temperature oscillations the calculated temperature amplitude 0.10 (°C) represents 99.34 % of temperature attenuation and corresponds to the depth of 10.0 m. The annual penetration depth represents approximately septuple of the diurnal penetration depth. The time lag for diurnal temperature oscillations corresponds to 1,583 min (approximately 26 h), while the annual time lag corresponds approximately to 292 days. All the recorded and calculated data represent the eastern side of Pravcicka Brana Rock

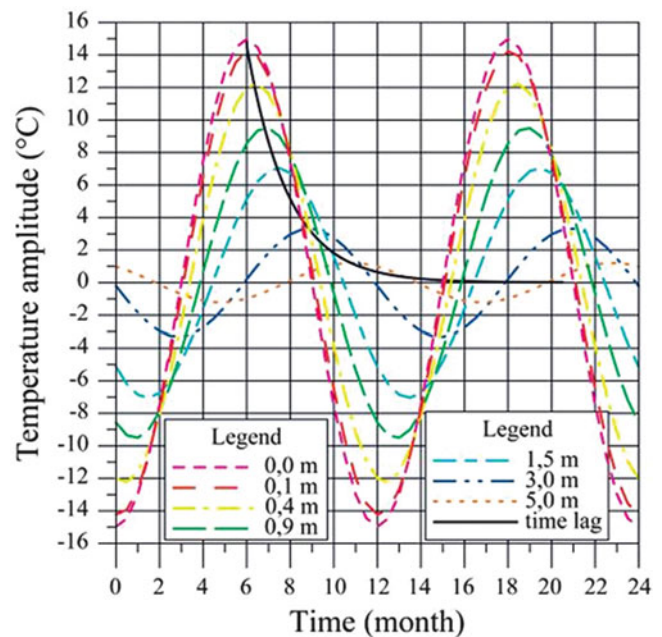


Fig. 2 Rock mass response to long-term (annual) temperature oscillations based on temperature records

Arch (western side data are very similar despite the different orientation).

From the annual temperature distribution inside the rock mass is clearly defined that the greatest differences in

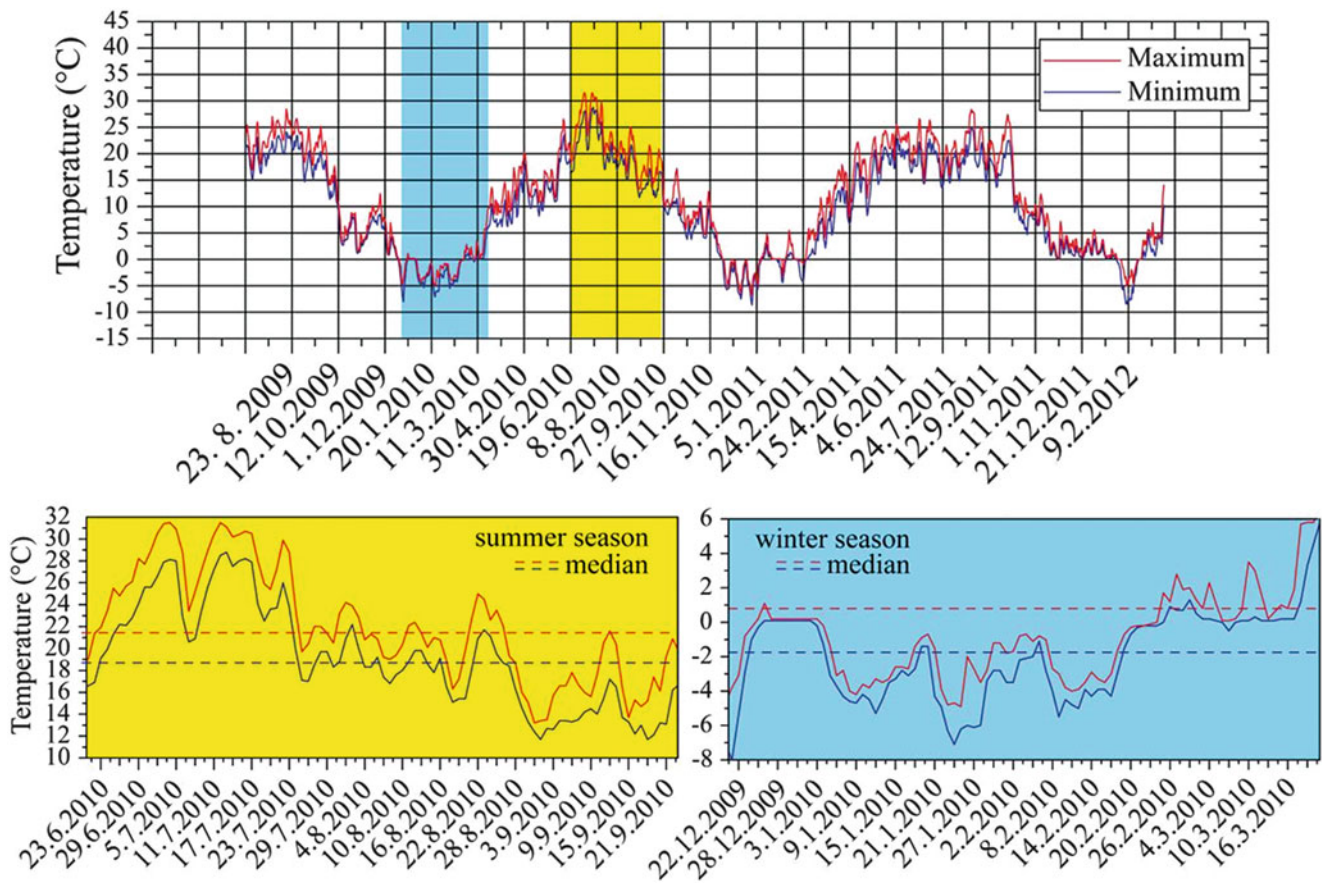


Fig. 3 Temperature oscillations recorded at the depth of 0.40 m

temperature oscillations were observed in summer; at the rock surface the mean values are as follows: median $T_{\max} = 29.1\text{ }^{\circ}\text{C}$ and median $T_{\min} = 15.6\text{ }^{\circ}\text{C}$ (in winter season 0.9 to -3.1) while at the depth of 0.40 m (Fig. 3) median $T_{\max} = 21.4\text{ }^{\circ}\text{C}$ and $T_{\min} = 18.7\text{ }^{\circ}\text{C}$ for summer period and median $T_{\max} = -0.8\text{ }^{\circ}\text{C}$ and $T_{\min} = -1.75\text{ }^{\circ}\text{C}$ for winter period were estimated.

From curves in Fig. 3 and 4 is clearly visible that for both diurnal and annual cycles the largest extremes between T_{\max} and T_{\min} are in summer period, while in winter period the situation is opposite. As far as the temperature attenuation (decay), time lag and the penetration of diurnal temperature wave concerns, expressed in m or in $\%$, the calculated temperature amplitude $0.01\text{ }^{\circ}\text{C}$ represents 99.9% of temperature.

Pravcicka Brana Rock Arch Versus Deformation Controlled by the Temperature

Since the displacement monitoring records confirmed both reversible and irreversible displacements the thermo-mechanical model we set up confirmed that the temperature

oscillations induce stress changes through thermo-elastic expansion and contraction. Since the displacement monitoring records confirmed both reversible and irreversible displacements, both depended on thermal dilation as a result of thermal loads triggered by diurnal and annual temperature oscillations we tried to set up a model of temperature distribution and kinematic behaviour of the beam at two selected points (assigned A, B) where the displacements in X (horizontal) and Y (vertical) axis were monitored. The input represent continuous time series of data acquired from 3 years temperature monitoring at different depths at three locations at the eastern part of sandstone arch tie beam. The model (Fig. 5) was prepared using commercial software UDEC and the results are corresponding to long term displacement records. The results we gained confirmed that the temperature oscillations induce stress changes through thermo-elastic expansion and contraction but there were not observed any significant displacements controlled by the temperature. According to the model calculations (Fig. 5) the rate of reversible displacement reaches the value from 2.2 to $2.8 \cdot 10^{-2}\text{ cm}$ in x axis and approximately the same rate of displacement was estimated in y axis for point A. For point B were estimated also reversible

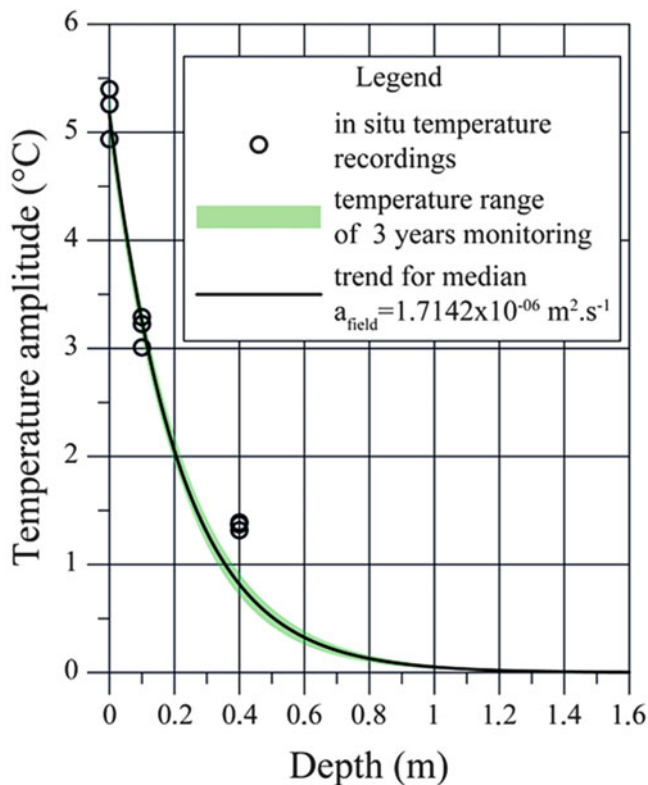


Fig. 4 Curve showing the penetration of the diurnal temperature wave calculated according to 3 years temperature recordings from three different depths the eastern side of Pravcicka Brana Rock Arch (western side data are very similar despite the different orientation)

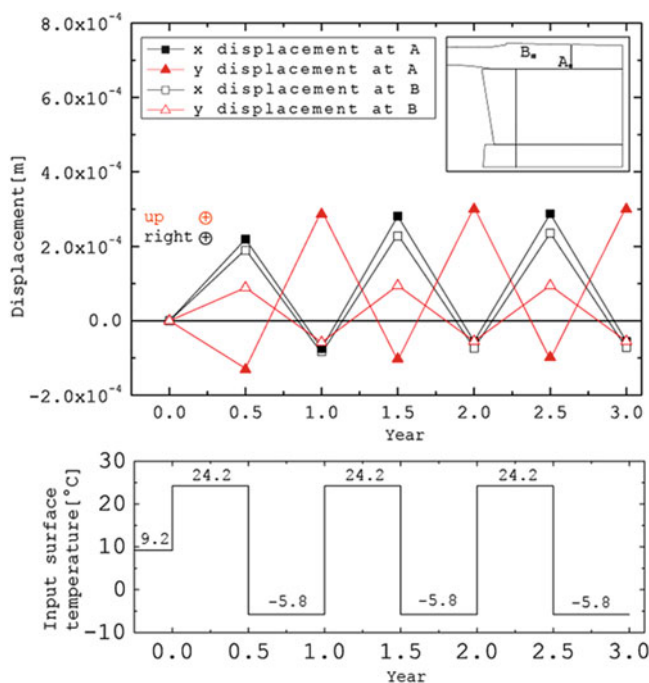


Fig. 5 Computed displacements at monitored points A and B placed near the edge of the tie beam of the Pravcicka Brana Rock Arch as a result of thermo-mechanical model with input temperatures based on in situ records acquired during three annual cycles

movements with the rate of displacement in x axis reaching almost the same values as at point A, differences are in y axis where the the movements reach low values (approx $1.0 \cdot 10^{-2}$ cm) and are synchronous with x axis (both axis have the same trend). This confirms the idea that in summer period the tie beam of the rock arch has the tendency to upward bending where in the upper part of the tie beam tension and at the bottom of it compression occur, in the winter period the movements are of opposite character and downward bending prevail.

Conclusion

The temperature oscillations at the tie beam of the sandstone rock body are of elastic character (reversible), small in magnitude and do not bring at present any potential collapse hazard to Pravcicka Brana Rock Arch. On the other hand cyclic and reversible movements produce shear stress along horizontal joint and once if the shear strength (mechanical parameters of sandstone of rock arch are very low) of the sandstone will be reached, collapse may occur. Far greater danger for this beautiful nature heritage site at present pose the triggers of different character e.g. rock deterioration due to high degree of weathering and tectonic setting.

Acknowledgments This work was supported by the Slovak Research and Development Agency under the contract No. APVV-0641-10, No. APVV-0330-10 and APVV SK-CN-0017-12 Landslide hazard and risk assessment for UNESCO World Heritage Site, Danxia, China as well as by Int. Consortium on Landslides Project IPL-101-2 Landslides monitoring and slope stability at selected historic sites in Slovakia.

References

- Bakun-Mazor D, Hatzor YH, Glaser SD, Santamarina JC (2011) Climatic effects on key-block motion: evidence from the rock slopes of Masada World Heritage Site. In: 45th US Symposium in Rock Mechanics (American Rock Mechanics Association). San Francisco, CA. pp 480–487
- Carslaw HS, Jaeger JC (1959) Conduction of heat in solids, 2nd edn. Oxford University Press, Oxford, p 517
- Clément C (2008) Auscultation d'un versant rocheux par mesures de déformations thermo-mécaniques. In: XXVI^{èmes} Rencontres Universitaires de Génie Civil, 4–6 Juin, Nancy, France, 8 p
- Clément C, Gunzburger Y, Merrien-Soukatchoff V, Dünner C (2008) Monitoring of natural thermal strains using hollow cylinder strain cells: the case of a large rock slope prone to rockfalls. In: Tenth international symposium on landslides and engineered slopes, June 30–4 July, Xi'an, China, 7 p
- Grøneng G, Christiansen H, Nilsen B, Blikra LH (2011) Meteorological effects on seasonal displacements of the Aknes rockslide, western Norway. Landslides 8:1–15
- Gunzburger Y, Merrien-Soukatchoff V (2011) Near-surface temperatures and heat balance of bare outcrops exposed to solar radiation. Earth Surf Process Landforms 36(12):1577–1589
- Gunzburger Y, Merrien-Soukatchoff V, Senfaute G, Pigeo JP (2004) Field investigations, monitoring and modeling in the identification

- of rock fall causes. In: Lacerda W, Ehrlich M, Fontoura S, Sayão A (eds) Landslides evaluation and stabilization, Proceedings of the Ninth International Symposium on Landslides. Taylor and Francis, London, pp 557–556
- Gunzburger Y, Merrien-Soukatchoff V, Senfaute G, Pigué JP (2005) Influence of daily surface temperature fluctuations on rock slope stability: case study of the Rochers de Valabres slope (France). *Int J Rock Mech Min Sci* 42(3):331–349
- Hall K, André MF (2001) New insights into rock weathering from high-frequency rock temperature data: an Antarctic study of weathering by thermal stress. *Geomorphology* 41:23–35
- Hall K, Hall A (1991) Thermal gradients and rock weathering at low temperatures: some simulation data. *Permafrost Periglacial Process* 2(2):103–112
- Inigo AC, Vicente-Travera S (2002) Surface-inside (10 cm) thermal gradients in granitic rocks: effect of environmental conditions. *Build Environ* 37(1):101–108
- Kerr A, Smith BJ, Whalley WB, McGreevy JP (1984) Rock temperatures from southeast Morocco and their significance for experimental rock-weathering studies. *Geology* 12:306–309
- Matsuoka N, Sakai H (1999) Rockfall activity from an alpine cliff during thawing periods. *Geomorphology* 28:309–328
- McGreevy JP, Whalley WB (1982) The geomorphic significance of rock temperature variations in cold environments. A discussion. *Arctic Alpine Res* 14:157–162
- McKey CP, Friedmann EI (1985) The cryptoendolithic microbial environment in the Antarctic cold desert: temperature variation in nature. *Polar Biology* 4:19–25
- Pasten C (2013) Geomaterials subjected to repetitive loading: implications on energy systems. PhD thesis. Georgia Institute of Technology, Atlanta, GA
- Richter D, Simmons G (1974) Thermal expansion behavior of igneous rocks. *Int J Rock Mech Min Sci and Geomechanics Abstracts* 11:403–411
- Vargas JE, Velloso R, Chávez L, Gusmão L, Amaral C (2013) On the effect of thermally induced stresses in failures of some rock slopes in Rio de Janeiro, Brazil. *Rock Mech Rock Eng* 46:123–34
- Varilova Z, Zvelebil J (2005) Sandstone relief geohazards and their mitigation: rock fall risk management in the Bohemian Switzerland National Park. *Ferrantia* 44:53–58
- Vlcko J, Jezný M, Pagáčová Z (2005) Influence of thermal expansion on slope displacements. In: Sassa K, Fukuoka H, Wang F, Wang G (eds) Landslides: risk analysis and sustainable disaster management. Proceedings of the first general assembly of the international consortium on landslides, Washington. Springer, 7, pp 71–74
- Vlcko J, Greif V, Gróf V, Jezný M, Petro L, Brček M (2009) Rock displacement and thermal expansion study at historic heritage sites in Slovakia. *Environ Geol* 58:1727–1740
- Warke PA, Smith BJ (1994) Short-term rock temperature fluctuations under simulated hot desert conditions: some preliminary data. In: Robinson DA, Williams RBG (eds) Rock weathering and landform evolution. Wiley, Chichester, pp 57–70
- Warke PA, Smith BJ, Magee RW (1996) Thermal response characteristics of stone: implications for weathering of soiled surfaces in urban environments. *Earth Surf Process Landforms* 21:295–306
- Watson AD, Moore DP, Stewart TW (2004) Temperature influence on rock slope movements at Checkerboard Creek. In: Landslides: evaluation and stabilization. Proceedings of ninth international symposium on landslides. London, Taylor and Francis Group, pp 1293–1298



Risk Assessment and Countermeasure of Rock Falls in Sanbang Mountain of Jeju Island, Korea

Su-Gon Lee, Stephen R. Hencher, Gi-Hyong Cho, Ji-Won Kim, Sung-Bu Cho, Ho-Dam Lee, Sun-Hyun Park, Paul Lee, Gun-Su Kim, and Young-Suk Lee

Abstract

This study concerns Sanbang Mt. (476 m in height) on Jeju Island in Korea, located to the south of the Korean peninsula. The mountain and is a natural heritage site and attracts many tourists due to its beauty. The mountain largely comprises trachyte with well-developed columnar joints, which are 1–2 m in diameter and 10–50 m in height. Many rock falls occur from these columnar joints almost every year and threaten a highway located at the foot of mountain. This paper discusses a risk assessment of the rock fall hazard and the design of mitigation measures to reduce the risk.

Keywords

Rock fall • Sanbang Mt • Korea • Columnar joint • Ring net • Natural heritage site • Jeju Island

Introduction

This study concerns the risk from rock fall from Sanbang Mt. in Jeju Island and the design of remedial measures to mitigate the risk. The mountain is located close to the southeastern coast of the island and a highway runs around

the mountain at a height of about 400 m above sea level. The mountain is made up of trachyte which is pervasively columnar jointed at the surface with spacing typically of 1–2 m and vertical persistence of about 50 m (KIGAM 2000a, b). Some blocks are even larger where incipient fractures have not yet developed to become full mechanical discontinuities. Rock falls occur frequently and sometimes impact the highway (Fig. 1).

Figure 1 View of Sanbang Mountain with near vertical columnar jointing in the background. Note man standing on large fallen block and line of road between man and the rock cliff behind.

In February 2005 an intensive geotechnical and engineering geological study was conducted to investigate the extent of the rock fall hazard and to consider how the risk could be reduced to an acceptable level (Nam Jeju Gun 2005). From that study, a system of rock catch nets was proposed as the most suitable countermeasure on the basis of safety, economic efficiency and appearance. This paper discusses the original study, its findings and a review of performance after 7–8 years in 2012 and 2013 (Seojuepo-Si 2013).

S.-G. Lee (✉) • J.-W. Kim • S.-B. Cho • H.-D. Lee • S.-H. Park
Department of Civil Engineering, University of Seoul, Seoul, South Korea
e-mail: sglee@uos.ac.kr

S.R. Hencher
Department of Earth Science, University of Leeds, Leeds, UK
Halcrow China Limited, a CH2MHILL company, Hong Kong, China
e-mail: s.hencher@see.leeds.ac.uk

G.-H. Cho • P. Lee
Department of Urban Infrastructure Engineering, Ulsan National Institute of Science and Technology, Ulsan, South Korea

G.-S. Kim
Department of Civil and Environmental Engineering, University of Ulsan, Ulsan, South Korea

Y.-S. Lee
Department of Electronic Engineering, Hanyang University, Seoul, South Korea

Main Subject

Rock Fall Hazard

One hazard derives from loose rock and other debris on the upper surface of the mountain which dips towards the highway at about 25°.

However the main hazard derives from the many steeply dipping rock joints in the rock face with a very high



Fig. 1 View of Sanbang Mountain with near vertical columnar jointing in the background

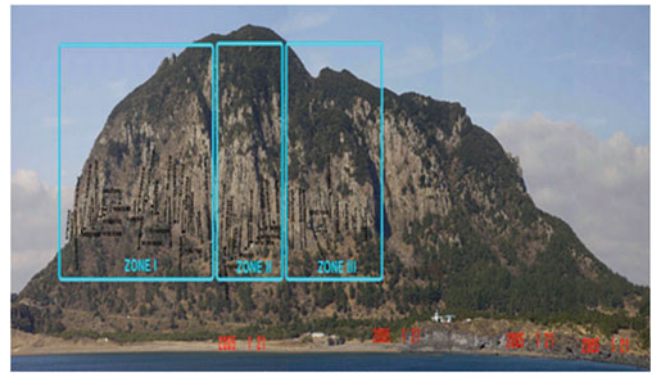


Fig. 3 Three hazardous zones identified on Sanbang Mt

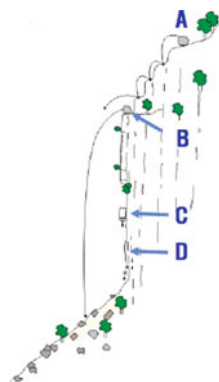
probability of toppling failure (as evident from field observation). Tree roots on the rock cliff are opening many of these joints.

The rock falls on the slope were classified into four types, from Type A to D in order to define appropriate mitigation measures as illustrated in Fig. 2.

Identification of Hazardous Zones and Evaluation of Risk

The orientation of joints and the intervals of crevices were investigated by field mapping on the cliff of Sanbang Mt. as well as remotely using telescopic observation, aerial photographs and 3-D laser scanning. Seventy-three regions were judged to be the most hazardous and these situations were analysed individually. For further analysis and design the cliff face was divided into three zones as shown in Fig. 3. Stereographic analysis was carried out for each region as illustrated in Table 1 to supplement the direct observation of judged hazard.

The falling height, volume, weight and average energy of potential rock falls were analyzed using ROCKFALL software developed by Rocscience (2004), to optimise design of



Type A: Rocks falling from upper surface, possibly bouncing before becoming airborne

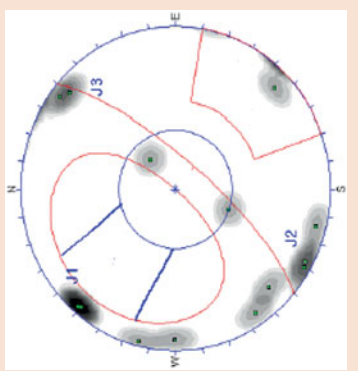
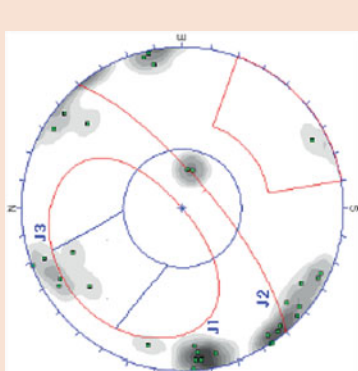

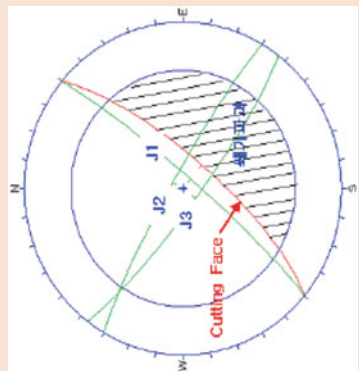
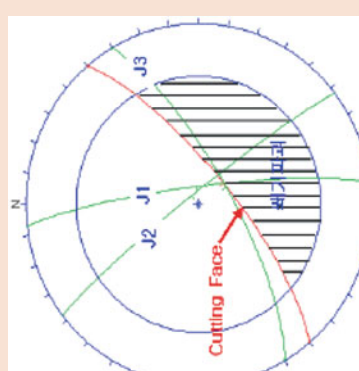

Type B: Rocks falling from the upper part of the cliff directly impacting the highway, possibly after bouncing and sliding.

Type C: Rocks falling from the middle part of the cliff.

Type D: Rocks falling from the lower part of the cliff.

Fig. 2 Rock fall origins for analysis

Table 1 Analysis on geological structure

	Zone I	Zone II	Zone III
Classification Analysis using stereographic projection			
Probability of wedge failure	Plane failure and toppling failure potential 	Mostly toppling failure potential 	Toppling failure possibility 
	Wedge failure possibility	No apparent risk of wedge failure	No apparent risk of wedge failure

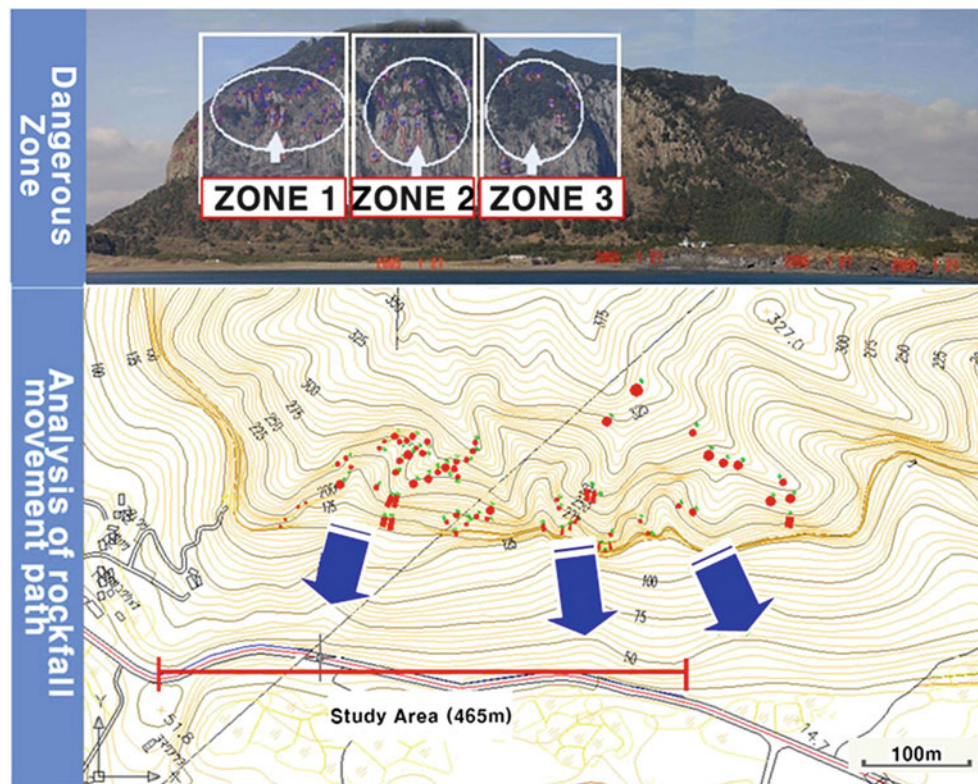


Fig. 4 73 blocks selected to be most dangerous by telescopic observation, aerial photographs and 3-D laser scan (red dots indicate the most hazardous 73 rock blocks; blue arrows indicate the main lines of rock fall)

rock fall protection measures. These analyses were carried out for the 73 hazards judged to be most dangerous, with a concentration on 15 areas, which were investigated intensively. The falling energy of rock fall was analyzed for each zone; falling energies were mostly of the order of $300 \text{ t}\cdot\text{m}$ but in some cases were much higher, of the order of $1,000\text{--}4,000 \text{ t}\cdot\text{m}$ (Fig. 4). Zone 1 showed the highest hazard level, followed by Zone 2 and Zone 3; Zone 1 also showed the strongest falling energy (Fig. 5).

Protection Works

One of the constraints of the design was to avoid spoiling the scenic beauty of the site. Design concentrated on the main hazard rockfall hazard of blocks with volume: $2.0\text{--}4.2 \text{ m}^3$ and energy: $20\text{--}200 \text{ t}\cdot\text{m}$. To provide protection, ring nets, developed by Switzerland's Geobruigg, were judged to be most suitable to be installed at locations indicated schematically in Fig. 6 (not to scale). Ring Net RX-300 (with capacity 3,000 kJ) were proposed around the valley at Zone I because of high-calculated impact energies. Ring Nets RX-150 (with capacity 1,500 kJ) were proposed for Zones II and III where the impact energies were lower.

Performance

Following construction of Ring Nets, site visits were conducted after 7–8 years in 2012 and 2013. A few rock blocks were observed in Ring Nets. This indicates that Ring Nets is a useful protection measure for rock fall.

Conclusions

There is a high risk from rock fall to a highway that runs around the base of Mt. Sanbang, a highly visited tourist destination on Jeju Island in Korea. Hazards were investigated by field mapping and remote examination, including 3D laser scanning. It was identified that the greatest risk (hazard frequency and consequence) derived from block falls less than 5 m^3 . It was considered most effective and environmentally friendly to design protection against such falls using a series of ring nets. In some areas, where there was a danger of rocks falling in excess of 5 m^3 , in-situ reinforcement was recommended using cable tie backs, buttressing and local anchoring.

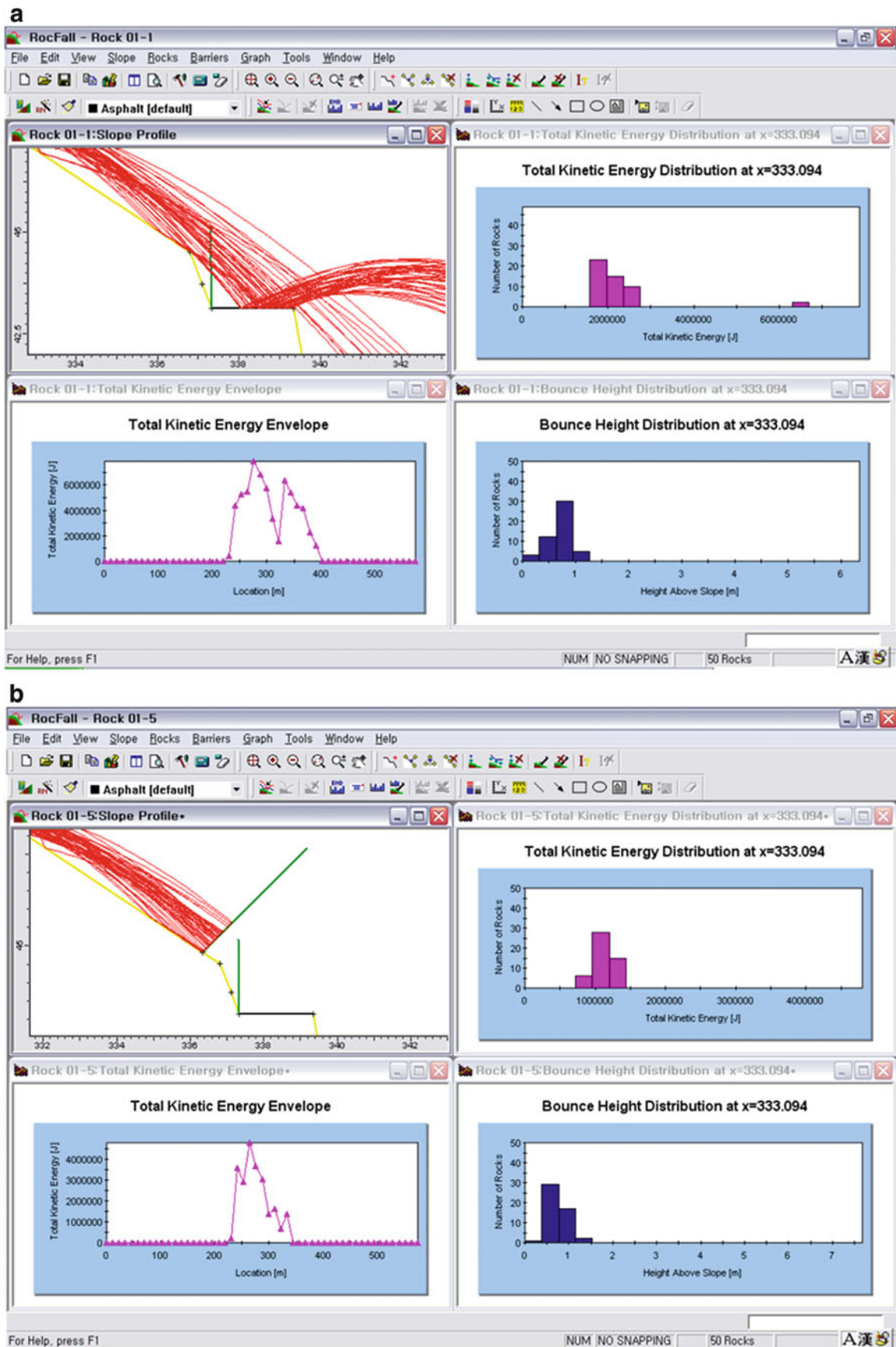


Fig. 5 Analysis of effectiveness of rock fall-protection fence (a) and additional protective wall (b)

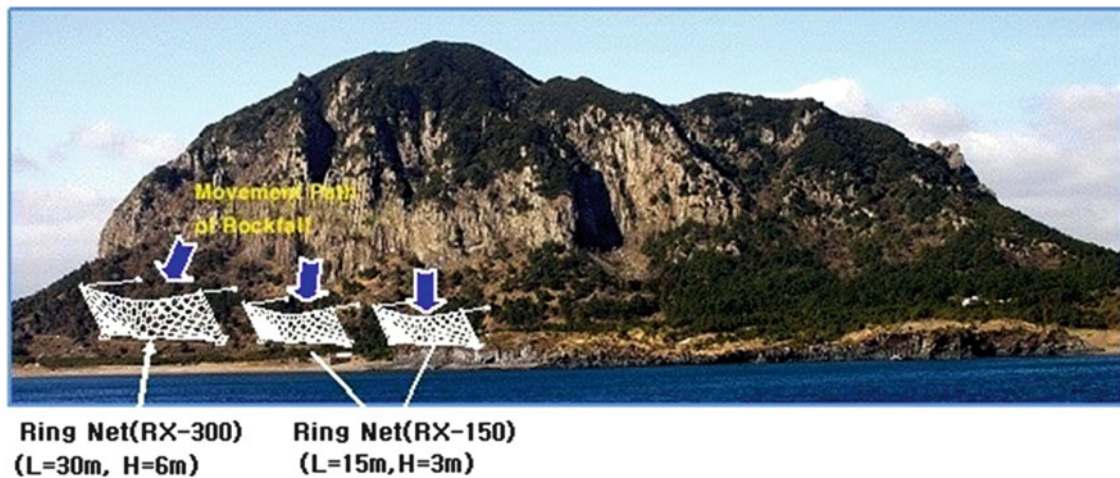


Fig. 6 Countermeasures against Rockfall

References

- Korea Institute of Geology, Mining and Materials (2000a) A report on the geological map of Moseulpo and Hallim (1:50,000)
- Korea Institute of Geology, Mining and Materials, Mining and Materials (2000b), An explanation on the geological map of Jeju (Baeka Island and Jinnampo; 1:250,000)
- Nam Jeju Gun (2005) A report on the safety of the slope in the danger zone of Sanbang Mt
- Rocscience (2004) Risk analysis of falling rocks on steep slope, Rock-Fall (V4.0)
- Seojuepo-Si (2013) The 2nd report on the safety of the slope in the danger zone of Sanbang Mt

Part VI

Urban Landslides



Introduction: Urban Landslides

José Chacón

Abstract

This introduction provides some clues, aims and scope intended for the presentation of papers and also to define the objectives expected for session C6. Authors dealing with Urban Landslides are invited to contribute with their papers and also participating in the final session.

Landslide is one of the geological processes inducing changes in the regional morphology of any mountains chain leading to the evolution of its relief along time.

Beside a purely geomorphological interest in featuring every detail of its morphological evolution also landslide is a mass movement requiring a given number of mechanical conditions to be triggered and before that starting moment also a given set of preparatory determinant factors permitting the un-balanced slope evolution.

Natural hazard is assessed, after the definitions by Varnes (1984), as the “the probability of occurrence within a specified period of time and within a given area of a potentially damaging phenomenon” affecting the “element at risk” or “the population, properties, economic activities, including public services, etc. in a given area with “a given vulnerability defined as the degree of loss when affected by a natural phenomenon such as any of type of landslide”.

These definitions made possible the identification and assessing of natural risks also based on Varnes (1984) definitions of the specific risk for each element at risk depending on the probability of occurrence of that particular landslide and the corresponding vulnerability value or the final total risk, for that landslide event, integrating specific risks for the different elements at risk, as distributed in the threatened area. Following these definitions a large set of papers have been published in the last decades concerning

different tools for assessing landslide hazard and risks as mapping (Chacón et al. 2006; Borghuis et al. 2007; Corominas et al. 2014); activity and diachroneity (Chacón et al. 2010; Fernández et al. 2012); showing advances on geotechnical analysis of mass properties in soil or rocks (Tacher et al. 2005; Blijenberg 2007; Pinyol and Alonso 2010) and determination of triggering factors as rainfall or earthquakes (Crosta et al. 2012).

It is in this context in which a session on Urban Landslides was proposed, by considering this scenery as associated to the highest values of the element at risks including the human victims and life losses, beside with landslides affecting crucial infrastructures as highways, roads, dams, energy plants, etc.

Nine papers have been presented in this session covering very different but representative study cases on: (a) deep landslides (Ancona landslide by Toffani et al.; Calaiza and Marina del Este landslides by Chacón et al.; rockfall by Frattini et al.) or shallow landslides (Antonina, Brazil by Picanço et al.; slumps in Saiha town, North-East India, Laldinpuia; rockfall by Frattini et al.); (b) landslides affecting highly developed urban areas Ancona landslide by Toffani et al.; Calaiza and Marina del Este landslides by Chacón et al., landslides in La Paz, Bolivia by Roberts; or affecting small villages and less developed contexts (Hurricane Mitch 1998, Tegucigalpa, Honduras by Hirota and Kamiya); (c) on soils or rocks (Laipuitlang rockslide, West India, Laldinpuia, and Singh); (d) triggered by rainfalls (Hurricane Mitch 1998, Tegucigalpa, Honduras by Hirota and Kamiya; Antonina, Brazil, Picanço et al.); or earthquakes (Ancona landslide by Toffani et al.) or

J. Chacón (✉)
Department of Civil Engineering, University of Granada, Granada,
Spain
e-mail: jchacon@ugr.es

(e) finally based on engineering geology and landslides mapping (Antonina, Brazil by Picanço et al.; Chacón et al.) or geotechnical analysis (Ancona landslide by Toffani et al.; Putrajaya, Malaysia, slope cut by Soon Min et al.; rockfall by Frattini et al.).

The variety and quality of the few presented examples gives a good idea of the complexity of Urban Landslides, therefore providing a good introduction for an interesting discussion on the present state-of-the-art and further possible developments.

References

- Blijenberg HM (2007) Application of physical modelling of debris flow triggering to field conditions: limitations posed by boundary conditions. *Eng Geol* 91(1):25–33
- Borghuis AM, Chang K, Lee HY (2007) Comparison between automated and manual mapping of typhoon-triggered landslides from SPOT-5 imagery. *Int J Remote Sens* 28:1843–1856
- Chacón J, Irigaray C, Fernández T, El Hamdouni R (2006) *Bull Eng Geol Environ* 65:341–411. doi:10.1007/s10064-006-0064-z
- Chacón J, Irigaray C, El Hamdouni R, Jiménez-Perálvarez JD (2010) Diachroneity of landslides. In: Williams AL et al (eds) *Geologically active*. Taylor and Francis Group, London. ISBN 978-0-415-60034-7999-1006
- Corominas J, Van Westen C, Frattini P, Cascini L, Malet J-P, Fotopoulou S, Catani F, Van Den Eeckhaut M, Mavrouli O, Agliardi F, Pitilakis K, Winter MG, Pastor M, Ferlisi S, Tofani V, Hervas J, Smith JT (2014) Recommendations for the quantitative analysis of landslide risk. *Bull Eng Geol Environ*. doi:10.1007/s10064-013-0538-8
- Crosta GB, Agliardi F, Frattini P, Soso R (eds) (2012) *SafeLand deliverable 1.1: landslide triggering mechanisms in Europe: overview and state of the art. Identification of mechanisms and triggers*. Available at <http://www.safeland-fp7.eu/>
- Fernández T, Jiménez JD, Delgado J, Cardenal FJ, Irigaray C, Chacón J (2012) Methodology for landslide susceptibility and hazard mapping using GIS and SDI 8th International Symposium on Geoinformation for Disaster Management. *Gi4DM 2012*. 13 p. 13–16 December, 2012, Enschede, The Netherlands
- Pinyol NM, Alonso EE (2010) Criteria for rapid sliding II: thermohydro-mechanical and scale effects in Vaiont case. *Eng Geol* 114:211–227
- Tacher L, Bonnard C, Laloui L, Parriaux A (2005) Modelling the behaviour of a large landslide with respect to hydrogeological and geomechanical parameter heterogeneity. *Landslides* 2:3–14
- Varnes D (1984) *Landslide hazard zonation: a review of principle and practice*. UNESCO, Paris, 60 p



Typology of Rainfall-Triggered Landslides in the Urban Area of Antonina, Southern Brazil

Jefferson Picanço, Carolina Athayde Pinto, Maria José Mesquita, Mayra Moraes, Luiz Felipe Soares, and Francisco Cardoso

Abstract

The Disaster of March 11, 2011, in Paraná state, Southern Brazil, was triggered by concentrated rainfall in a short time, after an unusually wet and warm hot season. In Antonina, the little town most severely affected, the event triggered dozens of landslides in the urban area, with two deaths and about a thousand of affected people. Analysis of the landslide typology showed a correlation between geology and geomorphology of slopes in the urban area. Where granitic rocks occur, it develops a steep relief is and a relatively thick and heterogeneous silty weathering mantle, generated landslides in first order headwater drainages. Some of these landslides, coalescing along drainages, gave rise to highly destructive debris flows, such as the neighbourhood of Laranjeira, with a death and the destruction of several houses. On the Caixa D'Água hill, where predominate mafic rocks (gabbro, mylonitic gabbro and diabase dikes), the landslides occurred on clayey steep slopes, controlled by a large diabase dike contact, causing hyperconcentrated flows in embedded drainages, provoked one death and the destruction of houses at the foot of the slope. In other areas dominated only by mafic rocks (gabbros and amphibolites), it develops concave slopes, with thicker and clayey weathering mantle. In these areas, landslides were mainly rotational. Where mylonitic rocks occur, we observe only shallow translational landslides. The strong correlation between typology of landslides, geomorphology (slope, drainage) and its connection with the geology (rock types, structures) is an important factor for future studies in the area of risk.

Keywords

Landslide typology • Shallow translational landslides • Rotational landslides • Urban areas

Introduction

Natural disasters cause hundreds of thousands of deaths every year worldwide, exacerbated by the different degree of vulnerability of affected societies (ISRD 2012). The march/2011 disaster in Paraná state coastal areas was caused

by intense rainfall in a short period of time, just after an unusual rainy summer.

The accumulated rain between 10 and 11 March was more than 400 mm (Picanço and Nunes 2013). The town of Antonina suffered floods with widespread landslides and debris flow in urban zone, provoking 2 deaths, 200 injured and 2,340 disaloged people (Table 1). This work discusses the relationships between mass movements, geomorphology and geology the Bom Brinquedo Hill, in urban zone of the city, which are the site of most of landslides in that event.

J. Picanço (✉) • C.A. Pinto • M.J. Mesquita • M. Moraes • L.F. Soares • F. Cardoso
Geosciences Institute, State University of Campinas (UNICAMP), R. João Pandiá Calógeras, 51, Campinas, São Paulo, Brazil
e-mail: jeffpicanco@ige.unicamp.br; carolina.athp@gmail.com; maria.mesquita@ige.unicamp.br

Table 1 Damage evaluation (source: Civil Defense Paraná State 2011)

Town	Disaloped people	Injured	Deaths
Antonina	1,160	200	2
Morretes	1,180	21	1
Total	2,340	221	3

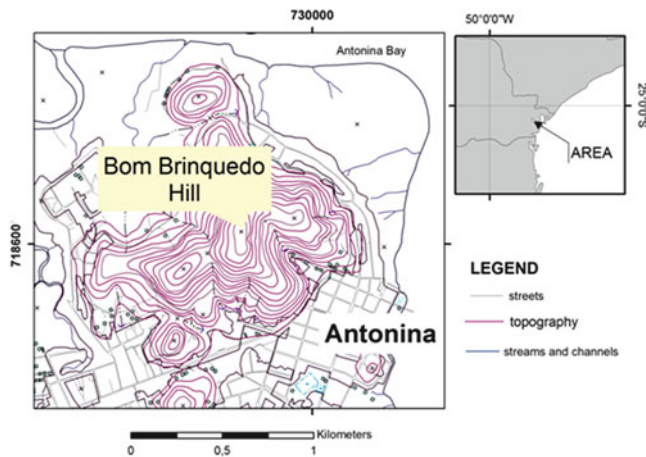


Fig. 1 Localization of the Bom Brinquedo Hill

Materials and Methods

The field surveys aimed the discrimination of different rock types and characterization of mass movements in Antonina urban area (Fig. 1).

The work was developed from aerial photography and online topographic 1:5,000 charts. The contour lines have equidistance of 10 m. The digital data were processed with ArcMap® software. The landslide data were obtained from fieldwork and movies from helicopter flights taken shortly after the climatological event. It was generated lithological map, slope or declivity map and landslides Inventory Map from Bom Brinquedo Hill.

The Geology of Bom Brinquedo Hill

The Bom Brinquedo hill presents four main rock types (Pinto et al. 2013, Fig. 2): (1) undifferentiated meta-mafic rocks; (2) Antonina Granite; (3) mylonites and “filonites” from both previous rocks; and (4) Mesozoic diabase dikes.

The heavily weathered meta-mafic rocks, mostly metabasalts, are amphibolites appearing only at the west end of the hill. It belongs to the Luiz Alves complex (Siga 1995).

The Antonina Granite belongs to Rio do Poço magmatic Suite (Cury 2009). The rocks have sienite to monzogranitic composition, divided into two facies: biotite granite and leucogranite (Pinto et al. 2013). The biotite granite has

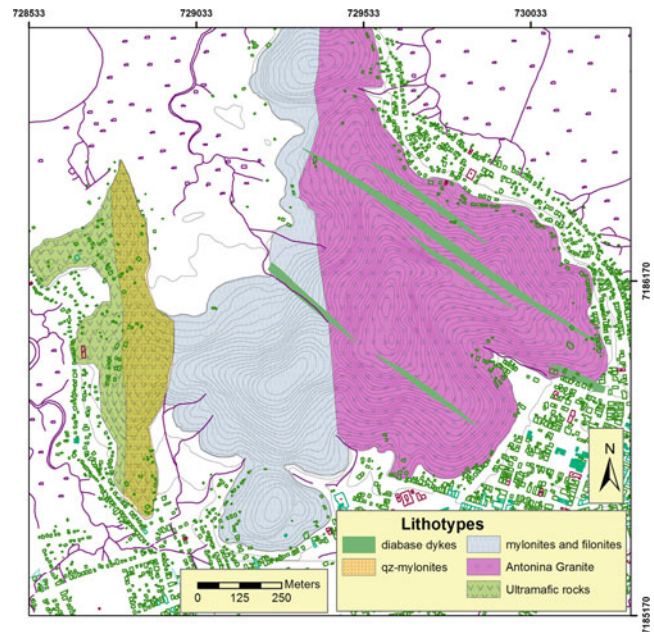


Fig. 2 Lithotype map of Bom Brinquedo Hill (Pinto et al. 2013)

equigranular to porphyritic medium grained texture, with plagioclase phenocrysts and quartz, feldspar and biotite matrix.

The leucogranite has a porphyritic pegmatoid texture, with alkali feldspar phenocrysts. The matrix is mostly quartz and feldspar with minor mica, apatite and allanite. Both facies have secondary epidote, biotite, muscovite, chlorite, carbonate, white mica and opaque minerals. The granite is locally deformed, with the development of protomylonites, mylonites, quartz mylonites and filonites (Pinto et al. 2013). These rocks present a mylonitic foliation (S_m) marked by the orientation of porphyroclasts of feldspar, quartz ribbons and levels of white mica, epidote and chlorite.

The granitic rock types are usually weathered with regolith thickness between 5 and 15 m, associated with lower declivity or slope angle. The steepest slopes have frequent rock outcrops and litholytic soils.

The milonites and filonites represents a thick zone from the contact between the Antonina granite and Luiz Alves metamafics (Fig. 2), comprising mostly quartz mylonites and biotite chlorite filonites. The quartz-mylonite is composed of quartz (80 %), muscovite (12 %) and opaque minerals (8 %). The biotite-chlorite filonite is characterized by a foliation with white mica, biotite and chlorite. Plagioclase is partially broken and replaced by carbonate. This later mineral occurs infilling irregular cavities and in small venules.

The fourth unit in Bom Brinquedo hill is composed of diabase dikes cutting the older units. The diabase dykes have metric to decametric widths and hundreds of meters long. Rocks are dark, fine-grained, locally porphyritic. Are associated with the Ponta Grossa arch Mesozoic dyke

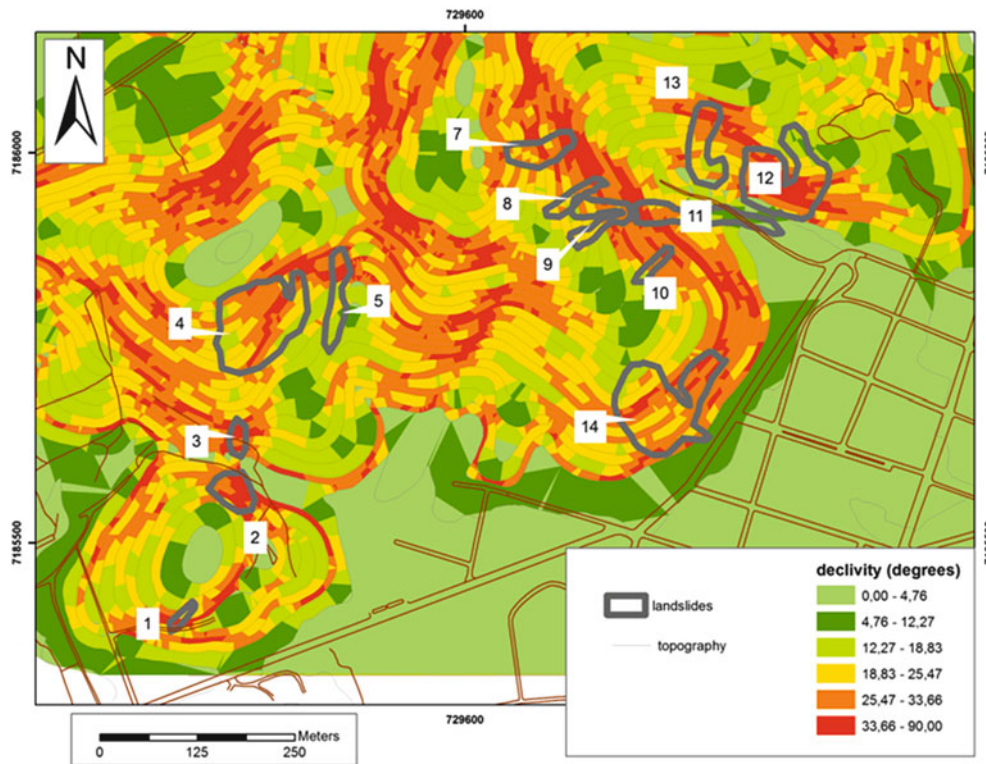


Fig. 3 Slope angle (Declivity) and landslide inventory map of southern—and most urbanized zone—of the Bom Brinquedo Hill. The number represents the single landslides characterized in Table 2

swarms. Although negligible in areal extension, the diabase dikes act as local hydrogeological barriers, changing substantially the properties of the slopes (Fernandes et al. 2004).

Analysis of Landslides

The gravitational landslides in the southern portion of the Bom Brinquedo Hill—the most urbanized area (Fig. 3) were carefully analysed, taking into account parameters such as: (1) lithotype; (2) regolith; and (3) type of landslide; (4) impact; (5) the influence of drainage; and (6) slope, as listed in Table 2.

The 1–4 landslides group was associated with biotite-filonite lithotype. Most of these landslides were shallow planar type, with rupture surface not reaching the bedrock. The greatest impact was with n°4, but that was an area of poultry, with little risk.

The 5–13 landslides occurred in granite saprolite. These landslide types are varied, related or not with drainage. The landslides n°5 and n°9 have evolved to debris flow. The catastrophic debris flow (landslide n°11) is associated with the n°9, having destroyed several houses, with one casualty.

The other landslides were shallow landslides associated with high slope in the area of positive relief breaks, without

strong association with drainage. Approximately five houses were destroyed by these landslides. The presence of a small diabase dike in this area might have been a predisposing factor for the occurrence of the landslide.

The landslides that have evolved to debris flow, the rupture occurred on the bedrock. In most areas of granite lithotype, however, the rupture occurred within the regolith.

Conclusions

From the analysis of the mass movements in the urban area of Antonina, it is observed that the most important predisposing factors were: (1) slope angle (declivity); (2) the saprolite type; and the presence of positive relief breaks. The slope hydrology associated with the proximity to drainage channels, also proved to be important, although it deserves more specific analysis beyond the scope of this study.

The granitic saprolite were most affected by landslides, while the area of occurrence of biotite-filonites and mylonites were also affected by small shallow landslides. It was noted that landslides occurred in areas with slopes of medium to high, with a value between 17° and 40°, a value close to that expected theoretically.

Table 2 Inventory, characteristics and impacts of landslides at Bom Brinquedo hill

N°	Lithotype/saprolite	Soil characteristics	Landslide type	Impact	Drainage	Slope
1	Biotite filonite	Medium/shallow	Slump	Negligible	Outside the drainage perimeter	Low (13 a 20°)
2	Biotite filonite	Medium/shallow	Shallow planar	Minor impact	Up to 25 m of drainage	Medium to high (>20°)
3	Biotite filonite	Medium/shallow	Shallow planar	Little impact	Up to 25 m of drainage	Medium to high (>20°)
4	Biotite filonite	Medium/shallow	Shallow planar, large-sized	Displacement of trees	Outside the perimeter drainage, advancing toward up to 5 m away	Medium to high (>20°)
5	Granite saprolite	Residual soil (4 m thick)	Headwater Slump	Minor	Within 5 m of the drainage perimeter	Medium to high (>20°)
7	Granite saprolite	Residual soil (>3.5 m)	Planar with minor flow	Medium impact, destroying tourist trail, and overthrow large trees	Outside the drainage perimeter	Medium to high (>20°)
8	Granite saprolite	Residual soil and coluvium (>3.5 m)	Planar; overthrow of large trees	Medium impact, destroying tourist trail	Outside the drainage, moving toward it	Medium to high (>20°)
9	Granite saprolite	Residual soil (~3.0 m)	Complex landslide, with gullies	Material is deposited downstream forming debris flow material (landslide n° 11)	Outside the drainage perimeter	Medium to high (>20°)
10	Granite saprolite	Residual soil	Shallow planar	n/d	Outside the drainage perimeter	Medium to high (>20°)
11	Granite saprolite	n/d	Debris flow	Large debris flow	Within drainage perimeter	Low
12	Granite saprolite	Residual soil	Planar	Destruction of houses and felling trees	Outside the drainage perimeter	Medium to high (>20°)
13	Granite saprolite	Residual soil	Planar with gullies	High impact, destroying two houses	Outside the drainage perimeter	Medium to high (>20°)
14	Granite saprolite	Residual soil (variable thickness)	Complex landslide	Great impact, destroying four houses	Outside the drainage perimeter	Medium to high (>20°)

The analysis showed that the landslides tend to begin in the area of positive relief, which are also areas of maximum infiltration of least resistance and upper slope (Augusto Filho 1992).

The debris flow (landslides 5 and 11) were initiated in areas with positive relief break, associated with drainage. In these areas, the disruption take place in bedrock, and the intensive gullies produced large amounts of material, which turned out to start the debris flow. Much of the impacts and dangers caused by the gravitational mass movements in the region of the Bom Brinquedo hill catastrophic event of March 2011, were related to this type of phenomenon.

Acknowledgments The research group “Analysis of gravitational mass movements in the catastrophic event of March 2011 on the Paraná coast” is grateful to Prof. Renato Lima, former CENACID president,

and Geol. Rogério Felipe (MINEROPAR) by the support and the field work discussions.

References

- Augusto Filho (1992) Caracterização Geológico-Geotécnica Voltada à Estabilização de Encostas: uma Proposta Metodológica. Proceedings of 1a Conferência Brasileira Sobre Estabilidade de Encostas (COBRAE), vol 2, pp 721–733, Rio de Janeiro
- Civil Defense Paraná State (2011) Notícias. URL <http://www.defesacivil.pr.gov.br/modules/noticias/article.php?storyid=885&tit=Boletim-das-chuvas-no-Estado-atualizado-13h> last accessed 8 Apr 2012
- Cury LF (2009) Geologia do Terreno Paranaguá. DR thesis, Instituto de Geociências, Universidade de São Paulo, Brazil
- Fernandes NF, Guimaraes RF, Gomes RAT, Vieira BC, Montgomery DR, Greenberg H (2004) Topographic controls of landslides in Rio de Janeiro: field evidence and modeling. *Catena* 55:163–181

- International Strategy for Reduction of Disasters (ISRD) (2012) Making cities resilient. URL: <http://www.unisdr.org/we/campaign/cities> last accessed 8 Apr 2012
- Picanço JL, Nunes LH (2013) A severe convective episode triggered by accumulated precipitation in the coast of Parana State, Brazil. In: Proceedings of 7th European conference of severe storms, 2013, Helsinki. 7th European Symposium on Severe Storms. Helsinki, ESSL, pp 4–14
- Pinto CA, Mesquita MJ, Picanço JL, Moraes M (2013) Caracterização Petrográfica do Granito Antonina e Rochas de Cisalhamento Associadas. In: Proceedings of Simpósio Nacional de Estudos tectônicos. Chapada dos Guimarães (MT), maio 2013. CD-ROM
- Siga Junior O (1995) Domínios tectônicos do sudeste do Paraná e nordeste de Santa Catarina: Geocronologia e evolução crustal. DR thesis, Instituto de Geociências, Universidade de São Paulo, Brazil



Rockfall Runout Modelling for Hazard Characterization and Countermeasure Design in Urban Area

Paolo Frattini, Giovanni B. Crosta, and Andrea Valagussa

Abstract

The analysis of rockfall risk along transportation facilities and residential areas requires the identification of potential unstable blocks and the modelling of rockfall runout in order to quantify the expected damages to structures and to support the design of countermeasures. This paper presents several approaches for the characterization of rockfall hazard for the southwestern slope of Mont La Saxe (Courmayeur, Aosta Valley, Western Italian Alps), from where several blocks detached in 2011, causing one victim and the interruption of the main road for almost one year. The propagation of each block over a complex topography represented by a 2 m gridded LiDAR DEM was simulated by using the 3D rockfall simulation model Hy-STONE (Crosta et al. *Geophys Res Abstr* 6: 04502, 2004). 330,180 blocks were simulated using a stochastic approach for restitution and friction coefficients in order to account for uncertainty in model parameters. For the main road and the exposed buildings, a detailed analysis has been performed, by mapping the type of impact, the kinetic energy and the velocity of blocks potentially impacting the structures and the height of trajectories passing through. For the most exposed elements, energies in excess to 10,000 kJ, and heights up to 50 m above the ground were foreseen by the simulation. These results showed that a mitigation strategy was necessary to protect the road and the residential buildings. In order to support the dimensioning and the correct positioning of these countermeasures and to verify the efficiency of the works, we performed a number of simulations, including in the model the designed countermeasures.

Keywords

Rockfall • Danger • 3D runout modelling • Hy-STONE • Countermeasure efficiency

Introduction

Rockfalls pose problems to structures and infrastructures in mountain areas. Transport facilities along narrow valleys frequently lie below rocky cliffs potentially affected by rockfall (Pierson et al. 1990; Hungr et al. 1999). The protection of these facilities can be extremely expensive for communities,

due to the large size of affected areas and the difficulty to forecast rockfall initiation. For this reason, studies aimed at modelling rockfall hazard are fundamental to optimize the design of protection measures and to prioritise the works to be done along transportation corridors.

The main critical issues for rockfall studies at local scale are related to the availability of robust modelling tools capable to describe the rockfall motion over complex morphologies. This issue is normally tackled by using 2D mathematical models to simulate the propagation of block along pre-defined trajectories. This strategy has several limitations: the need to select a-priori the trajectory; the impossibility to model lateral dispersion due to

P. Frattini (✉) • G.B. Crosta • A. Valagussa
Department of Earth and Environmental Sciences, University of
Milano - Bicocca, p.zza Scienza 4, Milano 20126, Italy
e-mail: paolo.frattini@unimib.it; giovannibattista.crosta@unimib.it;
a.valagussa@campus.unimib.it

topographical irregularities; the difficult to systematically model rockfalls along an entire rocky cliff.

The simulation of rockfall runout is a complex problem that requires mathematical models to describe rockfall trajectories together with velocity, energy, and height of blocks at each location along the slope. Such descriptions are obtained by solving kinematic or dynamic equations of motion. 3D models are becoming increasingly available in the recent years (Guzzetti et al. 2002; Agliardi and Crosta 2003; Crosta et al. 2004; Dorren et al. 2006; Lan et al. 2007). They overcome the limitations of 2D models by exploiting the three-dimensional form of the topography provided by DEMs. This is not the case, however, when a hydrologic approach (i.e. flow direction) is used to derive fall paths, when several unconstrained empirical rules are combined to decide possible block behaviours, or when results are interpolated between different trajectories. Three-dimensional models are powerful, but delicate tools and require a complete understanding of process and model parameters both for calibration and hazard zonation.

In this paper, we present the 3D simulation of potential rockfall propagation. This simulation allowed assessing (i) the potential impact of blocks to structures and infrastructures, (ii) the efficiency of countermeasures for the protection of elements at risks, and (iii) the performance required to mitigation structures.

Case Study

The south-western slope of Mont La Saxe (Courmayeur, Aosta Valley, Western Italian Alps) is a steep rock face hanging over the village of La Saxe and a main regional road (Fig. 1). On the 6th of January 2011, a few blocks detached from the rock face caused one victim and the interruption of the main road for almost one year. During 2011, other rockfalls occurred from the rock face. The slope is composed of Permian volcanic rocks (meta-granites and meta-rhyolites), belonging to the Mont de La Saxe Unit (Antoine et al. 1975). The metagranites are dominant in the study area, and they are composed of greyish aplitic granites with porphyritic texture, locally foliated, with cataclastic and mylonitic bands. Rock mass is characterized by intense fracturing with numerous open joint sets.

Rockfall Modelling

Analysis

Rockfall source areas have been identified with a purely morphometric approach based on the definition of slope angle thresholds (Fig. 2). This approach is repeatable, but the definition of the threshold implies a subjective judgement



Fig. 1 South-western slope of Mont La Saxe susceptible to rockfall. At the bottom of the slope, the endangered village, the main national road, and the old rock shed are visible

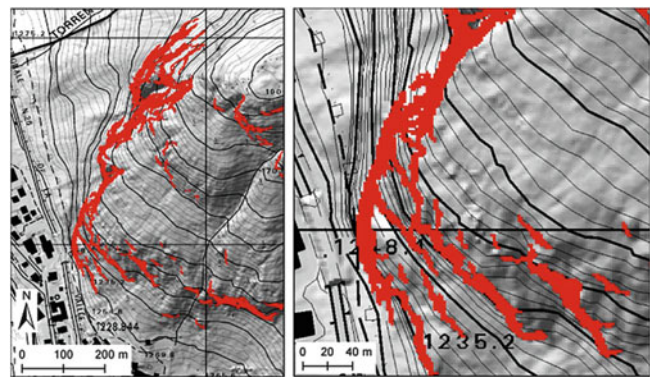


Fig. 2 Rockfall source areas (slope $> 65^\circ$) from a 2×2 m DEM

of the critical condition of the slope. The thresholds depends on the material strength and the structural setting (e.g., bedding attitude), but also on the resolution of the Digital Elevation Model (DEM) (Frattini et al. 2012). In this analysis, we used a high-resolution 2 m gridded LiDAR DEM, and we selected a slope threshold of 65° to map the source cliffs. Rockfall runout modelling was performed by using the 3D Hy-STONE model (Crosta et al. 2004; Frattini et al. 2012). The model core is a hybrid algorithm based on a three-dimensional extension of Pfeiffer and Bowen (1989) and Azzoni et al. (1995). Free fall, impact and rolling can be simulated with different damping relations. Topography is described by a DEM, and all relevant parameters are spatially distributed. The stochastic nature of rockfall processes and parameters are accommodated by slope morphology and roughness, and by the random sampling of most parameters from different probability density distributions (uniform, normal, exponential). Specific model components explicitly

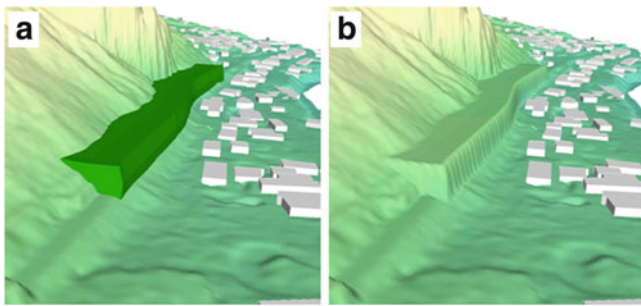


Fig. 3 Project of the final rock shed: TIN structure derived from the original CAD project; DEM modified to incorporate the rock shed

account for the interactions between blocks and countermeasures or structures. An elasto-viscoplastic damping model (Di Prisco and Vecchiotti 2006) has been also incorporated into the model to account for impact on soft ground. In addition, the geometric and dynamic effects of vegetation and fragmentation processes can be simulated (Crosta et al. 2006). The code accepts spatially distributed input data as raster matrices. The input are the location of source cells; the number, shape and mass of blocks; the initial conditions and the values of the damping coefficients that account for energy loss.

Results include rockfall frequency, trajectory height, rotational and translational velocity, and kinetic energy. At each computed point along fall paths, information is given on type of motion, locations of impacts and values of impact and rebound angle.

To calibrate the models, we partitioned the area into 18 unique condition sub-areas obtained by overlying land use and surface geology and existing countermeasures (rock shed). For each unit, we initially assigned restitution and rolling friction coefficients from the literature (Pfeiffer and Bowen 1989; Azzoni et al. 1995), and then we calibrated these values by fitting the runout of simulated trajectories to the historical events and to the location of large isolated boulders.

To account for the natural variability of rockfall in complex terrains, we varied stochastically the of normal and tangential restitution coefficients and rolling frictional angle according to a Gaussian distribution, with a standard deviation of 0.3. For the block size, we assumed an exponential distribution of volumes, with a modal value of 1 m³. We simulated 30 blocks from each source grid cell, for a total of 330,180 blocks.

During the analysis, we simulated different scenarios in order to support the design of optimal countermeasures. Here we present four scenarios: (i) “no action scenario”, without any defensive measure; (ii) “provisional rock shed scenario”, with a 150 m long defensive rock shed built during the emergency phase to allow the reopening of the road; (iii) “provisional rock shed + barriers” scenario, with the presence of several barriers on the slope in addition to the provisional rock shed; (iv) “final rock shed scenario”, with a 400 m long rock shed that is currently under project (Fig. 3).

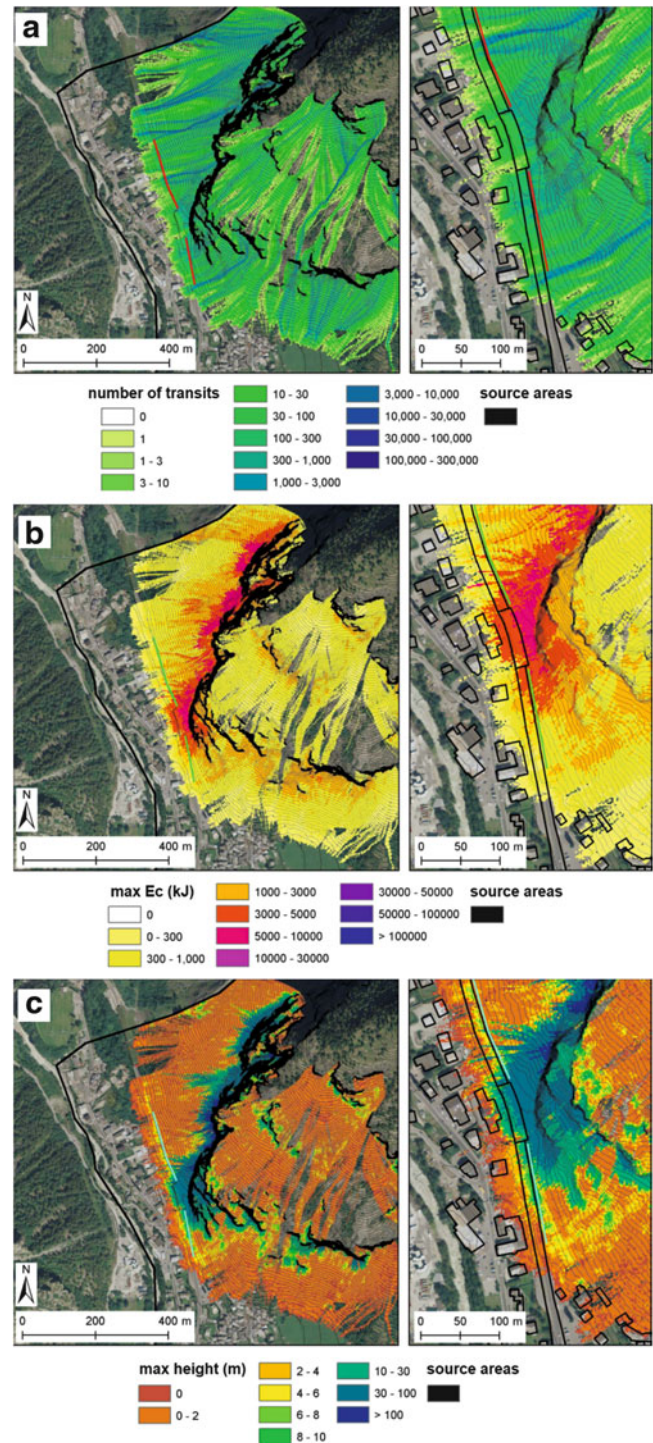


Fig. 4 Results of the “zero scenario”: (a) number of transits, (b) maximum kinetic energy, and (c) maximum height of trajectories passing through each grid cell. Existing catchnets and rock sheds are considered in the model

Characterization of Rockfall Danger

About 1 km of the main road and ten residential buildings lying below the rocky cliff are highly endangered by rockfalls (Fig. 4). The existing barriers along the main road are largely insufficient to arrest the potential rockfalls, which

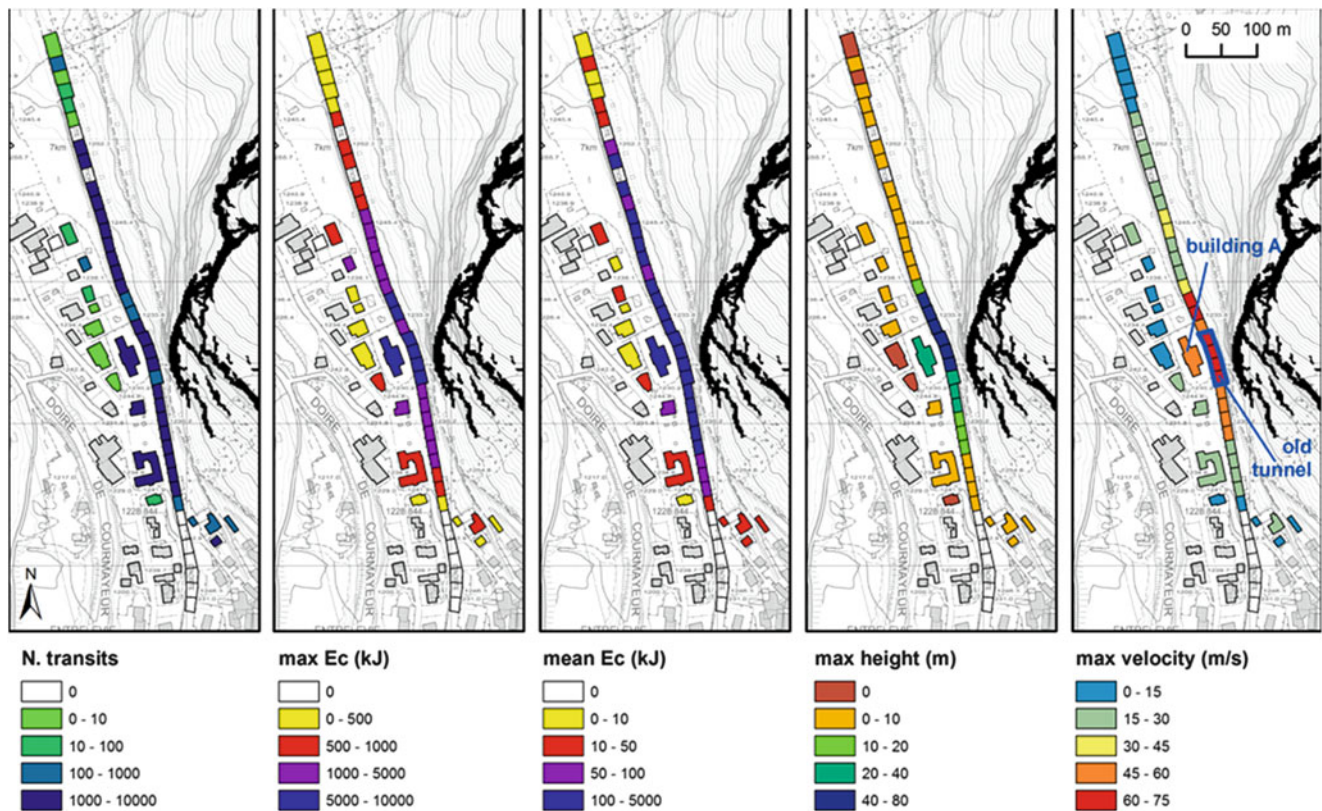


Fig. 5 Statistics of number of transits, kinetic energy, trajectory height and velocity for the elements at risk

present corridors with higher frequency as result of the complex morphology of the slope. This complex morphology requires 3D runout models that can be able to characterize convergence of trajectories into hollows and divergence along convex morphological features.

Expected kinetic energies are in excess of 5,000 kJ, with peaks of over 10,000 kJ in correspondence to the old rock shed. The height of the trajectories above the road can reach 30 m, making the use of barriers locally inadequate.

To better characterize the level of danger in correspondence to the elements at risk, we calculated, for each element, the statistics of the number of transits, the kinetic energy, the trajectory height and the velocity (Fig. 5). This allows to put in evidence that the most critical elements at risk are the central part of the main road and the building that lies just below the old rock shed (building A in Fig. 5). This building has been finally abandoned because practically impossible to protect.

Support for Countermeasure Design

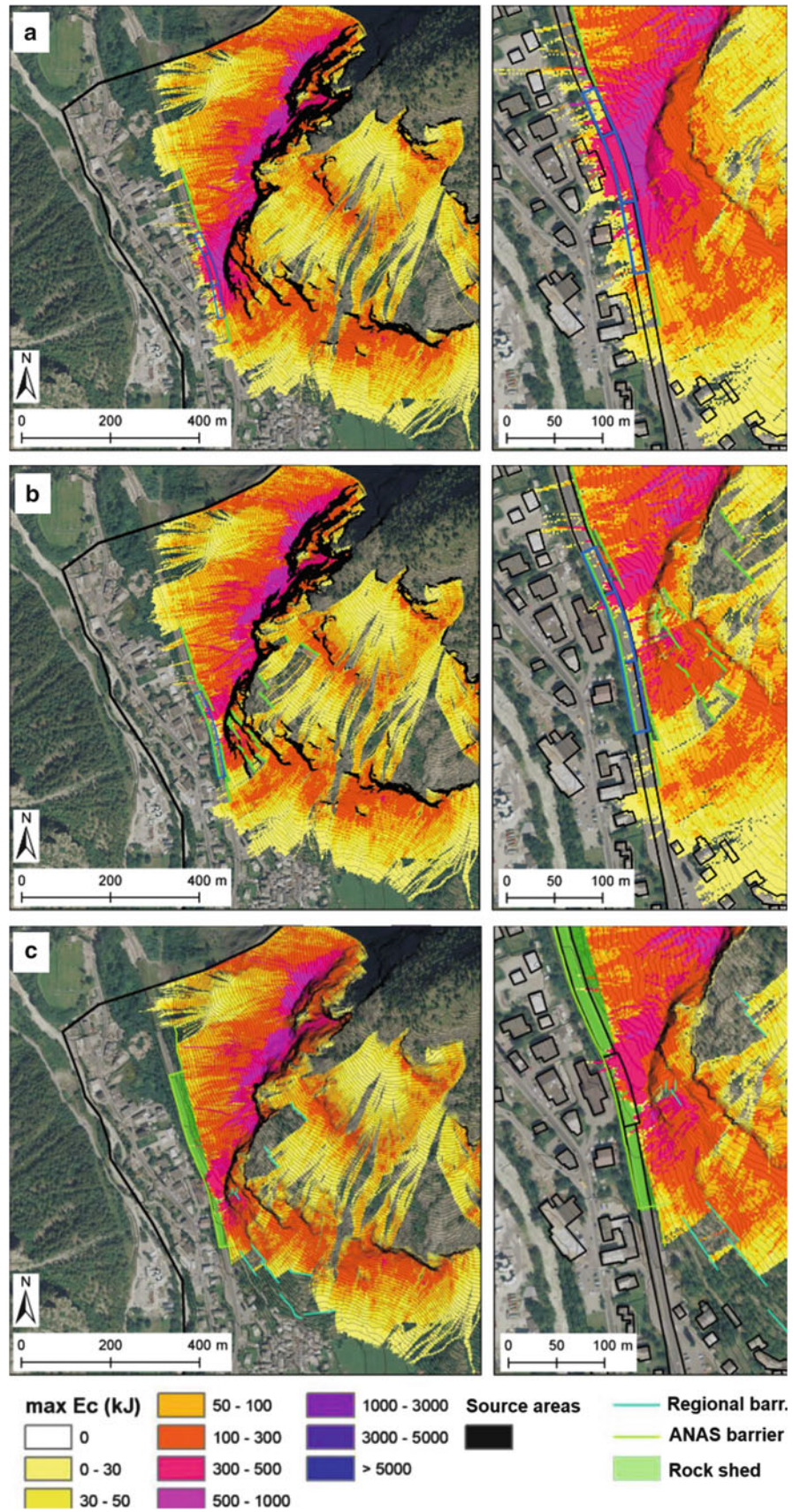
In order to protect the elements at risk, the Valle d'Aosta Regional Authority (responsible for the protection of buildings) and the Italian National Road Authority (ANAS, responsible for the road safety) decided to design more

extended countermeasures. To support the dimensioning and the correct positioning of these countermeasures and to verify the efficiency of the works, we performed a number of simulations, including in the model the designed countermeasures. Here we present three mitigation scenario.

The first scenario consists of the temporary rock shed that has been installed by ANAS during the emergency phase to allow the reopening of the road. The new rock shed consists in an extension of the older rock shed in both directions, by using a prefabricated steel structure. This scenario is able to protect the road in the central part of the area, but does not reduce hazard for the underlying buildings (Fig. 6a). Indeed, the presence of the rock shed locally increases the danger downward. The southern sector of the road is highly endangered and unprotected.

In the second scenario, the defensive measures consist of the ANAS temporary rock shed plus several flexible barriers installed along the slope by the Regional Authority in 2012 and 2013. These barriers are between 5 and 6 m high, with a resistance of 3,000–5,000 kJ. This scenario corresponds to the current situation (July 2013). The presence of barriers on the slope and along the rock shed allows for reducing the overall hazard for residential buildings and along the southern and northern part of the road (Fig. 6b). However, the scenario does not completely protect the elements at risk, especially in the southern part of the area.

Fig. 6 Kinetic energies associated to different mitigation scenarios: (a) provisional rock shed; (b) provisional rock shed + barriers; (c) final designed rock shed



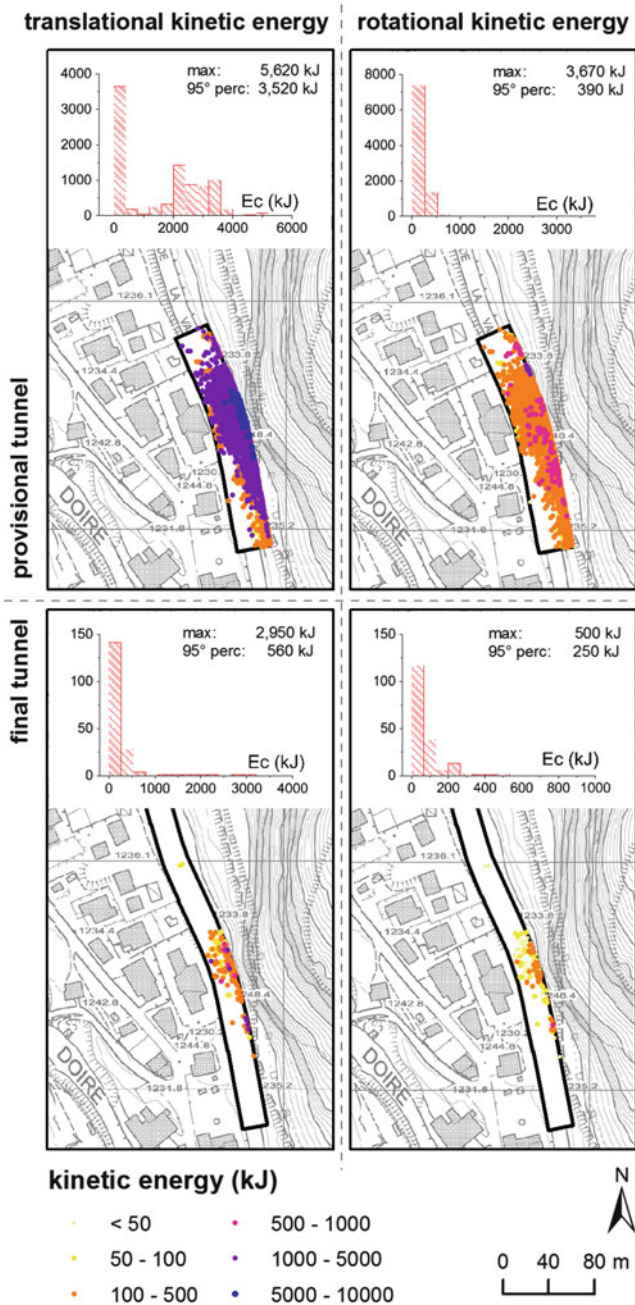


Fig. 7 Rotational and translational kinetic energies for blocks potentially impacting the top of the provisional and final rock sheds

The third scenario is still under a design stage, and consists of a completely new 400 m long rock shed that should replace the existing temporary rock shed.

In addition, on the top of the rock shed and in the southern and northern sector of the study area, 7,000 kJ flexible barrier should be installed. This scenario seems able to remove completely the rockfall danger in the urban area (Fig. 6c). The only building still endangered is building A (Fig. 5) that has been recently abandoned.

Rockfall modelling also provides support for the design of the defensive works. For calculating the loading capacity of the rock shed, we extracted the translational and rotational kinetic energy of blocks potentially impacting the rock shed roof covered with a cushion layer of granular material (Fig. 7).

According to the Italian standard (UNI 2012), the design kinetic energy for rockfall defensive works is the 95th percentile of the simulated energies, multiplied by a factor of safety of 1.02. Hence, for the final rock shed, the design kinetic energy for vertical impact on the roof of the rock shed amounts to 571.2 kJ for translational kinetic energy and 255 kJ for rotational kinetic energy, assuming a project block volume of 1 m³. The energy of blocks potentially impacting the provisional rock shed is higher due to the absence of effective barriers on the slope (Fig. 7).

Discussion

Rockfall runout modelling is fundamental for a complete characterization of rockfall danger in urban areas at the single building and road stretch scale, by considering type of impact (rolling, bouncing), height of impact (against walls or through roof), velocity and/or energy, transit across the road lanes with or without impact on the road surface.

Here, we show that 3D models are extremely useful where the slope morphology is complex, and where the available DEM resolution is high enough to describe such complexity. We also show that a GIS analysis of modelling results improves the visualisation of the rockfall danger along corridors or for specific elements at risk.

Rockfall modelling also allows a verification of the technical efficiency of countermeasures. This is fundamental for the selection of the most appropriate mitigation strategy, complemented with a risk analysis that would allow calculating costs and benefits of each mitigation option (e.g., Crosta et al. 2005). The final selection of the optimal mitigation strategy relies on the cost-benefit analysis.

Finally, 3D rockfall modelling also support the design of defensive works, by providing the relevant parameters (velocity of kinetic energy) needed for the dimensioning of the work.

Acknowledgments We thank Dr. M. Broccolato and Dr. D. Bertolo from Regione Autonoma Valle d'Aosta for making available topographic and geological data. Projects of the rock sheds were provided by ANAS spa.

References

- Agliardi F, Crosta GB (2003) High resolution three-dimensional numerical modelling of rockfalls. *Int J Rock Mech Mining Sci* 40 (4):455–471

- Antoine P, Pairis JL, Pairis B (1975) Quelques observations nouvelles sur la structure de la couverture sédimentaire interne du massif du Mont-Blanc, entre col Ferret (frontière italo-suisse) et la Tête des Fours (Savoie, France). *Géol Alpine* 51:5–23 (in French)
- Azzoni A, La Barbera G, Zaninetti A (1995) Analysis and prediction of rock falls using a mathematical model. *Int J Rock Mech Mining Sci Geomech Abstr* 32:709–724
- Crosta GB, Agliardi F, Frattini P, Imposimato S (2004) A three-dimensional hybrid numerical model for rockfall simulation. *Geophys Res Abstr* 6:04502
- Crosta GB, Frattini P, Fugazza F, Caluzzi L, Chen H (2005) Cost-benefit analysis for debris avalanche risk management. In: Hungr O, Fell R, Couture R, Eberhart E (eds) *Landslide risk management*. Balkema, Rotterdam, pp 517–524
- Crosta GB, Frattini P, Imposimato S, Agliardi F (2006) Modeling vegetation and fragmentation effects on rockfalls. *Geophys Res Abstr* 8:07694
- Di Prisco C, Vecchiotti M (2006) A rheological model for the description of boulder impacts on granular strata. *Geotechnique* 56:469–482
- Dorren LKA, Berger F, Putters US (2006) Real size experiments and 3D simulation of rockfall on forested and non-forested slopes. *Nat Hazards Earth Sys Sci* 6:145–153
- Frattini P, Crosta GB, Agliardi F (2012) Rockfall characterization and modeling. In: Clague JJ, Stead D (eds) *Landslides types, mechanisms and modeling*. Cambridge University Press, Cambridge, pp 267–281. ISBN 978-1-107-00206-7
- Guzzetti F, Crosta GB, Detti R, Agliardi F (2002) STONE: A computer program for the three-dimensional simulation of rock-falls. *Comput Geosci* 28:1081–1095
- Hungr O, Evans SG, Hazzard J (1999) Magnitude and frequency of rockfalls and rock slides along the main transportation corridors of south-western British Columbia. *Can Geotechn J* 36:224–238
- Lan H, Martin CD, Lim CH (2007) RockFall analyst: A GIS extension for three-dimensional and spatially distributed rockfall hazard modeling. *Comput Geosci* 33:262–279
- Pfeiffer TJ, Bowen TD (1989) Computer simulations of rockfalls. *Bull Assoc Eng Geol* 26:135–146
- Pierson LA, Davis SA, Van Vickie R (1990) Rockfall hazard rating system implementation manual. U.S. department of transportation, federal highway administration report, FHWA-OREG-90-01
- UNI, Ente Nazionale Italiano di Unificazione (2012) Rockfall protective measures. Part 4: definitive and executive design. UNI 11211-4:2012. UNI, Milano, Italy p 35 (in Italian)



Re-evaluation of Landslide Caused by Hurricane Mitch 1998, Tegucigalpa Honduras

Kiyoharu Hirota and Shizuka Kamiya

Abstract

This paper is concerned with the landslides caused by Hurricane Mitch in 1998 in the region of Tegucigalpa of Honduras. We have restudied the 17 localities of landslides which were earlier studied by JICA-project 2001. Besides these 17 localities we have studied three more sites of landslide for the purpose of gaining a better typology.

On three localities out of 17 mentioned above, *el Bambú*, *el Berrinche* and *el Reparto*, protection measures have been taken. In *el Bambú* bank works and drainage works were carried out in 2011. And in *el Berrinche* and *el Reparto* the works subsequently were carried out in 2013. Also installation of drainage well has finished in two localities.

In 2 of the 17 localities, *la Colonia Campo Cielo* and *la Colonia Canaán*, landslide activity is high. *Centroamérica* is stable but has a form of landslide.

11 of the 17 localities are stable, and it is difficult to find landslide-form. New landslides have been observed after heavy rain, for instance, in *el Guillén*, *la Colonia Miraflores Sur* and *la Colonia Altos de Loarque* in Tegucigalpa. Landslides frequently occur at the boundary of different geology and/or joints of rock.

Keywords

Landslide • Hurricane Mitch • Geology

Introduction

In the present paper we report results of a re-evaluation of the study on 17 localities carried out in 2001 as a JICA-project (JICA 2002). Tegucigalpa, the capital of Honduras was attacked by Hurricane Mitch 1998, which caused a great loss of human lives and delayed economic development for more than 10 years.

After Hurricane Mitch there has been no big natural disaster. On the other hand, occurrence of small scale

landslides became frequent, in particular at the time of heavy rainfall. Tegucigalpa is located in a basin which is about 1,000 m above the sea level and has a width of about 10 km. We put 17 localities on the map (Fig. 1).

In addition to the 17 localities of JICA-project 2001 we also studied three new sites (Hirota and Kamiya 2013). They are in, *el Guillén*, *la Colonia Miraflores Sur* and *la Colonia Altos de Loarque*. We would also like to discuss the landslides in these sites.

Features of the Studied Area

Geographical and Geological Settings

Basic geological feature of the region is as follows. Sandstone and siltstone of the “*Valle de Ángeles*” Group in Mesozoic lie on the basin, volcanic sediments like tuff, tuff

K. Hirota (✉)
Center for Disaster Management Informatics Research, Ehime
University, 3 Bunkyo-cho, Matsuyama 790-8577, Japan
e-mail: sbhirota@gmail.com

S. Kamiya
(independent), Ube, Yamaguchi Prefecture, Japan
e-mail: kamiyashizuka@gmail.com

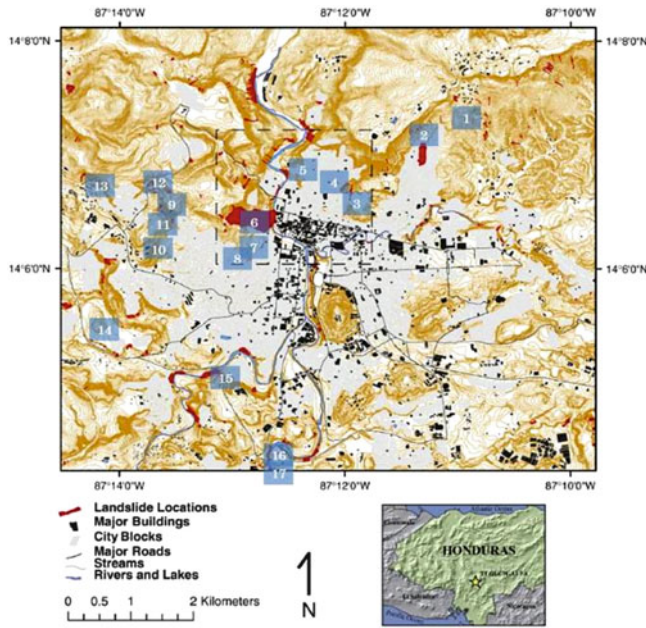


Fig. 1 Inventory of landslides triggered by Hurricane Mitch in Tegucigalpa, Honduras (adapted from Harp et al. 2009). Numbers: 1. *Canaán*, 2. *Reparto*, 3. *Bambú*, 4. *Bosque*, 5. *Buena Vista*, 6. *Berrinche*, 7. *Campo Cielo*, 8. *San Martín*, 9. *Flor 1*, 10. *Zapote Centro*, 11. *Zapote Norte*, 12. *Villa Unión*, 13. *Brasilia*, 14. *Centroamérica*, 15. *Nueva Esperanza*, 16. *Las Torres Este*, 17. *Las Torres Oeste*

breccia in Cenozoic and welded tuff lie upward in Tegucigalpa. The area studied in JICA (2002) is the patched area in the geological map of Tegucigalpa (Fig. 2).

Observation in 17 Localities

We revisited the 17 landslides localities in Tegucigalpa. Three sites taken measures of them are shown in Figs. 3, 4 and 5 (Maps are taken from JICA-project and air photographs from Google Earth).

The protection measures in *el Bambú*, drainage works and artificial bank, were completed in 2011 (Fig. 3).

El Reparto and *el Berrinche* are the areas where landslides are likely to cause (Figs. 4 and 5). The designed protection measure for *el Reparto*, the construction of drainage wells, was completed in 2012 (Drainage well was adopted to secure the stability of slope by diminishing groundwater).

In *el Berrinche*, drainage wells and surface drainages have been adopted and works have just finished in August 15 2013 (Fig. 5).

The landslide activity is highest in *la Colonia Campo Cielo* among 17 localities. The rock slide type landslide occurred in October 1 2012. We expect that under present conditions, soil flow type landslides would trigger rock slide type landslides.

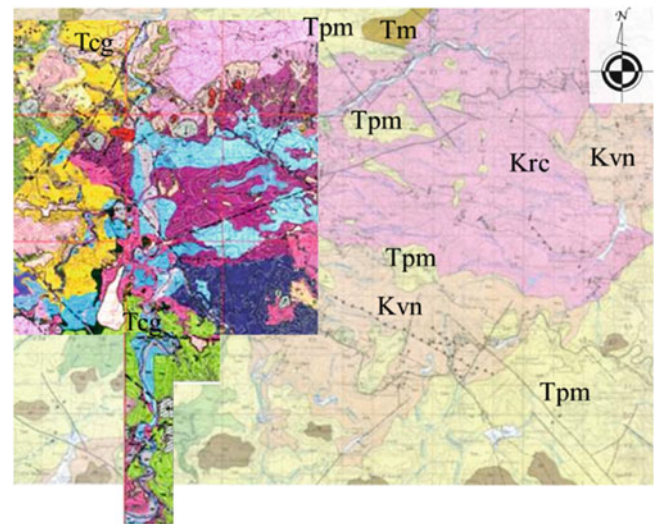


Fig. 2 Geologic Map of study area (compiled JICA-project Map into Geologic map of Tegucigalpa): **Tpm**, **Tcg**, and **Tm** (the Cenozoic Padre Miguel Group), **Krc** as Río Chiquito Formation and **Kvn** as the Villa Nueva Formation (the Mesozoic Valle de Ángeles Group)

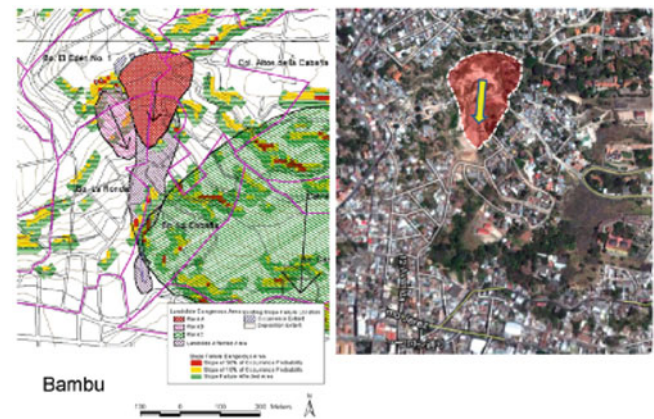


Fig. 3 Locality of *el Bambú*

In *la Colonia Canaán*, the land surface is relatively fragile. The protection measure for flow type landslide has been partially completed. The mountain slopes are stable under existing conditions. In *el Guillén*, south of *la Canaán*, a rotated type landslide with cracks has been observed.

In localities of *el Bosque*, *la Buena Vista*, *el San Martín*, *el Flor 1*, *el Zapote Norte*, *el Zapote Centro*, *la Villa Unión*,

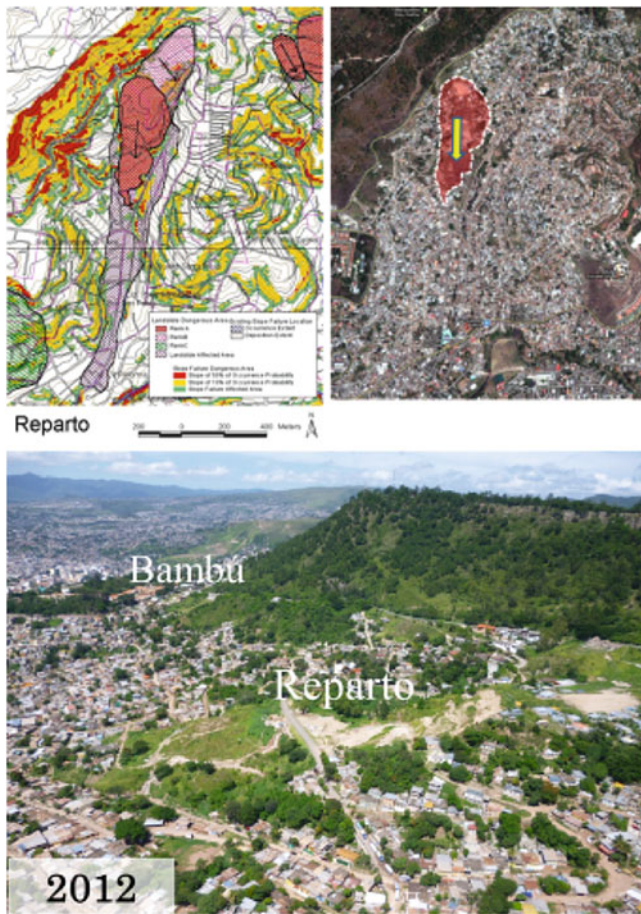


Fig. 4 Locality of el Reparto

la Brasilia, la Centroamérica, la Nueva Esperanza, Las Torres Este, and las Torres Oeste, the chance of occurrence of landslides is slim.

Observation in Other Areas

We have investigated three new active landslide sites other than those studied in JICA project 2001. These cases are important for figuring out the typology and finding appropriate protection measures to be taken in Tegucigalpa.

[La Colonia Altos de Loarque]

The site of landslide in La Colonia Altos de Loarque is at the south of Toncontín Airport (Fig. 6).

The landslide of la Colonia Altos de Loarque is typical “Slides” of Varnes (1987) which rotates three times from the vertical joints of tuff (Fig. 7).

The joints run parallel to each other in the direction of N50°W at the point of the crown of landslide. Slip clay has a

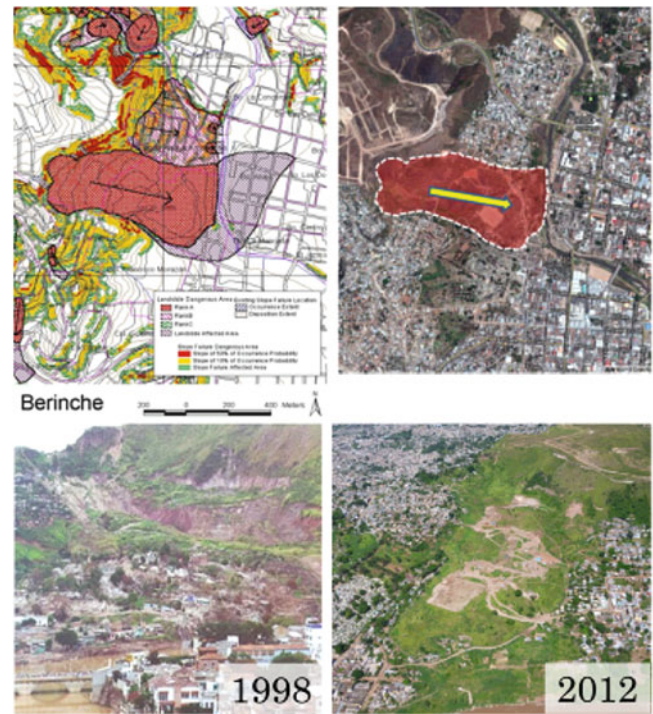


Fig. 5 Locality of el Berrinche

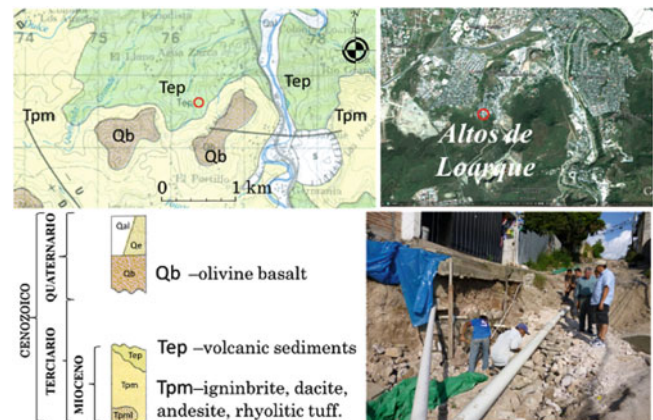


Fig. 6 Locality of the landslide in la Colonia Altos de Loarque. Qb: Quaternary Basalt, Tep and Tpm: Miocene deposits; sandstone, silt, conglomerate, tuff

residual angle of internal friction as high as 27.55° (Fig. 8; Hirota and Eveline 2013) in contrast to 24.0° the dip angle of the bed.

Besides, the clay mineral Vermiculite is not swelling (see Fig. 9).

Therefore one would expect that the area is safe from landslide. Nevertheless, it caused in la Colonia Altos de Loarque after intense rainfall. Then the reason for the landslide must be sought elsewhere. And we believe that rising groundwater level lowers the shear resistance and makes this site unstable and thus can lead to a landslide.

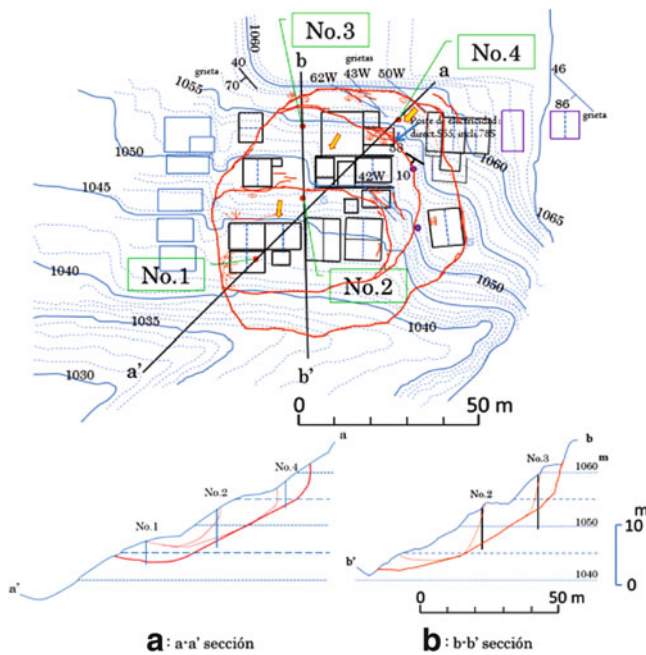


Fig. 7 Plane and its sections (after Hirota and Eveline 2013; Numbers in the figure indicate sites of boreholes)

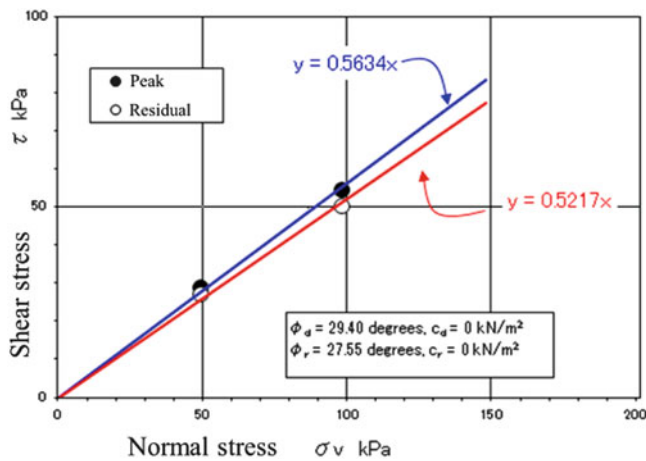


Fig. 8 Peak and the residual angles of internal friction (after Hirota and Eveline 2013)

[La Colonia Guillén]

In *La Colonia Guillén*, north of Tegucigalpa, there are two sites of landslide “*Reparto*” and “*Canaán*” (Fig. 10).

The landslide in *la Colonia Guillén* took place after intense rainfall.

First, the landslide took place downward from the road when Hurricane Mitch attacked the area in 1998. Second, the crown of the landslide appeared at the top of the area in October 2008. Since then landslides frequently occurred at the time of heavy rain (Fig. 11).

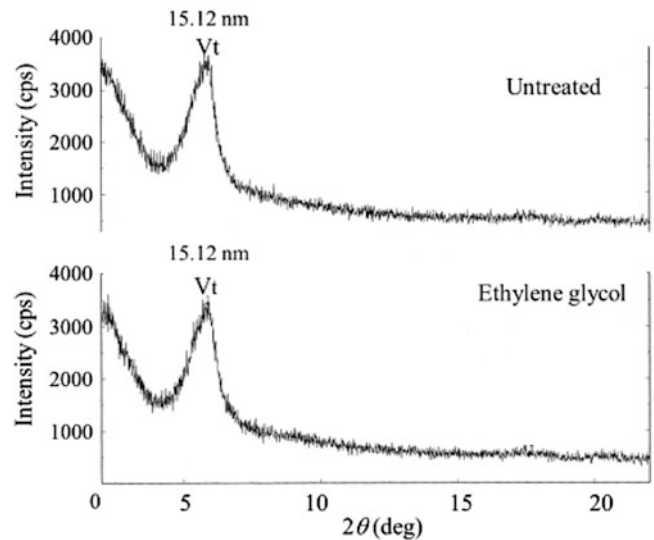


Fig. 9 X-ray diffraction patterns of the clay as untreated and Ethylene glycol states (after Hirota and Eveline 2013; Vt: Vermiculite, Mu: Muscovite)



Fig. 10 Locality of *la Colonia Guillén*

[La Colonia Miraflores Sur]

The landslide site of *la Colonia Miraflores Sur* is located at the north east of Toncontín (Fig. 12). The trigger of the landslide is the bank works on the head of the landslide which had slid. It is thus a case of artificially induced subsidence.

In November 15 2011, in a house under construction cracks were found after artificial bank slid. Later, the house was destroyed on March 2, 2012 (Fig. 13). Materials involved in the landslide are soils and weathering rocks.

After observation of landslides, we have done X-ray diffraction test of clay near the boundary of basement rock of the Group Valle de Ángeles and the body of the landslide.

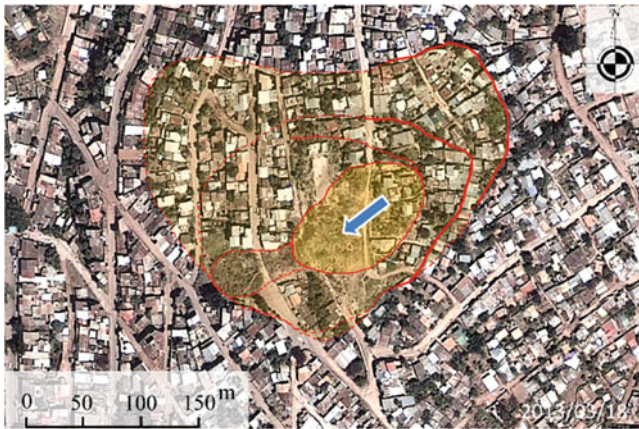


Fig. 11 Landslide of la Colonia Guillén



Fig. 12 Locality of la Colonia Miraflores Sur

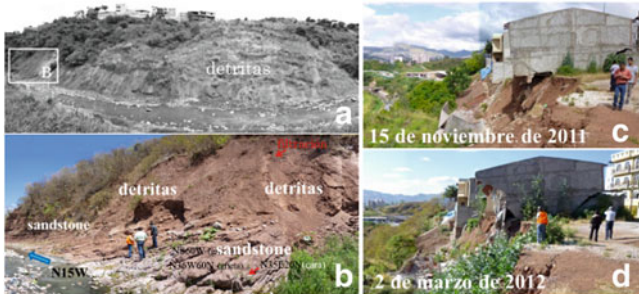


Fig. 13 Pie and Head of landslide in la Colonia Miraflores Sur (A, B: Toe, C: Head, November 15, 2011; D: Head, March 2, 2012)

The basement rock consists of stones such as siltstone and fine sandstone. The results of X-ray diffraction tests are shown in Figs. 14 and 15. Figure 14 indicates peaks Chlorite (Ch), Mica, Feldspar (Fld), Quartz (Qtz), and Hematite (He) in the bulk state.

Figure 15 shows X-ray diffraction patterns of materials obtained by the use of sedimentation method. States of materials are natural (untreated) and treated ethylene glycol. Peaks are due to Chlorite (Ch) and Mica. There is no clay mineral with expansion.

We think that the process of constructing house, bank works and erosion by the river increased the instability of the old landslide. In the analysis of landslide without

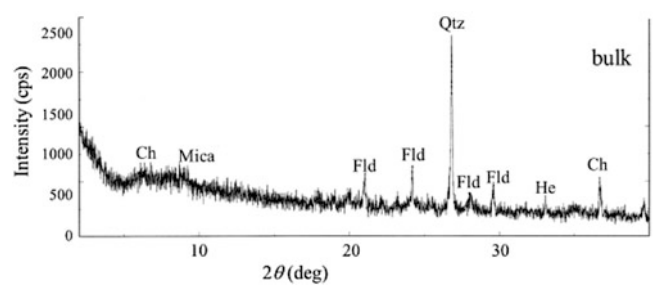


Fig. 14 X-ray diffraction pattern of the clay as bulk state (Ch: Chlorite, Fld: Feldspar, Qtz: Quartz, He: Hematite)

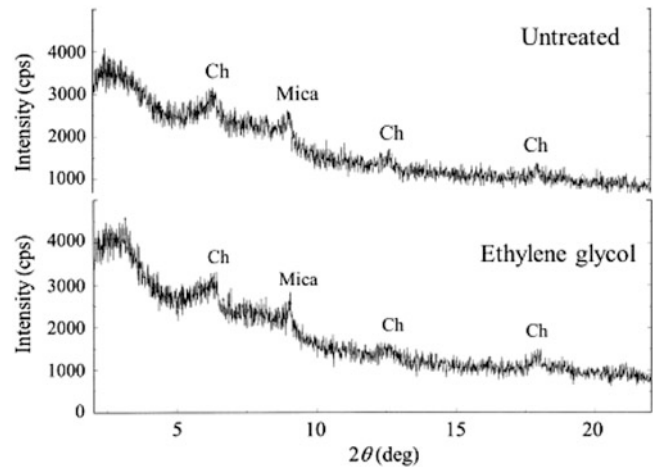


Fig. 15 X-ray diffraction patterns of the clay as untreated and Ethylene glycol states (Ch: Chlorite)

groundwater in the body of landslide, we set a condition of F (safety factor) as 1.00, of γ (soil density) as 1.8 t/m^3 , of ϕ (friction angle) as 15° . After getting the value c (cohesion), we analysed the safety state of landslide (Fig. 16).

Putting artificial bank on the toe of the landslide plays the most important role for the slope stability.

Data of Rainfall by Hurricane Mitch

Rainfall by Hurricane Mitch in the capital city of Tegucigalpa totaled 281 mm. This is however much less than that measured at Choluteca, which was more than three times the precipitation by hurricanes “Gilberto” and “Fifi” (Servicio Meteorologico Nacional, unpub. Data; after Harp et al. 2002). Rainfall values by Hurricane Mitch in Tegucigalpa is shown in Fig. 17.

During 3 days, October 29–31, 1998, total rainfall at Choluteca exceeded 900 mm. The river was dammed at approximately 12:30 a.m. on October 31, about 1 h after the peak flood flow of the Río Choluteca (Harp et al. 2002).

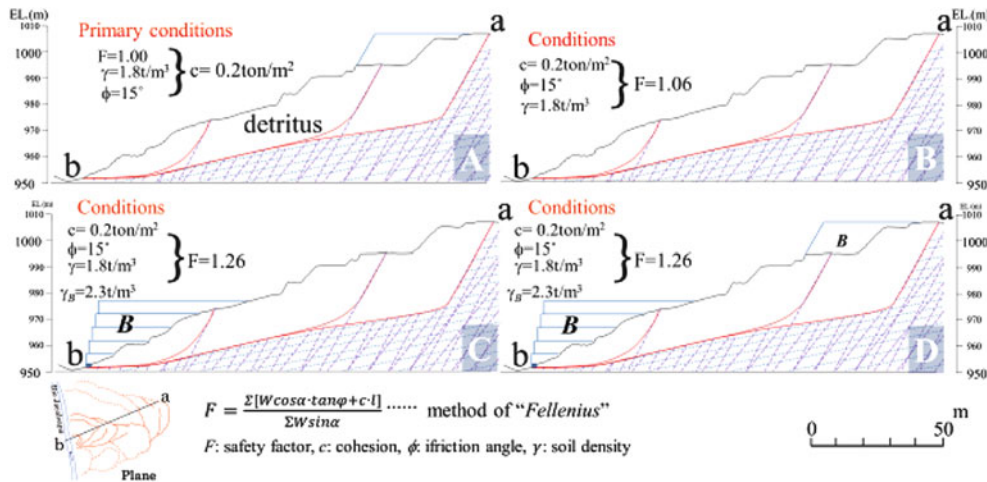


Fig. 16 Analysis of the stability

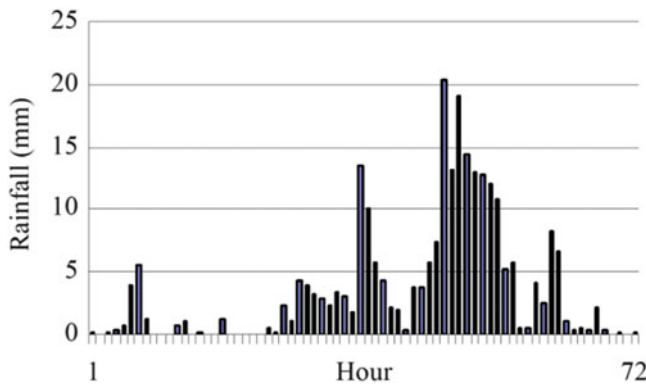


Fig. 17 Recorded rainfall at Toncontín during Hurricane Mitch (after JICA 2002)

Results

After the study of 17 localities, 3 localities, *el Bambú*, *el Reparto*, and *el Berrinche* were selected as appropriate sites where protections measures for landslide were to be provided.

In *la Colonia Campo Cielo*, nowadays practically all civil engineering works require detailed investigations leading to accurate knowledge of subsurface conditions in planning. In *la Colonia Canaán*, there is a flow of soil surface. In *el Bosque*, there is no landslide. In *la Buena Vista*, there are remains of rock falls. In *el San Martín*, there is no landslide. In *el Flor 1*, landslide is not expected to take place. In *el Zapote Norte*, there are remains of rock falls. There is no landslide. In *el Zapote Centro*, there is no landslide but there is erosion. In *la Villa Unión*, there is no landslide. In *la Brasilia*, there were debris flows. The mountain slopes are stable under existing conditions. In *la Centroamérica*, there

are remains of rock falls and small landslides. Slopes are stable under existing conditions.

In *la Nueva Esperanza*, *Las Torres Este*, and *Las Torres Oeste*, there are remains of rock falls. Erosion by el Río Choluteca affects stability of cliff. There are remains of rock falls. In these three regions landslides have the same pattern of slide back away for the upper part of the slope. Landslides are concentrated in the high relief, north-west of the province Tegucigalpa, although some isolated scars have been found in the south and southwest.

Discussion








[Typology of Landslides]

Varnes (1978) introduced five types for classification of landslides: Falls, Topples, Slides (including Rotational and Translational slides), Lateral spreads, and Complex (Table 1).

The result of our study shows that landslides in Tegucigalpa can be classified into Falls-type, Slides-type, and Flows-type of Varnes (1978).

In Falls-type landslide, there are six localities: *Bosque*, *Buena Vista*, *Zapote Norte*, *Zapote Centro*, *Nueva Esperanza*, and *Las Torres Este*. In Slides-type landslide, there are 5 localities including a part of *Berrinche*, a part of *Campo Cielo* in JICA-project, *Guillén*, *Altos de Loarque*, and *Miraflor Sur* without JICA-project. In Flows-type landslide, there are 11 localities: *Bambú*, *Reparto*, *Berrinche*, *Campo Cielo*, *Canaán*, *San Martín*, *Flor 1*, *Villa Unión*, *Brasilia*, *Centroamérica*, and *Las Torres Oeste*.

Table 1 Abbreviated version of Varnes’ classification of slope movements (adapted from Varnes 1978)

Type of movement		Type of material		
		Bed rock	Engineering soils	
			Predominantly coarse	Predominantly fine
	Falls	Rock fall	Debris fall	Earth fall
				
	Topples	Rock topple	Debris topple	Earth topple
				
Slides	Rotational	Rock slide	Debris slide	Earth slide
				
	Translational			
				
	Lateral spreads	Rock spread	Debris spread	Earth spread
				
	Flows	Rock flow (deep creep)	Debris flow	Earth flow
			(soil creep)	
	Complex	Combination of two or more principal types of movements		
				

[Factors of Landslides]

Intense rainfall, relief, slope angle, slope form, and slope exposure are recognized as factors in slide formation and distribution. They are classified into internal and external factors.

Internal factors are geology, geological structure as fault and joints, and geomorphological features. External factors are rainfall, cutting and artificial bank, and fluidity of groundwater. In *el Bambú, el Reparto, el Berrinche, el Campo Cielo, el Guillén, and el Miraflores Sur*, fault is an important geological factor which forms joints in the same direction and separates blocks of rocks by pairing joints. In the case of Rock slide type, joints induce formation of cracks at the crown and they trigger the landslide.

Many landslides in Tegucigalpa are caused by intense rainfall and fluidity of groundwater (external factor), and by joints of rocks (internal factor). The drainage of surface and underground water are the urgent problems to be solved. A study of the drainage may provide useful information, for instance: distribution of underground water and its direction of fluid.

Landslides called “Rock Slides” in Tegucigalpa are now almost stable after the first slip slide. It is solely due to the high value of residual shear stress of the slip clay of landslide. Furthermore groundwater level is very much influenced by intense rainfall. Ground water is very important. The height of the water table as well as its variation should be measured all year around. These points deserve further attentions.

Acknowledgments We are grateful to Dr. Ryuichi Yatabe and Dr. Netra P. Bhandary of Ehime University for making available for us apparatuses of X-ray analysis and Ring-shearing test, and to graduate students of Ehime University Mr. Deepak Raj Bhat and Miss Manita Timilsina (present: in Nepal) for supports in experiment. We would also like to thank Mr. Masahiko Hayashi of Earth System Science Co., Ltd. for providing helpful advice during this study and Dr. Yasushi Fujimoto of Cherry Consultants Inc. for interesting discussions.

References

- Harp EL, Castañeda M, Held MD (2002) Landslides triggered By Hurricane Mitch in Tegucigalpa, Honduras. USGS Open-File Report 02-33:1–11
- Harp EL, Reid ME, Mckenna JP, Michael JA (2009) Mapping of hazard from rainfall-triggered landslides in developing countries: examples from Honduras and Micronesia. *Eng Geol* 295–311
- Hirota K, Eveline L (2013) A case study of landslide at Altos de Loarque, Tegucigalpa, Honduras. First Central American and Caribbean Landslide Congress (CD document)
- Hirota K, Kamiya S (2013) A re-evaluation of landslide occurred by Hurricane Mitch 1998, Tegucigalpa Honduras. First central American and Caribbean landslide congress (CD document)
- JICA (2002) The study on flood control and landslide prevention in Tegucigalpa metropolitan area of the republic of Honduras (official document). Final Report in English version
- Varnes DJ (1978) Slope movement types and processes. In: Schuster RL, Krizek RJ (eds) Special Report 176: landslides: analysis and control. Transportation and Road Research Board, National Academy of Science, Washington DC, 11–33



11th May, 2013 Laipuitlang Rockslide, Aizawl, Mizoram, North-East India

Laldinpuia, S. Kumar, and T.N. Singh

Abstract

On 11th May 2013, a catastrophic rock slide occurred after cyclonic storm with heavy rainfall at Laipuitlang with $23^{\circ}44'60''$ N in latitudes and $92^{\circ}43'16''$ S in longitudes, Aizawl, the state capital of Mizoram, India. The landslide has a total area of 3,885 sq. m and a run-out distance of about 55 m. Estimated volume of debris is approximately 8 mm^3 . From the thick debris, 17 corpses were unearthed, 8 persons were rescued alive, and 10 houses are completely destroyed. It originated in the silty-sandstone bedding, highly weathered, steep slope with unsafe cutting for road and building construction. It was observed that over-weight building at the crown increased the tragic disaster. Schmidt hammer (N/NR type) was employed for measuring rebound value strength of rock and degree of weathering.

Keywords

Aizawl • Laipuitlang • Rockslide • Schmidt hammer • Silty-sandstone

Introduction

At the early Saturday morning on 11th May, 2013, a rockslide occurred at the slope of Laipuitlang, border of Ramhlun Venglai municipal local council area of Aizawl, Mizoram, India (Figs. 1 and 2). The incidence situated near PWD Side Office (Mechanical Sub-Division), Aizawl, located between $23^{\circ}44'60''$ N and $92^{\circ}43'16''$ S at 1,120 m above mean sea level. Seventeen persons were found dead under the thick debris, and 8 persons were rescued by the

State Disaster Search & Rescue Team. The rockslide badly affected and destroyed 15 houses (seven RCC buildings and eight Assam Type buildings) including community hall and an evacuated four storeyed RCC building of Public Works Department (PWD), Government of Mizoram (Fig. 2).

The area had experienced huge rockslide in 1957 and 1968 due to cutting of rock bed for one-time quarrying. The surrounding localities also experienced an anthropogenic induced landslide. On the 5th May of 2002, rockslide at Ramhlun affected one person died and concrete building collapse at the toe of the same dip direction after unsafe cutting of the rock bed and heavy rainfall. In 2007, on 25th November, rockslide affected Ramhlun South area after unsafe cutting of the rock bed for building construction. This rock bed was successfully mitigated using rock bolt in 2009.

The tension cracks first observed at the walls of building and slope face on June 2010. On September 2012, tension cracks were observed at the rock bed and soil, retaining walls and PWD RCC building which occurred at the crown along Laipuitlang road. Geologists' from the Directorate of Geology & Mineral Resources (Government of Mizoram) strongly suggested that PWD building was to be vacated,

Laldinpuia (✉)
Department of Geology, Pachhunga University College, Aizawl
796001, Mizoram, India
e-mail: dinpuiaageo@gmail.com

S. Kumar
Department of Geology, Mizoram University, Aizawl 796004,
Mizoram, India
e-mail: shivamzu@gmail.com

T.N. Singh
Department of Earth Sciences, I.I.T Bombay, Powai, Mumbai 400076,
Maharashtra, India
e-mail: tnsiitb@gmail.com

and to be demolished as preventive measures. But, before taking action for demolished, the 11th May 2013 rockslide destroyed the building and also observed as that this increased the catastrophic disaster for settlements at the toe region.

Geological Setting

Geology of the Study Area

The area falls under Bhuban Formation of Surma Group (Miocene to Upper Oligocene). The main rock type was brownish silty sandstone, and thinly intercalated by shale. The joint bedding of the rock thickness was generally about 3 m. The sliding rock mass was about 1.83 m thick. The joint set in this rock bed veering $N20^{\circ}$ to $23^{\circ}E$, $N65^{\circ}E$ width and $N75^{\circ}W$ (Geological & Mineral Resources Directorate unpublished report, 2012). The bedding was covered by thin soil and poor vegetation. The general slope of the failure surface was 48° . The general strike direction of the area was $N45^{\circ}E$ and $S40^{\circ}W$, and dip amount ranges between 43° and 47° due east respectively. But, at about 2 m from the south of rupture surface, the dip direction slightly change towards south-east with amount 51° . Tuikhurhlu stream flowing and spring water was also occurred between these different dip directions (Fig. 3).

The bedding of the rock was disturbed by water from the surrounding seepage and rainfall, and unsafe cutting at the southern side for building construction. A tension cracks are

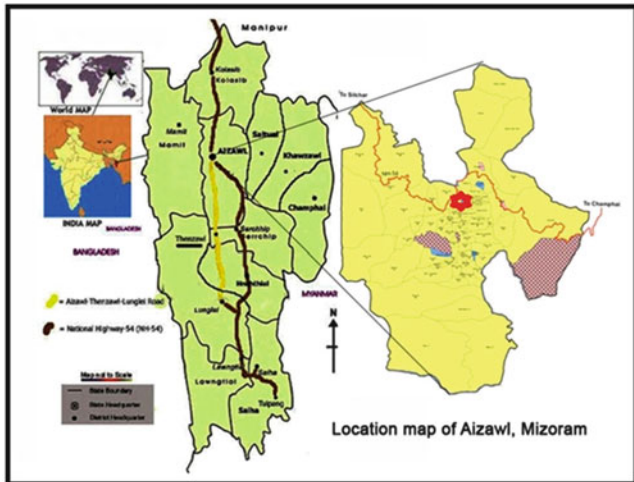


Fig. 1 Location map of Laipuitlang, Aizawl (Laldinpuia et al. 2013)

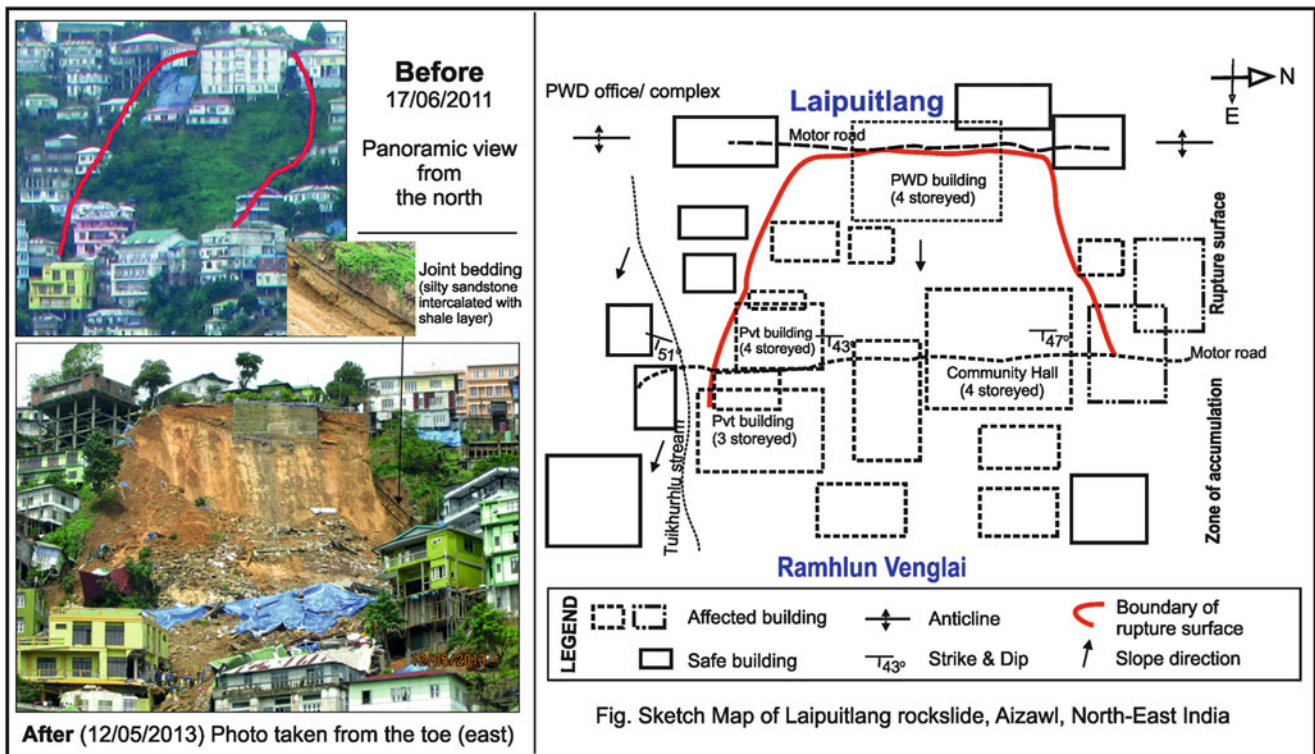


Fig. 2 Pre-event photo and after rockslide; sketch map showing general geology and settlements



Fig. 3 Dip direction changes at short distance

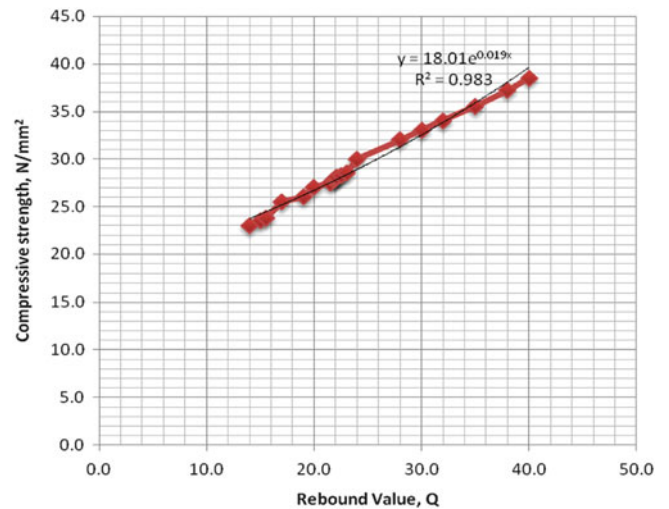


Fig. 5 The Hammerlink custom curve for Schmidt Hammer (N/NR type) reading



Fig. 4 Photograph showing joint bedding, tension cracks and zone of accumulation



Fig. 6 ‘Highly decomposed’ and weathered rock

observed at the crown along the motor road (Laipuitlang road), and north of the minor scarp, but not observed on the slope face (Fig. 4).

The hardness of the rock type obtained in terms of compressive strength. This compressive strength value was calculated from the rebound value using Schmidt Hammer (Day and Goudie 1977). The compressive strength of the main rock type silty-sandstone ranges between 14.0 and 40.0 N/mm² respectively. Most of the rock strength was confined between 20.0 and 24.0 N/mm² (Fig. 5). In field identification test, the rock strength can be termed as ‘moderately weak’ (Geotechnical Engineering Office 1998). The differences of the rebound values may be related to

degree of weathering (White et al. 1998). The northern site shows less value as compared to the southern site of the area, as also observed as northern rock type shows higher weathered. The Hammerlink custom curve was given at Fig. 5.

Triggering Mechanism

The Aizawl and its surrounding areas are highly susceptible to landslide. Landslides reported in and around Aizawl area are mainly caused by heavy rainfall, unsafe cutting, steep

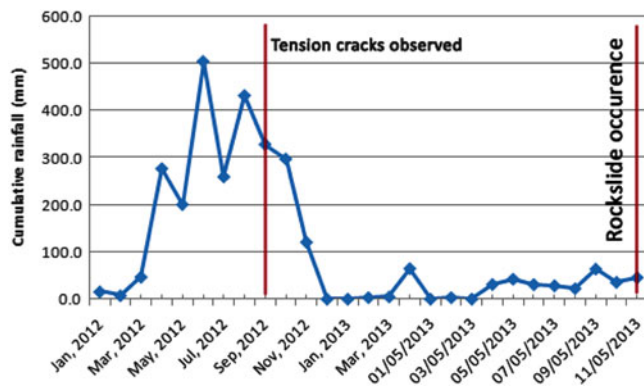


Fig. 7 Cumulative rainfall data, January 2012 to 10th May, 2013 (Directorate of Mizoram Science & Technology, Government of Mizoram)



Fig. 8 Effects of rockslide

slope, human interference and immature rock (Kumar et al. 1996; Laldinpuia et al. 2011; Lawmkima et al. 2011).

The rock type at the slope face observed as ‘highly decomposed’ classified as ‘Grade-IV’ in rock material decomposition grades (Geotechnical Engineering Office 1998; Fig. 6). The rock bedding was not massive, widely spaced, soft and porous; silty sandstone, brown sandstone intercalated by thin layer of shale (Fig. 4). Water infiltration was high due to poor drainage systems, leakage of a feet diameter water supply pipe, and seepages from in and

around surrounding settlements. These factors may increase weathering rate.

The area receives high rainfall, this may added decrease in binding forces between the rock bedding, thus caused prominent tension cracks, which observed at the crown and middle of the present rupture surface on September 2012 (Wieczorek 1996; McSaveney and Davis 2007). After continuous rainfall, and cyclonic storm with heavy rainfall, a disastrous rockslide took place on an early morning of 11th May 2013 (Figs. 7 and 8).

Unsafe cutting for road and construction of building decrease shear strength at the toe region (Zaruba and Mencl 1982). The respective area experienced tension cracks after unsafe cutting followed by rainfall at the middle of the rock bed for building construction on June 2010. This unsafe cut off initiates the movement. The most disastrous rockslide occurred in Mizoram in the year 1992 at Hlimen, claimed 66 lives was also took place after unsafe cutting of bedding (Kumar et al. 1996).

A huge four-storeyed RCC building located at steep slope of the crown that increased the force of gravity, acting driven force towards the slope direction. It was observed that this huge building increased the catastrophic disaster for settlements at the toe region.

Conclusion

The 11th May 2013 Laipuitlang rockslide is one of the disastrous catastrophic events in Mizoram. The occurrence influenced strengthening and improvement of Disaster Management in the State.

Field observations and history of the study area reveals that rockslide due to weathered joint bedding, steep slope, heavy rainfall, water seepage, unsafe cutting of rock bed and overweight building construction.

Further research on laboratory testing of rocks and more rigorous slope stability analyses are needed to suggest suitable mitigation measures.

Acknowledgments We are grateful to the local council authorities of Laipuitlang and Ramhlun Venglai and for providing us necessary information.

References

- Day MJ, Goudie AS (1977) Field assessment of rock hardness using the Schmidt test hammer. Br Geomorphol Res Group Tech Bull 18:19–29
- Geotechnical Engineering Office (1998) Guide to rock and soil description. Reprinted November 2000, Hong Kong
- Kumar S, Singh TN, Sawmliana C (1996) On the instability problems in South Hlimen landslide, Mizoram. Indian J Eng Mat Sci 4:78–80
- Laldinpuia, Kumar S, Singh TN (2011) Geotechnical studies of landslides at Ramhlun Vengthar, Aizawl, Mizoram. Mem Geol Soc India 77:251–258

- Laldinpuia, Kumar S, Singh TN (2013) The 2013 rockslide disaster of Aizawl, Mizoram, India. *Sci Vis* 13(2):58–63
- Lawmkima H, Tiwari RP, Kumar S (2011) Geomechanical analysis of sairang landslide near Aizawl, Mizoram. In: Singh TN, Sharma YC (eds) *Slope stability (natural and made slope)*. Vayu Education of India, New Delhi, pp 76–90
- McSaveney M, Davies T (2007) Rockslides and their motion. In: Sassa K, Fukuoka H, Wang F, Wang G (eds) *Progress in landslide science – part II*. Springer, New York, pp 113–133
- White K, Bryant R, Drake N (1998) Techniques for measuring rock weathering: application to a dated fan segment sequence in southern Tunisia. *Earth Surf Process Landforms* 23:1031–1043
- Wieczorek GF (1996) Landslide triggering mechanisms. In: Turner AK, Schuster RL (eds) *Landslides: investigation and mitigation*, Special Report 247, Transportation Research Board, p 76
- Zaruba Q, Mencl V (1982) Landslide and their control. *Dev Geotech Eng* 31:121–122



Geological Investigation of Slumping Localities in Saiha Town, Southern Mizoram, North-East India

Laldinpuia

Abstract

Saiha town experienced transverse cracks after continuous heavy rainfall on June 2002. Again, long monsoon in 2010 caused slumping in Saiha town. The slumping localities suffered mass movement after cloud burst on the 16th and 17th May 1995. Prominent transverse cracks and local faults were observed on October 2010 at the rupture surface of slumping localities namely New Colony-I, New Colony-III, College Veng and Council Veng, Saiha. About 310 houses were affected. The geological field investigations revealed that the nature of transverse cracks and structure of the slumping area.

Keywords

Middle Bhuban Formation • Saiha • Slump • Transverse cracks

Introduction

Slump or rotational slide is the downward rotation of regolith that occurs along a curved surface. This type of mass movement is common where clays are underlain by impervious strata, and the mass is generally inclined into the slope (Selby 1993; Zaruba and Mencl 1982).

The immature topography, receiving higher rainfall and the thick regolith of the town caused more geological hazards like mass movement. Saiha town experienced the largest mass movement in Mizoram on 16th and 17th May 1995 after cloud burst, and due to improper drainage system, geologically weak strata and poor vegetation. 20 people lost their valuable lives, 13 people are seriously injured and 67 houses are completely destroyed in Saiha town (Laldinpuia 2012).

Study Area

Saiha is the southernmost town in Mizoram; it is the district capital of Saiha District as well as headquarters of Mara Autonomous District Council (MADC). It is located at a distance of about 315 km from Aizawl *via* Thenzawl-Lunglei road. The town is approachable by NH-54. State Highway connected from Tuipang and from Sangau by seasonal road. It can also approach by the State Helicopter Service. It falls under Survey of India Toposheet No. 84 B/15 and situated in between 22°29'–22°30' latitude and 92°58'–93° longitude. The specific study area—New Colony and College Veng localities are situated at the western side of Saiha town, while Council Veng at the eastern side (Fig. 1).

The anticline ridge of Civil Hospital road breaks up the location of New Colony-College Veng block to Council Veng block.

Saiha town receives high rainfall with an average of 2,577.29 mm per annum (Fig. 2), i.e. highest in the state, and receives about 128 days annually. During winter the temperature ranges from 8 to 22 °C and the temperature ranges from 18 to 27 °C during summer.

Laldinpuia (✉)
Department of Geology, Pachhunga University College, Aizawl
796001, Mizoram, India
e-mail: dinpuiageo@gmail.com

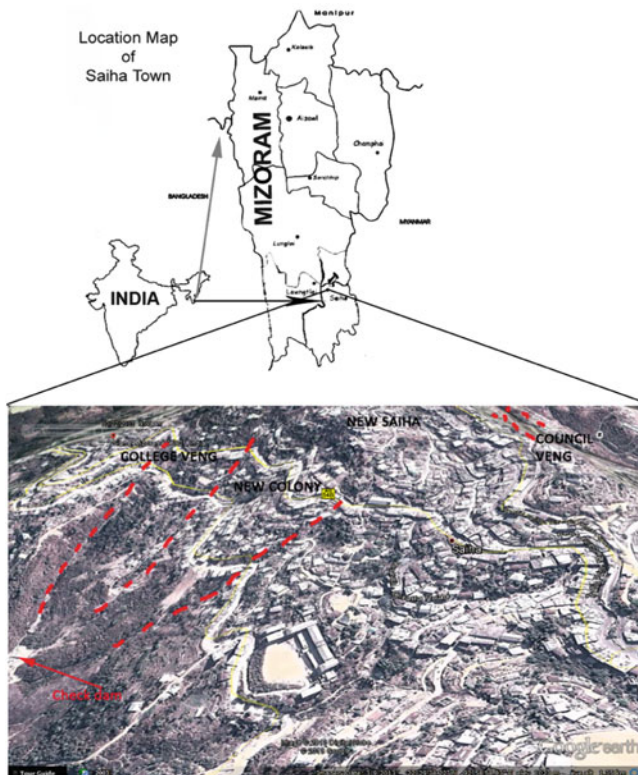


Fig. 1 Location of study area, Saiha

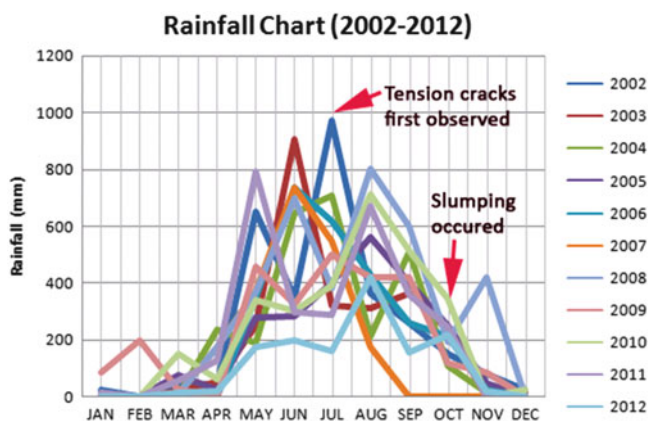


Fig. 2 Rainfall data (After Department of Agriculture, Government of Mizoram)

Geological Setting

Saiha town is made up of Middle Bhuban Formation of Surma Group. The main rock types are shale, sandstone and siltstone. There are many local fault lines, which controlled the stream lines. Since, shale is the main rock type, it easily weathered by the action of water, then transformed into clays (Osipo et al. 2005; Wen et al. 2004). These

weathered products are observed along the stream line and along the NH-54B road section. Medium to fine grained grey to yellow bedded sandstones are mostly deposited along the stream. There is no proper bed rocks exposure. The general strike of the beds trends $N5^{\circ}W/N5^{\circ}E-S5^{\circ}E/S5^{\circ}W$ with dip ranges from 30 to 65° either towards east or west. Development of joints and faults are abundance. But, proper beddings and outcrops were not observed at the slumping area.

The slopes are characteristically steep, ranges from 35° to almost vertical, i.e. 90° . Because of thick regolith and/or debris (2–20 m), the slope morphology is changes. High rate of erosion at the toe regions results vertical slope. The western limbs of the anticlines are usually steeper than the eastern limbs.

Methods

The present geological investigation was based on field study (Anbalagan et al. 2007). During geological field work, Brunton Compass and Silva Compass were used for measuring dip and strike amount and direction. GPSMAP78SC (Garmin) used for geographical location, and measuring tape for determination of the length and wide of transverse crack. Trees, buildings, and ruler marked stick are based for measuring the rate of subsidence. Tilting angle of trees and sinking of the stick (positioned at the contact between disturbed and undisturbed) were examined twice a day at the same time constantly for 3 weeks in the month of October, 2010.

The cracks observed at the wall and floor, conjunction between the column and the skirting of the affected buildings were also examined and measured. These short-time measurement, and field investigations during the month of December, 2011 and June, 2013 observed that a continuous movement of these slumping localities, and may be unsafe settlement area if not mitigate at the correct time.

Observations

New Colony

The slumping area covering an area of about 200 sq. m, coordinates between $N22^{\circ}29'26.46''-E092^{\circ}58'53.94''$ at the southern main scarp and $N22^{\circ}29'27.84''-E092^{\circ}58'55.32''$ at the northern main scarp. At the toe region, along NH-54B, it coordinates between $N22^{\circ}29'32.34''-E092^{\circ}58'48.48''$ at 979 m in south and $N22^{\circ}29'31.8''-E092^{\circ}58'54.9''$ in north. The height of main scarp to the down thrown ranges from 1.5 to 7 ft respectively, and the height distance between the main scarp at $N22^{\circ}29'26.46''-E092^{\circ}58'53.94''$ (1,078 m) and toe

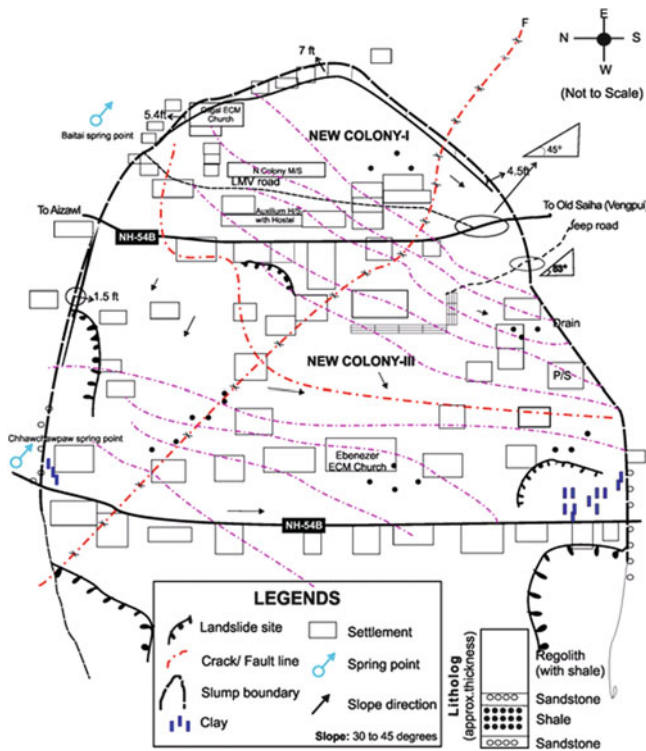


Fig. 3 New Colony-I and III

(bottom of earth flow) at $N22^{\circ}29'41.7''$ and $E092^{\circ}58'45.78''$ (881 m) is 197 m. The area comprises two village councils viz. New Colony-I and New Colony-III respectively (Fig. 3).

According to local people, the northern side of New Colony-I & III area suffered huge landslides in around 1920, again in 1960 and 1995. Transverse cracks were noticed from 23rd July, 2002. 10 transverse cracks along NE-SE & NS direction were identified during geological field work on October, 2010. About 180 houses were affected including one boarding school, i.e. Auxilium H/S, one middle school, i.e. New Colony M/S and one primary school, i.e. New Colony-III P/S, and ECM Church, Gilgal. These transverse cracks were about 1–13 inches wide and about 5–32 m (Fig. 4). One big transverse crack (fault) along NW-SE direction was observed, which severely affected four residential houses. Reconstruction of Cheinal chava (*'chava' means 'stream'*) was suggested to catch the drains from upper crown of the slump. ECM Church (Gilgal) situated at the border of northern slumping area was badly affected, and the District Disaster Management Authority (SDMA) ordered on the 17th June, 2013 to evacuated and dismantled the building.

There was no proper bed rock and outcrops exposed in this area. The geological structures in this area differed considerably. At the border of New Colony and College Veng, between $N22^{\circ}29'33.36''$ and $E092^{\circ}58'56.58''$ along the NH-54B road section, 13 in. thick grey sandstone



Fig. 4 Photograph of some of the transverse cracks in New Colony

intercalated with 2 in. shale bed of about 12 ft thick exposed was observed. This bed strikes $N80^{\circ}W$ and dip amount was 29° due east.

The CCI College Veng block of New Colony-III area was observed as the most vulnerable disastrous subsidence area in the town due to weak resisting nature at the toe portion (Fig. 4). It was situated between $N22^{\circ}29'30.18''$ and $E092^{\circ}59'1.74''$ at the crown at the height of 1,075 m to $N22^{\circ}29'41.1'$ and $E092^{\circ}58'46.86''$ at the toe at the height of 880 m. No bed rock was observed, only thick regolith about 24 m. The fishpond of about 70 sq. m situated near CCI church may increase the gravitation force. The resisting force at the toe region was weak due to high erosion, thick regolith and no proper bedding. 4 transverse cracks of about 1–6 in. wide, along NW-SE direction were observed at the toe region. 2 houses situated near the coordinates between $N22^{\circ}29'37.44''$ and $E092^{\circ}58'51.24''$ at the height of 968 m are highly vulnerable to sliding shown in Fig. 5.

College Veng

About 60 houses affected by slumping in College Veng area (Fig. 6). The area is situated between $N22^{\circ}29'32.16''$ and $E092^{\circ}59'2.7''$ at the crown at 1,081 m to $N22^{\circ}29'36.66''$ – $E092^{\circ}58'57''$ at the toe. 6 transverse cracks along NS, NE-SE, EW & NW-SE directions were observed. These transverse cracks are about 1–5 in. wide. At Seidia chava, at $N22^{\circ}29'35.94''$ and $E092^{\circ}59'5.94''$ at 1,056 m, there was an exposure of shale bed along the NH-54 road striking $N20^{\circ}E$ and dip $17^{\circ}W$, this type of rock bed exposed again at $N22^{\circ}29'38.2'$ and $E092^{\circ}58'43.87''$ at 881 m striking $N50^{\circ}E$ and dip amount is $13^{\circ}W$. After suggestion

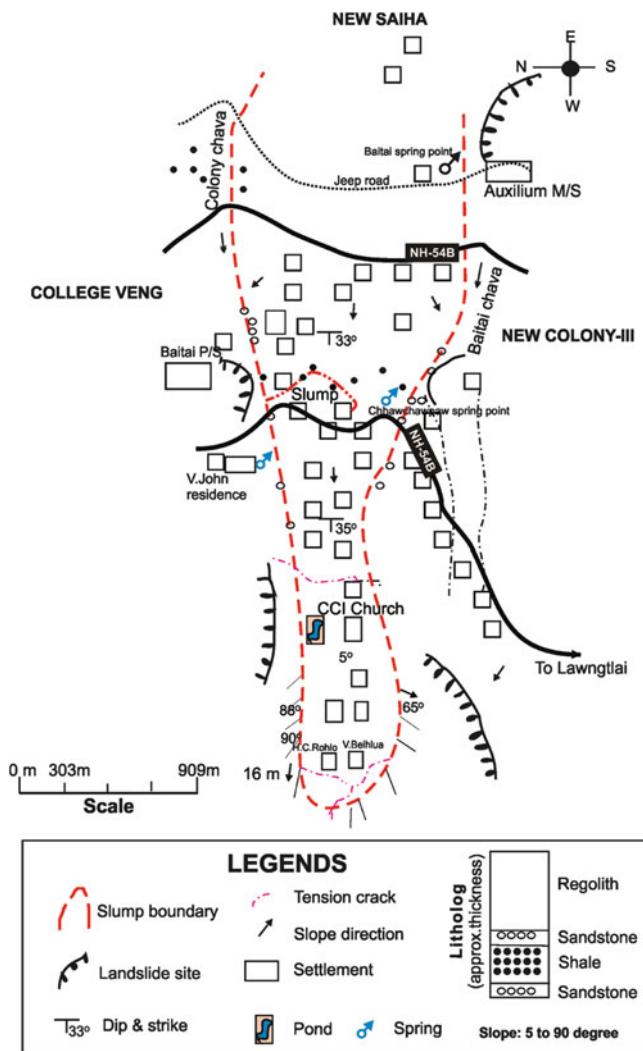


Fig. 5 CCI College Veng block of New Colony III

(Laldinpuia 2012), check dam was constructed at Seidia chava at the side of V. John residential compound. The check dam was also observed as positive. Garbion wall type was suggest at above the bridge to increase toe resisting force, and to prevent slump along the road of National Highway situated at the height of about 80 m.

Council Veng

Council Veng subsidence area was noticed from 1989, and again in 1995. About 40 houses are affected in this subsidence. The main scarp situated at $N22^{\circ}29'16.92''$ and $E092^{\circ}58'58.8''$ at the height of 1,136 m and the toe at $N22^{\circ}29'9.6''$ and $E092^{\circ}58'55.32''$ at 1,020 m (Fig. 7). On September 2010, an area of about 20 sq. m slumping was observed, destroyed one kutchha house.

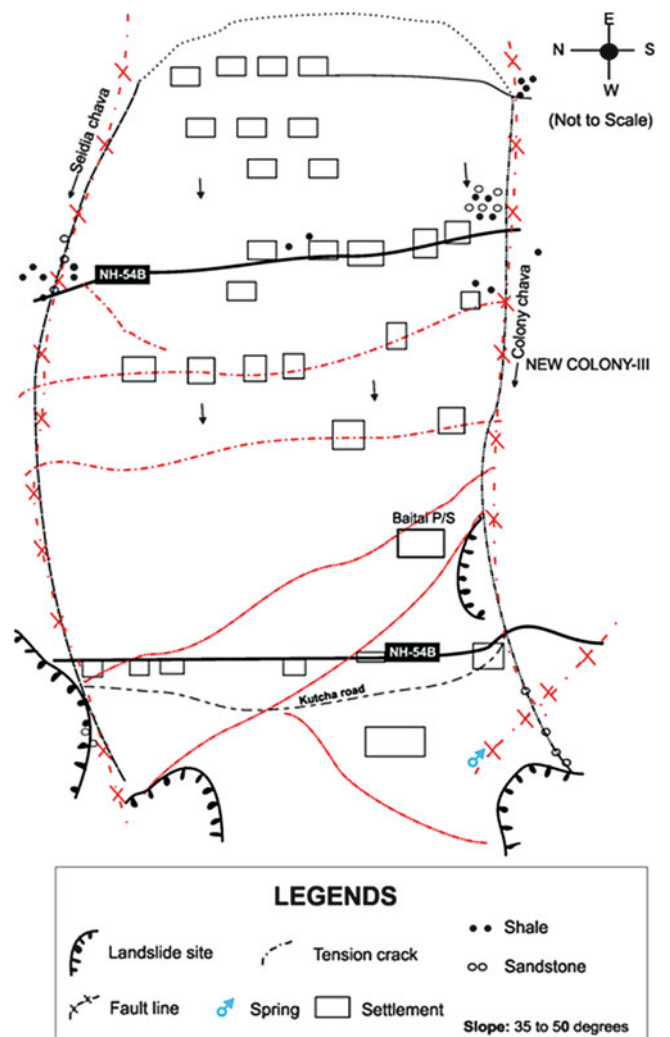


Fig. 6 Affected area of College Veng

There was no proper rock bed in the area. About 7 ft siltstone was exposed at the toe, at $N22^{\circ}29'8.4''$ and $E092^{\circ}58'54.78''$ at 1,020 m near Region stream striking $N42^{\circ}W$ and dip $20^{\circ}E$. Bluish weathering shale of about 3 ft thick was observed at $N22^{\circ}29'14.04''$ and $E092^{\circ}58'56.04''$ at the height of 1,126 m near the LIKKB church. One transverse crack was observed along NS-direction at the toe of Civil Hospital hill. The height of the main scarp to the nearest down thrown ranges from 8 to 20 ft.

Discussion

The rate of slumping increased during monsoon period, and generally slows in another season. The slumping may be due to heavy percolation of rain water into thick regolith develops pore pressure and reduced resisting force,

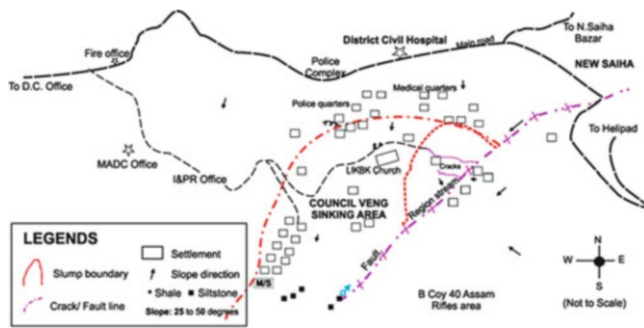


Fig. 7 Council Veng

steepness of the slope accelerate gravitational force of the soil and high erosion rate at the toe region. Stable rock bedding strata was not observed even at the toe region indicated that weak in resisting force.

Neither proper drainage system nor systematic household seepages was constructed at the study area. Suitable drainage system should be constructed at the crown and failure surface to catch rainfall and households seepages. To increase resisting force, breast wall, retaining wall, toe wall and check dam should installed at suitable places.

The life span of such recommended mitigation measures may depend on legislation. Construction of RCC building should be banned in the slumping localities. Building should

be completed with suitable drainage system, house gutter and water reservoir. Implementation of building bye-law or building regulation for Saiha town was strongly suggested.

Acknowledgments The author express appreciate to the authorities of Mara Autonomous District Council (MADC) for funding field investigation surveys and to the local people of the study area for helping in field works.

References

- Anbalagan R, Singh B, Charabarty D, Kohli A (2007) A field manual for landslide investigations. DST, New Delhi, pp 10–27, 28–50
- Laldinpuia (2012) Case study: Saiha sinking area. In: Saiha disaster management plan 2012, D.C. Saiha, Mizoram, pp 50–53
- Osipo VI, Gratchev IB, Sassa K (2005) The mechanism of liquefaction of clayey soils. In: Sassa K, Fukuoka H, Wang F, Wang G (eds) Landslides – risk analysis and sustainable disaster management. Proceedings of the first general assembly of the International Consortium on Landslides, Springer, Germany, pp 127–132
- Selby MJ (1993) Hillslope materials and processes. Oxford University Press, Oxford, pp 200–401
- Wen BP, Duzgoren-Aysin NS, Aydin A (2004) Geochemical characteristics of the slip zones of a landslide in granitic saprolite, Hong Kong: implications for their development and microenvironments. *Environ Geol* 47:140–154
- Zaruba Q, Mencl V (1982) Landslide and their control. *Dev Geotech Eng* 31:99–105, 282



Probabilistic Back Analysis of a Cut Slope: A Case Study of Slope Failure Event in Precinct 9, Putrajaya, Malaysia

Soon Min Ng, Mohd Ashraf Mohamad Ismail, and Ismail Abustan

Abstract

This paper presents a case study of slope failure in Precinct 9, Putrajaya, Malaysia in which back analysis was performed to investigate the main causes of slope failure. The catastrophic slope failure incident has caused 23 cars to be buried and evacuation of 1,000 people from their houses. Recorded data showed that it had been raining heavily with a total cumulative rainfall of 210 mm prior to the slope failure occurrence. Site investigation that comprised of soil boring and geophysical electrical resistivity survey was initially carried out to obtain information such as subsurface characteristics and groundwater condition. Relevant information such as shear strength parameters, soil profile and groundwater level will be then utilized for the modeling and analysis. Sensitivity analysis suggested that the slope failure is most likely to be caused by the fluctuations of groundwater level that increased the pore water pressure thereby reducing the shear strength. Due to the high degree of uncertainty in the slope stability parameters to be analyzed, probabilistic method was implemented in this study. Two approaches namely the limit equilibrium and shear strength reduction finite element methods were used to perform the stability analysis and the results from both analyses were compared. For finite element analysis, the principle of Point Estimate Method (PEM) was adopted where solutions were computed at various estimation points and then combined with proper weighting in order to get an approximation of the distribution of the output variables. Results from the back analysis may then be utilized for remedial works and redesign of the failed slope.

Keywords

Probabilistic back analysis • Slope stability • Limit equilibrium analysis • Shear strength reduction • Point estimate method

Introduction

It is important to understand the causes and nature of slope failure prior to design or determine a remedial measure for the slope. Generally, there may be more than a single factor that can cause slope failure (Duncan and Wright 2005). One of the

methods to obtain information on the conditions in the slope at the time of failure is to study the failed slope. For a failed slope, the factor of safety is considered to be unity (1.0) at the time of failure. By using this information and the appropriate method of analysis it is possible to develop a slope model during failure. The developed slope model can provide a better understanding of slope failure and can be used as a basis for analysis of remedial measures. The process of determining the conditions and establishing a suitable model of the failed slope is known as back analysis. Back analysis is preferred when there are significant limitations in the use of laboratory and in-situ test results to accurately characterize the soil. However,

S.M. Ng (✉) • M.A. Mohamad Ismail • I. Abustan
School of Civil Engineering, Universiti Sains Malaysia (USM),
Engineering Campus, 14300 Pulau Pinang, Malaysia
e-mail: soonmin1612@hotmail.com; ceashraf@eng.usm.my;
ceismail@eng.usm.my

there are several studies that describe the limitations of back-analyses (Azzouz et al. 1981; Leonards 1982; Duncan and Stark 1993; Gilbert et al. 1998; Tang et al. 1999; Stark and Eid 1998). Although these studies described many of the weaknesses in back analysis, a reliable back analysis requires accurate information such as geometry, material properties and pore water pressure distribution which are representative to the real system (Deschamps and Yankey 2006). In addition, there are also numerous studies that have applied the back-analysis technique for the estimation of soil parameters and the results produced were satisfactory (Sonmez et al. 1998; Jiang and Yamagami 2008; Sharifzadeh et al. 2010).

Two methods that are commonly used to perform back analysis are the deterministic and probabilistic methods. Deterministic back analysis is aimed to determine a set of parameters that would result in slope failure while probabilistic back analysis method developed a range of possibilities that caused slope failure and the probability of each possibility is assessed.

According to Zhang et al. (2010), probabilistic method has the advantages over deterministic method that include: (1) it provides a logical way to incorporate information from other sources in the back analysis and (2) it is capable of back analyzing multiple sets of slope stability parameters simultaneously. However, the only possible disadvantage of probabilistic back analysis method is the difficulties for implementation compared to deterministic back analysis method. In recent years, the applications of probabilistic analysis to numerical modeling of soil and rock slopes have been widely used (Griffiths and Fenton 2004; Hammah et al. 2008). Numerical methods such as the finite element method (FEM) have been successfully applied to slope stability analysis and with the advancement of computers, the computation of probability slope stability analysis has become faster and less intensive.

In this paper, back analysis of slope failure in Putrajaya, Malaysia is carried out. Initially, site investigation that consist of borehole drilling and geophysical resistivity survey were performed to collect information such as subsurface and groundwater conditions for the study area. The back analysis that utilized soil parameters obtained from laboratory testing was performed using both limit equilibrium and finite element with shear strength reduction method. Three parameters namely cohesion, friction angle and groundwater level that mainly affect the slope stability were assessed. Finally, the main cause of slope failure was identified.

Project Background

Putrajaya is an urban area with approximately 49 km² of land that serves as the federal administrative centre of Malaysia. On 23rd March 2007, a massive slope failure



Fig. 1 Location of slope failure in Precinct 9, Putrajaya

occurred at Precinct 9, Putrajaya burying 23 vehicles at 4.30 am. It had been raining heavily in Putrajaya since the evening of 21st March 2007 until the early morning of 22nd before the slope failure occurred. Although no casualties or injuries were involved, about 1,000 residents residing in the three blocks of government quarters adjacent to the slope failure area were forced to vacate their homes.

The slope failure occurred on the western side of a 50 m ridge with a 36 million water tank located on the crest. The water tank is partially buried on a part of the hill that has been cut to prepare a flat side for it. The distance of the tank to the edge of the ridge where the slide occurred is about 25 m. The study area is underlain by graphitic quartz mica schist from Kajang Formation. Based on historical site investigation, the rocks in this area consist of interbedded sandstone, shale and actinolite schist (Ahmed et al. 2011). Figure 1 shows the location of the slope failure in Precinct 9, Putrajaya.

Site Investigation

Soil investigations that consist of boreholes and geophysical surveys were carried out immediately after failure to identify the root causes followed by determining an efficient remedial work. A total of 17 boreholes were carried out using rotary wash boring method. Besides, geophysical electrical resistivity survey for a total of 9 lines was conducted to characterize the subsurface geology including hydrogeological condition of the study area. Figure 2 shows the 9 resistivity survey lines and 14 boreholes for site investigation in the study area. Soil samples were also collected from the site to determine the soil parameters input via laboratory testing for modeling and analysis. Rainfall data recorded by a rain gauge station located at Precinct 2, Putrajaya was presented in Fig. 3. High intensity of rainfall of 140 and 60 mm were recorded 2 days prior to the slope



Fig. 2 Location of boreholes and resistivity survey lines

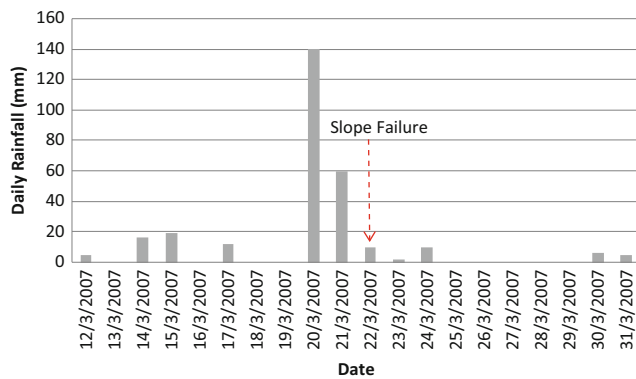


Fig. 3 Rainfall intensity data

failure. On the day of the slope failure which is 22nd March 2007, the rainfall intensity was only 10 mm.

Results from Geophysical Resistivity Survey

All the resistivity profiles were obtained using the Schlumberger array. A three-dimensional resistivity model was developed to map the overall subsurface based on the resistivity values obtained for the study area. Based on the 3D model as shown in Fig. 4, it can be observed that the area of slope failure is located within the area of low resistivity. To clearly investigate the subsurface, two resistivity lines adjacent to the slope failure zone were cut through the 3D model. Figure 5 shows the resistivity survey lines for R2 and R6 with total length of 100 m and 80 m respectively. From both the pseudo sections, it can be interpreted that the slope failure section comprised of a large zone with low resistivity values ranges from 0 to 100 Ωm . These zones can be interpreted as zone with high seepage inflow or presence of groundwater (Keller and Frishcknecht 1996). This interpretation may also suggest that saturated fractured schist is present underneath the slope failure zone. Borelogs from BH3 also shows a soft layer of silt up to 6 m followed by

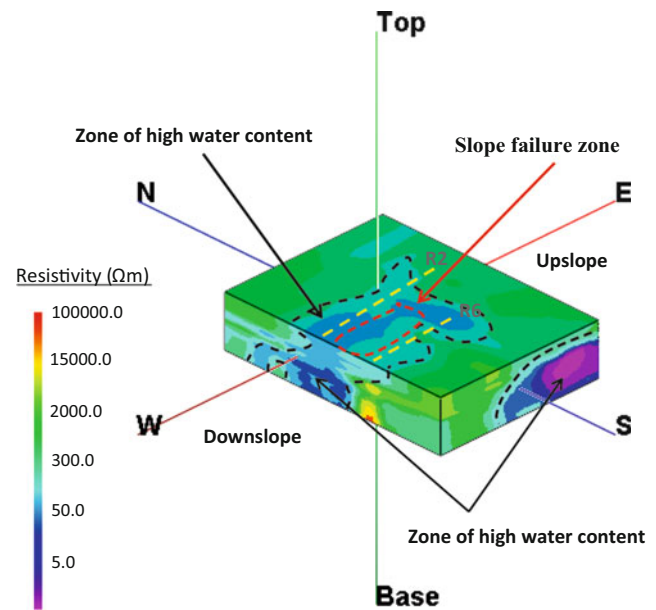


Fig. 4 3-Dimensional resistivity model

1.5 m of hard layer which is underlain by rock with an RQD of 13 %.

Results and Discussion

The factors that initiated the slope failure may be complex and cannot be analyzed using simple static analysis. Therefore, in this study a combination of both limit equilibrium and finite element method were utilized to maximize the advantages of both approaches. The uncertain parameters that were investigated to cause slope failure are cohesion, friction angle and pore water pressure. Based on the post failure site investigation and laboratory testing of soil samples, the input parameters that will be used for the analysis were presented in Table 1. Figure 6 shows the conceptual model of the slope developed for analysis. The groundwater levels measured from ground level of boreholes after the slope failure event were 5.8 m at the crest of the slope and 0 m at the toe of the slope respectively. Therefore, the boundary conditions for groundwater level during failure applied in the analysis were assumed to be less than the measured values.

In this study, the Point Estimate Method (PEM) developed by Rosenblueth (1975) was applied to Finite Element Shear Strength Reduction Method in performing the probabilistic slope stability analysis for the initial stage. Then it is followed by a comparison with limit equilibrium method (LEM) using Bishop’s method for validation purpose. Sensitivity analysis was also carried out using LEM to determine the response of each variable to the stability of slope. Slide 6.0 and Phase2 8.0 software developed by Rocscience

Fig. 5 (a) Resistivity survey line R2. (b) Resistivity survey line R6

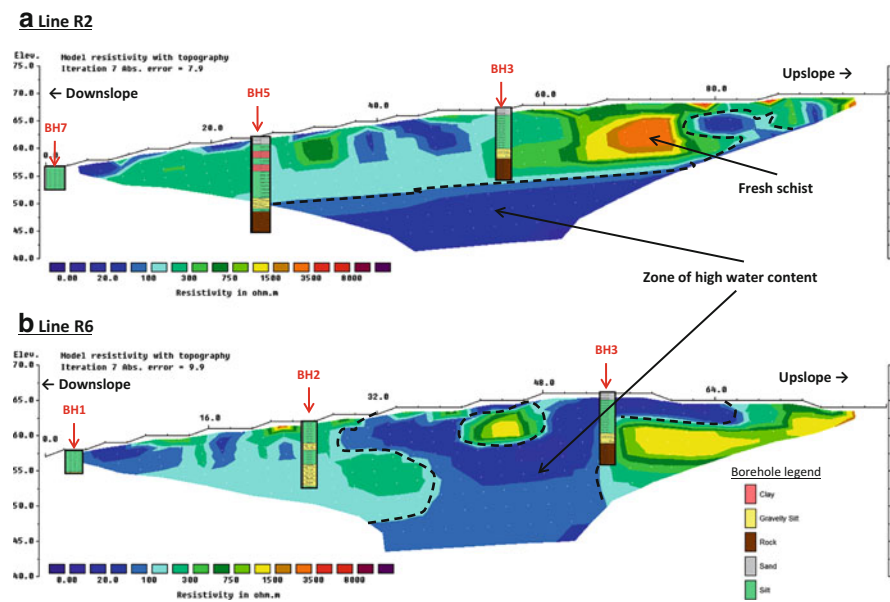


Table 1 Input parameters for stability analysis

Material parameter	Silt	Gravelly silt
Unit weight (kN/m ³)	18.67	17.79
Cohesion (kPa)	14	36
Friction angle (°)	23	18
Hydraulic conductivity (m/s)	1.17×10^{-10}	2.42×10^{-10}

Inc were used for limit equilibrium and finite element analysis respectively.

Table 2 shows the result obtained from both LEM and FEM-SSR probabilistic analysis for initial condition. It is noticed that the results produced from both methods is close to each other where the probability of failure is only 1 %. As rain started to fall, transient infiltration boundary condition was applied on the slope surface based on the historical rainfall data. From the limit equilibrium analysis using Bishop's method, the factor of safety obtained decreases as rainfall infiltration increases as shown in Fig. 7. However during the time of slope failure, the FOS obtained was 1.185 and the result is considered as safe since the FOS more than 1. This is mainly due to the various uncertainties subjected to the slope such as modeling errors, errors in input parameters etc. Hence, the back analysis was proceeded with sensitivity analysis.

Figure 8 presents the results of sensitivity analysis of both soil types for shear strength parameters cohesion and friction angle. It was observed that the cohesion and friction angle for gravelly silt does not affect the stability of slope with the changes of shear strength parameters. However for silt, slope failure will occur when the cohesion and friction angle values are less than 16.25 kPa and 20.3° respectively.

Hence, the cohesion and friction angle of silt during slope failure is deduced to be less than these values.

Besides the shear strength parameters, another possible cause of slope failure is the fluctuations of groundwater level specifically the initial groundwater level at the upslope. A coupled analysis of seepage and stability was applied to address this problem by varying the initial boundary conditions of total head to determine the changes of FOS. The results show that the total head at the upslope during failure was 24.4 m as presented in Fig. 9. This can be inferred as the groundwater level at the crest of the slope is approximately 2.2 m measured from the ground level. With this finding and also the results from geophysical survey, these have proved that the study area has existing high groundwater level which tends to destabilize the slope. This condition has caused the slope vulnerable to failure and failure will be triggered when rainfall raises the groundwater level that reduces the shear strength. Based on the 3-D resistivity model and soil boring data, the high groundwater level is mainly caused by the highly fractured saturated rocks where the groundwater flows from the South-East part of the study area to the slope failure zone.

As a remedial action, the usage of horizontal drains with the length of up to 24 m was installed to lower down the groundwater level. Horizontal drains are found to be very effective if is properly located (Rahardjo et al. 2003). For this case study, horizontal drains have been proven effective based on the observation from site measurements and instrumentation monitoring installed at the top, mid and bottom of the slope. Piezometric water level remains almost constant

Fig. 6 Conceptual model for the slope

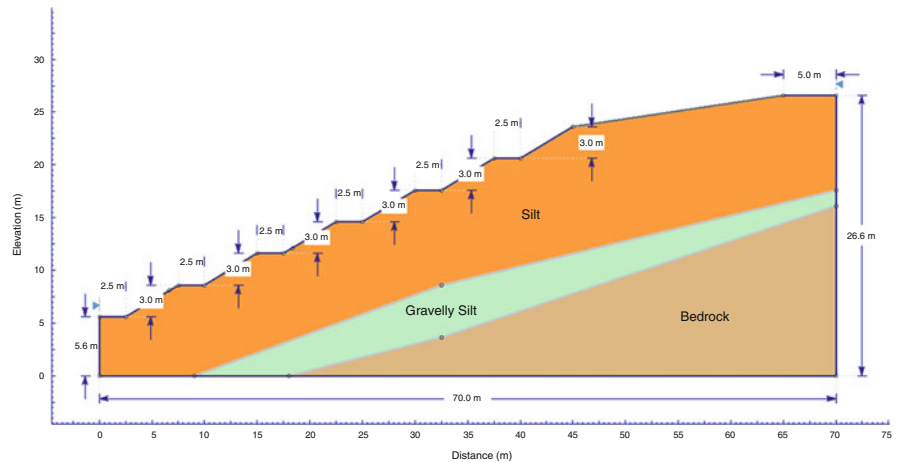


Table 2 Comparison of factor of safety by LEM and FEM-SSR

	LEM	FEM-SSR
Mean FOS	1.237	1.380
Probability of failure (%)	1.17	1.21

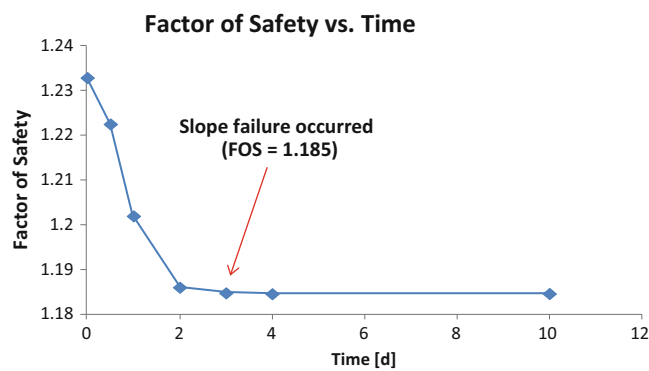


Fig. 7 Factor of safety vs. time using limit equilibrium Bishop’s method

and inclinometers show a minimum lateral movement even during continuous heavy rainfall (Ahmed et al. 2011).

Conclusion

Based on the back analysis carried out, it can be concluded that the slope failure that occurred in Precinct 9, Putrajaya, Malaysia is caused by the high existing groundwater level that put the slope in a condition that is vulnerable to failure. As heavy rainfall occurred, it has triggered the failure by increasing the groundwater level. When groundwater level increases, shear strength of the soil namely cohesion and friction angle decreases thereby reducing the stability of slope.

The zones with high yield of water caused by the highly fractured rocks were indicated through geophysical electrical survey and soil boring. The combination of these

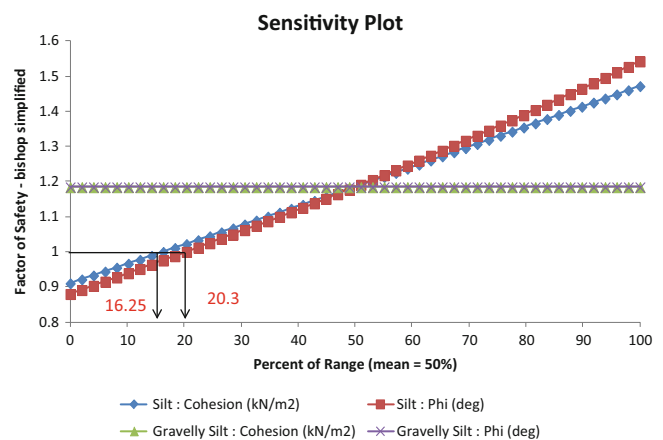


Fig. 8 Sensitivity plot for soil type silt and gravelly silt

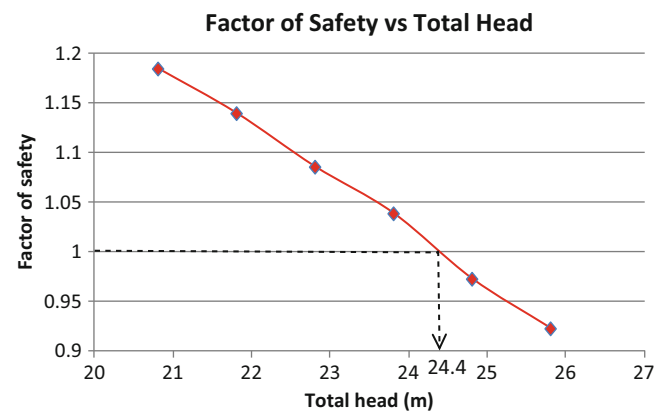


Fig. 9 Changes of FOS with respect to various boundary conditions of total head

methods provides reasonable indication of zone with high water content. Hence, the reason behind the high existing groundwater level is mainly due to the groundwater flow from the South-East of the study area.

Back analysis has been proven to be one of a useful tool for forensic investigation of slope failure. With combination of both limit equilibrium and finite element shear strength reduction methods, the results obtained can be compared and validated correctly. However, the limitations and reliability of this approach is always effected by the data quality. Hence, the back analysis approach must be applied carefully and the results must be interpreted with caution.

Acknowledgments The authors would like to express their appreciation to Universiti Sains Malaysia Research University (RU) Grant (1001/PAWAM/814192) for the financial support to carry out this research. In addition, the authors would also like to acknowledge Putrajaya Corporation and Kumpulan Ikram for the permission to carry out this research at the site and the cooperation given to make this research a success.

References

- Ahmed J, Ghazali MA, Mukhlisin M, Alias MN, Taha MR (2011) Effectiveness of horizontal drains in improving slope stability: a case study of landslide event in Putrajaya Precinct 9, Malaysia. In: *Unsaturated soils: theory and practice 2011*. Jatisankasa, Sawangsuriya, Soralump and Mairaing. Kasetsart University, Thailand, pp 753–758
- Azzouz AS, Baligh MM, Ladd CC (1981) Three-dimensional stability analyses of four embankment failures. In: *Proceedings of the 10th international conference on soil mechanics and foundation engineering*, vol 3, Stockholm, pp 343–346
- Deschamps R, Yankey G (2006) Limitations in the back-analysis of strength from failures. *J Geotech Geoenviron Eng* 132(4):532–536
- Duncan JM, Stark TD (1993) Soil strengths from back analysis of slope failures. In: *Stability and performance of slopes and embankments II* ASCE, pp 890–904
- Duncan JM, Wright SG (2005) *Soil strength and slope stability*. Wiley, Hoboken, NJ, 247p. ISBN 978-0-471-69163-1
- Gilbert RB, Wright SG, Liedtke E (1998) Uncertainty in back analysis of slopes: Kettleman Hills case history. *J Geotech Geoenviron Eng* 124(12):1167–1176
- Griffiths DV, Fenton GA (2004) Probabilistic slope stability analysis by finite elements. *J Geotech Geoenviron Eng* 130(5):507–518
- Hammah RE, Yacoub TE, Curran JH (2008) Probabilistic slope analysis with the finite element method. In: *Proceedings of the 41st US symposium on rock mechanics and the fourth US-Canada rock mechanics symposium*, Asheville, NC, USA
- Jiang JC, Yamagami T (2008) A new back analysis of strength parameters from single slips. *Comput Geotech* 35(2):286–291
- Keller GV, Frischknecht FC (1996) *Electrical methods in geophysical prospecting*. Pergamon, Oxford
- Leonards GA (1982) Investigation of failures. *J Geotech Eng Div* 108(2):185–246
- Rahardjo H, Hritzuk KJ, Leong EC, Rezaur RB (2003) Effectiveness of horizontal drains for slope stability. *Eng Geol* 69(3):295–308
- Rosenblueth E (1975) Point estimates for probability moments. *Proc Natl Acad Sci USA* 72(10):3812–3814
- Sharifzadeh M, Sharifi M, Delbari SM (2010) Back analysis of an excavated slope failure in highly fractured rock mass: the case study of Kargar slope failure (Iran). *Environ Earth Sci* 60(1):183–192
- Sonmez H, Ulusay R, Gokceoglu C (1998) A practical procedure for the back analysis of slope failures in closely jointed rock masses. *Int J Rock Mech Min Sci* 35(2):219–233
- Stark TD, Eid HT (1998) Performance of three-dimensional slope stability methods in practice. *J Geotech Geoenviron Eng* 124(11):1049–1060
- Tang WH, Stark TD, Angulo M (1999) Reliability in back analysis of slope failures. *Soils Found* 39(5):73–80
- Zhang J, Tang WH, Zhang LM (2010) Efficient probabilistic back-analysis of slope stability model parameters. *J Geotech Geoenviron Eng* 136(1):99–109



A New Appraisal of the Ancona Landslide

Veronica Tofani, Andrea Agostini, Teresa Nolesini, Luca Tanteri, Ascanio Rosi, and Nicola Casagli

Abstract

On the night of December 13th 1982, the city of Ancona suffered the catastrophic reactivation of an old and large landslide located along the coast to the West of the town. According to its morphological and kinematic characteristics, the Ancona landslide can typologically be defined as a deep-seated, multiple, compound and recurrent landslide.

After the 1982 event, several geological and geotechnical investigations were carried out; furthermore, a complex network of monitoring instruments has been installed. All these data have been of key importance in identifying the superficial and in depth extension of the landslide, the sliding surfaces, the failure mechanisms, the triggering factors and monitoring the deep on-going deformations.

The outcomes of past and new geotechnical investigations and all the data coming from the 30-year readings of the monitoring instruments have been integrated in order to redefine and update the actual location of the sliding surfaces. According to the new analysis, the landslide involves four main sliding surfaces with different extensions and maximum depths.

Stability analyses have been performed using the newly derived sliding surface geometries. The analyses have been carried out for five different stratigraphic-geotechnical scenarios, showing in each cases a stability slope condition near the limit equilibrium.

Keywords

Central Apennines • Urban landslide • Coastal landslide • Analytical modelling • Landslide monitoring

Introduction

Slopes along the medio-Adriatic coast are often affected by landslides. All these sliding phenomena are similar in their geomorphological and geological characteristics (e.g. Cancelli et al. 1984). Among them, one of the most representative examples is the one that involves the north-facing slope of Montagnolo Hill, on the coastal area to the west of

the Ancona (Marche region, Italy) (Fig. 1). Mass movements on this slope have been known for a long time and, on December 13th, 1982, after a period of intense rainfall, the slope suffered a catastrophic acceleration of the landslide movement, which damaged or destroyed hundreds of buildings, involving also the railway and the roads that run along the coast; fortunately there were no fatalities.

In 2002, the Marche Region assigned the Ancona Municipality the responsibility of creating an Early Warning System with the main goal of enabling the population to live with the landslide: this policy is directed not to a removal of the risk (the stabilization was unacceptable for the high cost and environmental impact) but to a reduction of the same (Cardellini and Osimani 2008). The complex network of

V. Tofani • A. Agostini (✉) • T. Nolesini • L. Tanteri • A. Rosi • N. Casagli
Department of Earth Sciences, University of Florence, Via La Pira 4,
Florence 50121, Italy
e-mail: veronica.tofani@unifi.it; andrea.agostini@unifi.it; teresa.nolesini@unifi.it

instruments installed makes the Ancona landslide one of best monitored in the world.

In this work, in the context of the necessary periodical geological investigation required by the adopted policy, we present a new revalidation of the main sliding surfaces, based on a comparative analysis of all the old and recent geological data and readings of the monitoring instruments. New landslide modeling has been carried out using the newly derived sliding surface geometries, allowing a revised interpretation of the degree of instability and of geotechnical features related to the instability conditions.

Geological and Geomorphological Setting

From the regional point of view, the Ancona area is part of the external Marche domain of the thrust system forming the Central Apennines (Bally et al. 1986).

In the study area the outcrop consists almost exclusively of sediments of the Plio-Pleistocene foredeep sequence, belonging to the Argille Azzurre formation. The Lower and Middle Pliocene sediments are represented by gray–blue (20–40 cm thick) marly clay (up to 60 cm thick) with thin sandy and silty interlayers. The Pleistocene deposits rest unconformably on the underlying sediments and are characterized by an alternation of pelitic and arenaceous layers (Argille Azzurre arenaceous-pelitic lithofacies) with a maximum outcropping thickness of ~300 m in the area.

The main structures (Fig. 1) interesting these sediments are the “Tavarnelle” syncline (which crosses the whole landslide area and exerts a main structural constraint on the layer arrangement) and the normal faults that cut the slope with a roughly E–W local orientation, results of a Pliocene compressive tectonic phase. The transverse faults with NNE–SSW orientation (Crescenti et al. 1983; Cello and Coppola 1989) are instead the result of the latest (Pleistocene-to date) phase and are probably still active and indicated as sources of historical earthquakes (Michetti and Brunamonte 2002).

From the geomorphological point of view, the slopes in the Plio-Pleistocene sediments are gentle, with moderate elevation and steepness variable between 5° and 15°. In detail, the Montagnolo slope, presents steeper areas, with inclination that reaches 25–30°, and morphological elements like scarps, steps, closed depressions (trenches) and reverse slopes (Coltorti et al. 1985, 1986) characteristic of deep-seated movements.

Landslide Description

The investigated slope has a history of gravitational movements in the past centuries (Segré 1920; Crescenti 1986). The origin of the movements must to be related to the Quaternary (i.e. Dramis et al. 2002).

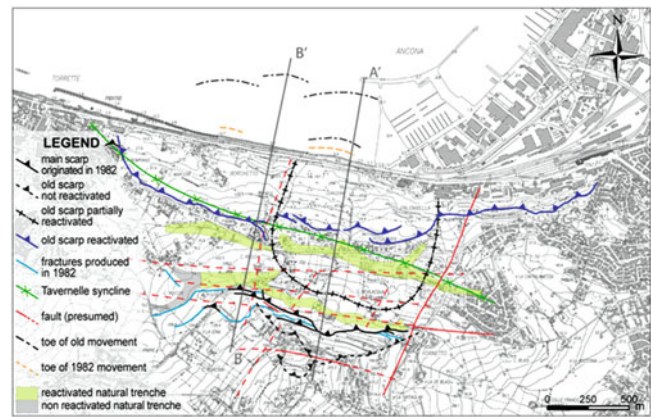


Fig. 1 Main geological and geomorphological features interesting the Ancona landslide area

The 1982 reactivation started without warning, lasted only a few hours and affected the whole area simultaneously (~3.4 km², with maximum width of ~2 km near the coastline, ~180 × 10⁶ m³ in volume). About 8 m of horizontal displacement and 3 m of uplift were recorded at the base of the slope; upslope, the recorded horizontal displacement was up to 5 m, together with settlements in the order of 2.5 m (Crescenti et al. 1983; Cotecchia 2006; Cardellini and Osmani 2008). The main direction of displacement was roughly South to North.

This phenomenon reactivated most of the main pre-existing morphological characters, inherited from earlier landslides, and resulted also in some new sliding surface and deformations zones (Cotecchia 2006).

The main geomorphological features are summarized in Fig. 1.

The dynamical evolution and the geomorphological characteristics indicate that main movement of the studied landslide was very deep, probably more than 100 m (Crescenti et al. 1983, 2005; Coltorti et al. 1985, 1986; Dramis et al. 2002), as confirmed by studies that followed the 1982 event. All the studies allowed a conceptual scheme of the landslide to be drawn. It is possible to recognize three main bodies (Body A, very deep and with huge areal dimensions, characterized by rather limited movements during 1982 event; Body B, superimposed on the Body A, interesting the central part of the slope, which was involved in more intense deformations during the 1982 event; Body C, in the lower part of the slope, partly reactivated in 1982) with movement intermediate between rotational and translational (Cotecchia 2006). The sliding surfaces of the three main deep landslides converge at depth into a single shear band with ductile behavior and low strength, and should emerge off-shore, at a maximum distance from the coast line of over 250 m (Cotecchia 2006). Following its characteristics, the Ancona landslide can be defined, according to Cruden and Varnes (1996), as a deep-seated, multiple, compound (roto-translational movement) and recurrent (slow, continuous movement, with short and sudden accelerations) landslide.

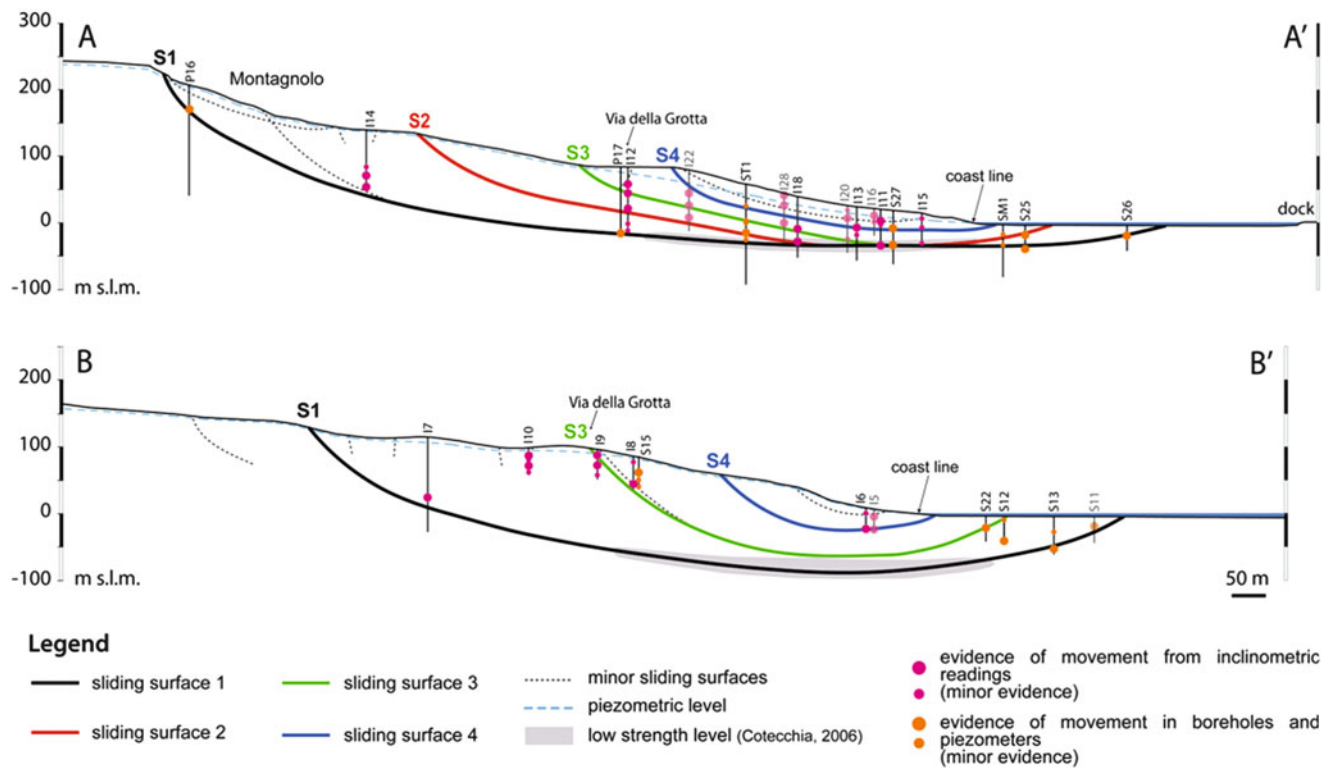


Fig. 2 Schematic representation of the section AA' and BB' (see Fig. 1 for location); the newly defined sliding surfaces are represented. Geotechnical investigations beyond 200 m from the section trace are in transparency. The movement evidences recognized along each log are

pointed out with *purple circles* for inclinometers and *orange circles* for boreholes and piezometers; *smaller circles* indicates minor movement evidences

Methods

Integrated Analysis of the Geotechnical Investigations

The Ancona landslide has been extensively studied and several methods have been used to define the causes and conditions of landslides (Cotecchia 2006). Among all of them, more than 150 exploratory boreholes have been drilled since the event of 1982. 68 boreholes are equipped with inclinometers and 42 with piezometers. The Ancona municipality carried out the last geotechnical campaign in 2011, with 6 new boreholes, 5 over water and 1 over land, to better define the submerged part of the landslide.

The geological and geotechnical outcomes at our disposal, coming from past and new investigations and from the 30-year readings of the monitoring instruments have been reworked and reinterpreted in order to redefine and update the actual location of the main sliding surfaces of the Ancona landslides. This data analysis has allowed to draw a new and comprehensive reconstruction of the landslide geometry and to define four main sliding surfaces (Fig. 2). The sliding surfaces proposed in all the previous

works (i.e. Segré 1920; Coltorti et al. 1985; Esu 1986; Cotecchia 2006) have been taken in account and all the geomorphological features have been recorded. To reconstruct the geometry, depth and organization of the sliding surfaces, two sections has been taken as representative of the central and wider portion of the landslide (AA' and BB'; Fig. 1), and crossing the entire area from the top of the hill to a few hundred meters over the coast line. The two sections are roughly parallel to the local direction of movement and overlaid all the main structures already described in literature.

The detection of the depth at which movement evidences occur have been based on inclinometric readings and the identification of structures which may be related to kinematic phenomena (i.e. highly fractured bands, high plasticity levels, chaotic levels with sudden changes of strata orientation not correlated with the local geological attitude, alteration surfaces). Each identified movement has been weighted on the base of its soundness and reliability as well as of its distance from the section trace and compared with respect to the information gave by the closest investigations and with respect to the geomorphological features (main scarps, natural trenches, fractures, etc.) identified in its immediate neighborhood.

Landslide Modeling

In order to qualitatively define the landslide stability conditions, analytical modeling implemented through the limit equilibrium method has been performed.

The main problem related to the modeling of the Ancona landslide is the transition from the geological model to geotechnical model of the slope. Given the geological and geomorphological complexity of the landslide, the geotechnical parameters obtained from laboratory tests are roughly adaptable to the complexity of the landslide body. The mechanical behaviour of the slope is thus not controlled only by the intrinsic strength of the clay but a major role is also played by the geometry, frequency and strength of the discontinuities (Cotecchia 2006).

In order to obtain the input parameters for the stability analyses many geotechnical test have been performed on the samples taken at different depth in the on land boreholes. All the samples can be classified as inorganic clay (USCS) with high plasticity CH (sample 1, 3) or low plasticity CL (sample 2). The Pliocene clay are overconsolidated and their compressibility, as obtained from oedometer test results, was rather low ($C_c = 0.30\text{--}0.35$). The unit weight (γ) varies between 20.3 and 21.7 kN/m³, depending on the degree of saturation, while the consistency index is around 1. Effective shear strength angles, ranging between 20° and 27°, have been obtained through a direct shear test while effective residual shear angles, ranging between 11° and 15°, have been obtained from an ring shear apparatus.

The analytical model performed with SLOPE/W software has been carried out for both sections (AA' and BB') and for all the main sliding surfaces identified (Fig. 2). In order to define the actual stability we have accounted for a complex geotechnical representation of the slope, which include the effects of the water level (pore water pressures along the sliding surface have computed hydrostatically based on the distance from the water level) and a deep level of Pliocene clay (Fig. 2) with low strength parameters and ductile behaviour recognized by Cotecchia (2006). Moreover, the effect of the water weight on the submerged portion of the slope has been taken into account considering an unit weight for the sea water of 10.052 kN/m³.

In order to obtained more representative strength parameters, back-analysis of the slope failure has been carried out. The back-analysis has been conducted with SLOPE/W software applying Morgenstern–Price limit equilibrium method Morgenstern and Price (1965) to all the sliding surfaces of section AA'. The results show that the residual friction angles range from about 16° for the deeper sliding surface S1 to about 12° for shallower sliding surface (S4). These obtained values has to be considered residual values for the shallowest sliding surfaces (S2, S3, S4) while have to considered has “intermediate” shear strength parameters, for the deepest sliding surface (S1).

In addition to peak and residual strength parameters, also intermediate strength parameters have been considered in order to take into account the probable recovery of strength of the Pliocene clay from the last event of 1982 (mostly to be ascribed to a progressive reduction of the fractures width).

In synthesis, combining the strength parameters obtained with the different methods used in the slope analysis, five different geotechnical and stratigraphic scenarios have been analyzed (Table 1).

Results

Reconstruction of the Main Sliding Surfaces

The integration of the different data available led to the identification and definition of four main sliding surfaces (Fig. 2).

Section AA' crosses all the main landslide bodies and the four proposed main sliding surfaces (Fig. 2). The deepest sliding surface (S1, 110 m b.g.l.) emerges at sea at a maximum distance estimable in about 300 m from the coast line as already proposed by Cotecchia (2006). Surfaces S1, S2 and S3 coalesce at depth (approximately 40 m below the sea level) in the deep low strength clay level with ductile behavior (Cotecchia 2006). Surface S4 almost coincides with the shallow landslide called “Barducci landslide” (cfr. Segrè 1920).

Section BB' crosses the landslides bodies defined by the sliding surfaces S1, S3 and S4. Sliding surface S2 does not intersect this section since its extension is limited and probably controlled by two NE-SW transverse faults (Fig. 1). Sliding surface S1 represent the deepest along this trace and reach 85 m b.g.l. and the toe is located at about 250 m from the coast line. Sliding surfaces along section BB' do not converge along the low strength level even if surface S1 crosses it for a big portion of its length.

Analytical Modelling

The results of the stability analysis carried out on the section AA' shows that surface S1, for all the scenarios analyzed, presents the lowest values of Factors of safety (FS) and thus it can be considered as the most critical in terms of instability conditions. Scenario 1 presents the highest values of FS for all the sliding surfaces while scenario 2 the lowest ones (Table 2).

The values of Factor of Safety related to all the sliding surfaces of section BB' are in general lower compared to section AA' (Table 3). The sliding surfaces S3 and S4 present values near the unit except for the scenarios 1 and 3, which consider peak strength parameters. These results are in agreement with the movements observed in the event

Table 1 Stratigraphic and geotechnical scenarios applied in the landslide modelling analysis

Scenario	Geological and geotechnical conditions
Scenario 1	Homogenous Pliocene clay with peak strength parameters ($c' = 10$ kPa and $\phi' = 23^\circ$)
Scenario 2	Homogenous Pliocene clay with residual strength parameters ($c' = 0$ kPa and $\phi' = 12^\circ$)
Scenario 3	Pliocene clay with peak strength parameters ($c' = 10$ kPa and $\phi' = 23^\circ$) and low strength level with residual strength parameters ($c' = 0$ kPa and $\phi' = 12^\circ$)
Scenario 4	Homogenous Pliocene clay with “intermediate” strength parameters ($c' = 10$ kPa and $\phi' = 17^\circ$) as in Cotecchia (2006)
Scenario 5	Pliocene clay with “intermediate” strength parameters ($c' = 10$ kPa and $\phi' = 17^\circ$) and low strength level with residual strength parameters ($c' = 0$ kPa and $\phi' = 12^\circ$)

Table 2 Factors of Safety (FS) computed for all sliding surfaces of section AA' according to the analysed scenarios

	S1	S2	S3	S4
Scenario 1	1.6	1.8	1.9	1.8
Scenario 2	0.8	0.8	0.9	0.9
Scenario 3	1.3	1.4	1.6	1.8
Scenario 4	1.2	1.3	1.4	1.4
Scenario 5	1.0	1.1	1.3	1.4

of 1982, during which the most significant displacements are registered for the shallowest sliding surface.

Discussion and Conclusion

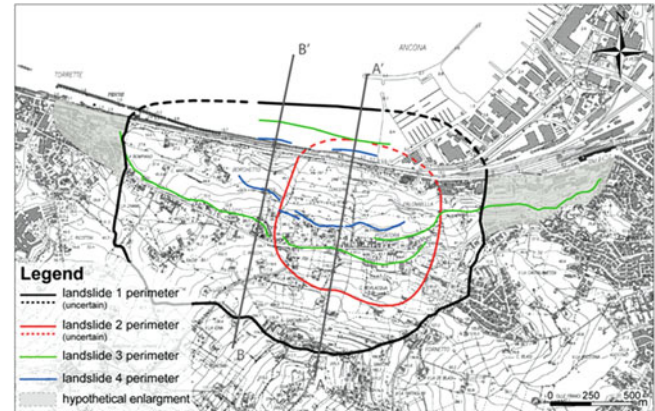
The results of past and new geotechnical investigations and all the data coming from the 30-year readings of the monitoring instruments have been integrated in order to redefine and update the actual location of the sliding surfaces along two longitudinal sections of the landslide. The accurate reconstruction of the actual underground 3D location of the sliding surfaces of the Ancona landslide is impossible due to the lack of a complete database of movement measurements; anyhow it has been possible, based on geomorphological evidence and on pre existing inventory maps, to infer the landslide perimeter outside the analysed sections. In particular four main bodies and associated perimeters, related to the four main sliding surfaces detected, have been defined and mapped (Fig. 3).

In syntheses the main outcomes of the work are:

- four main sliding surfaces with different extensions and depths, which range from around 110 m b.g.l. to 30 m b.g.l. have been identified. The deepest surfaces converge at depth in a low strength level as hypothesized by Cotecchia (2006) and exit near or beyond the coast line (with a maximum distance of around 300 m).

Table 3 Factors of Safety (FS) computed for all sliding surfaces of section BB' according to the analysed scenarios

	S1	S3	S4
Scenario 1	2.0	1.5	1.4
Scenario 2	1.0	0.7	0.7
Scenario 3	1.4	1.3	1.4
Scenario 4	1.4	1.1	1.0
Scenario 5	1.2	1.0	1.0

**Fig. 3** Perimeters of the four main bodies of the Ancona landslide (uncertain perimeters are indicated with the dashed line)

- the stability analysis, applied to five different stratigraphic-geotechnical scenarios, describes a slope condition near to the limit equilibrium, with FS values equal to 1 or slightly higher.
- the scenario that better describes the stability condition of the Ancona landslide is constituted by Pliocene Clay with intermediate strength parameters and a deep low strength level with residual strength parameters.

The outcomes of this work will be of help to further develop the early warning system of the landslide adopted as the current risk management strategy. Furthermore the newly defined landslide perimeters should be considered as input data for any land planning policies in order to provide recommendations and prescriptions in the area with highest landslide risk.

References

- Bally AW, Burbi L, Cooper C, Ghelardoni R (1986) Balanced section and seismic reflection profiles across the Central Apennines. Mem Soc Geol It 35:237–310
- Cancelli A, Marabini F, Pellegrini M, Tonnetti G (1984) Incidenze delle frane sull'evoluzione della costa adriatica da Pesaro a Vasto. Mem Soc Geol It 27:555–568

- Cardellini S, Osimani P (2008) Living with landslide: the Ancona case history and early warning system. In: Proceedings of the 1st World landslide forum, Tokyo, pp 473–476
- Cello G, Coppola L (1989) Modalità e stili deformativi dell'area Anconetana. *Studi Geologici Camerti* 11:37–47
- Coltorti M, Dramis F, Gentili B, Pambianchi G, Crescenti U, Sorriso-Valvo M (1985) The december 1982 Ancona landslide: a case of deep-seated gravitational slope deformation evolving at unsteady rate. *Zeitschrift für Geomorphologie* 29(3):335–345
- Coltorti M, Dramis F, Gentili B, Pambianchi G, Sorriso-Valvo M (1986) Aspetti geomorfologici della frana di Ancona. In: "La grande frana di Ancona del 13 Dicembre 1982". *Studi Geologici Camerti, Special Number: 29-40*
- Cotecchia V (2006) The Second Hans Cloos Lecture. Experience drawn from the great Ancona landslide of 1982. *Bull Eng Geol Env* 65: 1–41
- Crescenti U (1986) Notizie Precedenti. In: "La grande frana di Ancona del 13 Dicembre 1982". *Studi Geologici Camerti, Spec. Numb.: 13-23*
- Crescenti U, Ciancetti GF, Coltorti M, Dramis F, Gentili B, Melidoro G, Nanni T, Pambianchi G, Rainone ML, Semenza E, Sorriso-Valvo M, Tazioli GS, Vivalda P (1983) La grande frana di Ancona del 1982. In: Collana "Problemi del territorio". Spoleto 4-7 maggio 1983. *Atti XV Convegno Nazionale di Geotecnica. Atti Congr. vol. III*
- Crescenti U, Calista M, Mangifesta M, Sciarra N (2005) The Ancona landslide of December 1982. *Giornale di Geologia Applicata* 1:53–62
- Cruden DM, Varnes DJ (1996) Landslide types and processes. In: Turner AK, Schuster RL (eds) *Landslides investigation and mitigation, Spec. Rep. 247*. Transportation Research Board, National Research Council, Washington
- Dramis F, Farabollini P, Gentili B, Pambianchi G (2002) Neotectonics and large-scale gravitational phenomena in the Umbria-Marche Apennines, Italy. In: *Seismically induced ground ruptures and large scale mass movements. Field excursion and meeting 21–27 September 2001*. APAT, *Atti 4/2002*, pp 17–30
- Esu F (1986) Analisi delle condizioni di stabilità. In: "La grande frana di Ancona del 13 Dicembre 1982". *Studi Geologici Camerti, Special Number: 29-40*.
- Michetti AM, Brunamonte F (2002) Some remarks on the relations between the 1972 Ancona earthquake sequence and the Ancona landslide. In: *Seismically induced ground ruptures and large scale mass movements. Field excursion and meeting 21–27 September 2001*. APAT, *Atti 4/2002*, pp 31–34
- Morghestern NR, Price WE (1965) The analysis of the stability of general slip surface. *Geotechnique* 15:79–93
- Segré C (1920) Criteri geognostici per il consolidamento della falda franosa del Montagnolo, litorale Ancona-Falconara. *Boll Soc Geol It* 38:99–131



Urban Landslides at the South of Sierra Nevada and Coastal Areas of the Granada Province (Spain)

José Chacón, Clemente Irigaray, Tomás Fernández del Castillo, Rachid El Hamdouni, Jorge Jiménez-Perálvarez, Pedro Alameda, José Moya, and José Antonio Palenzuela

Abstract

The Southern flank of Sierra Nevada and coastal Mediterranean areas of South Spain, in the Andalusian Granada Province, a high number of urban settlements and roads have been affected by landslides and instability problems since the fifties. In this period, a very quick economic development with an intense annual increase of touristic demand gave place to rapid enlargements of formerly small villages, and the widespread land-use change from agricultural to urban not only around the pre-existing urban centres, but also in many new developed lands along the coast for urbanization or leisure services. This Mediterranean coast, in the uplifting section of the Eurasia and African plates, is mainly excavated on metapelites of the Betic Cordillera Internal Zone, showing very inclined if not vertical slopes on Lower Triassic to Paleozoic series of marble, schist, phyllite and quartzite units, very deformed and weathered, so giving place to instability problems which are described in this paper.

Keywords

Landslide activity and diachroneity • Coastal areas • Mediterranean Sea • South Spain

Introduction

A review of study cases is presented in this paper, following accumulated experience in the University of Granada (Spain) Research Group 121: Environmental Investigations, Terrain Engineering and Geological Hazards. The described

events occurred mainly since the eighties, although some of the landslides are also old “dormant” types reactivated by different factors (Fig. 1). The descriptions and identification of landslides follow mainly the proposal Varnes (1978), the landslides activity concepts and classification published by WP/WLI (1993a, b) and the diachroneity concept and classification proposed by Chacón (2008) and Chacón et al (2010). The incidence of these landslides on the affected urban areas is also summarized.

In addition some of the main landslides in the Southern slopes of Sierra Nevada, near the coastal border are here presented with the main results on its activity and diachroneity.

J. Chacón (✉) • C. Irigaray • R. El Hamdouni • J. Jiménez-Perálvarez • P. Alameda • J.A. Palenzuela
Department of Civil Engineering, Section of Terrain Engineering,
University of Granada, Granada, Spain
e-mail: jchacon@ugr.es; clemente@ugr.es; rachidej@ugr.es;
jorgejp@ugr.es

T. Fernández del Castillo
Department of Photogrammetry and Mapping Engineering, University
of Jaen, Jaen, Spain
e-mail: tferman@ujaen.es

J. Moya
Department of Terrain Engineering, University of Cataluña, Barcelona,
Spain
e-mail: jose.moya@upc.es

Geographical and Geological Settings

The Betic Cordillera is a branch of the Alpine belts resulting from the tectonics closure of the Tethys and the collision between the Eurasian and African Plates (Fig. 1).

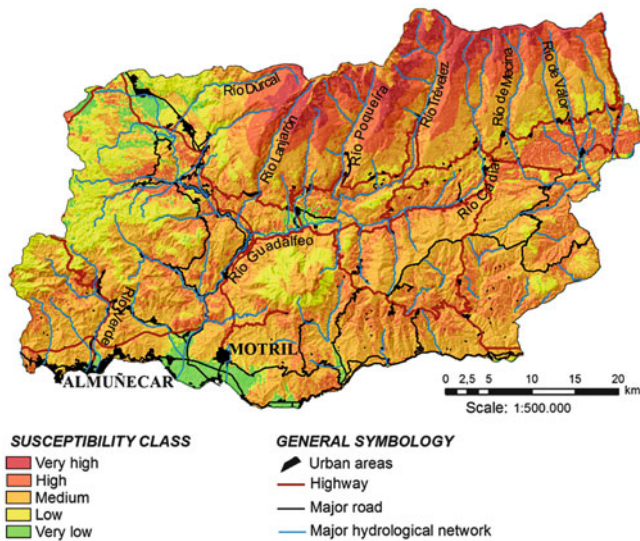


Fig. 3 Landslide susceptibility map of the Southern Granada Province (Spain) (Chacón et al. 2007)

Landslides on Coastal Urban Areas

Provide the appearance of new urbanised areas along the coast in the process of development starting at the late sixties, in 1970 a landslide occurred in the eastern Punta de la Mona, where a project of building the “Marina del Este” dock and urbanization, the excavated coastal slope of weathered schist and quartzite. It was a combined planar to rotational slide affecting the coastal slopes and the “Peñón de las Caballas” few metres away in the Sea. The project of stabilization included an underground tunnel of drainage, several pumping wells and two lines of anchored walls; afterward the project was finished and the urbanization and dock were built up. Since this event a number of other urbanizations were affected mainly, but not only, during the widening of the former 340 National Coastal Road to Malaga, originally too narrow and therefore slope excavations took place along the road in the section of the Granada Province where scarped coastal cliffs on metamorphic schist and quartzite appear.

In this area excavations at the feet of the slopes gave place to the extensional opening of previously existing sets of rock joints or discontinuities triggering slides with different degree of development. A very useful tool in the preliminary assessment of slopes was the analysis of fabric of discontinuities to plot its trends and also values of aperture or extension as percentage of the accumulated measured amount.

(a) Equiareal diagram of a Schmidt net plotting of 350 discontinuity poles. Concentrations of 1–2; 2–4; 4–10 and 10–18 %.

The trend of opening of discontinuities was coherent with the overall slope dipping and also with the former structural setting of the joint families (Fig. 5a, b) and gave information about the instability process. The observation of local discontinuities aperture and its distribution around previously existing rockblock boundaries is determined by the structural fabric.

(b) Plot of amount of joint aperture measured in mm perpendicular to each joint. Accumulated extension was 2,062 mm.

This assessment, supported by the structural analysis of discontinuities is helpful particularly in the preliminary and early stages of the slide development, when still the measured displacement is limited although with damaging consequences to the affected buildings.

At the late seventies a project of improvement of the main coastal road (N340) was developed, and its width increased three to four more metres, with slope excavations along the road belt. By that time a number of recently built urbanizations were scattered along the road, and some instability problems affected the housing and internal ways along the eighties. This was the case of several urbanizations as for instead “Monte de los Almendros”, “Costa Aguilera”, “El Pargo”, “Alfamar” or “El Montañés” in the districts of Salobreña and Almuñecar (Granada, Spain) (Fig. 4).

All these urbanizations, more or less hardly damaged, have in common the type of foundation terrain: very weathered brown to dark grey schist and quartzite with several families of discontinuities, and a thin cover of colluvial deposits. Also in common is the use of extensive infill on the excavated slope to arrange the urbanized areas. This sort of infill, frequently extended in summer dry conditions, commonly far from its optimum wetness and, because the rapidness of the works, with compaction below the maximum, leads to differential settlements and also is affected by shallow landslides after period of rains or associated to water infiltration from breakdown of water pipelines, when not from open fine cracks in swimming pools or from waste water pipes.

Rainfalls and Landslides in the Coastal Areas

A record of the last 65 yearly rain periods shows a trend to shortening the time between new historical records (Fig. 6). Although a variable sinuosity in the plotted record featuring probably the need of longer set of data to attain reliable conclusions, the last two maximum rain peaks are observed in a 1996–1997 and only 5 years later, in 2011–2012, suggesting effects to be accounted in the new paradigm of climate change.

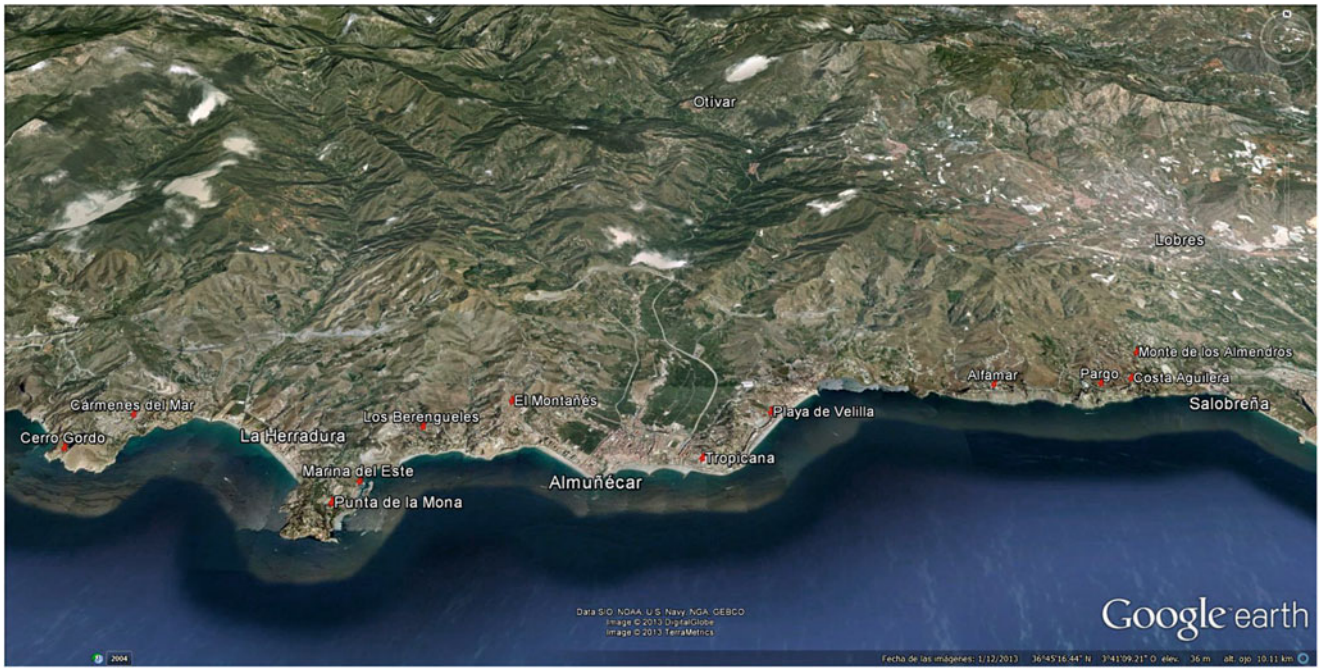


Fig. 4 Distribution of landslides in urban areas in the Mediterranean coast of the Granada Province (Andalusia, Spain). The affected urban areas are marked by red spots and the extent of damage varies from few houses to about 80

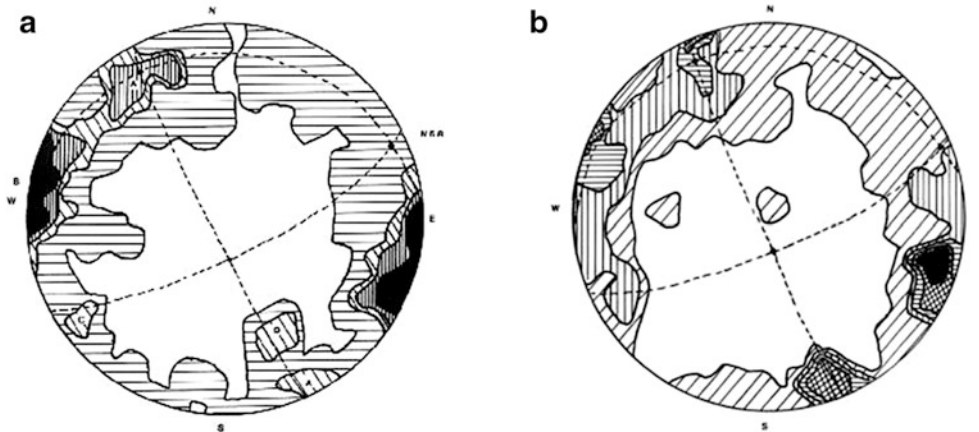


Fig. 5 Example of (a) equiareal projection of poles, and (b) amount of aperture of 350 discontinuities in a rock mass affected by rock slide in Costa Aguilera

Nevertheless not all these rainy events triggered landslides in the area, otherwise permanently affected by accidental breakdown of pipe line at very local or municipal levels. Therefore not always the observed geotechnical problems were directly related to excess of rainfall but with bad practice in pipes installation.

A longer recording of relationships between rains and sliding was obtained by dendrochronology of inclined pine trees growing on Cerro Gordo slide, were extensive damages affected great number of villas, evidencing a diachronic evolution of the landslide.

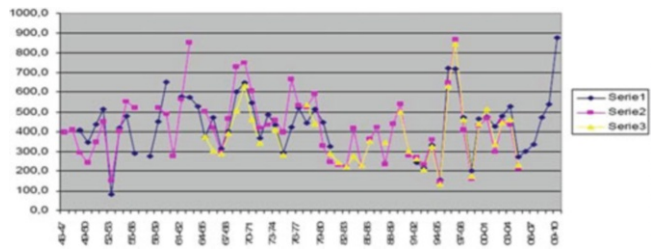


Fig. 6 Rainfall series in three villages of the coastal area of Granada Province (Almuñécar, Salobreña and Motril). See Fig. 4 to see villages setting

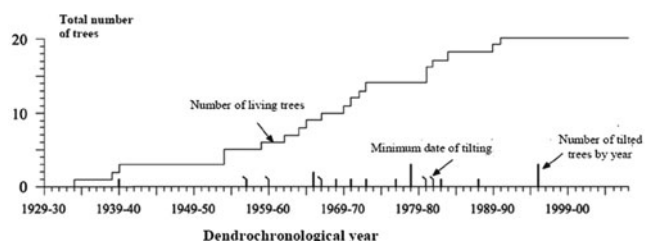


Fig. 7 Testing an inclined pine tree in Cerro Gordo landslide (*above*) and plotting of results obtained from dendrochronological analysis of samples (*below*)

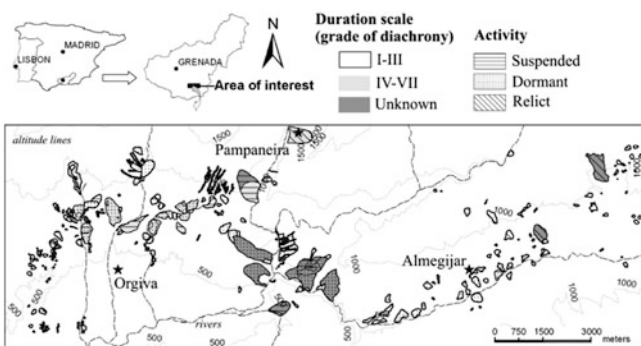


Fig. 8 Inventory of landslides in the Guadalfeo River showing data of scale and degree of diachrony

The results show (Figs. 7, 8) slope movements since 1934 associated to some of the rainy years shown in Fig. 6.

Timing of Landslides

Landslide Activity and Diachroneity

Concerning the identified deep-seated landslides, as the Calaiza landslide in Eastern Cerro Gordo (Fig. 9), dormant or very slow to suspended are the most predominant degree of activity (WP/WLI 1993a, b). The Calaiza landslide, known by drilling and inclinometry made by private



Fig. 9 *Above*: An empty exhausted block slide at the Western slope of Cerro Gordo; *Middle*: An urbanization built up on the previously existing Calaiza landslide in the Eastern slope of Cerro Gordo, causing damaging consequences. *Below*: slide on Alfamar urbanization. See Fig. 4 for setting of these examples

companies in the early eighties, shows *very slow* velocity (WP/WLI 1995) until the date of triggering may correspond to a Pre-Historical scale with *diachroneity* of *degree IX* (Table 2, Chacón 2008, 2009; Chacón et al. 2010).

Also the fairly well known landslide at La Serreta de Tablones (Fernández et al. 2009) considered in dormant stage of activity, was shown to be active with very low velocity by DinSAR assessment.

These two study cases suggest that deep-seated landslides in the Southern Granada Province may be very slowly active

Table 2 Time scale and degree of diachroneity of landslides (Chacón 2008, 2009; Chacón et al. 2010)

Scale: Contemporary (Present to 1900); Historical (1899 to 0); Pre-Historical (0 to 5,000 y.b.C.); Hyper historical (>5,000 y.b.C.)		
Degree	Diachroneity (years)	Equivalent units
I	$0-10^{-7}$	0–3.15 s
II	$10^{-7}-10^{-6}$	3.15 s–3.15 m
III	$10^{-6}-10^{-4}$	3.15–52.6 m
IV	$10^{-4}-10^{-2}$	52.6 m–3.65 d
V	$10^{-2}-10^{-1}$	3.65–36.5 d
VI	$10^{-1}-10^0$	36.5 d–1 y
VII	10^0-10^1	1–10 y
VIII	10^1-10^2	10–100 y
IX	10^2-10^3	100–1,000 y
X	$10^3-2 \times 10^3$	1,000–2,000 y
XI	$2 \times 10^3-5 \times 10^3$	2,000–5,000 y
XII	5×10^3	>5,000 y

movements with limited damaging consequences only if they are not affecting building areas, as the Calaiza landslide (Fig. 9), where really thick infilling layers below the urbanizations increase the damaging effects. Nevertheless more data are necessary to obtain definitive conclusions.

Also at a regional scale, recent inventories in the Guadalfeo River basin lead to differentiate landslides, following Table 2, by scale and degree of activity (Fig. 8, Jiménez-Perálvarez et al. 2011). Some of these landslides are also affecting nearby areas of some villages in the Southern slopes of Sierra Nevada.

Discussion

Despite the moderate concentration of landslides inventoried at the Southern slopes of Sierra Nevada, its damaging consequences are more visible in urban areas, and particularly in the nearest coastal areas.

A first reason for the persistence of damages in unstable slopes excavated on rock massif is related with difficulties of some geotechnical consulting to approach their reports by using appropriated rock engineering instead of the more common geotechnical methods based on soil mechanics.

A second reason comes from limitation of the usual building foundations reports to identify overall instability problems without previous studies on the general slope stability conditions to support decisions on land-use changes by planners and politicians.

Finally, this hazard context frequently becomes even more dangerous by the quick extension of huge amounts of soil infilling on the excavated slopes, a common practice in coastal building processes, in order to arrange the villas in stepped slopes with views to the Sea as an added value.

Acknowledgments The support by the Andalusian Plan of Research of the Groups RNM 121: Environmental Investigations, Terrain Engineering and Geological Hazard (University of Granada).

References

- Chacón J (2008) Los conceptos actuales de susceptibilidad, peligrosidad y riesgo, en la prevención de movimientos de ladera, con ejemplos de aplicaciones prácticas. In: Lima RE, Leite JC (eds) Desastres e riscos geológicos em Curitiba e litoral. Roteiro de Excursao Técnica, 43 p. CENACID. UFP, 44^o Congresso Brasileiro de Geologia. Publicação Especial, Curitiba, Brasil
- Chacón J (2009) Diacronía de los movimientos de ladera. In: Alonso E, Corominas J, Hürlimann M (eds) VII Simposio Nacional sobre Taludes y Laderas Inestables, 12pp
- Chacón J, Fernández del Castillo T, Hernández del Pozo JC (1992) Movimientos de ladera en la costa granadina al W de Salobreña. III Congreso Geológico de España, vol 2, pp 610–619
- Chacón J, Irigaray C, Fernández T (2007) Movimientos de Ladera, pp 45–82; in Ferrer M, (Coord) Atlas de Riesgos Naturales en la Provincia de Granada. Diputación de Granada-IGME, Spain, 190 pp.
- Chacón J, Irigaray C, El Hamdouni R, Jiménez-Perálvarez JD (2010) Diachroneity of landslides. In: Williams AL et al (eds) Geologically active: Proceedings 11th IAEG Congress. Auckland, New Zealand. Taylor & Francis Group, London, pp 999–1006
- El Hamdouni R, Irigaray C, Fernández del Castillo T, Sanz de Galdeano C, Chacón J (1997) Inventario de movimientos de ladera en el entorno del embalse de Béznar (Granada). In: IV Simposio Nacional sobre taludes y laderas inestables. vol II, pp 731–740
- Fernández del Castillo T, Brabb E, Delgado F, Martín-Algarra A, Irigaray C, Estévez A, Chacón J (1997) Rasgos geológicos y movimientos de ladera en el sector Izbor-Velez Benaudalla de la cuenca del río Guadalfeo (Granada). In: IV Simposio Nacional sobre Taludes y Laderas inestables, vol II, pp 795–808
- Fernández del Castillo T, Irigaray C, Chacón J (1994) Large scale analysis and mapping of determinant factors of landsliding affecting rock massifs in the eastern Costa del Sol (Granada, Spain) in a GIS. In: 7th International IAEG congress, Lisboa, 1994, vol VI. Balkema, Rotterdam, pp 4649–4658
- Fernández P, Irigaray C, Jiménez-Perálvarez JD, El Hamdouni R, Crosetto M, Monserrat O, Chacón J (2009) First delimitation of areas affected by ground deformations in the Guadalfeo River Valley and Granada metropolitan area (Spain) using the DInSAR technique. Eng Geol 105, 1–2, 23; 84–101
- Irigaray C, Fernández del Castillo T, El Hamdouni R, Chacón J (1999) Verification of landslide susceptibility mapping. A case study. Earth Surf Process Landforms 24:537–544
- Jiménez-Perálvarez JD, Irigaray C, El Hamdouni R, Fernández P, Chacón J (2011) Landslide-susceptibility mapping in a semi-arid mountain environment: an example of the southern slopes of Sierra Nevada (Granada, Spain). Bull Eng Geol Environ 70:265–277
- Varnes DJ (1978) Slope movement types and processes. In: Schuster RL, Krizek RJ (eds) Landslides: analysis and control. Transportation Research Board. Special Report 176:11–33
- WP/WLI (1993a) A suggested method for describing the activity of a landslide. Bull IAEG 47:53–57
- WP/WLI (1993b) Multilingual landslide glossary. BiTech Publishers Ltd., Canada
- WP/WLI (1995) A suggested method for describing the rate of movement of a landslide. Bull IAEG 52:75–78, Paris



Recent Landslide Activity in La Paz, Bolivia

Nicholas J. Roberts, Bernhard Rabus, Reginald L. Hermanns,
Marco-Antonio Guzmán, John J. Clague, and Estela Minaya

Abstract

Landslides are a major threat in La Paz, Bolivia, yet knowledge of landslide activity in the city has improved little since the 1970s. Landslides have received little consideration during La Paz's recent rapid expansion, contributing greatly to high levels of landslide risk. We provide new knowledge on landslide hazard with three datasets: a landslide inventory based on eight decades of aerial photographs and orbital imagery; recent ground displacements measured with RADAR interferometry (InSAR); and field-based characterization of dozens of landslides that have occurred since 1994. Over 100 landslides have happened in La Paz and adjacent areas since the start of the twentieth century and many slopes throughout the area are slowly moving at rates of centimetres to decimetres per year over areas of ~1 ha to nearly 20 km². Most historic failures have occurred at the margins of larger paleolandslides or near buried culverted rivers, indicating the important influence of long-term natural landscape processes and anthropogenic slope modification. Homogenous Distributed Scatterer InSAR (HDS-InSAR)—a novel technique that increases the density of targets available for slope deformation monitoring—provides excellent results in a range of environments in La Paz and the surrounding area. Results derived from HDS-InSAR could guide ground-based monitoring and physical slope mitigation in La Paz. However, a reduction of the growing landslide risk in the city requires changes to urban planning and policy, and greater use of scientific knowledge.

Keywords

Urban landslide hazard • Homogenous distributed scatterer InSAR • Multi-temporal landslide inventory • Achocalla Earthflow • Paleolandslides

N.J. Roberts (✉) • J.J. Clague
Simon Fraser University, Centre for Natural Hazard Research, 8888
University Drive, Burnaby, Canada V5A 1S6
e-mail: nickr@sfu.ca

B. Rabus
MacDonald, Dettwiler and Associates Ltd, 13800 Commerce Parkway,
Richmond, Canada V6V 2J3

R.L. Hermanns
Geological Survey of Norway, P.O. Box 6315 Sluppen, Trondheim
7490, Norway

M.-A. Guzmán
Universidad Mayor de San Andrés, Instituto de Investigaciones
Geológicas, Pabellón 3, Campus Universitario Cota Cota, La Paz
35140, Bolivia

E. Minaya
Observatorio San Calixto, Indaburo 944, La Paz 12656, Bolivia

Introduction

La Paz is one of the world's most landslide-prone cities. It experiences damaging landslides nearly every year, which are responsible for numerous deaths and large losses of public infrastructure, private property, and livelihoods. Landslide risk has increased since the early twentieth century due to a rapidly increasing population and settlement in unstable parts of the city. Currently, self-built settlements on the steep slopes surrounding the city centre (Fig. 1) house the majority of the city's inhabitants (O'Hare and Rivas 2005; UNDP 2007).

Current understanding of landslide activity in the city is inadequate, lacking many important details. Landslide maps dating from the mid-twentieth century identify unstable

areas, but focus on large paleolandslides and provide few details on landslide mechanism or frequency. No new maps have been created over the past forty years despite the increased exposure of the population to landslides. Even basic details of many historic events, including landslide location, type, and timing, are limited.

A better understanding of landslides in La Paz is a prerequisite for assessing the hazard and ultimately reducing the landslide risk. Hazard is currently evaluated based on the location of historic events in an incomplete catalogue (O'Hare and Rivas 2005). Because nearly half of La Paz is considered unstable for construction (BRGM-BCEOM 1977), this approach cannot properly guide risk reduction strategies.

We investigate landslide activity in La Paz since the early twentieth century using an updated landslide inventory, field investigations, and applied remote sensing. The objective of this research is to provide an improved understanding of landslide activity, causes, and triggers. This knowledge can aid risk reduction by identifying priority areas for planning, monitoring, and remediation.

Geologic and Geomorphic Context

Slopes of the La Paz valley system are predisposed to instability by geology and physiography. Río La Paz and its tributaries have incised 350–700 m of weakly lithified, late Miocene to Pleistocene sediments of the Altiplano plateau over the past million years. The steep valley-wall slopes are in a state of disequilibrium and prone to failure. Geologic and geotechnical mapping shows that many slopes have experienced repeated failures (Dobrovolsky 1962; BRGM-BCEOM 1977). Several large ($>1 \text{ km}^2$) landslides occurred in the La Paz area between ca. 11 and ca. 1.5 ka BP (Hermanns et al. 2012). Benching of slopes and infilling of gullies for development in recent decades has resulted in additional, localized landslides (Roberts et al. 2010).

Most of the historic landslides that have been investigated lack thorough documentation, in part because they are quickly obscured by re-grading and resettlement. Investigations of single events are limited to basic characterization of metrics, morphology, lithology, and impacts (Guzmán 2007; Quenta et al. 2007). A few studies document a small number of landslides of a particular type or events within a specific area, with some attention to causation (Roberts et al. 2010; Hermanns et al. 2012). Most historic events are several hectares to tens of hectares in size, but large failures affecting areas up to $\sim 2 \text{ km}^2$ have also occurred (Hermanns et al. 2012; Aguilar 2013). Most failures are sufficiently slow (decimetres per second) to allow residents to escape, although with much loss of property. Some failures, however, have been more rapid and have claimed several tens of lives (O'Hare and Rivas 2005). Slow

continuous slope creep has been inferred from ground deformation, particularly cracking and settling of roads and buildings at head scarps and lateral margins, but is essentially undocumented.

Methods

We created a landslide inventory for La Paz and adjacent areas from newspaper reports, aerial and orbital imagery, scientific publications, and field investigation. Aerial photographs (1935, 1955, 1976, 1996, and 2004) provide details for most of the past century at intervals of 20 years or less. High-resolution optical satellite images, including those available in GoogleEarth, provide information for the past decade at intervals ranging from several years to several months. In combination with geologic maps, the imagery provides the location, type, source material, and general timing of landslide events. Field mapping and characterization, together with reports in newspapers and other archival sources, provide additional information about some events, particularly those of the past 2 decades. In addition, we have inspected over 25 landslides that have occurred since 1994.

We detected and characterized slow ground deformation over a 40-month period (October 2008 to December 2011) by interferometric synthetic aperture RADAR (InSAR) analysis of a 24-day repeat stack of fine beam mode RADARSAT-2 scenes. Seven of the possible 51 scenes during this period were not acquired due to satellite planning conflicts. We applied Homogenous Distributed Scatterer InSAR (HDS-InSAR) to the stack of 44 acquired scenes. HDS-InSAR is a novel InSAR technique that uses an adaptive neighbourhood filter to identify pixel clusters forming coherent distributed targets; point targets are represented by single-pixel clusters. The interferometric signal of individual targets (single pixels and pixel clusters) is then modeled to determine displacement histories (Rabus et al. 2012). By increasing the density of specific targets for deformation tracking, HDS-InSAR improves on Persistent Scatterer InSAR (PS-InSAR), which utilizes only stable point targets (Kampes 2006). We estimated true landslide velocities using long-term average line-of-sight displacement rates and the angle between the satellite's line-of-sight and inferred landslide motion vectors.

Results

Over 100 landslides have occurred in the La Paz area since the start of the twentieth century. They range in area from 10^2 m^2 to 10^6 m^2 . Only six landslides exceed 1 Mm^3 in volume: five in the twenty-first century—2002, 2003, 2004, 2005, and 2011 (Hermanns et al. 2012)—and one in the late

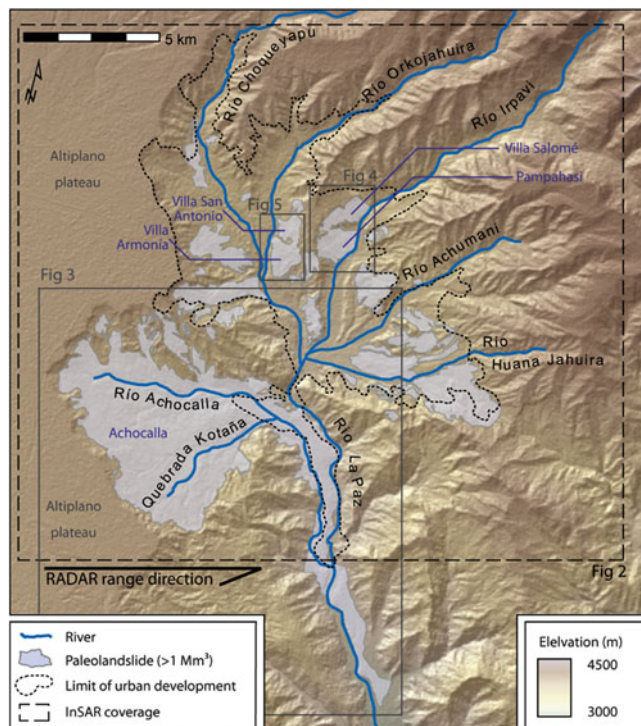


Fig. 1 Setting of La Paz showing the extent of urban development, distribution and extent of paleolandslides, and locations of other figures in this paper. Paleolandslides mentioned in the text are labeled in blue

nineteenth century (described briefly by Sanjinés 1948). Nearly 60 % of the inventoried events post-date the most recent comprehensive map of landslide features in the city (BRGM-BCEOM 1977), highlighting how outdated existing maps are.

There are several spatial clusters of historic landslides. Most occur in previously failed material or artificial fill. Landslides are particularly common near the limits of paleolandslides mapped by Dobrovolny (1962) and BRGM-BCEOM (1977). Lateral margins of numerous small landslides since the 1980s correspond to gullies that were previously culverted and filled in the course of land remediation for development (Roberts et al. 2010).

Information on 65 twentieth-century and twenty-first-century events is available from published accounts, newspaper articles, and local records. Together, these events caused 61 deaths, displaced nearly 13,000 people, and destroyed over 1,700 homes. These are likely minimum numbers, as many events are inadequately documented.

Results from HDS-InSAR show motion at numerous sites during the entire 40-month InSAR monitoring period throughout the city and surrounding area (Fig. 2). The most spatially extensive movements are within areas previously mapped as large paleolandslides (Figs. 1 and 2) in the predominantly fine-grained, Miocene-Pliocene La Paz Formation. Many of these areas are near the confluences of the Ríos

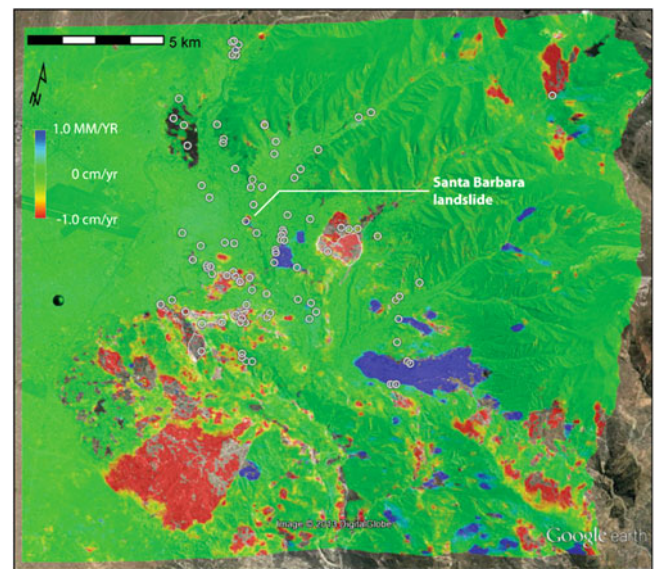


Fig. 2 Overview of historic landslides (white circles) and InSAR-measured displacements in the La Paz area. Displacements rates are average annual line-of-sight rates toward (positive) and away from (negative) the satellite. Base image is high-resolution optical satellite imagery draped over a DEM in GoogleEarth. See Fig. 1 for locations of mapped paleolandslides and locations of Figs. 3–5

Orkojahuara, Impavi, Achumani, and Huana Jahuira and are densely populated. Numerous slow-moving landslides occur in the Achocalla Basin, in valleys south of La Paz, and far to the north in the vicinity of the city's water sources (Fig. 2). HDS-InSAR results also indicate motion at sites of known recent activity, such as the Santa Barbara landslide (Fig. 2), which has repeatedly damaged buildings and roads over the past 200 years (Sanjinés 1948; Dobrovolny 1962).

Brief descriptions of three localities below demonstrate the range of landslide types and hazard issues in the La Paz area. Cited displacement rates are in the inferred direction of landslide movement.

Achocalla Earthflow

The Achocalla earthflow is one of the largest non-volcanic landslides in South America (Hermanns et al. 2008) and one of the largest earthflows in the world. It resulted from the failure of 2–3 km³ of the La Paz Formation and overlying gravels that underlie the Altiplano plateau just south of La Paz. Debris flowed around an intact hill of La Paz Formation and underlying Devonian rocks at the mouth of the Achocalla Basin (Dobrovolny 1968) and filled over 17 km of the Río La Paz valley to depths as much as 120 m. Failure was rapid enough to block Río La Paz, impounding a lake in the southern part of the current city of La Paz. Hermanns et al. (2012) obtained a calibrated radiocarbon age of 11,485–10,965 year BP on plant material in lacustrine

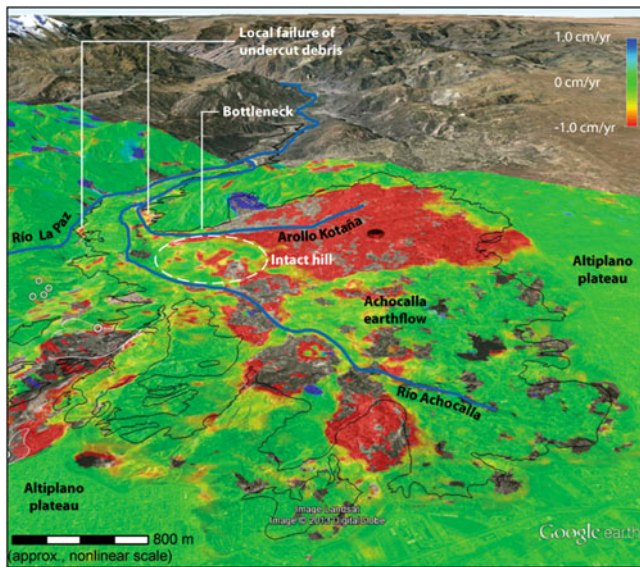


Fig. 3 Oblique view of the Achocalla Basin showing InSAR-measured displacements, historic landslides (*white circles*), and paleolandslides (*black outline*) including the area of the Achocalla earthflow. Base image is high-resolution optical satellite imagery draped over a DEM in GoogleEarth

sediments up-valley of the landslide dam. Debris remaining in the basin created by the earthflow includes large faulted blocks of the Altiplano fill sequence, whereas debris in the La Paz valley is largely folded and disaggregated (Hermanns et al. 2012). We have found no record of historic landslides in the Achocalla Basin, and no recent landslides are apparent on aerial photographs or satellite images.

About half of the Achocalla earthflow is moving at rates of up to ~ 20 cm/a (Fig. 3). Motion terminates abruptly along northeast-trending lateral limits that parallel morphologic lineaments mapped by Lavenu (1977) (Fig. 3). The headscarp above the left lateral limit of the deformation is the only location in the La Paz area where measurable deformation extends to the Altiplano surface, although for only about 800 m; the abrupt southwest limit of deformation on the Altiplano (Fig. 3) is parallel to nearby neotectonic faults (Lavenu 1977). Alignment of the limits of the deforming part of the Achocalla earthflow with faults and large-scale morphologic features suggests that tectonic discontinuities may influence movement. Depletion of earthflow material through the bottleneck at the lower end of the basin is required for kinematic freedom of upslope material, but no movement through this bottleneck is evident in the InSAR data (Fig. 3). This condition may indicate either accumulation of mass and stress on the upslope side of the bottleneck, requiring eventual release, or sufficient erosion at the bottleneck by Arolo Kotaña to maintain movement upslope.

We have identified several small instabilities in the vicinity of the Achocalla earthflow. Two elongate areas of ~ 50 ha on the down-valley side of the intact hill of Devonian rock described by Dobrovoly (1962) (Fig. 3) are moving at rates of 5–10 cm/a and are likely shallow earthflows unrelated to the Achocalla earthflow. A faster (up to ~ 24 cm/a) earthflow at the lower portion of the right lateral margin of the Achocalla earthflow appears to coalesce with it (Fig. 3). Localized displacements up to ~ 4 cm/a along incised edges of the debris tongue in the La Paz valley (Fig. 3) are likely driven by fluvial undercutting.

Pampahasi Landslides

The 2011 Pampahasi landslide is the largest and most damaging landslide in La Paz in at least 400 years. It affected an area of nearly 2 km^2 only a few kilometres from the city centre, displaced $\sim 6,000$ people (Aguilar 2013), many of whom are still housed in temporary shelters, and interrupted water service to $\sim 300,000$ more people for a period of several months (Hermanns et al. 2012; Aguilar 2013). The failure occurred within deposits of the Pampahasi paleolandslide (BRGM-BCEOM 1977) and partially reactivated the lower part of the 2009 Villa Salomé landslide, which had already been terraced by the city and was beginning to be informally resettled. The landslide developed over a four-day period starting on 29 February 2011; no lives were lost due to the slow rate of movement. Based on field observations of ground deformation in the area, Quenta and Calle (2005) alerted city officials to the possibility of a large landslide of similar magnitude to, although smaller than, the 2011 failure. In response to the field observations as well as reports from local residents of damaged roads and houses, the city had been monitoring deformation along the headscarp of the paleolandslide for several years prior to the failure. Total vertical displacements of ~ 0.5 m were observed over the monitoring period.

Most of the Pampahasi paleolandslide shows displacement at rates of 1–10 cm/a during the 30 months before and 10 months following the 2011 failure, with motion terminating abruptly at the headscarp and lateral margins (Fig. 4). Thus, the 2011 landslide was likely caused by long-term deformation of the paleolandslide deposit. Further, the failure did not stabilize this slope. This example suggests that InSAR-measured movement can improve forecasting of the spatial extent of rapid failures in the La Paz area. Gaps in displacement data (Fig. 4) are the result of aliasing and decorrelation between images due to major changes in topography and surface conditions, for example destruction

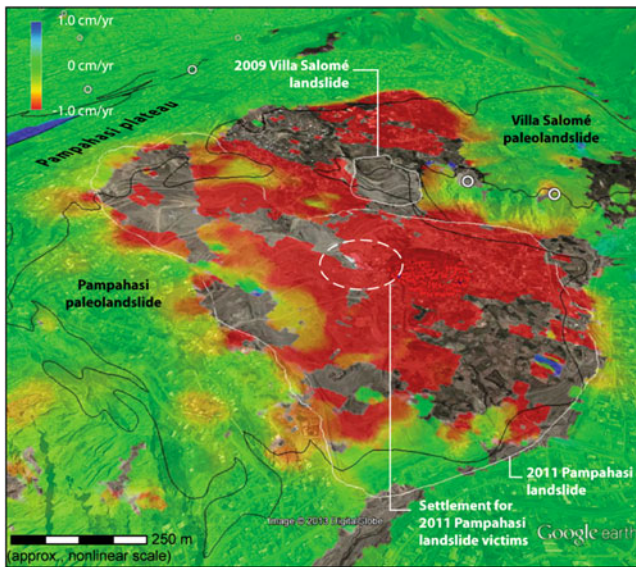


Fig. 4 Oblique view of the Pampahasi and Villa Salomé paleolandslides showing InSAR-measured displacement, historic landslides (*white circles*; *white outlines* for 2009 Villa Salomé and 2011 Pampahasi landslides), paleolandslide areas (*black outline*), and resettlement location. Base image is high-resolution optical satellite imagery draped over a DEM in GoogleEarth

of infrastructure and terracing related to the 2009 Villa Salomé and 2011 Pampahasi landslides. A temporary settlement for victims of this landslide was established in one such cleared area in the middle of the still-deforming slope, and is still being used (Fig. 4).

The InSAR data do not show acceleration in movement leading up to the 2011 failure. Thus, prediction of time of failure using InSAR alone would not have been possible. Accelerated displacement behind the headscarp and upper right lateral margin (Fig. 4) in the months following the landslide reflects continued destabilization along the high steep scarp formed during the 2011 failure. Headscarp retrogression in the years since the disaster has necessitated repeated evacuations at the edge of the Pampahasi plateau. Similar deformation patterns with displacement rates up to 5 cm/a occur in the headscarp region of the adjacent Villa Salomé paleolandslide (Fig. 4), suggesting that it could similarly cause a large damaging landslide in the future.

Villa San Antonio and Villa Armonía Landslides

The highest concentration of damaging landslides in recent decades is at the edge of the city centre (Fig. 5). Eight landslides have occurred along a 1,600-m length of the left bank of Río Orkojahuirra over the past 20 years; five events alone happened since 2000 in the neighbourhood of Barrio Retamani, which measures only 15 ha. The slope comprises

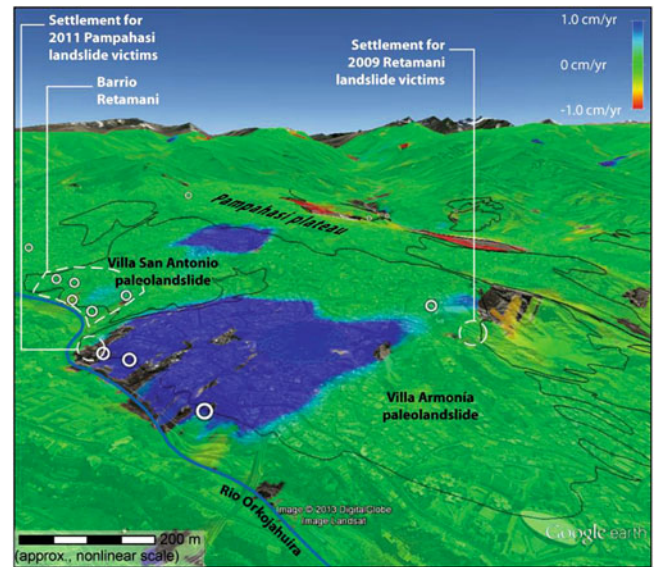


Fig. 5 Oblique view of the Villa San Antonio and Villa Armonía paleolandslides showing InSAR-measured displacement, historic landslides (*white circles*), paleolandslide areas (*black outline*), and temporary resettlement locations. Base image is high-resolution optical satellite imagery draped over a DEM in GoogleEarth

intact La Paz Formation overlain by deposits of the Villa San Antonio and Villa Armonía paleolandslides (BRGM-BCEOM 1977) (Fig. 5). Localized development of these slopes began about 1950, and by the 1980s many of the previously existing deep gullies in the paleolandslide deposits were culverted and in-filled to increase land area for housing (Roberts et al. 2010).

The upper part of the Villa San Antonio paleolandslide at the west edge of the Pampahasi plateau shows movement (~ 3 cm/a) throughout the InSAR-monitoring period (Fig. 5). A small localized area in the central part of the toe of the paleolandslide is also moving (~ 1 cm/a). Four of the recent failures in Barrio Retamani occurred at the edge of the deforming toe region (Fig. 5); lateral margins of all four coincide with buried streams and three of the four failed during the final months of the rainy season. The fifth recent landslide in Barrio Retamani occurred 150 m from the active area at the toe of the paleolandslide (Fig. 5), but was triggered by construction activity on a near-vertical slope forming the headscarp of a pre-1935 landslide. It appears that long-term activity of the Villa San Antonio paleolandslide preconditions historic failures, but leakage of buried culverted streams commonly triggers them.

Approximately one-third of the Villa Armonía paleolandslide is currently active (Fig. 5). Displacement in the inferred direction of movement is ~ 15 cm/a in the central part of the active area; displacement decreases to ~ 3 cm/a in the slope below, which was mapped previously as undeformed La Paz Formation by Dobrovolsky (1962) and

BRGM-BCEOM (1977). Three landslides occurred between 1994 and 2003 at toe of the Villa Armonía paleolandslide near the limit of deformation detected by InSAR. A temporary settlement for victims of the 2011 Pampahasi landslide is located in this area, only 300 m from two of the historic landslides (Fig. 5). In contrast, the permanent resettlement for 85 families displaced by the 2009 Retamani landslide appears to be on stable ground along the upper left lateral margin of the Villa Armonía paleolandslide (Fig. 5).

Displacement at the up-slope limits of deformation for both paleolandslides decreases from several centimetres per year to zero over distances of only several tens of meters. These abrupt changes are comparable to patterns recorded at the headscarp of the Pampahasi paleolandslide prior to the 2011 landslide (Fig. 4) and suggest that similar, but smaller failures are possible at the Villa San Antonio and Villa Armonía paleolandslides.

Discussion and Conclusion

Our investigation provides the first comprehensive characterization of landslide activity in the entire La Paz valley. In addition to frequent historic landslides, several ancient landslides, including the Achocalla, Pampahasi, Villa Salomé, Villa Armonía, and Villa San Antonio paleolandslides, show displacements of up to decimetres per year throughout the period of InSAR monitoring that are probably indicative of long-term activity.

Historic landslides in the La Paz area are related to long-term landscape evolution and recent anthropogenic modification of slopes. Most historic landslides occur near the limits of large slow-moving paleolandslides where differential movement is greatest. One or both lateral margins of a number of historic landslides correspond to locations of buried culverted streams, suggesting that failure on developed slopes may be triggered by subsurface water.

Most of the currently active paleolandslides in the city are densely populated and experiencing ongoing development. The southeast half of the Achocalla Basin, which is currently moving, is largely undeveloped; the mostly stable northwest half contains rural settlements and pasture land. Given their proximity to the city and favourable climate, these areas will likely become urbanized in future decades. Slow-moving landslides to the north of the city pose a risk to its water supply. Failures in vicinity of the La Paz's reservoirs or along aqueduct routes could disrupt water delivery to large portions of the city for weeks or months, as happened following the 2008 Represa Hampaturi landslide (Hardy 2009) and the 2011 Pampahasi landslide (Hermanns et al. 2012; Aguilar 2013).

This study includes the first application of HDS-InSAR for detecting and monitoring of landslides. The

technique enhances displacement records available for landslide characterization by combining benefits of differential InSAR and PS-InSAR. It supplements the high density of point scatterers in urbanized areas with signals from homogenous coherent surfaces such as pavement and sports fields. In areas of low building density or natural terrain, it preserves the relatively few, high-spatial resolution signals provided by point scatterers. In this application, ground deformation data are missing only in areas of dense tree and shrub cover or where major terrain changes related to rapid landslides and subsequent terrain modification produce decorrelation and aliasing between RADAR scenes. Under conditions present in the La Paz area, the HDS-InSAR technique provides detailed information on temporal and spatial deformation of large paleolandslides (tens of hectares and larger), and facilitates identification and characterization of landslides as small as one hectare. However, as with all InSAR methods, the technique cannot detect motion perpendicular to the line-of-sight of the sensor.

If appropriately used, the improved knowledge of landslide activity in La Paz provided by our investigation will aid in the reduction of landslide-related losses. Details on the location and drivers of instability can support appropriate long-term planning, as well as siting of temporarily settlements to house those displaced by landslides. Currently both new development and resettlement of landslide victims commonly occur on slowly moving slopes prone to repeated failure. Knowledge of the extent and rate of movement can guide ground-based monitoring efforts to provide additional details on landslide activity and can help assess what physical mitigation measures, if any, are appropriate.

Unfortunately, past science-based recommendations to avoid development in unstable areas (Dobrovolny 1962; BRGM-BCEOM 1977), including the slope affected by the 2011 Pampahasi landslide, have not been heeded. Poor urban planning decisions in the past are a major contributor to the current high landslide risk in La Paz (UNDP 2007). Evidence of actively moving slopes provided by HDS-InSAR and recognition that most historic landslides are related to slow-moving paleolandslides and buried culverted streams provide much-needed support for future restrictions on development. The crucial next step is communicating and disseminating information to decision makers in the city.

References

- Aguilar OQ (2013) Detección de cambios de uso del suelo en la zona de Callapa afectada por el megadeslizamiento (La Paz – Bolivia). In: Proceedings of XIV Encuentro de Geógrafos de América, April 2013, Lima, Perú, 20p

- BRGM-BCEOM (1977) Mapa de Constructibilidad, Cuenca de La Paz y sus Alrededores. Plan de Desarrollo Urbano Ciudad de La Paz. Honorable Alcaldía Municipal, La Paz, Bolivia. 1:25,000. 1 sheet.
- Dobrovolny E (1962) Geología del valle de La Paz. Departamento Nacional de Geología del Ministerio de Minas y Petróleo, La Paz, Bolivia. Boletín No 3, 152p
- Dobrovolny E (1968) A postglacial mudflow of large volume in the La Paz Valley, Bolivia. US Geological Survey Professional Paper 600-C, pp 130–134
- Guzmán M A (2007) Deslizamiento rotacional de Cuarto Centenario. Movimientos en masa en la región Andina: Una guía para la evaluación de amenazas. Servicio Nacional de Geología y Minería, Publicación Multinacional No 4, pp 198–204
- Hardy S (2009) Ruptura del abastecimiento de agua potable. Sistema Hampaturi-Pampahasi, La Paz, enero-febrero de 2008. Bulletin de L'Institut Français d'Études Andines 38(3):545–500
- Hermanns RL, Fauque L, Fidel Small L, Welkner D, Folguera A, Cazas A, Nuñez H (2008) Overview of catastrophic mega-rockslides in the Andes of Argentina, Bolivia, Chile, Ecuador and Peru. In: Proceedings of 1st world landslide forum, 18–21 November 2008, Tokyo, Japan, pp 255–258
- Hermanns RL, Dehls JF, Guzmán MA, Roberts NJ, Clague JJ, Cazas Saavedra A, Quenta G (2012) Relation of recent megalandslides to prehistoric events in the city of La Paz, Bolivia. In: Proceedings of 2nd North American symposium on landslides, 3–6 June 2012, vol 1. Banff, Canada, pp 341–347
- Kampes BM (2006) Radar interferometry: persistent scatterer technique. Springer, Dordrecht, 211p
- Lavenu A (1977) Neotectónica de los sedimentos Plio-Cuaternarios de la cuenca de La Paz (Bolivia). Rev Geoci UMSA 1(1):31–56
- O'Hare G, Rivas S (2005) The landslide hazard and human vulnerability in La Paz City, Bolivia. Geogr J 17(3):239–258
- Quenta G, Calle A (2005) Diagnostico de estabilidad de la zona Valle de las Flores. Servicio Nacional de Geología Técnico de Minas. 12p
- Quenta G, Galarza I, Teran N, Hermanns RL, Cazas A, García H (2007) Deslizamiento traslacional y represamiento en el valle Allpacoma, Ciudad de La Paz, Bolivia. Movimientos en masa en la región Andina: Una guía para la evaluación de amenazas. Servicio Nacional de Geología y Minería, Publicación Multinacional No 4, pp 230–234
- Rabus B, Eppler J, Sharma J, Busler J (2012) Tunnel monitoring with an advanced InSAR technique. In: Proceedings of radar sensor technology XVI, 23–25 April 2012, Baltimore, Maryland. SPIE vol 8361, 10p
- Roberts NJ, Minaya E, Guzmán MA, Zabala M, Clague JJ, Hermanns RL (2010) Overview of recent landslides in barrio Retamani, La Paz, Bolivia. In: Resúmenes Extendidos del XV Congreso Peruano de Geología, 27 September–1 October 2010. Cusco, Perú, pp 328–331
- Sanjinés AG (1948) Síntesis histórica de la vida de al cuidada, 1548–1948. 1° premio de la Alcaldía, La Paz, Bolivia. 86p.
- UNDP (2007) Catalogue of municipal management tools in risk reduction and emergency preparedness in Andean capital cities – La Paz, Bolivia. UNDP, La Paz, Bolivia, 74p

Part VII

Landslides in Cold Regions



Introduction: Landslides in Cold Regions

Ying Guo, Marina O. Leibman, Marten Geertsema, and Sumio Matsuura

Abstract

The areas we called the cold regions refers to permafrost, seasonal frozen soil and the short-term frozen soil. Their total area has accounted for about 50 % of the whole land area, and permafrost distribution accounts for about 25 % of the Earth's land surface. In Wlf3-C7 session—landslides in cold regions, for same study area and same study object in cold regions, researchers adopted different method, began with different perspective. In the context of climate change, their research contain landslides mechanism, geomorphologic identification and classification, environment geological conditions change, even the plants-soil-permafrost systems in landslide zone.

Keywords

Landslide • Cold regions • Climate change

WLF3-C7 session—Landslides in Cold Regions is organized by ICL-CRLN (International Consortium on Landslides in Cold Regions Landslide Network). The session includes 15 research papers coming from several cold region countries: Canada, China, Japan, Kyrgyzstan and Russia.

The speakers will cover the topics of landslides in cold regions from a variety of perspectives, in the context of climate change. Topics include landslide mechanisms, geomorphologic identification and classification, environmental changes, and plant-soil permafrost systems in landslide-affected zones.

Y. Guo (✉)
Northeast Forestry University, Heilongjiang, China
e-mail: samesongs@163.com

M.O. Leibman
Earth Cryosphere Institute, Siberian Branch, Academy of Sciences,
Tumen, Russia

M. Geertsema
Ministry of Forests, Lands, and Natural Resource Operations, Prince
George, BC, Canada

S. Matsuura
Disaster Prevention Research Institute, Kyoto University, Kyoto, Japan

For the same study area and object in cold regions, researchers adopted different methods and a variety of approaches such as environmental, geological, geochemical, climatic and more. These studies can be divided into the following topics:

Landslides in High Latitude Permafrost Lowlands and Hilly Area

Several papers are dealing with landslide-affected area on Russian lowlands, specifically Central Yamal. Dr. Marina O. Leibman suggests classification, mechanisms, and landforms specific for this area. Dr. Anatoly A. Gubarkov studies cryogenic landslides in paragenetic complexes of slope and channel processes. Dr. Ksenia Ermokhina and Dr. Olga Khitun present vegetation dynamics of landslide affected slopes including those of different age. Dr. Nataliya Ukraintseva studies plant-soil-permafrost system on landslide-affected slopes using geochemical methods. Dr. Artem Khomutov suggests a method of landsliding hazard assessment.

Chinese scholars Prof. Wei Shan studied the landslides near the southern boundary of high-latitude permafrost which is located in the Northwest Section of Lesser

Khingan: landslide formation mechanisms, landslide movement characteristics and the effect of climate change on permafrost distribution and degradation, etc. Dr. Ying Guo studied the effect of plant roots on soil cutting slope stability in seasonal permafrost regions of China.

Landslides in Steep Mountain Area Triggered by Permafrost Degradation, Snow and Glaciations

Canadian scholar Dr. Kenneth Hewitt studied the relationship between landslides and glaciations in the area of

Karakoram and NW Himalaya Inner Asia. Dr. Marten Geertsema studied the effect of climate change and permafrost degradation on permafrost landslides in northeast British Columbia.

Japanese scholar Dr. Sumio MATSUURA studied the effects of deep snowpack on the changes in pore water pressure of a landslide moving body.

Kyrgyz scholars Dr. Isakbek Torgoev studied the effects of glaciations and permafrost thaw on the stability of open pit wall and waste dumps.

This session will update the progress of research and allow for exchanges of ideas on landslides in cold regions.



Vegetation Dynamics of Landslide Affected Slopes (Central Yamal)

Ksenia Ermokhina

Abstract

One of the topical issues arising due to the development of natural resources and the climate change in the Arctic Region is the prediction of ecosystems' dynamics, based on the study of tundra biota response to the different natural and anthropogenic impacts. The cryogenic landslides' process appears to be one of the determining factors of the ecotopes' transformation in the various tundra regions including the Central Yamal. The process is influencing vegetation of vast areas, its structure and dynamics. The structure of plant communities is an important factor of the cryogenic landslides' activation. The ecotopes of the later vegetation demutation stages' communities are the most resistant to the development of the process. These communities have a closed shrub cover of *Salix glauca* (that is often 1–1.5 m high). At the subclimax stage this cover gets thinned, and the mosses begin to dominate by the phytomass. In subclimax communities there are no plants with extensive root systems capable to “retain” the structure of the active layer; therefore their ecotopes turn out to be extremely non-resistant to the development of the landslide process. Geochemical processes proceeding in the active layer also lead to the ecosystem destabilization through slow accumulation of secondary clay minerals on the border between active layer and permafrost. These minerals play a significant role in cryogenic landslides' development. The strain in upper deposits' horizons, which is also necessary for the landslide process activation, is accumulated gradually.

Keywords

Dynamics of vegetation • Cryogenic landslides • Phytoindication • Yamal peninsula

Introduction

The vegetation of tundra zone is very dynamic, and its dynamics is considerably determined by the exogenous geomorphologic processes. The cryogenic landslides' process appears to be one of the determining factors of the ecotopes' transformation in the various tundra regions including the Central Yamal. The process is influencing on vegetation of vast areas, its structure and dynamics.

Fieldworks were carried out by K.A. Ermokhina and N.G. Ukraintseva in 1997–2002, 2010 on the “Vaskiny Dachi” (key-site of the Institute of the Earth Cryosphere SB RAS, the site was created to study cryogenic landslides in the Central Yamal, Fig. 1). During the fieldworks 165 geobotanical relevés were made, also the above-ground phytomass, plant, soil and groundwater samples were taken. The complex lab tests of the samples including plants' ash-content and above-ground phytomass values were implemented by specialists of the Vernadsky Institute of Geochemistry and Analytical Chemistry RAS.

K. Ermokhina (✉)
Earth Cryosphere Institute, Siberian Branch, Russian Academy of Sciences, Malygin street, 86, Tyumen 625000, Russia
e-mail: diankina@gmail.com



Fig. 1 Study area

Key Site Characteristics

The study territory is situated in the northern part of the Yamal's subarctic tundra (subzone D) within flat accumulative-erosion plain with two-level structure of relief. The upper level is presented by outliers of the marine (Upper Pleistocene) and above-floodplain (Upper Pleistocene—Holocene) terraces, whereas lower level is presented by the flat flood-plain surfaces of the Sejaha, Mordyjaha and Nadujaha rivers (Tsibulskiy et al. 1995). Maximum depths of relief dissection run up to 50 m. Due to the fact that the permafrost of this territory has not been thawing during the Holocene optimum, marine clayey deposits, wide spread here, conserved high mineralization level (Leibman and Kizyakov 2007).

As usual slopes in the Central Yamal occupy much more area than near-watershed subhorizontal surfaces. Widespread cryogenic landslide's processes impact on structure of ecosystems to great extent here, forming swell-and-swale topography with dammed lakes. Area of potential landslides activity accounts for 45 % of the subarctic Yamal tundra (Tentyukov 1998), area of cropped out saline ground can reach 100 m² and more (Ukrainitseva 1997). Dissolution of chemical compounds, contained in cropped out permafrost deposits, results in sharp increasing suprapermafrost

groundwater mineralization after the landslide disturbance (Leibman and Kizyakov 2007). Landslide slopes are the systems of landslides of different age with representative set of elements: landslide shearing surfaces, landslide bodies and landslide separation walls. As usual the longitudinal profile of these slopes has not poised yet. Nowadays three age groups of Yamal cryogenic landslides are distinguished in the literature (Leibman et al. 2000; Ukrainitseva 1997)—young landslide structures (landslides occurred about 35 years ago), the old landslides (up to 300 years ago) and the ancient ones (300–2,000 years old).

Vegetation of Landslide Affected Slopes

Vegetation cover of marine terraces' slopes is mosaic, and the plant communities representing the elements of this mosaic are covering different areas (in general, from 50 to 150 m²). Vegetation cover's specifics do not depend on the absolute altitudes, slope inclinations and expositions due to the general topography flatness. The only natural agents under these landscape and geomorphologic conditions responsible for important differences in communities' conditions, are the cryogenic landslides, which are often transforming the whole active layer (the thickness of which in this area is about 0.5–1 m). Vegetation is represented here by the composition of dwarf birch-willow (*al. Equiseto–Salicion glaucae*), dwarf birch (*as. Vaccinio–Betuletum nanae*), grass-moss (*as. Luzulo–Polytrichetum juniperinum*) tundras and fragments of the forb-grass meadows (*as. Alopecuretum pratensis*).

Vegetation classification was carried out in accordance to the Braun-Blanquet method (Yermokhina and Myalo 2012). One alliance, integrating two associations, and three independent associations were identified. The communities of *Equiseto–Salicion glaucae* alliance are typical for the areas disturbed by the cryogenic landslides in different extent and periods of time. Landslide ecotopes' diversity determines differences of the species composition and vegetation communities' structure within the union (Table 1, Fig. 2).

According to the classification by B.A. Yurtsev (1995), landslide processes are disastrous in relation to vegetation. Cryogenic landslides form new ecotopes with diverse conditions. Considering the ecotopes' vegetation specifics and scale of their transformation, we have united "landslide" ecotopes into four types: the central and the peripheral parts of landslide shearing surfaces, the central and the peripheral parts of landslide bodies.

The certain set of syntaxa is linked to each ecotopes' type (Table 2, the reliability of their relation with types of ecotopes exceeds 0.70). *Poo–Caricetum concolor* association communities tend to the central parts of the landslide structures, whereas *Bistorto–Betuletum nanae* association tend to the contour parts.

Table 1 The main vegetation features on slopes of marine terraces

Vegetation syntaxa	Equiseto–Salicion glaucae Alliance		Vaccinio–Betuletum nanae association	Luzulo–Polytrichetum juniperinum association	Alopecuretum pratensis association
	Poo–Caricetum concolor association (1)	Bistorto–Betulion nanae association (2)			
Differential species of associations	<i>Carex concolor</i> , <i>Poa alpigena</i> subsp. <i>colpodea</i> , <i>Ranunculus borealis</i>	<i>Betula nana</i> , <i>Vaccinium vitis-idaea</i> subsp. <i>minus</i> , <i>Bistorta viviparum</i> , <i>Dicranum elongatum</i>	<i>Betula nana</i> , <i>Vaccinium vitis-idaea</i> subsp. <i>minus</i>	<i>Luzula confusa</i> , <i>Polytrichum juniperinum</i>	<i>Alopecurus pratensis</i>
Plant communities layers	Shrubs, dwarf shrubs and grasses, moss-lichenous layer	Shrubs (frequently), dwarf shrubs and grasses, moss-lichenous layer	Dwarf shrubs and grasses, moss-lichenous layer	Grass and moss-lichenous layers	Grass layer and rarely moss layer
Dominating species	<i>Salix glauca</i> , <i>Equisetum arvense</i> subsp. <i>boreale</i> , <i>Carex concolor</i> , <i>Poa alpigena</i> subsp. <i>colpodea</i> , <i>Ranunculus borealis</i>	<i>Salix glauca</i> , <i>Betula nana</i> , <i>Vaccinium vitis-idaea</i> subsp. <i>minus</i> , <i>Equisetum arvense</i> subsp. <i>boreale</i> , <i>Bistorta viviparum</i> , <i>Dicranum elongatum</i>	<i>Betula nana</i> , <i>Vaccinium vitis-idaea</i> subsp. <i>minus</i>	<i>Polytrichum juniperinum</i> , <i>Polytrichum strictum</i>	polydominant grass community, rich in graminoids
Total projective cover (PC)	65–95 %	65–90 %	85 %	97 %	55 %
Average PC of shrub layer	8–75 %	0–61 %	0 %	0 %	0 %
Average PC of dwarf shrubs and grasses layer	40–64 %	35–87 %	50 %	74 %	49 %
Average PC of moss component	28–80 %	30–85 %	84 %	96 %	26 %
Average PC of lichen component	1–6 %	0–8 %	7 %	2 %	0 %

Equiseto–Salicion glaucae Alliance

Differential species: *Salix glauca*, *Equisetum arvense* subsp. *boreale*

Poo–Caricetum concolor association

Differential species: *Carex concolor*, *Poa alpigena* subsp. *colpodea*, *Ranunculus borealis*

1. Salicetosum polaris Subassociation

Differential species: *Salix polaris*, *Poa arctica*, *Dryas octopetala*, *Polytrichum juniperinum*

2. Calamagrostietosum holmii Subassociation

Differential species: *Calamagrostis holmii*

3. Drepanocladetosum uncinati Subassociation

Differential species: *Drepanocladus uncinatus*

4. Veratretosum lobeliani Subassociation

Differential species: *Veratrum lobelianum*

5. Caricetosum arctisibiricae Subassociation

Differential species: *Carex arctisibirica*

6. Typicum Subassociation

Typical subassociation, faithful species: *Salix glauca*, *Equisetum arvense* subsp. *boreale*, *Carex concolor*, *Polemonium acutiflorum*

7. Caricetosum lachenalii Subassociation

Differential species: *Carex lachenalii*

Bistorto–Betulion nanae association

Differential species: *Betula nana*, *Vaccinium vitis-idaea* subsp. *minus*, *Bistorta viviparum*, *Dicranum elongatum*

1. Typicum Subassociation

Typical subassociation, faithful species: *Salix glauca*, *Betula nana*, *Dicranum elongatum*, *Vaccinium vitis-idaea* subsp. *minus*

2. Festucetosum rubrae Subassociation

Differential species: *Alopecurus pratensis*, *Festuca rubra* subsp. *arctica*, *Ranunculus borealis*

3. Peltigeretosum aphthosae Subassociation

Differential species: *Polemonium acutiflorum*, *Aulacomnium turgidum*, *Peltigera aphthosa*

4. Veratretosum lobeliani Subassociation

Differential species: *Veratrum lobelianum*

5. Poetosum arcticae Subassociation

Differential species: *Poa arctica*, *Carex arctisibirica*

6. Eriophoretosum vaginati Subassociation

Differential species: *Nardosmia frigida*, *Eriophorum vaginatum*, *Stellaria palustris*

7. Poo–Calamagrostietosum holmii Subassociation

Differential species: *Poa alpigena* subsp. *colpodea*, *Calamagrostis holmii*

Fig. 2 Vegetation prodromus of landslide affected slopes

The analysis showed that after destruction of the original vegetation cover features of seral changes of vegetation on the substratum revived by the landslide would depend on the

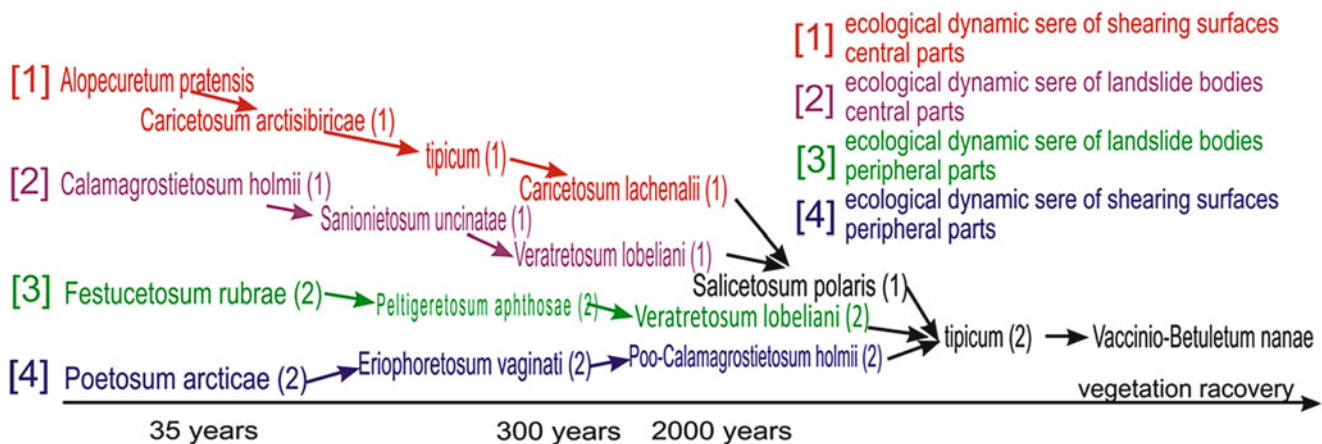
formed landslide element (landslide body or shearing surface) and on the site position relative to the landslide movement axis (central or peripheral).

Table 2 Distribution of syntaxa by ecotopes' types

Central parts of shearing surfaces	Peripheral parts of shearing surfaces	Central parts of landslide bodies	Peripheral parts of landslide bodies	Stable slopes ^a	Snow patch sites on stable slopes
<i>Alopecuretum pratensis</i>	<i>Poetosum arcticae</i> (2)	<i>Calamagrostietosum holmii</i> (1)	<i>Festucetosum rubrae</i> (2)	<i>Salicetosum polaris</i> (1)	<i>Luzulo-Polytrichetum juniperinum</i>
<i>Caricetosum arctisibiricae</i> (1) ^b	<i>Eriophoretosum vaginati</i> (2)	<i>Drepanocladetosum uncinati</i> (1)	<i>Peltigeretosum aphthosae</i> (2)	<i>tipicum</i> (2)	
<i>tipicum</i> (1)	<i>Poo—</i>	<i>Veratretosum lobeliani</i> (1)	<i>Veratretosum lobeliani</i> (2)	<i>Vaccinio-Betuletum nanae</i>	
<i>Caricetosum lachenalii</i> (1)	<i>Calamagrostietosum holmii</i> (2)				

^aStable slopes—slopes without noticeable landslide relief (the area more than 500 m²)

^bHere and further: (1)—subassociations of Poo-Caricetum concolor association, (2)—subassociations of Bistorto-Betuletum nanae association

**Fig. 3** The seral system of vegetation for landslide's slopes of marine terraces

Primary vegetation successions are developed on the central parts of shearing surfaces, in other types of ecotopes they proceed as secondary (because here fragments of parent vegetation are preserved and these ecotopes border on undisturbed sites for a long distance). Successions on the central parts of the thick landslide bodies can also proceed as the primary ones. Snow patches' sites occupied by *Luzulo-Polytrichetum juniperinum* association can be altered by the landslides, and then demutation processes would develop in these areas depending on the disturbance specifics. For every of identified ecotopes' type the ecologic dynamic series of communities performing vegetation succession during ecotope changing process can be composed.

Vegetation Dynamics and Succession Mechanisms

The seral system of vegetation forming under the landslide processes, which take place on marine terraces' slopes of the Central Yamal, was composed using the obtained data (Fig. 3). The vegetation ecological dynamic series' length

depends on the scale of the parent ecotope conditions' transformation, caused by the cryogenic landslide. The ecological dynamic sere of communities on the central parts of shearing surfaces is the longest, including the most number of syntaxa. This observation corresponds to the fact, that these ecotopes suffer the most changes and, therefore, development of these ecotopes takes the most time and the major number of seral stages. Peripheral ecological dynamic series are the shortest and contain only five syntaxa (two latter are common). With the vegetation recovering the convergence of the ecological dynamic series is observed, this indicates the gradual equation of different ecotopes' ecological conditions.

Canonical correspondence analysis of the dynamic changes has demonstrated that demineralization of groundwaters is the essential factor, influencing the successions. This factor's significance decreases in proportion to the vegetation recovering. Obtained data on occurring parallel changes in accumulation of chemical elements by the plants also give an evidence of the correlation between vegetation dynamics and groundwaters' mineralization changes.

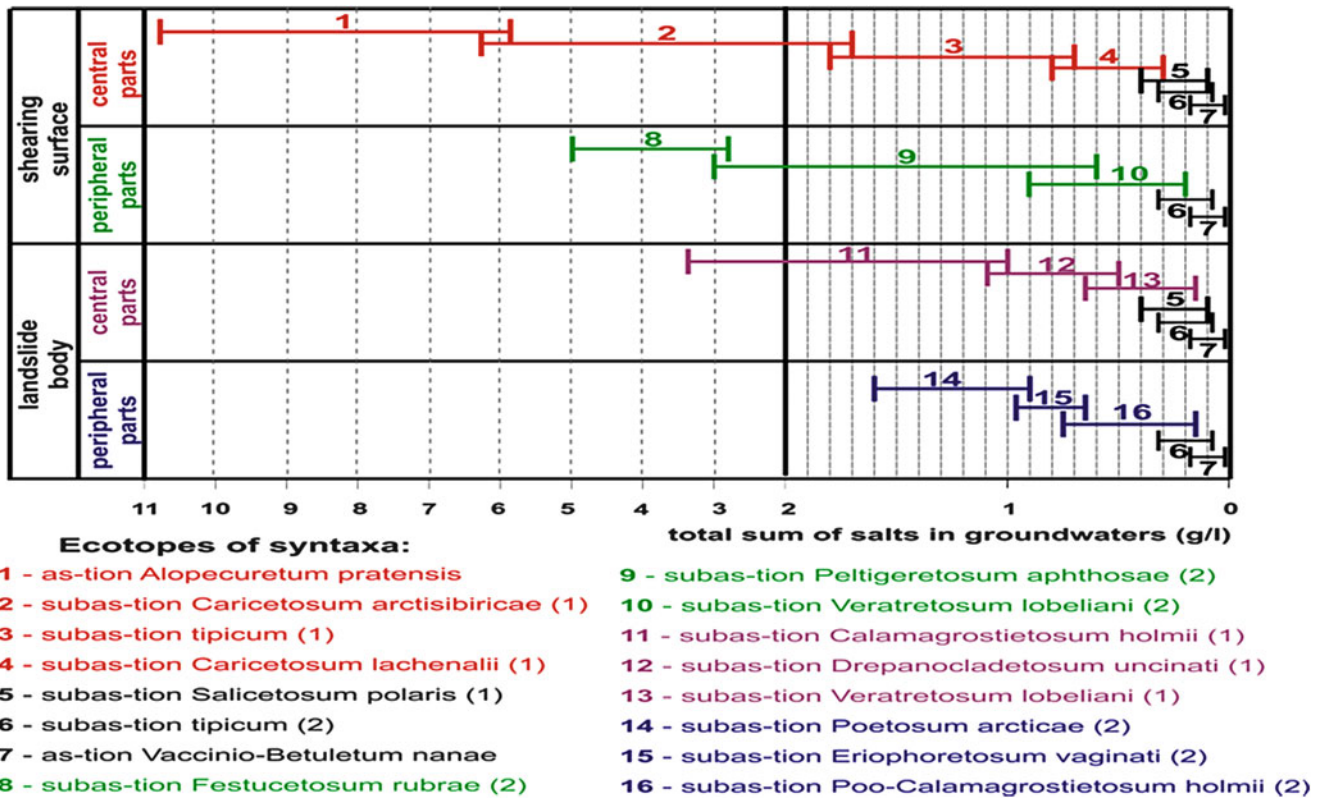


Fig. 4 Ecological-dynamic series and the change of salt content in groundwaters

The effect of groundwaters' demineralization is the most apparent in the ecological dynamic sere of the central parts of shearing surfaces, it is followed by the series of peripheral parts of shearing surfaces and the central parts of landslide bodies. The factor's impact on communities of the ecological dynamic series is the least pronounced within sere, formed on the landslide bodies contours. The factor's manifestation is directly associated with the scale of parent ecotope's transformation caused by cryogenic landslide.

In order to detect the phytoindicators of landslide's age and landslide structures' type the conjugated analysis of the parametric changes in the vegetation communities and their ecotopes has been carried out. The parameters under study are naturally varied; therefore the analysis took into account standard deviation as well as mean values of them (Rozenberg 1998; McCune et al. 2002; Puzachenko 2004). Statistical computations were conducted in Statistica 6.0 application, reliability estimation of the revealed relations was carried out by the B.V. Vinogradov's phytoindication methodic (1964). Relationship between changes of the parameters' values has been specified on the basis of the correlation analysis. The closeness and specifics of the relations were estimated by the Pearson correlation coefficient, widely applied in the geobotanical studies.

Total sum of salts and Cl, SO₄, Ca, Mg and K contents values in groundwaters were estimated for ecotopes of the

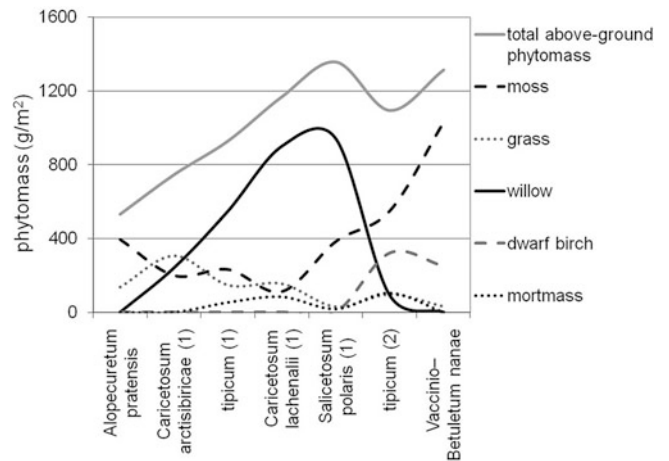


Fig. 5 Change of average phytomass values in the communities of ecological dynamic sere in the central parts of shearing surfaces

identified syntaxa. Distribution of these indexes for the groundwaters' samples is approximated by the normal probability law. Confidence intervals of the chemical elements' and compounds' contents have been built up for every syntaxon's ecotope separately so that 70 % of cases would enter them (B. V. Vinogradov's scale has a 60 % limit for using the indicator, 1964). The results are presented on the Fig. 4, they clearly show how syntaxa range in the ecologic series.

Obtained data reveals one of succession mechanisms in the vegetation communities, which proceed along with the ecotope's recovering after landslide disturbance. This confirms the fact, that vegetation dynamic changes on the marine terraces' slopes are based on the occurrent desalinization of groundwaters.

Decrease of sums of salts and mass contents of chemical elements values in groundwaters takes place in every identified ecotopes' type in proportion to the landslide structures' age increasing. In general the concentration of Cl, SO₄, Ca, Mg and K decreases sharply on the freshly exposed surfaces; the decreasing is very smooth on the ancient landslide structures.

Changes in the groundwaters' geochemical composition correlate with the dynamics of the communities' phytomass of the marine terraces' slopes' seral system (Fig. 5).

Phytomass increase is registered in every ecologic dynamic series up to the subclimax stage. This borderline in the dynamics of groundwaters' mineralization is characterized by changing water type from fresh to ultrafresh (according to Perelman's classification 1982). Most probably this correlation can be explained by the application of the additional mineral nutrition for the plants of the early and intermediate recovering succession stages due to dissolution of the chemical elements and compounds contained in the permafrost deposits. This supposal comports with N.G. Ukraintseva's conclusions (Ukraintseva 1997; Ukraintseva 2008). At the subclimax stage phytomass' amounts at first decreases and then increases. This fact results from the change of the predominating structural phytomass' parts: at this stage willow's part (*Salix glauca* makes about 95 %) in the communities sharply decreases, while the moss's part increases to the same extent. This process reflects the approaching of the ecotope conditions to the parent ones.

The species wealth of syntaxa is the maximum at the presubclimax succession stage, while the species saturation during the seral changes of vegetation remains almost the same. The early succession stages are characterized by the domination of long-quitch grasses with a pioneer strategy; their role gradually decreases along with vegetation recovering. In the course of succession the part of erect dwarf shrubs and firm bunchgrasses increases.

Phytoindication of Landslide Disturbances

The revealed vegetation relation to groundwater mineralization, as well as already known dependence of groundwater mineralization on the landslide age, was used to build up the indication chain "vegetation → groundwater mineralization → age of the landslide structure".

The marine terraces' slopes in the Central Yamal are complex landslide systems of different age generations, which are often overlapping each other. This fact complicates the visual identification of landslide structures in the relief. The set of vegetation indicators associated with the cryogenic landslide age, the type of the formed landslide structure, the mineralization level and the geochemical composition of groundwaters was identified on the basis of the succession changes' analysis: (1) syntaxa differential species; (2) indicator species (defined on the basis of their coenotic optimum position in the seral vegetation system); (3) total above-ground phytomass of vegetation communities, *Salix glauca* and moss phytomass; (4) set of vascular plants' biomorphes. The indicators' set includes physiognomic features of vegetation communities closely related to the objects of indication and characterized by the distinct dynamics depending on the dynamics of indicated objects (Yermokhina and Myalo 2012). To introduce age characteristics, we used the radiocarbon dating of landslide structures' age carried out by Leibman and Kizyakov (2007) at this key site.

Conclusions

With the unpoised longitudinal slope profile, the landslide process's development is possible at any stage of the vegetation recovering. Nevertheless, the structure of plant communities is an important factor of the cryogenic landslides' activation. The ecotopes of the later vegetation demutation stages' communities are the most resistant to the development of the landslide process. These communities have a closed shrub cover of *Salix glauca* (that is often 1–1.5 m high). At the subclimax stage the shrub cover gets thinned, and the mosses begin to dominate by the phytomass. *Betula nana* in these communities is short growing and doesn't form an independent layer. In subclimax communities there are no plants with extensive root systems capable to "retain" the structure of the active layer; therefore their ecotopes turn out to be extremely non-resistant to the development of the landslide process. On the other side, geochemical processes proceeding in the active layer also lead to the ecosystem destabilization through slow accumulation of secondary clay minerals on the border between active layer and permafrost. These minerals play a significant role in cryogenic landslides' development (Tentyukov 1998). The strain in upper deposits' horizons, which is also necessary for the landslide process activation (Leibman and Kizyakov 2007), is accumulated gradually (about 300 years). Therefore, ecotopes where the cryogenic landslide occurred long time ago turn out to be more exposed to the new landslides as compared to recently disturbed ecotopes.

References

- Leibman MO, Kizyakov AI (2007) Thaw slumps of Yamal and the Yugorskiy Peninsula. IKZ SO RAN, Moscow, 206 pp
- Leibman MO, Kizyakov AI, Archegova IB, Gorlanova LA (2000) Thaw slump stages at the Yugorskiy Peninsula and in Yamal// *Kriosfera Zemli* 4(4):67–75
- McCune B, Grace JB, Urban DL (2002) Analysis of ecological communities. MjM Software, Gleneden Beach, OR, 300 pp
- Perelman AI (1982) Natural waters geochemistry. Nauka, Moscow, 115 pp
- Puzachenko YG (2004) Mathematic methods in environmental and geographic studies. Akademiya, Moscow, 408 pp
- Rozenberg GS (1998) Quantitative phyto-indication methods // Environmental monitoring. Biological and physical-chemical monitoring methods. Part III. N. Novgorod, pp. 5–27
- Tentyukov MP (1998) Landscapes geochemistry in Central Yamal, Yekaterinburg izd-vo UrO RAN, 104 pp
- Tsibulskiy VR, Valeeva EI, Arefjev SP, Meltser LI, Moskovchenko DV, Gashev SN, Brusynina IN, Sharapova TA (1995) Yamal environment, vol 2. IPOS SO RAN, Tyumen
- Ukrainitseva NG (1997) Yamal willow shrub tundra as an indicator of surface deposits salting // Basic research results for the Earth's cryosphere in the Arctic and the Subarctic Regions Novosibirsk: Nauka, pp 182–187
- Ukrainitseva N (2008) Vegetation response to landslide spreading and climate change in the West Siberian Tundra. In: Proceedings of the ninth international conference on Permafrost / Institute of Northern Engineering, University of Alaska Fairbanks, 2008, V.2, pp 1793–1798
- Vinogradov BV (1964) Phytoindicators and their use in natural resources study. Vyssh.shk, Moscow, 328 pp
- Yermokhina KA, Myalo EG (2012) Phytoindicators of landslide disturbances in the Central Yamal tenth international conference on Permafrost. Vol. 2: Translations of Russian contributions. Co-edited by Drozdov DS, Romanovsky VE. The Northern Publisher, Salekhard, Russia, pp 531–536.
- Yurtsev BA (1995) Anthropogenic dynamics of vegetative cover in the Arctic and the subarctic regions: principles and methods of investigation. Trudy Botanicheskogo instituta im. V.L. Komarova RAN, Edition 15, 185 pp



Landslides in the Isolated Patches Permafrost Zone, Northeastern British Columbia (NTS Mapsheet 94G East Half)

Marten Geertsema and Vanessa N Foord

Abstract

Landslides are common in the east half of map sheet 94G in northeastern British Columbia, an area with patchy permafrost. Landslide frequency in the area has accelerated in the last decades. The increased activity may be, in part, due to the result of thawing permafrost under a warming climate, and due to an increase in precipitation. A landslide rupture surface in permafrost, however, has been substantiated in only one of the cases in this study.

Keywords

Landslides • Permafrost • Climate warming • British Columbia

Introduction

Landslides associated with permafrost degradation have been reported in mountain and subpolar regions around the world (e.g. Dramis et al. 1995; Leibman 1995; Davies et al. 2001; Harris et al. 2001; Gruber and Haeberli 2007; Huggel et al. 2012). In Canada much work has been done above 60°N (e.g. Aylsworth et al. 2000; Dyke 2000; Lewkowicz and Harris 2005; Lipovsky and Huscroft 2007), but in northern British Columbia (BC) the link between thawing permafrost and landslides has only recently received attention (Geertsema et al. 2006, 2007).

BC has seen an increase in large landslides in recent years (Geertsema et al. 2006). Certain areas of northeastern BC stand out in that they have particularly high numbers of low-gradient landslides in cohesive sediments as well as steeper landslides on mountain slopes. In this paper we bring together preliminary landslides, climate trends and permafrost observations for the east half of NTS map sheet 94G (Fig. 1).

Setting

The east half of map sheet 94G is located on the Alberta Plateau and the eastern part of the northern Rocky Mountains (Holland 1976). The plateau comprises dissected uplands and lowlands underlain by flat-lying sedimentary rock (Lane et al. 1999). Here low plateaux, mesas, and cuestas are dissected by the major rivers, and have undergone back-weathering by landsliding. Cliff-forming sandstone of the upper Cretaceous Dunvegan Formation overlies weak shale of the Fort St. John Group. Quaternary sediments are dominated by clay-rich tills and lake sediments derived from shales (Bednarski 1999, 2000, 2001). Much of the unconsolidated sediment has been reworked into colluvium by landslides.

The east half of 94G was covered by both the Cordilleran and Laurentide ice sheets and was partially inundated by large post glacial lakes at the end of the Wisconsinan Glaciation (Mathews 1980; Bednarski 1999, 2001; Dyke et al. 2001). A date on wood charcoal on Lake Peace sediments overlying Laurentide ice sheet till in the Fort St. John region gave an age of $13,970 \pm 170$ ^{14}C yr BP (Catto et al. 1996).

The associated biogeoclimatic zone is the Black and White Boreal Spruce zone (Meidinger and Pojar 1991). It is dominated by cold continental Arctic air in the winter and moist Pacific and Arctic air masses in the summer

M. Geertsema (✉) • V.N. Foord
Ministry of Forests, Lands, and Natural Resource Operations, Prince
George, BC, Canada V2L 5G4
e-mail: marten.geertsema@gov.bc.ca; vanessa.foord@gov.bc.ca

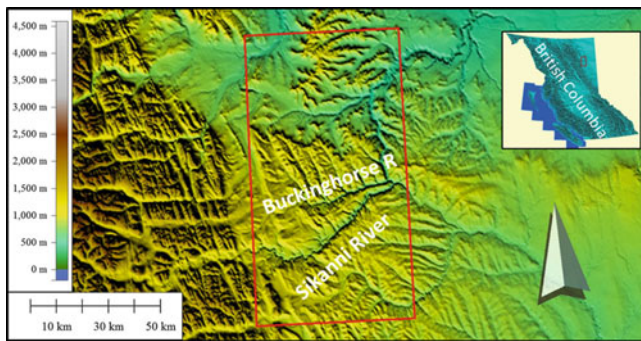


Fig. 1 Northeastern British Columbia. The red outlined area shows the east half of NTS map sheet 94G

(Demarchi 1996). Our study area is in the “isolated patches” permafrost zone (Heginbottom et al. 1995).

Climate

Holocene Climate

The climate has fluctuated throughout the post-glacial period, at millennial, century, and decadal scales (Clague 1989). Some of the climate changes were, if not global, at least hemispherical, while others were regional phenomena. Global cooling occurred during the Younger Dryas (just before the Holocene) and was also associated with the 8200 year BP drainage of Glacial Lake Agassiz which disrupted the thermohaline circulation in the North Atlantic Ocean. Local glacial advances occurred several times during the Holocene in the Canadian Cordillera and these were sometimes asynchronous with advances elsewhere. The most recent period of significant global cooling, the Little Ice Age (LIA), began about 1550 AD and persisted to 1850 AD.

Although no proxy paleoclimate records exist for the study area, inferences can be made from other studies in western Canada. The early Holocene was relatively warm and dry in western North America. Muskeg did not begin to form in northeastern BC until about 5–6,000 years ago (MacDonald and McLeod 1996). It is conceivable that permafrost may have expanded in northeastern BC during the cold periods such as the Younger Dryas, the mid Holocene period of muskeg expansion, and the LIA.

Historic Climate

The instrumental climate record in northern BC is a century old and has been analyzed in detail by Egginton (2005). However the record for our study area is shorter. The

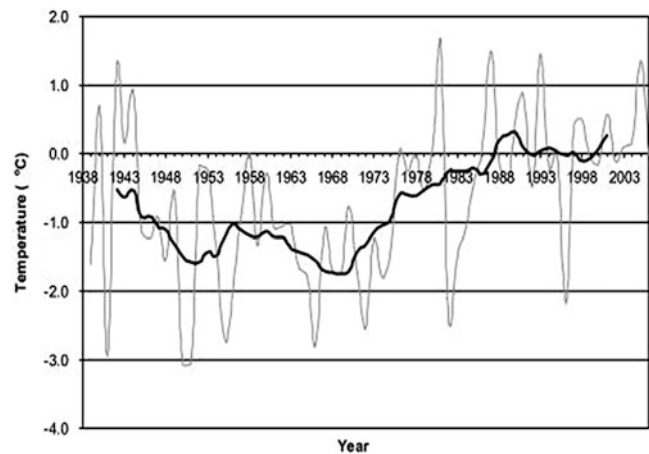


Fig. 2 Annual mean temperature of northeastern British Columbia with a 10 year moving average. The past two decades have experienced a shift in annual mean temperature to above freezing conditions

weather record of the area spans 1938–2006. The annual total precipitation over this period is approximately 500 mm (40 % snow) and the annual mean temperature is -0.5°C (annual mean maximum and minimum of 5.0°C and -6.3°C , respectively). This is however, locally variable, based on elevation and aspect.

Both precipitation and temperature have increased over the instrumental record. Annual total precipitation has increased by 5.9 % and annual mean temperature by 1.1°C (statistically significant at 90 % confidence). Summer precipitation has increased by 17 %. Significant warming has occurred in the last two decades. Figure 2 plots mean annual temperature for the area with a 10 year moving average. The plot shows that mean annual temperature has shifted to above freezing in the last two decades. Climate conditions in the region are influenced by the Pacific Decadal Oscillation (PDO), in which both the previous cold phase and current warm phase are apparent in the Fort Nelson temperature record (Egginton 2005).

Permafrost

Permafrost distribution is relatively well-documented north of 60°N latitude in Canada. Long-term monitoring of permafrost (summarized by Smith et al. 2005), the development of a Cryosolic Soil Order (Soil Classification Working Group 1998), and pipeline feasibility studies have all occurred in Canada’s territories that lie north of this latitude (Dyke and Brooks 2000). Very few studies on permafrost distribution (Bonnaventure et al. 2012) have been made in BC, although Hasler and Geertsema (2012) have prepared a provisional map to assist resource planning. The need has been realized in that an increase in landslides in northern BC

appears to be, in part, related to permafrost degradation (Geertsema et al. 2006).

The construction of roads and pipelines, have led to the discovery of permafrost in the study area. The presence of permafrost is noted at 18 locations. Permafrost has been observed at elevations as low as 735 m in our study area. We observed permafrost in peat plateaux (palsas), but not in adjacent fens. We also observed permafrost in a fresh landslide scar in a steep north-east facing talus slope, 3 m below the ground surface in September 2008. The distribution of permafrost appears, at best, patchy, but more work is needed.

Landslides

Landslide Classification

Landslide classification remains debated in the literature. The main classifications used in Canada are those of Cruden and Varnes (1996) and Hungr et al. (2001). The problem is to large degree a scale issue. Some properties remain unknown unless the landslide is inspected on the ground and material and rupture surfaces are characterized. For the purposes of this paper we use *landslide* as a generic term for mass movement. *Flow* implies movement with distributed shear surfaces or evidence of liquefaction and extensive remoulding. On aerial photos unvegetated lobes and bowls, narrow transport zones and fans indicate flowing. *Slide* refers to movement along a discrete shear surface. Displaced rafts of standing trees usually indicate sliding, although coherent flakes can sometimes be transported in a flow. In many cases sliding and flowing is evident in the same landslide. They may then be referred to as an *earth slide—earth flow* (Cruden and Varnes 1996) or a *flowslide* (Hungr et al. 2001).

Recent Landslides

Landslides are common in the east half of map sheet 94G. Virtually all the slopes of incised streams and escarpments are landslide colluvium. Landslides occur both in soil and rock and involve sliding (rotational and translational) and flowing. Where landslides involve soil, they usually occur in low plastic cohesive tills and lake sediments with low clast contents, and often in buried valleys (Geertsema et al. 2006). Reactivation and slow creep of colluvial toe slopes is an important process in the area (Larry Dyke and Wendy Sladen, personal communication). Many of the landslides occur on low gradients between 6 and 10° (Geertsema and Cruden 2008).



Fig. 3 Slow movement commonly precedes catastrophic landsliding. Low-gradient landslides usually involve reactivation of older landslides. Movement is evidenced by minor scarps (*arrows*), trees of various ages and tension fractures (*lower image*)

Slow movement preceding more rapid movement is common in the area. Low-gradient landslides usually involve reactivation of older landslides. Years of slow sliding may occur in source areas prior to catastrophic failure. Displacement is evidenced by minor scarps, tension fractures, and trees of various ages (Fig. 3).

Landslides have also occurred on steeper slopes. A recent debris slide—debris flow on Pink Mountain (occurred on a rupture surface at the upper boundary of permafrost). The landslide occurred on a 32, matrix-supported talus slope. The rupture surface, and upper boundary of ice-rich permafrost was 3 m below the pre-slide surface. The total travel distance of the landslide was 260 m.

This Buckingham River area has an unusually high concentration of recent low-gradient landslides for northern BC (Fig. 4). The plotted landslides, shown on a SPOT image, have occurred between 1993 and 2005. The zones of depletion are perched above stream levels—the streams being incised into bedrock, ruling out bank erosion as a trigger. The long runout landslides differ in moisture content and legacies. Two AMS radiocarbon dates of buried wood in a lateral scarp yielded 255 ± 15 ^{14}C yr BP and

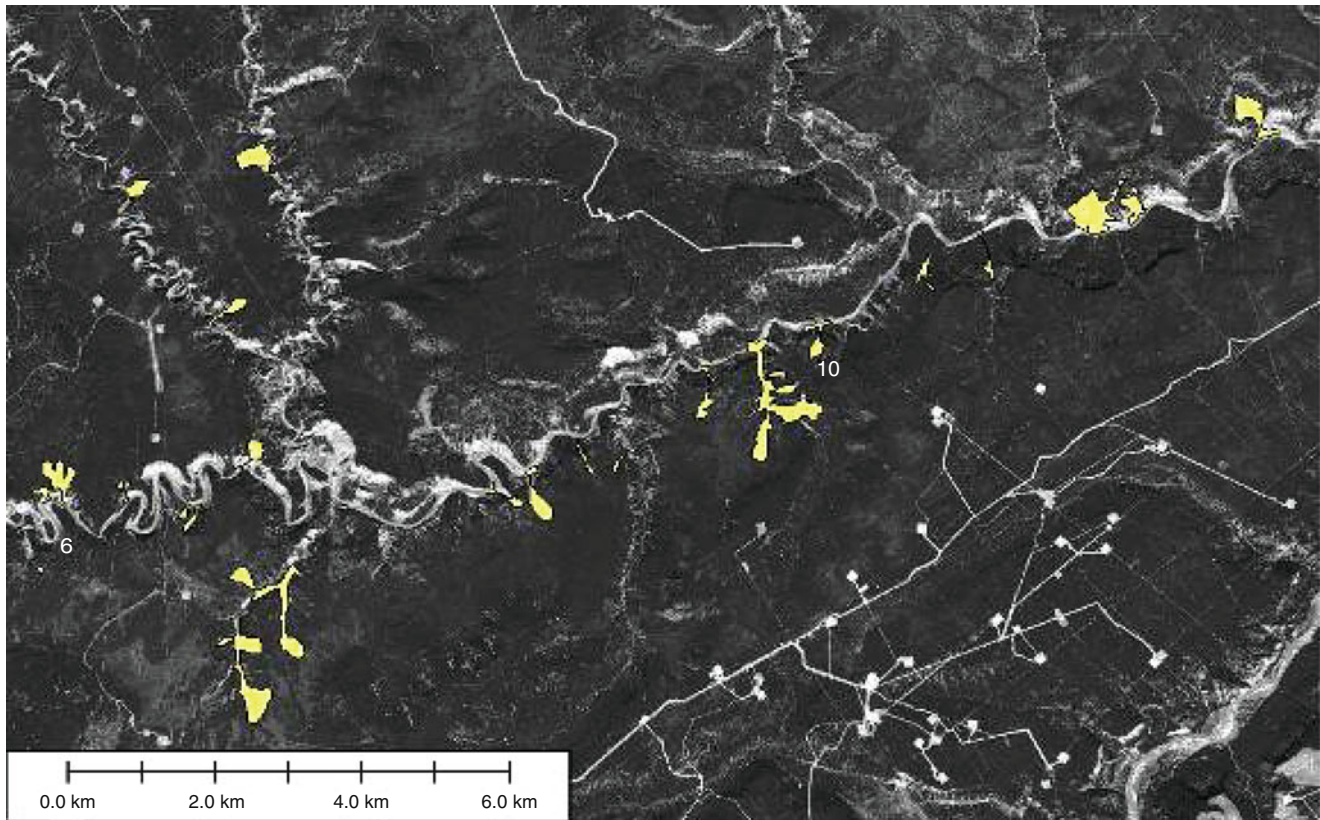


Fig. 4 Long runout landslides (yellow) in the Buckingham River area plotted on a 2004–05 5 m SPOT image. (s5_094g_2004_2005_utm10_5m_pan_enh). The landslides were only delineated if they post-dated a 19 September 1993 Landsat 7 image

$3,780 \pm 15$ ^{14}C yr BP (UCIAMS 23831 and 23832, respectively), confirming the long term movement history of these slopes.

Discussion/Conclusion

Large landslides have been increasing in northern British Columbia in the last decades (Geertsema et al. 2006, 2007). In the east half of map sheet 94G numerous long-runout flowslides have occurred since 1993, especially along Buckingham River. During this period the climate has become wetter, (17 % wetter in summer) and mean annual temperature is now above freezing.

The pattern of slide reactivation starting with shallow failures and progressing to deeper landslides was observed over wide areas, particularly in the 1990s. Around the same time there were also several successive summers of higher than average precipitation (Egginton 2005). However, earlier cycles of higher precipitation had had much less impact on slope stability and so it appears that thawing of permafrost may have been a major factor in the landslide movement patterns.

Recent permafrost degradation has been established as playing a role in increased landslide activity (e.g.

Aylsworth et al. 2000; Dyke 2000; Lewkowicz and Harris 2005; Lipovsky and Huscroft 2007). But earlier cycles of degradation have also been related to landslide activity. For example, post-LIA warming has been associated with increased debris flow activity in the mountains of central and northern Europe (van Steijn 1996). It's possible that a northward and upward moving "front of aggression" of increased landslide activity may occur as permafrost continues to degrade.

References

- Aylsworth JM, Duk-Rodkin A, Robertson T, Traynor JA (2000) Landslides of the Mackenzie valley and adjacent mountainous and coastal regions. In: Dyke LD, Brooks GR (eds) The physical environment of the Mackenzie Valley, Northwest territories: a base line for the assessment of environmental change, vol 547, Geol Surv Canada Bull., pp 167–176
- Bednarski JM (1999) Preliminary report on mapping surficial geology of Trutch map area, northeastern British Columbia. In: Current Research 1999-A, Geological Survey of Canada, pp. 35–43
- Bednarski JM (2000) Surficial geology Trutch, British Columbia. Geological Survey of Canada Open File 3885, Map, scale 1: 250 000

- Bednarski JM (2001) Drift composition and surficial geology of the Trutch map area (94G), northeastern British Columbia. Open File D3815, CD
- Bonnaventure PP, Lewkowicz AG, Kremer M, Sawada MC (2012) A permafrost probability model for the southern Yukon and northern British Columbia, Canada. *Permafrost Periglac Process* 23:52–68
- Catto N, Liverman DGE, Bobrowsky PT, Rutter N (1996) Laurentide, Cordilleran, and Montane Glaciation in the Western Peace River – Grand Prairie Region, Alberta and British Columbia, Canada. *Quaternary Int* 32:21–32
- Clague JJ (1989) Quaternary Geology of the Canadian Cordillera; Chapter 1. In: Fulton RJ (Ed) *Quaternary Geology of Canada and Greenland*, Geological Survey of Canada, No. 1, pp 15–96
- Cruden DM, Varnes DJ (1996) Landslide types and processes. In: Turner AK, Schuster RL (eds) *Landslides investigation and mitigation*. National Research Council, Transportation Research Board Special Report 247: 36–75
- Davies MCR, Hamza O, Harris C (2001) The effect of rise in mean annual temperature on the stability of rock slopes containing ice-filled discontinuities. *Permafrost Periglac Process* 12:137–144
- Demarchi DA (1996) An introduction to the Ecoregions of British Columbia. British Columbia Wildlife Branch, Ministry of Environment, Lands and Parks, Victoria, BC
- Dramis F, Govi M, Guglielmin M, Mortara G (1995) Mountain permafrost and slope stability in the Italian Alps: The Val Pola landslide. *Permafrost Periglac Process* 6:73–82
- Dyke AS, Andrews JT, Clark PU, England JH, Miller GH, Shaw J, Veillette JJ (2001) Radiocarbon dates pertinent to defining the Last Glacial Maximum for the Laurentide and Innuitian ice sheets. Open File report 4120, Geological Survey of Canada
- Dyke LD (2000) Stability of permafrost slopes in the Mackenzie Valley. In: Dyke LD, Brooks GR (eds) *The physical environment of the Mackenzie Valley, Northwest territories: a base line for the assessment of environmental change*. Geological Survey of Canada, Bulletin 547; pp 177–186
- Dyke LD, Brooks GR (eds) (2000) *The physical environment of the Mackenzie Valley, Northwest Territories: a Base Line for the Assessment of Environmental Change*. Geological Survey of Canada, Bulletin 547; 208
- Egginton VN (2005) Historical climate variability from the instrumental record in northern British Columbia and its influence on slope stability. MSc thesis. Simon Fraser University, Burnaby, BC
- Geertsema M, Cruden DM (2008) Travels in the Canadian Cordillera. In: 4th Canadian Conference on Geohazards. Quebec, PQ
- Geertsema M, Clague JJ, Schwab JW, Evans SG (2006) An overview of recent large catastrophic landslides in northern British Columbia, Canada. *Eng Geol* 83:120–143
- Geertsema M, Egginton VN, Schwab JW, Clague JJ (2007) Landslides and historic climate in northern British Columbia. In: McInnes R, Jakeways J, Fairbank H, Mathie E (eds) *Landslides and climate change—challenges and solutions*. Taylor and Francis, UK, pp 9–16
- Gruber S, Haeblerli W (2007) Permafrost in steep bedrock slopes and its temperature-related destabilization following climate change. *J Geophys Res* 112; F02S18, doi: 10.1029/2006JF000547.
- Hasler A, Geertsema M (2012) Provisional permafrost Map of British Columbia. Province of BC. <http://www.env.gov.bc.ca/esd/distdata/ecosystems/Permafrost/PermaFrostModel/>
- Harris C, Davies MCR, Etzelmüller B (2001) The assessment of potential geotechnical hazards associated with mountain permafrost in a warming global climate. *Permafrost Periglac Process* 12:145–156
- Heginbottom JA, Dubreuil MA, Harker PT (1995) National Atlas of Canada, 5th edn, Canada. Permafrost, Plate 2.1, (MCR 4177), 1:7 500 000 scale
- Holland SS (1976) Landforms of British Columbia: a physiographic outline. British Columbia Department of Energy, Mines and Petroleum Resources, Bulletin 48:138
- Huggel C, Clague JJ, Korup O (2012) Is climate change responsible for changing landslide activity in high mountains? *Earth Surf Process Landforms* 37(1):77–91
- Hungry O, Evans SG, Bovis M, Hutchinson JN (2001) Review of the classification of landslides of the flow type. *Environ Eng Geosci* 7:221–238
- Lane LS, Cecile MP, Currie LD, Stockmal GS (1999) Summary of 1998 fieldwork in Trutch and Toad River map areas, Central Forelands NATMAP Project, northeastern British Columbia. In: *Curr Res 1999-E*, Geological Survey of Canada, pp 1–8
- Leibman MO (1995) Cryogenic landslides on the Yamal Peninsula, Russia: preliminary observations. *Permafrost Periglac Process* 6:259–264
- Lewkowicz AG, Harris C (2005) Frequency and magnitude of active-layer detachment failures in discontinuous and continuous permafrost, Northern Canada. *Permafrost Periglac Process* 16:115–130
- Lipovsky P, Huscroft C (2007) A reconnaissance inventory of permafrost-related landslides in the Pelly River watershed, central Yukon. In: Emond DS, Lewis LL, Weston LH (eds) *Yukon exploration and geology 2006*. Yukon Geological Survey, p. 181–195
- MacDonald GM, McLeod TK (1996) The Holocene closing of the ‘Ice-Free’ corridor: A biogeographical perspective. *Quaternary Int* 32:87–95
- Mathews WH (1980) Retreat of the last ice sheets in northeastern British Columbia and adjacent Alberta. *Geol Surv Canada Bull* 331:21
- Meidinger DV, Pojar JJ (1991) *Ecosystems of British Columbia*. BC Ministry of Forests, Special Report Series 6:330
- Smith SL, Burgess MM, Riseborough D, Mark Nixon F (2005) Recent trends from Canadian permafrost thermal monitoring network sites. *Permafrost Periglac Process* 16:19–30
- Soil Classification Working Group (1998) *The Canadian system of soil classification*. Agriculture and Agri-food Canada publication 1646 (Revised). 187 pp
- van Steijn H (1996) Debris flow magnitude-frequency relationships for mountainous regions of Central and Northwest Europe. *Geomorphology* 15:259–273



Cryogenic Landslides in Paragenetic Complexes of Slope and Channel Processes in the Central Yamal Peninsula

Anatoliy Gubarkov and Marina Leibman

Abstract

The paper discusses development of a number of cryogenic and channel processes as well as their paragenetic complexes. In small river basins these complexes form (a) landslide-affected slopes and landslide cirques, (b) river valleys. Up to half of the small river basins' area in the upstream is subject to cryogenic processes. The vast majority (80 %) of these processes are cryogenic landslides. Other slope processes are interconnected to cyclicity of cryogenic landsliding. They appear between the landsliding cycles, lasting 200–400 years. Cryogenic landsliding within a paragenetic complex of processes is a leading and fast process. Between the active phases of cryogenic landsliding, thermoerosion and thermokarst develop. These processes can be considered accompanying slower processes.

Lowering of the surface per landsliding cycle is on average 0.9 m in the upper part of the slope and up to 1.6 m in the lower part. This corresponds to the surface denudation of 4–6 mm per year. Subsequent processes of thermoerosion and thermokarst are responsible for lowering of the surface to significantly higher degree (0.6–1.05 m).

Keywords

Paragenesis of processes • Cycle of processes • Cryogenic landslides • Thermoerosion • Landslide cirque • River valley • River channel processes

Introduction

Cryogenic landslides in the Central Yamal Peninsula are one of the most common processes (Ananieva 1997; Baulin et al. 1996, 2003; Baranov and Posnanin 1999; Leibman et al. 2003). There are cryogenic landslides of shearing and flowing mechanisms named accordingly (Kaplina 1965; French 1998; Lewkowicz 1990; Harris and Lewkowicz 1993; Leibman et al. 2003).

The majority of cryogenic processes are characterized by relation to one or more associated processes (Ershov et al. 1989; Washburn 1979). In the upper reaches of small rivers slope processes are the most common. One of those is cryogenic landsliding which leads to the formation of landslide cirques (Leibman et al. 2003).

Cryogenic landslides in the central Yamal are one of the most common processes. A large area of slope surfaces is influenced by landslides along with other cryogenic processes. The closest paragenetic relations exist between the cryogenic landslides and thermoerosion (Gubarkov and Leibman 2007). Immediately after the cryogenic landslide event melting of ground ice and the formation of a new active layer start. Against this background, the activity becomes erosional and thermoerosion of thawed permafrost is activated by water flows, generated by rainfall and snow-melt. Observations show that erosion/thermoerosion of the shear surfaces formed after the last extensive cryogenic

A. Gubarkov (✉)
Tyumen State Oil-Gas University, Volodarskiy str., 38, 625000
Tyumen, Russia
e-mail: agubarkov@rambler.ru

M. Leibman
Siberian Branch, Russian Academy of Sciences, Earth Cryosphere
Institute, Malygin Street, 86, Tyumen 625000, Russia
e-mail: moleibman@mail.ru

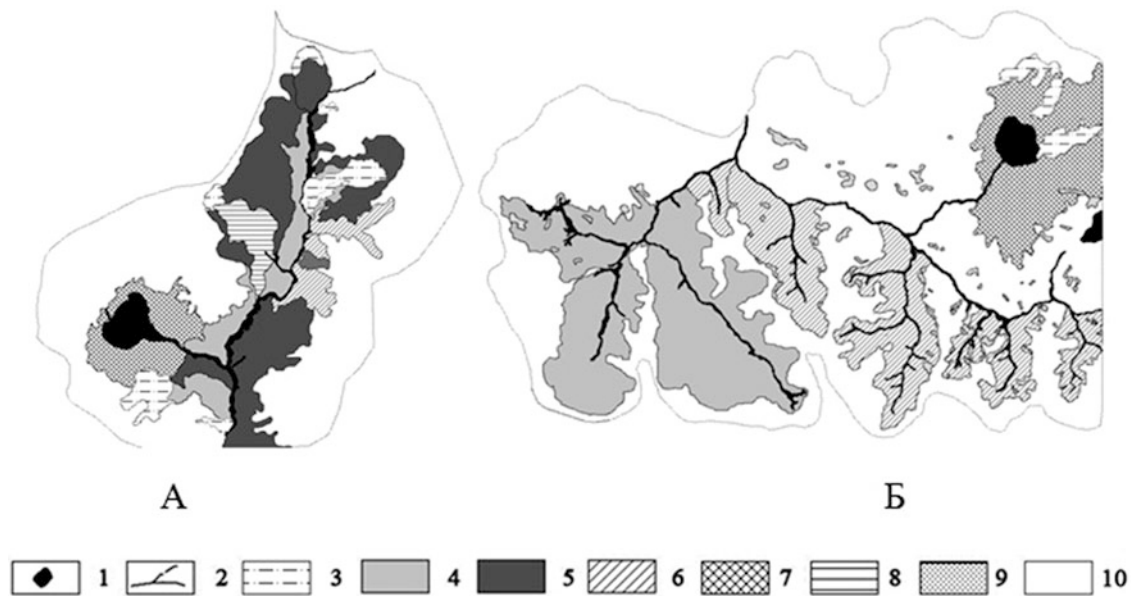


Fig. 1 Upper reaches of the Panzanana-yakha (a) and Halmer-yakha (b) river basins. Key: 1—lakes; 2—permanent and temporary streams; 3—modern cryogenic landslides; 4—middle aged cryogenic landslide

surfaces; 5—ancient cryogenic landslide surfaces; 6—ravine network; 7—hasyreis; 8—outlier without active denudation; 9—areas of deflation; 10—watershed area

landsliding in 1989, have continued for more than 20 years, as they are unevenly and slowly re-vegetating (Ermokhina 2009).

It is known that cryogenic landslides are cyclical and take place once between 200 and 400 years, an average of 300 years (Leibman et al. 2003). Each landslide cycle is accompanied by erosion/thermoerosion which leads to the formation of landslide cirques of different size and depth. With the increase of the number of cryogenic landsliding cycles on the same surface, the depth of landslide cirques increases. Sequential impact of cryogenic landsliding and thermoerosion on the slopes leads to a certain surface denudation. The depth of the concavity depends on the geomorphic level and geocryological conditions.

Cryogenic Landsliding in the Basins (Valleys) of the Small Rivers

Most of the slopes in the valleys of small rivers with headwaters on the III–V marine terraces were formed by paragenetic complexes of cryogenic and hydrological processes (Gubarkov and Leibman 2010). Most often, the leading slope process in the formation of the valleys is cryogenic landsliding. Cryogenic landslides belong to the rapid exogenous processes (Sukhodrovsky 1979; Leibman et al. 2003). Speed of the landsliding on the same territory is high as compared to the phases that separate them. Slow processes are also involved in the denudation of the surface that was exposed by cryogenic landslide. Only a certain combination

of factors can prepare the next cycle of cryogenic landsliding. The main processes between cycles of landsliding are mud flows and thermoerosion, while in case of exposure of tabular ground ice this is termodenudation.

Dokuchaev (1878) was the one to draw attention to the change in the width of river valleys in Russia. At present the main causes of changes in the river valleys have been established (Simonov 1972; Karasev and Khudyakov 1984). The following factors are the leading ones: tectonic, glacial, landfall and accumulative. The impact of cryogenic processes on change of the river channel width in the Yamal Peninsula is mainly noted in their upper reaches (Baulin et al. 2003 and others).

In the upper reaches of the rivers originating on the high geomorphologic levels (marine terraces) the cryogenic slope processes, such as cryogenic landslides, became dominant. The cryogenic landslide bodies enter the riverbeds, cover them and, in some cases, part of the valleys of small rivers as well. When the stream water is dammed, ponds are formed with heavily processed shores, which leads to the widening of the bottom of the river valley. Since the study area is located in the zone of continuous permafrost, expansion of river valley is also due to thermokarst accompanied by local slope processes.

In the upper reaches of Panzanana-yakha and Halmer-yakha rivers the valleys are shaped by a number of cryogenic processes (Fig. 1). Thus, the area of cryogenic landslides on the Panzanana-yakha river make up 39 %, on the Halmer-yakha river 18 %, on hasyreis and lakes 7 and 8 %, in each valley respectively, in thermoerosion ravines 4 and 11 %. On

Table 1 Number of site, cross-section and morphometric characteristics of the Panzanana-yakha river valley

No. of site	No. of cross-section	Distance from the river source (km)	Width of the river valley bottom (m)
1	1–3	0.2	3.7
2	3–7	0.6	17.6
3	7–9	0.9	5.7
4	9–14	1.1	11.0
5	14–18	1.7	25.1
6	18–21	2.0	18.9
7	21–22	2.1	11.9

the edges and upper parts of slopes in the Halmer-yakha valley sandy hollows result from deflation (2 % coverage), which is absent in the upper reaches of the Panzanana-yakha river. The rest of the area of the valleys belongs to the flat surface and slightly sloped watershed areas without active cryogenic processes (50 and 61 %). Area ratio shows that the number of cryogenic landslides is the largest within surfaces of upstream river basins subject to cryogenic processes.

Research of the valley banks in the upper reaches of the rivers showed that their formation is highly dependent on time, frequency and place of cryogenic landslide location. Field and remote-sensing data indicate that cryogenic landslide shear surfaces could be divided into three groups: ancient, old, and modern. The oldest surfaces in the study area are under the age of 1800–2200 years (Leibman et al. 2003). Cryogenic landslide surfaces ratio is distributed as follows. The ancient surfaces in the valley of Panzanana-yakha river occupy 61 % of the total area of cryogenic landslides, in the Halmer-yakha river valley they are absent; old surfaces occupy 25 and 92 %, modern—14 and 8 %, respectively.

In the valleys of the rivers under study distribution of the surface area controlled by cryogenic processes is very different. Leading process in the valleys of both rivers are cryogenic landslides. Area and length of the ravine system in the Halmer-yakha river valley are increasing, indicating a more active thermoerosion as compared to the Panzanana-yakha river valley. The significant specific feature of the upper reaches of the Halmer-yakha river is deflation, mainly distributed in edge part of ravine network in the form of local windblown sand hollows.

According to the results of high-resolution satellite imagery interpretation for Panzanana-yakha river valley in the upstream, the width of the valley bottom has been measured every 100 m from the source to the middle reaches of the river at every point. Analysis of the data showed that the bottom, depending on one or several principal and related cryogenic processes could be divided into seven sites (Table 1).

Depending on the intensity, sequence and duration of the cryogenic processes the width of the river bottom changes.

Table 2 The average depth (m) of the of landslide cirque bottoms for 1 landslide cycle

Number of cycles	Period (years)	Cross-section		
		Upper	Middle	Lower
3	600–1200	–1.17	–1.27	–1.30
5	1000–2000	–1.14	–1.24	–1.90
Average	200–400	–1.15	–1.25	–1.60

Table 3 The average denudation (mm) for different number of cycles of landsliding and thermoerosion

Number of cycles	Period (years)	Cross-section		
		Upper	Middle	Lower
3	600–1200	–3.9	–4.2	–4.3
5	1000–2000	–3.8	–4.1	–6.3

On the sites with cryogenic landslides the width of the river valley narrows by 2–3 times compared to the dammed by cryogenic landslides and flooded areas. Unlike Panzanana-yakha river, there are no dammed water bodies in the bottom of the Halmer-yakha river valley, which results in minor differences in the width of the bottom along entire river channel.

High activity of cryogenic landsliding and accompanying paragenetically related processes leads to increased turbidity of the water flows, most clearly seen in the middle and lower reaches of the river. In the middle reaches there is a sharp decrease of turbidity compared to the upstream. Maximum turbidity in the upper reaches for the observation period was in 2007 (5,120 g/m³, Table 2), while in the middle reaches it did not exceed 3 g/m³ and increased up to 33 g/m³ towards the river mouth. Similar relations were observed in the previous years of observation.

Table 3 shows the total volume of rocks involved in the sediment runoff in the Panzanana-yakha river basin over 4 years of observation, during the predominance of slow cryogenic processes between active phases of cryogenic landsliding. It suggests that, all types of processes in the valley move around 80 m³ of deposits per year.

During the cryogenic landsliding one landslide alone in the valley is able to move ten times more material from the slopes into the river bed. In 1989, the volume of the largest landslide in the Panzanana-yakha river valley was 6,000 m³, which is 75 times greater than the total annual solid runoff during the entire period between landslide cycles. In the same year the landslide volume in the Halmer-yakha river valley was about 800,000 m³, which is more than 10,000 times greater than the average annual sediment runoff. Such volumes of sediment yield from the riverbed by the water flows last for a long time. In fact, the river channel runs at a new level that is several meters higher than the previous level.

Cryogenic landslides form dammed lakes that exist for years and increase the time of water exchange in small rivers

up to 10 times (Gubarkov and Leibman 2010). Thus, even a single cryogenic landslide can regulate the water flow of small watercourses for several or dozens of years.

During the existence of “dams”, the dammed lakes accumulate different amounts of material from ravine network. This amount depends on the lifetime of the “dam” and amount of suspended matter yielded into the dammed lake. After breaking of the “dam” the entire layer of accumulative sediment is not eroded at the bottom of the dammed lake. The remaining sediment forms steps in the channel, which being vegetated become resistant to erosion. In the upper reaches of the Panzanana-yakha river there were 7 vegetated steps and 3 newly formed that were non-vegetated as yet. Height of the formed steps increases downstream from 1.2 to 1.9 m. This is due to a combination of factors, ranging from the source to the middle reaches of the river. Increase in the height of steps downstream to the boundary between upper and middle reaches of the river is connected to the new manifestations (which have appeared for the first time) of thermokarst along the river channel. Height difference occurs with the formation of hydraulic height and the removal of washed out sediment. A significant factor in the formation of steps are temporary or permanent streams flowing into the mainstream at the step toe. They provide higher removal of sediment, additional income of turbulent heat in the lower part of the step, standing water in the hydraulic jump, and have a warming effect on permafrost.

Studies have revealed the relationship between cryogenic and hydrological processes affecting small river valleys in the upper reaches and determining their morphometric and hydro-morphometric characteristics. From the combination of slope cryogenic manifestations (especially landslides and thermoerosion) the upper reaches of small rivers are characterized by the complex relationships. This results in complexes of cryogenic landforms and channel forms, united in a system of paragenetic complexes.

Study of Landslide Shear Surfaces

Because of cryogenic landsliding, subsequent erosion and thawing of ground ice at the formation of a new active layer cause subsidence of the surface to a certain degree. Figure 2 shows the shear surface and the depth of erosion troughs within, for a different number of landsliding cycles. Initial landslides on the surfaces not exposed to cryogenic landsliding earlier, are up to 1.8 m deep against the undisturbed slope surface. The depth of thermoerosion trough does not exceed 0.2 m.

Landslides embedded into each other with the formation of a landslide cirque are examined on the example of one of the landslides on the bank of the Panzanana-yakha river. On the satellite image one can see three shear surfaces that are

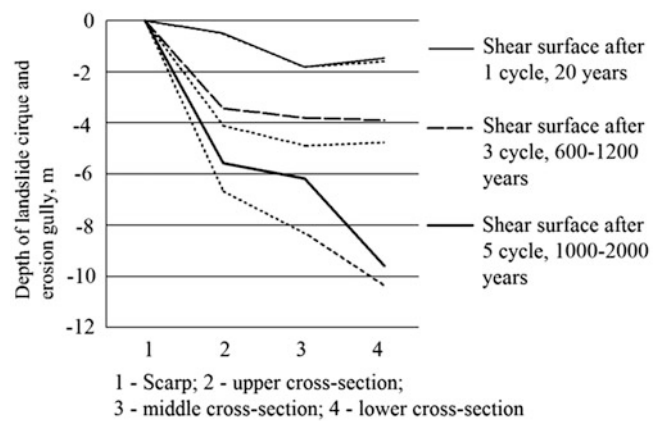


Fig. 2 Relation of the depth of shear surfaces to a number of landslide and erosion cycles in the landslide cirques

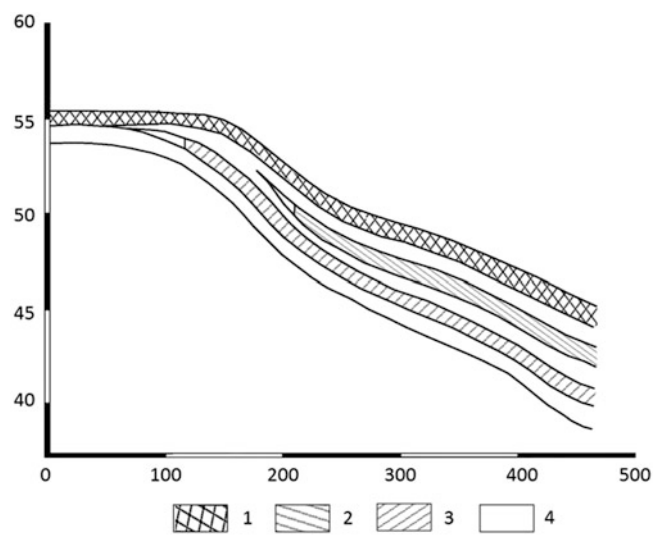


Fig. 3 Landslide and erosion cycles in the landslide cirque in the Panzanana-yakha river valley. Key: 1, 2, 3—900, 600, 20 year old landslide cycles, respectively; 4—erosion cycles separating landslide cycles

different in age. Their width is slightly different and the length varies significantly (Fig. 3).

As a result of the three landslide cycles and the same number of erosion cycles overall, the lowering of the surface amounts to 4.2 m, which means that each landslide and erosion cycle lowers the surface to 1.2–1.3 m over a period of 200–400 years (Leibman and Kizyakov 2007). Surface which underwent at least 5 cycles of landsliding is lowered by 9.5 m, i.e., each landslide cycle deepened it by 1.9 m. It is possible that the additional lowering of this surface was due to thermokarst, thawing of ground ice and subsequent subsidence.

Depths of landslide cirques and the number of landslide cycles (according to Leibman and Kizyakov 2007; Gubarkov and Leibman 2012) allows calculating the value

of the surface lowering in time intervals that make up these cycles (200–400 years). Compared were upper, middle and lower cross-sections of a landslide cirque given 3 or 5 landslide cycles (Table 2).

There is little difference in the rate of surface lowering for all cross-sections in a 3-cycle case ranging between 1.17 and 1.30 increasing from upper to lower cross-section (see Table 2). Given a 5-cycle case, the range of lowering depths is 1.14 to 1.90. Such an increase in the lowering rate for the lower cross-section may be associated with intense thermokarst.

Measurements of thickness of 156 landslide bodies at the site “Vaskiny Dachi” showed that each landslide cycle is responsible for 0.3 to 1.0 m, averaging 0.55 m lowering of the landslide cirque surface. Therefore, its lowering due to erosion and thermokarst subsidence has an average range of 0.6 m in the upper part of the slope and 1.05 m in the lower part (Table 2). Cryogenic landsliding triggers other processes that produce thermodenudation of the same intensity in the upper cross-section and twice as intensive in the lower cross-section.

The averaged value of surface lowering through alternating the main paragenetically associated slope cryogenic processes for three to five landslide cycles is 3.8–6.0 mm per year (Table 3). Middle and lower parts of the slopes have a greater potential of lowering compared to the upper part of the slope. The values obtained are close to the estimate of denudation obtained by Voskresenskiy (2001) for the Arctic Plains, which he estimated to be 6 mm per year.

Cryogenic landslides change the slope topography. It is the landsliding and subsequent lowering of the shear surface due to the erosion and thermokarst that create conditions for increased snow accumulation, which leads to an increase in the depth of the active layer. Seasonal thawing is increased due to the warming action of water dammed by landslide bodies in summer. In reservoirs dammed by landslides, there is thermokarst subsidence. In gullies and ravines, cut deep into the the shear surfaces of cryogenic landslides we observe increased snow accumulation, which prevents freezing in winter, but also contributes to the increased thawing in the summer (Voskresenskiy 2001). In addition, the gullies and ravines experience a temporary warm influence of runoff in summer during the rainfall.

Measurements of the active layer on the shear surfaces of cryogenic landslides, erosion network and on the adjacent undisturbed surface were conducted on 6 landslide shear surfaces. Measurements were carried out along the profiles shown on Fig. 1. The average depth of the active layer on the shear surfaces exceeds the depth of active layer at the adjacent undisturbed surface by 43 %. Erosion network on the shear surface increases the depth of thawing by additional 10 %. The maximum difference in the depth of thaw is noted in the middle cross-section of the shear surfaces, where it

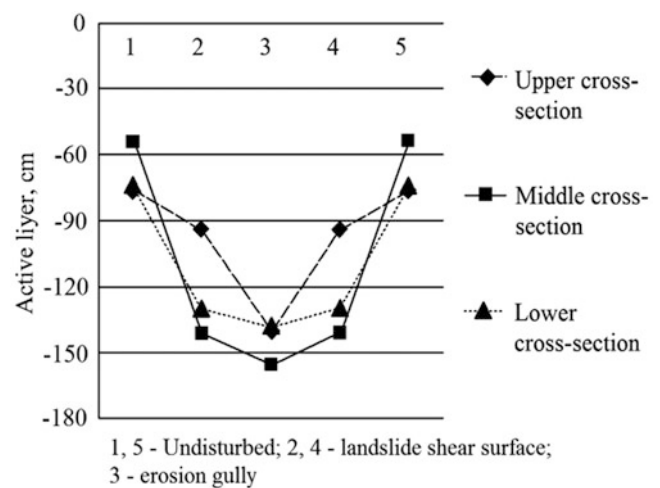


Fig. 4 Averaged active layer depth on the shear surfaces of cryogenic landslides, in ravines and adjacent undisturbed surface in a landslide cirque with three cycles of landsliding

may be two or more times deeper (Fig. 4). Given the warming impact in areas of erosion or damming of water, thawing can increase up to three times compared to the adjacent undisturbed surface.

Wider landslides or landslide cirques would allow snow redistribution from central parts towards the scarp and side walls where increased snow accumulation may be observed. In such cases, we observe the maximum thaw near the scarp and side wall foot.

Conclusions

Main factors of landslide cirque formation are cryogenic landslides, thermoerosion and thermokarst. The rate of processes varies. Cryogenic landsliding is a rapid process, thermoerosion has an active phase and gradually slows down, and thermokarst belongs to the slow cryogenic processes.

Denudation in the formation of landslide cirques by various cryogenic processes consists of two components. The first process is the cryogenic landsliding, the contribution of which is about half of the total lowering of the surface in the upper part of the slope and about a third in the lower. Subsequent processes are thermoerosion and thermokarst, which lower the surface even more.

Lowering of surface in the landslide cirques per a landslide cycle (200–400 years) on the average affects 0.9 m in the upper part of the slope and up to 1.6 m in the lower part. This corresponds to the denudation of 4–6 mm per year.

Acknowledgments This study was supported by the Interdisciplinary Integration Grants No. 122 and No. 144 of the SB RAS, Science School Grant #5582.2012.5, and RFBR Grant #13-05-91001-AHΦ_a to the Earth Cryosphere Institute SB RAS.

References

- Ananieva GV (1997) Especially engineering permafrost northern segment of the projected route of the railway Ob-Bovanenkovo. In: Results of basic research of the Earth Cryosphere in the Arctic and Subarctic. Nauka, Novosibirsk, pp 116–123 (In Russian)
- Baulin VV, Aksenov VI, Dubikov GI et al (1996) Engineering-geological monitoring of Yamal oil- and gas-fields. In: VII. Geocryological conditions of Bovanenkovsky gas-fields assimilation. IPOS SO RAN, Tyumen, 240 pp (In Russian)
- Baulin VV, Dubikov GI, Aksenov VI et al (2003) Permafrost conditions Harasavey and Kruzenshternovsky gas condensate fields (Yamal Peninsula). Geos, Moscow, 180 pp (In Russian)
- Baranov AV, Posnanin VL (1999) Thermoerosional processes. In: Erosion processes of Central Yamal. Gomel, St. Petersburg, pp 176–188 (In Russian)
- Dokuchayev VV (1878) Ways of formation of river valleys of the European Russia. St. Petersburg, 127 p (in Russian)
- Ermokhina KA (2009) Phyto-indication of exogenous processes in the tundras of Central Yamal. Dissertation. Moscow University, Moscow, 24 p (In Russian)
- Ershov ED et al (1989) Geocryology of the USSR. Western Siberia. Nedra Publisher, Moscow, 454 p (in Russian)
- French HM (1998) Permafrost, real estate and climate change: the case of Thompson. Northern Manitoba. Biuletyn Peryglacjalny, Canada, pp 35–44
- Gubarkov AA, Leibman MO (2007) Erosion processes on the share surfaces of cryogenic landslides: a case study at Vaskiny Dachi Station. In: Proceedings of the international conference “cryogenic resources of polar regions”, Salekhard, Russia, June 2007 II, pp 136–138 (in Russian)
- Gubarkov AA, Leibman MO (2010) Bead-shaped channel forms as an evidence of paragenesis of cryogenic and hydrological processes in the small-river valleys of central Yamal. Kriosfera Zemli (The Earth Cryosphere) XIII(1):41–49, In Russian
- Gubarkov AA, Leibman MO (2012) Cryogenic and hydrological processes in the small-river valleys of Central Yamal. In: Processes of self-organization in erosion-channel systems and dynamics of river valleys. Tomsk. <http://www.channel2012.ru/congeo.htm> (In Russian)
- Harris C, Lewkowicz AG (1993) Micromorphological investigations of active-layer detachment slides, Ellesmere Island, Canadian Arctic. In: Proceedings of the 6th international conference on permafrost, South China University of Technology Press, Beijing, China, pp 232–237
- Kaplina TN (1965) Cryogenic slope processes. Nauka Publisher, Moscow, 296 p (In Russian)
- Karasev MS, Khudyakov GI (1984) River systems: on the example of the Far East. Nauka, Moscow, 143 pp (In Russian)
- Leibman MO, Kizyakov AI (2007) Cryogenic landslides of the Yamal and Yugorsky Peninsulas. Earth Cryosphere Institute SB RAS, Moscow-Tyumen, 206 p (in Russian)
- Leibman MO, Kizyakov AI, Sulerzhitsky LD, Zaretskaya NE (2003) Dynamics of the landslide slopes and mechanism of their development on Yamal peninsula Russia Permafrost. In: M Phillips, SM Springman, LU Arenson (eds) Proceedings of the 8th international conference on permafrost, Zurich, 21–25 July 2003. Balkema, Lisse, pp 651–656
- Lewkowicz AG (1990) Morphology, frequency and magnitude of active-layer detachment slides, Fosheim Peninsula, Ellesmere Island, N.W.T. In: Proceedings of the 5th Canadian permafrost conference, Quebec, June 1990. Edited by M.M. Burgess, D.G. Harry, D.C. Segó. Laval University, Quebec, Collection Nordicana No. 54, 1990, 111–118
- Simonov YG (1972) Regional geomorphological analysis. Nauka, Moscow State University, Moscow, 252 pp (In Russian)
- Sukhodrovsky VL (1979) Exogenous transformation of relief in the permafrost zone. Nauka, Moscow, 280 pp (In Russian)
- Voskresenskiy KS (2001) The modern relief-forming processes on plains of the Northern Russia. Moscow State University, Moscow, 264 (In Russian)
- Washburn AL (1979) Geocryology: a survey of periglacial processes and environments. E. Arnold, London, 406 p



The Impact of the Shrub Roots on the Stability of Soil Cut Slope in Seasonal Frozen Regions

Ying Guo, Wei Shan, Hua Jiang, and Zhaoguang Hu

Abstract

In seasonal frozen regions of Northeast China, soil cut slope along the highway instability often occurs during the spring period of snow melt, which seriously affected the safety of highway operations. The protection methods of planting shrubs such as *Amorpha fruticosa* (AF) and *Lespedeza sp.* (LP) are better than other engineering protection methods. A comprehensive study on the shrub protection on the cut slope is carried out by combining results of on-site monitoring and testing, indoor laboratory and finite element numerical simulation. The study results show that: the shrub roots could reduce soil moisture in the shallow slope largely by root absorption of water, leaves transpiration, which can reduce the loss of soil shear strength during the spring period of snow melt. At the same time, shrub roots could improve the shear strength of slope soil body effectively, because the roots could form a root-soil body, and thus enhance the slope stability. Using soil physical and mechanical parameters obtained from field monitoring and laboratory tests, finite element simulation verified the correctness of our analysis results.

Keywords

Soil slope • Landslides • Root-soil body • Freeze-thaw • Soil moisture

Introduction

Heilongjiang province is located in the most northern area of China, from N43.5° to N53.5°, across nearly 10 latitudes, its total distance reaches 1,200 km from the southern to the northern. The annual average temperature is $-4.6\text{ }^{\circ}\text{C} \sim 4.0\text{ }^{\circ}\text{C}$, and the temperature difference between its north and its south areas is nearly $9\text{ }^{\circ}\text{C}$. Since 2008, the new highway passes through 3,042 km in Heilongjiang Province, and the total length of it is 4,000 km. During the construction of the highway, there were large numbers of soil cut slopes because of the excavation mountains. These slopes are often unstable

and slumping occurs, especially in the spring during melting and the rainy summer. This is because the cut slopes are newly exposed to the natural environment, and affected by precipitation and freeze-thaw cycles. This slope instability threatens the safety of highway operations, and destroys the landscape along the highway. In order to solve this problem, many slope protection methods are adopted, such as stone pitching, reinforced concrete anchors, geonet and so on, but none of them is entirely satisfactory. According to our survey, we find that the slopes planted with naturally-growing shrubs have a better performance.

At present, there is little study on freeze-thaw instability of cut slopes and its protection measures. In China, the study of frozen slopes is mainly on the Qinghai-Tibet Plateau permafrost regions (Zhou and Guo 1982; Jin 2004; Li et al. 2003). There are many differences for cut slope failure mechanism between high latitude frozen regions in Northeast China and high altitude frozen regions in Qinghai-Tibet Plateau. Frozen regions in Northeast China have obvious

Y. Guo (✉) • W. Shan • H. Jiang • Z. Hu
Northeast Forestry University, Hexing Road No. 26, Harbin 150040,
China
e-mail: samesongs@163.com; shanwei456@163.com;
jianghua3433@163.com; huzhaoguang008@163.com



Fig. 1 Study area and study section

seasonal characteristics because of its air temperature and repeated freeze-thaw cycles.

There are many studies on the reinforcement mechanism of shrubs, such as laboratory simulation (Deng et al. 2007), absorption of water model for plant roots (Ji et al. 2006), and mechanical models of root-soil (Cheng et al. 2006), but none of them have considered the influence of freeze-thaw cycles.

The main reason for shallow landslides on soil cut slopes is, during the freezing period, the water in the soil is transferred to the freezing front, resulting in greatly increased water content in shallow slopes. The association and arrangement among soil particles is changed after frost heaving in subzero temperatures, and the mechanical properties of the soil changed also (Liu et al. 2011; Guo and Shan 2011). In the spring melting period, the frozen layers in shallow slopes are thawed, which are influenced by many factors such as precipitation, increasing temperature and so on. The melting water is prevented from infiltrating by the frozen layer underneath, resulting in a rapidly increasing water content in the layer above the frozen layer, reaching a saturated or over-saturated state. This results in the effective stress reduction within the slope and then part or all of the shallow slope slides down along the “water saturation layer” under gravity (Niu et al. 2004).

Relying on the highway expansion project of TongSan Highway from Jiamusi to Harbin, the study area is located on the side of a widening area from K560 + 090 to K565 + 690 (Fig. 1). The terrain graph fluctuation of the study area is bigger, average height of the cut slopes is 5–15 m, and average ratio of the slope is 1.5–1.75. The soil is sandy clay, and its natural density is 1.8 ~ 2.1 g/cm³. The climate of this region is continental monsoon climate of middle

medium latitudes, and it is characterized by shorter summers and longer winters. Average annual precipitation is 570 mm, which is concentrated from June to September. The average temperature in January is –19 °C, and in July is 23 °C. The maximum freezing depth is 1.8 m ~ 2.2 m.

In this paper, through means of a digging pit and sampling, soil physical parameters of different depths in different slope-turf slope or shrub slope are obtained. Through laboratory test, soil mechanics indicators are obtained. Stability factor for turf slopes and shrub slopes are calculated by finite element analysis. Combining these comprehensive analyses, the impact of the shrub roots of on the stability of a soil cut slope is obtained.

Soil Physical Parameters Along the Cut Slope Depth

Two study sites are selected, one is in the K560 +700 (Site A, height 5.6 m, slope ratio 1.75) with planting turf (TU), another is in K563 +870 (Site B, height 15.3 m, slope ratio 1.75) with planting *Lespedeza* sp. (LP). Three pits with 240 cm depth are dug in the middle part of Site A, top and middle of Site B (Site B-1, Site B-2), soil natural density and soil moisture every 20 cm depth in each pit are measured, then dry soil density and permeability coefficient (Per. Co.) in different depth are obtained in a laboratory test (Fig. 2a–d). Basic physical parameters of the soil are shown in Table 1.

It can be seen from the curves that there is a difference between the TU slope and LP slope within 30–140 cm depth in dry soil density, moisture, and permeability coefficient

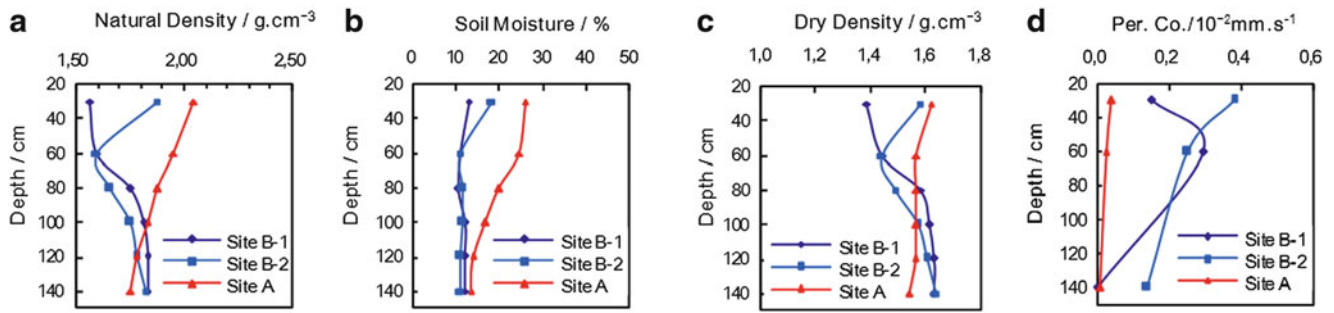


Fig. 2 The curves for soil physical parameters at depth in TU slope and LP slope[(a) Natural density; (b) Moisture; (c) Dry density; (d) Permeability coefficient (Per. Co.)]

Table 1 Basic physical properties of silty clay

Liquid limit (%)	Plastic limit (%)	Plasticity index	Maximum dry density (g/cm ³)	Optimum water content (%)
32.5	18.7	13.8	1.90	13

(Per. Co.). The reason for it is because of freeze-thaw action and plant roots: field test found that the roots of turf are mainly within 30 cm depth, the roots of LP are within 140 cm, the lateral roots are within 60 cm, and the main roots are within 100–140 cm. So the shrub roots could reduce soil moisture on the shallow slope more than turf roots and by root water absorption and leaves transpiration, and at the same time, they could increase soil permeability by roots distribution in the soil.

The Impact of Plant Roots on the Moisture of Slope Soil

In order to verify the impact of root water absorption on soil moisture, from February to May in 2008, we compare the slope soil moisture test between *Amorpha fruticosa* (AF) slope, *Lespedeza sp.* (LP) slope and turf (TU). The method used is digging pit and sampling it every 10 cm, and then measuring soil moisture on-site. The pit depth is 180 cm. The pits of AF slope are in middle of the slope located K562 +725–K562 +750. The pits of TU slope are in middle of the slope located K563 +800–K563 +820. The pits of LP slope are in middle of the slope located K563 +840–K563 +865. The test results are shown in Fig. 3.

Figure 3a–c is soil moisture curve of three plants, three moisture curve measured on different dates and an average value curves (av.) of all three. The av. Curve shows some inflection points along the depth. In Fig. 3a, the first inflection points in av. curve is 20 cm in depth (moisture 12.89 %), the second is 70 cm in depth (moisture 14.53 %), and the third is 90 cm in depth (moisture 17.83 %). In Fig. 3b, the first is 10 cm in depth (moisture 13.52 %), the second is 60 cm in depth (moisture 10.75 %), and the third is 100 cm in

depth (moisture 16.33 %). In Fig. 3c, the first is 20 cm in depth (moisture 23.72 %), the second is 40 cm in depth (moisture 20.95 %), and the third is 50 cm in depth (moisture 22.27 %). The fourth is 70 cm in depth (moisture 20.34 %). The fifth is 80 cm in depth (moisture 22.34 %). The sixth is 90 cm in depth (moisture 20.10 %). In Fig. 3a–c, inflection points of soil moisture always appear within 10–20 cm in depth no matter which plant is on the slope. This moisture wave is caused by evaporation in shallow slopes.

Putting the av. curves of LP, AM and TU in Fig. 3d, within the range of 70 cm depth, the mean moisture in LP slope (14.39 %), AM slope (13.69 %) is lower than that in TU slope (21.78 %) significantly. Three mean moisture curves become close from 70 cm depth, and are parallel substantially from depths of 100cm. The average soil moisture of LP slope, AM slope, and TU slope within 70–100 cm depth are: 17.43 %, 15.30 %, 20.99 %, within 100–180 cm depth are: 17.75 %, 17.09 %, 18.29 %.

Figure 3 shows: (1) Because the main root and most lateral roots of LP and AM distributed in 0–100 cm depth, the roots could reduce the soil moisture within 0–100 cm depth. (2) For root absorption of moisture, and leaves transpiration, AMs better than LP, as turf is minimal in contribution to the moisture reduction in the shallow slope.

Moisture Migration During Soil Freezing and Thawing

In Fig. 3d, there are some waves in soil moisture curves, and the reason is ice segregation and moisture migration during the freezing process. In the pit, we found fragments of frozen fringe (shown in Fig. 4a), ice segregation in the frozen soil cracks, and ice lenses (shown in Fig. 4b).

In the process of freezing or thawing, soil pore water, and capillary water could move directly under a certain temperature gradient. This would rearrange soil particles again and form ice, in the form of layers, bands or veins, called ice segregation. When water encountered frozen ice during segregation, “cementing ice segregation” will occur, and will

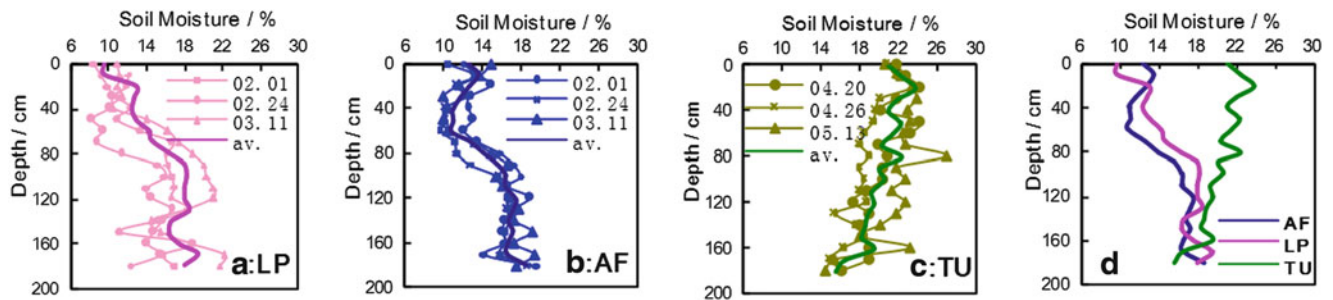


Fig. 3 The soil moisture curve in the slope (Feb. ~ May. in 2008) [(a) LP slope; (b) AF slope; (c) TU slope; (d) Average value of moisture]

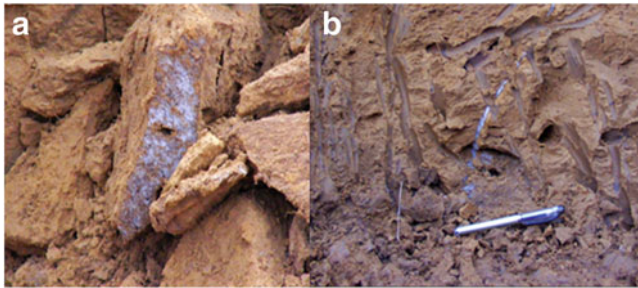


Fig. 4 (a) Fragments of frozen fringe; (b) Cracks segregation-ice and ice lenses

form a block-like cold structure referred to as ice lenses. The process of soil freezing and thawing is the process of heat transferring: in soil freezing process, when the temperature of soil particles drops to a certain degree, the latent heat of soil pore water releases completely, and water begins to turn into ice crystals, or wrap soil particles, forming a cementation body. Unfrozen water will move from the area of higher temperature to that with lower temperature and then become ice after releasing their latent heat—at this point, ice lenses form. The above process is not continuous because different soil moisture has different latent heat, and thus ice segregation and ice lenses are not forming continuously during freezing.

Combining above analysis, within 0–100 cm depth of LP, AM slope, the reason for soil moisture curve wave (see Fig. 3) is caused by root absorption and ice segregation together. Within 100–180 cm depth, the wave is mainly caused by ice segregation only. For TU slope, the moisture wave is caused by ice segregation only.

In Situ Direct Shear Tests of Root-Soil Body

In order to evaluate the anchoring effect of shrub roots on the slope body, near the section (K562 +715–K562 +760, K563 +830–K563 +880), contrast test of in-situ direct shear between root-soil body (AM and LP) and no-root-soil body (TU) is conducted. In-situ direct shear apparatus is designed,

for and effective shear area of shear box is $50 \times 50 \text{ cm}^2$, the shear plane is parallel to the slope surface, the depth is 50 cm. The test results are shown in Fig. 5.

Figure 5 is the curve between shear stress and shear displacement for the soil with AF roots, LP roots and without any roots. It can be seen from the curve that maximum shear stress with AF root systems is 17.4 kPa, and with LP root systems is 15.88 kPa. The shear displacement for them corresponds to 14 mm. The shear stress and shear displacement of the soil without any roots are about half of the soil with AF roots and LP roots. AF and LP have a different failure process, in AF curve, there is a second peak value of shear stress is 13.2 kPa, and corresponding shear displacement is 299 mm; in LP curve, there is only one peak value of shear stress, and shear stress decreases gently with increasing shear displacement. Because AF root system has stronger lateral roots, when the main root is cut and shear stress has reached the first peak, the lateral roots are pulled from curved to straight until cut again (giving the second peak). But the lateral roots of LP are long and straight, and weakly bonded to soil particles, so there is only one peak value of shear stress.

The Test of Soil Mechanics Indicators

After on-site investigation, the distribution of soil moisture, soil dry density and other physical indicators are obtained, and shows results of the soil sample having different soil moisture, soil dry density (DD), with roots or without roots. The sampling method of those samples with roots is to put fine linen in soil sample and apply a temperature of 60° . Then these samples are subjected to a triaxial test, which indicates the shear strength indicator for each for different freeze-thaw cycles (FTC) (see Fig. 6). The dry density of the soil sample in FTC is 1.615 g/cm^3 .

In Fig. 6 (first line a ~ d: moisture-cohesion curve), soil cohesion always increases with an increase in soil moisture, whether they have or don't have roots in them. It does not matter how many freeze-thaw cycles they underwent. The cohesion reaches the peak value when soil moisture is

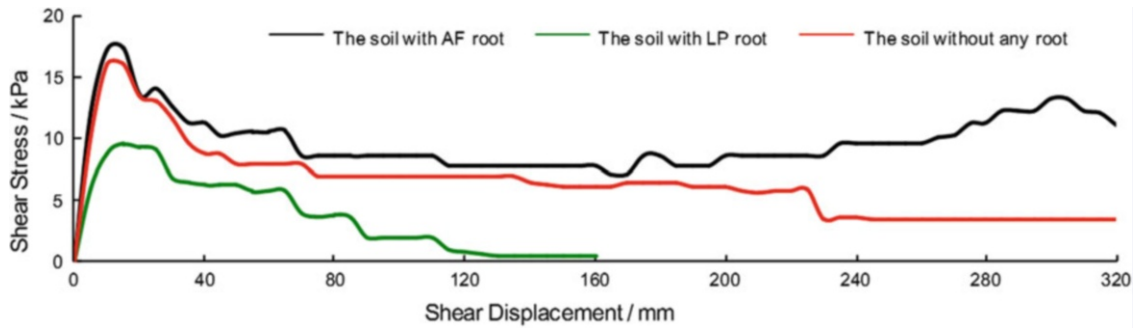


Fig. 5 The curve of shear stress-displacement for soil and root-soil

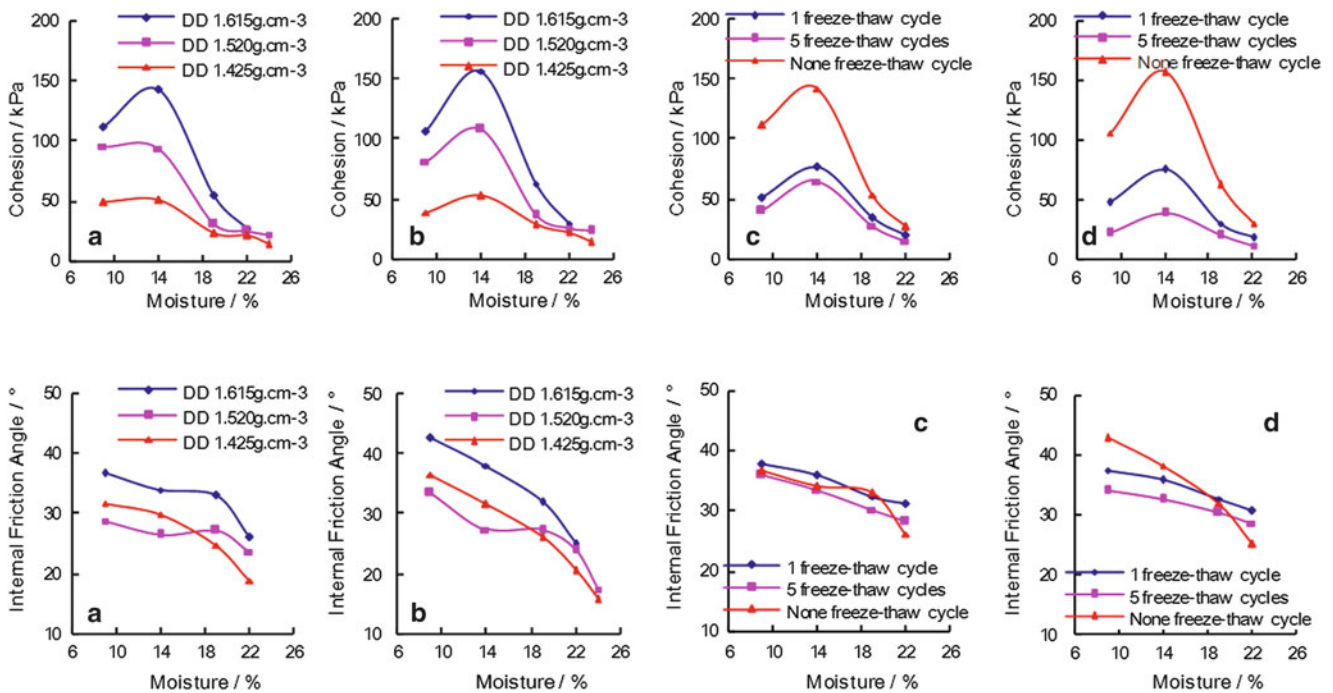


Fig. 6 Moisture-cohesion curve (first line) and moisture-friction curve (second line) [(a) soil without FTC; (b) root-soil without FTC; (c) soil after FTC; (d) root-soil after FTC]

around 14 % (optimum moisture), after that, soil cohesion decreases with soil an increase in moisture. Dry density also is one of the main factors, and soil cohesion significantly improves with the increasing soil dry density, especially when the soil moisture is less. When the soil dry density is bigger, soil samples with roots and without roots, it was found that the roots in the soil sample improved soil cohesion significantly. In the freeze-thaw cycle, the dry density of soil sample is 1.615 g/cm³ soil, and cohesion decreases with the increasing freeze-thaw cycles, especially after the first freeze-thaw cycle. The sample with roots have bigger declines of soil cohesion after several freeze-thaw cycles.

In Fig. 6 (second line a, b: moisture-friction curve without FTC), whether the soil having roots or not, soil internal

friction angle always declines with increasing soil moisture, the higher the soil moisture is, the faster soil internal friction angle declines, because higher soil moisture means soil body is closer to its saturation state, and thus have a stronger lubrication of soil pore water. About the influence of soil dry density, whether the soil samples have roots or not, when soil moisture is less than 18 %, internal friction angle of the soil with dry density 1.520 g/cm³ is smaller, when soil moisture is more than 18 %, internal friction angle increases with increasing soil dry density.

In Fig. 6 (second line c, d: moisture-friction curve with FTC). This is the contrast test of different freeze-thaw cycles. The dry density of soil sample in FTC is 1.615 g/cm³. First, whether the soil has roots or not, and undergo freeze-thaw cycle or not, soil internal friction angle decrease

Table 2 Soil physical parameters of TU slope and LP slope (used in simulation)

	No.	Depth (m)	Dry density (g/cm ³)	Water content (%)	
	1	0–0.8	1.425	10.9 (4.26)	31.0 (5.5)
Turf	2	0.8–1.5	1.520	8.8	
Slope	3	1.5–2.0	1.520	10.2	
	4	>2.0	1.615	13.0	
	1	0–0.8	1.425	7.2 (4.26)	21.2 (5.5)
LP	2	0.8–1.5	1.520	7.3	
Slope	3	1.5–2.0	1.520	9.9	
	4	>2.0	1.615	13.0	

Note: The dates in parentheses is the date soil moisture measured. That is April 26, 2009 and May 5, 2009. The initial state is the state of April 26, from then to May 5, the deformation caused by soil moisture increasing, the safety factor of the slope is calculated. Other moisture data in the table is the moisture measured on April 26, 2009 in TU slope and LP slope

Table 3 Soil mechanical parameters of TU slope and LP slope (used in simulation)

	No.		Water content (%)	Density (g/cm ³)	Cohesion (kPa)	Internal friction angle (°)	Elastic modulus (MPa)	Poisson ratio
	1	Soil	10.9	1.58	49.8	30.7	21	0.39
Turf		Soil	31.0	1.865	4.2	3.7	0.4	0.45
Slope	2		8.8	1.654	95.8	28.9	28	0.38
	3		10.2	1.675	95.5	28.3	28	0.38
	4		13.0	1.825	136.3	27.5	36	0.33
	1	Root-soil	7.2	1.528	48.7	30.5	21	0.39
LP		Root-soil	21.2	1.727	16.4	20.3	10	0.42
Slope	2		7.3	1.631	96.5	29.6	28	0.38
	3		9.9	1.670	95.6	28.4	28	0.38
	4		13.0	1.825	136.3	27.5	36	0.33

with increasing soil moisture. Secondly, there're different between freeze-thaw cycles. For the soil without roots, after the first freeze-thaw cycle, internal friction angle improve largely when soil moisture is less than 17 %. After five freeze-thaw cycles, internal friction angle comes back to the level of none freeze-thaw cycle. For the soil with roots, its internal friction angle decreases with increasing freeze-thaw cycles, but declines when the rate is lower.

Stability Analysis of Freeze-Thaw for the Slope with Different Plant

Using finite element analysis software COMSOL, adopting physical parameters of Site A (TU slope), Site B (LP slope) separately, stress and strain conditions are simulated in Site A section.

First, the slope body in Site A is divided into four layers, and soil units divided is triangular, which combine with the actual situation of Site A and take account in the impact of freeze-thaw and precipitation on soil moisture. Secondly, stress and strain conditions are simulated separately using

the physical parameters of TU slope and LP slope. The physical parameters are shown in Table 2 (the data come from Fig. 2 The curve of soil physical parameters along the depth in TU slope and LP slope), mechanics parameters are shown in Table 3 (the data come from Fig. 6 Moisture-cohesion curve and moisture-friction curve). Figure 7a, b are total displacement nephogram for TU and LP parameters, and the soil moisture adopted here is the moisture measured on-site. From April 26 to May 5, maximum displacement of LP parameters caused by soil moisture is 7.132×10^{-2} cm, TU parameters is 4.46 cm, and is 62.54 times for LP slope. The reinforcement effect of LP is obvious. Concerning factor of safety of slope stability, TU parameters are 1.069, and LP parameters are 4.720. Figure 7c is total displacement nephogram after strength reduction (TU slope, Site A). The maximum displacement before slope failure is 19.05 cm, and occurred in the middle of the slope. Figure 7d is plastic strain nephogram before slope failure (TU slope, Site A). The maximum plastic displacement before slope failure occurred at 80 cm away from the slope top, which is fully consistent with the actual state (see Fig. 8).

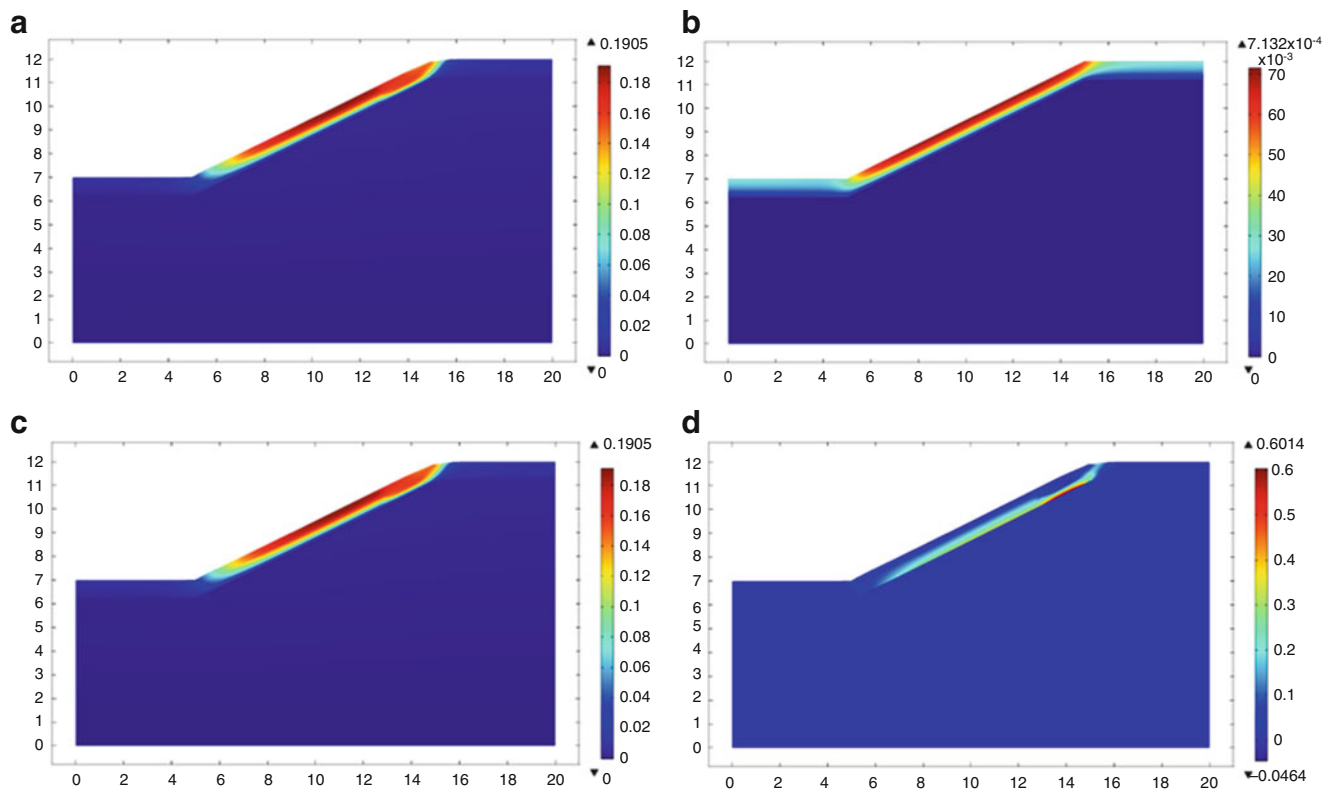


Fig. 7 Calculation nephogram. (a) The soil nephogram of total displacement caused by different moisture (TU slope parameters); (b) Root-soil nephogram of total displacement caused by different moisture (LP slope parameters); (c) Nephogram of total displacement after strength reduction (before destruction, TU slope parameters); (d) Nephogram of equivalent plastic strain after strength reduction (before destruction, TU slope parameters)

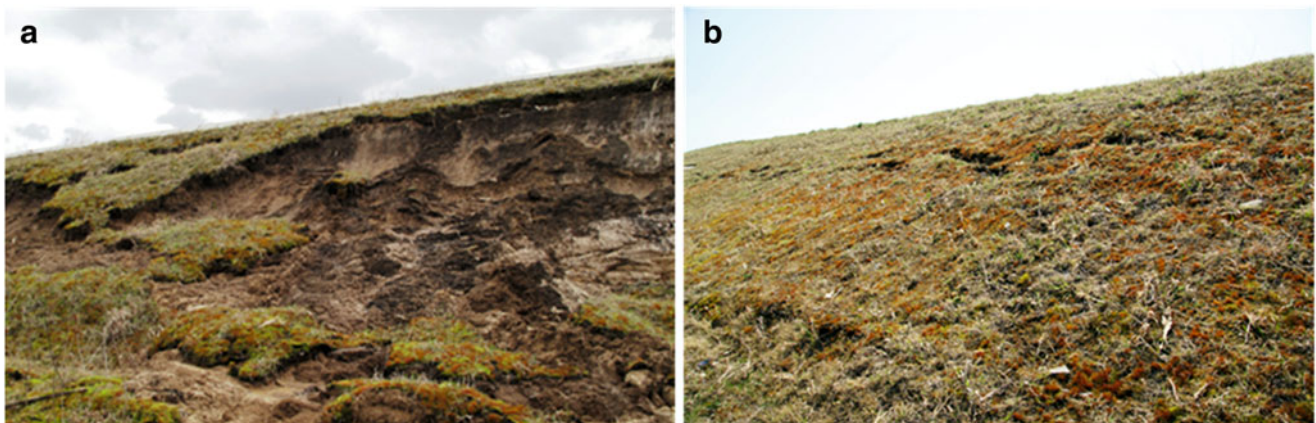


Fig. 8 (a) Creep deformation of the slope (Site A); (b) Crack in the middle of the slope (Site A)

Conclusions

1. Affect freeze-thaw action and plant roots, in the range of seasonal freezing depth, show that soil density and soil permeability is not uniform.
2. Plants could absorb water through their roots, and evaporate water through their leaves. Evaporation is the need of

plant body, as well as the driving force of root water absorption. The roots of shrub on the slope could adjust slope moisture, this functions is different from the length and shape of the roots. The lateral roots of LP, AF mainly is distributed within a 0–70 cm depth. Compared with turf slope, within the depth of 0–70 cm, LP, AF roots can

reduce soil moisture 7.39–8.09 %. The main root of LP, AF is distributed in 0–100 cm depth, within the depth of 70–100 cm, compared with turf slope, LP, AF roots can reduce soil moisture 3.56–5.69 %. Within the depth of 100–180 cm, the roots of LP, AF also can reduce soil moisture, but the effect is not obvious.

In the freezing process, freeze segregation is the main driving force of soil moisture migration. The roots in a shallow slope are able to adjust the soil moisture and then reduce the segregation effect.

Shrub roots in the slope can effectively improve slope soil shear strength, and shear distance. This function is different from the shrub kind and roots shape. Situ direct shear test results showed that: the shear strength of the soil with LP, AF root is two times that of the soil without roots. The shear strength of AF has two peak values because of its roots shape, and has a better stabilizing effect.

3. Triaxial test results showed that: soil cohesion always increases with soil and increase in moisture. The cohesion reaches the peak value when soil moisture is around 14 % (optimum moisture), after that, soil cohesion decrease with soil moisture increase. The soil internal friction angle always declines with increasing soil moisture; the more soil moisture there is, the faster its decline. The roots (fine linen) in the soil could improve soil cohesion and internal friction angle, especially with less soil moisture and larger soil density. Freeze-thaw cycles could decreases soil cohesion rapidly, especially after the first freeze-thaw cycle. Freeze-thaw cycles also could cause the soil internal friction angle to decline, but there is some increase after the first freeze-thaw cycle, and then decline in later freeze-thaw cycles. The performance of the soil with roots in the freeze-thaw cycle is similar to the soil without roots.
4. Based on the data of field monitoring and laboratory test, finite element analysis showed that: For the same slope

(Site A), it is in the critical state when TU slope parameters is adopted in simulation, and it is in steady state when LP slope parameters is used. So the shrubs on the slope can adjust soil moisture, increase soil shear strength, and improve slope stability.

Acknowledgements The authors would like to express our thanks for the support provided by the science and technology research project of Heilongjiang provincial Education Department (12533017).

References

- Cheng H, Xie T, Tang C et al (2006) Overview of mechanism of plant roots improving soil reinforcement and slope stabilization. *Chin J Bull Soil Water Conserv* 26(1):97–102, in Chinese with English abstract
- Deng WD, Zhou QH, Yan QR (2007) Test and calculation of effect of plant root on slope consolidation. *Chin J Highw Trans* 20(5):7–12, in Chinese with English abstract
- Guo Y, Shan W (2011) Monitoring and experiment on the effect of freeze-thaw on soil cut slope stability. *Procedia Environ Sci* 10:1115–1121
- Ji XB, Kang ES, Chen RS et al (2006) Research advances about water-uptake models by plant roots. *Chin J Acta Bot Occidentalia Sin* 26(5):1079–1086, in Chinese with English abstract
- Jin DW (2004) Slope stability study on permafrost area of Qinghai-Tibet Plateau. D.E thesis, Chang'an University, Xi'an, China (in Chinese with English abstract)
- Liu HJ, Guo Y, Shan W et al (2011) Instability of soil cutting slopes caused by freeze-thaw and reinforcement mechanism by vegetation. *Chin J Geotech Eng* 33(8):1197–1204, in Chinese with English abstract
- Niu FJ, Cheng GD, Lai YM et al (2004) Instability study on thaw slumping in permafrost regions of Qinghai-Tibet Plateau. *Chin J Geotech Eng* 26(3):402–406, in Chinese with English abstract
- Zhou YW, Guo DX (1982) Principal characteristics of permafrost in China. *Chin J Glaciol Geocryol* 4(1):1–19, in Chinese with English abstract



Formation Mechanism and Deformation Characteristics of Cut Layer Rock Landslide in Island Permafrost Region

Hua Jiang, Wei Shan, Zhaoguang Hu, and Ying Guo

Abstract

The Bei'an to Heihe Expressway in China's Heilongjiang province has been built by widening an existing second-class highway. These widening efforts have been hindered by the location of the old road, as some sections of the subgrade to be widened traverse the Lesser Khingan Mountains. These sections are located in an island permafrost region and experience landslides, which are influenced by the landform, geological conditions, rainfall, and freeze/thaw cycle and remain unstable. In this study, we investigated the K177 landslide site of the Bei'an to Heihe Expressway. We conducted geological surveys, topographic mappings, and geological explorations of the area, and performed field monitoring, indoor tests, and theoretical analyses to study the formation mechanism and deformation characteristics of the landslide. It was concluded that the rupture surface of the landslide is located in completely weathered mudstone. Further, atmospheric precipitation, snowmelt water, and water from the thawing seasonally frozen soil act as continuous water sources for the landslide. Surface water and ground water replenish the Cretaceous pore water through infiltration. Lateral runoff through the surface causes thermal shrinkage cracks in the shallow, high-permeability layer of rock and soil. Low-permeability mudstone with a loose structure forms an aquiclude, while completely weathered mudstone above the aquiclude, which is influenced by the Cretaceous pore water, softens and forms the rupture surface. Hence, landslide movement is affected by changes in slope moisture and the groundwater level, with the landslide exhibiting a low angle and intermittent creep.

Keywords

Expressway • Landslide • Formation mechanism • Deformation characteristics • Island permafrost region

Introduction

The Bei'an to Heihe Highway traverses an island permafrost area in northern China (Meng et al. 2001). This originally second-class highway, which contains a 3 km-long subgrade section, experienced a landslide during construction in 1999.

As a result, the route was relocated to the ridge where the geological conditions were relatively more stable (Liu et al. 2003; Liu and Mao 2003; Liu 2007), as shown in Fig. 1. In order to meet the economic and social development needs along the route, the second-class highway was unilaterally widened into an expressway. Some sections of the expressway are situated in the landslide body and are affected by the landform, topography, geology, rainfall, freeze/thaw cycle, and other such factors. The foundations of some of these sections are unstable, resulting in enormous difficulties in the widening and expansion of the expressway.

H. Jiang • W. Shan (✉) • Z.G. Hu • Y. Guo
Northeast Forestry University, Hexing road, 26, Harbin 150040, China
e-mail: jianghua3433@163.com; shanwei456@163.com;
huzhaoguang008@163.com; samesongs@163.com



Fig. 1 Aerial view of the Bei'an to Heihe Expressway expansion project

Because the triggering factors, topography, lithology, geological structure, and hydrogeological conditions of each landslide are different, their formation mechanisms are not identical (Li 2010; Yin et al. 2010). Therefore, there is a need for a comprehensive analysis of the formation mechanism of different types of landslides, their scale, and the hazards associated with them. Such an analysis should allow one to accurately determine the characteristics, for occurrence reason, and development mechanism of landslides, so that effective prevention measures can be taken during expressway construction (Wang and Yu 2008).

Geological Environment of Study Area

Climate and Environment

The study area is located in the central region of China's Lesser Khingan Mountains. The area has a continental monsoon climate. In the spring, the temperature rises quickly; the summers are not very warm; the rainy season sees the temperature drop rapidly; and the winters are long and cold. The annual average temperature is $0.6\text{ }^{\circ}\text{C}$, the lowest temperature is $-48.1\text{ }^{\circ}\text{C}$, and the highest temperature is $35.2\text{ }^{\circ}\text{C}$. In October, the ground begins to freeze, and melts in April the following year. The annual average freezing index is $3,000\text{--}3,300\text{ }^{\circ}\text{C}\cdot\text{d}$, and the frost-free period is approximately 96 days. The maximum seasonal freezing depth is $2.26\text{--}2.67\text{ m}$. Thus, the period from April to September is the period when the seasonally frozen soil melts; the

seasonally frozen soil melts completely by early July in the dry areas and by late October in the swamp areas (Shan et al. 2012). "Khingian-Baikal" type permafrost is distributed in the area. The permafrost is more widespread in the relatively low-lying areas and is also thicker in these areas. Its degradation occurs in the following order: first the sunny slopes degrade, then the shady ones. Similarly, first, the mountains degrade and then do the valleys.

The study area is located in the Sunwu-Heihe district, where the increase in the temperature has been the highest over the past 50 years, as per the meteorological data from the Sunwu weather station for 1954 to 2011. The annual average temperature has increased from $-1.6\text{ }^{\circ}\text{C}$ in 1954 to $1.2\text{ }^{\circ}\text{C}$ in 2011, with change being $2.8\text{ }^{\circ}\text{C}$, as shown in Fig. 2. In the past decade, owing to changes in the climate and environment, the permafrost has become more vulnerable. For instance, the permafrost degradation process has accelerated, with the permafrost layer decreasing in thickness and its temperature rising. Thus, in the areas around the road traversing the Lesser Khingan Mountains, the occurrence of small-scale landslides has increased significantly.

Geological Environment

In June 2009, we carried out geological investigations and topographical surveys in the K177 +400–K179 +200 sections of the Bei'an to Heihe Expressway expansion project. The results of these surveys are shown in Fig. 3.

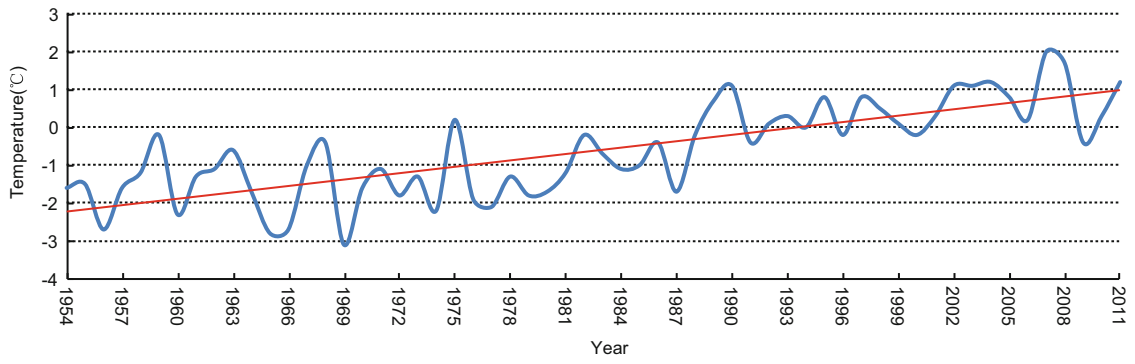


Fig. 2 Annual average temperature of Sunwu (1954–2011)

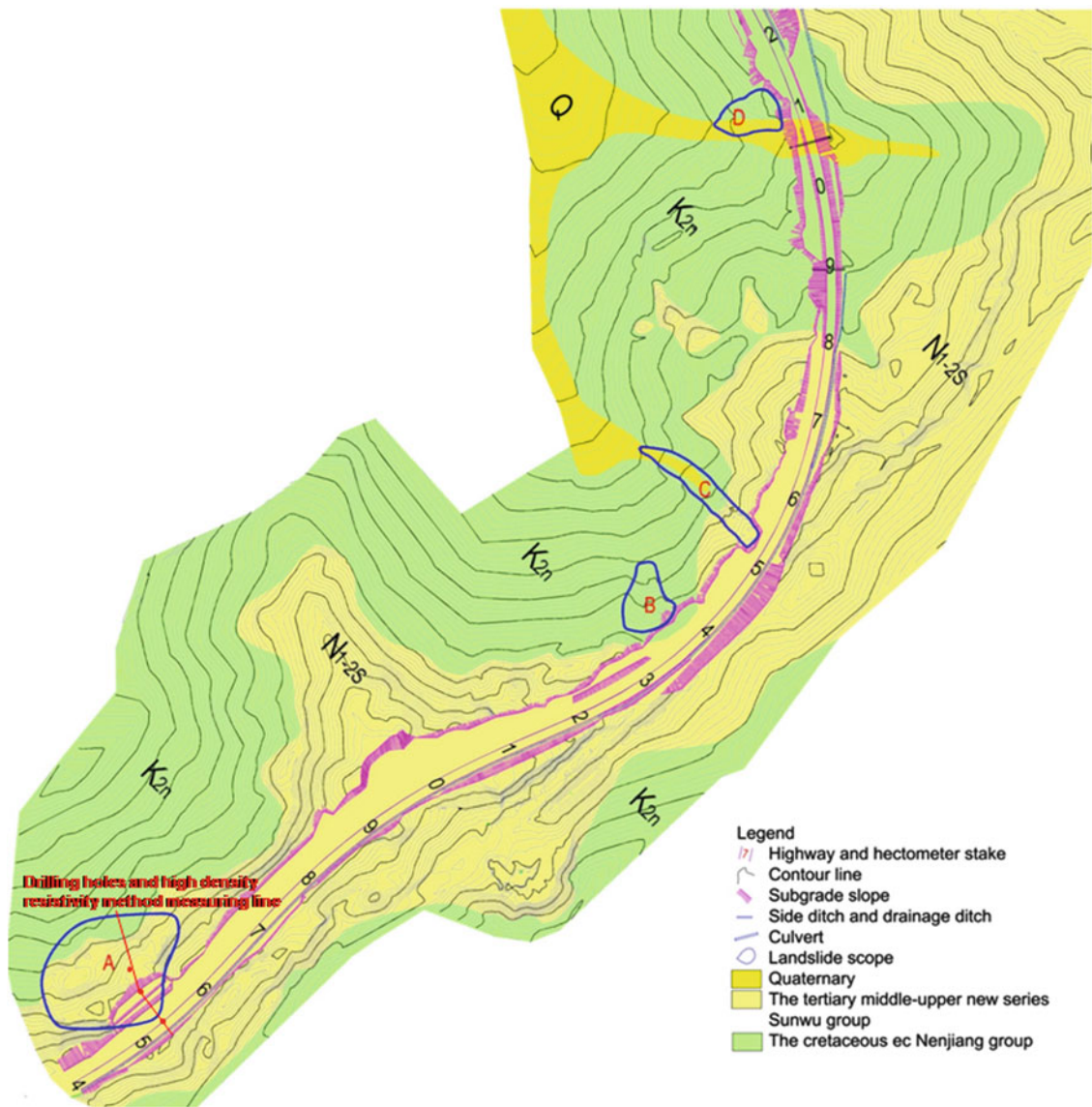


Fig. 3 Geologic and topographic map of the K177 +400–K179 +200 sections of the Bei'an to Heihe Expressway expansion project

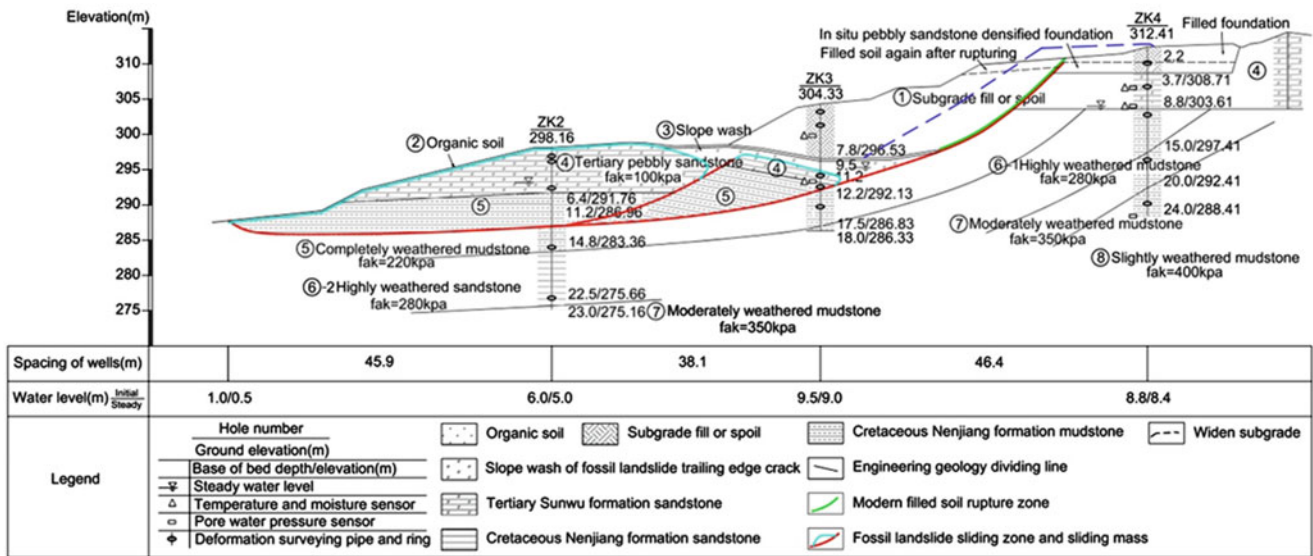


Fig. 4 Engineering geological profile of the landslide

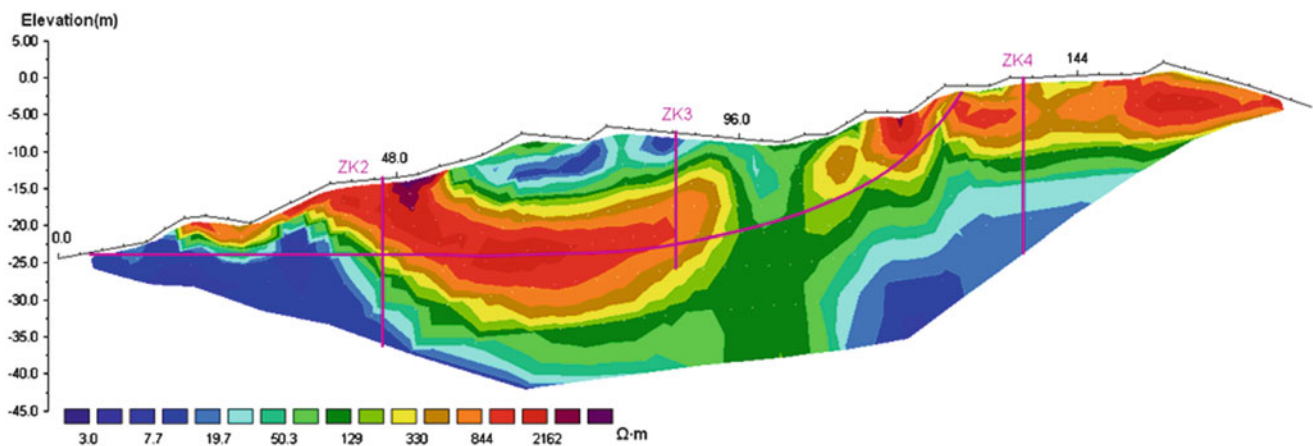


Fig. 5 Resistivity distribution diagram of the landslide

The tectonic study area is in the Wuyun-Jieya new rift zone; in the south is the Shuhe upwarping zone and in the north is the Handaqi virgation (Jiang and Shan 2012). The following strata are exposed: the upper Cretaceous Nenjiang formation, the Tertiary Pliocene series Sunwu formation, and the Quaternary Holocene series modern river alluvium and stack layers. In the study area, rock is bedded. In addition, there is weak cementation and poor weathering resistance. The weathering depth is high, and the surface is significantly weathered. On the basis of the properties of the aquiferous medium and the water supply and drainage conditions, the groundwater can be divided into three types: Quaternary pore water, Tertiary pore water, and Cretaceous pore water. Four landslides have affected the stability of the widened subgrade, as shown in Fig. 3; in this study, we focused on the K177 landslide.

Geological Exploration of Landslide Area

To survey the geological conditions of the landslide, we drilled three holes and arranged a resistivity measuring line in the area; their positions are shown in Fig. 3. On the basis of the results of the geological survey, we drew the engineering geological profile of the K177 landslide and its resistivity distribution diagram; these are shown in Figs. 4 and 5, respectively. Deformation-monitoring equipment, as well as temperature, moisture, and pore water pressure sensors were embedded in the holes.

The ground surface of the upper part of the landslide area was mainly subgrade soil, which consists of pebbly sandstone. Owing to the Cretaceous mudstone and sandy mudstone, the structure of this part was loose and water saturated

Table 1 Physical parameters of the various rock and soil samples

Rock and soil sample	ω (%)	ρ (g/cm ³)	Gs (g/cm ³)	e	Sr
Pebbly sandstone	25.8	1.84	2.57	0.76	0.87
Shallow mudstone	27.7	1.85	2.64	0.82	0.89
Sliding zone mudstone	30.1	1.87	2.67	0.86	0.94
Deep mudstone	27.2	1.79	2.76	0.96	0.78

As a result, it exhibited low resistivity, as can be seen from the resistivity distribution diagram. The ground surface of lower part of the landslide area was mainly pebbly sandstone, and it exhibited high porosity and poor integrity. This resulted in high resistivity, as can also be seen from the resistivity distribution diagram. The shallow area of the landslide consisted of completely weathered mudstone and had a loose structure, resulting in the development of fractures. As a result, it exhibited high resistivity. The deep area of the landslide consisted of completely weathered mudstone and had a compact structure. It exhibited moderately high resistivity. Owing to repeated dislocations, the sliding zone, which consisted of completely weathered mudstone, was found to have experienced cyclic shear. It had a completely crushed structure and exhibited very high resistivity.

On the basis of the results of the geological and geophysical investigations, it can be concluded that the landslide is a cut rocky layer type and that its sliding surface is located in completely weathered mudstone. The ground surface of the landslide area consists mainly of pebbly sandstone and subgrade soil. In addition, it has a high void ratio and weak integrity, and provides a smooth passage for infiltrating water. The shallow area consists of completely weathered mudstone, and exhibits fractures and high permeability. The deep area consists of completely weathered mudstone, has a compact structure, and exhibits low permeability. Atmospheric precipitation and surface water replenish the Cretaceous pore water through infiltration; while ground water adds to the Cretaceous pore water owing to lateral runoff. Water penetrates downward through the shallow rock and soil layer and accumulates on the sliding surface. Hence, the water content of the mudstone layer increases gradually, and reaches saturation, resulting in a significant decrease in shear strength.

Experimental Determination of the Physical and Mechanical Indexes of Various Landslide Rock and Soil Samples

Through geological explorations, we determined the engineering geological and hydrogeological conditions corresponding to the landslide as well as the cause of the

landslide. On the basis of results of the geological explorations, we formulated a laboratory test plan, collected various rock and soil core samples, and determined their physical and mechanical indexes.

Basic Physical Indexes

The basic physical parameters of the rock and soil samples, including their water content, wet density, and the specific gravity of the soil grains, reflect the condition of the samples. The basic physical indexes were measured in the laboratory and the corresponding conversion indexes were calculated using the relevant formulas; the indexes are listed in Table 1.

It can be seen from the index values that, in the case of the surface consisting of the completely weathered pebbly sandstone, the shallow and completely weathered mudstone, and the sliding zone, which consisted of completely weathered mudstone, the structure was loose and the water content was high. In particular, for the sliding zone, the water content was as high as 30.1 % and approached the saturation level. On the other hand, for the deep completely weathered mudstone, the water content was low.

Permeability

Infiltration is a phenomenon in which a liquid moves in a layer of rock and soil. The permeability coefficient is the primary index for evaluating the permeability of a layer of rock and soil. We determined the permeability coefficients of the various samples for different water contents; the results are shown in Fig. 6.

It can be seen from the results that the matric suction decreased sharply and the permeability coefficient increased rapidly with an increase in the water content. The permeability coefficients corresponding to the unsaturated and saturated states varied significantly, with the difference being approximately 10^3 times in the case of mudstone and greater than 10^6 times in the case of sandstone. In the landslide area, the permeability coefficient of the completely weathered pebbly sandstone was large; its saturated permeability coefficient was 1.04×10^{-4} cm/s, suggesting that its permeability was high. On the other hand, the permeability

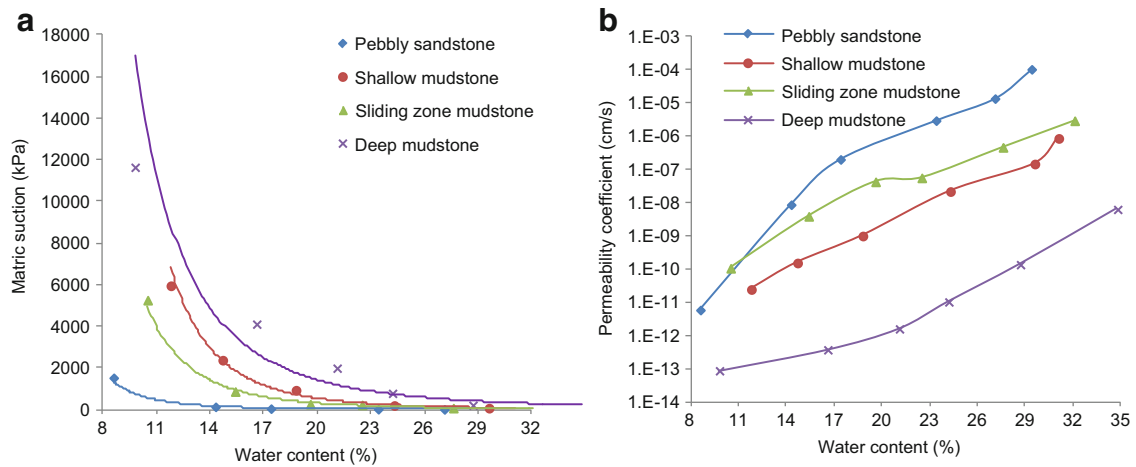


Fig. 6 (a) Soil-water characteristics and (b) change in permeability coefficient with water content

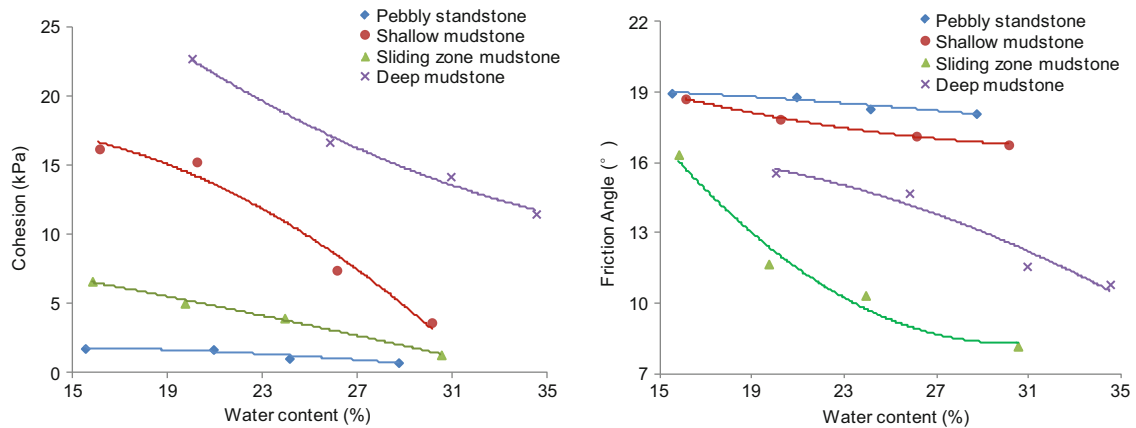


Fig. 7 Change in shear strength with water content

coefficient of the shallow area, which consisted of completely weathered mudstone, decreased markedly with an increase in the water content. Finally, the permeability coefficient of the deep area, which consisted of completely weathered mudstone, was very small, indicating that its permeability was very low.

Shear Strength

The shear strength of a layer of rock and soil is its ability to resist shear failure and is an important mechanical property. It is the key factor determining the slope stability of the layer. According to Coulomb's law, the shear strength of a layer of rock and soil is attributable to both cohesion and internal friction. We measured the shear strengths of the various samples for different water contents; the results are shown in Fig. 7.

The results showed that, in the case of the completely weathered pebbly sandstone, cohesion was very low and its

shear strength was mainly owing to friction. Further, the effect of the water content on shear strength was almost negligible; the cohesion and friction angle at saturation were 0.78 kPa and 18.1°, respectively. In the case of the shallow, completely weathered mudstone, the shear strength was owing to both cohesion and friction. In addition, the cohesion was highly dependent on the water content, but the friction angle was not. For the upper and lower ends of the range of water contents tested, the maximum decreases in the amplitude were 77.4 % and 10.5 %, respectively; in addition, the cohesion and friction angle at saturation were 3.67 kPa and 16.78°, respectively. In the case of the sliding zone consisting of completely weathered mudstone, the rock and soil layer was found to have experienced repeated shearing; hence, its structure was completely destroyed. Therefore, its shear strength was attributable mainly to friction. The cohesion and friction angle were dependent on water content. For the upper and lower ends of the range of water contents investigated, the maximum decreases in the amplitude were 78.4 % and 50.0 %, respectively. The cohesion

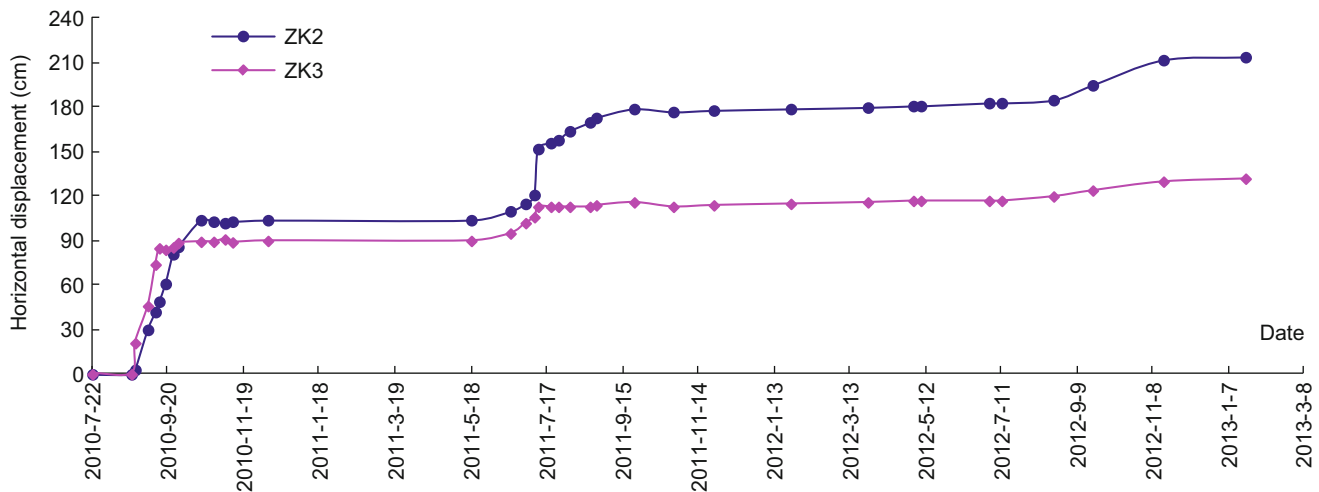


Fig. 8 Change in horizontal displacement at ZK2 and ZK3 with time

and friction angle at saturation were 1.34 kPa and 8.18° , respectively. In the case of the deep, completely weathered mudstone, the shear strength was attributable to both cohesion and friction. Both factors were dependent on the water content. For the highest and lowest water contents investigated, the decreases in amplitude were 49.3 % and 30.6 %, respectively. Finally, the cohesion and friction angle at saturation were 11.51 kPa and 10.82° , respectively.

In Situ Monitoring of Landslide Area

The embedding of the surveying and monitoring equipment was completed in July 2010, and we began collecting data on July 22, 2010. 32 days later, we found that the ZK2 and ZK3 deformation monitoring pipes had been sheared at depths of 11.0 m and 12.1 m, respectively, from their original positions. The temperature, moisture, and pore water pressure sensors had also been sheared. Thus, it was determined that a landslide had occurred in the area. We used the global positioning system (GPS) to monitor the surface horizontal displacement at the monitoring points ZK2 and ZK3; the results are shown in Fig. 8. We also employed a borehole incline tube to monitor the relative horizontal displacement of the rock and soil layer at ZK2 and ZK3; these results are shown in Fig. 9. Finally, we employed sensors to monitor the temperature, moisture, and pore water pressure of the rock and soil layer at the monitoring point ZK4; the results are shown in Figs. 10, 11 and 12.

As shown in Fig. 8, the landslide began on August 22, 2010, and reached a steady state on November 8, 2011. At this point, there was no further horizontal displacement and respectively reached 103 cm and 91 cm in 74 days. The

landslide exhibited more sliding on May 18, 2011, and reached a steady state on November 16, 2011. At this point again, there was no further horizontal displacement, 212 cm and 230 cm in 451 days. Thus, the landslide exhibited intermittent sliding and the horizontal displacement in the front was greater than that at the rear. We performed a cutting slope treatment on the widening subgrade on September 15, 2010. Prior to the treatment, the surface horizontal displacement at ZK2 was significantly less than that at ZK3. After the treatment, however, the surface horizontal displacement at ZK2 was significantly larger than that at ZK3. This shows that the stress state of the slope is affected by the slope cutting treatment, which can change it from one corresponding to pushing to one corresponding to pulling.

We set anti-landslide piles at the toe of the slope of the widened subgrade on April 18, 2011. It can be seen from Fig. 9 that, prior to this, the internal horizontal displacement of the rock and soil layer decreased with an increase in depth at ZK2. The anti-landslide piles change the stress state of the slope, and the sliding zone moves to a position 7–8 m under the ground. Hence, the horizontal displacement at this position is the greatest. The internal horizontal displacement of the rock and soil layer decreased with an increase in the depth at ZK3; the horizontal displacement 0–9 m under the ground was significantly larger than that for greater depths, because the soil 0–9 m under the ground is mainly of subgrade type, and its structure is loose and softened by water. The interface between the subgrade soil and the original ground surface readily forms a secondary sliding surface.

According to the monitoring data for ZK4, in the investigated region, the ground surface began to freeze early on 10th November, and the seasonally frozen soil had

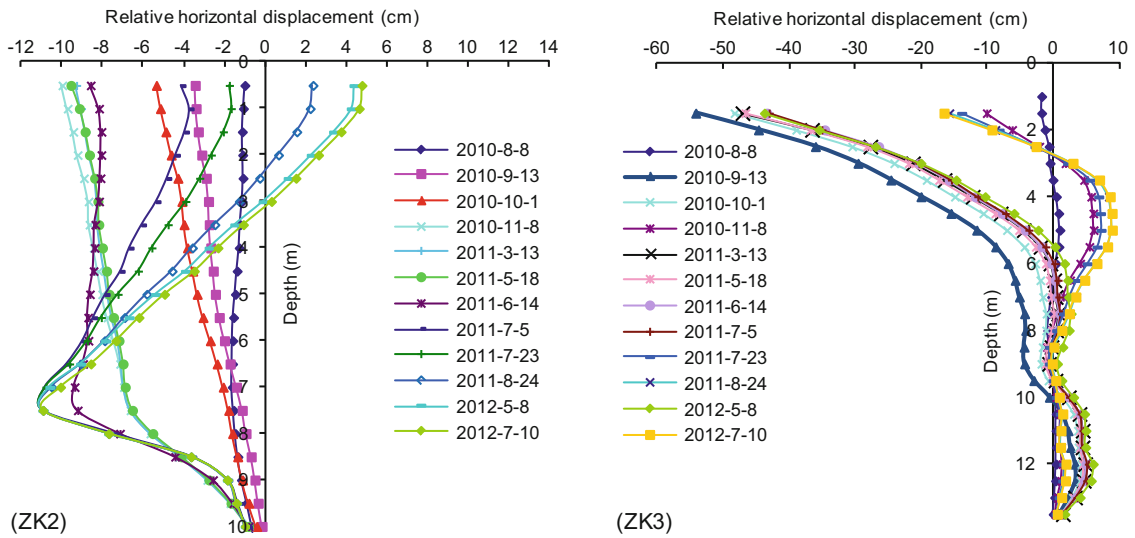


Fig. 9 Change in relative horizontal displacement in the rock and soil layer at different depths at ZK2 with time

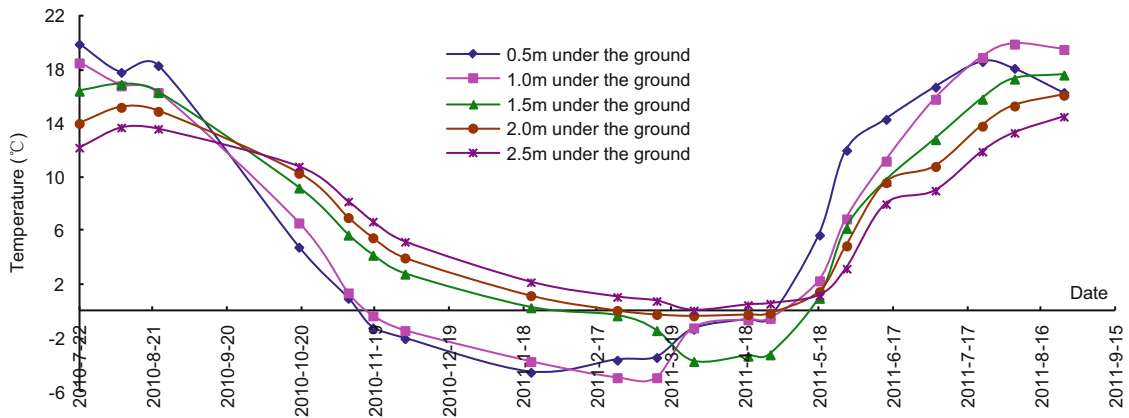


Fig. 10 Change in ground temperature at ZK4 with time

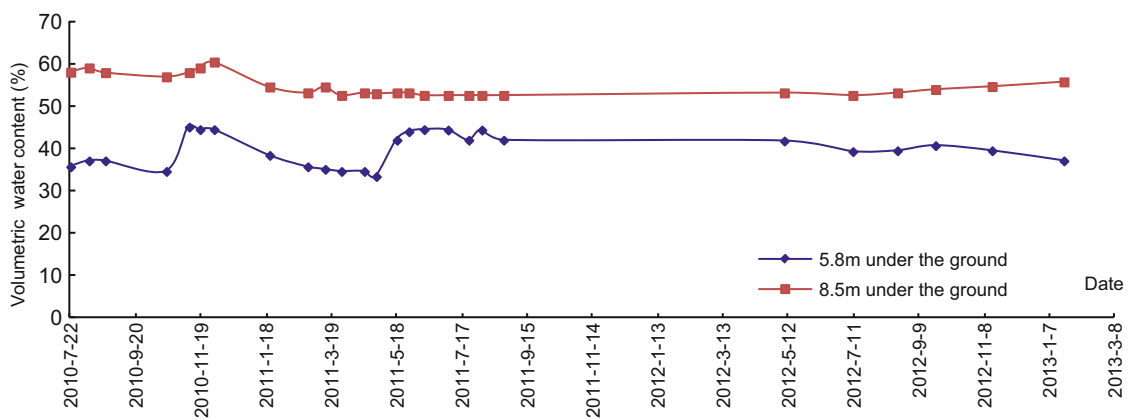


Fig. 11 Change in volumetric water content at ZK4 with time

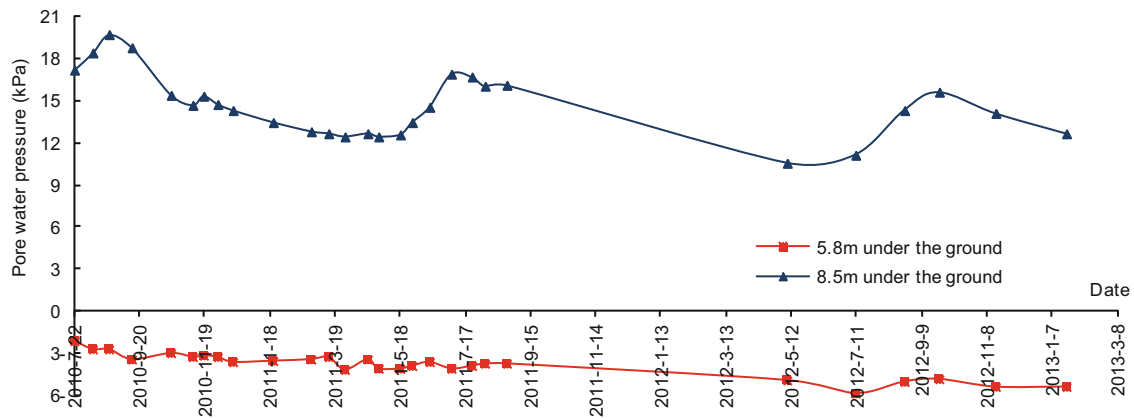


Fig. 12 Change in pore water pressure at ZK4 with time

melted completely by the middle of May next year. The depth of the seasonally frozen soil layer was approximately 2.5 m. The rock and soil layer 5.8 m under the ground was in an unsaturated state. Its pore water pressure did not change significantly; however, its volumetric water content increased rapidly in the rainy season and during the spring melt period. On the other hand, the rock and soil layer 8.5 m under the ground was in a saturated state. Its pore water pressure exhibited a rapid increase during the rainy season and the spring melt period.

On the basis of the monitoring data collected from the landslide region, it can be concluded that the regional temperature, atmospheric precipitation, and pore water pressure have a significant effect on landslide movement. In the spring melt period, the accumulated snow and the seasonally frozen soil melt completely. As a result, the pore water pressure begins to increase, and the landslide begins to creep. In the summer, strong rainfall further increases the pore water pressure rapidly to its peak value, accelerating the movement of the landslide. In the autumn, the ground temperature drops, atmospheric precipitation reduces, and the pore water pressure decreases. Therefore, the rate of landslide movement decreases gradually, with the landslide eventually reaching a steady state.

Conclusions

The K177 landslide is a cut layer rocky-type landslide. The landslide area surface is mainly composed of Tertiary pebbly sandstone whose saturated permeability coefficient is 1.04×10^{-3} cm/s; its high permeability results in it acting as a good channel for infiltrating water. Surface water and atmospheric precipitation replenish the Cretaceous pore water through infiltration, while mountain groundwater supplies the Cretaceous pore water through runoff. The shallow mudstone develops fissures, has a saturated permeability coefficient of 2.93×10^{-6} cm/s, and thus exhibits strong

permeability. On the other hand, the structure of the deep mudstone is dense. It has a saturated permeability coefficient of 6.24×10^{-9} cm/s, and thus exhibit slow permeability. Water penetrates downwards and accumulates in the sliding zone. As a result, the water content of the mudstone layer increases gradually and reaches a point of saturation. The cohesion and friction angle of the mudstone decrease to 1.34 kPa and 8.18° , respectively, resulting in slope instability.

The stress state of the slope is affected by slope cutting treatments, changing from one corresponding to pushing to one corresponding to pulling. Anti-landslide piles also change the stress state of the slope, with the sliding zone in the middle part of the landslide exhibiting an upward trend.

The regional temperature, precipitation, and pore water pressure have a marked effect on the movement of the landslide. In the spring melt period, the accumulated snow and the seasonally frozen soil melt completely, increasing the pore water pressure and causing the landslide to creep. In the summer, strong rainfall further increases the pore water pressure rapidly to its peak value, accelerating landslide movement. In the autumn, the ground temperature drops, atmospheric precipitation reduces, and the pore water pressure decreases, causing the rate of landslide movement to decrease gradually. The landslide eventually reaches a steady state.

Thus, in the investigated region, the movement of landslides is affected by changes in slope moisture and in the groundwater level. Further, the landslides have low angles and exhibit intermittent creep.

Acknowledgements This work was financially supported by the key science and technology project of Heilongjiang Communications Department "Study on Subgrade Stability Controlling Technology of Freeway Expansion Project Permafrost Melt and Landslides Sections" (2011318223630).

References

- Jiang H, Shan W (2012) Formation mechanism and stability analysis of Bei'an to Heihe Expressway expansion project K178 landslide. *Adv Mater Res* 368–373:953–958
- Li D (2010) Common types and treatment of expressway landslide in Guizhou mountain area. *J China Foreign Highway* 30(4):68–69, in Chinese
- Liu JH (2007) Geological Hazards Summary of Heihe-Bei'an Highway K62-K69 Section. *Commun Sci Technol Heilongjiang* 30(7):21–23, in Chinese
- Liu JP, Mao JB (2003) Heihe-Bei'an highway geological disasters abstract. *Commun Sci Technol Heilongjiang* 26(11):1–2, in Chinese
- Liu YH, You DF, Ni DY (2003) Subgrade Landslide Treatment Measure of Heihe-Bei'an Highway. *Commun Sci Technol Heilongjiang* 26(5):30, in Chinese
- Meng FS, Liu JP, Liu YZ (2001) Design principles and frost damage characteristics of frozen soil roadbed along the Heihe-Bei'an Highway. *J Glaciol Geocryol* 23(3):307–311, in Chinese
- Shan W, Jiang H, Hu ZG (2012) Island permafrost degrading process and deformation characteristics of expressway widen subgrade foundation. *Disaster Adv* 5(4):827–832
- Wang YC, Yu ZX (2008) The mechanism and control measures of several landslides in New River Highway. *Highway* (2):110–115 (in Chinese)
- Yin ZQ, Cheng GM, Hu GS (2010) Preliminary study on characteristic and mechanism of super-large landslides in Upper Yellow River since late Pleistocene. *J Eng Geol* 18(1):41–51, in Chinese



Dynamics of Vegetation on Cryogenic Landslides of Different Age in Central Yamal (West Siberian Arctic)

Olga Khitun, Irina Czernyadjeva, and Marina Leibman

Abstract

Active layer detachment slides of different age were examined in the Central part of Yamal peninsula (West Siberian Arctic) in the subzone of northern hypocoarctic tundra. Plant communities on the shear surface, on displaced blocks with preserved but degrading initial tundra vegetation and on undisturbed surroundings were described. In the processes of recovery pioneer grass-dominated communities on relatively dry surfaces and Equisetum-dominated communities in wet cracks were replaced by *Salix reptans*-graminoid communities. Vegetation on displaced blocks also transformed to the similar communities. On the oldest completely recovered landslides *Salix reptans*-graminoid communities with thin moss stratum occur both on former shear surface and on washed out remnants of blocks. Ancient landslides are indicated by willow copses and mesophytic herbaceous communities.

Keywords

Cryogenic landslides • Re-vegetation • Succession • Mosses

Introduction

Cryogenic landslides are common in Central Yamal and play an important role in formation of the local landscapes (Leibman and Kizyakov 2007). They are also an important disturbance factor affecting vegetation (Rebristaya et al. 1995; Cannone et al. 2010). Landslides alter both topography and soil and create new habitats available for colonization (Geertsema and Pojar 2007). Vegetation on disturbed surfaces differs essentially from adjacent undisturbed tundra both in terms of floristic composition and projective cover (Rebristaya et al. 1995; Walker and Walker 1991). The aim

of this paper is to reveal the relationship between landslide age and vegetation cover in Low Arctic (northern hypocoarctic tundra subzone according to Yurtsev 1994).

Study Area and Materials

Regular observations on different cryogenic landslides are ongoing from 1987 at “Vaskiny dachi” field lodge located in Central Yamal on watershed of Se-yakha and Mordy-Yakha rivers. Late Pleistocene marine terraces are formed there by salty clayey deposits with high ground ice content and cryogenic detachments occur there periodically. Due to the particular meteorological conditions during 1988 and 1989 (Leibman 1995) numerous landslides occurred in 1989 in the Central Yamal. Several 10–20 years older landslides (their age was estimated with the help of available aerial photos from different years) were also found in the area as well as several concave surfaces were dated as ancient landslides aged 300–2,300 years (Leibman and Kizjakov 2007). Botanical observations were carried out in

O. Khitun (✉) • I. Czernyadjeva
Komarov Botanical Institute Russian Academy of Sciences, Professor
Popov street 2, St. Petersburg 197376, Russia
e-mail: khitun-olga@yandex.ru; irinamosses@gmail.com

M. Leibman
Earth Cryosphere Institute, Siberian Branch, Russian Academy of
Sciences, Malygin street 86, Tyumen 625000, Russia
e-mail: irinamosses@gmail.com

1991–1993 and in 2012. Vegetation on 14 landslides of different aged and adjacent undisturbed terrain was described, here we describe four examples. Taxonomy of vascular plants follows Arctic flora of the USSR (1961–1987), of mosses—Ignatov et al. (2006).

Results

Vegetation on Young Landslides Formed in 1989

One of the most spacious active-layer detachments occurred in 1989 was studied in detail. We refer to it as “L1” in this paper. It was located on NE slope of lake depression, ca 3° steep. The range of movement of L1 was 180 m, including 120 m shear surface, its width was 50 m. As in 1991 projective cover (PC) of shear surface was less than 1 %, we mapped each individual plant or small group which allowed to see re-vegetation pattern: narrow (<0.5 m) stripe along the scarp by the perimeter of the shear surface, around the detached blocks of ground with preserved original vegetation, along the run-off troughs and in frontal part. Those places were somewhat sheltered from the wind and upper layer of ground did not dry out there as fast as in the central part of the shear surface. Monitoring during 1991–1993 did not show essential changes in PC of species on shear surface except for some increase in moss growth in 1993. In the first 3 years 21 species of vascular plants and 11 species of green mosses established on the exposure. Most of species recorded on the shear surface were present in small abundance in the adjacent tundra community—*Salix nummularia*-*Carex arctisibirica*-moss-lichen tundra on one side and wet low willow (*Salix glauca*)-cotton grass (*Eriophorum polystachyon*)-moss tundra on the other (lower) side of the landslide. The most active colonizer during the first years was *Equisetum boreale* which formed small patches (max 0.5 m² but with PC up to 80 %) in narrow stripe along scarp. Solitary individuals of grasses and sedges from surrounding communities (*Alopecurus alpinus*, *Arctagrostis latifolia*, *Calamagrostis holmii*, *Poa alpigena* subsp. *alpigena*, *Festuca ovina*, *Eriophorum polystachion*, *Carex arctisibirica*) penetrate onto the exposure, also few herbs. Whereas ten species absent in surroundings (*Deschampsia borealis*, *Trisetum spicatum*, *Poa alpigena* subsp. *colpodea*, *Puccinellia sibirica*, *Phippsia concinna*, *Draba hirta*, *Tanacetum bipinnatum*, *Tripleurospermum hookeri*, *Senecio congestus*, *Artemisia tilesii*) were actively colonizing shear surface. Shrubs (*Betula nana*, *Salix glauca*) preserved on the detached blocks were damaged and had bad vitality, tundra moss turf was degrading, whereas horse-tail was increasing its cover (from “+” to 1–2 %), and in cracks

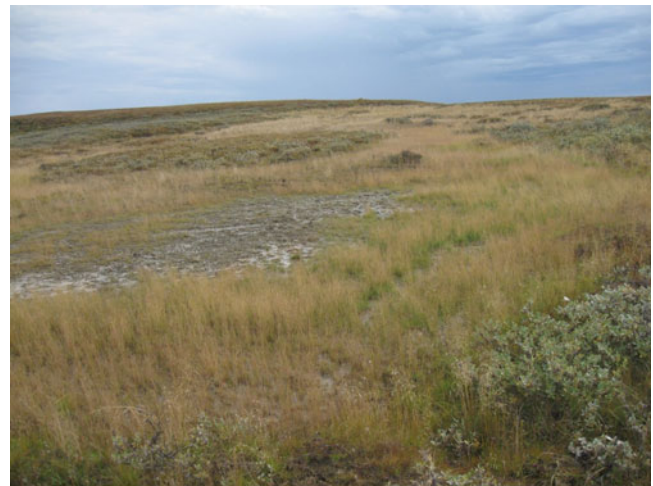


Fig. 1 Landslide No 1 in august of 2012, 23 years old. Pale colour in the upper part of the shear surface—drier convex parts with *Deschampsia borealis* dominated groupings with PC up to 60 %; in wet concave areas—*Puccinellia sibirica* dominated groupings with PC up to 40 % and in the periphery of the shear surface in rather moist conditions (greenish in the right low part of the photo)—*Calamagrostis holmii* with some addition of *Festuca rubra* subsp. *arctica* and *Poa alpigena* ssp. *colpodea* with PC up to 60–70 %

dissecting the blocks moss species typical for disturbed habitats (*Bryum* sp., *Ceratodon purpureus*, *Eurynchium pulchellum*, *Syntrichia ruralis*) appeared. Around the blocks development of mosses was recorded (from protonema in 1991 to plants with sporogones in 1993), both pioneer (*Bryum* spp., *Ceratodon purpureus*, *Dicranella crista*, *Distichium capillaceum*, *Funaria hygrometrica*, *Pohlia proligeraly*, *Hennediella heimii*, *Leptobryum pyriforme*) and typical tundra species (*Aulacomnium turgidum*, *Hylocomnium splendens*, *Polytrichum juniperinum*).

When we re-visited L1 in 2012 the PC on the shear surface was 60 % on average (30–90 % in different parts of it). Groupings with different dominated species could be distinguished in the different parts of the shear surface. In shallow run-off channels sedge-moss wet communities with 90 % cover has formed. Pioneer mosses (*Bryum knowltonii*, *B. triquetrum*, *Dicranella palustris*, *Leptobryum pyriforme*, *Pohlia nutans* and all those mentioned above found in 1993) and also *Drepanocladus aduncus*, *D. polygamus*, *Sanionia uncinata*, *Brachythecium jacuticum*, *B. turgidum* play important role in re-vegetation and stipulate the formation of organic horizon. After 20 years it has reached 0.5–1 cm depth. Grasses play the main role in stabilizing the surface (Fig. 1). Indicator of salted ground, *Carex glareosa*, never grows in undisturbed tundra but in Yamal it is strictly associated with landslides (and coastal habitats) and after 20 years we found it on the shear surface. Main dominant in water runs was *Eriophorum scheuchzeri*. Active regeneration of willows was recorded, mainly from seeds (numerous

seedlings up to 3 cm height) but also from roots (around the displaced blocks). This pattern was observed on all landslides formed in 1989.

Vegetation on Landslides Formed 30–40 Years Ago

Age of landslide No 2 (L2) in 1991 time we estimated as ca. 10–15 years. Its movement range was comparable with L1—150 m length and shear surface 120 m. It was located at NNW ca 5° steep slope in the run-off depression. Undisturbed communities surrounding landslide were *Salix nummularia*-*Betula nana*-moss-lichen tundra and low willow (*Salix glauca*)-cotton grass-moss moist tundra in run-off depressions. The shear surface of L2 was rather densely covered by pioneer vegetation groupings. According to dominated species we distinguished several zones, or patches, which we joined in four groups depending on topography, moisture and vegetation. In group I we included narrow (<80 cm) stripe along the perimeter of the landslide where conditions were obviously more favorable for plants and especially mosses. It was re-vegetated by protonema of mosses and also pioneer mosses (*Ditrichum cylindricum*, *Henediella heimii* var. *arctica*, *Dicranella crispera*) and also liverworts, which all together cover up to 20 % of the surface. Solitary shoots of vascular plants (*Equisetum arvense*, *Eriophorum polystachion*, *Poa alpigena*) also were recorded. In group II we included patches located on the shear surface differing by the surface moisture and topography: (1) drier, more convex zone with *Tripleurospermum hookeri* and *Puccinellia sibirica* as dominants covering together up to 40–45 % of the surface; (2) more gentle and not so dry sites relatively closer to the sides of the shear surface where *Deschampsia borealis* dominated and pioneer mosses spread actively, with total PC up to 40 % in this zone; (3) deep and wet erosional trough with solitary specimens of *Puccinellia sibirica*, *Deschampsia borealis*, *Tripleurospermum hookeri* (PC < 5 %); (4) distal part of this trough—more gentle and wide was re-vegetating actively by *Equisetum arvense* (its PC increased from 1991 to 1993 from 40 % to 60 %) and sparse *Dupontia fisheri*. In group III we included displaced small blocks of ground, which were washing out and grasses from initial tundra vegetation were spreading onto the shear surface. *Alopecurus alpinus* was the most vigorous and abundant, but *Arctagrostis latifolia* and *Calamagrostis neglecta* started to colonize as well. In group IV we included big blocks of the landslide body with preserved tundra communities.

In 2012 (Fig. 2) *Deschampsia borealis* became dominant practically on the whole shear surface (PC = 20–40 %) except for the wettest parts where *Eriophorum scheuchzeri*



Fig. 2 Landslide No 2 in August of 2012, its age estimated as ca 35 years. Shear surface became smoother and pioneer vegetation became more uniform, though still it is possible to distinguish patches with different dominants

and *Dupontia fisheri* were dominating, presence of *Carex glareosa* was also recorded at this time in wet parts, abundance of *Puccinellia sibirica* and *Tripleurospermum hookeri* decreased a little, and PC of *Poa alpigena* ssp. *colpodea* increased up to 10 % (compare to ca. 1 % in 1991). Vegetation on the displaced blocks of tundra does not change and plants have better vitality than in 1991. Tundra mosses (*Hylocomium splendens*, *Polytichum juniperinum*, *Aulacomnium turgidum*) completely recovered on the blocks. Also lichens (*Peltigera* spp.) became abundant.

Vegetation on Old Landslides

Landslide no 3 (L3) was formed before 1965, probably in the beginning of 1960s. It is located in shallow depression on the gentle (3°) W slope of the creek valley. Its length—ca. 100 m, width—80 m. L3 is surrounded by hummocky low-willow (*Salix glauca*, *S. lanata*)—*Betula nana*-*Carex arctisibirica*-moss tundra. Shear surface and remnants of the transported blocks of the landslide body were practically leveled and in more smooth completely re-vegetated concave parts *Salix reptans*—*Eriophorum polystachion*-moss (*Sanionia uncinata*, *Drepanocladus arcticum*) community with up to 80 % moss cover and up to 30 % of willow (up to 20 cm high) cover occur. In wetter (lower on slope) parts *Dupontia fisheri* and *Carex concolor* dominating wet meadow was formed with presence of *Carex glareosa*. Completely degraded remnants of transported blocks and elevated parts of shear surface were covered with grass (*Deschampsia borealis*)—willow (*Salix reptans* and *Salix glauca*) community with thin moss cover including both

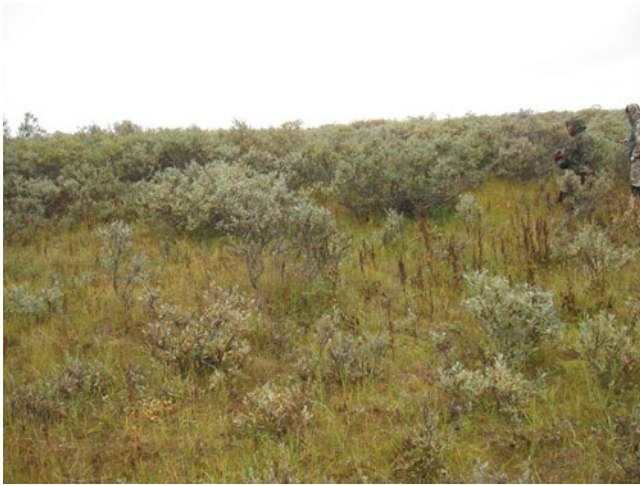


Fig. 3 1,000 year old landslide cirque with mesic herbaceous community and willow (L4). August, 2012

pioneer and tundra mosses and also *Peltigera* spp. and *Stereocaulon* sp. lichens. Principal change in moss composition was found at this site, even more pronounced after 20 years.

Vegetation on Ancient Landslides

As ancient landslides (dated 300–2,000 years old) were recognized concave parts on the slope of the creek valley occupied by low willow (*Salix glauca*, *Salix lanata*)-herbaceous-moss communities where *Carex lachenalii* is one of the main dominants and herbs (*Trollius asiatica*, *Veratrum lobelianum*, *Ranunculus borealis*, *Polemonium acutiflorum*, *Equisetum boreale*) are abundant (Fig. 3). *Sanionia uncinata* and *Brachythecium jacuticum* were dominating in rather well developed moss cover including also such species as *Polytrichum alpinum*, *Plagiothecium denticulatum*, *Bryum pseudotriquetrum*, *Sciuro-hypnum latifolium*.

Discussion and Conclusions

In process of re-vegetation of exposed mineral surface in Low Arctic lowland Yamal graminoids are playing the most important role forming pioneer grouping. Few species can dominate, *Deschampsia borealis* and *Puccinellia sibirica* are always the most active colonizers. That is typical for the West Siberian Arctic on a whole (as we could observe also in Gydan and Tazovsky peninsulas) but in other parts of the Arctic pioneer communities on shear surfaces can incorporate bigger number and abundance of herbs (Cannone et al. 2010). Re-vegetation pattern described above for L1 was observed on other landslides formed in 1989, comparing their vegetation and what we had seen on L2 in 1991, we can conclude

Table 1 Total number of species, number of green moss species and total projective cover (PC) on shear surface of four model landslides (L1–L4)

	L1	L2	L3	L4
Total no of species	41/50	30/48	31/44	43
No of green mosses	19/25	15/20	10/16	14
Total PC, %	1/60	50/70	90/90	100

Number before slash—recorded in 1993, number after slash—recorded in 2012. For L4 only 2012 data was available

that such pioneer grass-dominated groupings with abundance of pioneer mosses form during first 5–7 years and continue to occupy shear surface for at least 30 years. Respectively age of L3 probably can be adjusted a little—it was most likely formed in the middle of 1950s. In contrast to two younger landslides at the stage of L3 change in moss composition occur—reduce in number of pioneer mosses and increase in number of tundra mosses. This tendency was even more pronounced in 2012. During 20 years between surveys at least six very common tundra species (*Aulacomnium turgidum*, *A. palustre*, *Tomentypnum nitens*, *Straminergon stramineum*) penetrated into willow-cotton-grass community on shear surface which now does not differ from similar communities in undisturbed run-off depressions. Naturally, no pioneer species were found on ancient shear surface. Total number of species on shear surface varies both between landslides and between years (Table 1). Some increase in number of species occurred on all landslides, except for the ancient (which was not identified in 1991). Projective cover increased dramatically on L1 during the 20 years, whereas for L3 change is practically invisible. Increase of total PC on L2 happened mainly due to the increase of area of wetter densely re-vegetated parts with *Dupontia* dominated community.

In the process of active layer detachment dramatic change of geophysical environment occur: organic layer is destroyed, pH of upper horizon of the ground changed to closer to neutral values (ca 6 vs. 4.4 under tundra turf), salty horizons became exposed. In Yamal obligate halophyte *Carex glareosa* (and in Gydan peninsula even *Carex maritima*) are characteristic for landslides and even serve as indicators of ancient landslides, facultative halophyte *Tripleurospermum hookeri* is one of co-dominants in pioneer groupings on young landslides. No one dwarf shrub species was recorded on any of landslides, whereas undisturbed communities surrounding landslides contained *Vaccinium vitis-idaea* and *Salix nummularia*. We can only speculate that probably higher salt content prevented it.

Two processes are ongoing during the re-vegetation of landslides. Stage of pioneer groupings continues 20–40 years and results in formation of

Tripleurospermum hookeri-grass communities on dry surfaces and cotton-grass-Dupontia wet meadows in run-off depressions. Afterwards willows started to colonize shear surface both as seedlings and vegetative re-growth. On old landslides shear surface is occupied by herbaceous-willow communities. On the other hand tundra vegetation on replaced blocks of landslide body is degrading and after long time is transforming also into grass-willow communities, along with the process of washing out of these blocks. Those grass-willow communities is a long-term stage in revegetation of landslides.

On a whole landslides can be considered as a factor promoting habitat diversity and respectively biodiversity. Numbers of vascular species and mosses in different undisturbed communities surrounding landslides were varying between 20 and 30 species which is significantly fewer than on shear surface (Table 1). Though recovery of shear surface occur very slow in the Arctic compare to warmer zones. Mosses play active role in re-vegetation of shear surface. After many decades very stable mesophytic herb communities replace grass grouping. Willows (*Salix lanata*, *S. glauca*) obviously prefer sites with mineral enrichment and high (up to 1.5 m) willow copses which are unusual for this latitude are marking the sites of ancient landslides (Ukrantzzeva 1998). Vegetation can serve as a good indicator for estimating the age of the young landslides but this data can have only local implementation. Rates and patterns of re-vegetation differs greatly within the Arctic (see also Cannone et al. 2010).

References

- Arctic flora of the USSR. I–X. 1960–1987. Nauka Printing House. Moscow-Leningrad
- Cannone N, Lewkowicz A, Guglielmin M (2010) Vegetation colonization of permafrost-related landslides, Ellesmere Island, Canadian High Arctic. *J Geophys Res* 115:G04020. doi:[10.1029/2010JG001384](https://doi.org/10.1029/2010JG001384)
- Geertsema M, Pojar J (2007) Influence of landslides on biophysical diversity—a perspective from British Columbia. *Geomorphology* 89:55–69
- Ignatov MS, Afonina OM, Ignatova EA (2006) Check-list of mosses of East Europe and North Asia. *Arctoa* 15:1–130
- Leibman MO (1995) Cryogenic landslides on the Yamal peninsula, Russia: preliminary observations. *Permafrost Periglac Process* 6:259–264
- Leibman MO, Kizyakov AI (2007) Cryogenic landslides of the Yamal and Yugorsky peninsulas. Rosselkhosakadmija Print. Moscow, 206p. ISBN 5-85941-206-1
- Rebristaya O, Khitun O, Chernyadjeva I, Leibman M (1995) Dynamics of vegetation on cryogenic landslides in Central Yamal. *Bot Z* 80 (4):31–48
- Ukrantzzeva NG (1998) Specific of distribution of shrub tundras on Yamal. Materials of Moscow Centre of Russian Geographical Society. *Biogeography* 7:46–53
- Walker DA, Walker MD (1991) History and pattern on disturbance in Alaskan Arctic terrestrial ecosystems: a hierarchical approach to analyzing landscape change. *J Appl Ecol* 28:244–276. doi:[10.2307/2404128](https://doi.org/10.2307/2404128)
- Yurtsev BA (1994) Floristic division of the Arctic. *J Veg Sci* 5:765–776



Assessment of Landsliding Hazard in Typical Tundra of Central Yamal, Russia

Artem Khomutov and Marina Leibman

Abstract

The paper is presenting assessment of cryogenic landsliding hazard based on differentiation of landscapes in Central Yamal. Analysis of a landslide pattern shows that all modern cryogenic landslides are located on concave slopes, representing ancient landslide-affected area. Modern landsliding impact increases from low to high geomorphic levels. Landscape complexes are associated into five groups according to predicted cryogenic landsliding hazard degree. Grouping of landscape complexes is based on (1) differentiation of landscape conditions more or less favourable for cryogenic landsliding and (2) the latest cryogenic landslide occurrence. Landslide distribution within a landscape unit determines its sensitivity to landslide re-occurrence, the larger the area of disturbance by modern landsliding the more sensitive is a landscape complex. At the same time, directly disturbed by the latest landslides areas within a landscape unit are considered non-hazardous because the re-occurrence of cryogenic landsliding on such locations in coming centuries is mostly improbable.

Keywords

Cryogenic landsliding • Cryogenic translational landslides • Landscape complexes • Landscape map • Landslide impact • Landslide hazard

Introduction

On Central Yamal, cryogenic landsliding is a major surface process to control landscape dynamics.

Development of cryogenic landsliding in the areas of the shallow occurrence of tabular ground ice should be considered the most hazardous type of slope instability. Landsliding on such slopes can re-occur even in case of insignificant increase of summer air temperatures combined with minimal technogenic impact (Leibman and Kizyakov 2007; Burn and Zhang 2009).

The slopes with seasonal ground ice that is formed at the base of the active layer in a certain combination of climatic factors over a period of several years are less sensitive to the impact (Leibman 1997). Cryogenic landsliding along such icy surfaces (cryogenic translational landslides or active-layer detachments) can re-occur at the same site once in a few hundred years (Leibman et al. 2003). However, this periodicity is not fixed in time, and the adjacent areas may be subject to landsliding any time under the significant increase of summer precipitation and a simultaneous increase of air temperature. Cryogenic translational landslides (CTL) are the largest in size and, consequently, in mass in the area under study. This is why they are so hazardous.

Assessment of the landslide hazard use qualitative estimates based on identification of sites with different character of landslide activation (Kazakov and Gensiorovskii Yu 2008). To ensure landslide control during construction,

A. Khomutov (✉) • M. Leibman
Earth Cryosphere Institute, Siberian Branch, Russian Academy of Sciences, Malygin street, 86, Tyumen 625000, Russia
e-mail: akhomutov@gmail.com; moleibman@mail.ru



Fig. 1 Study area

assessment of the landslide situation is carried out using both qualitative and quantitative methods (Postoev et al. 2008).

For the study area, one of the first attempts to estimate the potential hazard of cryogenic landsliding activation was undertaken by Ukraintseva (Ukraintseva et al. 1992). It was qualitative expert judgement based on the analysis of changes in slope processes distribution on Bovanenkovo gas field. Expert judgement is proposed as a kind of rapid testing and alternative to quantitative methods requiring long-time special stationary observations (Ershov 1989; Grechishchev 1981). Ermokhina (Ermokhina 2009; Ermokhina and Ukraintseva 2003; Ermokhina and Myalo 2012) assessed probability of landslide process activation on Yamal Peninsula using vegetation as an indicator of land surface processes. Because of active exploitation of northern gas fields in cryolithozone characterized by active surface processes, the wider application of digital airborne and space borne data related to assessment of a landslide hazard became a timely issue.

Study Area

Estimation of the landslide hazard was carried out at the Vaskiny Dachi key site located in the watershed of Se-Yakha and Mordy-Yakha rivers on marine and coastal-marine plains of Central Yamal (Fig. 1).

The study area is a hilly plain. The highest elevations (up to 58 m altitude) are found within flat-topped remnants of the Salekhardskaya (Vth) Marine Plain. The territory is intensely dissected by narrow river valleys and gullies. The dissection depth is up to 50 m. Most of the territory (about 60 %) is represented by gentle slopes with gradient up to 7°; slopes with gradient between 7° and 50° (observed maximum in the area) occupy approximately 10 % of the area; and the

remaining 30 % include floodplains, lake depressions, and narrow-topped ridges (Leibman et al. 2003).

Active slope processes are typical for the outliers of marine terraces composed of ice-rich deposits with tabular ground ice. On the slopes with the shallow occurrence of tabular ground ice, thermocirques are developing, which transform into landslide cirques as the tabular ground ice is exhausted (Leibman 2005).

Vaskiny Dachi key site is located in the typical (moss and lichen) tundra subzone, gradually changing to the low-shrub tundra subzone (Trofimov 1975), bioclimatic subzone D according to Circumpolar Arctic Vegetation Map (CAVM Team 2003; Walker et al. 2009).

Methods

On our opinion, expert approach based on a CTL origin in the region of interest, combined with a landscape approach best suits assessment of cryogenic landsliding hazard. Main attention is given to the cryogenic landslides of 1989 as a large-scale natural landsliding experiment providing enough data for both conceptual and statistical output.

We offer special landscape zoning suitable for analysis of landslide hazard. Firstly, geomorphic levels with specific geology, topography, and slope length are subdivided, according to Leibman and Kizyakov (2007). Higher geomorphic levels provide greater amplitude of the relief, longer slopes, and respectively probability of large-scale landsliding (Leibman 2005). Then, landforms where cryogenic landsliding activation is probable were assigned. Separated were subhorizontal surfaces and bottoms where cryogenic landslide formation is impossible, and tops where landslides are improbable. Estimation of the landslide hazard on the slopes is based on previously developed conceptual models of cryogenic landsliding (Leibman and Kizyakov 2007). Analysis of a landslide pattern shows that all modern cryogenic landslides are located on concave slopes. As concave slopes on our opinion are resulting from ancient landsliding, it means that modern landslides inherit ancient landslide slopes (Leibman 2005). But new landslides are less probable on concave slopes already affected by modern landsliding than on concave slopes with only ancient landslides. Conditions necessary for landslide activation include thick organic canopy on the surface and high degree of cryodiagenesis of active layer deposits.

Landslide hazard is defined as a probability of surface disturbance due to a landslide body displacement (“outflow of material zone”), formation of a landslide shear surface (“transit zone”), and depositing of a landslide body (“accumulation zone”). Landsliding affects all the landforms. The watershed edges are in the zone of outflow, with subsidence cracks and suffusion subsidence. The slope surface in the

transit zone is exposed that leads to the change of surface lithology, specific soil process and vegetation succession, activation of thermoerosion. The landslide body is unloaded at the lower part of the slope, into the valley, or gully in the accumulation zone. This leads to the change of the hydrological regime, blocking of slope and valley water flow and forming of backwater lakes with thermokarst activation (Gubarkov and Leibman 2010).

Method used for assessment of cryogenic landslides involves an integrated landscape approach (Khomutov and Leibman 2010) combined with the concept of cryogenic landslide mechanisms (Leibman 2001; Leibman and Kizyakov 2007; Leibman and Egorov 1996). A full range of landscape factors directly or indirectly affecting the probability of cryogenic landsliding activation are considered.

To analyze modern landsliding impact, 19 landscape complexes were subdivided within main landforms (hill tops, slopes of various gradient and valley bottoms).

Distribution of CTL that of 1989 were mapped and their number and area calculated within each of 19 landscape units.

Three groups of the landslide coverage area are: (1) less than 0.002 km², (2) from 0.002 to 0.01 km², and (3) more than 0.01 km².

Results

Modern Landsliding Impact

At Vaskiny Dachi most of the largest landslides (with area more 0.01 km², and up to 0.08 km² each) are found on poorly drained lengthy gentle and concave ancient-landslide-affected slopes, and subhorizontal hummocky-tussocky slopes adjacent to hilltops.

Landslides with area of 0.002–0.01 km² generally are linked to all the landscape complexes, more often to landslide-affected concave shrubby slopes. Single landslides of this type occur on rather drained subhorizontal slopes with hummocky and tussocky tundra adjacent to hilltops, and drainage hollows, ravine, gully, and small stream valley slopes.

Small landslides (area less than 0.002 km²) are widely distributed on steep slopes of ravine and stream systems and frequently are linked to boundaries between these landscape complexes and rather drained edges of subhorizontal watersheds undercut by ravines and stream valleys, as well as lake depressions.

Modern landsliding impact differs within the same landscape complexes appearing on different geomorphic levels: Vth Marine plain, IVth Coastal-marine plain, IIIrd Alluvial-marine plain, IIrd river terrace, Mordy-Yakha river flood plain. Landscape complexes are associated in five groups

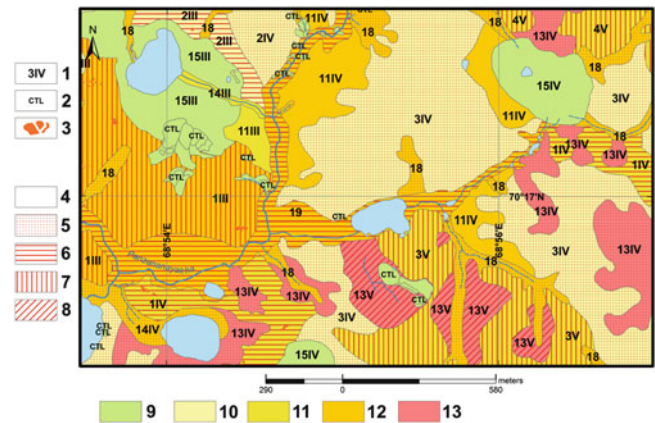


Fig. 2 Map of modern landslide impact and landslide hazard within subdivided landscape complexes. (1) landscape complexes, (2) cryogenic translational landslides of 1989, (3) windblown sands; Degree of modern landsliding impact: (4) none (0 %), (5) low (0–1 %), (6) moderate (1–5 %), (7) high (5–10 %), (8) largest (10 % and more); Degree of cryogenic landsliding hazard: (9) impossible, (10) minimal, (11) average, (12) serious, (13) maximal

according to the modern landsliding impact (Fig. 2, Table 1). Generally, impact of modern landsliding on landscape complexes increases from low (II–III) to high (IV–V) geomorphic levels.

The largest landsliding impact occurred on concave ancient-landslide-affected slopes (unit 13, Fig. 2) and gentle slopes with tussocky shrub-sedge-moss cover (unit 12, Fig. 2) on Vth Marine plain. These landscape units are affected by CTL of 1989 landsliding event on the area of 16 and 20 %, respectively.

Though in general watersheds (units 1–4) are not landslide-affected, landsliding here affects edge parts of the watershed landscapes by landslides on concave slopes and steep slopes of drainage hollows (unit 14), ravines (unit 18) and small stream valleys (unit 19).

Modern landsliding impact on landscape complexes does not exceed 20 %. Therefore, at least 80 % of each landscape unit surface can be affected by cryogenic landslides in nearest future. The activation of cryogenic landslides in the next 300 years is improbable on the surfaces affected by modern landsliding (Leibman and Kizyakov 2007) because of active thermoerosion and poor organic cover. Thus conditions necessary for landslide activation, namely thick organic canopy and high degree of cryodiagenesis of active layer form on the landslide shear surface for hundreds of years.

Cryogenic Landsliding Hazard

Landscape complexes affected by modern landslides are considered more sensitive to landsliding if the area affected by CTL of 1989 is larger. Parts of such landscape complexes without modern landslides are considered most hazardous.

Table 1 Degree of modern landsliding impact (1) and cryogenic landsliding hazard (2) at Vaskiny Dachi Research Station landscapes

1	2				
	Impossible	Minimal	Average	Serious	Maximal
None (0 %)	7II, 7III, 7IV, 8II, 8IV, 9 F, 15II, 15III, 15IV, 16III, 16IV, 17, CTL of 1989	3III,4II, 4III, 5II, 6III, 6IV, 10II, 10III, 10IV	2 V, 11II, 11III, 14III	11IV, 11 V	–
Low (0–1 %)	–	2IV, 3IV, 4IV	14II	14IV, 18	13IV
Moderate (1–5 %)	–	2III	1IV, 1 V, 12IV	19	13III
High (5–10 %)	–	–	3 V, 4 V	1III, 14 V	–
Largest (>10 %)	–	–	–	–	12 V,13 V

Note: V, Marine plain, IV, Coastal-marine plain, III, Alluvial-marine plain, II, River terrace, F, River flood plain



Fig. 3 Example of landscape without modern landslide impact and impossible landslide hazard (unit 7)



Fig. 4 Example of landscape with **moderate** landslide impact and minimal landslide hazard (unit 2III)

According to this principle and based on the analysis of modern CTL coverage within different landscape complexes and geomorphic levels, landscape complexes are associated into five groups of hazard degree: impossible, minimal,



Fig. 5 Example of landscape with high landslide impact and average landslide hazard (unit 4 V)

average, serious and maximal (Fig. 2, Table 1), based on estimation of geomorphic features, slope steepness, drainage, microrelief, vegetation associations and former landslide activity.

Maximal hazard of cryogenic landsliding remains on concave shrubby slopes (unit 13) of all geomorphic levels. Hazard of large-scale landsliding on gentle shrubby/partly shrubby slopes (units 11 and 12) increases from lower to higher geomorphic levels. Hazard of small-scale landsliding on subhorizontal surfaces (units 1–4) increases if deeply dissected by ravine (unit 18) and small stream valleys (unit 19), but without obvious relation to their geomorphic level.

Examples of landscapes characterized by different degree of impact/hazard are presented on photographs (Figs. 3, 4, 5, and 6).

Discussion

Existing for Central Yamal landslide risk assessment methods are qualitative or semi-quantitative in nature. Ukraintseva et al. (1992) identifies on the map natural



Fig. 6 Example of landscape with largest landslide impact and maximal landslide hazard (unit 13 V)

complexes, characterized by development of modern cryogenic processes, including slope ones, as a results of field surveys and expert judgement using analysis of landscape structure and engineering and permafrost changes. Her map of 1:100,000 scale covers IIIId alluvial-marine plain and river terraces.

Prediction of slope-process activation is based on the distribution of modern processes (the more widely and evenly distributed processes are, the more risky is the area). This method does not take into account our findings that the same area can become a scene for new landsliding only after several hundred years, excluding cases of close to the surface location of massive ground ice. This method was suggested and applied in the Bovanenkovo gas field area where it is acceptable because of low topography (from IIIId alluvial-marine plain to Se-Yakha river floodplain). Ermokhina (2009) estimates the likelihood of re-occurrence of landslides on landslide slope based on the degree of recovery of vegetation. Her method works on the ancient landslide slopes and does not assess other surfaces.

South of Bovanenkovo in the area of Research station Vaskiny Dachi with much more complicated geomorphology, high geomorphic levels, deeper in general massive ground ice position in the section, and much lower degree of anthropogenic impact, different approach is needed and suggested in this paper. Also based on relatively similar understanding of the process activation reasons, we suggest quantitative analysis of process coverage which was made possible by long-term detailed field study of landslide distribution and different mechanisms of its development (Leibman and Egorov 1996; Leibman et al. 2003; Khomutov and Leibman 2010). Also recently much more detailed remote-sensing data became available which in cooperation



Fig. 7 Cryogenic landslide on watershed edge next to concave shrunken slope (unit 13), detected in 2012 field season

with field survey of landscape structure allowed quantitative analysis with the addition of detailed landscape approach. Map of modern landsliding impact (Fig. 2) shows the degree of surface disturbance by modern landslides. The higher the degree, the more sensitive is a landscape complex to cryogenic landsliding. Simultaneously areas directly affected by modern landslides are attributed to low landslide risk, as the repetition of the landslide process cannot be on the surface with immature active layer and low degree of re-vegetation. The Map of cryogenic landsliding hazard (Fig. 2) being compared to other landslide prediction maps showed that in general the area of potential landslide risk match. However, our Map access landslide hazard in much more detail and is based on a longer and much more detailed ground truth and high-resolution remote-sensing data interpretation. During the 2012 field season, we observed two newly formed cryogenic landslides (Fig. 7) within units 13 and 18, and a thermocirque in unit 13 most probably activated by CTL. All of these cryogenic landsliding objects are linked to landscape complexes estimated as maximal landslide sensitivity (hazard degree), which proves applicability of the suggested method.

Conclusions

Method of cryogenic landsliding hazard analysis is based on quantitative assessment and expert judgment of modern landslide distribution and their parameters in different landscapes.

The application of the suggested risk assessment method reveals the following:

Very high cryogenic landsliding hazard on concave shrunken slopes is characteristic of all geomorphic levels except Mordy-Yakha river flood plain and 2nd river terrace.

Risk of large-scale landsliding on gentle shrunken/partly shrunken slopes increases from low to high geomorphic levels. Small-scale landsliding on subhorizontal surfaces increases with the degree and depth of dissection by ravine and small stream valleys independently of geomorphic level.

Landscapes in the key area are characteristic of typical tundra in the North of West Siberia. Therefore, the method tested at the key site can be applied to other plains of typical tundra zone with widely distributed tabular ground ice triggering cryogenic landsliding.

The application of the method of cryogenic landsliding hazard analysis using modern landsliding impact study and based on a landscape approach is quite effective at low labor costs. If high resolution satellite images for the area of interest are available, the method described in this paper is easy to apply with a minimum field investigations. Field work is needed just to refine local features for correct remote differentiating of landforms and vegetation cover on landscape base map. The combination of the suggested landscape method with the phytoindication method suggested by Ermokhina (2009) surely allows the most accurate prediction of landslide activation, but it is connected with more detailed field study.

Acknowledgments This study was supported by the Interdisciplinary Integration grants No. 122 and No. 144 of the SB RAS, Science School Grant #5582.2012.5, and RFBR grant #13-05-91001-AHΦ_a to the Earth Cryosphere Institute SB RAS.

References

- Burn CR, Zhang Y (2009) Permafrost and climate change at Herschel Island (Qikiqtaruk), Yukon Territory, Canada. *J Geophys Res* 114, F02001. doi:10.1029/2008JF001087
- CAVM Team (2003) Circumpolar Arctic vegetation map conservation of Arctic Flora and Fauna (CAFF) Map No. 1. US Fish and Wildlife Service, Anchorage, AK
- Ermokhina KA (2009) Phyto-indication of exogenous processes in the tundras of Central Yamal. Candidate dissertation, Moscow University, Moscow, 24p (in Russian)
- Ermokhina KA, Myalo EG (2012) Phytoindicators of landslide disturbances in the Central Yamal. In: Drozdov DS, Romanovsky VE (eds) Tenth international conference on permafrost. Translations of Russian contributions, vol 2. The Northern Publisher, Salekhard, pp 531–536
- Ermokhina KA, Ukraintseva NG (2003) Ecosystem response on dynamics of cryogenic landslides in the subarctic tundras (Yamal peninsula). In: Arctic-Alpine ecosystem and people in a changing environment. Book of Abstracts. Polar Environmental Centre, Tromsø, Norway, p 97
- Ershov ED (ed) (1989) *Geocryology of the USSR: Western Siberia*. Nedra, Moscow, 454p (in Russian)
- Grechishchev SE (ed) (1981) Guidelines for prediction of cryogenic physical-geological processes developing in the exploited areas of the Far North. VSEGINGEO, Moscow, 78 pp (in Russian)
- Gubarkov AA, Leibman MO (2010) Bead-shaped channel forms as evidence of paragenesis of cryogenic and hydrological processes in the small-river valleys of Central Yamal. *Earth Cryosphere XIV* (1):41–49
- Kazakov NA, Gensiorovskii Yu V (2008) Exogenous geodynamic and fluvial processes in the low-mountain area of the Sakhalin Island as the risk factors for “Sakhalin-2” oil and gas pipelines. *Environ Geosci Eng Geol Hydrogeol Geocryol* 6:483–496 (in Russian)
- Khomutov AV, Leibman MO (2010) Landscape pattern and cryogenic landsliding hazard analysis on Yamal peninsula, Russia. In: Thermal state of frozen ground in a changing climate during the IPY. Abstracts from the third European conference on permafrost. The University Centre in Svalbard, p 254
- Leibman MO (1997) Cryolithological peculiarities of the seasonally thawed layer on slopes in relation to the landslide process. *Earth Cryosphere I*(2):50–55 (in Russian)
- Leibman MO (2001) Procedures and results of active-layer measurements in marine saline deposits of Central Yamal. *Earth Cryosphere V*(3):17–24 (in Russian)
- Leibman MO (2005) Cryogenic slope processes and their geocologic consequences under the tabular ground ice distribution. Doctor of science dissertation, Tyumen, 40p (in Russian)
- Leibman MO, Egorov IP (1996) Climatic and environmental controls of cryogenic landslides, Yamal, Russia. In: Senneset K (ed) *Landslides*. Balkema Publishers, Rotterdam, pp 1941–1946
- Leibman MO, Kizyakov AI (2007) Cryogenic landslides of the Yamal and Yugorsky peninsulas. In: Melnikov VP (ed) *Earth Cryosphere Institute SB RAS, Moscow-Tyumen*, 206p. ISBN 5-85941-206-1 (in Russian)
- Leibman MO, Kizyakov AI, Sulerzhitsky LD, Zaretskaya NE (2003) Dynamics of the landslide slopes and mechanism of their development on Yamal peninsula Russia Permafrost. In: Proceedings of the 8th international conference on permafrost, 21–25 July 2003, Zurich, Switzerland, pp 651–656
- Postoev GP, Lapochkin BK, Kazeev AI, Nikulshin AS (2008) Natural and human-induced processes assessment of landslide hazard at the construction sites. *Environ Geosci Eng Geol Hydrogeol Geocryol* 6:547–557 (in Russian)
- Trofimov VT (ed) (1975) *Yamal Peninsula (engineering-geological outline)*. Moscow University Press, Moscow, 280 pp (in Russian)
- Ukraintseva NG, Shuvalova EM, Vasiliev AA (1992) Assessment of potential hazard of slope processes activation on area of Bovanenkovo gas field. In: Grechischev SE (ed) *Methods of research of cryogenic physical-geological processes*. VSEGINGEO, Moscow, pp 109–113 (in Russian)
- Walker DA, Leibman MO, Epstein HE et al (2009) Spatial and temporal patterns of greenness on the Yamal Peninsula, Russia: interactions of ecological and social factors affecting the Arctic normalized difference vegetation index. *Environ Res Lett* 4:045004



Cryogenic Landslides in the Arctic Plains of Russia: Classification, Mechanisms, and Landforms

Marina Leibman, Artem Khomutov, and Alexandr Kizyakov

Abstract

The paper is discussing the theory of cryogenic landslides. Suggested is classification of cryogenic landslides based on several attributes: mechanisms, specific landforms, and other manifestations of landsliding characteristic of the Arctic plains of Russia. The theory results from long-term field study at research station “Vaskiny Dachi” in Central Yamal, key sites on Yugorsky peninsula, as well as occasional observations in other areas of the Russian Arctic. Two main types of cryogenic landslides are identified: retrogressive thaw slumps (earth/mud flows) and translational landslides (active-layer detachments). Distinguished are several stages of landform development resulting from landsliding, passing from thermocirques to landslide cirques. Landslide cirques are considered to start as a subsequent stage of decadent thermocirque after the ground ice layer is exhausted or buried by landslide masses. Cryogenic landslides are climate-related features and for this reason are indicators of past and modern climate fluctuations.

Keywords

Cryogenic landslides • Thermocirque • Landslide cirque • Active layer • Transient layer • Massive ground ice

Introduction

The detailed study of landslides in permafrost zone was undertaken after the widespread landslide event in the North of West Siberia, especially on Yamal Peninsula, and Canada in 1988–1990 (Lewkowicz 1988; Leibman et al. 2003). Forcing factors and mechanisms are analysed in Leibman and Egorov (1996) and Lewkowicz (1990). General aspects of cryogenic landsliding within the Arctic are discussed in Voskresenskiy (1999), Harris and Lewkowicz

(2000), French (2007). The latest monograph reviewing previous knowledge and suggesting classifications and mechanisms based on extensive field study in north of West Siberia is published by Leibman and Kizyakov (2007).

This paper is devoted to cryogenic landslide classification, mechanisms for their activation, and landforms resulting from landslides of various mechanisms specific for the Arctic plains.

Key Site Characteristics

Vaskiny Dachi research polygon is located at the watershed of Se-Yakha and Mordy-Yakha rivers (Fig. 1), and comprises a number of highly-dissected alluvial-lacustrine-marine plains and terraces. Deposits are sandy to clayey. Massive ground ice including tabular ice and polygonal ice wedges,

M. Leibman (✉) • A. Khomutov
Earth Cryosphere Institute, Siberian Branch, Russian Academy
of Sciences, Malygin street, 86, Tyumen 625000, Russia
e-mail: moleibman@mail.ru; akhomutov@gmail.com

A. Kizyakov
Faculty of Geography, Moscow State University, Leninskie Gory,
Moscow 119991, Russia
e-mail: akizyakov@mail.ru

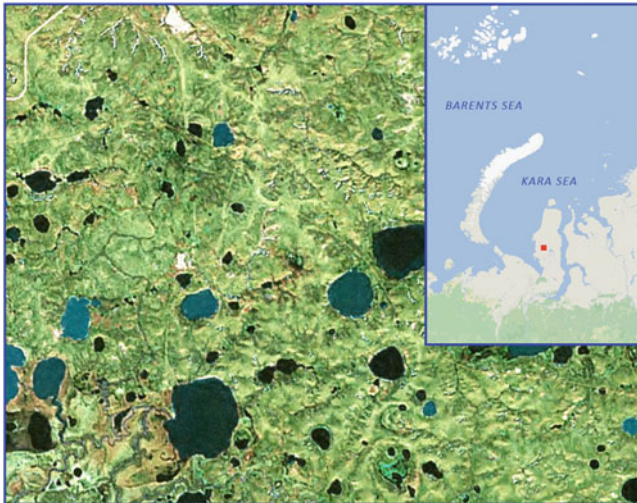


Fig. 1 Study area



Fig. 2 New exposure of tabular ground ice, Yamal Peninsula

are found within the geological section. Maximum elevations are up to 58 m above sea level. Maximum depths of dissection comprise 20–50 m.

Up to 60 % of the study area is represented by gentle slopes (gradient less than 7°), steep slopes (more than 7°) occupy about 10 % of the area, the rest 30 % being hilltops, river valleys and lake depressions.

Study area is characterized by continuous permafrost up to 400 m thick, and even more. Average annual ground temperature at the depths of zero annual amplitude ranges between 0 and -9°C .

The last decade, due to warm summers several new exposures of tabular ground ice formed by landslide activity (retrogressive thaw slumps, Fig. 2).

Table 1 Mechanisms and classification of cryogenic landslide process

Cryogenic translational landslides (active-layer detachments, block glides)	Cryogenic earth flows (mudflows, retrogressive thaw slumps)
Rather dry and dense sandy-silty active-layer deposits	Water-saturated viscous-flow silty-clayey active-layer deposits
Result of upward freezing of the active-layer and subsequent thaw of the ice at the active-layer base	Result of massive ice and/or ice-rich permafrost thaw
Inter-annual active-layer dynamics	Local lowering of permafrost table
Landslide body is a one piece or broken into several pieces block with well expressed vertical sidewalls along the perimeter	Landslide body is a spread flow with parabolic outlines, with floating pieces of turf (sod) overgrown by shrubs on top

Mechanisms and Classification of Cryogenic Landslides

Landslides in general are known to be triggered by high pore pressure due to water saturation (e.g. Schuster and Krizek 1978). In permafrost zone water saturation is provided by atmospheric precipitation together with the melt of ground ice in the active layer or/and upper permafrost. The shear surface coincides with the lithological boundary or with permafrost table depending on which is closer to the surface (Leibman et al. 2003).

The cause for a high pore pressure is at the same time an indicator of a landslide mechanism. For Arctic plains, such as North of West Siberia, we subdivide two different mechanisms of landsliding, two sets of forcing factors, triggers, and landforms. The name of process in a reference to the mechanism of landsliding in Table 1 is translation of Russian terms (in the parenthesis are more or less equivalent terms used in the English cryogenic-landslide literature).

Cryogenic Translational Landslides

Left column of Table 1 presents mechanism resulting from a rapid thaw of ice-bearing deposits at the active layer base (transient layer after Shur 1988). Accumulation of segregation ice at the active-layer base and formation of the transient layer is due to the active layer depth decrease in the course of several years cooling observed on Yamal in 1985–1988 (Leibman and Egorov 1996). Intensive heat flux in the late summer and heavy rainfalls linked to this period both cause relatively rapid thaw of the icy layer at the active-layer base (about 17 cm as measured from July 15 to August 14 in 1989, about 75 % higher than in other years,



Fig. 3 Crack filled with suspension pressed out due to high pore pressure (*left pane*) and edge crack (*right pane*), Yamal Peninsula



Fig. 4 Cryogenic landslide body on Yamal Peninsula

(Leibman and Egorov 1996), excess water accumulates in the active layer because of low filtration ability of silty soils (first centimetres per day, Leibman et al. 1993), and pore pressure rises dramatically. Gravity causes displacement of blocks, “floating” on the layer with excess pore pressure, broken up by frost, desiccation, or edge cracks (Leibman and Egorov 1996, Fig. 3).

Blocks preserve integrity due to structural bounds, formed by multiple freeze-thaw, drying-liquefaction and desiccation of the middle portion of the active layer by two-sided freeze back (Lewkowicz 1990; Leibman et al. 2003, Fig. 4).

Cryogenic Earth/Mud Flows CEF/CMF

Right column of Table 1 presents mechanism resulting from thaw of the massive ground ice (see Fig. 2). CEF/CMF are also referred to as retrogressive thaw slumps. This type of sliding mechanism is linked to the areas where massive ground ice is close to the surface (Burn and Lewkowicz 1990) and is occasionally involved into seasonal thaw through the natural or technogenic disturbance, or noticeable summer warming (Fig. 5).



Fig. 5 Cryogenic mud flow on Yugorsky Peninsula

At the exposures, thawing ice causes failures of overlaying deposits liquefied by meltwater and produce mudflows with pieces of turf, floating onto the flow. When exposures are covered with talus, portion of meltwater is absorbed by slope deposits and then earth flows form (Leibman and Kizyakov 2007).

Differently from Cryogenic translational landslides (CTL), CEF/CMF can develop every year until massive ground ice is within the zone of seasonal thaw. CMF are formed during the entire warm period at the ice exposures, CEF form only during warm years, mainly at the end of the warm period under the maximum thaw depth. Rain water is not as crucial for CEF/CMF, as is for CTL because massive-ice melt-water provides enough moisture for embodiment of the landslide potential on slopes (Kizyakov et al. 2006).

Landforms Produced by Landsliding

Landslide-affected slopes present a specific set of morphological elements: (a) cirque-shaped depressions, landslide scarp and shear surface (denudation and transition zone, Fig. 6); and (b) deformed hillocks and terraces, landslide bodies (accumulation zone, see Figs. 4 and 5).

On our opinion, modern landforms produced by landslide activity are inheriting those resulting from past thermokarst events of Holocene climatic optimum. At that time tabular ground ice bodies were involved in permafrost degradation from the surface, and in the areas with water outflow slope depressions—thermocirques formed through CEF/CMF. These landforms are continuously developing until now, more actively at the sea coast (Kizyakov et al 2006; Khomutov and Leibman 2008).

Evolution of thermocirques leads to flattening of slopes, revegetation of former exposures and thus transformation of thermocirques into landslide cirques. The reason is exhausting



Fig. 6 Cryogenic landslide: scarp and shear surface, Yugorsky peninsula

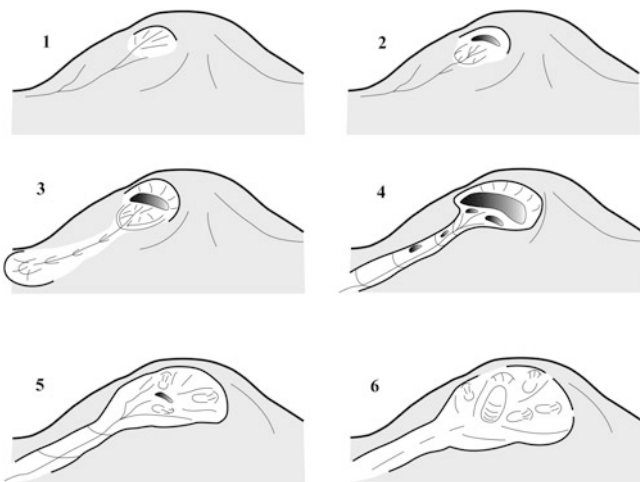


Fig. 7 Evolution of thermocirque into a landslide cirque: (1) initial lowering of the surface; (2) initial exposure of massive ground ice, CEF development; (3) expansion of landsliding; (4) widening and deepening of concavities; (5) burial of concavities by landslide bodies; (6) extinction of thermodenudation, development of CTL

or burying of near-surface layers of tabular ground ice, cooling of climate which causes formation of transient layer immediately beneath the modern active layer, and finally replacement of CEF by CTL to form landslide cirques as shown on a sketch (Fig. 7).

To evaluate the potential for activation of thermocirque development, we introduce the concept of landform development phase. The active phase is characterized by a combination of climatic conditions over the years which favors CEF/CMF (warming and massive ice thaw, significant summer rainfall is a favor as well). Passive phase coincides with the cold dry periods.

While stages of thermocirque development, probably, last for centuries, phases are controlled by short-term climate

variations and last for several years or decades. The last stage of thermocirque development coincides with the first stage of the landslide cirque. Further development of the latter is under the influence of climatic factors, as described above.

Within a single CTL “sub-stages” of development can be subdivided: (1) initial landsliding event; (2) development of deep erosion troughs on the shear surface; (3) sedimentation and vegetation recovery in the rear of the landslide, flattening of the erosion troughs; (4) overgrowing the shear surface, its leveling and wetting of the shear surface; and finally, (5) new landsliding. As follows from our observations in the key area “Vaskiny Dachi”, the first two sub-stages last for the period of more than 15 but less than 50 years. Sub-stage 3 takes 200 years or more.

Landslide cirque is harder to interpret when new landslides are not in view. At Research Station Vaskiny Dachi we observed modern landslides which occurred in 1989 and thus were able to distinguish these landforms of older age including ancient ones, dated to be between 300 and 2,100 years old (Leibman et al. 2003).

Thus, main landforms resulting from multiple landsliding events at the early stages of development are thermodenudation cirques, turning into the landslide cirques at the later stages. Periods of landsliding activation are separated by periods of relative stability needed to recover the stress state of slopes and terrain conditions favourable for landsliding of CTL type. These conditions include formation of dense vegetative canopy, cryogenically-transformed slope deposits (looser at the top and bottom and compact in the middle), flattened concave surface without marked drainage pattern, then the slope is ready to respond to the proper climatic conditions, such as several years of cooling and reducing the active-layer depth (to form icy transient layer), consequent warm summer (to thaw the transient layer), and high summer precipitation (to dramatically rise pore pressure within the active layer).

Conclusions

Cryogenic landslides are the main relief-forming process on the Arctic Plains of the North of West Siberia. Specific landforms of Central Yamal peninsula include concave slopes with mosaic vegetative cover represented by various pioneer to mature vegetative communities, patches of high willow shrubs, and heterogeneous mesorelief. These are shown to be landslide cirques formed by a series of landslide events during the late Holocene.

Cryogenic landslides are climate-related features and for this reason are indicators of past and modern climate fluctuations. The landsliding activation is controlled, first, by increasing atmospheric precipitation, and second, rise of summer air temperature.

Climate warming is followed by ground temperature rise and thus the southern limits of CTL occurrence should probably move northward where conditions for the ice formation at the active-layer base still preserve. As to CEF/CMF, their northern limits probably shift further northward due to active-layer thickening towards the deep-seated massive ice bodies.

Prediction of the landslide activation due to climate change is a complicated multi-factor analysis and can't be reduced to just the climate warming model.

Acknowledgements This study was supported by the Interdisciplinary Integration grants No. 122 and No. 144 of the SB RAS, Science School Grant #5582.2012.5, and RFBR grant #13-05-91001-AHΦ_a to the Earth Cryosphere Institute SB RAS.

References

- Burn CR, Lewkowicz A (1990) Retrogressive thaw slumps. *Can Geogr* 34(3):273–276
- French HM (2007) *The periglacial environment*, 3rd edn. Wiley, Chichester, 458 p. ISBN 978-0-470-86589-7
- Harris C, Lewkowicz AG (2000) An analysis of the stability of thawing slopes, Ellesmere Island, Nunavut, Canada. *Can Geotech J* 37(2):449–462
- Khomutov AV, Leibman MO (2008) Landscape factors of thermodegradation rate at the Yugorsky peninsula coast. *Kriosfera Zemli (The Earth Cryosphere)* XII(4):24–35 (in Russian)
- Kizyakov AI, Leibman MO, Perednya DD (2006) Destructive relief-forming cryogenic processes at the coasts of the Arctic plains with tabular ground ice. *Kriosfera Zemli (The Earth Cryosphere)* X(2):79–89 (in Russian)
- Leibman MO, Egorov IP (1996) Climatic and environmental controls of cryogenic landslides, Yamal, Russia. In: *Proceedings of the seventh international symposium on landslides*, 17–21 June 1996, Trondheim, Norway, pp 1941–1946
- Leibman MO, Kizyakov AI (2007) *Cryogenic landslides of the Yamal and Yugorsky Peninsulas*. Earth Cryosphere Institute SB RAS, Moscow-Tyumen, 206p. ISBN 5-85941-206-1 (in Russian)
- Leibman MO, Rivkin FM, Saveliev VS (1993) Hydrogeological aspects of cryogenic slides on the Yamal peninsula. In: *Proceedings of the seventh international conference on permafrost*, vol 1, 5–9 July 1993, Beijing, China, pp 380–382
- Leibman MO, Kizyakov AI, Sulerzhitsky LD, Zaretskaya NE (2003) Dynamics of the landslide slopes and mechanism of their development on Yamal peninsula Russia Permafrost. In: *Proceedings of the 8th international conference on permafrost*, 21–25 July 2003, Zurich, Switzerland, pp 651–656
- Lewkowicz AG (1988) Slope processes. In: Clark MJ (ed) *Advances in periglacial geomorphology*. Wiley, New York, pp 325–368. ISBN 0471909815
- Lewkowicz AG (1990) Morphology, frequency and magnitude of active-layer detachment slides, Fosheim Peninsula, Ellesmere Island N W T. In: *Proceedings of the 5th Canadian permafrost conference*, vol 54, Quebec, Canada, June 1990. Laval University, Quebec, Collection Nordicana, pp 111–118
- Schuster RL, Krizek RJ (1978) *Landslides: analysis and control*. National Academy of Sciences, Washington, DC, 234 p. ISBN 0309028043
- Shur Yu L (1988) *Upper horizon of permafrost and thermokarst*. Nauka Publisher, Siberian Branch, Novosibirsk, 213 p (in Russian)
- Voskresenskiy KS (1999) Landslides-flows and thermokarst. In: Sidorchuk AY, Baranov AV (eds) *Erosion processes of Central Yamal*. S-PGU Press, St-Petersburg, Russia, pp 133–139 (in Russian)



Fluctuations in the Pore-Water Pressure of a Reactivated Landslide in a Snowy District

Sumio Matsuura, Takashi Okamoto, Hikaru Osawa, Tatsuya Shibasaki, Kazutoki Abe, and Yasuhiko Okada

Abstract

Pore-water pressure fluctuations and water that reaches the ground surface (MR) were monitored in a reactivated landslide which is located in a heavy snow district of Japan. Observations of pore-water pressure inside the moving landslide mass revealed that changes in pore-water pressure during snow cover periods were quite different from those in other periods. These results suggest that the hydrological properties of a moving landslide mass are strongly affected by snow load.

Keywords

Piezometer • Hydrologic coefficient • Snow load

Introduction

Gently sloping mountains composed of Neogene soft rocks are widely distributed over the area facing the Sea of Japan. In this area, landslides frequently occur in the snowmelt season of March to May since huge amounts of meltwater flow out from thick snow accumulations (Aoyama et al. 1984).

Therefore, landslide researchers have believed that most of the landslides are activated in the snowmelt season by meltwater. However, recent advanced monitoring has revealed that some landslides remain inactive even during the snowmelt period in spite of active movement before the snow cover period (Sato et al. 2004). In many cases, these

types of landslides have a relatively shallow slip surface and are relatively small in size (Matsuura et al. 2003).

Therefore, snowpack which accumulates to 3–5 m in depth during the winter season has some effect on the landslide movement, but the mechanism is not still clear. We observed pore-water pressure fluctuation and the water that reached the ground surface, both of which are closely related to landslide movement.

Monitoring Method

We set the research site in a typical re-activated landslide of a Neogene deposit area where thick snow accumulation occurs every winter. This landslide is an elongated shape of approximately 300 m in length, 50–70 m in width and has a relatively shallow slip surface from –5 to –7 m in depth (Fig. 1).

Movement of this landslide is the largest from autumn to early winter, while very little movement occurs in the snowmelt period. This landslide may be classified into four blocks, that is to say upper, middle, lower, and terminal blocks. A piezometer consisting of a strain-type pressure gauge of 50 kPa full scale was mounted in the moving landslide body of the lower block at –2.85 m below the surface (Fig. 2). The space around the piezometer was filled

S. Matsuura (✉) • H. Osawa • T. Shibasaki
Kyoto University, Disaster Prevention Research Institute, Gokasho,
Uji, Kyoto 611-0011, Japan
e-mail: matsu03@scs.dpri.kyoto-u.ac.jp

T. Okamoto • Y. Okada
Forestry and Forest Products Research Institute, 1 Matsunosato,
Tsukuba, Ibaraki 305-8687, Japan
e-mail: okataka@ffpri.affrc.go.jp

K. Abe
Nihon University, College of Bioresource Science, 1866 Kameino,
Fujisawa, Kanagawa 252-0880, Japan
e-mail: kazuab@brs.nihon-u.ac.jp

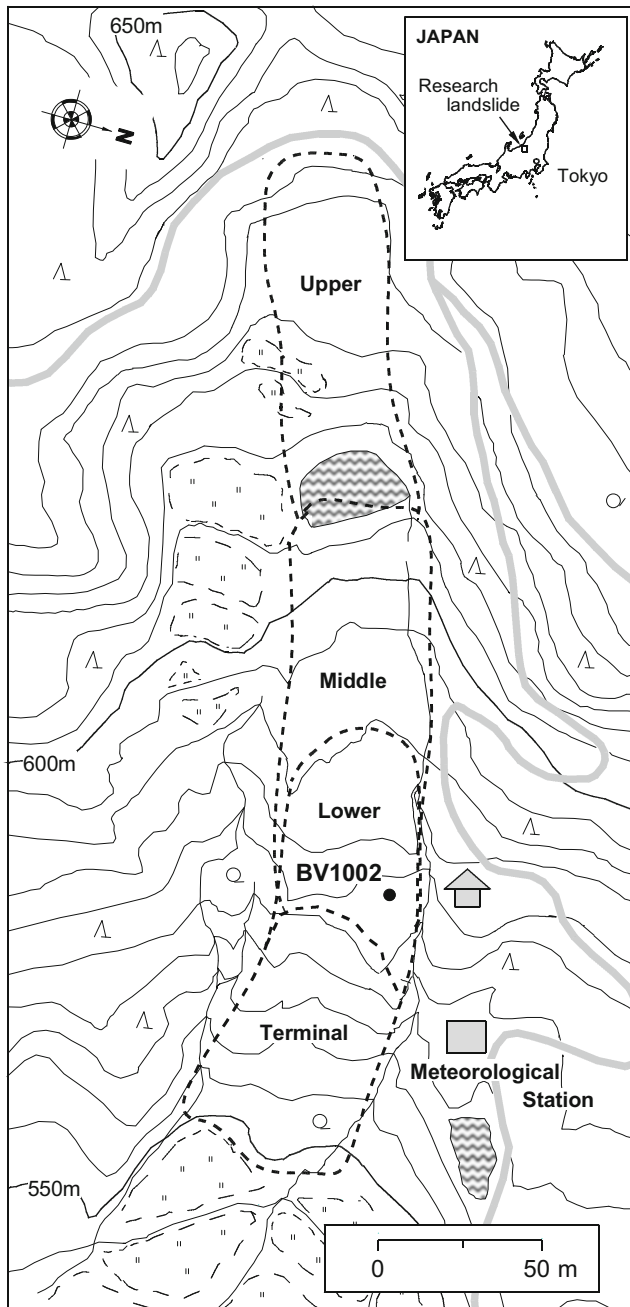


Fig. 1 Geomorphological map of the research landslide

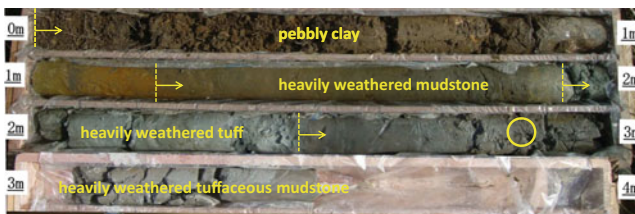


Fig. 2 Core sample of BV1002

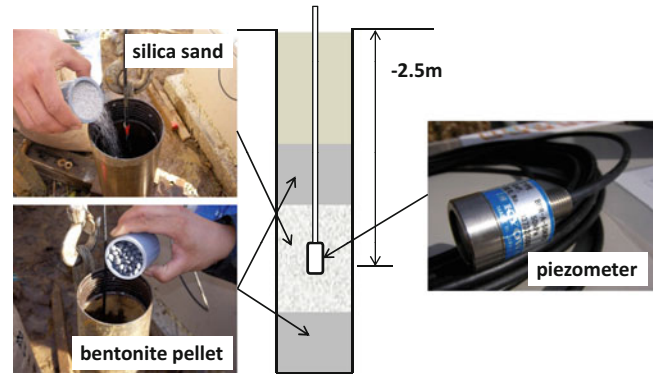


Fig. 3 Piezometer installation in borehole

with silica sand and top-and-bottom spaces were plugged with bentonite pellets (Fig. 3). The water that reaches the ground (hereafter referred to as MR) was observed using lysimeters with a tipping-bucket discharge gauge at a meteorological station.

Results and Discussion

Figure 4 shows the observed time series data of pore-water pressure and MR from September 1, 2011 to June 15, 2012. The response of pore-water pressure to rainfall was quite sensitive during the pre-snow cover period. However, pore-water pressure did not fluctuate due to less than 1 mm/d of MR when snow began to cover the ground. On the other hand, MR of 30–70 mm/d was observed almost every day in snowmelt period. However, there was relatively little increase in pore-water pressure for individual events.

We examined the response characteristics of the pore-water pressure for MR in the snowmelt period, especially during the pre-snow cover and snow cover periods. We compared the (ΔP) value, which is the integrated value of excess pore-water pressure, to time and (ΔMR), which is the total amount of MR in one event (Fig. 5). As a result, pore-water pressure responded sharply to the MR (rainfall) in the pre-snow cover period, while the response value decreased 1/50 to 1/200 in the snowmelt period. There were significant differences between the two periods (Fig. 6).

In addition, the response ratio ($\Delta P / \Delta MR$) of the events, which had a distinct peak both in pore-water pressure and MR in the snowmelt period, was calculated (Fig. 7). According to the results, the response ratio of 0.01–0.03 in the middle snowmelt period gradually increased, reaching 0.06–0.18 in the late snowmelt period.

The 2011–2012 winter season was very cold and a large amount of snow fell (Figs. 8 and 9). The maximum snow

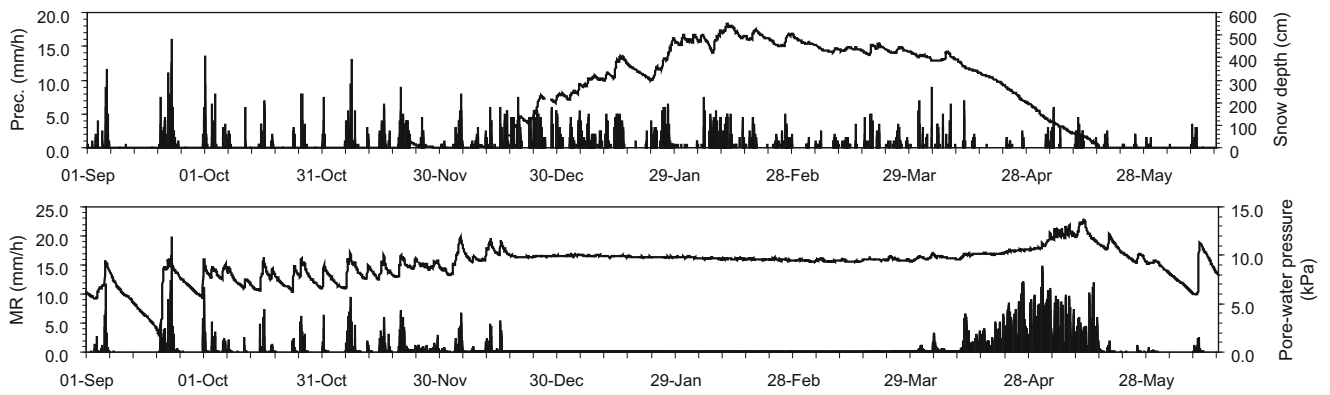


Fig. 4 Results of observations (2011–2012)

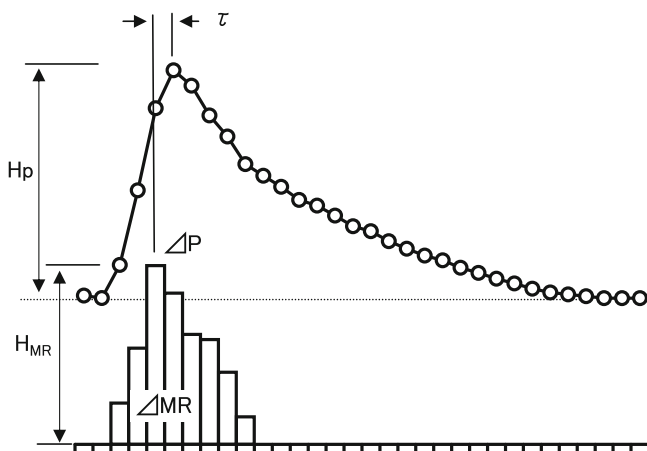


Fig. 5 Pore-water pressure response to MR

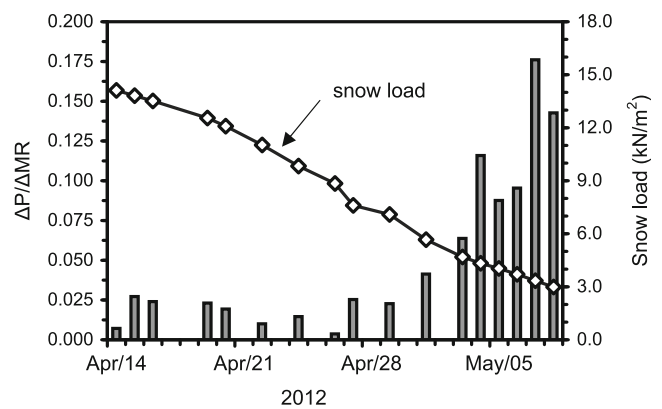


Fig. 7 Change in $\Delta P/\Delta MR$

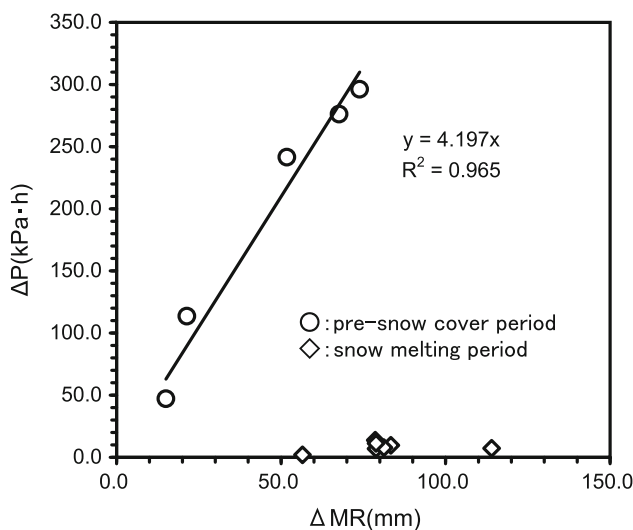


Fig. 6 Relationship between ΔMR and ΔP

depth was recorded at 551 cm on February 11, 2012 (Fig. 4). The maximum water equivalent of snow was 1,870 mm on March 15, which corresponds to 18.3 kN/m² in terms of snow load. Assuming that large snow load affected the response characteristics of the pore-water pressure, we compared the response ratio with the snow load (Fig. 10). The response ratio rapidly increased when the snow load decreased to around 5–6 kN/m², and these data can be approximated by an exponential function.

Therefore, the response characteristics of the pore-water pressure seem to be greatly affected by the snow load. In other words, the moving landslide body consisting of weathered soft rocks and clays was consolidated by snow load, which might have changed hydrogeological properties of the moving body such as void ratio.

On the other hand, the response ratio was relatively small, approximately 0.2, immediately after the disappearance of the snow. This value was far below the value of 3.0–5.0



Fig. 8 Meteorological station in the snow cover and post-snow cover periods



Fig. 9 Snow survey in a deep snow accumulation

during the pre-snow cover period. However, the response ratio tended to rise after the disappearance of snow. It appears that the consolidated moving body did not rebound immediately even if the snow load was removed; rather, it gradually bulged with a certain velocity. We plan to further investigate this phenomenon by conducting field tests and detailed analyses.

References

Aoyama K, Nakamata S, Ogawa S (1984) Consideration on the relations between landslide and snow in Niigata prefecture. *J Jpn Landslide Soc* 21(3):11–16 (in Japanese with English abstract)
 Matsuura S, Asano S, Okamoto T, Takeuchi Y (2003) Characteristics of the displacement of a landslide with a shallow sliding surface in a heavy snow district of Japan. *Eng Geol* 69:15–35
 Sato H, Shiraishi S, Ito T (2004) The behavior of the Tertiary landslides through the snowy period in Niigata prefecture, central Japan. *J Jpn Landslide Soc* 41(1):37–42 (in Japanese with English abstract)

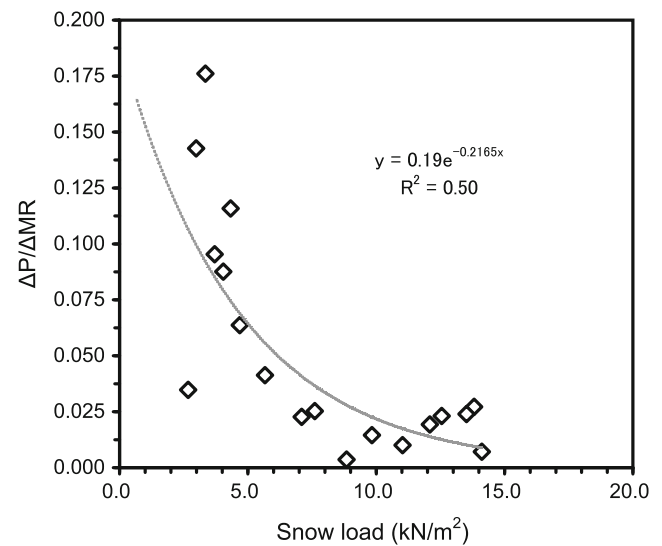


Fig. 10 Relationship between snow load and $\Delta P/\Delta MR$



Landslide Deformation Monitoring and Analysis of Influence Factors at K178 + 530 of the Bei'an to Heihe Expressway

Zhaoguang Hu, Wei Shan, and Hua Jiang

Abstract

A landslide occurred at the end of July 2010, at the K178 + 530 section of the Bei'an–Heihe expressway in the Northwest Lesser Khingan Mountains of China. The landslide is located on the left of the road embankment. Waste from road construction, subgrade fill, and surface soil slid along the valley, seriously damaging the road. The landslide is located in the permafrost area of the island. Owing to the atmospheric precipitation, the presence of permafrost, regional climate conditions, and special geological conditions, landslides occur annually from late May to early November. The area is in a relatively stable state during winter. These seasonal landslides have seasonal, gradual, low angle characteristics. By November 2012, the studied landslide had moved a distance of up to 104.15 m at the rear edge and 24.8 m at the leading edge. With the soil at the rear of the landslide decreasing and the recorded movement of the landslide over time, the landslide deformation appears to show an apparent attenuation trend. This article reports on a 2-year geological survey monitoring the surface deformation and soil geothermal changes. Research and analysis of the deformation features and effects of the landslide, and large scene survey and monitoring information can provide valuable information for analyzing soil landslides occurring in high latitude permafrost areas. Research results of steady disaster control and the optimization of artificial slope design hold important reference value for high-latitude permafrost area landslides.

Keywords

High latitude permafrost • Landslide • Deformation monitoring • Influence factors

Introduction

Landslides are a natural phenomenon occurring owing to the effects of river scour, groundwater activities, earthquakes, artificial cutting of slopes, and other factors on the rocks and soils of slopes, further influenced by gravity (Gu et al. 2009; He 1991). Landslides are common on mountainous highways owing to the geology, geomorphology, hydrology, and climatic conditions of the region. Landslides on

mountains frequently interrupt the flow of traffic along the mountainous expressways (Liu et al. 2007; Qiao 2002). Large-scale landslides can block rivers, destroy roads, damage roadside buildings, and disrupt local facilities (Li et al. 2003; Ma et al. 2006; Zhu et al. 2004).

Currently, research on the characteristics of landslide formations on mountains at high latitudes in the Lesser Khingan Range of the Heilongjiang Province, China, is in its initial stages (Shan et al. 2008). This article reports on the results of a 2-year geological survey monitoring the surface deformation and geothermal changes in the soils on slopes as well as on the effects of the landslide. Large scene surveys such as this can provide valuable information on the landslides that occur at high latitudes in permafrost areas;

Z. Hu • W. Shan (✉) • H. Jiang
Northeast Forestry University, Harbin, China
e-mail: huzhaoguang008@163.com; shanwei456@163.com;
jianghua3433@163.com

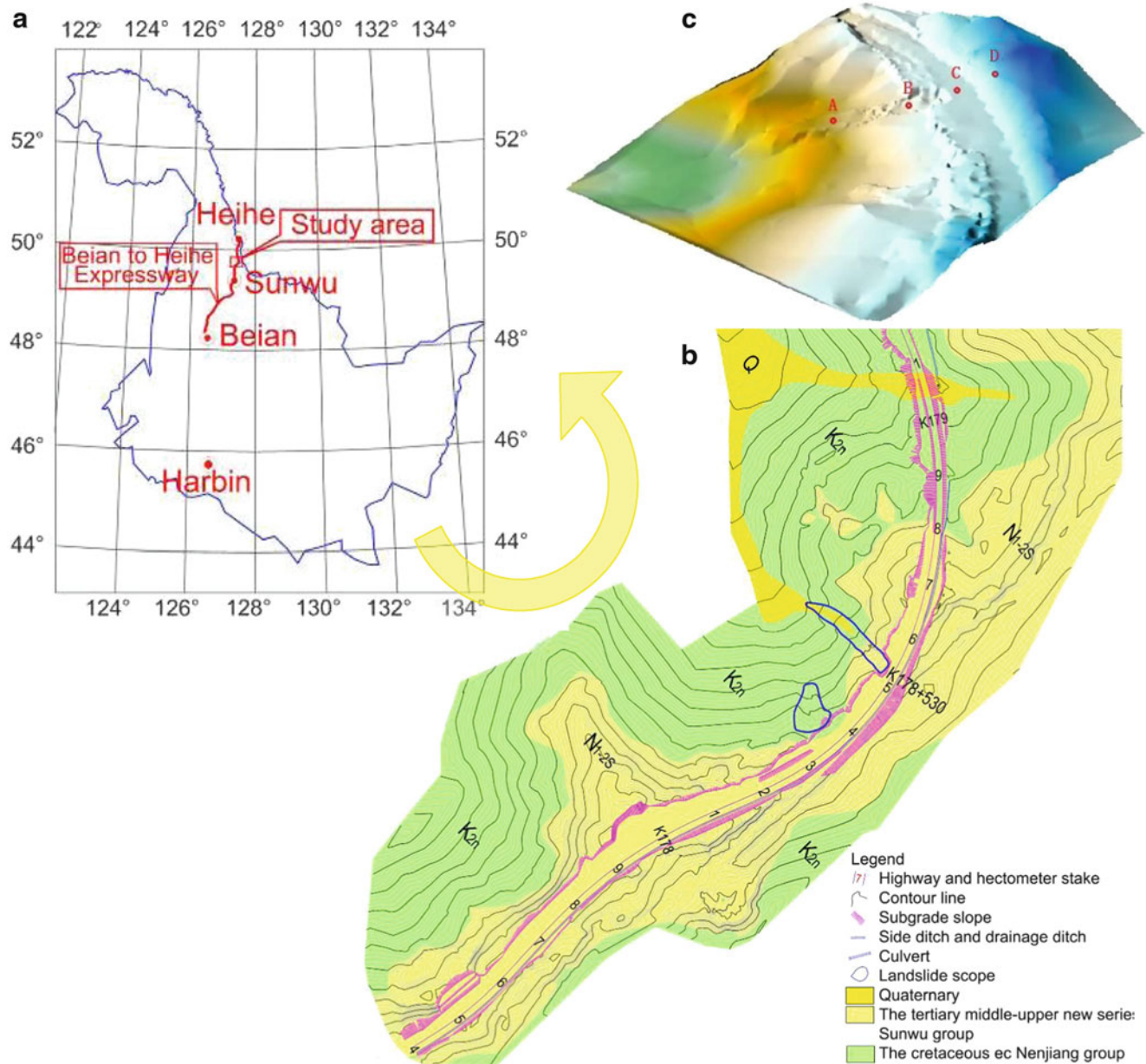


Fig. 1 (a) Satellite image showing the geographic position of the K178 + 530 landslide indicated by the red line. (b) Geographical position of the K178 + 530 landslide shown on a topographic and geological composite map. (c) K178 + 530 boreholes A–D drilled in the area

they aid in disaster control and evaluate the optimal artificial slope required to prevent landslides in landslide-prone highway areas.

Regional Natural Geographical Conditions

The geographic position of the study area is shown in Fig. 1. The landslide of interest is located in the central region of the Lesser Khingan Range. The spring season in this area is brief and warm, followed by a hot and rainy summer. With the onset of a short autumn season, the temperature falls rapidly,

leading to a long and cold winter. The annual average temperature in the area is -0.8°C . The average annual precipitation is 510–572 mm. Rainfall mostly occurs in the months of July to September and accounts for about 60 % of the total annual precipitation. The first snow generally occurs during the last third of October, and the last snow, at the end of March or during early April. During winter, the maximum depth of the frozen area is 2.30–2.50 m below the ground. The geomorphology of the study area is dominated mainly by low mountains and hills, and the topographic relief is large in the high latitude permafrost region (Hu and Shan 2011).

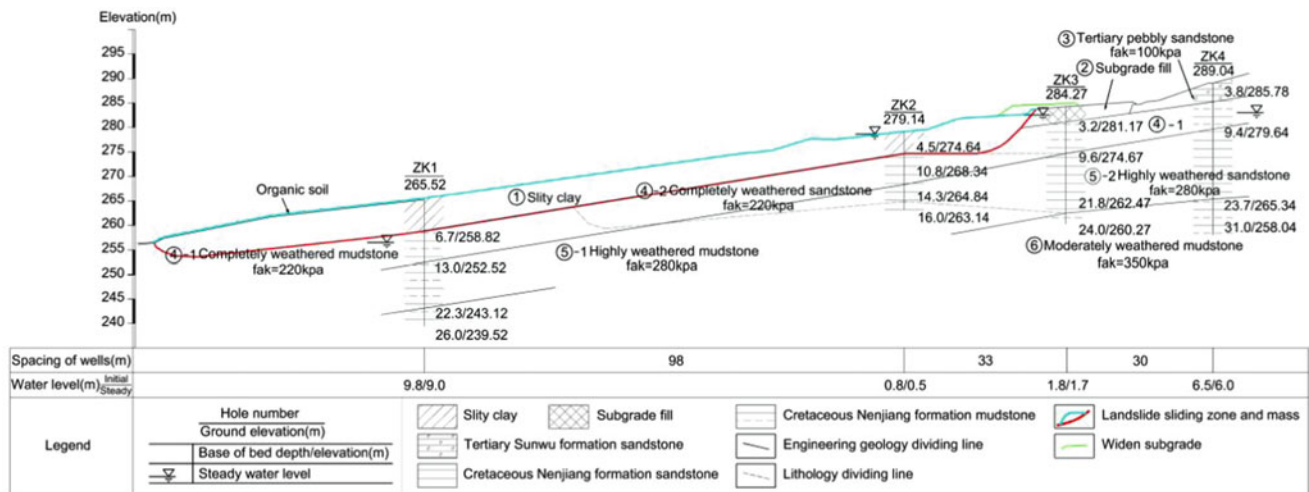


Fig. 2 Geological cross section of K178 + 530

K178 + 530 is located on the left of the road embankment. The abandoned soil and the subgrade fill soil slide along the gully. The 178 + 530 landslide is tongue-shaped; its width is 2,030 m, and its acreage is about 5,000 m². The distance from the toe of the landslide to its rear edge is about 200 m, and the elevations of the toe and the rear edge are 254 m and 285 m, respectively. The leading edge of the landslide pushes up the humus soil of the original ground surface, which consequently slides forward. The arcuate dislocation in the rear edge was in the range of the wider subgrade. There, the trees tilt at the leading edge of the landslide.

Geology of the Study Area

In order to gain insight into the subsurface characteristics of the landslide, we conducted a drilling exploration; we drilled four holes, the depths of which ranged from 14 to 26 m. Their arrangement is shown in Fig. 1.

In the research section, the soil distribution is listed as follows: quaternary loose sediment, tertiary pebbly sandstone, cretaceous mudstone, and sandstone (Fig. 2). The subgrade fill soil or the waste from the road construction is yellow and waterlogged; it comprises mainly loose materials, including the tertiary pebbly sandstone, cretaceous mudstone, and sandy mudstone. The clay in the soil is yellow, soft, and plastic when saturated, and it is tough and strong when dry. Silty clay is located at depths of 1.5–3.8 m and 0–6.7 m in the upper section and in the mid-to-lower sections of the landslide, respectively. More than one intercalated sand layers exist within the silty clay layer; the thickness of a single sand layer ranges from 1 to 10 cm. The presence of these sand layers greatly increases the permeability of the soil. The tertiary pebbly sandstone layer comprising large clasts and sand minerals is located at depths of 3.8–4.5 m on the upper section of the landslide. This layer is weathered, slightly wet, and unconsolidated with loose sand

having good gradation and good water permeability. The weathered siltstone is yellow in color and is located at a depth of 4.5–14.3 m at the upper section of the landslide. The siltstone has a sandy structure with bedding and poor water permeability. The slightly weathered mudstone is yellow or greyish-black, and it has a muddy and layered structure, poor water resistance, and poor water permeability. The strongly weathered mudstone is unconsolidated, greyish-black with a layered and muddy structure. The moderately weathered mudstone is brown and greyish-black with a muddy and layered structure.

Factors Influencing the Formation of Landslides

The formation and development of the K178 + 530 landslide is mainly influenced by the topography, geology, hydrology, climate, specific geography, intense freeze-thaw erosion, and human engineering activities.

During the rainy season and the thawing period in spring, the landslide formations are particularly feasible. Tympanite deformations in landslides aid permeation and stockpiling. Highly permeable surface soil, grit, and silty clay provide passage for water infiltration. The infiltration capacity of the lower mudstone and siltstone layers is very small, forming a combined impermeable layer. The infiltration of rainwater, snowmelt water, fissure water, and thawing frozen soil are cut off by the frozen soil and lower impervious layers in the process of infiltration. This impedance to the groundwater flow is the main cause of landslides in the area. The landslide first began moving in late July 2010. Freezing and thawing affect the movement of the landslide heavily, inducing intermittent sliding that result in drumlins.

The slip surface of the upper section of the landslide is at a depth of 4.5 m, located at the interface between the gravel sand and siltstone layers. The slip surface of the middle and

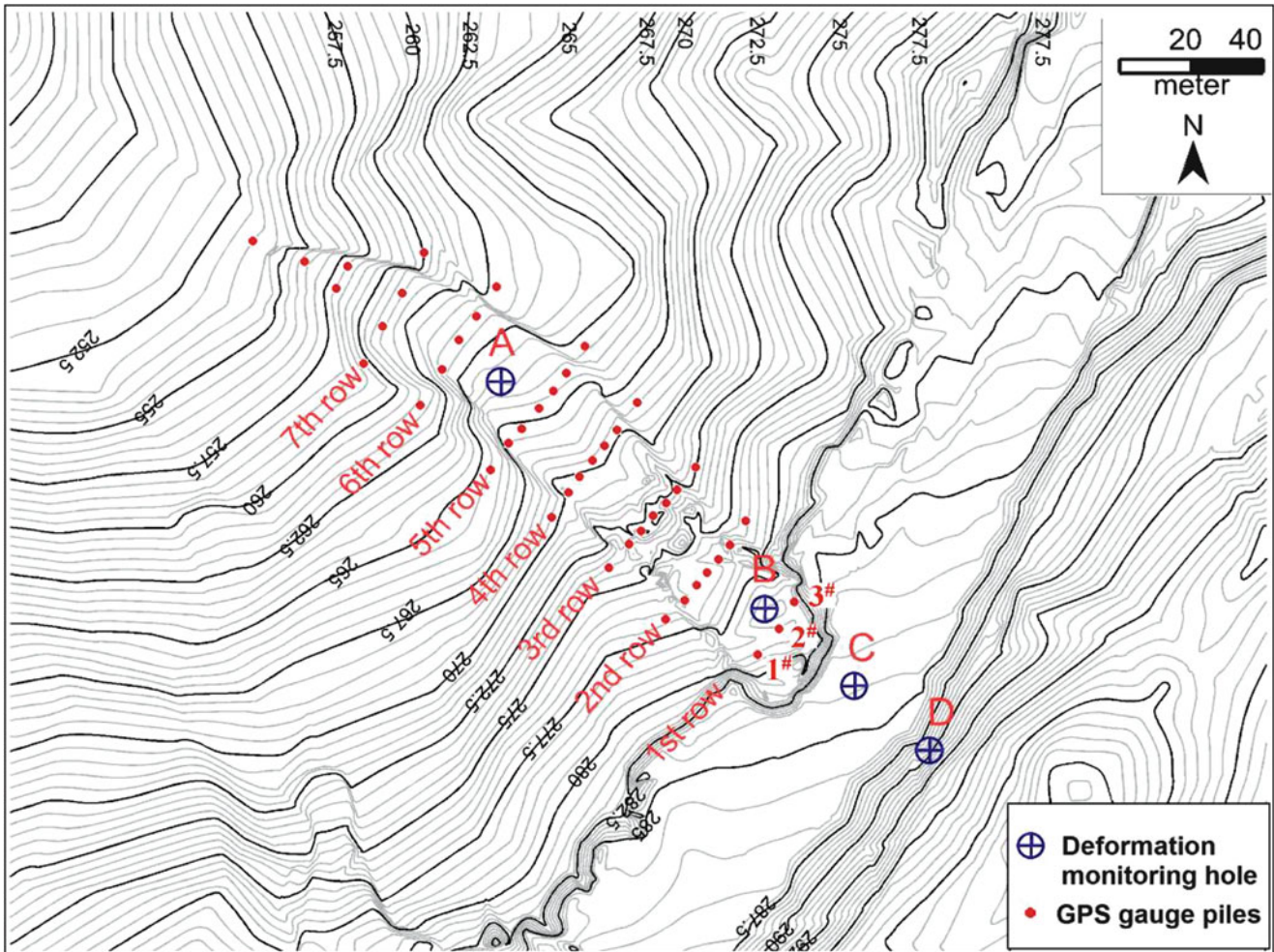


Fig. 3 Layout of GPS gauge piles along the length of the landslide

lower sections is at a depth of 6.5 m, at the interface of the silty-clay and mudstone layers.

GPS Monitoring of the Landslide Deformation

GPS Monitoring Sites Arrangement

On September 13, 2010, two deformation monitoring pipes and sensors were bored on the landslide body at respective depths of 4.2 m and 6.5 m. We employed a GPS to monitor the movement of the landslide by arranging nearly 49 GPS gauge piles at different positions on the landslide (Fig. 3).

From the rear edge of landslide to the leading edge, we arranged 11 rows of gauge piles on both sides of the outside of the landslide, as well as at the center of the top and close to the rear edge of the landslide. The distance from the first row to the rear edge of the landslide is 15 m, and the gauge numbers run from 1 to 3 (left to right). The distance from the second row to the rear edge of the landslide is 30 m, and that

from the third row through the seventh row to the rear edge of the landslide is 50 m, 70 m, 93 m, 119 m, and 134 m, respectively. The rest of the gauge piles are distributed along the leading edge of the landslide. These GPS monitoring piles can monitor the sliding conditions at the proximal, middle distal, and lateral sections of the landslide. Data collection was carried out from September 13, 2010 to November 16, 2012, for a total of 793 days.

Motion Characteristics of Gauge Piles at Different Positions

Figure 4 shows the horizontal and vertical sliding displacement curves of monitoring pipes A and B, respectively. We know that the landslide started moving on July 22, 2010, and continued moving until mid-November 2010. After that, towards winter, the ground surface began to freeze and remained stable until May 2011, at the end of which, the sliding commenced once again. The displacement values of

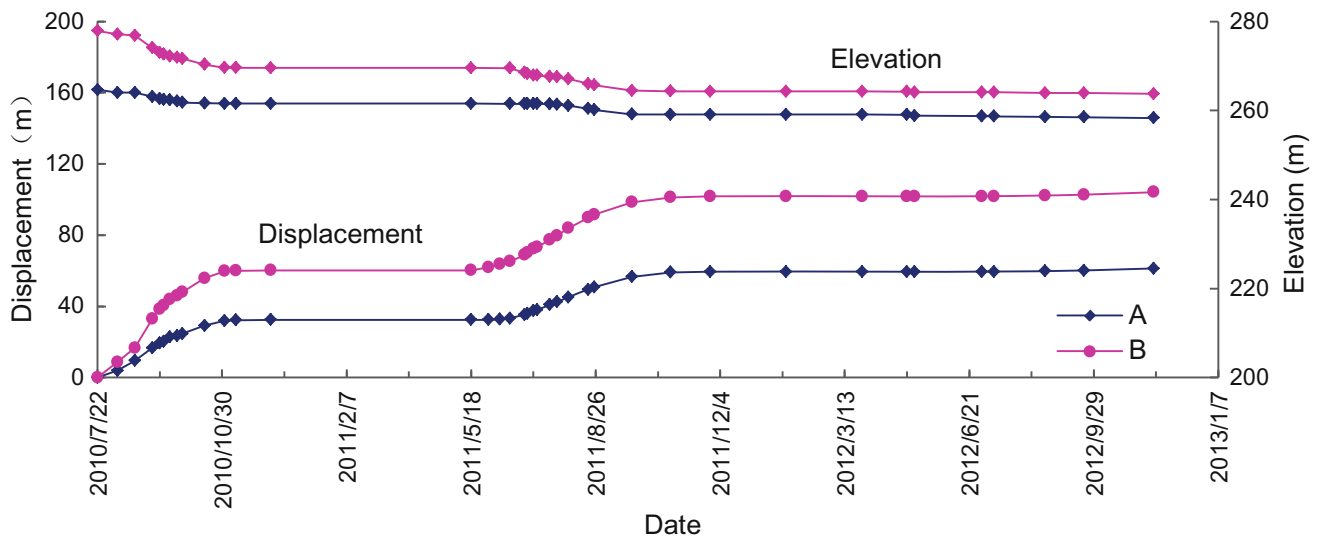


Fig. 4 Horizontal and vertical sliding displacement curve of deformation monitoring pipes A and B

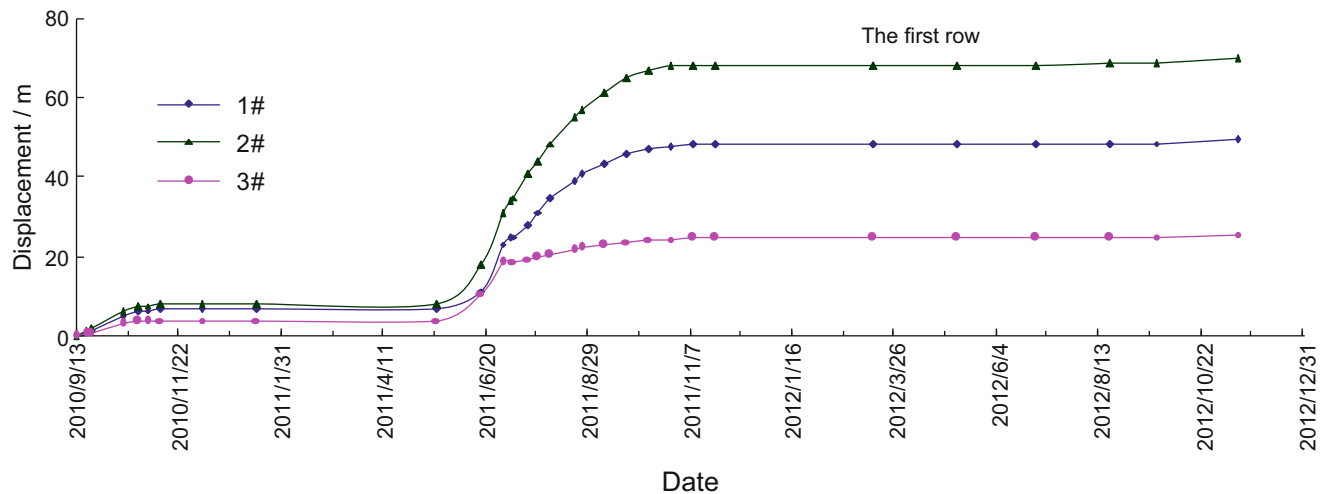


Fig. 5 Sliding displacement graph for the first row of gauge piles

the two monitoring points were not consistent with each other. For example, in late May 2011, monitoring point B had already started to slide, whereas monitoring point A was still stationary. This shows that the trailing edge was the first to begin sliding. More than 10 days later, the leading edge of the landslide began to slip, showing increased displacement values compared to those at the front of the landslide. These sliding and deformation characteristics show that the landslide is a push-type landslide. Figure 5 shows the first row of gauge piles to slide in the study area. From September 13, 2010 to November 2010, 1#, 2#, and 3# gauge piles were displaced by 6.90 m, 8.05 m, and 4.12 m, respectively. In early June 2011, the landslide began to mobilize again, and by July 1, 2012, the sliding displacements of 1#, 2#, and 3 gauge piles were 48.03 m, 68.08 m, and 24.63 m, respectively (for 658 days of monitoring). The slip rate exhibited at

the center of the landslide body (2# gauge pile) was higher than that exhibited near the edges (1# and 3# gauge piles).

Figure 6 shows the sliding displacement graph of the second row of gauge piles. From the sliding displacement graphs of the front and second rows of gauge piles, it is evident that the landslide was mobile during September 13 to mid-November 2010, after which, the land surface began to freeze, rendering the landslide immobile until the end of May 2011. From early June 2011, the landslide began moving again. The sliding displacement values for gauge piles at the center of the landslide are distinctly larger than the values for those closer to the edges.

From the longitudinal section in the center of the landslide (Fig. 7), we observed that the gauge pile displacement from the first row through the seventh row during September 13, 2010 to September 25, 2011, were 65.01 m, 71.31 m,

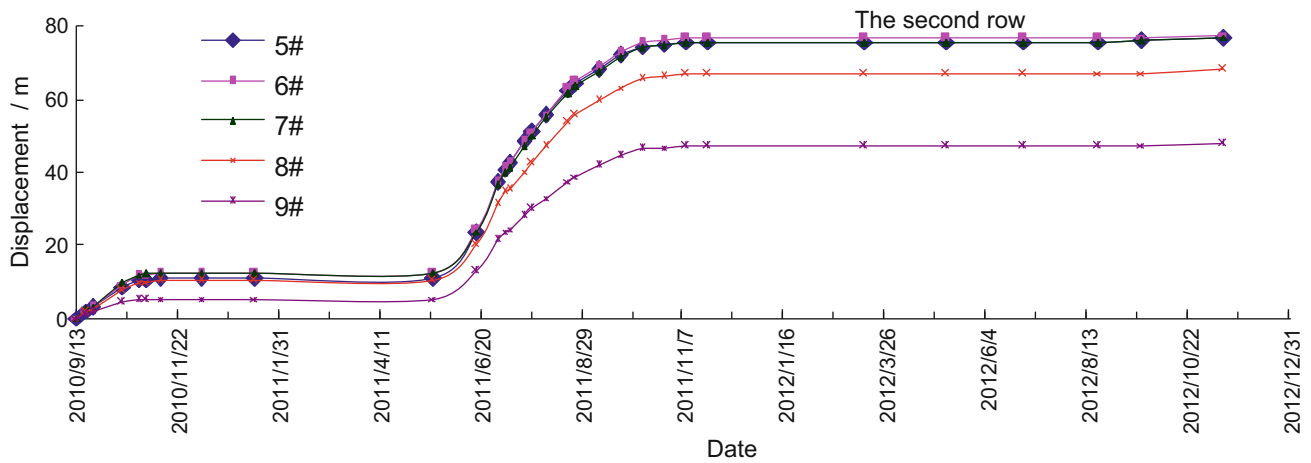


Fig. 6 Sliding displacement graph for the second row of gauge piles

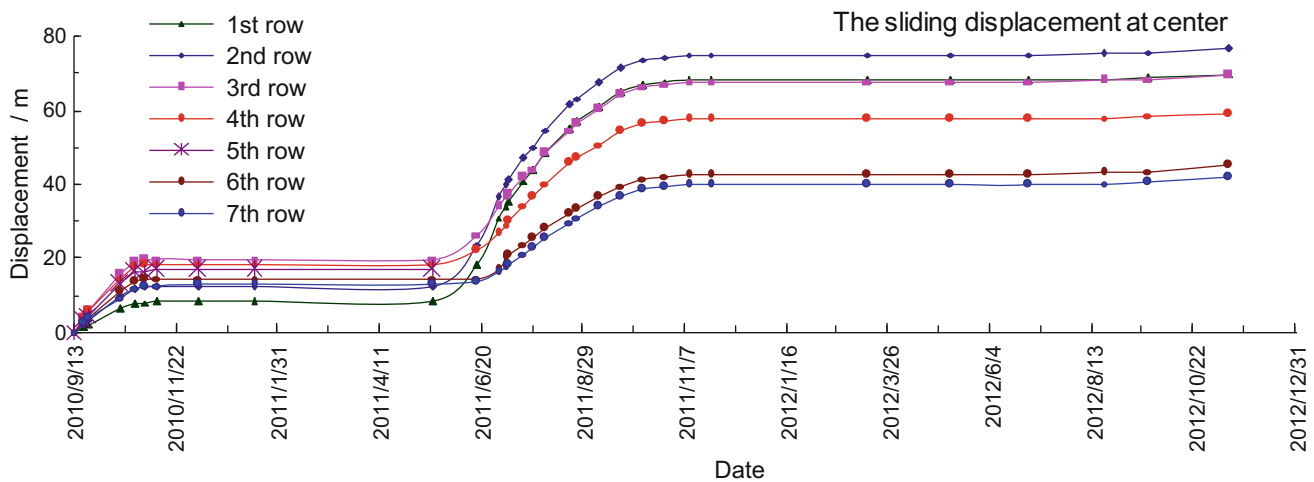


Fig. 7 Gauge pile displacement curve along the middle of the landslide

64.20 m, 54.23 m, 46.37 m, and 39.43 m, respectively. This slide displacement graph shows different values for different gauge pile positions at the same time. The sliding displacement of the middle and upper sections is the greatest.

Figure 8 shows the K178 + 530's landslide perimeter variations. This figure shows that the landslide's trailing edge has been expanding towards the road, which would eventually result in a road hazard. From July to November 2010, the front section of the landslide advanced by 15.5 m, and from July 2010 to August 2012, the landslide advanced by 28.5 m.

Conclusions

This article reports on the drilling exploration and GPS location monitoring of the K178 + 530 landslide in order to evaluate the mechanism of landslide formation, the movement characteristics of the landslide in a permafrost area, and the apparent shape and internal dynamic variations

of landslide soil. From this analysis, we obtained the following conclusions:

1. The landslide is superficial, occurring parallel to bedding. The soil of the sliding surface is silty clay, which is loose and plastic when dry. Snowmelt water, rainwater, and fissure water are the water sources to the landslide. Tympanite cracks along the slope facilitate the infiltration of atmospheric precipitation into the landslide. The soil provides the passage for water to infiltrate the landslide, whereas the mudstone and sandstone layers with low permeability form an aquifuge. The silty clay above the aquifuge facilitates the saturation of infiltrating water, forming the displacement surface. Freezing and thawing result in intermittent slide, bench slope, and drumlin formation along the landslide slope.
2. The sliding velocity of the landslide varies largely between different seasons. From mid-November to late May of the following year, the rainfall was very low,

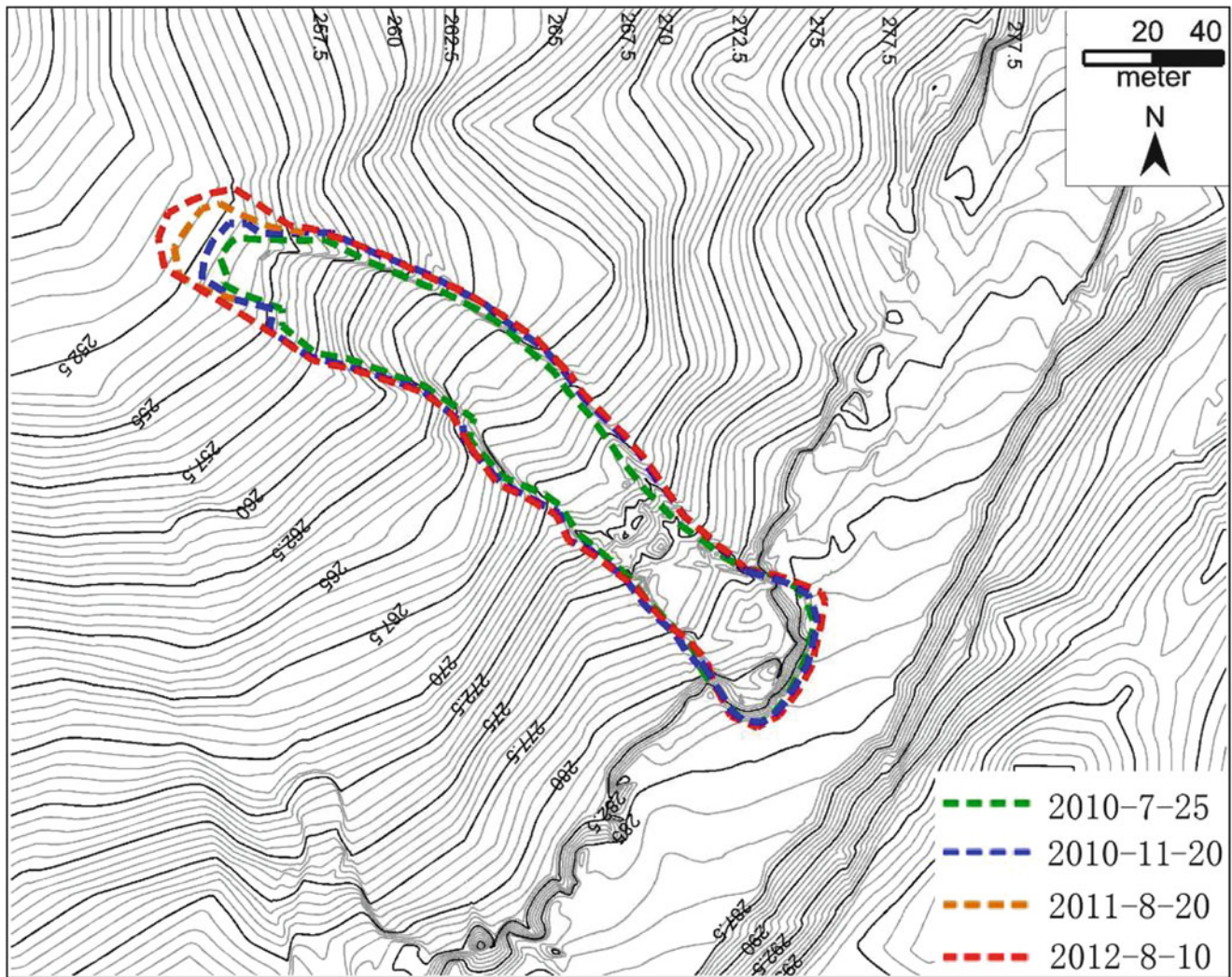


Fig. 8 Topographic map showing the variations in the perimeter of the K178 + 530 landslide

the surface layer of ground was frozen, and the landslide remained stable. In late May 2011, owing to the melting of the frozen ground and snow cover followed by infiltration, the landslide began mobilizing once again. The displacement velocity of the landslide was greatest during the period from late May to mid-June 2011. The sliding velocity of the rear edge of the landslide was 0.89 m/day, the sliding velocity of middle landslide was 0.37 m/day, and the sliding velocity near the toe was 0.16 m/day. The sliding velocity began decreasing in late June 2011; that of the rear edge was 0.51 m/day, that of middle of the landslide was 0.30 m/day, and that near the toe was 0.11 m/day. After mid-October, the sliding velocity began decreasing, averaging at 0.08 m/day.

3. Landslide displacement occurs at different rates in different sections, as shown by the bedding plane displacement. Within the same cross section of the landslide, the sliding

displacement in the center is largest and the sliding displacement near the flanks is the smallest. The trailing edge of the landslide creeps continuously towards the road, increasing the hazard that this erosional feature poses to commuters.

Acknowledgments This work was financially supported by Heilongjiang Communications Department project, and it is a subtopic of the western communication science and technology project "Study on Subgrade Stability Controlling Technology of Expressway Expansion Project Permafrost Melt and Landslides Sections."

References

- Gu TF, Wang JD, Lu X, Meng YL (2009) Characteristics and stability analysis of accumulations landslide No.3 in Tuoba of Southeast Tibet. *J Nat Disast* 1:32–38

- He YX (1991) Application of D.C. electric sounding for the permafrost exploration along Xinjiang-Xizang highway [J]. *J Glaciol Geocryol* 13:255–260
- Hu ZG, Shan W (2011) Application of geological drilling combined with high-density resistance in Island structure permafrost survey. The international conference on electronics, communications, and control (ICECC, 2011)
- Li TL, Zhao JL, Li P (2003) Analysis on the characteristics and stability of the No.2 landslide of 102 landslide group on Sichuan-Tibet Highway. *J Catastrophol* 18(4):40–45
- Liu LH, Zhu DY, Liu DF (2007) Discussion on multiple solutions of safety factor of a slope. *Rock Soil Mech* 28(8):1661–1664
- Ma LF, Niu FJ, Yang NF (2006) Analysis on ground temperature changes and landslide process of thaw slumping in permafrost regions. *Hydrogeol Eng Geol* 3:53–56
- Qiao JP (2002) Structure and shape of landside. *Chin J Rock Mech Eng* 21(9):1355–1358
- Shan W, Liu HJ, Yang L et al (2008) Study of regularity of variation of water content in shallow layer of soil road cutting slopes in seasonally frozen-ground region. *Rock Soil Mech* 29(suppl):335–340
- Zhu Y, Rao Z, Wu B (2004) Organic and gas geochemistry of gas hydrate-bearing sediments from Mallik 5L-38 production research well [J]. *Mackenzie delta, Canada, geological survey of Canada. Bulletin*. 68(2):311–319



Rockslides in the Open Pit of Kumtor Goldmine (Kyrgyzstan)

Isakbek Torgoev and Almazbek Torgoev

Abstract

The high-elevation Kumtor mine is located in the Central Tien Shan in the permafrost and active glaciers area. This area is characterized by extreme continental climate. The average annual temperature in the mine area is $-7.8\text{ }^{\circ}\text{C}$ with fluctuations in the average minimum temperature of $-28.8\text{ }^{\circ}\text{C}$ in January up to $1.7\text{ }^{\circ}\text{C}$ in July. The average annual precipitation is 350–400 mm, a quarter of which falls as rain and the rest in the form of snow. Harsh climatic conditions in the area, the presence of mountain glaciers and permafrost rocks, diversity of terrain, rock types, seasonal freezing and melting of the rocks and soil together with global warming and large-scale anthropogenic impact cause active development of cryogenic gravitational processes. The most dangerous among them are repeated slumping and sliding of the north-eastern wall of the Central pit. The report presents the results of geotechnical studies and analysis of the main reasons for the failure of the pit walls, which include melting of the permafrost rocks at the top of the pit and glacial water inflow into the tectonic disruption zone.

Keywords

Permafrost • Glaciers • Pit • Landslides • Sliding • Wall

Introduction

The Kumtor mine is one of the largest gold mines in the Tien Shan. The deposit is mined by the joint Kyrgyz-Canadian company “Kumtor Operating Company” (KOC). Among geotechnical problems that seriously complicate the planned gold production at this high-elevation mine there are mass gravitational movements on the high and steep walls in the north-eastern part of the Central pit (Thalenhorst et al. 2012).

I. Torgoev (✉)

Institute of Geomechanics and Development of Subsoil of the National Academy of Sciences of the Kyrgyz Republic, SEC “Geopribor”, Mederova str., 98, Bishkek 720017, Kyrgyzstan
e-mail: geopribor@mail.ru

A. Torgoev

Department of Geology, University of Liege, Sart Tilman, 4000 Liege, Belgium
e-mail: torgoeval@yahoo.com

The first failure of the north-eastern wall of the pit occurred in August 2001. This failure did not result in any victims, therefore, no special attention was paid to this. The second collapse of more than 2.7 million m^3 of rock was on 8 July 2002. As a result of the second failure one person died, the drilling equipment worth over 300,000 dollars was destroyed and the ore mining was suspended, as the access to the gold bearing stockwork zone was temporarily unavailable. Collapse of the wall led to a significant decrease in the gold production for a long period. Mining operations on the described part of the pit resumed only at the end of 2005. The next large-scale collapse has occurred on 13 July 2006 at the same part of the pit, again above the stockwork zone, which mining was planned for 2006–2007. For safety reasons, the mining of this site has been postponed again and the gold processing plant had to process low-grade ores, which also affected the final production figures for 2006–2007.

One of the main reasons for the repeated failures of the abovementioned wall of the Central pit was the errors and

miscalculations in the pit design. First of all, these errors were due to inappropriate consideration of permafrost and glaciological features of the gold deposit area. Man-made pressure on the glaciers and fragile permafrost rocks increases with the mining of the deposit, thus causing the development of dangerous natural and man-made processes. Massive slides and rockslides are among these processes and discussed below.

Permafrost Characteristics of the Deposit Area

The Kumtor mine is located in one of the largest glacial and permafrost areas in Central Asia (Fig. 1). Permafrost rocks in the Tien Shan emerged due to the neotectonic uplifting of this mountainous area and the planetary climate cooling in the Neogene-Quaternary period. With time permafrost areas increased in size and merged into a continuous frozen ground massive as a result of the ongoing uplift. Harsh climatic conditions with long winters, short summers and relatively low level of precipitation in winter contributed to preservation of permafrost, or so-called “permafrost rocks” (PFR). Geological engineering (geotechnical) conditions in the mine area are determined by the distribution, abundance, capacity, temperature, composition and structure of the seasonally thawed rocks and permafrost rocks.

The area of the Kumtor mine is characterized by continuous permafrost rocks distribution. The thickness of permafrost rocks varies from 350 to 370 m at the elevation of 4,200 m and down to 110 m at the elevation of 3,950 m. The regional permafrost temperatures below the depth of seasonal thawing layer (STL) ranges from $-2.6\text{ }^{\circ}\text{C}$ to $-5.6\text{ }^{\circ}\text{C}$. The thickness of seasonal thawing layer without the impact of the construction work and man-made effects is 1.5 down to 2 m depending on the exposure of the slopes.

Permafrost rock mass is a set of rocks with not only different ages and differences in lithology and mineral and petrographic features, but also with a set of specific cryogenic features. Frozen rocks composing the pit walls in the Kumtor mine are divided into frozen rocks with ice inclusions, and rocks without such inclusions. Cryogenic structure of frozen bedrock is determined by the extent and type of initial fracturing and the degree of weathering. The highest ice content is registered in the areas of fragmentation with typical tectonic breccias and ice cement.

The waste rocks and gold bearing rocks are in the frozen state during the biggest part of the year. However, in case of the open pit mining under the intense solar radiation, there are significant changes in the strength of host rocks caused by rapid changes in the daily and seasonal temperature. Geotechnical tests showed that compression resistance of the rocks in the hanging wall is 81.2 MPa in the dry state and 59.6 MPa in water saturated state. It should be



Fig. 1 General view of the pit as of 2008: the *yellow ellipse* shows the collapse area in the upper north-eastern part of the pit area in 2002 and 2006

emphasized that the strength of the hanging wall phyllite after 25 cycles of freezing and thawing decreases to 41.5 MPa, which is almost two times less than initial value. Physical and mechanical properties of the host phyllites are: Young’s modulus -70 GPa ; Poisson’s ratio -0.25 ; bulk density -2.75 g/cm^3 ; cohesion -5.54 MPa ; and the internal friction angle -60° .

Central Pit of the Kumtor Mine

Kumtor mine is composed of the phyllites with schistosity and folding. The deposit itself is associated with two mineralized zones of the Kumtor fault (KR) with a width of about 400 m and a length of 10 km, which coincide with the length of mining concession area. The rocks in the ore zone are characterized by quartz-feldspar-pyrite mineralization.

From the point of view of the pit walls stability, the most important characteristic of the geological structures is spatial orientation of these structures. The Kumtor ore-bearing north-east stretching fault is represented by the zone of strong fragmentation, boudinage, crumples and limonitization of rocks and is an ancient upthrust-overthrust zone, which has changed due to modern tectonic displacements. The influence of the Kumtor fault zone appears in the form of sub-parallel cracking in all mineralization zones, and in cracking perpendicular to the fault zone. Faults, thrusts and foliation are the structures that predetermine stability of the pit walls, and their influence is clearly evident in the large-scale failures of the walls discussed below.

Big geological structures at the Kumtor mine, which can cause large surface disruptions include the main fault that stretches north-east to south-west. This fault zone is oriented sub-parallel to the KR zone. These structures also include faults outgoing from the main faults that are dipping in the western and north-western directions. In addition to the abovementioned fault structures, there are also horizontal faults of south and southeast directions.

The weak north-east wall is the highest in the Central pit. The elevation of the crest of this wall is up to 4,342 m above sea level, the bottom of the pit at the end of the mining will be at around 3,500 m, and the maximum height of the eastern wall will reach 842 m. North-east wall of the Central pit is situated in the hanging wall. The high and initially steep north-eastern wall of the Central pit (Fig. 1) is composed of frozen and extremely altered phyllite melonites, which are intensively crushed under the impact of mining operations and thawing. Since the abovementioned wall of the Central pit is high, there is the probability for the failure along the sliding surface in the intact rock mass.

The construction of the pit wall was designed based on the recommendations of the geotechnical company “Golder Associates inc.” (GA), presented in the feasibility study in 1993. A modified Bishop method of slope stability analysis based on the computer program CPLOPE specifically developed by GA was used to evaluate stability of the walls of the Central pit. Most of the benches of the Central pit were put in a limit conditions, the pit wall is formed mainly by benches of 24 m heights (3–8 m) with a safety berm of 12 m width between them. With the bench angle of 63.4° , the angle of the wall was 45° (Thalenhorst et al. 2012). Deviation from these parameters was made for the highest (550 m) north-eastern part of the Central pit. The safety berm width in this area was increased to 21 m leading to a decrease of the wall angle value down to 36° with the same bench angle. The same design parameters were set for the north-western and western walls, which are formed in the Kumtor fault breccias zones.

Massive Failures in the North-Eastern Wall of the Central Pit

Out of the three massive failures in the north-eastern wall, the greatest damage was caused by the second one (Fig. 2a), which occurred on July 8, 2002 at 14:53 pm, about 1.5 h after a massive explosion on the block on the elevation 4,010 m.

The week before this failure, the drilling works started on the bench of 4,018 m, which was directly beneath the collapsed wall; the drilling works lasted until the collapse. The failed area was between the benches of 4,298 and 4,018 m, i. e., the height of the sliding area was 280 m, the width at the base was 270 m (Fig. 2a), the average depth of the failure area from the surface of the wall was 40 m. As it can be seen from Fig. 2b, a steeply dipping geological structure formed the crest of the sliding area. A vertical crack was formed in the southern part of the sliding mass, which then spread to the north. The horizontal separation crack on the top of the slope appeared a moment before the whole mass slid down the slope. After the failure of the whole mass the steep walls were formed in some places that further experienced smaller

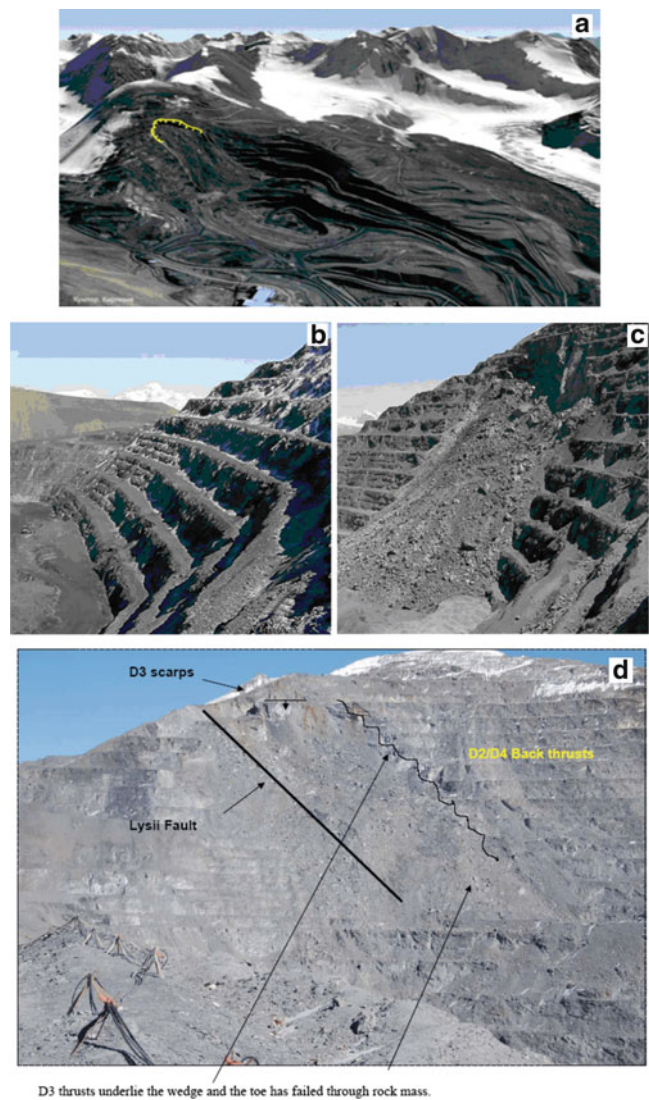


Fig. 2 Unstable wall of the KOC Central pit: (a) a general view of the Central pit after the landslide on July 8, 2002; (b) and (c) photo of the site before and after the collapse of July 8, 2002; (d) a graphical representation of the mechanism of the collapse in the north-eastern part of the pit wall (Thalenhorst et al. 2012)

slides until July 14, 2002. The groundwater (filtration, water accumulation, ice schlier) was observed neither before, during, nor after the collapse on 8 July 2002 (Fig. 2c).

According to the eyewitnesses, a number of the failure parameters were beyond the typical characteristics of large slides that occurred in the pits. Thus, a very unusual fact was a strong fragmentation of the failed mass, which crushed into stone, gravel and sand. According to some witnesses, extremely unusual was the speed and almost explosive nature of the collapse. Most large-scale slides are characterized by a progressive dynamics and occur for a longer time. In this case it happened within 10 s only. A few minutes before the collapse, a small falls of stones was recorded in the upper benches. Available information does

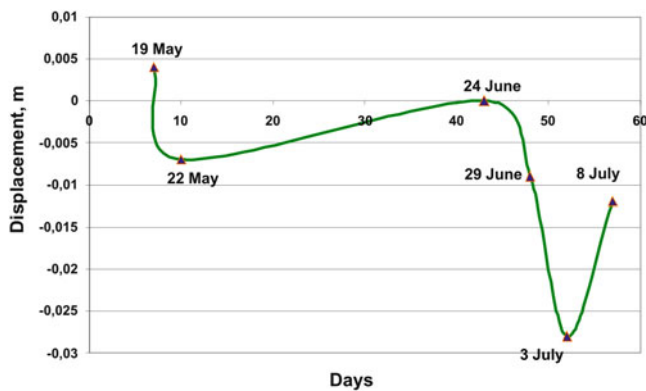


Fig. 3 Displacement at the monitoring point 4 situated on the bench 4,082 m—positive direction is to the east

not contain any specific evidence about any seismic events in the area near the mine and extreme hydro meteorological conditions prior to the collapse, which could play the role of a collapse trigger. There were five geodetic monitoring points in the collapse zone, the monitoring was conducted once a week. However, according to the KOC geotechnical service, observations showed no signs of the destructive process, that is, no deformations that are typical for such slides or precursors that precede large-scale displacement of the rock mass were recorded.

Several expert committees have expressed different opinions regarding the causes of the mass collapse of the north-eastern wall of the Central pit. However, until now experts cannot come to a common opinion. It should be noted that among various opinions and hypotheses there is an assumption that a deep rock burst took place in this area of the Central pit. The basis for this conclusion was the evidence of some eyewitnesses for rapid explosive nature of this collapse.

In addition, based on the author's opinion, this hypothesis is supported by a step-like alternating displacement of rocks (Fig. 3) recorded by the KOC's geodetic monitoring system on this place 5 days before the slide, which was found during retrospective analysis of the data after the collapse.

However, when comparing the graphs of the point 4 displacement on the 4,082 m bench, with the graphs of changes in the soil temperature at a depth of 50 cm (Fig. 4), it is clear that the alternating displacement of the point 4 substantially repeat the temperature change of the soil, i.e., are likely caused by thermal deformation of the wall surface. In addition, for reasonable prove of the rock burst hypothesis there are no data on the stress-deformational state of the massive prior and after the collapse, in particular, instrumental data on measuring the parameters and directions of strains in the massive. Finally, it is unlikely that the rock burst would occur three times in the same place of the wall.

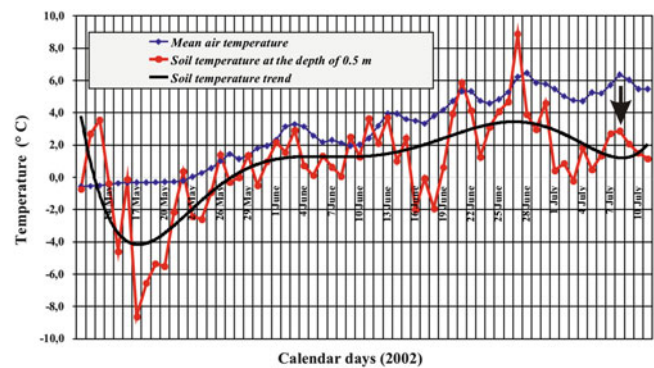


Fig. 4 The change of air and soil temperature at a depth of 50 cm based on the observation data for the period 11 May–11 July 2002. The arrow shows the time of the wall sliding on July 8, 2012

After the third failure, the consulting company SRK Consulting hired by the KOC, conducted a geotechnical (drilling) and structural-geological studies in the slide area in order to determine the mechanism of sliding and develop measures to ensure stability of the pit walls (Bruce et al. 2008). Based on the collapse analysis, it was recognized that the slide was caused by the increase in pore pressure in the massive due to Lysyi glacier melting water inflow—seepage areas appeared near the top of slide scarp. It should be noted that rapid air and soil temperature changes typical for the Kumtor conditions are accompanied by phase transformation of water into ice and vice versa.

The initial design of the Central pit was revised based on these studies. In order to improve the stability, the slope angle of the wall was decreased at this dangerous part from the original value of 36° down to 30° (Bruce et al. 2008). Tab.1 presents the results of stability analysis for north-eastern wall of the Central pit for slope angles 37° and 30° made by GA.

According to the standards the $SF > 1.2$ is considered to be acceptable value. Previous geotechnical investigations and monitoring of the walls performed by the GA showed that the part of the wall between elevation 4,070 and 3,950 m was in a frozen state. In this case, the slope can be considered to have dry conditions or at least without water saturation and should therefore be stable ($SF > 1.2$). However, the upper part of the wall had and still has open cracks, from which water is flowing out, possibly under the pressure. Table 1 indicates that for water-saturated conditions the slope is unstable even when the slope angle is 30° (Bruce et al. 2008). In order to reduce the impact of hydraulic pressure on the wall stability, GA recommended to set up a water recharge wells, and to remove the ice in the crest part to minimize the volume of melt water going into the pit.

In addition, geotechnical research and structural-geological mapping made by SRK Consulting helped to understand causes for failures of the north-eastern wall of

Table 1 Calculated FS values for the north-eastern wall of the central pit (Bruce et al. 2008)

Slope angle (°)	FS for water saturated conditions	FS for dry conditions
37	0.8	1.2
30	1.0	1.4

the pit, which was triggered by the massive explosion. Large shallow wedge in the tectonic thrust D3 zone formed the collapse surface along the line of intersection with the thrust Lysyi (Fig. 2d). In addition, based on the opinion of SRK Consulting, one of the collapse causes was thawing of permafrost rocks at the top of the pit and water saturation of the tectonic dislocation zone caused by melt glacial water (Bruce et al. 2008). In our opinion, melt glacier water in a daily freeze-thaw condition caused extension effect on the rocks (phyllites) in the pre-wall zone along faults and cracks. As it is known, when water freezes, its volume increases by 9.2 %. According to the laboratory studies, pressure on the sides of the cracks during water freezing can reach the value of 10^7 Pa (10 MPa). This is enough for the destruction of some massive rocks, in particular weathered phyllites.

Discussions

As it was noted above, the sliding area before the mining activity was composed of frozen, extremely altered phyllites-melonites, which tend to be crushed during the mining operations and thawing (Rogers 2001). Perhaps this has led to a strong fragmentation of the collapsed rock masses. In addition, it should be noted that it is not by chance that all three collapses occurred in July–August, i.e. during the period of maximum thawing of the rocks in the pit walls. In addition, ongoing climate change resulted in increase of the average air temperature, which finally affected the temperature of the rocks in pre-wall part. Most likely this effect has led to separation of the seasonal freezing layer from the permafrost rocks. This factor is of particular importance for the north-eastern wall of open pit since this part was mined much earlier than other parts of the pit. Apparently, the initiation of the sliding was also affected by seasonal deformations of the pre-wall part of the slope. It was probably provided through repeated freezing and thawing of crushed phyllites in the tectonic disruption zone including extension effect. The situation in the top clearly pointed to the fact that the collapse occurred along the steeply dipping fault (Fig. 2b).

Bjerrum and Jorstad (1968), studied around 300 unstable rock slopes and concluded that the effects of frost, chemical weathering, temperature changes, direct exposure to water and snow cover (in our case, ice) make impossible long-term

stability of steep slopes composed of fractured rocks, unless they are covered with a protective layer of gravel or steepness of the slope below the angle of the natural slope for these rocks ($\approx 37^\circ$).

According to Bjerrum and Jorstad (1968), the FS values cannot be determined by theoretical calculations, since it is impossible to define the relative value of the factors mentioned above. Therefore, the best method would be to compare the designed slopes with already existing. However, the empirical approach does not provide consideration for slopes stability (or instability) mechanism. Therefore, theoretical studies (calculations) are desirable, even if they cannot provide reliable estimates.

It was noted above that the repeated failures in the unstable north-eastern wall occurred after the mass explosions—these explosions were the triggering mechanism of sliding in the Central pit walls. Mass explosions occur in the pit every day, the total mass of explosive is 15–20 tons. According to the KOC for the period of 1996–2011, 280,000 tons of explosives were used in the pits. Research of the seismic impact of the mass explosions on the boards of the Central pit has shown that in case of explosion in the pit bottom, the vertical component of seismic vibrations velocity is three or more times greater than the horizontal component. It results in vertical uplift of rocks in the upper part, which in combination with thawing leads to sliding (Lewis et al. 2006).

In our opinion, the permafrost and hydrogeological features together with structural-geologic and geodynamics factors contributed to the initiation of sliding in the north-eastern wall of the Central pit. In the conditions of global warming and human impact these factors include: separation of seasonally thawing layer from permafrost rocks due to the increasing mean annual temperature; sharp temperature fluctuations, causing seasonal and daily deformations due to freezing and thawing of phyllites and water in pre-wall part; wedging and lubricating effect of the Lysyi glacier meltwater and reducing rock (phyllite) strength as a result of repeated freezing and thawing. As it was noted above, the phyllites, composing the north-eastern wall, showed almost two times strength reduction resulted from several cycles of freezing and thawing.

Due to security reasons the mining of stockwork zone in the north-eastern part of the Central pit is currently postponed until 2015.

References

- Bjerrum L, Jorstad F (1968) Stability of rock slopes in Norway. Publ Norges Geotekniska Institut 79:1–11
 Bruce I, Redmond D, Thalenhorst H, (2008) Technical Report on the 2007 Year-End Mineral Reserves and Resources Kumtor Gold

- Mine Kyrgyz Republic for Centerra Gold In. and Cameco Corporation. Toronto, Canada Strathcona Mineral Services Limited, p 163
- Lewis E, McNee D, Kutuzov B (2006) The study of seismic impact of mass explosions on the Kumtor mine pit walls. *Mount Mag* (in Russian) 8:48–50
- Rogers T (2001) Kumtor gold mining company - a flagship mining industry of Kyrgyzstan. *Mount Mag* (in Russian) 4:1–8
- Thalenhorst H, Redmond D, Raponi TR, Vdovin V (2012) Technical report on the Kumtor gold project Kyrgyz Republic for Centerra Gold Inc. Centerra Gold, Totonto, p 179



Mass Movement in the Waste Dump of High-Altitude Kumtor Goldmine (Kyrgyzstan)

Isakbek Torgoev and Bektur Omorov

Abstract

The movement of waste rocks dumps together with ice, stored on the glaciers of the high-altitude Kumtor gold mine is reviewed in this paper. This mining site is located in the central part of the Tien Shan (Kyrgyzstan). There are no other cases around the world, when the waste rocks and removed ice were stored on the active mountain glaciers. The landslide has formed in the area of dumps, stored on the Davydov glacier, and the displacement velocity has dramatically increased in spring 2013. Due to the accelerated movement of rock-ice mass, a number of Kumtor mine infrastructural units was destroyed with economic losses of about USD 100 million. This article presents the results of monitoring of the landslide displacements and provides analysis of the causes for its acceleration. The potential environmental impact of further development of the gravitational mass movement and impact on the Kumtor gold mine facilities were assessed.

Keywords

Kumtor gold mine • Glaciers • Permafrost • Rock dumps • Landslide

Introduction

Mining of mineral deposits in the polar and high-altitude regions are often accompanied by the gravitational mass movements involving consolidated masses of ice, snow and crushed rocks, which may also occur in the waste rock dumps. The landslides in such kind of dumps are often referred as Rock Glaciers, widely spread in the high-altitude zone of Tien Shan Mountains. The Rock Glaciers are the natural accumulations of ice and debris that independently move under the effect of gravity (Barsch

1996). Some researchers define Rock Glacier as a major form of permafrost terrain, which, from one side, has strong similarity with glaciers situated in the valley, and, from another side, has landslide features (Gorbunov et al. 1992).

The big landslide with volume about 200 million m³ was formed in the dumps stored in the basin of the Davydov glacier. This landslide consists of mixture of waste rock and removed glacier ice. Accelerated movement of the landslide in April 2013 caused destruction of several infrastructural units resulting in large economic losses. There was a risk that this mass movement will transform into the debris flow with high environmental impact possibly resulted from the contamination of the Naryn River Basin (Syrdariya).

Instability of the massive dumps on the Kumtor mine glaciers is considered to be unique problem and this paper describes the reasons caused gravitational mass movement, which involved waste rock and removed ice. This paper also presents the results of geotechnical investigations and monitoring of the landslide displacements, which were characterized by the rapid acceleration.

I. Torgoev (✉) • B. Omorov
Institute of Geomechanics and Development of Subsoil of the National Academy of Sciences of the Kyrgyz Republic, SEC "Geopribor", Mederova str., 98, Bishkek 720017, Kyrgyzstan
e-mail: geopribor@mail.ru; geopribor@mail.ru

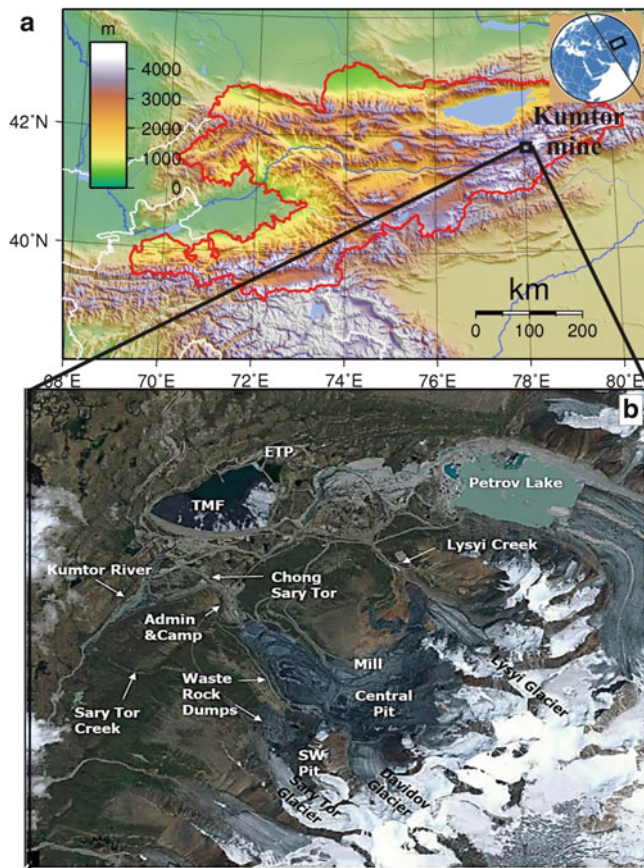


Fig. 1 (a) Map of Kyrgyzstan with the location of Kumtor gold mine; (b) main natural and technogenic sites of the mine

Basic Information on the High-Altitude Kumtor Mine and Davydov Glacier Area

Kumtor gold mine is located in the area of Central Tien-Shan Mountains, at altitudes of 3,900–4,400 m (Fig. 1a). The project is implemented by the joint Kyrgyz-Canadian venture “Kumtor Operating Company” (KOC) in the zone of active glaciers (Fig. 1b) and the continuous permafrost rocks (PF). This mine site is situated in the Ak-Shyrak mountain range, which is one of the largest areas of modern glaciers in Kyrgyzstan.

Landslide occurred in the dumps stored in the valley of Davydov glacier, which is located in the northwest slope of Ak-Shyrak ridge (41°51'N; 78°12'E), between the Lysyi and Sary Tor glaciers (Fig. 1b). The length of Davydov glacier before mining activity was about 6 km, the area of the glacier was around 11.6 km². The total ice volume in glacier before mining activity was estimated around 720 million m³. According to the radar geophysical survey, provided in 1985, the maximum ice thickness reached the value of 130 m. The results of thermodrilling and thermometry indicated that Davydov glacier has polythermic structure

including cold ice on top of the glacier and warm ice at the bottom (Vasilenko et al. 1988). Based on the results of combined survey in 1985 it was concluded that there is water in the lower part of glacier, which is present even in winter. This water content probably strongly affects the dynamic characteristics of the glacier. The presence of water in the lower part of glacier was fully confirmed by drilling in 2009. The lower part of the glacier is the boundary between bottom moraine-ice and the underlying bedrocks. Based on velocity measurements in different parts of the glacier it was concluded that the movement occurs in form of a single block of ice sliding along the bed. Displacement velocity in the lower part of Davydov glacier in the period prior to the mining was around 15–20 m/year, which included total glacier displacement and intra-block displacements.

Ore mining, post-processing and storage of the massive waste dumps in Kumtor area are seriously complicated by the presence of active glaciers and permafrost state of soil and rocks. In addition, the mining in target area is complicated by geological structure, faults of different scales together with high seismic activity. The seismicity of the area is $M = 8$ on the Richter scale with the earthquake repeatability of 1–2 times per 500 years. According to GPS measurements, the horizontal displacement of the earth surface in Kumtor area is 10 mm/year and is mainly directed to the north. The reported glaciological, cryogenic and seismotectonic conditions of this mountainous region predetermine the poor stability and high vulnerability of rock and ice mass in relation to anthropogenic impacts, in particular, to the formation of the massive dumps on them.

Kumtor Mine Waste Rock Dumps

As of middle 2013, over 1.0 billion tons of waste rocks and more than 100 million m³ of glacier ice were mined and moved to the dumps of the Kumtor mine. This huge mass of rock and ice was stored in the Lysyi, Davydov and Sary Tor glaciers basins (Fig. 1b). Waste rocks were mostly dumped on the surface of the moving glaciers. The majority of waste rock and glacial ice was stored on the Davydov glacier (Fig. 1b). Thus, according to KOC, for the period from 1995 to 2012, the amount of waste rocks stored in the basin of this glacier is more than 278 million m³ or 775 million tons.

From the very beginning of operations in 1995, joint (non-separate) storing of waste rocks and glacier ice has been carried out. The main feature of the dumps structure is blocky composition of the rock material, alternating with ice. According to the designers, the presence of ice inside the dumps must have contributed to the conservation of cold in the dump mass, thus ensuring the stability of the frozen dumps on the glacier.

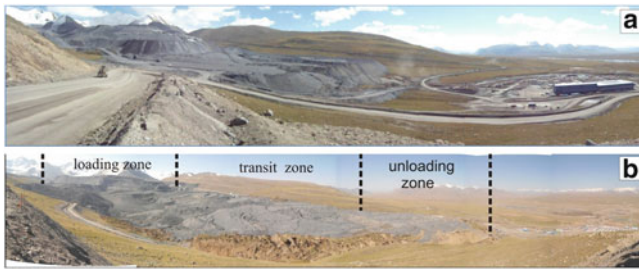


Fig. 2 The view to the waste rock dumps, situated in the valley of Davidov glacier: (a) situation as of August, 05 2012; (b) situation as of August, 09 2013

By the end of 2012, the total volume of glacial ice, stored in mixture with waste rocks in the Davydov glacier basin, has exceeded 100 million m^3 . Consequently, glacier ice takes more than 35 % of the dumps volume placed on the Davydov glacier.

In course of the mining operation, it became clear that excessive loading of the Davydov glacier with waste rocks and glacial ice lead to the squeezing of ice from the thick dumps. It also became clear that excavation and removing of ice to ensure safe access to SB area (south-west part of the Central pit) has led to a big change in the natural glacier regime. While in the beginning of dumps formation the velocity vectors in different parts of glacier were consistent, after significant load of the glacier with waste rocks the velocity and direction of the movement of its mainstream part changed dramatically. There was gradual narrowing of the ice flow parts in the middle and lower parts of glacier (ice damming). According to the geodetic monitoring results, acceleration of displacement in the narrowed ice flow parts was recorded, especially in the tongue part. With further accumulation of waste dumps and expansion of the Central pit, three separate parts formed in the glacier. In the area of the ice flow the dumps have also started their sliding.

Sliding in the Waste Dumps

The targeted landslide occurred in the lower part of dump situated in Davydov glacier basin (Figs. 1b and 2). As of July 30, 2013, the length of the landslide active part exceeded 2.3 km, width was around 1.06 km, the area—2.44 km^2 . The coordinates of the front part of landslide are the next: $\varphi = 41.87401^\circ N$; $\lambda = 78.15566^\circ E$, its height is around 43–50 m, and the slope angle is close to the angle of the natural slope.

Landslide has three main parts, which present the main parts of loading, transit and unloading of waste rocks and ice sliding mass (Fig. 2b). The loading area is presented by the thickness down to 180 m from the surface to the bottom of the Davydov glacier moraine. The length of the loading area



Fig. 3 The view to the front part of the sliding mass (June, 2013), showing the destruction of the administration building and mine infrastructure damage

along the thalweg of the valley reached the value of 1.0 km. Based on the topographic surveys the total volume of waste rock and ice in this area was more than 120 million m^3 . Starting from April 2013, dumping of waste rock in this area was terminated.

The transit area is presented by the mass of waste rock and ice, where the basic deformation of the block slumping occurs. On the surface of the transit area the arc-shaped transverse tensile cracks are well expressed, as well as hummocky topography expressed in the direction parallel to the general slope and indicating the dumps movement (Fig. 2b). The average thickness of the transit zone in spring 2013 was about 100 m, its length was around 1.4 km, the estimated volume of moving rocks and ice is more than 70 million m^3 .

The discharge (unloading) zone is presented by the tongue part of the sliding dump, near the constantly moving front part. The length of this zone within the contours of the landslide body was about 400 m, the average thickness is 85 m, the estimated volume is around 1.2 million m^3 .

By all indications, the dumps move in form of block displacements in all three parts. Landslide itself is moving the moraine deposits of the Davydov glacier in front of it, like a bulldozer (Fig. 3).

The average slope of the surface of the sliding dumps varies in the range of 4–6°. On the top, they have hummocky, stepped surface, sometimes covered with glacial ice, removed from the upper parts of the Davydov glacier. In the beginning 2013, the open ice area was more than 20 % of the total area of sliding dumps.

According to information provided by the KOC geotechnical service, the ice-rock mass of dumps formed in the Davydov glacier valley moves along an inclined surface (12–16°) presented by permafrost rocks lying under a layer of moraine deposits. This conclusion on the morphology of the sliding surface is based on the exploration drilling, according to which at a depth of 30–40 m from the lower dump surface, the ice layers and lenses of ice were found. Cohesion of the moraine material at depths of 19–33 m increased from 85.0 to 105.0 kPa, angle of internal friction is between 40° and 42°, plasticity decreased from 11.0 to 8.4.

The physical and mechanical properties of loose moraine deposits are defined by the ice content in dump. The degree of deformation of frozen soil also depends on the ice content in the upper layers of permafrost. The average ice content is around 15–20 %, maximum is up to 30–40 %. Areas with high ice content in the rocks and soils are strongly exposed to the deformations under the man-made load and/or exposure. For these reasons, the moraine material on the slopes and in the glaciers valleys are unfavorable for building of various facilities on them, including the waste rock dumping.

It should be noted that the dumps stored on Davydov glacier made the barrier for the natural movement of the glacier ice. The position of dumps put the barrier for melt water runoff, finally causing an increase in water pressure at the border between the glacier and the bottom moraine. High fracturing of the glacial ice under the dumps weight, and the high permeability of waste rock fragments caused almost complete water infiltration in the dump mass. High water content in the dumps in combination with the seismic impact can lead to the transformation of current sliding of rock and ice mass into a mudflow, which could pose a serious threat to the personnel and facilities of the mine, located downstream. KOC is constantly pumping out water from reservoirs formed at the sliding dumps in order to avoid water infiltration into the dumps. These reservoirs get water from Chong Sarytor River, which was blocked by the sliding mass. Compared to previous years, water discharge in the Chong Sarytor River downstream from dumps has dropped almost two times, reaching the value of 1.3 m³/s in the period of intense glacier melting.

Dumps Sliding Dynamics

Figure 4 presents the displacement velocity dynamics in the lower (dump 31), middle (dump 32) and upper (dump 33) parts of the sliding mass. These graphs were based on the results of the geodetic monitoring for the period from January 2012 till August 2013. As can be seen from the graphs, the dump sliding velocities are not the same in different parts of dump mass. According to the monitoring data, in the course of 2012, the average velocity in the tongue part of sliding mass was 1.5 m/day. Acceleration of displacement with velocities over 1.5 m/day was recorded in the beginning of April 2013. The maximum velocity of the rock-ice mass sliding has recorded in mid-April with value of 5.2 m/day in its tongue part, when sliding mass reached the number of buildings and infrastructure.

It has resulted in destruction of buildings, where the KOC administrative and technical services were located (Fig. 3). The Kumtor mine infrastructure (power lines, power substation, motor vehicle repair shops, etc.) were also under the threat of destruction. The total amount of losses associated

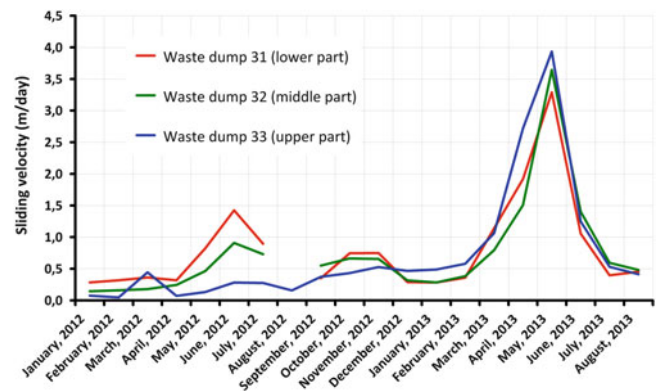


Fig. 4 Average sliding velocity dynamics for different parts of the landslide for the period 2012–2013

with the urgent need to move the mine facilities is estimated at a sum of USD 100 million. Because of the accelerated movement of dumps, the company terminated the further storing of the waste rocks at the foot of Davydov glacier.

In the second half of May and in June, 2013 a gradual decrease in velocity to about 0.5 m/day was recorded. One of the main reasons for the dramatic acceleration of the dump movement was the excessive dumping of waste material in the upper part, in the area where valley inclination changes from steep to slightly inclined. Apparently, the dumps formed in the steep part of the valley, moved down, and triggered sliding of mass situated in less inclined valley.

At present time sliding mass is separated into three blocks (Fig. 2b): the lower part, moving at an average velocity of 0.40 m/day; the middle and upper parts, which move with a higher speeds (up to 0.45 m/day) and appear to slide over the lower part. The upper part is situated in the loading zone, and, despite the termination of dumping of waste rocks, is still mobilized for a possible acceleration in the near future.

It was noted above that sliding of dumps in Davydov glacier basin is similar with Rock Glaciers widely spread in the nival-glacial zone of the Tien Shan. However, the literature review suggest that the velocity values for the viscoplastic flow of active Rock Glaciers in Tien Shan are normally up to several meters per year, sometimes reaching the values of up to 14 m/year (Gorbunov et al. 1992). Obviously, these velocities are significantly less than the velocities observed in target area. For example, only for 6 months, from October 2012 to May 2013, the total displacement reached the value of 300 m.

Rock and ice sliding in some extreme cases (earthquakes, abnormal rainfall or a combination of them) can result in a rapid sliding of huge masses of ice-rock material in shape of mudflows/debris flows. Such scenario of the rock-ice sliding in the current climate warming conditions seriously threat to the environment, since debris flows or mudflows moving towards Kumtor River can be a source of systematic and

long-term contamination of the Naryn-Syrdarya Rivers basins. In addition, in case of transformation of the sliding mass into the mudflow/debris flow, it is possible that Kumtor mine infrastructure, including living camp, may be affected by it. It should be noted that living camp of Kumtor mine site currently accommodates more than 1,200 people.

Discussions

The stripping of Kumtor mine glaciers was a unique and doubtful experiment in the history of mining in glacial areas. At present time, the sources of big problems for Kumtor mine future activity are originated from a large-scale and high velocity sliding of the ice-rock mass. This sliding occurs in the dumps, situated in Davydov glacier valley with possible environmental threats in form of surface water pollution in Kumtor-Naryn River basin.

The main causes of geotechnical problems in dumps of Kumtor mine are the errors in choosing right place for dumps storage, including waste rock storage on the surface of active glaciers. The mistakes also included incomplete account for glaciological features, permafrost characteristics and geological environment in glacial-nival belt of Tien Shan. Cryogenic gravitational processes observed at the mine have significant

impact on the environmental conditions of the target area. Such kind of gravitational processes are the major factors complicating the geotechnical situation in the area of Kumtor mine and represent the greatest threat to its infrastructure and facilities. At present time, the most important issues include the selection of the safe sites for further dumping and relocation of buildings/infrastructure threatened by sliding mass. At the moment, the dumps are piled on the neighboring glaciers Lysyi and Sarytor. By the end of 2013, it is planned to place: in the Sary Tor River valley—around 40 million m³ of waste rocks and 19 million m³ of ice, in the Lysyi glacier—over 9 million m³ of waste rock and 8 million m³ of ice.

References

- Barsch D (1996) Rockglaciers: indicators for the present and former geoecology in high mountain environments. Springer, Berlin, 331 p
- Gorbunov AP, Titkov SN, Polyakov VG (1992) Dynamics of rock glaciers of the Northern Tien Shan and the Djungar Ala Tau, Kazakhstan. *Permafrost Periglac Process* 3(1):29–39
- Vasilenko EV, Gromyko AN, Dmitriev DN, Macheret YuYA (1988) The structure of the Davydov glacier according to the radio sounding and the thermal drilling data. *Data of Glaciological Studies* 62: 208–215 (in Russian)



Study of Plant-Soil-Permafrost System on Landslide-Affected Slopes Using Geochemical Methods on Yamal, Russia

Nataliya Ukraintseva, Marina Leibman, Irina Streletskaya, and Tatiana Mikhaylova

Abstract

Interrelation between the height and productivity of willow tundra, and activation of cryogenic landsliding is discussed. Cryogenic landslides on saline marine sediments in Typical tundra subzone of the Yamal Peninsula show specific features. Landslide process causes desalinization of marine sediments and enriches the active layer with salts. Landforms of the landslide-affected slopes can serve as indicators of permafrost table change, heterogeneity of saline composition of near-surface sediments.

It is suggested that high willow canopies are indicators of ancient landslide activity. Landslide-affected slopes significantly differ by structure of phytomass from stable surfaces (background): on landslide slopes willow proportion in phytomass reaches 50–80 %, while background surfaces are dominated by moss (60–70 %). The total above-ground phytomass on ancient landslides (an average of about 1,600 g/m²) is much higher than on stable surfaces (an average of about 1,200 g/m²).

Most informative landslide age indicators are: salinity of sediments and ground water, macro- and trace-element concentration, ash content in willow leaves and grasses. Concentration of chemical elements can either increase with age, or decline. This is obviously due to the mobility of an element migrating in the active layer.

Keywords

Cryogenic landslides • Soil and plant geochemistry • Willow shrubs

Introduction

Cryogenic landslides are widespread on the Arctic plains (Geertsema and Pojar 2007; Harry and Dallimore 1989; Matsuda et al. 1988; etc). Landslides of permafrost zone

(active-layer detachment slides after Lewkowicz (1990), etc.) are known to move over an active layer base. The permafrost table serves as a landslide shear surface. In Yamal Peninsula (North of West Siberian Lowland) landslides are widely distributed in a Typical Tundra subzone. They actively change the primary surface of ancient marine plains and terraces. Landslide activation took place in late 1980s with the main event in 1989.

Specific features of Yamal landslides are connected to marine origin of permafrost deposits underlying active layer. Exposure of the frozen saline marine sediments due to landslide disturbance triggers their desalinization. In addition to the mechanical dislocation of active-layer deposits by a landslide, lateral redistribution of elements within the active layer is observed (Dubikov 2002; Leibman and Streletskaya 1997; Ukraintseva 1997, 2008).

N. Ukraintseva (✉) • M. Leibman (✉) • T. Mikhaylova
Earth Cryosphere Institute, Siberian Branch, Russian Academy of Sciences, Malygin street, 86, Tyumen 625000, Russia
e-mail: ukraintseva@mail.ru; moleibman@mail.ru; korobova.tatiana@gmail.com

I. Streletskaya
Faculty of Geography, Moscow State University, Leninskie Gory, Moscow 119991, Russia
e-mail: irinastrelets@gmail.com



Fig. 1 Study area. Research station “Vaskiny Dachi” (red square) and sites of landslide observations (blue circles). Dashed red line is the southern limit of the frozen saline marine deposits (after Dubikov 2002)

It was noted that abnormally high willows (up to 1–1.5 m high) characterize landslide-affected areas in Typical tundra subzone of West Siberian lowland. The area of high-willow tundra coincides with the limits of distribution of saline marine deposits near the surface (Fig. 1). In Southern tundra subzone, where permafrost degraded in Holocene optimum and temporarily thawed, saline deposits were washed out and desalinized, willows were replaced by dwarf birch/moss communities on the stabilized landslide slopes.

Cryogenic landslides are cyclic in time—various parts of the landslide-affected slopes are periodically involved in the movements after a certain period of recovery (Leibman et al. 2012). The landslide age, defined by direct observation, analysis of multi-temporal images, and radiocarbon dating of buried organic matter, varies from less than 100 to more than 2,000 years.

Paper presents: 1) stages of landslide shear surface revegetation, 2) chemical composition of ground water and water extraction from active-layer deposits, and 3) concentration of trace elements in soils and plants.

Paper is based on the data obtained in field in Central Yamal since 1988.

Study Area and Methods

The study area is located in the vicinity of Bovanenkovsky gas field and Research station «Vaskiny Dachi». It comprises a highly dissected plain in the Typical Tundra bioclimatic subzone (Bioclimatic subzone D, after Walker et al. 2011), with continuous permafrost, rather thick (0.8–1.2 m) active layer in sandy and clayey deposits, often saline due to marine origin.

Geochemical features were studied at 80 selected points along 10 transects of total length 6 km. Sampled were vegetation, active-layer and ground water. The technique

of laboratory tests was described earlier (Ukraintseva 2008). The main ion concentration in ground water and filtered water extraction out of sediments were determined by standard chemical methods at the Dokuchaev Soil Institute in Moscow (analysts RV Grishina and NS Nikitina). X-ray–fluorescent analysis of air-dried and homogenized plants and sediments was carried out with the help of XRF spectrometer ORTEC-TEFA (analysts SE Sorokin and AT Savichev, Dokuchaev Soil Institute, Moscow).

Vegetation Recovery Stages on the Landslide-Affected Slopes

Anomaly of high willow distribution on Yamal Peninsula and other areas of the Arctic plains was known long ago (Andreev 1970; McKendrick 1987; Sturm et al. 2001; etc.). However, authors did not link them to geochemical features of the active layer, caused by landslide activity. Willow shrubs were associated with climate change, warming and “greening” (Walker 1987; Walker et al. 2011; Forbes et al. 2010). Numerous studies are devoted to geochemistry of shrub tundra (Tentyukov 1998; etc.) with no mentioning of slope processes as controls. The predominance of high willow shrubs (*Salix glauca*) on landslide-affected slopes was noticed by Matsuda et al. (1988); Rebristaya et al. (1995); Ukraintseva (1997).

Our study shows, that dominating communities on hilltops and stable slopes (A3) are the undershrub/grass/moss and moss/lichen tundra. These are the background communities for a subzone of Typical Tundra.

Three age generations of landslides were subdivided: 1, young, came off in 1989–1991, directly observed, 2—old (under 100 years old, detected by clearly observed landforms, poorly vegetated shear surface, and 3—ancient (300 to more than 2,000 years determined by radiocarbon dating) (Ukraintseva 2008).

The first stage is considered when bare patches alternate with pioneer herbages, such as *Puccinellia sibirica*, *Deshampsia* sp., *Phippsia concinna*, *Tripleuro-spermum Hookerii* etc. on young surfaces (B1, Fig. 2). The second stage comprises colonization by meadow sedge/grass communities (*Calamagrostis* sp., *Poa alpigena* subsp. *colpodea*, *Carex* sp., *Polemonium acutiflorum*, *Equisetum arvense* subsp. *boreale* etc.) with active willow restoration (old shear surfaces B2). The third, final stage comprises colonization by the high willow communities (ancient shear surfaces B3, Fig. 2).

On young landslide bodies (C1, Fig. 3) low shrubs (willow, dwarf-birch) are dominating, moss cover degrades, pioneer vegetation appears. On the old bodies (C2) willow/meadow communities with mosses replace C1-type. Dense willow canopy covering moss/herbaceous communities



Fig. 2 Landslide shear surfaces of various age: young (*left pane*), ancient (*right pane*)



Fig. 3 Landslide bodies of various age: young (*left pane*), ancient (*right pane*)

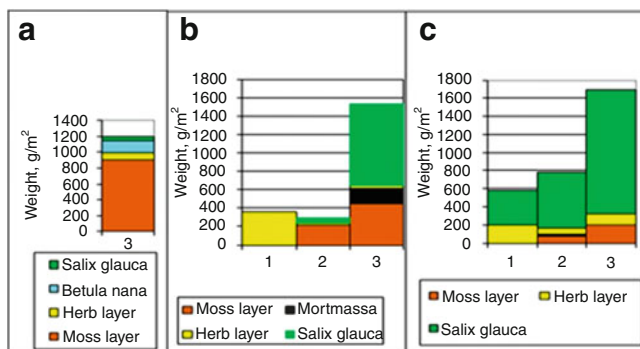


Fig. 4 Total aboveground phytomass (mean values) of vegetation at ‘background’ surfaces (*a*) and landslide-affected slopes: shear surfaces (*b*) and landslide bodies (*c*). (1)—young, (2)—old, (3)—ancient

ominate on ancient landslide bodies (C3, Fig. 3). Thus, high willow canopies are indicators of an ancient landslide activity.

The total aboveground phytomass on ancient landslides (B3, C3) on average is about 1,600 g/m² compared to 1,200 g/m² of A3 (Fig. 4). On A3 moss coverage is 100 %, and willows—less than 10–15 %.

On the landslide-affected slopes the willow quota increases up to 50–80 %, and less than 40–80 % is covered by mosses.

Chemical Composition of Ground Water and Water Extraction from Active-Layer Deposits

Analyzed are water-soluble salts (ions) in active-layer deposits. Water-soluble salts are most mobile; rapidly move both vertically and laterally (Streletsky et al. 2003).

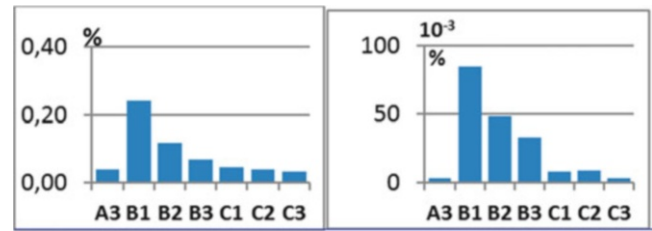


Fig. 5 Concentration of water-soluble salts (*left pane*) and Cl-ion in the solution (*right pane*) in active-layer deposits

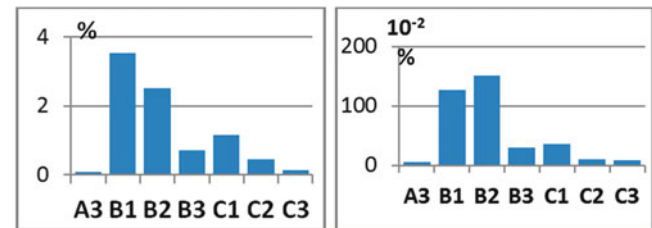


Fig. 6 Concentration of water-soluble salts (*left pane*) and Cl-ion in the solution (*right pane*) in ground water of landslide slopes

These salts are also most approachable for plants, forming growing substrate for plant roots. Figure 5 shows two main parameters characterizing marine origin of the active layer deposits and permafrost. These parameters are: concentration of water-soluble salts (% in solution), and concentration of Cl-ion in the solution (10⁻³ %) (after Dubikov 2002).

Young shear surfaces (B1) are characterized by maximum values of all the parameters which are 5–10 times higher than respective parameters on the stable surfaces (A3). The same trends are observed on the landslide bodies: maximum values are on young landslide bodies (C1) reducing in the sequence old (C2) > ancient (C3) landslide bodies. At the same time, parameters on the landslide bodies are slightly higher compared to the stable surfaces and substantially lower than on shear surfaces of the same age.

Ground water of landslide slopes is highly heterogeneous in both ionic structure and their concentration (Fig. 6). A3 are characterized by low concentration of water-soluble salts (0.05–0.1 g/l, averaging at 0.09 g/l), and domination of Ca-cation, Mg-cation and SO₄-anion. On shear surfaces desalination starts after permafrost deposits of marine origin get involved in seasonal thaw. First most mobile Cl-ion and Na-ion move into ground water. Their high concentration indicates recent landslide event.

Ion concentration on the young shear surfaces on average exceeds 3 g/l (even more being 100 times higher than background salinity), and abruptly reduces on ancient shear surfaces (down to 0.7 g/l). Ion concentration within ancient shear surfaces is heterogeneous ranging between 0.3–0.5 g/l and 4–5 g/l. This indicates that the areas of salt accumulation and salt washout exist simultaneously in ground water on the

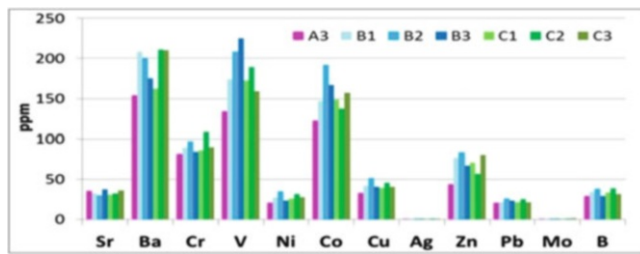


Fig. 7 Trace elements in the active layer deposits (average values for different landforms on landslide-affected slopes)

ancient landslides depending on surface topography. Ion structure changes from Cl-HCO_3 to HCO_3 . Na^+ domination is replaced by Ca^{2+} and Mg^{2+} .

Gross Concentration of Trace Elements in Soils and Plants

According to semi-quantitative spectral analysis of 40 chemical elements on 235 soil samples in the study area most common are 15 (Fig. 7). These elements are found in all collected samples, their relative abundance varies markedly over the landforms. Age differences are clearer visible on the shear surfaces of landslides. Landslide bodies in their trace-element composition are similar to the hilltops and stable slopes (A3), their geochemical evolution in time depends on their location on the slope which controls inflow of matter in the respective location.

Four minerals which are most significant: barium, vanadium, cobalt and zinc (Fig. 7). Their concentration on landslide slopes are 1.2–1.5 times higher compared to the stable surfaces. Barium concentration is the highest on the young landslide shear surfaces (B1) and gradually decreases towards old (B2) and ancient (B3) shear surfaces. Vanadium, however, significantly increases from B1 towards B3.

The maximum concentration of cobalt and zinc, as well as chromium, nickel, copper and boron are typical for B2, while both B1 and B3 show lower concentration. Obviously, these differences are related to the mobility of elements. Most mobile in active-layer deposits is barium, it is gradually washed out of marine sediments. Vanadium is the most inert, its relative abundance increases with time due to the reduction in the proportion of more mobile elements. The remaining trace elements are intermediate in abundance: in the beginning their share increases, and then, on the old shear surfaces, where element migration is reduced and may even be the inflow of matter, their share gets significantly reduced.

Thus, increase in the concentrations of some trace elements on the shear surfaces of landslides is induced by the chemical composition of the original marine substrate.

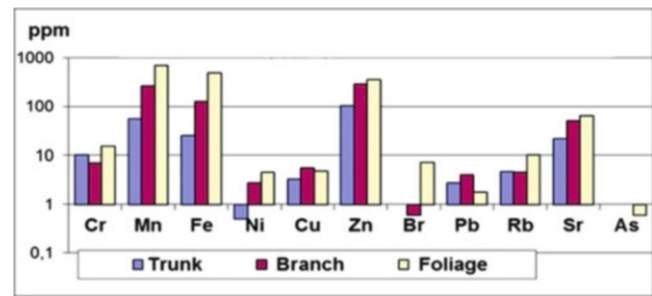


Fig. 8 Average trace-element concentration in various parts of willow shrub

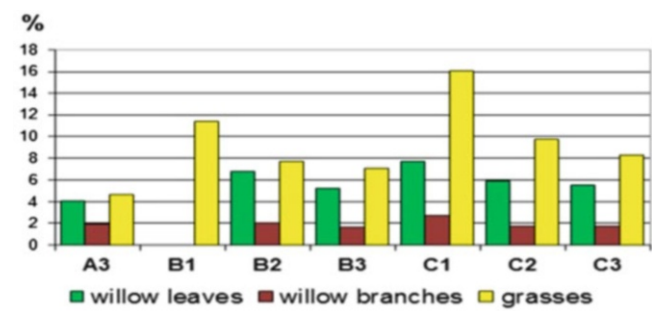


Fig. 9 Ash content in plants

In stable areas concentration of trace elements decreased with time through numerous cycles of freeze-thaw (frost weathering) and groundwater action in the warm seasons.

The concentration of trace elements in plants varies not only by groups of plants, but also by landforms on landslide slopes, as well as by landslide age. Despite the richness of trace element composition in the active layer deposits of the landslide slopes, the oppressed mosses accumulate trace elements in much smaller concentrations.

In the willow shrubs concentration of trace elements is most sustained in space on the landslide slopes of the same age. Willows show maximum for zinc, strontium, manganese and iron concentrations (Fig. 8). Strontium (which can replace calcium) helps build a large willow “skeleton”: the trunk and branches, zinc increases frost-resistance of willows, allowing it to create stable groups in the typical tundra subzone (Rebristaya et al. 1995; Ukraintseva 1997; Tentyukov 1998).

Ash content successively decrease from younger to older surfaces and on landslide slopes is much higher compared to background surfaces, especially in grasses and willow leaves (Fig. 9). This allows using trace-element concentration and ash content as indicators of landslide’s relative age. Most trace elements are actively accumulated in mosses. Willows, though having less total concentration of trace elements compared to mosses, show maximum for zinc, strontium, manganese and iron concentrations (Fig. 8). Strontium (which can replace calcium) helps build a large willow

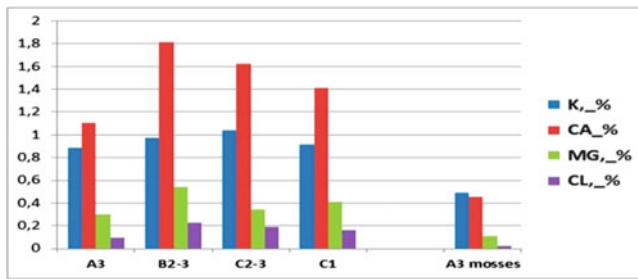


Fig. 10 Macroelements in willow leaves and mosses

“skeleton”: the trunk and branches, zinc increases frost-resistance of willows, allowing it to create stable groups in the typical tundra subzone (Rebristaya et al. 1995; Ukrantseva 1997; Tentyukov 1998).

Ash content successively decrease from younger to older surfaces and on landslide slopes is much higher compared to background surfaces, especially in grasses and willow leaves (Fig. 9).

The use of X-ray fluorescence analysis allowed determining not only the trace elements, but also macroelements in the willow leaves. Characteristic is a significant increase in calcium, magnesium and chlorine concentrations on landslide slopes compared to stable areas. But even in the under-shrub-lichen-moss communities on hilltops dwarf willows accumulate much more macroelements than mosses (Fig. 10).

After the landslide event Gramineae create pioneer groups on the exposed shear surfaces, tolerate high salinity of soil water (halophytes are marked among). On old landslides grasses predominate in the understory of willow shrub communities, only on ancient landslides gradually giving way to mosses (Ukrantseva 2008).

Conclusions

Field data confirms the relationship of height and productivity of willow shrubs with activation of cryogenic processes in the region with saline deposits of marine origin. It is established that azonic high-willow canopy is an indicator of ancient landslide activity, and areas of its distribution can be used for mapping landslides on aerial and satellite images.

Offered is a variety of methods to estimate the relative age of landslides.

Landslide-affected slopes are very different by the structure of phytomass from the stable surfaces: on landslide slopes willow share reaches 50–80 % and background are dominated by moss (60–70 %). Bulk phytomass on ancient landslides (about 1,600 g/m²) is much higher than on stable surfaces (about 1,200 g/m²).

The chemical composition of sediment and plants within cryogenic landslides, developing in saline

permafrost, changes dramatically depending on the age of the landslide. Most informative in estimation of the landslide age are: salinity of ground water and active-layer deposits, ash content, macro- and trace-element concentration in willow leaves and grasses. Concentration of chemical elements on landslides can either increase with age, or decline. This is obviously due to the mobility of an element and rapidness of its migration in the active layer.

Acknowledgements The study was supported by grants 11-05-00544-a, 11-05-10084-k, 10-05-10027-k from the RFBR; Grant SS 5582.2012.5 from the President of the Russian Federation for Science Schools and international projects RISES, TSP and CALM. Authors express their gratitude to SE Sorokin and RV Grishina for performing chemical tests.

References

- Andreev VN (1970) Some geographical laws in distribution of above-ground phytomass in tundra zone in connection with progress to the north of tree-shrubs vegetation. In: Biological basis of nature usage in the North. Komi, Syktyvkar, pp 6–13 (in Russian)
- Dubikov GI (2002) Composition and cryogenic structure of permafrost in West Siberia. GEOS, Moscow, 246 p (in Russian)
- Forbes BC, Fauria MM, Zetterberg P (2010) Russian Arctic warming and ‘greening’ are closely tracked by tundra shrub willows. *Global Change Biol* 16:1542–1554
- Geertsema M, Pojar JJ (2007) Influence of landslides on biophysical diversity — a perspective from British Columbia. *Geomorphology* 89(1):55–69
- Harry DG, Dallimore SR (1989) Permafrost, ground ice and global change in the Beaufort Sea coastlands, vol 3. GEOS, Moscow, pp 48–53
- Leibman MO, Streletskaya ID (1997) Land-slide induced changes in the chemical composition of active layer soils and surface-water run-off, Yamal Peninsula, Russia. Proceedings of the international symposium on physics, chemistry, and ecology of seasonally frozen soils, Fairbanks, pp 120–126
- Leibman MO, Gubarkov AA, Khomutov AV, (2012) Research station Vaskiny Dachi. Excursion guidebook. In: Tenth international conference on permafrost, Salekhard, Russia, 25–29 June 2012. Pechatnik, Tyumen, p 50
- Lewkowicz AG (1990) Morphology, frequency and magnitude of active-layer detachment slides, Fosheim Peninsula, Ellesmere Island NWT. In: Burgess MM, Harry DG, Sego DC (eds) Proceedings of the 5th Canadian permafrost conference, Quebec, Canada, June 1990. Laval University, Quebec, Collection Nordicana 54, pp 111–118
- Matsuda K et al (1988) Observations of geomorphic and vegetational changes caused by thermal erosion of an involuted hill in Tuktoyaktuk, N.W.T., Canada. In: Characteristic of the massive ground ice body in the Western Canadian Arctic related to paleoclimatology. *Inst. Low Temp. Sci., Hokkaido Univ.*, 1984–1985, pp 24–42
- McKendrick JD (1987) Plant succession on disturbed sites, North Slope, Alaska, U.S.A. *Arct Alp Res* 19(4):554–565
- Rebristaya OV, Khitun OV, Chernyadyeva IV, Leibman MO (1995) Dynamics of vegetation on the cryogenic landslides at the central part of Yamal Peninsula. *Bot J* 80(4):31–48 (in Russian)
- Streletsky DA, Streletskaya ID, Rogov VV, Leibman MO (2003) Redistribution of ions within the active layer and upper permafrost, Yamal, Russia. In: Phillips M, Springman SM, Arenson LU (eds)

- Permafrost: proceedings of the 8th international conference on permafrost, Zurich, Switzerland, 20–25 July 2003, vol 2. A.A. Balkema, Zurich, pp 1117–1122
- Sturm M, Racine C, Tape K (2001) Increasing shrub abundance in the Arctic. *Nature* 411:546–547
- Tentyukov MP (1998) Geochemistry of landscapes of Central Yamal. Ekaterinburg. IB Komi SC UD RAS, 101 p (in Russian)
- Ukraintseva NG (1997) Willows tundra of Yamal as the indicator of salinity of superficial sediments. In: Results of basic research of Earth cryosphere in Arctic and Subarctic. Nauka, Novosibirsk, pp 182–187 (in Russian)
- Ukraintseva NG (2008) Vegetation response to landslide spreading and climate change in the West Siberian tundra. In: Proceedings of the ninth international conference on permafrost, University of Alaska Fairbanks, vol 2, pp 1793–1798
- Walker DA (1987) Height and growth rings of *Salix lanata* ssp. *richardsonii* along the coastal temperature gradient of northern Alaska. *Can J Bot* 65:988–993
- Walker DA, Forbes BC, Leibman MO, Epstein HE, Bhatt US, Comiso JC, Drozdov DS, Gubarkov AA, Jia GJ, Karlejaärvi E, Kaplan JO, Khumutov AV, Kofinas GP, Kumpula T, Kuss P, Moskalenko NG, Reynolds MK, Romanovsky VE, Stammer F, Yu Q (2011) Cumulative effects of rapid land-cover and land-use changes on the Yamal Peninsula, Russia. In: Gutman G, Reissel A (eds) Eurasian Arctic land cover and land use in a changing climate, vol 4. Springer, New York, NY, pp 206–236. doi:[10.1007/978-90-481-9118-5_9](https://doi.org/10.1007/978-90-481-9118-5_9)



Permafrost Distribution Study Based on Landsat ETM+ Imagery of the Northwest Section of the Lesser Khingan Range, China

Chunjiao Wang, Wei Shan, Ying Guo, Zhaoguang Hu, and Hua Jiang

Abstract

The northwest section of the Lesser Khingan Range is close to the southern permafrost boundary in China. Global warming and permafrost degradation have exacerbated local landslides and other natural disasters. Land surface temperature is used as an index of the Earth's surface energy balance and climate change. In order to study regional surface temperature change and permafrost degradation laws as well as to conduct an in-depth study of their influences, we used Landsat ETM+ imagery and applied remote sensing thermal infrared methods using the ENVI software to calculate surface emissivity. Using the radiative transfer equation method, we produced four surface temperature maps of the northwest section of the Lesser Khingan Range, China. Using the ArcGIS software, we produced two views of an initial permafrost distribution map. Through analysis of elevation, aspect, and slope distribution, the initial permafrost distribution map produced correlates well with on-site investigations and geophysical survey results, showing clear "Khingian-Baikal type" permafrost features. This study shows that the permafrost distribution maps generated from Landsat ETM+ data by ground temperature inversion for the study area can assist research into permafrost degradation mechanisms and the disasters they cause.

Keywords

Permafrost distribution • Climate change • Lesser Khingan • Landsat ETM+

Introduction

Permafrost is a product of heat and mass transfer between the atmosphere and lithosphere. The planar distribution of permafrost is directly affected by multiple complex factors. At a global scale, the northeastern permafrost zone in China is one of the regions that have been significantly affected by climatic warming and human activities. In recent decades, regional permafrost degradation has been significant, and its main natural causes are global warming (especially winter warming), precipitation, snow periods, thickness, and other

factors related to climate change (Ruixia He et al. 2009). Urbanization and human activities such as major construction projects in the northeastern permafrost zone in China have also had a profound impact on the permafrost and the rest of the local environment, leading to rapid, large-scale, permafrost degradation, which can cause landslides and thaw settlement, posing a threat to the safety of human structures. Our local permafrost distribution study presents an important contribution to the understanding of the underlying principles of permafrost degradation and the early warning signs of associated geological disasters.

Permafrost in China is mainly distributed in the northeast, Greater and Lesser Khingan Mountains, Western High Mountains, and the Tibetan Plateau, and covers a total area of approximately 2.15 million km². This area accounts for 22.3 % of the national land area. If we also include seasonally frozen ground with depths greater than 0.5 m,

C. Wang • W. Shan (✉) • Y. Guo • Z. Hu • H. Jiang
Northeast Forestry University, Harbin, China
e-mail: zlj_832008@126.com; shanwei456@163.com;
samesongs@163.com; huzhaoguang008@163.com;
jianghua3433@163.com

permafrost then accounts for 68.6 % of the national land area. The northeastern permafrost terrain mainly comprises hills and mountains present at high latitudes rather than at high altitudes. Due to the impact of the Siberian high pressure, the area is the coldest natural region in China (Zhou and Guo 1982). High latitude and high altitude permafrost are significantly different. Permafrost at high latitudes formed in the Early Pleistocene during a stage of bipolar ablation degradation, which was mainly controlled by a characteristic regional horizontal distribution of climate. They are composed of widely distributed, isolated zones with thicknesses greater than those of permafrost at high altitudes. In high latitude permafrost areas, the undulation of regional weather in a horizontal direction is not large, the annual temperature differences are relatively large, and the annual variation in ground temperature with depth is relatively small (Zhang and Cai 1984). In northeast China, high latitude permafrost zones mainly develop into the “Khangai–Baikal type,” in which the permafrost is more developed and has greater thickness in low-lying areas. Their degradation begins with increased warming of slopes by the Sun, with high areas and hill tops being affected first followed by shady slopes, and low areas and hill bottoms (Wei Shan et al. 2013).

In 1974, the National Institute of Building Sciences Construction Committee constructed a 1:17,000,000 graph of the standard frost line of northeast and north China (Building Sciences Institute of National Construction Committee 1974). In 1975, Boliang TONG constructed a 1:25,000,000 permafrost distribution map of China (Lanzhou Institute of Glaciology and Desert 1975) with modifications and supplements by Youwu ZHOU (Zhou and Cui 1980). This permafrost distribution map reveals the initial permafrost distribution and landform types in China. In 1977, Dongxin GUO collaborated with the staff of the Forestry Survey and Design Institute in Yakeshi and the third Design Institute of the Railways Ministry to construct a 1:2,000,000 permafrost zoning map of the Greater and Lesser Khangai Range of northeast China. In 1980, Boliang TONG established a 1:600,000 permafrost map for the area along the Qinghai-Tibet Highway. In 1982, Xiaozu XU compiled a 1:4,000,000 map of the permafrost distribution in China on the basis of data gathered in 1978 (Ding and Xu 1978).

Based on the thermal view, permafrost regions are geological reservoirs of natural history; their existence is mainly controlled by upper and lower boundary conditions and the nature of the soil itself. The upper boundary of permafrost is the ground surface; it is usually described by the ground-atmosphere system heat balance equation. The ground surface temperature can indirectly indicate the upper distribution limits of permafrost. Owing to the fact that temperature data is easier to obtain and that there is a linear interrelated relationship between ground surface temperature and atmospheric temperature for a single case of surface conditions,

permafrost researchers use temperature as a division index, and further classify its distribution by ground-atmosphere temperature differences. This is done through a regression analysis according to the relationship of annual average temperature, latitude, and altitude. The data obtained is used to delineate the range of different types of permafrost on topographic maps (Xu and Guo 1982).

With the development of satellite detection systems, different types of sensors can obtain a variety of information related to the Earth’s surface. LANDSAT are terrestrial exploration satellite systems launched by the United States. The first satellite, LANDSAT1 was launched in 1972. The satellite LANDSAT7, is equipped with an Enhanced Thematic Mapper Plus (ETM+). It detects passive responses of the earth’s surface to solar and thermal radiation. There are eight band sensors covering different wavelength ranges from infrared to visible light (<http://datamirror.csdb.cn/landsat/files/17slcon.jsp>).

With the development of satellite detection systems, it is possible to use thermal infrared remote sensing technology to invert the collected surface temperature data. The advantages of satellite thermal infrared remote sensing are high monitoring precision (0.2–0.5 °C), the ability to collect a large amount of information, and fewer restrictions. Currently, thermal infrared sensing technology is the main method used to obtain high spatial ranges of land surface temperature distributions. Since 1961, there have been successful applications of thermal infrared remote sensing to invert land surface temperatures in the Lordsburg District in New Mexico, the Wairakei District in New Zealand, Reykjavik in Iceland, and the Michoacan area in Mexico.

In this paper, we used data collected on June 4, 2011; May 3, 2011; August 23, 2011; and October 10, 2011 for four LANDSAT ETM+ remote sensing imageries according to the radiative transfer equation method used to invert regional surface temperatures. ENVI software was used to read the collected data and to conduct radiometric calibration and regional cropping. The ground surface emissivity and blackbody radiation brightness values were calculated using ENVI for the thermal infrared band by making use of Planck’s equation. Two images were created from the ArcGIS software and the initial permafrost distribution in the study area was classified according to ground temperature.

Method

We used four Landsat ETM+ imageries to conduct land surface temperature inversions. The data acquisition dates are 2011–05–03, 2011–06–04, 2011–08–23, and 2011–10–10.

Vegetation coverage F_v was obtained by the use of the mixed pixels decomposition method. The entire imagery was divided into water, vegetation, and buildings, and the specific calculation formula is as follows:

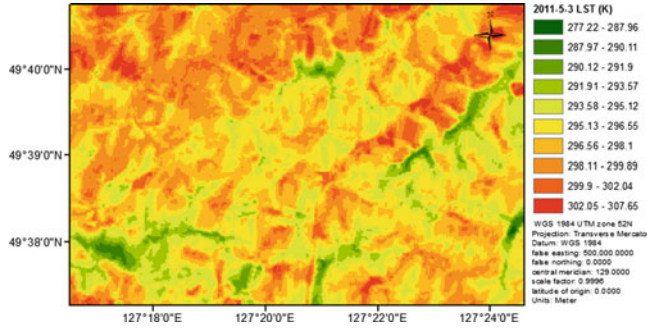


Fig. 1 May 3, 2011 temperature inversion result

$$F_v = (NDVI - NDVI_s) / (NDVI_v - NDVI_s) \quad (1)$$

According to previous research, remote sensing images can be divided into three types: water, towns, and natural surfaces. The emissivity of water is 0.995, the emissivity of the natural surface and the towns were calculated according to the following formulas (2) and (3):

$$\varepsilon_{surface} = 0.9625 + 0.0614F_v - 0.0461F_v^2 \quad (2)$$

$$\varepsilon_{building} = 0.9589 + 0.086F_v - 0.0671F_v^2 \quad (3)$$

In the formulas above, $\varepsilon_{surface}$ and $\varepsilon_{building}$ represent the emissivity of natural surfaces and towns, respectively.

The thermal infrared radiation brightness value L_λ was received by the satellite sensor and consists of three parts: the atmospheric upwards radiation brightness L_\uparrow , energy received from ground radiation brightness after passing the atmosphere, and the energy when atmospheric energy radiates downward and is reflected after reaching the ground. Thermal infrared radiation brightness values received by satellite sensors can be written as (radiative transfer equation):

$$L_\lambda = [\varepsilon \cdot B(T_s) + (1 - \varepsilon)L_\downarrow] \cdot \tau + L_\uparrow \quad (4)$$

ε is the surface emissivity, T_s is the ground surface temperature, $B(T_s)$ is the blackbody thermal brightness value under T_s , τ is atmospheric transmittance in the thermal infrared band. Radiation brightness $B(T_s)$ of blackbodies with temperature T in the thermal infrared band is determined by:

$$B(T_s) = [L_\lambda - L_\uparrow - \tau \cdot (1 - \varepsilon)L_\downarrow] / \tau \cdot \varepsilon \quad (5)$$

Subsequently, we determined the radiation brightness of blackbodies with temperature T in the thermal infrared band. According to the inverse function of Planck's formula, we calculated the ground surface temperature T_s using:

$$T_s = K_2 / \ln(K_1 / B(T_s) + 1) \quad (6)$$

Temperature inversion results displayed in ArcGIS are shown in Figs. 1, 2, 3, and 4.

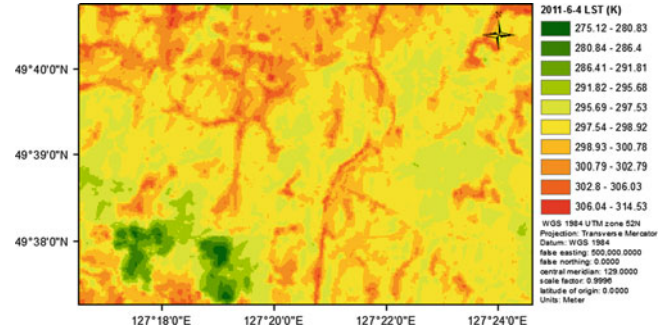


Fig. 2 June 4, 2011 temperature inversion result

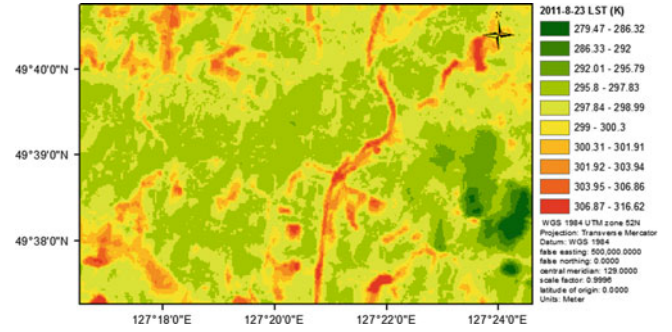


Fig. 3 August 23, 2011 temperature inversion result

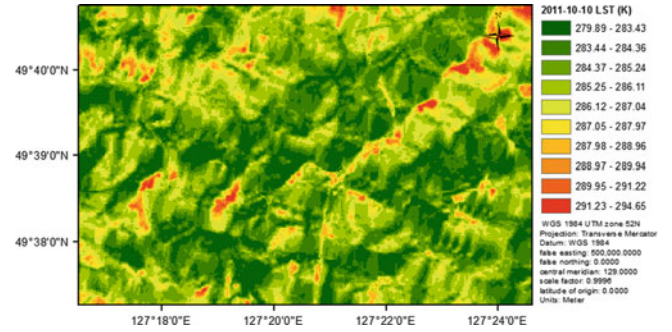


Fig. 4 October 10, 2011 temperature inversion result

Results and Discussion

The results of the temperature inversions were affected by cloud cover in the research area on June 4, 2011, and August 23, 2011, and therefore, we have shown only the inversion results for May 3, 2011 and October 10, 2011. We inputted the temperature data into ArcGIS to classify the results through human-computer interaction in order to adjust the range of variables, conduct raster data calculations and intersection operations, and overlay the results on satellite imagery for June 15, 2004. As shown in Fig. 5, we obtained a map showing the upper limits of permafrost distribution and these calculated results are consistent with results of previous studies. Figure 6 shows comparison maps in which permafrost melting traces and permafrost distributions are shown.

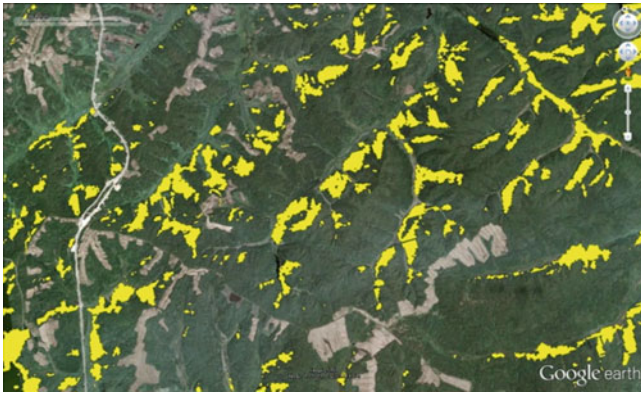


Fig. 5 Map showing the upper limit of permafrost distribution (based on Landsat ETM+ images)

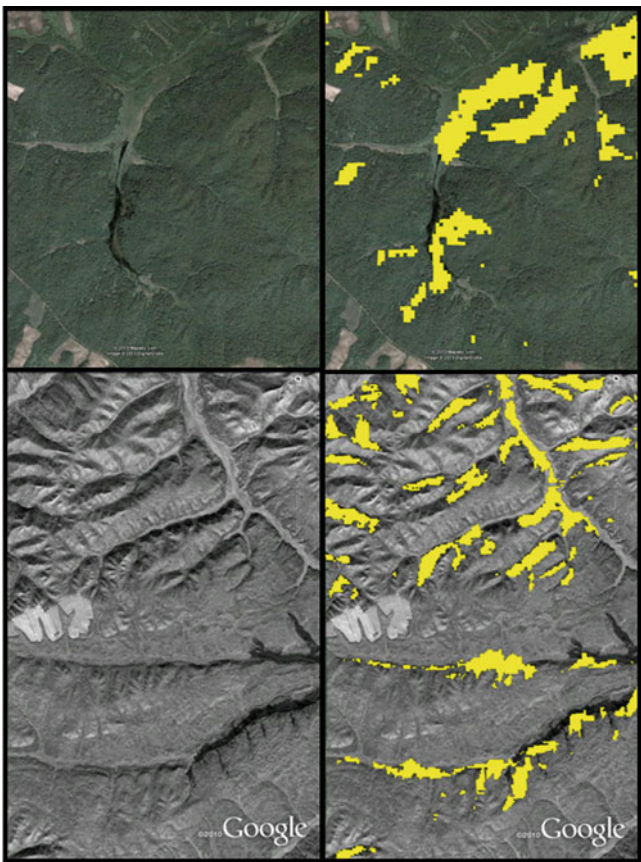


Fig. 6 Comparison map showing permafrost melting traces and permafrost distribution

We compared the areas with the most intense permafrost distribution to isolated permafrost areas using the distribution controls of height, slope and aspect. Classification analysis was conducted between the DEM of permafrost intensive areas and the DEM of isolated permafrost areas (Figs. 7 and 8). We then produced an elevation distribution map of permafrost intensive zones in the study area and

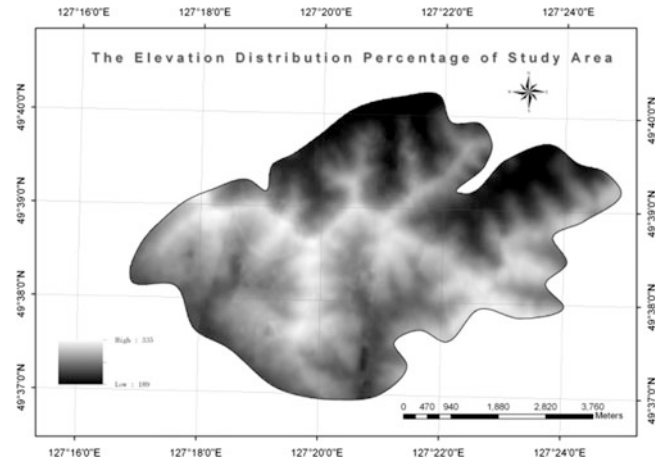


Fig. 7 Elevation distribution analysis map of the study area

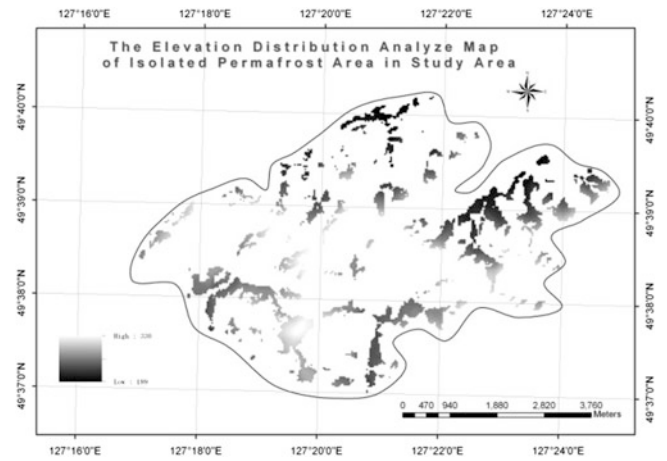


Fig. 8 An elevation distribution analysis map of isolated permafrost zones in the study area

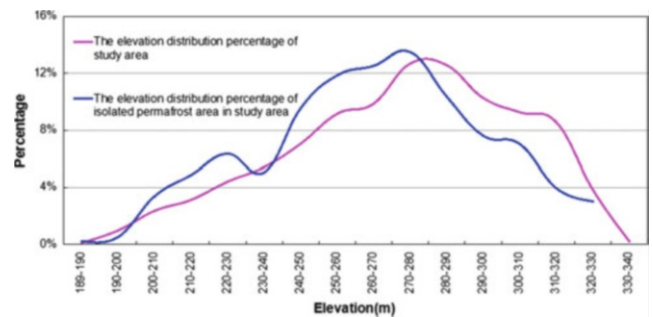


Fig. 9 An elevation distribution graph of the study area and isolated permafrost areas within the study area

isolated permafrost zones in the study area (Fig. 9). The blue curve in Fig. 9 shows the elevation distribution of isolated permafrost areas and the red curve shows the elevation distribution of the permafrost intensive zones. According to our analyses, the elevation range in the study area is 189–335 m with an average value of 273.37 m. The

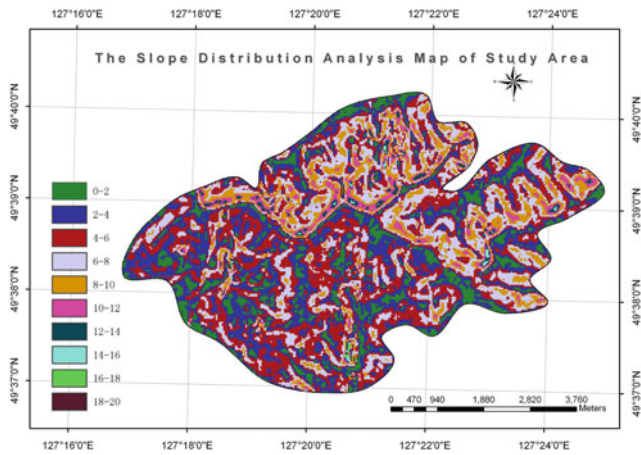


Fig. 10 A slope distribution analysis map of the study area

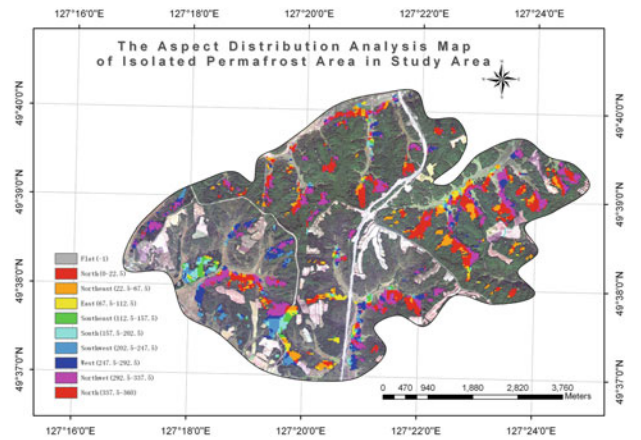


Fig. 13 An aspect distribution analysis map of isolated permafrost areas in the study area

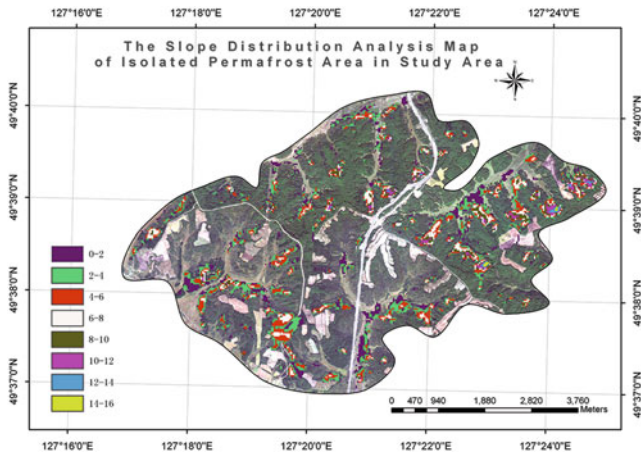


Fig. 11 A slope distribution analysis map of isolated permafrost areas in the study area

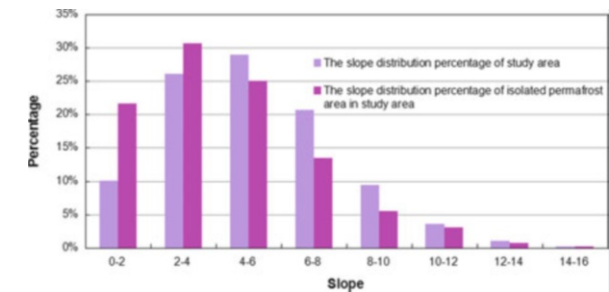


Fig. 14 A slope distribution histogram of the study area and isolated permafrost areas within the study area

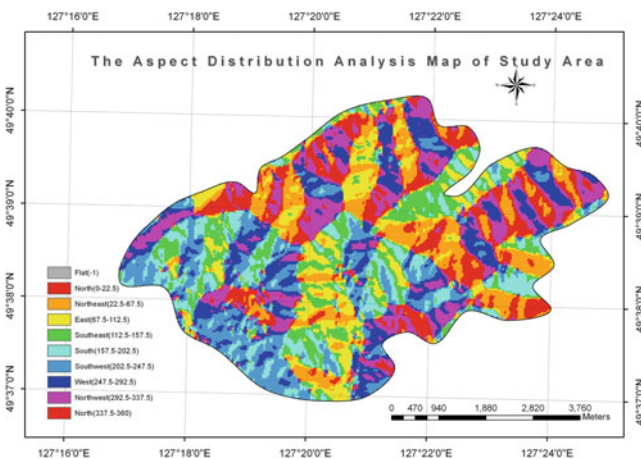


Fig. 12 An aspect distribution analysis map of the study area

permafrost intensive areas have an elevation range of 189–330 m, with an average value of 265.57 m. The difference in average heights is 7.8 m.

The slope and aspect distribution map were compared on the basis of the DEM (Figs. 10, 11, 12, and 13). The slope distribution histogram of the study area and isolated permafrost zones is shown in Fig. 14, which indicates that permafrost in the study area is primarily distributed on the north and northwest slopes, which accounts for 29.2 % and 26.3 % of the area, respectively, or a total of 55.5 % of the study area. Therefore, this demonstrates that the regional permafrost distribution on shady slopes is greater than that on sunny slopes. In the aspect distribution histogram of the study area and the isolated permafrost areas in study area (Fig. 15), at the 0–2° interval, the permafrost distribution is significantly greater than the distribution proportion of the study area. In the 2–4° interval, the permafrost distribution ratio is slightly larger than the rest of the study area, which is consistent with the characteristic that permafrost are always located in low-lying areas and at the toe of slopes.

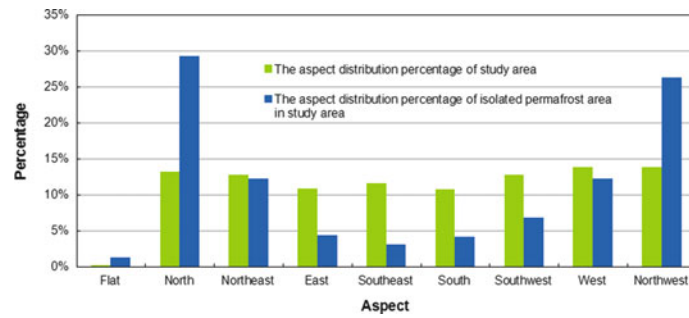


Fig. 15 An aspect distribution histogram of the study area and isolated permafrost areas in the study area

The data analysis results show that the permafrost distribution presents clear permafrost features indicative of the “Khangai–Baikal type.” Our study confirms the reliability of permafrost distribution maps.

Conclusions

Using LANDSAT ETM+ remote sensing data sources, we were able to apply thermal infrared remote sensing methods for surface temperature inversion. By overlaying the results onto Google Earth imagery and performing further calculations using ArcGIS we combined RS and GIS technology, allowing us to obtain preliminary permafrost distributions in our study area. Our distribution map is in agreement with geophysical survey results, and show clear “Khangai–Baikal type” permafrost features. Ground temperature inversion was conducted using Landsat ETM+ regional remote sensing images and through studies of the regional permafrost distribution. These results have great significance for studies into permafrost degradation and may provide an early warning for geological disasters induced by permafrost degradation. In the future, we will work on the refinement and further analysis of permafrost distribution maps.

References

- Building Sciences Institute of National Construction Committee (1974) Industrial and civil building foundation design specifications TJ7-74. China Building Industry Press, Beijing, China, 102 p
- Ding DW, Xu BZ (1978) The permafrost plane division indicators and signs. Chinese geographical society glaciology conference selection papers. Science Press, Beijing, China. <http://datamirror.csdb.cn/landsat/files/l7slcon.jsp>
- He RX, Jin HJ et al (2009) Permafrost degradation and the Cause in northern part of Northeast China. *Glaciol Cryopedol* 31(5):829–834
- Lanzhou Institute of Glaciology, Geocryology and Desert (1975) Permafrost. Science Press, Beijing, China, 124 p
- Shan W, Jiang H et al (2013) Occurrence mechanism and movement characteristics of landslides in Bei’an to Heihe expressway area in China under the climate change. In: *Landslide in cold regions in the context of climate change*. Springer, Germany, pp 23–37
- Xu XZ, Guo DX (1982) 1:4000,000 China permafrost distribution map. *Glaciol Cryopedol* 4:18–25
- Zhang Y, Cai SQ (1984) Qinghai-Tibet Plateau permafrost distribution characteristics and comparison with the permafrost in high-latitude regions. *Qinghai-Tibet Plateau geological proceedings*
- Zhou YW, Cui ZJ (1980) Permafrost and periglacial geomorphology. *China Natural Geography (landscape chapter) Chapter IX*. Science Press, Beijing, China
- Zhou YW, Guo DX (1982) The main features of permafrost in China. *Glaciol Cryopedol* 4(1):1–19



Transglacial Hazards: Karakoram and NW Himalaya, Inner Asia

Kenneth Hewitt

Abstract

In high mountain environments glacial and landslide hazards can be causally interdependent. They help prepare, trigger, transform or constrain each other, and related geohazards. Interactions between massive rock slope failures (MRSFs) and glaciers are examined, with examples from the Greater Karakoram Himalaya region. The MRSFs of interest generate rock avalanches. Rock avalanches and glacial processes affect each other in several ways, may include off-ice as well as on-ice landslide effects and are identified as transglacial hazards. Verticality is a key concern as gravity driven processes in high relief areas pass through different clima-geomorphic regimes with effects on the nature and severity of the landslides and secondary hazards associated with them. Since 1985 fourteen such MRSFs have been reported in the region. The recent record, if at all representative, suggests as many as 50 MRSFs per century in these glacier basins, and 5,000 in the Holocene. Climate change may affect recent events through rock wall debuttressing where glaciers retreat, or from degrading permafrost. However, MRSFs are especially identified with earthquakes. Geomorphic evidence suggests concentrated landslide episodes from large earthquakes, and the region may be subject to rare mega-quakes. Of the many more prehistoric rock avalanches identified from deposits in ice-free areas, more than 30 descended out of glacier basins. Short case histories illustrate the different styles of event and hazard potential. They include some mass flow events with longest run outs and greatest catastrophic potential. Risk profiles are complicated and compounded by landslide and glacier impoundments, glacier advances including surges, and outburst floods. Landslide-driven thickening, advances and deposits out-of-phase with climate complicate the glacial record. Rapidly growing mountain populations and towns, resource activity and infrastructure projects, increase exposure to the risks involved.

Keywords

Cryosphere hazards • Rock avalanches • Transglacial processes • Risk assessment

Introduction

The largest concentration of perennial snow and glaciers in the Indus basin and, indeed, all of High Asia, is in the Karakoram Himalaya, about 20,500 km². The nearby Hindu Raj, Hindu

Kush east slopes, Nanga Parbat and Zaskar Himalaya comprise a further 4,500 km² in the transHimalayan Upper Indus Basin (Hewitt 2013). The size and reach of the largest glaciers are directly proportional to the elevation and extent of each range at high altitude. Most of the largest valley glaciers outside high latitudes are found in the main or Mustagh (=“ice mountains”) Karakoram. While termini descend as low as 2,300 m elevation, most glaciers and all the larger ones originate in the highest mountains. Many have elevation ranges exceeding 3,000 m and some over 5,000 m. In the lower parts of the

K. Hewitt (✉)
Cold Regions Research Centre, Wilfrid Laurier University, Waterloo,
Canada N2L 3C5
e-mail: khewitt@wlu.ca

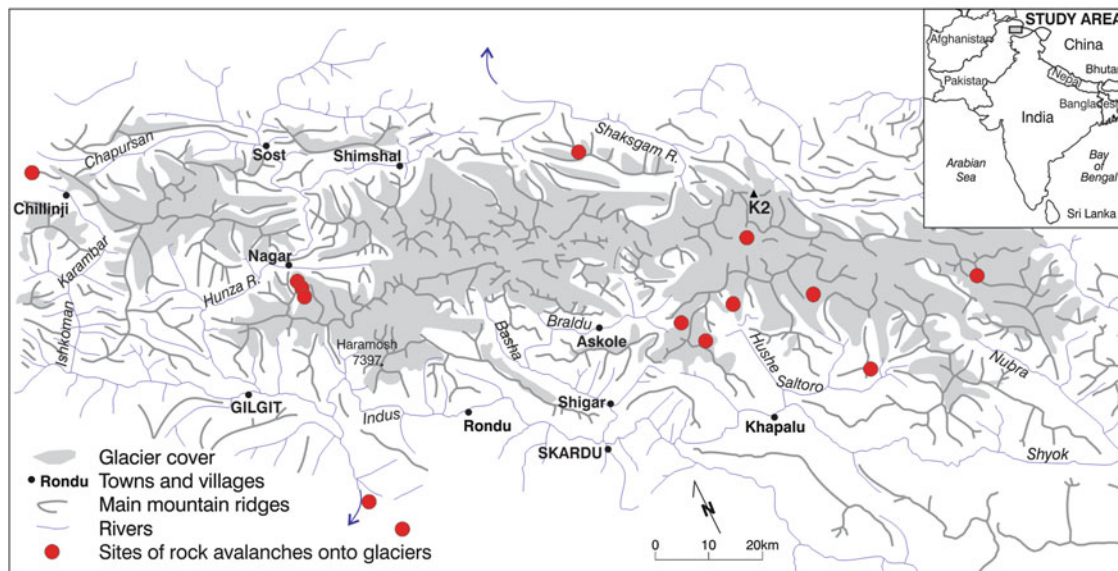


Fig. 1 Reported occurrence of rock avalanches onto glaciers, 1980s to the present

glacial zone, below 5,500 m or so, and above about 3,500 m, are thousands of rock glaciers. Permafrost and periglacial processes prevail in seasonally snow free off-ice areas in glacier basins, and over a much greater surrounding region.

The dominant landforms in the glacial zone and most glacier basins are steep rock walls. A survey of the largest Karakoram glaciers, about 2/3rds of its total glacierized area, shows that over 65 % of their basins consists of steep rock walls; more than 70 % of their frigid upper source areas (ibid, p.73). These exposed rock slopes mostly exceed 45°, rock wall surfaces amounting to more than twice their plan areas. It does mean the perennial snow zone and glaciers are constantly affected by slope processes driven by extreme gravitational forces, and interact with them. Most snow descends to the glaciers in snow avalanches. Along with rock falls from exposed slopes, these are pervasive, all-year processes.

Recently, evidence has grown of massive rock slope failures (MRSFs) in or affecting glacier basins, a set of rarer but catastrophic geohazards. The landslides of interest are of large size and high mobility; bedrock failures or collapse involve more than one million m³. Where they occur on steep, high rock walls there is rapid descent with intensive crushing and pulverising of the rock mass. It gives rise to long and high speed run out of debris, velocities typically exceeding 100 km/h; the rock avalanche. Recent reports show rock avalanches descend on glaciers at least once in 2 years across the Greater Karakoram region (Fig. 1). If at all representative, it suggests as many as 5,000 in the Holocene. If, as seems likely, major concentrations of events occur during and after large earthquakes, there would be many more.

These processes pose direct and indirect dangers for society. Their relatively rare occurrence and the very limited exposure of humans on the glaciers themselves reduce the threat. However, great risks, and the most lethal calamities,

Table 1 Classes of MRSFs affecting glaciers, and numbers (Italics) identified in the upper Indus Basin

I Entirely glacial zone rock avalanche (RA) events:	
I a. Rock wall failure, movement and emplacement within one glacier basin	8
1b. RA from a tributary, (partly) emplaced on a main glacier	4
II RAs that originate in glacier basins and travel onto ice free valley floors:	
II a. wholly emplaced in the valley of the source glacier	1
II b. originate in tributary glacier basin, emplaced in ice-free main valley	9
IIc. RAs transformed by incorporated snow, ice, water and sediments	4
III RAs from ice free valley walls that travel over active glacier tongue	8
IV RAs in ice free areas affect glaciers up-valley	96

arise where the landslides travel beyond the glacier into areas with human settlements, activities and infrastructure.

The type of landslide involved has been discussed in detail elsewhere (Hewitt 1998; Hewitt et al. 2008). The scale and reach of the landslides reflect a special role of glacial conditions in mass movement (Evans and Clague 1988). A range of indirect or secondary hazards also arise, including thickening and sudden advance of the glacier, impounding of melt water and outburst floods, and during the subsequent erosion history of landslide-, and glacier-disturbed valleys. Rather than just landslides or glacial hazards alone, risks arise from the interactions or overlaps between glaciers and other earth surface processes (Hewitt 2009). This identifies a set of transglacial conditions and hazards—glacial developments arising from, and partly dependent on, non-glacial processes and vice versa (Iturrizaga 2006). Four main classes of event can be recognised in terms of landslide-glacier interactions (Table 1). Eleven of those in recent

Table 2 Historical reports of RAs on glaciers and types involved

Glacier	River basin (Lat; Long.)	Date	Type
Bualtar Gl.	Hispar (36 08; 74 44)	1890 s	Ia
Kondus Gl.	Saltoro (35 28; 76 39)	1980s(?)	Ia
Bualtar Gl.	Hispar (36 08; 74 44)	1986	Ia (3 RAs)
Masherbrum Gl.	Hushe (35.33; 76.19)	1988 (?)	Ia
Lokpar- Aling Gl.	Hushe (35 29; 76 14)	1990 (?)	Ib
Chillinji Gl.	Karambar (36.46; 74.02)	1991	Ia
Chhelish	Das Bar (36.35; 76.16)	2000s(?)	Ib
Buldar Gl. Nanga P.	Buldar-Indus (35.24; 74.4)	2002	Iib
North Te-Rong Gl.	Nubra (35.20; 77.18)	2002	Ib
Chhichi Gl. NP	Astor (35.04; 74.34)	2005	Ia
Khai-Khai Gl. Baltoro	Braldu (35.47; 76.29)	2008	Ia
E.Ching Khang Gl	Braldu (35.34; 76.07)	2008 (?)	Ia
Gayari, unnamed	Saltoro (35.09; 76.57)	2012	Iib

decades were Type I, and just two, Type II (see Table 2). The latter, lethal events at Buldar, 2002 and Gayari, 2012, had relatively local impact but are indicative of the risks from a recurrence of much larger prehistoric events. The Attabad 2010 event has some elements of a Type IV event. The lake stretched back to the terminus of Ghulkin Glacier and continues to affect sediment delivery conditions in the Hunza system. It will help to understand the developments and risks involved by first describing selected examples.

Case Histories

Chillinji Glacier, Type Ia

First observed in June 1992 a rock avalanche had been emplaced mid-glacier, possibly in late 1991 or early 1992. The debris covered almost 2 km². Vertical sections through the openwork cover of boulders indicated a deposit thickness between 3 and 5 m. By 2009 the debris front had been carried 3 km down the glacier, roughly 176 m per year. Although shedding material down ice slopes at the margins, the main rock-avalanche deposit remained intact and largely unmodified (Figs. 2 and 3). It is raised 10–20 m on a

platform of ice protected from ablation, which had reached a steady state position by 1994. Presumably ice flow from beneath compensates for continuing absent or low ablation. A zone of accelerated and thickened ice over-riding the margins was observed in 1994, 1 km in front of the landslide debris which presumably travelled ahead of the landslide to reach the tongue first. However, to 2004 Chillinji terminus showed no change in position or character. Then, in 2005, there was a sudden advance of about a kilometre. The landslide debris was 2.5 km above the location of the former, stable terminus, and 3.1 km from the extended one. The terminal lobe spread across the Karambar River, but it has maintained a channel under the ice. Chillinji dammed the river in the past and may do so again as landslide-thickened ice reaches the terminus (Hewitt 1998; Hewitt and Liu 2010). Locally, the route to Karambar Pass, a bridge, and settlement for migrants were damaged.

Chillinji illustrates how the usual picture of glacial fluctuations and sedimentation regulated by climate are altered. For the past 23 years, and for some decades into the future, the landslide influences glacier dynamics, mass balance, ice margin conditions and sedimentation. Its debris alters rates and patterns of glacier ablation, surface elevation, and movement geometry. The patterns, pace and composition of sediment delivery change as landslide material is dispersed and modified by glacial activity. For the half-century or more required to fully disperse the landslide materials, they strongly buffer glacier conditions against climate. In this case, despite evidence of climatic warming there has been thickening not thinning, advance not retreat, a more vigorous tongue with increased sediment transport and release, not less. When most glaciers in the western Karakoram and Hindu Raj were retreating or stable, there was positive mass balance and advance with attendant secondary hazards (Hewitt 2005; Gardelle et al. 2012).

Lokpar-Aling Type Ib

In 1992 a sudden advance of the Aling Glacier was reported. An outburst flood destroyed a summer pasture village just below the glacier, damaged bridges, and eroded cropland down Hushe valley. Inspection showed the surge had been of Aling's steep, right bank tributary, the Lokpar. Moreover, large parts of the Lokpar tongue and lower ablation zone were blanketed in rock avalanche debris (Figs. 4 and 5). A huge, high bulb of Lokpar ice dammed the main glacier, where the surge was stalled by a marked narrowing of the main valley. The steep, 200 m-high ice front advanced the terminus slowly to 2011. The lower Aling remained a sluggish ice stream buried in supraglacial moraine and partly vegetated. The outburst flood came from breaching of an ice margin lake at the intersection of Lokpar and Aling. Local

Fig. 2 Chillinji Glacier basin, on-ice rock avalanche and surrounding features in 2009

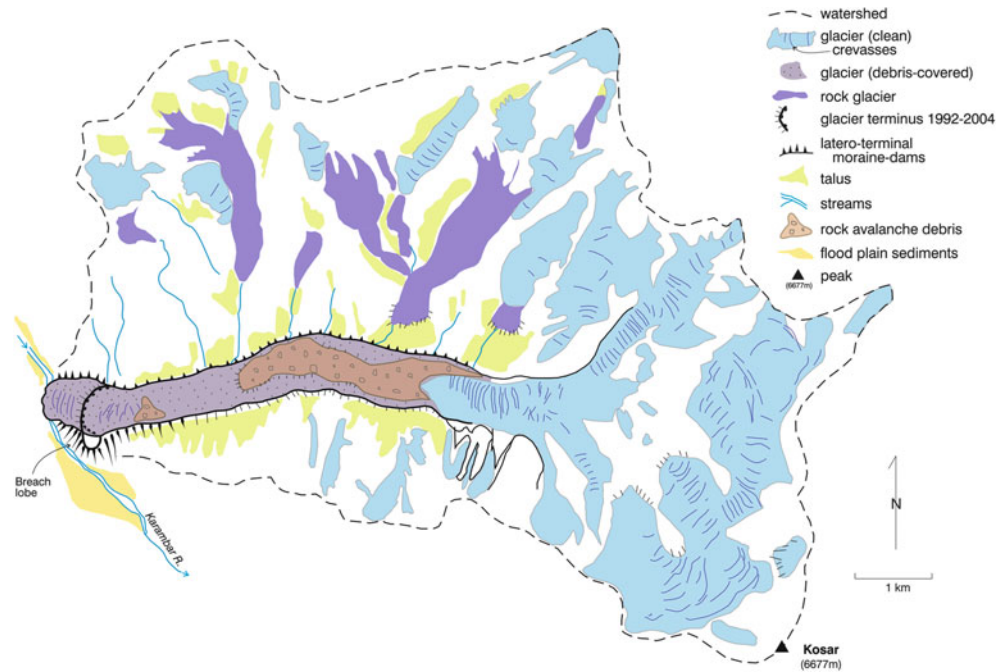
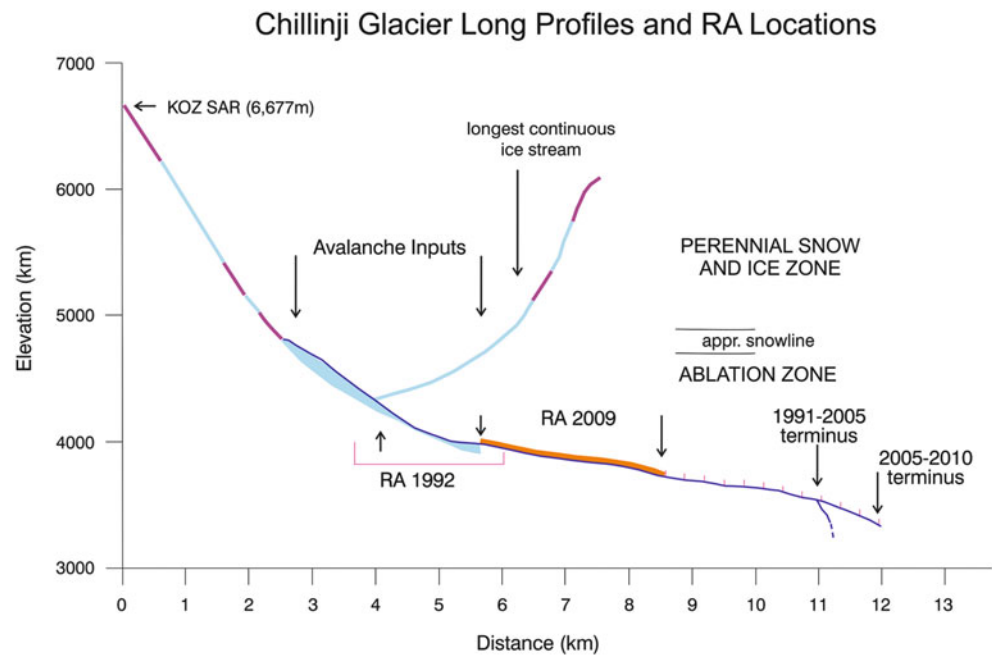


Fig. 3 Vertical profile of Chillinji Glacier and on-ice rock avalanche deposits in 1992 and 2009



guides said the lake had existed for some generations, at least. It is not known exactly when the rock avalanche occurred, or how soon after the glacier surged but the two seem closely related. Possibly, the rock avalanche helped trigger or preempt the surge cycle as at Bualtar in 1987 (Gardner and Hewitt 1990), or was triggered by it. Certainly, its debris protects the lower glacier from ablation and is partly responsible for two decades of advance. Once more, this is contrary to most glaciers in the Hushe Basin, notably the Aling, although some others advanced again after 1995 (Hewitt 2005). The

GLOF triggered from a lake that had been stable for a century or more further complicates the risk profile.

Buldar, Type IIa (Lat. 35.24; Long. 74.4)

During the 2002, Astor valley earthquake, a MRSF and rock avalanche descended from a steep, left bank tributary of Buldar Glacier, northwest of Nanga Parbat (8,125 m) summit. It spread over ice and moraines left by post-Little Ice

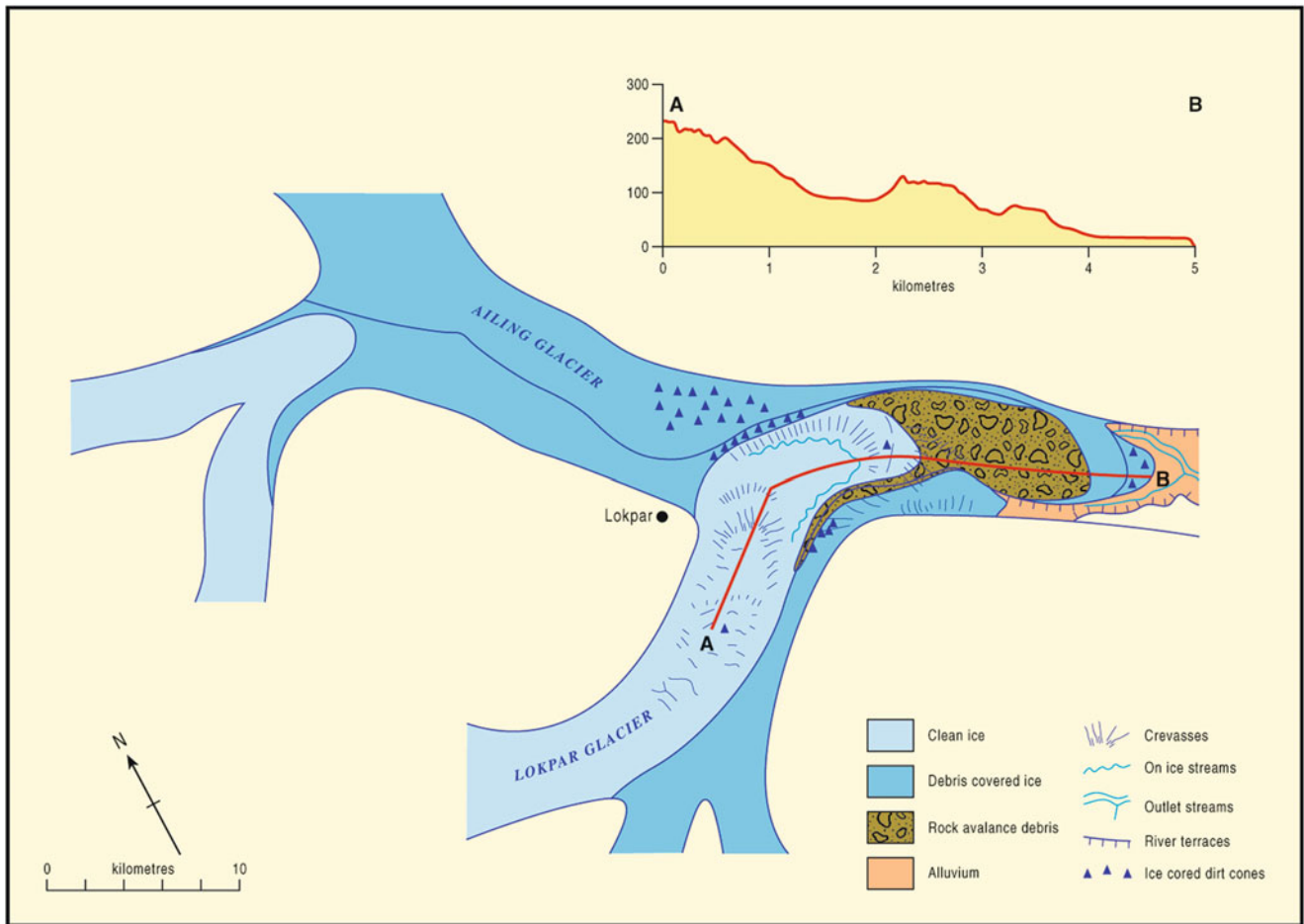


Fig. 4 Map of the Lokpar-Aling RA and surge, summer 1994. Since then the terminus has advanced another 2 km and the high-stand ice subsided



Fig. 5 View of Lokpar-Aling terminus, 1994 after the surge. On-ice grey rubble is part of rock avalanche

Age retreat. It continued 1–2 km over pro-glacial areas including pastures and an occupied summer village. Some 30 villagers were killed, the worst concentration in the earthquake. By 2006 a lake 1 km long, and a series of other smaller lakes, lay below Buldar Glacier terminus

impounded by the ridges and mounds of the landslide. Detachment zone elevation and conditions suggest the slope had been weakened by degrading of permafrost. It appeared frozen before the event, but melt water streams were in the detachment zone afterwards. It illustrates the added dangers when these landslides travel beyond the glaciers into inhabited areas. Fortunately, it was not large enough to reach more populated areas and Karakoram Highway where the valley joins the main Indus. It is indicative of the threat from larger prehistoric cases.

Moni-Iskere Glacier-Sassi, Prehistoric Event, Haramosh; Type IIc (Lat. 35.51 N; Long. 74.44E)

The Indus crosses the Raikot-Sassi fault, bounding the NW-Himalayan syntaxis at Sassi village (Khan et al. 2000). There are remnants of several rock avalanches around the Sassi-Indus junction. Conspicuous lighter coloured deposits record a huge mass flow, tracable up the Phuparash River to Iskere, and to Moni Glacier on Haramosh Peak (7,397 m). The most likely explanation is a MRSF on the mountain flanks,



Fig. 6 View eastwards up the Indus River to the eroded Sassi mass flow deposit (middle ground). The Indus flows in channels superimposed on bedrock from the Sassi and other landslides (Hewitt 1998)

possibly including large volumes of ice, that travelled over the Moni where more snow and ice were entrained to generate a debris avalanche or mass flow of exceptional mobility, run out exceeding 25 km. It is likely the mass flow continued beyond the junction up and down the Indus. Large amounts of debris between 100 and 200 m thick, and as much as a kilometre wide, remain along the lower Phuparash and at the Indus junction. Reconstruction is difficult due to post-emplacment erosion, and burial of material by other landslides, but total mass probably exceeded 1.5 km³. The Indus and upper Phuparash were dammed. Subsequently, the Indus cut through the barrier and flows in epigenetic rock gorges (Fig. 6). There are no age determinations but this is certainly a Holocene event, probably from the latter half.

This is one of several cases where MRSF and a rock avalanche travelled over a glacier to become a complex mass flows with exceptional run-out (Hewitt et al. 2008). It may be compared, in varying degrees, to the Huascaran 1970 landslide that destroyed the town of Yungay, Peru, the 2002 Kolka-Karmadon event in Caucasus Mountains, North Ossetia (Huggel et al. 2005), and the prehistoric Horcones event on Mt. Aconcagua, Argentina (Fauqué et al. 2009). The Sassi-Iskere event needs more attention, as does evidence of comparable events in the Chitral Hindu Raj around the junction of the Booni and the Miragram with Yarkhun valley, and in Chumarkhan Gol.

Risk Conditions and Geohazards

Rock avalanche mobility is modified by travel over glaciers. Smooth ice surfaces or incorporation of snow, ice, melt water or wet sediment from the glacier, can reduce friction

and amplify the reach of long run out events (Evans and Clague 1988; Dutto and Mortara 1991). In this environment, the behaviour of the landslide, the debris it emplaces and response of the glacier create a series of secondary hazards. When rock avalanche debris blankets the ice it disturbs ice dynamics and mass balance. Ice thickening and accelerated movement may lead to over-riding of ice-free margins and advance of the terminus. Glacier activity leads to rapid modification, transport and dispersal of landslide debris. MRSFs and long-runout landslides can be involved in other catastrophic, cryosphere risks such as large GLOFs (Hewitt and Liu 2010), large debris flows (Santi et al 2010), and exceptional ice advances, notably of surge-type glaciers as indicated at Bualtar and Lokpar-Aling (Hewitt 2013, Chap. 9). Developments can be out of phase with climatic conditions and glacier behaviour in the rest of the mountain region, or exaggerate them in the glaciers affected.

Type III and IV interactions introduce further transglacial hazards. The former are only known at sites of prehistoric landslides, but involved large, long-lived lakes impounded at glacier termini. The vast lake sediments indicative of an impoundment above Malagutti Glacier in Shimshal, for example, was actually sealed by a rock avalanche from the wall opposite the terminus. Similar developments applied with Batura Glacier dams evidenced by lake sediments in the Bilgim Platt section of the Hunza River (Hewitt 2006). Examples of Type IV include the on-going impact of Attabad landslide on sedimentation around the terminus of the upstream Ghulkin Glacier, and the hazards of frequent dust and sand storms from glacial sediment exposed in flats as lake level is reduced. In fact, behaviour and sedimentation of ice tongues in almost every headwater stream of the Gilgit, Hunza and Indus in the Karakoram, Hindu Raj and Nanga Parbat, are affected by existing or former cross-valley rock avalanche barriers up-, and downstream, and by on-going base level control.

Risk assessments depend on landslide frequency and how far past incidence is a guide to the future. In the past 25 years, 14 rock avalanches are known that travelled on glacier surfaces (Table 2; Fig. 1). If at all representative, this would indicate more than 5,000 in the Holocene or the equivalent of 4.3 per km² of the existing glacierized terrain. It has been suggested recent events reflect global climate change, an important consideration. However, it is also likely most past and some recent events have been missed. When triggered by earthquakes or severe weather the chances of direct observation are small. As well as rugged terrain and difficult access, rapid burial of landslide debris by snow, reduce the chances they will be found. In the longer term, dispersal by ice movement and ablation intervene to erase the record (McSaveney 2002, p. 68). Large earthquakes are likely to trigger more events. In the region, a potential of rare mega-earthquakes has been proposed (Feldl and Bilham 2006;

Hewitt et al. 2011). Their absence in recent centuries may mean long-term incidence or worst-case scenarios are underestimated. The need for a concerted effort to fully identify on-going risks seems urgent, especially for proposed infrastructure, including large dams, transport corridors, and tourist destinations.

References

- Dutto F, Mortara G (1991) Grandi frane storiche con percorso su ghiacciaio in Valle d'Aosta. *Revue Valdôtaine d'Histoire Naturelle* 45:21–35
- Evans SG, Clague JJ (1988) Catastrophic rock avalanches in glacial environments. In: Bonnard C (ed) *Proceedings of the 5th International Symposium on Landslides*, 2. Balkema, Rotterdam, pp 1153–1158
- Fauqué L, Hermanns R, Hewitt K, Rosas M, Wilson C, Baumann V, Lagorio S, Di Tommaso I (2009) Mega-deslizamientos de la pared sur del Cerro Aconcagua y su relación con depósitos asignados a la glaciación pleistocena. *Revista de la Asociación Geológica Argentina* 65(4):691–712
- Feldl N, Bilham R (2006) Great Himalayan earthquakes and the Tibetan Plateau. *Nature* 444:165–170
- Gardelle J, Berthier E, Arnaud Y (2012) Slight mass gain of Karakoram glaciers in the early twenty-first century. *Nat Geosci* 5:322–325. doi:10.1038/NGEO1450
- Gardner JS, Hewitt K (1990) A surge of Bualtar Glacier, Karakoram Range, Pakistan - a possible landslide trigger. *J Glaciol* 36:159–162
- Hewitt K (1998) Himalayan Indus streams in the Holocene: Glacier- and Landslide-‘Interrupted’ fluvial systems. In: Stellrecht I (ed) *Karakoram-Hindu Kush-Himalaya: dynamics of change part I*. Rudiger Koppe, Koln, pp 1–28
- Hewitt K (2005) The Karakoram Anomaly? Glacier expansion and the ‘elevation effect’, Karakoram Himalaya, Inner Asia. *Mt Res Dev* 25:332–348
- Hewitt K (2006) Glaciers of the Hunza Basin and related features, chapter 5. In: Kreutzmann H (ed) *Karakoram in transition: culture, development and ecology in the Hunza Valley*. Oxford University Press, Oxford, pp 49–72
- Hewitt K (2009) Rock avalanches that travel onto glaciers: disturbance regime landscapes, Karakoram Himalaya, Inner Asia. *Geomorphology* 103:66–79
- Hewitt K (2013) Glaciers of the Karakoram Himalaya: glacial environments, processes, hazards and resources, Springer Earth Sciences and Advances in Asian Human-Environmental research. Springer Science Media, Heidelberg
- Hewitt K, Liu J (2010) Ice-dammed lakes and outburst floods, Karakoram Himalaya: historical perspectives and emerging threats. *Phys Geogr* 31(6):528–551
- Hewitt K, Clague JJ, Orwin J (2008) Legacies of catastrophic rock slope failures in mountain landscapes. *Earth Sci Rev* 87:1–38
- Hewitt K, Clague JJ, Gosse J (2011) Rock avalanches and the pace of late Quaternary development of river valleys in the Karakoram Himalaya. *Geol Soc Am Bull* 123(9–10):1836–1850
- Huggel C, Zraggen-Oswald S, Haeblerli W, Käab A, Polkvoj A, Galushkin I, Evans SG (2005) The 2002 rock/ice avalanche at Kolka/Karmadon, Russian Caucasus: assessment of extraordinary avalanche formation and mobility, and application of QuickBird satellite imagery. *Nat Hazard Earth Syst Sci* 5:173–187
- Iturrizaga L (2006) Transglacial landforms in the Karakoram (Pakistan): a case study from Shimshal Valley. In: Kreutzmann H (ed) *Karakoram in transition: culture, development and ecology in the Hunza Valley*. Oxford University Press, Karachi, pp 96–108
- Khan MA, Treloar PT, Searle MP, Jan MQ (Eds.) (2000) *Tectonics of the NangaParbat Syntaxis and Western Himalaya*. Geological Society, UK, Special Publication, #170
- McSaveney M (2002) Recent rock falls and rock avalanches in Mount Cook National Park, New Zealand. In: Evans SG, DeGraff JV (eds) *Catastrophic landslides: effects, occurrence, and mechanisms*, vol 15, *Rev Eng Geol.*, pp 35–70
- Santi PM, Hewitt K, VanDine DF, Barillas Cruz E (2010) Debris-flow impact, vulnerability, and response. *Nat Hazard* 56(1):371–402

Landslides in Coastal and Submarine Environments



Introduction: Landslides in Coastal and Submarine Environments

Michael Strasser, Yonggang Jia, Yasuhiro Yamada, and Roger Urgeles

Abstract

Lack of direct observations and restricted access limits our current knowledge about submarine and coastal landslides. Open research questions remain regarding landslide recurrence rates, trigger mechanisms, failure dynamics, their impact on coastal and seafloor infrastructure and their role in causing subsequent effects such as tsunamis. The session C8 of the 3rd World Landslide Forum addresses causes and consequences of hazardous mass movements in coastal and marine areas. The session highlights the role of innovative marine-geophysical, -geological, and -geotechnical surveys and site-investigation techniques in coastal and subaquatic landslide research, hazard assessment and mitigation. This introductory paper to the C8 section of the WLF3 volume provides a brief overview on the general topic and presents the compendium of seven papers contributed by landslide experts from different parts of the world to document detailed case studies on coastal and submarine landslides as well as landslide tsunamis.

Keywords

Coastal landslides • Submarine mass movements • Landslide tsunami

Introduction

The morphology of coastal cliffs and submarine continental slopes around the world, as well as the flanks of oceanic islands are marked with major landslide scars. Many of the submarine landslides involve large portions of sea floor, sometimes thousands of square kilometers, and their formation represents an important mechanism for transferring

sediments into the deep sea (e.g. Masson et al. 2006; Lee et al. 2007; Yamada et al. 2012; Talling et al. 2013; Urgeles and Camerlenghi 2013). Sand-rich gravity flow deposits form some of the World's largest petroleum and gas reservoirs, while mud-rich deposits are hypothesized to sequester globally significant volumes of organic carbon (e.g. Galy et al. 2007; Ogiesoba and Hammes 2012; Beaubouef and Abreu 2010). The geohazards associated with coastal and submarine slope failures include destruction of coastal and sub-sea infrastructure such as pipelines and cables and the generation of tsunamis, (Yamada et al. 2012; Urgeles and Camerlenghi 2013). Most landslides that cause tsunamis result in more local effects than comparable earthquake-induced tsunamis due to different source characteristics (e.g. Satake 2012). Volcanic flank collapses may also cause tsunamis inducing distant destruction (Ward and Day 2001), although their tsunamigenic potential is highly disputed (e.g., Hunt et al. 2011).

Given that 30 % of the World's population lives within 60 km of the coast, the hazard posed by coastal and

M. Strasser (✉)
ETH Zurich, Geological Institute, Sonneggstrasse 5, 8092 Zürich,
Switzerland
e-mail: michael.strasser@erdw.ethz.ch

Y. Jia
Ocean University of China, Qingdao 266100, China

Y. Yamada
Department of Civil and Earth Resources Engineering, Kyoto
University, Kyoto 615-8540, Japan

R. Urgeles
Institut de Ciències del Mar (CSIC), 08003 Barcelona, Spain

submarine landslide is expected to grow as global sea level rises (Yamada et al. 2012). Furthermore, the demand for growth of residential, commercial and infrastructure development along the coast and offshore has increased in recent years necessitating a better knowledge of coastal and submarine mass movements and their consequence for reliable hazard assessment and mitigation measures.

The causes of submarine mass movements are manifold but not yet well understood. Surprisingly many of the larger landslides are associated with much gentler slopes than required to destabilize the sea floor under static conditions (e.g. Masson et al. 2006; Lee et al. 2007). Slope failure is often attributed to some combination of earthquake triggering, rapid sedimentation, the presence of mechanically weak layers, excess pore pressures, steeping from tectonic, diapiric or erosional activity, and volcano development (e.g. Sultan et al. 2004; Lee et al. 2007; Urgeles and Camerlenghi 2013), but only for very few slope failures a robust scientific case has been made.

Although wave action is the obvious mechanism for coastal erosion and subsequent onset for landslide activity, there are many geological and climatic factors (e.g. coastal rock and/or soil type and strength, land use cover, permeability, pore water pressure, rainfall etc.) that are considered key preconditioning factors for coastal landslides (e.g. Budetta et al. 2000; Thornton and Stephenson 2006; Lim et al. 2011). Assessing the relative contribution of these factors in controlling coastal cliff stability is essential to understand the fundamental processes of coastal landslide initiation and to gain a firm understanding towards providing measures to mitigate against coastal landslide hazard.

The complex nature of coastal and submarine mass movements and their consequences calls for a multidisciplinary approach including state of the art coastal, seafloor and sub-seafloor mapping, investigations of physical properties, modeling of landslides and associated tsunamis as well as risk assessment. This section C8 of the 3rd World Landslide Forum (WLF3) volume compiles a good selection of contributions documenting detailed case studies that use various investigation and analysis techniques to provide new insights into the processes and factors that govern coastal and submarine mass movements and their consequences such as landslide tsunamis.

Contributions to Research on Coastal Landslides and Volcanic Island Flank Collapses

Two papers by Benac et al. (2014) and Kaya and Topal (2014) investigate landslides along the Mediterranean Sea coast of Croatia and Turkey, respectively. These studies document the role of different bedrock types and strength vs. hydrology and coastal wave action on the mode of

landslides in areas highly relevant for tourism. Kaya and Topal (2014) perform engineering geological studies including laboratory experiments and limit equilibrium slope stability analysis to identify potential hazards from sliding and rockfalls in a coastal area near Kusadasi, Turkey, and propose nature-friendly solutions in order to prevent or minimize the hazards. The identification of potential hazards from marine erosion and slope movements along the SE coast of the Krk Island, Croatia, by Benac et al. (2014) is further complemented by numerical wave models and subsequent analysis of the impact of prevailing coastal processes on hazard exposure in future raising sea level scenarios.

A massive flank collapse involving an estimated volume of $\sim 30 \text{ km}^3$ on Ta'u Island, Samoan Archipelago, is investigated by Williams et al. (2014). By applying exposure dating on the remnant landslide scarp using the cosmogenic nuclide ^{36}Cl , the flank-collapse is dated to $22.4 \pm 1.8 \text{ ka}$. While this event occurred before the Samoan and surrounding Island Nations were inhabited, the authors discuss the need to identify and date other such volcanic island flank collapses throughout the Pacific in order to further improve our spatial and geochronological understanding of such events and to assessing with more confidence the hazard potential of similar flank-collapses in the future.

Contributions to Submarine Landslide Research

Two papers contributed to WLF3 session C8 present reflection seismic and sedimentary core data to document submarine landslides emplaced in $>1,000 \text{ m}$ water depth in the Qiongdongnan Basin, South China Sea (Wang et al. 2014) and in the Ligurian Sea of the Northwestern Mediterranean (Ai et al. 2014). Wang et al. (2014) use high resolution 3D seismic data to characterize the internal structure and kinematic indicators of three submarine mass-transport deposits (MTDs) emplaced since about 0.78–1.8 Ma. The data reveals mass-transport direction from the shelf edge/upper slope system offshore central Vietnam to the deep Qiongdongnan Basin. Timing and source of MTDs suggest a causal link between Quaternary high sedimentation rate to the shelf/upper slope in the Western South China Sea influenced by the eccentricity scale sea-level change and the emplacement of MTDs.

Ai et al. (2014) present geophysical, sedimentological and geotechnical results of two submarine landslides that occurred along the tectonic and seismically active Ligurian margin. Results from laboratory geotechnical experiments on samples retrieved from the headscars of the landslides constrain input parameters for infinite slope

limit equilibrium stability analyses under both static and earthquake seismic loading conditions. Results reveal stable slopes under static conditions and allow the author to estimate critical earthquake intensities needed to initiate slope failure, which would be equivalent to a nearby Magnitude 5–5.3 earthquake.

Contributions to Landslide Tsunami Research

Towards reliable assessment of tsunami hazard from submarine landslides, numerical simulation techniques need to integrate calculations of the landslide dynamics, of the resulting tsunamigenic impulse and of tsunami propagation. Several tsunami research groups worldwide have developed codes for such numerical simulations (see review by Heidarzadeh et al. 2014). In this section of the WLF3 proceedings two studies are presented that use the codes developed by the University of Bologna Tsunami Research Team to (1) test the hypothesis that a submarine landslide triggered the historically documented tsunami of 1977 in the harbour of Gioia Tauro, Italy (Zaniboni et al. 2014) and (2) to evaluate the potential tsunami hazard from submarine landslides offshore southern Calabria, Italy, where a prehistoric submarine landslide has been identified on new multibeam bathymetry data (Ceramicola et al. 2014).

The results obtained by Zaniboni et al. (2014) fit well with the observations of tsunami height and inundation in the harbour, as well as with reported cable breaks offshore, thus strengthening the hypothesis of such landslide as the source for the 1977 tsunami. The authors further discuss this event to be considered as paradigmatic of a category of coastal hazards: small submarine landslides occurring close to populated coasts may pose considerable risk, even if only at a local scale.

Ceramicola et al. (2014) present a reconstruction of the geometry and dynamics of one of the largest seabed features, the Assi failure, on the relatively steep submarine slope off southern Calabria, and use it as input to numerical landslide tsunami modeling. The results indicate that within 8 min waves just over 1 m in height affect the southern Calabrian coast where their capacity to cause damage could be amplified in small harbours. This allows the authors to suggest that tsunamis represent a hazard for Ionian coastal areas, and call for accurate monitoring and further study.

Acknowledgments This session is co-sponsored by the International Geoscience Program “Earth’s continental Margins: Assessing the Geohazard from submarine Landslides” IGCP-585, funded by the International Union of Geological Science (IUGS) and the United Nations Educational, Scientific and Cultural Organization (UNESCO).

References

- Ai F, Förster A, Stegmann S, Kopf A (2014) Geotechnical characteristics and slope stability analysis on the deeper slope of the Ligurian margin, Southern France. In: Sassa K et al (eds) *Landslide science for a safer geoenvironment*, vol 3. Springer, Heidelberg
- Beaubouef RT, Abreu V (2010) MTCs of the Brazos-Trinity slope system; thoughts on the sequence stratigraphy of MTCs and their possible roles in shaping hydrocarbon traps. In: Mosher et al. (eds) *Submarine mass movements and their consequences*. *Adv Nat Technol Hazard Res* 28: 475–490
- Benac C, Dugonjić Jovančević S, Ružić I et al (2014) Marine erosion and slope movements: SE coast of the Krk Island. In: Sassa K et al (eds) *Landslide science for a safer geoenvironment*, vol 3. Springer, Heidelberg
- Budetta P, Galiotta G, Santo A (2000) A methodology for the study of the relation between coastal cliff erosion and the mechanical strength of soils and rock masses. *Eng Geol* 56(3–4):243–256
- Ceramicola S, Tinti S, Zaniboni F et al (2014) Reconstruction and tsunami modeling of a submarine landslide on the Ionian margin of Calabria (Mediterranean Sea). In: Sassa K et al (eds) *Landslide science for a safer geoenvironment*, vol 3. Springer, Heidelberg
- Galy V, France-Lanord C, Beyssac O, Faure P, Kudrass H, Palhol F (2007) Efficient organic carbon burial in the Bengal fan sustained by the Himalayan erosional system. *Nature* 450(7168):407–410
- Heidarzadeh M, Krastel S, Yalciner AC (2014) The state-of-the-art numerical tools for modeling landslide tsunamis: a short review. In: Krastel S et al (eds) *Submarine mass movements and their consequences*. *Adv Nat Technol Hazard Res* 37: 483–496
- Hunt JE, Wynn RB, Masson DG et al (2011) Sedimentological and geochemical evidence for multistage failure of volcanic island landslides: a case study from Icod landslide on north Tenerife, Canary Islands. *Geochem, Geophys, Geosyst* 12:12
- Kaya Y, Topal T (2014) Assessment of rock slope stability for a coastal area near Kusadasi, Aydin, Turkey. In: Sassa K et al (eds) *Landslide science for a safer geoenvironment*, vol 3. Springer, Heidelberg
- Lee HJ, Locat J, Desgagnés P, et al (2007) Submarine mass movements on continental margins. In: Nittrouer CA et al (eds) *Continental margin sedimentation: from sediment transport to sequence stratigraphy*. pp 213–273
- Lim M, Rosser NJ, Petley DN et al (2011) Quantifying the controls and influence of tide and wave impacts on coastal rock cliff erosion. *J Coast Res* 27(1):46–56
- Masson DG, Harbitz CB, Wynn RB et al (2006) Submarine landslides: processes, triggers and hazard prediction. *Philos Trans R Soc A: Mathematical, Physical and Engineering Sciences* 364(1845):2009–2039
- Ogiesoba O, Hammes U (2012) Seismic interpretation of mass-transport deposits within the upper Oligocene Frio formation, south Texas Gulf Coast. *Am Assoc Petrol Geol Bull* 96:845–868
- Satake K (2012) Tsunamis generated by submarine landslides. In: Yamada Y et al. (eds) *Submarine mass movements and their consequences*. *Adv Nat Technol Hazard Res* 31: 475–484
- Sultan N, Cochonat P, Canals M et al (2004) Triggering mechanisms of slope instability processes and sediment failures on continental margins: a geotechnical approach. *Mar Geol* 213(1–4):291–321
- Talling PJ, Paull CK, Piper DJW (2013) How are subaqueous sediment density flows triggered, what is their internal structure and how does it evolve? Direct observations from monitoring of active flows. *Earth-Sci Rev* 125:244–287
- Thornton LE, Stephenson WJ (2006) Rock strength: a control of shore platform elevation. *J Coast Res* 22(1):224–231

- Urgeles R, Camerlenghi A (2013) Submarine landslides of the Mediterranean Sea: trigger mechanisms, dynamics and frequency-magnitude distribution. *J Geophys Res Earth Surf* 118(4):2600–2618
- Wang D, Wu S, Yao G, Lü F, Strasser M (2014) Analysis of Quaternary mass transport deposits based on seismic data in southern deep-water region of Qiongdongnan Basin, South China Sea. In: Sassa K et al (eds) *Landslide Science for a safer geoenvironment*, vol 3. Springer, Heidelberg
- Ward SN, Day S (2001) Cumbre Vieja Volcano - potential collapse and tsunamis at La Palma, Canary Islands. *Geophys Res Lett* 28(17):3397–3400
- Williams S, Davies TR, Barrows TT et al (2014) Flank-collapse on Ta'u Island, Samoan Archipelago: timing and hazard implications. In: Sassa K et al (eds) *Landslide science for a safer geoenvironment*, vol 3. Springer, Heidelberg
- Yamada Y, Kawamura K, Ikehara K, et al (2012) Submarine mass movements and their consequences. 1-12
- Zaniboni F, Armigliato A, Elsen K et al (2014) The 1977 Gioia Tauro harbour (South Tyrrhenian Sea, Italy) landslide-tsunami: numerical simulation. In: Sassa K et al (eds) *Landslide science for a safer geoenvironment*, vol 3. Springer, Heidelberg



Geotechnical Characteristics and Slope Stability Analysis on the Deeper Slope of the Ligurian Margin, Southern France

Fei Ai, Annika Förster, Sylvia Stegmann, and Achim Kopf

Abstract

Submarine slope failures of various types and sizes are common along the tectonic and seismically active Ligurian margin, northwestern Mediterranean Sea, primarily because of seismicity up to $\sim M6$, rapid sediment deposition in the Var fluvial system, and steepness of the continental slope (average 11°). We present geophysical, sedimentological and geotechnical results of two distinct slides in water depth $>1,500$ m: one located on the flank of the Upper Var Valley called Western Slide (WS), another located at the base of continental slope called Eastern Slide (ES). WS is a superficial slide characterized by a slope angle of $\sim 4.6^\circ$ and shallow scar (~ 30 m) whereas ES is a deep-seated slide with a lower slope angle ($\sim 3^\circ$) and deep scar (~ 100 m). Both areas mainly comprise clayey silt with intermediate plasticity, low water content (30–75 %) and underconsolidation to strong overconsolidation. Upslope undeformed sediments have low undrained shear strength (0–20 kPa) increasing gradually with depth, whereas an abrupt increase in strength up to 200 kPa occurs at a depth of ~ 3.6 m in the headwall of WS and ~ 1.0 m in the headwall of ES. These boundaries are interpreted as earlier failure planes that have been covered by hemipelagite or talus from upslope after landslide emplacement.

Infinite slope stability analyses indicate both sites are stable under static conditions; however, slope failure may occur in undrained earthquake condition. Peak earthquake acceleration from 0.09 g on WS and 0.12 g on ES, i.e. $M5-5.3$ earthquakes on the spot, would be required to induce slope instability. Different failure styles include rapid sedimentation on steep canyon flanks with undercutting causing superficial slides in the west and an earthquake on the adjacent Marcel fault to trigger a deep-seated slide in the east.

F. Ai (✉)

MARUM-Center for Marine Environmental Sciences, University of Bremen, Leobener Straße, 28359 Bremen, Germany

Faculty of Geosciences, University of Bremen, Leobener Straße, 28359 Bremen, Germany

State Key Laboratory of Geomechanics and Geotechnical Engineering, Institute of Rock and Soil Mechanics, Chinese Academy of Sciences, 430071 Wuhan, China

e-mail: aifei@uni-bremen.de

A. Förster

Institute of Geosciences and Geography, Martin-Luther-University Halle-Wittenberg, von Seckendorff Platz 3, 06120 Halle (Saale), Germany

e-mail: annika.foerster@geo.uni-halle.de

S. Stegmann • A. Kopf

MARUM-Center for Marine Environmental Sciences, University of Bremen, Leobener Straße, 28359 Bremen, Germany

Faculty of Geosciences, University of Bremen, Leobener Straße, 28359 Bremen, Germany

e-mail: stegmann@uni-bremen.de; akopf@uni-bremen.de

K. Sassa et al. (eds.), *Landslide Science for a Safer Geoenvironment*, Vol. 3,

DOI 10.1007/978-3-319-04996-0_84, © Springer International Publishing Switzerland 2014

Keywords

Submarine slope failure • Geotechnical characteristics • Slope stability analysis • Ligurian margin

Introduction

Submarine slope failures represent the main agents of sediment transport from continental slope to deep ocean, and one of the most common geohazards impacting on both offshore infrastructures (e.g. pipeline, cables and platforms) and coastal areas (e.g. slope failure-induced tsunamis) (Locat and Lee 2002). Slope failures are generally controlled by long-term preconditioning factors (e.g. high sedimentation rate, weak layer and oversteepening) and short-term triggering mechanisms (e.g. earthquake, anthropogenic activity) (Sultan et al. 2004). However, the exact causes for the different slope failure styles are still poorly understood.

The Ligurian margin, northwestern Mediterranean Sea, is one of most intensely studied natural laboratories for landslide initiation in seismically active areas because of its steep topography with numerous landslide scars of different size. Previous slope stability analyses in the region mainly focused on the 1979 Nice Airport Slide or the upper slope of Ligurian margin (Cochonat et al. 1993; Mulder et al. 1994; Sultan et al. 2004; Dan et al. 2007; Leynaud and Sultan 2010; Stegmann et al. 2011). This study presents two distinct slides (WS and ES) along the deeper slope of Ligurian margin (1,500–2,000 m below seafloor (mbsf)). Klauke and Cochonat (1999) and Migeon et al. (2011) concentrated on the morphologies of slope failure and qualitatively identified their triggering mechanisms. Kopf et al. (2008) and Förster et al. (2010) characterized the architecture and evolution of the slope failures. Our study presents geotechnical properties of sediments from undeformed, headwall and deposit areas of WS and ES. Those results are used for infinite slope stability of undeformed sediments under various conditions to (1) identify the preconditioning factors and (2) quantify the influence of earthquakes as a key factor in slope failing mechanisms in this densely populated area.

Geological, Geomorphological and Lithological Setting

The Ligurian Basin is considered as a back-arc basin, that formed by continental rifting and drifting during the late Oligocene from the southeastward rollback of the Apennines-Maghrebides subduction zone (Larroque et al. 2012 and references therein). Currently, active basin deformation occurs offshore at a slow rate of ~ 1.1 m/ka NNW-SSE, which

involves moderate seismic activity with common earthquake magnitudes of M2.2 to M4.5 (Fig. 1a). However, earthquake magnitudes up to M6.8 (e.g. 1887 Ligurian earthquake) are documented at the Ligurian margin (Larroque et al. 2012). The Marcel Fault shows evidence of present activity that three moderate earthquakes (M3.8–M4.6) took place around this fault over the last 30 years (Larroque et al. 2012 and Fig. 1b).

The northern upper continental slope of the Ligurian Basin is eroded by two major canyons (Var canyon and Paillon canyon), which coalesce at a depth of 1,650 m (Cochonat et al. 1993 and Fig. 1b). A single channel was formed at the confluence of the two canyons and divided into three parts: upper, middle and lower valleys. The walls of Upper Valley are highly dissected by small retrogressive failure events (Migeon et al. 2011) such as that west of Cap Ferrat Ridge called Western Slide (WS). It is characterized by shallow headwalls (< 30 m) with high slope gradients of $\sim 4.6^\circ$ (Fig. 1c and Fig. 2a). A slope failure east of Cap Ferrat Ridge is termed Eastern slide (ES) and shows deep slide scars (80–120 m) and a lower slope gradient of $\sim 3^\circ$ (Fig. 1c and Fig. 2b).

Recent processes of sediment transport and deposition in the Var Upper Valley were mainly dominated by hyperpycnal-flow activity, failure-induced turbidity currents, and hemipelagic emplacement (Migeon et al. 2011). The lithostratigraphic succession of WS is characterized by homogenous, fine-grained hemipelagic clayey silt with some coarse-grained sand intervals (Kopf et al. 2008 and Fig. 3a). Areas east of Cap Ferrat Ridge are not connected to major fluvial input of the Var system and receive only hemipelagic sediments (Klauke et al. 2000). The sediments are generally composed of well-bioturbated, homogenous, fine-grained hemipelagic deposits (Kopf and Cruise 2008 and Fig. 3b).

Materials and Methods

Laboratory Tests

The principal data set for this study is based on six gravity cores from undeformed slope, headwall and deposit areas of the WS and ES events. Water content was measured by a GeoTeK Multi Sensor Core Logger (MSCL) on the archive halves at 2 cm intervals. Undrained shear strength (S_u) was estimated using a Mennerich Geotechnik (Germany) vane shear apparatus and Wykeham Farrance cone penetrometer.

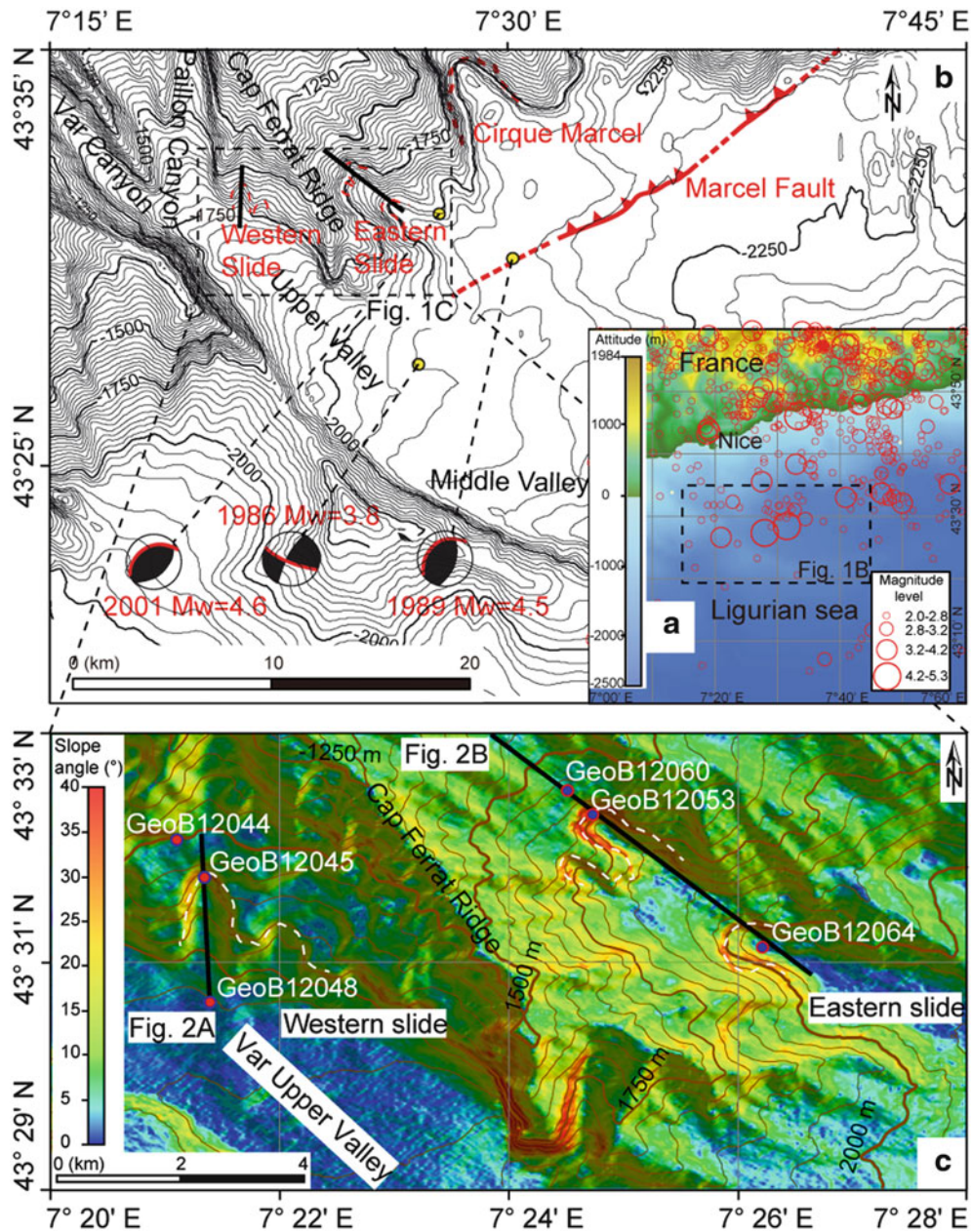


Fig. 1 (a) Map showing the location of the study area, red circles indicate earthquake records of the Ligurian margin from 1980 to 2010 (catalogue from the Bureau Central Sismologique Français). (b) Bathymetric map of deeper slope of Ligurian margin with focal mechanisms of the moderate earthquakes associated with the Marcel Fault (taken

from Larroque et al. 2012). (c) Slope-gradient map of WS and ES. Circles indicate core locations. Dashed white lines mark the headwalls of both slides (revised after Förster et al. 2010). Black lines indicate the locations of seismic profiles shown in Fig. 2b

Grain size distribution analysis using the Beckman Coulter LS 13320 particle size analyzer and Atterberg limits using the Casagrande apparatus and rolling thread method were carried out. Oedometer tests were performed using a GIESA uniaxial incremental loading oedometer system. The drained sediment strength parameters (cohesion c' and internal friction angle ϕ') were determined using a displacement-controlled direct shear apparatus built by GIESA (Germany).

Slope Stability Analysis

The 1D infinite slope stability analysis is used to calculate the factor of safety (FS). For static conditions the FS calculation after Morgenstern (1967) follows:

$$FS = \frac{S_u}{\gamma' z \sin \theta \cos \theta} \quad (\text{undrained}) \quad (1)$$

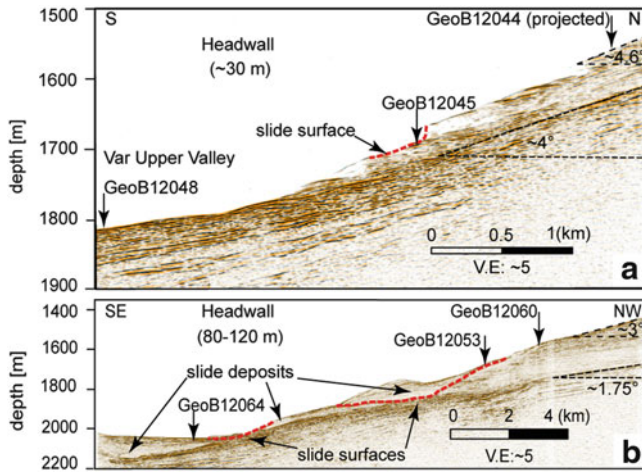


Fig. 2 Seismic profiles of WS (a) and ES (b) (modified after Förster et al. 2010). Note that the bulge in panel B does not show the real morphology of the headwall but is an artefact because the profile crosses the flank of slope

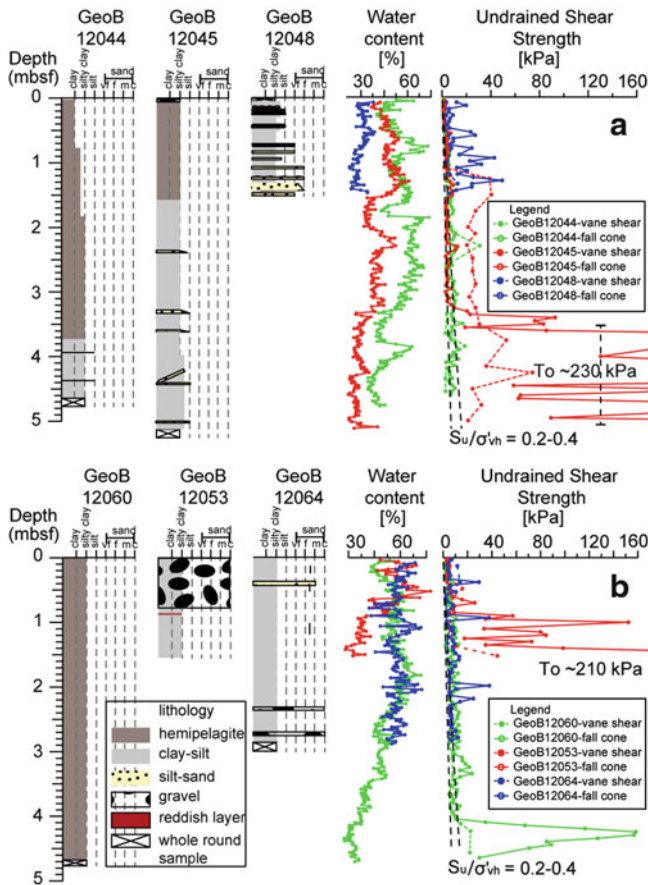


Fig. 3 Lithology, Water content as representative for physical properties and undrained shear strength of the sediments from WS (a) and ES (b)

$$FS = \frac{c' + \gamma'z(\cos^2 \theta - \lambda^*) \tan \phi'}{\gamma'z \sin \theta \cos \theta} \quad (\text{drained}) \quad (2)$$

Where θ is slope angle and λ^* is overpressure ratio ($\lambda^* = \Delta u / \sigma'_{vh}$), Δu is overpressure, σ'_{vh} is vertical effective stress for hydrostatic conditions ($\sigma'_{vh} = \gamma'z$). γ' is buoyant weight, z is overburden depth.

Pseudostatic analysis was used for evaluation of slope stability under earthquake, which is assumed the integrated horizontal ground acceleration $k g$ (where k is the seismic coefficient and g is the acceleration due to gravity) to be applied over a time period long enough for the induced shear stress to be considered constant while the overpressure that may be generated during an earthquake is not taken into account for the slope stability analysis (see Mulder et al. 1994):

$$FS = \frac{S_u}{\gamma'z[\sin \theta \cos \theta + k(\gamma/\gamma') \cos^2 \theta]} \quad (\text{undrained}) \quad (3)$$

$$FS = \frac{c' + \gamma'z(\cos^2 \theta - \lambda^*) \tan \phi'}{\gamma'z[\sin \theta \cos \theta + k(\gamma/\gamma') \cos^2 \theta]} \quad (\text{drained}) \quad (4)$$

Where γ is unit weight.

Results

Physical and Geotechnical Properties

Water content and undrained shear strength of sediments are presented in Fig. 3. Sediments from undeformed slopes have high values of water content ($\sim 60\%$), while lower values ($\sim 30\%$) are seen in deeper parts of sediment cores from the headwall. Sediments from the ES deposit area have similar water content as sediments from the undeformed upslope region. Low water content ($\sim 30\%$) of sediments from the deposit area of WS is attributed to coarse-grained materials. Undrained shear strength of sediments from undeformed slope gradually increase with depth to ~ 20 kPa at 5 m core depth with value of S_u/σ'_{vh} ranging between 0.2 and 0.4 which indicate normal consolidated state for marine sediments (Cochonat et al. 1993). Sediments from headwall have low shear strength (0–20 kPa) and increase rapidly up to ~ 200 kPa at 3.65 m for WS and 1.0 m for ES.

The dominant lithology is clayey silt (with $\sim 20\%$ clay) with an intermediate plasticity according to our Atterberg limit measurements. Oedometer tests indicate sediment from the undeformed slope of WS is underconsolidated (overconsolidation ratio (OCR) = $\sigma'_{pc}/\sigma'_{vh}$) = 0.62, $\lambda^* = 1 - \text{OCR}$ = 0.38) and normally consolidated (OCR = 0.99, $\lambda^* = 0$)

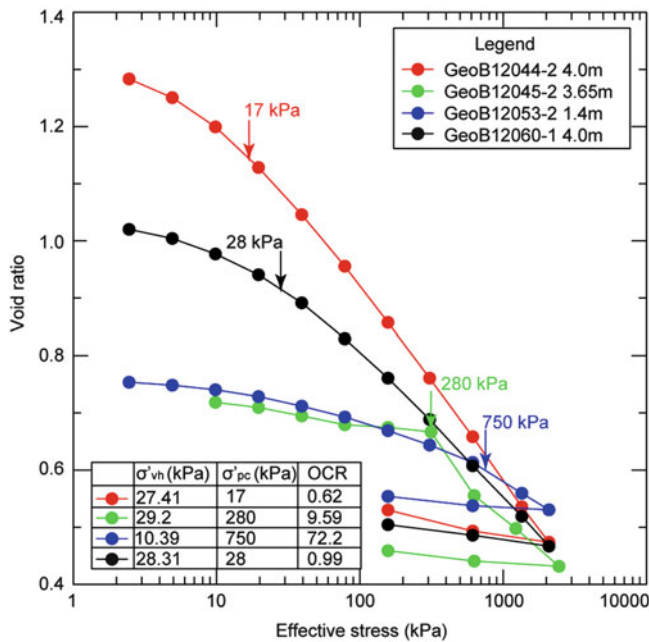


Fig. 4 e-log (σ'_v) curves from oedometer tests with calculated preconsolidation stress (σ'_{pc}) and overconsolidation ratio (OCR)

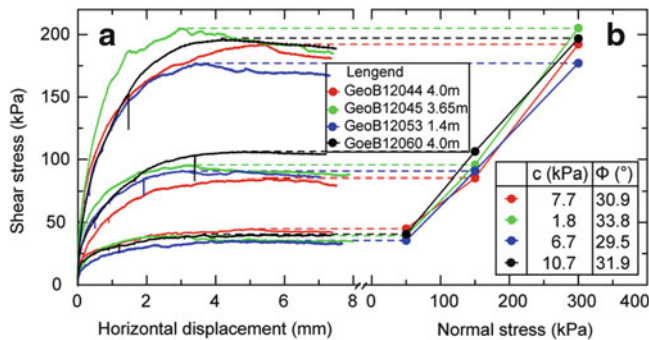


Fig. 5 (a) Direct shear test protocols shown as shear stress versus horizontal displacement. (b) Mohr-Coulomb failure planes obtained from peak shear strength values

for ES whereas sediments below the slip surface near the headwall are strongly overconsolidated (OCR = 9.6 for WS, OCR = 72.2 for ES) (Fig. 4). The calculated thickness of removed overburden material are 31 m for WS and 100 m for ES using the equation of Silva et al. (2001). This is consistent with the depth estimates based on seismic profiles (Fig. 2). Drained direct shear test results are presented in Fig. 5. Values of c' are lower in sediments from WS (1.8–7.7 kPa) than in ES (6.7–10.7 kPa) whereas values of ϕ' are slightly higher in sediments from WS (30.9–33.8°) than in ES (29.5–31.9°).

Slope Stability Analysis

Factors of safety for four different scenarios were calculated using Eqs. (1–4) with two parameters changing within a certain range while all others were kept constant (for details see Table 1). The undrained shear strength-depth relation was obtained using fall cone tests data with linear regression. We assume λ^* of WS is 0.38 due to underconsolidated state and no overpressure in ES because of its normal consolidation state. Our data suggest that both slopes appear to be presently stable under both undrained and drained static conditions. The results further indicate that the slope angle has a stronger influence on slope stability than slope failure depth (Fig. 6). The minimum horizontal acceleration coefficient required to trigger slope failure (FS = 1) was back-calculated based on Eqs. (3) and (4). For the undrained earthquake case, a value of $k = 0.08$ is needed to trigger slope failure for ES, while a lower value of $k = 0.06$ is needed to fail the WS slope.

Discussion

Preconditioning Factors of WS and ES: Superficial Failure vs. Deep-Seated Failure

WS is affected by superficial failures with shallow headwall (~30 m vertical displacement) while ES shows deep-seated failure with deeper scars (~100 m). Previous studies in the Ligurian margin have shown that the slope angle is a governing factor for sediment failure (e.g. Cochonat et al. 1993 and Migeon et al. 2011). High slope angles ($>5^\circ$) promote regular small-volume failure events, which prevent the area to build a thick, potentially unstable sediment package. Sedimentation rates are assumed to be higher near WS on the flank of Var Upper Valley than in the ES region due to regular sediment supply by hyperpycnal flows (Klaucke et al. 2000). On the other hand, hyperpycnal flows are also involved in the gradual undercutting at the base of canyon walls leading to local oversteepening (Migeon et al. 2011). High slope angles with high sedimentation rates and effect of hyperpycnal flows promote superficial failure in WS whereas relative lower slope angle, lower sedimentation rates and without reworking by bottom currents promote the accumulation of a thick but more stable sediment succession in the ES region. The latter then serve as prerequisite and sufficient material resources for deep-seated failure and larger volumes of slid material.

Table 1 Parameters used for slope stability calculations

Parameter	WS GeoB12044				ES GeoB12060			
	US	DS	UE	DE	US	DS	UE	DE
S_u (kPa)	1.46z +3.3	32.5			1.7z +5.0	260.0		
z (m)	<i>1–50</i>	30			<i>1–300</i>	100		
θ (°)	<i>1–10</i>				<i>1–10</i>			
c' (kPa)	–	5	–	5	–	9	–	9
ϕ' (°)	–	32	–	32	–	30	–	30
γ (kN/m ³)	–		17.1		–		17.4	
λ^*	–	0.38	–	0.38	–	0	–	0
k	–		<i>0–0.1</i>	<i>0–0.3</i>	–		<i>0–0.1</i>	<i>0–0.3</i>
γ' (kN/m ²)	7.31				7.62			
g (m/s ²)	9.81				9.81			
FS/ k	2.8/ –	>7/ –	1/ 0.06	1/ 0.14	4.5/ –	>7/ –	1/ 0.08	1/ 0.23

US Undrained Static, DS Drained Static, UE Undrained Earthquake, DE Drained Earthquake, numbers in italics indicate variable parameters

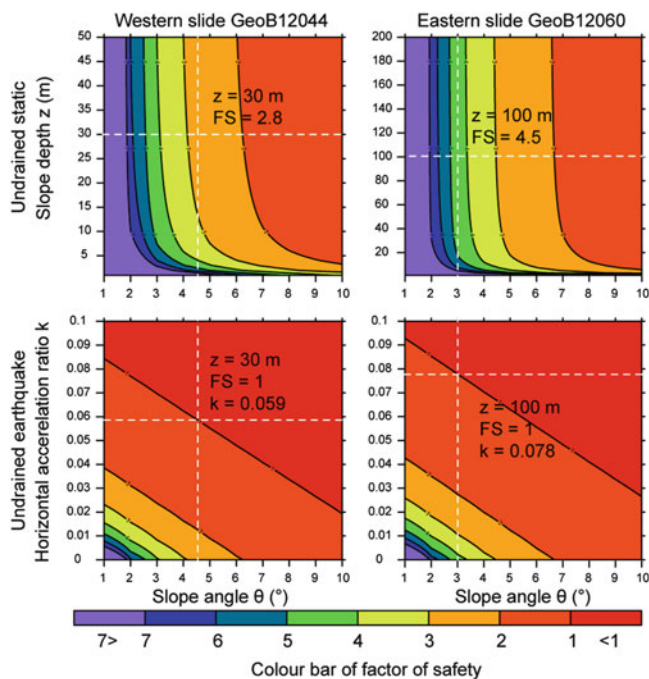


Fig. 6 Undrained slope stability analyses and back-calculations of pseudostatic horizontal acceleration ratio for WS (GeoB12044) and ES (GeoB12060). Dashed white lines indicate current mean values of the parameters for static analysis and values of pseudostatic horizontal acceleration required to trigger slope failure (FS = 1)

The Influence of Earthquake to the Slope Stability

Superficial failures frequently occur in oversteepened, underconsolidated sediments resulting from high sedimentation rates, while deep-seated failures probably require external constraints such as seismic loading on the sediments to induce slope instability. When considering acceleration-induced earthquakes as a static parameter, it is reasonable

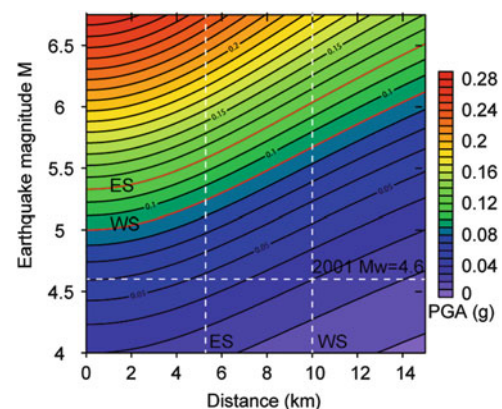


Fig. 7 PGA estimates using an empirical attenuation equation after Bindi et al. (2011). Dashed white lines indicate the 2001 earthquake and the distances between the slope scarps of WS and ES to the epicenter of the 2001 earthquake. Red lines indicate the PGA needed to currently trigger slope failure at WS and ES

to assume a drained pseudostatic model (Mulder et al. 1994). Critical pseudostatic acceleration as the average equivalent uniform shear stress imposed by seismic shaking represents ~65 % of the effective seismic peak ground acceleration (PGA) (Strasser et al. 2011). WS is more vulnerable in undrained conditions where a PGA of 0.09 g (PGA = 0.06 g/0.65) is sufficient to fail the slope. In our study, PGA has been estimated using an empirical attenuation equation after Bindi et al. (2011) (Fig. 7). Over the past 30 years, earthquakes with magnitudes 3.8–4.6 have occurred around the Marcel Fault in distances as close as 10 km to WS and 5.6 km to ES (Larroque et al. 2012 and Fig. 1b). Despite this short epicentral distance, PGA induced by the M4.6 2001 earthquake (0.03 g for WS and 0.05 g for ES) is still insufficiently strong to trigger instability in either WS or ES. The attenuation relationship indicates that moderate earthquake activity of M5.0 on the

spot or stronger earthquakes (e.g. $M = 6.1$) in epicentral distances < 15 km are required to fail the WS slope. In the ES area, moderate earthquakes with $M 5.3$ on the spot or $> M6.5$ earthquakes at distances < 15 km are required to trigger slope failure. From Mulder et al. 1994, PGA ranging from 0.095 g to 0.26 g could be expected for earthquakes with return periods ranging from 100 to 1,000 years, respectively. We propose that seismic triggers may have been required for the deep-seated failure in the ES area, but certainly also affected the instability of superficial failure in the WS region.

Conclusions

In summary, we have demonstrated how geotechnical properties of sediments and slope stability analysis of two distinct types of slope failure (superficial failure and deep-seated failure) control the Ligurian Margin. Consolidation test results can be used to calculate the amount of sediment removed by slope failure, which is consistent with depth estimates from seismic profiles. The slope angle seems to have a stronger influence on slope instability than slope failure depth below seafloor. For better assessment the potential instability in this tectonic active area, dating of different failure events is mandatory to correlate these data to real seismic events. However, the risk assessment shows that a large-size failure only requires moderate earthquake magnitudes, similar to (or even lower than) those of the 1887 historical event. Given the societal loss associated with a tsunamigenic landslide at the French Riviera, more detailed work has to be carried out in this direction.

Acknowledgments We thank the captain and crew of the RV Meteor for their support during the cruise M 73/1. This study is funded through DFG-Research Center/Cluster of Excellence “The Ocean in the Earth System” as well as the Chinese Scholarship Council. We also like to acknowledge the reviewers, Yasuhiro Yamada and Michael Strasser, for their constructive remarks.

References

- Bindi D, Pacor F, Luzi L, Puglia R, Massa M, Ameri G, Paolucci R (2011) Ground motion prediction equations derived from the Italian strong motion database. *Bull Earthquake Eng* 9(6):1899–1920
- Cochonat P, Bourillet JF, Savoye B, Dodd L (1993) Geotechnical characteristics and instability of submarine slope sediments, the nice slope (N-W Mediterranean Sea). *Mar Georesour Geotechnol* 11(2):131–151
- Dan G, Sultan N, Savoye B (2007) The 1979 Nice harbour catastrophe revisited: trigger mechanism inferred from geotechnical measurements and numerical modelling. *Mar Geol* 245 (1–4):40–64
- Förster A, Spieß V, Kopf AJ, Dennielou B (2010) Mass wasting dynamics at the deeper slope of the Ligurian margin (Southern France). Submarine mass movements and their consequences advances in natural and technological hazard research. Springer, Dordrecht, Heidelberg, London, New York, pp 66–77
- Klaucke I, Cochonat P (1999) Analysis of past seafloor failures on the continental slope off Nice (SE France). *Geo-Mar Lett* 19 (4):245–253
- Klaucke I, Savoye B, Cochonat P (2000) Patterns and processes of sediment dispersal on the continental slope off Nice, SE France. *Mar Geol* 162(2–4):405–422
- Kopf A, Cruise Participants (2008) Report and preliminary results of Meteor Cruise M 73/1: LIMA-LAMO (Ligurian Margin Landslide Measurements & Observatory). *Berichte Fachbereich Geowissenschaften, Universität Bremen*, 264; 161p
- Larroque C, Scotti O, Ioualalen M (2012) Reappraisal of the 1887 Ligurian earthquake (western Mediterranean) from macroseismicity, active tectonics and tsunami modelling. *Geophys J Int* 190(1):87–104
- Leynaud D, Sultan N (2010) 3-D slope stability analysis: a probability approach applied to the nice slope (SE France). *Mar Geol* 269 (3–4):89–106
- Locat J, Lee HJ (2002) Submarine landslides: advances and challenges. *Can Geotech J* 39(1):193–212
- Migeon S, Cattaneo A, Hassoun V, Larroque C, Corradi N, Fanucci F, Dano A, Mercier de Lepinay B, Sage F, Gorini C (2011) Morphology, distribution and origin of recent submarine landslides of the Ligurian Margin (North-western Mediterranean): some insights into geohazard assessment. *Mar Geophys Res* 32(1–2):225–243
- Morgenstern N (1967) Submarine slumping and the initiation of turbidity currents. *Mar Geotechnique* 189–220
- Mulder T, Tisot J-P, Cochonat P, Bourillet J-F (1994) Regional assessment of mass failure events in the Baie des Anges, Mediterranean Sea. *Mar Geol* 122(1–2):29–45
- Silva AJ, LaRosa P, Brausse M, Baxter CD, Bryant WR (2001) Stress states of marine sediments in plateau and basin slope areas of the northwestern Gulf of Mexico. *Offshore Technology Conference*
- Stegmann S, Sultan N, Kopf A, Apprioual R, Pelleau P (2011) Hydrogeology and its effect on slope stability along the coastal aquifer of Nice, France. *Mar Geol* 280(1–4):168–181
- Strasser M, Hilbe M, Anselmetti F (2011) Mapping basin-wide subaquatic slope failure susceptibility as a tool to assess regional seismic and tsunami hazards. *Mar Geophys Res* 32 (1–2):331–347
- Sultan N, Cochonat P, Canals M, Cattaneo A, Dennielou B, Hafidason H, Laberg JS, Long D, Mienert J, Trincardi F, Urgeles R, Vorner TO, Wilson C (2004) Triggering mechanisms of slope instability processes and sediment failures on continental margins: a geotechnical approach. *Mar Geol* 213(1–4):291–321



Reconstruction and Tsunami Modeling of a Submarine Landslide on the Ionian Margin of Calabria (Mediterranean Sea)

Silvia Ceramicola, Stefano Tinti, Filippo Zaniboni, Daniel Praeg, Peter Planinsek, Gianluca Pagnoni, and Edy Forlin

Abstract

The Ionian margins of Calabria are affected by repeated sediment failures, recorded by slide scars at seabed and stacked slide deposits. We present a reconstruction of the geometry and dynamics of one of the largest seabed features, the Assi failure on the relatively steep slope off southern Calabria, and use it as input to numerical modeling to evaluate the potential tsunamigenic hazard. The Assi failure is up to 6 km wide and at least 18 km long, and involved the displacement of ca. 2 km³ of sediment, inferred to have taken place within the last 4,000 years in two main phases. The first and larger phase is used as input to the tsunami modeling, on the assumption that the slide moved in a single step as a coherent mass of 1.85 km³, in order to evaluate the most disruptive possible consequences. The results indicate that within 8 minutes, waves just over 1 m in height affect the southern Calabrian coast between Monasterace and Roccella Jonica, where their capacity to cause damage could be amplified in small harbours. This shows that tsunamis represent a hazard for Ionian coastal areas, and calls for accurate monitoring and further study.

Keywords

Ionian Sea • Calabrian margin • Morpho-bathymetry • Sub-bottom profiles • Submarine failure • Tsunami modeling

Introduction

Submarine landslides are important agents for downslope sediment transport and seafloor geomorphic change, and potential tsunamigenic events that represent geohazards for

coastal communities. The tectonically-active Ionian Margins of Calabria (IMC, Fig. 1) provide an interesting natural laboratory to study such processes. The seabed dynamics of the IMC are being examined in the context of the Italian projects MaGIC (Marine Geohazards along the Italian Coasts) and RITMARE (La Ricerca Italiana per il Mare). Integrated seabed mapping during MaGIC has shown the margins to be characterized by numerous slide scars, interpreted as the sign of recurrent slope failures (Morelli et al. 2011; Ceramicola et al. 2014). One of the largest geomorphic features is the Assi slide, located within 10 km of the coast (Fig. 1). Information on this feature is available from both swath bathymetric data and high-resolution sub-bottom profiles. The objective of this study is to present a reconstruction of the geometry, volume and dynamics of the Assi slide and its environs, and use it as input to a model of tsunami generation and propagation.

S. Ceramicola (✉) • D. Praeg • E. Forlin
OGS (Istituto Nazionale di Oceanografia e di Geofisica Sperimentale),
Borgo Grotta Gigante 42/c, 34010 Sgonico (TS), Italy
e-mail: sceramicola@inogs.it; dpraeg@inogs.it; eforlin@inogs.it

S. Tinti • F. Zaniboni • G. Pagnoni
Dipartimento di Fisica e Astronomia, Università di Bologna, viale
Carlo Berti Pichat 6/2, 40127 Bologna, Italy
e-mail: stefano.tinti@unibo.it; filippo.zaniboni@unibo.it;
gianluca.pagnoni3@unibo.it

P. Planinsek
Via Doberdò 26/2 Opicina, Trieste, Italy
e-mail: pitplan@gmail.com

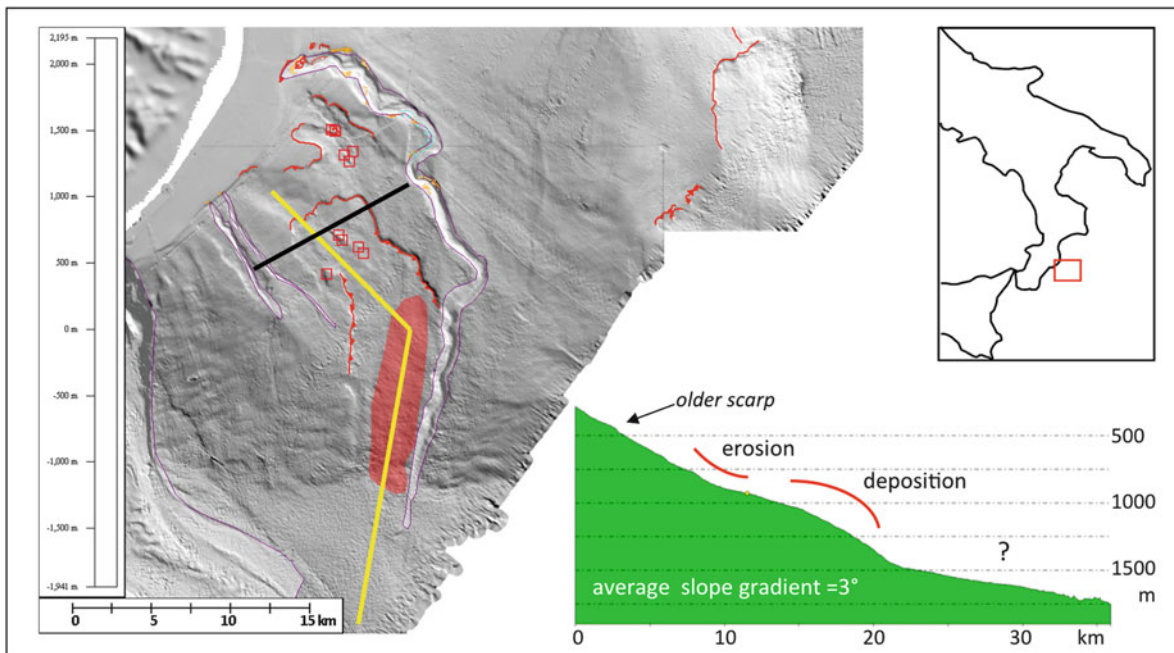


Fig. 1 Study area location on the Ionian margin of Calabria. Main figure: shaded relief from DEM of multibeam data acquired by OGS; submarine canyons are indicated in white, red lines denote seabed

scarp, the elongated red area indicates deposited material. Inset shows a bathymetric profile along the axis of the Assi slide (yellow line). Black line shows location of Fig. 2

Regional Setting

The IMC forms part of a broader accretionary prism that records the NW subduction of Ionian lithosphere beneath the Tyrrhenian Sea (Sartori 2003), a process associated with historical seismic activity (DISS Working Group 2010). The SE advance of the accretionary prism over the last ~10 Ma has slowed or ceased since 0.8–0.5 Ma (Mattei et al. 2007), coincident with a km-scale differential uplift of onshore areas (Westway 1993). Uplift has contributed to the steep (3–8°) bathymetric slope offshore southern Calabria, which is incised by canyon systems that reflect sediment transport into the deep-water Spartivento and Crotona fore-arc basins (Sartori 2003). The open slopes between the canyons are marked by scarps (<50 m) interpreted to indicate recurrent failures (Fig. 1).

Methods and Data

High-resolution geophysical data were acquired by the R/V OGS Explora during campaigns in 2005 and 2009. Swath bathymetric data were acquired over an area of about 30,000 km² using Reson 8150 (12 kHz) and 8111 (100 kHz) multibeam systems, to obtain DEMs of variable

cell size (5–50 m). Sub-bottom profiles consist of about 10,000 line-km of Chirp data (2–7 kHz). Our interpretive method consists of integrating seabed morpho-bathymetric elements with acoustic facies identified on the sub-bottom profiles, in order to identify the principal sedimentary features of the margin and reconstruct their dynamics.

Calculations of the slide dynamics, of the resulting tsunamigenic impulse and of tsunami propagation are performed using three numerical codes developed and maintained by the University of Bologna Tsunami Research Team. Code UBO-BLOCK1 solves equations of motion accounting for gravity, buoyancy and all interactions between the sliding mass (discretized into a chain of interacting, volume-conserving blocks) and the environment, to obtain the slide acceleration, velocity, position and shape at each time step. These elements are used to compute the tsunamigenic impulse via code UBO-TSUIMP, which filters the perturbation provided by the slide motion through the sea depth (cutting the higher frequencies), and computes the forcing term used as input for the tsunami model. The tsunami propagation is simulated by code UBO-TSUFUD, implementing the non-dispersive Navier-Stokes equations with the shallow water (SW) approximation. For a more detailed description of the codes, see Tinti et al. (1997), for applications see Tinti et al. (2006, 2011) and Zaniboni et al. (2013).

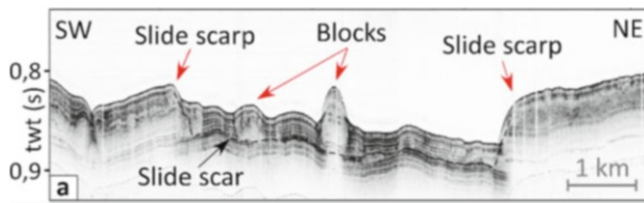


Fig. 2 Chirp sub-bottom profile across the upper part of the Assi slide (location in Fig. 1). Black dashed line marks the low-angle unconformity at the base of the slide deposits

Results and Discussion

Seabed Mapping

The Assi failure lies off southern Calabria on an open slope between the large Siderno canyon system to the west and the smaller Assi canyon to the east (Fig. 1). Morphobathymetric data reveal a number of arcuate scarps indicative of sediment failure, including several on the upper slope in water depths of 150–500 m (Fig. 1). Downslope, the Assi slide is apparent as a seabed scarp up to 50 m high, defining an elongated slide scar up to 6 km wide and at least 18 km long, extending across water depths of 500–1,400 m (Fig. 1). The slide scar has a minimum width of 3.1 km in water depths of 730 m; above this narrowing, its axis is of NW-SE orientation, whereas below it is of N-S orientation (both parts are perpendicular to the regional slope). Bathymetric profiles along the slide show concave upper and convex lower profile (Fig. 1). The lowest parts of the slide intersect the Assi canyon, and the slide has no apparent expression on the adjacent floor of the Spartivento basin (Fig. 1).

Sub-bottom profiles across the Assi slide show it to contain both stratified and unstratified deposits, above a low-angle basal unconformity (Fig. 2). The upper part of the slide consists mainly of stratified deposits and unstratified blocks that have seabed expression (Fig. 2), while the lower part contains more mixed acoustic facies. The slide is observed to truncate sediments that include unstratified layers interpreted as older debris flow deposits (Fig. 2), including near-seabed layers seen to be linked to the seabed scarps observed upslope (Fig. 1).

Reconstruction of Failure Dynamics

We interpret this part of the slope to have been affected by at least three phases of failure (Fig. 3). The oldest phase (SLIDE 1) is associated with scarps on the upper slope (Fig. 1) and unstratified deposits on the slope below that are truncated by the younger Assi slide (Fig. 2). The Assi

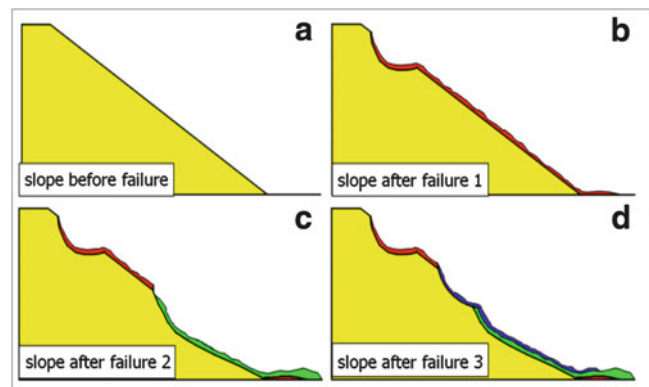


Fig. 3 Reconstruction of failure dynamics along the Calabrian Ionian margin

slide itself provides evidence of two phases of failure: the N-S oriented lower slide (SLIDE 2), which we infer to be older, and the NW-SE oriented upper slide (SLIDE 3). The Assi slide extends over an area of ca. 90 km² and we estimate that it mobilised a total ca. 2 km³ of sediment during the two events (Fig. 3).

The age of the three slide events (Fig. 3) has been estimated from the thickness of a layer of sediment observed on sub-bottom profiles to overlie the slide deposits across the slope (e.g. Fig. 2). On the upper slope above SLIDE 1, this deposit is 6 m thick, whereas downslope above both SLIDES 2 and 3 it is 4 m thick. Post-LGM sedimentation rates for this area are taken from Zecchin et al. (2011) to be about 1.4 mm/year. This yields an estimated age of ca. 4300 year for SLIDE 1 and an age of ca 2850 year for SLIDES 2 and 3. The comparable thickness of this deposit across SLIDES 2 and 3 supports an interpretation of them as linked events, SLIDE 3 having formed by retrogressive failure after the larger SLIDE 2 (Fig. 3).

The first phase of the Assi slide (SLIDE 2, Fig. 3c) is the largest of all the failures to have affected this steep open slope. In the following, we focus on SLIDE 2 (hereafter simply referred to as the Assi slide) to model the failure dynamics and evaluate its tsunamigenic potential.

Numerical Modeling of the Assi Slide

The material mobilised during SLIDE 2 was used for the tsunami modeling, assuming that the material failed in a single step and remained a coherent mass. This represents a ‘worst-case’ scenario, chosen in order to evaluate the strongest possible consequences.

The calculation of the slide dynamics is performed using the numerical code UBO-BLOCK1: the sliding mass is discretized into a chain of interacting, volume-conserving blocks, whose centre of mass move along a predefined

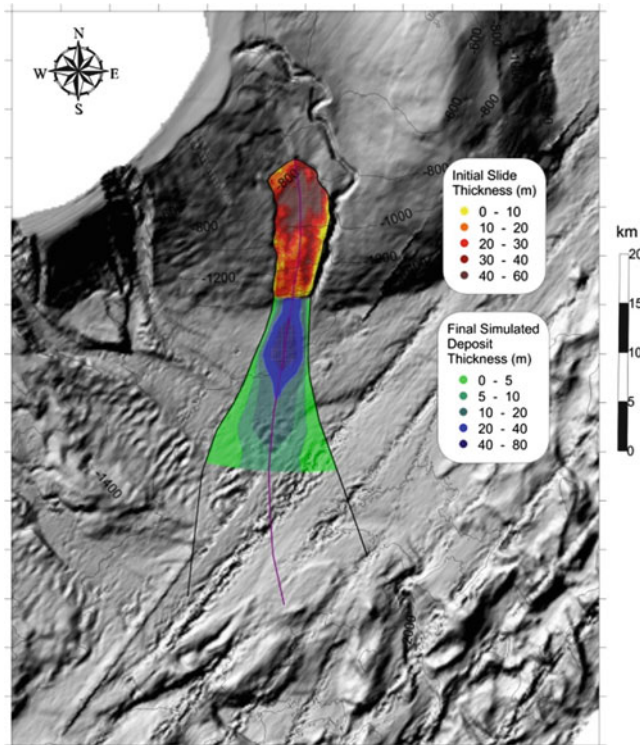


Fig. 4 Reconstruction of the initial thickness (yellow-red-brown colour scale) of the Assi slide and computed final deposit (green-blue scale). The purple line marks the trajectory of the centres of mass, while the two black side-boundaries account for lateral spreading

trajectory (Fig. 4, purple line). The inputs required by the numerical code are: the undisturbed sliding surface; the initial thickness of the mass; the trajectory of the centres of mass of the partition blocks (mostly based on the maximum local slope); and the lateral boundaries governing the spreading of the slide. Initial slide thickness was reconstructed by filling the present sea-bottom scar (Fig. 4). The sliding surface was deduced from the present bathymetry, neglecting the presence of possible deposits at the base of the slope.

The result is a mass of 1.85 km^3 volume, mainly concentrated upslope between 800–900 m water depths (see major thickness marked by the brown area in Fig. 4). The area covered by the initial mass ranges about 66 km^2 , for a mean thickness of 28 m. Most of the deposit remains at the toe of the margin, where the slope reduces, at about 1,500 m water depth (Fig. 4), while the frontal part reaches deeper sea down to 1,700 m, for a runout of more than 20 km.

As concerns dynamics, the Assi slide is characterized by a slipping time of over 18 min. In the acceleration phase, the mass seems to move not coherently, as testified by the spreading of the velocities of individual blocks (black dots in Fig. 5). The mean velocity reaches a peak of about 23 m/s after more than 11 min. A fast deceleration phase follows, due to the mass reaching gentler slopes. The Froude number

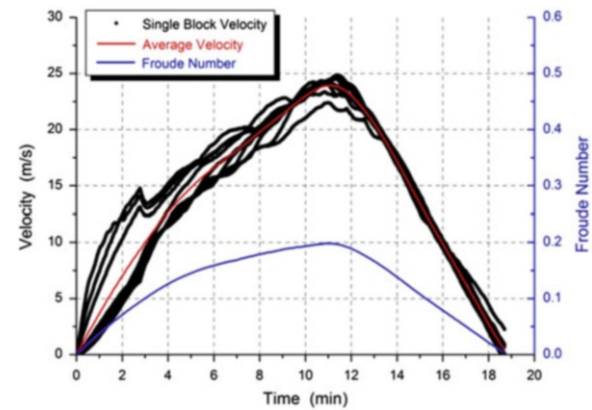


Fig. 5 Average velocity (red line) and individual centre of mass velocities (black dots) vs. time. The Froude number value is marked in blue

is also given in Fig. 5: this parameter is obtained as the ratio between the horizontal component of the sliding velocity and the phase velocity of the generated water wave: when it is close to the resonance condition, (i.e. the value 1), the energy transferred from the slide to the waves is maximum. The highest Froude number is relatively low, 0.2, far from the critical value, and is attained in correspondence of the velocity peak, after around 11 min. Afterwards, the Froude number decreases rapidly as the result of a double effect: the slide slows down (hence, the numerator of the ratio decreases), and the water becomes deeper (hence, the denominator of ratio increases).

Simulation of the Tsunami Propagation

The computational domain is composed of a regularly-spaced grid, 200 m step, focused on the Ionian Calabrian coast and visible in Fig. 6

Figure 6 reports the propagation of the Assi landslide tsunami at different time steps over the smaller computational domain. Initially the wave propagates almost radially from the source ($t = 3 \text{ min}$ sketch in Fig. 6), with a negative leading front moving northward, and a leading crest moving southward, in the direction of the sliding motion. Between 6 and 8 min, the tsunami hits the Calabrian coast and begins to deform, and the wave front orients almost parallel to the coast. The coastal stretch between Monasterace and Roccella Jonica is the first one attacked by the tsunami (a sea withdrawal of about 1 m). South of this area, in direction of Siderno, a first positive arrival (meaning sea invasion) is observed, while moving northward the tsunami first manifests as a negative signal.

Such features are confirmed by the virtual marigrams, reported in Fig. 7: the maximum peak-to-peak water elevation,

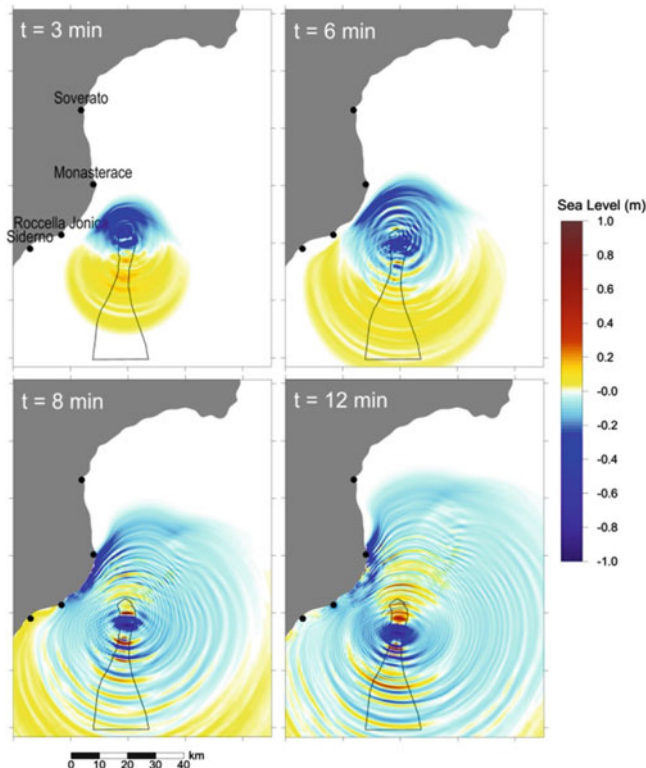


Fig. 6 Propagation of the tsunami over the smaller computational grid at different time steps. Cyan-blue scale stands for sea withdrawal, yellow-red-brown for sea level increasing. The black line marks the slide motion boundary

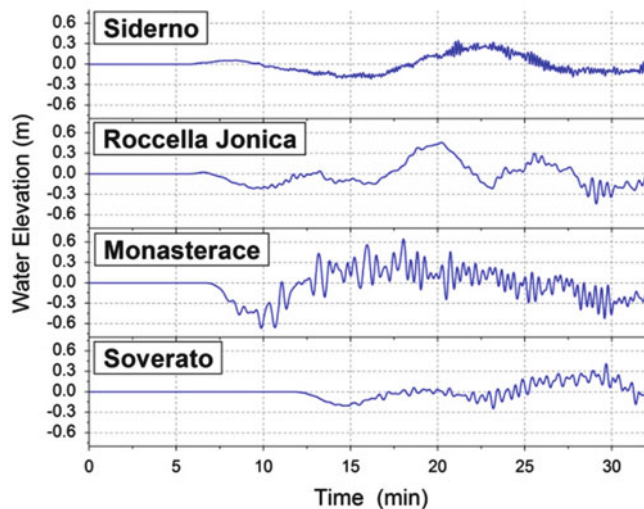


Fig. 7 Virtual tide gauge records (geographical locations in Fig. 6)

about 1.2 m, is found in Monasterace, where a first sea withdrawal of about 60 cm occurs 10 min after the landslide beginning and is followed by an equivalent maximum 7–8 min later.

The marigrams show also two more relevant features that are typical of the landslide-induced tsunamis: (1) the high-

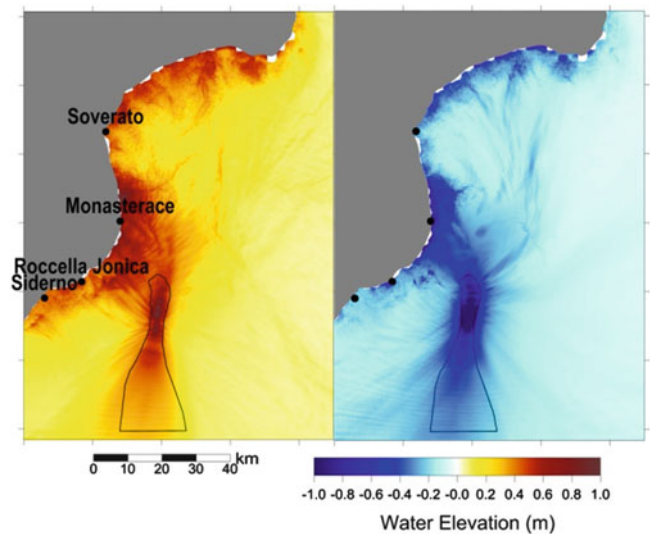


Fig. 8 Maximum and minimum water elevation over each node of the smaller computational grid

frequency signals (associated to the short wavelength waves in the fields of Fig. 6, $t = 8$ min and $t = 12$ min) overlapping the main wave; (2) the rapid amplitude decay with the distance from the source. In general the main perturbation shows a periodicity of about 8 min, and the first tsunami signal takes at least 7 min after the beginning of the landslide motion to affect the closer coast.

The maximum and minimum water elevation over each point of the computational domain (Fig. 8) provides a good description of how the tsunami energy distributes: in general, velocity and height of the wave is governed mainly by the sea depth, meaning that bathymetry plays the key role in driving the tsunami propagation.

In the case of Assi landslide, the main signals are clearly deviated north-westward, towards Monasterace and Roccella Jonica, while a small part of the energy departs north-eastward, as evidenced by the beam in that direction. This kind of maps can have immediate and important applications in the study of hazard along the coast.

Conclusions

This study presents the first attempt to evaluate the potential tsunamigenic hazard associated to submarine mass movements along the Ionian margins of the Mediterranean Sea, using a combination of seabed mapping and tsunami modeling. Seabed mapping shows the Assi slide to be the most recent and largest failure to have affected the steep open slope south of Calabria. The Assi slide is inferred to have taken place in two retrogressive phases, of which the first and larger was used to estimate the volume of mobilised material ($\sim 1.85 \text{ km}^3$), as input to modeling the failure dynamics and tsunamogenic potential.

The coastal areas along the southern part of the margin between Monasterace and Roccella Jonica, including the village of Riace Marina, are found to be the most susceptible to tsunamis generated by the Assi slide: within 8 minutes they are affected by waves with maximum peak-to-peak elevations just over 1 m in height. Such waves are not catastrophic, but would be able to cause damage, especially within the small harbors characteristic of the coast, where wave effects can be amplified by resonance and multiple. Moreover, the wave could pose threat to coastal populations, especially if occurring during the season of major tourism flow.

More generally, the unpredictability of the sliding phenomena, their proximity to the coast and the corresponding shortness of the lead time (in this case about 7 minutes), the large number of possible tsunami sources related to evidence of repeated episodes of failure along the margin, suggest that tsunamis represent a recurrent hazard for Ionian coastal areas and thus need accurate monitoring and further study.

Acknowledgments Geophysical data were acquired and analysed in the framework of the MaGIC Project (Marine Geohazards along the Italian Coasts) funded by the Italian Department of Civil Protection and by the RITMARE Project (La Ricerca Italiana per il Mare) funded by MIUR (Italian Ministry of University and Research).

References

- Ceramicola S et al (2014). Submarine mass-movements along the slopes of the active Ionian continental margins and their consequences for marine geohazards (Mediterranean Sea). In: Krastel S et al (eds) Submarine mass movements and their consequences, 6th international symposium. Advances in natural and technological hazards research, Ch. 26. Springer, pp 295–306
- Ceramicola S et al (2012) Potential tsunamigenic hazard associated to submarine mass movement along the Ionian continental margin (Mediterranean Sea). *Geophys Res Abst* 14:EGU2012–1410808
- Ceramicola S et al (2011). Seabed mapping for marine geohazard assessment on the Ionian Calabrian margin. Marine geo-hazards in the Mediterranean, Nicosia, Cyprus, 2-5 February 2011; CIEM Workshop Monographs, n. 42, pp 59–65
- DISS Working Group (2010) Database of Individual Seismogenic Sources (DISS), Version 3.1.1: A compilation of potential sources for earthquakes larger than M 5.5 in Italy and surrounding areas. <http://diss.rm.ingv.it/diss/>
- Mattei M, Cifelli F, D'Agostino N (2007) The evolution of the Calabrian Arc: evidence from paleomagnetic and GPS observations. *Earth Planet Sci Lett* 263:259–274
- Morelli D et al (2011) Geomorphic setting and geohazard-related features along the Ionian Calabrian margin between Capo Spartivento and Capo Rizzuto (Italy). *Mar Geophys Res*. doi:10.1007/s11001-011-9130-4
- Planinsek P et al (2011) Reconstruction of a submarine landslide and related tsunami from morpho-bathymetry and sub-bottom data on the Ionian Calabrian margin (Medit. Sea) The Second World Landslide Forum, Rome, Abstracts
- Sartori R (2003) The Tyrrhenian back-arc basin and subduction of the Ionian lithosphere. *Episodes* 26(3):217–221
- Tinti S, Bortolucci E, Vannini C (1997) A block-based theoretical model suited to gravitational sliding. *Nat Hazard* 16:1–28
- Tinti S, Pagnoni G, Zaniboni F (2006) The landslides and tsunamis of the 30th of December 2002 in Stromboli analysed through numerical simulations. *Bull Volcanol* 68:462–479
- Tinti S et al (2011) Numerical simulation of the tsunami generated by a past catastrophic landslide on the volcanic island of Ischia, Italy. *Mar Geophys Res* 32:287–297
- Westaway R (1993) Quaternary uplift of Southern Italy. *J Geophys Res* 98:21741–21772
- Zaniboni F et al (2013) The potential failure of Monte Nuovo at Ischia Island (Southern Italy): numerical assessment of a likely induced tsunami and its effects on a densely inhabited area. *Bull Volcanol* 75:763. doi:10.1007/s00445-013-0763-9
- Zecchin M et al (2011) Cliff overstep model and variability in the geometry of transgressive erosional surfaces in high-gradient shelves: The case of the Ionian Calabrian margin (southern Italy). *Mar Geol* 281:43–58



Marine Erosion and Slope Movements: SE Coast of the Krk Island

Čedomir Benac, Sanja Dugonjić Jovančević, Igor Ružić, Martina Vivoda, and Josip Peranić

Abstract

This paper presents the interaction of the marine erosion and slope movements on the south eastern coastal area of the Krk Island, Croatia. Larger parts of the coastal bedrock are carbonate rocks, and smaller parts are marls and flysch. The bedrock is occasionally covered with Quaternary sediments, which are characterized in terms of engineering soil properties. Complex geological fabric of the coastal area around Stara Baška settlement, in the south western part of the Krk Island, caused different movements on the coast. Due to the different grade of fissuring and karstification, as well as different weathering grade, carbonate and siliciclastic rock mass have wide range of resistance to the sea effects including wave attack. Exposure to the wave attack generated due to winds from the south directions contributes to the decreased resistivity. Additionally, occasional torrent flows and intensive erosion cause sporadic higher slope instability. The effect of the previously registered extremely high tides, as well as the possible hazard increase due to the estimated sea level rise, is also analysed in the paper.

Keywords

Coast • Marine erosion • Landslide • Adriatic Sea • Sea-level

Introduction

This paper describes problems of marine erosion and slope instabilities in the coastal area around Stara Baška Settlement on the south eastern coast of island Krk (Croatia, north eastern channel part of the Adriatic Sea, Fig. 1). Construction of large number of facilities, new bathing areas and engineering works in the existing small port are planned inside this coastal area in the future.

Due to expressed susceptibility to accelerated marine erosion and sliding, it will be necessary to perform certain

investigations in the phase of urban planning. Regarding mentioned problems and with the aim to get the reliable input parameters, it will be important to perform geotechnical and oceanographic investigations prior to any engineering work. Without them, there is a real risk to choose inappropriate project solution and to aggravate the existing conditions, or to violate the ecological balance during or after construction works.

Geologic, Hydrologic and Oceanographic Settings

The altitudes around Stara Baška settlement are formed in Upper Cretaceous and Palaeogene limestones, dolomitic limestones and dolomitic breccias (Velić and Vlahović 2009). This carbonate rock mass has different degree of fissuring and karstification, and forms typical bare karstic landscape (Figs. 2 and 3).

Č. Benac • S. Dugonjić Jovančević (✉) • I. Ružić • M. Vivoda • J. Peranić
Faculty of Civil Engineering, Geotechnical Department, University of Rijeka, Radmile Matejčić 3, Rijeka 51000, Croatia
e-mail: cedomir.benac@gradri.uniri.hr; sanja.dugonjic@gradri.uniri.hr; igor.ruzic@gradri.uniri.hr; martina.vivoda@gradri.uniri.hr; josip.peranic@gradri.uniri.hr



Fig. 1 Position of investigated area

Palaeogene siliciclastic rocks consist of marls and flysch (siltstones with sandstone intrabeds) and they are situated in a relatively narrow coastal zone (Fig. 2). A large part of the siliciclastic bedrock is covered by Quaternary sediments: The western part (Zone A in Fig. 2) is covered by talus breccias and the eastern part by mixture of silty clay and carbonate rock fragments (Area B in Fig. 2). Outcrops of siliciclastic rock mass are visible only in narrow coastal zone (Fig. 3).

Karstified carbonate rock mass has a high permeability. For this reason great part of precipitations can penetrate in karstic aquifer. Surface flows are here visible in dry valleys during periods of heavy rainfall (Fig. 2). On the other hand, siliciclastic rocks mass is impermeable and subsurface (hypodermic) groundwater flows through the cover sediments toward the coast.

Kvarnerić is a relatively enclosed channel part, and fetch areas are limited (Fig. 1). Most frequent are low and moderate winds, silent periods are frequent, while the storm winds (speed over 30 m/s) are rare (Leder et al. 1998). North eastern wind bora has the highest frequency and reaches maximum speeds, but waves are moderate due small fetches. In contrast, winds from the south east generate the highest waves. Figure 4 shows SWAN wave model results (Booij et al. 1999). The model simulations were generated on Kvarner bathymetry, with constant wind speed 25 m/s, from south eastern wind direction. It can be seen that Rab Island protects the coastal area of Krk Island from SE wind waves. The significant wave height increases towards the west (to Cres Island) from 2.4 to 4.2 m. Taking into account the influence of waves on coastal processes, it can be concluded that waves with estimated wave heights up to 2.4 m in the area of Stara Baška coast are big enough to have influence on erosion of the coastal area and landslide hazard increase.

As result of climate changes, accelerated sea level rising is expected in twenty-first century. In the Mediterranean Sea, sea level rise could come up to +60 cm in 100 year period (Antonioli and Silenzi 2007). Direct consequence will be more frequent occurrence of extreme sea level heights (ita. *acqua alta*) in the Kvarner area (Benac et al. 2007).

Extremely high tides were recorded on mareograph located in Bakar in 2008, measuring +117 cm above the mean sea level and +122 cm in 2012. Such high levels occurred during strong south eastern winds.

Marine Erosion

Intensity of marine erosion in the carbonate rocks depends of the degree of fissuring and rock mass weathering in the coasts of Kvarner area (Juračić et al. 2009). Slow processes of bioerosion prevail on massive and blocky rock mass. In more fissured and karstified rock mass mechanical destruction is visible.

Intensity of marine erosion in some coastal parts formed in siliciclastic rocks depends greatly on the geological setting and on the deformation degree, which is a function of the Geological Strength Index (GSI). In relatively resistant sandstones, disintegration and slow erosion processes are notable, while in silts and marls the influence of waves is expressed Table 1).

Where silt and marls bedrock is exposed, high cliffs up to 10 m are formed, with narrow beaches underneath. Beach bodies are mixture of fine grained gravel and sand, left after washing out rock mass particles. Beaches partly have the role to protect the coast from wave impacts. Namely, in shallow water, waves deform far away from the coast line, and beaches take over most of their energy (Masselink and Hughes 2003). There are sporadic talus breccias blocks visible on the coastal boundary, fallen from the cliff peaks. They have the role of natural wave breakers (Fig. 5).

According to the damages on facilities, and especially to the morphological expression on the coast, two landslides in phase of creeping can be located (Figs. 2 and 6). Since their foot reaches the sea, continuous erosion, especially in time of storms and high tides, is present (Fig. 6). In these landslide zones, numerous damages are visible on present facilities (damages on coastal roads and concrete structures in small ports, fractures visible on facilities etc.).

Discussion and Conclusions

The area around Stara Baška settlement is in delicate geodynamic balance. Main causes are the geological setting, hydrological and hydrogeological conditions as well as direct coast exposure to the wave impacts. Over the past few decades, unplanned expansion of settlements

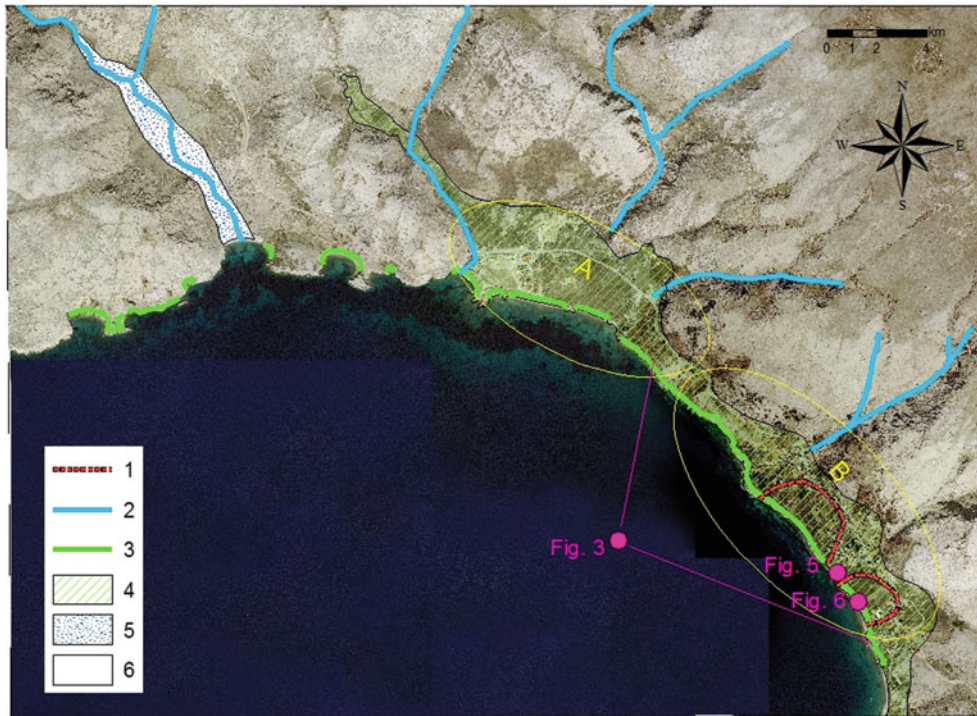


Fig. 2 Simplified engineering geological map: 1-position of landslides; 2-periodical surface (torrent) flow; 3-exposed coastal erosion; 4-siliciclastic rock mass covered by Quaternary sediments;

A-talus breccia; B-mixture of silty clay and carbonate rock fragments; 5-gravely torrent sediments; 6-carbonate rocks (according to Benac et al. 2013)

Fig. 3 Stara Baška settlement (photo: Ž. Gržančić)



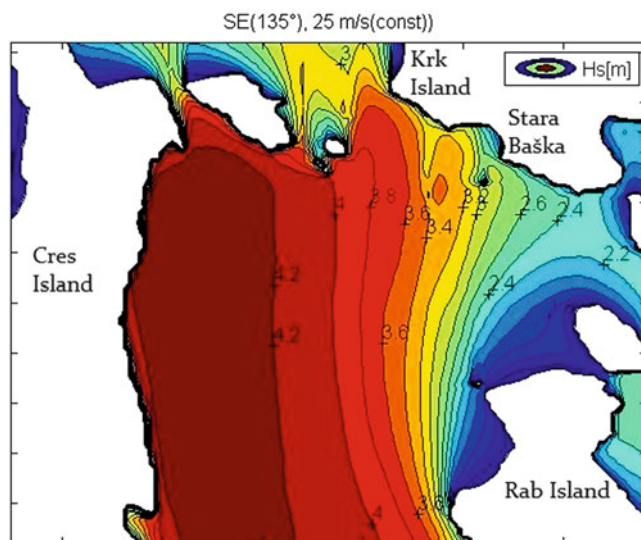


Fig. 4 Significant wave height (m)—SWAN wave model, Kvarneric NE part, constant wind speed: 25 m/s, wind direction: SE—135°

and more intense construction of facilities, mainly for tourism purposes, and lack of the corresponding drainage system for faecal and atmospheric water, numerous problems caused by groundwater and periodically activated landslides appeared. Instabilities are caused by weathering of superficial flysch deposits, erosion at the foot of the landslide and unfavourable hydrological conditions that cause the shear stresses to exceed the soil strength, may have initiate the sliding. After long rainy periods, the fissure-joint system in the deeper flysch layers, which act as watertight zones, cannot completely drain the infiltrated water, resulting in the rise of the groundwater level in the vertical joints and in a subsequent increase in pore pressures, driving slope failure initiation.

Almost all concrete structures, which were generally built, were destroyed during one or at most few years after the construction, due to intense erosion of major coastal part.

After extremely high tides recorded in 2008 and in 2012, traces of increased coastal erosion and numerous damages of coastal structures through the whole Kvarner area were visible. On the coast around Stara Baška settlement, the effects of destruction due to the wave's impact are often expressed. Namely, narrow gravel shoreline, which stretches along major part of the coast, absorbs most of the wave mechanical energy at the mean sea level. However, during extremely high tides, waves cross the beaches, eroding them in the returning current, performing the direct impact on the steeper coastal part and underwashing the coast at the same time. The results are landslides on cliffs and movements of the sliding bodies.

Table 1 Relation between Geological Strength Index (GSI) of siliciclastic rock mass (flysch), prevailing coastal processes and hazard degree regarding marine erosion

GSI ^a	Prevailing coastal processes	Exposure/hazard degree ^b	
		±0 cm	+60 cm
A	Weathering	Low	Low
B–C	Weathering/low erosion	Low	Low/moderate
D–E	Low erosion	Low	Moderate
F	Moderate erosion	Moderate/high	High
G–H	High erosion	High	High

^aGSI classification (Hoek and Marinos 2001)

^bCurrent state and expected sea level increase in 100 years (Antonioli and Silenzi 2007)



Fig. 5 Cliff and rocky blocks (photo: Č. Benac)

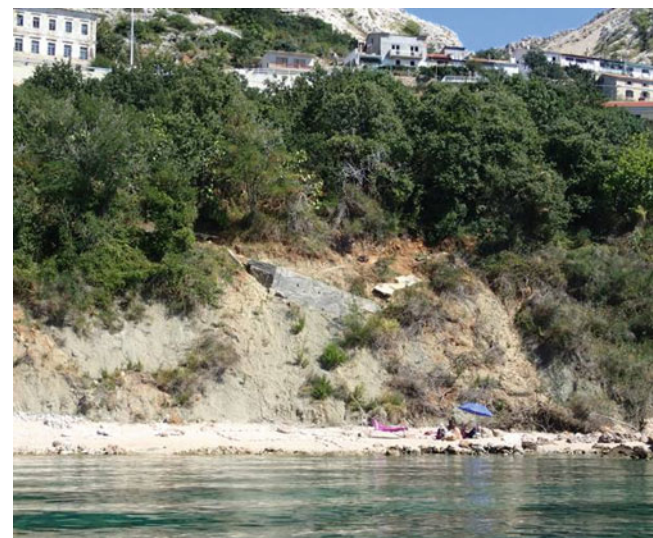


Fig. 6 Eroded landslide foot in the coast (photo: Č. Benac)

In combination with high waves from south eastern direction, coastal erosion can be expected, especially in parts formed in siliciclastic rocks. Analysis of extremely high sea levels in case of mareograph in Bakar, shows probability of more frequent flooding in lower and flattened coastal parts in comparison to the present situation.

References

- Antonioli F, Silenzi S (2007) Variazioni relative del livello del mare e vulnerabilità delle pianure costiere italiane. *Quad Della Soc Geol Italiana* 2:1–29
- Benac Č, Ružić I, Žic E (2007) Coastal vulnerability in the Kvarner area. *Mar Almanac* 44:201–214
- Benac Č, Juračić M, Matičec D, Ružić I, Pikelj K (2013) Fluviokarst vs. karst: examples from the Krk Island, Northern Adriatic, Croatia. *Geomorphology* 184:64–73
- Booij N, Ris RC, Holthuijsen LH (1999) A third-generation wave model for coastal regions. 1. Model description and validation. *J Geophys Res* 104(7):649–666
- Hoek E, Marinos P (2001) Estimating the geotechnical properties of heterogeneous rock masses such as flysch. *Bull Eng Geol Environ* 60(2):85–92
- Juračić M, Benac Č, Pikelj K, Ilić S (2009) Comparison of the vulnerability of limestone (karst) and siliciclastic coasts (example from the Kvarner area, NE Adriatic, Croatia). *Geomorphology* 107(1–2):90–99
- Leder N, Smirčić A, Vilibić I (1998) Extreme values of surface wave heights in the Northern Adriatic. *Geophysics* 15:1–13
- Masselink G, Hughes MG (2003) Introduction to coastal processes and geomorphology. Arnold, London, p 354
- Velić I, Vlahović I (2009) Geologic map of Republic of Croatia, scale 1:300.000. Croatian Geological Institute, Zagreb



Assessment of Rock Slope Stability for A Coastal Area Near Kusadasi, Aydin, Turkey

Yavuz Kaya and Tamer Topal

Abstract

The study area, which will be open to tourism in Kusadasi (Aydin), has steep and high cliffs near the Aegean coast in Turkey. In the area where some slidings and rockfall problems occurred in the past, the geological hazards should be investigated and nature-friendly remedial measures should be taken. The aim of this study is to perform engineering geological studies to (1) search for geological hazards, (2) identify slope stability problems, and (3) recommend nature-friendly solutions in order to prevent/minimize the hazards. To accomplish these tasks, a geological survey was performed involving collection of rock samples and information on rock discontinuities by means of scanline surveys. Furthermore, in situ and laboratory tests were performed. The combined data set allowed performing slope stability and 2D rockfall analyses for different slope conditions. Flysch-like sedimentary material is the main lithological unit in the study area. This flysch consists of alternating sandstone-claystone-marl sequences. It is generally gray, light brown, thin to thick bedded and moderately weathered. The pervasive discontinuity is the bedding plane. Additionally, there are joints developed in two different directions. In this study, outcomes of the slope stability and 2D rockfall analyses along 43 profiles are presented with possible remedial measures.

Keywords

Rockfall • Stability analysis • Kusadasi • Turkey

Introduction

Kusadasi is a touristic coastal town in Turkey. A coastal area located about 5 km south of Kusadasi (Fig. 1) is now under rehabilitation and will be open for tourism in the next few years. However, this area is affected by landslide and rockfall problems where steep and high cliffs occur. Nature-friendly remedial measures are therefore required for the area.

The aim of this study is to understand slope stability and rockfall problems, to analyze the rockfall problems in 2D and to recommend nature-friendly solutions in order to prevent/minimize the hazards.

Y. Kaya (✉) • T. Topal
Department of Geological Engineering, Middle East Technical
University, Ankara 06800, Turkey
e-mail: ykaya@metu.edu.tr; topal@metu.edu.tr

Geology

The study area is located in the western part of the Büyük Menderes Graben. The Menderes Massif metamorphic rocks comprise the basement of the study area (Yilmazer et al. 1994).

Various geological units crop out in the broader study area (Fig. 2). These are from older to younger: Schists (Upper Paleozoic), marbles (Middle Triassic-Cretaceous), meta-flysch (Upper Cretaceous) and continental carbonates (Middle-Upper Miocene). Most relevant rocks for the here presented study are the Miocene continental carbonates comprising gray, light brown, thin to thick bedded, moderately weathered, alternation of weak sandstone-claystone-marl.

The study area is located in an earthquake zone where expected peak horizontal ground acceleration values within



Fig. 1 Location map of the study area

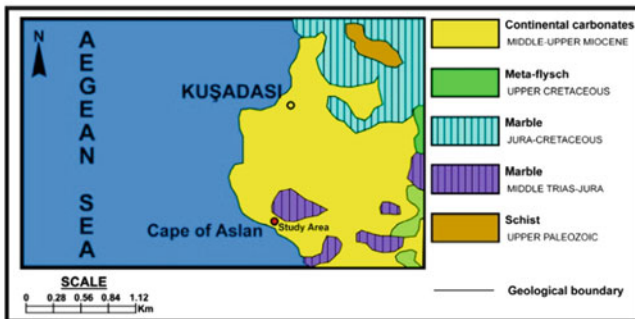


Fig. 2 The geological map of the study area and its close vicinity

50 years may exceed 0.4 g with %90 probability according to the Earthquake Zoning Map of Turkey (GDDA 1996).

Data Collection

Data collection was performed by means of field and laboratory studies. In the field, soil and rocks were investigated in terms of engineering geological properties. Data on discontinuities were collected according to Priest (1993) by means of a scan-profile

survey along 10 profiles. Schmidt rebound hardness measurements were performed and field rockfall tests with 66 block samples were performed along the two different sections to assess the coefficient of restitution, which is one of the most important parameters affecting the rockfall analyses. Samples were also collected for laboratory studies.

The rocks in the study area are generally gray, light brown, thin to thick bedded and moderately weathered. They consist of alternation of sandstone-claystone-marl. The most pervasive discontinuity is the bedding plane. Additionally, there are joints developed in two different directions. The orientation of the major discontinuity sets are related to the deformation of the layers with respect to the formation of anticlines and synclines in the region.

In the laboratory, unit weight, effective porosity, water absorption and point load strength tests were performed on ten samples taken from the field according to ISRM (1981) and ISRM (1985). According to the tests performed on the samples (Table 1), the dry and saturated unit weights are 23.60 kN/m³ and 24.48 kN/m³, respectively. Effective porosity and water absorption values are 9.01 % and 3.89 %, respectively. According to the point load strength test results, the average $I_{s(50)}$ value is 6.06 MPa. Because the

Table 1 Laboratory results of the samples taken from the field

Tests performed	Number of samples	Average value
Unit weight-dry (kN/m ³)	10	23.60
Unit weight-saturated (kN/m ³)	10	24.48
Point load strength (MPa)	10	6.06
Effective porosity (%)	10	9.01
Water absorption by weight (%)	10	3.89

claystone is very weak, the sampling could not be performed in this lithology. The sampled rocks have moderate unit weight and porosity according to Anonymous (1979).

Slope Stability Analyses

In the past, planar failures occurred in the northern sector of the study area. For most of the study area, however, orientation of discontinuities does not favor planar failure. Wedge failure is only likely to occur around Section 6 and 7 (see Fig. 3 for location of profiles) with very small block size at the upper levels of the slope. Therefore, even if the initial movement of the small blocks may be controlled by wedge failure, the movement will then take the form of rockfall. The toppling failure-type does not exist in the study area. Because the cliffs at the coast are steep and high, circular rock mass failure and rockfall analyses were carried out along 43 cross-sections.

Rock Mass Stability Analyses

The required rock mass shear strength parameters for the limit equilibrium analyses were obtained for 43 cross-sections (see Fig. 3) by using RocLab 1.032 (Rocscience 2011). Because of the blocky structure and very poor surface conditions, the Geological Strength Index (GSI) value was defined as 33. A uniaxial compressive strength (σ) = 35 MPa, an intact rock parameter (m_i) = 5 and a Disturbance Factor (D) = 0.7 were used as input values in the RocLab software. The uniaxial compressive strength value was obtained by correlating the average Schmidt hammer hardness and unit weight values. The rock mass shear strength parameters (c and ϕ) were assessed by considering the height of every cross-section.

The obtained shear strength values for highly jointed rock mass were used in Slide 5.1 software (Rocscience 2004a). Limit equilibrium analyses were performed separately for three different conditions at every cross-section (original slope, inclined slope and inclined with one-bench slope). The rock mass was divided into 30 slices and analyzed with the Simplified Bishop Method. A maximum seismic load coefficient of 0.15 g is considered for the pseudostatic analysis. This value corresponds to reasonable maximum horizontal ground

acceleration expected to occur in the study area as located in a first degree earthquake zone of Turkey. Since the groundwater is not encountered in the area, the analyses were performed in dry conditions. However, the saturated unit weight value was used to represent the conditions after a rainy period. A typical example of limit equilibrium analysis for the 39th section of the original slope is given in Fig. 4. The factors of safety values for all slope types are much higher than 1.5 for all three slope conditions. Therefore, circular mass failures are not expected in the cliffs of the study area, even during earthquake shaking.

2D Rockfall Analyses

To perform the 2D rockfall analyses, the dimensions of the blocks must be defined in the field. The dimension of the blocks prone to fall was defined by analyzing the dimension and positions of the fallen blocks and using the scan-line survey data performed at ten locations. In this context, the representative blocks were selected. 66 rock blocks that fell along profile 13 and profile 39 (Fig. 3) were used to define the normal and tangential coefficient of restitutions (R_n and R_t). The RocFall 4.0 software (Rocscience 2004b) was used for the 2D rockfall analyses. The R_n and R_t values are found to be 0.28 ± 0.06 and 0.72 ± 0.13 , respectively for section 13 by using back analysis method. For section 39, R_n and R_t values are 0.30 ± 0.13 and 0.64 ± 0.24 , respectively. The 2D rockfall analyses were carried out along 43 profiles (Fig. 3) to define the rockfall end point. Because of the different material properties observed at the sites, the R_n and R_t values obtained from profile 13 were used for the cross-sections between 1 and 17, and the R_n and R_t values obtained from the profile 39 were used for the cross-sections between 18 and 43. The other parameters used in the analyses are given in Table 2. The 2D rockfall analyses were performed separately along the 43 profiles for the original slope, inclined slope and benched slope (Fig. 5) For some original slope rockfall scenarios, some blocks could even reach the sea. This also applies for the inclined, and inclined with one-bench slope model scenarios. When the rockfall end points were considered for all slope conditions (Fig. 6), it is clear that the rockfall blocks act in falling mode and stop at a shorter distance in the original slope conditions. For the original slope these blocks describe a falling mode style.

On the other hand, rolling and bouncing movements are dominant in the other two slope conditions (inclined and benched slopes) and the end points imply a larger run-out. These slopes may therefore pose a danger for people near the coast. Based on this, the profile of the existing slope must be preferred over the inclined and benched slopes. The maximum bouncing height is 5.75 m at the middle of the profile 33 and the bouncing height significantly decreases near the coast, where protection walls with lower height will need to be built.

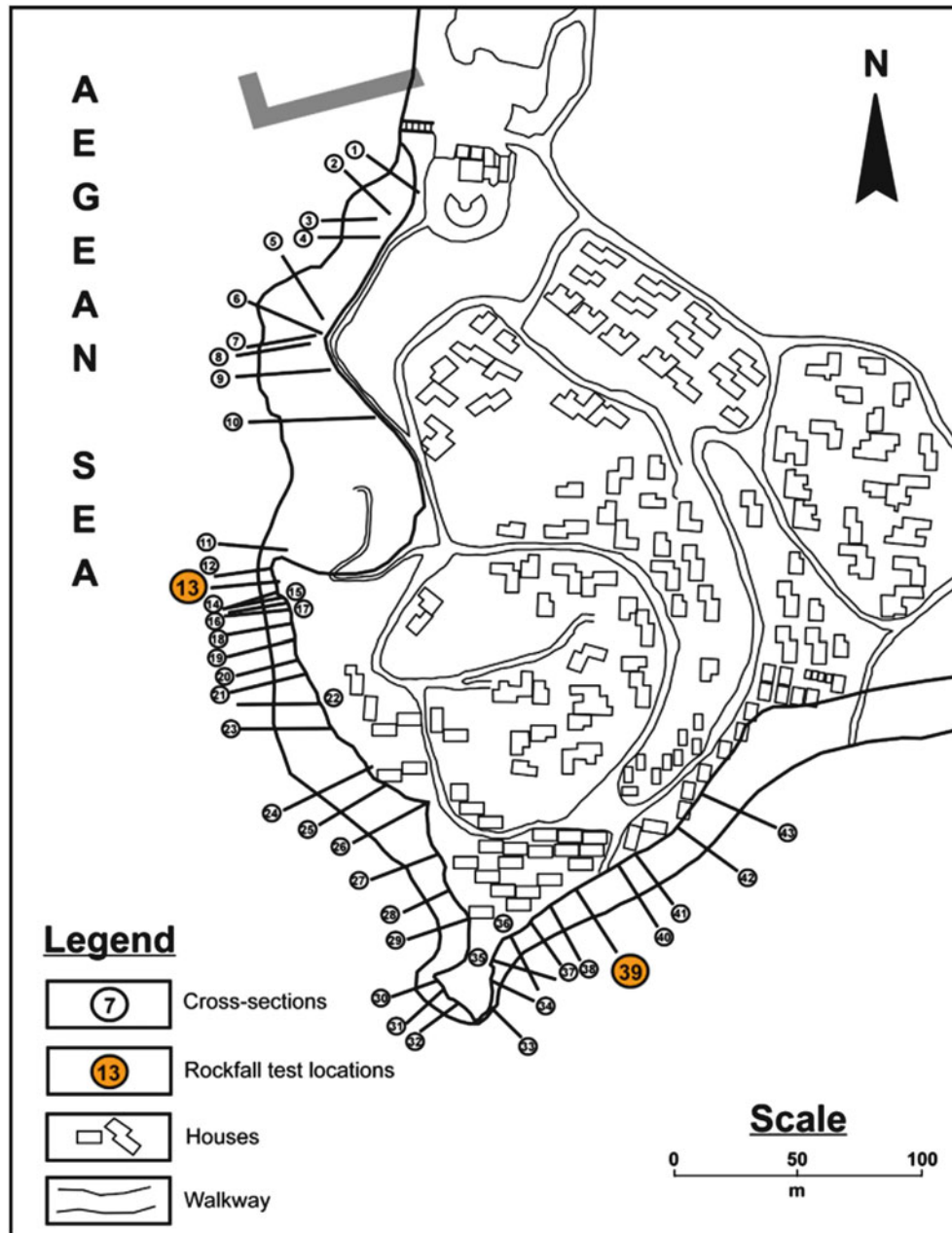


Fig. 3 Locations of the cross-sections for the rockfall analyses

Remedial Measures

Block Removal

As revealed from the rockfall analyses, the blocks falling from the cliffs can be dangerous, particularly if the end points are considered. Today, the rock blocks with falling potential are removed at first, according to general rockfall remedial works applied worldwide. In a similar way, all rocks having the potential of falling controlled by fracture

must be removed. The intact fallen blocks can be used in building the protection wall. After opening the area for public use, controls must be periodically performed at the end of each winter and the blocks having tendency to fall must be removed if necessary.

Drainage

In the study area, there is a drain line at the crown of the cliffs but some deficiencies were observed in the drain lines

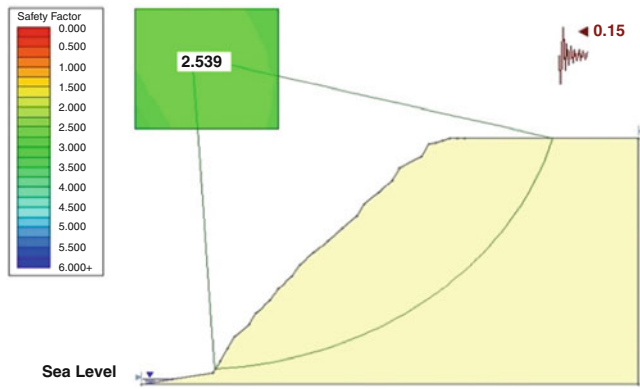


Fig. 4 The result of limit equilibrium analysis for the 39th section of the original slope

Table 2 The parameters used in the 2D rockfall analyses

Parameters	Value
Total number of fallen blocks	1,000
Friction angle (degrees)	20
Slope roughness	0
Block weight (kg)	88
Initial velocity (m/s)	1.5
Minimum velocity cut-off (m/s)	0.1
Number of throws	1,000
Sampling interval	100

in some locations. Additionally, the drain line turning with a right angle in the north of the study area is not suitable for draining water. For these two reasons, new drain lines (top width = 50 cm, base width = 30, depth = 40 cm) must be built and the formers removed. In this way, the drain lines, which must always be kept clear, will prevent the flow of rain water into the cliffs and its damage.

Greening (Vegetation)

The study area is quite green in comparison to its vicinity. Sliding and rockfall problems do not occur in those areas where shrub kind vegetation is very dense. For this reason, the greening of the poorly vegetated areas will not only improve the surrounding beauty but also reduce geological hazards (sliding, erosion, rockfall, etc.). Greening must be planned as soon as possible.

Filling the Caverns

The rock units consisting of alternating sandstone-claystone-marl have been carved by wave action. Small-scale collapses occurred in the areas with large caverns. Because these

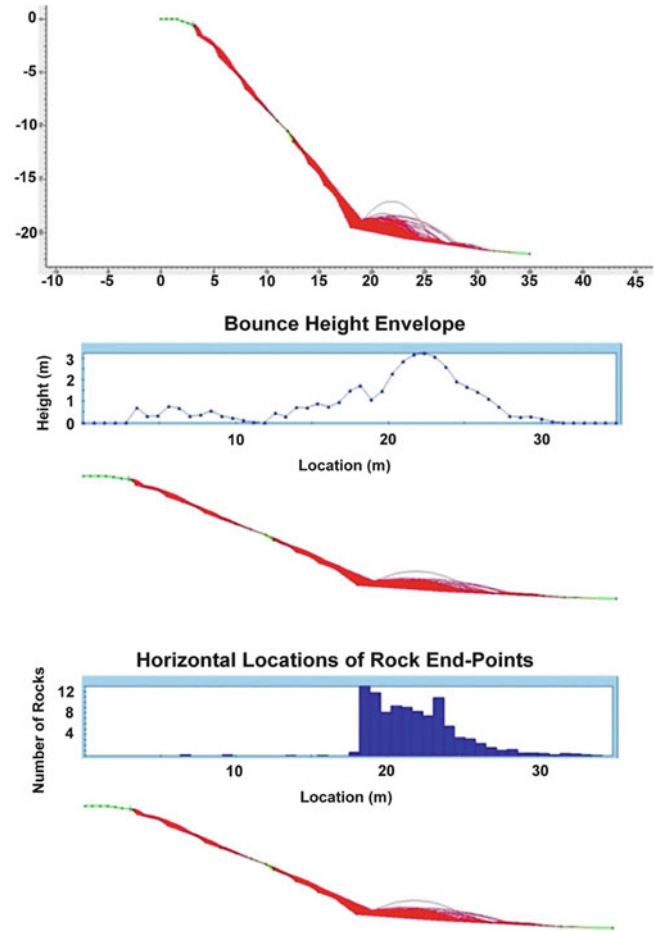


Fig. 5 A typical rockfall analysis of the slope for the 39th section

caverns are potentially dangerous, they must be filled fully as early as possible with the natural stones.

Wall Building

According to the rockfall analyses in the study area, many blocks may reach the coast when falling. This situation would be dangerous for people at the coast. The evaluation was carried out by considering the bounce heights of the rock blocks, and the nearest points to the coast where the energy of the block and bounce height attenuate were defined. The locations of optimal wall points were defined using this approach.

By considering the environment, the intact rocks around the study area can be used to build the wall. The wall height for the whole area is proposed to be 1.5 m. Energy absorbers such as gravels should be installed with ~30 cm thickness at the back side of the wall to attenuate the energy of blocks and decrease the bounce height. In case the material

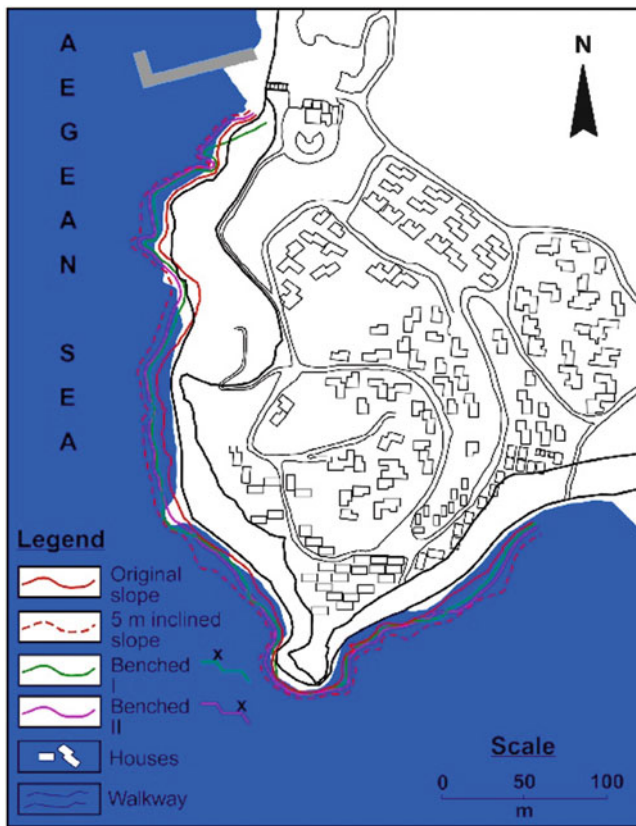


Fig. 6 Map showing rockfall end points obtained from 2D analysis for all conditions

collected from the back of the wall is removed every year, the wall is expected to function for many years.

This wall will reduce the danger derived from rockfall and minimize the undercutting formed at the coast. Vegetation can be applied on this wall by covering the whole wall.

Erosion Prevention

The slope in the north of the study area has the character of a soft soil rather than a rock. Soil erosion occurs occasionally. In this area, there are densely spaced iron rods to prevent the erosion. This approach prevented the erosion to some extent but it could not be effective because of the limited application area. Instead of iron rods, small terracing, wooden rods and deep-rooted vegetation must be applied.

Conclusions

This study is aimed to investigate the slope instability problems, to analyze the rockfall problems in 2D and to

recommend nature-friendly solutions in order to prevent/minimize the hazards.

The study area of Kusadasi (Aydin) which will be open to tourism soon, has steep and high cliffs near the coast.

Geological field studies have shown that the bedding plane and two families of joints are present in the sedimentary rock across every investigated profile except one.

Laboratory studies show that soil and rock units have moderate unit weight and porosity as well as low water absorption and point load strength values.

The study reveals that rockfall is the main geohazard problem although local sliding and erosion problems also exist. The 2D rockfall analyses performed indicate that many blocks may reach up to the shore and this situation would be dangerous for tourists.

To protect the tourists from the geological hazards (sliding, erosion, rockfall, etc.), block removal, drainage, greening, cavern-filling, wall building and erosion prevention are suggested.

Acknowledgments The authors gratefully acknowledge to Diana Tourism Company and its employees for their help and support throughout the field works. Thanks are due to the reviewers for their valuable and constructive comments to improve the quality of the paper.

References

- Anonymous (1979) Classification of rocks and soils for engineering geological mapping. Part 1. Rock and soil materials. *Bull Int Assoc Eng Geol* 19: 64–371
- GDDA (1996) Earthquake zoning map of Turkey. Earthquake Research Department, General Directorate of Disaster Affairs, Ministry of Reconstruction and Resettlement of Turkey
- ISRM (1981) Rock characterization, testing and monitoring. International Society for Rock Mechanics Suggested Methods. Pergamon, Oxford, 211 p
- ISRM (1985) Suggested method for determining point load strength. *International Journal of Rock Mechanics and Mining Sciences and Geomechanics Abstracts* 22: 51–60
- Priest SD (1993) Discontinuity analysis for rock engineering. Chapman & Hall, London, 473 p
- Rocscience (2004a) Slide 5.1-2D limit equilibrium slope stability analysis, Rocscience User's Guide 196 p
- Rocscience (2004b) RockFall 4.0-, Scientific Software-Statistical Analysis of Rockfalls, Rocscience User's Guide 59 p
- Rocscience (2011) RocLab 1.032- Rock mass strength analysis using the Hoek-Brown failure criterion, RocLab User's Guide 25 p
- Yilmazer S, Şaroğlu F, Özgür R, Açıkgöz S, Ercan T, Gevrek İA, Yıldırım N, Aydoğdu Ö (1994) Kuşadasi-Davutlar (Aydin) Arasinin Jeolojisi ve Jeotermal Olanaklarının Değerlendirilmesi. *Türkiye 6. Enerji Kongresi, İzmir, Teknik Oturum Tebliğleri c. 1*, 156–167



Analysis of Quaternary Mass Transport Deposits Based on Seismic Data in Southern Deep-Water Region of Qiongdongnan Basin, South China Sea

Dawei Wang, Shiguo Wu, Genshun Yao, Fuliang Lü, and Michael Strasser

Abstract

Mass transport deposits (MTDs) were identified in Quaternary sedimentary sequences of the southern deep-water (water depth 1,000–1,500 m) region of the Qiongdongnan Basin, South China Sea. Based on high resolution 3D seismic data, seismic amplitude and coherence data are obtained and used to analyse MTDs. Through the seismic profile, two-way-travel time (TWT) time map, time thickness and time slice of target strata, profile characteristics and internal structure of MTDs are revealed. MTDs are characterized of mounded, hummocky, chaotic, low amplitude and discontinuous seismic reflection. MTD-internal thrusts and basal groove marks indicate mass-transport direction from WSW to ENE, suggesting MTD source in the shelf edge/upper slope system offshore central Vietnam, where mountainous rivers deliver high amount of terrigenous clastics. Since about 0.78–1.8 Ma, three depositional cycles characterized by basal MTDs overlain by turbidite channel levee systems have been emplaced in the study area. Timing and source of MTDs suggest a causal link between Quaternary high sedimentation rate to the shelf/upper slope in the Western South China Sea influenced by the eccentricity scale sea-level change and the emplacement of MTDs.

Keywords

Deep-water • Mass transport deposits • Qiongdongnan basin

Introduction

In this paper, 3D seismic data were used to study mass transport deposits (MTDs) in the deep-water area of Qiongdongnan Basin (QDNB). The study area, on the north-western slope of the South China Sea (SCS, Fig. 1), includes

the southern part of QDNB. The MTDs affect the Yinggehai Formation of Quaternary age (Wang et al. 2009). We aim to understand the nature of the Quaternary MTDs, including their seismic characteristics, architecture, distribution, transporting direction and formation mechanism.

D. Wang (✉) • S. Wu

Key Laboratory of Marine Geology and Environment, Institute of Oceanology, Chinese Academy of Sciences, Qingdao 266071, China

Marine Oil & gas Research Center, Institute of Oceanology, Chinese Academy of Sciences, Qingdao 266071, China
e-mail: wangdawei@qdio.ac.cn

G. Yao • F. Lü

PetroChina Hangzhou Institute of Geology, Hangzhou 310023, China

M. Strasser

Geological Institute, ETH Zurich, 8092 Zurich, Switzerland

Geological Setting

The QDNB is located on the northwest slope of the SCS (Fig. 1a). As other basins along the northern SCS margin, QDNB was also formed by lithospheric stretching during the Paleocene and Oligocene, followed by thermal subsidence (Li et al. 1998). In the QDNB the rift phase was associated with the initial opening of the SCS in the Eocene and Oligocene (Ru and Pigott 1986), and post-rift subsidence followed after Early Miocene (~21 Ma) (Fig. 1c). The

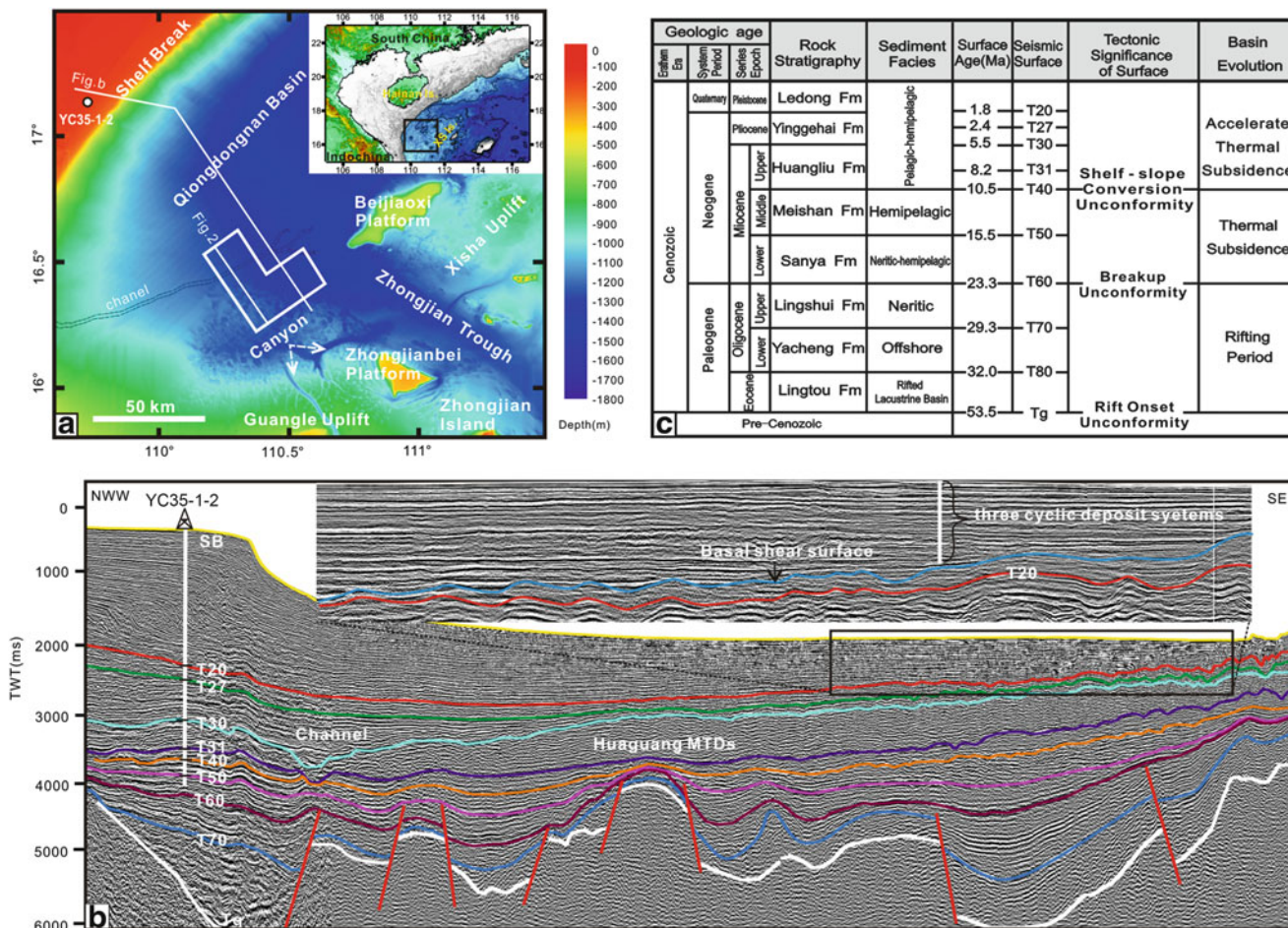


Fig. 1 (a) Bathymetry of study area, (b) seismic profile and (c) stratigraphic column of the Qiongdongnan Basin and major tectonic events affecting the South China Sea. The polygon in the central of a is the location of 3D seismic data which we will discuss in this paper. The black dash lines highlights the submarine channel, which cuts the

uppers slope and into the lower slope and the study area from the West. The white lines show the location of 2D seismic data shown in b. The black circle denotes the location of the well YC35-1-2. The well picks and 2D seismic data in b were used to constrain the age of the bury MTDs after 1.8 Ma(sequence boundary T20)

terrigeneous sediments were transported from two main sources during the Cenozoic: the South China Block and Indochina Peninsula (Yao et al. 2008). Sediment sources for the basins on the SCS western shelf and slope are mountainous rivers that are draining into the SCS along the Vietnam coast (Schimanski 2002). These small narrow mountainous rivers are prominent in the central part of the coast. A submarine channel cuts the upper and lower slope and feeds into the study area from the West. Many MTDs and channel leveed systems from Miocene to recent were found in the deep-water region of QDNB (Wang et al. 2009, 2013; Yuan et al. 2009; Sun et al. 2011) (Fig. 1b).

Data and Methods

The data used in this paper include high resolution 2D/3D seismic data acquired by the China National Petroleum

Corporation in 2005 and drilling data from well YC35-1-2 (Fig. 1a). The 3D seismic data, with dominant frequencies of 40–60 Hz and cell size of 12.5×25.0 m, cover an area of $1,200 \text{ km}^2$. The seismic stratigraphy was mapped and geological ages of the MTDs were determined using seismic stratigraphic correlation to the well stratigraphy (Fig. 1) and previous research results.

In general, MTDs are characterized by mounded, hummocky, low amplitude, chaotic and translucent seismic reflections, surrounded by undisturbed sedimentary strata. Headwalls, lateral walls, top surfaces and basal surfaces can be identified in seismic profiles. The headwalls and lateral walls are continuous normal faults or escarpments (Gee et al. 2006; Bull et al. 2009; Moscardelli and Wood 2008; Perov and Bhattacharya 2011), and they form continuous boundaries between undisturbed and disturbed sedimentary strata. The bottom surface of the MTDs is a shear erosional surface, while the top surface is the continuous

surface between the lower chaotic strata and upper continuous strata. By recognizing diagnostic slide characteristics and calculating thicknesses of MTDs, we can determine the transport direction of the MTDs, the sedimentary depocenter and the source region. The high resolution 3D seismic data enable us to map the distribution of MTDs, and to evaluate possible trigger mechanisms.

Results

Seismic Facies and Seismic Stratigraphy

The reflection seismic data of the Quaternary successions comprise three seismic facies characterized by (1) continuous, parallel reflection pattern, (2) sub-parallel continuous-to-sub-continuous and undulating reflections, and (3) incoherent or internally deformed to chaotic reflection pattern (Fig. 2).

The latter seismic facies (3) is typical for MTDs (e.g. Bull et al. 2009), which thus are identified as seismic intervals of distorted and discontinuous reflections, bounded above, below and laterally by continuous or weakly deformed reflections.

Seismic facies 1 typically includes strata below and outside of the MTDs while seismic facies 2 overlies MTDs. The stratigraphically superimposed repeated succession of these seismic facies has been interpreted by Sun et al. (2011) as three main depositional elements within a cyclic depositional system (CDS; including an MTD overlain by a channel leveed system (CLS); Fig. 2). Seismic stratigraphic correlation to drilling data from well YC35-1-2 (shown in Fig. 1b) constrain the age of the oldest of this three MTDs to be younger than lower Pleistocene (<1.8 Ma) but older than middle Pleistocene (>0.78 Ma).

In the following sections, we focus on detailed characterization of the lowermost MTD complex.

Basal Shear Surface, Top Surface and Lateral Margin

The basal shear surface of the lowermost MTD unit is a distinct high-amplitude, negative polarity reflective event (e.g. seismic profiles shown in Figs. 2 and 3). We interpret this basal surface as the slide plane for the MTD. The time structure map of the basal surface shows that the surface is shallower in the north-west and deeper in the south-east (Fig. 3a). This suggests overall flow direction from north-west to south-east in the study area.

The lateral margins of the MTD are distinctly recognized in seismic profiles perpendicular to the inferred flow

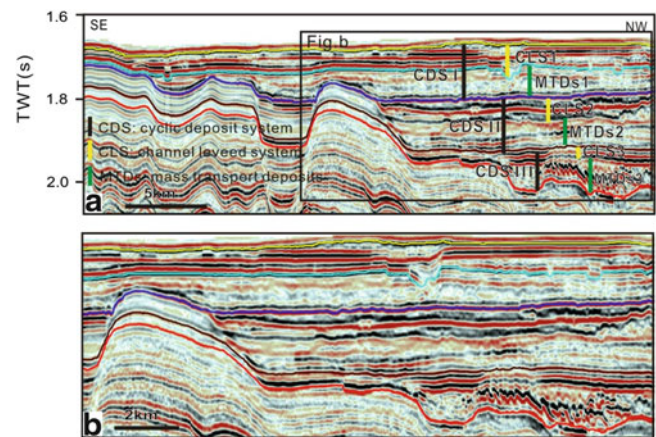


Fig. 2 (a) Three cyclic deposit systems are identified in seismic profiles. Location of seismic line is shown in Fig. 1a. (b) Enlargement of the seismic line. The MTDs discussed in this paper is the lowest one, MTD3. An evolution from MTDs to channel leveed system is characteristics of every cyclic deposit system

direction as abrupt lateral boundaries between the inner highly chaotic or weakly reflective seismic facies and the outer continuous undisturbed facies (Fig. 3d). The lateral margin forms a steeper escarpment in the proximal region, while it is gentler along the transport direction and disappears in the distal region.

The top surface of MTDs is a distinct high-amplitude, positive polarity reflective event (e.g. Seismic profiles showed in Figs. 2b and 3d). The MTD is overlain by younger gravity flow deposits in a channel leveed complex (Sun et al. 2011).

MTD-Internal Thrust Faults

Thrust faults are observed within the MTD northwest of an underlying morphologic high shown in the coherency map Fig. 3b and the seismic profile of Fig. 3d. In the coherency map shown in Fig. 3b, a series of parallel NE-SW white curves depict the distribution and trend of thrust faults. The horizontal slice shows a slight curvature of trend lines. The flow direction of MTD is from NW to SE based on this curvature convex to SE and the trend of thrust faults in this region. The dip of the thrust faults agrees with this flow direction as well. Transport direction from NW-SE is also inferred from the location and distinct boundary of thrust faults relative to the underlying morphologic high. We didn't identify thrust faults in other region within the study area. Therefore, it is inferred that the thrust faults were formed due to the morphological high, which acted as confinement to the NW-SE flowing mass, resulting in compressive plastic deformation and thrusting in the proximal region of MTD.

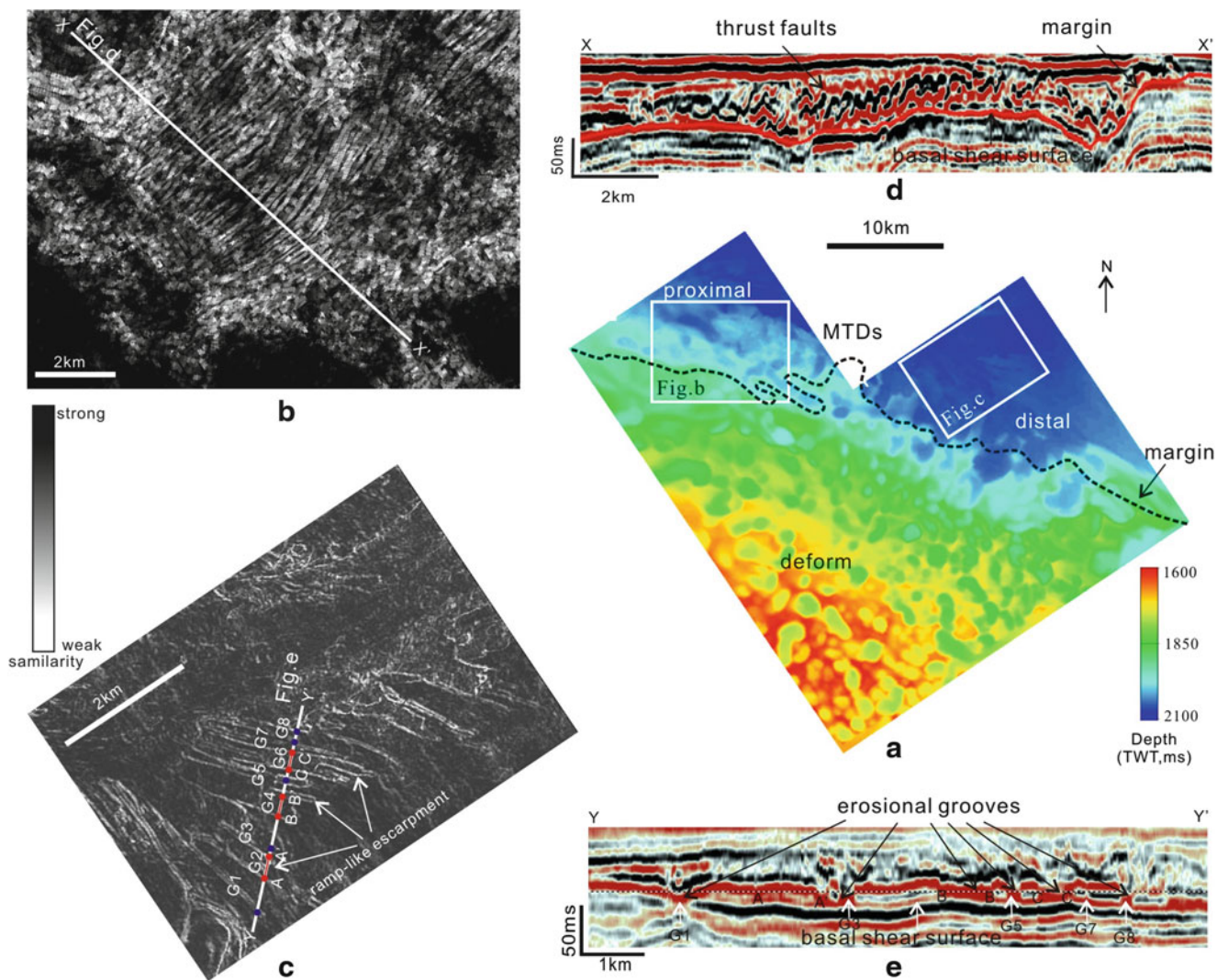


Fig. 3 (a) TWT time map of the basal surface of the lower MTD3 which deposited in the north-eastern deeper region of the study area (north of the *black dashed line*). (b, c) Horizontal slice of coherence body (produced from a surface within the MTD and paralleling the basal surface of the MTD; *white colour* indicates weak similarity in the slice of coherent body) and (d, e) seismic profiles showing different

seismic characteristics along the transport-direction from NW-SE: (d) Thrust faults were found in the proximal region and (e) the erosional grooves were identified in the distal region (see text for explanation of groove annotation G1–G8 and discussed intervals A–A', B–B', and C–C')

Erosional Grooves

A series of erosional grooves were identified within the basal shear surface in the distal region of the MTD. In the horizontal slice of coherence body shown in Fig. 3c, the white lines present the margin of grooves, which are depicted as black region between almost parallel white lines parallel to the NW-SE flow direction. The width of the largest grooves can be more than 600 m, such as G2, G4 and G6 (i.e. red lines between points A and A', B and B', C and C' shown in Fig. 3c). In contrast the width of the smaller grooves G1, G3, G5, G7 and G8 (i.e. blue points shown in the Fig. 3c) is more difficult to quantify in coherency maps because the distance

between the margins is close to the resolution of the coherence map. However, all grooves are distinct in the seismic profile (Fig. 3e).

It is generally accepted that erosional phenomenon like striations and grooves can form during gravity flow processes on the basal surface, and that they can be preserved at the base of the MTD after the gravity flow deposited (e.g. Bull et al. 2009). Three different types of SE-terminations of grooves were recognized (Fig. 3c): The first one is the block in the front of grooves, such as G1. We interpret that G1 is the striation along one outrunner block. The second is the irregular ramp-like escarpment, which is the asymmetrically closed white line shown in Fig. 3c in the front of the large

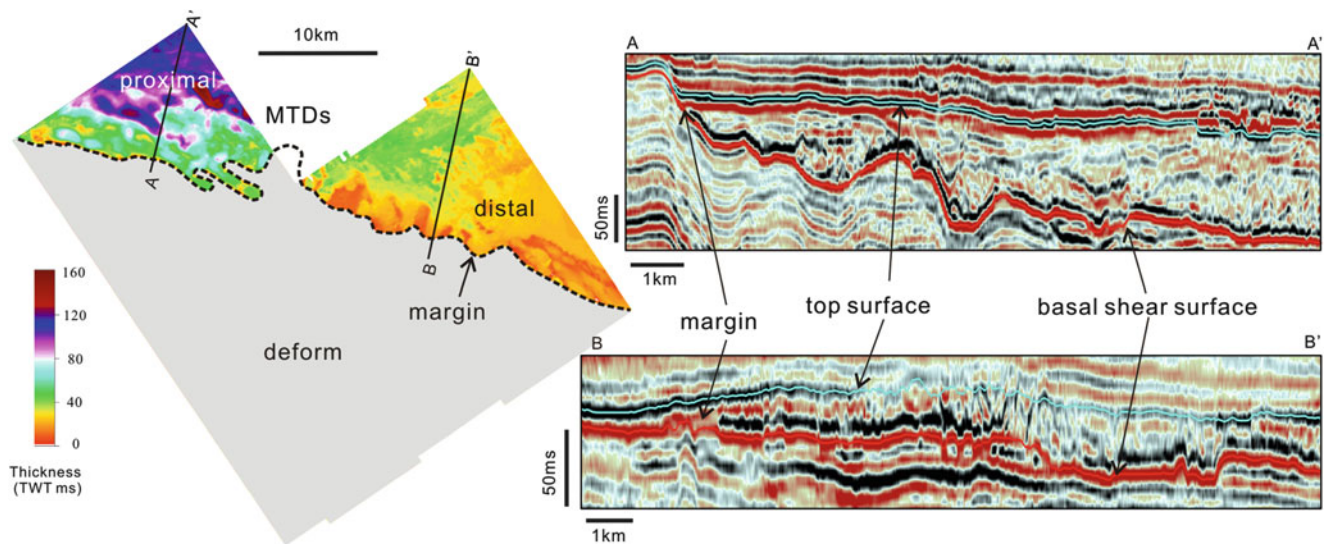


Fig. 4 Isopach map and seismic profiles show the thickness distribution of the lower MTD in the study area along its transport direction from WNW and ESE: The MTD mainly deposited in the proximal region

Table 1 The major mountain rivers out the study area in the central coast of Vietnam

River	Length (km)	Slope (1:)	M.A.R (10^6 m^3)	Peak dis. (m^3/s)
Dai Giang	158	52	7,490	6,710
Kien Giang	96	50	4,032	2,110
Thu Bon	205	39	20,400	10,600

grooves G2, G4 and G6. Those front white lines represent the margin of the gravity flow erosion from strong to weak in the toe region. In contrast, groves G3, G5, G7 and G8 terminate to the SE without characteristic seismic reflection pattern. Therefore, we infer that there are two mechanisms to form the grooves in the study area. One is the striation of blocks, which are drifted by gravity flow and produce outrunner blocks in the toe region of MTD, the other is the basal erosion of gravity flow which maybe high velocity.

MTD Thickness

The thickness of the lowermost MTD ranges from 12.5–80 ms (Fig. 4) and varies from proximal to distal along the flow direction of the MTD. The thickness in the proximal area is generally more than 25 ms, with maximum thickness up to 80 ms. Assuming an interval velocity in the order of 2,500 m/s, the range of MTD thickness in this proximal area would be 62.5–200 m. In contrast the maximum thickness is only ~20 ms (~50 m, assuming an interval velocity of 2,500 m/s) in the distal region. Thus, the main MTD depocenter was in the north-west region of study area.

Discussion

The Source Area of MTDs and High Sedimentation Rates on the Steep Shelf Off the Central Coast of Vietnam

Multiple lines of evidence from our 3D seismic data analysis (see Sect. 2 above) and the channel on the seabed shown in Fig. 1a constrain the main source of the MTDs to be to the west of the study area. According to these kinematic indicators and the general trend of the bathymetry to the west as shown in Fig. 1a, the MTDs are most likely sourced from the shelf/upper slope region (N $16^{\circ}00'00''$ – $16^{\circ}30'00''$) off the coast of central Vietnam.

There are numerous mountainous rivers draining from the high rising hinterland into the SCS in the region of the central coast of Vietnam. Three major rivers, as shown in Table 1, and characterized by Tung et al. (2008) deliver large amounts of sediments to the narrow, steep shelf and upper slope.

The Thu Bon river, which is the closest one to the study area, is only 205 km in length, but conveys high amounts of

terrigenous clastics. The peak discharge of this river can be up to $10,600 \text{ m}^3/\text{s}$ and the mean annual runoff (M.A.R.) is $20,400 \times 10^6 \text{ m}^3$. With current day sea level conditions, the distance from the mouth of the Thu Bon river (N $15^\circ 52' 20''$, E $108^\circ 23' 38''$) to the lower shelf break at $\sim 300 \text{ m}$ water depth is only ca. 116 km. Holocene sedimentation rates on the shelf offshore this river mouth, reconstructed from core data by Schimanski (2002) confirm very high sedimentation ranging between 10.1–124.5 cm/ka (for cores No. 18396 and 18422, respectively; see Schimanski 2002).

During Pleistocene sea level low stands, the mouth of the Thu Bon river can seaward jump 100 km (according to the current water depth of 120 m and adopting the 120 m as a typical amplitude of sea-level change). Even larger amount of sediments are expected to have been delivered to shelf-break and upper slope during this period. The narrow and steep shelf, in particular during sea level low stands thus likely facilitated sediment delivery to the deep-water region of QDNB by either “catastrophically” remobilizing thick piles of sediment deposited near the shelf break in large mass transport events (resulting in the MTDs) and/or by high density fluid or gravity flow that would form the channel levee complexes in our study area.

Discussion About Factors Controlling MTD Emplacement

The regular pattern of at least three cyclic deposit systems in the study area (CDS, see Sect. 2.1 above and Fig. 2) emplaced since 0.78–1.8 Ma (mean value of age uncertainty is $\sim 1.29 \text{ Ma}$) suggests repeatedly recurring preconditioning factors facilitating large scale sediment remobilization events along the outer shelf/upper slope region of the western SCS offshore central Vietnam. Following MTDs emplacement an evolution from MTDs to channel leveed system is found to adapt to every cyclic deposit system.

We reconstruct a mean period of cyclic deposit systems of ~ 0.43 Million years (range of uncertainty from age constraints from well YC35-1-2 ~ 0.26 – 0.6 Ma). This value is similar to the period of eccentricity variation, 0.413 Ma (of ± 0.012), as the Milankovitch cycles. Although, large uncertainties in dating the MTDs in our study area remain, the apparent correlation allows for formulation of the hypothesis that there is a causal relationship between Pleistocene eustatic sea-level changes on the eccentricity cycle time-scales and formation of large MTDs and channel leveed systems in the Qiongdongnan Basin. However, we need more core data and better age constraints to prove this hypothesis.

Conclusion

Mass transport deposits (MTDs) were identified in Pleistocene sedimentary sequences of the upper-slope in southern deep-water region of the Qiongdongnan Basin, South China Sea. The high resolution deep-water 3D seismic data shows typical characteristics of MTDs such as mounded, hummocky, chaotic, low amplitude and discontinuous seismic reflection, and indicators such as margin, thrust faults and erosional grooves. Source of MTDs is inferred to be on the outer shelf/uppermost slope off the central coast of Vietnam. There, mountainous rivers transport a lot of terrigenous clastics from the highland of Vietnam into western area out of research area to form the steep and narrow shelf and upper slope, in particular during Pleistocene sea level low stands. The repeated occurrence of three cyclic deposit systems reveals that with evolutions from MTDs to channel leveed system is a regular pattern with periods of about 430 ka suggests that eccentricity scale sea level change is the most convincing governing factor controlling mode and pattern of sediment transport from the mountains regions to the Qiongdongnan Basin and emplacements of large scale MTDs.

Acknowledgments We acknowledge Dr. Yasuhiro Yamada for constructive comments, which greatly improve this manuscript. And we thank China National Petroleum Company and China National Offshore Oil Cooperation for their permissions to release the seismic and well data. This work was supported by the National Natural Science Foundation of China (40906028 and 91228208) and Strategic Priority Research Program of the Chinese Academy of Sciences XDA11030103.

References

- Bull S, Cartwright J, Huuse M (2009) A review of kinematic indicators from mass-transport complexes using 3D seismic data. *Mar Petrol Geol* 26:1132–1151
- Gee M, Gawthorpe R, Friedmann S (2006) Triggering and evolution of a giant landslide, offshore Angola revealed by 3D seismic stratigraphy and geomorphology. *J Sediment Res* 76:9–19
- Li ST, Lin CS, Zhang QM (1998) Dynamic process of episodic rifting in continental marginal basin and tectonic events since 10 Ma in South China Sea. *Chin Sci Bull* 43(8):797–810
- Moscardelli L, Wood LJ (2008) New classification system for mass transport complexes in offshore Trinidad. *Basin Res* 20:73–98
- Perov G, Bhattacharya JP (2011) Pleistocene shelf-margin delta: intradeltaic deformation and sediment bypass. Northern gulf of Mexico. *AAPG Bull* 95:1617–1641. doi:10.1306/01271109141
- Ru K, Pigott JD (1986) Episodic rifting and subsidence in the South China Sea. *AAPG Bull* 70(9):1136–1155

- Schimanski A, (2002) Holocene sedimentation on the Vietnamese shelf: from source to sink. PhD Dissertation, Christian Albrecht University, Kiel, Germany
- Sun QL, Wu SG, Lüdmann T, Wang B, Yang TT (2011) Geophysical evidence for cyclic sediment deposition on the southern slope of Qiongdongnan Basin. South China sea. *Mar Geophys Res* 32: 415–428
- Tung TT, Stive MJF, van de Graaff J (2008) Stabilization of tidal inlets along the central coast of Vietnam. COPEDEC VII, Dubai, UAE. Paper 190
- Wang D, Wu S, Dong D, Yao G, Cao Q (2009) Seismic characteristics of quaternary mass transport deposits in Qiongdongnan basin. *Mar Geol Quater Geol* 29(3):69–74
- Wang D, Wu S, Qin Z, Spence G, Lü F (2013) Seismic characteristics of the Huaguang mass transport deposits in the Qiongdongnan Basin. South China Sea: implications for regional tectonic activity. *Mar Geol* 346:165–182
- Yao GS, Yuan SQ, Wu SG, Zhong C (2008) The double provenance supply depositional model and its exploration prospect in the deep-water of Qiongdongnan Basin. *Petrol Explorat Dev* 35(6):685–691. doi:[10.1016/S1876-3804\(09\)60101-4](https://doi.org/10.1016/S1876-3804(09)60101-4)
- Yuan SQ, Wu SG, Lüdmann T, Yao GS, Lü FL, Cao F, Wang HR, Li L (2009) Fine-grained Pleistocene deepwater turbidite channel system on the slope of Qiongdongnan Basin, northern South China Sea. *Mar Petrol Geol* 26:1441–1451. doi:[10.1016/j.marpetgeo.2009.03.007](https://doi.org/10.1016/j.marpetgeo.2009.03.007)



Flank-Collapse on Ta'u Island, Samoan Archipelago: Timing and Hazard Implications

Shaun P. Williams, Tim R. Davies, Timothy T. Barrows, Matthew G. Jackson, Stanley R. Hart, and Jim W. Cole

Abstract

A discrepancy between the cartographic depiction of Ta'u Island, Samoan archipelago, in 1849 and its present geomorphology, leads to the impression that a massive collapse involving an estimated 30 km³ occurred on the island's southern flank less than 170 years ago. It is likely that this flank-collapse, whenever it occurred, generated a tsunami with regional impacts. Here we apply exposure dating to the remnant landslide scarp using the cosmogenic nuclide ³⁶Cl, to show that the flank-collapse occurred 22.4 ± 1.8 ka during the last glacial maximum (LGM). The collapse may have been triggered due to volcanic-related processes, but it is also possible that climatic-eustatic sea-level during the LGM may have played a role in influencing failure of the flank. We confirm that the initial cartographic depiction of Ta'u in 1849 was incorrect, and that this prehistoric landslide-tsunami was not a societal hazard at the time of its occurrence. This is because the Samoan and surrounding Island Nations were only inhabited about 3 ka or so. Nevertheless, we suggest that geomorphic features similar to the Ta'u flank-collapse on analogous islands and seamounts in the Pacific likely represent signatures of landslide-tsunamis in the past. We conclude that there is a need to identify and date other such features in the Pacific, in order to further improve our spatial and geochronological understanding of these events. There is also a need to identify flank features that have not yet failed, and assess the likely mechanisms that could potentially trigger failure. By doing this, we can start assessing with more confidence the hazard potential of similar flank-collapses in future—a risk that is presently under-represented.

Keywords

Flank-collapse • ³⁶Cl • Exposure dating • Samoa

S.P. Williams • T.R. Davies (✉) • J.W. Cole
Department of Geological Sciences, University of Canterbury,
Christchurch 8140, New Zealand
e-mail: shaun.williams@pg.canterbury.ac.nz; tim.davies@canterbury.ac.nz; jim.cole@canterbury.ac.nz

T.T. Barrows
University of Exeter, Geography, College of Life and Environmental
Sciences, Exeter EX4 4RJ, UK
e-mail: T.Barrows@exeter.ac.uk

M.G. Jackson
Department of Earth Science, University of California Santa Barbara,
Santa Barbara, CA 93160, USA
e-mail: jackson@geol.ucsb.edu

S.R. Hart
Department of Geology and Geophysics, Woods Hole Oceanographic
Institution, Woods Hole, MA 02543, USA
e-mail: shart@whoi.edu

Introduction and Background

Ta'u is the easternmost volcanic island in the Samoan archipelago, South Pacific, and lies within the Manu'a Group of American Samoa (Fig. 1a). It is the youngest island formed from the Samoan volcanic hotspot, which currently lies about 45 km to the East (Hart et al. 2000, 2004).

Geologically, it is in its shield-building stages of volcanism which commenced about 300 ka (Natland and Turner 1985; Hart et al. 2004; Koppers et al. 2008). However, the nature of the 1866–1867 submarine eruption of Pomasame volcanic cones reported in Turner (1889), is not well understood (Williams 2009). These cones were mapped during surveys reported in Fenner et al. (2008), and lie about 2 km

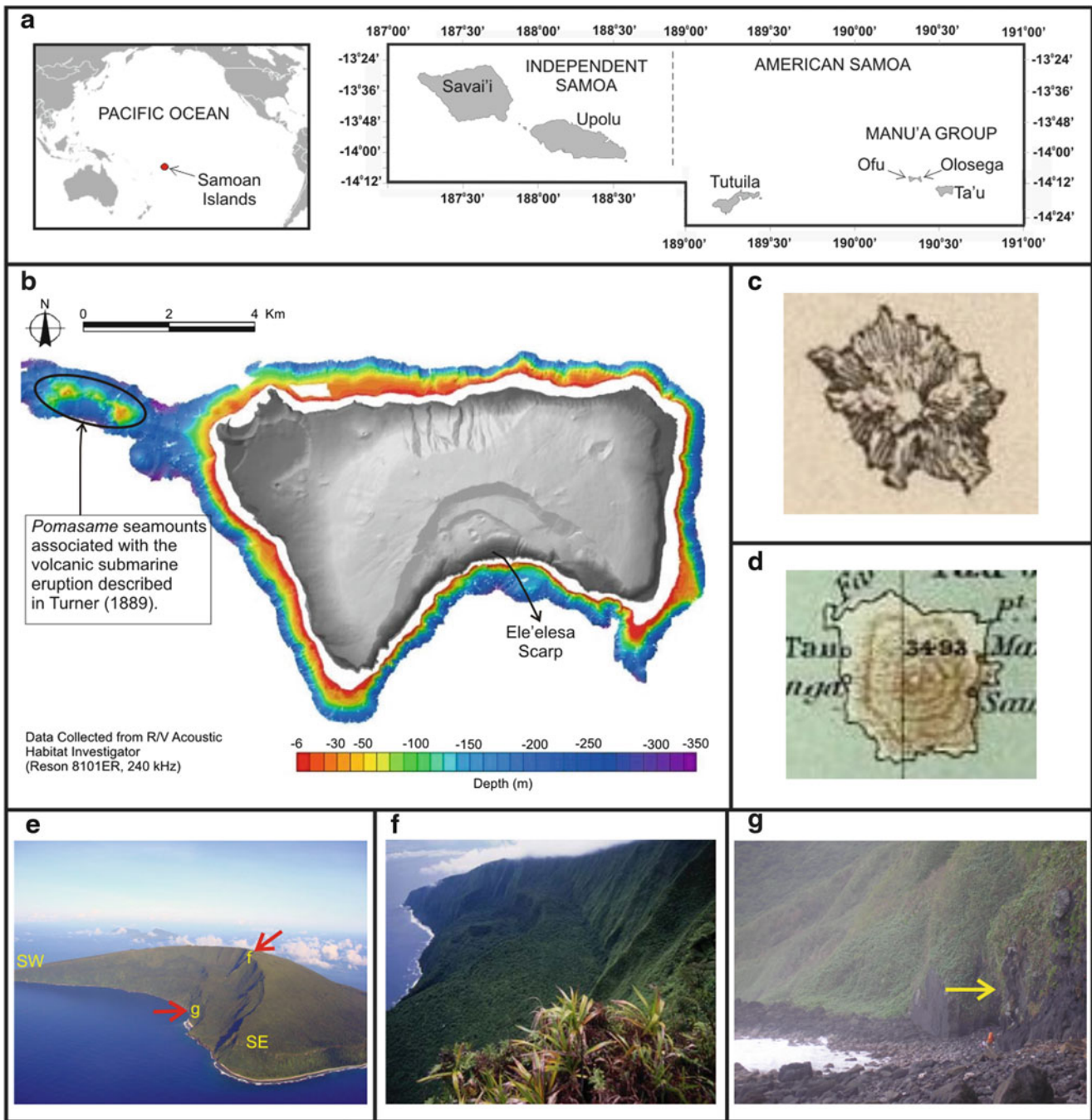


Fig. 1 (a) Location of the Samoan Islands (b) Ta'u Island and offshore bathymetry (Map source: American Samoa Department of Wildlife and Conservation) (c) Depiction of Ta'u in Wilkes (1849) based on 2 days of survey data collection in October 1839 (d) Depiction of Ta'u in

Turner (1889) based on survey data of Wilkes (1849) (e) South flank of Ta'u (Photo by Michael Tenant) (f) Summit (~925 m), view looking west (Photo by Mark Rauzon) (g) Sampled outcrop in this study

NW of Ta'u along the submarine ridge connecting it to neighbouring Ofu and Olosega islands (Fig. 1b).

The southern flank of Ta'u exhibits a series of down-faulted benches which are likely remnants of a large-scale flank-collapse involving an estimated 30 km³ (Williams 2009; Williams et al. 2012). Further, it was recognized that

this flank-collapse could have occurred more recently than the year 1839 (Williams 2005, 2009; Williams et al. 2012); although there was little tsunami evidence in the historical record to suggest it did (NGDC 2010).

The likelihood of a recent historical collapse stemmed from the cartographic depiction of Ta'u in Wilkes (1849)

Table 1 Site data

Sample (field code)	Longitude (°W)	Latitude (°S)	Altitude (m)	Horizon correction	Thickness (cm) ^a
TAVI-06	169°26'50	14°14'56	8	0.50	5.5

^a $\rho = 3.0 \text{ g cm}^{-3}$; $\Lambda = 160 \text{ g cm}^{-1}$

Table 2 Major element data (wt.%)

SiO ₂	Al ₂ O ₃	Fe ₂ O ₃	TiO ₂	MgO	MnO	CaO	K ₂ O	Na ₂ O	P ₂ O ₅
50.74 ± 0.31	13.11 ± 0.14	9.91 ± 0.09	3.69 ± 0.10	6.39 ± 0.05	0.14 ± 0.004	12.47 ± 0.12	0.78 ± 0.03	2.63 ± 0.30	0.04 ± 0.001

Table 3 Trace element data (ppm)

[B] ^a	[Cl]	[Sm]	[Gd]	[Th]	[U]	Cross section (10 ⁻³ cm ² g ⁻¹)
5.0 ± 2.0	54.4 ± 1.2	7.62 ± 0.04	7.44 ± 0.07	3.23 ± 0.10	0.72 ± 0.02	7.84 ± 0.10

^aEstimated from similar rocks

and Turner (1889) (Fig. 1c, d). The island was depicted as having a much more symmetrical geomorphic structure than its present day planform (Williams 2009; Williams et al. 2012) (Fig. 1e, f). Further, the depictions were based on the initial survey data of Ta'u collected on October 8–10, 1839, and the island was described as having the form of a regular dome (Dana 1849; Wilkes 1849; Turner 1889).

Geomorphic interpretations in Williams (2009) and Williams et al. (2012), suggested that the collapse occurred after the LGM sea-level low-stand, which was assumed to have been ~18 ka. The estimated volume of material that would have collapsed based on the Ta'u depiction in Turner (1889) was about 30 km³, and would have most likely generated a tsunami with regional impacts.

Conservative numerical modeling of the likely event in Williams et al. (2012) strengthens this landslide- tsunami hypothesis. However, it was suggested that if the event was younger than 1839, the impacts of the tsunami would not have gone unnoticed by local inhabitants. The absence of any such event occurring within recorded history (both written and oral), led to the suggestion that the event was much older than 1839, and that the depiction of Ta'u in Wilkes (1849) was incorrect.

Here we investigate this hypothesis. We use ³⁶Cl cosmogenic surface exposure dating of a basalt sample obtained from the Ele'elesa scarp to infer the likely age of the collapse. We discuss the implications of the result with respect to the depiction of Ta'u in Wilkes (1849), as well as to the associated geo-climatic context of collapse occurrence. The nature and implications of the event in a regional hazard and risk context are also considered.

Methods and Results

Field Sampling

A basalt sample was obtained from a massive outcrop on the Ele'elesa scarp (Table 1 and Fig. 1g), which is the lower expression of the collapsed block mass that formed the south flank benches.

³⁶Cl Cosmogenic Surface Exposure Dating

The extraction of ³⁶Cl was undertaken at the Exeter Cosmogenic Nuclide Laboratory at the University of Exeter. Total ³⁶Cl was measured on the whole rock because the fine-grained nature prevented effective mineral separation. The concentrations of major target elements for ³⁶Cl production were determined using X-ray fluorescence. The concentrations of trace elements with large neutron capture cross sections (Gd, and Sm) and neutron-producing elements (U and Th) were measured by inductively-coupled plasma mass spectrometry. Chlorine content was determined by isotope dilution. The isotopic ratio of ³⁶Cl/Cl was measured by accelerator mass spectrometry on the 14UD accelerator at the Australian National University (Fifield et al. 2010). Major and trace element abundances and neutron capture cross sections are listed in Tables 2 and 3.

The ³⁶Cl exposure age was calculated as detailed in Barrows et al. (2013) (Table 4). The production rate was scaled using the scheme of Stone (2000). All analytical

Table 4 ^{36}Cl exposure ages

Field code	Lab code	$[^{36}\text{Cl}]_c$ ($\times 10^4 \text{ g}^{-1}$) ^a	$[^{36}\text{Cl}]_r$ ($\times 10^3 \text{ g}^{-1}$) ^b	Exposure age (ka)
TAVI-06	ANU-225-19	5.84 ± 0.435	4.88 ± 0.19	22.4 ± 1.8

Data are normalised to the GEC standard ($^{36}\text{Cl}/\text{Cl} = 444 \times 10^{-15}$). Carrier $^{36}\text{Cl}/\text{Cl} = <1 \times 10^{-15}$. ^{36}Cl decay constant $2.3 \times 10^{-6} \text{ year}^{-1}$

^aC = cosmogenic component

^bR = nucleogenic component

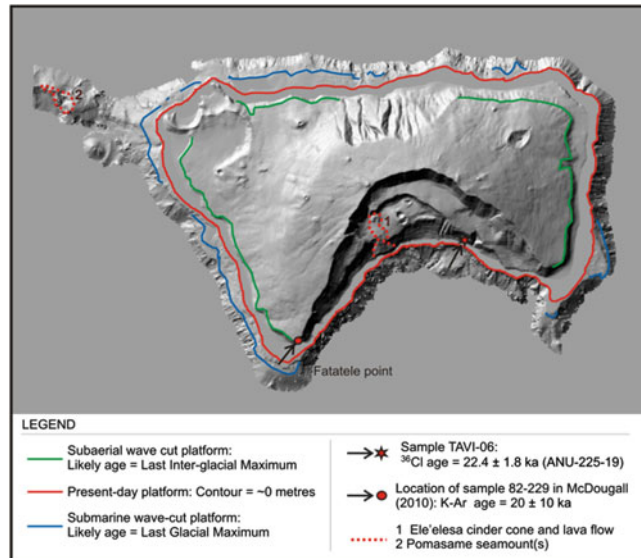


Fig. 2 Digital elevation model of Ta'u showing locations of reported ages and geomorphic features (DEM data obtained from the National Park of American Samoa)

errors are fully propagated, and the age in the text is reported at one standard deviation (68 % probability).

Discussion and Interpretations

Timing of Collapse

The ^{36}Cl exposure age was calculated at $22.4 \pm 1.8 \text{ ka}$ and is interpreted to be indicative of the timing at which the scarp was first exposed to cosmic rays after flank collapse. This assumption is based on the location of the sample relative to the implied collapsed-mass deduced from Wilkes (1849) (Fig. 2). If the collapse was younger than 1839, then the scarp which the sample was obtained would have only recently been exposed to cosmic rays. That is, it is likely to have been less than a few hundred years old or so.

The calculated exposure age of $22.4 \pm 1.8 \text{ ka}$ is unambiguously much older than 1839. This implies that there is a 68 % probability that collapse occurred between 24.2 and 20.6 ka, likely corroborating the suggestion in Williams et al. (2012) that the initial depiction of Ta'u in Wilkes (1849) could have been incorrect.

The proposed maximum relative collapse age of $\sim 18 \text{ ka}$ in Williams et al. (2012), was suggested based on geomorphic

indicators. Subaerial and submarine wave-cut platforms assumed to represent the last interglacial and glacial sea-level high- and low-stands, respectively, are both absent on the southern flank. It was thus inferred that the collapse occurred after the formation of the more recent submarine wave-cut platform; which may have formed during the LGM-associated sea-level low-stand.

The timing of the collapse is also associated with the K-Ar age of a basalt sample (Sample Lab Code 82-229), collected from the densest part of the least weathered lava flow from the southwest coast at Fatatele point reported in McDougall (2010). An age of $20 \pm 10 \text{ ka}$ at one standard deviation was obtained for the sample. This indicates that the island was volcanically active around that time; which was interpreted to be pre-collapse in age.

Nature of Collapse

The association of the collapse with the timing of the LGM is interesting. The LGM is the most recent period in Earth history characterised by global ice-sheet maxima and sea-level and temperature minima (Lambeck et al. 2001; Clark et al. 2009).

Paradoxically, it is generally accepted that large-scale volcanic flank collapses typically occurred during (or associated with the onset of), warmer, wetter, interglacial period climates and rising sea-levels (McMurty et al. 2003; McGuire 2012).

However, McGuire (2012) cautioned that this acceptance does not dismiss the likelihood of collapses occurring during colder, drier climates and lower (or rapidly falling) sea-levels. He suggested that a sudden reduction of the buttressing effect as huge volumes of water were removed from the flanks of a volcano could favour collapse. Rapid changes between cold and dry to warm and wet climates, and vice-versa, were also suggested to have an effect on rapid sea-level changes which in turn would increase collapse potential. This process though is ambiguous, because there is little evidence to suggest a distinct association between rapid climatic-eustatic sea level changes and their influence on collapse behaviour.

Nevertheless, the interpretation here that the Ta'u collapse occurred after sea-level reached its minimum at this site likely suggests that it occurred during the onset of warmer climates and rising sea-level; even though post-LGM sea-level rise is thought to have only commenced about 16 ka (Lambeck et al. 2001). Further investigation is needed to resolve this enigma.

The likelihood of the collapse being triggered by an earthquake was investigated in Williams (2009). It was suggested that the potential for collapse being triggered by an earthquake with similar peak ground accelerations (0.4 g) to those in Samoa's seismic history was low. However, this interpretation did not account for the long-term effects of earthquakes experienced over geologic time. Further investigation is needed to understand the likely long-term seismic influence on collapse potential.

In Williams et al. (2012), it was suggested that the lava flows from the intra-caldera cinder cone which flow over the Ele'elesa scarp were possibly indicative of an association between the eruption and the collapse. Although this could be the case, it is also likely that the eruption could be much younger. In the absence of a geochronological age for this eruption, an association between the two cannot be stated definitively.

Conversely, the collapse age is associated with the timing of likely active volcanism in the area reported in McDougall (2010). His suggestion that the timing of this volcanism was pre-collapse in age is also likely; implying that volcanic-related processes may have been associated with triggering the collapse. However, the large uncertainty of ± 10 ka for the age of this volcanism limits a definite association with the ^{36}Cl collapse age reported here.

Conclusions and Hazard Implications

We interpret the ^{36}Cl surface exposure age of 22.4 ± 1.8 ka to be indicative of the age of the Ta'u flank collapse. Further, we surmise that the depiction of Ta'u as a complete edifice in Wilkes (1849) was incorrect. It is likely that the time spent in the field surveying the Manu'a Group in October 1839 was most likely insufficient to gather accurate data from Ta'u, leading to the inaccuracies in its depiction.

Current available geochronological and geomorphic evidence in Williams (2009), McDougall (2010), Williams et al. (2012) and this study, suggests that a volcanic-related mechanism is likely to have been responsible for triggering the collapse. Dating the upper and adjacent scarps as well as the Ele'elesa cinder cone flow would aid in elucidating this dilemma.

Whilst we recognise that climatic-eustatic conditions during the LGM may have played a role in influencing flank failure, the potential for these processes to trigger collapse is not well understood. More investigation is needed to understand, verify, or dismiss the likely associations.

The landslide-tsunami associated with the collapse modelled in Williams (2009) and Williams et al. (2012), is confirmed to not have been a hazard at the time of its occurrence. This is because the Samoan and surrounding Island Nations were first inhabited about 3 ka or so (Petchev 2001; Bedford and Sand 2007).

Nevertheless, evidence of likely active volcanism associated with the timing of the collapse (McDougall 2010; Williams et al. 2012), coupled with the recent eruption of the Pomasame submarine cones in 1866–1867 (Turner 1889), imply that volcanism could presently be in a temporary state of quiescence. Thus there may be a present and future eruptive hazard. Coupled with the understanding that large-scale flank-collapses typically occurred (or tend to occur) during warmer, wetter, interglacial climates comparable to present and projected conditions (McGuire 2012), the likelihood of a future collapse exists.

Further, there is a possibility that the northern flank could undergo similar large-scale collapse and generate a tsunami with likely regional impacts. More investigation is needed to understand the nature, likelihood, and hazard implications of such an event occurring in future.

Further, we suggest that the Ta'u flank-collapse represents similar processes in comparable volcanic settings. We propose that analogous geomorphic features on other volcanic islands and seamounts in the Pacific likely represent forensic signatures of landslide-tsunamis in the past. We conclude that there is a need to identify and date such features, in order to further our spatial and temporal understanding of these processes. The need to identify flank features that have not yet failed and assess the likely mechanisms that could potentially trigger failure is important. This would enable more confidence in interpreting the hazard potential of similar flank-collapses in future—a risk presently under-represented.

Acknowledgments We thank Rhea Workman for her help in the initial conception of this study. We also thank Leilua Mase Akapo, Peter Craig, Rise Hart, Paul Brown, Leoso Leoso, Dino Ta'aga, Tavale Ta'aga, Ionatana Lealamanu'a, Koli Maeata, Douglas Fenner, Anekant Wandres, Janet Warburton, John Southward, Pat Roberts, Joan Williams, Jim Williams, Cathy Higgins, and Alison Green for their help and advice regarding field logistics in 2008. The National Park of American Samoa is also thanked for permitting us to conduct research in the Ta'u National Park.

The field component of this study was funded in 2008 by NZAID and the Mason Trust, University of Canterbury. The exposure dating was implemented via collaboration between the Department of Geological Sciences, University of Canterbury, and Geography, University of Exeter.

References

- Barrows TT, Almond P, Rose R, Fifield LK, Mills S, Tims SG (2013) Late Pleistocene glacial stratigraphy of the Kumara-Moana region, West Coast of South Island, New Zealand. *Quaternary Science Reviews* 74:139–159
- Bedford S, Sand C, (2007) Lapita and Western Pacific Settlement: Progress, prospects and persistent problems. In: Bedford S, Sand C, Connaughton S P (eds) *Oceanic explorations: Lapita and Western Pacific Settlement*, Terra Australis 26. The Australian National University E Press, Canberra. ISBN 9781921313332. pp 1–15

- Clark PU, Dyke AS, Shakun JD, Carlson AE, Clark J, Wohlfarth B, Mitrovica JX, Hostetler SW, McCabe AM (2009) The last glacial maximum. *Science* 325:710–714
- Dana JD (1849) United states exploring expedition during the years 1838-1842 under the command of Charles Wilkes U.S.N., Vol X, geology. United States Navy, Philadelphia, pp 307–336
- Fenner D, Speicher M, Gulick S, et al. (2008) The state of coral reef ecosystems of American Samoa. In: Waddell JE, Clarke AM (eds). The state of coral reef ecosystems of the United States and Pacific freely associated states: 2008, NOAA Technical Memorandum NOS NCCOS 73. NOAA/NCCOS center for coastal monitoring and assessment's biogeography team, Silver Spring, MD. pp 307–351
- Fifield LK, Tims SG, Fujioka T, Hoo WT, Everett SE (2010) Accelerator mass spectrometry with the 14UD accelerator at the Australian National University. *Nucl Instrum Meth Phys Res B* 268:858–862
- Hart SR, Staudigel H, Koppers AP, Blusztajn J, Baker ET, Workman R, Jackson M, Hauri E, Kurz M, Sims K, Fornari D, Saal A, Lyons S (2000) Vailulu'u undersea volcano: the new Samoa. *Geochem Geophys Geosyst* 1(2000GC000108):13
- Hart SR, Coetzee M, Workman RK, Blusztajn J, Johnson KTM, Sinton JM, Steinberger B, Hawkins JW (2004) Genesis of the Western Samoa seamount province: age, geochemical fingerprint and tectonics. *Earth Planet Sci Lett* 227:37–56
- Koppers AAP, Russell JA, Jackson M, Staudigel H, Konter J, Hart SR (2008) Samoa reinstated as a primary hotspot trail. *Geology* 36(6):435–438
- Lambeck K, Yokoyama Y, Purcell T (2001) Into and out of the last glacial maximum: sea-level change during oxygen isotope stages 3 and 2. *Quater Sci Rev* 21:343–360
- McDougall I (2010) Age of volcanism and its migration in the Samoa Islands. *Geol Mag* 147(5):705–717
- McGuire B (2012) Waking the giant: how a changing climate triggers earthquakes, tsunamis, and volcanoes. Oxford University Press, Oxford, p 318. ISBN 9780199592265
- McMurtry GM, Watts P, Fryer GJ, Smith JR, Imamura F (2003) Giant landslides, mega tsunamis, and paleo-sea level in the Hawaiian Islands. *Mar Geol* 203(2004):219–233. doi:10.1016/S0025-3227(03)00306-2
- Natland JH, Turner DL (1985) Age progression and petrological development of Samoan shield volcanoes: evidence from K-Ar ages, lava compositions and mineral studies. In: Brocker TM (ed) Geological investigations of the northern Melanesian borderland: Houston, Texas, Council for Energy and Mineral Resources, Circum-Pacific Council for Energy and Mineral Resources Earth Science Series. 3: 139–172
- NGDC and ITIC (2010) TsuDig WDC-MGG Historical Tsunami GIS version 0.5 beta, March 2010. National Geophysical Data Center and The International Tsunami Information Center, A UNESCO/IOC – NOAA Partnership. CD ROM
- Petchey FJ (2001) Radiocarbon determinations from the Mulifanua Lapita site, Upolu, Western Samoa. *Radiocarbon* 43(1):63–68
- Stone JO (2000) Air pressure and cosmogenic isotope production. *J Geophys Res* 105:23753–23759
- Turner GA (1889) Samoa. *Scottish Geograph Mag* 5:235–256
- Wilkes C (1849) Narrative of the United States exploring expedition during the years 1838-1842, vol I. United States Navy, Philadelphia, USA
- Williams S (2005). Ta'u through the Hourglass: an alternative look. Enduring resources earth science education, Earthref.org. URL: <http://earthref.org/ERESE/projects/ALIA/reports/report-taumorphology.htm>. Last Accessed 21 Aug 2013
- Williams SP (2009) Ocean-island flank collapse on the south of Ta'u, Manu'a Group, Samoa Islands: Implications for risk management. MSc Thesis, Department of Geological Sciences, University of Canterbury, Christchurch, New Zealand p 129 URL: <http://hdl.handle.net/10092/3784>
- Williams S, Davies T, Cole J (2012) Catastrophic flank collapse on Ta'u Island and subsequent tsunami: Has this occurred during the last 170 years. *Sci Tsunami Hazard* 31(3):178–198



The 1977 Gioia Tauro Harbour (South Tyrrhenian Sea, Italy) Landslide-Tsunami: Numerical Simulation

Filippo Zaniboni, Alberto Armigliato, Katharina Elsen, Gianluca Pagnoni, and Stefano Tinti

Abstract

On July 12th, 1977, waves 5 m high hit the harbour of Gioia Tauro, provoking relevant damages on facilities and infrastructures, but fortunately no casualties. The source was supposed to be a submarine mass failure, ranging 5 million m³ and occurring in very shallow water at the heads of a canyon just in front of the port. The sliding mass cut a cable at 600 m depth, meaning that it travelled more than 15 km far from the source. In this work we reconstruct the hypothesized mass failure, compute the slide dynamics and simulate the generated tsunami through numerical modelling. The results obtained fit well with the observations, strengthening the hypothesis of such a landslide as the source for the 1977 tsunami. This event can be considered as paradigmatic of a category of coastal hazards: small submarine landslides occurring close to populated coasts may pose considerable risk, even if only at a local scale.

Keywords

Submarine landslides • Numerical modelling • Landslide tsunami

Introduction

Small landslides along continental margins are very frequent, due to continuous supply of sedimentary material to the submerged slopes, that can be mobilized by seismic shaking or simply by gravitational instability. The tsunami generated by these events, even if unlikely to produce effects on the regional scale, need particular attention when assessing hazard at the local scale.

In the Mediterranean Sea one can find many near-shore areas with steep submarine slopes incised by canyons. The margins of the Balearic Sea, the coasts of Sardinia and Corsica, the Ligurian Sea, southern Tyrrhenian Sea, the Ionian Sea, the slopes along the Hellenic Arc are the most

known, and many potentially tsunamigenic occurrences have been identified here (see Papadopoulos et al. 2007; Camerlenghi et al. 2010).

One of the most known and significant events of this kind was the 1979 Nice slide (France), in the Ligurian Sea, where a part of the harbour still in construction, close to the Nice international airport, slid into the sea as a consequence of a submarine collapse at its foot: a tsunami was generated, provoking huge damages to infrastructures, seven victims among the workers in the construction site and probably 1 casualty in Antibes-La Salis, 10 km far from the source, where waves 3.5 m high were observed and the sea penetrated 150 m inland (Assier-Rzadkiewicz et al. 2000; Sahal and Lemahieu 2011).

In this paper we study a similar event that took place in Gioia Tauro (southern Tyrrhenian Sea, Italy, see map in Fig. 1), where on July 12th, 1977, after a 2–3 m sea withdrawal, a 5 m tsunami hit the western dock of the harbour and provoked conspicuous damages.

It was immediately clear that sea waves were associated neither with stormy weather nor with seismic shaking, and

F. Zaniboni (✉) • A. Armigliato • K. Elsen • G. Pagnoni • S. Tinti
Dipartimento di Fisica e Astronomia, Università di Bologna, viale
Carlo Berti Pichat 6/2, Bologna 40127, Italy
e-mail: filippo.zaniboni@unibo.it; alberto.armigliato@unibo.it;
katharina.elsen2@unibo.it; gianluca.pagnoni3@unibo.it; stefano.tinti@unibo.it

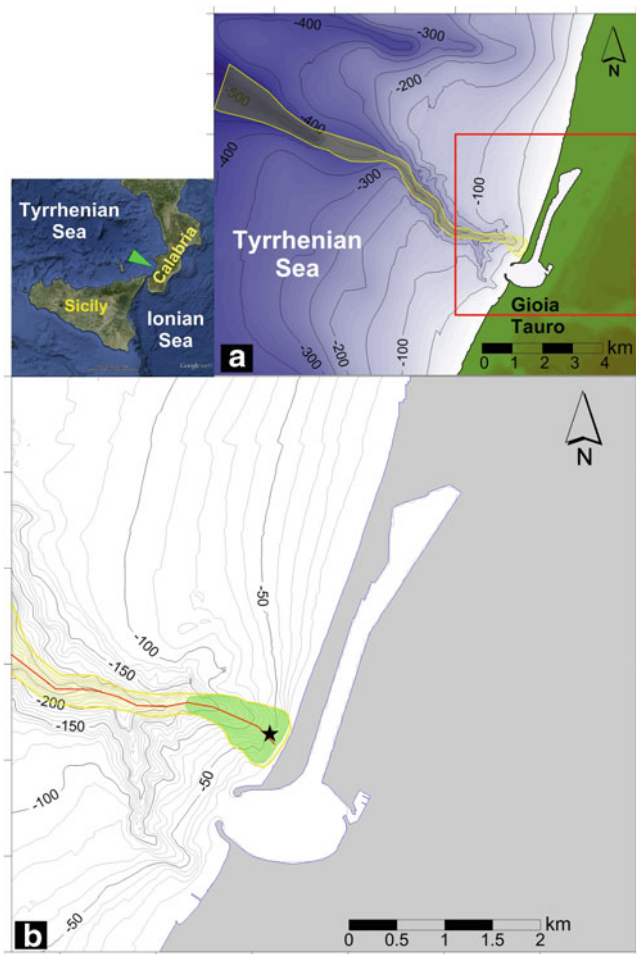


Fig. 1 Map of the investigated area. Panel **a** shows the bathymetry offshore Gioia Tauro partly including the canyon. The *yellow* contour encloses the surface swept by the mass flow. Panel **b** focuses on the Gioia Tauro harbour (*red square* in panel **a**): the green area is the footprint of the reconstructed sliding mass, following the hypothesis by Colantoni et al. (1992) who place the upper part where the *black star* is located. The *red line* marks the trajectory of the centre of mass of the elements forming the slide

detailed morpho-bathymetry surveys were undertaken soon after the event to search for evidences of underwater mass mobilization. The main target of the survey was the Gioia Tauro canyon, whose head is located just in front of the port entrance, at about 10–15 m depth (Fig. 1, panel a) and that elongates down to 700 m depth to a distance of more than 15 km from the coast.

The results of the surveys evidenced a lack of mass of about 5.5 million m^3 just at the head of the canyon (Fig. 1, panel b, evidenced by the black star): this feature was associated with the generation of the tsunami (Colantoni et al. 1992). The dislocated mass evolved into a turbidity current that flew along the canyon and cut a cable at about 600 m depth, 14–15 km far from the coast, 52 min after the

slide motion started: a mean velocity of about 15–17 km/h was then inferred (Colantoni et al. 1992).

Numerical Methods

Following a strategy repeatedly applied by some of the authors (for example in Lo Iacono et al. 2012; Zaniboni et al. 2013) to study tsunamis induced by landslides, the first step of the analysis is the reconstruction of the sliding mass and the simulation of its motion. The second step is the computation of the impulses imparted by the moving mass to the ocean, and the final step is the simulation of the tsunami propagation.

The motion of the mass is computed via the code UBO-BLOCK1, created and maintained by the University of Bologna tsunami research team (Tinti et al. 1997). It implements a Lagrangian approach to landslide modelling, splitting the sliding mass into a “chain” of interacting blocks, with centre of mass (CoM) moving along a predefined trajectory (Fig. 1, panel b). All the forces acting on the blocks are projected along this path: the equations are solved numerically. The blocks are allowed to change shape, but do conserve their volume, and cannot separate from each other. The code needs as input the undisturbed sliding surface, the upper surface of the sliding body, the CoM path and the lateral boundaries controlling slide spreading during the motion. It is worth pointing out that the partition blocks are not real physical blocks but numerical discretization blocks that can represent a vast range of rheology from rigid body dynamics to fluid like flows like turbidity currents, by changing parameters accounting for the block-block interaction.

The impulses imparted by the slide to the sea are computed by an intermediate code, UBO-TSUIMP, that maps the Lagrangian grid of the code UBO-BLOCK1 into the Eulerian grid of the tsunami propagation code. Further UBO-TSUIMP accounts for transferring the mass flow impulse from the sea floor to the sea surface by filtering wavelengths much shorter than the sea depth.

The tsunami propagation is simulated by solving the non-linear Navier-Stokes equations in the shallow water approximation, with the slide impulse introduced as a forcing term. The numerical computation is performed by the code UBO-TSUFD, developed by the same tsunami research team, adopting a finite difference resolution scheme with a staggered-grid technique. Though the code can be used on a system of nested different-resolution grids, it was applied in this study only on a single grid domain. Some examples of the applications of such codes, with further details on the landslide and tsunami modelling, can be seen in Tinti et al. (2011), Tonini et al. (2011), Zaniboni et al. (2013).

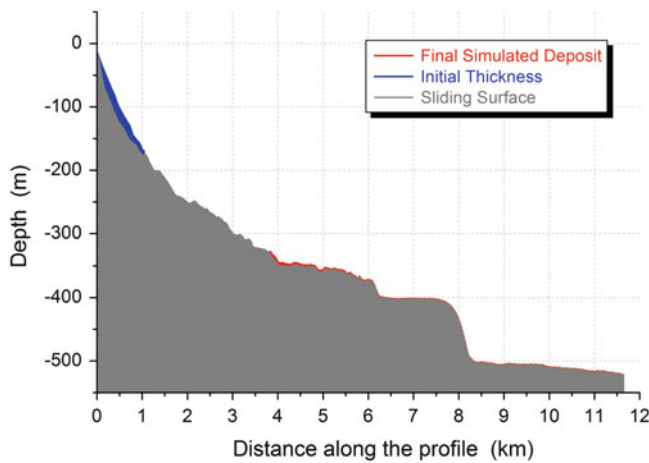


Fig. 2 Profiles of the sliding surface (grey), of the initial sliding mass (blue) and of the simulated final deposit (red), sliced along the CoM trajectory (red line in Fig. 1, panel b)

Data Elaboration

The bathymetry of the Gioia Tauro canyon has been reconstructed by digitizing maps found in Colantoni et al. (1992): the integration of them with GEBCO and SRTM databases allowed us to realize a regularly-spaced computational grid, with 40 m step, covering also the harbour of Gioia Tauro and the adjacent coastline, providing the input to UBO-TSUFDF for the computation of the tsunami propagation and inland inundation.

As concerns the input for the mass flow code, the sliding surface was simply obtained by the reconstructed bathymetry, delimiting the lateral spreading of the slide motion as shown in Fig. 1, panel a, by the yellow boundary. The initial sliding mass (green area in Fig. 1, panel b) has been reconstructed following suggestions found in Colantoni et al. (1992): its upper part is found in correspondence of the black star of Fig. 1 (panel b), and it extends along the canyon down to about 200 m depth. As visible in Fig. 2, the initial mass is relatively thin: the reconstructed volume is about 5.7 million m^3 , fully compatible with Colantoni et al. (1992) analysis, over an area of 0.4 km^2 , for a mean thickness of about 14 m. The predefined CoM follows the maximum local slope, mainly on the canyon bottom.

Landslide Numerical Simulation

The application of UBO-BLOCK1 provides the complete dynamics of the sliding mass, accounting also for its shape changes, relevant for the evaluation of the tsunami impulse.

The simulation shows that the front block reaches the end of the computational domain, at about 500 m depth, almost

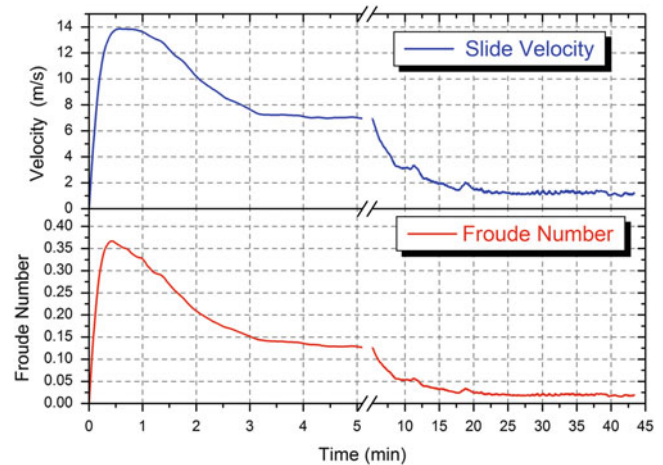


Fig. 3 Velocity (upper graph) and Froude number (lower graph) vs. time. The slide velocity is intended as the average, at each time step, among the velocities of the individual CoM. The same stands for the Froude number. Notice the break of the time axis at about 5 min, with a zoomed scale on the left to better represent the initial features of the motion

12 km far from the source (Fig. 2), after about 43 min, spreading and reducing considerably its mean thickness at about 1 m. Here the computation is stopped, even if a residual mean velocity (over 1 m/s) characterizes the slide (Fig. 3), meaning that the mass would continue its motion towards deeper sea bottom.

The dynamics of the slide is characterized by an initial high acceleration phase, the mass reaching 14 m/s (over 40 km/h) within 1 min, corresponding to the peak of the Froude number computation (Fig. 3). This is obtained by the ratio between the horizontal component of the slide velocity and the phase velocity of the tsunami (namely \sqrt{gh} , with g gravity acceleration and h sea depth), and indicates the coupling between the two motions: the closer is its value to 1, the more efficient is the energy transfer from the slide to the tsunami. In this case the maximum value of the Froude number occurs after about 30 s, in correspondence of the peak of velocity, then the value diminishes both because of the decreasing velocity and due to the increasing sea depth.

In summary, the motion duration is about 2,600 s, and the distance covered almost 12 km: the mean velocity turns out to be 4.6 m/s (i.e. around 17 km/h), fully compatible with the analysis made in Colantoni et al. (1992).

Tsunami Propagation

After the simulation of the sliding motion, the tsunamigenic impulse is evaluated and provided to UBO-TSUFDF as the forcing term causing the perturbation of the sea surface. The simulation of the propagating tsunami is performed over the

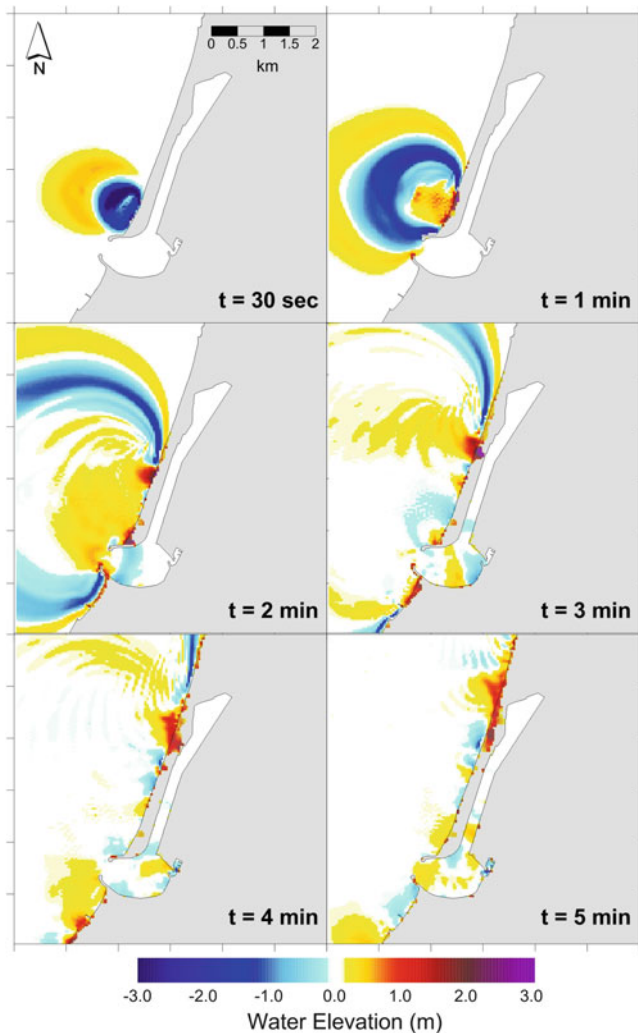


Fig. 4 Tsunami propagation over the computational domain comprehending the Gioia Tauro harbour and surrounding coasts. Positive signals, meaning sea level growth, are marked by the yellow-red scale, negative signals, meaning sea withdrawal, with the cyan-blue scale

computational domain covering the harbour of Gioia Tauro and areas around.

The propagation sketches, reported in Fig. 4, show that the tsunami takes less than 1 min to reach the narrow strip of land enclosing the harbour. The first evidence is a strong sea lowering by at least 2 m, well visible in the $t = 30$ s sketch, while a positive front spreads towards the open sea. After around 1 min, the area that was affected by the sea retreat experiments a positive arrival at least 2 m high, while the negative perturbation reaches the entrance of the port in the south. To the north, the negative signal is preceded by a

small positive wave, coming from the faster, circular propagation of the tsunami towards the open sea. The subsequent sketches evidence many interesting features. Outside the harbour, to the north, it is possible to notice the formation of a sequence of positive-negative oscillations, which are trapped waves due to the interaction between the wave and the coast. With increasing distance from the source, the tsunami hits the coast with an almost parallel front. Moreover, in the northern part of the land strip separating the harbour basing from the sea, the tsunami penetrates inland, due to the lower topography in this zone, and reaches also the inner part of the harbour, with waves exceeding 3 m.

The tsunami propagates inside the harbour only after 2–3 min, losing strength due to protection given by the southern part of the land strip, 5–6 m high. In the $t = 5$ min sketch one can observe the northward propagation of a small tsunami wave along the inner basin.

Virtual marigrams are shown in Fig. 5, computed over the point outside (1, 2) and inside (3–6) the inner basin of the Gioia Tauro harbour.

Marigrams 1 and 2 confirm what was observed from the propagation sketches in Fig. 4, i.e. the first negative signal hitting the coast, with sea retreat of more than 2 m: notice that this is in full agreement with the few observations available and reported in Colantoni et al. (1992). After this, further oscillations of minor entity are observed for at least 30 min.

When entering the inner basin (point 3), a strong negative first signal (almost 1 m) is again observed, around 2 min after slide initiation, followed by a long series of oscillations. This is observed for all the other inner marigrams, with the first signal reducing when moving inside the basin, but oscillations amplifying considerably. This is due to the large number of reflections inside the harbour, and to resonance phenomena: narrow-mouthed basins communicating with the sea are characterized by standing oscillations, which dominant frequency is known as Helmholtz mode and is typical of harbours and fjords, that can contribute to intensify considerably the effects of the tsunami. After 30 min, indeed, oscillations of more than 1 m peak-to-peak are still visible in marigrams 4, 5 and 6, accounting for this effect and constituting a serious problem for boats and infrastructures inside the harbour. Also the frequency of such perturbation appears to very stable, around 2 min, that is a typical period of resonance of small, enclosed basins (Bressan et al. 2013).

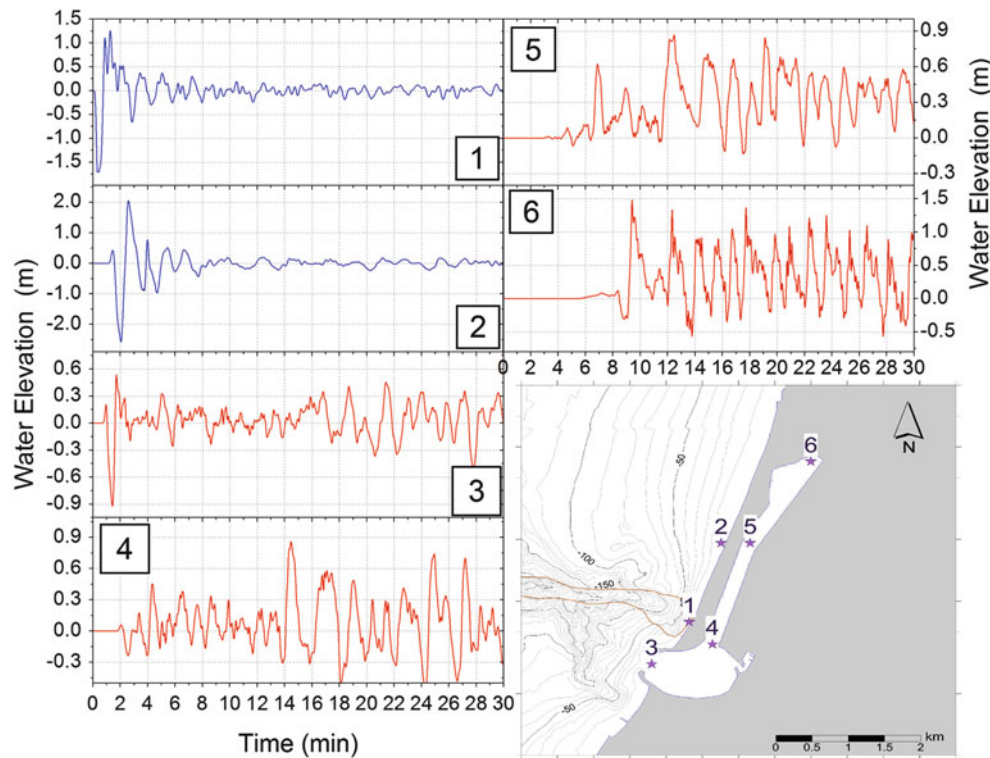


Fig. 5 Virtual marigrams (in blue the ones outside of the harbour, in red the ones located inside) computed in six nodes of the computational grid

Discussion and Conclusions

The July 12th, 1977 tsunami in the harbour of Gioia Tauro is a case of a tsunamigenic mass flow that was not given too much attention by modern research. Though, it represents a known documented proof that small landslides can generate relevant damages (and also casualties) on a local scale.

In this study we have investigated the hypothesis that the tsunami was produced by a 5.5 million m^3 mass that detached from the head of the Gioia Tauro canyon, rapidly evolved into a turbidity current and flowed to deep water (a cable at 600 m depth was cut about 50 min after the mass started to fail).

The slide motion has been computed via the code UBO-BLOCK1, providing the tsunamigenic impulse for the propagation of the tsunami, simulated through the finite difference code UBO-TSUFD. The computational grid, 40 m regularly-spaced, encloses the area of the Gioia Tauro harbour.

The simulated slide dynamics shows good agreement with the observations: the mass exits the computational domain, at 500 m sea depth, after about 43 min, with a mean velocity of about 17 km/h. The maximum velocity, over 40 km/h, is attained after around 30 s, corresponding to the most tsunamigenic phase.

The generated tsunami manifests through a negative first signal hitting the coast 30 s after the beginning of the sliding motion. A train of oscillations propagates northward, reaching over 3 m elevations in the northern part of the land strip protecting the harbour from the sea, where the water penetrates inland for tens of meters. The perturbation enters the inner basin after 1 min, but continues to affect it for over 30 min, with a long series of oscillations with 2 min period. This feature is explained by the fact that tsunami loses energy slowly through the narrow harbour mouth, and that the harbour behaves as a resonator amplifying selectively the frequencies corresponding to its proper modes of oscillation, and mostly the Helmholtz mode.

Further, it was also shown that the tsunami radiating offshore becomes rapidly negligible due to the combined effect of the geometrical spreading and the wave height lowering due to propagation towards deeper waters.

This study confirms that tsunamis generated by small-volume coastal mass movements produce only local effects in the stretch of coast in front of the slide source, and very little effects elsewhere. However, they cannot be neglected, since they can produce damage through waves several meters high, through flooding low-lying areas and through persistent and dangerous wave agitation in coastal semi-closed basins.

References

- Assier-Rzadkiewicz S, Heinrich P, Sabatier PC, Savoye B, Bourillet JF (2000) Numerical modelling of a landslide-generated tsunami: the 1979 nice event. *Pure Appl Geophys* 157:1707–1727
- Bressan L, Zaniboni F, Tinti S (2013) Calibration of a real-time tsunami detection algorithm for sites with no instrumental tsunami records: application to stations in eastern Sicily Italy. *Nat Hazards Earth Syst Sci Discuss* 1:2455–2493
- Camerlenghi A, Urgeles R, Fantoni L (2010) A database on submarine landslides. Submarine mass movements and their consequences. In: Mosher DC et al. (eds) *Advances in natural and technological hazards research*, Vol 28, © Springer Science + Business Media B.V. 2010. [10.1007/978-90-481-3071-9_41](https://doi.org/10.1007/978-90-481-3071-9_41)
- Colantoni P, Genesseeux M, Vanney JR, Ulzega A, Melegari G, Trombetta A (1992) Processi dinamici del canyon sottomarino di Gioia Tauro (Mare Tirreno). *Giornale di Geologia* 54:199–213 (in Italian)
- Lo Iacono C, Gràcia E, Zaniboni F, Pagnoni G, Tinti S, Bartolomé R, Masson D, Wynn R, Lourenço N, Pinto de Abreu M, Dañobeitia JJ, Zitellini N (2012) Large and deep slope failures in the Gorringe Bank. Evidence for landslide-generated tsunamis along the SW Iberian Margin. *Geology* 40:931–934. doi:[10.1130/G33446.1](https://doi.org/10.1130/G33446.1)
- Papadopoulos GA, Daskalaki E, Fokaefs A (2007) Tsunamis generated by coastal and submarine landslides in the Mediterranean Sea. In: Lykousis V, Sakellariou D, Locat J (eds) *Submarine mass movements and their consequences*. Springer, Heidelberg, pp 415–422
- Sahal A, Lemahieu A (2011) The 1979 Nice airport tsunami: mapping of the flood in Antibes. *Nat Hazards* 56:833–840. doi:[10.1007/s11069-010-9594-6](https://doi.org/10.1007/s11069-010-9594-6)
- Tinti S, Bortolucci E, Vannini C (1997) A block-based theoretical model suited to gravitational sliding. *Nat Hazards* 16:1–28
- Tinti S, Chiocci FL, Zaniboni F, Pagnoni G, de Alteriis G (2011) Numerical simulation of the tsunami generated by a past catastrophic landslide on the volcanic island of Ischia, Italy. *Marine Geophys Res* 32(1):287–297. doi:[10.1007/s11001-010-9109-6](https://doi.org/10.1007/s11001-010-9109-6)
- Tonini R, Armigliato A, Pagnoni G, Zaniboni F, Tinti S (2011) Tsunami hazard for the city of Catania, eastern Sicily, Italy, assessed by means of Worst-case Credible Tsunami Scenario Analysis (WCTSA). *Nat Hazards Earth Syst Sci* 11 (1217–1232):2011. doi:[10.5194/nhess-11-1217-2011](https://doi.org/10.5194/nhess-11-1217-2011)
- Zaniboni F, Pagnoni G, Tinti S, Della SM, Fredi P, Marotta E, Orsi G (2013) The potential failure of Monte Nuovo at Ischia Island (Southern Italy): numerical assessment of a likely induced tsunami and its effects on a densely inhabited area. *Bull Volcanol* 75:763. doi:[10.1007/s00445-013-0763-9](https://doi.org/10.1007/s00445-013-0763-9)

Natural Dams and Landslides in Reservoirs



Introduction: Natural Dams and Landslides in Reservoirs

Alexander Strom, Hans-Balder Havenith, and Fawu Wang

Abstract

Introduction describes briefly main problems that are highlighted in the papers selected for the C9 session of the WLF3 “Natural dams and landslides in reservoirs”. Various aspects of interaction between water bodies and surrounding slopes and of the stability of natural and artificial dams are discussed.

Keywords

Landslide • Natural dam • Reservoir • Debris flow • Geophysical method • Displacement wave

Introduction

The session “Natural Dams and Landslides in Reservoirs” of the Third World Landslide Forum was proposed considering the success of the “Landslides and Reservoirs” session of the Second Forum in 2011 in Rome. This time we also include natural (i.e. landslide) dams in the session title because about one half of the papers are devoted to the related hazards such as inundation and outburst floods, which could be even much more disastrous than the direct impacts of the original mass movement.

15 papers are included in the full-color Forum proceedings and several more in the mono-color book. Authors from eight countries—Belgium, Canada, China, Japan, Kyrgyzstan, Netherlands, Norway and Russia discuss various aspects of interaction between water bodies and surrounding slopes and of the stability of natural and artificial dams. Most of the presenters are from China and some papers are

written by Chinese researchers in cooperation with scientists from other countries. This is not surprising, because it is China that hosts the Third Forum and, even more, considering stunning development of hydraulic engineering in China during last decades and attention paid by Chinese authorities to protect hydraulic schemes and people living on reservoirs’ banks from slopes’ instabilities.

Several papers describe landslides on the banks of the Three Gorges Reservoir—the world-largest hydraulic scheme where the stability of the reservoir banks became a critical issue. Landslides in other parts of China, at the Daxishan reservoir in North-Eastern part of the country, at the Dadu River (Sichuan), and at the Jinsha River (Jinsha is the Chinese name for the upper stretches of the Yangtze River) are described as well. Authors investigate geological conditions favorable for the reservoir-induced landslides formation, monitoring data, role of reservoir level fluctuation on slopes stability, effect of slope failures that collapse into the water and create large waves that pose threat both for water transport and along-banks road systems. Special attention is paid to geotechnical tests and to physical experiments aimed to model various phenomena caused by the reservoir-slopes interaction as well as the stability of natural landslide dams. Some papers provide recommendations on how to stabilize slopes and to decrease risk of their uncontrolled failure.

Analysis of catastrophic debris flow mechanism and of its disastrous effects on the hydraulic power plant in Ethiopia

A. Strom (✉)
Geodynamics Research Center – Branch of the JSC,
“Hydroproject Institute”, Moscow, Russia
e-mail: strom.alexandr@yandex.ru

H.-B. Havenith
Department of Geology, Liege University, Liege, Belgium

F. Wang
Department of Geoscience, Shimane University, Shimane, Japan

extends the session topic. This natural disaster affected the diversion scheme far away from the headrace reservoir, but it highlights the necessity of thorough analysis of the potentially hazardous sites for hydraulic engineering. Powerful highly mobile debris flows represent “remote hazard” and the possibility of their occurrence must be considered during an engineering-geological survey for various hydraulic structures, with or without reservoirs.

An interesting global overview of the disasters caused by the displacement waves from subaerial landslides is presented by the Canadian-Norwegian team. Special attention was paid to the remote character of the related hazards—landslide-generated waves might affect sites far away from the unstable slope. Assessing related hazards requires a regional analysis even if only one particular site or settlement has to be protected.

A paper presented by a joint Belgium-Kyrgyz team is partly related to both topics of our session—reservoir landslides and natural dams. The Kambarata-2 dam in Kyrgyzstan is an artificial structure, partially created by a large-scale explosion, but the method used for its monitoring—the electrical tomography—can be used for natural landslide dams monitoring as well.

Geophysical methods described in several papers provide powerful tool for a better understanding of the internal

structure of landslide dams and for their stability assessment. Besides electrical tomography the novel method of the multichannel analysis of surface waves was applied to study interiors of both earthquake- and rainstorm-triggered landslide dams in Japan and China. Results of these investigations are presented in the session proceedings along with data on the progressive failure of landslide dams caused by the internal erosion and piping obtained during physical experiments. These methods could be used to study the internal structure of landslide dams all over the world, the gigantic Usoi blockage in Pamirs—the largest historical landslide dam that forms 500 m deep reservoir storing 17 cubic kilometers of water, in particular. Despite almost century-long studies of this unique phenomenon, the extensive additional investigations are necessary to propose optimal technical measures that will ensure its long-term safety.

Besides the analysis of the selected case studies the general concept of the coseismic landslide dam hazard assessment, including cascade events was proposed in the paper written by international Chinese-Belgian-Dutch team.

We hope that the results of investigations presented in this book will help to develop a safer mode of reservoirs’ operation and to reduce risk of uncontrolled and sudden failure of landslide dams all over the World.



Catastrophic Debris Flow in the Hako Creek: Tributary of the Wabi Shebelle River, Ethiopia

Anatoliy Zhirkevich

Abstract

Origin and evolution of the unusual catastrophic debris flow that caused breakdown of the Malka Wakana Hydroelectric Power Plant in the upper reaches of the Wabi Shebelle River, in the Ethiopian upland, are described. Debris flow affected the lower part of the small Hako Creek valley only. Most of material mobilized by debris flow came from thick debris accumulation at the foot of the waterfall and its activation was caused by flood originated due to heavy rain.

Keywords

Hydraulic power plant • Debris flow • Rainstorm • Debris mobilization

Introduction: The Malka Wakana Hydroelectric Power Plant

The Malka Wakana Hydroelectric Power Plant (HPP) is located in the upper reaches of the Wabi Shebelle River valley that crosses the eastern flank of the Ethiopian plateau—the plain elevated up to 2,500–2,530 m a.s.l. The river is about 1,600 km long and its catchment area at the project site is 5,300 km². The powerhouse of the diversion scheme was placed at the Hako Creek mouth (Fig. 1).

The Ethiopian plateau at the HPP area is characterized by mixed subequatorial and tropical monsoon climate influenced by high altitude of the region. Mean annual temperature is 13–14 °C (+28 maximum and –10 minimum). Precipitation is due to equatorial monsoons mainly; annual rainfall is about 700 mm, 85–95 % of which occur during long rainy season from March to November. Maximal daily rainfall may exceed 100 mm.

The hydrological regime of the Wabi Shebelle River close to the HPP site is characterized by rainfall floods of variable duration and intensity. The highest floods have been

recorded from July till November, while maximal yearly discharges were recorded during the second rainy season, usually in August.

Mean annual discharge at the HPP site is 26.2 m³/s, while maximal discharge estimate based on the analysis of past flood traces is 365 m³/s. The maximal design water level at the power plant site (at the Hako creek mouth) is about 2205.2 m a.s.l. that corresponds to the flood of 0.01% excess probability which discharge with warranty correction is 860 m³/s (Malka Wakana 1985).

The Malka Wakana HPP was constructed at the river section where the morphology of its valley changes abruptly. Upstream from the dam site the valley is shallow and river has relatively low terraced banks. 300 m downstream from the dam site shape of the valley converts into narrow canyon up to 300 m deep. The valley was eroded through volcanic rocks—tuffs and lavas.

The hydraulic scheme includes the dam with the spillway and bottom outlet, the headrace canal with additional spillway, penstocks, powerhouse, tailrace and the 230 kV substation (see Fig. 1). The powerhouse, tailrace and transformers were placed on the right bank of the Wabi Shebelle River and occupy part of the Hako Creek valley bottom. This area at 2,205–2,211 m a.s.l. was covered by coarse angular boulders, partially mixed with modern gravelly-pebbly alluvium. Abandoned buried channels of

A. Zhirkevich (✉)
JSC “Hydroproject Institute”, Volokolamskoe Shosse 2, 125993
Moscow, Russia
e-mail: anzhir@yandex.ru

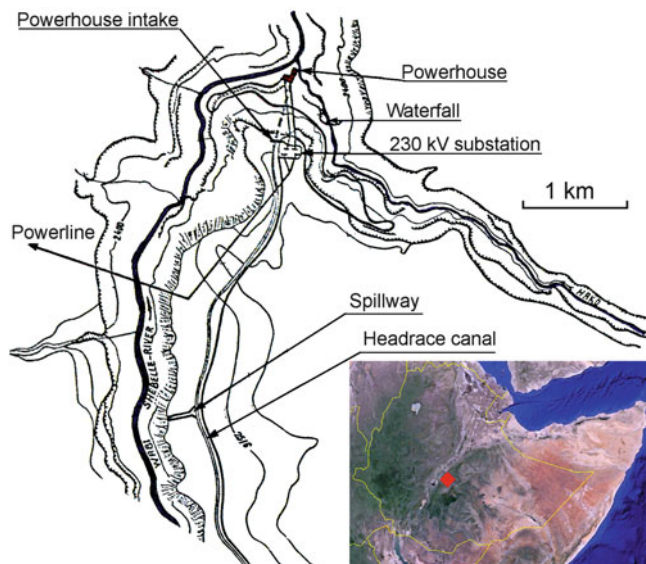


Fig. 1 Schematic layout of the Malka Wakana HPP at the confluence of the Wabi Shebelle River and the Hako Creek. Position of the HPP is shown on the Google Earth image

both streams incised up to 2,170 m a.s.l. (30–35 m deeper than the present day riverbed) and filled by the alluvium and talus were discovered close to the site. The powerhouse was located at the level of 2,208 m a.s.l.—about 3 m above the design level of the 0.01% flood.

However, on August 31, 1991 the powerhouse was affected by powerful debris flow from the Hako Creek that caused temporary breakdown of the power plant.

The Hako Creek Morphology

The Hako Creek valley is 34 km long and has catchment area of 157 km². At its section where the valley is incised in the plateau the riverbed gradient is about 55–57 ‰. During the dry season it is a small stream, which discharge does not exceed few cubic meters per second. However, its maximal flood discharge in the rainy season can reach 76–92 m³/s with 1.0–0.5 % exceedance probability. Talus accumulations composed of large blocks of basalts and ignimbrites with detritus and sandy-loamy fill are developed on the slopes of the Hako Creek canyon that inherit the southeast-northwest trending fault zone.

At the lower part of the canyon with 100 m overall drop at a distance of 500 m (Fig. 2) there is a waterfall, which height was about 3 m in 1982 and increased up to 8 m in 1991 (Fig. 3).

No evidence of debris flow activity in the Hako Creek have been found during field explorations performed in 1982–1983 for the Malka Wakana Project (Malka Wakana 1985).

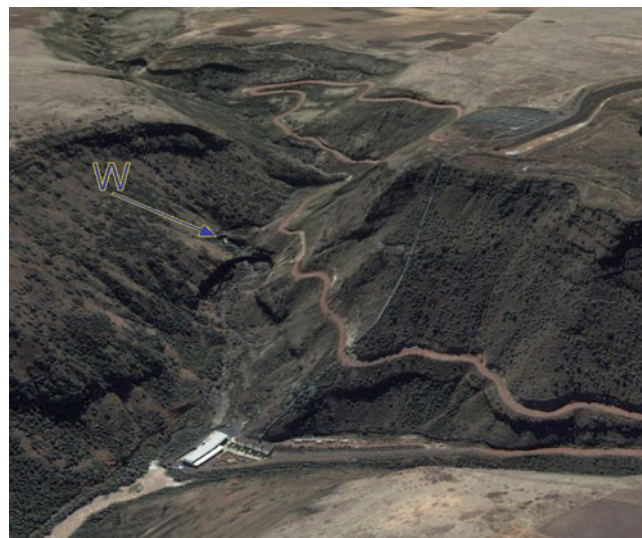


Fig. 2 Shape of the Hako Creek valley and location of the Malka Wakana HPP Powerhouse. Arrow marked by W indicates the waterfall shown in Fig. 3



Fig. 3 The Hako Creek waterfall after the August 31, 1991 debris flow

The 1991 Hako Creek Debris Flow

Causes and triggers of debris flows are variable. However, the entire Ethiopian plateau and the Wabi Shebelle River basin in particular can be hardly classified as the debris flow prone region. The upper reaches of the Hako Creek passes through the planar area and can be classified as the sluggish river. Thus, origination of the debris flow in the Hako Creek valley was completely unpredictable.

According to the field inspection, aerial observations and eyewitness interviewing performed immediately after the event it was found that an intensive rainstorm had occurred on August 31, 1991 in the central part of the Hako Creek basin, over its right bank mainly. It lasted for 2 h, from 13–30 till 15–30. 1.5–2 h later after rainstorm had started the flood discharge of about $50 \text{ m}^3/\text{s}$ was recorded at the Hako village located on the plateau. It increased downstream and reached $80\text{--}90 \text{ m}^3/\text{s}$ where the creek is crossed by the road that goes to the HPP. Flood caused temporary damming of the stream by trees and bushes where it was crossed by the bridges, and subsequent breach of such dams. It resulted in wavy motion of water in the stream. However, no evidence of debris flow formation was observed upstream from the waterfall. This process started just at the waterfall where large amount of loose material had accumulated immediately below the waterfall during the long period of time. Just this section of the valley with channel slope and flood discharge exceeding critical values was the source of the 1991 debris flow.

Amount of loose material that had accumulated below the waterfall and could be mobilized by debris flow (PDFM—the potential debris flow massif—term proposed by Yu.B. Vinogradov 1977, 1980) was estimated as $800\text{--}1,000 \text{ m}^3$, according to comparison of the waterfall height measurements made in 1982 and 1991. This over-wetted material was mobilized and, due to high channel gradient started moving downstream. Amount of water that had triggered the debris flow motion was, likely, not very large and this process occurred within 2–3 min when peak flood discharge reached $90\text{--}95 \text{ m}^3/\text{s}$.

Further, while debris flow had moved along the stream, the entrainment of saturated debris that had collapsed from valley slopes took place (Fig. 4). There was significant amount of talus on the slopes, part of which came from the construction of the road that passes along the canyon wall (see Fig. 2) This material entrained by debris flow tripled the latter's initial volume, which increased its disastrous consequences significantly (Figs. 5, 6 and 7).



Fig. 4 Minor slope failures on the Hako Creek valley slopes eroded by debris flow downstream from the waterfall that had delivered additional material to the stream

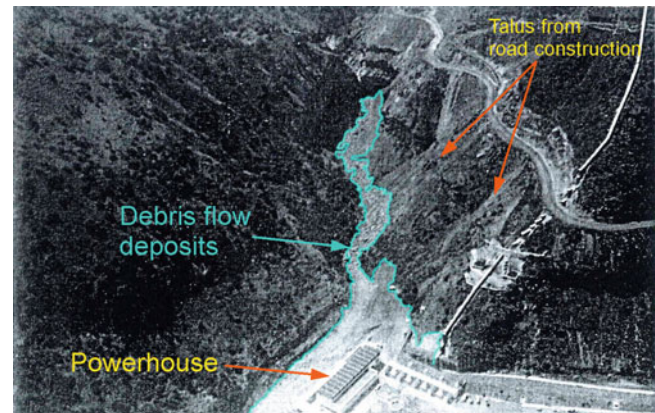


Fig. 5 Deposits of the 1991 Hako Creek debris flow downstream from the waterfall. View from helicopter



Fig. 6 1991 Debris flow deposits at the Malka Wakana powerhouse



Fig. 7 View on the powerhouse from the Hako Creek valley after the disaster



Fig. 9 Mobilization of debris at the slope break where the unnamed creek falls into the Cherek River valley



Fig. 8 Huge boulders transported by the 1991 Hako Creek debris flow. The diameter of the largest one exceed height of the staying person (marked by yellow oval)

Coarse material carried by debris flow formed elongated levees nearby the powerhouse that appeared to be not protected from such events.

Debris flow power could be estimated based on the size of boulders (Fig. 8).

1991 Debris Flow Mechanism

Field inspection of the 1991 Hako Creek debris flow effects allow to classify this phenomenon as the high-density mud-and-stone debris flow with volume content of solid particles (including boulders up to 2–3 m in diameter) up to 85–90 % and density up to 2,350–2,400 kg/m³, while density of its solid phase was 2,600 kg/m³.

Comparison of the 1991 Hako Creek debris flow parameters with those of debris flows described in the Guidelines (1976) or in the Handbook (1976) shows that,

according to these Regulations, we must study almost each rainstorm flood with high (limiting) saturation by solid particles (suspended stream). Volume of the deposits that could be transported by such stream is determined by the transporting capacity of the water flow. It seems, however, that the 1991 Hako Creek debris flow mechanism had differed from that of the typical debris flow: while usually solid particles saturate flowing water, here, in contrast, water falling from the waterfall saturated loose sediments at its base, which, finally, fluidized. The debris flow formation was associated not with gradual increase of the erosion intensity with increasing of flood and of its saturation by solids, but with abrupt displacement of the entire mass of saturated and fluidized loose deposits when the shearing load exceeded the shear strength.

Similar phenomenon was observed during construction of the Upper-Balkar midget power plant in Caucasus. It appeared that an imperceptible runlet, dry during most of the year can produce debris flow-like processes at the break of slope on the bank of the Cherek River main stream (Fig 9).

Relatively large amount of mobilized material required special measures to protect the construction site.

1991 Debris Flow Parameters Assessment

Maximal discharge of debris flow at the Malka Wakana powerhouse site could be estimated according to (Smirnov et al 1968) considering the hydraulic parameters of the stream after debris flow (cross section, plot of discharge vs. water level $Q = f(H)$) and approximate estimate of the flow rate calculated according to Guidelines (1985).

The surficial debris flow rate was calculated according to (2):

$$V_{cn} = \frac{2.1R}{l} \sqrt{R \sin \alpha} \quad (1)$$

where R —hydraulic radius; α —slope angle of the stream bed; l —scale of turbulence, calculated from nomographic charts (Guidelines 1985) compiled according to (2):

$$l = \frac{\sqrt{(S_T d_{80})^2 + (\wp R)^2}}{3.2 \left[\left(\frac{R}{d_{80}} \right)^{0.125} - \left(\frac{d_{80}}{R} \right)^{0.125} + 3 \right]} \quad (2)$$

where S_T —bulk concentration of the debris flow solid fraction; d_{80} —diameter of fraction corresponding to the 80% occurrence (considered here provisionally by analogy with complete curves of the debris flow prone soils grain size composition); \wp —the Karman parameter calculated according to (3):

$$\wp = 0.4 \frac{1 + S_T \left(\frac{\rho_T}{\rho_o} - 1 \right)}{1 + 2.5 S_T} \quad (3)$$

where ρ_T —density of the solid fraction; ρ_o —density of debris flow;

Mean debris flow rate V_c is taken as 0.8 of the surficial one.

The scale of turbulence value can vary from 0.3 to 0.5. Thus, considering the hydraulic radius from 2 to 10 and slope angles from 3° to 25° , the debris flow rate would vary from 5 to 10 m/s. To calculate maximal discharge we took debris flow rate of 6 m/s, which gives the discharge at the power house side up to 1,200–1,500 m³/s.

Such discharge exceeded the site level of 2008 m a.s.l. and resulted in inundation of the power house and its partial filling by the liquid component of debris flow saturated by solid particles—by mud similar to the concrete mix. It caused temporary breakdown of the HPP with capacity of 153 MW producing 543 million kWh.

The remedial works and restoration of the power plant were funded by insurance company, since both occurrence of debris flow and its consequences were considered as an unpredictable event which was not envisaged by the design (Malka Wakana 1985) and, thus, should be covered by

insurance. During restoration the stone masonry dike aimed to protect the powerhouse was constructed with due regard to the 1991 debris flow.

Conclusions

The phenomena that occurred in the Hako Creek valley on August 31, 1991 represent a special type of debris flow associated with the abrupt mobilization of large amount of water-saturated and fluidized loose deposits when the shearing load exceeds its shear strength. Such debris flows may occur at waterfalls or sharp breaks of stream's profile, which should be taken into consideration when constructing any structures in the river valleys in rugged terrain.

Special engineering-hydrological, meteorological and engineering-geological investigated must be performed at such sites. It should be pointed out that minor streams, which do not pose obvious threat due to their small dimensions and negligible discharge during most of the year could produce, nevertheless, destructive debris flows. Though such phenomena are rare, they must be taken into consideration to ensure structures' safety.

Acknowledgments I want to thank Alexander Strom for the translation of the manuscript and useful discussions.

References

- Guidelines on assessment of the debris flows design parameters VSN 03-76 (1976) Hydrometeoizdat, Leningrad (in Russian)
- Guidelines on the design of debris flow protection structures P-814-84 (1985) Hydroproject Institute, Moscow (in Russian)
- Handbook on debris flows study (1976) Hydrometeoizdat, Leningrad (in Russian)
- Malka Wakana HPP detail design (1985) Final edition, vol I, Summary; 2. Natural Conditions. Hydroproject Institute, Moscow
- Smirnov IP, Degovets AS, Zhirkevich AN (1968) Procedure of calculation of the main parameters of debris flows in Kazakhstan induced by rainstorms. In: Proceedings of the X-th all-union debris flow conference, Erevan. Publishing house of the Armenian Academy of Sciences (in Russian)
- Vinogradov YUB (1977) About the structure and dynamics of debris flow material. In: Debris Flows, Issue 2. Kazark Scientific hydro-meteorological institute. Hydrometeoizdat publishing house, Moscow branch (in Russian)
- Vinogradov YUB (1980) Study of debris flows. Hydrometeoizdat, Leningrad (in Russian)



A Conceptual Event-Tree Model for Coseismic Landslide Dam Hazard Assessment

Xuanmei Fan, Runqiu Huang, Cees J. van Westen, Qiang Xu, Hans-Balder Havenith, and Victor Jetten

Abstract

Earthquakes may trigger a series of multiple cascading geohazard phenomena. For example, coseismic landslides may block rivers and form landslide dams, which occur frequently in tectonically active mountains with narrow and steep valleys. The catastrophic release of water masses from landslide-impounded lakes is capable to produce outburst floods and debris flows, causing loss of lives, housing and infrastructure. Quantifying the probability of these cascading phenomena following a triggering event has been a main research challenge. This study creates a conceptual event tree model for hazard assessment of earthquake-induced landslide dams, with the involvement of many discussions amongst specialists in different fields. Event tree (ET) is a graphical, hierarchical and tree-like representation of possible events, which has been successfully applied in the volcano hazard assessment, but the application in landslide research is rather limited. We attempt to elaborate the event tree model by applying it in estimating the hazard of landslide dams induced by the Wenchuan earthquake. The model starts from a scenario-earthquake on a known possible active faults; the model then progressively assesses the susceptibility to coseismic landslides and landslide dams, and, finally, provides an estimate of dam-break flood hazard. According to the literature and our best understanding of the seismic hazard, we suggested or proposed possible methods to estimate the probabilities at successive nodes, the cascading events.

Keywords

Wenchuan earthquake • Event-tree model • Landside dam • Hazard assessment

X. Fan (✉) • R. Huang • Q. Xu

The State Key Laboratory of Geohazards Prevention and
Geoenvironment Protection, Chengdu University of Technology,
Chengdu, Sichuan 610059, China
e-mail: fanxuanmei@gmail.com

C.J. van Westen • V. Jetten

Faculty of Geo-Information Science and Earth Observation (ITC),
University of Twente, 7500 AE, P.O. Box 217, Enschede, The
Netherlands

H.-B. Havenith

Department of Geology, University of Liege, Liege, Belgium

Introduction

On May 12, 2008, a devastating earthquake of magnitude M_w 7.9 hit China's Sichuan province. The quake, originating in the Longmen Shan fault zone at the eastern margin of Tibetan Plateau, was the country's largest seismic event in more than 50 years. In addition to the immediate devastation through shaking, the earthquake triggered more than 60,000 destructive landslides (Görüm et al. 2011) over an area of 35,000 km²; the landslides caused about one-third of the total number of fatalities. More than 800 landslides during the earthquake blocked rivers, and thus produced numerous quake lakes that posed a serious threat to people downstream (Fan et al. 2012a, b).

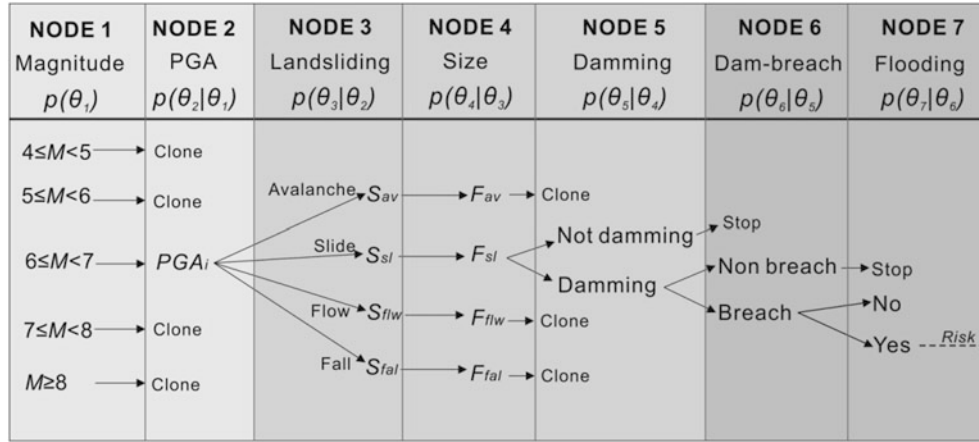


Fig. 1 A conceptual event tree scheme for the earthquake-triggered geohazards. The seven steps of estimation progress from general to more specific events, which are explained in the text. Note that any branch that terminates with “Clone” is identical to the subsequent central branch. For example, at NODE 1, the other magnitude bins are identical to the central $6 \leq M < 7$ branch. At NODE 2, the PGA stands for the peak ground acceleration that is commonly used to

represent amplitude of ground shaking. At NODE 3, the S_{av} - S_{fal} represents the spatial probability (susceptibility) of different types of landslides (av = avalanche, sl = slide, flw = flow, fal = fall types) given specified seismic source parameters (i.e. magnitude, fault type and length, PGA etc). At NODE 4, the F_{av} - F_{fal} means the size-frequency distribution of different types of landslides

It is well known that earthquakes may trigger a series of multiple cascading geohazard phenomena. Quantifying the probability of these cascading phenomena following a triggering event is an important research challenge. Event trees (ET) are recognized as a useful framework for discussing, from a probabilistic point of view, all the possible outcomes of adverse events (Newhall and Hoblitt 2002). Basically, an ET is a graphical, hierarchical and tree-like representation of possible events in which branches are logical steps from a general prior event through increasingly specific subsequent events (intermediate outcomes) to final outcomes. In this way, an event tree shows the most relevant possible outcomes produced by the interactions among different hazardous events, i.e. cascading effects.

Marzocchi et al. (2004) developed the Bayesian event tree (BET) based on the event tree scheme created by Newhall and Hoblitt (2002), because the Bayesian approach can estimate the uncertainty and determine the posterior probability on the basis of a prior probability distribution. BET is regarded as a flexible tool to quantify the probabilities of any specific series of events, by combining all the relevant available information such as theoretical models, empirical and deterministic models, prior knowledge and beliefs, monitoring data and any kind of historical data. This method has been well developed and widely applied in the short- and long-term volcanic hazard assessment (i.e. Marzocchi et al. 2010). However, few studies have been done on applying the event tree approach in landslide hazard assessment (i.e. Wong et al. 1997), let alone the application in seismically triggered geohazards.

A Conceptual Event-Tree Model for the Coseismic Landslide Dam Break Flood Assessment

A conceptual ET model for the earthquake-triggered hazard sequence was constructed, after many discussions with specialists in different fields (Fig. 1). A conditional probability, written in the form of $p(\theta_n|\theta_{n-1})$, is the probability of event n given that event $(n-1)$ has occurred. As defined by Newhall and Hoblitt (2002), the probability of any outcome, $p(\theta_n)$, is the product of the probability of an initial event, $p(\theta_1)$, and all further conditional probabilities, as shown in Eq. (1). The possible events at each node do not need to be mutually exclusive or exhaustive.

$$p(\theta_n) = p(\theta_1) \cdot p(\theta_2|\theta_1) \cdot p(\theta_3|\theta_2) \cdot \dots \cdot p(\theta_n|\theta_{n-1}) \quad (1)$$

In the conceptual ET model, we define the probability for the subsequent outcomes at each node as follows:

$p(\theta_1)$ Probability that a given magnitude earthquake will be triggered by known active faults (seismogenic zones) in a region of interest;

$p(\theta_2|\theta_1)$ Probability that, given seismic source parameters (i.e. magnitude, distance to seismic source, fault type, geometry etc.) and site-specific parameters, the peak ground acceleration (PGA) in a certain area will reach a specified value;

$p(\theta_3|\theta_2)$ Probability that, given above seismic source parameters and ground motions, landslides with a specified type will happen in a certain area;

- $p(\theta_4|\theta_3)$ Probability that, given the certain type of landslide occurrence, it will be of a specified size (in terms of landslide area or volume);
- $p(\theta_5|\theta_4)$ Probability that, given a specified landslide size and type, the landslide will reach and block a river with a certain width, forming a landslide dam;
- $p(\theta_6|\theta_5)$ Probability that, given a landslide dam formation, it will break;
- $p(\theta_7|\theta_6)$ Probability that, given the dam breach, it will cause flooding to the exposures at downstream.

The ET starts from an assumed earthquake from known possible seismogenic faults, progressively develops to more specific levels, therefore it can also be called a scenario-based ET. Note that NODE 1 focuses on different known active fault zones (the seismic sources on which future earthquakes are likely to occur); NODE 2 is about ground motion variation in a region, which can be terrain or geological-unit based considering the site amplification effects; NODE 3 estimates the spatial probability (susceptibility) of coseismic landslides, which are normally grid-based; NODE 4 and 5 are specific for each potential landslide site; NODE 6 is then focusing on individual landslide dams; and NODE 7 is different for each area downstream of a potential dam site. NODE 2, 3 and 7 are spatial maps with probabilities, while the probability of the other nodes can be estimated as a single value. The ET can be extended for risk assessment by adding some nodes at the right side of NODE 7, for example, the probability that there will be exposed individuals or buildings given a specified flooding area; the probability that, given a certain type of elements at risk, the degree of damage (vulnerability) will reach a certain value; and the probability that losses will be caused by a specified flood.

General Illustration of the Event-Tree Model

At **NODE 1**, the different earthquake magnitude bins are determined based on the classification of NEIC (National Earthquake Information Center). The earthquakes with the magnitude lower than 4 are not considered, since these hardly triggered any catastrophic landslides according to the review on earthquake-induced landslides by Keefer (2002). $p(\theta_1)$, the magnitude recurrence probability can be estimated by a statistical model, the Gutenberg-Richter magnitude-frequency power-law, using historic earthquake catalog of the known active fault zone.

NODE 2 is the probability of reaching a certain PGA level given specified seismic source parameters and site-specific parameters of a certain area. The intensity and duration of earthquake induced ground shaking at a site is a function of three main factors: earthquake source, medium

of propagation as well as physical and geotechnical characteristics of the site denoted as site effects (Kramer 1996; Shafique et al. 2011). The commonly used method for estimating ground motion is a simplified empirical attenuation models based on strong motion data.

NODE 3 is actually the susceptibility assessment of coseismic landslides of a certain type, which can be defined as a function of relevant spatial factors (i.e. seismic, geological, topographic and hydrological factors)

$$S = f(L|X_1, \dots, X_n) \quad (2)$$

Equation (2) expresses the joint conditional probability that a given region will be affected by future landslides of a certain type given the n variables X_1, X_2, \dots, X_n in the same region. There are a variety of methods available for landslide susceptibility assessment, including heuristic, deterministic and statistical approaches (see van Westen et al. 2008 for an overview).

NODE 4 is the size probability of a certain type of coseismic landslides. The exact size of landslides is not possible to be predicted beforehand, due to the intrinsic complexity of landslide failure mechanisms, site-specific geomorphology, geological and tectonic setting. In case that there are available landslide inventories or an event-based inventory, the landslide size probability can be assessed by a magnitude (size)-frequency analysis. The landslide size can be fitted to various statistic distributions as reviewed by van den Eeckhaut et al. (2007).

NODE 5 is the probability that a landslide of a certain type and size from a specific area can dam a river with a certain width. This can be solved by the empirical model, together with the landslide susceptibility assessment at NODE 3 and size-frequency distribution at NODE 4. The dam-formation threshold volume for a certain type of landslides was determined based on the empirical runout model as well as the correlation between river width and required damming volume, which allows a landslide to reach and block a river with a certain width.

NODE 6 is the dam-break probability. This node relates to the stability of landslide dams, which is a function of their geometry, internal structure, material properties, lake volume, inflow rate, and seepage processes (Costa and Schuster 1988; Korup and Tweed 2007). We tried to link the landslides and the consequent dam typology to the dam stability (Fan 2013). It is believed that the dams composed by large boulders or almost intact rock strata are more stable than those composed by unconsolidated fine debris.

NODE 7 is the dam-break flood probability. This node requires dynamic hydraulic modelling to estimate the spatial variation of flood parameters. The dam-break flood probability is controlled by the discharge capacity of the river that flows into the dammed lake and the probable flood parameters (flood

peak discharge, depth, velocity and duration) that are determined by the lake volume, dam-breach process and downstream terrain. The flood parameters can be estimated by physically-based numerical models and GIS-based hydraulic models as discussed in Fan et al. (2012c).

At the regional scale or in an emergency situation, the NODE 6 and 7 can be combined and simplified in order to rapidly assess the potential hazard of landslide dams.

Discussion

This study presents a basic framework, the “Event Tree Model”, to assess the multi-hazard associated with a high-magnitude earthquake. This approach has been successfully applied in volcanic hazard assessment, but the application in earthquake-induced landslide research still needs to be tested in more regions. Future research is directed towards the improvement of the shortcomings of this method (that lacks a spatial capability), and better illustrating the model by giving a calculation example. Such a model needs to be integrated with GISs to cope with data with dynamical position and attributes. In addition, further effort is needed to assign conditional probabilities, with their confidence boundaries, to each of the primary and secondary branches (nodes).

References

- Costa JE, Schuster RL (1988) The formation and failure of natural dams. *Geol Soc Am Bull* 100:1054–1068
- Fan X (2013) Understanding the causes and effects of earthquake-induced landslide dams. PhD Thesis, University of Twente, Enschede, the Netherlands
- Fan X, van Westen CJ, Xu Q, Görüm T, Dai F (2012a) Analysis of landslide dams induced by the 2008 Wenchuan earthquake. *J Asian Earth Sci* 57:25–37
- Fan X, van Westen CJ, Korup O, Görüm T, Xu Q, Dai F, Huang R, Wang G (2012b) Transient water and sediment storage of the decaying landslide dams induced by the 2008 Wenchuan earthquake, China. *Geomorphology* 171–172:58–68
- Fan X, Tang CX, van Westen CJ, Alkema D (2012c) Simulating dam-breach scenarios of the Tangjiashan landslide dam induced by the Wenchuan earthquake. *Nat Hazards Earth Syst Sci* 12:3031–3044
- Görüm T, Fan X, van Westen CJ, Huang R, Xu Q, Tang C, Wang G (2011) Distribution pattern of earthquake-induced landslides triggered by the 12 May 2008 Wenchuan earthquake. *Geomorphology* 133(3–4):152–167
- Keefer DK (2002) Investigating landslides caused by earthquakes – a historical review. *Surv Geophys* 23(6):473–510
- Korup O, Tweed F (2007) Ice, moraine, and landslide dams in mountainous terrain. *Quaternary Sci Rev* 26(25):3406–3422
- Kramer SL (1996) Geotechnical earthquake engineering. I. K. International Publishing House Pvt. Ltd, New Delhi, India
- Marzocchi W, Sandri L, Gasparini P, Newhall C, Boschi E (2004) Quantifying probabilities of volcanic events: the example of volcanic hazard at Mount Vesuvius. *J Geophys Res* 109
- Marzocchi W, Sandri L, Selva J (2010) BET_VH: a probabilistic tool for long-time volcanic hazard assessment. *Bull Volcanol* 72:705–716
- Newhall C, Hoblitt R (2002) Constructing event trees for volcanic crises. *Bull Volcanol* 64(1):3–20
- Shafique M, van der Meijde M, Kerle N, van der Meer F (2011) Impact of DEM source and resolution on topographic seismic amplification. *Int J Appl Earth Obs Geoinf* 13(3):420–427
- Van Den Eeckhaut M, Poesen J, Govers G, Verstraeten G, Demoulin A (2007) Characteristics of the size distribution of recent and historical landslides in a populated hilly region. *Earth Planet Sci Lett* 256(3–4):588–603
- Van Westen CJ, Castellanos E, Kuriakose SL (2008) Spatial data for landslide susceptibility, hazard, and vulnerability assessment: an overview. *Eng Geol* 102(3–4):112–131
- Wong HN, Ho KKS, Chan YC (1997) Assessment of consequence of landslides. In: Cruden D, Fell R (eds) *Landslide risk assessment*. A. A. Balkema, Rotterdam, pp 111–149



Analysis of Waves Generated by Zhaojun Bridge Rockfall in Xingshan County, Three Gorges Reservoir, on December 28, 2012

Huang Bolin, Yin Yue-ping, Wang Shichang, and Liu Guangning

Abstract

Rockfall waves generally cause damages to coastal infrastructures and people's lives and properties. This paper presents and analyzes case about damages to the bridge and human activity areas caused by waves generated by rockfall. Based on the field survey on Zhaojun Bridge Rockfall in Xingshan County, Three Gorges Reservoir, it establishes a FSI (Fluid-solid Interaction) simplified model integrating RNG (Re-Normalisation Group) turbulence model and GMO (General Moving Objects) collision model through FLOW-3D, with simulated block volume of 6,240 m³. FSI analysis results show that the maximum wave generated by rockfall was 35 m, the body wave generated was about 1.2 m, the energy transfer rate is about 0.9 %. The direction of wave movement (145°) was skew with the running direction of Zhaojun Bridge (86.5°), and the major attack point of this accident was located on the east side of the Bridge. Simulation results are relatively consistent with the actual investigation. Impulse wave spray will also cause damages to economy and living zone. The key to wave hazards is the relative spatial relationship between human activity areas and waves. The FSI model based on the Navier-Stokes (N-S) equation can be used to analyze this relative relationship and provide reference for the study on the rockfall waves in tributary shallow waters.

Keywords

Rockfall wave • Fluid-solid interaction (FSI) • Spray • Three Gorges Reservoir • Shallow water

Introduction

Since the Three Gorges Reservoir launched 175 m impoundment, its tributaries have witnessed several rockfalls, and geological disasters along tributaries have gradually come

into eyesight. The greatest difference between the trunk stream and tributaries in the reservoir region is that tributaries enjoy shallower waters, and rockfall waves in shallow waters have highly non-linear and huge spray effects, so it is difficult to be studied.

With the development of CFD (Computational Fluid Dynamics) technology and computer hardware, hydromechanics N-S equation can be used to analyze the rockfall wave problem in this shallow water. B. H. Choi et al. (2008) adopted RANS (Reynolds-averaged Navier–Stokes equations) system to carry out 3D solitary wave run-up analysis, while Silvia Bosa and Petti (2011) simulated the wave event of Vaiont landslide with mobile wall through 3D shallow-water wave model. F. Montagna et al. (2011) conducted 3D island landslide wave study with FLOW-3D,

H. Bolin (✉) • W. Shichang • L. Guangning
Wuhan Center of China Geological Survey, Guanggu Road 69#,
Wuhan 430223, China
e-mail: bolinhuang@aliyun.com; 94789070@qq.com;
125299542@qq.com

Y. Yue-ping
China Institute for Geo-Environment Monitoring, Dahuisi Road 20#,
Beijing 100081, China
e-mail: yinyueping0712@qq.com

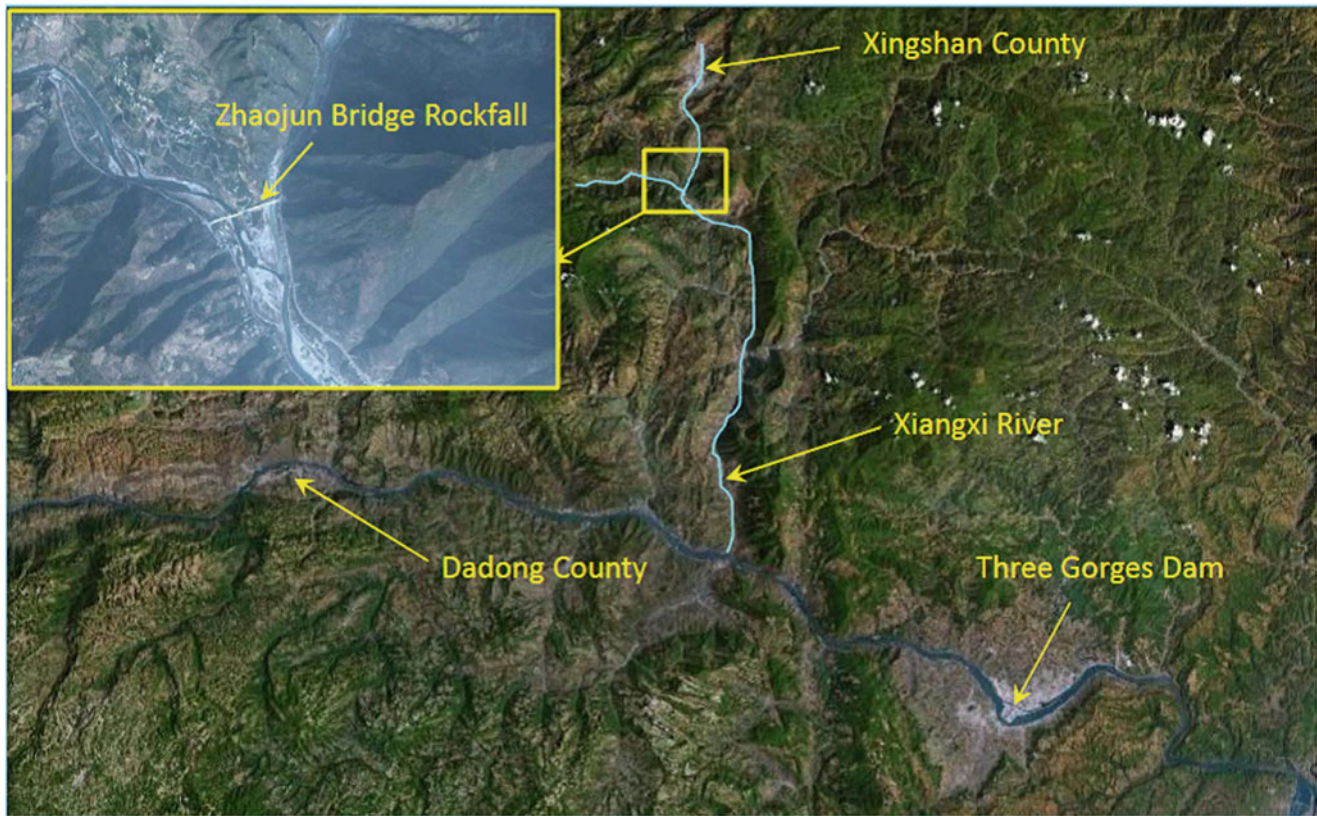


Fig. 1 Location map of the Zhaojun Bridge Rockfall

and carried out contrastive analysis with physical testing. M. Pastor et al. (2009) conducted studies on several disastrous landslide waves integrating 3D SPH (Smoothed Particle Hydrodynamics) method with FEM (Finite Element Method). Stéphane Abadie et al. (2010) conducted simulation studies on the waves generated when 3D sliding mass entered the water with two-phase flow N-S (Navier-Stokes) equation. With the method of hydromechanics, they respectively carried out studies on their study objects, but all are unrelated to shallow-water rockfall wave problems.

This paper takes Zhaojun Bridge Rockfall waves over the Xiangxi River in the Three Gorges Reservoir as an example, adopts the method of hydromechanics to study the rockfall waves in shallow waters, and provides reference for the study on rockfall waves.

Overview of Zhaojun Bridge Rockfall and Waves over the Xiangxi River in the Three Gorges Reservoir

The Zhaojun Bridge Rockfall occurred on the Xiangxi River, a tributary of the Three Gorges Reservoir, around 10:00 A.M. on Dec. 28, 2012, when the reservoir level was about 175 m a.s.l. Failure took place in the west side of the Shendu River mouth, 57.5 m away from Zhaojun Bridge that

strides over two rivers. The middle pier of the Bridge is located on a spur, and the rockfall was located on the north side of the Shendu River mouth (Fig. 1).

The orientation of the Zhaojun Bridge deck is 86.5° , with about 14.1 m elevation difference apart from 175 m a.s.l. water level.

The detached rock mass was thin in the rear edge and gradually became thicker downwards, forming a roughly elongated oblique triangular pyramidal block. The top of the collapsed rock body was at 221.5 m a.s.l., the base elevation at 184.4 m a.s.l., so the collapsed rock mass was about 36.9 m high and about 32.2 m wide at its middle and lower parts. Its maximum thickness was about 13 m, and the volume—about $6,000 \text{ m}^3$. The center of gravity of rockfall was about 190 m a.s.l. The sliding bed of the rockfall was unsmooth, with a rugged shape, and was dipping about $139^\circ \angle 64^\circ$. In the main sliding direction, the horizontal distance from the front edge of the rockfall to the Bridge was 55.7 m. The exposed rock stratum belonged to Member 4 of the Lower Triassic Jialing River Formation (T_{1j}^4), the lithology was light gray thick & thin-bedded dolomite, containing argillaceous dolomite limestone interbedded with multilayer salting-in breccia, the middle and upper parts were interbedded with brecciated limestone. Bedding orientation is $230^\circ \angle 54^\circ$. Three groups of joint fissures are developed in rock stratum dipping $139^\circ \angle 64^\circ$, $195^\circ \angle 40^\circ$ and $45^\circ \angle 75^\circ$



Fig. 2 Overview of the Zhaojun Bridge Rockfall

respectively, with relatively developed bedding planes (Fig. 2).

As reported by local residents, the rockfall collapsed as a single body. Waves generated when the rockfall fell into water had 2 m run up above the bridge deck. A passenger car was impacted, two pedestrians were hurt by rolling rocks, and the wave run-up on the opposite bank was 3.4–5.2 m, which caused damages to some farmlands and vendor stalls on the deck, and certain economic loss to local residents.

Numerical Model of the Zhaojun Bridge Rockfall Wave

The formation of waves caused by reservoir bank collapse is a very complicated process. Rocks are disintegrated in the movement, interact with water body and produce waves after falling into water. To simplify this complicated FSI motion problem, this paper introduces FLOW-3D software, meanwhile, Zhaojun Bridge dangerous rock body instability is simplified into block instability to simulate the wave caused by block insatiability.

FLOW-3D is general-purpose CFD software developed by Flow Sciences, which dates from Los Alamos National Laboratory in 1980. In Euler equation frameworks such as conservation of mass, momentum conservation and energy conservation, FLOW-3D employs finite volume difference method to approximate discretization computational domain to solve the equations. This software has a large number of models used to simulate phase transition, non-Newtonian fluid, porous media flow, surface tension effect, two-phase flow and so on. FLOW-3D solves the 3D transient Navier–Stokes equation with FAVOR (Fractional Area/Volume Obstacle Representation) and VOF (Volume-of-Fluid) techniques, which can offer extremely accurate and detailed Free Surface flow field information. FAVOR and

VOF techniques allow defining solid boundary within Euler grid and tracking fluid boundary while the CFD responds to solid boundary. Using this method, solid matters will independently form a grid, which can efficiently and precisely define the geometric shape. FLOW-3D's FAVOR and VOF techniques provide it with unique accuracy and authenticity in the description of free surface flow (Flow Science 2012).

FLOW-3D has many different turbulence models used to simulate turbulence, including Prandtl mixing length model, $k-\epsilon$ equation, RNG equation and LES model (Large Eddy Simulation model). Meanwhile, in the FLOW-3D, there is a special GMO collision computational model, which can allow users to predict the movement of objects in fluid. GMO will simulate rigid body motion, which can be a specified movement pattern or flow coupling calculation. In case of a specified movement pattern, the flow will be affected by the movement of objects, while the movement of objects will not be affected by the fluid. In case of flow coupling, the movement of objects and the flow are dynamically coupled (interactive). In both of two modes, there are 6 degrees of freedom. During calculation, there might be many types of moving objects, and they may collide with each other. Collision analysis can adopt elastic collision, local plastic collision and full plastic collision. Elastic collision refers to no energy loss caused by the collision among moving objects in the process of movement. Full plastic collision refers to complete energy loss after the collision among moving objects. The collision analysis adopts the overall friction coefficient and the overall collision recovery coefficient for control. The collision recovery coefficient is between 0 and 1, wherein, 0 represents full plastic while 1 represents full elastic. This paper adopts RNG equation and GMO model coupled model for analysis and calculation (Serrano-Pacheco et al. 2009; Basu et al. 2009; Das et al. 2009; Choi et al. 2007).

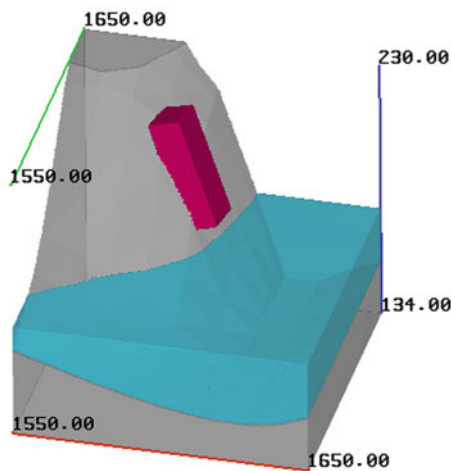


Fig. 3 FLOW generalized calculation model

A slope valley model 1.6 km long in X direction, 1.5 km wide in Y direction and 1 km high in Z direction has been created according to the slope valley topography of Zhaojun Bridge Rockfall. And a GMO rock body 40 m long, 12 m wide and 13 m thick (with density of $2,450 \text{ kg/m}^3$) has been established according to the rockfall volume investigation. Block volume is $0.624 \times 10^4 \text{ m}^3$, the drop of gravity center is 200 m, and the initial state is still. According to (Zhang et al. 2011) the limestone area rockfall collision recovery coefficient used for calculation is 0.72. We took a $100 \times 100 \times 96 \text{ m}$ wave forming area as the computational domain. It adopts 0.5 m computational grids for discretization, and there are a total of 7.68 million grid cells, including 200 grids in X direction, 200 grids in Y direction, and 192 grids in Z direction. The boundary conditions for k- ϵ turbulence model: outflow boundary in X, Y directions, free surface boundary in Zmax direction (water pressure at 0 and air interface), impermeable wall boundary in Zmin direction (waterproof boundary). The initial condition for k- ϵ turbulence model: still water surface and water level at 175 m. The boundary conditions for GMO model: gravitational acceleration in Z direction, closed boundary for 3D slopes (inaccessible areas), while other areas are open areas (accessible areas). The initial condition for GMO model: still. The analog computation time is set at 10 s (Figs. 3 and 4).

This coupling calculation model carried out computing for about 15.8 h at LENOVO THINK work station and formed 54.2 G of the resulting data files.

During the rockfall collapse, the potential energy of the rock body turned into kinetic energy that increased continuously while the speed increased. Around 3.3 s, the speed reached the maximum of about 18.8 m/s, and the kinetic energy also reached the maximum of about $2.06 \times 10^9 \text{ J}$. At this time the center of gravity of the rock body was

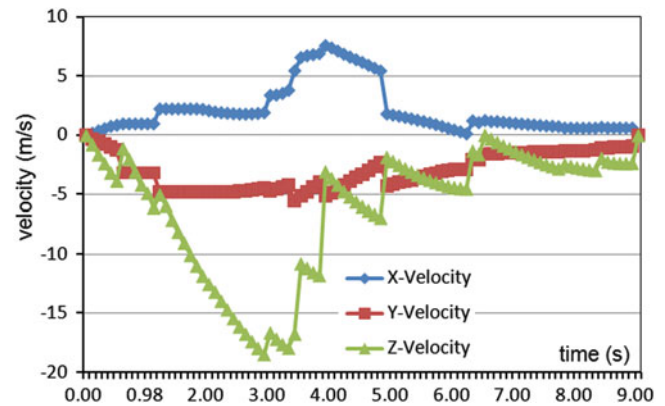


Fig. 4 The velocity process line of rock block

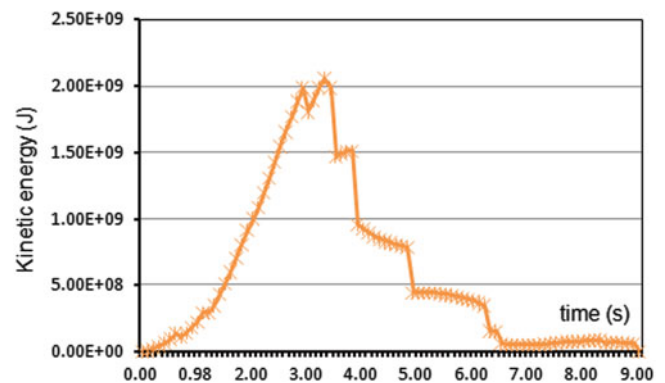


Fig. 5 The kinetic energy process line of rock block

175 m a.s.l., and at 4.4 s, the whole rock completely fell into water. The collapse of the rock into the water was a turning point in the conversion process from potential energy into kinetic energy. After its caving into the water, the total kinetic energy of GMO began to decline (Fig. 5). Before entering the water, the total energy of rock GMO was $8.1 \times 10^{11} \text{ J}$, the energy acquired by fluid was $8.0 \times 10^9 \text{ J}$, and above 99 % was potential energy. Compared with the total energy of the rock, the energy transfer rate was about 0.9 %, indicating that only a small percentage of rock energy was delivered to the water body, while the majority was lost in the slope movement.

Analysis on the Numerical Results of Zhaojun Bridge Rockfall Waves

After entering the water, first of all, craters formed around the rock body, the water body around craters combed upwardly and outwardly along the rock walls and made huge spray, about 35 m higher than the water level which is 30 m away from the banks, and then scattered into the water. A circular body wave began to form with the entry

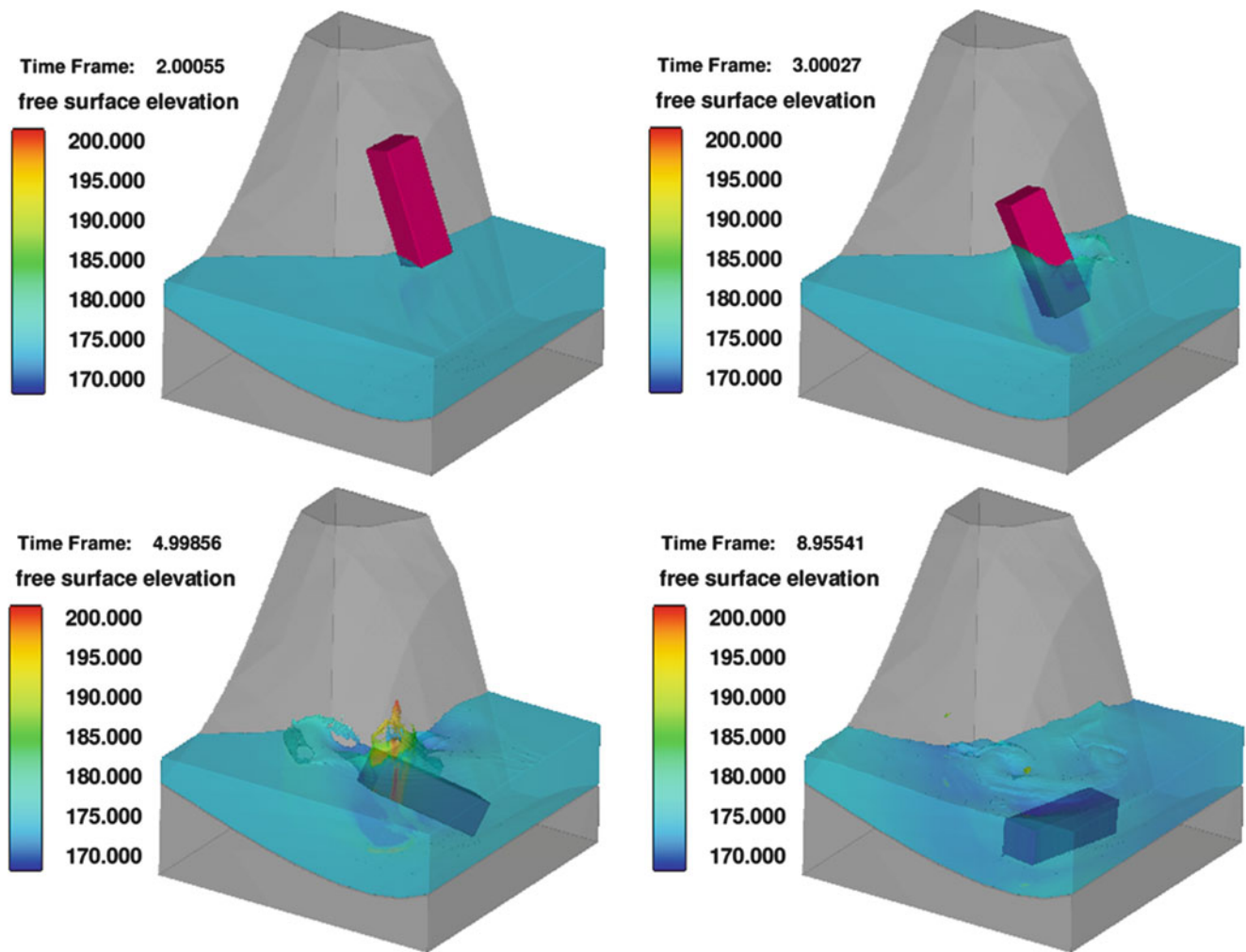


Fig. 6 The moving instantaneous picture of rock block

point as the center of circle, after the formation of waves, they were spread circle by circle. The maximum wave height was about 1.2 m, which is around 50 m away from the banks (Fig. 6).

This forming process of rockfall waves took 9 s. After formation, waves began to spread outwardly, which was very sudden and harmful. This was proved by witnesses during survey. Some stall keepers at the bridgehead witnessed the sudden rockfall and the fast rising of water body over the deck, which attacked them. The spray even hit the road sign at the bridgehead. Zhaojun Bridge was 14 m above the water surface, while the road sign was 10 m above the deck, so the wave spray was at least 24 m high. This was close to 35 m wave spray in simulation. According to the witnesses, the waves receded quickly, and except for the Bridge, other areas met very small waves. This was consistent with the computing result of small wave height.

When waves formed, they were about 30 m away from the banks, the moving distance was more than 62 m, and the

moving direction was about 135° . The moving direction of waves was skew with the running direction of the Bridge (86.5°), and the Bridge was some 57 m away from the banks and within the attack scope of waves. Therefore, the water wall formed by huge waves rushed at the bridgehead in an oblique direction and unexpectedly attacked those pedestrians and vehicles on the deck. Since the waves were huge and close to the human living area, they caused harms. Instead, the small and quickly receded body wave caused no harm.

Discussion

According to the statistics of Fritz (2002), rocks with volume less than $10,000 \text{ m}^3$ cause smaller waves, being less harmful. But he ignored the situation described in this paper, namely, when the wave is formed close to the living area, the body wave will not cause severe harms, but the water wall made of

huge waves could damage living area. Therefore, the key to wave hazards is the relative spatial relationship between human activity areas and waves.

Meanwhile, Zhaojun Bridge Rockfall wave event revealed people's ignorance and underestimation on geological disasters and wave hazards. When the disaster occurred, some stall keepers and pedestrians noticed the rockfall, but instead of identifying wave hazards, they rushed to the Bridge to watch the rockfall. Therefore, while promoting the publicity of geological disasters, we should also strengthen education on geological disasters & wave hazards and remind people that any link in a disaster is extremely hazardous and cannot be ignored.

The numerical simulation analysis on Zhaojun Bridge Rockfall waves shows that the study on dangerous rock body waves in the vicinity of living areas can use the FSI analysis of N-S equation, which can study the affected range of waves to the living area and provide technical support for geological disaster prevention and warning.

Conclusion

This paper adopts the CFD software of GMO collision model to predict the whole wave forming process of Zhaojun Bridge Rockfall and draws the following conclusions and suggestions:

- 1) 3D hydromechanics and solid mechanics coupling analysis on waves can acquire intuitive results from micro to macro and analyze the spread of waves in shallow waters, which will become the development trend of wave study.
- 2) This paper establishes an FSI model integrating RNG turbulence model and GMO collision model in which there are a total of 18.27 million grid cells, and the assumed GMO volume is $0.624 \times 10^4 \text{ m}^3$. The largest wave spray formed is 35 m, the body wave height formed is about 1.2 m, and the energy transfer rate is about 0.9 %.
- 3) The direction of wave movement is skew with the running direction of Zhaojun Bridge, and the bridge living area is the attack point of this accident. The key to wave hazards is the relative spatial relationship between human

activity areas and waves. The FSI model of N-S equation can be used to analyze this relative relationship.

Acknowledgement This work was supported by China Geological Survey (ID: 1212011014027) and National Natural Science Foundation of China (ID: 41372321). The authors would like to thank Ms. Cui and engineer Yu Zubing from Flow Science.

References

- Abadie S, Morichon D, Grilli S, Glockner S (2010) Numerical simulation of waves generated by landslides using a multiple-fluid Navier–Stokes model. *Coast Eng* 57:779–794
- Basu D, Green S, Das K, Janetzke R, Stamatakos J (2009) Numerical simulation of surface waves generated by a sub-aerial landslide at Lituya Bay, Alaska. *Proceedings of OMAE 2009, 28th international conference on ocean, offshore and arctic engineering*. pp 1–14
- Bosa S, Petti M (2011) Shallow water numerical model of the wave generated by the Vajont landslide. *Environ Model Software* 26:406–418
- Choi BH, Kim DC, Pelinovsky E, Woo SB (2007) Three-dimensional simulation of tsunami run-up around conical island. *Coast Eng* 54:618–629
- Choi BH, Pelinovsky E, Kim DC, Didenkulova I, Woo SB (2008) Two- and three-dimensional computation of solitary wave runup on non-plane beach. *Nonlin Process Geophys* 15:489–502
- Das K, Janetzke R, Basu D, Green S, Stamatakos J (2009) Numerical simulations of tsunami wave generation by submarine and aerial landslides using RANS and SPH models. *Proceedings of OMAE 2009, 28th international conference on ocean, offshore and arctic engineering*. pp 1–14
- Flow Science Inc (2012) Flow-3D user manual. Flow Science Inc., Santa Fe, NM
- Fritz HM (2002) Initial phase of landslide generated impulse waves. The thesis for Ph.D., VAW, ETH, Zürich
- Montagna F, Bellotti G, Di Risio M (2011) 3D numerical modeling of landslide-generated tsunamis around a conical island. *Nat Hazards* 58:591–608
- Pastor M, Herreros I, Fernández Merodo JA, Mira P, Haddad B, Quecedo M, González E, Alvarez-Cedrón C, Drempevic V (2009) Modelling of fast catastrophic landslides and impulse waves induced by them in fjords, lakes and reservoirs. *Eng Geol* 109:124–134
- Serrano-Pacheco A, Murillo J, García-Navarro P (2009) A finite volume method for the simulation of the waves generated by landslides. *J Hydrol* 373:273–289
- Zhang G, Xiang X, Tang H (2011) Field test and numerical calculation of restitution coefficient of rockfall collision. *Chin J Rock Mech Eng* 30(6):1266–1273



Development Characteristics of the Landslides in Jurassic Red-Strata in the Three Gorges Reservoir, China

Haibo Miao, Kunlong Yin, and Bin Lin

Abstract

Landslides in Jurassic red-strata make up a great part of geo-hazards in the Three Gorges Reservoir (TGR) in China. They are mainly large thick-bedded, which usually developed in J_{2s} and J_{3p} , and located within the influence zone of reservoir water level fluctuation and human engineering activities from the view of the distribution of elevation. This kind of landslides mainly distributes in the linear-shaped bank slope, and secondly, in convex and ladder-shaped bank slope. When the linear-shaped bank slopes between 10° and 20° , large scale landslide would probably develop, and usually a thick-bedded one; when between 20° and 30° , relatively huge scale landslide with mega-thick layer could develop; whereas in nearly horizontal slope (gradient $< 10^\circ$), large thick-bedded landslide casually appears. While the gradient of nonlinear bank slope is between 10° and 20° , the huge and large scale landslides would mostly develop, both of which could form thick-bedded or mega-thick-bedded landslide; when the gradient of bank slope is between 20° and 30° , or between 30° and 40° , large thick-bedded landslide grows better, nevertheless, huge scale landslide with mega-thick layer and medium scale landslide occasionally appear.

According to the combined features of bank slope formation lithology, landslides in Jurassic red-strata in TGR can be divided into three categories, each class corresponding to a failure mode, respectively. They are: the layered bank slope controlled by soft layer (class I), the layered bank slope controlled by weak substrate (class II), and the layered bank slope controlled by bedding and structural surface (class III). Among them, the first class is divided into five subclasses based on the syntagmatic relation among the gradient of sliding bed rock (θ), the angle between slope aspect and sliding bed rock inclination (δ) and slope aspect.

Keywords

Landslides • The Three Gorges Reservoir • Jurassic red-strata • Development characteristics

H. Miao (✉) • B. Lin
School of Civil Engineering and Architecture, Anhui University of
Science and Technology, Shungeng Middle Road, 168, Huainan
232001, China
e-mail: mhblowal@gmail.com; linbin8910@126.com

K. Yin
Faculty of Engineering, China University of Geosciences,
Wuhan 430074, China
e-mail: yinkl@126.com

Introduction

The Three Gorges Reservoir (TGR) is the area with a large number of geological disasters in China, which developed in all strata, especially in Jurassic stratum. The Jurassic lithology in TGR is the continental lake facies sedimentary rocks, the colours of which are mainly fuchsia, maroon, or red brown; therefore, the Jurassic stratum is often called “red-strata” by Chinese academe (Li and Wang 2002; Chen et al. 2004; Xu and Zhou 2010). According to the incomplete

statistics, among the landslides in TGR of the second and the third phase of mitigating and monitoring projects, the landslides in Jurassic red-strata are more than 70 % (Chai et al. 2009). From the lithology structure of Jurassic red-strata in TGR, the interbedding layer of thick silty-sandstone and thin sandy-mudstone is an important reason for the development of weak bands with high content of clay mineral like montmorillonite and illite in the long geological history (Jian et al. 2005, 2008), which caused some typical landslides, such as Chonggang landslide (Yin and Wu 1998), four landslide groups in Wanzhou area (Jian et al. 2009), Jipazi landslide (Huang 2007), Qianjiangping landslide (Wang et al. 2004; Liao et al. 2005) and so on. With the formal operation of water storage and the further expansion of human engineering activities in TGR, the deformation and stability of reservoir bank in Jurassic red-strata will directly restrict the sustainable development of economy to reservoir area, and also affect people's life and property security. In result, it has been one of the most important environmental and geological problems.

In this paper, 60 typical landslides which developed in Jurassic red-strata were selected as the research sample (Table 1). The characteristics of development of these landslides were investigated from three aspects like distribution, landform of bank slope, and the structure of bank slope.

Characteristics of Development of the Landslides in Jurassic Red-Strata in TGR

Distribution

The characteristics of the distribution were analyzed from the lithology of sliding bedrock, the range of elevation, volume of sliding mass and the thickness of sliding mass, which is illustrated in Fig. 1.

According to landslide samples with the lithology of Jurassic strata in TGR showed in Fig. 1a, 30 landslides developed in upper Shaximiao formation of middle Jurassic (J₂s), distributed in the area from Fengjie to Chongqing. In addition, 11 landslides developed in Penglaizhen formation of upper Jurassic (J₃p), distributed in the region from Zhongxian to Fengdu mainly.

The lithology of J₂s is the interbedded layer of thin to middle-thick fuchsia pack-sandstone, calcareous siltstone, silty mudstone and fine grained feldspar quartz sandstone, where the silty mudstone is the thin weak band. The lithology of J₃p is the gray middle-thick feldspar quartz sandstone with the interlayer of fuchsia calcareous and clayey siltstone, which is rich in clay mineral like montmorillonite and illite. This kind of lithology shows that argillation of weak interlayer and distension of clay mineral is the important factor for the landslides in Jurassic red-strata in TGR.

As shown in Fig. 1b, Based on the classification of landslide scale, about 78.3 % are large-scale landslides with the volume range from 10^6 m^3 to 10^7 m^3 . According to classification of sliding mass thickness, 48 landslides are thick-bedded landslides with the thickness range from 6 to 20 m, and the others are mega-thick-bedded landslides with the thickness more than 20 m, which is showed in Fig. 1c. Moreover, it can be seen that the elevation of leading edge is from 100 m to 175 m, and the trailing edge is from 250 m to 400 m in Fig. 1d. In addition, the elevation distribution of the landslides has three features which are listed as follows. Firstly, the leading edges of the landslides are all in the influence of impoundment of TGR, and most of the shear openings are in the hydro-fluctuation belt that has 30 m of perpendicular throw, as a result, the leading edges of landslides will be affected by erosion, scour and infiltration from reservoir water. Secondly, the trailing edges of the landslides are all in the range of large scale immigrant relocation construction. Also, the unreasonable excavation and preloading will further intensify the deformation and/or the failure. Thirdly, when the difference of elevation between leading and trailing edge is in the range of 100–200 m, the landslides mostly developed, which can be found from Fig. 1e, f.

Landform of Bank Slope

Regional geographic and geomorphic conditions usually control the distribution and development characteristics of landslides. For the slope unit, the landslide occurs on the slope should needs a certain shape, gradient and free surface conditions. Qiao (2002) and Chai (2008) analyzed the landslides development through the slope gradient and slope surface shape. In this paper the relationship between the landslide development and geomorphic characteristics of bank slope in Jurassic red-strata in TGR were investigated from slope shape and slope gradient.

(a) Slope shape

According to the characteristics of the slope surface shape in Jurassic red-strata in TGR, four kinds of shapes were used in the present research, which is illustrated in Fig. 2. They are linear, concave, convex and ladder shape. The relationships among the volume, thickness and slope surface shape were showed in Fig. 3. The results show that: landslides in Jurassic red-strata mainly developed in linear-shaped bank slope, and then developed in convex and ladder-shaped bank slope.

(b) Slope gradient

The gradient is an important factor inducing the failure of slope. Duo to the difference of surface shape of bank slope, the relationship between gradient of linear-shaped slope and nonlinear-shaped slope (including concave,

Table 1 Statistical table of the main landslides in Jurassic red-strata in the Three Gorges Reservoir (60 landslides)

Number	Elevation (m)	Volume (10^4 m ³)	Average thickness (m)	Lithology	Stratum attitude	Slope aspect (°)	Gradient of slope (°)	Type of slope	Slope shape
1	135–423	1,600	40	J _{1x}	10°∠36°	340	25–45	Dip	Ladder
2	135–520	9,000	50	J _{1x}	25°∠27°	10	10–30	Dip	Ladder
3	135–425	864	30	J _{2q}	25°∠30°	323	19	Oblique	Linear
4	125–300	525	35	J _{3s}	30°∠58°	51	10–30	Dip	Ladder
5	160–370	315	20	J _{3p}	30°∠15°	64	27–35	Oblique	Concave
6	160–355	180	15	J _{1–2n}	120°∠25°	140	15	Dip	Linear
7	170–375	700	20	J _{1–2n}	130°∠25°	130	5–35	Dip	Ladder
8	140–405	420	15	J _{1–2n}	100°∠25°	40	20	Oblique	Linear
9	140–350	448	18	J _{1–2n}	110°∠32°	66	15	Oblique	Linear
10	110–430	2,400	35	J _{2q}	140°∠30°	140	30	Dip	Linear
11	150–250	168	15	J _{1–2n}	258°∠46°	82	15–40	Reverse	Convex
12	150–500	350	20	J _{1–2n}	270°∠43°	81	10–50	Reverse	Convex
13	160–360	433	20	J _{2s}	180°∠22°	345	18	Reverse	Linear
14	150–345	248	20	J _{2s}	223°∠12°	190	10–20	Oblique	Convex
15	130–300	283	15.8	J _{2s}	150°∠42°	39	20	Oblique	Linear
16	150–333	587	20	J _{2s}	210°∠15°	358	13–22	Oblique	Convex
17	170–310	452	20	J _{2s}	325°∠12°	33	25–40	Oblique	Ladder
18	99–400	948	15	J _{2s}	182°∠29°	160	27	Dip	Linear
19	150–331	605	30.5	J _{2s}	140°∠12°	315	13–30	Reverse	Ladder
20	125–285	1,350	25	J _{2s}	345°∠10°	335	7–24	Dip	Ladder
21	135–330	947	23	J _{3p}	177°∠34°	160	30	Dip	Linear
22	165–305	639	11	J _{2s}	220°∠20°	312	20–30	Oblique	Convex
23	158–320	995	18	J _{2s}	120°∠11°	85	15	Oblique	Linear
24	140–326	352	20	J _{2s}	115°∠7°	265	10–30	Reverse	Convex
25	94–307	2,882	30.5	J _{3p}	167°∠41°	165	25	Dip	Linear
26	135–380	315	12.5	J _{2s}	330°∠37°	340	16–45	Dip	Concave
27	115–250	246	12.5	J _{2s}	321°∠10°	310	20–30	Dip	Convex
28	70–380	1,500	50	J _{3p}	180°∠24°	195	8–40	Dip	Concave
29	135–250	360	15	J _{2s}	315°∠18°	310	20	Dip	Linear
30	160–328	215	20	J _{3s}	306°∠5°	298	8–26	Dip	Convex
31	120–225	1,350	20	J _{2x}	300°∠15°	291	10–30	Dip	Ladder
32	130–250	318	15	J _{2x}	305°∠12°	297	15	Dip	Linear
33	125–270	247	13.5	J _{2s}	340°∠20°	245	10–30	Oblique	Concave
34	120–290	280	17.5	J _{2x}	305°∠12°	294	15	Dip	Linear
35	120–245	300	25	J _{2s}	290°∠25°	293	17	Dip	Linear
36	117–250	360	22.5	J _{2s}	330°∠5°	292	25	Oblique	Linear
37	110–325	903	20	J _{2s}	155°∠15°	158	15–60	Dip	Concave
38	130–325	2,500	20	J _{2s}	354°∠10°	354	5–25	Reverse	Ladder
39	120–320	1,544	15	J _{2s}	170°∠5°	350	5–25	Reverse	Convex
40	120–250	216	20	J _{2x}	279°∠15°	270	10–20	Dip	Concave
41	120–255	810	15	J _{2s}	305°∠17°	305	15–25	Dip	Convex
42	113–335	880	20	J _{2s}	317°∠10°	305	10–50	Dip	Convex
43	110–295	210	17.5	J _{2s}	290°∠25°	293	13	Dip	Linear
44	147–450	1,547	17	J _{3s}	170°∠6°	50	25	Oblique	Linear
45	150–340	666	15	J _{2s}	250°∠4°	238	10–35	Dip	Ladder
46	147–400	48.5	10	J _{2s}	170°∠10°	102	25–45	Oblique	Convex
47	140–255	148	12.5	J _{3p}	325°∠21°	303	10–18	Dip	Convex
48	168–325	200	12.5	J _{3p}	300°∠20°	5	25	Oblique	Linear
49	176–300	26	12	J _{1–2z}	320°∠20°	301	18	Dip	Linear
50	143–275	112	10	J _{3p}	310°∠20°	290	18	Dip	Linear
51	145–240	175	10	J _{2s}	332°∠17°	330	20	Dip	Linear
52	170–270	288	10	J _{3p}	305°∠20°	250	9	Oblique	Linear

(continued)

Table 1 (continued)

Number	Elevation (m)	Volume (10^4 m^3)	Average thickness (m)	Lithology	Stratum attitude	Slope aspect ($^\circ$)	Gradient of slope ($^\circ$)	Type of slope	Slope shape
53	170–250	109	17	J _{3p}	$135^\circ \angle 7^\circ$	247	25	Oblique	Linear
54	160–250	131	15	J _{3p}	$342^\circ \angle 12^\circ$	42	15–25	Oblique	Convex
55	160–268	176	9	J _{3p}	$282^\circ \angle 17^\circ$	282	18	Dip	Linear
56	130–276	490	14	J _{2s}	$320^\circ \angle 14^\circ$	250	11	Oblique	Linear
57	140–288	112	11.5	J _{1-2z}	$155^\circ \angle 27^\circ$	85	15	Oblique	Linear
58	161–343	220	15	J _{2s}	$185^\circ \angle 3^\circ$	315	8–18	Oblique	Convex
59	162–300	221	15	J _{2s}	$185^\circ \angle 3^\circ$	335	5–15	Reverse	Convex
60	180–329	80	8	J _{2s}	$255^\circ \angle 10^\circ$	340	10–20	Oblique	Convex

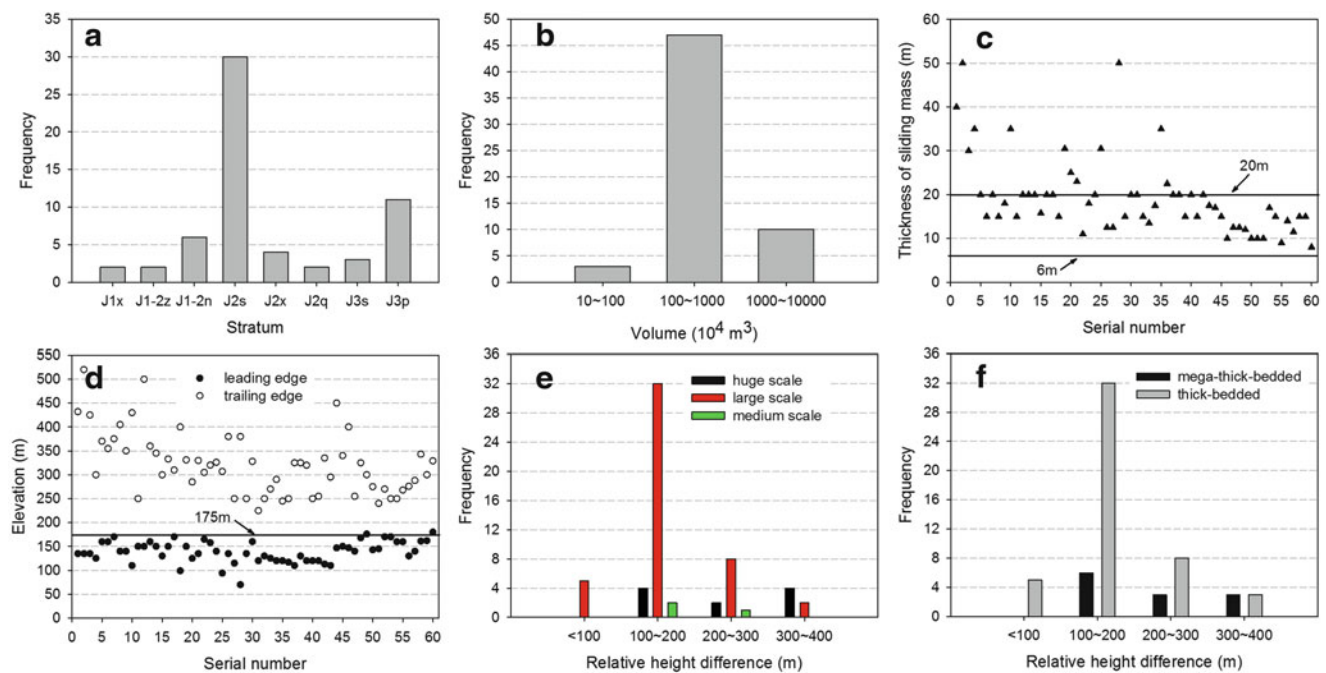


Fig. 1 Distribution of the landslides in Jurassic red-strata in TGR. (a) Lithology of sliding bed rock, (b) volume of sliding mass, (c) thickness of sliding mass, (d) elevation of leading edge and trailing

edge, (e) volume of the landslides in different height difference, and (f) thickness of the landslides in different height difference

convex and ladder-shaped slope) and landslide development are illustrated in Fig. 4. The results show that: firstly, when the gradient of linear-shaped bank slope is in the range of 10° – 20° , the large scale landslides mostly developed, and often are thick-bedded landslides. When the gradient of linear-shaped bank slope is from 20° to 30° , the huge scale and mega-thick-bedded landslides comparative well developed, whereas few large scale and thick-bedded landslides developed in nearly horizontal bank slope with the gradient less than 10° . Secondly, in the nonlinear-shaped bank slope where the gradient is from 10° to 20° , the huge and large scale landslides are mostly developed and are thick-bedded landslides predominantly. However, when the gradient is from 20° to 30° and 30° to 40° , the large and thick-

bedded landslides mostly developed, whereas occasionally huge scale and mega-thick-bedded landslides and medium scale landslides developed.

Structure of Bank Slope

The bank slope is characterized by rock mass structure and stratum lithological combination (Yin 2005; Hu and Zhao 2006). The main features of rock mass structure are the gradient of sliding bed rock (named θ) and bank slope type. For θ , 10° , 20° , 45° are selected as the division criterion. When θ is smaller than 10° , the slope is nearly horizontal. When θ is smaller than 20° but large than 10° , the slope is gently inclined. When θ is between 20° and 45° , the

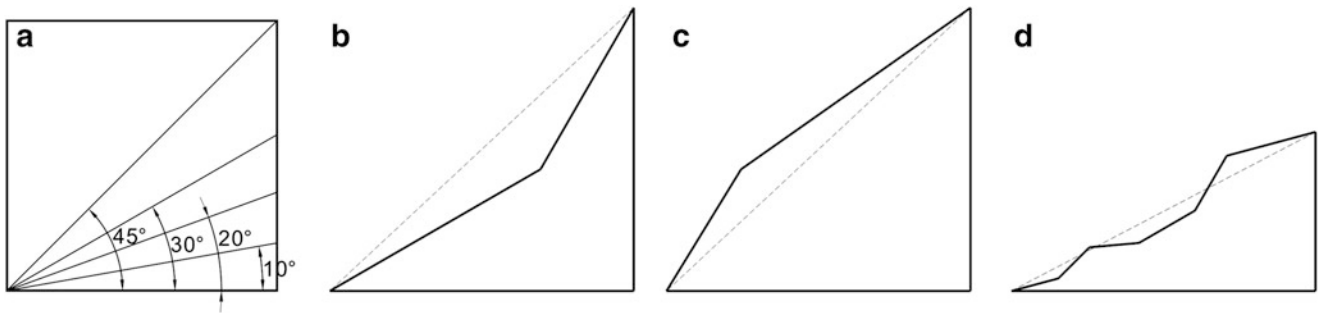


Fig. 2 Shape of bank slope. (a) Linear-shaped bank slope, (b) concave-shaped bank slope, (c) convex-shaped bank slope, and (d) ladder-shaped bank slope

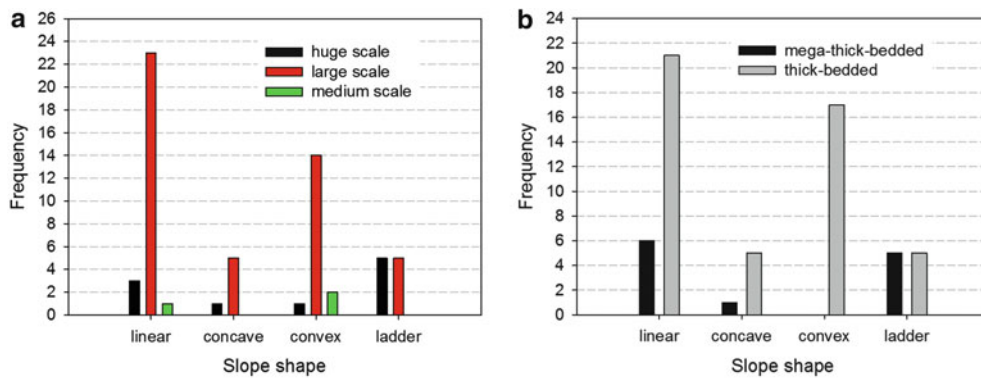


Fig. 3 Relations between bank slope shape and landslides development. (a) The volume of landslides in each slope shape, and (b) the thickness of landslides in each slope shape

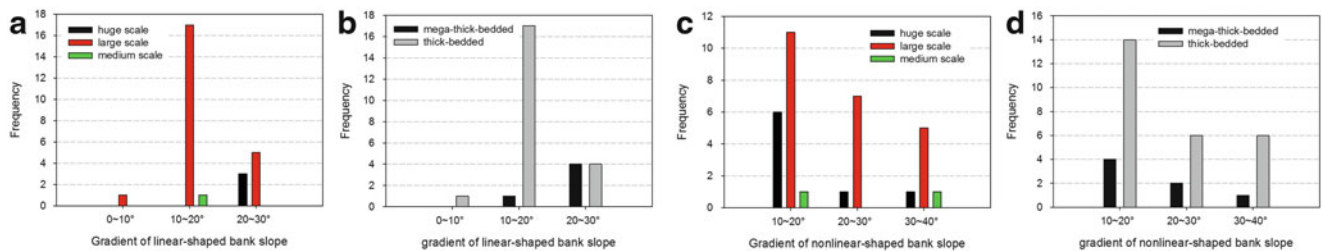


Fig. 4 Relations between landslides development and gradient of bank slope (in linear and nonlinear-shaped bank slope respectively). (a) The volume of landslides in each range of gradient of linear-shaped bank slope, (b) the thickness of landslides in each range of gradient of linear-shaped bank slope, (c) the volume of landslides in each range of gradient of nonlinear-shaped bank slope, and (d) the thickness of landslides in each range of gradient of nonlinear-shaped bank slope

slope is medium inclined, and for the steep slope θ is larger than 45° . The type of bank slope is controlled by the angle (δ) between slope aspect and sliding bed rock inclination. It has been reported that the failure type and strength both have marked difference when δ was smaller or larger than 30° (Bai et al. 2005). In view of the above analysis, 30° was selected as the criterion in this paper, i.e. $\delta \leq 30^\circ$, dip slope; $30^\circ < \delta < 150^\circ$, oblique slope; $150^\circ \leq \delta \leq 180^\circ$, reverse slope.

linear-shaped bank slope, (c) the volume of landslides in each range of gradient of nonlinear-shaped bank slope, and (d) the thickness of landslides in each range of gradient of nonlinear-shaped bank slope

The clear stratification is the most prominent feature in the diagenetic process for Jurassic red-strata in TGR. The difference of stratum lithology combination appeared because of the different ancient landform and paleoclimate environment. According to the control layer of bank slope stability, the bank slope in Jurassic red-strata is divided into three categories, namely, layered slope controlled by weak layers (class I), layered slope controlled by weak bases (class II), and layered slope controlled jointly by layers and

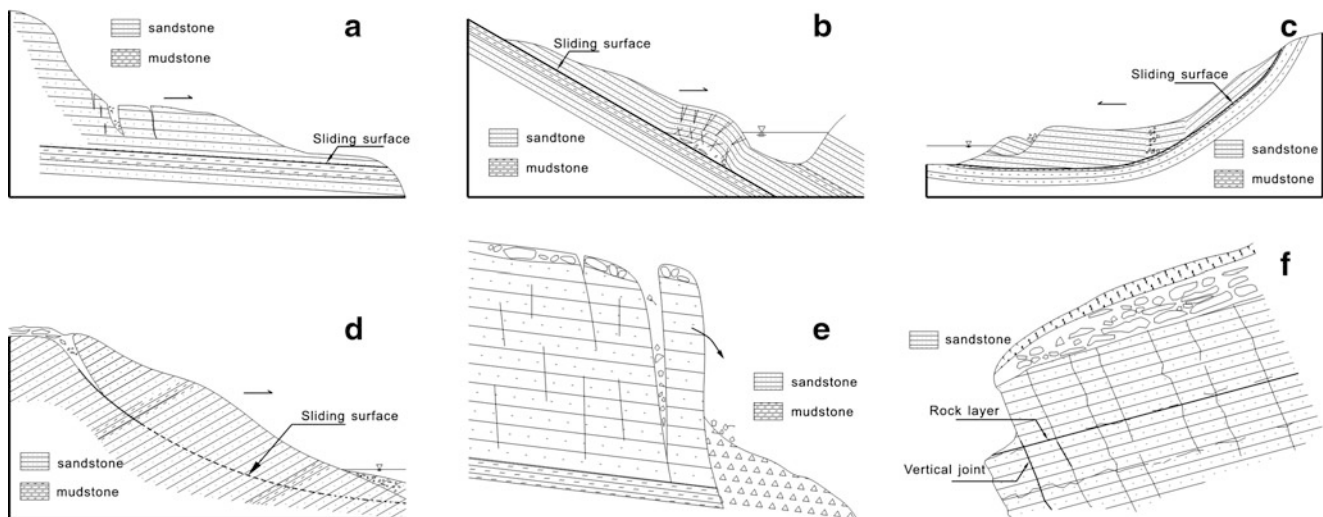


Fig. 5 Failure modes of the landslides in Jurassic red-strata bank slope. (a) Class I1, (b) Class I2, (c) Class I3, (d) Class I4, (e) Class II, and (f) Class III

structure surface (class III). For class I, bank slope can be further divided into five subclasses on the basis of syntagmatic relation among the gradient of sliding bed rock (θ), δ and slope aspect.

I1: Nearly horizontal—gently inclined-layered dip bank slope ($\theta \leq 20^\circ$, $\delta \leq 30^\circ$)

This kind of bank slope distributed in synclinal valley section, for example, in the region near Wanzhou. The bank slope is mainly composed of Jurassic sand-mudstone interbedding, which shows a ladder shape with the average gradient of 20° . The groundwater existing in the slope presents as interlayer water, usually the sandstone near the underlying mudstone roof is the rich water belt, effects of argillization, softening, dilation, etc., mainly occurs in the mudstone roof.

The main deformation of this kind of bank slope shows the plastic flow of mudding interlayer or weathered mudstone along the mudstone roof, which will further pull the upper sandstone and cause slip pull-apart deformations, and then gradually form tensile crack, in turn, develop into small scale local secondary landslides. What's more, with cracks deepening and widening, the trailing edge of the landslide occurs collapse rockfalls due to the unloading effect. With heavy rainfall, the water in tensile crack may lead to the whole horizontal pushing type sliding, which is shown in Fig. 5a.

I2: Medium inclined-layered dip bank slope ($20^\circ < \theta \leq 45^\circ$, $\delta \leq 30^\circ$)

The bank slope is mainly composed of Jurassic sand-mudstone interbedding, and the whole slope shows a linear shape. The gradient of the slope is almost in accordance with the stratum gradient, about 30° . The groundwater existing in the slope presents as multilayer interlayer water or confined

aquifer, and the roof and floor of the mudstone both appear the phenomenon like argillization, softening, dilation, etc.

Usually, this kind of bank slope is monoclinic, which will be significantly affected by river incised action, in turn easily broaden the river valley, therefore, it provides a good free surface condition for landslide sliding, moreover, the average slope gradient and stratum gradient, nearly 30° , also provide enough gravitational potential energy for landslide sliding. The main deformation of this kind of slope presents the plastic flow of mudding interlayer or weathered mudstone along the mudstone roof, which extrudes the front sandstone resist-sliding section, and causes its uplift and curve, consequently, the resist-sliding section suffers shear failure under the effect of gravitational potential energy, and then leads to integral sliding. Deformation mode is given priority to sliding—bending—cutting form, which would develop into dip—reverse layer landslides as shown in Fig. 5b.

I3: Layered dip bank slope with the variable gradient ($0^\circ \leq \theta \leq 45^\circ$, $\delta \leq 30^\circ$)

This bank slope is most in the convergence area of the fold, such as the river valley section of Fengjie and Yunyang. The weak layer in profile presents a chair or wave shape (in presence of the secondary fold). The average slope gradient approximates the whole stratum inclination, generally about 30° – 35° . The groundwater existing in the slope presents as multilayer interlayer water or confined aquifer, and the mudstone roof and floor both appear the phenomenon like argillization, softening, dilation, etc.

The bank slope deformation is mainly slipping—bending. The plastic flow of mudding interlayer or weathered mudstone along the mudstone roof leads the steep rock layer in trailing edge to drive and extrude the gently inclined layer in

leading edge. The joints and fissures usually develop in the core of a fold, where the rock mass is broken and occur shear failure easily. In result, this kind of bank slope is most likely to develop into sliding—bending or dipping—cutting layer landslides, which is shown in Fig. 5c.

I4: Layered reverse bank slope ($10^\circ < \theta \leq 45^\circ$, $150^\circ \leq \delta \leq 180^\circ$)

Most bank slopes of this type are located in the other side of layered dip bank slope; whose average slope gradient is between 30° and 40° . The groundwater existing in the slope presents as phreatic water living in the surface weathering unloading section.

Since the stratum in this kind of bank slope is anti-dipping strata, the failure of slope occurs under the action of structure plane combination. The deformation mode of bank slope is mainly bending—cracking and creep sliding—cracking. The former usually occurs in gently to medium inclined reverse bank slope, presenting as the crack of weathering fissure section. The cut-through slip surface forms in result of crack tracking stratum plane, which thus cause the shallow cutting-layered landslide; the latter usually occurs in the steep reverse bank slope, in which the hard rock alternates with the soft rock. The large deep cutting-layered landslide developed after the creep sliding and tensile crack, which is shown in Fig. 5d.

I5: Layered oblique bank slope ($0^\circ < \theta \leq 45^\circ$, $30^\circ < \delta < 150^\circ$)

Landslides developed in oblique bank slope are only second to that in dip bank slope. Since the condition of bank slope failure cannot be formatted by the rock plane itself, the sliding and/or collapse will occur easily by structure plane combination like joints and fissures. Moreover, the bigger the angel between strata inclination and bank slope aspect is, the more stable the bank slope becomes.

II: Nearly horizontal—gently inclined-layered bank slope with weak bases ($\theta \leq 20^\circ$)

This kind of bank slope usually has a high and steep terrain. The section facing Yangtze River in the bank slope is usually collapse deposits, and the trailing edge of the bank slope is the bedrock scarp. The lithology is composed of overlying thick sandstone and underlying thin weak layers of mudstone. The groundwater lies in fracture of sandstone and mudstone roof.

The deformation mode of bank slope is mainly plastic flow—tilting failure with tensile crack. The plastic flow usually occurs due to the gravity of thick sandstone overlying on thin weak layer. While the tensile crack in the upper sandstone with vertical joints appears because of the base sliding, which easily cause the collapse and tilting failure as shown in Fig. 5e.

III: Layered bank slope controlled jointly by layers and structure surface

In this kind of bank slope there are usually two groups of structural joints which are nearly orthogonal. One of them is parallel to the strike direction of layer with the length about meters or hundred meters. In the conditions of unloading of the leading edge of bank slope or a good free surface, the lansliding or collapse will easily happened, which is shown in Fig. 5f.

Conclusions

Sixty typical landslides in Jurassic red-strata in TGR are selected as the statistical analysis sample. In the aspects of landslide distribution, landform of bank slope, and the structure of bank slope, this paper draws the following conclusions.

Landslides in Jurassic red-strata in TGR usually developed in J_2s and J_3p , and located within the influence of reservoir water level fluctuation and human engineering activities from the view of the distribution of elevation. This kind of landslides mainly distributes in the linear-shaped bank slope, and secondly, in convex and ladder-shaped bank slope. When the gradient of linear-shaped bank slope is between 10° and 20° , large scale landslide would probably develop, and is usually a thick-bedded one; when between 20° and 30° , huge scale landslide with mega-thick layer could relatively develop; whereas in nearly horizontal slope (gradient $< 10^\circ$), large thick-bedded landslide casually appears. While the gradient of nonlinear—shaped bank slope is between 10° and 20° , the huge and large scale landslides would mostly develop, both of which could form thick-bedded or mega-thick-bedded landslide; when the gradient of bank slope is between 20° and 30° , or between 30° and 40° , large thick-bedded landslide grows better, nevertheless, huge scale landslide with mega-thick layer and medium scale landslide occasionally appears.

Landslides in Jurassic red-strata in TGR can be divided into three categories; each class corresponds to a failure mode, respectively. They are: the layered bank slope controlled by soft layer (class I), the layered bank slope controlled by weak substrate (class II), and the layered bank slope controlled by bedding and structural surface (class III). Among them, the first class is divided into five subclasses based on the syntagmatic relation among the gradient of sliding bed rock (θ), the angle between slope aspect and sliding bed rock inclination (δ) and slope aspect.

Acknowledgments This study was supported by the National Natural Science Foundation of China (No. 41101515, No. 41202247 and No. 41240023). Also this study was partially supported by the Fundamental Research Funds for the Central Universities, China University of Geosciences (Wuhan), No. CUGL110203.

References

- Bai YF, Zhou DP, Feng J (2005) Upper limit of angle between strikes of slope and strata for dip slope. *J Southwest Jiaotong Univ* 40(3): 326–329
- Chai B (2008) Systematic research on rock mass structure of Three Gorges Reservoir shoreline slope in the new Badong country. PhD Thesis, Chinese University of Geosciences, Wuhan, China
- Chai B, Yin KL, Jian WX, Dai YX (2009) Analysis of water-rock interaction characteristics and bank slope failure process of red-strata. *J Cent South Univ* 40(4):1092–1098
- Chen Q, Kou XB, Huang SB, Zhou YJ (2004) The distributes and geologic environment characteristics of red beds in China. *J Eng Geol* 12(1):34–40
- Hu HT, Zhao XY (2006) Studies on rockmass structure in slope of red bed in China. *Chin J Geotech Eng* 28(6):689–694
- Huang RH (2007) Large-scale landslides and their sliding mechanisms in China since the 20th century. *Chin J Rock Mech Eng* 26(3): 434–454
- Jian WX, Yin KL, Ma CQ, Liu LL, Zhang C (2005) Characteristics of incompetent beds in Jurassic red clastic rocks in Wanzhou. *Rock Soil Mech* 26(6):901–905, 914
- Jian WX, Yin KL, Luo C, Yao LL, Zhang C (2008) Slip zone characteristics of Anlesi landslide in Wanzhou of Three Gorges Reservoir area. *Earth Sci J China Univ Geosci* 33(5):672–678
- Jian WX, Wang ZJ, Yin KL (2009) Mechanism of the Anlesi landslide in the Three Gorges Reservoir, China. *Eng Geol* 108(1–2):86–95
- Li TY, Wang JL (2002) Chinese red beds and landforms. *J Sichuan Normal Univ* 25(4):427–431
- Liao QL, Li X, Li SD, Dong YH (2005) Occurrence, geology and geomorphy characteristics and origin of Qiangjiangping landslide in Three Gorges Reservoir area and study on ancient landslide criterion. *Chin J Rock Mech Eng* 24(17):3146–3153
- Qiao JP (2002) Structure and shape of landslide. *Chin J Rock Mech Eng* 21(9):1355–1358
- Wang FW, Zhang YM, Huo ZT, Matsumoto T, Huang BL (2004) The July 14, 2003 Qiangjiangping landslide, Three Gorges Reservoir, China. *Landslides* 1(2):157–162
- Xu RC, Zhou JJ (2010) Red bed and dam, 2nd edn. China University of Geosciences Press, Wuhan, pp 1–20. ISBN 9787562525363
- Yin YP (2005) Human-cutting slope structure and failure pattern at the Three Gorges Reservoir. *J Eng Geol* 13(2):145–154
- Yin KL, Wu YP (1998) Systematic research of one special paleo-landslide in the Three-Gorges Reservoir. *Chin J Geol Hazard Control* 9(S):200–206



Influence of Geotechnical Properties on Landslide Dam Failure Due to Internal Erosion and Piping

Austin Chukwueloka Okeke, Fawu Wang, and Yasuhiro Mitani

Abstract

Landslide dams are formed in valley-confined settings where favourable conditions like earthquakes, oversteepened slopes, rainfall and snowmelt affect relatively weathered bedrocks, leading to downslope movement of mountain materials which, under favourable geomorphic setting, block river valleys creating barrier lakes. Landslide dams may fail by overtopping or by internal erosion and piping. Presently, stability assessments of landslide dams are done considering the geomorphic characteristics of the blockage mainly, without analyzing the properties of the dam materials. This paper presents results of experiments carried out to study the influence of geotechnical properties of landslide dams to failure by internal erosion and piping. The dam models were made up of mixed and uniform soils of varying grain sizes and other index properties. The results show that characteristic properties of dam materials such as density, soil type, dispersion, degree of compaction, hydraulic conductivity and soil gradation affect the stability of dams and control the time and magnitude of the resulting flood. The present study provides new idea and insight on stability analysis of landslide dams considering sparse research results on material properties of landslide dams, which is relevant in numerical simulation of dams, flood routing and early warning system development.

Keywords

Landslide dam • Piping • Laboratory experiments • Internal erosion • Geotechnical properties • Monitoring sensors

Introduction

Landslide dams, levees, embankment dams and other natural dams sometimes fail by internal erosion and piping. This has been found to depend solely on the internal structures and material characteristics of the blockages. Recent studies and inventories of 204 known cases of failed landslide dams show that their life span range from several minutes to 20,000 years, depending on: (1) the material composition and internal structure of the dam, (2) the size, volume and

shape, and (3) the rate of inflow into the blockage (Costa and Schuster 1988; Peng and Zhang 2012). Numerous assessment methods developed for predicting landslide dam stability and longevity consider only the geometry of the blockage. For example, Korup (2004) carried out a quantitative analysis of $n = 232$ landslide dam cases in New Zealand and proposed three dimensionless indices, the Backstow Index, the Basin Index I_a and the Relief Index I_r , based on landslide dam height H_d . The author reported that geomorphometric parameters such as landslide dam height H_d , landslide dam volume V_d , lake volume V_l , catchment area A_c , and local relief H_r , are major parameters used in assessing landslide dam stability, excluding other variables such as climatic factors and lithologic characteristics of the dam material. Casagli and Ermini (1999) analyzed several cases of landslide dams in the

A.C. Okeke (✉) • F. Wang • Y. Mitani
Research Center on Natural Disaster Reduction, Shimane University,
1060 Nishikawatsu-cho, Matsue, Shimane 690-8504, Japan
e-mail: elo_destiny@yahoo.com; wangfw@riko.shimane-u.ac.jp

Northern Apennines and defined a landslide dam assessment method known as the Blockage Index (*BI*):

$$BI = \log\left(\frac{V_d}{A_b}\right) \quad (1)$$

Where V_d is the landslide volume (m^3), and A_b the catchment area (km^2). The Blockage Index was further modified by Ermini and Casagli (2003) by adding another geomorphic parameter, H_d to define an index known as the Dimensionless Blockage Index (*DBI*):

$$DBI = \log\left(\frac{A_b \times H_d}{V_d}\right) \quad (2)$$

The disadvantage of using geomorphic analysis in stability assessment of landslide dams is due to the fact that some of the major factors that determine the stability and longevity of landslide dams, such as material composition and geotechnical properties of dam materials are not considered in the method. However, numerous approaches have been adopted for the study and evaluation of internal structures and geotechnical properties of landslide dams (Dunning 2006). The influence of grain size distribution on stability and longevity of landslide dams has been reported in several literature (Shugar and Clague 2011; Casagli et al. 2003). The nature of soil material such as the degree of consolidation, percentage clay content, coefficient of uniformity and other index properties, influence the overall strength of dams and control permeability, seepage and internal erosion in landslide dams.

This research aims at studying the effect of geotechnical properties of landslide dam materials to failure by internal erosion and piping by building laboratory-scale landslide dam models with mixed and homogeneous silica sands of varying geotechnical properties.

Experimental Setup

The experiments were carried out in a transparent flume box $2 \text{ m} \times 0.45 \text{ m} \times 0.45 \text{ m}$ in size. The flume box was tilted to make a bed slope of 5° . Two drainage outlets of diameter, 4 cm each were bored at the downstream end of the flume to allow steady discharge of sediment-laden water. Two intelligent CMOS multi-function analog laser sensors were attached to a wooden overboard to measure pre-failure crest settlement associated with the onset of internal erosion and piping. To obtain characteristic concave-upward curvature of the dams during internal erosion and piping, one of the sensors (H_{d1}) was positioned directly above the center of the dam crest, while the other sensor (H_{d2}), was positioned

0.07 m away from the central part of the crest. The measurements were made by allowing maximum vertical distance of 0.25 m between the dam crest and the sensor heads (Fig. 1a). Lateral displacement and downstream transport of dam materials were measured with a linear displacement transducer (LDT), which has maximum response speed of 0.2 m/s and measuring range of 1.0 m (Fig. 1b). The transducer was fixed at the upper end of the flume box while a thin metallic wire attached to the sensor was connected to a plastic ball of similar weight with the materials used in the experiments. The ball was buried at the center of the dam crest, while the outer end of the metallic wire, suspended by a known weight was made to pass through four stationary pulleys. Recalibrated pore water pressure sensor with rated capacity of 50 kPa was used to track transient changes in upstream water level. The pore water pressure sensor was fixed at a stationary position near the upstream dam toe to ensure accurate measurement and recording of data (Fig. 1c). Upstream water was recharged from a drainage hose fed by a water tap. The inflow rate was set at constant rate of $120 \text{ cm}^3/\text{s}$ by a flow-meter fixed at the upper part of the flume box (Fig. 1d). A turbidity sensor (VisoTurb^(R) 700 IQ SW) was inserted into one of the drainage outlets to measure the rate of internal erosion and sediment transport processes in the dam models and to obtain transient changes in turbidity of the sediment-laden water. This was done since internal erosion process begins with selective removal of fines within the interstitial pores of sand materials. All the sensors were connected to a standard real time monitoring and recording unit comprised of a universal recorder (KYOWA, EDX-100A) and a computer. Two digital video cameras were strategically positioned to record the failure sequence of the dam models. Schematic diagram of the experimental setup with location of sensors and work station used in recording of data is shown in Fig. 2.

Properties of the Materials and Dam Model Construction

The dam materials are composed of mixed and homogeneous samples of industrial silica sand numbers 4, 5, 6, 7, and 8 in varying proportions (Table 1). The grain shapes are generally sub-angular to sub-rounded containing high amount of quartz and sparse distribution of feldspars. The sand samples, composed of varying properties such as grain size distribution, permeability, density, percentage clay content, degree of saturation and plasticity index were used to build landslide dam models of uniform height (H_d) and crest width of 0.25 and 0.01 m, respectively (Fig. 3a). About 40 kg of each material was rigorously mixed in an industrial mixer.

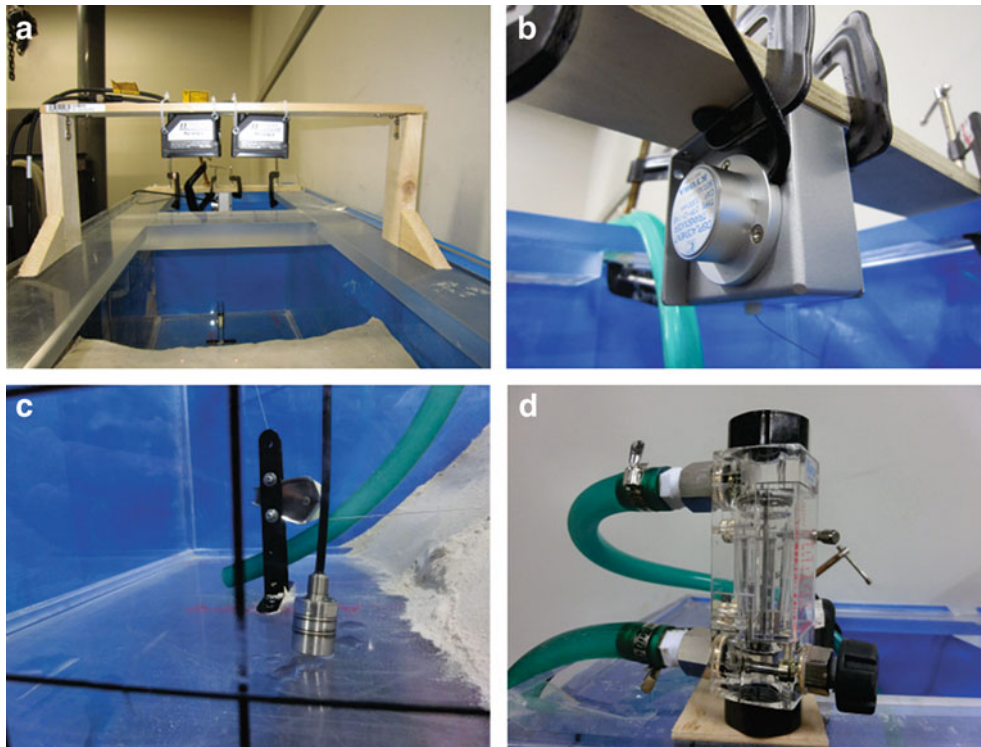


Fig. 1 Location of sensors used in the experiments showing: (a) laser displacement sensors; (b) linear displacement transducer; (c) upstream water probe; (d) upstream flow-meter

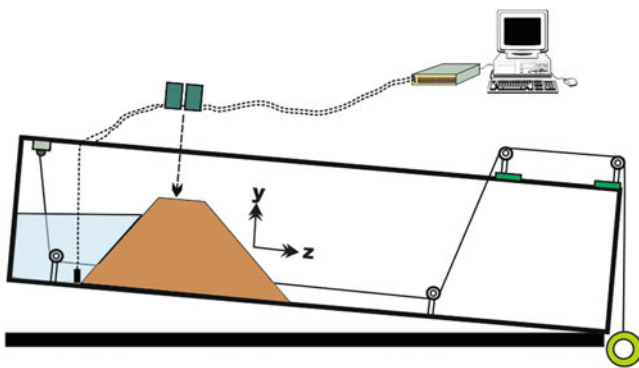


Fig. 2 Experimental set up with sensor positions

The dams, built 0.4 m away from the upstream water inlet, were uniformly compacted by gently tapping each 5 cm-thick sand laid in the flume box with a wooden mallet. Friction was increased at the sides of the flume by ensuring maximum compaction of sands near the flume wall and reducing void spaces between the sand particles and the flume wall. Internal erosion was initiated by laying uniformly sized pebbles encased in a plastic mesh at the center of the dam model (Fig. 3b). The encased pebbles were laid such that a flume bed slope of 10–12° was obtained. A plastic ball attached to the linear displacement transducer was laid in the dam and kept at critical tension by a

Table 1 Summary of percentage composition of materials used in the experiments

Sample name	Percentage composition
Dam mix A	20 % of silica sands 4, 5, 6, 7 and 8
Dam mix B	70 % of SS-5 and 30 % of SS-8
Dam mix C	70 % of SS-6 and 30 % of SS-8
Dam mix D	70 % of SS-8 and 30 % of SS-4
Dam mix E	SS-4 100 %
Dam mix F	SS-5 100 %
Dam mix G	SS-6 100 %
Dam mix H	SS-7 100 %
Dam mix I	SS-8 100 %

suspended weight. The dams were built at constant upstream and downstream slope angles of 35° and 50°, respectively.

Experimental Results and Discussions

General Features

The generalized failure sequence observed in all the experiments are: pipe development, pipe gross enlargement, crest settlement, hydraulic fracturing, progressive sloughing, collapse of dam crest and breach. Figure 4 shows observed erosional stages of dam mix G and I. Internal erosion begins

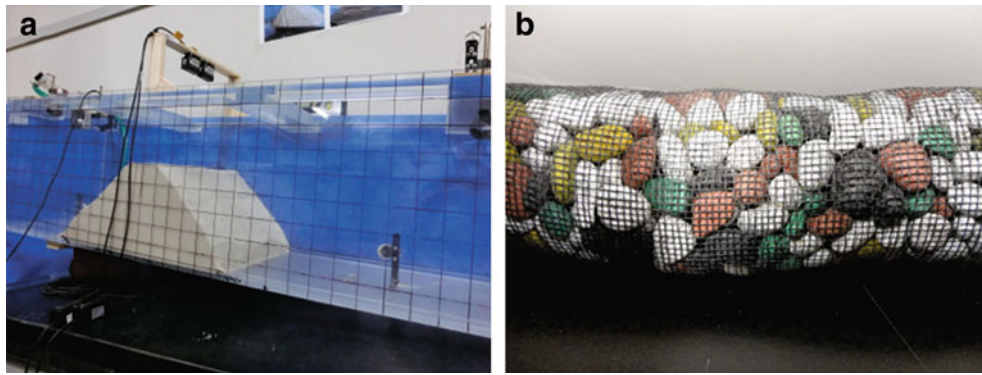


Fig. 3 (a) Location of 0.25 m thick dam model at the upper part of the flume box; (b) pebbles used as drainage channel

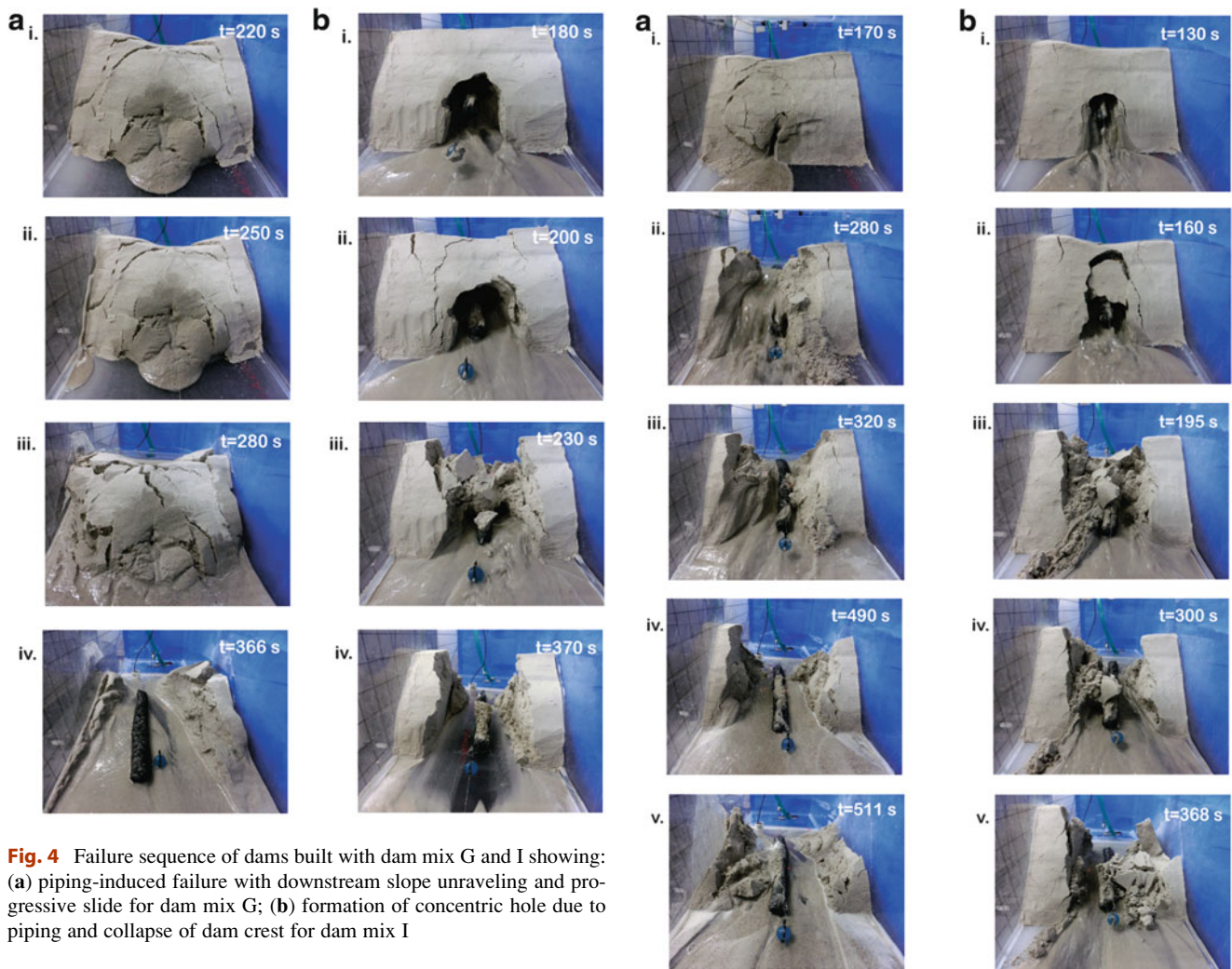


Fig. 4 Failure sequence of dams built with dam mix G and I showing: (a) piping-induced failure with downstream slope unraveling and progressive slide for dam mix G; (b) formation of concentric hole due to piping and collapse of dam crest for dam mix I

as soon as the level of the upstream lake reaches the height at which the pebbles were laid. At the downstream dam face, concentrated seepage paths (pipes) develop with low outburst of sediment-laden water. This is preceded by gross enlargement of the pipe with high velocity outburst floods.

Fig. 5 Failure sequence of dams built with dam mix B and dam mix F showing: (a) piping-induced failure coupled with late stage overtopping failure for dam mix B; (b) piping and instantaneous collapse of dam crest for dam mix F

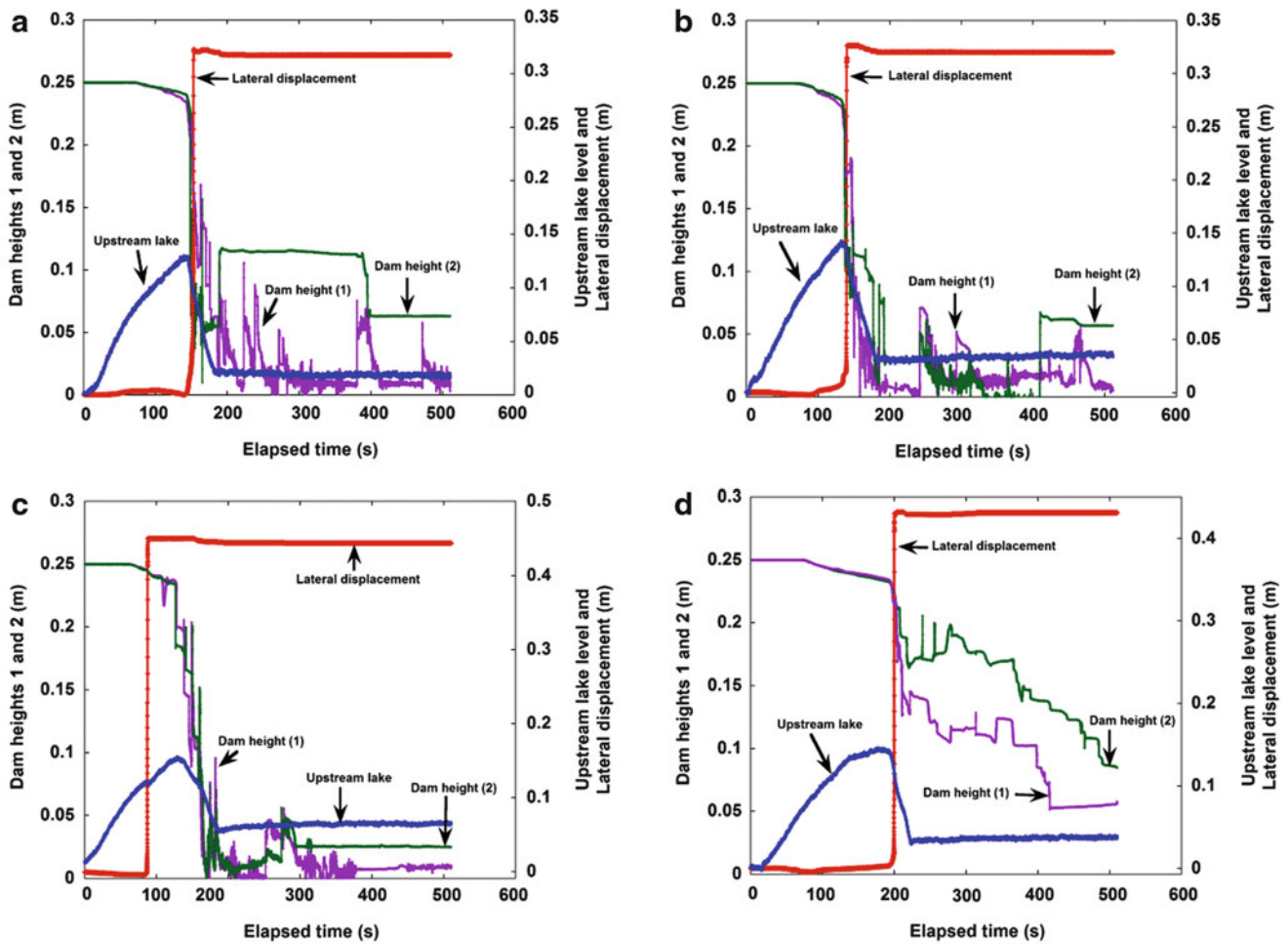


Fig. 6 Stage hydrographs and failure sequence of dams built with mixed materials of dam mix A, B, C and D

The removal of internal materials of the dams leads to crest settlement with the formation of cracks running parallel to the downstream slope. The duration and longevity of the dam crest depends on the shear strength of the soil material and the tractive force which is directly related to the velocity of the intergranular flow. Dam breach occurs with collapse of the dam crest leading to steady rise in upstream lake. Downstream erosion continues when the erosive force of the upstream lake is able to dislodge the dam material. The formation of a wide breach channel marks the end of the failure process. However, these processes vary with the material composition of the dams.

The formation of concentric seepage paths depends on the ability of the material to support the dam crest (Fig. 4b-i). In contrast to dam mix I, backward erosion and formation of concentric pipes do not occur in dams composed of clean sands of very low fine content (Fig. 4a-i). The appearance of concentrated seepage zone with very low muddy leakages at the downstream slope exit is followed by settlement of the dam crest (Fig. 4a-ii). This is preceded by progressive sloughing and undercutting of the downstream dam toe

leading to the formation of very steep and unstable slope surfaces. In some cases, the failure is enhanced by concentrated leakages that originate from crevasses and fractures trending along the crest down to the downstream slope toe. Gradual unraveling of the downstream slope and increased seepage forces, with the lowering of the crest due to internal erosion and effect of pore water pressure leads to instantaneous failure by sliding (Fig. 4a-iii). This process has been attributed to the effect of grain size distribution which controls the overall behavior of landslide dams. Figure 5 shows observed erosional processes of dam mix B and F composed of mixed silica sand nos. 5 and 8, and homogeneous samples of silica sand no. 5, respectively. Failure sequence of the dam built with dam mix F (Fig. 5b) starts with initial bulging at the downstream toe due to increased pressure of the erosive forces within the dam. The effect of internal erosion and high pore water pressure within the dam is shown by the concave-upward curvature of the dam crest. Crest settlement is followed by the formation of fractures and gradual undercutting of the downstream slope toe due to the effect of the growing outflow water and developing pipe.

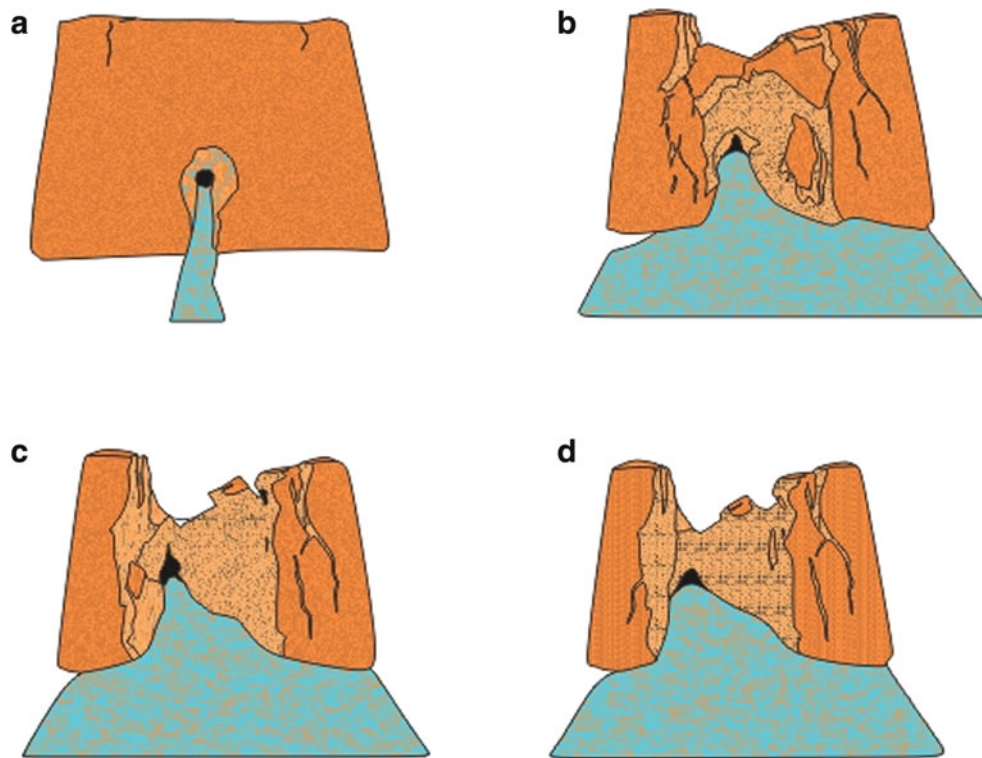


Fig. 7 Failure stages of dam built with dam mix D showing: (a) initial stage of piping; (b) collapse of dam crest; (c) downstream slope unraveling; (d) breach

The unraveling of the downstream slope leads to gradual lateral spread which continues until the upstream lake flows over the dam crest. This failure style is relatively different from the one shown in Fig. 5a which is composed of gap graded material. Also, the strength of the two dams can be evaluated from the final breach formation time, T_b . Evidence of suffusion is visible in the dam built with dam mix B due to the formation of defined seepage path from which high turbidity sediment-laden water flowed until the shear strength of the dam material reduced drastically. This led to the collapse of the dam crest and consequent overtopping flow of the upstream lake (Fig. 5a-iii). The relative difference in tractive force, velocity of the seepage flow and erodibility of the dam sediments can be seen from the final breach morphology formed at the end of the two failure processes. This is due to the difference in shear resistance of the two materials, coefficient of uniformity, permeability and the size of pore spaces between the sand grains.

(a) *Case I—Analysis of dams composed of mixed materials*

Figure 6 shows stage hydrographs and failure sequence of dams built with homogeneous materials of dam mix A, B, C and D. The overall failure mechanism observed in these experiments is primarily contributed by piping. Analysis of all the results show that strength properties

of the dam materials decreased from dam mix D to dam mix C. The relative high strength properties of dam mix D is shown by its ability to form dam roof which lasted for a longer period of time (Fig. 7). This is evidenced from the relative low uniformity coefficient and maximum dry density of dam mix D (ρ_{dmax} , 1.65 and C_u , 1.86) with respect to dam mix A, B and C (ρ_{dmax} , 1.74, 1.72 and 1.63, and C_u , 1.94, 2.62 and 1.75, respectively).

(b) *Case II—Analysis of dams composed of homogeneous materials*

Figure 8 shows results of analysis of geotechnical properties of dams built with dam mix E, F, G and I. Initial concave-upward curvature of the dam crests formed due to removal of internal materials of the dams is observed from plotted values of dam heights 1 and 2. The overall sediment transport pattern is influenced by the characteristic properties of the dam materials which include unit weight, permeability, porosity, density and coefficient of uniformity.

Analysis of dam mix E, F and G shows that dam built with dam mix G lasted longer than those built with dam mix E and F, even at higher permeability values of dam mix E with respect to dam mix F and G. However, for the same upstream discharge velocity, thickness of the

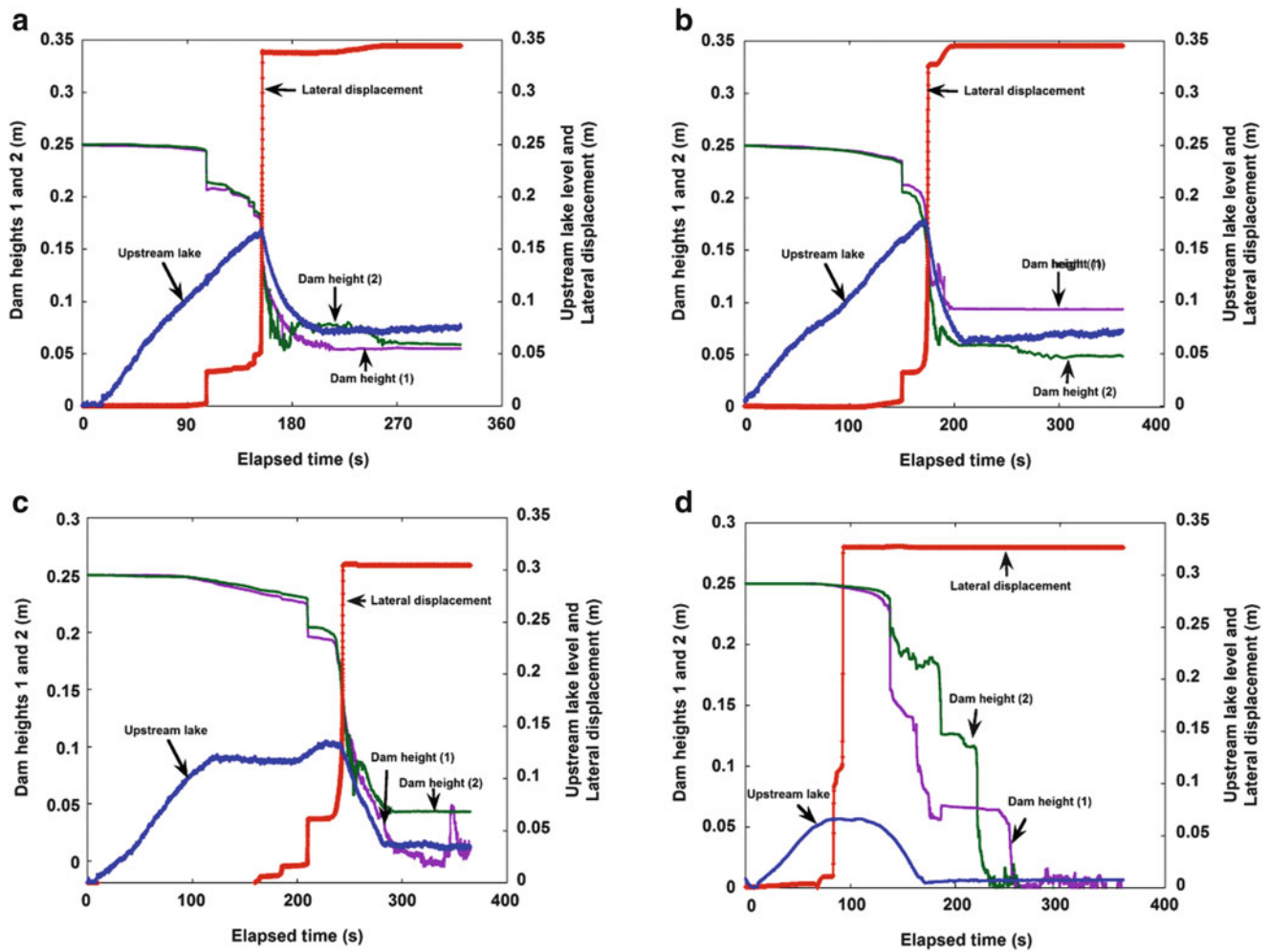


Fig. 8 Stage hydrographs and failure sequence of dams built with homogeneous materials of dam mix E, F, G and I

uneroded sediments at the bottom of the breach channel increased from dam mix G to E; this can be attributed to the relationship between intergranular flow velocity and shear resistance of the dam materials. For all the experiments conducted with homogenous dam materials, only dam mix H and I were able to support a roof (Fig. 9), while others failed by piping coupled with late stage overtopping due to downstream slope unraveling.

(c) *Case III—Influence of dam materials on the overall behavior of dams*

Figure 10 shows transient behavior of the dams due to the effect of piping and internal erosion. Values obtained from transient decrease in dam heights at the middle part of the dam crests (H_{dl}) are plotted against the elapsed time. Failure sequence of dams built with homogeneous materials of dam mix E, F and G is shown in Fig. 10b. The plot shows significant difference in downstream erosion of sediments. Thicknesses of uneroded

sediments deposited at the floor of the breach channel are 0.1 m, 0.05 m and 0.01 m for dam mix E, F and G, respectively.

This variation in thickness of dam sediments at the floor of the breach channel is found to depend on permeability and erosive forces of the upstream lake. The relative difference in index properties of the dam materials influenced the failure mechanism of the dams (Fig. 10a, b). The relationship between erosive forces of the upstream lake and density of the sediments is illustrated by the thickness of uneroded dam sediments at the floor of the breach channel.

Conclusions

Series of experiments were conducted to study the influence of geotechnical properties of landslide dam materials to failure by internal erosion and piping. Soil particle density was observed as the major factor controlling the development of internal erosion, notwithstanding high

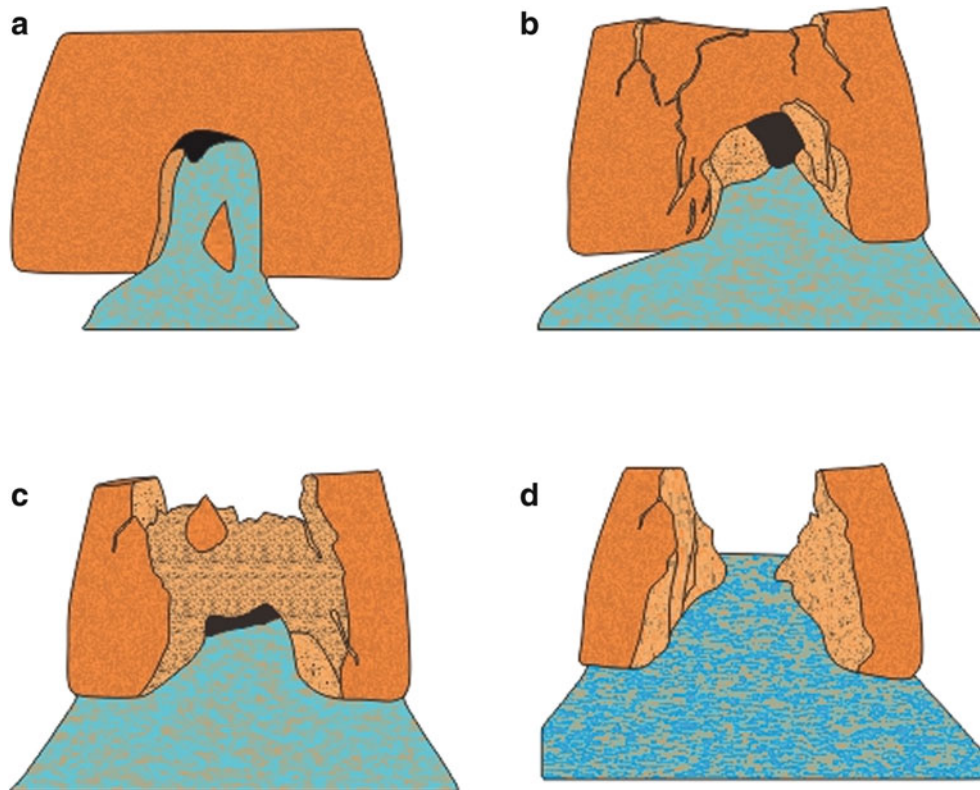


Fig. 9 Failure stages of dam built with dam mix I showing: (a) piping; (b) pipe development; (c) onset of breaching; (d) final breach morphology

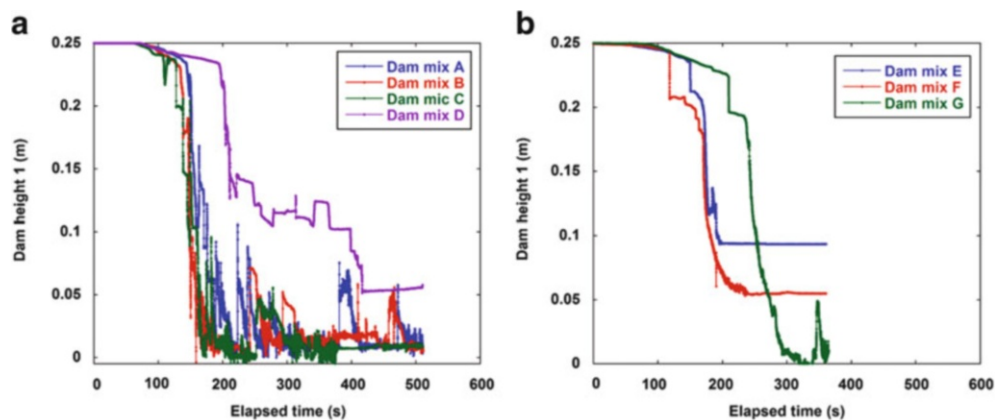


Fig. 10 Analysis of transient changes in: (a) dams built with reconstituted materials of dam mix A, B, C and D and, (b) homogeneous materials of dam mix E, F and G

permeability values of some of the materials. This may be due to the minimum shear resistance which must be overcome by the seeping water to dislodge the soil particles. Results obtained shows that the dam built with dam mix D materials posed high resistance to failure with respect to other constituted soil materials. This could indicate that there is a critical value of uniformity coefficient and pore size at which the dam models can withstand the onset of internal erosion and piping.

References

- Casagli N, Ermini L (1999) Geomorphic analysis of landslide dams in the Northern Appennine. *Tran Jap Geomorph Union* 20(3):219–249
- Casagli N, Ermini L, Rosati G (2003) Determining grain size distribution of material composing landslide dams in the Northern Appennines: sampling and processing methods. *Eng Geol (Amsterdam)* 69:83–97
- Costa JE, Schuster RL (1988) The formation and failure of natural dams. *Geol Soc Am Bull* 100:1054–1068

- Dunning SA (2006) The grain-size distribution of rock avalanche deposits in valley-confined settings. *Ital J Eng Geol Environ* 1:117–121
- Ermini L, Casagli N (2003) Prediction of the behaviour of landslide dams using a geomorphological dimensionless index. *Earth Surf Process Landforms* 28:31–47
- Korup O (2004) Geomorphometric characteristics of New Zealand landslide dams. *Eng Geol* 73(1):13–35
- Peng M, Zhang LM (2012) Breaching parameters of landslide dams. *Landslides* 9(1):13–31
- Shugar DH, Clague JJ (2011) The sedimentology and geomorphology of rock avalanche deposits on glaciers. *Sedimentology* 58(7):1762–1783



Sarez Lake Problem: Ensuring Long-Term Safety

Alexander Strom

Abstract

The main ambiguities related to the Usoi natural dam and the Sarez Lake evolution are described. They are predetermined by insufficient knowledge of the geological structure of the dam and valley slopes and by uncertain seismological conditions of the region. All these uncertainties do not allow to guarantee long-term (decades–centuries) safety of the Sarez Lake without special technical measures aimed to reduce risk of the Usoi dam breach. These laborious and time-consuming measures could be implemented while the situation remains stable.

Keywords

Sarez Lake • Usoi dam • Rockslide • Seismicity

Introduction: Brief Overview of Past Studies

The Sarez Lake formed in 1911 by the seismically triggered Usoi rockslide is the World-deepest natural reservoir that stores about 17 km³ of water and represents potential threat to the communities in Tajikistan, Afghanistan, Uzbekistan and Turkmenistan.

During the 100-years long history of studies different opinions on the lake safety were asserted. Some experts (Bukinich 1913; Rodionov 1931) expected that the dam would be either overtopped or eroded by the upslope advancing canyon relatively soon (within several decades). On the contrary, Shpilko (1914), Preobrajensky (1920), Lange (1926, 1929), Selivanov and Andreev (1959) concluded that blockage is a stable long-living feature that should sustain even in case of overflow.

Besides expectations that the dam could be overtopped by rising water, another threatening phenomenon was the rapid growth of the erosional canyon on the downslope face of the dam fed by seeping water and by debris flows from the

remnants of Usoi-Dara glacial valley. Fortunately in late 40th rockfall from the headscarp cliff diverted these debris flows towards the lake (Paramonov 1969). Later the lake level growth and the advance rate of the erosional canyon towards the dams' crest slowed down. However, in the same time a new problem was revealed: the possibility of large-scale slope failure into the water body that could produce a surge wave large enough to destroy the dam's crest became the main concern (Sheko 1968; Sheko and Lehatinov 1970; Fedorenko 1988). Since 1967 site investigations were concentrated on the right bank of the lake, 4–5 km upstream from the Usoi dam where the so called "Right-bank Landslide" was identified. Its volume estimates varied from 300 million m³ up to 2 km³.

This assumption is opposed by N. Ischuk who disclaimed the landslide nature not only of this part of the valley slope, but of many other sites around the Sares Lake and within the entire Pamirs (N. Ischuk 2011a, b).

Recently an early warning system was installed with the financial support of World Bank (Stucky 2001); it aimed to detect evidence of upcoming dam breach and to alarm people living in the river valleys downstream that might be affected by an outburst flood. Now there is a general consensus that the Usoi blockage in its present state can be considered as a stable feature that should not

A. Strom (✉)
Geodynamics Research Center – Branch of JSC "Hydroproject
Institute", Volokolamskoe Shosse, 2, 125993 Moscow, Russia
e-mail: strom.alexandr@yandex.ru

fail catastrophically in the near future (Alford and Schuster 2000).

But what about its long-term evolution with due regard to the river damming events and their evolution worldwide and considering scarcity of our knowledge of the feature in question?

Main Ambiguities of the Sarez Lake Safety Assessment

Due to the enormous size of the Usoi dam, site remoteness and difficult access conditions we still have resulted that till now, about 100 years after the event, we have quite limited knowledge of the internal structure of the blockage, its grain-size composition, of lake banks structure and stability. It predetermines uncertainty of the lake evolution scenarios except for data on the slow gradual rise of the water level with seasonal variations derived from long-term hydrological measurements (Biedermann and Attewill 2002).

Additional ambiguity is provided by inevitable uncertainty of seismic hazard assessment of the Sarez Lake region where historical records on hazardous natural phenomena are available for not more than 150–200 years, which is much shorter than the recurrence interval of large intracontinental earthquakes.

Ambiguities of the Usoi Dam Structure and Evolution

Lack of data on the dams' body internal structure and grain-size composition prevents reliable prediction of its behaviour both in "static" conditions and, especially, under seismic loading. Qualitative assumptions suggest several possible effects. First, seismic shaking could cause dams' compaction, its crest settlement and some blocking of seepage ways, which would lead to the dams' freeboard decrease.

Another scenario implies deformations of the blockage downstream face—i.e. development of secondary landslide within the dams' body. It seems to be quite realistic since the potential sliding surfaces have been formed already either during rockslide collision with the valley left bank and lateral spreading of the dams' body (Strom 2010a), or afterward, but in any case during the 1st years after dam formation (Paramonov 1969). Secondary sliding formed well-expressed bow-shape scarps along the dam crest affecting not only meta-sediments of the topmost part of the dam, but also marble and gypsum debris of its lowest proximal part as well (Fig. 1).

The comparison of the Usoi dam map compiled in 1915 by Prof. Preobrazhensky with stereoscopic aerial images made in 1951 (Paramonov 1969) shows that main

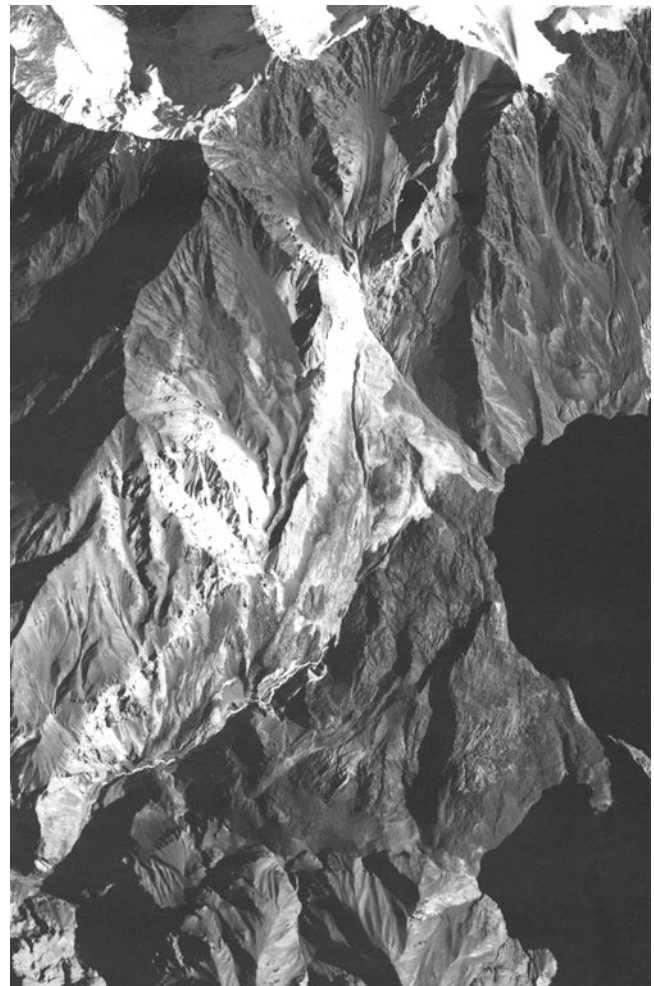


Fig. 1 Bow-shape scarps on the downstream face of the Usoi blockage marking secondary landslides (white arrows)

deformations of the dams' surface took place at its lower-most proximal part where a distinct bow-shape scarp extends from the topmost central part of the blockage (see Fig. 1). These movements could be associated with the erosional canyon growth or just with some internal deformations of the dams' body. It is obvious that strong earthquake(s) would increase the probability of such secondary sliding.

Activation of secondary sliding could affect filtration in an unpredictable way. Blocking of seepage ways would cause lake level growth, while increasing filtration could intensify erosion, both surficial and internal. The latter strongly depends on the grain-size composition of the Usoi dam interiors. The latter is not known, since no borehole deep enough to clarify it have been drilled yet.

However, detailed studies of a large number of deeply eroded large rockslide dams in different parts of the World (McSaveney and Davies 2006; Brückl and Heuberger 2001; Pollet and Schneider 2004; Dunning et al. 2005; Poschinger et al. 2006; Hewitt 2002; Strom 1994, 2006; Abdrakhmatov

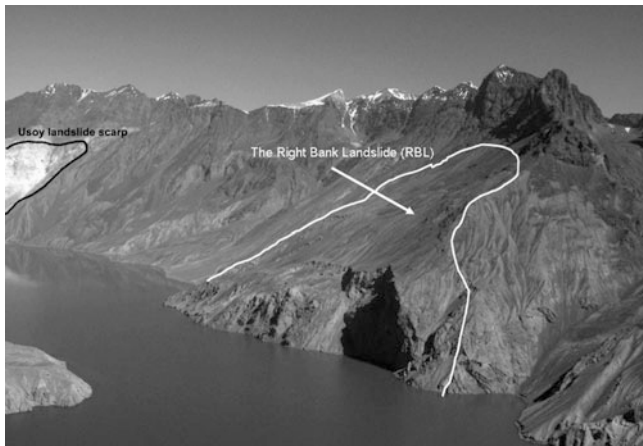


Fig. 2 The Sarez Lake right bank slope with distinct evidence of landslide undercutting. Photo courtesy A. Ischuk

and Strom 2006) show that practically all of them are characterized by a coarse blocky carapace overlying a giant “internal core” of intensively crushed and compacted material.

The same internal structure is assumed for the Usoi natural dam. Since the boundary between the blocky unit and crushed material may be sharp (similarly to many other deeply eroded blockages), concentrated seepage through the voids in the blocky part could entrain fine-grained material provoking internal erosion and piping.

Such composition could favour a catastrophic dams’ breach: removal of the coarse carapace by erosion or by a surge wave would lead to erosion of shattered material of the dam’s interior by powerful turbulent flow as it happened in 1963 during the Issyk dam breach (Gerasimov 1965; Strom 2010b).

Concluding this section I want to cite a passage from Goncharov and Skomarovskiy (2006): “*Centuries-old experience in the hydraulic engineering have produced the inviolable statement – if something uncontrolled takes place on the downstream face of the dam – this structure is doomed*”. It is obvious that the Usoi dam and, especially, its downstream face are subjected to such uncontrolled phenomena – erosion and secondary sliding that could be intensified by seismic shaking.

Ambiguities of the Sarez Lake Banks Stability Assessment

Uncertainty of the Sarez Lake long-term safety is increased by the possibility of slope failures along the lake banks that can induce powerful surge wave. From my point of view, the key problem is not if the so called “Right-bank Landslide” (RBL—Fig. 2) really exists, but if this slope (and slopes at

other lake banks as well) will be stable in a long-term perspective, especially in case of a strong earthquake.

Seismically induced landslides might occur both on “prepared” and on “unprepared” slopes (Fedorenko 1988). Considering the 1911 event, one could ask if anybody, armed by all modern facilities and techniques, would have been able to predict this rockslide several years before. Data on the pre-failure state of this slope are scarce, but, if there would have been any abnormal phenomena really indicating upcoming collapse (frequent rock-falls, strange sounds, etc.) people from Usoi village who survived must have remembered them. However, none of these indications had been reported. Most likely, this gigantic collapse was unpredictable.

In the same way, the next strong earthquake could trigger another large landslide, especially where the more than 1 km high slope has been un-buttressed by the existing landslide (see Fig. 2). Several more or less disastrous scenarios of such phenomena have been proposed and, again, scarcity of data does not allow us to make sound conclusions on their reliability.

Ambiguities of the Seismic Hazard Assessment

All the above uncertainties are increased at a large extent by high seismicity of the Sarez Lake area. Its seismic hazard is predetermined by frequent deep-focus earthquakes from the Pamirs—Hindu Kush zone at a depth of 100–300 km with large (up to ~7.5–8.0) magnitudes and by large crustal earthquakes similar to the 1911 one that had triggered the Usoi landslide as it was proposed by Ambraseys and Bilham (2012).

According to PSHA earthquakes with return period of ~100 years can produce mean peak ground acceleration (PGA) of 0.2 g at the site, while assumed maximum credible crustal earthquake of $M = 7.9$ can produce mean PGA of 0.213 g with a return period slightly above 130 years (Stucky 2001; A. Ischuk 2011). However, the statement that “the earthquakes with return periods >100 years and peak ground accelerations >0.20 g are unlikely to occur close to Lake Sarez” (Stucky 2001; A. Ischuk 2011, p. 428) means that such “extreme” seismic effects can be ignored, is incorrect. From my point of view these PGA estimates seem to be too low, moreover, considering that the return period of MCE and MDE strong motion used for high dams design is much longer than 100 years (ICOLD 1989).

According to Ambraseys and Bilham (2012) the source of the 1911 earthquake with $M_s = 7.7 \pm 0.3$ ($M_w \approx 7.7$) with rupture length of about 50–80 km and 6–10 m mean slip was associated with a fault zone passing, most likely, along the Bartang River valley, about 20 km north-west from the dam. Considering the typical recurrence interval of high-magnitude crustal earthquakes it is really unlikely that

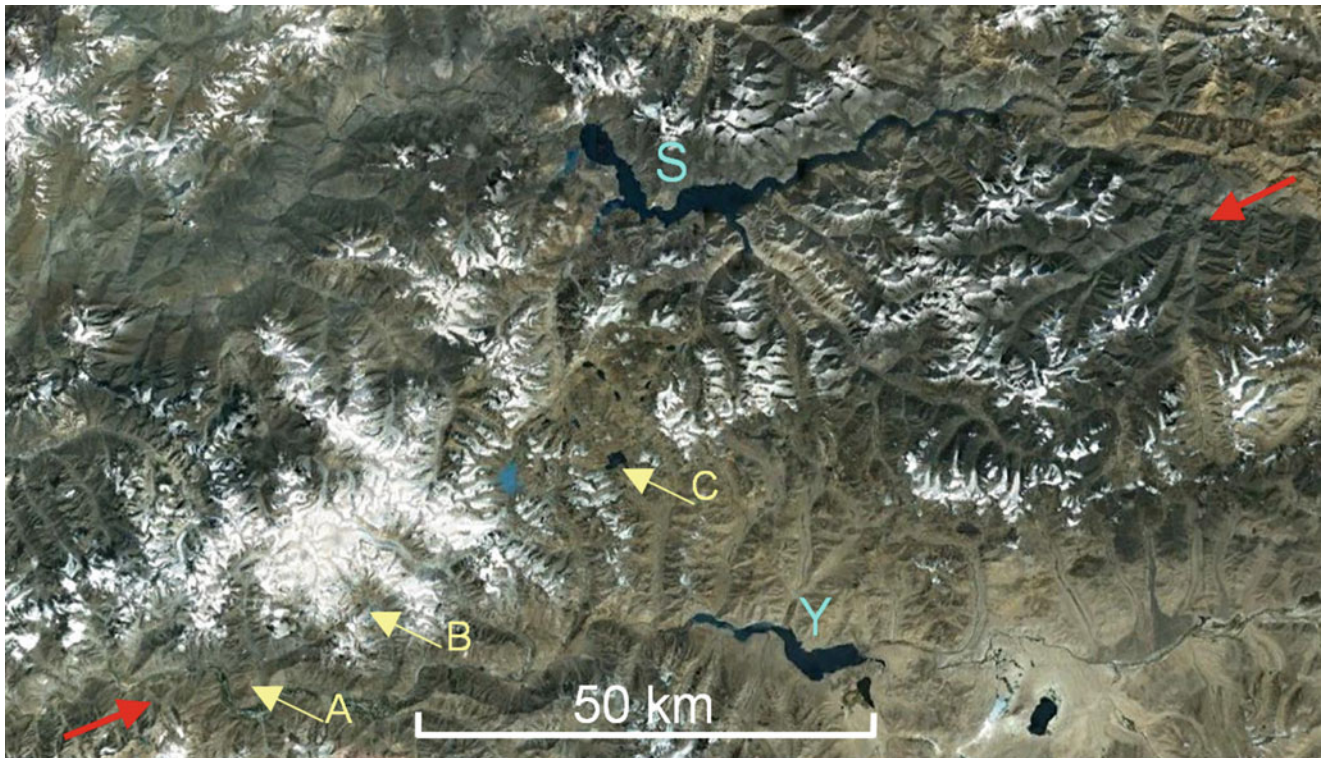


Fig. 3 Space image of the Bartag River–Gunt River water divide. *S* the Sarez Lake, *Y* the Yashilkul Lake. *Red arrows* mark the Pathur–Nemos active fault. Sites shown in Fig. 3 are indicated by *yellow arrows*

large earthquake would occur in the same source zone during the next decades.

This source zone, however, is not the only one in the vicinity of the Sarez Lake where large earthquake could occur. For example, the distinct Pathur–Nemos active fault of a length more than 100 km passes 35 km south from the Usoi dam (Fig. 3). Evidence of recent faulting (Fig. 4) show that this fault zone can be capable for large earthquakes. Based on the conservative approach required by ICOLD (1989) for unique dams it can be assumed that such fault zone could generate earthquakes up to M 7.5. (Wells and Coppersmith 1994), which intensity at the Usoi dam area might exceed 8 points on the macroseismic scale and, thus, PGA might exceed abovementioned values provided by PSHA calculations.

Besides, in rugged Pamirs terrain, strong motion parameters at the particular site could differ significantly from the mean PGA estimates. Real intensity amplification at the dams' crest and on suspicious slopes is unknown, which increases the uncertainty of possible seismic effects on the dam and Lake banks.

Discussion

Most of all natural dams failed (Costa and Schuster 1988), many of them catastrophically, and some after centuries or even millennia of “safe” existence (Strom 2010b; Hermanns et al. 2011; Hewitt 2011; Weidinger 2011). The uniqueness of each case study requires thorough analysis of the whole set of influencing factors, rather than more formal probabilistic assessment of the breach hazard based on the statistical analysis of river-damming events worldwide.

Rockslide dams that sustain overflow without any catastrophic effects such as the prehistoric Yashilkul dam 50 m high and 3.5 km wide (along the stream) in the Pamirs (see Fig. 3) are characterised by a combination of low-gradient profile and coarse blocky carapace. In such conditions overflowing or seeping is not strong enough to remove or erode the carapace.

Another combination of factors supporting long-term stability of rockslide dams and their gradual breach after overtopping is the position of the lowermost part of the

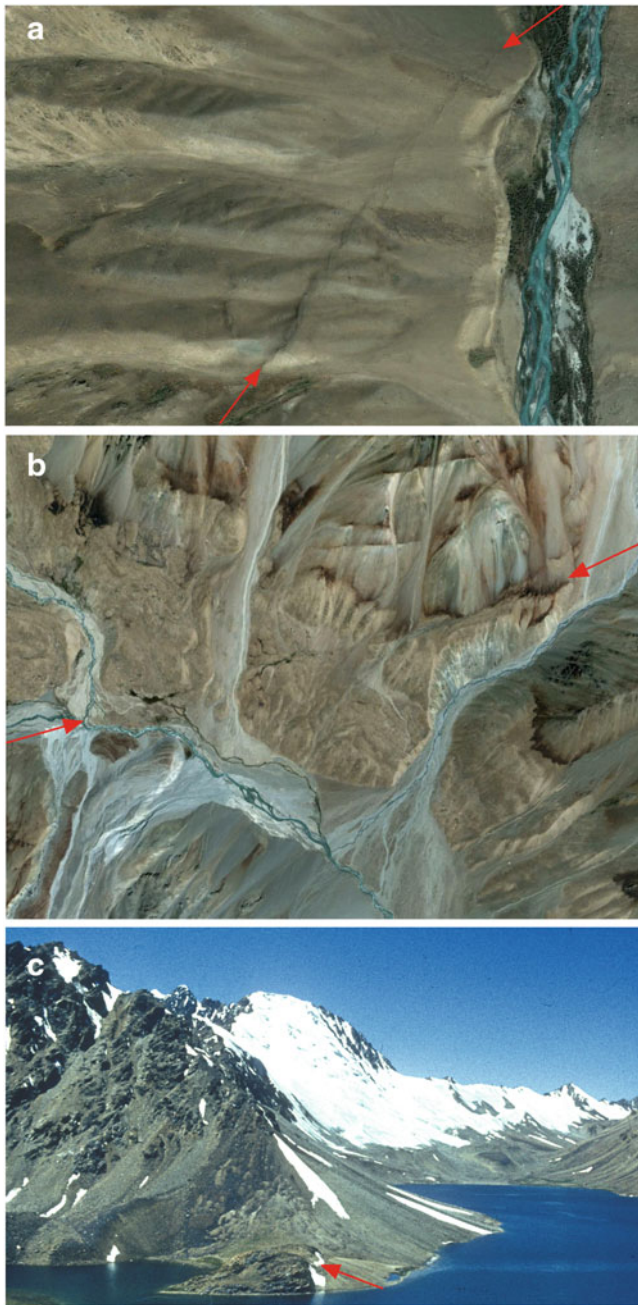


Fig. 4 Surface ruptures along the Psathur-Nemos active fault. (a) at the right bank of the Pathur River valley; (b) across moraine deposits in the upper reaches of the Shazud River valley; (c) small scarp at the southern bank of the Chapdara Lake marked by *arrow* reflects latest offset, while high escarpment covered by snow (at the background)—cumulative effect of multiple displacements

dams' crest relative to the local bedrock topography. If outflow takes place along the distal edge of the blockage or along some topographic lowering outside the landslide body, there is a good chance that erosion would reach bedrock soon. Higher erosional resistance of the bedrock would result in a gradual decrease of the dammed lake level, as it occurred, for example, at the Beshkiol landslide in the Naryn River valley (Korup et al. 2006).

In contrast, landslide dams with pronounced proximal lowering, as the Usoi one, are more susceptible to a catastrophic breach in case of overtopping since erosion starting at this part of the dams' crest would go through loose material up to a significant depth. Moreover, proximal lowering at the dams crest is often filled by subsequent rockfalls debris that could be less compact than the main landslide material and more erodible.

As an example, the Aksu rockslide dam comparable in size with the Usoi blockage had been breached soon after impoundment (Strom 2010b), due to absence of lake sediments upstream, though it had blocked a small river and should be considered as a stable feature according to low Dimensionless Blockage Index (DBI) value (Ermini and Casagli 2003) (Table 1). Likely, the same occurred with the 800 m high Rio Laja dam in Argentina (Hermanns et al. 2011). I assume that the critical factor determining such behaviour is the steepness of the downstream face of compact dams that increase the erosional power of overflowing or seeping water significantly (Strom 2010b).

It should be pointed out that even the centuries-old existence of some landslide-dammed lakes cannot guarantee that they will remain safe forever if a combination of their morphological and structural peculiarities facilitates dams' breach. It can be illustrated by the catastrophic outburst floods from the Issyk Lake in 1963, from the Yashinkul Lake in 1966 [both in Kyrgyzstan; see Strom (2010b)] and the 1914 Rio Barrankas disaster in Argentina (Hermanns et al. 2011). I want to point out that all breached dams listed in Table 1 had low DBI value, thus being "stable" features. Nevertheless, each of these dams was breached by some extreme event after several hundreds years of safe evolution.

It seems that such "delayed" breach is more typical of landslide-dammed lakes located in the arid climatic zone than of those in the wet (monsoon) climatic zone with large annual peak discharges. The latter fail rather soon after impoundment that can be exemplified by the 1841 Indus, 1858 Hunza, 1894 Gohna, 1985 Bairaman or 1993 La Josefina disasters (Evans et al. 2011; King et al. 1989; Delaney and Evans 2011).

Century-long survival of the Sarez Lake, despite large DBI of the Usoi dam (3.55, see Table 1), according to which it should be classified as an unstable feature (Ermini and Casagli 2003), is the geomorphic and hydrological anomaly, possible due to lucky balance between the inflow in the lake and filtration through the dam, which retention depends on numerous factors hardly predictable in the long-term perspective.

Conclusions

The comparison of the Usoi dam with other natural blockages shows that many of its morphological and structural peculiarities are favourable for failure: enormous height and relative compactness that increase erosional potential of water flowing on the downstream face of the blockage;

Table 1 Main parameters of the Usoi dam and of some breached dams from arid regions of Central Asia (Strom 2010a, b) and Argentina (Hermanns et al. 2011)

Dams' name and volume (m ³)	Dams' height (m)	Catchment area (km ²)	DBI
Usoi: 2,200 × 10 ⁶	550	14,166	3.55
Aksu: 1,500 × 10 ⁶	400	329	1.94
Issyk: 25 × 10 ⁶	100	189	2.87
Yashinkul: 25 × 10 ⁶	100	107	2.63
Rio Barrankas: 1,300 × 10 ⁶	160	1,923	2.37
Rio Laja: 1,000 × 10 ⁶	800	106	1.98

prominent lowering at its proximal part composed of most erodible material; distinct evidence of downstream face deformations combined with deep erosional canyon. These factors are characterised by a high level of uncertainty caused by an inadequate knowledge of the internal structure and composition of the dams' body as well as of the stability of lake banks; the ambiguous situation is exacerbated by the uncertainty of strong motion assessment. All these do not allow us to guarantee the long-term safety of the Sarez Lake without technical measures aimed to reduce risk of the dam breach.

I would not discuss various technical solutions here in detail, but just want to mention that those that could affect filtration through the dam and/or erosion on its downstream face (see e.g. Papyryn 1989) could lead to uncontrolled effects and, thus cannot be accepted.

However, in any case such measures would be laborious and time-consuming and, if some changes indicating the possibility of dams' failure will be detected there could be not enough time to perform adequate construction works. Thus, to guarantee permanent safety of the Sares Lake and the sustainable development of the Bartang–Pianj–Amu-Darja River valleys, necessary measures should be implemented while situation remains stable.

Acknowledgments I want to thank Hans-Balder Havenith for useful discussions and Anatoly Ishuk for kind permission to use his photograph of the right bank of the lake.

References

- Abdrakhmatov K, Strom A (2006) Dissected rockslide and rock avalanche deposits; Tien Shan Kyrgyzstan. In: Evans SG, Scarascia Mugnozza G, Strom A, Hermanns RL (eds) Landslides from massive rock slope failure. NATO science series: IV: earth and environmental sciences, vol 49. Springer, Heidelberg, pp 551–572
- Alford D, Schuster RL (eds) (2000) Usoi landslide dam and Lake Sarez: an assessment of hazard and risk in the Pamir Mountains, Tajikistan, United Nations. ISDR Prevention Series No. 1, 113p
- Ambraseys N, Bilham R (2012) The Sarez-Pamir earthquake and landslide of 18 February 1911. *Seismol Res Lett* 83(2):294–314
- Biedermann P, Attewill L (2002) Evolution of seepage through landslide dams: the case of Usoi Dam in Tajikistan. Paper presented at IAHR Symposium, St. Petersburg, 8 p
- Brückl J, Heuberger H (2001) Present structure and prefailure topography of the giant rockslide of Köfels. *Zeitschrift für Gletscherkunde und Glazialgeologie* 37:49–79
- Bukinich DD (1913) Usoi earthquake and its consequences. Russian records, No. 187, Wednesday, August 14, 1913 (in Russian)
- Costa JE, Schuster RL (1988) The formation and failure of natural dams. *Geol Soc Am Bull* 100:1054–1068
- Delaney KB, Evans SG (2011) Rockslide dams in the Northwest Himalayas (Pakistan, India) and the adjacent Pamir Mountains (Afghanistan, Tajikistan), Central Asia. In: Evans SG, Hermanns R, Strom AL, Scarascia-Mugnozza G (eds) Natural and artificial rockslide dams, vol 133, Lecture notes in earth sciences. Springer, Heidelberg, pp 205–242
- Dunning SA, Petley DN, Rosser NJ, Strom AL (2005) The morphology and sedimentology of valley confined rock-avalanche deposits and their effect on potential dam hazard. In: Hungr O, Fell R, Couture R, Eberhardt E (eds) Landslide risk management. Balkema, Amsterdam, pp 691–704
- Ermini L, Casagli N (2003) Prediction of the behavior of landslide dams using a geomorphological dimensionless index. *Earth Surf Proc Land* 28:31–47
- Evans SG, Delaney KB, Hermanns RL, Strom AL, Scarascia-Mugnozza G (2011) The formation and behaviour of natural and artificial rockslide dams; Implications for engineering performance and hazard management. In: Evans SG, Hermanns R, Strom AL, Scarascia-Mugnozza G (eds) Natural and artificial rockslide dams, vol 133, Lecture Notes in Earth Sciences. Springer, Heidelberg, pp 1–75
- Fedorenko VS (1988) Rockslides and rock falls and their forecast. Moscow State University Publishing House, Moscow (in Russian)
- Gerasimov V (1965) The Issyk catastrophe in 1963 and its effects on geomorphology of the Issyk River Valley. *Trans All-Union Geogr Soc* 97(6):541–547 (in Russian)
- Goncharov VS, Skomarovskiy AN (2006) Study of the filtration through the Usoi blockage. Unpublished report, <http://www.sarezsite.eu.pn> (in Russian)
- Hermanns RL, Folguera A, Penna I, Fauqué L, Niedermann S (2011) Landslide dams in the Central Andes of Argentina (Northern Patagonia and the Argentine Northwest). In: Evans SG, Hermanns R, Strom AL, Scarascia-Mugnozza G (eds) Natural and artificial rockslide dams, vol 133, Lecture Notes in Earth Sciences. Springer, Heidelberg, pp 147–176
- Hewitt K (2002) Styles of rock avalanche depositional complexes conditioned by very rugged terrain, Karakoram Himalaya, Pakistan. In: Evans SG, DeGraff JV (eds) Catastrophic landslides: effects, occurrence, and mechanisms, reviews in engineering geology, vol XV. Geological Society of America, Boulder, CO, pp 345–377
- Hewitt K (2011) Rock avalanche dams on the Trans Himalayan Upper Indus streams: a survey of late quaternary events and hazard-related characteristics. In: Evans SG, Hermanns R, Strom AL, Scarascia-Mugnozza G (eds) Natural and artificial rockslide dams, vol 133, Lecture notes in earth sciences. Springer, Heidelberg, pp 177–204
- ICOLD (1989) Selecting seismic parameters for large dams. Guidelines, Bulletin 72, Paris, 78p.

- Ischuk AR (2011) Usoi Rockslide Dam and Lake Sarez, Pamir Mountains, Tajikistan. In: Evans SG, Scarascia Mugnozza G, Strom A, Hermanns RL (eds) Landslides from massive rock slope failure NATO Science Series: IV: Earth and Environmental Sciences, vol 49. Springer, Dordrecht, pp 423–440
- Ischuk NR (2011a) The origin of the mountain river closures in Tajikistan. Abstract book of the Second World Landslide Forum, Rome, p. 393
- Ischuk NR (2011b) The role of glacial deposits in forming modern mountain lake dams in the Pamirs. *Georisk* (1): 16–29 (in Russian)
- King J, Loveday I, Schuster RL (1989) The 1985 Bairaman landslide dam and resulting debris flow Papua New Guinea. *Q J Eng Geol* 22:257–270
- Korup O, Strom AL, Weidinger JT (2006) Fluvial response to large rock-slope failures—examples from the Himalayas, the Tien Shan and the New Zealand Southern Alps. *Geomorphology* 78:3–21
- Lange OK (1926) Expedition on the Usoi blockage and the Sarez Lake survey. *Natl Econ Central Asia* (10): 76–79 (in Russian)
- Lange OK (1929) Present-day state of the Usoi blockage, vol XIX. Transactions of the Central-Asian Geographical Society, Tashkent (in Russian)
- McSaveney MJ, Davies TRH (2006) Rapid rock-mass flow with dynamic fragmentation: inferences from the morphology and internal structure of rockslides and rock avalanches. In: Evans SG, Scarascia Mugnozza G, Strom A, Hermanns RL (eds) Landslides from massive rock slope failure, vol 49, NATO science series: IV: Earth and environmental sciences. Springer, Dordrecht, pp 285–304
- Papyryn LP (1989) Method of the Sarez Lake water level lowering. Express-Information of TadjikNIINTI, Dushanbe (in Russian)
- Paramonov BA (1969) Formation of the Usoi blockage relief. *Rep Moscow Univ* (5): 110–112 (in Russian)
- Pollet N, Schneider J-L (2004) Dynamic disintegration processes accompanying transport of the Holocene Flims sturzstrom (Swiss Alps). *Earth Planet Sci Lett* 221:433–448
- Poschinger A, Wassmer P, Maisch M (2006) The flims rockslide: history of interpretation and new insights. In: Evans SG, Scarascia Mugnozza G, Strom A, Hermanns RL (eds) Landslides from massive rock slope failure, vol 49, NATO science series: IV: Earth and environmental sciences. Springer, Dordrecht, pp 329–356
- Preobrajensky IA (1920) The Usoi landslide. *Geol Commun. Papers on Applied Geol* 14: 21p (in Russian)
- Rodionov NE (1931) Hydrology of the Usoi blockage, vol LXIII. Transactions of the Stage Geographical Society, Moscow (in Russian)
- Selivanov PI, Andreev VI (1959) About water level behaviour and possible evolution of the Sarez Lake. *Meteorol Hydrol* (3) (in Russian)
- Sheko AI (1968) The Usoi blockage stability and the Lake Sarez breach assessment. *Bull Moscow Nat Invest Soc Geol Sect* (4) (in Russian)
- Sheko AI, Lehatinov AI (1970) The Usoi blockage stability assessment, Tajikglavgeologia unpublished report (in Russian)
- Shpilko GA (1914) The 1911 earthquake in Pamirs and its effects. *Proc Russian Geogr Soc* 3:69–94 (in Russian)
- Strom AL (1994) Mechanism of stratification and abnormal crushing of rockslide deposits. In: Proceedings of 7th international IAEG congress, vol 3. Balkema, Rotterdam, pp. 1287–1295
- Strom AL (2006) Morphology and internal structure of rockslides and rock avalanches: grounds and constraints for their modelling. In: Evans SG, Scarascia Mugnozza G, Strom A, Hermanns RL (eds) Landslides from massive rock slope failure. NATO science series: IV: Earth and environmental sciences, vol 49. Springer, Dordrecht, pp 305–328
- Strom AL (2010a) Evidence of momentum transfer during large-scale rockslides' motion. In: Williams AL, Pinches GM, Chin CY, McMorran TG, Massei CI (eds) Geologically active. Proceedings of the 11th IAEG congress, Auckland, New Zealand, 5–10 September 2010. Taylor & Francis Group, London, pp 73–86
- Strom AL (2010b) Landslide dams in Central Asia region. *Landslides J Jpn Landslide Soc* 47(6):309–324
- Stucky Consulting Engineers (2001) Design report – monitoring and early warning systems/studies on long term solutions: Lake Sarez risk mitigation project. Renens, Switzerland
- Weidinger JT (2011) Stability and life span of landslide dams in the Himalayas (India, Nepal) and the Qin Ling mountains (China). In: Evans SG, Hermanns R, Strom AL, Scarascia-Mugnozza G (eds) Natural and artificial rockslide dams. Lecture notes in earth sciences, vol 133. Springer, Heidelberg, pp 243–277
- Wells DL, Coppersmith KJ (1994) New empirical relationships among magnitude, rupture length, rupture width, rupture area, and surface displacement. *Bull Seism Soc Am* 1994(84):974–1002



Geophysical Monitoring of Artificial Landslide Dam of Kambarata Hydro Power Plant-2 (Kyrgyzstan)

Isakbek A. Torgoev, Hans-Balder Havenith, and Almaz D. Torgoev

Abstract

One of the main stages of the Kambarata HPP-2 construction, which is situated on Naryn River (Kyrgyzstan), was the design of a unique dam. This dam was formed under the difficult seismic-tectonic conditions of Central Tien-Shan. The applied method of dam construction was not a traditional one, but one which used explosive energy. An oriented large-scale explosion (around 2,600 tons of explosives) blasted a rock mass from the right slope of Naryn river basin, downstream from Kambarata river mouth. The big explosion initiated the failure of an artificial landslide which dammed Naryn River—the volume of landslide dam was around 1.8 mln. m³ and its height was 35 m. Since the explosion did not produce the designed dam properties (60 m of height and 3 mln. m³ of volume) there was a need to apply traditional methods of dam construction in order to reach the planned elevation of 961 m. The monitoring of the dam and the surrounding rock massif was set up study their geotechnical properties and filtration anisotropy. Water inflow in the dam and the surrounding rock massif was mapped on the basis of an electrical resistivity survey and regular piezometric observations. The latter started in 2010 and revealed the gradual clogging of dam's body. Additional measures to insure the impermeability of the dam include the construction of a continuous concrete screen along the whole face of the dam. The interest of this study for landslide dam research is related to the fact that here we provide an insight to the internal structure of a dam that partly consists of landslide material.

Keywords

Hydro power plant (HPP) • Artificial landslide dam • Geophysical monitoring

Introduction

The Kambarata HPP-2 (KHPP-2) is situated on Naryn River, Kyrgyzstan (Fig. 1) and was partially constructed as an artificial landslide dam. Big-scale explosion initiated rock mass failure from the right slope of Naryn River, which finally dammed it and was the basis for KHPP dam (Torgoev et al. 2013).

Explosion itself can be considered as a trigger event which initiated the release of gravitational energy concentrated in the massif of rock mass presented in river canyon. This method of dam construction has special

I.A. Torgoev (✉)
Institute of Geomechanics and Development of Subsoil of the National Academy of Sciences of the Kyrgyz Republic, SEC “Geopribor”, Mederova str., 98, Bishkek 720017, Kyrgyzstan
e-mail: geopribor@mail.ru

H.-B. Havenith • A.D. Torgoev
Department of Geology, University of Liege, B-4000, Sart Tilman, Liege, Belgium
e-mail: hb.havenith@ulg.ac.be; torgoeval@yahoo.com



Fig. 1 The map of Kyrgyzstan with indication of KHPP-2 position

features, since the river valley should be blocked by a rockslide-fall induced by blasting.

It was planned that the oriented big explosion would initiate rockslide failure, which would lead to the river damming with a volume of 3 mln. m³ and a height of 60 m. But in reality the dam was significantly less than planned—the volume 780,000 m³ demanded additional activity on dam filling up to the planned elevation of 961 m using traditional methods.

Dynamic compaction of failed rock mass in the dam was not enough since explosion did not reach the planned parameters. It resulted in the water outflow in the lower part of dam which was already registered 12 h after river damming. Later, 18 h after damming, water outflow reached 8–9 m³/s, while water level difference from both sides of dam reached the value of 35 m.

Monitoring system was set up to survey the change of dam state, since KHPP-2 was considered to be unique construction. In order to control water inflow, a piezometric survey together with geophysical investigations were carried out in 2010 and 2012, respectively. This paper presents the results of water inflow monitoring and discusses obtained results.

General Info on KHPP-2

KHPP-2 includes the 60 m high dam, power station penstock and spillway. The KHPP-2 reservoir has a volume of 70 mln. m³ and extends 16 km upstream from the Kambarata River estuary. The dam is located on top of alluvial sediments with a thickness of 10–14 m, density 2.1 tons/m³ and gravel filtration coefficient $K_f = 0.1$ cm/s (100 m/day). The



Fig. 2 General view (to the east) of KHPP-2 dam, situated on the Naryn River

underlying bedrock has a density 2.71 tons/m³ and filtration coefficient $K_f = 1 \times 10^{-3}$ to 3×10^{-3} cm/s. The KHPP-2 dam consists of inhomogeneous rocks presented by sandstone, siltstone and mudstone fragmented during big-scale explosion.

The main geometric and hydrogeologic parameters of the dam (Fig. 2) are the following: height—60 m; crest elevation—961.0 m; width along the upper part—230.5 m; width along the middle part—444.5 m; slope 1:2.5; maximal value of water pressure on the dam—51.8 m, minimal value of water pressure on the dam—48.3 m. Physical and mechanical properties like strength, deformability, water permeability are dependent on the grain-size distribution and rock mass compaction resulted from big-scale

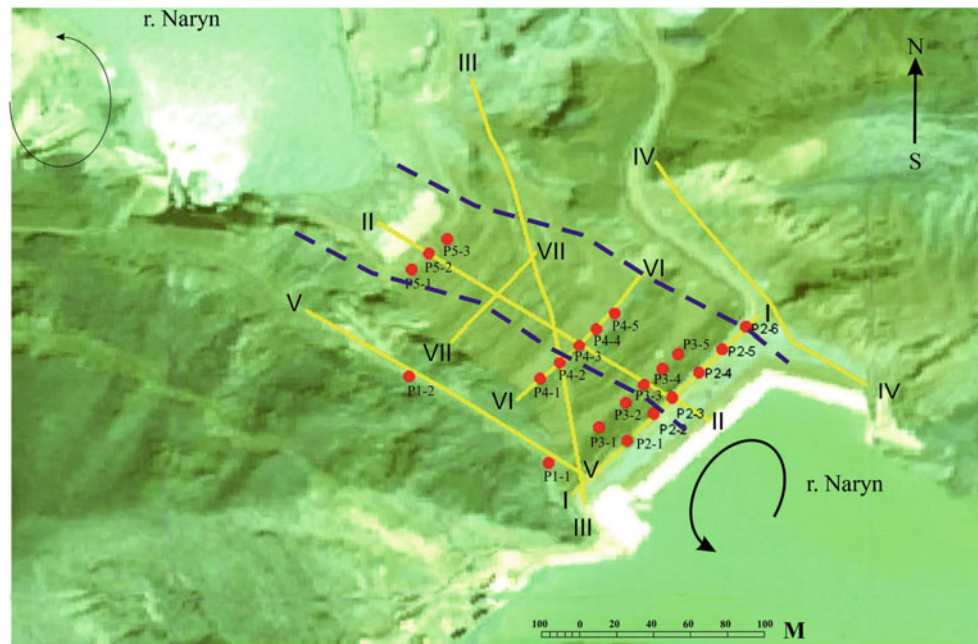


Fig. 3 Electrical tomography profiles (yellow lines) and piezometric boreholes (red dots), installed on KHPP-2 dam (blue lines show Naryn River channel before explosion)

explosion. Owing to the calculations the values of density (ρ) and filtration coefficient (Kf) are the next: for the main part of dam $\rho = 2.1 \text{ tons/m}^3$, $Kf = 0.2\text{--}0.5 \text{ cm/s}$ (200–500 m/day); for the part, which is consist of rock fragments $\rho = 2.1 \text{ tons/m}^3$, $Kf = 0.08 \text{ cm/s}$ (80 m/day); for the part of dam below 935.0 m, which is consist of gravel $\rho = 1.8 \text{ tons/m}^3$, $Kf = 0.0012 \text{ m/s}$; for the part of dam upper than 935.0 m, which is consist of gravel $\rho = 2.1 \text{ tons/m}^3$, $Kf = 0.0008 \text{ m/s}$; for water-proof layer $\rho = 2.2 \text{ tons/m}^3$.

There is a need for monitoring of the dam state not only because the explosion did not produce the required size of dam, but also because there are special tectonic features in the dam surroundings, like the Southern fault, which lies on the river bottom and has modern displacement amplitude of 3.5 m. It should be noted, that the surroundings of KHPP-2 are characterized by high seismic activity—this area has the probability of $M = 7.5$ earthquakes owing to seismic zoning map for the territory of Kyrgyzstan. For example, Susamyр earthquake ($M = 7.4$) occurred in 1992 was situated around 60 km to the north–east from KHPP-2 site.

Monitoring Methods

A resistivity survey (with electrical tomography) was used to study water infiltration through KHPP-2 dam. The surveys provided in different periods of time give the information about the change of filtration properties in dam and surrounding bedrock. Electrical tomography measured

apparent resistivity values using low frequency alternating current and applying Wenner-Schlumberger array with electrode spacing of 4 m. The type of equipment is GeoTom-MK1E100 RES/IP/SP made by GEOLOG2000 company (Augsburg, Germany). There were totally 100 electrodes connected to 400 m long cable using 50 % overlapping during profile extension. Since the biggest spacing of feeding electrodes (max LAB) was 400 m, the maximum penetration depth was around 80–90 m.

In addition, in 2010 there were piezometric boreholes installed on the dam. It is clear that combination of electric survey together with piezometric observation provide the full and reliable estimation of underground water conditions. Figure 3 presents the position of VES profiles and piezometric boreholes on the surface of KHPP-2 dam.

Survey Results

Figures 4 and 5 presents the results of electrical tomography along two crossing profiles I-I and II-II together with geological cross-sections and graphical representation of ground water level change in the upper part of dam and in the piezometric boreholes. As it can be seen, the distribution of apparent resistivity values is inhomogeneous in both profiles—the dam itself is characterized by wide diapason of resistivity values changing from tens up to several thousand $\text{Ohm}\cdot\text{m}$. It can be explained by inhomogeneous composition of dam—low values of apparent resistivity

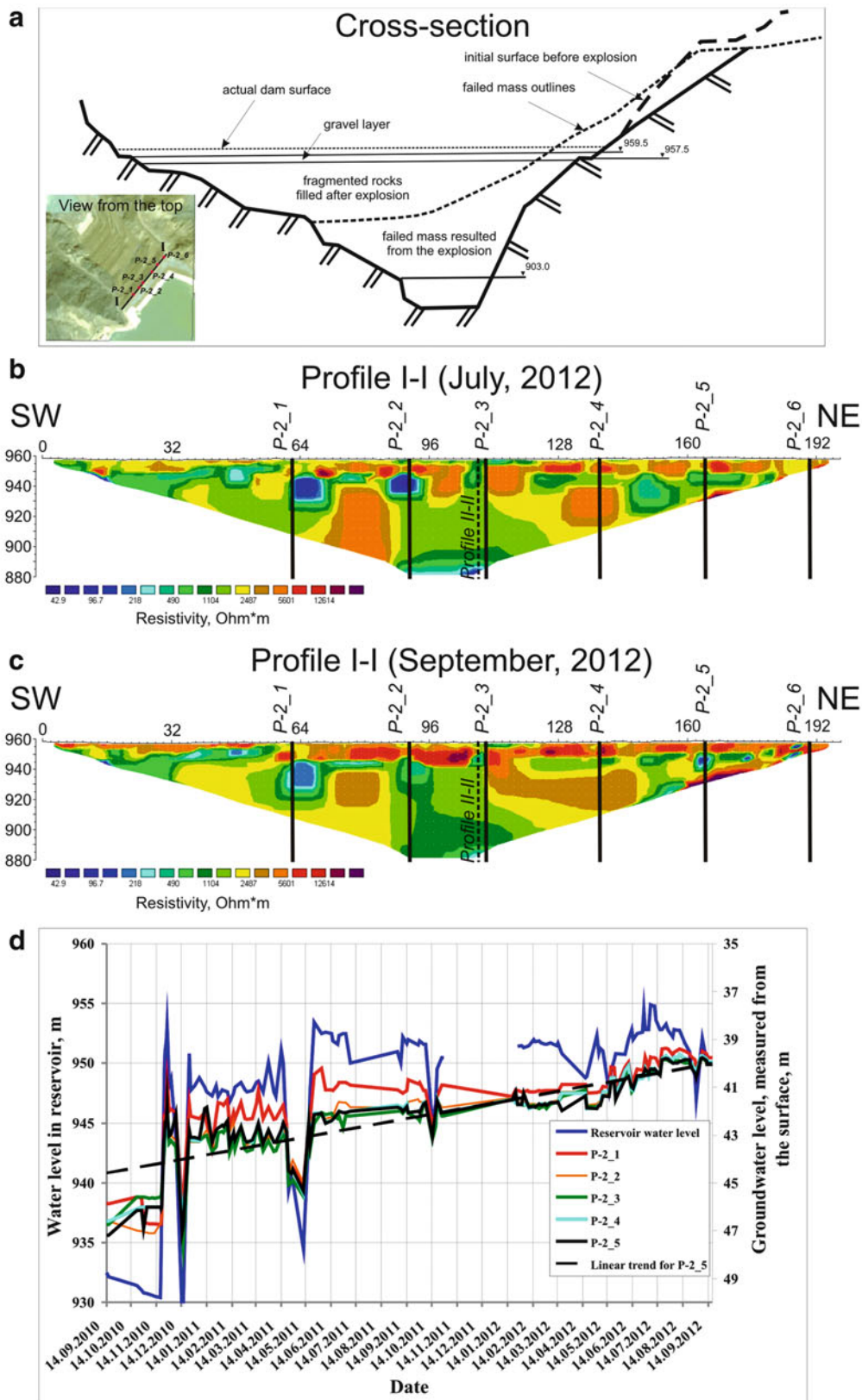


Fig. 4 (a) Cross-section of the dam, of electrical tomography profiles and piezometric boreholes position; (b) electrical tomography profile I-I, surveyed in July, 2012; (c) electrical tomography profile I-I, surveyed

in September, 2012; (d) the results of piezometric survey compared with the change of water reservoir level

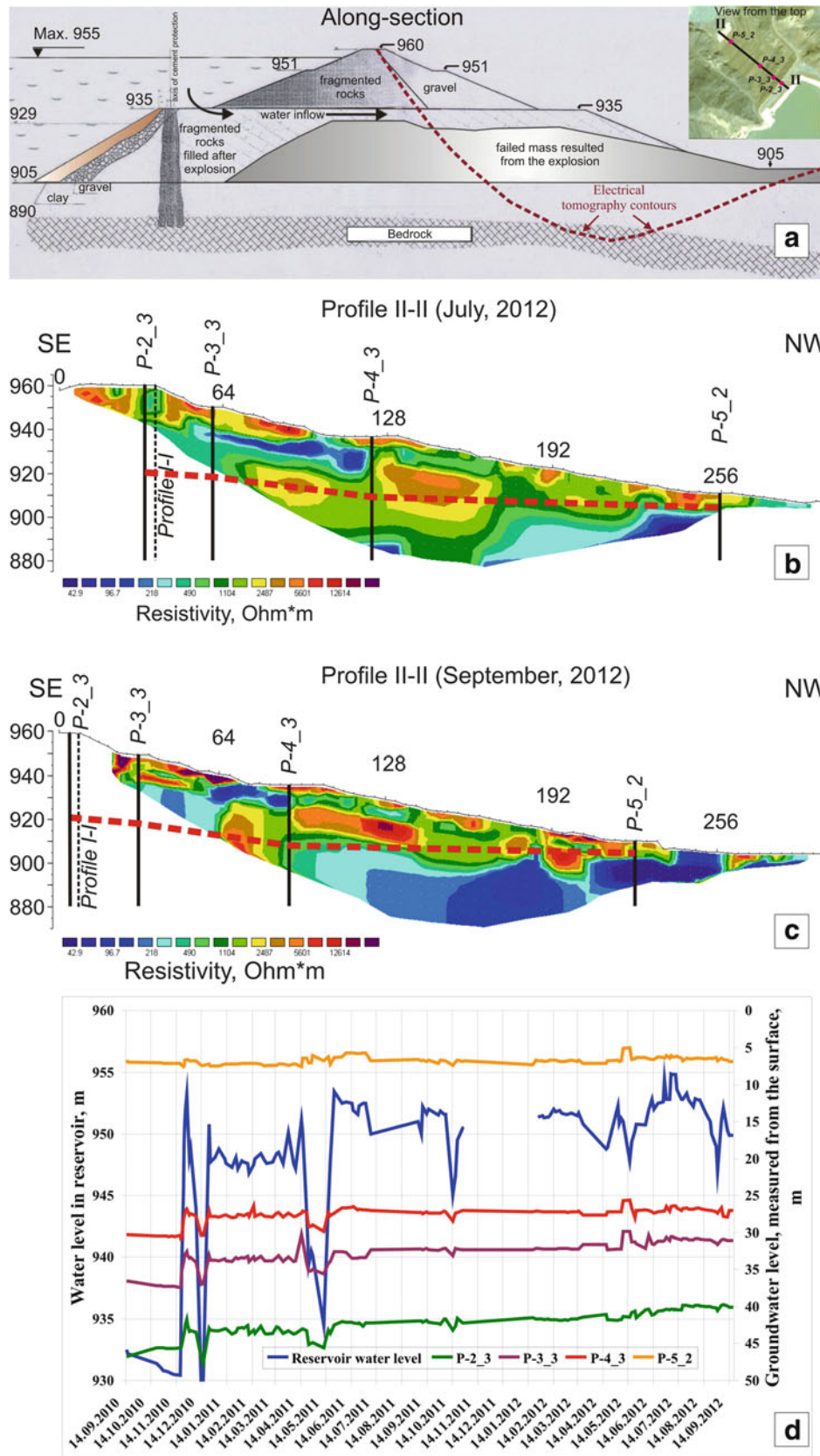


Fig. 5 (a) Cross-section of the dam, electrical tomography profiles and piezometric boreholes position; (b) electrical tomography profile II-II, surveyed in July, 2012 (red dotted line shows underground water level); (c) electrical tomography profile II-II, surveyed in September, 2012; (d) the results of piezometric survey compared with the change of water reservoir level

10–100 Ohm*m correspond to rock and soil with high water content, while high resistivity values indicated low water content of composing material.

As it can be seen in Fig. 4a there are several layers presented in the dam of KHPP-2: failed mass resulted from the explosion, which is highly compacted by explosion energy; the mass of fragmented rocks filled on the previous layer directly after explosion using traditional methods (dozers); the layer of boulders and rock fragments of different size filled on the elevation above 935.0 m; loam-pebble layer filled over polyethylene screen in the upper part of the dam; antifiltration cement layer.

There are two low resistivity zones in the upper part of Profile I-I, each of them 8–9 m wide and located at an elevation of 935 to 945 m (Fig. 4b, c). These zones are surveyed by boreholes 2.1 and 2.2 and can be interpreted as zones with high water content caused by water inflow. These zones are more pronounced in the profile, surveyed in July (Fig. 4b), since that time water reservoir level was higher than in September. Figure 4a indicates that these water saturated zones are situated within the fragmented rocks filled by the dozers and other equipment. High water content in these zones is caused by high values of water permeability of this layer, which was constructed after explosion. Cross-section II-II (Fig. 5b) indicates this zone, which is situated between boreholes 2.3 and 4.3. It should be noted that above-described zones of high water content between boreholes 2.1 and 2.2 correspond with the zones of cracking and subsidence on the dam surface appeared in November 2011. It is also important to note that there is no water-proof cemented layer like one which is situated at the rims of the dam. Water-proof cemented layer was designed using special technology involving boreholes and cement filling. That is why when water level in reservoir is high there is some water inflow through the areas which do not have water-proof layer. Figure 4b shows that when water level in reservoir is the highest there is one more zone of high water content at the elevation below 900 m. This zone is connected with alluvial sediment of Naryn River and caused by water inflow along the bottom of the dam. Figure 4d presents the change of water level in reservoir together with the change of ground water level in piezometric boreholes 2.1–2.5 installed close to reservoir. Since these boreholes are the closest to the reservoir the change of groundwater level in these boreholes is directly connected with the change of water level in reservoir. Moreover these boreholes should better indicate the effectiveness of water-proof layer comparing to the boreholes situated further from reservoir. The comparison of water level change in reservoir and underground water change in closest boreholes showed, that there was almost synchronous dynamics from the start of survey in September, 14 2010 till the beginning of 2012. Since the beginning of 2012 situation changed almost in all

boreholes, sometimes showing opposite dynamics, especially in periods of rapid water accumulation in the reservoir and when the water level reached the elevation 950.0–955.0 m. It can be seen that starting from the beginning of 2012 underground water level is less impacted by water level in reservoir. This fact shows that dam material gradually becomes impermeable owing to natural processes of clogging by river sediments. Figure 5b, c shows cross-section II-II together with the cross-section of the dam (Fig. 5a). It can be seen that two zones with high water content visible on Profile I-I are connected with water inflow from reservoir in the elevation below 940 m. Figure 5a shows the most probable way of water inflow. Most probably water flows along the contact between fragmented rocks filled after explosion and failed mass resulted from the explosion at the elevation around 935 m. Both profiles in Fig. 5b, c clearly indicated the zone of high water content at 935 m, even though visual inspection on the surface did not show water outflow on the surface neither in July, nor in September 2012. There is piezometric borehole 4.3 close to this zone of high water content—groundwater level in this borehole stays at the same value during all observation period (Fig. 5d) with some changes caused by rapid change of water reservoir level. The same type of groundwater level change is observed in borehole 5.2, installed in the lower part of dam. It should be noted that all piezometric boreholes along profile II-II (2.3, 3.3, 4.3 и 5.2) are situated within the rims of former river channel (Fig. 3). Borehole 3.3 and, especially, borehole 2.3 indicate the rising trend of underground water level (Fig. 5d) which can be connected with gradual clogging of failed mass resulted from the explosion. Geoelectric profile II-II (Fig. 5b, c) also indicated another zone with high water content situated in the lower part of dam, below 910 m. This zone is probably caused by water flow along alluvial deposits and partially by water infiltration in the lower part of the dam. As it can be seen this zone becomes more pronounced in September, 2012 comparing to July, 2012. Most probably, the size of this zone grew as the result of high water level in the river normally observed in spring-summer time.

As it was noted above, non-successful explosion resulted in the fact, that planned parameters of the dam were not reached. It is true for the height, volume and dimensions of the failed mass. It resulted in water overflow and infiltration almost directly after explosion. Further filling activity and design of the crest of the dam was provided in these conditions of overflowing water, when discharge reached the values of 8–9 m³/s in December, 23 2009. Obviously, this water overflow left the traces and spatial dimensions which still can be observed in the dam. So, there are the reasons to conclude that high water content between 50 m and 120 m of Profile II-II at the elevation below 940 m (Fig. 5b) resulted from the water overflow that took place almost directly after big-scale explosion.

Conclusions

The combined survey of the KHPP-2 dam provided by piezometric observations and electrical tomography showed a roughly 8 m thick zone of water infiltration. This zone is situated to the south-west from the longitudinal axis of dam and is represented by two low resistivity zones in the profile along in the crest of the dam. This water inflow is in the upper part of fragmented rocks filled after explosion. This zone overlies the compacted mass, failed by explosion. The latter had produced a relatively impermeable crushed rock mass that enables dam stability. This crushed rock mass can be considered as similar to the one produced by a natural rockslide-fall.

The view from the top indicates that water inflow contours are mainly within the rims of the former river channel, and arose 12 h after explosion as the result of water overflow and filtration into the dam. It should be noted, that cracks and subsidence at the dam crest were found in 2011 exactly in the area of fragmented rocks, situated above this underground water flow.

Electrical and piezometric measurements also showed that natural clogging of the dam material contributes significantly to its impermeability. This process is also likely to contribute to the impermeability of natural rockslide dams in general.

Ongoing studies focus on the seismic stability of such a hybrid blast- rock-fill dam structure since the area is highly prone to seismic activity.

Acknowledgments Electrical tomography equipment was provided within the frame of NATO Science for Peace project LADATSHA, SFP983289.

Reference

Torgoev I, Havenith H-B, Strom A (2013) Impact of 300-t blast on unstable slope near the Kambarata-2 HPP site, Kyrgyzstan. *Landslide science and practice*, 6:37–42



Using Microtremor Array Survey to Evaluate the Possibility of Piping-Induced Landslide Dam Failure

Fawu Wang, Hisao Hayashi, Austin Chukwueloka Okeke, Yasuhiro Mitani, Hufeng Yang, Yohei Kuwada, and Shinya Baba

Abstract

Landslide dams are formed when landslides move into mountain valleys, and potential flooding to the downstream area becomes secondary hazard of landslides. Sometimes, the potential flood threatens larger areas and more population than that by the landslide itself, so it is very important to find a quick method of evaluating the possibility of landslide dam failure. Generally, landslide dam failure can be caused by overtopping and piping. It is relatively easier to predict failure triggered by overflow because water level in the upstream area can be monitored. For those failure caused by piping, it is difficult to be predicted, because piping depends on the internal structure and composition of the landslide dam. If the internal structure of the landslide dam can be clarified, then it will become possible to evaluate the possibility of piping-induced landslide dam failure. In this paper, the possibility of using microtremor array survey to understand the internal structure of landslide dam and evaluate the potential of piping failure is examined.

Keywords

Landslide dam • Piping failure • Internal structure • Micro-tremor survey

Introduction

Landslide dams, also known as natural dams, form when landslides or debris flows move into steep valleys, and create barrier lakes. Because landslide dams are formed in natural processes, their structure and stability can be very different. Depending on the rate at which water level rise in the barrier lake and the structure of the landslide dam, the impoundment can collapse within a short period of time or last for several hundred years. Generally, when landslide dam fails, it results into flooding in the downstream area, and leads to severe loss

of lives and property. For landslide disaster reduction, it is important to evaluate the failure potential of a landslide dam and predict the failure time. Figure 1 shows an image of a landslide dam. The dimension of landslide dams may depend on the scale of the landslide, its structure, slope angle of the valley it dammed, and the width of the valley. When the landslide is a large scale translational slide or rotational slide, the structure of the landslide dam may still be intact and the stability of the landslide dam may be high, while, when a landslide dam is caused by debris flow, or a long travelling landslide, the structure of the landslide dam may be weak and the stability of the landslide dam may be low.

Landslide dams are widely distributed in mountainous areas of the world. Their failures usually threaten local people and communities. Generally, there are three failure modes of landslide dams. Most landslide dams fail by overtopping with subsequent dam breach and erosion by the overflowing stream. Another mode of landslide dam failure is by piping which usually takes place inside the dam as a result

F. Wang (✉) • A.C. Okeke • Y. Mitani • H. Yang • Y. Kuwada
Shimane University, Research Center on Natural Disaster Reduction,
1060 Nishikawatsu, Matsue 690-8504, Japan
e-mail: wangfw@riko.shimane-u.ac.jp

H. Hayashi • S. Baba
Geo-X Consultants Corporation, 3-148-1 Miyahara, Kita-ku, Saitama
331-0812, Japan
e-mail: hayashi@geo-x.co.jp

of the structural characteristics of materials composing the dam. When compared with other modes of failure such as overtopping, predicting landslide dam failure by piping is more complicated and difficult, because what happens inside a landslide dam is relatively complex and invisible. In this paper, a new geophysical exploration method is used to analyze the internal structures of two landslide dams, and the possibility of detecting piping process is discussed using case studies.

Principle of Microtremor Chain Array Survey

Multichannel Analysis of Surface Waves (MASW) is a geophysical technique employed in seismic exploration for evaluating subsurface geology such as internal structural style of strata, bed thickness, lithologic variations,

subsurface fluid system and aquifer characteristics. MASW has a lot of advantage over conventional seismic methods because it is relatively portable, environmentally friendly, safe, and less time consuming. A type of MASW, called the microtremor array survey, is a passive surface wave technique used in the measurement of natural and artificial surface waves. Passive surface wave technique has the capability of obtaining phase velocity structure to depths of more than 100 m, provided there is a wave source and space for the receivers. A lot of researchers have reviewed the physics and principles of microtremor method used in seismic geophysics for estimating phase velocities (Okada 2003; Park et al. 1999; Arai and Tokimatsu 2005).

In the ground surface of the Earth, microtremors are caused by lots of natural phenomena and artificial operations. As shown in Fig. 2, microtremors can be caused by ocean waves, vehicular vibration on roads. Also wind in forests, ocean currents and tides, and others can generate micro-motion. Microtremor array survey (MAS) makes use of the micromotion to explain underground structures (Okada 2003). The micromotion can be measured with seismometers. Because micromotion comes from different sources in different amplitudes, a dispersion phenomenon exists in their phase velocities, i.e., those microwaves with different frequencies or wavelengths show different phase velocity when they travel in the ground layer with different shear wave (S-wave) velocity. By separating those microwaves with different frequencies, the MAS can get the dispersion curves, i.e., the relationship between phase

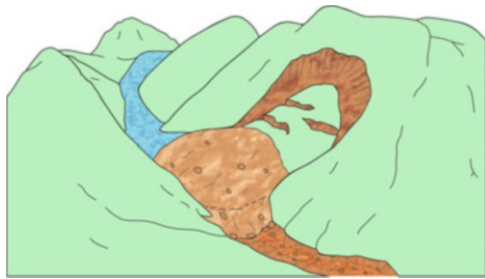


Fig. 1 An image of landslide dam

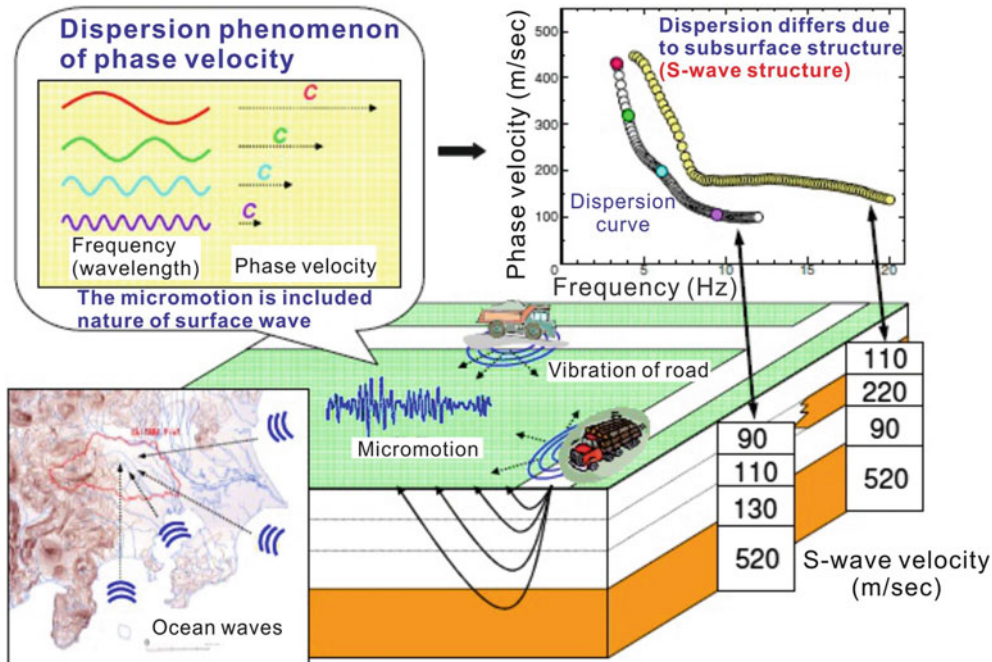


Fig. 2 Principle of microtremor array survey (MAS) method

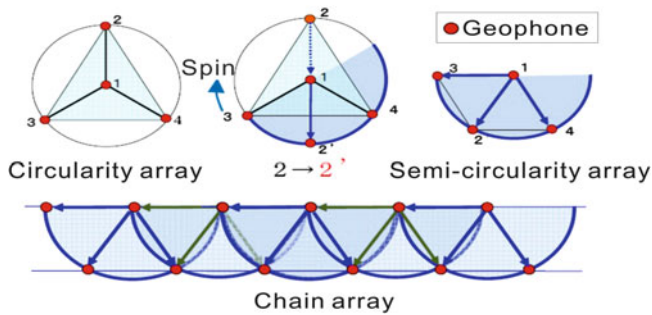


Fig. 3 Chain array method of geophone arrangement used in the investigation

velocity and frequency for the measured target ground. The result of MAS is a one-dimensional (1D) section showing the S-wave velocity change with depth. The advantage of the MAS is that it can give out the S-wave structure of the measured point.

The microtremor wave-field consists of fundamental-mode surface waves which can provide seismic information. It has enhanced velocity studies of subsurface structures by enabling passive seismic investigations to be processed and interpreted to yield a phase velocity depth profile (Roberts and Asten 2004). This is enhanced by applying a low-frequency wave-field transform-Fast Fourier Transformation (FFT) or Spatial Autocorrelation (SPAC) to separate Raleigh energy from that of other waves.

Hayashi et al. (2010) proposed a method of obtaining 2D section of a survey line using microtremor chain array survey (MCAS). In contrast with the MAS method measuring an isolated point, MCAS measures micromotion in a continuous line of interconnected geophones that constitute a chain (Fig. 3).

The seismometers are located at points in which equilateral triangles are formed. For each triangle, phase velocity change with depth can be obtained. Combining all of the phase velocity change in the center of all the triangles, a continued 2D section of phase velocity structure can be obtained (Fig. 4).

For purpose of assessing the potential of piping in a landslide dam, visual 2D section of the phase velocity is very useful. The measured lines should be located across the valley in which the landslide dam is formed. To obtain a 3D phase velocity structure of a landslide dam, parallel monitoring lines are necessary to cover the whole landslide dam. The disadvantage of the MCAS method is that it is difficult to give out the S-wave velocity structure in 2D section, because of the nonlinear property of the relationship between phase velocity and frequency. If the 2D S-wave velocity structure is needed, the MCAS and MAS measurement should be conducted in the same site. By comparing the S-wave velocity structure and phase velocity structure in

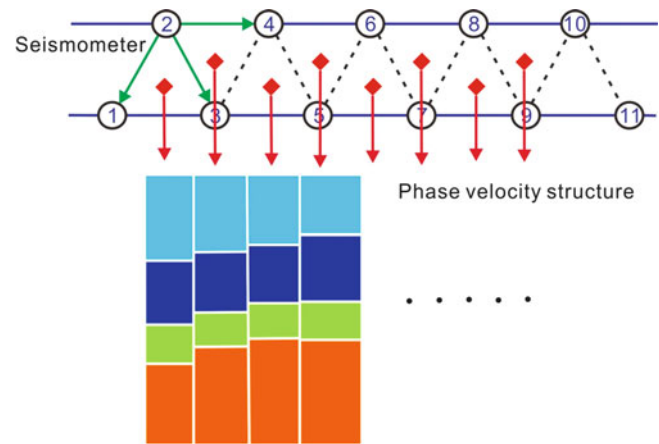


Fig. 4 The principle of the microtremor chain array survey (MCAS) method

some typical reference points, the 2D S-wave velocity structure can be estimated.

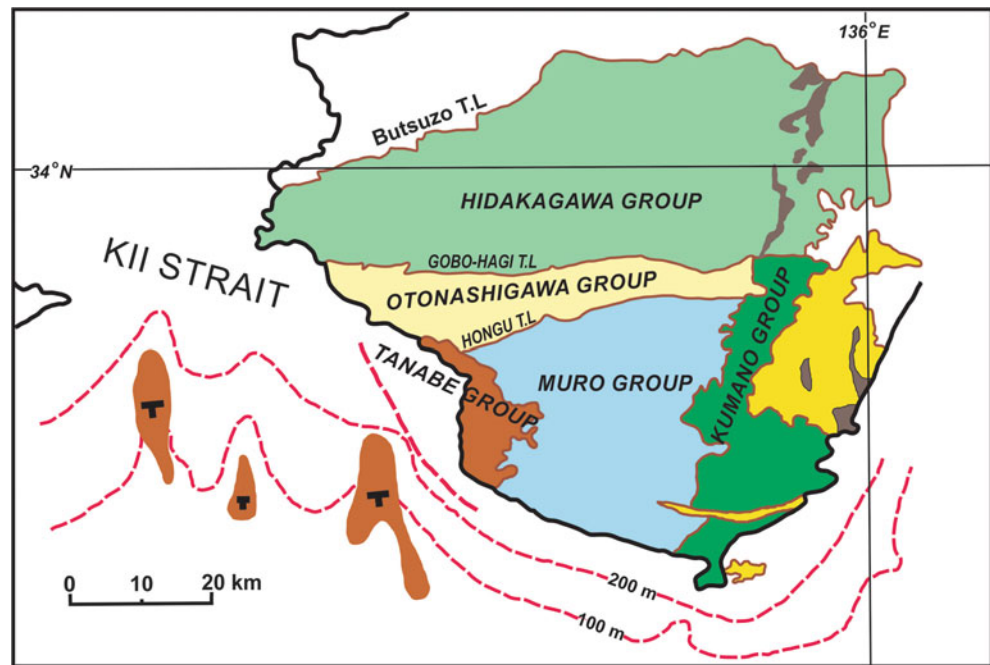
Applications to Landslide Dams in Kii Peninsula

Geologic Setting of the Kii Peninsula

The Kii Peninsula is located in the southern region of mainland Japan (Lat: 34N, Long: 136E), and bestrides Mie, Nara, Osaka and Wakayama prefectures. The Japan Median Tectonic Line (MTL) and other crushed zones created by fault movements are distributed all over the Peninsula. Across the Yoshinogawa River, the MTL divides Nara Prefecture into northern lowlands and southern Yoshino mountain region. The latter is dominated by chains of mountains which include Mount Odaigahara (1,695 m), Mount Shakka (1,800 m), Mount Sanjo (1,719 m) and Mount Hakkenzen (1,915 m). Majority of those strata are made up of accretionary prisms formed by the subduction of the oceanic plate.

The Kii Peninsula is underlain by deposits of the Shimanto Supergroup which is divided into three Groups: Upper Cretaceous Hidakagawa, Paleogene Otonashigawa and Muro Groups with Miocene Kumano and Tanabe Groups overlying them (Taira et al. 1982). The Shimanto belt has a regional extent of 2,000 km, extending from the Kanto Mountains to the Nansei Islands. Overlying the geosynclinal sediments of the Shimanto Supergroup are the Early to Middle Miocene sediments with scattered outcrops of Neogene Igneous rocks. In the Kii Peninsula, the Shimanto belt is divided into two sub-belts by the Gobo-Hagi Tectonic Line. The northern belt is the Cretaceous Shimanto belt, while the Southern belt is the Paleogene to recent Shimanto belt. The Northern Shimanto belt is defined as an accretionary complex formed during the Upper Cretaceous, composing sediments of the Hidakagawa Group

Fig. 5 Geologic map of Kii Peninsula (after Taira et al. 1982)



(Taira et al. 1982), while the southern belt is underlain by sediments of the Otonashigawa and Muro Groups. The strata in the northern belt dip northward at high angles, generally trending east–west. Structural features of this belt are folds and reverse faults with dip direction to the north, upturned strata and disjointed beds. The Otonashigawa and Muro Group are less commonly sheared compared to the Hidakagawa Group. However, these groups dip steeply to the north, with several structural features such as faults, disjointed beds and folds (Fig. 5).

Overview of the 2011 Typhoon-Induced Landslide Disasters in the Kii Peninsula

The Kii Peninsula has been considered as one of the regions prone to deep catastrophic landslides and associated mass movements (SABO 2010). The passage of a severe tropical cyclone, Typhoon Talas (named Typhoon 12 in Japan), over the Japanese archipelago in September 2011 brought a cumulative precipitation of 1,000 mm to 1,500 mm in the southern part of the Kii Peninsula, and 2,436 mm in 5 days in some districts in Nara Prefecture (Figs. 6 and 7).

The Typhoon originated from the Mariana Islands and advanced to the northern part of the South Seas before its course was shifted to the west, passing the Japanese mainland in the early hours of 4 September. The arrival of the cyclone destroyed inhabited areas and affected municipal buildings, leading to infrastructural damage worth close to 600 million USD. Data obtained from Erosion and

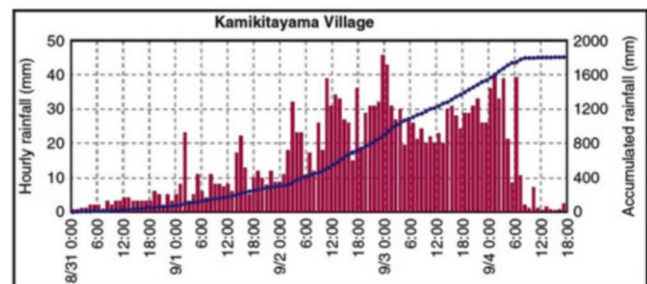


Fig. 6 Time-series data of rainfall in Kamikitayama village, Nara Prefecture, between 31 August and 4 September, 2011 (Hayashi et al. 2013)

Sediment Control Division of the Ministry of Land, Infrastructure, Transport and Tourism show that in Nara Prefecture alone, 14 fatalities were recorded while 10 people were declared missing. About 13 houses were inundated by debris flow and floods, 50 houses were completely destroyed, while 70 houses were partially destroyed. Wakayama Prefecture recorded 52 deaths with 5 people declared missing. A total of 1,985 houses were partially destroyed, and a record 2,642 buildings were flooded with complete destruction of 365 buildings (Fujita 2012). About 207 landslides, landslide dams, debris flows and other sediment-related disasters were triggered in 21 prefectures with Mie, Nara and Wakayama Prefectures recording the highest number of cases. The volume of sediments produced by the effect of the cyclone was estimated to be about 100 million m³. Field investigations carried out immediately after the disaster confirmed that deep-seated catastrophic landslides were triggered in 72 locations

and 17 landslide dams were formed in different locations as a result of these deep-seated landslides, 5 of which were

discovered to be at risk of failure due to the rate of rise in level of barrier lakes created by the impoundments (SABO 2012).

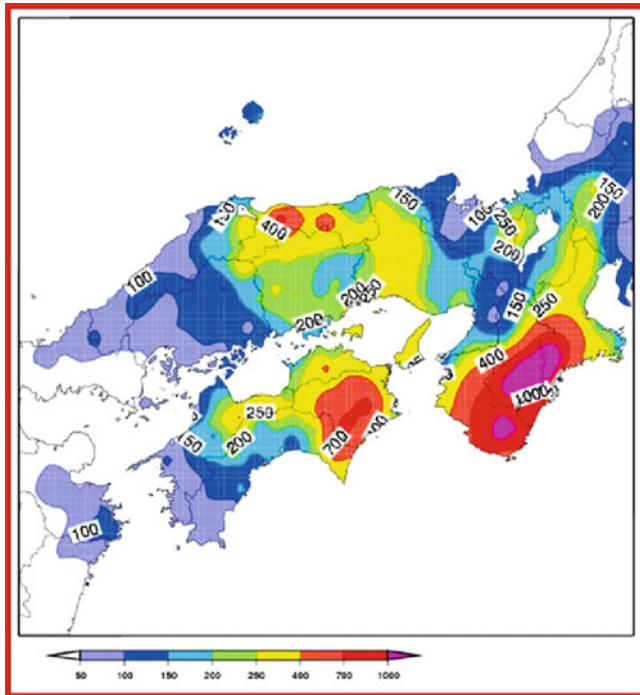


Fig. 7 Rainfall distribution map of mainland Japan for 4 September, 2011

Application of the MCAS Method to Two Landslide Dam Sites

To understand the internal structures of the landslide dams, two separated field investigations were carried out on selected landslide dams in those areas in 2012 using microtremor chain array survey (MCAS) (Okeke 2013).

1. Akatani Landslide Dam

On 3 September 2011, Akatani landslide dam was formed after the occurrence of a landslide in Akatani District, within the Kawarabi River Basin. The landslide destroyed some camp sites downslope of the mountain area and recorded no fatality. Material of the landslide dam is mainly composed of weathered blocks of sandstone and mudstone with detached fragments of intrusive rocks. The landslide is 30 m deep, with length and width of 1,100 and 460 m, respectively, while height and volume of the impoundment are 85 m and 9.4 million m³, respectively. To avert secondary disaster, geotechnical remediation work was carried out on the impoundment by laying 2–3 m diameter discharge pipes inside the impoundment to lower the barrier lake (Fig. 8a, b, c, d).

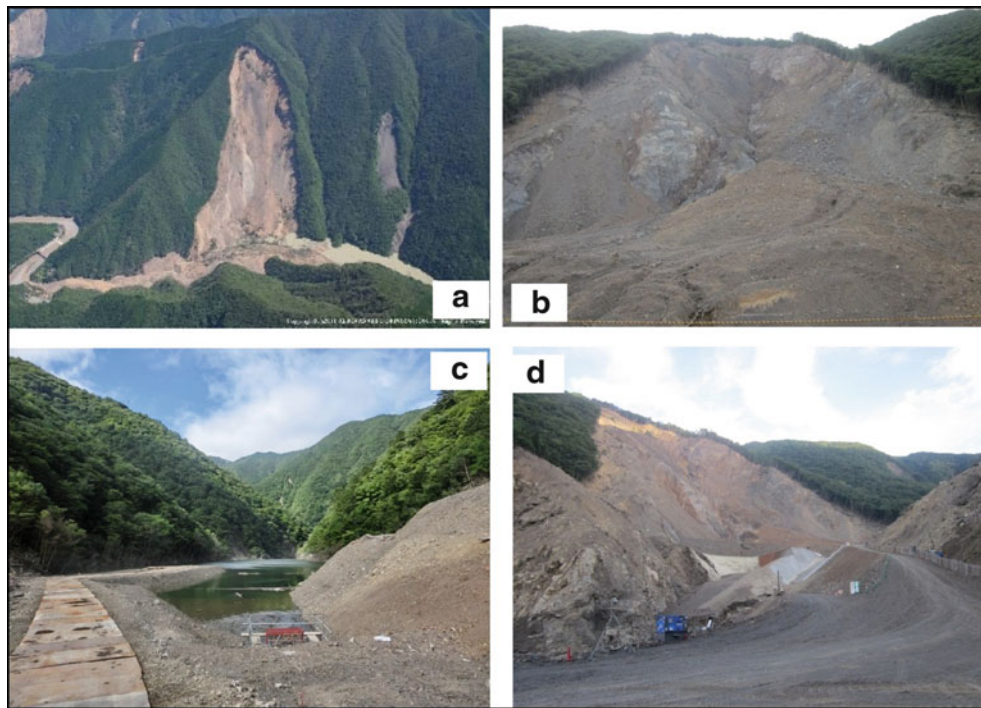


Fig. 8 Akatani landslide dam. (a) Aerial view (Photo courtesy of Aero Asahi) of the site few hours after the landslide dam was formed. (b) Front view. (c) Upstream side of the landslide dam. The *red gate*

shows the entrance of a draining pipe through the landslide dam from upstream to downstream. (d) Downstream side of the landslide dam



Fig. 9 Kuridaira landslide dam. (a) Aerial view (Photo courtesy of Aero Asahi) of the site few hours after the landslide was formed. (b) Front view of the main scarp and main sliding body. (c) Stabilized

section of the upstream dam axis with the barrier lake. (d) Stabilized part of the downstream dam face with internal pipes installed to lower the upstream lake level



Fig. 10 Chain array method of geophone arrangement at station D–D' on Akatani landslide dam (geophone inserted at the top right corner)

2. Kuridaira Landslide Dam

Kuridaira landslide dam was formed about the same time from deep-seated collapse of a relatively weathered mountain slope in Kuridaira, Totsukawa Village, Nara Prefecture. The landslide is 60 m deep, with length and width measuring up to 950 and 650 m, respectively. The

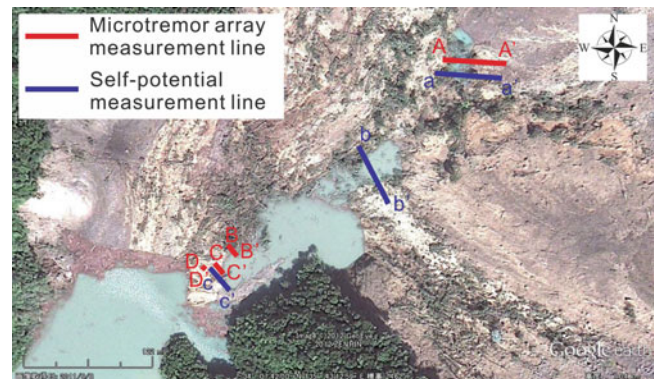


Fig. 11 Measure lines of microtremor chain array survey on Akatani landslide dam

height of the dam is about 100 m with volume of approximately 13.9 million m^3 (Fig. 9a, b, c, d).

3. Microtremor Array Survey and Result

In this study, microtremor chain array survey was carried out on Kuridaira and Akatani landslide dams. Extent of the survey line depends on topographic constraints such as availability of continuous planar surfaces, passage of subsurface drainage pipe and surface geology of the area. The geophones were arranged in a continuous triangular form of 3 m between adjacent stations (Fig. 10).

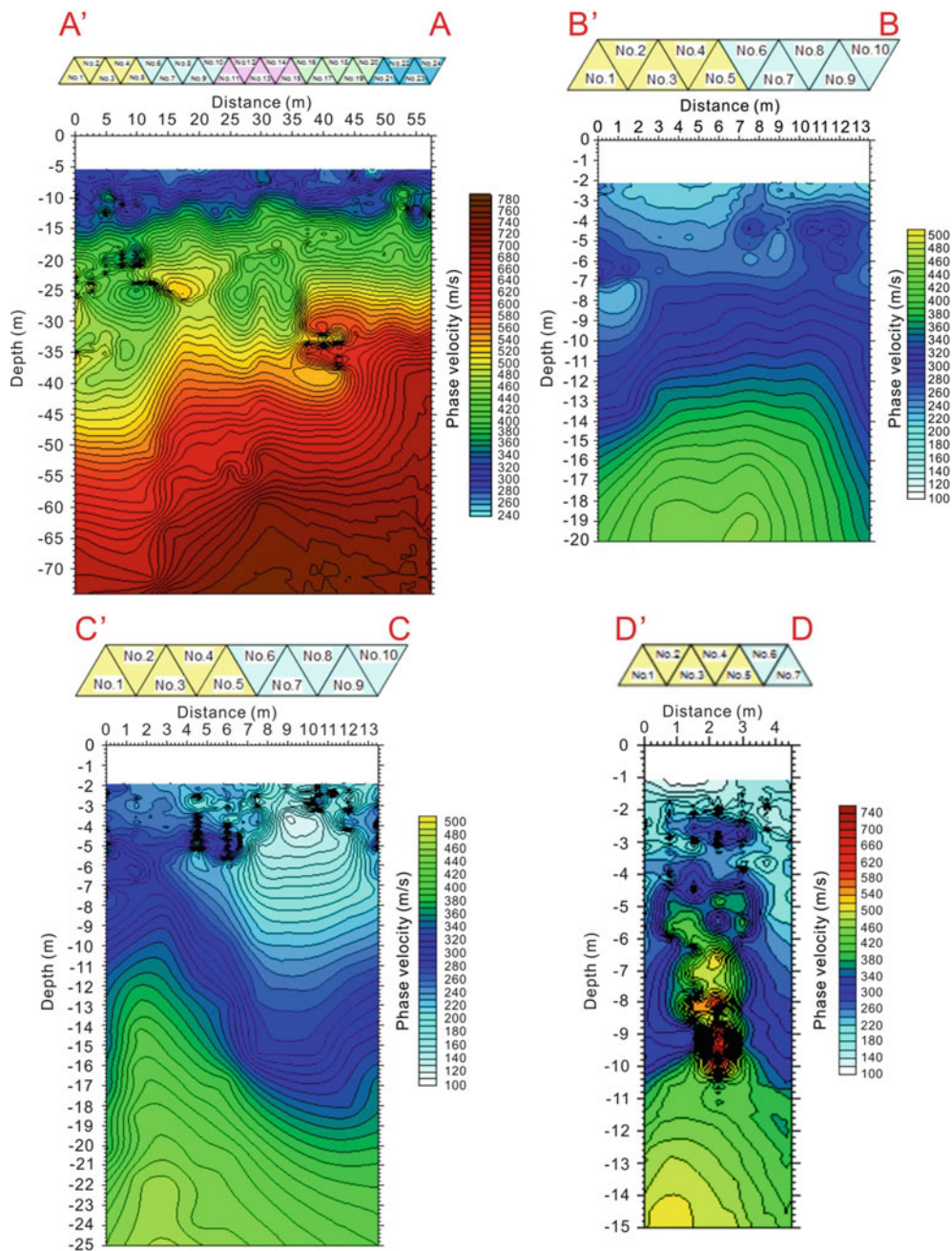


Fig. 12 Microtremor array survey results from Akatani landslide dam. D'-D is a profile section over a drainage pipe through the landslide dam

(a) Measurement results on the Akatani landslide dam
 At Akatani landslide dam, four lines with horizontal distance, for A-A' line, 3 m, B-B' line, 3 m, C-C' line, 3 m, and D-D' line, 1.5 m, were studied. Three of the investigation lines are close to the upstream lake (Fig. 11). Results of the survey show that phase velocity values on Akatani landslide dam range from 100 to 740 m/s. Lower values of phase velocity were obtained at the downstream side of Akatani landslide dam at

depth range of 20 m to 25 m (Fig. 12). The result of D-D' line shows different pattern with others. Some concentric holes were detected; these may be caused by underground movement of water in the drainage pipe installed after the formation of the landslide dam. One major significance of using MCAS in evaluating piping in landslide dams is the ability of the method to detect and record noise and other wave signals generated by the movement of groundwater beneath the survey line.

(b) Measurement results on the Kuridaira landslide dam

A horizontal interval of 10 m was covered on the central part of Kuridaira landslide dam along the direction of flow of the river (Fig. 13). Result of phase velocity obtained from Kuridaira landslide dam at depth range of 75 m to 85 m ranges from 620 to 680 m/s (Fig. 14).

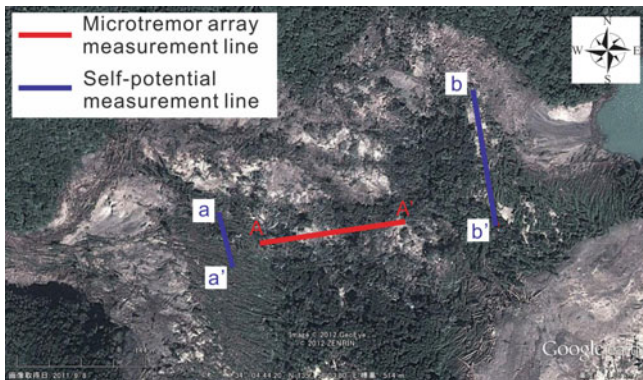


Fig. 13 Measure line of microtremor chain array survey on Kuridaira landslide dam

The relative high phase velocities obtained from the survey, especially on Kuridaira landslide dam, could be related to the geotechnical properties of the dam materials.

Conclusions

The microtremor chain array survey has proven to be useful in understanding the internal structures of landslide dams by measuring phase velocity of materials composing landslide dams. Furthermore, when piping flow exists in a landslide dam, the noise generated by movement of underground water can be detected by the microtremor chain array survey as a source of tremor. The application of MCAS in the two landslide dams in Nara prefecture showed high potential for using MCAS in evaluating the possibility of piping failure of landslide dams. More data and case studies will be reviewed to have better understanding of the process.

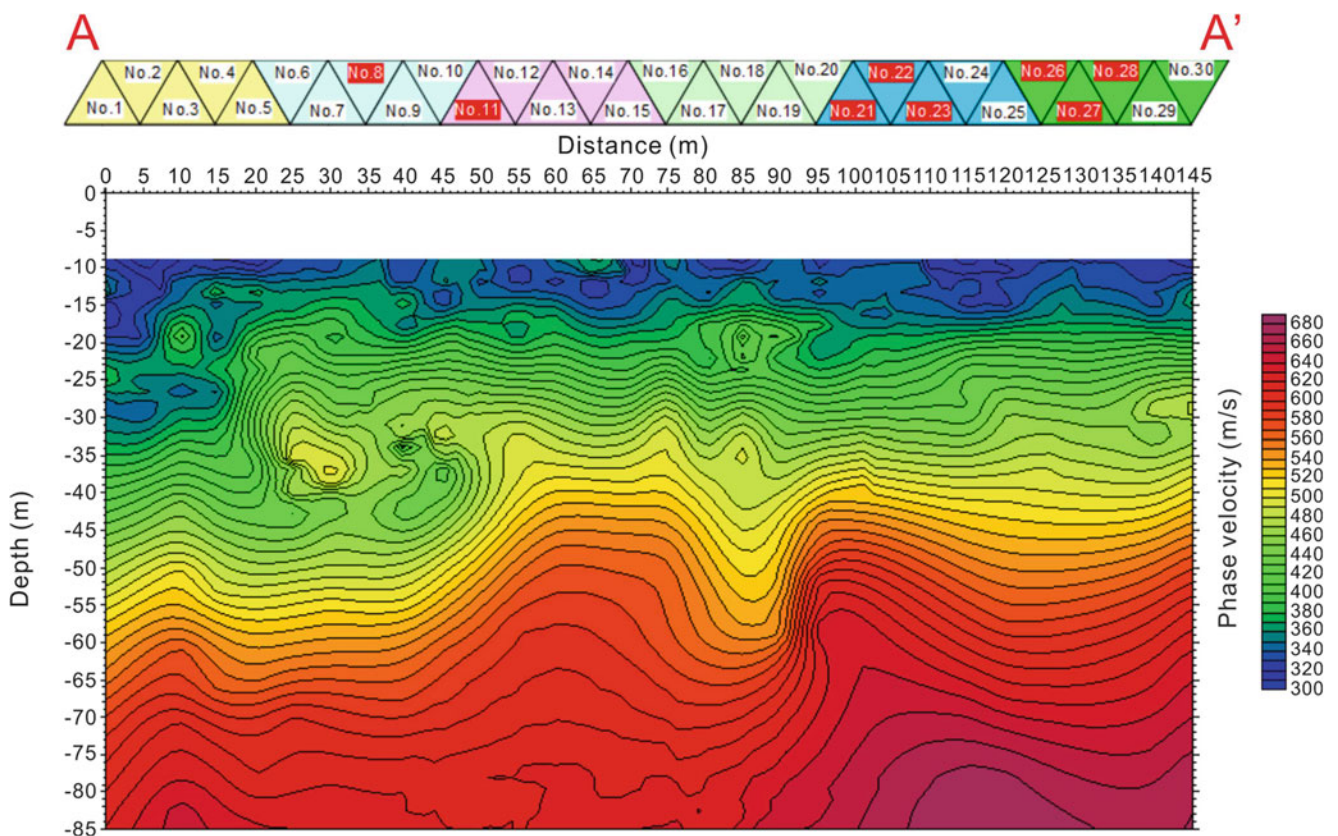


Fig. 14 Microtremor array survey result from Kuridaira landslide dam

References

- Arai H, Tokimatsu K (2005) S-wave velocity profiling by joint inversion of microtremor dispersion curve and horizontal-to-vertical (H/V) spectrum. *Bull Seism Soc Am* 95(5):1766–1778
- Fujita M (2012) Huge sediment disasters due to Typhoon Talas. In: The 3rd International Workshop on multimodal sediment disasters
- Hayashi H, Matsuoka T, Mizuochi Y, Ono M (2010) Two dimensional microtremors survey – Chain array survey method. *Geotech Engr Mag JGS* 58(8):10–13
- Hayashi SI, Uchida T, Okamoto A, Ishizuka T, Yamakoshi, T, Morita K (2013) Countermeasures against landslide dams caused by Typhoon talas 2011. *Tech Monitor*, pp 20–26
- Okada H (2003) The microtremor survey method. Society of exploration Geophysicists with the cooperation of Society of Exploration Geophysicists of Japan [and] Australian Society of Exploration Geophysicists, vol 12
- Okeke AC (2013) Field and laboratory study of internal erosion and piping in landslide dams. Master thesis of Shimane University, Japan. 82p
- Park CB, Miller RD, Xia J (1999) Multichannel analysis of surface waves. *Geophysics* 64(3):800–808
- Roberts JC, Asten MW (2004) Resolving a velocity inversion at the geotechnical scale using the microtremor (passive seismic) survey method. *Explor Geophys* 35(1):14–18
- SABO (2010) Press release dated August 11 2010, on assessed map of the relative susceptibility to deep catastrophic landslides. Division of the River Bureau, The Ministry of Land, Infrastructure, Transport and Tourism, and the Public Works Research Institute. http://mlit.go.jp/report/press/river03_hh_000252.html (in Japanese)
- SABO (2012) Press release dated September 10 2012, on survey of deep catastrophic landslides at the stream (small watershed) level. Division of the River Bureau, The Ministry of Land, Infrastructure, Transport and Tourism, and the Public Works Research Institute. http://mlit.go.jp/report/press/mizukokudo03_hh_000552.html (in Japanese)
- Taira A, Okada A, Whitaker JH, Smith AJ (1982) The Shimanto Belt of Japan: Cretaceous-lower Miocene active-margin sedimentation. *Geol Soc Lond* 10:5–26 (Special Publications)



Impact of Water Level Fluctuation on the Reservoir Landslide Stability

Qiang Yang, Zhennan Ye, Weicui Ding, and Youlong Gao

Abstract

Taking Sidaoqiao landslide in Wushan County in Three Gorges Area as an example, this paper explore the impact of reservoir water level rising and falling at different rate on the stability of typical gravel soil accumulation landslide by establishing the landslide seep model and slope model with the Seep module and Slope module in Geostudio and calculating the landslide seepage field and stability coefficient. Results showed that the impact of reservoir water level fluctuation on landslide stability was controlled by several factors such as hydrodynamic pressure, hydrostatic pressure, uplift force, variation in physical–mechanical properties (the value of c , ϕ etc.). When the water level fluctuates at a high rate, before the stability coefficient reaches the maximum value, the landslide stability is mainly affected by the hydrostatic pressure; while after the maximum value, with water further infiltrating into or draining out of the slope, it is mainly affected by the variation in physical and mechanical properties and the uplift force. When the water level fluctuates at a lower rate, the pore water pressure, uplift force and physical and mechanical properties are the dominant factors.

Keywords

Three Gorges Area • Gravel soil • Landslide • Reservoir water level fluctuation • Stability

Introduction

During the normal operation of the Three Gorges Reservoir, the water level fluctuates periodically within the range of 145–175 m every year, resulting in a 30 m hydro-fluctuation belt. As the water level fluctuates, the original limit

equilibrium state of the geological environment has been changed, which inevitably affect the formation and development of landslide and other geological hazards, in addition to the particularity of the geological conditions and the complexity of the geological environment, which makes the Three Gorges Area a severely afflicted area of geological disasters (Xiao et al. 2005; Zeng 2011; Lian et al. 2011). There are a large amount of gravel soil accumulation landslides from Badong to Fengjie in the Three Gorges Area, which have better permeability and larger slide band and affected zone, which make them more sensitive to the water-level-fluctuation. After the impoundment of the Three Gorges reservoir, the rise of the underground water level and the fluctuation of the reservoir water level, which have changed the seepage field, will greatly affect the stability of the slopes along the river. The impact of the water level fluctuation on the stability of the landslides has attracted extensive attention by experts and scholars (Yin 2003; Ding et al. 2004; Zheng et al. 2004).

Q. Yang (✉) • Y. Gao
Center for Hydrogeology and Environmental Geology, CGS,
Baoding 0711051, China
e-mail: yang5359535@126.com; gemcgao@163.com

Z. Ye
China University of Geosciences, Beijing 100083, China
e-mail: yzn0414@126.com

W. Ding
Institute of Geology Chinese Academy of Geological Sciences,
Beijing 100037, China
e-mail: dingweicuis@163.com

Working on this research is of great scientific value and practical significance to the study of gravel soil accumulation landslides, and it also helps to understand similar landslides.

The change of hydrodynamic condition is the dominant factor that leads to reservoir landslides. So far there is little research on the impact of the reservoir water level fluctuation on landslides stability. Besides, most of the previous studies have concentrated on qualitative description and simple calculation. The numerical simulation and general mechanic calculation means with a model that is not refined enough and is calibrated with macro phenomena or little monitoring data lack of the long-term continuous multi-monitoring data. Therefore, collecting various parameters more accurately, establishing a relatively refined model and adopting the multiple real-time continuous monitoring data as the basis for model calibration to ensure the overall accuracy of the simulation results and provide more effective data to further study on the impact of reservoir water level fluctuation on the landslide stability.

Main Factors of Water Level Fluctuation Affecting the Stability of Landslide

In the process of the reservoir water level fluctuation, the seepage field of the slide body that submerged in the river changes, which would affect the original equilibrium state in the slide body, reduce the stability coefficient of the slope, and lead to landslide. The main factors that lead to the reduction of the stability coefficient are as follow (Liu et al. 2006; Zhu et al. 2002; Wang 2005; Wu 2009).

Uplift Force Change Caused by Variation of the Submerged Part of Landslide

In the water level fluctuation process, the submerged landslide segment varied. The uplift force on the slide body varied with the water infiltrating or draining out of the slide mass. The uplift force act opposite as the body weight, and would reduce the effective weight of the toe of the landslide, decreasing the resistance force of the entire slide body and consequently lowering its stability. When the lower part of the sliding surface is flat, the uplift force would act on a relatively large area, the abovementioned effect is especially significant.

Variation in Pore Water Pressure During Water Level Fluctuation

A rise in the reservoir water level, especially a rapid increment, would lead to a quick increment in hydrostatic

pressure and an infiltration hydrodynamic pressure, which would helps to stabilize the landslide. On the contrary, when the reservoir water draws down quickly, ground water level in the slope would also decline but with a certain lag behind the reservoir water table, resulting in a higher ground water level than the one with the same water table when it is rising. Therefore, a large hydraulic gradient occurred in the cutting slope, which would easily induce reservoir landslide. This effect is marked especially when the permeability of the bank slope is very small.

Variation in Physical–Mechanical Properties of Slip Soil in the Submerged Landslide

The seepage field in the submerged landslide body would vary as the reservoir water level fluctuates. Then the physical–mechanical properties (especially the shear strength parameters) would change with continuous infiltration or drainage, changing stability of the entire landslide. At the same time, the matric suction in the slip soil would vary as the water content of the slip body change, leading to a change in the stress state of the soil, along with the landslide stability.

General Situation of Typical Landslide

Sidaoqiao landslide was developed in the west of Wushan town. The slide body is 100–250 m wide, about 600 m long, 14–43 m thick in average, with an area of about $11 \times 10^4 \text{ m}^2$, and a volume of about $268 \times 10^4 \text{ m}^3$. The back of the landslide is in the shape of round-backed arm-chair, with the back wall of 280–360 m high and with a slope of about 40° . The shear outlet of the landslide lies on the gully mouth, above the Yangtze River high floodplain, with an elevation of 100–150 m. Generally, the Sidaoqiao landslide extends along Sidaogou in the north-south direction, and the main sliding direction is $150\text{--}170^\circ$.

The sliding body was mainly composed of gravel soil, sliding cataclastic rock mass, fragment stone soil and gravelly silt or silty clay. From the top to the bottom, the fine grained soil was gradually reduced with increasing fragment stone content. T2b2 strongly weathered amaranth argillaceous siltstone and mudstone was exposed locally. The slide body is highly permeable, while the mud layers between the sliding bodies are water proof. The sliding zone is 1–4 m thick, mainly composed of yellow-pale or amaranth gravelly silt, silty clay, clayey gravel and mud, in plastic or soft-plastic state. Part of the slide zone was with striation and polished surface, and some segments were muddy with water.

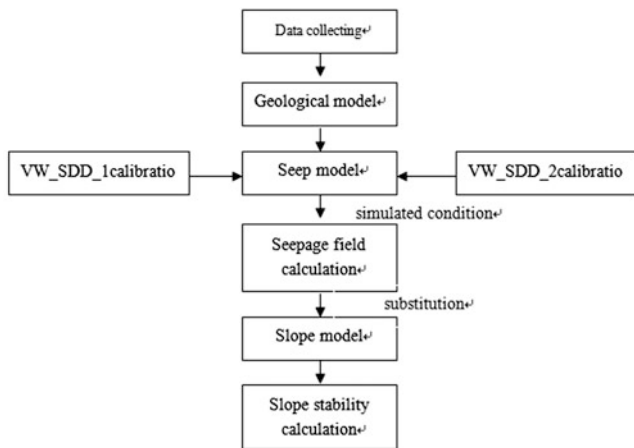


Fig. 1 Flowchart of model establishment, correction and calculation

The front of the landslide was greatly affected by water level fluctuation, with strong reservoir bank reformation.

Influence of Reservoir Water Level Fluctuation on the Landslide Stability

Flow Path of Simulation

Based on previous survey and test data, the geologic model was built with geoscience software Geostudio, and the seep model was established with the Seep module and calibrated with long sequences of real-time monitoring pore water pressure data (VW_SDD_2, VW_SDD_3). The time length of calibration data was a life cycle for the reservoir water level. The seepage field was first simulated at various conditions, and then subject to calibration. Then the calibrated seep model was imported into Slope module to calculate the stability coefficient in different seepage fields the reservoir water level rising and falling at various rates. Then the results were analyzed to explore the influencing factors of landslide stability under different conditions. Figure 1 shows the model establishment, optimizing and calibration, and calculation process.

Model Establishment

Based on survey data, the main sliding profile could be grouped into three layers: backfill, gravel and slip soil (main and secondary slip zone), and the parameters for each soil layer were collated. The corresponding model was built with Seep and Slope module in Geostudio. The seep model and stability model is shown in Fig. 2, and the parameters used are list in Table 1.

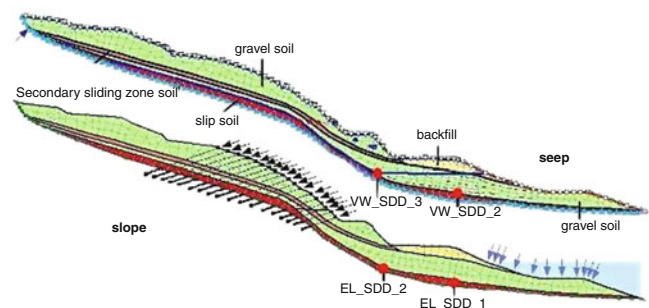


Fig. 2 The seep and slope model of main slip section

Model Calibration

The seep model was calibrated repeatedly according to the long-period real-time monitoring data obtained pore water pressure gauge VW_SDD_2 and VW_SDD_3 that installed in the middle or lower part of the slip band. The comparison diagram of the final simulated result and the monitoring data is as shown in Fig. 3.

It could be seen that the values of simulated and real-time monitored pore water pressure from VW_SDD_2 and VW_SDD_3 were quite close both in overall trend and single data, which could indicate good calibration in turn. It could also be concluded that the simulated seepage field was consistent with the one in situ under reservoir water level fluctuation, and that the model could give reasonable calculation results.

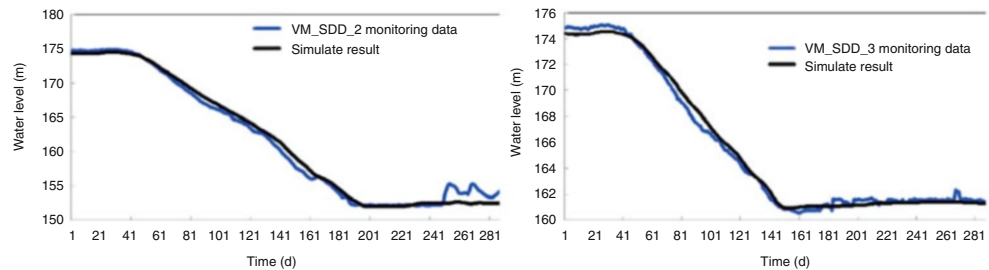
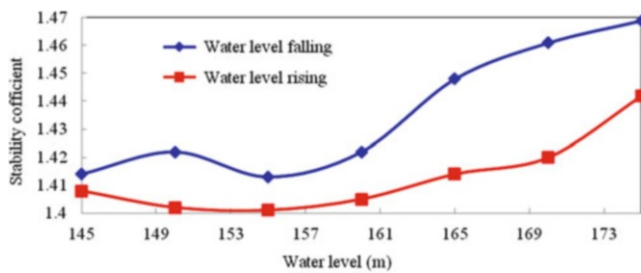
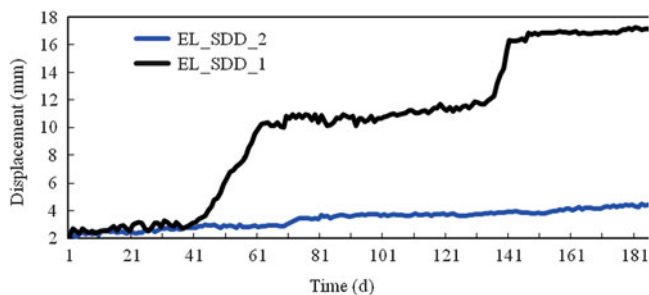
The seep field was simulated at the reservoir water level of 145, 150, 155, 160, 165, 175 m respectively in one fluctuation cycle. Then the simulated seep model was imported to the Slope module to calculate the landslide stability coefficient, as shown in Fig. 4. Figure 5 shows the monitored displacement from two points in the low part of the landslide (the location of the monitor points is shown in Fig. 2).

It could be seen from Fig. 4 that with the reservoir water level naturally falling, the stability coefficient of the landslide was first reduced to a minimum value at 155 m of water table, and then continuously and slowly increased.

The Sidaoqiao landslide is a typical gravel soil accumulation landslide. At the beginning drawdown process of the reservoir water level, the ground water in the slope body drained out quickly. The hydrostatic pressure was reduced and dynamic water pressure was locally raised, which was weakening the landslide stability. At the same time, the uplift force declined and the shear strength of the slip soil was strengthened, which helped to stabilize the landslide. However, the former effect was stronger than the latter one, so the stability coefficient of the landslide was reduced at first. With the groundwater draining out, when the stability coefficient reached the lowest point, the second abovementioned effect,

Table 1 Parameters for the Sidaoqiao landslide

Soil type	Density γ (kN/m ³)	Cohesion c (kPa)	Inner friction angle ϕ (°)	Residual water content (m ³ /m ³)	Saturated water content (m ³ /m ³)	AEV (kPa)	Permeability (m/d)
Backfill	28	20	22	0.18	0.43	2.5	0.025
Gravel soil	20.14	24	22.1	0.04	0.3	0.06	8
Slip soil	18.8	48.5	15.2	0.22	0.5	11.8	0.005

**Fig. 3** The comparison diagram of VW_SDD_2 and VW_SDD_3 simulation and monitoring results**Fig. 4** Stability coefficient of Sidaoqiao landslide under different water levels**Fig. 5** Deep displacement monitoring data in the lower part of landslide

i.e. the effect stabilize the landslide, became stronger than the first one, and the stability coefficient began to continuously raise. During this process, different water falling rates would result in various stability coefficient varying tend.

During the reservoir water level naturally increasing, the stability coefficient was firstly raised then reduced and then continuously increased again. At the beginning stage, the uplift force rose, with the shear strength of slip soil weakened and increasing dynamic water pressure, which is adverse to stabilize the slope and weaker than the hydrostatic

pressure which helped to stabilize the slope. Therefore the stability coefficient began to continuously rise until the reservoir water level reached 150 m. Then the adverse effect became stronger than the stabilizing effect the hydrostatic pressure brought about, and the stability coefficient began to decline until the reservoir water level reached 155 m. After that, the hydrostatic pressure turned to be the dominant factor, significantly greater than the adverse effect from dynamic water pressure, uplift force and weakened shear strength of slip soil, and the stability coefficient gradually increased to a maximum value during the water table reaching 175 m.

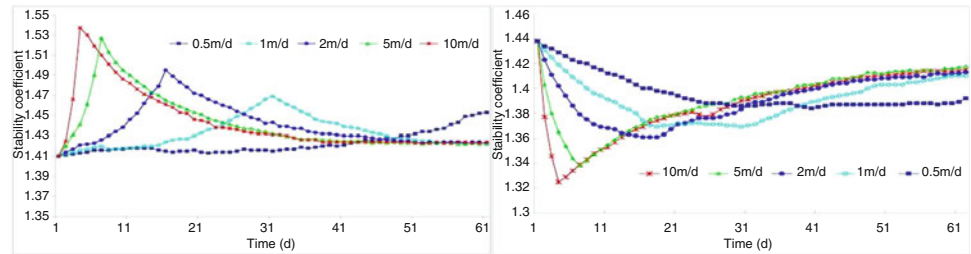
Calculation results from Fig. 4 indicated that the landslide kept stable. And monitoring data in Fig. 5 showed that in a reservoir water level fluctuation cycle, the displacement of slip zone was relatively small, 17 mm at most, indicating that the landslide was creeping very slowly, which was consistent with simulated results. It could be concluded that the model was reliable and the simulated results were quite reasonable.

Influence of Reservoir Water Level Fluctuation on Landslide Stability

As is well known, the reservoir water level rising and falling rates are crucial to reservoir landslide development. Different rising and falling rates would result in different seepage field variation, and then affect the landslide stability. Therefore, it is of great significance to understanding the disaster mechanism and model to simulate the landslide stability under different seepage field variation when reservoir water level rising and falling at different rates especially at large rates, and to explore the relation between different

Table 2 The simulation conditions

Condition	Water level variation (m)	Original state (m)	Water level rising/falling rate (m/d)
Condition 1	145–175	145	0.5, 1, 2, 5, 10
Condition 2	175–145	175	

Fig. 6 Stability coefficient changes under different water level rising/falling rates from 145 m/175 m**Table 3** The changing patterns in stability when water level rising/falling from 145 m/175 m

Rise/fall rate (m/d)	Time to extreme value (D)		Time to steady state (D)		Variation in stability	
	Rise	Fall	Rise	Fall	Rise (increment)	Fall (reduction)
10	3	3	22	55	0.014	0.023
5	6	6	28	58	0.011	0.02
2	15	15	35	58	0.013	0.025
1	30	30	50	58	0.013	0.027
0.5	60	60	60	58	0.043	0.046

reservoir water level, different rising/falling rates and landslide stability. The simulated conditions were listed in Table 2.

Figure 6 shows that the calculated stability coefficients at different reservoir water level rising rates under Condition 1, and that the stability coefficients at different falling rates under Condition 2. The stability coefficients were listed in Table 3. As shown in Fig. 6, during the reservoir water level rising from 145 m to 175 m at different rates, when the rising rates were greater than 1 m/d, the landslide stability coefficient tended to increase quickly firstly, then gradually decreased to a stable value. When the rising rates were smaller than 1 m/d, the landslide stability coefficient tended to decrease firstly and then gradually increase. It could be seen from Table 3 that the greater the rising rates, the quicker the max/min stability coefficient could be reached, and vice versa. During the reservoir water level rising process, the stability coefficient was increased by 0.013 when the rising rates were greater than 1 m/d, and by 0.043 at rising rate of 0.5 m/d. When the rising rates were great, before the water level reached 175 m, the hydrostatic pressure acted dominantly in controlling landslide stability, then the landslide stability coefficient gradually increased. After the water level reached 175 m, with reservoir water infiltrating into the landslide, the uplift force increase, and the physical and mechanical properties of slip soil (the value of c , ϕ etc.) were gradually reduced. Then the stability coefficient gradually decreased to a stable state. When the rising rates were small, the landslide stability was controlled by reservoir water hydrostatic pressure, dynamic pressure,

uplift force and variation of shear strength of slip soil, and the stability tendency was controlled by the dominant influencing factor. As a whole, during the reservoir water level rising, the landslide kept stable.

As shown in Fig. 6, during the reservoir water level decreasing from 175 m at different rates, when the falling rates were greater than 1 m/d, the landslide stability coefficient tended to decrease quickly firstly, then gradually rise to a stable value. When the falling rates were smaller than 1 m/d, the landslide stability coefficient tended to decrease gradually, then increase slowly to stable. Similar to water level rising process, it could be seen from Table 3, that the greater the falling rate, the quicker the min stability coefficient could be obtained. The time needed for the stability coefficient to recover to stable at different rates were quite similar, about 56 days. During the reservoir water level falling process, stability coefficient was decreased by 0.024 when the falling rates were greater than 1 m/d, and by 0.046 at falling rate of 0.5 m/d. When the falling rates were greater than 1 m/d, before the water level reached 145 m, the hydrostatic pressure acted dominantly in controlling landslide stability. So with reservoir water level falling, hydrostatic pressure decreased with hydrodynamic pressure locally increased, then the landslide stability coefficient gradually declined. After the water level reached 145 m, with groundwater drain out from the landslide, the uplift force decreased and hydrodynamic pressure locally increased, and the physical and mechanical properties of slip soil (the value of c , ϕ etc.) were gradually strengthened. Then the landslide stability

was mainly controlled by variation of shear strength of slip soil, and the stability coefficient gradually increased to a stable state.

When the falling rates were smaller than 1 m/d, the landslide stability was mainly controlled by reservoir water hydrostatic pressure at the beginning stage. With reservoir water level falling, the hydrostatic pressure and uplift force decreased with hydrodynamic pressure raised, which was adverse to landslide stability and exceed the effect of shear strength strengthen of slip soil. So the slope stability coefficient was gradually decreased to min. After that, the effect of shear strength strengthening of slip soil become dominant, and the landslide stability gradually increased to stable. Similarly, during the reservoir water level falling, the landslide also kept stable.

Conclusions

1. Based on survey data and laboratory test data, the seep model and slope model were established with the Seep module and Slope module in Geostudio, and calibrated by long-period real-time monitoring data in reservoir water level fluctuation cycle. The calibrated results and calculated landslide stability indicated that the seep model was quite reliable and reasonable. During the reservoir water level naturally rising, the calculated landslide stability increased firstly then decreased, and then continuously increased. When the reservoir water level falls, the calculated landslide stability coefficient gradually decreased to a min value and then gradually increased. However, the landslide kept stable in whether condition. Comparing the calculated landslide stability at different reservoir water level and real-time monitoring displacement, the seep model and the slope model could give reasonable results and the simulated results was consistent with that in field.
2. When the reservoir water level rises at different rates, the quicker the water rise, the more impact the landslide stability would suffer. Before the water level rises to 175 m, the hydrostatic pressure would be the dominant factor controlling slope stability, and the landslide stability coefficient continuously increases. After the water level reached 175 m, with reservoir water infiltrating into the landslide, the uplift force increase, and the physical and mechanical properties of slip soil (the value of c , ϕ etc.) were gradually reduced. Then the stability coefficient gradually decreased to a stable state.
3. When the reservoir water level falls at different rates, the quicker the water falls, the quicker the landslide stability falls. At beginning, the hydrostatic pressure and the uplift force decreased with hydrodynamic pressure locally increased, then the landslide stability coefficient gradually declined. After the water level reached 145 m, the landslide stability was mainly controlled by variation of shear strength of slip soil, and the stability coefficient gradually increased to a stable state.
4. The impact of reservoir water level fluctuation on the stability of gravel soil accumulation landslide was controlled by several factors such as hydrodynamic pressure, hydrostatic pressure, uplift force, variation of physical—mechanical properties (the value of c , ϕ etc.). It is a relatively complex process, and the variation tendency of stability depends on the dominant factor.
5. Sidaoqiao landslide keeps stable during the reservoir water level rising and falling. During the reservoir water level rising, the greater the rising rates, the quicker the max/min stability coefficient could be reached. The stability coefficient was increased by 0.013 when the rising rates were greater than 1 m/d, and by 0.043 at rising rate of 0.5 m/d. During the reservoir water level falling, the greater the falling rate, the quicker the min stability coefficient could be obtained. The time needed for the stability coefficient to recover to stable at different rates were quite similar, about 56 days. During the reservoir water level falling process, the stability coefficient was decreased by 0.024 when the falling rates were greater than 1 m/d, and by 0.046 at falling rate of 0.5 m/d.

References

- Ding X, Fu J, Zhang Q (2004) Stability analysis of landslide in the south end of Fengjie Highway Bridge with fluctuation of water level of the Three Gorges Reservoir. *Chin J Rock Mech Eng* 23(17): 2913–2919
- Lian Z, Tan J, Yan J, Wang N (2011) Analysis of bank slope stability under rainfall and reservoir level fluctuation. *Safety Environ Eng* 18(2):14–22
- Liu C, Chen C, Feng X (2006) Study on mechanism of slope instability due to reservoir water level rise. 26(5): 769–773
- Wang X (2005) Research on the effect to the bank slope in impounding and drawdown of Three Gorges reservoir water level. Chengdu University of Technology, Chengdu
- Wu Z (2009) The influence of water level fluctuation on the bank slope stability. *Disaster Contr Eng* (1): 1–6
- Xiao X, Li T, Zhang Z (2005) Causes analysis and the stability assessment of Yanjiapo Landslide in the Three Gorges Reservoir area. *Chin J Geol Hazard Contr* 16(1):39–43
- Yin Y (2003) Seepage pressure effect on landslide stability at the Three Gorges Reservoir area. 14(3): 1–8
- Zeng G (2011) Stability analysis of landslide under reservoir water level fluctuation. *J Chin Three Gorges Univ (Nat Sci)* 33(4):15–18
- Zheng Y, Shi W, Kong W (2004) Calculation of seepage forces and phrcatic surface under drawdown conditions. *Chin J Rock Mech Eng* 23(18):3203–3210
- Zhu D, Ren G, Nie D, Ge X (2002) Effecting and forecasting of landslide stability with the change of reservoir water level. *Hydrogeol Eng Geol* (3): 6–9



Stability Analysis of Reservoir Slope Considering the Change of Mechanical Parameters of the Materials

Ming Zhang and Ruilin Hu

Abstract

Mechanical actions of the reservoir water including hydrostatic and hydrodynamic water pressures are mostly considered in the stability computation of the reservoir slope under water level change; while reduction of the mechanical properties including friction angle (φ) and cohesive strength (c) due to water immersing is always neglected due to the difficulties in building the numerical model and obtaining the change of the parameters. The factor of safety computed with this neglecting is obviously unreliable. Taking the Xiazanri slope on the Jinsha River for example, the paper proposes a systematic method to compute the stability of reservoir slope considering the reduction of mechanical parameters. Large-scale in-situ horizontal push-shear tests were used to obtain the mechanical parameters of the materials under natural condition and after immersed. Seepage numerical modeling was used to obtain the seepage fields at each step, which were imported into the stability computation model. The material regions were redrawn along the water table to assign the different mechanical parameters above and below the water table. Through above method, factor of safety considering the change of mechanical parameters could be obtained. The results show that under two conditions (considering the change of materials and not), the changing laws of the factors of safety of the slope are the same as the reservoir water level increases. They both decrease at first and increase afterwards; however, compared with the latter, the factor of safety under the former condition decreases by as much as 35.34%. Therefore, considering the change of mechanical parameters in stability analysis of the reservoir slope is a necessity in engineering design.

Keywords

Reservoir slope • Stability analysis • Change of mechanical parameters • Water table • In-situ horizontal push-shear tests

Introduction

Influence of water level change of the reservoir on the stability of the slope is not only the mechanical action including hydrostatic and hydrodynamic water pressures, but also change of mechanical parameters of the slope materials. After physical and chemical reactions between the materials and reservoir water, the friction angle (φ) and cohesive strength (c) decrease markedly, which leads to sharp reduction of the stability of reservoir slope.

The reduction of mechanical parameters of the materials due to reservoir water has been gradually considered to be one

M. Zhang (✉)

Faculty of Engineering, China University of Geosciences, No. 388, Lumo Road, Wuhan, Hubei Province 430074, China
e-mail: zhangming8157@126.com

R. Hu

Institute of Geology and Geophysics, Chinese Academy of Sciences, Beijing 100029, China
e-mail: hurl@mail.igcas.ac.cn

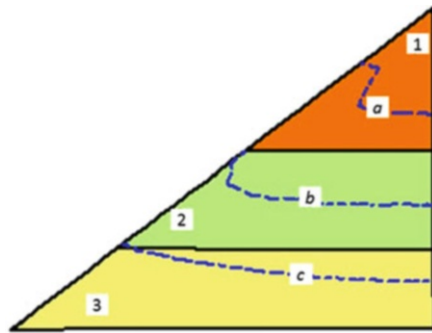


Fig. 1 Water tables of groundwater in a reservoir slope as the water level increases

of the important reasons leading to landslide (Xu et al. 2004). However, there are still many difficulties in the research including obtaining the reductions of mechanical parameters and building the computation model based on these reduced parameters. Therefore, many studies neglected the reductions of the mechanical parameters and only consider the mechanical actions of the reservoir water on the slope (Zhu et al. 2002; Liao et al. 2005, 2006; Huang and Xu 2005; Qiao et al. 2005; Liu et al. 2005a, b). The mostly used method in stability computation of reservoir slope with increasing water level is to consider the hydrostatic and hydrodynamic actions of the reservoir water. The conclusion obtained through this way is that factor of safety firstly decreases and then increases when the reservoir water rises from the slope toe to the crown (Zhu et al. 2002). The mostly used method in stability computation of reservoir slope with decreasing water level is to consider only the hydrodynamic water pressure and buoyancy of the water on the soil. However, the reduction of mechanical parameters of the slope material can reach as much as by 73.1 % due to reaction between water and the materials (Peng and Liu 2000), which means that this reduction cannot be neglected.

Considering the reduction of the mechanical parameters in the stability computation of reservoir slope has mainly two difficulties:

1. How to obtain the mechanical parameters of the slope materials after immersing for different time. The material of the reservoir slope is always the mixture of soil and stones with diameters of several millimeters to several meters. The obtained parameters in laboratory are unreliable. Due to the limit of sample size, stones larger than a certain size is got rid of the sample. Furthermore, it is very difficult to keep the sample the original state in laboratory, not to mention obtaining the exact parameters of the materials after immersed by reservoir water.
2. How to build the computation model with those natural and reduced parameters. Taking Fig. 1 for example, the reservoir slope contains three different materials numbered as 1, 2 and 3. The reservoir water increases at a certain speed, c, b and a are the water tables at 1st, 2nd and third day. At the

third day, the materials under the water table c has been immersed for 3 days, the materials between water tables b and c has been immersed for 2 days, and the materials between water tables a and b has been immersed for 1 day, the material above the water table is in the natural condition. Even the same material experiencing different immersing time has different mechanical parameters, which leads to difficulties in building the computation model. Taking Xiazanri slope consisting of materials of accumulation bodys on Jinsha River, Yunnan Province for example, this study proposes a systematic method to compute the factor of safety of reservoir slope considering not only the hydrostatic and hydrodynamic water pressures, but also the reduction of mechanical parameters.

Characteristics of the Xiazanri Slope

The Xiazanri slope (Fig. 2) is situated on left bank of the Jinsha River and is only 100 m upstream from the dam of the Liyuan water power station, which is going to impound water in 2015. The slope distributes between 1,560 m and 1,680 m in elevation. The area is about 1.2 km², and the volume is about $5,084 \times 10^4$ m³ (KHIDRI 2007). The stability of the Xiazanri slope is a key factor to the safety of the dam and the nearby water resource facilities.

The field investigations including drillings and an adit (KHIDRI 2007) indicate that Xiazanri slope mainly consists of three layers of materials (Fig. 3): The first layer is a colluvial deposit, which is the mixture of soil and gravels with poor psephicity. The content of the gravels is about 80 %. The diameter of the gravels is mainly between 1 cm and 15 cm. The middle layer is a glacial till consisting of 60 % gravels with relatively good psephicity and 40 % of soil. The diameter of the gravels is mainly between 1 cm and 5 cm. The bottom layer is an alluvial deposit with clear stratifications and poor cementations. This layer consists of interbedding two layers: one is the gravel layer with gravels between 2 cm and 10 cm in diameter; the other one is gravels mingled with silt. The content of the gravels is about 80 %. This paper numbered the three materials as 1, 2 and 3.

In-Situ Horizontal Push-Shear Tests for the Mechanical Parameters of the Slope Materials

Mechanical parameters of the gravel soil mainly depend on its texture and gravel content, which are random in the natural condition. Furthermore, the sample in laboratory is difficult to keep its original natural texture. Therefore, the mechanical parameters of the gravel soil under the natural and immersed conditions are difficult to be obtained through laboratory tests.

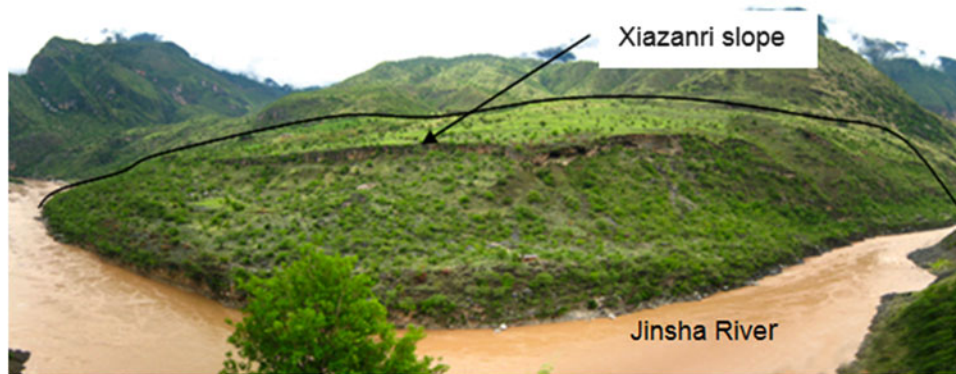


Fig. 2 The panorama of the Xiazanri slope

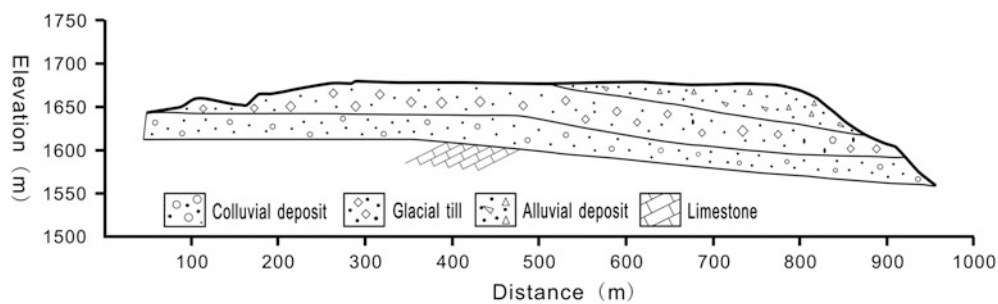


Fig. 3 The section map of the Xiazanri slope

There are usually two ways obtaining the mechanical parameters of the gravel soil. One is laboratory tests on the samples in which the gravels larger than a certain size is got rid of. The parameters obtained in this way will multiply an empirical coefficient according to the content and diameter of the gravels. Applications of this method show that the final results exists relatively large error. The other one is the in-situ test, the mostly used test is direct shear test, while the vertical counter load exerted on the sample needed is not always satisfactory.

This study used in-situ horizontal push-shear test to obtain the mechanical parameters (friction angle φ and cohesive strength c). As to the colluvial deposit, the tests were conducted directly on the ground surface. While the tests of the glacial till and the alluvial deposit were conducted in the adit, which was dug in order to investigate the structure of the slope.

The procedure of the in-situ horizontal push-shear test is as following:

- (1) Preparing the sample. Select the place where to conduct the test, and then cut the gravel soil to be a rectangular parallelepiped, which has three lateral exposure faces (Fig. 4).
- (2) Installing the equipments. First install an armor plate which transmits the push force of the jack to the sample

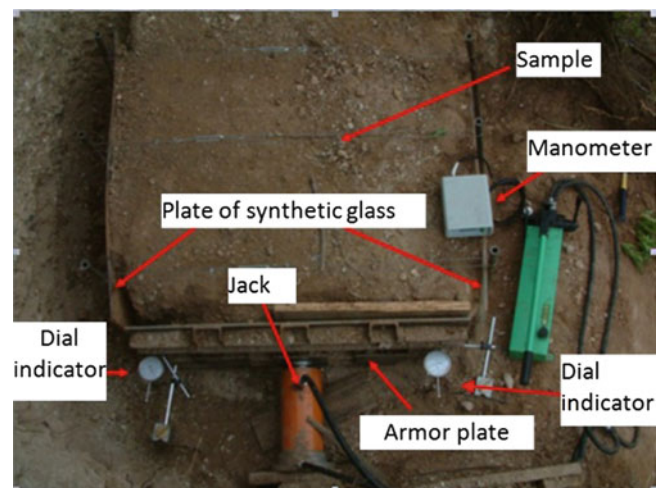


Fig. 4 Samples and equipments installed

on the thrust surface, one of three exposure faces. If there are spaces at local places between the armor plate and the sample, fill the space with fine sand and compact the sand. Install the jack behind the armor plate, and connect the jack and the manometer with a sensor, which translates the pressure the jack exerts on the plate to the manometer. Install and fix two plates of synthetic glass respectively on



Fig. 5 Horizontal push-shear in-situ test of saturated accumulation body

the lateral two exposure surfaces. If there are spaces between the plates and the sample, fill the spaces with fine sand and compact the sand. The two plates of synthetic glass can limit the lateral expansion of the sample during shear. Install two dial indicators on the armor plate to monitor its displacement. The sample and equipments after installments finished are shown in Fig. 4.

- (3) Conducting the tests. Exert the stress on the armor plate with the jack and add the stress gradually. During the course, the displacement of the armor plate is record by two dial indicators (the final displacement is equal to the average value of this two indicators), and the stress exerted on the plate is record by the manometer. As the displacement increases, the exerted stress first increases to a peak value and then decreases to a steady value. This peak value is the maximum horizontal push stress P_{max} . Release the horizontal push stress of the jack, and then exert the horizontal push stress in the same way at the second time and obtain a peak value of this pushing course, this peak value is the minimum horizontal push stress P_{min} .

After exerting the push stress for the second time, some local failure surfaces in the sample has been formed, continue to add the push stress until the connective failure surface forms. Remove the jack, and get rid of the gravel soil above the failure surface, which will emerge at the surface. Make one of the two bottom points of thrust surface the origin of coordinates, measure the coordinates (x, y, z) of the failure surface at certain intervals. According to the obtained coordinates, draw the failure surface.

- (4) Conduct three tests at typical points in each layer of material according to the above procedure.

The procedure how to calculate the values of c , φ was referred by Lin (1994). The parameters finally used in stability computation are the average value of the three tests.

In order to obtain the mechanical parameters of the materials after immersed by water, after preparing the sample of the above step (1), a closed embankment about 10 cm is built on the surface of the sample. The reservoir water is input into the embankment to a certain water level (Fig. 5). Keep the water level through supplementing the water as long as the water level decreases. After a period of time, the horizontal push test can be conducted according to the above procedure. In this study, we suppose that after immersing for one day, the parameters of the materials decrease to a minimum value and do not continue to decrease any more. Therefore, only the samples immersed by water for one day were tested. Because the water consumption used for tests was very large, the water level in the embankment decreased quickly, and the reservoir water was difficultly taken from the Jinsha River. The road from the water level to the test points was very steep (Fig. 2), and there was no electricity in this region, therefore pump could not be used. The water used in the tests was mainly obtained by manpower. Five hired local persons picked water by their shoulders.

The other parameters of the materials including saturated permeability coefficient, density were also obtained through field tests.

The parameters of three materials of the Xiazanri slope are shown in Table 1.

Stability Computations

This study conducted the stability computations using the Geostudio software. Its module Seep/w can model the change of the seepage field with the change of reservoir water level, and the module Slope/w can compute the factor of safety.

According to the impoundment plan of the water power station, the water level will increase by 120 m during 30 days. This study divides 30 days into six time steps in the computations. Therefore, the factors of safety of the Xiazanri slope under the natural condition and at the 5th, 10th, 15th, 20th, 25th and 30th days were computed.

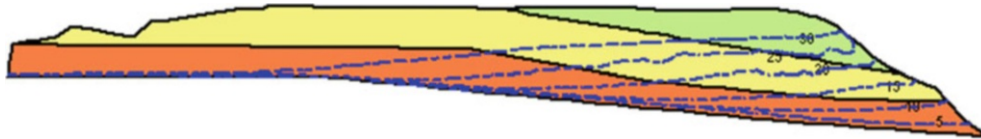
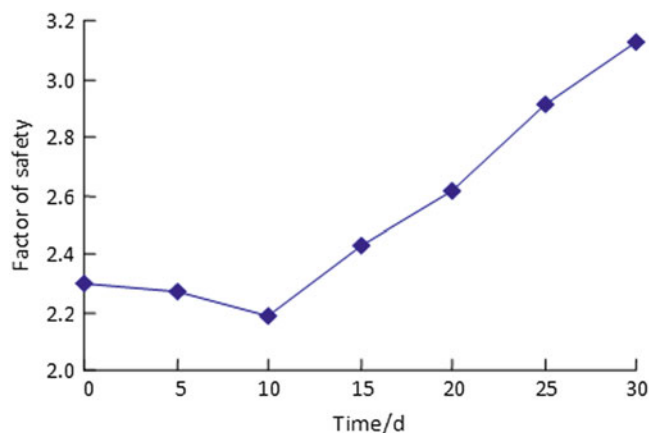
Stability Computations Not Considering Reduction of Mechanical Parameters

We firstly obtained the seepage fields at the 5th, 10th, 15th, 20th, 25th and 30th days using the Seep/w module (Fig. 6), and then the obtained seepage fields were imported into the Slope/w module to compute the factors of safety of the slope at each time step.

In this part of computations, reduction of the mechanical parameters of the slope materials was not considered. Only

Table 1 Parameters of three layers of materials of Xiazanri accumulation body

Material number	Density ρ ($\text{kg} \times \text{m}^{-3}$)	Ksat ($10^{-4} \text{ m} \times \text{s}^{-1}$)	φ ($^{\circ}$)		c (kPa)	
			Natural condition	Immersed for 1 day	Natural condition	Immersed for 1 day
1	957.60	2.08	50.58	42.38	12.32	5.03
2	1,845.79	7.67	30.60	18.92	13.52	11.96
3	1,873.10	2.13	28.17	10.70	5.32	2.04

**Fig. 6** Groundwater tables in the slope at each time step as reservoir water level increases (unit: m)**Fig. 7** Changing curve of factor of safety of the Xiazanri slope as water level increases (not considering the reduction of mechanical parameters due to water immersing)

the seepage field was imported into the slope model used built in Slope/w module for stability computing, therefore, only the hydrostatic and hydrodynamic water pressures were taken into account in computing the factor of safety of the slope. Figure 7 is obtained changing curve of factors of safety as the water level increases. From the Fig. 7, the initial factor of safety under the natural condition was 2.31, as the water level increases, the factor of safety firstly gradually decreases to 2.19 at the 2nd time step (the 10th day), then gradually increases afterwards to 3.13 finally at the 6th time step (the 30th day).

Stability Computations Considering the Reduction of Mechanical Parameters

The method to consider the reduction of mechanical parameters of the slope materials due to water immersing is as following:

1. Obtain the seepage fields at each time step with Seep/w module.
2. Import the corresponding seepage field into the slope model built in Slope/w module when computing the factor of safety at a certain time step. Redraw the material regions of the numerical model along the water table, and assign the different mechanical parameters above and below the water table.

For example, we want to compute factor of safety of the Xiazanri slope at the 6th time step (the 30th day). First, we import the seepage field at 6th time step into the Slope/w model (Fig. 7), if the reduction of mechanical parameters is not considered, there are three material regions in the numerical model. If the reduction of mechanical parameters is considered, the material regions must be redrawn along the water table (Fig. 8). After redrawing, there are six material regions in the numerical model, the original one material region is divided into two regions according to whether it has been immersed by water. Next, the parameters in Table 1 are assigned to the six material regions in Fig. 8.

3. Compute the factors of safety of the reservoir slope at each time steps.

Through the above method, six factors of safety considering the reduction of mechanical parameters as the water level increases are obtained. The changing curve is shown in Fig. 9.

Discussions

Comparing the Figs. 7 and 10, the changing laws of the factors of safety are the same as the reservoir water level increases. The factors of safety both considering and not considering the reduction of the mechanical parameters decrease first and then increase. The authors propose the reasons leading to this changing law are as follows: As the reservoir water firstly

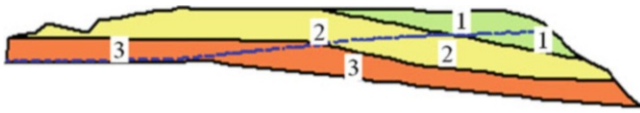


Fig. 8 Seepage field at the sixth step was imported into numerical model

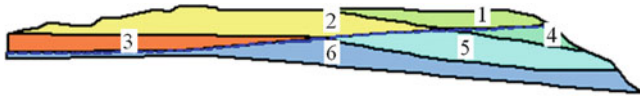


Fig. 9 The numerical model of Xiazanri slope after redrawing the material regions

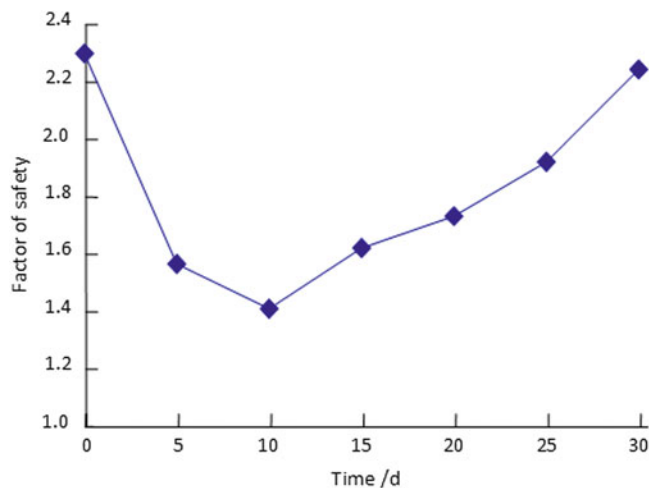


Fig. 10 Changing curve of factor of safety of the Xiazanri slope as water level increases (considering the reduction of mechanical parameters due to water immersing)

immerses the slope toe, the natural density of the gravel soil becomes to be the buoyant density, which means the resisting stress of the slope decreases. Therefore, the factor of safety of the slope decreases. As the water level continues to increase, the hydrodynamic stress acts inwards the slope and becomes larger with higher water level. Therefore, factor of safety of the slope increases gradually.

Although both the two factors of safety considering and not considering the change of mechanical parameters have the same changing law, they are different on two points.

1. The inflexion points emerge at the different time. The inflexion point of the former emerges at the 2nd time step; while the inflexion point of the latter emerges at the 3rd time step.
2. The former is much smaller than the latter as the reservoir water is at the same level. The maximum difference of two factors of safety is 35.34 %. In this study, due to the limit of the test condition, we suppose that reduction of the

parameters of the slope material occurs for only one day and obtain the parameters of materials immersed for only one day, which means the factors of safety computed based on the parameters under the real condition are even smaller.

To compute the factor of safety under the real condition at each time step, the actual parameters of the materials at each step must be obtained, which needs to conduct the in-situ horizontal push-shear tests on samples immersed for the corresponding time. Furthermore, the slope will be redrawn into not only six material regions. The number increases with the time steps. For example, the slope can be redrawn into 15 regions along the 6 water tables at the sixth time step (In Fig. 6, the slope is divided into 15 regions by 6 water tables.).

Conclusions

Taking the Xiazanri slope on the Jinsha River as an example, this study proposes a systematic method to compute the factor of safety of the reservoir slope considering the change of mechanical parameters due to water immersing. In-situ horizontal push-shear tests were conducted to obtain the mechanical parameters of the slope materials under natural condition and immersed for different time. Furthermore, the material regions in the numerical model built for stability computation were redrawn along the water tables obtained through seepage modeling. The changing curves of the factors of safety both considering and not considering the parameter reductions were obtained. The comparison indicates the changing laws of two factors are the same. They both decrease first and increase afterwards, while the times of inflexion points are different and the value of the former is much smaller than that of the latter. This means that considering the change of mechanical parameters of slope materials due to water immersing in the stability analysis of the reservoir slope is necessary.

References

- Huang B, Xu M (2005) Analyses of typical landslides in xiangxi river valley affected by impounding. *J Disaster Prev Mitig Eng* 26 (3):290–295
- Kunming Hydropower Investigation, Design and Research Institute (2007) Report on the Xiazanri large-scale accumulation body's stability study in dam site of liyuan waterpower station on Jinsha River during possibility study, 2007
- Liao H, Sheng Q, Gao S, Xu Z (2005) Influence of drawdown of reservoir water level on landslide stability. *Chin J Rock Mech Eng* 24(19):3454–3458
- Liao H, Gao S, Sheng Q, Xu Z (2006) Influence of permeability coefficient and reservoir water level variation on slope stability. *J Xi'an Jiaotong Univ* 40(1):88–92
- Lin Z (1994) Geotechnical testing and monitoring manual. Liaoning Science and Technology Publishing House, Shenyang, pp 521–522

- Liu X, Xia Y, Lian C, Zhang K (2005a) Research on method of landslide stability valuation during sudden drawdown of reservoir level. *Rock Soil Mech* 26(9):1427–1431
- Liu X, Xia Y, Zhang X, Guo R (2005b) Effects of drawdown of reservoir water level on landslide stability. *Chin J Rock Mech Eng* 24(8):1439–1444
- Peng M, Liu D (2000) Investigation on micro-mechanism for damage of contaminated soil by landslide. *Undergr Space* 20(3):259–263
- Qiao J, Luo X, Zhang L, Wang Z (2005) Study of some deposit slope's stability affected by water of three gorges reservoir. *J China Three Gorges Univ (Nat Sci)* 27(6):490–493
- Xu Z, Huang R, Yang L (2004) Some problems on chemical water-rock interaction in slopes. *Chin J Rock Mech Eng* 23(16):2778–2787
- Zhu D, Ren G, Nie D, Ge X (2002) Effecting and forecasting of landslide stability with the change with reservoir water level. *Hydrogeol Eng Geol* 3:6–9



Field Identification and Characteristics of the Ancient Shuangjiaping Translational Landslide

Zhao Yong, Xu Mo, Guo Jian, Kang Xiaobing, and Song Ci

Abstract

There are a lot of landslide bodies along the Dadu River, which could pose a threat to hydropower schemes and towns in mountain areas. Shuangjiaping ancient translational landslide is one of the classic cases. Since August 2010, after the Pubugou hydropower station reservoir impoundment, the ground and houses underwent deformation in the western part of accumulation body. The investigation showed that the deformation area is a part of an ancient landslide. Boundary conditions and deposits characteristics of landslide could be divided into four zones. It is concluded that the mechanism of this ancient landslide includes the of translational sliding, stopping and hanging in the air, air capturing, avalanche accumulating. At last, the means and evidences, how to distinguish this ancient landslide deposits in the field, are presented.

Keywords

Dadu river • Landslide accumulation body • Accumulation characteristics • Ancient translational landslide • Field identification

Introduction

Dadu River is an important tributary of Yangtze River and also an important hydropower base in China (Fu 2013). According to the investigation, a lot of landslides are distributed along the Dadu River (Wu 2013). These landslide deposits pose a threat to hydraulic schemes and towns. Therefore, it is important to carry out the work of identification, accumulation characteristics, and stability assessment of these landslide deposits.

These landslide deposits vary in size, formation mechanism, ages. Among them, some are giant ones owing to ancient earthquakes (Wu 2013) and some transformed from translational landslides induced by heavy rainfall. Translational landslides occur mainly in the interbedding sandstone and mudstone with gentle dip angle. This type of landslides is widely distributed in Sichuan basin and Three Gorges area, in where the Red Bed, red-colored clastic sedimentary deposits in the Mesozoic and Cenozoic era, is commonly spread, but seldom reported in other countries. There are some classic cases of this type, for instance, the abundant landslides occurred in the red bed area of eastern Sichuan basin after rainstorm in 1981 (Wang et al. 1982), a number of landslides located in Three Gorges area, such as Wanzhou landslide groups in Chongqing (Wu and Li 1994) and Zigui landslide (Dai et al. 2004). Tiantaixiang landslide, occurred in Xuanhan county of Sichuan on September 5, 2004, is a typical giant translational landslide, with strong destructive effect (Fan et al. 2008, 2009).

Z. Yong • X. Mo (✉) • G. Jian • K. Xiaobing • S. Ci
State Key Laboratory of Geohazards Prevention and Geoenvironment
Protection, Chengdu University of Technology, Chengdu 610059,
Sichuan, China
e-mail: xm@cdut.edu.cn

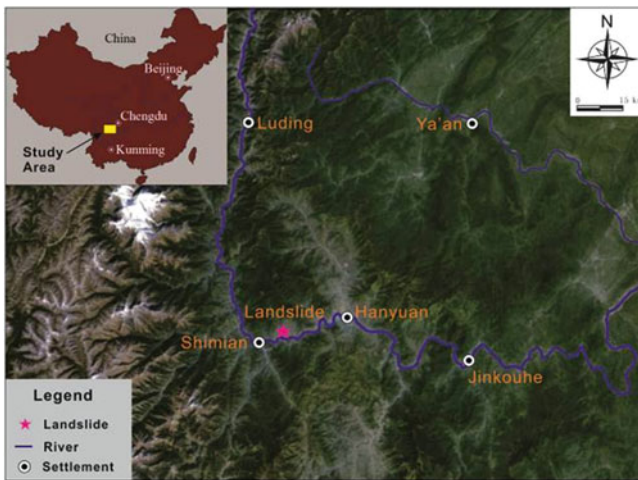


Fig. 1 Landslide location map

Location and Geological Setting

Location

Shuangjiaping landslide accumulation is located in Yingzheng village of Shimian county, on the left bank of the Dadu River, 10 km downstream from the urban area of Shimian County (Fig. 1). It is convenient to arrive the landslide area by the national road G108, passes in the middle of the landslide, and the expressway of Ya'an to Xichang, which is on the other side of the Dadu River.

Geological Setting

Shuangjiaping landslide is in the transitional zone of Western Sichuan Plateau and Sichuan basin. This area is middle-alpine gorge, steep slope on both banks and exposed bedrock. The strike of the mountains in the area is NE-SW, which northern part is generally higher than the southern one. The highest point is the peak of Liangtai mountain, 1,287 m, and the lowest is the regular water level of Pubugou reservoir, 850 m.

The landslide area belongs to the upper yangtze platform, located at the north part of the Sichuan-Yunnan meridional structural belt in the southeastern margin of the Tibetan Plateau. The Baiguowan group of Triassic system (T3bg) is widely exposed in landslide area, mainly composed of gray sandstone and argillaceous siltstone, marlstone with shale and gypsum bands. The strata are thick and with strike and dip $N70^{\circ}E/SE\angle 5^{\circ}-10^{\circ}$, two groups of vertical joints widely spread. The Quaternary system includes the residual colluvial deposit (Qcol + dl), landslide accumulation (Qdel) and pluvial deposit (Qal + pl).

Boundary and Accumulation Feature

Boundary

The Shuangjiaping landslide is an ancient translational landslide, having experienced the process of being push out, gravity bending failure, collapse and accumulation.

The front edge is up to the water level of Dadu River, the brick platform—big tension gully is the trailing edge, the west boundary is up to the intact bedrock and the east is a little gully. In a whole, this landslide accumulation is irregular and about 1,050 m long, 750 m wide (Fig. 2) It is about $50.4 \times 10^4 \text{ m}^2$ in area and $956 \times 10^4 \text{ m}^3$ in volume. The elevation of front edge is about 840 m and 1,060 m at the trailing edge.

Shuangjiaping landslide could be divided into four zones—A, B, C and D, in terms of geomorphology and structure of material, as showed in Fig. 2.

Accumulation Feature

Zone A

Zone A is in the upstream side of the landslide and is a low-lying depression, northward. The elevation of the front edge is about 840 m (covered in the water) and its trailing edge is 990 m, the height difference is 150 m. Zone A is about 550 m long, and 350 m wide It is about $20.3 \times 10^4 \text{ m}^2$ in area, $324.8 \times 10^4 \text{ m}^3$ in volume and the accumulation is 16 m thick on an average. Its western border is coincident with the ancient landslide and the eastern border is at the junction of Shuangjiaping village and the platform of brick factory, which is located in the central of this ancient landslide. The rear boundary is the upside platform of brick factory which is coincident with the trailing edge of the landslide and the front edge reaches to the water level. Cross-section of the zone A is shown on Fig. 3.

As for the material structure, zone A is composed of loose sediments with uneven thickness of 20–30 m. Because of the excavation, the thickness near the G108 is 10–15 m (see Fig. 3). Site survey and drilling reveals that the accumulation body is a thin layer of the gravels, breccia particles, sand. The landslide deposits in the middle mainly are composed of large stone, 1–3 m in diameter (Fig. 4) and there is gravelly soil among them. The lower part is composed of grayish yellow silty clay with 20–30 % gravels which are commonly angular to subangular and 2–7 cm in diameter. The lithology of the deposit is yellow gray sandstone and argillaceous stone. No sliding surface has been revealed by drilling.

The slope deformation caused by the water storage of Pubugou reservoir is concentrated in the zone A mainly,

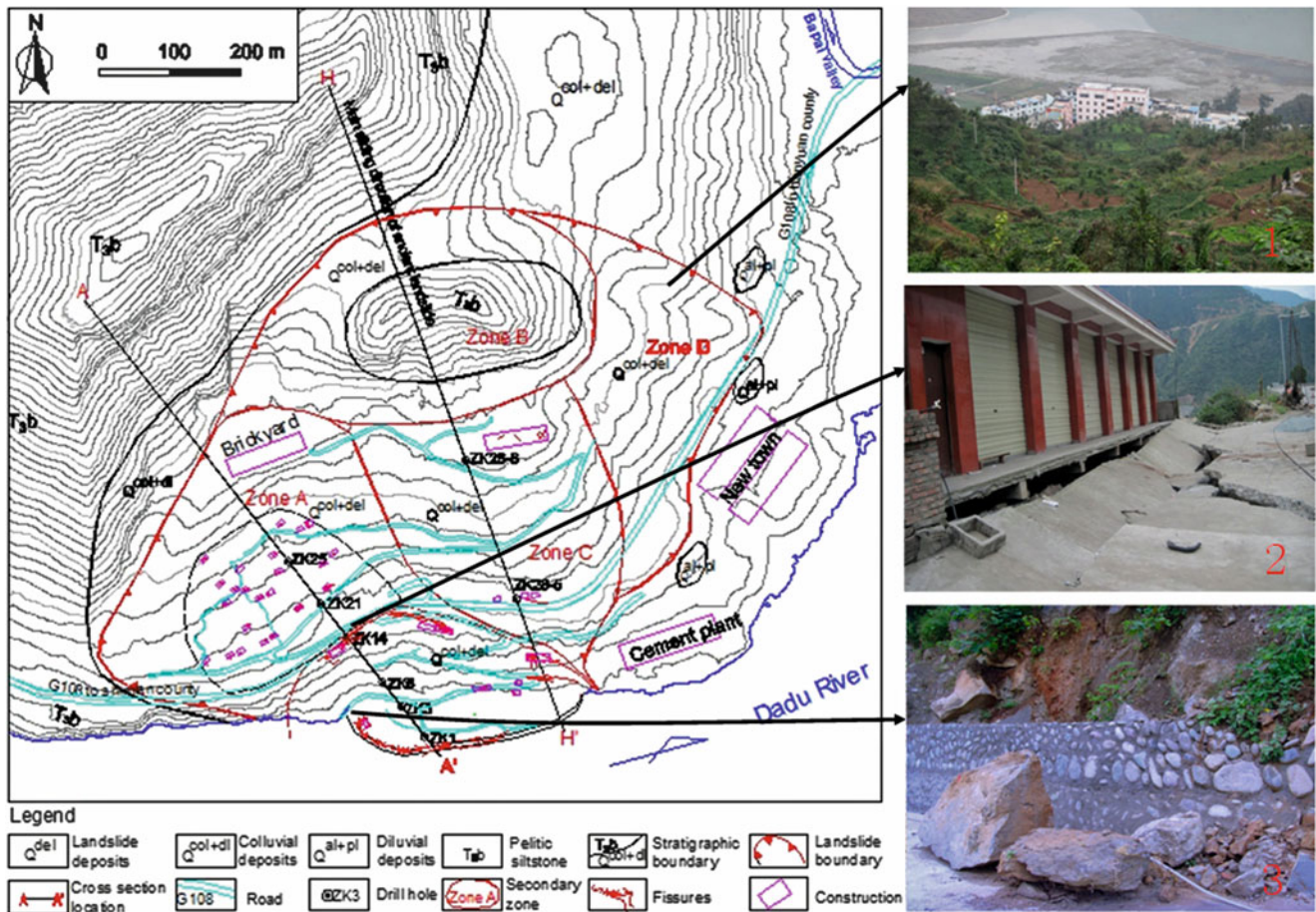


Fig. 2 The Shuangjiaping landslide accumulation (1) Little gully, eastern boundary of accumulation; (2) Tilted buildings and subsidence of ground surface; (3) Giant rocky blocks in the front edge of zone A

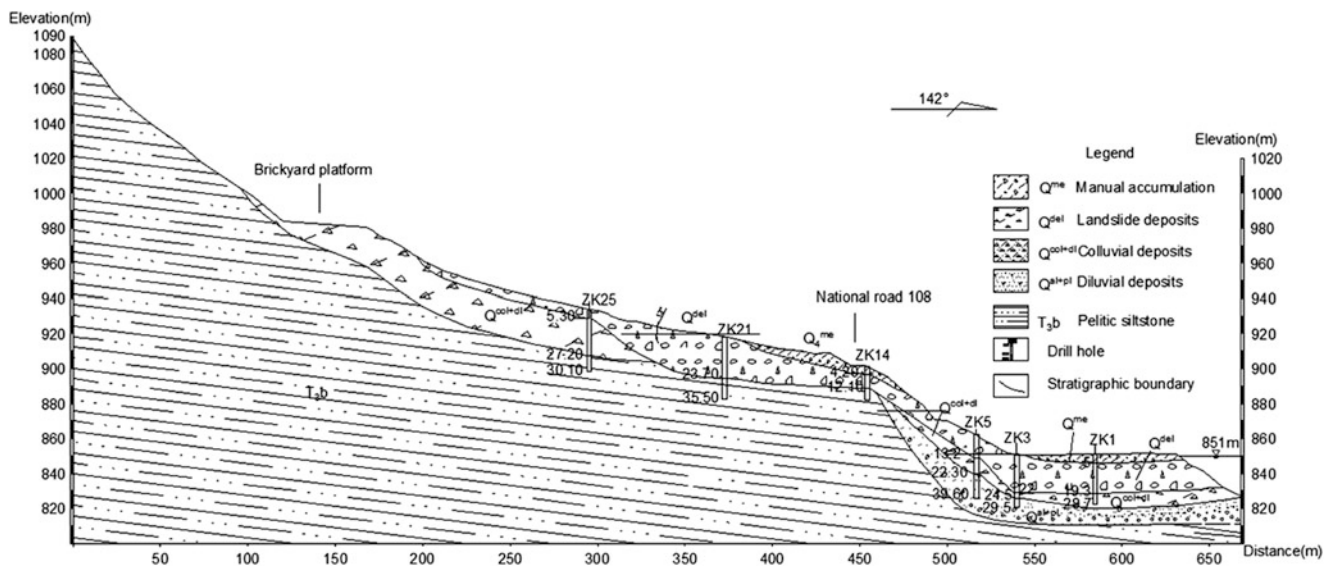


Fig. 3 Profile of zone A. A thin layer of particulate particles is on the top and the medium is a layer containing abundant giant rock

especially below the National road G108 and the neighboring houses. Subsidence and many long and large fissures appear on the road surface, the buildings are tilted.

On the whole, the distribution of the cracks present the trend of forming a trap type, boundary of a new landslide.



Fig. 4 Giant rock is exposed at the front part of zone A, next to a water channel

Zone B

Zone B is at the northern part of this landslide body, mainly including the displaced block, which is a isolate bar-type hill, like a lying peanut with long axis EW. Zone B is about 500 m long, 300 m wide. It is about $12 \times 104 \text{ m}^2$ in area and $216 \times 104 \text{ m}^3$ in volume.

The block retains the original order of stratum as “fake bedrock”, with gentle angles and an attitude of $N70^\circ E/SE \angle 5^\circ - 10^\circ$, which is same with the parent rock mass. There are two groups of weathering joints in the “fake bedrock”, with the attitude $N83^\circ W/SW \angle 85^\circ - 90^\circ$, $N3^\circ W/NE \angle 89^\circ$ respectively.

A thick layer of residual deposit is around the “fake bedrock”. The U -shape elongated depression in the trailing edge, about 70–90 m wide, and the middle part is higher than the both ends. 80 % of it is filled with residual deposit, 60–70 m thick approximately. The residual deposit is mainly composed of silty clay, angular stoned and a few granule particles (Fig. 5).

Zone C

Zone C is in the front of zone B, in the middle of the accumulation, which is a bulge ridge like a shield. Zone C is about 400 m long, 320 m wide. It is about $10 \times 104 \text{ m}^2$ in area and $300 \times 104 \text{ m}^3$ in volume.

According to drilling, the thickness of accumulation in this zone is about 30–60 m. The material structure is as same as zone A, mainly composed of giant block, which could reach several meters in diameter, and some largest blocks even keeps the original order (Figs. 6 and 7).

Found by exploration drilling and field investigation, there is a thick layer of sand under the frontier of zone C (Fig. 7), which means that the landslide buried the terrace. This terrace is the second one, about 20 m higher than the

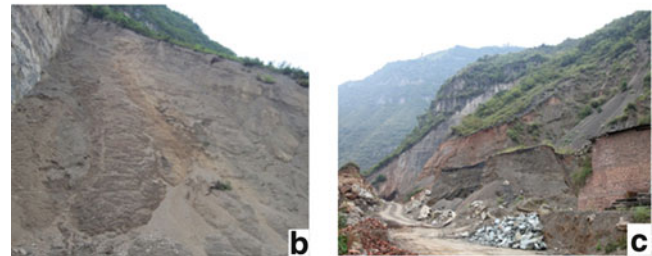


Fig. 5 Fake bedrock and residual deposit around. (a) Western part of zone B; (b) Residual deposits in tension gully; (c) Residual deposit in southern side of the fake bedrock



Fig. 6 Deposits of the zone C. (a) Big blocks at inner side national road G108; (b) Giant block, retaining the original bedding

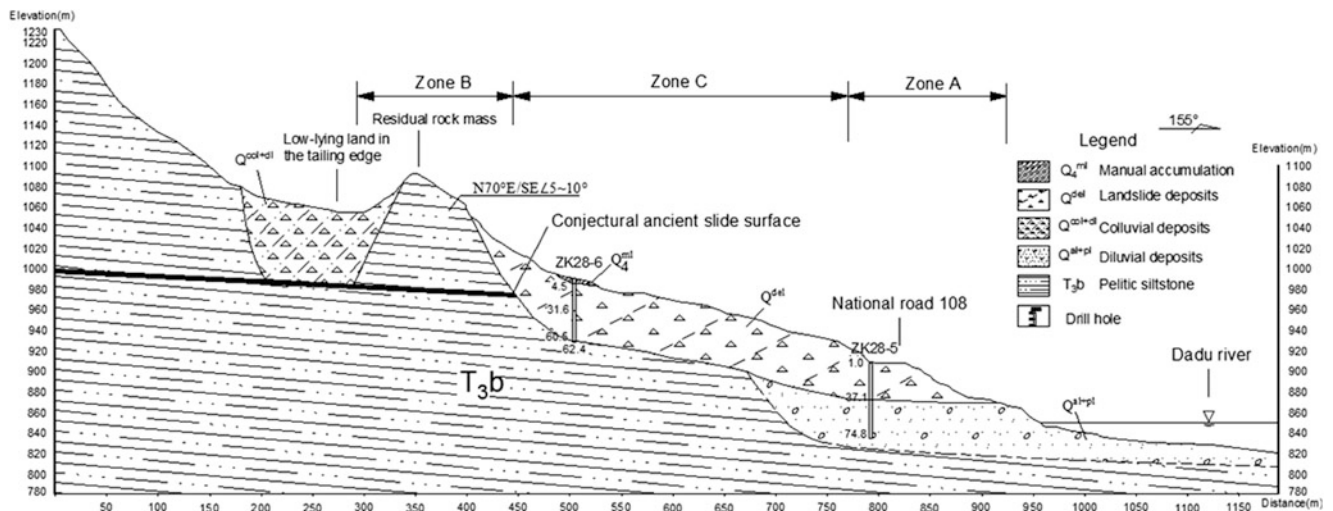


Fig. 7 Principal section of this accumulation. The direction is 156° that is estimated as the main sliding direction of ancient translational landslide

water level. No deformations occurred in zone C after the impoundment of Pubugou reservoir.

Zone D

Zone D is in the eastern part of the accumulation with irregular shape, which is about 360 m long, 280 m wide. It is about $8.2 \times 10^4 \text{ m}^2$ in area and $115.2 \times 10^4 \text{ m}^3$ in volume.

The deposits in this zone are thin, composed of shattered material mainly, without big blocks. The east boundary of zone D, as well as of the whole accumulation, is a little gully.



Fig. 8 Aerial image of landslide area, the gentle topography of landslide area and isolate rock mass in Zone B are both clearly classified

Identification Evidences

Shuangjiaping landslide has a long history and has experienced long-term geological transformation, so that many landslide features have disappeared and the original landform has changed a lot, with high vegetation coverage, which has brought much difficulty in landslide identification. However, there are still some evidences followed to identify this ancient landslide.

1. Saltation of topography

This landslide is located on the left bank of Dadu river, the upstream side of which is steep slope and majestic mountain. Contrarily, the topography becomes gently immediately in the landslide area, with a slope angle 10° – 20° , becoming a settlement of local resident, which is showed in the Fig. 8. The saltation of topography, like above, occurred in alpine gorge region, which is often

caused by landslide and will be the first evidence of landslide identification in field investigation.

In field investigation, the most attention is attracted by the isolate and bar-type rock mass in Zone B. Its existence makes the landslide area sharply different with the mountains around, easily recognized. And the big tension gully, negative relief, between the isolate rock mass and the parent rock mass, is also one of important evidences of landslide classification, showed in Fig. 9.

2. Saltation of characteristic of material structure

As mentioned previously, there are abundant giant blocks in the landslide accumulation and some even maintain the original order of stratum. This unit is overlaid by a thin layer of crushed material, composed of rubbles, angular



Fig. 9 The topography of eastern part of ancient landslide, the isolate and bar-type rock mass and the big tension gully could be seen clearly

stones and sand. On contrary, only lays a thin layer of particulate matter described above that is typical slope wash on the surface of outer area of west part of this landslide. Meanwhile, there is integrated bedrock exposure next to the eastern part of this landslide, with few slope wash. It is thus clear that the characteristic of material is widely different with surroundings, which is a strong evidence for identifying the ancient landslide as well.

Found by exploration drilling and field investigation, there is a thick layer of alluvial deposit under the landslide accumulation with obvious dual structure, which demonstrates that the landslide moved on the terrace.

3. Kinematic characteristic

According to the residential “fake bedrock” in Zone B and the giant block that retains the original order of stratum in Zone C, this ancient landslide accumulation is formed after a slide with short distance and low speed and accumulates in situ. And the giant rocks, keeping the original order of stratum in zone C, demonstrated that this landslide experienced gravity bending failure, collapse

and accumulation after being pushed out and did not move too far because of the gentle slope.

Conclusion

1. Shuangjiaping landslide could be divided into A, B, C and D four zones, in terms of geomorphology and structure of material.
2. Zone A and zone C are the main accumulation area, mainly composed of giant rock. Zone B is area of residential rock mass, in which the stratum retain the original order. Zone D is area of particulate matter. The characteristic of accumulation body is controlled by the original topography.
3. Shuangjiaping landslide accumulation is an ancient translational landslide, which have experienced the process of being push out, gravity bending failure, collapse and accumulation, etc.
4. The saltation of topography, saltation of material structure and kinematic characteristic are all could be the evidences of ancient landslide classification in field investigation.

References

- Dai FC, Deng JH, Tham LG et al (2004) A large landslide in Zigui County, Three Gorges area. *Can Geotech J* 41:1233–1241
- Fan XM, Xu Q, Zhang ZY et al (2008) Study on genetic mechanism of translational landslide. *Chin J Rock Mech Eng* 27(2):3753–3761
- Fan XM, Xu Q, Zhang ZY et al (2009) The genetic mechanism of a translational landslide. *Bull Eng Geol Environ* 68(2):231–244
- Fu XY (2013) Discussion of the leading role of hydropower exploration in Dadu River. *Sichuan Water Power* 32(1):88–95
- Wang LS, Li YG, Zhan Z (1982) The characteristics of the rock landslides of Sichuan basin in 1981. *Discov Nat* (1):41–45
- Wu JF (2013) Research on development characteristics and genetic mechanism of the seismic landslides in Daduhe River. Ph.D., Chengdu University of Technology, Chengdu, China
- Wu SM, Li YG (1994) Study on numerical simulation of landslide groups in Wanxian County. *Hydrogeol Eng Geol* 6:14–17



Field Monitoring and Stabilization Analysis of Landslide: A Case Study

Tingkai Nian, Dongchen Li, Kai Liu, Haiyang Xu, and Yanjun Zhang

Abstract

A series of geological surveys and explorations were performed to investigate the Daxishan reservoir landslide, which is the largest landslide in northeastern China. 16 boreholes equipped with full length inclinometer tubes were drilled in the landslide to investigate the movement characteristics of the landslide. Data obtained from the inclinometers were presented and analyzed to understand the movement mechanism of the landslide. Data from the inclinometer show that multiple sliding surfaces occurred in the landslide. Also, excavation done for the construction of Lvshunzhonglu road and rock-climbing center at the slope toe, induced the reactivation of the old landslide. Rainfall and change in groundwater table accelerated the sliding movement. Based on this comprehensive analysis, a row of piles is proposed to stabilize the landslide, and FEM, based on strength reduction technique is implemented to evaluate the whole stability of the stabilized landslide. Numerical results indicated that pile reinforcement scheme can improve the stability of the slope effectively.

Keywords

Landslide • Slope stability • Monitoring • Pile reinforcement • Sliding mechanism

T. Nian (✉)

State Key Laboratory of Coastal and Offshore Engineering, School of Civil Engineering, Dalian University of Technology, Dalian 116024, China

Key Laboratory of Marine Hydrocarbon Resources and Environmental Geology, Ministry of Land and Resources, Qingdao 266071, China
e-mail: tknian@dlut.edu.cn

D. Li

School of Civil Engineering, Dalian University of Technology, No. 2 Linggong Road, Dalian 116024, China

Central Southern China Electric Power Design Institute (CSEPD), Wuhan 430071, China
e-mail: lidongchen1987@163.com

K. Liu • Y. Zhang

School of Civil Engineering, Dalian University of Technology, No. 2 Linggong Road, Dalian 116024, China
e-mail: kliu@mail.dlut.edu.cn; zhangyanjun@mail.dlut.edu.cn

H. Xu

Shenzhen YJY Building Technology Co. Ltd., Shenzhen 518054, China
e-mail: xuhaiyangsailing@sohu.com

Introduction

Among all geological disasters, landslides, being second to earthquake, cause huge damage to lives and properties. In China over 2/3 areas are covered by mountains, which leads to a high frequency and large volume of landslides. Since 1980, many large-scale landslides came alive again, which led to more and more geological disasters, causing loss of more than five billion US dollars from economic statistics (Zheng et al. 2010). In recent decades, rapid development of economy, great increase in population and quick progress of urbanization makes more demand for land use. More and larger slopes are constructed by excavation, fill or other ways. More and more complex stability problems of slopes or landslides require to be solved immediately (Wang and Li 2009).

The Daxishan reservoir landslide is the largest landslide in northeastern China. Detailed information about the topography, geological formation, stratigraphy, and hydrogeological



Fig. 1 General view of Daxishan reservoir landslide

conditions of the landslide is described in this paper. Data obtained from inclinometer reading is presented and analyzed to understand the landslide movements. Anti-slide piles are proposed to reinforce the slope and the reinforcement effect is analyzed and evaluated by the shear strength reduction finite element method (Duncan 1996; Zienkiewicz et al. 1975; Griffiths and Lane 1999; Griffiths and Marquez 2007; Sainak 2004; Wei and Cheng 2009; Cai and Ugai 2000; Won et al. 2005; Kourkoulis et al. 2011).

Field Condition

General Description

The Daxishan reservoir landslide is located in the south of Liaotung Peninsula, China. Figure 1 shows its general view. The hill is heavily undulate with tectonic denudation physiognomy, and has rich vegetation resource with locally exposed rock mass. The landslide comes from the reactivation of part of an old landslide, which appeared before the Quaternary Period (Holocene). Geological survey and exploration reveals the range of the old and new landslide (Fig. 2). The longitudinal length along the sliding direction of the landslide is 415 m, from the reservoir bank to the slope shoulder. The lateral length is 275 m at the toe, 180 m in the middle and 135 m at the crest. The slope has a general inclination angle of about 35° and height of about 124 m. The thickness of the sliding mass ranges from 6 m to 38 m, with area of about $1.01 \times 10^5 \text{ m}^2$ and volume of about $3 \times 10^6 \text{ m}^3$.

The old landslide was in a relatively stable state, but it was disturbed by human activities, especially, from series of excavations, which removed much rock and soil mass at the slope toe, for the construction of the Lvshunzhonglu Road and the rock-climbing center. Then, part of the old landslide was reactivated. Since 2006, movement of the sliding mass started to accelerate, which caused great damage to the road and trestle. Figure 3 shows cracks at the toe of the slope and the surface of road. The road had to be renovated for many times. Until 2009, the landslide had caused direct economic loss of about six million US dollars. This may lead to some secondary geological disasters, like dam break of the Wangjiadian reservoir, which is a great threat to over 360 people living downstream.

Stratigraphy, Soil Properties and Hydrogeological Conditions

Drilling and sampling were performed to investigate the stratigraphy and soil properties of the landslide. Figure 2 shows the distribution of boring holes. Figure 4 and Table 1 show the distribution and properties of each stratum at the critical cross-section R2-R2'. The soil profile can be divided into three layers. The bedrock is composed of moderately weathered Quartzite and moderately-weathered Slate (Zwhg). The upper layer is composed of gravelly soil ($Q_3^{\text{al+pl}}$) with clay and 15–30 % pebbly sandstone. The middle layer is composed of silty-clay ($Q_4^{\text{al+pl}}$) with about 5 % gravel, having relatively weaker strength parameters and is regarded as a soft layer.

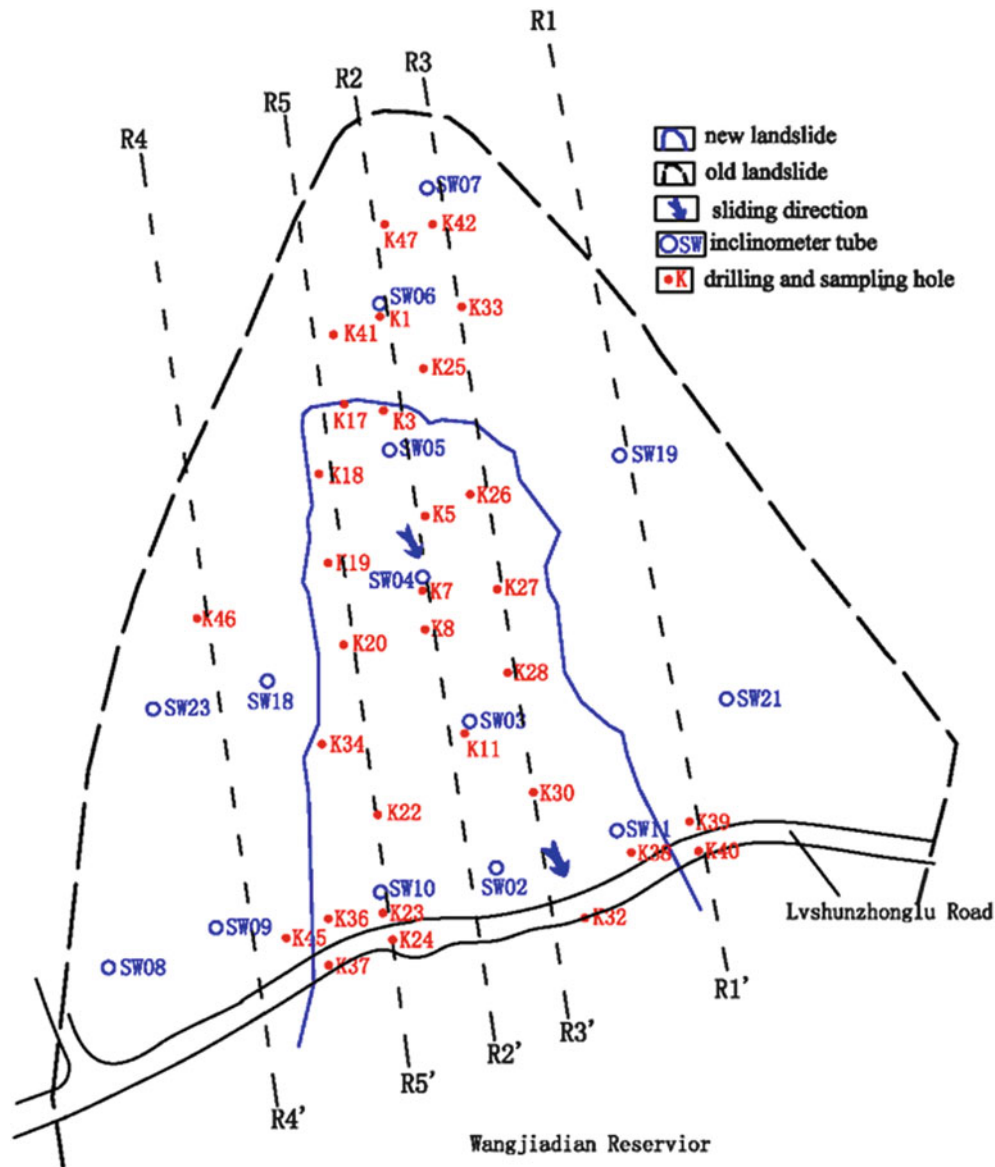


Fig. 2 Plane view of Daxishan reservoir landslide

There are two kinds of groundwater in this area: (1) pore water, mainly existing in the unconsolidated Quaternary diluvium, with depth of about 5–8 m and single-well water inflow of less than 100 m³/d. (2) Fissure water, mainly existing in cracks of weathered quartzite, and only arising during the rainy season, with flow rate of less than 2.0 m/s.

Monitoring Results from the Inclinometers

The inclinometer is an effective tool in investigating the movement depth inside the sliding mass and determining the position of the critical slip surface. 16 boreholes,

equipped with full length inclinometer tubes were drilled in the landslide at the beginning of 2010. The boreholes were distributed basically along the five longitudinal principal axes: R1R1'–R5R5' (showed in Fig. 2). The monitoring frequency is usually once a month and may increase during the rainy season or when the data from the inclinometer gives some significant clue. Figures 5, 6, and 7 show some results of three boreholes recorded from April, for data obtained from inclinometer reading was used to calibrate the monitoring equipment during the first quarter of 2010.

The accumulative horizontal displacement along the SW2 borehole tube gradually increased steadily from the bottom to 14 m depth. According to the sudden increase in

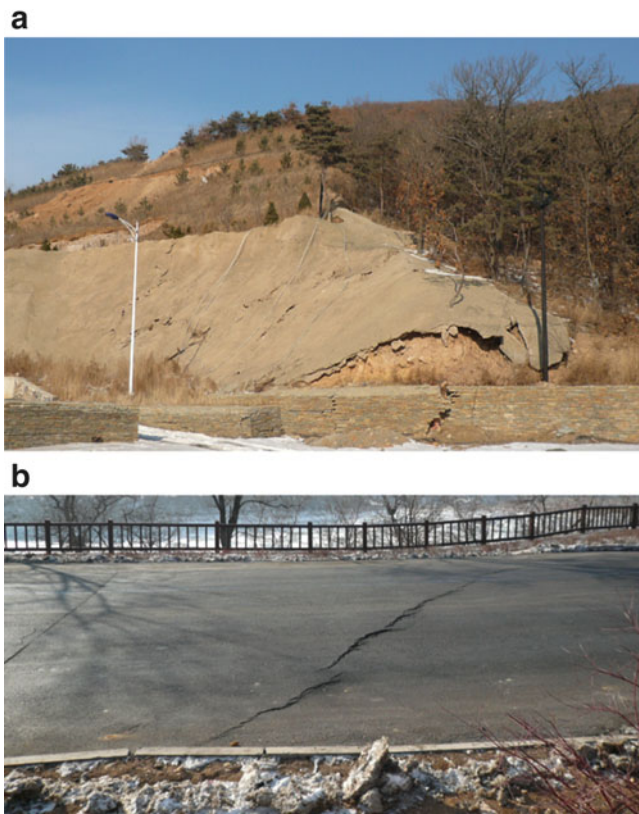


Fig. 3 Damage caused by the landslide. (a) Failure at the slope toe and (b) Crack on the surface of road

displacement at about 14 m depth, it is concluded that a shallow critical slip surface was initiated during this period. The displacement from the ground to 14 m depth showed no apparent changes and the displacement at the top of the borehole increased a lot from April to May, which suggested that the whole sliding mass above 14 m depth moved concurrently. The SW2 monitoring point is located near the toe of the new landslide (Fig. 2).

Accumulative horizontal displacement along the SW4 borehole tube presents two steps: (1) the sudden increase in displacement at 34 m depth indicated the initiation of a new critical slip surface and the concurrent moving of the whole sliding mass above 34 m depth from the middle to the end of April. The borehole tube was sheared off at the end of April. (2) Another new critical slip surface appeared at 26 m depth due to the sudden change of displacement during July and August; and the borehole tube was sheared off once more at the end of August. After August, the displacement from 26 m depth to the ground gradually increased and did not change much. It came to a relatively stable stage. The SW4 monitoring point is located near the middle of the new landslide (Fig. 2).

The accumulative horizontal displacement along the SW7 borehole tube showed a gradual growth from the bottom to the top and the overall displacement of the tube top

did not increase very fast as time went on. No apparent movement occurred at SW7 monitoring point near the shoulder of the old landslide.

Part of the old landslide reactivated and multiple sliding surfaces appeared from April to the rainy season. During this period, the sliding mass moved relatively faster, this agreed with the observed destructive condition of Lvshunzhonglu Road. The excavation done for several times, due to the construction of the road and the rock-climbing center, removed the rock and soil mass at the slope toe and induced the reactivation of the part of the old landslide. Rainfall and change of underground water accelerated the movement of the sliding mass.

Numerical Analysis of the Slope with Pile Reinforcement

A row of piles are proposed to stabilize the landslide. A numerical model, based on critical cross-section R2-R2', is established to investigate the reinforcement effect and the response of the piles. Shear strength reduction- finite element method is adopted. The soil is treated as elastic-plastic material and its strength parameters are listed in Table 1. The pile is treated as elastic material and its parameters are listed in Table 2. Normal interactive behaviour between the pile and the soil is selected as hard contact and the tangential friction coefficient is valued 0.3.

Figure 8 shows the factor of safety and critical slip surface for the stabilized slope. Clearly, the factor of safety increases about 30 % after pile installation. Without piles, the multiple sliding surfaces are presented, mainly through the soft layer (Fig. 8a).

Figure 9 shows the distribution of the displacement and moment along the pile. The part of the pile embedded in the bedrock (about 10 m) can be taken as a fixed end. So when the pile head is free, it deforms like a cantilever; when the pile head is hinged, it deforms like a beam with one fixed end and one hinged end. The peak value of the displacement and moment is far larger with free pile head than those with hinged pile head. The FOS is very close to each other with free or hinged pile head when the elastic modulus of pile is much larger than that of soil, but the restraint of the pile head can decrease the response of the pile effectively (Cai and Ugai 2000; Won et al. 2005).

Figure 10 shows the distribution of soil pressure along the pile. The distribution of soil pressure above the soft layer with 2 different pile heads (free and hinged) is nearly the same. As we know, the resistance provided by the pile and the soil pressure is a pair of interactive force, and the potential sliding mass is above the soft layer. So, the resistance provided to potential sliding mass by the pile with two different pile heads (free and hinged) is nearly the same,

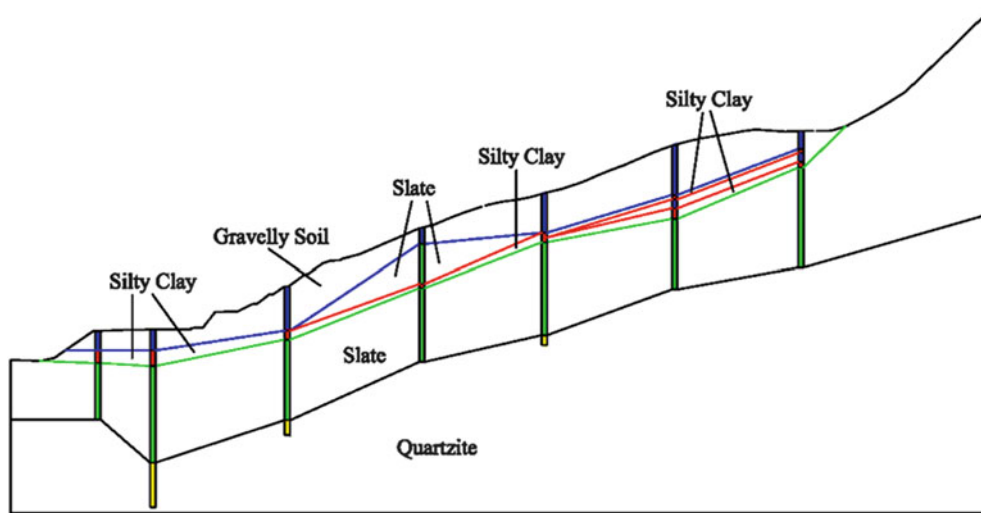


Fig. 4 Cross-sectional view of R2-R2' profile

Table 1 Soil and rock properties of each stratum

Soil type	Unit weight (kN/m ³)	Cohesion (kPa)	Friction angle (°)	Young's modulus (MPa)	Poisson's ratio
Gravelly soil	20.2	22.6	28.5	100	0.30
Silty clay	19.0	22.0	18.0	100	0.30
Moderately-weathered slate and Quartzite	26.0	100.0	60.0	900	0.25

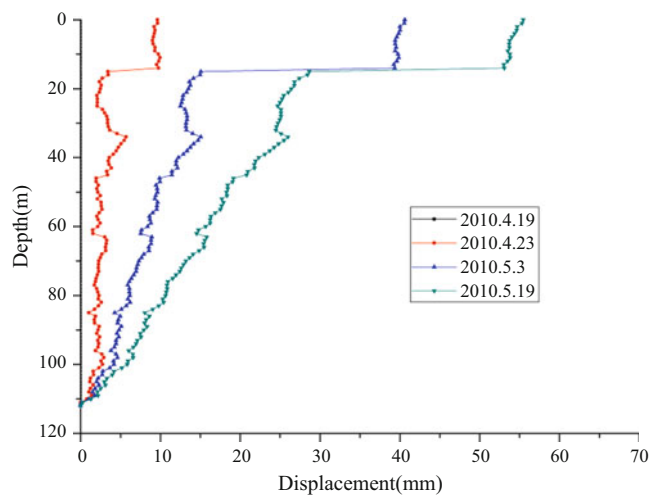


Fig. 5 Accumulative horizontal displ. of SW2 borehole

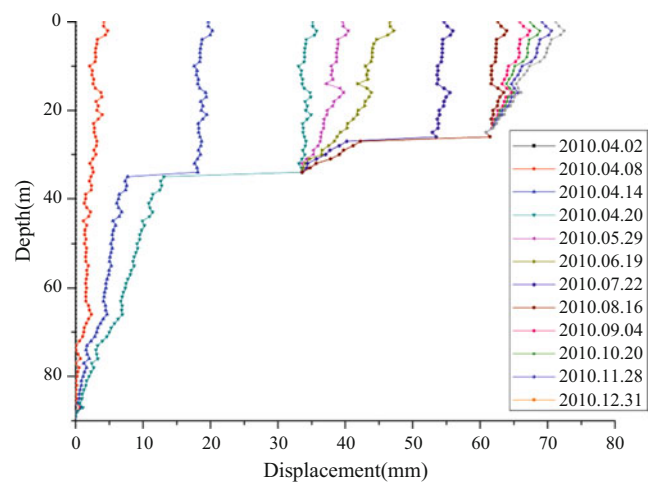


Fig. 6 Accumulative horizontal displ. of SW4 borehole

which explains why the FOS with two different pile heads are close to each other. The distribution of soil pressure below the soft layer (or inside the bedrock) with two different pile heads (free and hinged) vary greatly. The thrust force coming from the potential sliding mass has to be transferred to the bedrock through the pile when the pile head is free. While the thrust can be partly transferred to the structure used to restrain the pile head (anchor, as an example) when the pile head is restrained.

Conclusions

Geological investigation was performed to obtain information about the Daxishan reservoir landslide. The movement deep inside the landslide was obtained, based on monitoring data obtained from 16 inclinometer tubes. A numerical model based on SSR-FEM was used to analyze the effectiveness of pile reinforcement and response of the pile. The following conclusions were drawn:

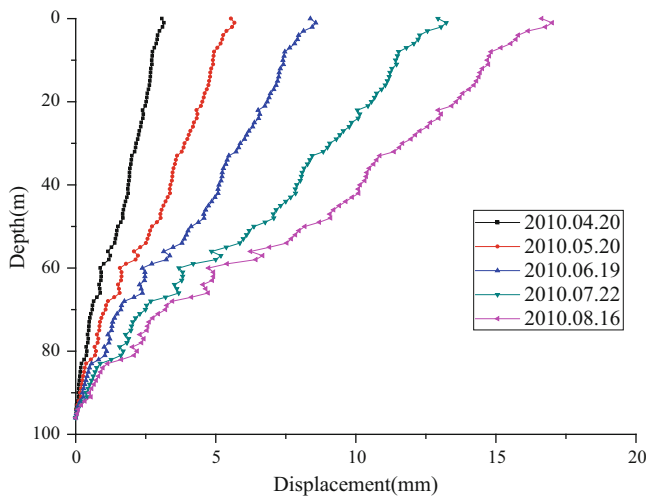


Fig. 7 Accumulative horizontal displ. of SW7 borehole

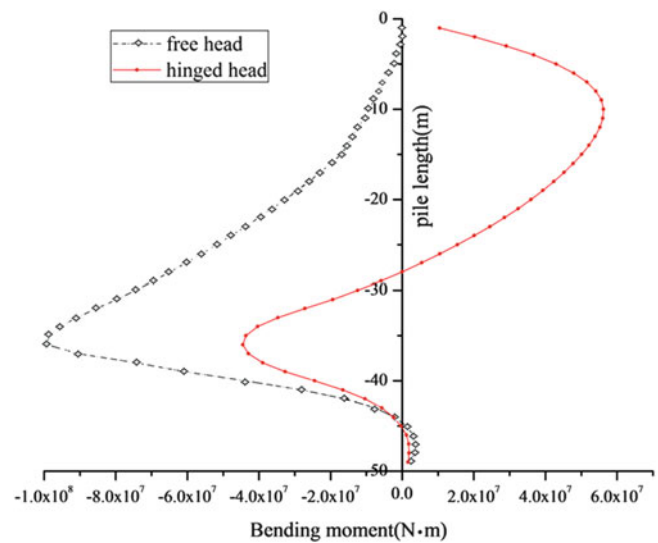


Fig. 9 Distribution of moment along the pile depth

Table 2 Parameters of the pile

Material	Unit weight (kN/m ³)	Diameter (m)	Spacing (m)	Length (m)	Young's modulus (MPa)	Poisson's ratio
Pile	24.0	4.0	10.0	50.0	100	0.2

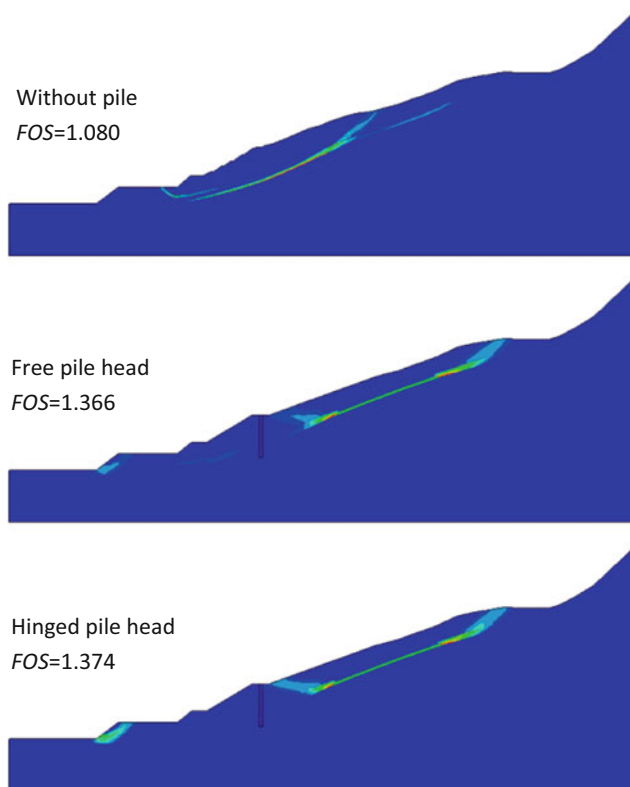


Fig. 8 Factor of safety and critical slip surface for slope

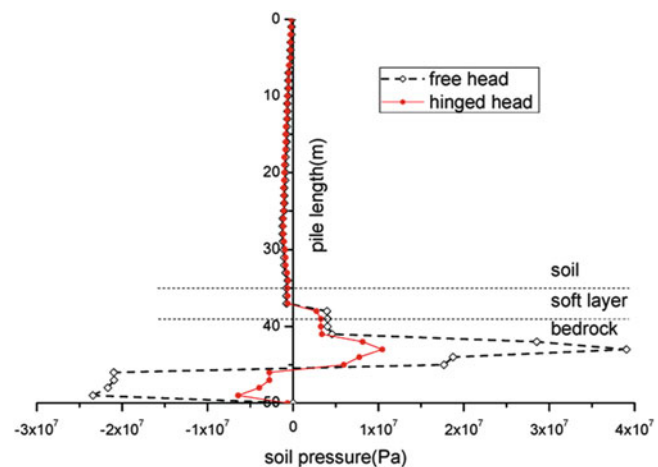


Fig. 10 The distribution of soil pressure along the pile

1. The excavation removed much rock and soil mass at the slope toe and induced the partial reactivation of the old landslide.
2. Multiple sliding surfaces arose in April and increased during the rainy season of 2010. Rainfall and the change of groundwater table accelerated the movement of the sliding mass.
3. The piles installed in the middle to lower part of the slope improved the stability of the slope effectively.

Acknowledgments The authors wish to acknowledge the support of the National Science Foundation of China (No.51179022), the Fundamental Research Funds for Central Universities (DUT12LK19) and Open Research Fund of Key Laboratory of Marine Hydrocarbon Resources and Environmental Geology (No.MRE201304), Ministry of Land and Resources.

References

- Cai F, Ugai K (2000) Numerical analysis of the stability of a slope reinforced with piles. *Soils Found* 40(1):73–84
- Duncan JM (1996) State of the art: limit equilibrium and finite element analysis of slopes. *J Geotech Eng* 122(7):577–596
- Griffiths DV, Lane PA (1999) Slope stability analysis by finite elements. *Geotechnique* 49(3):387–403
- Griffiths DV, Marquez RM (2007) Three-dimensional slope stability analysis by elasto-plastic finite elements. *Geotechnique* 57(6):537–546
- Kourkoulis R, Gelagoti F, Anastasopoulos I (2011) Slope stabilizing piles and pile-groups: parametric study and design insights. *J Geotech Geoenviron* 137(7):663–677
- Sainak AN (2004) Application of three-dimensional FEM in parametric and geometric studies of slope stability. In: Jardine RJ, Potts DM, Higgins KG (eds) *Advances in geotechnical engineering*, vol 2 (Skempton conference). Thomas Telford, London, pp 933–942
- Wang FW, Li TL (2009) *Landslides disaster mitigation in Three Gorges Reservoir, China*. Springer, Berlin
- Wei WB, Cheng YM (2009) Strength reduction analysis for slope reinforced with one row of piles. *Comput Geotech* 36(7):1176–1185
- Won J, You K, Jeong S (2005) Coupled effects in stability analysis of pile-slope systems. *Comput Geotech* 32(8):304–315
- Zheng YR, Chen ZY, Wang GX (2010) *Slope and engineering management of landslide*, 2nd edn. People's Communication Press, Beijing
- Zienkiewicz OC, Humpheson C, Lewis RW (1975) Associated and non-associated visco-plasticity and plasticity in soil mechanics. *Geotechnique* 25(4):671–689



Preliminary Global Catalogue of Displacement Waves from Subaerial Landslides

Nicholas J. Roberts, Robin McKillop, Reginald L. Hermanns, John J. Clague, and Thierry Oppikofer

Abstract

Displacement waves generated by subaerial landslides can have devastating effects and extend impacts of a landslide tens of kilometres or more. Most research has involved characterization of individual events and, in some cases, comparison of a few events. We have begun to broaden understanding of the phenomenon by compiling a preliminary global catalogue of landslide-generated displacement waves that provides insights into their geographic distribution, size, frequency, and range of mechanisms and impacts. The catalogue is based on a review of published case studies, tsunami catalogues, and the Norwegian national landslide database. It contains 254 events from the fourteenth century AD to 2012. Greater event density in regions with longer written histories, in areas with more settlement, and in the more recent part of the record suggests spatial and temporal biases in documentation and recording. Despite these biases, the spatial pattern of events suggests settings—likely determined by geologic, physiographic and tectonic controls—with elevated hazards that can help focus hazard investigation and mitigation. The diversity of events helps identify differences in displacement wave processes and their resulting impacts, such as wave run-up and travel distance.

Keywords

Landslide-generated displacement wave • Landslide tsunami • Global database • Coastal landslide hazard • Secondary effects of landslides

Introduction

Rapid entry of landslides into water bodies transfers energy that is subsequently dissipated through displacement waves (Hermanns et al. 2013). Depending on the size of the

landslide relative to the water body, the displacement wave may have the form of a frontal push wave or a more tsunami-like body wave (de Blasio 2011). These displacement waves can be an important element of risk from landslides in some areas, yet they remain poorly documented and understood.

A small number of well studied events demonstrates the potential devastating impacts of displacement waves generated by subaerial landslides (Fig. 1). Near-field run-up can be many times higher than that produced by seismogenic tsunamis, and can reach many hundreds of metres in exceptional circumstances (e.g. Lituya Bay, Alaska; Miller 1960). The long reach of displacement waves greatly extends hazard beyond the immediate area of the landslide. For example, the displacement wave generated by the explosive eruption of Krakatau in 1883 produced run-ups of over 35 m at distances of up to 60 km (Carey et al. 2000).

N.J. Roberts (✉) • J.J. Clague
Centre for Natural Hazard Research, Simon Fraser University,
8888 University Drive, Burnaby, BC, Canada V5A 1S6,
e-mail: nickr@sfu.ca

R. McKillop
Palmer Environmental Consulting Group Inc., 475 Howe Street #1030,
Vancouver, BC, Canada V6C 2B3,

R.L. Hermanns • T. Oppikofer
Geological Survey of Norway, P.O. Box 6315 Sluppen,
Trondheim 7490, Norway



Fig. 1 Effects of select events described in the text. (a) Vegetation stripped by the 2007 Chehalis Lake displacement wave, Canada (trimline in background adjacent to landslide and across the lake on the right ranges from 18 to 30 m above lake level). (b) Vegetation stripped by the 2007 Mentirosa displacement wave in Aysén Fjord, Chile. (c) Houses destroyed by the 1936 Loen Lake displacement wave, Norway

Rockslide-generated displacement waves in 1905 and 1936 at Lake Loen, Norway, claimed 137 lives (Jørstad 1968), and over 1,900 people lost their lives when a rockslide entered the Vajont reservoir in the 1963 and produced a huge displacement wave that overtopped the dam (Genevois and Ghirotti 2005). Built infrastructure and natural resources also can be damaged by displacement waves; for example marketable timber was destroyed at Chehalis Lake, British Columbia, in 2007 (Roberts et al. 2013) and fish farms were damaged at Aysén Fjord, Chile, in 2007 (Lastras et al. 2013).

The occurrence, behaviour, and effects of landslide-generated displacement waves are studied using a variety of approaches, including field investigation, simple physical modeling, and computational modeling. However, nearly all published studies have focused on single events or include a small number of related events, and thus provide an incomplete view of the phenomenon. To provide a broader understanding of landslide-generated displacement waves, we have compiled a global catalogue of displacement waves from subaerial landslides documented in the literature, tsunami catalogues, and the Norwegian national landslide database. Our catalogue, although preliminary, is the largest collection of landslide-generated displacement wave events available and includes details of their geographic distribution, size, frequency, and range of mechanisms and impacts.

Methods

Most of the events in the catalogue were compiled from a review of about 300 published papers, book chapters, and case study reports. A small number of events have been well described in many papers and reports (e.g. Lituya Bay, 1958; Vajont, 1963). Most events, however, are documented in a single publication (e.g. Lago Cabrera, 1965; Watt et al. 2009), commonly with little detail. Systematic review of tsunami catalogues identified additional events that do not appear to be reported in the scientific literature. We identified most of these poorly documented events using the NGDC (2013) online global database of historic tsunamis, which includes a summary of printed catalogues specific to oceans or regions. For some events the NGDC database infers a landslide cause only from the local nature of disturbance and the absence of seismic or meteorological triggers; such events with no identifiable landslide source were not included in the catalogue.

The catalogue for Norway is by-far the most complete in the world. We expanded on reported Norwegian events by reviewing accounts of landslides summarized from church records (Furseth 2006) and the Norwegian national landslide inventory database, which is a catalogue of mass movements in Norway since the fourteenth century (Hermanns et al. 2012). A review of these sources added 143 events to the 13 Norwegian events found during our initial search of the scientific literature.

Locations and sizes of most source landslides are approximate. Where possible, more precise landslide locations and improved metrics (e.g. landslide run-out, height of fall) were obtained using Google Earth and, for Norwegian events, aerial photographs and maps in the Norwegian Geologic Survey's geographic information system.

Event Distribution

The catalogue contains 254 events from the fourteenth century AD to 2012 (Fig. 2). Patterns in the global distribution of documented events reflect environmental factors that influence the occurrence of landslide-generated displacement waves and biases in their recording. Additionally, the regional concentrations in Norway (156 events), the Pacific Northwest of North America (18 events), and the European Alps (12 events) likely reflect the high level of landslide research in these regions and the ready availability of pertinent documents.

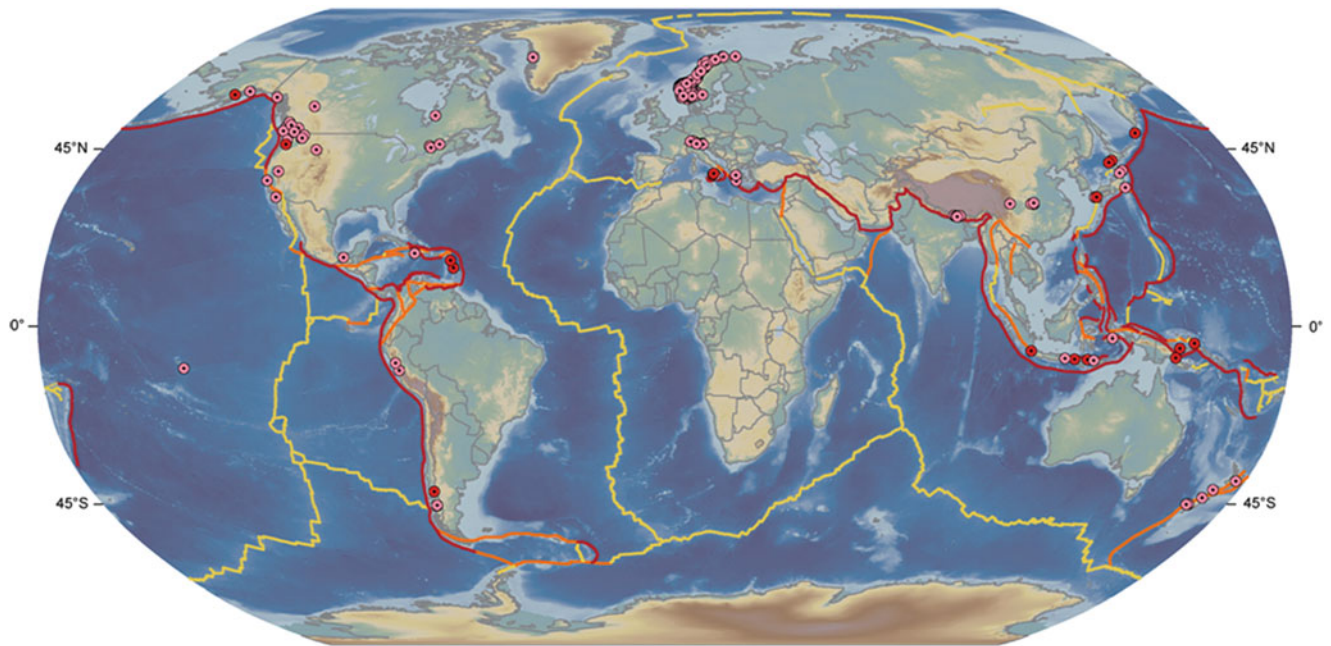


Fig. 2 Global map of landslide-generated displacement waves in the catalogue. Non-volcanic landslides are shown by pink circles; landslides from volcanoes are shown by red circles. Plate boundaries: convergent—red; divergent—yellow; and transform—orange

Reporting Bias

Biases in documentation and reporting undoubtedly influence the spatial and temporal distribution of events in the catalogue. Documentation of displacement waves in many regions is poor to nonexistent, or is in foreign-language literature that is difficult to access. Biases are manifested in high densities of reported events in regions with longer written histories and large populations (Fig. 2) such as Japan, the Mediterranean region, the European Alps, and Norway. All but one of the 53 pre-nineteenth century events are from these four areas (44 are from Norway alone). The exception is a rockslide-generated displacement wave mentioned in oral histories on the British Columbia coast that has been confirmed by an archaeological investigation and radiocarbon-dated to the mid- to late sixteenth century (Bornhold et al. 2007).

Greater event frequency in the more recent part of the record (Fig. 3a) reflects a temporal bias in event documentation and not a change in the frequency of landslide-generated waves. Details of early events are commonly sparse, and even the dates of several events prior to the mid-seventeenth century are uncertain.

Given increased reporting of events over the past century (Fig. 3a) and attendant global population growth, an upward trend in annual fatalities from landslide-generated displacement waves might be expected. The catalogue suggests, however, that a small number of random, high-fatality events dominate historic life loss from landslide-generated

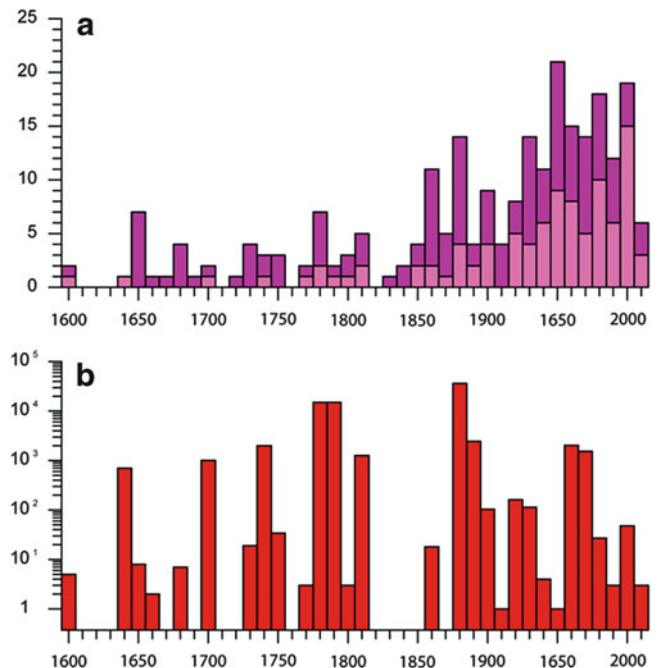


Fig. 3 Temporal distribution of landslide-generated displacement waves per decade since the seventeenth century. (a) Number of catalogued events outside Norway (pink) and in Norway (purple). (b) Total reported fatalities from events in the catalogue; all decades exceeding 100 deaths are dominated by a single high-fatality event, except the 1930s, which represents two events in Norway (Loen and Tafjord). Eight events in Norway (three in the sixteenth century, three in the eighteenth century, and two in the nineteenth century) are not included because their decades of occurrence are unknown

displacement waves (Fig. 3b). Each peak in Fig. 3b is largely or completely the result of a single disaster during a decade.

The large number of events in Norway suggests a severe under-representation in similar settings such as Western Canada and Chilean Patagonia. Similarly, the abrupt cut-off of events in the North American Cordillera at United States-Mexico border suggests underrepresentation of events in Mexico and probably Central America (Fig. 2).

Physiographic and Geological Patterns

Despite the aforementioned caveats, the spatial pattern of events highlights settings with elevated hazard. Events are most common in mountain belts, particularly at latitudes above about 45° (Fig. 2), where they typically result from rockslides, rock falls, and rock avalanches (e.g. Western Canada, western Norway, Chilean Patagonia). In these settings, recurrent Pleistocene glaciations have produced high, glacially oversteepened rock slopes that have not yet reached equilibrium. Most low-latitude (<45°) events are associated with flank collapses and large debris avalanches at active and dormant volcanoes (Fig. 2), or with failures of sea cliffs or river banks consisting of unconsolidated sediments or of poorly lithified or strongly jointed rocks. The low occurrence of non-volcanic events at low latitudes likely reflects the lack of glacial preconditioning of slopes for failure.

Many events cluster near convergent or transform plate boundaries, indicating an important role of earthquakes, volcanism, and the creation of relief through active tectonic processes. Earthquakes and volcanism are reported as triggers or major factors in, respectively, 23 and 10 events in the catalogue. Many events, however, are associated with passive plate interiors, including those in Norway. The concentration of documented events in the fjord district of western Norway is, in part, due to the high relief and steep slopes resulting from glacial erosion and glacio-isostatic uplift. Most events in areas of low relief in Central Canada and Scandinavia are associated with failures of sensitive glaciomarine clays exposed in river banks and along lakeshores.

There are concentrations of events in some areas for a variety of reasons. Valley walls inundated behind dams (e.g. Jones et al. 1961), are particularly susceptible to failure. Several events may result from a single earthquake, such as the 2007 Aysén Earthquake in Chile (Lastras et al. 2013). A single unstable slope may fail more than once, as happened at Vajont between 1960 and 1963 (Genevois and Ghirotti 2005). Repeated wave-generating slope failures have occurred in Loen Lake, Norway, with seven events between 1905 and 1950 alone, four of which produced run-ups in excess of 40 m (Hermanns et al. 2006).

Very few events have been reported from low-latitude regions far from plate boundaries, including Africa and

Australia, which are tectonically stable continents. Most African mountain ranges are ancient features with limited relief and gentle to moderate slopes; furthermore, they have not been glaciated during the Pleistocene. However, the lack of even a single historic event on these continents is most likely due to absent reporting.

Artificial Reservoirs

Artificial reservoirs are a common setting for landslide-generated displacement waves and deserve special attention. Twenty events in the global catalogue involved reservoirs. Marked fluctuations in reservoir levels can increase the possibility of landslides along their shorelines and thus displacement waves that can damage associated infrastructure and nearby settlements. Historic examples include Vajont and Lake Roosevelt in Washington State.

Reservoir failures are most common during initial filling or early operation when slopes first experience increased water content. Seven collapses of Pleistocene sediments generated displacement waves along the shores of Lake Roosevelt in the decade following its 1942 impoundment behind the Grand Coulee Dam (Jones et al. 1961), whereas only two documented waves have occurred since then, both in 2009. Two events were reported in Three Gorges Reservoir prior to the reservoir reaching its designed maximum level in 2010. Given the occurrence of several hundred additional landslides and existence of thousands of potentially unstable slopes along the shores of the 600-km long reservoir (Petley 2013), future displacement waves can be expected.

Not counting the 1963 Vajont disaster, five of the 20 reservoir events in the catalogue caused a total of 43 fatalities. Yet, in spite of the concentration of landslide-generated displacement waves at reservoirs, the majority of recent landslide-caused deaths related to dams occurred during construction and did not involve displacement waves (Petley 2013). However, large unstable reservoir slopes such as at Laxiwa Hydro-power Station, China (Zhang et al. 2013), show the potential for future, deadly and highly destructive, landslide-generated displacement waves in reservoirs. Large-scale hydroelectric reservoirs planned for coming years, particularly in the landslide-prone Himalaya region (Petley 2013), are likely to experience landslide-generated displacement waves.

Range of Impacts

Explosions of active coastal volcanoes and accompanying flank collapses and debris avalanches, such as those at Krakatau and Ritter Island in the nineteenth century, have generated the farthest reaching displacement waves. Run-ups of several tens of meters can occur farther than 75 km

from the landslide. A run-up of several meters occurred over 1,000 km from the 1741 Oshima-Oshima eruption in Japan. The four farthest reaching displacement waves in the catalogue were produced in open seas with only small landmasses and had effects over distances of 100–1,000 km. Such settings offer minimal near-field obstacles to wave propagation and provide distant shorelines for significant run-up before waves completely attenuate.

Six documented events produced maximum run-ups exceeding 100 m. All six events occurred in relatively small water bodies (narrow lakes or fjords) that were impacted by very rapid rockslides with volumes in excess of 10^7 m³. Maximum run-ups occurred on slopes directly opposite the point of entry of the landslide into the water body. All but the Spirit Lake event—triggered by the 1980 eruption of Mount St. Helens—occurred in previously glaciated, non-volcanic terrain. The 1958 Lituya Bay event had the largest run-up (524 m); the next largest is the Spirit Lake event (260 m). Two earlier events at Lituya Bay, one of which was dated by Miller (1960) from the age of a forest trimline, had maximum run-ups of 120 and 150 m. The occurrence of half the extreme run-up events in the catalogue at a single locality (Lituya Bay) suggests a site-specific role in generation of such large run-ups.

Fatal events are possible where fast-moving landslides produce high near-field run-ups in settled areas, or where particularly large landslides generate huge displacement waves that have a far-field reach. All of the four events with more than 2,000 fatalities occurred along populated coasts in Indonesia and Japan during the eighteenth and nineteenth centuries. These four events involved high-velocity rockslides and debris avalanches. Three of the four had volumes in the range of 10^8 – 10^9 m³; the fourth event lacks a reported volume, but occurred in conjunction with an earthquake-generated tsunami, which may account for the large number of fatalities. Four other events claimed between 1,000 and 2,000 lives. One each occurred along sea coasts of Indonesia, Italy, and Japan during the eighteenth and nineteenth centuries; the fourth was the 1963 Vajont catastrophe. Reliable characterization of economic impacts is currently not possible because of the dearth of information on losses. Long-term and less tangible secondary impacts are almost completely lacking.

The geomorphic signature of landslide-generated displacement waves is important in the recognition and characterization of past events, but has not been systematically studied. Most details of geomorphic impacts are from detailed descriptions of a small number of events (e.g. Lituya Bay, Miller 1960; Lago Cabrera, Watt et al. 2009; Chehalis Lake, Roberts et al. 2013). For most events, geomorphic features are mentioned briefly, or not at all. Most geomorphic features produced by landslide-generated displacement waves are similar to those produced by tsunamis

triggered by earthquakes and submarine landslides (Dawson 1994), although they are more localized and vary more with distance. Features include erosional scarps in soil, stripping of vegetation, rafting of vegetation and construction material, nearshore traction and rotation of boulders, sedimentary bedforms, fine sediment and organic debris deposits near the limit of wave run-up, and erosional backwash channels. Such features provide insight into wave run-up, direction, velocity, and depth, and thereby aid in analyzing hazards from future events and in calibration of numerical and physical models.

Conclusions

Although in a preliminary state, our catalogue aids in the global characterization of landslide-generated displacement waves and provides important insights into preconditions and possible impacts of future events. The phenomenon is more widespread and more frequent than previously recognized. Glacial, tectonic, volcanic, and anthropogenic preconditioning is particularly important in the production of landscapes susceptible to landslides that generate displacement waves. In such settings, landslide-generated displacement waves should be an important consideration in hazard assessments. Furthermore, the cases in the catalogue demonstrate the wide range of possible events and their impacts. The latter includes the potential for large loss of life and damage stemming from possible near-field run-ups over 100 m and wave effects up to many tens or even hundreds of kilometers from the source.

The catalogue is particularly comprehensive for Norway—over 60 % of the events in the catalogue are Norwegian, including the earliest reliably reported events. The quality of the Norwegian record is due to the nation's extensive and long-settled fjord coastline, and to a well funded undertaking to produce a nationwide landslide database. Elsewhere, even in densely populated areas with long written histories, many events are certainly unreported. Events prior to the mid-twentieth century and smaller events are most likely to be underreported.

During the next several years, we will expand and improve the catalogue. Details of some events in the catalogue are tenuous or lacking, and characterization of many known events is incomplete, particularly for older events and those in less studied regions. We intend to incorporate an event validity scale, as is common for historic catalogues of tsunamis and earthquakes, to reflect our confidence in the documented events. As we better quantify metrics for individual events, it may be possible to explore basic empirical relationships, such as maximum run-up as a function of landslide and water-body properties.

The most important step, however, in improving the catalogue is adding missing events. We invite colleagues

in geosciences and related fields to help us expand the catalogue by identifying and detailing events unknown to us. Records in some regions appear to be particularly incomplete, given the presence of conditions likely to favour the occurrence of landslide-generated displacement waves: Mexico and Central America, the Central Andes of South America, Central Asia and the Karakoram, and the Arctic shores of Canada and Russia. Specific localities that are particularly vulnerable to landslide-generated displacement waves also require further attention. For example, many un-catalogued landslide-generated displacement waves likely have occurred and will occur in the future in Three Gorges reservoir. It is by far the largest reservoir in the world, was recently impounded, and is in a region predisposed to landslides by geologic, climatic, and tectonic factors. Similar hotspots in the future will likely include proposed hydroelectric projects in Central Asia. Events are also likely in high mountain areas experiencing large and rapid loss of glacier ice due to glacial debuitressing of unstable rock slopes.

References

- Bornhold BD, Harper JR, McLaren D, Thomson RE (2007) Destruction of the first nations village of Kwalate by a rock avalanche-generated tsunami. *Atmos Ocean* 45(2):123–128
- Carey S, Sigurdsson H, Mandeville C, Bronto S (2000) Volcanic hazards from pyroclastic flow discharge into the sea: examples from the 1883 eruption of Krakatau, Indonesia. *Geological Society of America Special Paper* 345, 14p
- Dawson AG (1994) Geomorphological effects of tsunami run-up and backwash. *Geomorphology* 10:83–94
- de Blasio FV (2011) Introduction to the physics of landslides: lecture notes on the dynamics of mass wasting. Springer, Dordrecht, 408p
- Furseth A (2006) *Skredulykker i Norge*. Tun Forlag, Oslo, 207p
- Genevois R, Ghirotti M (2005) The 1963 Vaiont landslide. *Giornale di Geologia Applicata* 1:41–52
- Hermanns RL, Blikra LH, Naumann M, Nilsen B, Panthi KK, Stromeyer D, Longva O (2006) Examples of multiple rock-slope collapses from Kofels (Otz valley, Austria) and western Norway. *Eng Geol* 83:94–108
- Hermanns RL, Hansen L, Sletten K, Böhme M, Bunkholt H, Dehls JF, Eilertsen R, Fischer L, L'Heureux J-S, Høgaas F, Nordahl B, Oppikofer T, Rubensdotter L, Solberg I-L, Stalsberg K, Yugsi Molina FX (2012) Systematic geological mapping for landslide understanding in the Norwegian context. In: Eberhardt E, Froese C, Turner AK, Leroueil S (eds) *Landslide and engineered slopes: protecting society through improved understanding*. Taylor & Francis, London, pp 265–271
- Hermanns RL, L'Heureux J-S, Blikra LH (2013) Landslide triggered tsunami, displacement wave. In: Bobrowsky PT (ed) *Encyclopedia of natural hazards*. Springer, Dordrecht, pp 611–615
- Jones FO, Embody DR, Peterson WL (1961) Landslides along the Columbia River valley, northeastern Washington. US Geological Survey Professional Paper 367, 98p
- Jørstad FA (1968) Waves generated by landslides in Norwegian fjords and lakes. Norwegian Geotechnical Institute Publication 79, pp 13–32
- Lastras G, Amblas D, Calafat AM, Canals M, Frigola J, Hermanns RL, Lafuerza S, Longva O, Micallef A, Sepúlveda SA, Vargas G, De Batist M, Van Daele M, Azpiroz M, Bascuñán I, Duhart P, Iglesias O, Kempf P, Rayo X (2013) Landslides cause tsunami waves: insights from Aysén Fjord, Chile. *EOS Trans Am Geophys Union* 94(34):297–298
- Miller DJ (1960) Giant waves in Lituya Bay, Alaska. US Geological Survey Professional Paper 354-C, 86p
- NGDC (National Geophysical Data Center) (2013) NOAA/WDS Global Historical Tsunami Database, Boulder, CO, USA. http://www.ngdc.noaa.gov/hazard/tsu_db.shtml. Last accessed 30 Sept 2013
- Petley D (2013) Global losses from landslides associated with dams and reservoirs. In: Proceedings of the international conference on Vajont – 1963-2013 – thought and analyses after 30 years since the catastrophic landslide, 8-10 October 2013. Padua, Italy. Italian Journal of Engineering Geology and Environment Book Series, vol 6, pp 63–72
- Roberts NJ, McKillop RJ, Lawrence MS, Psutka JF, Clague JJ, Brideaus M-A, Ward BC (2013) Impacts of the 2007 landslide-generated tsunami in Chehalis Lake, Canada. In: Margottini C, Canuti P, Sassa K (eds) *Landslide science and practice*, vol 6. Springer, Berlin, pp 133–140
- Watt SFL, Pyle DM, Naranjo JA, Mather TA (2009) Landslide and tsunami hazard at Yate volcano, Chile as an example of edifice destruction on strike-slip fault zones. *Bull Volcanol* 71:559–574
- Zhang D, Wang G, Yang T, Zhang M, Chen S, Zhang F (2013) Satellite remote sensing-based detection of the deformation of a reservoir bank slope in Laxiwa Hydropower Station, China. *Landslides* 10:231–238



Internal Structure of Landslide Dams Triggered by Earthquake/Rainfall and Their Instability

Gonghui Wang

Abstract

The internal structure of landslide dams plays a key role in their stability; however, it has not been much studied, probably due to the difficulty in obtaining information on internal structure in most cases. Here, we examined the shear-wave-velocity structure of some landslide dams by a surface-wave technique called multichannel analysis of surface waves (MASW). During the 2008 Wenchuan earthquake ($M_w 7.9$), more than 800 landslide dams formed. Those dams with a high risk of collapse threatened rescue activities, and almost all of the large landslide dams were treated by digging a spillway immediately after the earthquake. Although the risk of collapse of many landslide dams was eliminated or lowered, not all of the countermeasures were based on well controlled methods. On 3–4 September 2011, extensive landslides were induced in Kii Peninsula in Japan by the heavy rainfalls during Typhoon Talas, some of which formed big landslide dams. To analyze the internal structure of the dams triggered by earthquake and rainfall, and to assist in carrying out reliable countermeasures, the detailed geophysical investigations of the dam bodies were carried out. Based on these landslides geological and geomorphological features and movement mechanisms, as well as on the data about internal structures of landslide dams, their instability potential was analyzed.

Keywords

Landslide dam • Earthquake • Rainfall • Internal structure • Stability

Introduction

During the 2008 Wenchuan ($M_w 7.9$) earthquake, more than 800 landslide dams were formed (Fan et al. 2012), greatly hindering the recovery and reconstruction in the affected area. Almost all of the landslide dams failed naturally or were removed artificially soon after the quake. However, some larger landslide dams still remain, impounding large volumes of water and keeping a risk of outburst flooding.

It is well known that once a landslide dam is formed, emergency countermeasures are always needed to prevent or

mitigate the potential outburst flooding disaster due to landslide dam failure. To assist in assessing the risk of outburst flooding due to landslide dam failure, we performed field surveys of some landslide dams that were formed during the 2008 Wenchuan earthquake in Sichuan, China, and also some landslide dams formed during the 2011 Typhoon Talas in Kii Peninsula, Japan. We investigated the geological and topographical characteristics of these landslides, processes of their formation and the internal structure of the landslide dams. In this paper, through studying two coseismic landslide dams (Donghekou and Tangjiashan in Sichuan, China) (Fig. 1a) and one rainfall-induced landslide dam (Akatani, Japan) (Fig. 1b), we examine their possible deposition features related to their internal structures. We also discuss the dam's formation and stability.

G. Wang (✉)
Research Center on Landslides, DPRI, Kyoto University, Gokasho, Uji,
Kyoto 611-0011, Japan
e-mail: wanggh@landslide.dpri.kyoto-u.ac.jp

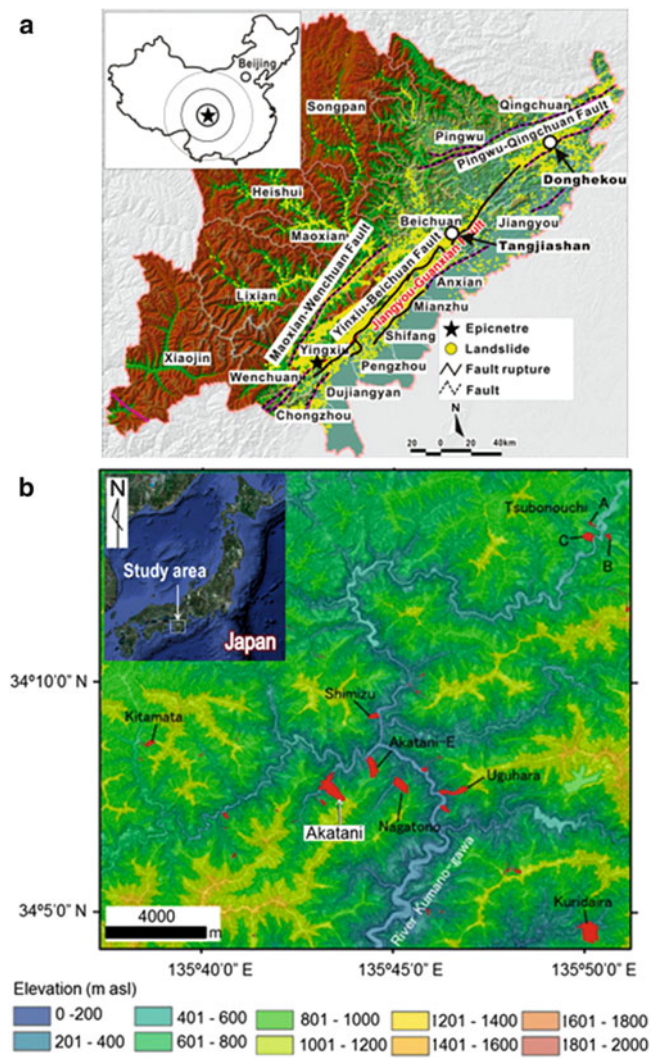


Fig. 1 (a) Epicenter of the 2008 Wenchuan earthquake and distribution of landslides triggered by the earthquake. Arrows mark the studied landslide dams; (b) locations of some large deep-seated landslides triggered by the 2011 Typhoon Talas in Kii Peninsula (after Chigira et al. 2013)

Landslide Dams Studied

Landslide Dams Triggered by Wenchuan Earthquake, China

Wenchuan earthquake ($M_w 7.9$) occurred on May 12, 2008, with the hypocenter being at 30.99°N , 103.36°E , at a depth of 19 km in Sichuan province, China (Fig. 1). The earthquake occurred in the Longmen Shan thrust zone (about 60 km wide), which is located on the eastern boundary area of the Tibetan plateau, and is one of the most significantly deformed regions in China, with many seismically active faults. In Wenchuan earthquake area, the rocks in the vicinity of the Longmen Shan thrust zone are mainly

composed of Triassic granite, metamorphosed sandstone, phyllite, sandy slate and dolomite (Ma 2002). The rocks are closely jointed due to strong tectonic movement in this area.

During the earthquake more than 60,000 landslides were triggered (Gorum et al. 2011) and more than 800 landslide dams were formed (Fan et al. 2012), of which 104 had heights of >10 m, impounding $>10,000$ m³ of water, and with catchment areas >20 km². Based on the scale of the landslide dam, the possible peak value of outburst flooding, and the possible downstream flooding area, the degree of risk of each landslide dam was placed into one of three risk categories (high, medium and low). Of the landslide dams, 6 were at high risk, 25 were at medium risk and 73 were at low risk (Liu 2008; Yin 2008). Urgent countermeasures had been carried on many of these sites.

Donghekou landslide (Fig. 2) is located in Qingchuan County, about 250 km northeast of Chengdu. Bedrock in Donghekou area is mainly dolomite, limestone, sandstone, carbon siliceous slate, and phyllite. The landslide originated from a slope facing the confluence area of Qingzhu River and its tributary, Hongshi River. There is a fault passing through the source area. The N-W side of the fault is mainly composed of limestone, whereas the S-E side of strongly weathered slate forming the main source of the landslide. The displaced mass had a total volume of 10^7 m³. It traveled about 2 km with an elevation drop of about 500 m, passing through the residential areas before depositing on a rice paddy. Four villages were buried by this landslide, and about 780 people were killed. Both rivers were dammed by the debris pile (about 700 m long, 500 m wide and 15–25 m high). The resultant barrier lake overflowed after a few days, and the dam partially collapsed. Fortunately, no further human damage occurred downstream.

Tangjiashan landslide (Fig. 3) is located at 31.837°N , 104.432°E , on the right bank of the Tongkou River, 6.5 km upstream of Beichuan Town. The river here was 100–130 m wide and 0.5–4 m deep. The landslide occurred on a dip slope that was mainly composed of moderately to highly weathered siltstone, siliceous rocks and mudstone of the Qingping Group, from the lower Cambrian, dipping parallel to the slope (Yin et al. 2009; Chigira et al. 2010). The displaced landslide material spanned the entire valley floor and ran up to the opposite valley side, blocking the river and producing the largest landslide dam in the affected area. The dam has a volume of 2.04×10^7 m³, height of 82–124 m, length (across the river) of 803 m, and width (along the river) of 611 m. The impounded lake has an upstream catchment area of 3,550 km² and a maximum capacity of 3.16×10^8 m³. Figure 4 presents the longitudinal section along line I-I' in Fig. 3, and section of dam body along the original river. Based on the geological survey and boring exploration, the geological structure of the dam body was

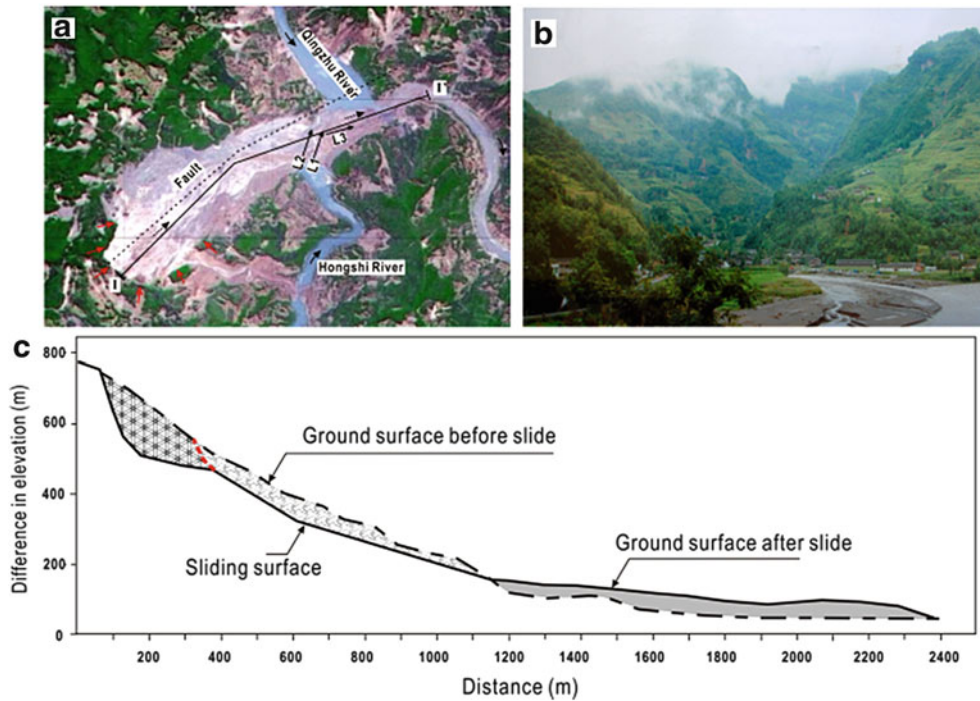


Fig. 2 Donghekou landslide: (a) aerial view; (b) view from the toe part before the quake; (c) longitudinal section along the main sliding path (after Yin 2008). L1, L2, L3: S-wave survey lines. Arrow presents the extending direction of the survey line



Fig. 3 Tangjiashan landslide dam. (a) Aerial view; (b) view of the dam body; (c) view of the dam after construction of spillway (June 8, 2008); (d) view of the dam body with sudden breaching on June 10, 2008

inferred to be consisted of four differing layers from the top to the bottom as shown in Fig. 4 (Fan et al. 2012). The top layer is about 5–15 m thick, and consist of loose soil with

rock fragments (<5 cm) mainly. The second layer about 10–30 m thick is composed mainly of strongly weathered rock blocks (6–40 cm in diameter) and angular boulders

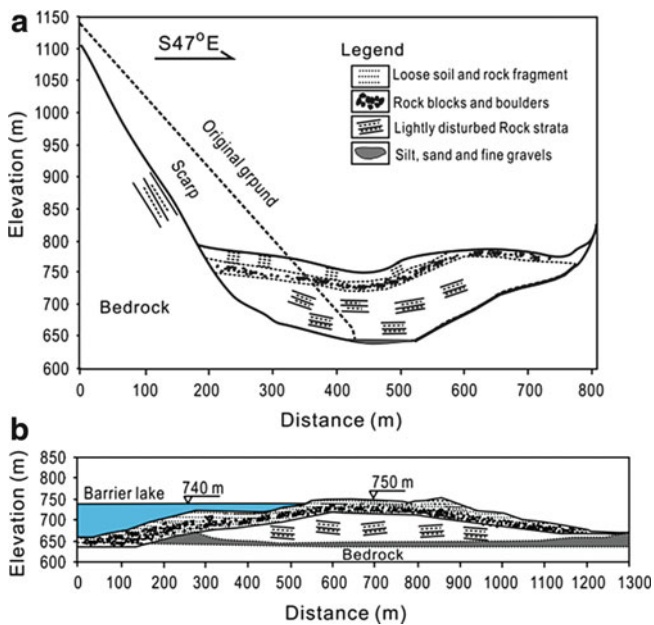


Fig. 4 (a) Geological profile (T–T' in a) of the Tangjiashan landslide; (b) longitudinal cross-section of the dam body along the valley (after Fan et al. 2012)

(1–2 m). The third layer 50–67 m thick, is composed of huge massifs comprising partly intact rock strata and retaining the original structure. The fourth (bottom) layer (about 6–16 m) consist of silt, sand and fine gravels mostly from the alluvial deposits of the original river bed.

Akatani Landslide Dam in Kii Peninsula, Japan

Typhoon Talas hit the Japanese Island during September 2–5, 2011, and brought heavy rainfall in a wide area of west Japan, especially in Kii Peninsula. The rainfall from August 31 till September 4 exceeded 1,000 mm over two thirds of the Kii Peninsula, and gave a new record of 2,349 mm at Kami-Kitayama rainfall observation site. During this period, more than 70 large (volume > 100,000 m³) deep-seated landslides were triggered (Chigira et al. 2013). 17 landslide dams were formed. According to a Japanese law, emergency countermeasures had been performed soon on five large ones with high risk of secondary disaster. Among these five landslide dams, one formed by a landslide on the Akatani River valley slope (hereinafter called Akatani landslide dam) (Fig. 5) was the most dangerous, presenting high possibility of abrupt breaching.

Akatani landslide area is mainly composed of sandstone, tuffaceous shale, alternate layer of sandstone and shale (Fig. 6). The landslide had a width of 300 m at the upper part of the source area, 500 m at the toe part along the river,



Fig. 5 Akatani landslide dam (Google Earth image) and geophysical survey line (S3)

and a thickness of 80–100 m on the slope. The volume of displaced materials was estimated to be 8.2 million m³ (Chigira et al. 2013). The landslide had a length of about 1,100 m with a difference of 550 m in elevation. The displaced materials blocked Akatani River, forming an 80 m high landslide dam. The impounded lake has an upstream catchment area of 13.8 km² and a maximum capacity of 9×10^5 m³.

Due to the high potential of overtopping and abrupt failure and threat to many downstream residents, a real-time monitoring system was promptly set at the barrier lake to monitor the water level. It was found that the dam body suffered overtopping erosion during the Typhoon Roke (2 weeks after Typhoon Talas), which resulted in the occurrence of a drainage channel of about 4 m deep on the dam body. Nevertheless, no collapse failure occurred.

Internal Structure of the Landslide Dams

Detailed boring exploration is not always available to study the geological structure of landslide dam, because the time before the overtopping is normally very limited. To understand the internal structure of the landslide dams, we used a surface-wave method known as multichannel analysis of surface waves (MASW) (Hayashi and Suzuki 2004) to measure the shear-wave velocity profile (Vs) of the dam body. This method enables us not only to investigate the geological structure of the dam body, but also to obtain data on the geotechnical property of the soil layers of the dam body (Wang et al. 2013).

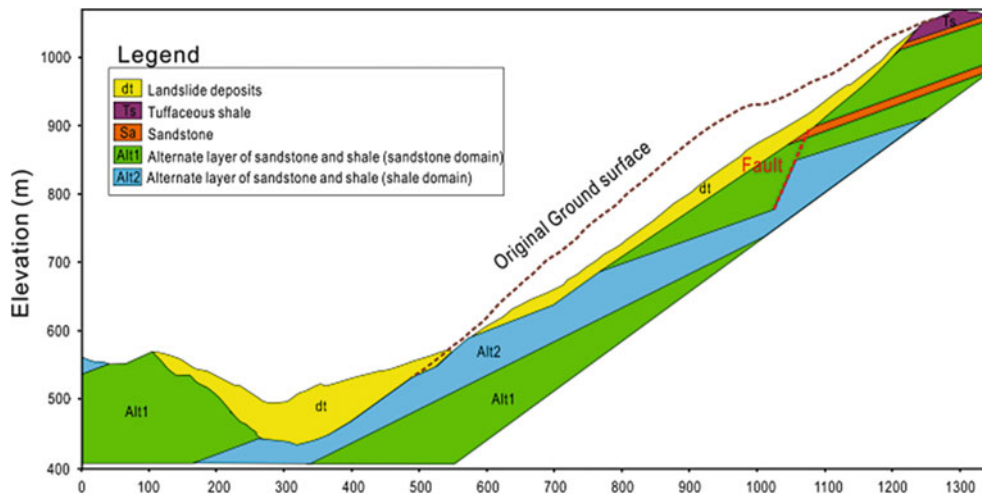


Fig. 6 Geological profile along line T-T' in Fig. 5 (after Inaba et al. 2013)

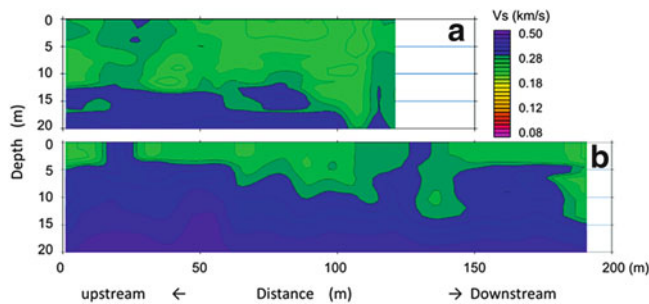


Fig. 7 Shear-wave velocity (V_s) profiles along traverse line L2 (a) and L1 (b), respectively

For Donghekou landslide dam, the survey was performed along three lines (L1–L3) as shown in Fig. 2a. The V_s profiles along L2 and L1 are presented in Figs. 7a and 7b, respectively. These two lines are parallel to the drainage channel of the Hongshi River with the distance between them being about 70 m. As shown in Fig. 7b, the upper weak layers have smaller V_s values (250–300 m/s) and become thicker in the downstream direction. However, these layers are separated by a harder layer with greater V_s (300–340 m/s), and can be divided into three sub-zones. This harder soil layer/belt might result from big massifs or angular boulders wrapped up in the landslide debris. Three layers with V_s ranging from 330 to 470 m/s can be identified in the bottom of the profile. These layers can be regarded as the original ground where a road had passed before the earthquake. Therefore, the boundary showing large contrasts in V_s could be regarded as the boundary between the landslide debris and original ground. The V_s profile along L2 (Fig. 7a) showed that the weak soil layer ($V_s = 250$ –300 m/s) is thicker than at L1, and the landslide deposits are even thicker than the maximum depth (20 m) available by the applied survey method. A harder soil layer/zone was also

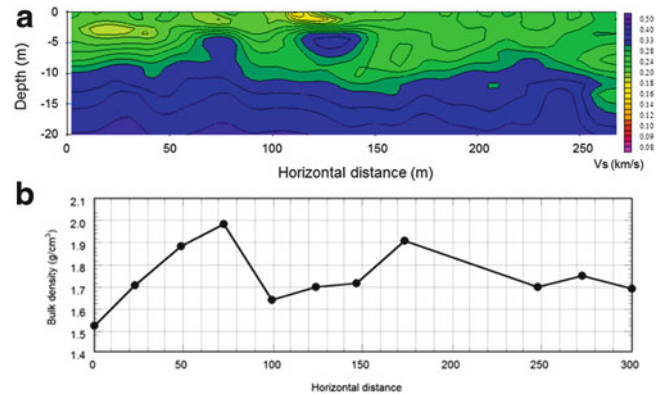


Fig. 8 (a) Shear-wave velocity (V_s) profile along traverse line L3; (b) variation of bulk density along the main sliding direction with origin starting from survey line L1 approximately (after Zhang et al. 2011)

wrapped in the upper weak soil layer, and their locations are almost the same as at L1. This evidenced that the harder layer/belt of big rock massifs or boulders extended at least a distance >100 m. The V_s profile along L3 showed that the surficial soil layers have small V_s values (180–270 m/s) (Fig. 8). The contrasts in the V_s values indicated that the landslide deposits might have a thickness of about 10 m in average. There is a domain on the middle part of the survey line (110–140 m) and 7–10 m deep where the shear velocity is greater (ranging from 300 to 360 m/s). This domain might result from the wrapping of big rocks and boulders. In this area, a lot of big boulders sized 2–3 m in diameters were deposited.

For the Tangjiashan landslide dam, we surveyed the dam along the spillway (Fig. 9) and along a line crossing the dam body on its downstream part (Fig. 10) by means of MASW. During our survey time, the water level (spillway bed) was lowered to 710 m, and the start point is about 13 m above the

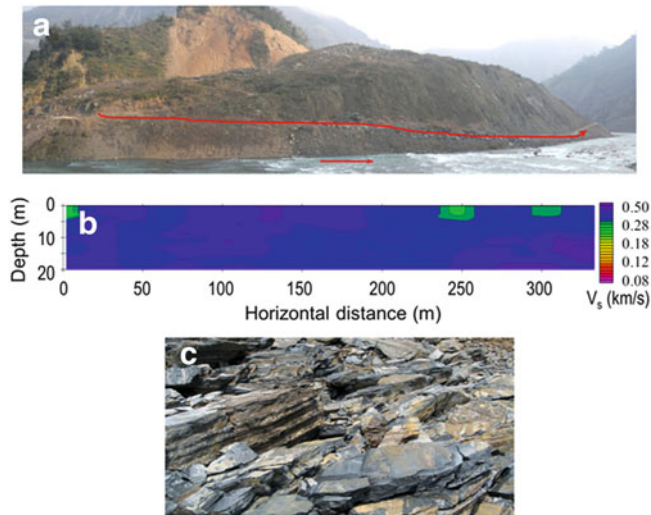


Fig. 9 MASW survey along the spillway on Tangjiashan dam. (a) Survey line; (b) shear wave velocity profile; (c) outcropped rock layers on the dam body

river bed. According to Fig. 4, the survey line is within the third layer where the rock massifs retaining the original structure are relatively less disturbed. The Shear wave velocity profile (Fig. 9a) revealed that there is a hard rock layer with greater V_s values at the upstream part of the survey line (near the inlet of drainage channel), and this layer was underlain by a relatively weaker layer that outcropped downstream (after 200 m from the start point). Below this weaker layer is another hard layer with greater V_s value. This kind of interlayers of hard rock and weak rock showed good consistency with the original rock strata of the slope. The dipping angle of these layers shown in Fig. 9b also showed good consistency with the outcropped rocks as presented in Fig. 9c. Considering the interlayer structure of the dam body and the height of starting point above the river bed, the hard rock layer in the inlet of the drainage channel may be thin, according to Fig. 9b. In this case, if the weak layer on the downstream be eroded, scouring could result in retrogressive failure upwards, and then result in failure of the bed rock near the inlet of the channel. It is noted that this engineering-treated drainage channel suffered breaching during a flood in July, 2013, and lowered for another 10 m approximately.

Result of survey on the downstream toe part of Tangjiashan landslide dam (along the line crossing the river) (Fig. 10) showed that dam body is inhomogeneous. The domain (area of LS in Fig. 10) of landslide distal toe (deposits on the opposite bank) consist of loose debris with low shear wave velocity, and some loose materials are sandwiched in the hard soil layers. These loose materials might result from the deposits of loose soils on the toe part of the slope as well as from alluvial deposits on the river bed.

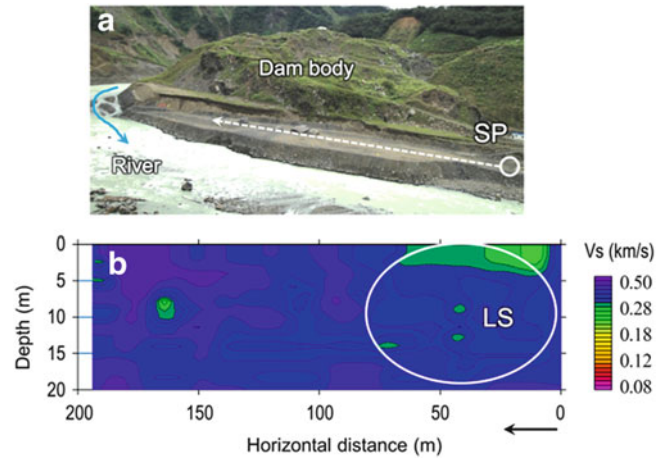


Fig. 10 MASW survey on downstream part of Tangjiashan landslide dam. (a) Survey line; (b) Shear wave velocity profile. LS: low shear wave velocity domain

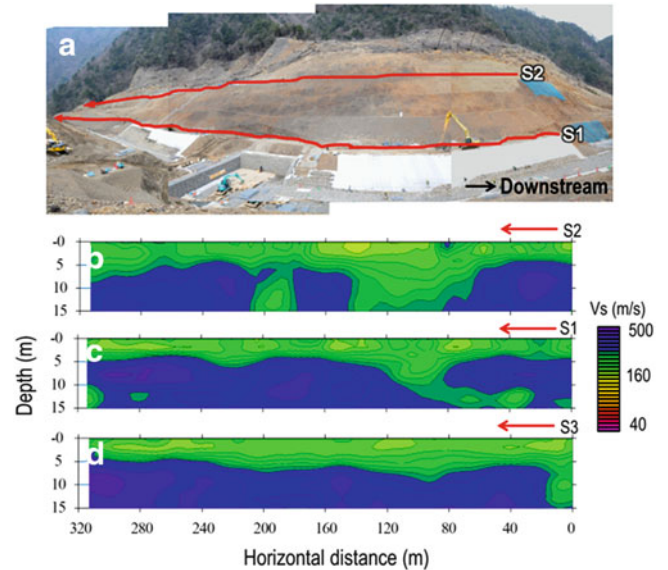


Fig. 11 (a) View of Akatani landslide dam body and survey lines. (b–d) Shear-wave velocity (V_s) profiles along traverse lines S1, S2 in (a) and line S3 in Fig. 5, respectively

For Akatani landslide dam, two survey lines (S1 and S2 shown in Fig. 11a) were allocated on the dam body along the drainage channel that was under construction as one of the emergency countermeasure. The third survey line (S3 in Fig. 5) was at the downstream part of the dam body along the river bed, where the main material are deposits of fine debris originating from fluidized landslide debris. The shear wave velocity profiles along S1 and S2 are presented in Figs. 11b and 11c, while that along S3 in Fig. 11d, respectively. It is seen from Fig. 11b, c that the surficial layer (about 5 m thick in general) has its shear wave velocity in the range of 160–260 m/s, showing that this layer consists

of loosely deposited landslide material. It is also noted that the loose debris was thicker (10–15 m) on the domain of 60–140 m starting from the original point of the survey line. The V_s profile along S3 (Fig. 11c) showed that the thickness of landslide deposits on the downstream of dam body is about 4–6 m and the deposits have a smaller V_s value (<200 m/s).

Discussion

In the stability analysis of landslide dam, two different approaches, the topographical approach (Costa and Schuster 1988, 1991; Casagli and Ermini 1999; Ermini and Casagli 2003) and the hydraulic approach (Mizuyama et al. 1987, 1989; Takahashi and Kuang 1988; Takahashi and Nakagawa 1993), have been developed to analyze the possible longevity of the dam and the flood profile when the dam is breached. The topographical characteristics and the breaching failure mechanisms due to overtopping have been widely examined. An approach termed the *Dimensionless Blockage Index (DBI)* proposed by Ermini and Casagli (2003) had been widely used.

$$DBI = \log(A_b \times H_d / V_d) \quad (1)$$

where A_b is the catchment area (km^2); H_d is the landslide dam height (m); V_d is the landslide dam volume ($\times 10^6 \text{ m}^3$). Based on the analysis of numbers of recorded landslide dams, Ermini and Casagli (2003) recognized three “domains” for the dimensionless blockage index (1) when $DBI < 2.75$, the landslide dam lies in the stability domain; (2) when $2.75 < DBI < 3.08$, the landslide dam is in the uncertain domain; and (3) when $DBI > 3.08$, the landslide dam is in the instability domain.

Using Eq. (1), we calculated the DBI for three above-mentioned landslide dams, and the values are 4.36, 4.16 and 2.1, for Donghekou, Tangjiasha and Akatani cases, respectively. Therefore, Donghekou and Tangjiashan landslide dams could be regarded to lie in the instability domain. In Fig. 12, we superimposed the plot of catchment area against V_d/H_d together with those obtained by Ermini and Casagli (2003), where SD means the stability domain, UD instability domain. Since the Donghekou landslide dam suffered outburst breaching, and abrupt dam breaching also occurred in the Tangjiashan landslide dam after the drainage channel was constructed, we concluded that the risk of abrupt breaching of these large landslide dams formed in the 2008 Wenchuan earthquake is correctly indicated by DBI . However, the Akatani landslide dam also suffered abrupt breaching after the occurrence of overtopping, although its DBI is less than 2.75. This improper performance of DBI in the prediction of the stability of a

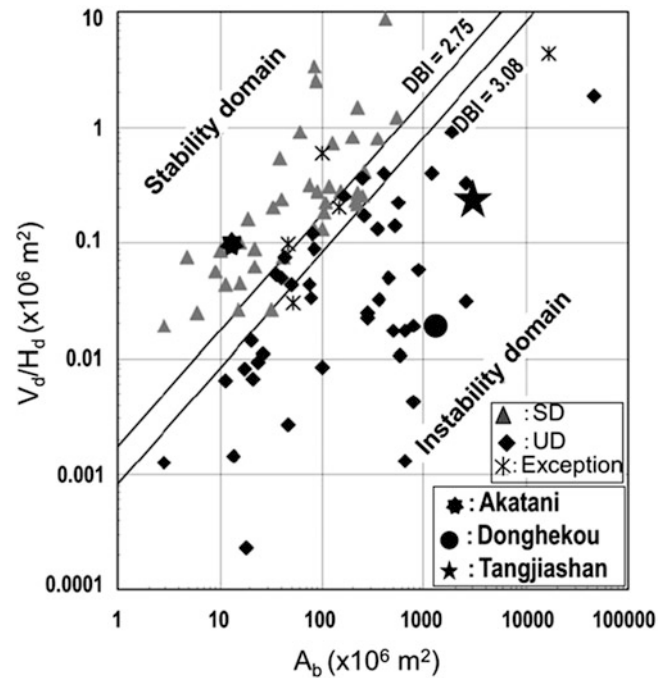


Fig. 12 Stability analysis using Dimensionless Blockage Index (after Ermini and Casagli (2003)). Filled triangles: intact landslide dams; filled diamonds: collapsed landslide dams

given landslide dam may be due to the fact that the DBI is based on topographic features of the landslide dam and the upstream catchment area, without consideration of the dam’s geotechnical properties. Such anomalous behavior has also been reported by Strom (2010), who suggests that additional quantitative parameters characterizing landslide dams and dammed lakes should be used in the stability analysis of landslide dams. This may be further proved by the Tangjiashan case. Because the artificial drainage channel had been reinforced by concrete structures, and it has been deemed that the dam body will be stable since then. Nevertheless, these concrete structures had also been destroyed by the floods during heavy rainfall. Therefore, the internal structure of the dam shown in Fig. 9b implies that another possible process, scouring on the weaker layer, may result in failure of the hard layer and then further breaching of the dam.

Hydraulic prediction of downstream flooding due to failure of a landslide dam is of great importance to the assessment of potential damage downstream and effective evacuation. By now, some approaches to this kind of hydraulic prediction have been proposed, based on experimental work on landslide dams consisting of homogenous soil layers. However, as revealed by these V_s profiles of differing landslide dams, a landslide dam normally consists of heterogeneous debris.

We surveyed the shear-wave velocity profiles of several large landslide dams formed in the 2008 Wenchuan

earthquake, and found that those dams abruptly breached during the construction of the sluiceway had shear-wave velocity values smaller than 250 m/s (Wang 2011). It is known that the standard penetration test *N* value of a soil layer has a positive correlation with the shear-wave velocity (Imai and Tonouchi 1982). A higher shear-wave velocity value means that the soil layer has greater penetration resistance, indicating that the soil layer is more tightly consolidated. It is noted that at present there is no accepted rapid approach to predict the stability of a landslide dam immediately after its formation. However, we expect that a method combining the Dimensionless Blockage Index and shear-wave velocity survey results could be developed so that the risk of abrupt breaching of a landslide dam can be assessed rapidly and more reliably. In the future, we plan to carry out similar geophysical surveys on more landslide dams with differing topographic, geological and movement characteristics to develop a physically based method of assessing the breaching risk of landslide dams.

Conclusions

Based on the field survey of three landslides, some conclusions are made.

1. Landslide dams formed by landslides with differing geological, topographical and movement features have differing internal structures. A seismic geophysical survey of the landslide dams revealed that the soil layers inside the landslide dams were not homogenous. Those soil layers with small *V_s* values suffered abrupt breaching after the overtopping.
2. The main body of Donghekou landslide dam had smaller *V_s* than other two landslide dams in general, identifying that the debris of long-traveled landslide was normally loosely deposited and can suffer abrupt breaching after the occurrence of overtopping.
3. The main body of Tangjiashan landslide dam consisted of alternate layers of hard and weak rocks, and the original geological structures were less disturbed. The toe part of the landslide deposits (on the opposite bank of the river) is consisted of loose debris with small *V_s*.
4. Akatani landslide dam triggered by rainfall had a very loose surficial layers on the dam body, which suffered overtopping breach although its *DBI* index showed that the dam is in the stable domain.
5. Those soil layers with smaller *V_s* (say 300 m/s) are prone to suffer from abrupt breaching due to overtopping.

Acknowledgement This research was supported by the Opening Fund of State Key Laboratory of Geohazard Prevention and Geoenvironment Protection (Chengdu University of Technology) (Nos. SKLGP2011K012), a scientific research grant from the MEXT

of Japan (Grant No. 21403002), and a 2009 special event fund for promotion of disaster prevention research, DPRI, Kyoto University (SA21-06). I am grateful to Prof. Runqiu Huang in Chengdu University of Technology, Prof. Toshitaka Kamae and Prof. Masahiro Chigira in Kyoto University, Dr. Araiba Kiminori in National Research Institute of Fire and Disaster, Japan, Dr. Sergio Lourence in Cardiff University, Dr. Alexander Strom in Geodynamics Research Center of Hydroproject Institute, Russia, Dr. Fanyu Zhang in Lanzhou University, for their help and valuable discussions on this work.

References

- Casagli N, Ermini L (1999) Geomorphic analysis of landslide dams in the Northern Apennine. *Trans Jpn Geomorphol Union* 20:219–249
- Chigira M, Wu XY, Inokuchi T, Wang G (2010) Landslides induced by the 2008 Wenchuan earthquake, Sichuan, China. *Geomorphology* 118:225–238
- Chigira M, Tsou C, Matsushi Y, Hiraishi N, Mastuzawa M (2013) Topographic precursors and geological structures of deep-seated catastrophic landslides caused by Typhoon Talas. *Geomorphology* 201:479–493
- Costa JE, Schuster RL (1988) The formation and failure of natural dams. *Geol Soc Am Bull* 100:1054–1068
- Costa JE, Schuster RL (1991) Documented historical landslide dams from around the world. U.S. Geological Survey Open-File Report 91-239, pp 1–486
- Ermini L, Casagli N (2003) Prediction of the behaviour of landslide dams using a geomorphological dimensionless index. *Earth Surf Process Landforms* 28(1):31–47
- Fan X, Gorum T, van Westen CJ, Korup O, Xu Q, Dai F, Huang R, Wang G (2012) Transient water and sediment storage of the decaying landslide dams induced by the 2008 Wenchuan earthquake, China. *Geomorphology* 171–172:58–68
- Gorum T, Fan XM, van Westen CJ, Huang RQ, Xu Q, Tang C, Wang G (2011) Distribution pattern of earthquake-induced landslides triggered by the 12 May 2008 Wenchuan earthquake. *Geomorphology* 133(3–4):152–167
- Hayashi K, Suzuki H (2004) CMP cross-correlation analysis of multi-channel surface-wave data. *Explor Geophys* 35:7–13
- Imai T, Tonouchi K (1982) Correlation of *N*-value with *S*-wave velocity and shear modulus. In: Proceedings of the 2nd European symposium on penetration testing, Amsterdam, pp 57–72
- Inaba H, Ogawauchi Y, Oyama M, Kitagawa S (2013) Geological survey results of Akatani area with occurrence of deep-seated landslide triggered by 2011 Typhoon Talas. In: 46th annual conference of research presentation, Japan Civil Engineering Consultants Association, No. 113-1, 12 Sept 2013, 6p (in Japanese)
- Liu N (2008) Lesson from the countermeasures on lowering the risk of the dammed lakes formed by large landslides during the 2008 Wenchuan earthquake. *J China Water Resour* 16:1–7 (in Chinese)
- Ma LF (ed) (2002) Geological atlas of China. Geological Publishing House, Beijing, 348p
- Mizuyama T, Ishikawa Y, Fukumoto A (1987) Landslide dams outburst due to seepage. *Annu Public Works Res Inst* 2744:18–91 (in Japanese)
- Mizuyama T, Ishikawa Y, Fukumoto A (1989) Landslide dams outburst and its countermeasure. *Civ Eng J* 31–11:50–56 (in Japanese)
- Strom A (2010) Landslide dams in Central Asia region. *J Jpn Landslide Soc* 47(6):309–324
- Takahashi T, Kuang SF (1988) Hydrograph prediction of debris flow due to failure of landslide dam. *Annu Disast Prev Res Inst Kyoto Univ* 31(B-2):601–615

- Takahashi T, Nakagawa H (1993) Flood and debris flow hydrograph due to collapse of a natural dam by overtopping. *J Hydrosoci Hydraul Eng JSCE* 37:699–704
- Wang G (2011) Formation of large scale landslide dams and failure prediction. In: *Proceedings of 2011 landslide symposium, Kansai Branch of Japan Landslide Society*, pp 65–80 (in Japanese)
- Wang G, Huang R, Kamai T, Zhang FY (2013) The internal structure of a rockslide dam induced by the 2008 Wenchuan (M_w 7.9) earthquake, China. *Eng Geol* 156:28–36
- Yin YP (2008) Researches on the geo-hazards triggered by Wenchuan Earthquake, Sichuan. *J Eng Geol* 16:433–444 (in Chinese)
- Yin YP, Wang FW, Sun P (2009) Landslide hazards triggered by the 2008 Wenchuan earthquake, Sichuan, China. *Landslides* 6 (2):139–152
- Zhang LM, Xu Y, Huang RQ, Chang DS (2011) Particle flow and segregation in a giant landslide event triggered by the 2008 Wenchuan earthquake, Sichuan, China. *Nat Hazards Earth Syst Sci* 11:1153–1162



Influence of Water Level Drawdown on Landslide Movement in Reservoir

Hufeng Yang and Fawu Wang

Abstract

Water level variation is one of the main triggering factors of landslides in reservoirs. In the Three Gorges Reservoir, China, the field monitoring data of the Shuping landslide shows that the sliding deformation accelerates during water level drawdown. In order to study the influence of water level drawdown on landslide movements in the reservoir, series of slope model tests were conducted to simulate the response of water level drawdown on the slope. The movement of slopes with different soil permeability is presented along with the generation and dissipation of pore water pressure in the slopes under water level variation. Experimental results show that the permeability of slope material controls the dissipation of pore water pressure in the slope under water level drawdown. However, if the permeability is high enough, the effect of the permeability change on the dissipation time of pore water pressure will not be obvious. During the mitigation and prevention of landslide with low permeability soil in reservoir, more attention should be focused on the drainage of ground water to quickly reduce the pore water pressure after water level drawdown in reservoir.

Keywords

Landslide • Model test • Water level drawdown • Reservoir

Introduction

Mass movements along reservoir slopes can occur as a result of either filling or drawdown of a reservoir (Schuster 1979). Globally, the water level variation has triggered several catastrophic landslides in reservoirs (Müller 1964; Wang et al. 2004; Du 2006). In China, the Three Gorges Dam constructed on the Yangtze River is one of the largest hydro-electricity projects in the world. The reservoir water level changes between 145 and 175 m every year for power generation and

flood prevention. Many landslides were triggered by the water level variation in the Three Gorges Reservoir (Ding et al. 2004; Wang et al. 2004, 2007; Huang et al. 2007, 2012).

The Shuping landslide is one of the landslides reactivated by the initial impoundment of the Three Gorges Reservoir in 2003. Wang and his research team (Wang et al. 2008) had established a monitoring system to obtain the relationship between slope deformation and water level variation. The movement of the landslide is related to the change in the water level according to the results obtained from long period of monitoring. The progressive movement was found to be more active during periods of water level drawdown (Wang et al. 2013). In order to study the influence of water level drawdown on landslide movement on the reservoir banks, series of slope model tests were conducted to simulate the response of water level drawdown on slopes. The movement of slopes with different soil permeability was presented along with the generation and dissipation of pore water pressure in the slopes under water level variation. In addition,

H. Yang (✉)
Department of Geoscience, Shimane University, Nishikawatsu 1060,
Matsue 690-8504, Japan
e-mail: yanghufeng@gmail.com

F. Wang
Research Center on Natural Disaster Reduction, Shimane University,
Matsue 690-8504, Japan
e-mail: wangfw@riko.shimane-u.ac.jp

experimental results were combined with the field monitoring data to understand the movement characteristic of the Shuping landslide during water level variation in the reservoir.

Model Test Apparatus

Model tests were conducted in a water tank. Figure 1 shows the arrangement of the experimental apparatus for the slope model test. The water tank is 115 cm long, 55 cm high and 57 cm wide. A plastic ball was buried in the slope model to monitor the slope movement. This ball was connected to a linear displacement transducer (LDT) to get the displacement data. The LDT has rated capacity of 1 m and accuracy of 0.1 mm, which is enough to monitor the slope movement. The other side of the ball was connected to a balance weight determined by the friction force between the wire and soil and the rotating pulley. The balance weight ensures free movement of the plastic ball within the soil when the movement of the slope model occurs. A box covers the pulley in the slope model to separate it from the sand. This makes sure that the pulley freely rotates without the resistance between the sand and pulley. Three pore water pressure sensors were installed at the flume bottom. The three pore water pressure sensors have uniform capacity of 50 kPa with accuracy of 0.001 kPa. Pore water pressure sensor No. 1 (P1) is used to measure the water level variation in water tank. Pore water pressure sensor No. 2 (P2) and No. 3 (P3) were used to measure the generation and dissipation of pore water pressure in the slope body during water level variation in water tank. Two video cameras positioned at the top and side view, were used to monitor the event. The rise-rate of the water level was controlled by the recharge rate using a water tap. Three mini water pumps were used to control the discharge of water from the water tank. The various usage of three pumps were used to simulate the various drawdown-rates of the water level in water tank.

Soil Properties

Silica sand No. 8, No. 7, and No. 6 were used to construct the slope models. Figure 2 shows the grain size distribution of the samples. According to the international scale, recommended by the International Society for Soil Mechanics and Foundation Engineering (ISSMFE), silica sand No. 6 used in the model tests is medium sand, while silica sand No. 7 and No. 8 are classed as fine sand. Table 1 shows the properties of samples silica sand No. 8, No. 7 and No. 6. The coefficients of saturated permeability (k_s) of the samples were obtained through constant head permeability test. As we know, the density of the sample affects the permeability. The density of soil sample used for permeability test is same with the slope material after the construction of the slope model. The initial water content of the sample was kept at 5.0%. The wet soil sample was kept in a

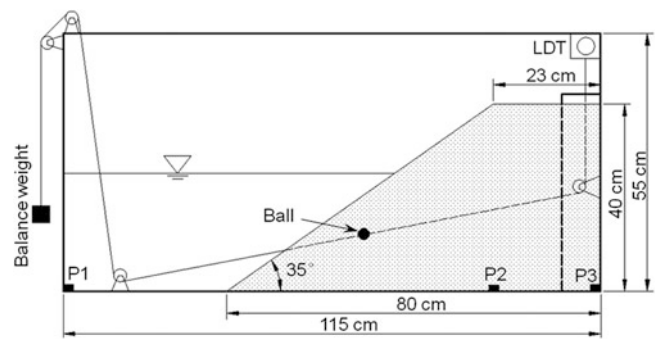


Fig. 1 Arrangement of the experimental apparatus for model test

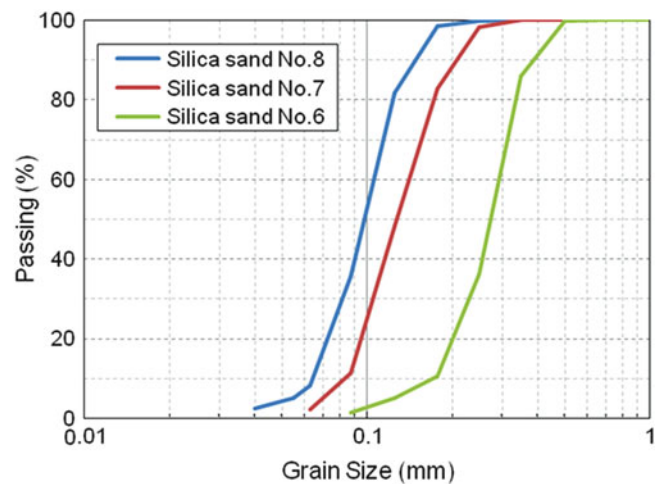


Fig. 2 Grain size distribution of silica sand No. 8, No. 7 and No. 6

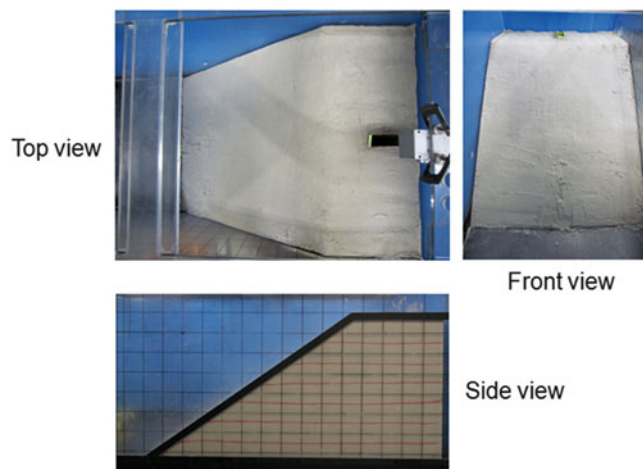
sealed box for one night before constructing slope model. The purpose is to make sure that moisture is dispersed evenly. The water content value shown in Table 1 was the actual water content of the sample used for the construction of slope model.

Slope Model Construction

All the transducers were installed before building the slope model in the water tank. A careful placement of the sample inside the water tank is very important to obtain a homogeneous slope model. The sample was placed inside the tank in horizontal layers. Each layer had a thickness of 5 cm. Sample was covered with a piece of wood board, and was drummed five times using a wood mallet. The layer surface was roughed using a steel brush to avoid obvious stratification before laying the next layer sample. For each 10 cm thickness, red color marked layers were positioned at their respective locations during building of the slope model. The purpose is to monitor the failure process during the water level rise and drawdown. Figure 3 shows the top, front and side view of the slope model in the water tank. The length of the top and bottom of the slope model are 23 and 80 cm,

Table 1 Properties of samples silica sand No. 8, No. 7 and No. 6

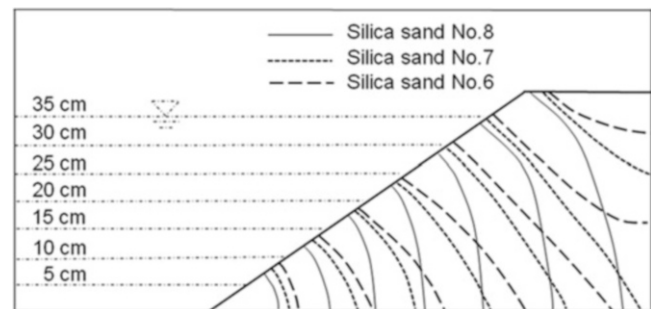
Properties	Silica sand No. 8	Silica sand No. 7	Silica sand No. 6
Specific gravity, G_s	2.663	2.664	2.664
Constrained grain size, D_{60} (mm)	0.107	0.142	0.298
Mean grain size, D_{50} (mm)	0.100	0.127	0.278
Grain size D_{30} (mm)	0.083	0.106	0.232
Effective grain size, D_{10} (mm)	0.065	0.086	0.175
Coefficient of uniformity, C_u	1.646	1.651	1.702
Coefficient of curvature, C_c	0.990	0.920	1.032
Density, ρ (g/cm ³)	1.19	1.20	1.32
Initial water content, w (%)	4.82	4.80	4.81
Coefficient of saturated permeability, k_s (m/s)	6.30×10^{-6}	1.50×10^{-5}	3.74×10^{-5}
Natural angle of repose ($^\circ$)	34	34	34

**Fig. 3** Slope mode in the water tank

respectively. The slope is 40 cm high. Slope angle is 35° . The width of the slope model is 57 cm.

Test Procedures

After the slope model construction, model tests were conducted under the water level rise and drawdown. The purpose of the water level rise in the first time is to saturate the slope model. Therefore, the rise rate of water level is quite slow. From the side view, we can observe that the wet front in the slope models moved forward gradually. Figure 4 shows the distribution of wet front of silica sand No. 8, No. 7 and No. 6 during water level rise, respectively. They comply with the general seepage phenomenon. In addition, this phenomenon reveals the slope is homogenous. Due to the different properties of silica sand No. 8, No. 7 and No. 6, especially the permeability, the pattern of the distribution of wet front during the water level rise is different. The difference shows that moisture in the high permeability soil moved faster than the low one.

**Fig. 4** The distribution of wet front during the water level rise by per 5 cm

When the water level reached to the maximum level, it was kept for one night to saturate the slope model. After that, water level drawdown test was conducted on the slope models. During this process, the slope movement and pore pressure change were recorded through our data acquisition system.

Results and Discussions

Slope Movement Under Water Level Drawdown

After the water in tank rose to a maximum level and saturated the slope, water level drawdown at the rate of 3.75 cm/min was carried out. The displacement of slope models of silica sand No. 8, No. 7 and No. 6 under water level drawdown is shown in Fig. 5. From the monitoring results, it can be observed that obvious movement of slopes of silica sand No. 8 and No. 7 occurred during water level drawdown. However, the slope of silica sand No. 6 remained stable during the whole test procedure. Compared with the displacement of slopes with water level drawdown, we can find that the slope of silica sand No. 7 stopped movement when water level dropped to the minimum level (10 cm). However, the slope of silica sand No. 8 kept moving when water level dropped to the minimum level (10 cm). Finally, the displacement of slope of silica sand No.

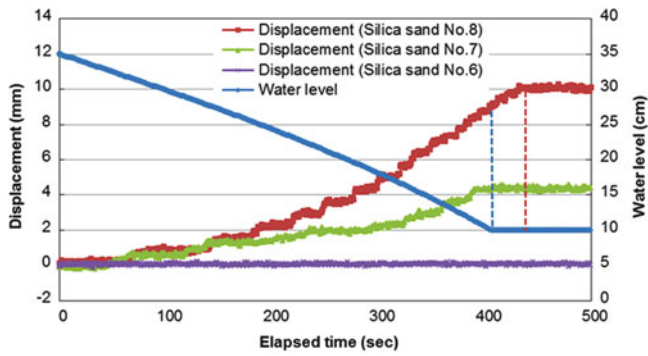


Fig. 5 Displacement of slopes under different soil permeability during tank water level drawdown

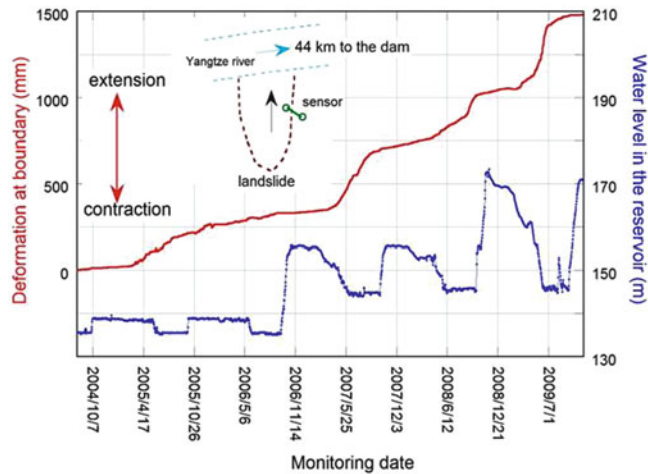


Fig. 6 Monitoring result of sensor at the east boundary of the Shuping landslide compared with the reservoir water level variation (Wang et al. 2013)

8 reached the maximum value after water level was kept at 10 cm for a few seconds.

The hydraulic boundary conditions and geometry are same for slopes of silica sand No. 8, No. 7 and No. 6. Compared with silica sand No. 7 and No. 6, the permeability of silica sand No. 8 is quite low (6.30×10^{-6} m/s) (Table 1). Therefore, the soil properties, especially the permeability, are the main controlling factor of different slope movement under water level drawdown.

Referring to the field monitoring result of extensometer at the east boundary of Shuping landslide in the Three Gorges Reservoir (Wang et al. 2013), the deformation of the landslide accelerated during reservoir water level drawdown (Fig. 6). In addition, there was a time lapse between deformation and water level drawdown, i.e. the main deformation of landslide occurred after reservoir water level dropped to a minimum level. This field monitoring result of the relationship between deformation and water level variation corresponds to what we obtained through model test on the slope of silica sand No. 8 (Fig. 5). Wang et al. (2007) described that the main component of sliding mass of the Shuping landslide is silty clay. The

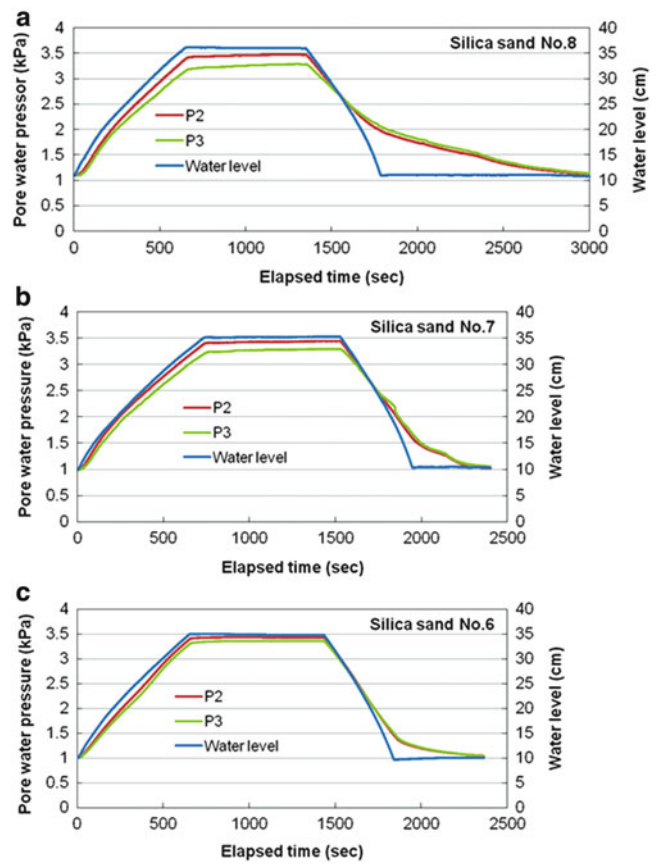


Fig. 7 Generation and dissipation of pore water pressure under slow water level rise and water level drawdown at an average rate of 3.75 cm/min

permeability of silty clay is quite low (10^{-6} – 10^{-8} m/s) according to the permeability and drainage characteristics of soils (Terzaghi et al. 1996). Combining the field monitoring result with slope model tests, we can find that the permeability of the sliding mass plays an important role in slope movement under water level drawdown in the reservoir.

Pore-Pressure Generation and Dissipation

From the above discussion, it can be observed that the hydraulic boundary condition and soil permeability control the transient behavior of the slope model, especially during the water level drawdown. Change in hydraulic boundary condition results in change of pore water pressure. Meanwhile, soil permeability affects the seepage in the slope. To identify the dominant parameter, the slope model tests with different soil permeability and different drawdown-rate of water level were conducted. Pore water pressure sensors No. 2 and No. 3 were used to monitor the pore water pressure changes in the slope body.

Figure 7 shows the generation and dissipation of pore water pressure under slow water level rise and water level

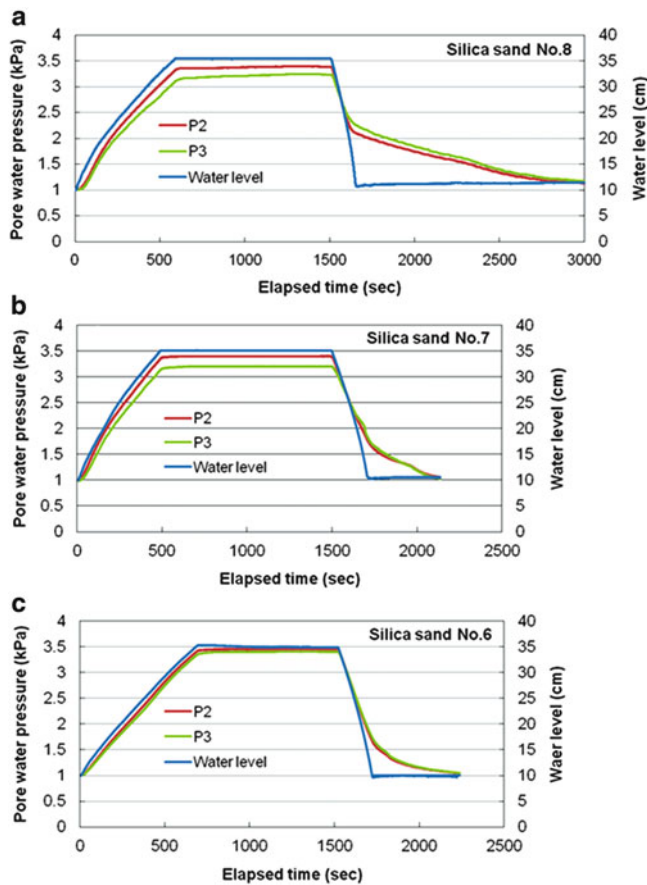


Fig. 8 Generation and dissipation of pore water pressure under slow water level rise and water level drawdown at an average rate of 11.25 cm/min

drawdown at the average rate of 3.75 cm/min. Compared with the monitoring results of slopes of silica sand No. 8, No. 7 and No. 6, we can find that the generation of pore water pressure in slope of silica sand No. 6 (high permeability) responds to water level rise in water tank immediately. However, there is a time delay between the water level rise in water tank and generation of pore water pressure in slopes of silica sand No. 7 and No. 8. Because the slope displacement occurred during water level drawdown, we will focus on the change of pore water pressure during this period. From the result, we can find that the dissipation time in the slope of silica sand No. 8 with low permeability (6.30×10^{-6} m/s) is about three times longer than for the slope of silica sand No. 7. The permeability of silica sand No. 7 and No. 6 is different. However, their dissipation time is almost same. For the rapid drawdown condition (Fig. 8), we can get the same conclusion. In addition, the difference on the dissipation time of each slope under different drawdown-rate of water level is not so big. Therefore, it can be observed that permeability controls the dissipation of pore water pressure under water level drawdown. However, if the permeability is high enough, the effect of the

increase in permeability on the dissipation time of pore water pressure is not obvious.

Experimental results can be applied to the Shuping landslide to explain its displacement features. Due to the low permeability value of silt clay, the dissipation of pore water pressure in landslide takes a long time after reservoir water level drawdown. High pore water pressure in the landslide reduces the effective strength of the soil. Water level drawdown (about 30 m) releases the load on the slope toe. Under the driving force from the weight of upper slope and seepage force, the displacement of the Shuping landslide shows obvious speedup after water level drawdown in reservoir. However, after the water level rise in the reservoir, displacement of the Shuping landslide slowed down. Therefore, during mitigation and prevention of the Shuping landslide, more attentions should be focused on the drainage of groundwater to quickly reduce pore water pressure after water level drawdown.

Conclusions

In order to investigate the mechanism of landslide movement under water level drawdown in a reservoir, series of slope model tests were conducted to simulate the response of water level variation on the slopes under different soil permeability. Based on the results of the experiments, conclusions can be summarized as follows:

1. Model test result conforms with the field monitoring result of the Shuping landslide in the Three Gorges Reservoir, China. Landslide movements accelerate during the periods of water level drawdown in reservoir.
2. The rate of water level drawdown and permeability of soil should be jointly considered to identify the generation and dissipation of pore water pressure in the slope. Normally, the permeability controls the dissipation time of pore water pressure under water level drawdown. However, if the permeability is high enough, the effect of the permeability change on the dissipation time of pore water pressure will not be obvious.
3. During mitigation and prevention of landslides with low permeability in reservoirs, more attentions should be focused on the drainage of groundwater to reduce pore water pressure after water level drawdown quickly.

References

- Ding X, Fu J, Zhang Q (2004) Stability analysis of landslide in the south end of Fengjie highway bridge with fluctuation of water level of Three Gorges Reservoir. *Chin J Rock Mech Eng* 23 (17):2913–2919
- Du B (2006) Tanyanguang landslide of Zhexi reservoir – the first large landslide induced by reservoir storage in China. In: *Symposium of the second conference of Chinese geotechnical and engineering*, vol 1

- Huang B, Chen X, Pen X, Zhang Y (2007) Deformation characteristic analysis of representative landslides in Xiangxi River valley in the Three Gorges Reservoir area. *Hydrogeol Eng Geol* 4:10–12, 30
- Huang B, Yin Y, Liu G, Wang S, Chen X, Huo Z (2012) Analysis of waves generated by Gongjiafang landslide in Wu Gorge, three Gorges reservoir, on November 23, 2008. *Landslides* 9(3):395–405
- Müller L (1964) The rock slide in the Vaiont valley. *Felsmechanik und Ingenieurgeologie (Rock Mech Eng Geol)* 2(3/4):148–212
- Schuster RL (1979) Reservoir-induced landslides. *Bull Int Assoc Eng Geol* 20(1):8–15
- Terzaghi K, Peck RB, Mesri G (1996) *Soil mechanics in engineering practice*, 3rd edn. Wiley, New York
- Wang F, Zhang Y, Huo Z, Matsumoto T, Huang B (2004) The July 14, 2003 Qianjiangping landslide, Three Gorges Reservoir, China. *Landslides* 1(2):157–162
- Wang F, Zhang Y, Wang G, Peng X, Huo Z, Jin W, Zhu C (2007) Deformation features of Shuping landslide caused by water level changes in Three Gorges Reservoir area, China. *Chin J Rock Mech Eng* 26(3):509–517
- Wang F, Zhang Y, Huo Z, Peng X, Araiba K, Wang G (2008) Movement of the Shuping landslide in the first four years after the initial impoundment of the Three Gorges Dam Reservoir, China. *Landslides* 5(3):321–330
- Wang F, Yin Y, Huo Z, Zhang Y, Wang G, Ding R (2013) Slope deformation caused by water-level variation in the Three Gorges Reservoir, China. In: Sassa K, Rouhban B, Sálvano B, McSaveney M, Bin H (eds) *Landslides: global risk preparedness*. Springer, Berlin, 370p. ISBN 10:364222086X

Landslide Technology and Engineering in Support of Landslide Science

Kyoji Sassa

The World Landslide Forum (WLF) is the triennial conference of the International Consortium on Landslides (ICL) and the International Programme on Landslides (IPL). The IPL is a programme of the International Consortium on Landslides, managed by ICL and its supporting organizations: UNESCO, WMO, FAO, UNISDR, UNU, ICSU, WFEO and IUGS. IPL and WLF contribute to the United Nations International Strategy for Disaster Reduction.

The World Landslide Forum provides an information and academic-exchange platform for landslide researchers and practitioners. It creates a triennial opportunity to promote worldwide cooperation and share new theories, technologies and methods in the fields of landslide survey/investigation, monitoring, early warning, prevention, and emergency management. The forum's purpose is to present achievements of landslide-risk reduction in promoting the sustainable development of society.

Advancements in landslide science and disaster-risk reduction are supported by developments in landslide technology and engineering. Here we invited ICL supporters who support the publication of the international full-color journal "Landslides: Journal of the International Consortium on Landslides", the companies advertising in the seven volumes of "Landslide Science and Practice: Proceedings of the Second World Landslide Forum 2011" and the companies exhibiting at the Third World Landslide Forum 2014 to introduce their landslide technology and engineering. Six companies applied to exhibit in this book: their names, addresses, contact information and a brief introduction are given below (in the order of receipt of application):

1. MARUI & Co. Ltd.

1-9-17 Goryo, Daito City, Osaka 574-0064, Japan
URL: <http://marui-group.co.jp/en/index.html>

Contact: hp-mail@marui-group.co.jp

MARUI & Co. Ltd is the leading manufacturing and sales company in Japan since 1920 of material testing machines for soil, rock, concrete, cement and asphalt. Marui engineers built and assisted in development of the series of stress and speed control ring-shear apparatus by DPRI and ICL to study landslides since 1982.

2. OSASI Technos, Inc.

65-3 Hongu-cho, Kochi City, Kochi 780-0945, Japan

URL: <http://www.osasi.co.jp/en/>

Contact: info-tokyo@osasi.co.jp

OSASI Technos, Inc. develops and markets the slope-disaster monitoring system called OSASI Network System (OSNET). The monitoring devices use a built-in lithium battery and operate without external electricity supply in mountainous areas. The system enables a network of up to 64 units with up to 1 km distance between units. OSNET is suitable for quickly establishing monitoring systems on landslides in emergencies.

3. Okuyama Boring Co., Ltd.

10-39 Shimei-cho, Yokote City, Akita 013-0046, Japan

URL: <http://www.okuyama.co.jp/>

Contact: info@okuyama.co.jp

The Okuyama Boring Company Ltd specializes in landslide investigation, analysis of landslide mechanisms, and design of landslide remedial measures. The company uses its own software to analyze the initiation and motion of landslides, including the tsunami generated by landslides into reservoirs.

4. Japan Conservation Engineers & Co., Ltd.

3-18-5 Toranomon, Minato-ku, Tokyo 105-0001, Japan

URL: <http://www.jce.co.jp>

Contact: hasegawa@jce.co.jp

Japan Conservation Engineers & Co, Ltd develops landslide-simulation software and shear-testing apparatus, including slip-surface direct-shear apparatus and ring-shear apparatus to measure the shear strength mobilized on the sliding surface of landslides. Japan Conservation Engineers is a consulting company for

K. Sassa (✉)

International Consortium on Landslides, Kyoto, Japan
e-mail: sassa@iclhq.org

landslide investigation, reliable monitoring, data analysis and the design of landslide-risk reduction works.

5. KOKUSAI KOGYO Co., Ltd.

2 Rokuban-cho, Chiyoda-ku, Tokyo 102-0085, Japan

URL: <http://www.kk-grp.jp/english/>

Contact: overseas@kk-grp.jp

Kokusai Kogyo has undertaken aerial surveys, infrastructure development projects for road and harbor facilities, and landslide-disaster prevention and mitigation works since its foundation in 1947. The company has recently developed remote-sensing technology using the laser profiler, satellite synthetic aperture radar, and a new monitoring system called <Shamen-net> integrating GPS and other monitoring devices, all of which contribute to landslide-disaster prevention and mitigation.

6. C.S.G. S.r.l. Centro Servizi di Geingegneria

Via Cazzolini, 15A - 15010 Ricaldone (AL), Italy

URL: <http://www.csgrl.eu>

Contact: csg@csgrl.eu

C.S.G. S.r.l. Centro Servizi di Geingegneria is a leader in the production of multi-parametric in-place borehole monitoring columns called DMS (patents). DMS columns have been installed in a number of important international sites, where continuous monitoring for Early Warning,

both in shallow landslides and deep-seated rockslides requires instrumentation with high-precision, accuracy and reliability. CSG pursues a high quality standard through rigorous laboratory calibration tests, and long-term stability and alignment tests within temperature-controlled vertical and inclined boreholes in field.

Full-color presentations from these six exhibitors focusing on their landslide technology are shown in the following pages.

The progress of landslide science is supported by advances in landslide technology. The success of landslide risk-reduction measures needs effective landslide engineering. The International Consortium on Landslides seeks expressions of interest in contributing to “Landslide Technology and Engineering to Support Landslide Science” at the Fourth World Landslide Forum to be held on May 29–June 2, 2017, in Ljubljana, Slovenia. We may call for presentations on landslide technology and engineering in the proceedings, as well as through exhibitions at the site. Those interested in this initiative are requested to contact the Secretariat of the International Consortium on Landslides <secretariat@iclhq.org>. We will send invitations to interested applicants when further details become available.

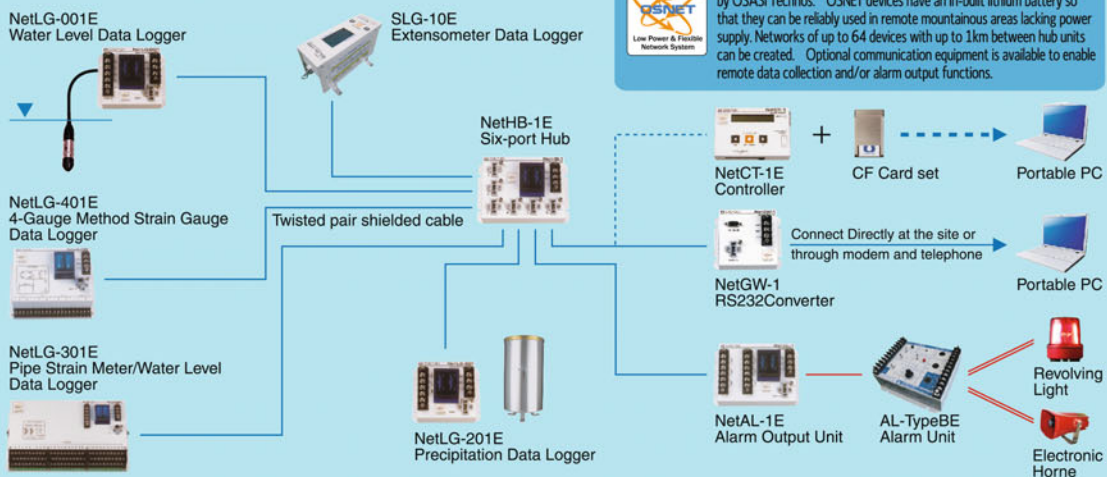


Web site : <http://www.marui-group.co.jp/en/>
E-mail : hp-mail@marui-group.co.jp
Address : 1-9-17 Goryo, Daito City, Osaka Prefecture,
574-0064, Japan
Phone : 81-72-869-3201 Fax : 81-72-869-3205

Slope Disaster Monitoring System

OSASI NETWORK System

EXAMPLE SETUP 2



OSNET is a network solution for disaster prevention monitoring developed by OSASI Technos. OSNET devices have an in-built lithium battery so that they can be reliably used in remote mountainous areas lacking power supply. Networks of up to 64 devices with up to 1km between hub units can be created. Optional communication equipment is available to enable remote data collection and/or alarm output functions.



We pass on voices of the earth.
OSASI Technos, Inc.



Corporate Headquarters / 65-3 Hongu-cho, Kochi-shi, Kochi 780-0945, JAPAN

Tel: +81-88-850-0535 Fax: +81-88-850-0530

Tokyo Headquarters / Sumitomoseimei Building 4F 1-10-2 nishishinbashi, minato-ku, Tokyo 105-0003, JAPAN

Tel: +81-3-5510-1391 Fax: +81-3-5510-1393

Kyushu Branch Office / Iwaho Building Ekiminami 4F 4-1-17 Hkaka Eki Minami, Hakata-ku, Fukuokashi, Fukuoka 812-0016, JAPAN

Tel: +81-92-434-9200 Fax: +81-92-434-9201

* Please note that specifications for the equipment are subject to change without notice.

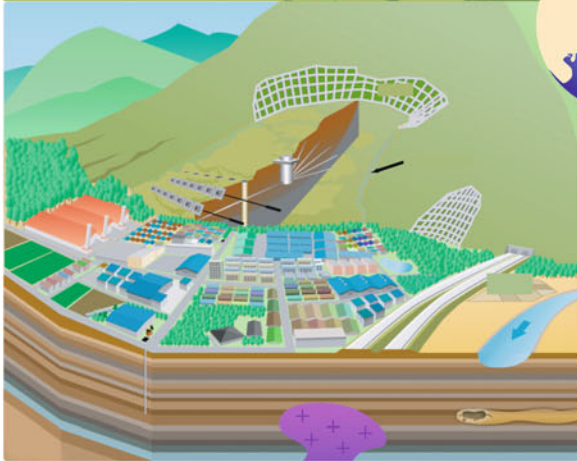
* For further detailed specifications, please visit our homepage at <http://www.osasi.co.jp/en/>

We keep a clean nature for the future.

Okuyama Boring Co., Ltd.

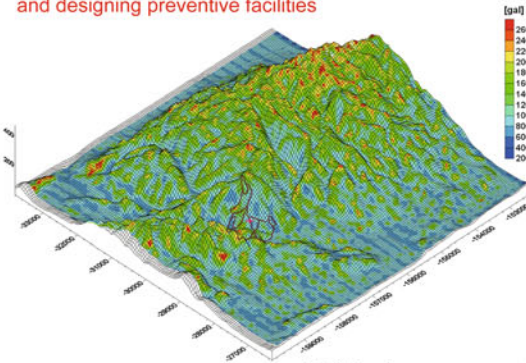


<http://www.okuyama.co.jp/>
 E-mail info@okuyama.co.jp



Landslide countermeasure works

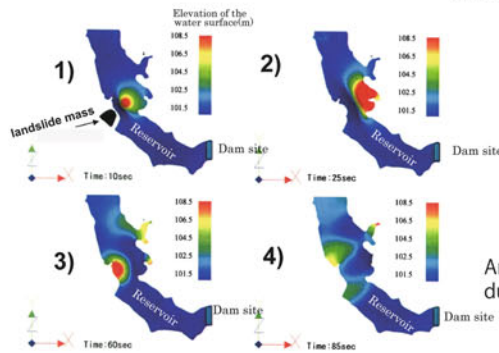
Landslide research, analysis and designing preventive facilities



3D Seismic response analysis



Ground anchor



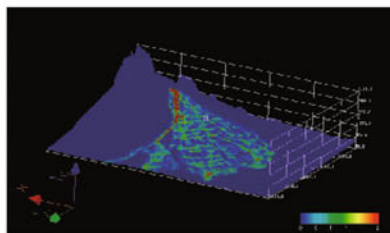
Analysis of water waves due to landslide



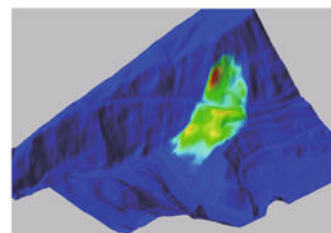
Water catchment well



Water catchment boring

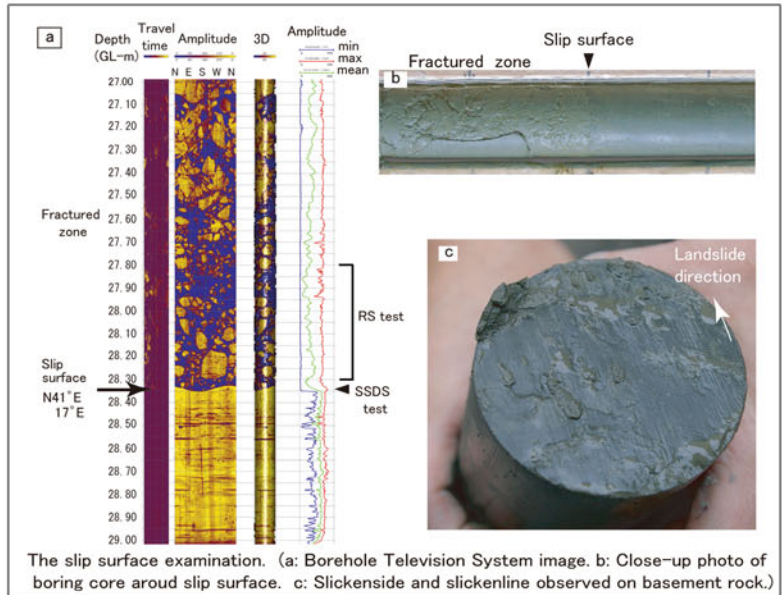


Flooding analysis in area with steep slope



Analysis of grain-fluid flow due to landslide

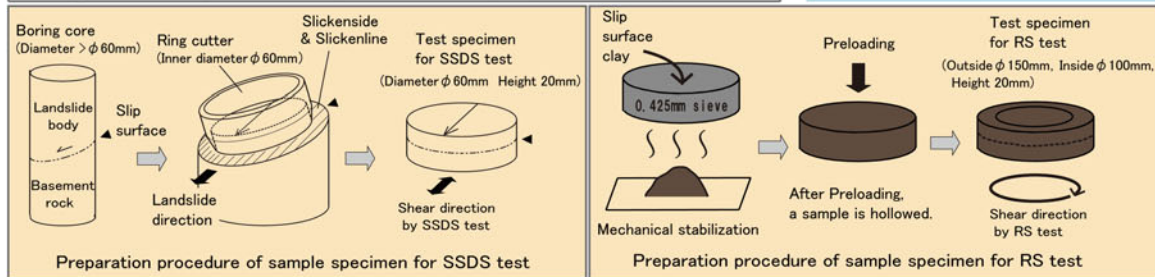
As for Landslide survey, we have various technologies for the slip surface examination.
 Slip Surface Direct Shear (SSDS) apparatus we have developed is the repeating one surface shearing testing apparatus which aims to measure the shear strength.
 This apparatus can exactly examine to the shear strength of the slip surface that will be demonstrated in the site.
 Ring Shear (RS) test is large displacement test which can obtain the fully softened strength and residual strength of the cohesive soil which constitutes a slip surface.



SSDS apparatus



RS apparatus



JAPAN CONSERVATION ENGINEERS&CO., LTD

URL:<http://www.jce.co.jp/>

HEAD OFFICE
 3-18-5, TORANOMON, MINATO-KU,
 TOKYO 105-0001, JAPAN
 TEL:+81.3.3436.3673
 FAX:+81.3.3432.3787

LABORATORY
 34-12, SHIMIZUMAE, MINAMIYANOME,
 FUKUSHIMA-SHI, FUKUSHIMA
 960-0112, JAPAN
 TEL:+81.24.555.0255
 FAX:+81.24.557.3966



Contribute to make Global society through the various technologies for the soil, water and nature.



Building sustainable cities of the future
Green communities

Geospatial advantage green communities

We have geospatial technology to create ever more accurate maps, essential for developing social infrastructure and nation building—the backbone of economic growth. We are providing total solutions that merge our geospatial and urban planning technologies with renewable energy sources and to create safer, disaster-resistant communities of the future.

Environment/energy



*Disaster prevention/
risk reduction*



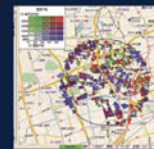
Supporting government



Social infrastructure



Business Solutions



Our Major Fields for international development



Disaster Prevention



Solid Waste Management



Water resource development



Survey and Mapping



KOKUSAI KOGYO CO.,LTD.

2 Rokubancho, Chiyoda-ku, Tokyo, Japan 102-0085

URL <http://www.kk-grp.jp/english> E-mail info_overseas@kk-grp.jp

ARE YOU DEALING WITH LANDSLIDES AND STABILITY PROBLEMS? **YES** **NO**

DO YOU NEED AN EARLY WARNING SYSTEM SAFE AND RELIABLE? **YES** **NO**

WOULD YOU LIKE TO KNOW THE DISPLACEMENTS EXTENT AND ITS DEPTH? **YES** **NO**

THE IDEA TO MONITOR IN CONTINUOUS PHENOMENA CONFORTABLY SIT IN YOUR OFFICE IS A DREAM? **YES** **NO**

DO YOU HAVE TO CROSS-CHECK THE DISPLACEMENTS, THE WATER TABLE, THE ACCELERATION, THE PORE PRESSURE DATA AND OTHER GEOTECHNICAL PARAMETERS? **YES** **NO**

DO YOU WISH A SOFTWARE THAT MANAGES ALL THE HARD JOB AND HELPS YOU? **YES** **NO**

The multiparametric column allows the measurement of the main geotechnical and mechanical parameters of soil and 2/3D structures, besides water table, temperature and acceleration in the same borehole. The column has digital sensors that transfer data to the control unit, placed on surface, which transmits data in real time to the final user and to the monitoring room.



Via Cazzulini, 15/A
 15010 RICALDONE (AL) ITALY
 Tel. +39 0144 74277
 Fax +39 0144 745914
 www.csgrl.eu
 csg@csgrl.eu

GEOTECHNICAL MULTIPARAMETRIC MONITORING COLUMNS

DMS column is like a "spiral cord", to be installed in place inside the borehole, composed by a sequence of hard tubular modules connected each other by special flexible joints having 2 or 3 freedom degrees that make possible to copy any deformation. These joints allow each module to perfectly fit the drilling hole and soil movements, maintaining the azimuthal direction.



**So...
 What you need is DMS**

- Continuous and multi-parametric data in the same borehole
- Fast and easy start up of the monitoring system
- Modular and retrievable system
- Advanced selection procedures
- High mechanical quality
- Advanced data processing software and graphical elaboration
- System developed for deep seated landslides and early warning
- Technical support and remote diagnostic
- After sale support and hire service
- Results and cost reduction

DMS



International Consortium on Landslides

An international non-government and non-profit scientific organization
promoting landslide research and capacity building for the benefit of society and the environment

President: Paolo Canuti (Prof. Emeritus, University of Firenze, Italy)

**Vice Presidents: Kaoru Takara (Kyoto University, Japan)/Yueping Yin (China Geological Survey)/
Claudio Margottini (National Institute for the Protection and Environmental Research (ISPRA), Italy)/
Irasema Alcantara-Ayara, (UNAM), Mexico**

Executive Director: Kyoji Sassa (Prof. Emeritus, Kyoto University, Japan)

ICL Supporting Organizations:

The United Nations Educational, Scientific and Cultural Organization (UNESCO) / The World Meteorological Organization (WMO) / The Food and Agriculture Organization of the United Nations (FAO) / The United Nations International Strategy for Disaster Reduction Secretariat (UNISDR) / The United Nations University (UNU) / International Council for Science (ICSU) / World Federation of Engineering Organizations (WFEO) / International Union of Geological Sciences (IUGS) / Government of Japan

ICL Members:

Albania Geological Survey / Federal University of Parana, CENACID-UPFR, Brazil/ Geological Survey of Canada / Chinese Academy of Sciences, Institute of Mountain Hazards and Environment / Northeast Forestry University, China / Bureau of Land and Resources of Xi'an, China / China Geological Survey / Nanjing Institute of Geography and Limnology, Chinese Academy of Sciences / Universidad Nacional de Columbia, Columbia / City of Zagreb, Emergency Management Office, Croatia /Croatian Landslide Group (Faculty of Civil Engineering, University of Rijeka and Faculty of Mining, Geology and Petroleum Engineering, University of Zagreb) / Charles University, Faculty of Science, Czech Republic / Institute of Rock Structure and Mechanics, Department of Engineering Geology, Czech Republic / Joint Research Centre (JRC), European Commission /Technische Universität Darmstadt, Institute and Laboratory of Geotechnics, Germany / Universidad Politecnica de Ingenieria, UPI, Honduras / National Institute of Disaster Management, India / University of Gadjah Mada, Indonesia / Agricultural Research and Education organization (AREO), Iran / Building & Housing Research Center, Iran / International Institute of Earthquake Engineering and Seismology (IIEES), Iran / University of Firenze, Earth Sciences Department, Italy / Italian Institute for Environmental Protection and Research (ISPRA) - Dept. Geological Survey, Italy / Forestry and Forest Product Research Institute, Japan / Japan Landslide Society / Kyoto University, Disaster Prevention Research Institute, Japan / Niigata University, Research Institute for Natural Hazards and Disaster Recovery, Japan / University of Tokyo (Institute of Industrial Science and Department of Civil Engineering, Geotechnical Engineering Group), Japan / Korea Forest Research Institute, Korea / Korea Infrastructure Safety & Technology Corporation, Korea /Korea Institute of Geoscience and Mineral Resources (KIGAM) /Korean Society of Forest Engineering / Mara University of Technology, Malaysia / Slope Engineering Branch, Public Works Department of Malaysia / Institute of Geography, National Autonomous University of Mexico (UNAM) / International Centre for Integrated Mountain Development (ICIMOD), Nepal / University of Nigeria, Department of Geology, Nigeria / International Centre for Geohazards (ICG) in Oslo, Norway /Grudec Ayar, Peru/ Moscow State University, Department of Engineering and Ecological Geology, Russia / Russian Academy of Sciences, Sergeev Institute of Environmental Geoscience (IEG RAS) / JSC "Hydroproject Institute", Russia / University of Belgrade, Faculty of Mining and Geology, Serbia / Comenius University, Faculty of Natural Sciences, Department of Engineering Geology, Slovakia / University of Ljubljana, Faculty of Civil and Geodetic Engineering (UL FGG), Slovenia / Geological Survey of Slovenia / Engineering Geoscience Unit, Council for Geoscience, South Africa / Central Engineering Consultancy Bureau (CECB), Sri Lanka / National Building Research National Organization, Sri Lanka / Taiwan University, Department of Civil Engineering, Chinese Taipei / Asian Disaster Preparedness Center, Thailand / Ministry of Agriculture and Cooperative, Land Development Department, Thailand / Institute of Telecommunication and Global Information Space, Ukraine / Institute Hydroingeo, State Committee of Geology of Uzbekistan / Institute of Transport Science and Technology, Vietnam

ICL Supporters:

Kawasaki Geological Engineering Co., Ltd., Tokyo, Japan / Marui & Co., Ltd., Osaka, Japan / Okuyama Boring Co., Ltd., Yokote, Japan / GODAI Development Corp., Kanazawa, Japan / Japan Conservation Engineers & Co., Ltd, Tokyo / Kokusai Kogyo Co., Ltd., Tokyo, Japan / Nippon Koei Co., Ltd., Tokyo, Japan / Ohta Geo-Research Co., Ltd., Nishinomiya, Japan / OSASI Technos Inc., Kochi, Japan / OYO Corporation, Tokyo, Japan / Sabo Technical Center, Tokyo, Japan / Sakata Denki Co., Ltd., Tokyo, Japan

Contact:

International Consortium on Landslides, 138-1 Tanaka Asukai-cho, Sakyo-ku, Kyoto 606-8226, Japan

Web: <http://icl.iplhq.org/>, E-mail: secretariat@iclhq.org

Tel: +81-774-38-4834, +81-75-723-0640, Fax: +81-774-38-4019, +81-75-950-0910